Proceedings of the Indian Academy of Sciences

(Chemical Sciences)

Volume 97, 1986

CONTENTS

norganic and Analytical

norganic complexation of nickel and cobalt in natural waters
Anil Kumar 1–7

A ruthenium(II) complex of *bis*(1-pyrazolyl) borate
M M Taqui Khan, K Veera Reddy, R C Bhardwaj and H C Bajaj 9–11

ome lanthanide metal complexes of *n*-isonicotinamidosalicylamidine
T R Rao, I A Khan and R C Aggarwal 13–18

Mixed ligand complexes of *bis*(acetylacetanato) nickel(II) and cobalt(II) with N and N,N′-substituted thioureas
G L Tembe, S B Kokatnur and A S R Murty 19–24

Structural studies of amino acid complexes—I EXAFS study of glutamic acid complex of copper *C K Bhaskare and S Y Kulkarni* 25–32

Preparation, characterization and thermal analysis of rare earth and uranyl hydrazinecarboxylate derivatives
G V Mahesh, P Ravindranathan and K C Patil 117–123

$RuCl_2(PPh_3)_3$ catalysed oxidation of secondary alcohols with N-methylmorpholine N-oxide *K Vijayasri, J Rajaram and J C Kuriacose* 125–132

Effect of dielectric constant of various mixed aqueous solvent on the proton-ligand and metal-ligand formation constants of N-methylisatin β-amidinohydrazone *K Sarkar and B S Garg* 133–139

Synthesis and spectral studies of tin(IV) complexes with Schiff bases derived from sulpha drugs *Anil Varshney and J P Tandon* 141–146

Water insoluble polyacrylamide XII: Polychelates based on poly (N-methacryloyl-*m*-amino benzoic acid)
Kishore Patel, Trishar Desai and Bhikhu Suthar 147–152

2-Hydroxy-1-naphthaldehyde guanylhydrazone as analytical reagent for

Synthesis, identification and analytical properties of the 2-pyrilidenimino benzohydroxamic acid
F Salinas, M Jiménez-Arrabal and I Durán Merás 159

Study of ternary complexes of substituted catechols and catecholamines
P K Bhattacharya, N A Emanuel and N D Kulkarni 529

Exchange reactions of copper complexes with amines
M N Patel and K B Patel 535

Influence of electrostatic effect on the stability of mixed-ligand complexes: Uranyl-complexone-phenol/phenolic acid ternary systems
Anushree Samanta, S N Limaye and M C Saxena 543

Instrumentation

Design and fabrication of an ultraviolet photoelectron spectrometer for the study of free molecules *V Jayaram and M S Hegde* 617

Organic

^{13}C NMR substituent induced chemical shifts in the side-chain carbons of α,β-unsaturated sulphones
C Sreenivasan, P K Ganesan, A Shanmugasundaram and N Arumugam 3

Photo-Fries reaction of 1-naphthyl cinnamate
T Jayachandran, T Manimaran and V T Ramakrishnan 4

Reaction of ethyl bromoacetate with substituted naphthoate ions
K Rajasekaran and C Gnanasekaran 4

Kinetics of the reaction of alkyl bromides with nucleophiles containing nitrogen atoms *T Janardhan Rao, G Punnaiah and E V Sundaram* 5

Semecarpuflavanone—a new biflavanone from *Semecarpus anacardium* Linn. *S S N Murthy* 6

Solid phase synthesis of the signal sequence of *E. coli* alkaline phosphatase
G Laxma Reddy and R Nagaraj 7

Abietane diterpene quinones and a new diterpene epoxide from *Salvia moorcraftiana* *Beena Bakshi, N B Mulchandani and J Shankar* 167

Molecular and crystal structure of 1-hydroxy-2-methyl-11-methylene-tricyclo $(5.3.1.0)^{2,7}$-undecan-5-one, $C_{13}O_2H_{18}$
S Krishnaswamy and Vasantha Pattabhi 547–553

Mechanism of the oxidation of alkyl aryl and diphenyl sulphoxides by peroxomonosulphate *R Suthakaran, P Subramanian and C Srinivasan* 555–563

Physical and Theoretical

Enthalpies of complex formation of dibutyl and tributyl amines with isomeric butanols *Shirish D Pradhan and Gopal Pathak* 77–81

Electronic and vibrational spectra of 2,4,6-trichloro- and 6-chloro-2,4-dimethoxypyrimidine *S L Srivastava, M Prasad and Ranjeet Singh* 83–90

QSAR studies on estrogen receptor binding affinity of 2-phenylindoles using first-order valence molecular connectivity *P Singh* 91–95

Infrared and Raman spectra of 2,4-dimethylaniline
A R Shukla, C M Pathak, N G Dongre, B P Asthana and Jacob Shamir 97–115

ESR Bonding parameter studies of single and mixed ligand complexes of copper(II)
Y Anjaneyulu, N V S Rao, R Prabhakara Rao and V G K M Pisipati 177–184

Reaction of 2-hydrazino-4-methyl-6-substituted quinones with ethylacetoacetate: A structural reinvestigation. *Radhe K Vaid and Shiv P Singh* 185–189

Vibrational-rotational $(v\text{-}j)$ levels of HD^+ evaluated in the adiabatic approximation for the electronic ground state $(1s\sigma_g)$
R S Bhattacharjee, R P Saxena, P K Srivastava and K V Sane 191–207

Electron impact ionization of amines using crossed electron-molecular beams *S V Krishna Kumar and D Mathur* 565–572

Reaction of the phosphate radical with amines—A flash photolysis study
P Subramanian, V Ramakrishnan, J Rajaram and J C Kuriacose 573–580

Underpotential deposition studies of copper on glassy carbon
S Jaya, T Prasada Rao and G Prabhakara Rao 581–586

Stereochemistry and structural phase transition of Cu(II) complexes containing orthophosphate ions and pyridine/picoline
M S Sastry and M D Sastry 587–592

SCF Perturbation calculations on metalloporphyrins
K K Bhattacharjee, J Subramanian, D P Santry and J H Fuhrhop 601–606

Exchange studies of sulphosalicylic acid in amberlite IRA 401 Cl anion exchange resin *Nooman A Khalaf and G S Natarajan* 607–615

Special issue dedicated to Professor K S G Doss on his eightieth birthday

Solvation model for inner-sphere nuclear reorganization in the photo-ionization of univalent anions in solution
Paul Delahay and Andrew Dziedzic 221–231

Proton and hydrogen transfer reactions in solution *P P Schmidt* 233–265

New theories for the electric double layer at a metal/electrolyte solution interface *Ezequiel Levia and Wolfgang Schmickler* 267–296

Calculation of the density profile of a system of hard spheres near a hard wall using the Henderson–Plischke and related approximations
Douglas Henderson and Michael Plischke 297–305

Spectral functions and Green's functions: A critique
A K Mishra and S K Rangarajan 307–331

The adsorption of D-(+)-xylose at the mercury-water interface
Roger Parsons and Robert Peat 333–347

Polymer films on electrodes. 21. Electrochemical behaviour of tetramethyl-tetraselenafulvalene incorporated into a Nafion-coated electrode
Roger D Moulton, Allen J Bard and Jack M Williams 349–357

High performance electrode materials for the hydrogen evolution reaction from alkaline media *B V Tilak, A C Ramamurthy and B E Conway* 359–393

Electrochemical reduction of 2-nitrobenzidine in methanol-water mixtures
S Aravamuthan, M S Sashidar, C Kalidas and C S Venkatachalam 395–401

Electrochemical reduction of some benzophenones in molten acetamide at 85°C *R Saraswathi and R Narayan* 403–416

Cyclic voltametric studies of dioxygen-bridged dinuclear cobalt(II) complexes *S Ilangovan and P Natarajan* 417–430

The translocation of cobalt dicarbamide anions across a lipid bilayer membrane: the effect of solution resistance

Use of programmed time-potential inputs in anodic stripping voltammetry with *in situ* sodium amalgamation
G Prabhakara Rao and A Varadharaj 449–455

In situ resistance measurement of a conducting polymer electrode
M Gholamian, T N Suresh Kumar and A Q Contractor 457–464

Applications of exponential relaxation methods for corrosion studies and corrosion rate measurement
V Lakshminarayanan and S R Rajagopalan 465–477

Electrobioluminescence—a novel method for understanding bioluminescent mechanisms
K S V Santhanam 479–494

Corrosion of austenite stainless steel in aqueous environments
J B Gnanamoorthy 495–511

Fuel cells: problems and prospects
A K Shukla, K V Ramesh and A M Kannan 513–528

Rapid Communications

Solution of difficult crystal structures: New, simple, economic and time saving approaches
S S Tavale and T N Guru Row 209–211

Reactions of halogens with 2,2′-azinobis-(3-ethylbenzothiazole-6-sulphonate) stopped-flow kinetics of formation of radical cations and dications
P Maruthamuthu, L Venkatasubramanian and P Dharmalingam 213–218

Magnetic properties of $Ca_2Fe_{2-x}Mn_xO_5^+$
A K Ganguli and J Gopalakrishnan 627–630

High T_c superconductivity in oxides derived from $La_{1.8}Sr_{0.2}CuO_4$
P Ganguly and C N R Rao 631–633

Subject Index 635–643

Author Index 643–647

Inorganic complexation of nickel and cobalt in natural waters

ANIL KUMAR

Chemical Engineering Division, National Chemical Laboratory, Pune 411 008, India
Present address: Laboratory of Professor Franck, Institute of Physical Chemistry
Electrochemistry, University of Karlsruhe, D 7500 Karlsruhe, West Germany

MS received 25 February 1985; revised 2 September 1985

Abstract. The distribution of nickel and cobalt species has been computed, based o
pH-dependent model of Zirino and Yamamoto. The media used in the pH range of 7 to
natural waters like fresh water, sea water and a mixture of them at different compositio
25°C temperature and 1 atm pressure. In fresh water, both nickel and cobalt dominate a
cations at lower pH, and as carbonato complexes at higher pH. In sea water, chloro comp
are significant. In mixtures of the two kinds of water, as might be found in a totally r
estuary, chloro complexes are important, varying slowly with pH. Sea water plays an impo
role in complexation. The present results are in excellent agreement with experimental
obtained by the resin exchange method.

Keywords. Nickel; cobalt; species pattern; pH; complexation; natural waters.

1. Introduction

Speciation calculations are of great significance in evaluating the fate of trace meta
biogeochemical cycles. In recent years, many theoretical and experimental studies
appeared on the equilibrium speciation of major and electrochemically active meta
natural waters. However, a few studies (Mantoura *et al* 1978; Turner *et al* 1981
reported on the behaviour of trace metals in fresh and sea water media.

In this paper, we report the results of computations of per cent species of nickel
cobalt in natural waters like fresh water and sea water at 25°C temperature and 1
pressure, using a modified pH dependent model of Zirino and Yamamoto (1972) in
pH range of 7 to 9. This may help us in understanding the nature of the var
complexes and their behaviour in natural waters. The calculations are further exter
to mixtures of different compositions of fresh and sea water for observing the cha
in the distribution of species in a completely mixed estuary.

2. Calculations

The model and appropriate mass balance equations used in the work are summar
elsewhere (Zirino and Yamamoto 1972; Long and Angino 1977). Thermodyna
equilibrium is assumed to exist and the pH range is 7 to 9 with an increment of 0·2. S
the concentrations of nickel and cobalt are very low, polynuclear and org
complexes are completely avoided (Helgeson 1969; Long and Angino 1977). Hu
acid complexes are also avoided as their stability constants are presently unavailab
a function of pH. The speciation of major elements was calculated by the mod

Table 1. End numbers on molal scale used as input.

Component	Fresh water[a]	Sea water[b]
Sodium	0·000274	0·4752
Potassium	0·000059	0·01
Magnesium	0·000168	0·054
Calcium	0·000375	0·0104
Chloride	0·00022	0·554
Sulphate	0·000955	0·0284
Effective ionic strength	0·0021	0·661
Total alkalinity	0·000955	0·00234

[a]Livingstone 1963; [b]Berner 1971.

Table 2. Stability constants ($\log \beta$) of various species of nickel and cobalt at 25°C.

Species	$\log \beta$
Nickel	
Cl^-	$\beta_{11} = 0{\cdot}73^a$, $\beta_{12} = 0{\cdot}72^b$
SO_4^{--}	$2{\cdot}32^b$
HCO_3^-	$2{\cdot}5^d$
CO_3^{--}	$5{\cdot}37^c$
OH^-	$4{\cdot}16^b$
Cobalt	
Cl^-	$0{\cdot}57^c$
SO_4^{--}	$2{\cdot}36^b$
HCO_3^-	$2{\cdot}4^d$
CO_3^{--}	$4{\cdot}91^c$
OH^-	$4{\cdot}15^b$

[a]Sillen and Martell 1964; [b]Sillen and Martell 1971; [c]Turner *et al* 1981; [d]Mantoura *et al* 1978.

Garrels and Thompson (1962). The compositions of fresh water and sea water used are listed in table 1. The ligands used for the complexation are OH^-, HCO_3^-, Cl^-, SO_4^{2-}, CO_3^{2-} and their stability constants (Mantoura *et al* 1978; Turner *et al* 1981; Sillen and Martell 1964, 1971) are listed in table 2. Tables 1 and 2 are inputs of calculations. Stability constants were also critically examined by Turner *et al* (1981).

The activity coefficients of metals and their complexes are calculated by the Davies equation (Davies 1962) as

$$-\log \gamma_i = 0{\cdot}5\, z^2 \left[I^{1/2}/(1+I^{1/2}) - 0{\cdot}3\, I\right], \tag{1}$$

where z is the charge on the ion and I is ionic strength. The use of MacInnes convention (MacInnes 1919) in calculating γ_i was avoided as it was not applicable to ionic strengths higher than 0·1. Activity coefficients of ion pairs (Reardon and Langmuir 1976) are given by

where $B = 0{\cdot}1, 0{\cdot}3$ and $0{\cdot}5$ for 1-1, 1-2 and 2-2 ion pairs respectively and γ_{IP} is the activity coefficient of the ion pair. Activity coefficients of major ions are calculated from Robinson and Stokes (1959), using the mean salt method (Millero and Schreiber 1982). The hydration model of Bates (1978) was also attempted, which gave unrealistic $\gamma_{Mg^{2+}}$ values and hence was dropped.

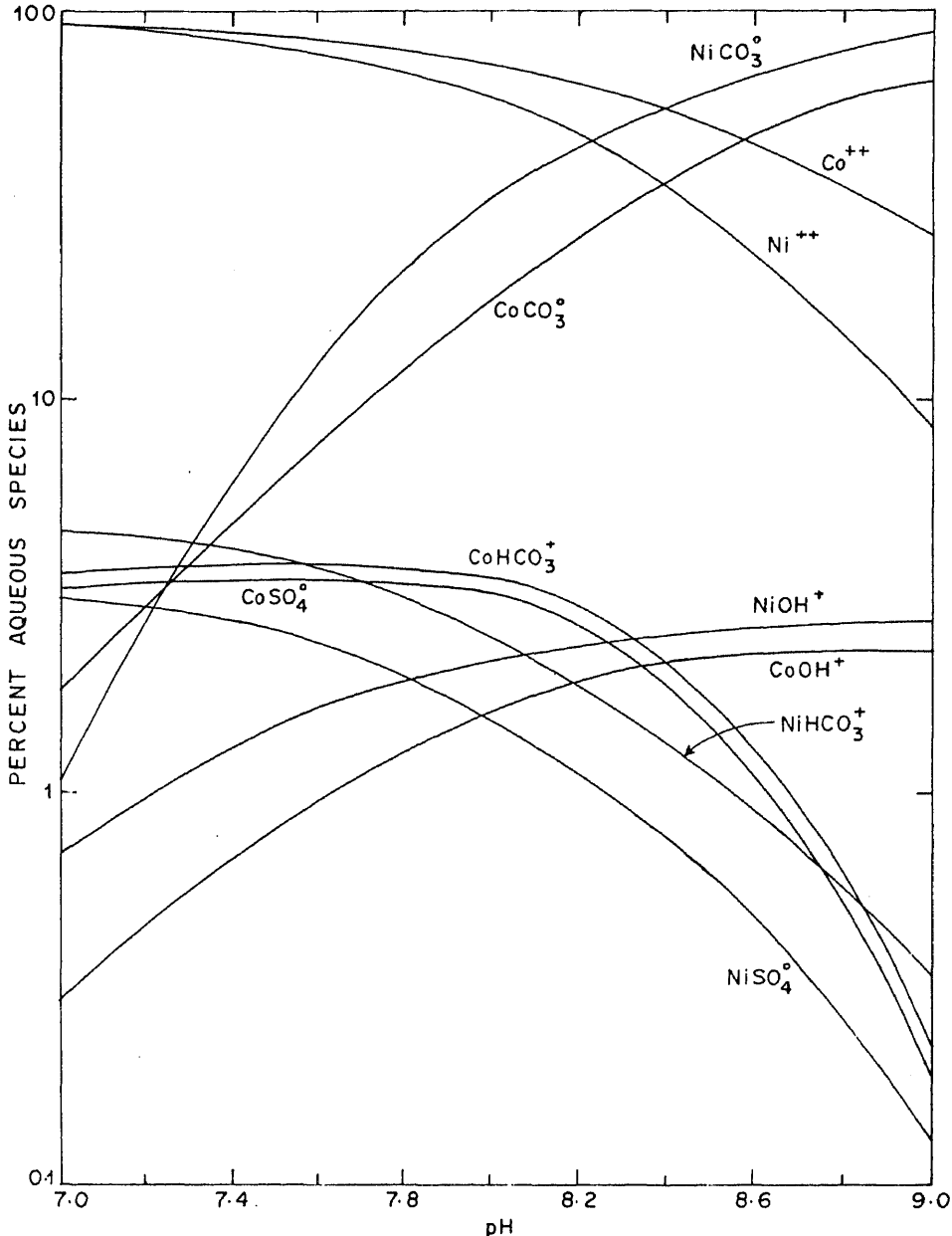

3. Results and discussion

The results obtained from computations are plotted as percent aqueous species (0·1 to 100%) on a log scale against pH. Distribution of different species of nickel and cobalt in 100% fresh water is shown in figure 1. Free Ni^{++} and Co^{++} both dominate upto pH 8·2, except that the magnitude of free Co^{++} is higher than free Ni^{++} as pH increases. Beyond pH 8·2, carbonato complexes dominate in both cases. Other complexes like sulphato, bicarbonato and hydroxy remain below 4% throughout. Table 3 shows a summary of values of percent of aqueous species of nickel and cobalt alongwith existing experimental and theoretical calculated values (Mantoura *et al* 1978; Turner 1981) for comparison.

In 100% sea water, both metals are complexed by about 50% in the forms of carbonato and chloro species. Figure 2 shows this fact, while table 3 compares our computed values at pH 8·2 of sea water. Present values at pH 8·2 for free Ni are slightly higher, otherwise the agreement is good. Unlike Turner *et al* (1981), the bicarbonato

Table 3. Chemical speciation (%) of nickel and cobalt in fresh and sea water.

Species	Fresh water pH 7	Fresh water pH 9	Sea water pH 8·2
		Nickel	
Ni^{++}	90·7	8·4 (9)[a]	36·1 (47)[a], (20)[b]
$NiCl^{+}$	—	—	27 (34)[a,c], (34)[b]
$NiCl_2^0$	—	—	5 (5·2)[b]
$NiSO_4^0$	3	0·3 (0·1)[a]	5 (4)[a,c], (4·4)[b]
$NiHCO_3^+$	4·5	0·30	6·2 (3·6)[b]
$NiCO_3^0$	1	88 (90)[a]	19 (14)[a], (45)[b]
$NiOH^+$	0·7	2·80 (2)[a]	1·7 (1)[a], (1·8)[b]
		Cobalt	
Co^{++}	90·8	28	47·4 (58)[a], (50)[b]
$CoCl^{+}$	—	—	29 (30)[a], (27)[b]
$CoSO_4^0$	3·4	0·20 (1)[a]	5 (5)[a], (5)[b]
$CoHCO_3^+$	3·7	0·2	6 (6)[b]
$CoCO_3^0$	1·8	69·3 (73)[a]	11 (6)[a], (10·5)[b]
$CoOH^+$	0·3	2·3 (7)[a,c]	1·6 (1)[a], (1·5)[b]

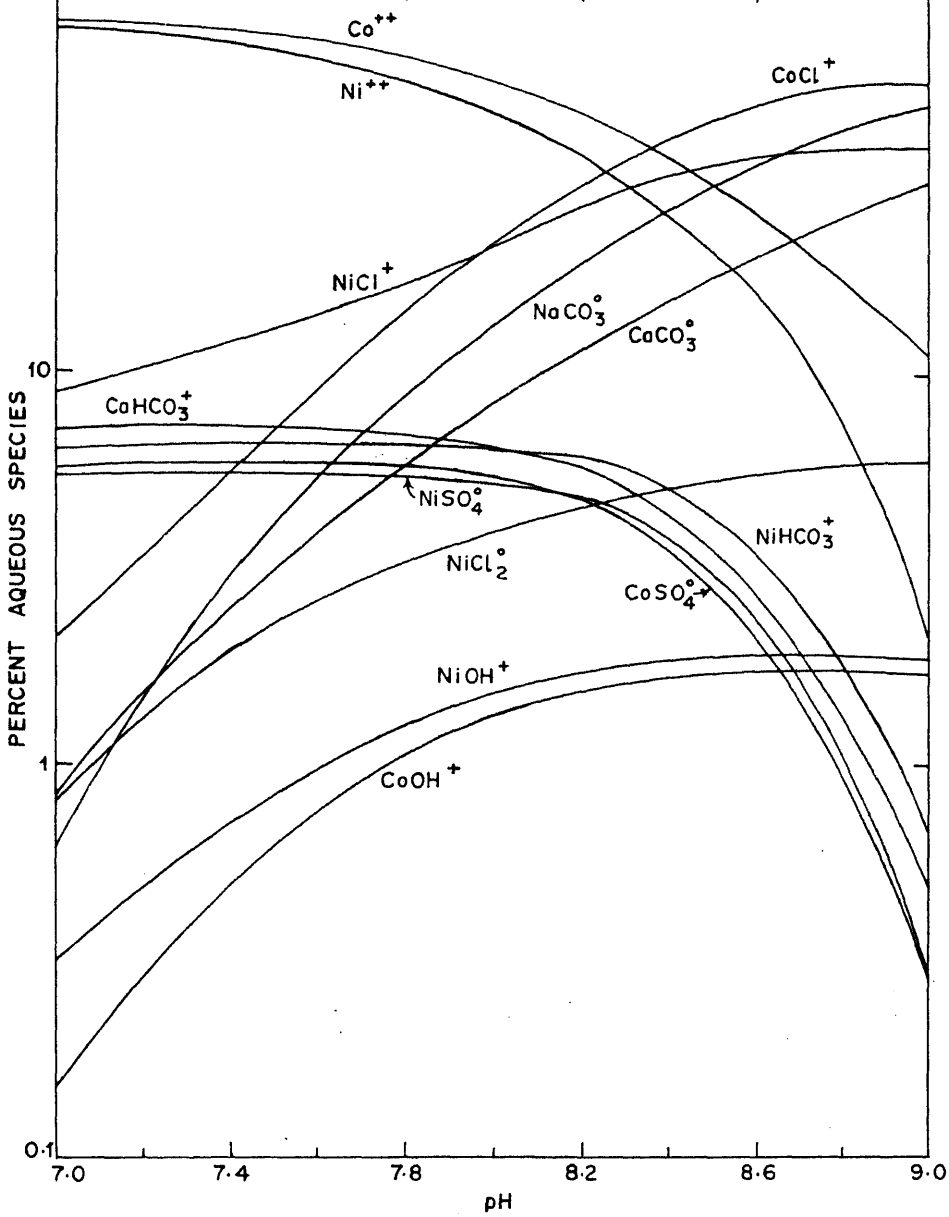

Figure 2. Inorganic complexation of nickel and cobalt in sea water.

complexes are also considered and their contribution is significant (6% at pH 8·2 in sea water).

Extensive computations based on the Long and Angino method (1977) were carried out to obtain graphic diagrams of various mixing ratios of fresh and sea water. To conserve space, only one mixing ratio of 25% sea water and 75% fresh water for both

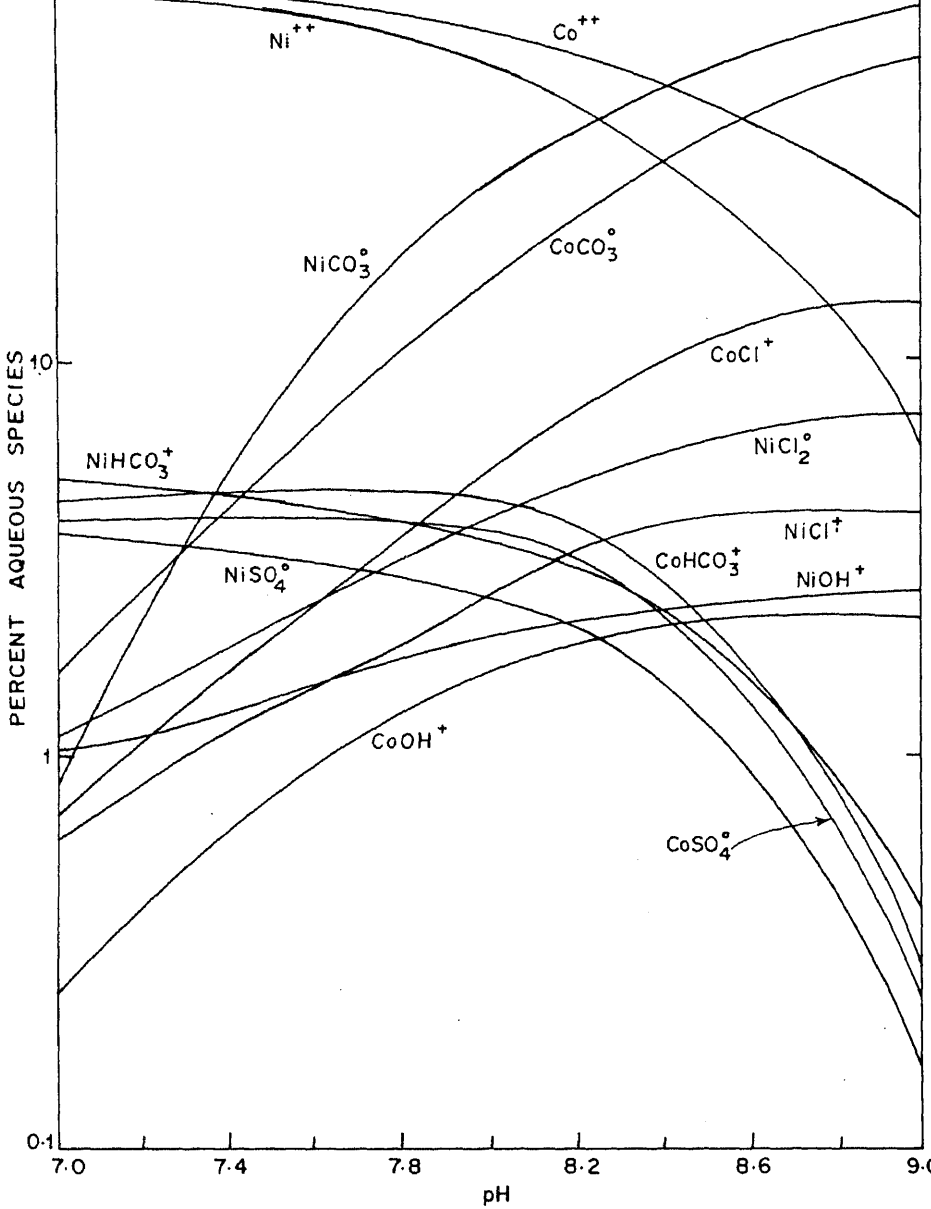

Figure 3. Inorganic complexation of nickel and cobalt in 25% sea water and 75% fresh water.

amount of sea water with fresh water, chloro complexes become significant in both the cases. This condition may be expected at nearshore environs such as deltas or estuaries. Carbonato complexes form more than 50% of the whole at higher pH ($NiCO_3^0$ 60 and $CoCO_3^0$ 50% at pH 9). Chloro complexes contribute 11 and 14% at pH 9 for nickel and cobalt respectively and show poor variation with increasing pH.

As one goes from pure fresh water to pure sea water, a higher order association of chloride complexes would be expected (as in zinc) but such a process does not occur in these metals. In the cases of very high concentrations of fresh water with low amounts of sea water, it is observed that the concentration of ligand controls the speciation pattern and a 5 to 10 per cent addition of sea water is enough for such a change. This type of behaviour may be expected by mixing solutions of high and low ionic strengths.

One important feature regarding nickel is observed on mixing a little fresh water ($\sim 10\%$) with sea water. In this solution, the $NiCl_2^0$ species is higher than $NiCl^+$ but as one progressively uses pure sea water, $NiCl^+$ dominates over $NiCl_2^0$ and thus the trend is reversed.

As a matter of fact, graphic diagrams for such theoretical computations depend on the selection of stability constants. This is the reason why our values of a few species differ from reported values. Since the values of stability constants used in this work are critically examined by Turner *et al* (1978), it is felt that results of the calculations are reliable. Until experimental results either by ESR or resin exchange techniques are made available, these values could be used. During the computations, various expressions (Mantoura *et al* 1978) for estimating the activity coefficients of metal ions and complexes were attempted. It however, does not make any significant impact on the final results and the conclusion drawn remains the same.

Acknowledgements

This work was carried out during the author's stay at NIO, Goa. Help rendered by the late C V G Reddy is gratefully acknowledged. The author thanks the referees for constructive criticism on the first draft of this paper.

References

Bates R G 1978 *Denki Kagaku* **46** 1978
Berner R 1971 *Principles of chemical sedimentology* (New York: McGraw Hill)
Davies C W 1962 *Ion association* (London: Butterworths)
Garrels R M and Thompson M E 1962 *Am. J. Sci.* **260** 57
Helgeson H C 1969 *Am. J. Sci.* **266** 729
Livingstone D A 1963 US Geol. Surv. Prof. Paper 440-G
Long D T and Angino E E 1977 *Geochim. Cosmochim. Acta* **41** 1183
MacInnes D A 1919 *J. Am. Chem. Soc.* **41** 1089
Mantoura R F C, Dickson A and Riley J P 1978 *Estuarine Coastal Shelf Sci.* **6** 387
Millero F J and Screiber D R 1982 *Am. J. Sci.* **282** 1508
Reardon E J and Langmuir D 1976 *Geochim. Cosmochim. Acta* **40** 549
Sillen L G and Martell A E 1964 *Stability constants of metal ion complexes* (London: Chemical Society) Publ. No. 17
Sillen L G and Martell A E 1971 *Stability constants of metal ion complexes* (London: Chemical Society) Publ. No. 25
Turner D R, Whitefield A E and Dickson A G 1981 *Geochim. Cosmochim. Acta* **45** 855
Zirino A and Yamamoto S 1972 *Limnol. Oceanogr.* **17** 661

Proc. Indian Acad. Sci. (Chem. Sci.), Vol. 97, No. 1, July 1986, pp. 9–11.
© Printed in India.

A ruthenium(II) complex of *bis*(1-pyrazolyl) borate

M M TAQUI KHAN*, K VEERA REDDY†, R C BHARDWAJ and H C BAJAJ

Coordination Chemistry and Homogeneous Catalysis Division, Central Salt and Marine Chemicals Research Institute, Bhavnagar 364002, India
† Department of Chemistry, Osmania University, Hyderabad 500007, India

MS received 3 January 1986; revised 26 March 1986

Abstract. A new neutral ruthenium(II) complex of dihydro-*bis*(1-pyrazolyl) borate is synthesised by the reaction of $RuCl_2(PPh_3)_3$ with the ligand in methanol and is characterised on the basis of IR and $^{31}P\{^1H\}$ NMR spectra.

Keywords. Pyrazolyl borate complex; ruthenium(II); uninegative chelating agents.

1. Introduction

The polypyrazolylborates are uninegative chelating agents in which the number of pyrazolyl groups attached to boron primarily determine the bonding modes of polypyrazolylborates to the metal ion. Chelates of Mn^{2+}, Fe^{2+}, Co^{2+}, Ni^{2+} and Cu^{2+} with pyrazolylborates were reported earlier (Trofimenko 1966, 1967a, b). As polypyrazolylborates exhibit remarkable hydrolytic and oxidative stability in their complexes it was considered important to prepare a ruthenium(II) complex in order to test its catalytic activity (Taqui Khan and Martell 1974). In this note we report the synthesis, characterization and structure of *bis*-(1-pyrazolyl)borate-*bis*-triphenylphosphineruthenium(II). The complex was characterised on the basis of elemental analysis, IR and $^{31}P\{^1H\}$ NMR spectra.

2. Experimental

Potassium dihydro*bis*-pyrazolylborate was used as received from Alfa Chemicals. $RuCl_2(PPh_3)_3$ was prepared by reacting $RuCl_3 \cdot xH_2O$ and triphenylphosphine by a reported procedure (Stephenson and Wilkinson 1966). The IR and far-IR spectra of the complex were recorded on a Beckman IR-Model-12 and Nicolet 200SX spectrometer, respectively. The conductivity was taken on a Digisun electronic conductivity meter. The elemental analysis was performed at the Australian Micro-analytical Service (AMDEL), Australia. The $^{31}P\{^1H\}$ spectrum was recorded on a Jeol FX-100 FT-NMR

A solution of $RuCl_2(PPh_3)_3$ (0·496 gm, 1 mM) in methanol was treated with potassium dihydrogenpyrazolylborate (0·372 gm, 2 mM). The mixture was refluxed for two hours till the yellow precipitate settled down. The yellow precipitate was filtered and washed with methanol and finally with an ethanol-water mixture. The complex was recrystallized with dichloromethane and dried in vacuum. Yield 0·39 gm (43%). Analytical data: found C = 62·58, H = 5·09 and N = 11·86%, calculated C = 63·50, H = 5·07 and N = 11·34%. The complex decomposes at 80°C.

3. Results and discussion

The complex is water insoluble and air stable. The conductivity data of the complex in CH_2Cl_2 shows that it is neutral. The far-IR spectrum of the complex shows a strong band at 620 cm^{-1} which is assigned to ν(Ru-N) stretching frequency. It also shows two bands at 528 and 550 cm^{-1} which can be assigned to ν(Ru-P) stretching frequencies indicating a *cis*-disposition of the two triphenyl phosphine groups. Absence of band around 300–350 cm^{-1} indicates the displacement of all the chloride groups from the coordination sphere of the metal ion.

The proton decoupled phosphorus-31 NMR spectrum gives two doublet centred at 78·201 and 74·174 ppm with $J(P_a\text{-}P_b)$ coupling constant equal to 20 Hz due to the two magnetically inequivalent phosphorus atoms of the two PPh_3 group. The doublet centred at 78·201 ppm can be assigned to the phosphorus atom P_a of PPh_3 which is at an equitorial position and the other doublet centred at 74·174 ppm can be assigned to P_b which is at an axial position. The larger downfield shift, δ(complex)-δ(free ligand) corresponds to the equitorial phosphorus which is closer to the metal ion than the axial

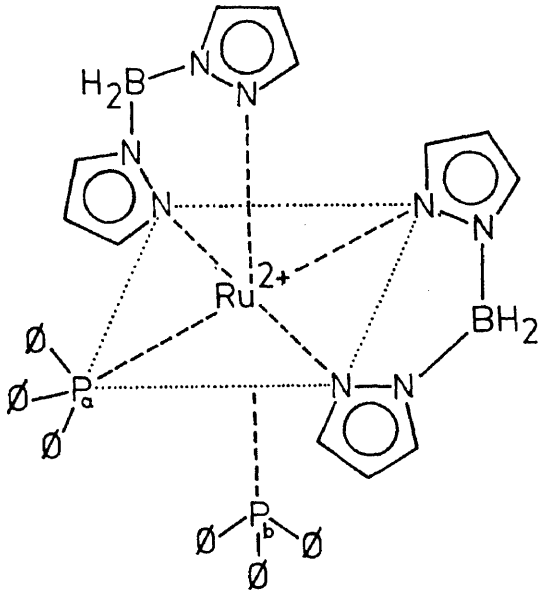

one (Bertrand and Plymale 1966). The low J(P-P) coupling constant of 20 Hz is typical for ruthenium complexes with a *cis*-disposition of phosphorus groups (Briggs *et al* 1984; Gill *et al* 1973). On the basis of the above physicochemical and spectral data a distorted octahedral structure can be proposed for the complex where two PPh_3 groups are *cis* to each other. The structure of the complex is shown in figure 1.

References

Bertrand J A and Plymale D L 1966 *Inorg. Chem.* **5** 879

Briggs J C, McAuliffe C A and Dyer G 1983 *J. Chem. Soc., Dalton Trans.* 423

Gill D F, Mann B E and Shaw B L 1973 *J. Chem. Soc. Dalton Trans.* 311

Stephenson T A and Wilkinson G 1966 *J. Inorg. Nucl. Chem.* **28** 945

Taqui Khan M M and Martell A E 1974 *Homogenous catalysis by metal complexes* (New York: Academic Press)

Trofimenko S 1966 *J. Am. Chem. Soc.* **88** 1842

Trofimenko S 1967a *J. Am. Chem. Soc.* **89** 3165

Trofimenko S 1967b *J. Am. Chem. Soc.* **89** 3171

Proc. Indian Acad. Sci. (Chem. Sci.), Vol. 97, No. 1, July 1986, pp. 13–18.
© Printed in India.

Some lanthanide metal complexes of n-isonicotinamidosalicylaldimine

T R RAO*, I A KHAN and R C AGGARWAL

Department of Chemistry, Faculty of Science, Banaras Hindu University, Varanasi 221 005, India

MS received 21 December 1985; revised 11 March 1985

Abstract. Trivalent lanthanide complexes of the type $K[ML_2]$ where M = La(III), Pr(III), Nd(III), Sm(III), Eu(III), Gd(III) and Dy(III) and H_2L = N-isonicotinamidosalicylaldimine, have been prepared and characterised. The nephelauxetic ratio($\bar{\beta}$), covalency (δ) and bonding parameter ($b^{\frac{1}{2}}$) of $K[NdL_2]$ have been calculated. Infrared spectral studies reveal that N-isonicotinamidosalicylaldimine acts as a dibasic tridentate ligand. A coordination number six has been proposed for the lanthanide metal ions.

Keywords. Lanthanide metal complexes; N-isonicotinamidosalicylaldimine; tridentate ligand; coordination number.

1. Introduction

The ligand N-isonicotinamidosalicylaldimine (*I*) has been reported to behave as a uninegative bidentate and dinegative tetradentate species with 3*d*-metal ions (Narang and Aggarwal 1975) and neutral bidentate and uninegative tridentate species with a main group element like Sn(IV) (Aggarwal and Vara Prasad Rao 1982). No report has been made on the coordinating behaviour of N-isonicotinamidosalicylaldimine towards lanthanides. In continuation of our earlier work on transition metal and lanthanide complexes of pyridine based hydrazides and their derivatives (Aggarwal and Rao 1977, 1978; Rao *et al* 1985, 1986), we report here the synthesis and structural investigations on N-isonicotinamidosalicylaldimine complexes of La(III), Pr(III), Nd(III), Sm(III), Eu(III), Gd(III) and Dy(III).

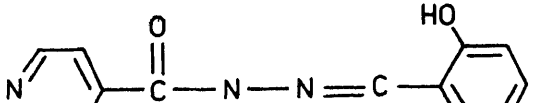

as such, and N-isonicotinamidosalicylaldimine was prepared as described in the literature (Sacconi 1953).

2.2 *Preparation of the complexes*

All the complexes were prepared by mixing together aqueous-ethanolic solutions of the ligand (2 mmol), KOH (4 mmol) and the appropriate metal chloride (1 mmol) and adjusting the pH of the solution to ~ 7·5 by the addition of a few drops of dil. HCl. The precipitated complexes were digested on a water bath for about 30 min, filtered, washed successively with water, and ethanol and dried at room temperature.

2.3 *Analyses of the complexes*

Lanthanides were gravimetrically estimated as oxides as well as oxalates after decomposing the organic matter with aqua regia and subsequently with concentrated H_2SO_4 (Kolthaff *et al* 1963). Hydrazine was estimated volumetrically after subjecting the complexes to acid hydrolysis. Nitrogen was microanalysed.

2.4 *Physical measurements*

Magnetic susceptibility measurements were carried out at room temperature on a Cahn-Faraday electrobalance and the molar conductance was determined on a WTW conductivity meter. The infrared spectra were recorded on Perkin-Elmer spectrophotometer, model 621 while the electronic spectra were obtained on a Cary-14 spectrophotometer.

3. Results and discussion

The analytical data (Table 1) of the complexes indicate 1:2 metal to ligand stoichiometry with the general formula $K[ML_2]$ where M = La(III), Pr(III), Nd(III), Sm(III), Eu(III), Gd(III) and Dy(III) and each ligand in the complex coordinates as a dinegative species as evidenced by IR and PMR spectra discussed later. The simultaneous behaviour of N-isonicotinamidosalicylaldimine as a uninegative and a dinegative species in the same complex molecule, as reported for its isomer (N-picolinamidosalicylaldimine) in Ln(III) complexes (Dutta and Das 1983), has been completely ruled out on the basis of spectral data. Further, in order to estimate quantitatively the ionic cation involved, we have prepared a new series of complexes, $Li[ML_2]$, [M = Pr(III), Nd(III), Sm(III) and Eu(III)] following the same synthetic routes as those of $K[ML_2]$ except that LiOH. H_2O has been used in place of KOH. The lithium present in the complexes has been qualitatively confirmed by the flame test as well as quantitatively estimated as $2Li_2O$, $5Al_2O_3$. The results agree well with the empirical formula $Li[ML_2]$. Further, their magnetic and spectral data have been observed to be identical with those of the corresponding $K[ML_2]$ complexes.

Table 1. Elemental analysis and general behaviour of N-isonicotinamidosalicylaldimine complexes.

Complex	Analysis found (Calc.) %			Molar conductance (mhos cm^2 mol^{-1})	μ_{eff} (BM)
	M	N	N_2H_4		
K[LaL_2]	21·03 (21·17)	12·50 (12·80)	9·65 (9·75)	25·37	Diamag.
K[PrL_2]	21·20 (21·41)	12·48 (12·76)	9·62 (9·72)	29·50	3·38
K[NdL_2]	21·59 (21·64)	12·43 (12·70)	9·55 (9·67)	38·35	3·63
K[SmL_2]	22·40 (22·52)	12·25 (12·58)	9·50 (9·56)	32·45	2·17
K[EuL_2]	22·39 (22·71)	12·30 (12·55)	—	46·61	4·06
K[GdL_2]	23·15 (23·32)	12·32 (12·45)	9·38 (9·49)	40·12	7·62
K[DyL_2]	23·41 (23·91)	12·28 (12·36)	9·36 (9·41)	38·94	9·88

Complex K[LaL_2] is light yellow and all the other complexes are yellow.

All the complexes are non-melting below 300°C and are insoluble in water and common organic solvents. They are, however, sparingly soluble in hot DMF and DMSO. The molar conductance values of their saturated solutions in DMF ($< 0{\cdot}001$ *M*) lie in the range 25·37–46·61 ohm^{-1} cm^2 mol^{-1} which are close to those reported for 1:1 electrolytes (Geary 1971). Thermal studies (ambient – 135°C) made on the complexes indicate no loss of weight.

3.1 *Magnetic moments*

The magnetic moments of Ln(III) complexes show little deviation from the Van Vleck values (Van Vleck and Frank 1929) since the 4*f*-electrons are well shielded by $5s^2p^6$ octet both in their spin and orbital motion and consequently indicate very little participation of the 4*f*-electrons in bond formation. All the complexes in the present study with the exception of K[LaL_2] show magnetic moments (table 1) corresponding to Van Vleck values (Van Vleck and Frank 1929).

3.2 *Electronic spectra*

The *f-f* transition bands show normally weak perturbation due to complexation. Spectra have been recorded for the neodymium(III) complex in its solid state as well as as saturated solution in DMF. The solid state and the solution spectra are similar indicating no appreciable change around the metal ion on going from the solid to the solution state. The hypersensitive bands ($^4I_{9/2} \rightarrow {}^4G_{5/2}$, $^2G_{7/2}$) show significant red shift compared to those of aquoneodymium(III) complex (Choppin *et al* 1966). The magnitude of the bathochromic shift of the bands indicates a meagre nephelauxetic effect upon complex formation (Misumi *et al* 1968). The nephelauxetic effect ($\bar{\beta}$), bonding parameter ($b^{\frac{1}{2}}$) and Sinha's parameter (δ) have been calculated (table 2) from the spectrum (Henrie and Choppin 1968; Sinha 1966). The nephelauxetic parameter ($\bar{\beta}$) is less than one which shows the covalent nature of the bonding between the metal ion and the ligand. Jorgensen ascribed the nephelauxetic effect to a decrease in coulombic interaction between the *f* electrons on the lanthanide atoms, that is, expansion of the

Table 2. Electronic spectral data of the Nd(III) complex of N-isonicotinamidosalicylaldimine.

Band max (cm^{-1})	Assignment	*Spectral parameter
11430	$^4I_{9/2} \rightarrow {}^4F_{3/2}$	
12426	$\rightarrow {}^4F_{5/2}$	
13385		
13515	$\rightarrow {}^4F_{9/2}$	$\bar{\beta} = 0{\cdot}9867$
13605		$b^{\frac{1}{2}} = 0{\cdot}0815$
16475	$\rightarrow {}^2H_{11/2}$	$\delta = 1{\cdot}347$
16950	—	
17155	$^4I_{9/2} \rightarrow {}^4G_{5/2}, {}^2G_{7/2}$	
19010	$\rightarrow {}^4G_{9/2}$	

*Spectral parameters are calculated for hypersensitive transition,

$$^4I_{9/2} \rightarrow {}^4G_{5/2}, {}^2G_{7/2}; \bar{\beta} = 1/n \sum_{n=1}^{n} \text{complex/aquo}$$

$$b^{\frac{1}{2}} = [\tfrac{1}{2}(1-\bar{\beta})]^{\frac{1}{2}}; \; \%\delta = [(1-\bar{\beta}/\beta] \times 100$$

amount of $4f$ ligand orbital mixing in the complex. Sinha's parameter is positive indicating the presence of weak covalent bonding is the Nd(III) complex.

3.3 *PMR spectra*

The PMR spectrum of N-isonicotinamidosalicylaldimine in DMSO-d_6 displays signals at δ12·18, 11·07, 8·71 and 7·45–6·20 assignable to the phenolic, imine (NH), azomethine and aromatic protons, respectively. In the spectrum of K[LaL_2], signals due to phenolic and imine protons totally disappear, while those of the azomethine and aromatic protons appear with slight broadening at almost the same positions as in the ligand. These observations can best be interpreted in terms of the loss of the amide proton through enolization and the deprotonation of the phenolic OH group and the subsequent coordination of the ligand as a dinegative tridentate species bonding through the enolic oxygen, azomethine nitrogen and the phenolic oxygen. The absence of any shift in the aromatic proton signals indicates the noninvolvement of the pyridine nitrogen in coordination.

3.4 *Infrared spectra*

The bonding sites of the ligand involved in coordination with the metal ion have been determined by a careful comparison of the IR spectra of the ligand and the complexes. The peaks appearing in the spectrum of the parent ligand at 1670, 1610, 1560, 1285 and 1270 cm^{-1} may respectively be assigned to amide I, ν(C=N), amide II, amide III and ν(C–O) modes (Aggarwal and Vara Prasada Rao 1982). All the amide bands disappear in the spectra of the complexes suggesting the destruction of the >C=O group by

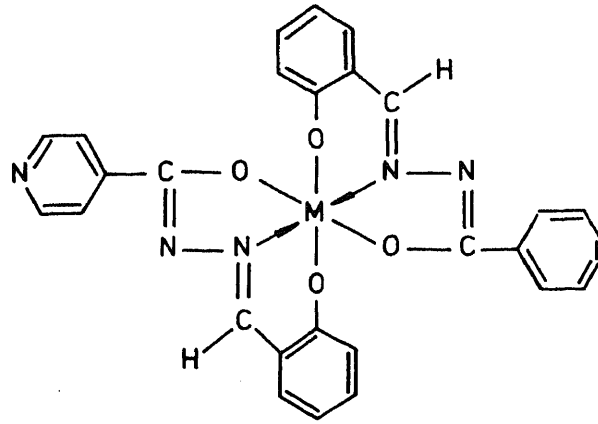

Figure 1. Structure of $[ML_2]^-$. M = La(III), Pr(III), Nd(III), Sm(III), Eu(III), Gd(III) and Dy(III).

20–25 cm^{-1} indicating coordination through the azomethine nitrogen and phenolic oxygen atoms. The destruction of the >C=O group via amide ⇌imidol tautomerism is further shown by the appearance of new peaks characteristic of $\nu(NCO^-)$ in the regions 1535–1530 and 1395–1390 cm^{-1}. Further, the bands due to the ring skeletal bending and in-plane and out-of-plane deformation modes of the pyridine ring appearing at 990, 675 and 440 cm^{-1} in the spectrum of the ligand remain almost unaltered in the spectra of all the complexes suggesting the noncoordination of the pyridine nitrogen.

The nonligand bands appearing in the 330–310 and 400–370 cm^{-1} regions in the spectra of all the complexes may tentatively be assigned to ν(M–N) and ν(M–O) modes respectively (Charpantier and Moeller 1970; Ngsee *et al* 1977). Based on elemental analysis and various physico-chemical studies, the structure shown in figure 1 has been proposed for the $K[LnL_2]$ complexes.

Acknowledgements

The authors are thankful to the Head of the Chemistry Department, for encouragement. One of them (IAK) thanks the CSIR, New Delhi, for a fellowship.

References

Aggarwal R C and Vara Prasada Rao D S S 1982 *Indian J. Chem.* **A21** 735
Aggarwal R C and Rao T R 1977 *Trans. Met. Chem.* **2** 201
Aggarwal R C and Rao T R 1978 *J. Inorg. Nucl. Chem.* **40** 1177
Charpantier J L and Moeller T 1970 *J. Inorg. Nucl. Chem.* **32** 3575
Choppin G R, Henrie D E and Buijs K 1966 *Inorg. Chem.* **5** 1743
Dutta R L and Das B R 1983 *Indian J. Chem.* **A22** 207
Geary W J 1971 *Coord. Chem. Rev.* 7 81

Kolthoff I M, Elving P J and Sandell E B 1963 *Treatise on analytical chemistry*, Part II (Interscience Publishers) vol. 8, p. 29
Misumi S, Kida S and Aihara M 1968 *Coord. Chem. Rev.* **3** 193
Narang K K and Aggarwal A 1975 *Indian J. Chem.* **13** 1072
Ngsee N, Latz H W and Hendricker D C 1977 *J. Inorg. Nucl. Chem.* **39** 71
Rao T R, Khan I A and Aggarwal R C 1985 *Curr. Sci.* **54** 218
Rao T R, Khan I A and Aggarwal R C 1986 *J. Less-Common Met.* **115** 325
Sacconi L 1953 *J. Am. Chem. Soc.* **75** 5437
Sinha S P 1966 *Spectrochim. Acta* **22** 57
Van Vleck J H and Frank A 1929 *Phys. Rev.* **32** 1494

Mixed ligand complexes of *bis*(acetylacetonato) nickel(II) and cobalt(II) with N and N,N′-substituted thioureas

G L TEMBE, S B KOKATNUR† and A S R MURTY*

Department of Chemistry, Karnatak University, Dharwad 580003, India
†B K Arts and Science College, Chikod 591201, India

MS received 9 February 1985; revised 4 December 1985

Abstract. Several mixed ligand complexes of nickel(II) and cobalt(II) acetylacetonates with N-substituted thioureas such as ortho, meta and para chlorophenyl, parabromophenyl and orthotolyl thioureas and N,N′-substituted thioureas such as N-benzoyl N′-ethyl thiourea, N-benzoyl N′-phenyl thiourea, N-benzoyl N′-*o*-chlorophenyl thiourea, N-benzoyl N′-*o*-tolyl thiourea, N-benzoyl N′-*o*-methoxyphenyl thiourea, N-benzoyl N′-cyclohexyl thiourea, N-benzoyl N′-2,5 dimethoxyphenyl thiourea, N-benzoyl N′-2,5 diethoxyphenyl thiourea, N-benzoyl N′-β-hydroxyethyl thiourea, N-benzoyl N′-furfuryl thiourea, N-benzoyl N′-orthohydroxyphenyl thiourea and N-phenyl N′-orthomethoxyphenyl thiourea, have been synthesized and characterized on the basis of elemental analysis, conductivity, molecular weight determination and magnetic moments. The nature of the bonding and the structure of the complexes have been proposed from the infrared and electronic spectral studies.

Keywords. Mixed ligand complex; acetylacetonates; nickel(II) and cobalt(II) thioureas; magnetic spectra.

1. Introduction

Although a considerable amount of work has been done on the complexes of metal β-diketones such as *bis*(acetylacetonato) nickel(II) with nitrogen and oxygen donor ligands (Misra and Ramanrao 1969; Graddon 1969; Syamal 1968), very few reports are available on the analogous sulphur-containing complexes (Misra and Ramanrao 1973). Hence, it was considered worthwhile to undertake a systematic study of the mixed complexes derived from N and N,N′ substituted thioureas with nickel(II) and cobalt(II) acetylacetonates.

2. Experimental

2.1. *Synthesis of ligands*

The N-substituted thioureas were prepared from the appropriate amines, ammonium or potassium thiocyanate and hydrochloric acid in accordance with published procedures (Kurzer 1958). The N,N′-disubstituted thioureas were synthesized employing benzoylisothiocyanate or phenyl isothiocyanate and the corresponding amines according to the method of Douglass and Dains (1934).

separated was filtered under suction, washed successively with alcohol and ether and dried in vacuum over P_2O_5.

2.3 *Analysis of complexes*

The complexes were analysed for nickel (gravimetric–dimethylglyoxime), cobalt (oxinate method–gravimetric), nitrogen and sulphur by standard methods (Vogel 1962). Analysis of carbon and hydrogen has been carried out by microchemical methods.

2.4 *Physico-chemical measurements*

Conductivity measurements of the complexes in dimethylformamide were carried out on an Elico conductivity bridge type CM-82 with a dip type conductivity cell having cell constant 0·63. The molecular weight of a few complexes was determined by the cryoscopic method using nitrobenzene as solvent. The magnetic susceptibility of the complexes at room temperature ($\sim 26°C$) was determined by the Gouy method using $Hg[Co(SCN)_4]$ as the calibrant. The infrared spectra (4000–625 cm^{-1}) of ligands and complexes, as KBr pellets, were recorded on a Perkin-Elmer model 257 spectrometer. Infrared spectra (200–10 cm^{-1}) were recorded on a Polytech FIR-30 spectrometer. The electronic spectra of the complexes in the solid phase (1500–350 nm) were taken on a Beckmann DMR-21 spectrophotometer.

3. Results and discussion

3.1 *Physical properties*

The mixed ligand complexes of nickel(II) and cobalt(II) acetylacetonates with N-benzoyl N′-aryl/alkyl substituted thioureas are greenish yellow and greenish brown respectively, and they are insoluble in common organic solvents. Chemical analysis data (table 1) reveal a 1:2 ratio for metal to ligand in the complexes under present study. The molar conductance values (0·5 to 15 mho cm^2 mol^{-1}) are too low to account for any anionic dissociation of the complexes.

3.2 *Infrared spectra*

The complexes exhibit intense hydrogen bonding as shown by some negative shift coupled with reduction in intensity for the νNH band (3320–3000 cm^{-1}).

A slight positive shift (2 to 16 cm^{-1}) for the ν_{asym} NCN + δNH_2 band in the region 1542–1475 cm^{-1} and a negative shift (2 to 15 cm^{-1}) for the νCS + νCN band in the region 769–701 cm^{-1}, coupled with reduction in intensity in the case of the complexes as compared to free ligands, reveal 'S' bonding of all thioureas [Jensen and Nielsen 1966] except for N-benzoyl, N′-β-hydroxy-ethyl thiourea (N-bz N′-β(OH)etu). Further the negative shift 2–28 cm^{-1}) for the νCS band in the region 695–650 cm^{-1} on com-

Table 1. Elemental analysis of complexes.

Complex number	Complex	% Ni/Co	%N	%S	%C	%H	Mol. wt.
1	$Ni(acac)_2(bz\text{-}o\text{-}Clptu)_2$*	7·14	6·81	7·56	—	—	887
		(6·97)	(6·70)	(7·65)			(838)
2	$Ni(acac)_2(bz\text{-}ptu)_2$	7·77	7·25	8·12	—	—	799
		(7·68)	(7·25)	(8·32)			(769)
3	$Ni(acac)_2(bz\text{-}o\text{-}totu)_2$	7·51	7·05	8·09	—	—	764
		(7·36)	(6·97)	(8·03)			(797)
4	$Ni(acac)_2(bz\text{-}etu)_2$	8·75	8·65	9·46	—	—	706
		(8·72)	(8·32)	(9·52)			(673)
5	$Ni(acac)_2(bz\text{-}o\text{-}meoptu)_2$	7·24	7·05	7·64	—	—	785
		(7·08)	(6·75)	(7·72)			(829)
6	$Ni(acac)_2(bz\text{-}cyhxtu)_2$	7·53	7·18	7·96	58·68	6·38	813
		(7·54)	(7·17)	(8·20)	(58·39)	(6·45)	(781)
7	$Ni(acac)_2(Ph\text{-}o\text{-}meoptu)_2$	7·57	7·59	8·27	58·86	5·62	723
		(7·59)	(7·24)	(8·33)	(59·00)	(5·47)	(773)
8	$Ni(acac)_2(bz\text{-}o\text{-}OHptu)_2$	7·36	7·01	8·20	—	—	—
		(7·32)	(6·97)	(8·01)			
9	$Ni(acac)_2(bz\text{-}\beta\text{-}OHetu)_2$	8·22	7·80	8·93	—	—	—
		(8·32)	(7·94)	(9·08)			
10	$Ni(acac)_2(bz\text{-}2,5\ dietoptu)_2$	6·17	5·84	6·66	—	—	903
		(6·20)	(5·92)	(6·78)			(945)
11	$Ni(acac)_2(bz\text{-}2,5\ dimeoptu)_2$	6·57	6·19	7·10	—	—	899
		(6·59)	(6·29)	(7·20)			(889)
12	$Ni(acac)_2(bz\text{-}furftu)_2$	7·44	6·99	8·08	55·32	4·86	758
		(7·55)	(7·20)	(8·24)	(55·61)	(4·93)	(777)
13	$Co(acac)_2(o\text{-}Clptu)_2$	9·40	9·11	10·05	45·97	4·62	—
		(9·39)	(8·89)	(10·17)	(45·72)	(4·48)	
14	$Co(acac)_2(p\text{-}Clptu)_2$	9·31	8·83	10·14	—	—	—
		(9·39)	(8·89)	(10·17)			
15	$Co(acac)_2(m\text{-}Clptu)_2$	9·41	9·12	10·32	—	—	—
		(9·39)	(8·89)	(10·17)			
16	$Co(acac)_2(o\text{-}totu)_2$	10·16	9·65	10·53	—	—	—
		(9·84)	(9·52)	(10·87)			
17	$Co(acac)_2(p\text{-}Brptu)_2$	8·26	8·24	8·74	40·26	3·84	—
		(8·21)	(7.79)	(8·90)	(40·07)	(3·92)	

*Abbreviations used: acac = acetylacetone; bz = benzoyl; Clptu = chlorophenyl thiourea; ptu = phenyl thiourea; totu = tolylthiourea; etu = ethyl thiourea; meoptu = methoxy phenyl thiourea; cyhxtu = cyclohexyl thiourea; furftu = furfuryl thiourea; Brptu = bromophenyl thiourea Ph = Phenyl.

plexation followed by the appearance of a ν M-S band at $\sim 340\ cm^{-1}$ also support 'S' coordination of the ligand to the central metal ion. However, in the case of the complex derived from N-bz N'-β(OH)etu, a marked negative shift for the δNH_2 band in the $1600\ cm^{-1}$ region and a slight positive shift with no reduction in intensity for the νCS and $\nu CS + \nu CN$ bands favour nitrogen bonding of the ligand to the central metal ion. The possibility of coordination through the 'O' of the >C=O of the benzoyl group is overruled as the band around $1650\ cm^{-1}$ remains unaffected on complexation.

The coordination of the 'O' of the >C=O group of the other ligand acetylacetone to

Table 2. Electronic spectral data of complexes in solid phase.

Complex number	ν_1 (cm^{-1})	ν_2 (cm^{-1})	ν_3 (cm^{-1})	ν_2/ν_1	B'	β	ν_2 (cm^{-1}) (calcd.)	% Distortion	LFSE kcal/mole	μ_{eff} (B.M.)
1	10889	17543	30383	1·64	1017	0·977	16644	5·40	37·3	2·88
2	10889	17543	29154	1·64	935	0·899	16808	4·37	37·3	2·90
3	8333	14814	25000	1·77	987	0·949	12798	15·75	28·6	2·86
4	11235	17182	30383	1·53	924	0·888	16591	3·56	38·5	2·85
5	10630	17391	29850	1·64	1023	0·984	16591	4·82	36·4	3·07
6	10500	17220	28540	1·64	950	0·914	17070	0·87	36·0	2·85
7	10526	16528	29850	1·57	986	0·948	14558	13·53	36·0	2·80
8	9525	17699	25000	1·85	941	0·905	15332	15·43	32·6	2·86
9	10000	16666	26315	1·66	865	0·830	16076	3·67	34·3	3·42
10	8368	17391	22727	2·07	1000	0·961	14286	21·73	28·7	2·87
11	8368	16949	23392	2·02	1015	0·976	13717	23·56	28·7	2·86
12	9090	17094	26019	1·88	1056	1·010	14993	14·01	31·2	2·89
13	8333	16100	19047	1·93	889	0·916	—	—	19·04	5·03
14	8333	16129	19230	1·94	901	0·920	—	—	19·04	5·24
15	8333	16339	19531	1·96	901	0·937	—	—	19·04	5·00

Free ion values: for $Ni^{2+} = 1040\ cm^{-1}$; for $Co^{2+} = 976\ cm^{-1}$.

$\sim 1575\,cm^{-1}$. This is also supported by the shift in νM-O of parent acetylacetonates ($\sim 430\,cm^{-1}$) to lower frequencies (Calvin and Wilson 1945; Haigh *et al* 1970).

3.3 *Electronic spectra*

Solid state electronic spectra of the present $Ni(acac)_2$ thioureas exhibit three bands at $\sim 10000\,cm^{-1}$ $[^3T_{2g} \leftarrow {}^3A_{2g}(F),\ \nu_1]$, $\sim 15000\,cm^{-1}$ $[^3T_{1g}(F) \leftarrow {}^3A_{2g}(F),\ \nu_2]$ and $\sim 29000\,cm^{-1}$ $[^3T_{1g}(P) \leftarrow {}^3A_{2g}(F), \nu_3]$. The ligand field parameters such as Dq, ν_2/ν_1, B' and β have been computed (Drago 1965). It is clear from the table (table 2) that the low value of ν_2/ν_1 supports the octahedral nature of these nickel(II) complexes. The percentage distortion and the extent of covalency of the metal to ligand bond are also shown in the above table.

The present mixed ligand complexes of $Co(acac)_2$ exhibit three low intensity bands in the regions: $\sim 8333\,cm^{-1}$ (ν_1), $\sim 16100\,cm^{-1}$ (ν_2) and $19000\,cm^{-1}$ (ν_3), corresponding to the transitions $^4T_{2g} \leftarrow {}^4T_{1g}(F)$, $^4A_{2g} \leftarrow {}^4T_{1g}(F)$ and $^4T_{1g}(P) \leftarrow {}^4T_{1g}(F)$, respectively. The ligand field parameters were calculated (Rastogi *et al* 1975) and are presented in table 2. The ligand field stabilization energy (LFSE) values for these compounds, ~ 30 kcal/mol for nickel(II) and ~ 19 kcal/mol for cobalt(II) agree fairly well with the values reported for octahedral complexes (Rastogi *et al* 1975; Eilbeck *et al* 1967) of Co(II) and Ni(II). The high B' and β values obtained here may be due to configurational interaction in the case of weak ligands such as the present thioureas (Lever 1968). However, the ν_2/ν_1 values (1·93–1·96) agree reasonably well with an octahedral stereochemistry for the present Co(II) complexes.

3.4 *Magnetic susceptibility measurements*

The effective magnetic moment (μ_{eff}) values at room temperature for Ni(II) and Co(II) complexes lie in the range 2·8–3·4 and 5·0–5·2 B.M. respectively. The higher μ_{eff} values compared to the spin only value of 2·8 B.M. (Ni^{2+})/3·87 (Co^{2+}) may indicate spin-orbit coupling.

4. Conclusion

On the basis of the above spectral, magnetic and analytical studies, the following tentative structure is proposed for $ML_2(acac)_2$ complexes:

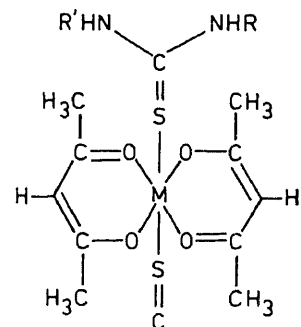

M = Ni(II) / Co(II)

Acknowledgement

We are thankful to the Head, RSIC, IIT, Madras for providing spectral facilities. One of the authors (GLT) is grateful to the CSIR, New Delhi, for the award of a Fellowship.

References

Calvin M and Wilson K W 1945 *J. Am. Chem. Soc.* **67** 2003
Douglass I B and Dains F B 1934 *J. Am. Chem. Soc.* **56** 1408
Drago R S 1965 *Physical methods in inorganic chemistry* (New York: Reinhold) p. 410
Eilbeck W J, Holmes F and Underhill A E 1967 *J. Chem. Soc. A* 757
Graddon D P 1969 *Coord. Chem. Rev.* **4** 19
Haigh J M, Slabbert N P and Thornton D A 1970 *J. Inorg. Nucl. Chem.* **32** 3635
Jensen K A and Nielsen P H 1966 *Acta Chem. Scand.* **20** 597
Kurzer F 1958 *Organic synthesis* (New York: John Wiley) vol. 31, p. 21
Lever A B P 1968 *Inorganic electronic spectroscopy* (New York: Elsevier) p. 187
Misra M K and Ramanrao D V 1969 *J. Inorg. Nucl. Chem.* **31** 3875
Misra M K and Ramanrao D V 1973 *J. Indian Chem. Soc.* **L** 460
Rastogi K D, Sharma K C, Dua S K and Teotia M P 1975 *J. Inorg. Nucl. Chem.* **37** 685
Syamal A 1968 *J. Inst. Chem. (India)* **40** 105
Vogel A I 1962 *Text book of quantitative inorganic analysis* (London: ELBS Longmans) pp. 256, 462 and 479

Structural studies of amino acid complexes-I
EXAFS study of glutamic acid complex of copper

C K BHASKARE* and S Y KULKARNI
Department of Chemistry, Shivaji University, Kolhapur 416 004, India

MS received 27 February 1984; revised 16 December 1985

Abstract. The ambiguity in the assignment of stereochemistry and co-ordination to Cu(II) complexes can be resolved by using x-ray absorption spectroscopic technique. The difficulty in the structural assignment of the Cu-glutamate complex is studied in detail. The Cu-acetylacetonate complex has also been studied as an example of square planar geometry. The Cu-glutamate complex is a distorted octahedral molecule.

Keywords. X-ray absorption spectra; EXAFS; distorted octahedral coordination; amino acid.

1. Introduction

In order to understand the exact role of metal ions in biological systems a study of the structure, physico-chemical aspects and reactivity of ligands occurring in living systems with biologically significant metals, is essential. Copper ion and amino acids constitute one such system.

Glutamic acid is a dibasic, tridentate ligand. A molecular disease 'sickle cell anemia' is due to the occurrence of valine in place of glutamic acid in haemoglobin (Horne 1978). A number of copper(II)-protein complexes containing this amino acid are isolated in plants. Copper uptake by roots of wheat plants may partly be through the glutamate complex (Touchton *et al* 1980). In lower animals like crabs and snails the oxygen carrier system is based on copper (Lippard 1979). Hence, the Cu-amino acid systems must be studied in details.

Solution chemistry of binary and ternary complexes of amino acids is well established, while the solid state and structural aspects are less explored. The physico-chemical properties of the compounds such as the charge on the metal ion, its relation to molecular symmetry, edge structure study and chemical bonding have not been studied extensively. In recent years, x-ray absorption spectral studies are assuming importance since the study of various aspects like the shape of the absorption discontinuity, edge shift, edge width and the profile of the absorption edge can be correlated to the stereochemistry of the molecule (Srivastava and Nigam 1973). The absorption characteristics, when studied upto a few hundred electron volts on the high energy side of the main absorption edge, constitute the x-ray absorption fine structure. The fine structure upto a few tens of electron volts in the vicinity of the absorption edge is known as the Kossel structure and beyond it is the Kronig fine structure. Several theories, grouped as long range order (LRO) and short range order (SRO) theories, are

* To whom all correspondence should be addressed.

wave functions due to scattering in the presence of absorbing atoms is the basis of the Lytle, Sayers and Stern (LSS) theory (Sayers 1970). The present communication reports the EXAFS data in the light of the LSS theory for six-coordinated copper glutamate and four coordinated copper acetyl acetonate complex.

2. Experimental

2.1 *Preparation of complexes*

Copper glutamate, $CuG \cdot 2H_2O$ (Shugan 1951) and copper acetyl-acetonate, $Cu(acac)_2$ were prepared by reported methods (Sharma 1956).

2.2 *X-ray absorption study*

The Cauchois type bent mica crystal spectrograph of 400 mm diameter was used for recording absorption spectra. The instrument could resolve the MoKα1·2 doublet. A Carl Zeiss photodensitometer was used for measuring the intensities of absorption bands from the photographic film.

3. Results and discussion

The d^9 configuration of Cu(II), as a result of the Jahn-Teller effect, shows tetragonally distorted octahedral coordination, and therefore, square-coordination cannot be sharply and easily differentiated from it (Cotton and Wilkinson 1970). Common techniques like electronic absorption and magnetic character cannot clarify this point. The molecular frame is known from x-ray diffraction data and disposition of atoms, bond distances and bond angles are known. However, the decision upon the relation between the central metal atom and the atoms occupying axial positions is difficult to arrive at.

It is observed that if interatomic distances between Cu and the axial atom (Cu-L_{ax} distances) are more than 3 Å, the distances between Cu and the atoms in the planar positions (Cu-L_{pl} distances) hardly change with further change in Cu-L_{ax}. The Cu-L_{pl} distance in such limiting instances is 1·9 Å. With further change in Cu-L_{ax} there is hardly any change in Cu-L_{pl}. This clue may be useful in deciding upon the coordination (Gazo *et al* 1976). Roughly this may be taken as a guide for clear choice of 4 to 6 coordination polyhedra. As a result of shortening of Cu-L_{ax} distance, Cu-L_{pl} distance increases and when Cu-L_{ax} = Cu-L_{pl} an undistorted octahedral structure is obtained. However, it can be said that if Cu-L_{ax} exceeds 2·75 Å there is no harm in regarding it as square planar geometry. What has been said above can be summarised by taking illustrative examples (table 1).

If a compound of category A or D is chosen, there is hardly any controversial situation. Categories B and C must be carefully examined. X-ray diffraction data and x-ray absorption data together solve the problem to a fair degree of satisfaction. In the present study, x-ray diffraction and x-ray absorption data already reported in the literature regarding one member of the B category, CuO, have been chosen, which are in favour of square planar geometry. Another example, $CuSO_4 \cdot 5H_2O$, belongs to the C

Table 1. Relation between axial and equatorial bond distances and stereochemistries of copper compounds.

Compound	Category	R-L_{pl}	R-L_{ax}	Remarks	Reference
Copper(tropolone)$_2$	A	1·91Å	3·30Å	Unambiguous examples of	McIntyre *et al* 1965
$Cu(C_6H_4OHCOO)_2 4H_2O$		1·88Å	3·00Å	square planar geometry	Hanic and Michalav 1960
$Na_2Cu(CO_3)_2$	B	1·93Å	2·77Å	May be regarded as square planar.	Healy and White 1972
CuO		1·95Å	2·78Å	Extreme elongation of the tetragonal geometry	Asbrink and Norrby 1970
$CuSO_4 5H_2O$	C	1·97Å	2·41Å	Not much elongated; tetragonal geometry;	Bacon and Curry 1962
Cu(phthalate)$_2 H_2O$		1·94Å	2·58Å	can be said to be distorted octahedron.	Prout *et al* 1971
$Cu(CH_3OCH_2COO)_2 2H_2O$	D	2·03Å	2·13Å	Fairly good examples of octahedral case,	Prout *et al* 1968
$CuCrO_4$		2·05Å	2·15Å	but distortion is still present.	Brandt 1948
$K_2PbCu(NO_2)_6$	E	2·11Å	2·11Å	Perfect octahedral at room temperature, between 276 K and 193 K it is orthorhombic	Isaacs and Kennard 1969 Joesten *et al* 1977
$Ca(Cu, Zn)_4(OH)_6 (SO_4)_2 3H_2O$		2·11Å	2·11Å	No distortion	Sabelli and Zanazzi 1968
$Cu(H_2O)_6SiF_6$		2·07Å	2·07Å		B J Temple (unpublished results)

category, in favour of octahedral geometry, but of course, distorted. This consideration is further applied to $Cu(acac)_2$. In the present study x-ray absorption spectral data for this compound are reported for the first time.

X-ray diffraction data for both $Cu(acac)_2$ and $CuG2H_2O$ have been taken from literature (Koyama *et al* 1953; Gramaccioli and Marsh 1966).

The reflectance spectra and magnetic data are in agreement with monomeric structures and are not given here.

Figure 1 shows the essential frameworks of the molecules. Table 2 contains XAS and various energy parameters calculated from the absorption data. Table 3 contains EXAFS data. Table 4 shows parameters related to the proposed stereochemistry. Figure 2 shows the absorption curves for the two compounds.

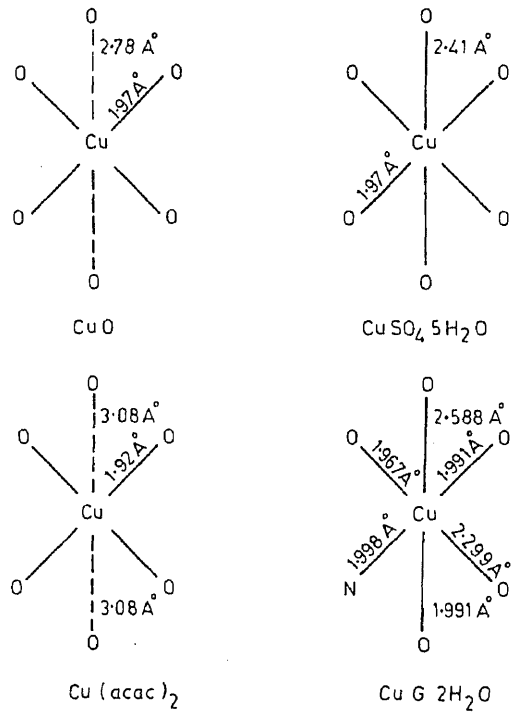

Figure 1. Essential framework of the copper compounds.

Table 2. Shifts* in K absorption edge (E_k), relative energy of principal absorption maxima edge width and energy parameter of Cu(II) compounds.

Compound	E_k	E_k	E_A	E_A	Edge width 10·6	Slope M	R_1-α (Å)
Copper sulphate pentahydrate	8986·69	6·4	8994·19	13·9	7·6	1·41	1·11
Copper oxide	8983·83	3·54	8999·58	19·29	9·98	2	1·57
Copper glutamate	8985·28	4·98	8992·76	12·465	7·48	2·28	2·2
Copper acetylacetonate	8987·99	7·65	8997·91	17·62	9·98	2	2·26

Table 3. EXAFS data of the copper compounds.

	Glutamate		Acetylacetonate		Oxide		Sulphate pentahydrate	
n Peak	Energy (eV) (±0·3)	Wave vector K (Å)$^{-1}$	Energy (eV) (±0·3)	Wave vector K (Å)$^{-1}$	Energy (eV) (±0·3)	Wave vector K (Å)$^{-1}$	Energy (eV) (±0·3)	Wave vector K (Å)$^{-1}$
0 *A*	7·5	1·40	7·5	1·40	15·7	2·03	8·7	1·51
1 α	24·9	2·56	27·4	2·59	27·2	2·67	22·4	2·43
2 *B*	46·1	8·48	42·4	3·34	28·7	2·79	52·4	3·71
3 β	52·4	3·71	47·4	3·55	43·8	3·39	72·3	4·36
4 *C*	57·3	3·88	52·4	3·71	66·1	4·16	109·7	5·37
5 γ	74·8	4·44	72·3	4·37	67·6	4·21	122·2	5·69
6 *D*	86·3	4·57	84·8	4·72	69·4	4·27	128·4	5·81
7 δ	99·5	5·11	94·7	4·99	—	—	142·1	6·11
8 *E*	106·0	5·28	105·0	5·25	—	—	154·6	6·38
9 ε	123·0	5·67	108·5	5·34	—	—	163·0	6·53
10 *F*	134·7	5·96	112·2	5·43	—	—	172·1	6·73
11	137·1	6·01	114·8	5·49	—	—	180·8	6·90
12 *G*	147·1	6·22	124·8	5·72	—	—	184·5	6·97
13 η	158·3	6·45	—	—	—	—	204·5	7·33
14 *H*	163·3	6·55	—	—	—	—	—	—
15 *O*	174·5	6·78	—	—	—	—	—	—
16 *I*	178·3	6·87	—	—	—	—	—	—
17 *i*	184·5	6·97	—	—	—	—	—	—
18 *J*	193·3	7·13	—	—	—	—	—	—

Table 4. Correlation between edge widths and coordination stoichiometry.

Complex	Coordination stoichiometry	$\Sigma(X_m - X_l)$	Edge width	Constant = $[\Sigma(X_m - X_l)EW]^{1/2}$
$CuSO_4 \cdot 5H_2O$	M:O:N	9·6	7·6	8·5
CuO	1:4	6·4	15·75	8·5
Cu-glutamate	1:5:1	9·1	7·48	8·25
Cu-$(acac)_2$	1:4	6·4	9·98	7·99

The EXAFS data on treatment with the Lytle theory (Lytle *et al* 1975) show the slope (M) of the plots of n vs k which can be used to find out the EXAFS parameter (R_1-α). This (R_1-α) EXAFS parameter can be used for explaining the nature of chemical bonding as follows:

In $CuSO_4 \cdot 5H_2O$, the copper atom is surrounded by an approximate square of four oxygen atoms and the fifth and sixth apices of the distorted octahedron of Cu^{+2} atom are occupied by two other oxygen atoms, at a non-bonding distance. In CuO the fifth and the sixth apices of the octahedron are occupied by two other Cu^{+2} ions at a non-bonding distance. This may also be true in the case of $Cu(acac)_2$, which may be due to the symmetrical position of 'acac' groups around Cu^{+2}, while the bonding is square planar.

However, drastic changes in EXAFS energy values and consequently in (R_1-α) parameters suggest that degree of covalency increases in the order $CuSO_4 \cdot 5H_2O$, CuO, $Cu \cdot \underline{G} \cdot 2H_2O$ and $Cu(acac)_2$. This is as per expectation, because $CuSO_4 \cdot 5H_2O$ and CuO are ionic solids. (R_1-α) value for $Cu \cdot G \cdot 2H_2O$ lies in between those for CuO and $Cu(acac)_2$ and this suggests distorted symmetry. This is because $Cu(acac)_2$ is the most symmetrical among the four compounds. By losing the charge on the central metal atom Cu-$G \cdot 2H_2O$ may lose its symmetry and the octahedron is distorted and this picture is reflected in the EXAFS study.

That the $Cu(acac)_2$ complex is four-coordinated and Cu-$G \cdot 2H_2O$ six-coordinated is further confirmed by the fact that the edge width for lower coordination is higher, while it is less for higher coordination. Table 2 shows that the edge width for $Cu(acac)_2$ is 9·98 and the reported value for CuO, which is four-coordinated, is 9·98. The edge width for Cu-$G \cdot 2H_2O$ is 7·48 and the reported value for $CuSO_4 \cdot 5H_2O$ which is *six*-coordinated, is 7·6 (Tunnel *et al* 1935). The octahedral Cu^{2+} complex has a d^9 configuration and the copper atom uses dsp^2 hybrid orbitals. In such a structure the M–O bond distance is necessarily more than that in tetrahedral sp^3 hybridization. Levine (1973) suggests that the bond distance d is inversely proportional to the fractional covalency and that a parallel trend is observed with respect to α also, that is, $d \propto V_{FC}$ and $d \propto 1/\alpha$ therefore $V_{FC} \propto \alpha$. It is obvious, therefore, that Cu–O bonds in $Cu \cdot G \cdot 2H_2O$ must be having predominantly covalent character. Moreover, copper complexes with distorted tetrahedral structure are orange in colour whereas $CuSO_4 \cdot 5H_2O$, $Cu(acac)_2$ and $Cu \cdot G \cdot 2H_2O$ are blue in colour and therefore, octahedral or square planar (Cotton and Wilkinson 1972).

Further, it has been shown that there is an empirical correlation between edge width

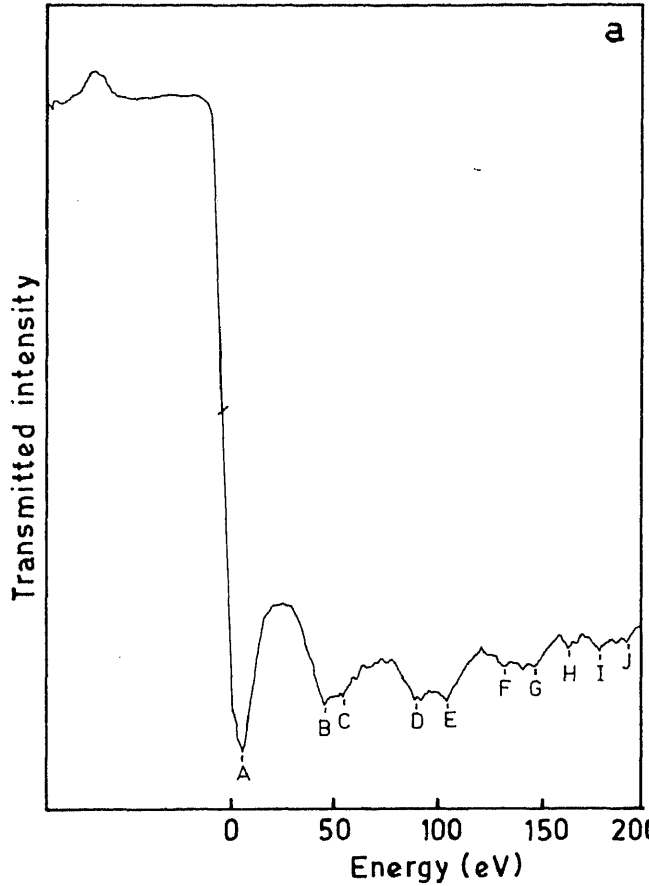
a
Transmitted intensity
A
B
C
D
E
F
G
H
I
J
0
50
100
150
200
Energy (eV)

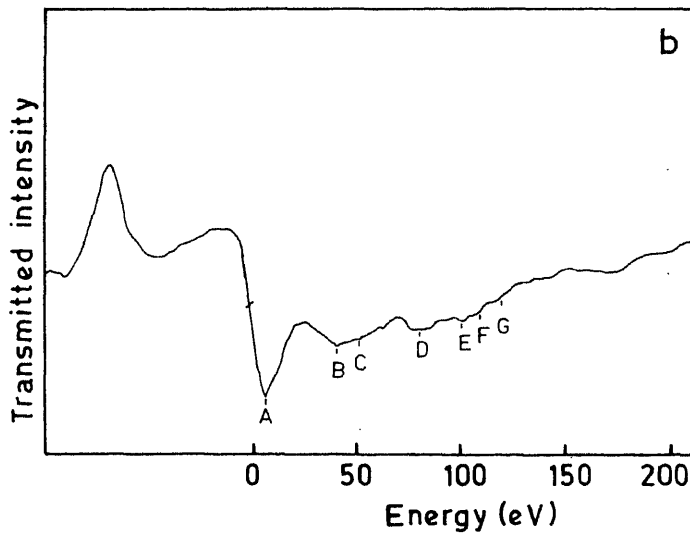
b
Transmitted intensity
A
B
C
D
E
F
G
0
50
100
150
200
Energy (eV)

This relation is valid for O_h geometry for $CuSO_4 5H_2O$ and $Cu \cdot G \cdot 2H_2O$ and square planar geometry for CuO and $Cu(acac)_2$ (Srivastava and Nigam 1973).

4. Conclusion

When the value of the EXAFS parameter $(R_1\text{-}\alpha)$ increases, the degree of covalency shows an increase in trend. In the two compounds studied in the present work the high values (around 2·3) for this parameter show a high degree of covalency in these complexes.

From substitution in the empirical formula $[\Sigma(X_m - X_l)EW]^{1/2}$ for $Cu(acac)_2$ as Cu_1O_4 and $Cu \cdot G \cdot 2H_2O$ as $Cu_1O_5N_1$, fairly constant values in the range 8 to 8·5 are obtained in conformity with a square planar structure for the former and an octahedral structure for the latter.

Acknowledgement

One of the authors, SYK, is thankful to the CSIR, New Delhi, for a fellowship.

References

Agarwal B K 1979 *X-ray spectroscopy* (Berlin: Springer-Verlag) p. 288
Asbrink S and Norrby L J 1970 *Acta Crystallogr.* **B26** 8
Bacon G E and Curry N A 1962 *Proc. R. Soc. London* **266** 95
Brandt K 1948 *Ark. Kemi. Mineral Geol.* **A17** 13
Cotton F A and Wilkinson G 1972 *Advanced inorganic chemistry* (New York: John Wiley) p. 912
Gazo J, Bersuker I B, Garaj J and Valach F 1976 *Coord. Chem. Rev.* **19** 260
Gramaccioli C M and Marsh R E 1966 *Acta Crystallogr.* **21** 594
Hanic F and Michalov J 1960 *Acta Crystallogr.* **13** 299
Healy P C and White A H 1972 *J. Chem. Soc., Dalton Trans.* 1913
Horne R A 1978 *Chemistry of our environment* (New York: John Wiley) p. 400
Isaacs N W and Kennard C H L 1969 *J. Chem. Soc. A* 386
Joesten M D, Hussain M S, Lenhert P G and Venables J H 1968 *J. Am. Chem. Soc.* **90** 5623
Koyama H, Saitoy and Kuroya H 1953 *J. Inst. Polytech. Osaka City Univ. Serec.* **4** 43
Levine B F 1973 *Phys. Rev.* **B7** 2591
Lippard S J 1971 *Progress in inorganic chemistry* (New York: John Wiley) p. 31
Lytle F W, Sayers D E and Stern E A 1975 *Phys. Rev.* **B11** 4825
McIntyre W M, Robertson J M and Zahrobsky R F 1965 *Proc. R. Soc. London* **289** 161
Nigam H L and Srivastava U C 1971 *Chem. Commun.* **14** 761
Prout C K, Armstrong R A, Carruthers J R, Forrest J G, Murray-Rust P and Rossotti J C F 1968 *J. Chem. Soc.* A2791
Prout C K, Carruthers J R and Rossotti F J C 1971 *J. Chem. Soc. A* 3350
Sabelli C and Zanazzi D F 1968 *Acta Crystallogr.* **B 24** 1214
Sayers D E, Stern E A and Lytle F W 1971 *Phys. Rev. Lett.* **27** 1204
Sharma B D 1956 *J. Amer. Chem. Soc.* **78** 892
Shugarm E A 1951 *Doklady Akad Nauk SSSR* **81** 853
Srivastava U C and Nigam H L 1973 *Coord. Chem. Rev.* **9** 703

^{13}C NMR substituent induced chemical shifts in the side-chain carbons of α,β-unsaturated sulphones

C SRINIVASAN*, P K GANESAN, A SHUNMUGASUNDARAM and N ARUMUGAM

School of Chemistry, Madurai Kamaraj University, Madurai 625 021, India

MS received 8 November 1985

Abstract. The ^{13}C NMR chemical shifts of α,β-unsaturated sulphones of the types E-2-aryl-1-phenyl-sulphonylethylenes (series I) and E-1-arylsulphonyl-2-phenylethylenes (series II) have been measured in $CDCl_3$ solution. The chemical shifts of the side-chain and a few ring carbons have been correlated with various single and multiparameter linear free energy relationships. Analysis of the ^{13}C NMR spectral data by a dual substituent parameter equation shows that the resonance effect is the dominant factor at C-α in series I and C-β in series II. The inductive effect is predominant at C-β in series I with a reverse substituent effect at this carbon atom. The reverse inductive contribution is explained in terms of π-polarisation mechanism.

Keywords. ^{13}C NMR chemical shifts; substituent effect; α,β-unsaturated sulphones; reverse substituent effect.

1. Introduction

The study of correlations between the Hammett substituent constants and ^{13}C NMR substituent induced chemical shifts (SCS) of side-chain carbon atoms of aromatic systems and the use of SCS to monitor the transmission of electronic effects in molecular structures, in general, and to understand the mode of transmission of long-range substituent effects in extended π-electron systems, in particular, are topics of current interest (Inamoto *et al* 1974; Dawson and Reynolds 1975; Solčániová *et al* 1976, 1982; Shapiro 1977; Bromilow *et al* 1981; Srinivasan *et al* 1985). In recent years SCS of C-α and C-β of ethenyl group in several conjugated systems (Happer 1976; Solčániová *et al* 1976, 1982; Bromilow *et al* 1977, 1981; Srinivasan *et al* 1985) have been correlated by the dual substituent parameter (DSP) extension of the Hammett approach and this has revealed new features of a very important mechanism for the transmission of substituent effects i.e. π-polarisation (Bromilow *et al* 1981; Brownlee and Craik 1981). It is, therefore, of interest to investigate whether this new phenomenon exists in other systems, notably in α,β-unsaturated sulphones. In this study, the ^{13}C NMR spectra of E-2-aryl-1-phenylsulphonylethylenes (series I) and E-1-arylsulphonyl-2-phenylethylenes (series II) have been recorded and the SCS analysed by the simpler single substituent parameter and DSP treatments. The results of the analysis have been compared with those of chalcones.

2. Experimental

All the α,β-unsaturated sulphones used in this study were prepared by literature methods (Baliah and Seshapathi Rao 1959; Srinivasan *et al* 1983). Their purity was checked by m.p. measurements and TLC analyses. The observed coupling constants (J = 15 Hz) for ethylenic protons in the ^{1}H NMR spectra of all the α,β-unsaturated sulphones indicate that they exist in an E-configuration. The ^{13}C NMR spectra were run on a Varian XL-100-A_{12} spectrometer, equipped with a Varian 620 L computer operating in the fourier transform mode at 25·2 MHz under noise-modulated proton-decoupled conditions with 2 kHz band width at 10 W for normal spectra and with upfield irradiation by 200 Hz at 8 W for off-resonance spectra. For the spectra 10,000 time-domain data points were used. The peak positions printed out in Hz units were converted into chemical shifts in ppm. Spectra were measured in dilute solution (~ 5 %) in $CDCl_3$. All shifts reported are referenced to TMS and estimated to be accurate to ±0·05 ppm. The correlation analyses were performed with a Micro 2200 Diskette Recorder (Hindustan Computers).

Table 1 (a). ^{13}C NMR chemical shifts[a] of E-2-aryl-1-phenylsulphonylethylenes (series I).

Substituent	C-3	C-2	C-1	C-β	C-α	C-1′	C-2′	C-3′	C-4′
				Series I					
H	130·30	131·35	135·01	145·14	130·23	143·53	131·79	132·14	136·18
p-OMe	117·29	130·15	127·64	145·01	127·26	143·94	132·03	133·16	135·91
p-Me	130·27	131·37	132·42	145·22	129·01	144·53	132·08	132·55	136·04
p-i-pr	129·78	131·35	132·85	145·16	129·02	145·34	131·64	132·20	135·98
p-F	119·24	133·33	131·64	143·92	—	—	130·43	132·13	136·43
p-Cl	130·38	132·04	133·63	143·68	130·81	142·99	132·16	132·59	136·26
p-Br	130·28	132·04	—	143·79	130·75	—	132·53	—	136·13
m-Cl	129·53	130·52	137·12	143·35	133·09	—	131·64	132·16	136·26
m-NO_2	128·07	130·59	136·87	142·15	133·03	142·02	132·26	132·26	136·56
p-NO_2	127·02	130·63	141·15	141·98	133·05	142·42	132·02	132·28	136·62

[a] Chemical shifts are in ppm relative to TMS.

Table 1 (b). ^{13}C NMR chemical shifts[a] of E-1-arylsulphonyl-2-phenylethylenes (series II).

Substituent	C-3′	C-2′	C-1′	C-α	C-β	C-1	C-2	C-3	C-4
				Series II					
H	131·25	132·14	143·53	130·23	145·14	135·01	131·79	130·30	134·05
p-OMe	117·31	132·53	131·92	130·78	144·03	—	131·73	131·17	—
p-Me	131·27	132·74	140·93	130·88	144·62	135·48	131·85	130·52	133·80
p-Cl	131·29	132·17	145·53	129·55	145·57	134·83	131·74	131·29	133·93
p-Br	132·86	131·84[b]	145·74	129·57	145·80	135·28	131·32	131·32[b]	134·04
p-NO_2	127·38	132·05	149·06	130·88	147·75	134·89	131·73	131·82	134·61

In the present study, the ^{13}CNMR chemical shifts of α- and β-carbons and the ring carbons of series I and II are given in tables 1a and b. Assignments of these carbons were made on the basis of the chemical shifts exhibited by the signals, the off-resonance decoupling technique and the relative signal intensity. All the ring carbons were identified by assuming the rule of additivity. The chemical shifts of the carbon atoms of the substituted ring were compared with the corresponding chalcones (Solčániová *et al* 1976), styrenes (Dhami and Stothers 1965; Hamer *et al* 1973) and phenyl methyl sulphones (Buchanan *et al* 1974). The signals due to C-α and C-β were readily identified by their splitting patterns and low intensities. These two carbons appear as overlapping multiplets due to long range coupling in the off-resonance proton-decoupled spectrum. The chemical shifts (in ppm relative to TMS) for C-α fall in the region 127·3–133·1 and 129·6–130·9 in series I and II, respectively, and for C-β fall in the region 142·0–145·2 and 144·0–147·8 in series I and II, respectively. The low field shift of C-α and C-β as compared to styrenes (116–126 ppm and 133–138 ppm, respectively) (Dhami and Stothers 1965; Hammer *et al* 1973) is presumably due to the greater electron-withdrawing ability of the phenylsulphonyl group attached to the neighbouring carbon. A similar trend in chemical shifts has been reported in the chalcones (Solčániová *et al* 1976), furan and thiophene chalcone analogues (Masumarra and Ballistreri 1980).

In series I, the chemical shift of C-α is more susceptible to the polar effects of substituents ($\Delta\delta \sim 6$ ppm), than that of C-β ($\Delta\delta \sim 3$ ppm). In series II, the effect is the opposite, i.e., the chemical shift of C-β is more sensitive ($\Delta\delta \sim 4$ ppm) than that of C-α ($\Delta\delta \sim 1$ ppm).

The SCS data of C-α and C-β in series I and II were correlated with the Hammett single parameter equation, employing σ or σ^+ or σ^+/σ^- constants, and the results of correlations with the best correlation coefficient for each carbon are set forth in table 2. While a fair correlation is obtained in series I for the SCS for C-α, correlation of the C-β SCS with substituent constants is poor. The correlation of SCS of C-β in series II is good. The correlation of chemical shifts of C-α of series II has not been attempted due to the poor spread of SCS ($\Delta\delta \sim 1{\cdot}33$) which is comparable to that reported for the

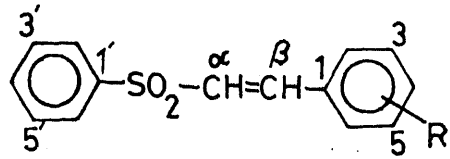

Series I

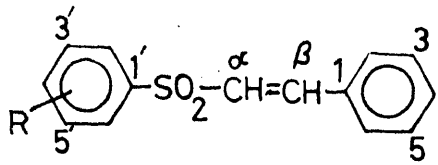

Series II

Table 2. Results of the statistical treatment on ^{13}C NMR chemical shifts with σ or σ^+ or σ^+/σ^- using the single parameter equation.

Series	Carbon chemical shifts	scale	ρ	r	s	n
I	C-α	σ^+/σ^-	$4{\cdot}66 \pm 0{\cdot}652$	0·988	0·461	9
	C-β	σ	$-3{\cdot}26 \pm 0{\cdot}691$	0·968	0·323	10
	C-1	σ^+/σ^-	$6{\cdot}22 \pm 1{\cdot}62$	0.960	1·15	9
II	C-β	σ^+/σ^-	$1{\cdot}89 \pm 0{\cdot}320$	0·992	0·173	6
	C-1′	σ^+	$10{\cdot}6 \pm 4{\cdot}89$	0·950	2·06	6

r = Correlation co-efficient; s = standard deviation; n = number of data points taken for consideration.

corresponding C-α in chalcones ($\Delta\delta \sim 1{\cdot}14$). The results of correlations for C-1 (series I), and C-1′ (series II) carbons are also included in table 2. The correlations for other carbons are poor.

Since the correlations with the single parameter equation are not excellent, the correlation of SCS of C-β in series I in particular being very poor, the SCS have been treated by the DSP equations (1) and (2).

$$\text{SCS} = \rho_I \sigma_I + \rho_R \sigma_R, \tag{1}$$

$$\text{SCS} = fF + rR. \tag{2}$$

The DSP method provides the relative magnitudes of various modes of transmission of substituent effects like ρ_I and ρ_R values which are not obtainable from single parameter treatment. By DSP treatment using (1), the correlations were done for each of the four resonance scales, viz, σ_R^0, $\sigma_R^{(BA)}$, σ_R^+ and σ_R^- and the results for the one with the lowest standard error are taken for consideration. The values of σ_I and σ_R used in the present analysis are those given by Ehrenson *et al* (1973) and F and R are those given by Swain and Lupton (1968). The results of the DSP equations are presented in table 3 for both the series I and II. Generally, electron-withdrawing substituents cause a downfield shift by decreasing the extent of shielding and electron-releasing substituents an upfield shift by increasing the shielding. Consequently, DSP treatment is expected to give a positive value of ρ_I and ρ_R. This is indeed the case for C-α carbon in series I. The chemical shifts of C-α carbon exhibit a normal substituent effect, the resonance effect being the predominant factor ($\rho_I = 6{\cdot}621$; $\rho_R = 11{\cdot}402$). Our recent DSP analysis of ^1H NMR SCS of H-α indicates that the resonance contribution to the chemical shift predominates over the field effect (Srinivasan *et al* 1983). The chemical shifts of C-β in series II also exhibit a normal substituent effect but the magnitudes of ρ_I and ρ_R are lower than those of C-α in series I ($\rho_I = 3{\cdot}029$; $\rho_R = 4{\cdot}247$). It is interesting to note that the resonance contribution is more than that of the inductive effect for C-β in series II, which is remarkably similar to the dominant resonance effect of the β-protons of series II as revealed by the DSP

Table 3. DSP analysis of SCS data of carbon atoms for *p*-substituted compounds.

Carbon Chemical shifts	Scale[a]	Equation	R	SE	n	CL (%)
C-α	σ_I, σ_R^0	SCS = 6·621 σ_I + 11·402 σ_R^0 ±0·387 ±0·583	0·997	0·269	7	99·9
	F, R	SCS = 3·718 F + 10·226 R ±0·624 ±1·291	0·989	0·607	6	99·5
C-β	σ_I, σ_R^0	SCS = −3·756 σ_I − 2·571 σ_R^0 ±0·215 ±0·315	0·993	0·157	8	99·9
	F, R	SCS = −2·368 F − 1·977 R ±0·144 ±0·294	0·994	0·151	7	99·9
C-β	σ_I, σ_R^0	SCS = 3·029 σ_I + 4·247 σ_R^0 ±0·121 ±0·162	0·999	0·073	6	99·9
	F, R	SCS = 1·716 F + 3·820 R ±0·130 ±0·270	0·997	0·127	6	99·9

multiple regression correlation coefficient; SE = standard error of the estimate; CL = confidence levels
d on F-test.
the DSP analysis the correlations were done for each of the four resonance scales (σ_R^0, $\sigma_R^{(BA)}$, σ_R^+, σ_R^-), and
results for the one with the lowest standard error are shown.

32), N-benzylidenebenzylamines (Arrowsmith *et al* 1978), N-methyl-4-styryl-
idinium iodides (Srinivasan *et al* 1985) and the others (Hamer *et al* 1973; Happer *et*
1977; Bromilow *et al* 1981; Butt and Topsom 1982) also show a normal substituent
ct at these carbons.

The notable feature of the study is that C-β in series I gives negative values for ρ_I and
indicating a reverse substituent effect.

As seen from the results of the DSP equation in table 3 for series I, the inductive effect
ntributes more to the chemical shifts of C-β than the resonance effect. The DSP
thod of analysis of SCS values in a series of several unsaturated systems of the type
C_6H_4—CH=CH–, show that the C-β leads to almost a constant ρ_I value of $\sim -3{\cdot}8$
e table 4). The near constancy and the negative ρ_I value in these cases have been
ributed to a π-polarisation mechanism postulated by Brownlee (Brownlee and Craik
81; Bromilow *et al* 1981). The π-polarisation mechanism occurs through space
eraction of the substituent dipole and the ethylenic π-electrons. According to this
ncept, polarisation of the conjugated styryl system, as a whole, does not play a
nificant part in the determination of ρ_I value for the C-β position. The present
estigation on ^{13}CNMR spectra in series I which is analogous to the systems
C_6H_4—CH=CH–, gives $\rho_I = -3{\cdot}8$ on DSP analysis by (1). Consequently, we attribute
s reverse substituent effect to the 'localised polarisation' involving the separate
larisation of ethylene, the phenyl π-system and the phenylsulphonyl group. It is
lependent of the nature of the α-substituent in the unsaturated system corroborating
ownlee's concept.

It is highly interesting to note that the plot of chemical shifts of C-β of sulphones
ries I) gives an excellent correlation with C-β of the corresponding chalcones

Table 3. DSP analysis of SCS data of carbon atoms for *p*-substituted compounds.

Series	Carbon Chemical shifts	Scale[a]	Equation	R	SE	n	CL (%)
I	C-α	σ_I, σ_R^0	SCS = 6·621 σ_I + 11·402 σ_R^0 ± 0·387 ± 0·583	0·997	0·269	7	99·9
		F, R	SCS = 3·718 F + 10·226 R ± 0·624 ± 1·291	0·989	0·607	6	99·5
	C-β	σ_I, σ_R^0	SCS = −3·756 σ_I − 2·571 σ_R^0 ± 0·215 ± 0·315	0·993	0·157	8	99·9
		F, R	SCS = −2·368 F − 1·977 R ± 0·144 ± 0·294	0·994	0·151	7	99·9
II	C-β	σ_I, σ_R^0	SCS = 3·029 σ_I + 4·247 σ_R^0 ± 0·121 ± 0·162	0·999	0·073	6	99·9
		F, R	SCS = 1·716 F + 3·820 R ± 0·130 ± 0·270	0·997	0·127	6	99·9

R = multiple regression correlation coefficient; SE = standard error of the estimate; CL = confidence levels based on F-test.

[a] In the DSP analysis the correlations were done for each of the four resonance scales (σ_R^0, $\sigma_R^{(BA)}$, σ_R^+, σ_R^-), and the results for the one with the lowest standard error are shown.

1982), N-benzylidenebenzylamines (Arrowsmith *et al* 1978), N-methyl-4-styryl-pyridinium iodides (Srinivasan *et al* 1985) and the others (Hamer *et al* 1973; Happer *et al* 1977; Bromilow *et al* 1981; Butt and Topsom 1982) also show a normal substituent effect at these carbons.

The notable feature of the study is that C-β in series I gives negative values for ρ_I and ρ_R indicating a reverse substituent effect.

As seen from the results of the DSP equation in table 3 for series I, the inductive effect contributes more to the chemical shifts of C-β than the resonance effect. The DSP method of analysis of SCS values in a series of several unsaturated systems of the type X–C_6H_4–CH=CH–, show that the C-β leads to almost a constant ρ_I value of $\sim -3{\cdot}8$ (see table 4). The near constancy and the negative ρ_I value in these cases have been attributed to a π-polarisation mechanism postulated by Brownlee (Brownlee and Craik 1981; Bromilow *et al* 1981). The π-polarisation mechanism occurs through space interaction of the substituent dipole and the ethylenic π-electrons. According to this concept, polarisation of the conjugated styryl system, as a whole, does not play a significant part in the determination of ρ_I value for the C-β position. The present investigation on ^{13}CNMR spectra in series I which is analogous to the systems X–C_6H_4–CH=CH–, gives $\rho_I = -3{\cdot}8$ on DSP analysis by (1). Consequently, we attribute this reverse substituent effect to the 'localised polarisation' involving the separate polarisation of ethylene, the phenyl π-system and the phenylsulphonyl group. It is independent of the nature of the α-substituent in the unsaturated system corroborating Brownlee's concept.

It is highly interesting to note that the plot of chemical shifts of C-β of sulphones (series I) gives an excellent correlation with C-β of the corresponding chalcones

Buchanan G W, Zamora C R and Clarke D E 1974 *Can. J. Chem.* **52** 3895
Butt G and Topsom R D 1982 *Spectrochim. Acta* **A38** 301, 649
Dawson D A and Reynolds W F 1975 *Can. J. Chem.* **53** 373
Dhami K S and Stothers J B 1965 *Can. J. Chem.* **43** 510
Ehrenson S, Brownlee R T C and Taft R W 1973 *Prog. Phys. Org. Chem.* **10** 1
Hamer G K, Peat I R and Reynolds W F 1973 *Can. J. Chem.* **51** 897
Happer D A R 1976 *Aust. J. Chem.* **29** 2607
Happer D A R, Mckerrow S M and Wilkinson A L 1977 *Aust. J. Chem.* **30** 1715
Inamoto N, Kushida K, Masuda S, Ohta, Satoh S, Tamura Y, Tokumaru K, Torik and Yoshida M 1974 *Tetrahedron Lett.* 3617
Masumarra G and Ballistreri F P 1980 *Org. Magn. Reson.* **14** 384
Shapiro M J 1977 *Tetrahedron* **33** 1091
Solčániová E, Toma S and Gronowitz S 1976 *Org. Magn. Reson.* **8** 439
Solčániová E, Hrnciar P and Liptaj T 1982 *Org. Magn. Reson.* **18** 55
Srinivasan C, Ganesan P K and Arumugam N 1983 *Indian J. Chem.* **B22** 646
Srinivasan C, Shunmugasundaram A and Arumugam N 1985 *Indian J. Chem.* **24B** 827
Swain C G and Lupton E C 1968 *J. Am. Chem. Soc.* **90** 4328

Photo-Fries reaction of 1-naphthyl cinnamate

T JAYACHANDRAN, T MANIMARAN and V T RAMAKRISHNAN*
Department of Organic Chemistry, University of Madras, Madras 600 025, India

MS received 12 February 1983; revised 25 November 1985

Abstract. The photo-Fries reaction of 1-naphthyl cinnamate afforded 2-cinnamoyl-1-naphthol. Likewise, 1-naphthyl *p*-methyl-cinnamate gave 2-(*p*-methylcinnamoyl)-1-naphthol. The product chalcones were cyclised into the respective flavanones.

Keywords. 1-Naphthyl cinnamate; 1-naphthyl *p*-methylcinnamate; 1-naphthyl α-methyl-cinnamate; 2-cinnamoyl-1-naphthol; 2-(*p*-methylcinnamoyl)-1-naphthol; 7,8-benzoflavanone; photo-Fries reaction.

1. Introduction

The photo-Fries reaction of aryl esters is known since 1960 when the first report on the photolysis of phenyl acetate appeared (see Bellus 1971 for a review). Since then studies were initiated on the mechanistic aspect as well as the synthetic applications of the photo-Fries reaction. In such a study, the synthesis of naturally occurring chalcones (2) and flavanones (3) by the photo-Fries reaction of aryl cinnamates (1) have been reported (Ramakrishnan and Kagan 1970).

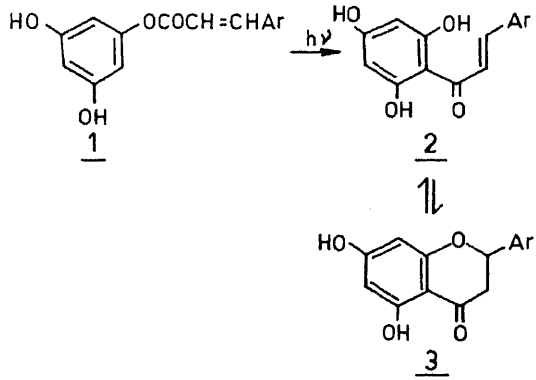

1 2 3

2. Results and discussion

We wish to report here the photo-Fries reaction of 1-naphthyl cinnamates (4). Irradiation (254 nm) of 1-naphthyl cinnamate (4a) in benzene solution in a Rayonet photochemical reactor for 10 hours furnished an orange red solid, mp 127–8°C. The

* To whom all correspondence should be addressed.

infrared spectrum showed the carbonyl absorption at 1630 cm^{-1}. The ^1H NMR showed aromatic protons (13H) at δ7·2–8·0 and an hydroxy proton at δ14·77. The mass spectrum showed the molecular ion at *m/e* 274 and the elemental analysis agreed with the molecular formula $C_{19}H_{14}O_2$. Based on the above data, a chalcone structure obtained by Fries reaction is evident for the orange-red product (5a). However, the position of the cinnamoyl group in the product was perplexing since no clue could be obtained from the complex ^1H NMR spectrum. The possible positions of the cinnamoyl group are 2,4,5 and 7 of 1-naphthol, based on the mechanism of Fries reaction (Bellus 1971). The chalcone (5a) when treated with hydrogen chloride gas in methanol solution gave a pale yellow solid, m.p. 112–3°C, showing the characteristic signals for a $CHCH_2$ system with geminal as well as *cis* and *trans* couplings in the ^1H NMR spectrum; hence the flavanone structure is imperative and could arise only from the 2-cinnamoyl-1-naphthol. Thus the photo-Fries reaction of 1-naphthyl cinnamate (4a) afforded 2-cinnamoyl-1-naphthol (5a).

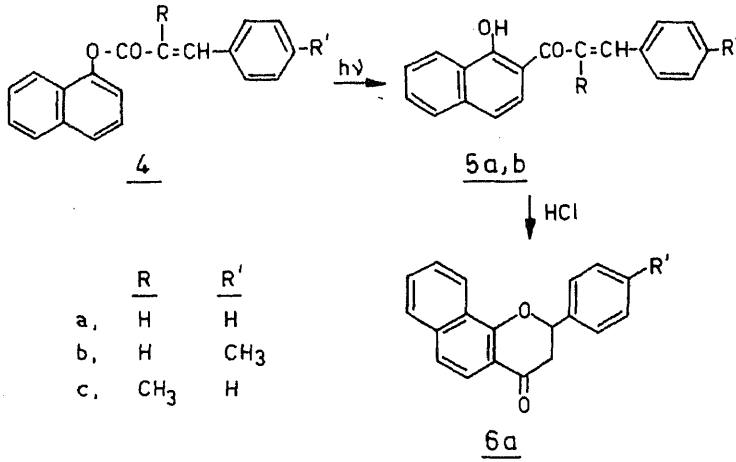

Likewise irradiation of 1-naphthyl *p*-methylcinnamate (4b) furnished an orange red solid, m.p. 147–8°, to which was assigned the chalcone structure, i.e. 2-(*p*-methylcinnamoyl)-1-naphthol (5b), based on its cyclisation into a flavanone with HCl gas. 1-Naphthyl α-methylcinnamate (4c) was also studied, which on irradiation furnished a mixture showing a yellow spot on TLC which however could not be separated by column or preparative thin layer chromatographic methods. While this study was in progress, a parallel report appeared on the photochemical reaction of 1-naphthylacetates, cyclohexane carboxylates and benzoates giving 2-acyl-1-naphthols, in connection with its synthetic usefulness for the synthesis of daunomycinone (Crouse *et al* 1981).

The photolysis of 2-naphthyl cinnamate in benzene, however, furnished only 2-naphthol. This marked difference in the photochemical reaction of 1-naphthyl and 2-naphthyl cinnamates is perplexing. Similarly, the interesting reaction observed

Melting points are uncorrected. Beckmann IR-20, Varian A-60 and T-60 and Varian MS-30 were used. Tetramethylsilane was used as internal standard for NMR.

3.1 *Preparation of* 1-*naphthyl p-methylcinnamate* (4*b*)

p-Methylcinnamoyl chloride (8·1 g, 50 mmol, prepared from *p*-methylcinnamic acid) and thionyl chloride (7·5 ml) in dry benzene were added dropwise to a solution of 1-naphthol (7·2 g, 50 mmol) and pyridine (4 ml) in dry benzene. The reaction mixture was stirred for 14 hours at room temperature and worked up by washing with dil. HCl, an ice-cold solution of sodium hydroxide and water. The organic layer was dried ($MgSO_4$) and concentrated to get ester (4b) 11·5 g, 80%) m.p. 109–111° (benzene-hexane); IR (KBr): 1720 cm^{-1}; ^1H NMR ($CDCl_3$–CCl_4): δ2·42 (*s*, 3H, CH_3), 6·73 (*d*, α-H, $J = 16$ Hz), 7·1–8·0 (*m*, 11H, Ar-H), 8·0 (*d*, β-H, overlapping with Ar-H); *m/e* 288 (M^+), 145, 143, 117, 91. Found: C, 83·60; H, 5·46; $C_{20}H_{16}O_2$ required C, 83·33; H, 5·55.

3.2 1-*Naphthyl* α-*methylcinnamate* (4*c*)

From α-methylcinnamoyl chloride and 1-naphthol (50 mmol) the ester (4c) was prepared (9·5 g, 66%) m.p. 98–9° (benzene-hexane); IR (KBr): 1750 cm^{-1}; ^1H NMR ($CDCl_3$–CCl_4): 2·37 (*s*, 3H, CH_3), 7·3–8·17 (*m*, 12H, ArH), 8·23 (*s*, β-H). *m/e*, 288 (M^+), 145, 143, 117, 91, 77. Found: C, 83·40; H, 5·56; $C_{20}H_{16}O_2$ requires C, 83·33; H, 5·55.

1-Naphthyl cinnamate (4a) was prepared as above from cinnamoyl chloride (50 mmol) and 1-naphthol (50 mmol) in 87% yield; m.p. 108–9° (benzene-hexane) (lit. m.p. 109–110°) (Jean d' Ans and Zimmer 1952).

3.3 *Irradiation of* 1-*naphthyl cinnamate* (4*a*)

The ester (4a) (1·0 g) in dry benzene (100 ml), taken in a quartz vessel, was flushed with nitrogen and irradiated in a Rayonet photochemical reactor Model RPR-208 equipped with eight RUL-208 lamps of wavelength 254 nm. The reaction was followed by TLC when the solution turned yellow. The irradiation was stopped after 10 hours, even though the TLC showed the presence of starting material (4a), since the formation of 1-naphthol increased with increase in irradiation time (as per TLC). The solution was concentrated and the mixture (showing only 3 spots on TLC) was chromatographed over a column of silica gel. Elution with hexane furnished 2-cinnamoyl-1-naphthol (5a) as an orange-red solid (0·2 g, 20%) m.p. 127–8°; IR ($CHCl_3$): 1630 cm^{-1}; ^1H NMR ($CDCl_3$): δ7·2–8·0 (*m*, 13H, Ar-H, α-H, β-H), 14·77 (*s*, 1H, OH); *m/e* 274 (M^+), 197, 171, 143, 142, 131, 115, 103, 91, 77. Found: C, 83·30; H, 5·15; $C_{19}H_{14}O_2$ requires C, 83·20; H, 5·10.

On elution with a mixture of benzene-hexane (1:9) the ester (4a) was obtained (60 mg, 6%); a 1:1 mixture of benzene-hexane eluted only a small quantity of 1-naphthol (30 mg).

3.4 *Irradiation of* 1-*naphthyl p-methylcinnamate* (4*b*)

A solution of the ester 4b (1·0 g) in dry benzene (100 ml) taken in a quartz vessel, was irradiated with 254 nm light for 10 hours under nitrogen atmosphere. The reaction

mixture was concentrated and the residue chromatographed over a column of silica gel. Elution with hexane afforded 2-(*p*-methylcinnamoyl)-1-naphthol (5b), as an orange-red solid (0·35 g, 35%); m.p. 147–8°; IR ($CHCl_3$): 1630 cm^{-1}; ^1H NMR ($CDCl_3$–CCl_4): δ2·37 (*s*, 3H, CH_3), 7·0–8·5 (*m*, 12H, Ar-H, α-H, β-H), 14·8 (*s*, 1H, OH); *m/e* 288 (M^+), 197, 171, 145, 117, 102, 91. Found: C, 83·52; H, 5·48; $C_{20}H_{16}O_2$ requires C, 83·33; H, 5·55.

Elution with a 1:9 mixture of benzene-hexane gave the ester (4b) (0·1 g, 10%), while a 1:1 mixture of benzene-hexane gave 1-naphthol (70 mg).

3.5 *Irradiation of* 1-*naphthyl* α-*methylcinnamate* (4c)

The ester 4c (1·0 g) in benzene solution (100 ml) was irradiated for 10 hr with 254 nm light. The yellow solution was concentrated and the residue chromatographed over a silica gel column. Elution with hexane furnished a brown liquid, showing a yellow spot on TLC, which, however, could not be purified further even by preparative TLC. Hence the suspected chalcone (5c) could not be characterized.

3.6 *Treatment of the chalcone 5a with HCl gas*

The chalcone (5a, 0·5 g) was dissolved in methanol and HCl gas passed through the solution and kept at room temperature for 2 days. After concentration under reduced pressure the residue obtained was chromatographed over a column of silica gel. Elution first with hexane furnished the starting material (5a) (25 mg, 5%) while later elutions with a mixture of benzene and hexane (1:9) yielded 7,8-benzoflavanone (6a) as a pale yellow solid (45 mg, 9%); m.p. 112–113° IR (KBr): 1670 cm^{-1}; ^1H NMR ($CDCl_3$–CCl_4): δ2·9–3·1 (*m*, 2H, CH_2), 5·5–5·75 (*dd*, 1H, C<u>H</u>–CH_2), 7·2–8·5 (*m*, 11H, Ar-H). Found C, 83·27; H, 5·08. $C_{19}H_{14}O_2$ requires C, 83·20; H, 5·10. The poor yield is probably due to loss of material in chromatography.

3.7 *Treatment of* 2-(*p-methylcinnamoyl*)-1-*naphthol* (5b) *with HCl gas*

Treatment of 5b (500 mg) in methanol with HCl gas, as above, followed by chromatography over a silica gel column furnished a light brown solid (50 mg) mp 120–1°, tentatively identified as 4′-methyl-7,8-benzoflavanone (6b); IR (KBr): 1660–70 cm^{-1}; ^1H NMR ($CDCl_3$–CCl_4): δ2·4 (*s*, 3H, CH_3), 2·85–3·2 (*m*, 2H, CH_2), 5·4–5·6 (*dd*, 1H, C<u>H</u>-CH_2), 7·1–8·2 (*m*, 10H, Ar-H).

Acknowledgements

We wish to thank Professors Walter Lwowski and J H Boyer for mass spectral data, Dr R Balasubramanian for microanalysis and Professor S Swaminathan for facilities and the UGC, New Delhi, for financial assistance.

References

Crouse D J, Hurlbut S L and Wheeler D M S 1981 *J. Org. Chem.* **46** 374
Jean d' Ans and Zimmer H 1952 *Chem. Ber.* **85** 585 *cf* 1953 *Chem. Abstr.* **47** 1666c
Manimaran T, Jayachandran T and Ramakrishnan V T 1980 *Proc. Indian Acad. Sci (Chem. Sci.)* **89** 301
Ramakrishnan V T and Kagan J 1970 *J. Org. Chem.* **35** 2901

Reaction of ethyl bromoacetate with substituted naphthoate ions

K RAJASEKARAN and C GNANASEKARAN*
Department of Chemistry, VHNSN College, Virudhunagar 626 001, India

MS received 17 October 1985; revised 25 March 1986

Abstract. Rate constants for the reaction of ethyl bromoacetate with three series of substituted naphthoate ions have been measured in an acetone-water mixture (90% v/v). Using σ_p values rate constants at 30° correlate well with the Hammett equation yielding $\rho = -0{\cdot}54$, $-0{\cdot}19$ and $-0{\cdot}25$ for (4, 1-), (6, 1-) and (6, 2-) series, respectively. Comparison of these ρ values with those of the reaction of phenacyl bromide reveals the failure of the reactivity-selectivity principle RSP in these reactions. Failure of RSP has been explained in terms of isoselective temperature.

Keywords. Ethyl bromoacetate; substituted naphthoate ions; Hammett equation; reactivity-selectivity principle; isoselective relationship.

1. Introduction

The reactivities of α-haloketones and α-haloesters towards nucleophilic reagents have been subjects of investigation over several decades. The reaction between α-halo compounds and nucleophiles is a simple S_N2 reaction. The formation of intermediates in these reactions has been ruled out by Thorpe and Warkentin (1973). Various mechanisms have been proposed to explain the activation caused by the α-carbonyl group. Dewar (1949) first suggested that the α-carbonyl group stabilises the transition state through resonance delocalisation and that the partial Nu · · · C and C · · · X bonds must be necessarily aligned with the π-plane of the carbonyl group so that the excess negative charge on the central carbon can be delocalised into the π* molecular orbital. This was supported by Bordwell and Brannen (1964). In a variation of this idea, Winstein *et al* (1951) postulated that delocalisation could be assisted by bridging of the nucleophile between the α-carbon and the carbonyl carbon in the transition state as shown in scheme 1. In contrast, Pearson *et al* (1952) invoked an electrostatic effect to explain the α-carbonyl enhancement. The carbonyl group induces an electron deficient centre at the carbon with the halogen atom, thereby attracting the nucleophile towards

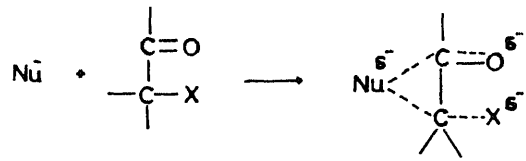

Scheme 1

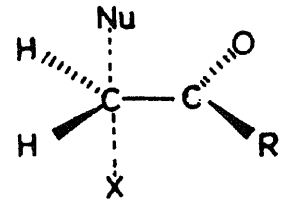

R = Ph or OEt

itself. Experiments conducted by Thorpe and Warkentin (1973) suggest that electrostatic effects are not the major reason for the rate enhancement. Evidence indicating a definite geometric requirement in the transition state was furnished by Bartlett and Trachtenberg (1958). Theoretical calculations conducted on the S_N2 transition state by Wolfe *et al* (1982) and Kost and Aviram (1982) indicate a perpendicular geometry for the transition state as shown below. It is only in such an arrangement that the developing partial negative charge on the α-carbon can be effectively delocalised into the π^*_{CO} orbital (consistent with Dewar mechanism) or the nucleophile undergo partial interaction with the carbonyl group leading to bridging (as in the Winstein scheme).

Although the kinetics of the reactions of α-haloketones with different kinds of nucleophiles have been studied, relatively little attention has been paid towards the reactivity of α-haloesters. In this paper, we report our investigations on the S_N2 kinetics of ethyl bromoacetate (EBA) with several substituted naphthoate ions.

2. Results and discussion

The reaction between EBA and the naphthoate ion follows second order kinetics and can be represented by (1).

$$X\text{-}C_{10}H_6COO^- + BrCH_2COOC_2H_5 \rightarrow$$
$$X\text{-}C_{10}H_6COOCH_2COOC_2H_5 + Br^- \qquad (1)$$

The products were found to be exclusively naphthoylglycolates, as characterised by their analytical data (table 1). The bimolecular rate constants for the reaction of EBA with several substituted naphthoate ions are given in table 2.

The second order rate constants for the reaction of 1-naphthoate ion with phenacyl bromide (PB) and EBA are respectively $2{\cdot}78 \times 10^{-2}$ dm^3 mol^{-1} s^{-1} (Rajasekaran and Gnanasekaran 1982) and $2{\cdot}48 \times 10^{-3}$ dm^3 mol^{-1} s^{-1} (table 2) at 35°. These values show that EBA is less reactive than PB. The electron withdrawing ability of the carbethoxy group is greater than that of the carbonyl group. Based on electronic effects alone it may be expected that EBA should react at a faster rate than PB if the activation caused by the α-carbonyl group is only due to inductive electron withdrawal as suggested by Pearson *et al* (1952). But the experimental results are quite contrary to this expectation and this suggests that the electrostatic effects are not the major reason for the rate enhancement of the reaction of α-halocompounds.

Table 1. Analytical data.

Substituent	m.p. (°C)	Molecular formula	Observed (%) C	Observed (%) H	Required (%) C	Required (%) H
		Ethyl 4-substituted 1-naphthoylglycolates				
H	35	$C_{15}H_{14}O_4$	70·0	5·0	69·8	5·4
F	64	$C_{15}H_{13}O_4F$	65·1	4·9	65·2	4·7
Cl	43	$C_{15}H_{13}O_4Cl$	61·7	4·6	61·6	4·4
CH_3	59	$C_{16}H_{16}O_4$	70·4	6·0	70·6	5·9
NO_2	216	$C_{15}H_{13}O_6N$	59·5	4·0	59·4	4·2
		Ethyl 6-substituted 2-naphthoylglycolates				
H	76	$C_{15}H_{14}O_4$	69·9	5·8	69·8	5·4
F	61	$C_{15}H_{13}O_4F$	65·4	4·9	65·2	4·7
Br	99	$C_{15}H_{13}O_4Br$	53·4	4·0	53·4	3·9
CN	91	$C_{16}H_{13}O_4N$	67·6	4·5	67·8	4·6
CH_3	88	$C_{16}H_{16}O_4$	70·5	6·1	70·6	5·9
OCH_3	82	$C_{16}H_{16}O_5$	66·8	5·7	66·7	5·6

Table 2. Rate constants for the reaction of ethyl bromoacetate with substituted naphthoate ions in 90% (v/v) actone-water mixture.

Substituent	10^4k / $mol^{-1}dm^3s^{-1}$ 30°	35°	40°	E_a / $kJmol^{-1}$	$\Delta H^{\neq}$ / $kJmol^{-1}$	$-\Delta S^{\neq}$ / $JK^{-1}mol^{-1}$
			Sodium 4-substituted 1-naphthoates			
OMe	21·0	28·9	41·6	51·9	49·4	132·2
CH_3	19·6	26·6	38·0	53·5	51·0	128·4
H	16·3	24·8	36·3	56·9	54·4	118·8
F	15·0	22·5	32·4	59·4	56·9	111·3
Cl	12·3	16·6	26·9	61·1	58·6	107·5
Br	12·3	16·2	26·4	61·1	58·6	107·5
NO_2	5·8	9·6	14·2	70·3	67·8	83·3
			Sodium 6-substituted 1-naphthoates			
OMe	17·4	25·2	37·0	59·0	56·5	111·3
CH_3	16·8	25·0	36·9	61·5	59·0	103·4
Cl	14·0	22·0	32·0	64·8	62·3	94·1
Br	14·0	22·0	32·0	64·8	62·3	94·1
CN	11·6	18·2	27·0	66·5	64·0	90·0
			Sodium 6-substituted 2-naphthoates			
OMe	10·0	17·0	25·0	74·5	72·0	65·7
CH_3	9·4	16·5	24·0	75·3	72·8	62·8
H	8·6	15·6	22·8	76·6	74·1	59·4
F	7·8	14·2	21·5	79·5	77·0	50·6
Cl	7·4	13·7	20·9	81·6	79·1	43·9
Br	7·4	13·7	20·9	81·6	79·1	43·9

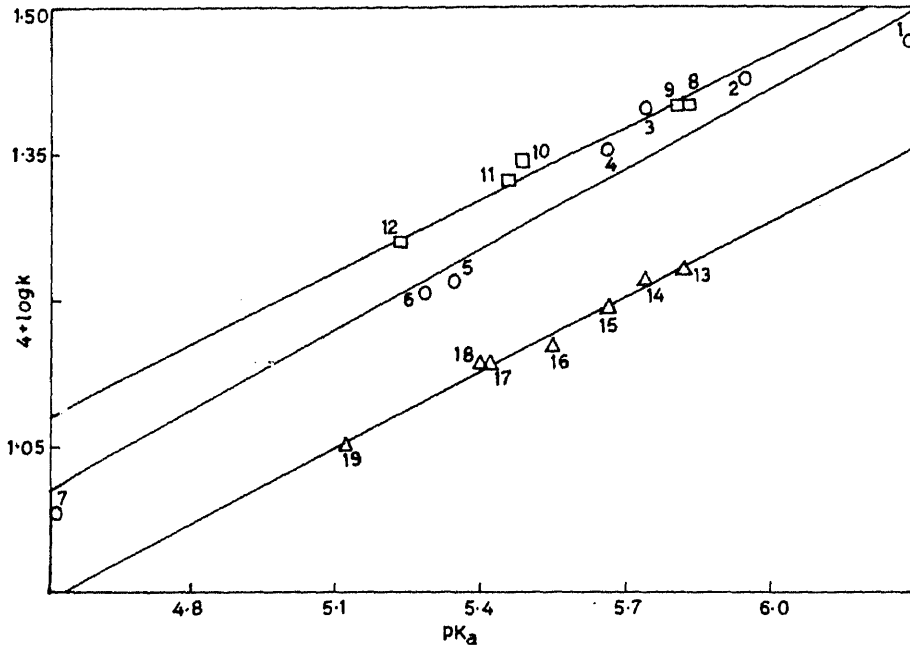

Figure 1. Brönsted plot for the reaction of EBA with substituted naphthoate ions. O: 4, 1-series; □: 6, 1-series; Δ: 6, 2-series.

rate of the reaction depends on the electron density on the oxygen atom of the carboxylate ion. The logarithm values of the rate constants are found to be linearly related to the pK_a of the corresponding naphthoic acids (figure 1). The Brönsted coefficients, α, are found to be 0·32, 0·28 and 0·28 for the (4, 1-), (6, 1-) and (6, 2-) series respectively at 35°. The smaller α values indicate little bond formation in the transition state (Mohanty and Nayak 1975).

The values of activation energy show a regular variation with nature of substituents; electron-attracting substituents increase and electron-releasing substituents decrease the activation energy. The entropies of activation are negative as expected for bimolecular reactions. The plots of $\Delta H^{\neq}$ versus $\Delta S^{\neq}$ are linear for all the three series. The linear relationship between $\Delta H^{\neq}$ and $\Delta S^{\neq}$ is indicative of a single mechanism operating throughout the series (Bowden *et al* 1964).

The rate data for the reaction of EBA with substituted naphthoate ions have been correlated with σ_p constants (table 3) and, for comparison, the rate data for the reaction of PB with naphthoate ions (Baliah and Ananthakrishna Nadar 1977; Ananthakrishna Nadar and Gnanasekaran 1975; Rajasekaran and Gnanasekaran 1982) have also been correlated with σ_p constants (table 3). Good correlations were obtained in all cases.

Table 3. Hammett reaction constants for the reaction of EBA and PB with naphthoate ions.

System	Reactant	Temperature (°C)	ρ	r	s
4,1-	EBA	30	−0·54±0·01	0·993	0·017
4,1-	EBA	35	−0·48±0·02	0·972	0·031
4,1-	EBA	40	−0·45±0·03	0·979	0·041
4,1-	PB	30	−0·59±0·03	0·980	0·042
4,1-	PB	35	−0·56±0·03	0·984	0·038
6,1-	EBA	30	−0·19±0·01	0·991	0·009
6,1-	EBA	35	−0·15±0·01	0·980	0·013
6,1-	EBA	40	−0·15±0·01	0·980	0·012
6,1-	PB	30	−0·17±0·01	0·983	0·011
6,1-	PB	35	−0·15±0·01	0·970	0·014
6,2-	EBA	30	−0·25±0·02	0·981	0·015
6,2-	EBA	35	−0·19±0·01	0·991	0·009
6,2-	EBA	40	−0·15±0·01	0·994	0·005
6,2-	PB	30	−0·39±0·04	0·925	0·039
6,2-	PB	35	−0·21±0·01	0·987	0·009

fact that EBA is less reactive than PB, the ρ values for the two reactions are almost the same and this indicates the failure of RSP in these reactions.*

When plots of selectivity log (k_{PB}/k_{EBA}) versus log $(k_{PB})_{rel}$ are made for the (4, 1-) and (6, 2-) series at 35°, all the substituents show almost the same selectivity. The selectivity will depend on temperature (Geise 1977) according to (2) if the competing reactions have different activation enthalpies.

$$\log k_2/k_1 = [(\Delta H_2^{\neq} - \Delta H_1^{\neq})/2{\cdot}303\,RT] - [(\Delta S_2^{\neq} - \Delta S_1^{\neq})/2{\cdot}303\,R] \quad (2)$$

The selectivity values will coincide at the isoselective temperature (T_{iso}), i.e. $\delta \log k_2/k_1 = 0$ and hence (2) reduces to (3).

$$[\delta(\Delta H_2^{\neq} - \Delta H_1^{\neq})/2{\cdot}303\,RT_{iso}] - [\delta(\Delta S_2^{\neq} - \Delta S_1^{\neq})/2{\cdot}303\,R] = 0. \quad (3)$$

Equation (3) can be rearranged as follows:

$$\delta(\Delta H_2^{\neq} - \Delta H_1^{\neq}) = T_{iso}\delta(\Delta S_2^{\neq} - \Delta S_1^{\neq}). \quad (4)$$

Thus the isoselective temperature can be obtained from the slope of the plot of $\delta(\Delta H_2^{\neq} - \Delta H_1^{\neq})$ versus $\delta(\Delta S_2^{\neq} - \Delta S_1^{\neq})$.

If the variation of the reactants x_m or the partners y_n can be described by linear free energy relationships, the reaction parameters of the individual series of reaction series are essentially equal at the isoselective temperature. The RSP is applicable only above or

* The referees have pointed out that "the breakdown of RSP is meaningful only for reactions proceeding by the same mechanism and this may not be the case in the systems studied, because carbonyl participation is conceivable for the reactions of PB but not for those of EBA. Also, the magnitude and variation in ρ values are too small to make a strong case for the failure of RSP. Finally, the most systematic way of examining the problem would be by studying the rate for different nucleophiles". Assuming that the failure of RSP is indeed

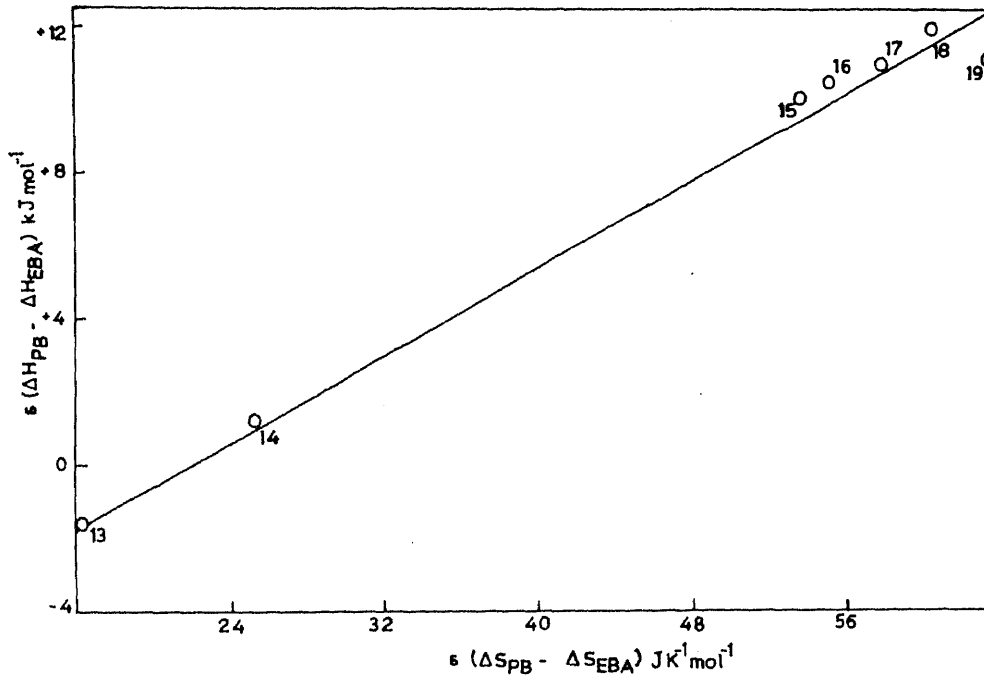

Figure 2. Plot of $\delta(\Delta H^{\neq}_{PB} - \Delta H^{\neq}_{EBA})$ versus $\delta(\Delta S^{\neq}_{PB} - \Delta S^{\neq}_{EBA})$ for 6, 2-series. $\Delta H^{\neq}_{PB}$ and $\Delta S^{\neq}_{PB}$ are from Ananthakrishna Nadar and Gnanasekaran (1975).

below the isoselective temperature (Giese 1977). A plot of $\delta(\Delta H^{\neq}_{PB} - \Delta H^{\neq}_{EBA})$ versus $\delta(\Delta S^{\neq}_{PB} - \Delta S^{\neq}_{EBA})$ is linear (figure 2; $r = 0{\cdot}990$; $n = 7$) for the (6, 2-) series and from the slope, the isoselective temperature is found to be 20°. A similar plot for the (4, 1-) series ($r = 0{\cdot}997$; $n = 7$) yields the isoselective temperature as 40°. The experimental and the isoselective temperatures are close to each other. This may be the possible cause for the failure of RSP in these reactions.

3. Experimental

All the naphthoic acids were prepared as described by Ananthakrishna Nadar and Gnanasekaran (1978) and converted into sodium salts. Acetone was purified by standard methods and the course of the reaction was followed by estimating the amount of bromide ion formed, by Volhard's method.

Acknowledgement

References

Ananthakrishna Nadar P and Gnanasekaran C 1975 *Indian J. Chem.* **13** 1237
Ananthakrishna Nadar P and Gnanasekaran C 1978 *J. Chem. Soc. Perkin* **2** 672
Baliah V and Ananthakrishna Nadar P 1977 *Indian J. Chem.* **B15** 272
Bartlett P D and Trachtenberg E N 1958 *J. Am. Chem. Soc.* **80** 5808
Bordwell F G and Brannen W T 1964 *J. Am. Chem. Soc.* **86** 4654
Bowden K, Chapman N B and Shorter J 1964 *J. Chem. Soc.* 3370
Dewar M J S 1949 *The electronic theory of organic chemistry* (Oxford: Oxford University Press)
Giese B 1977 *Angew. Chem., Int. Ed.* **16** 125
Hammond G S 1955 *J. Am. Chem. Soc.* 77 334
Kost D and Aviram K 1982 *Tetrahedron Lett.* 4157
Mohanty T R and Nayak P L 1975 *J. Chem. Soc. Perkin* **2** 242
Pearson R G, Langer S H, Williams F V and McGuire W J 1952 *J. Am. Chem. Soc.* **74** 5130
Rajasekaran K and Gnanasekaran C 1982 *Indian J. Chem.* **B21** 599
Thorpe J W and Warkentin J 1973 *Can. J. Chem.* **51** 927
Winstein S, Grunwald E and Jones W H 1951 *J. Am. Chem. Soc.* 73 2700
Wolfe S, Mitchell D J and Schlegel H B 1982 *Can. J. Chem.* **60** 1291

Proc. Indian Acad. Sci. (Chem. Sci.), Vol. 97, No. 1, July 1986, pp. 55–61.
© Printed in India.

Kinetics of the reaction of alkyl bromides with nucleophiles containing nitrogen atoms

T JANARDHAN RAO, G PUNNAIAH and E V SUNDARAM*
Department of Chemistry, Kakatiya University, Warangal 506 009, India

MS received 9 September 1985; revised 21 November 1985

Abstract. Kinetics of the reactions of propyl, propargyl and allyl bromides with anilines has been studied in methanol and dipolar DMF. All reactions were found to be of second order. The values of the Bronsted slope (0·4) suggested that bond formation occurs to a considerable extent in the transition state. Electron-donating substituents increased the rate, while electron-withdrawing groups decreased the rate. The magnitudes of the negative values (≈ 1) indicate that the reaction rate depends on the availability of electron-density on the nitrogen atom, which implies bond formation, suggesting that all the reactions are SN^2 in nature, forming a loose transition state. Isokinetic temperature values calculated from the three methods for the reaction of allyl bromide-anilines suggested that the reaction series in DMF is entropy controlled while in a methanol medium hydrogen bonding is responsible for the solute-solvent interactions.

Keywords. Kinetics; anilines; alkyl bromides; Hammett relationship; thermodynamic parameters; hydrogen bonding.

1. Introduction

The literature survey showed that work on bimolecular nucleophilic substitution reactions of alkyl bromides with anilines is meagre. Particularly, propyl, propargyl and allyl bromides have received little attention. Crocker and Jones (1959), and Panigrahi and Sinha (1977) studied the kinetics of allyl bromide with anilines to some extent but not of propyl and propargyl bromides. Vorob eV (1941) reported that the rate constants for the reaction of pyridineallyl bromide were greater than those of dimethyl aniline-allyl bromide.

Notwithstanding these results, the lack of a systematic investigation of the substituent effect and solvent effect is evident.

Para- and meta-substituted anilines can transmit the electronic effects to the reaction site through their inductance and resonance and this may be different in protic and aprotic solvents. Hence, in the present investigation the effect of the solvents methanol and DMF on the magnitude of the polar substituent effect at 30°C has been studied. The effect of temperature on the reaction of allyl bromide with selected nucleophiles has been studied to evaluate thermodynamic parameters.

2. Experimental

The various solid anilines are commercial products which are purified to constant

propargyl bromide (Fluka) and *n*-propyl bromide (BDH-AR) were distilled and collected at their respective boiling points. The purity of the compounds was checked by estimating the bromide present in the compound by Volhard's method. Methanol and DMF were purified by standard procedures and used for the experiment.

10 ml of nucleophile (0·02 M) and 10 ml of alkyl bromide (0·02 M) were placed separately in two boiling test tubes and placed in a thermostat for about 15 minutes to attain thermal equilibrium. The two solutions were mixed and a dry conductivity cell was placed in the reaction mixture. The progress of the reaction was followed by measuring the resistance of the reaction mixture using an Elico conductivity bridge type CM-82 T at known intervals of time.

3. Results and discussion

All reactions between alkyl bromides and aniline nucleophiles followed second order kinetics, first order each with respect to alkyl bromide and base, proved by the linear plots of $(R/R-R_\infty)$ versus time. The rate constants calculated by the procedure of Frost and Pearson (1970), were reproducible with an error of $\pm$ 2–3 %. Rate constants are given in table 1.

3.1 *Bronsted relationship*

Acid-base strength is used as a model process for correlating nucleophilic reactions not because it is a good model, but mainly because it is a convenient one. Correlations are sought between the logarithm of the rate constant and the pK_a of the reagent though such correlations are less susceptible to interpretation because the model process and the reaction under study are quite different. In our present study of para- and meta-substituted anilines in the three reaction series, all compounds react quite in consonance with their basicity. A good linear relationship between log k and pK_a is observed in protic methanol and aprotic DMF. From the slopes of the lines the Bronsted coefficients are calculated and recorded in table 1.

The Bronsted coefficient value of about 0·4 in methanol and DMF can be taken to imply that bond formation with the aniline base used occurs to a considerable extent in the transition state.

3.2 *Common mechanism*

In order to determine whether a common or a different mechanism operates in all the reactions log k propargyl bromide is plotted against log k_n-propyl bromide.

A fair linear relationship is observed in both the solvents with slopes equal to unity indicating the same mechanism. To confirm this hypothesis, a plot of log k_p-anisidine versus log k_p-Cl aniline is also drawn. A good linear plot is observed, though only three points on each straight line represent the solvents methanol and DMF. The slopes of these lines are approximately equal to one, implying that all the nucleophiles react by the same mechanism irrespective of different β-carbon hybridization in the substrates

3.3 *Substituent effect*

Examination of the rate constants that are listed in table 1, reveals that the rate depends on the electron-withdrawing or electron-releasing character of the substituent attached to the aromatic ring. It is evident that the electron-donating substituent in the aniline increases the rate, while electron-withdrawing groups decrease the rate.

A plot of log k against σ yielded a straight line. From the slopes of the linear plots of log k versus σ, the values of the reaction parameter are calculated and recorded in table 1. The magnitudes of ρ indicate the susceptibility of alkyl bromides to substituent electronic effects at the reaction site. The observed Hammett correlation (negative slope) indicates that the reaction rate depends on the availability of electron density on the nitrogen atom, which implies bond formation. Further the negative values of ρ (≈ 1) suggest that all the reactions are SN^2 in nature and form a loose transition state (Ballisteri *et al* 1976; Grob and Schlageter 1977).

3.4 *Temperature effect*

Reactions of all the nucleophiles with allyl bromide are studied in the temperature range 25–45°C in methanol and 30–50°C in DMF. The Arrhenius parameter ΔE and the thermodynamic parameters $\Delta S^{\neq}$, $\Delta H^{\neq}$ and $\Delta G^{\neq}$ are collected in table 2. Variation of ρ values has been recorded in table 3.

The isokinetic temperature β has been calculated by the following three methods and computed in table 4: (i) $\Delta H^{\neq}$ versus $\Delta S^{\neq}$ plot; (ii) Exner's plot; (iii) ρ temperature relation.

The values of isokinetic parameter β calculated from the above three relations are in good agreement with each other in DMF, but unsynchronised and inconsistent in methanol. This trend unequivocally proves that the reaction series in DMF is entropy controlled. Since the experimental temperature range (303–323° K) is above the isokinetic temperature for the solvent DMF, the increase in magnitude of the negative ρ values with increase in temperature is a characteristic phenomenon of entropy controlled reactions. Since the ρ value is insensitive to the variation of temperature in methanol medium, the β value cannot be calculated by the third method.

3.5 *Solute-solvent interaction*

To determine the nature of the reaction series in methanol, the help of Hepler's equation is invoked. Exner's relationship as well as the ρ-β relation failed to provide any conclusion in regard to the nature of the reaction series in methanol. But the conventional isokinetic plot of $\Delta H^{\neq}$ versus $\Delta S^{\neq}$ (figure 1) showed the tendency of scatter which is discriminating and characteristic of the nature and position of the groups. This observation together with the ideas put forward by Hepler (1963), Laidler (1959) and Ritchie and Sagar (1964), suggest that if the enthalpy and entropy changes are resolved into external and internal components, a relationship may exist between the external parameters. In this treatment external contributions to enthalpy and entropy are associated with solvent interactions, and internal contributions arise from differences in enthalpy and entropy within the reactant molecules and the transition state. If the reasonable assumption is made that the internal motions of the substituents

Table 1. Second order rate constants, Bronsted coefficients and reaction constants for the reactions of alkyl bromide with substituted anilines; their pK_a and σ values in the solvents DMF and MeOH.

hile	Ionisation constant at 30°C in H_2O	Substituent constant	DMF rate constant $k_2 \times 10^5$ M^{-1} sec^{-1}			MeOH rate constant $k_2 \times 10^5$ M^{-1} sec^{-1}		
			Allyl bromide	Propargyl bromide	*n*-propyl bromide	Allyl bromide	Propargyl bromide	*n*-propyl bromide
aniline	5·35	−0·27	813·00	457·00	23·00	169·00	79·40	4·27
niline	5·08	−0·17	501·00	308·00	17·01	141·00	56·20	3·24
	4·59	0·00	327·00	222·00	11·04	91·00	40·80	2·21
aniline	4·20	0·12	255·00	158·00	7·80	63·00	31·60	1·78
line	3·98	0·23	199·00	121·00	6·31	50·00	25·80	1·42
coefficient (α)	—	—	0·43	0·41	0·39	0·40	0·37	0·35
parameter	—	—	−1·28	−1·16	−1·08	−1·00	−0·95	−0·91

omide] = [propargyl bromide] = [nucleophile] = 0·01 M, temperature = 30°C [*n*-propyl bromide] = [nucleophile] = 0·05 M.

Table 2. Thermodynamic parameters for the reaction of allyl bromide with substituted aniline in the solvents DMF and MeOH at 30°C.

nt	Second order rate constant at 30°C $k_2 \times 10^5$ M^{-1} s^{-1}		Activation energy ΔE kcal/mole		Enthalpy of activation $\Delta H^{\neq}$ kcal/mole		Entropy of activation $-\Delta S^{\neq}$ e.u.		Free energy of activation kcal/mole		$\Delta H^{\neq} + 2{\cdot}303\,RT\rho\sigma$ kcal/mole (MeOH)
	DMF	MeOH	DMF	MeOH	DMF	MeOH	DMF	MeOH	DMF	MeOH	
	81·30	16·91	11·80	16·00	11·19	15·40	32·00	21·00	20·00	21·76	15·77
	50·10	14·10	12·30	14·77	11·69	14·16	31·00	25·30	21·07	21·84	14·39
	32·70	9·88	10·89	15·43	10·28	14·82	36·40	24·00	21·30	22·10	14·80
	25·50	9·51	10·22	16·05	9·61	15·44	39·20	22·50	21·48	22·27	15·20
	19·90	6·31	9·70	17·04	9·09	16·79	41·40	18·70	21·60	22·40	16·47

Table 3. Variation of ρ with temperature for the reaction of allyl bromide with substituted anilines in DMF and MeOH.

Temperature (K)	Reaction constant	
	DMF	MeOH
303	−1·28	−1·00
313	−1·35	−0·97
323	−1·42	−0·98

Table 4. Different β values for the reaction of allyl bromide with substituted anilines in DMF and MeOH.

Method	Value of β (K)	
	DMF	MeOH
$\Delta H^{\neq}$ versus $\Delta S^{\neq}$ plot	220	360
Exner's plot	225	151
ρ-temperature relation	200	—

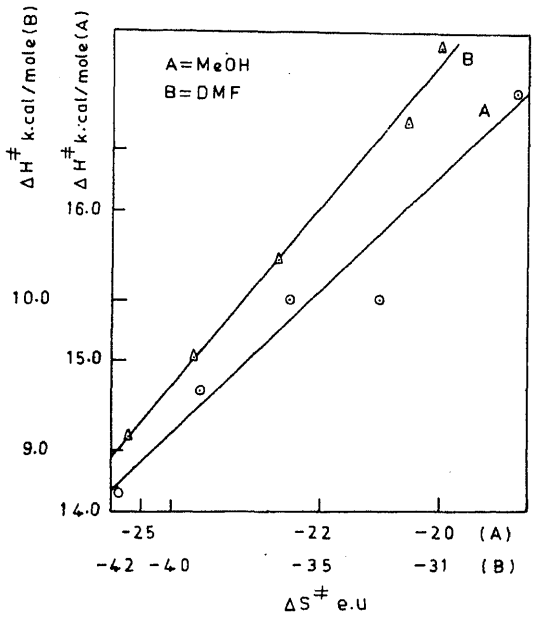

Figure 1.

following equations (Lee 1963, 1964) may be used as a test of external entropy and enthalpy relationship:

$$\Delta H^{\neq} + 2{\cdot}303\, RT\rho\sigma = b\,\Delta S^{\neq}$$

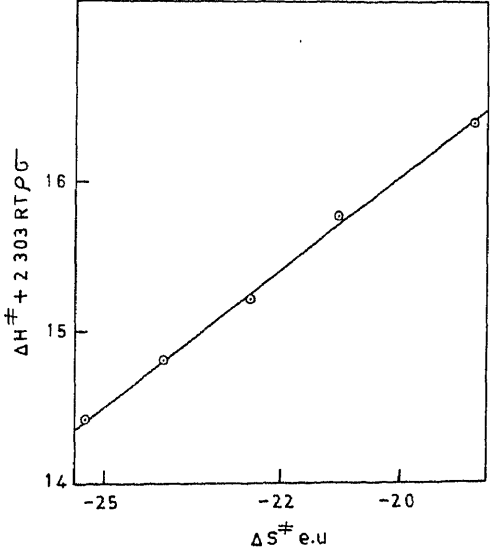

Figure 2.

30°C for the allyl bromide-aniline reaction (table 3), b is a constant, a characteristic of the reaction, which can be obtained from the slope of a plot of $\Delta H^{\neq} + 2{\cdot}303\,RT\rho\sigma$ against $\Delta S^{\neq}$. The fair linearity of figure 2 unequivocally supports the external contributions to the enthalpy and entropy due to the interactions between the solute and solvent, which may be assumed to arise from the hydrogen bonding between the methanolic proton and the nitrogen atom of the aniline.

3.6 *Effect of solvent on reaction constant*

The effect of the reaction medium on ρ is also an important factor. This effect may be related to the ease of transmission of electronic effects not only through the molecule but also by a field effect through the solvent. Though the dielectric constants of methanol and DMF are nearly the same, the ρ value is slightly higher in DMF compared to methanol. The higher values of ρ in DMF may be partly due to its polarising effect on the electrons of the nucleophile, whereby the substrate can easily discern the nucleophile, thus leading to the higher sensitivity of the reaction, and partly due to the hydrogen bonding in methanol.

Acknowledgements

The authors (GP and TJR) are thankful to the Principal, Arts & Science College, Warangal, for encouragement. One of the authors (TJR) is grateful to the UGC, New

References

Ballisteri F P, Mamo A and Maccarone E 1976 *J. Org. Chem.* **41** 336
Crocker H P and Jones B 1959 *J. Chem. Soc.* 1808
Frost A A and Pearson R G 1970 *Kinetics and mechanism* (New Delhi: Wiley Eastern) chap. 7 and p. 36
Grob C A and Schlageter M G 1977 *Helv. Chim. Acta* **60** 1884
Hepler L G 1963 *J. Am. Chem. Soc.* **85** 3089
Laidler K J 1959 *Trans. Faraday Soc.* **55** 1725
Lee I 1963 *J. Korean Chem. Soc.* **7** 221 and 238
Lee I 1964 *Chem. Abstr.* **61** 505e, 7770e
Panigrahi G P and Sinha T K 1977 *Indian J. Chem.* **B15** 561
Ritchie G D and Sagar W F 1964 *Prog. Phys. Org. Chem.* **2** 323
Vorob eV H K 1941 *Chem. Abstr.* **35** 3881

Semecarpuflavanone—a new biflavanone from *Semecarpus anacardium* Linn.

S S N MURTHY

Organic Chemistry Laboratories, School of Chemistry, Andhra University, Waltair 530003, India

MS received 12 October 1985; revised 11 April 1986

Abstract. A new biflavanone designated as semecarpuflavanone has been recently isolated from the alcoholic extract of the nut shells of *Semecarpus anacardium* Linn. It was dehydrogenated with iodine and potassium acetate in glacial acetic acid to the corresponding, relatively more stable biflavone known as SA4. The structure of semecarpuflavanone has been established through chemical and spectroscopic studies.

Keywords. *Semecarpus anacardium*; Anacardiaceae; biflavanones; semecarpuflavanone; biflavone SA4; PMR and mass spectra.

1. Introduction

Three new biflavanones, named as galluflavanone, jeediflavanone and semecarpuflavanone, besides the three known biflavanones (Prakasa Rao *et al* 1973), 1–3 have been recently isolated from the acetone soluble fraction of the ethanolic extract of the defatted nut shells of *Semecarpus anacardium* Linn. On the basis of spectral and chemical data, structures 4 and 5 have been already assigned to galluflavanone (Murthy 1983) and jeediflavanone (Murthy 1985), respectively. The present paper deals with the isolation and structure determination of semecarpuflavanone.

2. Results and discussion

Semecarpuflavanone (6) appeared as a fine microcrystalline pale yellow powder from acetone, $C_{30}H_{22}O_{10}$, m.p. 248–49°. Preliminary characterisation showed it to be a polyhydroxybiflavanone. It exhibited UV maxima in ethanol at 291 nm which underwent a bathochromic shift (291 → 312 nm) on addition of sodium acetate to the test solution, while with aluminium chloride no such shift was observed, indicating the absence of chelated hydroxyl groups in the biflavonoid. Further, in its PMR spectrum, no low field proton could be noticed. The above observation clearly revealed that there was at least one 7-hydroxyflavanone system (Horowitz and Jurd 1961; Mabry *et al* 1970) in the molecule.

The PMR spectrum (270 MHz, acetone-d_6) of semecarpuflavanone displayed signals due to six non-chelated D_2O exchangeable hydroxylic protons at τ 1·50 (*s*, 1H), 2·24 (*s*, 1H), 2·36 (*s*, 2H) and 2·74 (*s*, 2H). Hence, the biflavonoid linkage must only be through a C–C linkage since all the ten oxygen atoms in the biflavanone (6) are accounted for by the six non-chelated hydroxyl groups and four pyranone oxygen

mole of gallic acid suggesting that one of the side-phenyls is involved in the interflavonoid linkage.

On methylation with diazomethane, semecarpuflavanone gave a pentamethyl ether (7), $C_{35}H_{32}O_{10}$, m.p. 161–62°, whose PMR spectrum ($CDCl_3$) displayed a singlet signal at τ 1·48(1H) corresponding to the non-chelated D_2O exchangeable hydroxylic proton. Further, the biflavonoid (6) on acetylation with acetic anhydride and pyridine afforded a hexaacetate (8), $C_{42}H_{34}O_{16}$, m.p. 174–76°, while with dimethyl sulphate and K_2CO_3 in dry acetone, it gave a bichalcone hexamethyl ether (9), $C_{36}H_{34}O_{10}$, m.p. 199–201°. The PMR spectrum of compound 9 showed the presence of two chelated hydroxylic protons at τ -4·20 (*s*, 1H) and -4·30 (*s*, 1H).

When semecarpuflavanone pentamethyl ether was oxidised with neutral permanganate, both syringic acid and 2-hydroxy-4-methoxybenzoic acid (identified by mixed m.p. and IR) were obtained. Hence the diaryl system must contain the remaining two methoxyl groups which are placed by analogy and PMR spectral data at the B-4′ and D-7″ positions. Consequently the biflavonoid linkage must be either at the B-3′-D-8″ position or at the B-3′-D-6″ position. Since the parent compound contains no chelated hydroxyl groups, the positions at A-5 and D-5″ are free. Further, the PMR spectra of semecarpuflavanone and its three derivatives (7–9) clearly indicated the presence of two *ortho*-coupled protons which must correspond to ring D (see §3). On the basis of this observation, the biphenyl linkage at the B-3′-D-6″ position is eliminated from consideration and hence, semecarpuflavanone must have a C–C linkage at the B-3′-D-8″ position.

Semecarpuflavanone was dehydrogenated (Pelter *et al* 1971; Murthy *et al* 1981) with iodine and potassium acetate in glacial acetic acid to the corresponding, relatively more stable biflavone designated as SA4 which appeared as a light yellow powder from acetone, $C_{30}H_{18}O_{10}$, m.p. > 300°. Preliminary characterisation showed it to be a

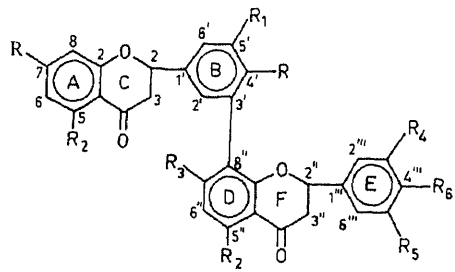

1 R = R_2 = R_4 = R_6 = OH, R_1 = R_3 = R_5 = H
2 R = R_2 = R_3 = R_6 = OH, R_1 = R_4 = R_5 = H
3 R = R_3 = R_6 = OH, R_1 = R_2 = R_4 = R_5 = H
4 R = R_1 = R_3 = R_4 = R_5 = R_6 = OH, R_2 = H
5 R = R_2 = R_3 = R_4 = R_6 = OH, R_1 = R_5 = H
6 R = R_3 = R_4 = R_5 = R_6 = OH, R_1 = R_2 = H
7 R = R_3 = R_4 = R_5 = OMe, R_6 = OH, R_1 = R_2 = H
8 R = R_3 = R_4 = R_5 = R_6 = OAc., R_1 = R_2 = H

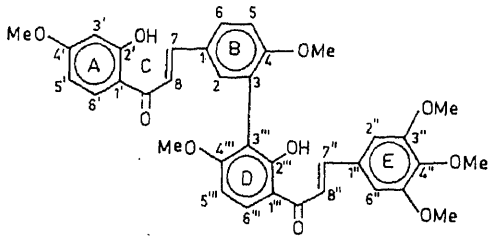

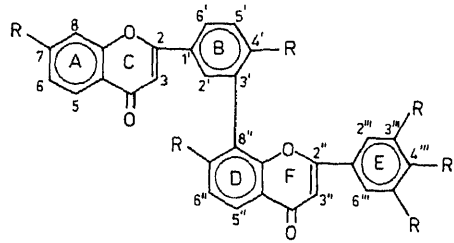

polyhydroxybiflavone. The PMR spectrum of SA4 (10) in acetone-d_6 indicated the presence of six non-chelated D_2O exchangeable hydroxyl groups at τ 1·54 (*s*, 1H), 2·14 (*s*, 2H), and 2·39 (*s*, 3H). On methylation with dimethyl sulphate and K_2CO_3, SA4 furnished a hexamethyl ether (11), $C_{36}H_{30}O_{10}$, m.p. 190–91°. Oxidation of 11 with neutral permanganate afforded only one mole of gallic acid tri-methyl ether suggesting that one of the side-phenyls is involved in the diaryl linkage.

The chemical shifts and multiplicity of protons in the PMR spectra of semecarpuflavanone (6), its three derivatives (7–9), compound SA4 (10) and its hexamethyl ether (11), fully supported the proposed structure of semecarpuflavanone (6) (see § 3).

Semecarpuflavanone pentamethyl ether (7) and SA4 hexamethyl ether (11) in their respective mass spectra showed the molecular ions (M^+) at *m/z* 612 and *m/z* 622. The peak at *m/z* 179 [3,5-$(H_3CO)_2$-4-OH-C_6H_2-CH=C^+H] arising from rings E and F in 7 not only revealed that these rings are not involved in the interflavonoid linkage but also indicated that the hydroxyl groups at positions 3‴ and 5‴ in ring E are methylated. The ion at *m/z* 151 corresponding to the fragment (12) appeared in the mass spectra of both the methyl ethers (7 and 11) indicating that the hydroxyl group at the A-7 position is methylated. The peak at *m/z* 281 corresponding to the fragment (13) in the pentamethyl ether could arise after two RDA fragmentations. There is another peak at *m/z* 282 corresponding to either of the ions (14) and (15) and these two are closely related to the fragment (13). Compound (11) also afforded the two central fragments at *m/z* 280 and *m/z* 281 corresponding to the ions (16) and (17). Similar crucial fragments were already reported in (−) succedaneaflavanone tetramethyl ether (Chen and Lin 1975) and morelloflavone heptamethyl ether (Karanjgaokar *et al* 1967). Compounds (7) and (11) showed the peaks, respectively, at *m/z* 566 and *m/z* 576, which are formed by the loss of 46 mass units. These fragments can be formulated respectively as (18) and (19) in which

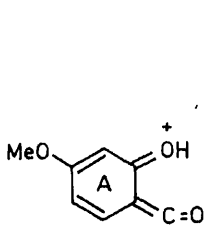

12

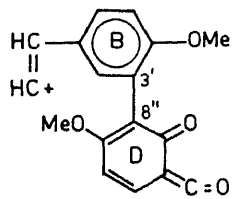

13

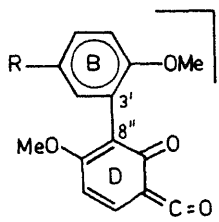

14 R = -CH=CH_2

16 R = -C≡CH

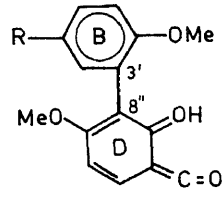

15 R = -CH=$\dot{C}$H

17 R = -C≡CH

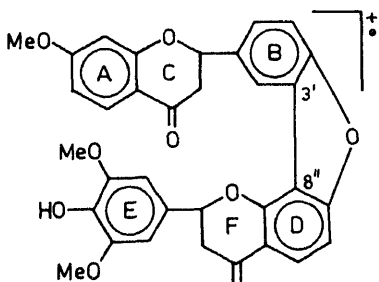

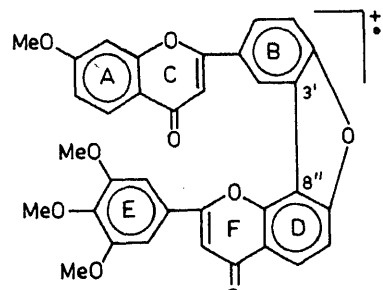

the methoxyl groups *ortho* to the biphenyl linkage cyclise to a furan ring (Natarajan *et al* 1969). Perhaps the most characteristic feature is the formation of the two fragments (13) and (18) in the pentamethyl ether (7) and the two peaks (16) and (19) in the hexamethyl ether (11) which could be sufficiently indicative or diagnostic of a C–C linkage. It may be mentioned here that similar fragments have been reported in (±) fukugetin heptamethyl ether (Konoshima *et al* 1969) and rhusflavanone (Lin and Chen 1973). Overall the mass spectral (MS) fragmentation pattern of semecarpuflavanone pentamethyl ether exhibits a close similarity to that of 2,3-dihydroamentoflavone hexamethyl ether (Varshney *et al* 1973) and GB-2 (Jackson *et al* 1971). Similarly, the MS fragmentation of SA4 hexamethyl ether showed a very close resemblance to that of amentoflavone hexamethyl ether (Natarajan *et al* 1969).

Based on the foregoing chemical and spectral evidences, structure (6) has been assigned to semecarpuflavanone with the biflavonoid linkage at the B-3′-D-8″ position.

3. Experimental

Equipment and methods used for UV, IR, PMR, MS, m.p., C and H analysis, TLC and PLC have been described elsewhere (Murthy 1985).

Isolation: On removal of solvent under reduced pressure, fraction FI (Murthy 1985) yielded a dark coloured mass from which the gummy material was separated by thorough maceration with *n*-hexane (50 ml × 3). The insoluble deep yellow residue (~ 18 gms) showed only one major spot on TLC besides a large tailing (chloroform:methanol, 5:1) and was adsorbed on silica gel (40 gms) and transferred over to a column of silica gel (110 gms, 100–200 mesh) set with chloroform. The column was eluted successively with chloroform, ether and acetone. The ether eluate afforded a deep pink colour with Mg-HCl. Hence, on removal of solvent under vacuum, the combined ether fractions furnished a yellow compound which contained two close running minor components on TLC (chloroform: methanol, 5:1) besides a small streak. The major component was separated by preparative TLC using chloroform: methanol (5:1) as the solvent for development. The compound so obtained still showed minor impurities on a thin layer chromatogram and hence it was filtered through a small column of silica gel with chloroform: acetone (5:2) as the eluent. The column fractions, on concentration under vacuum, yielded a pale yellow compound, semecarpuflavanone, which was found to be pure on a thin layer chromatoplate.

Semecarpuflavanone (6): It resisted crystallisation from normal organic solvents. On drying in a vacuum oven for six hours at 60°, semecarpuflavanone appeared as a pale yellow powder, $C_{30}H_{22}O_{10}$, m.p. 248–49°, yield: 525 mg. It gives a greenish-violet ferric reaction, a pinkish-red colour with Mg-HCl, an orange colour with $NaBH_4$-HCl and is readily soluble in aqueous NaOH giving a deep orange-yellow solution; UV (EtOH): nm, 221, 291, 333; + NaOAc, 223, 312, 335; + $AlCl_3$, 221, 292, 332; IR ν(nujol): 3520–3470 (*br*, OH), 3225 (OH), 1680 (flavanone carbonyl), 1600, 1580 (aromatic) cm^{-1}; Found: C, 66·04; H, 4·06; $C_{30}H_{22}O_{10}$ requires C, 66·42 and H, 4·09 %; PMR (270 MHz, acetone-d_6, τ values): 2·54 (*dd*, 1H, J = 2, 8·5 Hz, B-6′), 2·63 (*d*, 1H,

cis-protons, C-3, F-3″), 1·50 (*s*, 1H), 2·24 (*s*, 1H), 2·36 (*s*, 2H), 2·74 (*s*, 2H) [non-chelated D_2O exchangeable hydroxylic protons, A-7, B-4′, D-7″, E-3‴, 4‴, 5‴].

Semecarpuflavanone pentamethyl ether (7): Compound 6 (175 mg) in acetone (10 ml) was added to an ethereal solution of diazomethane till the yellow colour persisted. After the usual work-up, 7 appeared as yellow crystals from a chloroform and acetone mixture, $C_{35}H_{32}O_{10}$, m.p. 161–62°, UV (EtOH): nm, 220, 289, 332; IR ν(nujol): 3450 (OH), 2830 (OCH_3), 1685 (flavanone carbonyl), 1600, 1585 (aromatic) cm^{-1}; Found: C, 68·19; H, 5·22; OCH_3, 25·10; $C_{35}H_{32}O_{10}$ requires C, 68·62; H, 5·26 and OCH_3, 25·32 %; PMR (80 MHz, $CDCl_3$, τ values), 7·24 (*dd*, 2H, J = 3, 16 Hz, *cis*-protons, C-3, F-3″), 6·90 (*m*, 2H, *trans*-protons, C-3, F-3″), 4·60 (*q*, 2H, J = 4, 12 Hz, C-2, F-2″), 2·60–2·82 (*m*, 3H, B-2′, 5′, 6′), 3·10 (*s*, 2H, E-2‴, 6‴), 3·31 (*d*, 1H, J = 8 Hz, D-5″), 3·49 (*d*, 1H, J = 8 Hz, D-6″), 3·62 (*d*, 1H, J = 8 Hz, A-5), 3·88 (*dd*, 1H, J = 2, 8 Hz, A-6), 3·78 (*d*, 1H, J = 2 Hz, A-8), 1·48 (*s*, 1H, non-chelated D_2O exchangeable hydroxylic proton, E-4‴), 6·16 (*s*, 2 × 3H), 6·25 (*s*, 3 × 3H) [methoxyl groups, A-7, B-4′, D-7″, E-3‴, 5‴]; *m/z* (relative intensity) 612 $[M]^+$ (42), 597 $[M-15]^+$ (15), 582 $[M-2\times15]^+$ (7·6), 581 $[M-31]^+$ (8·5), 566 $[M-46]^+$ (8), 461 (11), 432 (10), 329 (9·5), 283 (6·8), 281 (29), 181 (57·5), 179 (64·6), 151 (100), 150 (72·5).

Semecarpuflavanone hexaacetate (8): To 6 (30 mg), a mixture of freshly distilled acetic anhydride (1 ml) and dry pyridine (1 ml) was added, heated on a steam-bath for four hours and worked-up in the usual manner. The hexaacetate (8) appeared as pale yellow crystals from a chloroform and methanol mixture, $C_{42}H_{34}O_{16}$, m.p. 174–76°, UV (EtOH): nm, 222, 288, 329; IR ν(nujol): 1755, 1745 ($OCOCH_3$), 1685 (flavanone carbonyl), 1600, 1580 (aromatic) cm^{-1}; Found: C, 63·06; H, 4·25; $C_{42}H_{34}O_{16}$ requires C, 63·48 and H, 4·28 %; PMR (80 MHz, $CDCl_3$, τ values), 7·26 (*dd*, 2H, J = 3, 16 Hz, *cis*-protons, C-3, F-3″), 6·86 (*m*, 2H, *trans*-protons, C-3, F-3″), 4·60 (*q*, 2H, J = 4, 12 Hz, C-2, F-2″), 2·65–2·83 (*m*, 3H, B-2′, 5′, 6′), 3·12 (*s*, 2H, E-2‴, 6‴), 3·30 (*d*, 1H, J = 8 Hz, D-5″), 3·48 (*d*, 1H, J = 8 Hz, D-6″), 3·64 (*d*, 1H, J = 8 Hz, A-5), 3·88 (*dd*, 1H, J = 2, 8 Hz, A-6), 3·80 (*d*, 1H, J = 2 Hz, A-8), 7·72 (*s*, 2 × 3H), 7·76 (*s*, 3 × 3H), 7·78 (*s*, 3H) [acetoxyl groups, A-7, B-4′, D-7″, E-3‴, 4‴, 5‴].

Bichalcone hexamethyl ether (9): A mixture of semecarpuflavanone (30 mg), freshly ignited potassium carbonate (0·5 gm) and dimethyl sulphate (0·3 ml) was refluxed in dry acetone (10 ml) on a water bath for several hours with occasional shaking. The inorganic salts were filtered off and washed well with hot acetone. The filtrate after solvent removal gave a residue which resisted crystallization from common organic solvents. On drying in a vacuum oven for six hours at 70°, 9 appeared as a pale yellow powder, $C_{36}H_{34}O_{10}$, m.p. 199–201°, yield: 25 mg. It furnished a red precipitate with antimony trichloride in carbon tetrachloride, a brown colour with neutral ferric chloride solution and was readily soluble in aqueous sodium hydroxide giving an orange-red solution. UV (EtOH): nm, 225, 381; + $AlCl_3$, 224, 436; + NaOAc, 223, 380; IR ν(nujol): 3460 (*br*, OH), 2830 (OCH_3), 1630 (chalcone carbonyl), 1595, 1580 (aromatic) cm^{-1}; Found: C, 68·67; H, 5·43; OCH_3, 29·52; $C_{36}H_{34}O_{10}$ requires C, 69·00; H, 5·47 and OCH_3, 29·71 %; PMR (80 MHz, $CDCl_3$, τ values), 2·62–2·86 (*m*, 3H, B-2, 5, 6), 3·10 (*s*, 2H, -E-2″, 6″), 3·20 (*d*, 1H, J = 8 Hz, D-6‴), 3·36 (*d*, 1H, J = 8 Hz, D-5‴), 3·62 (*d*, 1H, J = 8 Hz, A-6′), 3·84 (*dd*, 1H, J = 2, 8 Hz, A-5′), 3·78 (*d*, 1H, J = 2 Hz, A-3′), 2·22

hydroxylic proton, A-2'), −4·30 (*s*, 1H, chelated hydroxylic proton, D-2‴), 6·20 (*s*, × 3H), 6·26 (*s*, 4 × 3H) [methoxyl groups, A-4', B-4, D-4‴, E-3″, 4″, 5″]; *m/z* (relati intensity) 626 $[M]^+$ (41·5), 611 $[M-15]^+$ (11·5), 596 $[M-2\times15]^+$ (21), 595 [$-31]^+$ (7), 580 $[M-46]^+$ (7·5), 475 (10·5), 443 (9), 343 (10), 283 (9), 282 (8·5), 281 (26· 221 (14), 193 (50·5), 192 (44), 151 (100), 150 (76).

Dehydrogenation of semecarpuflavanone (6): Semecarpuflavanone (140 mg), potassiu acetate (1·5 gm) and iodine (0·3 gm) in glacial acetic acid (10 ml) were heated at refl temperature for three hours. The cooled mixture was poured into water and t reaction product was extracted with ethyl acetate. The solvent was removed und reduced pressure and a saturated solution of sodium metabisulphite (12 ml) was add to the residue to destroy excess iodine and the whole filtered. The filtrate w concentrated under vacuum when a yellow compound separated out, which has be designated as SA4.

Compound SA4 (10): It did not crystallize from normal organic solvents. Hence drying in a vacuum oven for six hours at 80°, SA4 appeared as a light yellow powd $C_{30}H_{18}O_{10}$, m.p. > 300°, yield: 105 mg. It gave a violet colour with neutral fer chloride solution, a deep pink colour with magnesium-hydrochloric acid and is read soluble in aqueous sodium hydroxide giving a deep orange-yellow solution; UV (EtO nm, 255, 302, 378; +NaOAc, 256, 327, 431; $+AlCl_3$, 255, 301, 379; IR *v* (nujo 3530–3290 (*br*, OH), 3170 (OH), 1685, 1680 (flavone carbonyls), 1600, 1585 (aromat cm^{-1}; Found: C, 66·65; H, 3·34; $C_{30}H_{18}O_{10}$, requires C, 66·92 and H, 3·37 PMR (270 MHz, acetone-d_6, τ values), 2·28 (*q*, 1H, $J = 2$, 8 Hz, B-6'), 2·43 (*d*, 1H, = 2Hz, B-2'), 2·84 (*d*, 1H, $J = 8$ Hz, B-5'), 2·90 (*d*, 1H, $J = 2$ Hz, E-6‴), 2·98 (*d*, 1H, = 2 Hz, E-2‴), 3·14 (*d*, 1H, $J = 8{\cdot}5$ Hz, D-5″), 3·34 (*d*, 1H, $J = 8{\cdot}5$ Hz, D-6″), 3·48 (*s*, 2 C-3, F-3″), 3·62 (*d*, 1H, $J = 8$ Hz, A-5), 3·74 (*d*, 1H, $J = 2$ Hz, A-8), 3·90 (*dd*, 1H, $J =$ 8 Hz, A-6), 1·54 (*s*, 1H), 2·14 (*s*, 2H), 2·39 (*s*, 3H) [non-chelated D_2O exchangeab hydroxylic protons, A-7, B-4', D-7″, E-3‴, 4‴, 5‴].

SA4 hexamethyl ether (11): SA4 (80 mg) was dissolved in dry acetone (10 ml). Fresh ignited potassium carbonate (0·8 gm) and dimethyl sulphate (0·5 ml) were introduc and the mixture was refluxed on a water bath for several hours till the reaction produ did not respond to the ferric reaction and then it was worked up as usual. T hexamethyl ether (11) appeared as light yellow crystals from a chloroform and methan mixture, $C_{36}H_{30}O_{10}$, m.p. 190–91°, UV (EtOH): nm, 252, 301, 374; IR *v* (nujol): 28 (OCH_3), 1690, 1680 (flavone carbonyls), 1595, 1580 (aromatic) cm^{-1}; Found: C, 69·2 H, 4·83; OCH_3, 29·64; $C_{36}H_{30}O_{10}$ requires C, 69·45; H, 4·86 and OCH_3 29·90 PMR (80 MHz, $CDCl_3$, τ values), 2·38–2·65 (*m*, 3H, B-2', 5', 6'), 2·92 (*s*, 2H, E-2‴, 6‴), 3· (*d*, 1H, $J = 8$ Hz, D-5″), 3·42 (*d*, 1H, $J = 8$ Hz, D-6″), 3·50 (*s*, 2H, C-3, F-3″), 3·59 (*d*, 1 $J = 8{\cdot}5$ Hz, A-5), 3·76 (*d*, 1H, $J = 2$ Hz, A-8), 3·88 (*dd*, 1H, $J = 2$, 8·5 Hz, A-6), 6·22 (*s*, × 3H), 6·30 (*s*, 4 × 3H) [methoxyl groups, A-7, B-4', D-7″, E-3‴, 4‴, 5‴]; *m/z* (relati intensity) 622 $[M]^+$ (82), 607 $[M-15]^+$ (38), 592 $[M-2\times15]^+$ (19·5), 591 $[M-31]$ (24), 576 $[M-46]^+$ (9), 560 $[M-2\times31]^+$ (6·5), 472 (11), 430 (10·5), 341 (8·5), 281 (280 (30), 195 (70·5), 192 (78), 151 (100), 150 (47·5).

Oxidation of semecarpuflavanone (6) *with neutral permanganate*: A mixture of semeca puflavanone (100 mg) and potassium permanganate (100 mg) in dry acetone (15 m was left at room temperature for one hour. The solvent was then evaporated and t

residue diluted with water. The manganous salts were decomposed with sulphur dioxide and extracted with ether. The ether extract was shaken with 1% aqueous sodium bicarbonate solution, acidified with dilute hydrochloric acid and again extracted with ether, dried and evaporated. The residue on crystallization from water afforded colourless needles, m.p. 250–51° (decomp.), yield: 14 mg; identical with an authentic sample of gallic acid (mixed m.p. and IR).

Oxidation of semecarpuflavanone pentamethyl ether (7) *with neutral permanganate*: A mixture of 7 (100 mg) and potassium permanganate (100 mg) in dry acetone (15 ml) was left at room temperature for one hour and worked up in the usual manner. The residue was extracted with hot benzene and concentrated, when a solid substance separated out. It appeared as colourless crystals from a chloroform and benzene mixture, m.p. 204°, yield: 12 mg; identical with authentic syringic acid (mixed m.p. and IR). The residual solid was crystallised from chloroform and methanol mixture as colourless needles, m.p. 155–56°, yield: 10 mg; identical with an authentic sample of 2-hydroxy-4-methoxybenzoic acid (mixed m.p. and IR).

Oxidation of SA4 hexamethyl ether (11) *with neutral permanganate*: Compound 11 (50 mg) was oxidised with neutral permanganate (50 mg) in dry acetone (10 ml) for one hour. After the usual working up of the reaction mixture, the residue on crystallization from a chloroform and methanol mixture appeared as colourless prisms, m.p. 172–73°, yield: 5 mg; identical with an authentic sample of gallic acid trimethyl ether (mixed m.p. and IR).

Acknowledgements

I am grateful to Professor L R Row for encouragement. My thanks are also due to Drs P A Ramaiah and M Bapuji for recording technical help.

References

Chen F C and Lin Y M 1975 *Phytochemistry* **14** 1644

Horowitz R M and Jurd L 1961 *J. Org. Chem.* **26** 2446

Jackson B, Locksley H D, Scheinmann F and Wolstenholme W A 1971 *J. Chem. Soc. C* 3791

Karanjgaokar C G, Radhakrishnan P V and Venkataraman K 1967 *Tetrahedron Lett.* 3195

Konoshima M, Ikeshiro Y, Nishinaga A, Matsura T, Kubota T and Sakamoto H 1969 *Tetrahedron Lett.* 121

Lin Y M and Chen F C 1973 *Tetrahedron Lett.* 4747

Mabry T J, Markham K R and Thomas M B 1970 *The systematic identification of flavonoids* (New York: Springer) pp. 165–171

Murthy S S N 1983 *Phytochemistry* **22** 2636

Murthy S S N 1985 *Phytochemistry* **24** 1065

Murthy S S N, Prakasa Rao N S, Anjaneyulu A S R and Ramachandra Row L 1981 *Planta Med.* **43** 46

Natarajan S, Murti V V S and Seshadri T R 1969 *Indian J. Chem.* 7 751

Pelter A, Rahman W, Warren R, Chexal K K and Handa B K 1971 *Tetrahedron* **27** 1625

Prakasa Rao N S, Ramachandra Row L and Brown R T 1973 *Phytochemistry* **12** 671

Varshney A K, Talat M, Khan N U, Rahman W, Hwa C W, Okigawa M and Kawano N 1973 *Indian J. Chem.* **11** 1209

Proc. Indian Acad. Sci. (Chem. Sci.), Vol. 97, No. 1, July 1986, pp. 71–75.
© Printed in India.

Solid phase synthesis of the signal sequence of *E. coli* alkaline phosphatase

G LAXMA REDDY and R NAGARAJ*

Centre for Cellular & Molecular Biology, Uppal Road, Hyderabad 500007, India

MS received 11 February 1986

Abstract. A synthetic peptide corresponding to the signal sequence of *E. coli* alkaline phosphatase has been synthesized by the solid phase method employing the transesterification method of cleavage from the resin. The protected peptide obtained after cleavage was purified to homogeneity by column chromatography on silica gel, followed by partition chromatography on Sephadex LH-20 using organic solvents like chloroform and methanol as eluants.

Keywords. Signal sequence; solid phase synthesis; transesterification; partition chromatography.

1. Introduction

Proteins destined for export in eukaryotic and prokaryotic cells are synthesized as precursors with amino terminal extensions (signal sequences) varying between 15–40 residues (Silhavy *et al* 1983). The signal sequences of secretory proteins are characterized by a positively charged region followed by a 15–20 residue stretch of apolar amino acids (Watson 1984). The precursor regions of mitochondrial proteins are much larger and apolar and charged residues are distributed uniformly (Hay *et al* 1984). Extensive studies using biochemical (Walter *et al* 1984), recombinant DNA (Lingappa *et al* 1984; Duffaud *et al* 1985) and genetic (Bankaitis *et al* 1985; Benson *et al* 1985) techniques have revealed the following facts: (i) there is no primary structure homology among signal sequences (ii) introduction of a charged amino acid in the hydrophobic region renders a signal sequence non-functional (iii) signal sequences can initiate export of cytoplasmic proteins and also target them to organelles like chloroplasts and mitochondria (iv) proteins that recognize signal sequences are components of the cells' export machinery.

In spite of the large amount of information available in the intracellular sorting of proteins, questions like, what are the common recognition elements in signal sequences? and how do signal sequences actually initiate translocation of polypeptide chains across membranes? are still unanswered. Structural and other physico-chemical studies on signal sequences which should help in answering these questions have been few (Briggs and Gierasch 1984; Katakai and Iizuka 1984; Laxma Reddy and Nagaraj 1985; Rosenblatt *et al* 1980; Shinnar and Kaiser 1984) presumably due to the difficulties in obtaining signal sequences in sufficient amounts. An approach based on chemical

proteins is technically very difficult (Ito 1982). In fact, the few structural studies that have been reported are based on synthetic signal peptides. In an effort to generate signal sequences in sufficient amounts for structural studies, which are amenable to post synthetic modifications, we had explored the transesterification method of cleavage in the solid phase synthesis of signal peptide fragments (Laxma Reddy and Nagaraj 1985) and obtained protected peptides in good yields which could be easily purified by column chromatography on silica gel employing organic solvents. In this paper we describe the synthesis of a 20-residue peptide corresponding to the signal sequence of *E. coli* alkaline phosphatase (Silhavy *et al* 1983) shown below, employing the transesterification method of cleavage.

Lys-Gln-Ser-Thr-Ile-Ala-Leu-Ala-Leu-Leu-Pro-Leu-Leu-Phe-Thr-Pro-Val-
1 5 10 15
Thr-Lys-Ala
20

2. Experimental

2.1 *Materials*

Amino acids, dicyclohexylcarbodiimide (DCC), diisopropylethylamine (DIEA), 1-hydroxybenzotriazole (HOBT) and chloromethylated polystyrene co 1% divinyl benzene (200–400 mesh, 1·03 m eq/gm) were purchased from the Sigma Chemical Co, Mo, USA. Trifluoro acetic acid (TFA) was from Fluka, Switzerland. Protected amino acids were prepared by established methods (Stewart and Young 1984). Dichloromethane (CH_2Cl_2) was distilled over P_2O_5 and Na_2CO_3. DIEA was distilled over ninhydrin. The protecting groups employed were *t*-butyloxycarbonyl (Boc) for α-NH_2 groups, benzyloxycarbonyl (Z) for ε-NH_2 group of Lys and benzyl (Bzl) for the OH of Ser.

2.2 *Assembly of the peptide chain*

The first amino acid (Ala at the 20th position) was attached to the resin by the cesium salt procedure of Gisin (1973). A substitution of 20% i.e. 0·2 mmol of Ala for 1 gm of resin was used for the synthesis. Substitution was estimated by the picric acid method (Gisin 1972). The Boc amino acids of Ser (OBzl), Thr, Ala, Phe and Val were coupled as symmetric anhydride which were prepared as follows: the Boc amino acid (1·2 mmols) was dissolved in CH_2Cl_2 cooled to 4°C and DCC (1·2 mmols) added. After 15 minutes at 4°C, the DCC urea was filtered off and the CH_2Cl_2 solution of the Boc amino acid symmetric anhydride was used for coupling. The Boc amino acids of Leu, Ile, Pro and Lys (ε-Z) were coupled with DCC. Boc Gln was coupled with DCC and HOBT in DMF/CH_2Cl_2 2:8 (*v*/*v*). Each coupling was performed twice. After the addition of Ala at the 16th position, each coupling was performed thrice. The couplings were monitored by the picric acid test (Gisin 1972). Solid-phase reactions were carried out on

symmetric anhydride method of coupling was not employed (9) 50% ethanol/CH_2Cl_2 wash, 15 ml, 3 × 2 min (10) CH_2Cl_2 wash, 15 ml, 3 × 2 min (11)–(14) were similar to operations (7)–(10). After step (14), chain termination was effected by acetylation with acetic anhydride:pyridine:benzene 1:3:3, 15 ml, 2 × 10 min. The coupling time for Boc Gln was 24 hours. At the end of the synthesis, the resin was washed with methanol and dried. The weight of the resin at the end of the synthesis was 1·3 g. About 100 mg of the resin was consumed for the amino acid analysis and the picric acid test during the course of the synthesis.

2.3 *Cleavage from solid support*

Cleavage of the peptide from the resin by transesterification was achieved as follows: a suspension of the peptide-resin (0·65 g) in 30 ml of anhydrous methanol and 4 ml of triethylamine was stirred under reflux for 4 hours. The resin was filtered and the methanol solution evaporated to yield the crude peptide. Three cycles of transesterification were carried out to ensure complete recovery of the peptide. From 0·650 g of resin, the amount of crude peptide obtained was 0·100 g.

2.4 *Purification by chromatography on silica gel*

The crude, fully protected peptide (80 mg) was first purified by column chromatography on silica gel (30 × 2 cm). The sequence of elution was as follows: (1) 200 ml $CHCl_3$ (2) 200 ml 2% MeOH/$CHCl_3$ (3) 200 ml 4% MeOH/$CHCl_3$ and (4) 1000 ml 5% MeOH/$CHCl_3$. About 400 fractions of 4 ml each were collected. Thin layer chromatography (tlc) profiles in 10% MeOH/$CHCl_3$ (peptides visualized by starch/KI) indicated that fractions 231–325 were similar. These fractions were pooled and evaporated to yield 20 mg of peptide which gave the following amino acid analysis on a LKB 4151 alpha plus analyzer after hydrolysis in TFA/HCl 1:2 in vacuum for 24 hours: Ser 0·55 (1), Lys 1·66 (2), Glx 0·64 (1), Thr 2·71 (3), Ile 0·50 (1), Ala 2·90 (3), Leu 4·58 (5), Pro 1·82 (2), Phe 1·00 (1), Val 1·20 (1). Values in parentheses indicate theoretical values. Since the amino acid analysis was not satisfactory and tlc indicated heterogeneity, the peptide was further purified by partition chromatography on sephadex LH-20 (Anggard and Bergkvist 1970).

2.5 *Purification by partition chromatography*

20 g of Sephadex LH-20 was refluxed in MeOH for 14 hours. The resin was filtered and air dried for 12 hours. The dry resin was allowed to swell in 30% MeOH/$CHCl_3$ for 2 hours. The peptide (20 mg) was dissolved in 0·5 ml 30% MeOH/$CHCl_3$, applied to the column (bed dimensions: 60 × 1 cm) and eluted with 30% MeOH/$CHCl_3$. Fifty fractions of 1 ml each at a flow rate 0·1 ml/min were collected. Pure peptide (homogeneous on tlc) was obtained in fractions 24–28. The remaining fractions (29–32) were pooled and the impure peptide was again purified in the same manner. The total yield of pure peptide was 10 mg.

The protecting groups were removed by treatment with TFA/thioanisole (Bodanszky

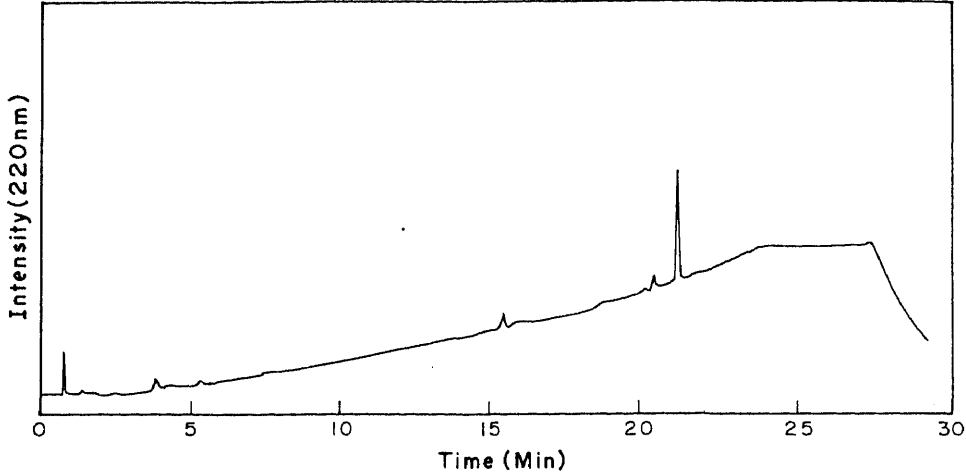

Figure 1. High pressure liquid chromatographic analysis of the synthetic *E. coli* alkaline phosphatase signal peptide. Conditions: solvent A = 50% MeOH/H_2O, solvent B = 0·05% TFA in MeOH, linear gradient of 0–100% B into A in 30 min, 0·25 ml/min; detection at 220 nm.

and Bodanszky 1984) and chromatographed on a small sephadex LH-20 column. The purified deprotected peptide was analysed by high pressure liquid chromatography on a Hewlett Packard C-18 microbore column (100 × 2·1 mm, 5 μM) in a Hewlett Packard HP 1090 instrument and was found to be homogeneous (figure 1). Amino acid analysis after hydrolysis in TFA/HCl 1 : 2 for 24 hours (Shinnar and Kaiser 1984) in vacuum was as follows: Thr 2·02 (3), Ser 0·59 (1); Glx 1·00 (1); Ala 3·17 (3); Val 1·00 (1); Ile 1·02 (1), Leu 5·19 (5); Phe 1·01 (1); Lys 2·20 (2); Pro 2·11 (2). Numbers in parentheses are theoretical values. The TFA/HCl method is known to yield low recovery of Thr and Ser as a result of partial degradation of these amino acids.

3. Results and discussion

The synthesis of the *E. coli* alkaline phosphatase signal peptide has been achieved on a solid support employing well established protocols for solid-phase peptide synthesis (Stewart and Young 1984). However, cleavage of the peptide from the solid support was accomplished by transesterification, a method not commonly used now-a-days. Although cleavage by anhydrous HF is extensively used in solid-phase peptide synthesis (Barany and Merrifield 1980) considerable difficulties were experienced in the purification of a signal peptide obtained by this method (Rosenblatt *et al* 1979). Apart from generating protected peptide suitable for post synthetic modifications for physico-chemical studies, the transesterification method of cleavage also aids in purification, as the protected peptides show good solubility in organic solvents. Since most signal sequences have amino acids with short side chains like Gly, Ala or Ser at the carboxy terminus, steric hindrance is unlikely to reduce yields in the transesterification reaction. Hence, in the solid-phase synthesis of signal sequences, cleavage by transesterification would be more advantageous than by other methods commonly

Acknowledgement

We thank Mr M V Jagannadham for amino acid analysis.

References

Anggard E and Bergkvist H 1970 *J. Chromatogr.* **50** 251
Bankaitis V A, Ryan P J, Rasmussen B A and Bassford P J Jr 1985 in *Current topics in membranes and transport* (ed.) F Bonner, New York: Academic Press, vol. 24, p. 151
Barany G and Merrifield R B 1980 in *The peptides* (eds) E Gross and J Meienhofer vol. 2 (New York: Academic Press)
Benson S A, Hall M N and Silhavy T J 1985 *Annu. Rev. Biochem.* **54** 101
Bodanszky M and Bodanszky A 1984 *Int. J. Pept. Protein Res.* **23** 287
Briggs S M and Gierasch L M 1984 *Biochemistry* **23** 3111
Duffaud G D, Lehnhardt S K, March P E and Inouye M 1985 in *Current topics in membranes and transport* (ed.) F Bonner vol. 24, p. 65 (New York: Academic Press)
Gisin B F 1972 *Anal. Chim. Acta* **58** 248
Gisin B F 1973 *Helv. Chim. Acta* **56** 1476
Hay R, Bohni P and Gasser S 1984 *Biochim. Biophys. Acta* **779** 65
Ito K 1982 *J. Biol. Chem.* **257** 9895
Katakai R and Iizuka Y 1984 *J. Am. Chem. Soc.* **106** 5715
Laxma Reddy G and Nagaraj R 1985 *Biochim. Biophys. Acta* **831** 340
Lingappa V R, Chaidez J, Yast S C and Hedgpeth J 1984 *Proc. Natl. Acad. Sci. (USA)* **81** 456
Rosenblatt M, Habener J F, Tyler G A, Shepard G L and Potts Jr J T 1979 *J. Biol. Chem.* **254** 1414
Rosenblatt M, Beaudette N V and Fasman G D 1980 *Proc. Natl. Acad. Sci. USA* 77 3983
Shinnar A E and Kaiser E T 1984 *J. Am. Chem. Soc.* **106** 5006
Silhavy T J, Benson S A and Emr S D 1983 *Microbiol. Rev.* **47** 313
Stewart J M and Young J D 1984 in *Solid phase peptide synthesis*, 2nd ed, (USA: Pierce Chemical Co)
Walter P, Gilmore A and Blobel G 1984 *Cell* **38** 5
Watson M E E 1984 *Nucleic Acids Res.* **12** 5145

Enthalpies of complex formation of dibutyl and tributyl amines with isomeric butanols†

SHIRISH D PRADHAN* and GOPAL PATHAK
Physical Chemistry Division, National Chemical Laboratory, Pune 411008, India

MS received 11 July 1985; revised 2 April 1986

Abstract. Enthalpies of complex formation (ΔH_c) of dibutyl and tributyl amines with the four isomeric butanols were determined at 30°C. The present data were compared with the previous data on isomeric butanols with monobutyl amine complexes. The ΔH_c in the case of *n*-alcohol has been found to decrease by about $4{\cdot}0 \pm 0{\cdot}4$ kJ/mole on replacement of each hydrogen atom of the NH_2 group. The branching of the butyl chain, also, decreases the strength of the complex due to steric hindrance.

Keywords. Calorimetry; amine-alcohol interactions; isomeric effect; steric effect; enthalpy of complexes.

1. Introduction

The study of interactions between associated liquids is of considerable academic and practical interest. In earlier work in this series we have reported the study of isomeric and steric effects of primary alcohols and amines on their intermolecular interactions (Pradhan and Pathak 1980a, b, 1984). The present investigation deals with the study of interactions between the molecules of dibutyl amine and tributyl amine with those of isomeric butanols. A comparison of the values of enthalpy of complex formation between dibutyl and tributylamines with isomeric butanol helps us in understanding the effect of the hydrogen atoms of the NH_2 group on the hydrogen bonded complexes, as well as the isomeric effect on the intermolecular interactions.

2. Experimental

n-Hexane (SD Chemicals, AR), isomeric butanols (BDH, AR), *n*-butyl amine, dibutyl amine and tributylamine (Fluka) were purified by fractional distillation. All the compounds were dried over freshly activated molecular sieves.

A 1:1 Complex of each system was prepared by making an equimolar mixture of amine and alcohol. The enthalpies of mixing of these complexes with *n*-hexane were measured at concentrations below the 0·05 mole fraction of the complex at 30°C using the dewar type calorimeter. Experimental details are given in an earlier communication (Pradhan and Pathak 1980).

† NCL Communication No. 3864

3. Results and discussion

The enthalpies of mixing of butanols-dibutyl amine and butanols-tributyl amine complexes with *n*-hexane have been reported in table 1. All the systems show endothermic behaviour due to the breaking of hydrogen bonded complexes. The partial molar enthalpies of the complex may therefore be taken as the enthalpy of complex formation (Savini *et al* 1965). The plot of $\Delta H/x_1x_2$ versus mole fraction of the complex (x_1) for dibutyl amine and tributyl amine complexes are presented in figures 1 and 2 respectively.

The enthalpies of complex formation obtained by extrapolating the $\Delta H/x_1x_2$ versus x_1 curves to infinite dilution ($x_1 \rightarrow 0$) for these systems are reported in table 2 along with the values for isomeric butanol-monobutyl amine systems for ready comparison. It may be observed from table 2 that in all the systems containing the isomers of alcohol,

Table 1. Enthalpies of mixing of butanol-dibutylamine and butanol-tributylamine complexes with *n*-hexane at 30°C.

	Dibutylamine			Tributylamine		
Alcohol	X_1	ΔH (J/mole)	$\Delta H/x_1x_2$ (kJ/mol)	X_1	ΔH (J/mole)	$\Delta H/x_1x_2$ (kJ/mol)
n-BuOH	0·0018	62 ± 0·5	34·5 ± 0·3	0·0014	42 ± 0·5	30·0 ± 0·3
	0·0020	65 ± 0·5	32·6 ± 0·2	0·0021	58 ± 0·5	27·7 ± 0·2
	0·0042	123 ± 0·5	29·4 ± 0·1	0·0029	76 ± 0·5	26·3 ± 0·2
	0·0048	139 ± 0·5	29·1 ± 0·1	0·0048	109 ± 0·5	22·8 ± 0·1
	0·0080	189 ± 1·0	23·8 ± 0·1	0·0095	183 ± 1·0	19·4 ± 0·1
	0·0095	211 ± 1·0	22·4 ± 0·1	0·0141	238 ± 1·0	17·1 ± 0·1
	0·0102	219 ± 1·0	21·7 ± 0·1	0·0147	236 ± 1·0	16·3 ± 0·1
	0·0201	332 ± 1·0	16·9 ± 0·1	0·0366	371 ± 2·0	10·5 ± 0·2
iso-BuOH	0·0024	74 ± 0·5	30·9 ± 0·3	0·0014	39 ± 0·5	27·9 ± 0·3
	0·0048	140 ± 0·5	29·3 ± 0·2	0·0028	73 ± 0·5	26·2 ± 0·2
	0·0080	207 ± 1·0	26·1 ± 0·1	0·0051	126 ± 1·0	24·8 ± 0·2
	0·0106	257 ± 1·0	24·5 ± 0·1	0·0094	202 ± 1·0	21·7 ± 0·1
	0·0137	300 ± 1·0	22·2 ± 0·1	0·0134	252 ± 1·0	19·1 ± 0·1
	0·0190	371 ± 2·0	19·9 ± 0·1	0·0180	289 ± 1·0	16·3 ± 0·1
sec-BuOH	0·0015	48 ± 0·5	32·1 ± 0·3	0·0021	59 ± 0·5	28·2 + 0·3
	0·0045	126 ± 0·5	28·1 ± 0·2	0·0030	80 ± 0·5	26·7 ± 0·3
	0·0097	235 ± 1·0	24·5 ± 0·2	0·0051	128 ± 1·0	25·2 ± 0·2
	0·0124	270 ± 1·0	22·0 ± 0·1	0·0064	151 ± 1·0	23·7 ± 0·2
	0·0184	334 ± 1·0	18·2 ± 0·1	0·0099	212 ± 1·0	21·6 ± 0·1
	0·0224	389 ± 2·0	17·8 ± 0·1	0·0137	254 ± 1·0	18·8 ± 0·1
	0·0337	466 ± 2·0	14·3 ± 0·1	0·0190	314 ± 1·0	16·9 ± 0·1
	0·0515	541 ± 2·0	11·1 ± 0·1	0·0302	411 ± 2·0	14·4 ± 0·1
tert-BuOH	0·0024	75 ± 0·5	31·3 ± 0·3	0·0018	50 ± 0·5	27·9 ± 0·3
	0·0052	146 ± 1·0	28·2 ± 0·3	0·0054	134 ± 0·5	24·9 ± 0·3
	0·0098	242 ± 1·0	24·9 ± 0·2	0·0099	218 ± 1·0	22·2 ± 0·2
	0·0125	280 ± 1·0	22·7 ± 0·2	0·0162	305 ± 1·0	19·1 ± 0·2
	0·0156	340 ± 1·0	22·1 ± 0·1	0·0262	362 ± 1·0	14·2 ± 0·1
	0·0173	350 ± 1·0	20·6 ± 0·1	0·0412	475 ± 2·0	12·0 + 0·1

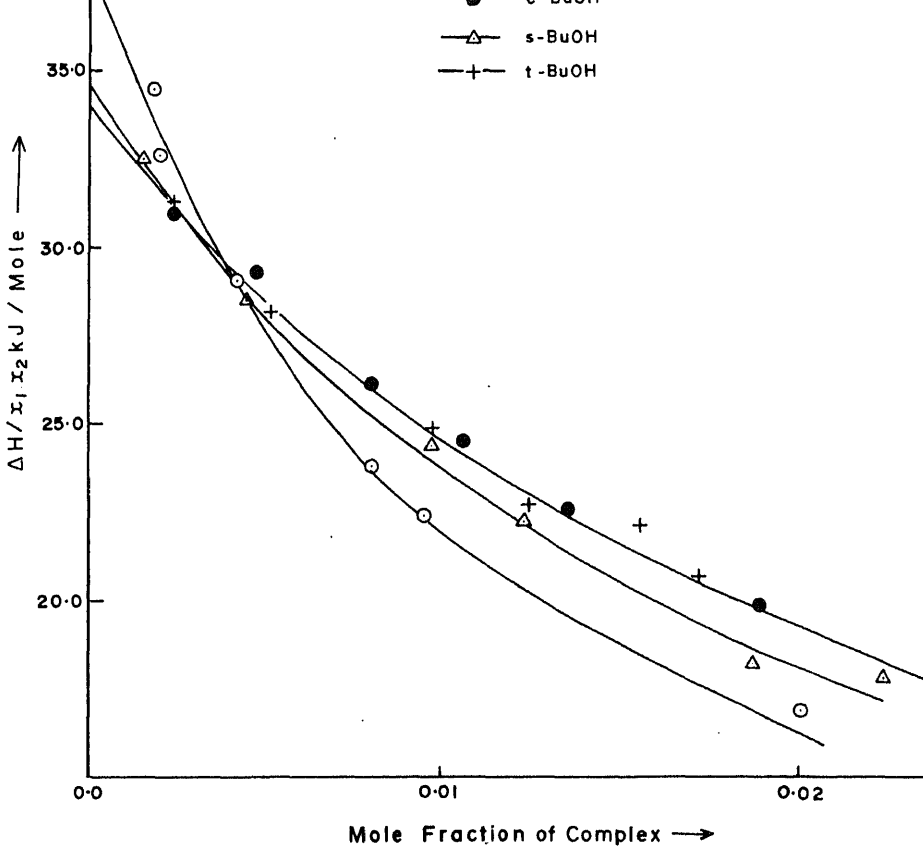

Figure 1. $\Delta H/x_1x_2$ versus mole fraction of the complex (x_1) for dibutyl amine complexes.

the enthalpy of complex formation decreases as

monobutyl amine > dibutylamine > tributyl amine.

Huyskins *et al* (1960) and Lambert *et al* (1963) from their studies on *n*-butyl amine-*n*-butanol system by NMR calorimetry and conductivity have concluded that *n*-butyl amine and *n*-butanol form a non-linear 1:1 type complex. The nitrogen of the NH_2 group is hydrogen bonded with the H of the OH of alcohol. The two hydrogen atoms of NH_2 group form two weak hydrogen bonds with the O of the OH group. The results of the present work support the Huyskins model of the complex, as the enthalpy of complex formation decreases by about $4{\cdot}0 \pm 0{\cdot}4$ kJ/mole on replacement of each hydrogen atom of the NH_2 group. It is seen from the tributyl amine-*n*-butanol complex that the strength of the –N – – – H bond is about $35 \pm 0{\cdot}4$ kJ/mole and the strength of the N–H – – – O–H bond is about $38{\cdot}4 \pm 0{\cdot}4$ kJ/mole.

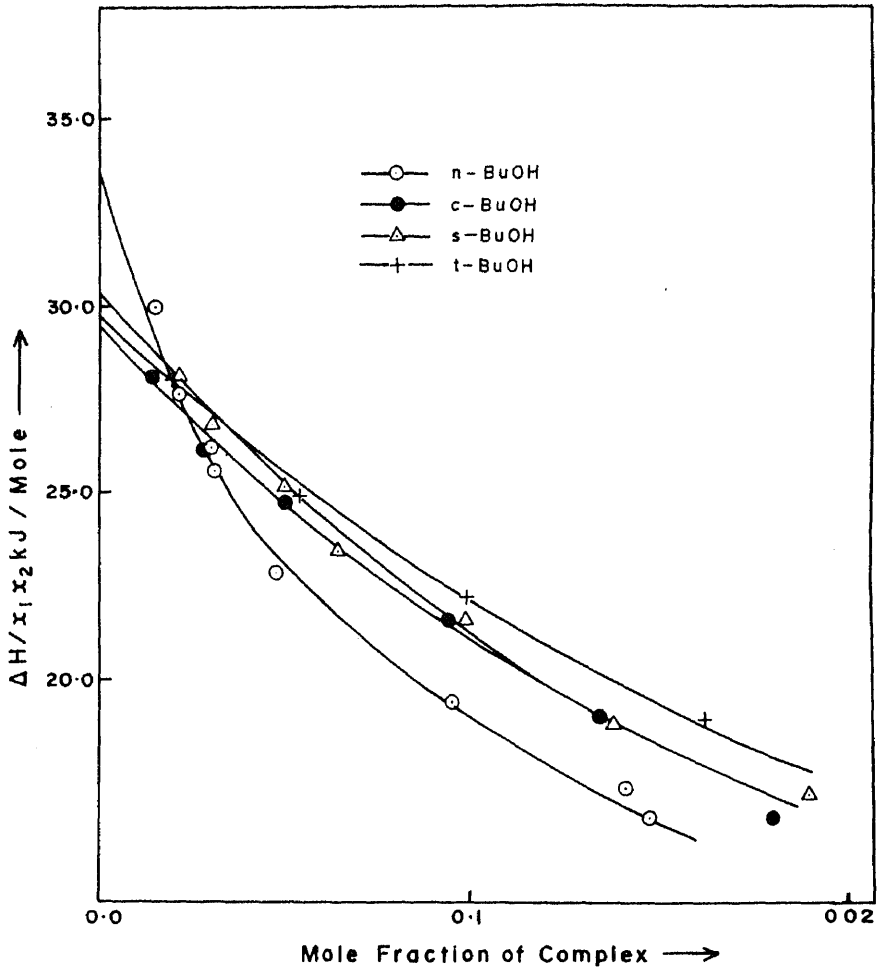

Figure 2. $\Delta H/x_1x_2$ versus mole fraction of the complex (x_1) for tributyl amine complexes.

Table 2. Enthalpies of mixing of 1:1 complexes of isomeric butanols with monobutyl amine, dibutyl amine and tributyl amine.

Alcohol	Monobutyl amine (kJ/mole)	Dibutyl amine (kJ/mole)	Tributyl amine (kJ/mole)
n-BuOH	$-42{\cdot}7 \pm 0{\cdot}4$	$-38{\cdot}4 \pm 0{\cdot}4$	$-34{\cdot}8 \pm 0{\cdot}4$
iso-BuOH	$-41{\cdot}9 \pm 0{\cdot}4$	$-34{\cdot}5 \pm 0{\cdot}4$	$-29{\cdot}5 \pm 0{\cdot}4$
sec-BuOH	$-40{\cdot}9 \pm 0{\cdot}4$	$-34{\cdot}5 \pm 0{\cdot}4$	$-29{\cdot}5 \pm 0{\cdot}4$
tert-BuOH	$-43{\cdot}1 \pm 0{\cdot}4$	$-34{\cdot}0 \pm 0{\cdot}4$	$-29{\cdot}8 \pm 0{\cdot}4$

For all the branched isomers of alcohols the enthalpy of complex formation with dibutyl amine is about $34{\cdot}5 \pm 0{\cdot}5$ kJ/mole. The decrease in the strength of the complex

also be noted that the enthalpy of complex formation between the branched chain alcohol and dibutyl amine is nearly equal to that between tributyl amine and the normal alcohol. In the latter case there is no H atom on the amino group to form the weak hydrogen bond with the oxygen of alcohol. It seems therefore that in the case of diamine and isomeric alcohol, the weak hydrogen bond formation between the H of the NH group and the O of the OH group does not take place because of the steric repulsion by the CH_3 group present on the alcohol skeleton.

The steric effect is also apparent in the case of branched alcohol and tri-butylamine complexes. The enthalpy of complex formation of these is lowest amongst the series and is of the order of $29{\cdot}7 \pm 0{\cdot}3$ kJ/mole.

References

Huyskens Zeeger Th and Huyskens P 1960 *Bull. Soc. Chim. Belg.* **69** 267

Lambert and Huyskens Zeeger Th 1963 *J. Chim. Phys.* **60** 435

Pradhan Shirish and Pathak Gopal 1980a *Proc. Indian Acad. Sci. (Chem. Sci.)* **89** 341

Pradhan Shirish and Pathak Gopal 1980b *Proc. Indian Acad. Sci. (Chem. Sci.)* **89** 349

Pradhan Shirish and Pathak Gopal 1984 *Proc. Indian Acad. Sci. (Chem. Sci.)* **93** 831

Savini C G, Winterhalter D R and Van Nesstie 1965 *J. Chem. Eng. Data* **10** 168

Electronic and vibrational spectra of 2,4,6-trichloro- and 6-chloro-2,4-dimethoxypyrimidine

S L SRIVASTAVA*, M PRASAD† and RANJEET SINGH‡

Department of Physics, University of Gorakhpur, Gorakhpur 273 009, India
† Department of Physics, St. Andrew's College, Gorakhpur 273 001, India
‡ Department of Physics, Shivapati degree college, Shohratgarh, Basti 272 205, India

MS received 24 June 1985; revised 16 December 1985

Abstract. This paper presents the investigations of the electronic and vibrational spectra of 2,4,6-trichloropyrimidine and 6-chloro 2,4-dimethoxypyrimidine. The electronic spectra have been recorded in the liquid and vapour states in the region 50000–28000 cm^{-1}. The n-π and π-π transitions are classified in each case. Infrared absorption spectra of 2,4,6-trichloropyrimidine in nujol have been recorded in the region 4000–400 cm^{-1}. It is concluded that substituents like Cl or OCH_3 do not have much influence on the sp^2 electron of the nitrogen atom of the ring. From infrared studies the mass-dependent modes and the modes insensitive to substitution have been pointed out. The assignments are tentative and are based on the group frequency approach and data available for similar molecules.

Keywords. UV and IR spectra; 2,4,6-trichloropyrimidine; 6-chloro-2,4-dimethoxypyrimidine.

1. Introduction

Amongst the three diazines, light absorption studies of pyridazine, pyrazine and their substituted analogues have been made purely for spectroscopic purpose. Thymine, cytosine and uracil are substituted pyrimidines and are well known for their biological activity. In the case of pyrimidine and substituted pyrimidines, the aim is two-fold. Spectroscopic interest apart, investigations have also been carried out on their biological activity by many workers. The role of substituents in pyrimidines is very important. In earlier investigations on di- and tri-substituted pyrimidines (Srivastava and Rohitashava 1981; Srivastava and Prasad 1982; Srivastava *et al* 1984, 1985), tautomeric structures have been reported with OH, NH_2 and SH groups arranged at different positions on the ring and their spectra interpreted in terms of the proposed structures. For the present, we have selected two molecules, 2,4,6-trichloropyrimidine and 6-chloro 2,4-dimethoxypyrimidine, to study the effect of substitution on the π-π and n-π systems of pyrimidine. If the substituents act as electron donors a blue shift of the n-π system will be observed, since they stabilize the ground state more than the upper state. Substituents which can act as electron acceptors behave quite differently and produce larger stabilization in the excited state than in the ground state and cause a red shift of the n-π bands. In addition, the infrared absorption spectra of both molecules have been recorded and the observed bands are interpreted in terms of ring vibrations and vibrations associated with the substituent groups/atoms.

2. Experimental

Attempts were made to photograph the absorption spectra on a Hilger medium quar spectrograph in the vapour phase but no discrete bands could be obtained for either the two molecules. Hence, we recorded the electronic spectra in vapour and liquid stat with absorbing path lengths of 5 and 1 cm, respectively, on a Carl Zeiss UV-VIS doub beam spectrophotometer in the region 50000–28000 cm^{-1}. For obtaining the requir amount of vapour for absorption, the tube was heated upto 50°C. The spectra in t liquid state recorded at room temperature are shown in figures 1 and 2. An analysis the bands along with their correlation with pyrimidine and a few monosubstitut pyrimidine is presented in tables 1 and 2, respectively, for the two molecules. T accuracy of measurement of these bands is $\pm 40\ cm^{-1}$. The infrared absorpti spectrum of 2,4,6-trichloropyrimidine was recorded in the vapour phase with a gas c of path length 10 cm. The band contours could not be recorded. For 6-chloro-2, dimethoxypyrimidine the nujol mull technique was employed. The infrared spectra both the molecules recorded in the region 4000–400 cm^{-1} on a Carl Zeiss Specord 75 are shown in figures 3 and 4. The accuracy of measurement for these bands is up $\pm 7\ cm^{-1}$.

3. Discussion

Substitution of chlorine atoms at the 2,4 and 6-positions in pyrimidine, which 1,3-diazine, does not alter the symmetry of the parent molecule. Hence, the C_{2v} poi group has been ascribed to this molecule. On the other hand, the C_s point group h been ascribed to 6-chloro-2,4-dimethoxypyrimidine as there is no plane of symmet other than that containing all the atoms.

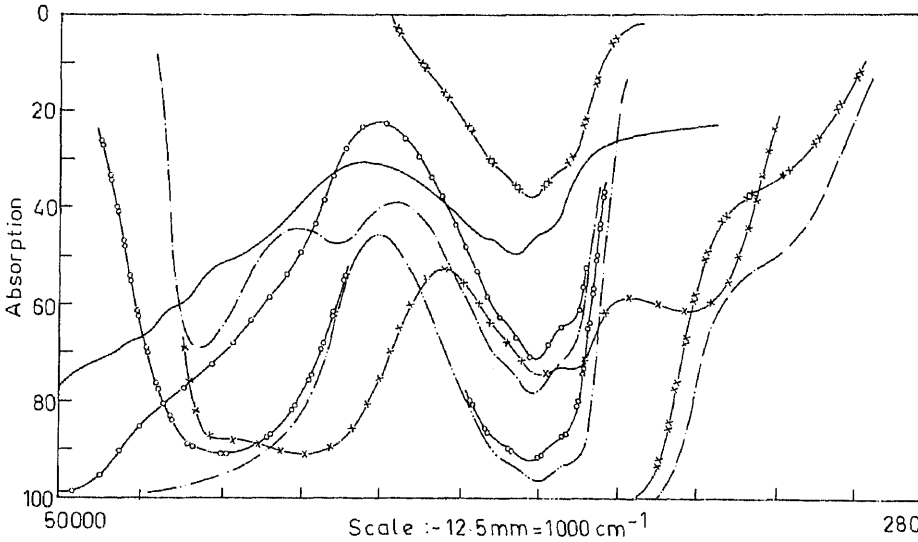

Figure 1. UV absorption spectra of 2,4,6-trichloropyrimidine in vapour (——), dioxa

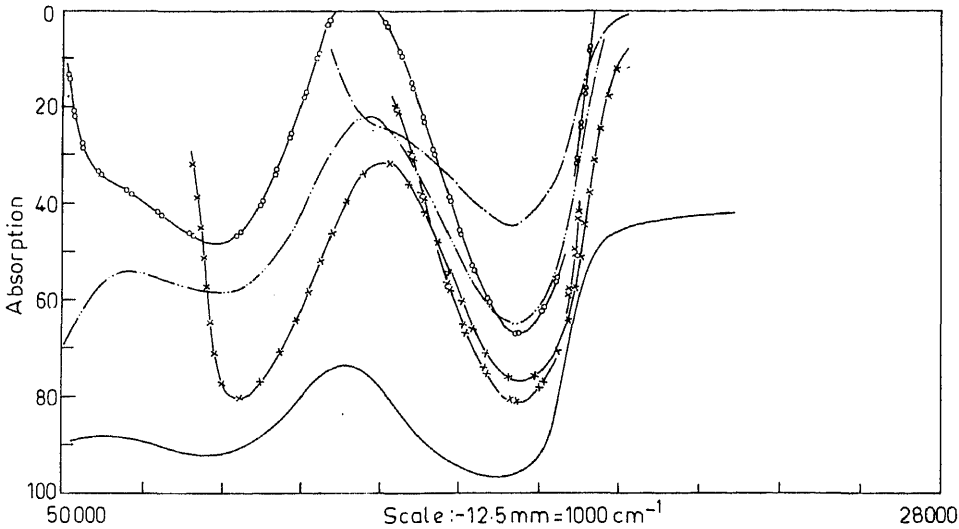

Figure 2. UV absorption spectra of 6-chloro-2,4-dimethoxy pyrimidine (explanation of symbols as in figure 1).

3.1 *Electronic spectra*

The vapour absorption spectra of 2,4,6-trichloropyrimidine show two absorption systems originating from π-π transitions. The analysis of the second π-π system shows the presence of ν_{12}, the ring-bending mode (880 cm^{-1}). This system appears with structure in all the solvents. In view of the accuracy of the bands it appears that the ν_{12} mode is excited. The first π-π system shows some structure in the vapour phase as well as in methyl alcohol but no analysis could be proposed because vibrational analyses at large energies are always doubtful due to the involvement of a large number of energy levels.

In addition to the π-π system, a transition due to the nonbonded electron of the ring nitrogen atom has also been found in solvents like dioxane, N/10 sodium hydroxide, chloroform and methyl alcohol. As expected, this system disappears in acidic solutions. The n-π and π-π systems show a blue and red shift respectively. This is in accordance with the general observations for such molecules (table 1). The intensities of the π-π transitions are greater as compared to the n-π transitions. In addition to the above transitions a band at 45200 cm^{-1} in the vapour phase, at 43000 cm^{-1} in dioxane and at 43800 cm^{-1} in N/10 sodium hydroxide, has been located. In the absence of any data no positive explanation for these bands could be made. In the electronic spectra of 6-chloro-2,4-dimethoxypyrimidine, one n-π and two π-π transitions have been classified. These show no structure either in the vapour phase or in solution. The presence of the n-π system has been noticed only in dioxane. The shift of the π-π and n-π systems follows the general pattern reported in the literature (table 2). These investigations lead to the conclusion that groups like Cl or OCH_3 when substituted around the ring show a blue shift in the case of n-π transitions and a red shift in the case of π-π transitions. Further,

Table 1. Ultraviolet absorption spectra of 2,4,6-trichloropyrimidine in the liquid and vapour states in the region 50000–28000 cm^{-1} and its correlation with pyrimidine and a few substituted pyrimidine

All values are in cm^{-1}

	Solvent	First π-π system	Second π-π system	n-π system	Assignment	Reference
	Cyclohexane	53000	41000	33600		Stern and
	Water	53200	41600	37400		Timmons 1970
	Ethylalcohol	—	41000	35800		
midine	Water	47800	39800	—		
midine	Water	47400	38800	—		
pyrimidine	Neutral solution	—	38597	—		Rao 1961
ropyrimidine	Vapour	46960, 47880, 48680	37600, 38480, 39360	—	37600=0, 0 band 38480=0, 0+880 39360=0, 0+2×880	Present work
	Dioxane	46560	37200, 38080, 39040	31840	37200=0, 0 band 38080=0, 0+880 39040=0, 0+2×880	
	Water	—	37080, 38000, 38960	—	37080=0, 0 band 38000=0, 0+920 38960=0, 0+2×920	
	N/10 sodium hydroxide	46320	36880, 37880	34000	36880=0, 0 band 37880=0, 0+1000	
	N/10 sulphuric acid	—	37080, 38000, 39000	—	37080=0, 0 band 38000=0, 0+920 39000=0, 0+2×920	
	Chloroform	—	37160, 38080, 39000	31680	37160=0, 0 band 38080=0, 0+920 39000=0, 0+2×920	
	Methylalcohol	45800, 46560	37240, 38160, 39120	32000	37240=0, 0 band 38160=0, 0+920 39120=0, 0+2×920	

Table 2. Ultraviolet absorption spectra of 6-chloro-2,4-dimethoxypyrimidine in the liquid and vapour states in the region 50000–28000 cm^{-1} and its correlation with pyrimidine and a few substituted pyrimidine

All values are in cm^{-1}

Molecule	Solvent	First π-π system	n-π system	Second π-π system	Reference
Pyrimidine	Cyclohexane	53000	33600	41000	
	Water	53200	37400	41600	Stern and
	Ethylalcohol	—	35800	41000	Timmons 1970
2-chloropyrimidine	Water	47800	—	39800	
5-chloropyrimidine	Water	47400	—	38800	
2-methoxypyrimidine	Cyclohexane	47604	33888	37868	Jaffe and
4-methoxypyrimidine	Cyclohexane	46497	37026	40310	Orchin
6-chloro-2,4-dimethoxy-	Vapour	46320	—	39000	
pyrimidine	Dioxane	—	42320	38560	
	Water	46000	—	38480	
	N/10 Sodium hydroxide	45560	—	38320	Present work
	N/10 Sulphuric acid	46000	—	38320	
	Chloroform	—	—	38480	
	Methyl alcohol	46080	—	38400	

3.2 *Vibrational spectra*

Both the molecules in the present study are trisubstituted pyrimidines. Only one C–H bond is present in each case. Vibrations of this bond involve C–H out of plane and in plane bending, and stretching modes. In the case of nearly all the aromatic molecules, the vibrations associated with the C–H bond and the functional groups are almost free of any influence of the substituents. With this in mind, the vibrations associated with the C–H bond and the attached functional groups of each molecule have been identified and presented in table 3.

The infrared absorption spectra of pyrimidine contain four bands at 1400, 1461, 1569 and 1610 cm^{-1}. These bands are analogous to the components of the e_{1u} 1485 and e_{2g} 1595 cm^{-1} modes of benzene. Spectra of substituted pyrimidines show that these vibrations are almost insensitive to substitution. Hence, the two pairs of bands at 1407 and 1433 and 1533 and 1560 cm^{-1} in 2,4,6-trichloropyrimidine and at 1400 and 1480 cm^{-1} and 1567 and 1580 cm^{-1} in 6-chloro-2,4-dimethoxypyrimidine have been assigned, respectively, to the ν_{19} mode and ν_8, the ring stretching mode.

Sabrana *et al* (1967) studied the spectra of pyrimidine and some of its deuterated analogues and have suggested that the ring breathing ν_1 mode is mass-dependent. Similar observations have been made in the spectra of trisubstituted benzenes also. Thus the strong bands at 833 and 827 cm^{-1} in the two respective molecules have been assigned to the ν_1 mode. The other ring vibrations which are not very sensitive to substituent effects are ν_{12} and ν_{14} modes. These are assigned and presented in table 3. The ν_6 mode which represents the ring-bending mode has been found to be mass-dependent by Sabrana *et al* (1967). This observation is true for substituted benzenes also. On the basis of data for trisubstituted benzenes, the pair of bands at 573 and

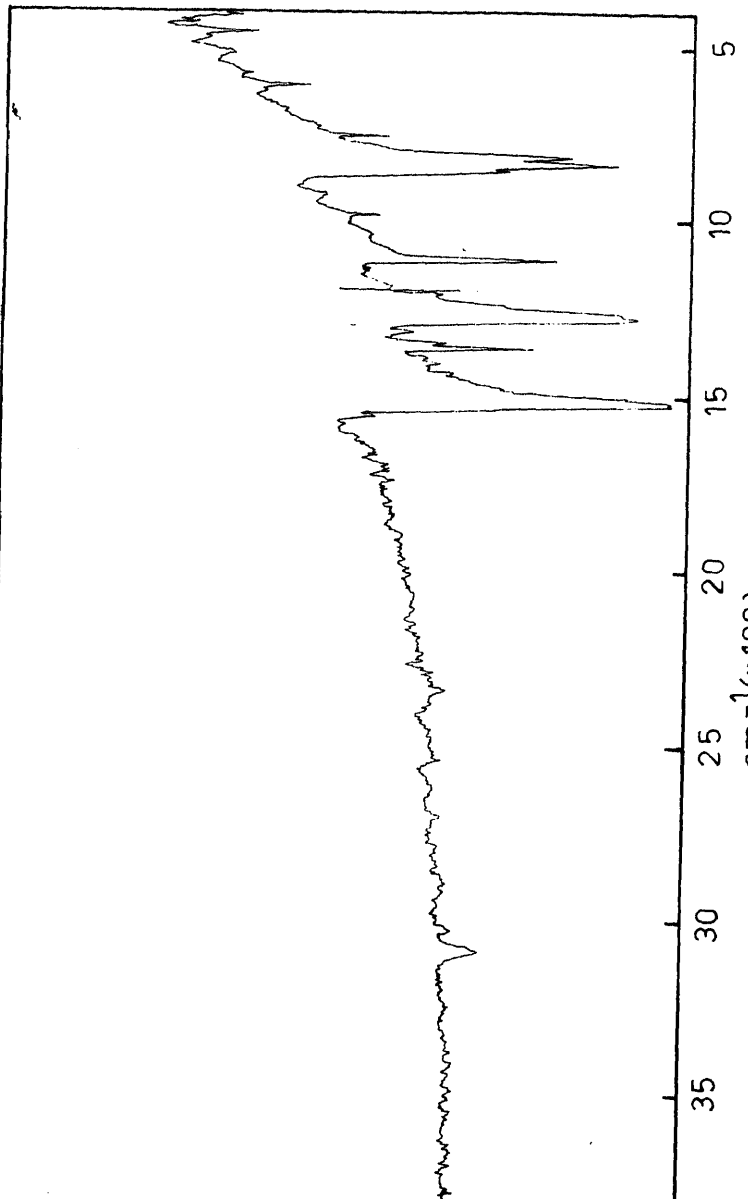

Figure 3. IR absorption of 2,4,6-trichloropyrimidine in vapour in the region 4000–400 cm^{-1}.

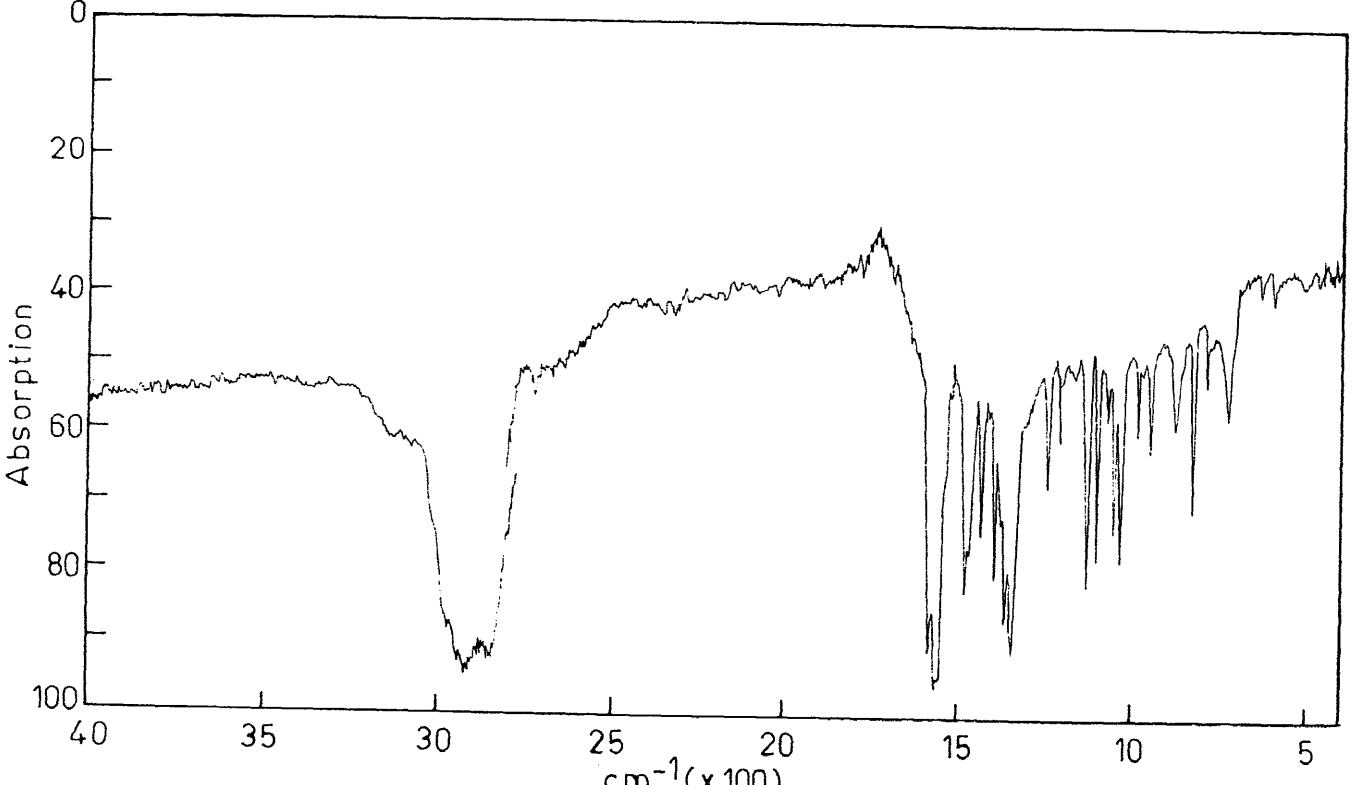

Figure 4. IR absorption of 6-chloro-2,4-dimethoxy pyrimidine in nujol in the region 4000–400 cm^{-1}.

Table 3. Correlation of fundamental vibrational frequencies of 2,4,6-trichloropyrimidine and 6-chloro-2,4-dimethoxypyrimidine with pyrimidine and their modal assignment.

All values are in cm^{-1}

Pyrimidine	2,4,6-trichloro-pyrimidine in the vapour phase	6-chloro-2,4-dimethoxy pyri-midine in nujol	Assignment
394	433 (*w*)	467 (*w*)	ν_{16}
—	460 (*ms*)	—	
—	473 (*w*)	500 (*w*)	β (C-Cl)
624	573 (*vw*)	600 (*w*)	
677	613 (*ms*)	633 (*w*)	ν_6
679	680 (*w*)	688 (*w*)	ν_4
—	733 (*vw*)	727 (*ms*)	ν (C-Cl)
—	760 (*s*)	—	
990	833 (*vvs*)	827 (*s*)	ν_1
806	813 (*vs*)	—	γ (C-H)
870	—	873 (*m*)	γ (C-H)
1065	1040 (*w*)	1033 (*s*)	ν_{12}
1071	1113 (*vs*)	1100 (*s*)	β (C-H)
—	—	1126 (*s*)	ν (C-OCH_3)
1291	1280 (*vs*)	1240 (*ms*)	ν_{14}
—	—	1367 (*s*)	CH_3 sym bending
—	—	1433 (*s*)	CH_3 asym bending
1400	1407 (*w*)	1400 (*s*)	ν_{19}
1461	1433 (*w*)	1480 (*s*)	
1569	1533 (*vs*)	1567 (*s*)	ν_8
1610	1560 (*w*)	1580 (*s*)	
—	—	2853 (*w*)	ν (C-H) aliphatic
—	—	2913 (*w*)	ν (C-H) aliphatic
3001	3033 (*w*)	—	ν (C-H)
3085	—	3083 (*w*)	ν (C-H)

vs = very strong, *s* = strong, *ms* = medium strong, *m* = medium, *w* = weak; ν = stretching, β = in plane bending, γ = out of plane bending, asym = asymmetric, sym = symmetric.

Acknowledgement

One of the authors (MP) is thankful to UGC, New Delhi for financial assistance.

References

Jaffe H H and Orchin M 1965 *Theory and applications of ultraviolet spectroscopy* (New York: John Wiley and Sons) p. 379

Rao C N R 1961 *Ultraviolet and visible spectroscopy* (London: Butterworths) p. 57

Sabrana G, Adembri G and Califano S 1966 *Spectrochim. Acta* **22** 1831

Srivastava S L and Rohitashava 1981 *Indian J. Phys.* **B55** 455

Srivastava S L and Prasad M 1982 *Indian J. Phys.* **B56** 358

Srivastava S L *et al* 1984 *Spectrochim. Acta* **A40** 675

Srivastava S L, Prasad M and Singh H S 1985 *Indian J. Phys.* **B59** 29

Proc. Indian Acad. Sci. (Chem. Sci.), Vol. 97, No. 1, July 1986, pp. 91–95.
© Printed in India.

QSAR studies on estrogen receptor binding affinity of 2-phenylindoles using first-order valence molecular connectivity

P SINGH

Department of Chemistry, Birla Institute of Technology and Science, Pilani 333 031, India

MS received 1 August 1985; revised 10 January 1986

Abstract. The estrogen receptor binding affinity of 2-phenylindoles is found to be significantly correlated with Kier's first-order valence molecular connectivity index. The correlation equations obtained provide a much simple rationale to design more potent compounds and help in predicting the potency of new compounds.

Keywords. Quantitative structure-activity relationship; 2-phenylindoles; estrogen receptor binding affinity; molecular connectivity.

1. Introduction

Recently von Angerer *et al* (1984) synthesised a series of 2-phenylindoles and screened them for their binding affinities for the calf uterine estrogen receptor by a competitive binding assay with 17β-[^{3}H] estradiol. The relative binding affinities (RBA) were given as 100 × the ratio of the molar concentration of 17β-estradiol and indole required to decrease the receptor bound radioactivity by 50%. Their results indicate a very sensitive dependence of binding affinity on structural modifications of these indoles. The maximum in binding affinity was qualitatively rationalized by two contrary effects: the favourable increase in lipophilicity in the centre of the molecule and the steric hindrance by larger groups. Also, the hydroxy groups in two aromatic rings of these compounds, at a certain distance were prerequisites for a strong binding interaction with the receptor site.

These results stimulated me to rationalize the process of structural modifications. In the simplest way this may be achieved by either analysing the relationship of the RBA with well known physicochemical parameters like π, σ, MR, ES, etc. or with molecular parameters like molecular connectivity χ and van der Waals volume V_w. Because of the lack of data on physicochemical parameters at present for these compounds, it is proposed to find the correlation of the RBA with molecular parameters. This shows the applicability of only one molecular parameter which can be well correlated with the RBA. This parameter is the first-order valence molecular connectivity ($^1\chi^v$). Though an attempt was also made to establish the relationship between V_w and RBA, the correlation equations obtained were not statistically sound.

The connectivity index, χ, has several versions (Kier and Hall 1976). The simplest as well as the extended versions in χ ($^n\chi$) are all calculated from a hydrogen-suppressed graph of the molecule. However, with the use of the connectivity index of various orders

and of all the χ's the best and most meaningful is the $^1\chi^v$, as it is an index of the lowe order that takes into account the branching in the molecules and is calculated with t consideration of the valence electrons of the atoms as well. In a number of cases (Ki and Hall 1976, 1977; Bindal *et al* 1980; Gupta *et al* 1982, 1983) this parameter was fou to be significantly correlated to biological activities. Further this molecular paramet has also been shown (Kier *et al* 1976) to be correlated separately with hydrophobici log P and molar refraction, R_m, accounting for steric bulk, for different series compounds.

2. First-order valence molecular connectivity

The first-order valence molecular connectivity index, $^1\chi^v$, as described by Kier and Ha (1976) encodes information about size, branching, cyclization, unsaturation a heteroatom content. It is defined as

$$^1\chi^v = \sum (\delta_i^v \delta_j^v)^{-1/2}$$

where δ_i^v and δ_j^v are atom connectivity terms indicating the number of non-hydroge atoms adjacent or connected to atoms i and j which are formly bonded, and t summation extends to all connections or edges in the hydrogen suppressed graph. δ^v f any atom is defined as

$$\delta^v = Z - N_H$$

where Z is the number of valence electrons of the atom and N_H is the number hydrogen atoms attached to it. Thus $^1\chi^v$ is calculated for the total structure of a giv compound supressing all the hydrogens. The calculated $^1\chi^v$ values, the indicat variables I_1 and I_2 and the log of relative estrogen receptor binding affinities, log RB for 2-(4-hydroxyphenyl) indoles and 2-(3-hydroxyphenyl) indoles are given in tables and 2, respectively. I_1 is used to distinguish the position of the hydroxyl functi present in the aromatic ring of the indole part. $I_1 = 1$ for X = 6-OH and $I_1 =$ for X = 5-OH. Similarly I_2 is used to differentiate the compounds of table 1 from t compounds of table 2.

3. Results and discussions

With the use of data as given in table 1, the most significant correlation equation, that surfaced by regression analysis, is (3). This equation correlates log RBA with $^1\chi^v$ in first and second powers and I_1.

$$\log \text{RBA} = 12{\cdot}585\ ^1\chi^v + 0{\cdot}880(^1\chi^v)^2 + 0{\cdot}127\ I_1 - 43{\cdot}825,$$

$$n = 26,\ r = 0{\cdot}893,\ s = 0{\cdot}481,\ F(3,22) = 28{\cdot}853,$$

where n is the number of compounds considered for analysis, r is the correlati coefficient, s is the standard deviation and F is the F ratio between the variances calculated and observed activities. For the present study however, compound 3 (table

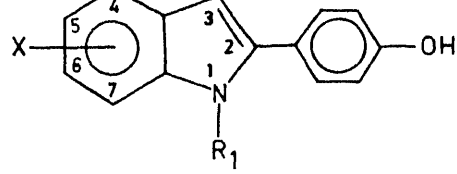

Compound number	R_1	R_2	$X=OH$ position	$^1\chi^v$	I_1	I_2	log RBA Obsd.[a]	Calc. (4)	Calc. (7)
1	H	H	6	5·334	1	1	−2·00	−1·68	−1·67
2	H	CH_3	6	5·756	1	1	−1·22	0·47	0·47
3	H	C_2H_5	6	6·317	1	1	−0·89[b]	—	—
4	CH_3	H	6	5·728	1	1	0·58	−0·54	−0·54
5	C_2H_5	H	6	6·304	1	1	1·20	0·62	0·62
6	C_3H_7	H	6	6·804	1	1	0·93	1·15	1·15
7	C_4H_9	H	6	7·304	1	1	0·63	1·23	1·22
8	CH_3	CH_3	6	6·150	1	1	1·00	0·37	0·37
9	C_2H_5	CH_3	6	6·726	1	1	1·52	1·10	1·10
10	C_3H_7	CH_3	6	7·226	1	1	1·11	1·24	1·24
11	i-C_3H_7	CH_3	6	7·116	1	1	1·11	1·25	1·25
12	CH_3	C_2H_5	6	6·711	1	1	0·77	1·08	1·08
13	C_2H_5	C_2H_5	6	7·287	1	1	1·32	1·23	1·23
14	C_3H_7	C_2H_5	6	7·797	1	1	1·28	0·87	0·87
15	H	H	5	5·334	0	1	−2·00	−1·68	−1·67
16	H	CH_3	5	5·756	0	1	−1·22	−0·47	−0·47
17	CH_3	H	5	5·728	0	1	−0·10	−0·54	−0·54
18	C_2H_5	H	5	6·304	0	1	0·76	0·62	0·62
19	C_3H_7	H	5	6·804	0	1	1·26	1·15	1·15
20	CH_3	CH_3	5	6·150	0	1	0·66	0·37	0·37
21	C_2H_5	CH_3	5	6·726	0	1	0·98	1·10	1·10
22	C_3H_7	CH_3	5	7·226	0	1	1·20	1·24	1·24
23	i-C_3H_7	CH_3	5	7·116	0	1	0·54	1·25	1·25
24	C_4H_9	CH_3	5	7·726	0	1	0·66	0·94	0·94
25	C_5H_{11}	CH_3	5	8·226	0	1	0·36	0·19	0·19
26	C_2H_5	C_2H_5	5	7·287	0	1	1·36	1·23	1·23
27	C_3H_7	C_3H_7	5	8·287	0	1	0·23	0·06	0·06

[a] Relative binding affinity for the calf uterine estrogen receptor, taken from von Angerer *et al* (1984);
[b] compound is excluded in the derivation of (4) and (7).

position 3 of the indole offers steric bulk and the hydrogen at position 1 of the indole probably decreases the hydrophobicity, as suggested by Fritsche (1964), as it forms hydrogen bridges with water molecules and prevents the hydrophobic interaction with the receptor site. The increase in steric hindrance and decrease in hydrophobicity, therefore, tends to decrease the binding action of this compound. Though (3) is quite

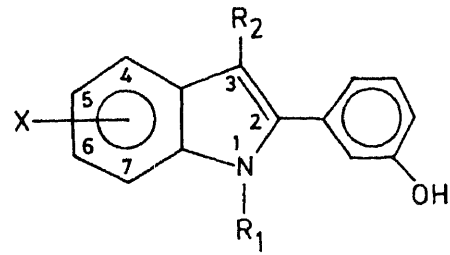

Compound number	R_1	R_2	$X=OH$ position	$^1\chi^v$	I_1	I_2	log RBA Obsd.[a]	log RBA Calc. (6)	log RBA Calc. (7)
1	C_2H_5	H	6	6·304	1	0	0·23	0·05	0·06
2	CH_3	CH_3	6	6·150	1	0	−0·26	0·07	−0·18
3	C_2H_5	CH_3	6	6·726	1	0	0·48	0·37	0·54
4	C_3H_7	CH_3	6	7·226	1	0	0·54	0·75	0·68
5	C_2H_5	H	5	6·304	0	0	0·23	0·05	0·07
6	CH_3	CH_3	5	6·150	0	0	−0·22	−0·07	−0·18
7	C_2H_5	CH_3	5	6·726	0	0	0·34	0·37	0·54
8	C_3H_7	CH_3	5	7·226	0	0	0·87	0·75	0·68

[a] See footnotes under table 1.

sound statistically, the coefficient associated with I_1 indicates that its contribution to the activity is very small. This implies that the binding action of the molecule will not be much effected by the presence of hydroxyl group either at position 5 or position 6 of indole. Therefore, deleting the variable I_1 an equally statistically significant parabolic equation (4) is obtained.

$$\log \text{RBA} = 12{\cdot}835\ {}^1\chi^v + 0{\cdot}899({}^1\chi^v)^2 - 44{\cdot}563,$$

$$n = 26,\ r = 0{\cdot}891,\ s = 0{\cdot}475,\ F(2, 23) = 44{\cdot}168. \tag{4}$$

The F value of the above equation is significant at 99% level [F^2_{23} (0·01) = 5·66] and accounts for 79% of variance (r^2 = 0·794). The calculated values of log RBA listed in table 1 are in close agreement with observed values.

Similarly using the data of table 2 for 2-(3-hydroxyphenyl) indoles the correlation equation (5) is obtained.

$$\log \text{RBA} = 9{\cdot}439\ {}^1\chi^v + 0{\cdot}648({}^1\chi^v)^2 - 0{\cdot}057\ I_1 - 33{\cdot}638,$$

$$n = 8,\ r = 0{\cdot}926,\ s = 0{\cdot}189,\ F(3,4) = 8{\cdot}08. \tag{5}$$

In this equation the coefficients of the $({}^1\chi^v)^2$ and I_1 variables show that activity is not going to be much effected if both of these are deleted. Thus a linear equation (6) is obtained.

$$\log \text{RBA} = 0{\cdot}761\ {}^1\chi^v - 4{\cdot}749,$$

$$n = 8,\ r = 0{\cdot}897,\ s = 0{\cdot}181,\ F(1, 6) = 24{\cdot}642. \tag{6}$$

The F value of (6) is significant at 99% level [$F_6^1(0{\cdot}01) = 13{\cdot}74$] and the calculated values of log RBA are tabulated in table 2. From the above discussion and from (4) and (6), it is quite evident that I_1 makes no significant contribution to the activity. Therefore, in 2-(4-hydroxyphenyl) or 2-(3-hydroxyphenyl) indoles the position of the hydroxyl group, either at 6 or 7 of the indole moiety will hardly matter as far as the binding action is concerned. Further (4) is parabolic and (6) is linear, therefore, it is considered appropriate to consider 34 compounds all together by taking another indicator variable I_2, which will differentiate the two sets of congeners. The second set of 8 compounds having linear variation of binding affinity with ${}^1\chi^v$ will fall on the ascending part of the parabolic variation of the first set of 24 compounds, as the sign of the coefficient of ${}^1\chi^v$ in both equations is the same. I_2 is assigned a value 1 for each of the compound belonging to a 2-(4-hydroxyphenyl) indoles and a value 0 for each of the remaining 2-(3-hydroxyphenyl) indoles. Therefore, I_2 will differentiate the positions of the hydroxyl groups either 4 or 3, in phenyl ring. Considering ${}^1\chi^v$, $({}^1\chi^v)^2$ and I_2 as independent variables and activity as a dependent variable for all 34 compounds from table 1 and table 2 the derived correlation is (7).

$$\log \text{RBA} = 12{\cdot}801\,{}^1\chi^v + 0{\cdot}897\,({}^1\chi^v)^2 + 0{\cdot}556\ I_2 - 44{\cdot}996,$$

$$n = 34,\ r = 0{\cdot}893,\ s = 0{\cdot}422,\ F(3, 30) = 39{\cdot}343, \qquad (7)$$

where the F value is again significant at the 99% level [$F_{30}^3(0{\cdot}01) = 4{\cdot}51$] and accounts for 79% of variance. This highly significant equation is therefore used to calculate the activity values for all the compounds of tables 1 and 2. The calculated values of activity, listed in these tables, are in close agreement with observed values. The positive coefficient of I_2 shows that there will be a significant increase in binding affinity of a compound, if it has a hydroxyl group in the para position of the phenyl ring. Similarly, as evident from the coefficients of ${}^1\chi^v$ and $({}^1\chi^v)^2$, the binding action of a compound increases as its molecular connectivity increases. But this does not mean that affinity can take any value as ${}^1\chi^v$ goes on increasing. After a certain optimum value of ${}^1\chi^v$, the affinity again starts decreasing, since there exists a parabolic variation between connectivity and binding affinity.

Thus ${}^1\chi^v$ plays an important role in the binding action of 2-phenylindole with estrogen receptor proteins. The correlation equations mentioned above describe the direct structural influence on binding affinity and are very useful in substituent selection while designing more potent compounds.

References

Bindal M C, Singh P and Gupta S P 1980 *Arzneim.-Forsch.* **30** 234

Fritsche H 1964 *Ber. Bunsenges. Phys. Chem.* **68** 459

Gupta S P, Bindal M C and Singh P 1982 *Arzneim.-Forsch.* **32** 1223

Gupta S P, Prabhakar Y S and Handa A 1983 *Res. Commun. Chem. Pathol. Pharmacol.* **42** 455

Kier L B and Hall L H 1976 *Molecular connectivity in chemistry and drug research*, (New York: Academic Press)

Kier L B and Hall L H 1977 *J. Med. Chem.* **20** 1631

Von Angerer E, Prekajac J and Strohmeier J 1984 *J. Med. Chem.* **27** 1439

Infrared and Raman spectra of 2,4-dimethylaniline

A R SHUKLA†, C M PATHAK*, N G DONGRE, B P ASTHANA and JACOB SHAMIR‡

Department of Physics, Banaras Hindu University, Varanasi 221 005, India
† Present address: Department of Non-Conventional Energy Sources, Block No. 14, CGO Complex, New Delhi 110 003, India
‡ Department of Inorganic and Analytical Chemistry, The Hebrew University of Jerusalem, Jerusalem, Israel.

MS received 7 November 1985

Abstract. The infrared spectra of 2,4 dimethylaniline have been recorded in the region 3600–100 cm^{-1}. The Raman spectra with polarization measurements have been recorded and investigated for the first time in the region 3500–100 cm^{-1}. New frequency assignments have been proposed assuming the molecule to possess an approximate C_s symmetry. Fifty normal modes of the molecule, out of a possible fifty four modes, have actually been observed and assigned including twenty seven hitherto unreported frequencies. The observed spectral changes give evidence of the presence of an intermolecular hydrogen bonding of an N–H . . . N type, and suggest a solid-solid phase transition between 223 and 123 K in the molecule.

Keywords. Infrared and Raman spectra; normal modes; spectral changes; hydrogen bonding; phase transition.

1. Introduction

The infrared spectra of 2,4 dimethylaniline (hereafter referred to as 2,4-DMA) were first investigated by Prasad (1975) who has reported the frequency assignment of only 23 modes out of a possible 54. Many of his assignments are open to question. It has been difficult to observe all the fundamentals in benzene derivatives (Varsanyi 1974) but there is often a possibility of observing more fundamentals (Hainer and King 1950) if the spectra are recorded at lower temperatures.

According to Varsanyi (1974) 2,4-DMA falls under the category of 1,2,4-tri-light benzene derivatives. Although the molecule, in a strict sense, possesses the C_1 symmetry, we have proposed the assignment of the ring modes assuming an approximate C_s symmetry.

Infrared spectra have been recorded at room temperature, 223 K and 123 K along with the spectra in the solution phase choosing CS_2 as solvent. The observed frequency shifts, bandwidth changes and intensity variations give evidence of the presence of intermolecular hydrogen bonding of the N–H . . . N type and suggest a solid-solid phase transition between 223 and 123 K.

2. Experimental

2,4 Dimethylaniline was obtained from Koch-Light, England. The reported purity of the sample was better than 98·5 %. However, the liquid was redistilled several times under reduced pressure before use. The experimental details of recording the infrared spectra at room temperature, 223 K and 123 K have already been described in an earlier communication (Shukla *et al* 1986) on 2,3 dimethylaniline (2,3-DMA). The far infrared spectra in the region 600–100 cm^{-1} and the Raman spectra along with polarization measurements were recorded as described in the above communication (Shukla *et al* 1986). The slit width used in recording the Raman spectra was 2·5–5·0 cm^{-1}.

The spectra recorded at different temperatures, in different spectral ranges, have been reproduced in figures 1 to 5. Some of the weak bands marked as *vw* or *vvw*, which are actually present in the recorded spectra, may not be perceptible in the figures due to reduction in size. The accuracy of measurement was nearly $\pm$ 2 cm^{-1}.

3. Frequency assignments

The frequency assignments for the ring modes, methyl groups and the amino group have been presented under three separate heads. Wilson's (1934) numbering has been strictly followed for the assignment of ring modes. Mulliken's (1955) numbering scheme has been followed only in a restricted sense such that fundamental vibrations in each of the three categories are numbered in the decreasing order of frequency. The observed fundamental frequencies associated with the methyl groups have been labelled as $\nu'_1, \nu'_2, \ldots \nu'_{14}$ and those associated with the amino group have been labelled as $\nu''_1, \nu''_2, \ldots \nu''_6$. The frequencies of the ring modes in 2,4-DMA have been compared with the corresponding modes in similar molecules (Green *et al* 1971), 1,2,4 trimethylbenzene (1,2,4-TMB) and 4-fluoro 1,2 dimethylbenzene (4F,1,2,-DMB) in table 1.

4. Normal vibrations associated with the benzene ring

4.1 *Spectra in the region* 3600–2800 cm^{-1}

The liquid and solid phase (123 and 223 K) infrared spectra and the Raman spectra at room temperature recorded in this region have been reproduced in figure 1. The Raman spectrum of 2,4-DMA shows a weak line at 3078 cm^{-1} but in the infrared spectrum a weak shoulder appears at 3079 cm^{-1} only at 223 K. Although another weak shoulder is seen in the infrared spectrum at 3096 cm^{-1}, the lines at 3078 and 3079 cm^{-1} are assigned to mode number 20b and the shoulder at 3096 cm^{-1} has been explained as a combination band. The two polarized Raman lines at 3050 ($\rho = 0{\cdot}44$) and 3017 cm^{-1} ($\rho = 0{\cdot}30$) and their infrared counterparts at about 3045 (obscured by a strong absorption) and 3010 cm^{-1} are assigned to modes 2 and 20b respectively

Table 1. Observed frequencies (cm^{-1}) in infrared and Raman spectra of 2,4 dimethylaniline with frequency assignments.

Infrared									Raman			Assignm
Room temperature			223° K			123° K			CS_2 solution		Room temperature			
Frequency	I	$\Delta\nu_{1/2}$ cm^{-1}	Frequency	I	$\Delta\nu_{1/2}$ cm^{-1}	Frequency	I	$\Delta\nu_{1/2}$ cm^{-1}	Frequency	I	Frequency	I	Polarisation	
3441	*s*	102	3420	*s*	108	3410	*s*	139	3477	*s*	3442	*vw*		$\nu_{asym}(\nu_1'')$
3354	*s*	92	3343	*s*	139	3341	*s*	156	3391	*s*	3370	*b*	*p*	$\nu_{sym}(\nu_2'')$
3223	*m*	68	3220	*s*	88	3220	*s*	120			3230	*w*	*p*	$2\times\nu_3''$
3126	*w*								3128	*w*				8b + 19
3096	*w, sh*		3096	*w, sh*		3098	*w, sh*							8a + 19
			3079	*w, sh*							3078	*w*		20a (ν_1)
3046	*m*		3042	*m*		3044	*m*		3046	*sh*	3050	*m*	*p*	$2(\nu_2)$
3008	*s*	50	3008	*s*	52	3011	*s*	49	3016	*s*	3017	*m*	*p*	20b (ν_3)
											3006	*sh*		$\nu_8' + \nu_3''$
2969	*m*	57	2966	*s*	61	2968	*s*	55	2972	*s*	2975	*w*	*p*	$\nu_{asym}(\nu_1'$
						2936	*s, sh*							$\nu_{asym}(\nu_2'$
2922	*s*	75	2921	*s*	80	2922	*s*	79	2923	*s*	2922	*ms*	*p*	$\nu_{sym}(\nu_3'$
2900	*s*		2897	*s*		2893	*s*		2893	*w, sh*				$2\times\nu_4'$
2859	*ms*	44	2857	*s*	45	2855	*ms*	44	2860	*s*	2864	*m*	*p*	$2\times\nu_6'$
						2813	*w, sh*							$\nu_7' + \nu_8'$
			2790	*w, sh*		2789	*w, sh*							7a + 19
2733	*w*	14	2733	*w*	14	2733	*w*	14			2736	*mw*	*p*	$2\times\nu_8'$
			2697	*w*		2697	*w*							8b + ν_4''
2664	*w*		2667	*w*		2667	*w*							8a + ν_4''
2625	*w*		2625	*w*		2633	*w*							8b + ν_{11}'
2602	*w*		2605	*w*		2610	*w*							$\nu_{11}' + 8a$
						2562	*w*							7b + ν_3''
2536	*w*					2537	*w*							8a + 17
						2514	*w*							7a + 13
2468	*w*		2468	*w*		2474	*w*							$\nu_5' + \nu_{11}'$
2443	*w*		2446	*w*		2448	*w*							$\nu_4' + \nu_{12}'$

Table 1. (*Continued*)

Infrared								Raman					
emperature		223° K			123° K			CS_2 solution		Room temperature			Assignment
I	$\Delta\nu_{1/2}$ cm^{-1}	Frequency	*I*	$\Delta\nu_{1/2}$ cm^{-1}	Frequency	*I*	$\Delta\nu_{1/2}$ cm^{-1}	Frequency	*I*	Frequency	*I*	Polari-sation	
w		2400	*w*		2400	*w*							ν'_5+17b
								2299	*w*				8a+1
					2136	*w*							8a+16a
					2084	*w*							ν''_3+16b
					2028	*w*							5+18a
					1973	*w*							$\nu'_{10}+7b$
w		1912	*w*		1915	*w*							$\nu'_{12}+7b$
		1872	*w*		1873	*w*							18a+1
w	32	1862	*w*	31	1863	*w*	32						$\nu'_{12}+5$
					1821	*w*							5+17b
w													5+7b
w	31	1751	*w*	32	1753	*w*							11+17b; 2×5
w		1720	*w*										$\nu'_{12}+4$
										1655	*w, sh*		5+12
s	46	1627	*s*	53	1629	*s*	73	1623	*vs*	1626	*ms*	*p*	$\beta_{sym}(\nu''_3)$
s		1609	*s*		1609	*s*				1613	*sh*		8b(ν_4)
m		1588	*ms*		1586	*ms, sh*				1589	*mw*	*p*	8a(ν_5)
					1548	*w*							$\nu'_{12}+6a$
vs	33	1515	*vs*	35	1513	*vs*	35			1515	*mw*	*p*	19b (ν_6)
		1505			1506								
w, sh					1498	*w, sh*							3+15
ms	37	1464	*ms*	30	1465	*s*	24			1463	*sh*	*dp*	$\delta^+_{asym}(\nu'_4)$
										1458	*mw*		$\delta^+_{asym}(\nu'_5)$
ms	31	1442	*s*	27	1442	*s*	24			1445	*mw*	*dp*	$\delta^+_{asym}(\nu'_6)$
										1438	*w, sh*		$\delta^+_{asym}(\nu'_7)$

1410	*m*	13	1410	*m*	12	1409	*m*	8			1411	*mw*	*dp*	19a (ν_7)
1379	*m*	11	1379	*m*	12	1380	*m*	14	1375	*m*	1381	*s*	*p*	$\delta_{sym}(\nu'_8)$
											1373	*w, sh*		$\delta_{sym}(\nu'_9)$
											1364	*w*		$10a+\nu''_4$
1313	*m*	9	1315	*m*	10	1318	*m*	12	1320	*m*	1313	*mw*	*p*	14(ν_8)
1290	*s*		1289	*s*		1289	*s*							3(ν_9)
1275	*s*	24	1273	*s*	26	1274	*vs*	25	1273	*vs*	1275	*s*	*p*	7a(ν_{10})
1240	*ms*	9	1239	*s*	9	1242	*s*	10	1237	*s*	1242	*m*	*p*	13(ν_{11})
1226	*mw, sh*		1226	*mw*		1229	*mw*							6b+4
1179	*w*		1179	*w*		1180	*w*							4+16b
1155	*ms*	13	1154	*ms*	16	1153	*s*	16	1150	*s*	1155	*m*	*p*	18a(ν_{12})
									1122	*w*	1120	*vw*		18b(ν_{13})
1076	*w*	19	1081	*w*	24	1085	*w*	25	1072	*w*	1076	*vw*		$\beta_{asym}(\nu''_4)$
1035	*m*	14	1034	*m*	14	1035	*m*	14	1030	*m*	1040	*w*	*p*	$\delta^-_{asym}(\nu'_{10})$
1012	*m*	12	1013	*m*	10	1013	*m*	10	1008	*m*	1011	*w*	*p*	$\delta^-_{asym}(\nu'_{11})$
984	*mw*	8	984	*mw*	9	985	*mw*	8	980	*mw*	982	*w*	*p*	$\delta^-_{asym}(\nu'_{12})$
									946	*mw*	950	*w, sh*		17b(ν_{22})
933	*mw*	16	933	*mw*	18	934	*mw*	18	930	*mw*	933	*s*	*p*	7b(ν_{14})
									883	*m, sh*				$\delta^-_{as}(\nu'_{13})$
875	*m*	15	876	*ms*	18	876	*s*	19	871	*m*	876	*vw*		5(ν_{23})
814	*vs*	30	817	*vs*	36	821	*vs*	40	812	*vs*	814	*vw*		11(ν_{24})
790	*b, sh*		787	*m*		790	*b, sh*							10b+16
											778	*vs*	*p*	12(ν_{15})
									765	*w*	759	*sh*		10a+6b
740	*ms*		744	*s*		743	*m*		744	*ms*				4(ν_{25})
716	*ms, sh*		714	*ms*					722	*m*	717	*vvs*	*p*	1(ν_{16})
668	*mb*													I(1−3)?
590	*vw*										588	*w, sh*		$\gamma_{sy}(\nu''_5)$
562	*sh*										560	*vs*	*p*	6a(ν_{17})
551	*s*													16a(ν_{26})
482	*mw*										482	*s*	*p*	6b(ν_{18})
											445	*m*	*p*	9b(ν_{19})
440	*s*													16b(ν_{27})
420	*sh*													I(0−2)?
379	*w*													I(1−2)?

Table 1. (*Continued*)

Infrared										Raman			
Room temperature			223° K			123° K			CS_2 solution		Room temperature			Assign
Frequency	I	$\Delta\nu_{1/2}$ cm^{-1}	Frequency	I	$\Delta\nu_{1/2}$ cm^{-1}	Frequency	I	$\Delta\nu_{1/2}$ cm^{-1}	Frequency	I	Frequency	I	Polarisation	
341	*mw*										341	*m*	*p*?	9a(ν_2
310	*w*													(ν_τ +
296	*w*													I(2 −
284	*mw*										284	*m*	*dp*	10a(ν
274	*vw*													$\tau'(\nu''_6)$
241	*mw*													10b(ν
231	*w*													(ν_τ −
211	*m*										210	*ms*	*p*?	15(ν_2
185	*w*										184	*w*		$\tau(\nu'_{14}$
158	*wb*										155	*w*	*dp*	17a(ν

Abbreviations:
$\Delta\nu_{1/2}$: Full width at half maximum; I: intensity; *p*: polarized; *dp*: depolarized; *b*: broad; *s*: strong; *m*: medium; *w*: weak; *ms*: medium strong; *mw*: medium weak; *vs*: very strong; *sh*: shoulder; *vvs*: very very strong.

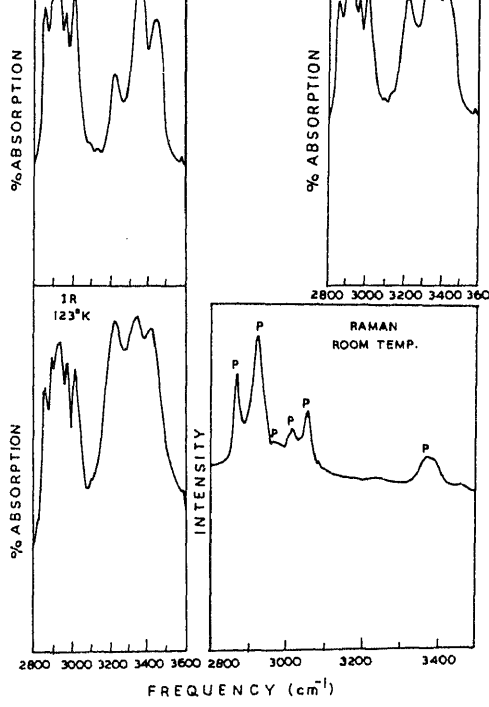

Figure 1. Infrared and Raman spectra of 2,4 dimethylaniline in the region 2800–3600 cm^{-1}.

4.2 *Spectra in the region* 1700–1100 cm^{-1}

The ring modes falling in this region are: the C–C stretching modes 8a, 8b, 19a, 19b, and 14; the C-*X* stretching modes 7a and 13, and the C–H in-plane bending modes 3 and 18a. Some bands are associated with normal modes of the NH_2 and CH_3 groups, whose assignments would be discussed separately.

In 2,4-DMA, like in 2,3-DMA (Shukla *et al* 1986), the frequency of the mode 8b is found to be higher than that of 8a and the frequencies of these modes for the two molecules are almost insensitive to substitution. The Raman spectrum shows a distinct, medium weak and polarized line ($\rho = 0{\cdot}56$) at 1589 cm^{-1} with a shoulder at 1613 cm^{-1} while the infrared bands at 1611 and 1590 cm^{-1} are only shoulders (figure 2). The infrared spectrum further shows a very strong band at 1510 cm^{-1} and a medium weak band at 1410 cm^{-1} in the predicted (Varsanyi 1974) frequency interval for modes 19b and 19a respectively. A weakly depolarized Raman line at 1411 cm^{-1} ($\rho = 0{\cdot}70$) and a polarized one at 1515 cm^{-1} ($\rho = 0{\cdot}50$) are observed with equal intensity. Prasad (1975) has observed only a single band at 1510 cm^{-1} which he has assigned to mode 19.

In the 1350–1250 cm^{-1} interval, one would expect three fundamentals corresponding to modes 14, 7a and 3. In substituted benzenes containing an NH_2 group, mode number 14 has usually been observed (Varsanyi 1974) at a higher frequency than the two other modes and this fact has been supported by a normal coordinate analysis

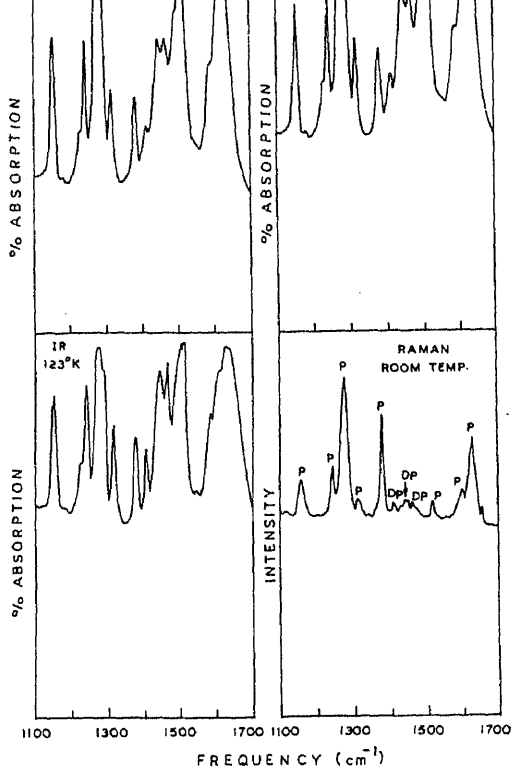

Figure 2. Infrared and Raman spectra of 2,4 dimethylaniline in the region 1100–1700 cm^{-1}.

performed by Abasbegovic *et al* (1977) for *p*-methylaniline. The frequency of mode 14 in 2,3-DMA (Shukla *et al* 1986) was found to be 1308 cm^{-1}. In the case of 2,4-DMA, an infrared band of medium intensity and a weak but strongly polarized line in the Raman spectra appeared at 1313 cm^{-1}. This frequency has been assigned to mode number 14. The C–NH_2 stretch has been reported to appear quite strongly in the infrared and Raman spectra of *p*-methylaniline (Abasbegovic *et al* 1977) and aniline (Evans 1960) at 1275 cm^{-1} with the Raman line being strongly polarized. In the spectra of 2,4-DMA (figure 2), a very strongly polarized and intense Raman line and a very strong infrared band have been observed at 1275 cm^{-1} and assigned to mode 7a (C–NH_2 stretch). Further, the infrared spectrum only shows a shoulder at 1290 cm^{-1} which has been assigned to mode 3.

In the 1250–1100 cm^{-1} interval, one would expect a C–CH_3 stretching mode number 13 and two C–H in-plane bending modes 18a and 18b. Although the frequency of an isolated C–*X* stretching mode is dependent on the mass of the linked atom (or group of atoms) and the strength of the C–*X* bond, the radial skeletal modes 1, 12, and 6 are known (Varsanyi 1974) to interact strongly with the C–*X* stretching vibration. Since two radial skeletal modes 1 and 12 have frequencies around 1000 cm^{-1} in benzene, the

C–X stretching mode in the case of light substituents will couple with modes 1 and/or 12, and as a result, its frequency increases above 1100 cm^{-1} while the frequency of mode 1 decreases below 900 cm^{-1}. This fact has been supported by normal coordinate calculations carried out on some disubstituted benzenes by Le Calve and Labarbe (1960). The observed frequencies at about 1240 cm^{-1} (figure 2) have been assigned to this mode number 13. The first bending mode 18a is assigned to the rather strong infrared and Raman bands at 1155 cm^{-1}. A weak infrared band (1122 cm^{-1}) and a very weak Raman line (1120 cm^{-1}) have been tentatively assigned to the second bending mode 18b. Prasad (1975) has reported only a single frequency at 1155 cm^{-1} and has assigned it to mode number 15, which is probably incorrect.

4.3 *Spectra in the region* 1100–600 cm^{-1}

The C–*X* stretching mode 7a, skeletal modes 1 and 12, out-of-plane wagging modes 17b, 5, and 11, and torsional mode 4 lie in this frequency interval. Six frequencies are reported for the first time. This region also contains bands corresponding to the normal vibrations associated with the methyl and amino groups, which will be discussed separately.

In benzene derivatives (Varsanyi 1974) some of the out-of-plane bending modes either appear with very weak intensity or do not appear at all in the infrared spectrum. Consequently, it is common practice (Green *et al* 1971; Kuwac and Machida 1978; Young *et al* 1951) to ascertain the frequency of such a mode, especially 17b, from the characteristic combination bands (Young *et al* 1951) in the region 2000–1800 cm^{-1}. However, in the case of 2,4-DMA, the solution phase infrared spectrum and the Raman spectrum (figure 3) show up a weak band around 950 cm^{-1} which has been assigned to mode 17b. The infrared band of medium intensity at 875 cm^{-1} has been assigned to mode number 5, which incidently has been observed at 871 cm^{-1} in 1,2,4-TMB (Green *et al* 1971). The frequency is significantly lower ($\approx$ 90 cm^{-1}) in 2,4-DMA than in 2,3-DMA (Shukla *et al* 1986). This change can be attributed to the relative position of the amino group with respect to the methyl groups in the two molecules. The very strong band at 814 cm^{-1} has been assigned to mode number 11.

The C–*X* ($X = CH_3$) stretching mode 7b in 2,4-DMA is expected at 820–1005 cm^{-1} but mode number 17b and the CH_3 rocking modes also fall in this region. The observed frequencies are given in table 1. The 985 cm^{-1} band was considered a suitable candidate for the CH_3-rock on the basis of its intensity in addition to the fact that this is a characteristic rocking frequency and has been observed at 991 cm^{-1} in 2,3-DMA (Shukla *et al* 1986). The strongly polarized Raman line at 933 cm^{-1} has a better claim for mode number 7b. If one compares this mode in 2,4-DMA with that reported (Shukla *et al* 1986) in 2,3-DMA (1128 cm^{-1}), one finds a difference of 200 cm^{-1} but similar changes have been reported in parent molecules (Green 1970), *o*-oxylene (1185 cm^{-1}) and *m*-xylene (903 cm^{-1}).

A very strong polarized Raman line at 778 cm^{-1} (figure 3) is the best candidate for mode number 12. This frequency does not appear in infrared spectra but a broad band is seen at lower temperatures at 790 cm^{-1} which is better explained as a combination band. A medium strong band observed at 740 cm^{-1} in the infrared spectra has been assigned to mode number 4. Prasad (1975) has reported a band at 735 cm^{-1} and has assigned it to mode 10 which does not seem justified as mode number 10 is actually a

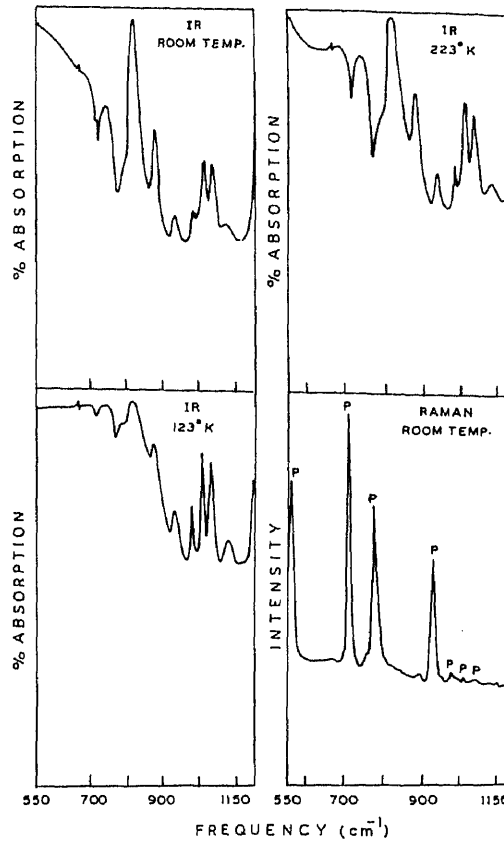

Figure 3. Infrared and Raman spectra of 2,4 dimethylaniline in the region 550–1150 cm^{-1}.

400 cm^{-1}. A very strongly polarized Raman line observed at 717 cm^{-1} and an infrared band of medium intensity at 716 cm^{-1} are assigned to mode number 1.

4.4 *Spectra in the region* 600–100 cm^{-1}

In this frequency interval, one would expect to observe the skeletal modes: 6a, 6b, 16a, and 16b; the C–*X* in-plane bending modes: 9a, 9b, and 15; and the C–*X* out-of-plane wagging modes: 10a, 10b, and 17a. In 2,4-DMA, eight frequencies have been observed for the first time.

In the spectra of 1,2,4-TMB (Green *et al* 1971), one finds that the highest frequency falling in this region corresponds to mode number 6a. Accordingly, the strong polarized Raman line at 560 cm^{-1} with its infrared partner appearing as a weak shoulder at 562 cm^{-1} (figure 5) can be assigned to mode 6a. In 1,2,4-TMB (Green *et al* 1971), a very strong band was observed in the infrared as the next lower frequency (540 cm^{-1}) which was assigned to mode 16a with its Raman partner not observed at all. In 2,4-DMA also, a

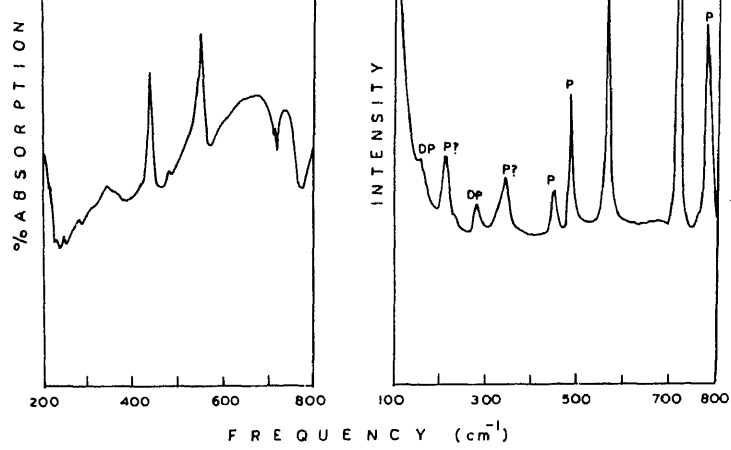

Figure 4. Infrared and Raman spectra of 2,4 dimethylaniline in the region 200–800 cm^{-1}.

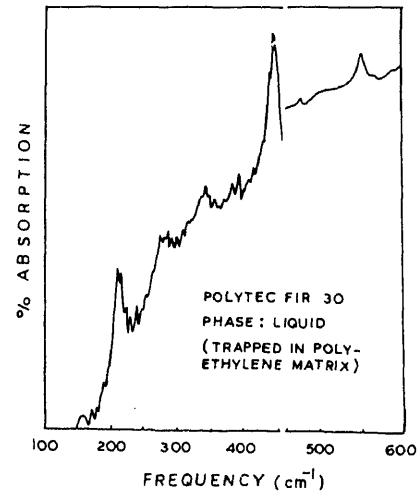

Figure 5. Infrared spectra of 2,4 dimethylaniline in the region 100–600 cm^{-1}.

Raman, $\rho = 0{\cdot}30$) is assigned to mode number 6b, its frequency being quite close to those in 1,2,4-TMB and 4F,1,2-DMB (Green *et al* 1971).

In 1,2,4-TMB and 4F,1,2-DMB (Green *et al* 1971), modes 16b and 9b have been assigned to two bands quite close to each other, the first is strong in the infrared spectrum, the second is a strong polarized Raman line. Accordingly, the polarized Raman line of medium intensity observed at 445 cm^{-1} in 2,4-DMA has been assigned to mode number 9b of a' symmetry and the strong infrared band at 440 cm^{-1} has been assigned to mode number 16b of a'' symmetry.

The predicted frequency range (Varsanyi 1974) for the in-plane C–*X* bending mode 9a is 200–345 cm^{-1}. In 4F,1,2-DMB (Green *et al* 1971), this mode appears in the infrared and Raman spectra at 343 cm^{-1}. In 2,4-DMA, a partially polarized Raman line ($\rho = 0{\cdot}67$) and an infrared band have been observed at 341 cm^{-1} (figures 4 and 5) and are assigned to mode 9a (a').

In the frequency interval 300–100 cm^{-1}, one would expect to observe the three C–*X* out-of-plane bends: 10a, 10b, and 17a in addition to a C–*X* in-plane bend (mode 15). The four frequencies of 2,4-DMA observed in this region have been assigned by comparison with the assignments (table 2) made for 1,2,4-TMB (Green *et al* 1971). Two of the infrared bands (figures 4 and 5), namely 211 cm^{-1} and 158 cm^{-1}, are observed in the polyethylene matrix.

5. Assignments of fundamental modes associated with substituent groups

In 2,4-DMA, a total of 24 fundamental frequencies would arise from the two methyl groups and the amino group. Eight new frequencies, five associated with the methyl groups and three with the amino group, have been observed and reported herein with appropriate assignments. All the observed fundamentals along with their assignments have been listed in table 3.

5.1 *Normal modes associated with the methyl groups*

5.1a *The stretching modes*: The infrared spectra of 2,4-DMA (figure 1) at room temperature shows a strong band at 2969 cm^{-1} (polarized Raman line at 2975 cm^{-1}) and another band at 2936 cm^{-1} recorded as a shoulder in the spectra at 123 K with its Raman partner appearing with a weak intensity. These are assigned as $\nu_{asym}(\nu'_1)$ and $\nu_{asym}(\nu'_2)$ respectively. Prasad (1975) observed only a shoulder at 2950 cm^{-1}.

The strong infrared band at 2922 cm^{-1} (figure 1) and the corresponding Raman line which is polarized, can be safely assigned to $\nu_{sym}(\nu'_3)$.

5.1b CH_3 *deformation modes*: Two strong infrared bands are seen at 1463 and 1444 cm^{-1} (figure 2, table 3) and the corresponding Raman lines are depolarized. Two more weak lines at 1458 and 1438 cm^{-1} are seen in the Raman spectrum only. We have assigned these frequencies, 1463, 1458, 1444 and 1438 cm^{-1} to the CH_3 asymmetric deformation modes δ^{+}_{asym} (table 3). One would expect to observe two asymmetric CH_3 deformation modes around 1375 cm^{-1} quite close to each other in accordance with the observed frequencies in 1,2,4-TMB (Green *et al* 1971). In the infrared spectra of 2,4-DMA a band of medium intensity at 1379 cm^{-1} (table 1) and the corresponding Raman line, strong and polarized ($\rho = 0{\cdot}30$) are assigned to δ_{sym} (ν'_8). A weak shoulder observed only in the Raman spectrum at 1373 cm^{-1} has been assigned to $\delta_{sym}(\nu'_9)$.

5.1c CH_3 *rocking modes*: In 2,4-DMA, one would expect 4 rocking modes and our recorded spectra (figure 3) reveal the presence of three distinct infrared bands at 1035,

Table 2. Ground state fundamental frequencies (cm^{-1}) of 2,4 dimethylaniline associated with the benzene ring in comparison with some similar molecules.

Designation of mode[a,b]	Description of mode	Expected range	1,2,4-TMB[c]	4F,1,2-DMB[c]	Present work					Earlier work[d]		
					IR	*I*	Raman	*I*	Polarization	IR	*I*	Assignment
Species a'												
ν_1	20a ν_{C-H}	3030–3125		3068 IR *w*	3079*	*w*	3078	*vw*				
ν_2	2 ν_{C-H}	3040–3100	3042 IR R *w s*	3058 IR *w*	3046	*m*	3050	*m*	*p*	3040	*sh*	7
ν_3	20b ν_{C-H}	2980–3050	3051 IR *sh*	3029 IR *m*	3008	*s*	3017	*m*	*p*	3020	*m*	7
ν_4	8b ν_{C-C}	1585–1645	1620 IR *s*	1624 IR *s*	1611	*s*	1613	*sh*		1610	*m*	8
ν_5	8a ν_{C-C}	1545–1605	1581 IR *w*	1593 IR *s*	1590	*m*	1589	*mw*	*p*	1590	*sh*	8
ν_6	19b ν_{C-C}	1415–1520	1507 IR *vs*	1506 IR *s*	1510	*vs*	1515	*mw*	*p*	1510	*vs*	19
ν_7	19a ν_{C-C}	1370–1455	1448 IR R *w p*	1416 IR *m*	1410	*m*	1411	*mw*	*dp*			
ν_8	14 ν_{C-C}	1235–1320	1348 R *vw*	1276 IR R *s p*	1313	*m*	1313	*mw*	*p*	1315	*w*	14
ν_9	3-β_{C-H}	1270–1310	1289 IR, R *vw p*		1290	*s*						
ν_{10}	7a ν_{C-X}	1215–1320	1246 IR R *vs p*	1253 IR R *s p*	1275	*s*	1275	*s*	*p*	1280	*s*	7a
ν_{11}	13 ν_{C-X}	1090–1235	1212 IR R *m p*	1189 IR R *s p*	1240	*ms*	1242	*m*	*p*	1245	*m*	13
ν_{12}	18a β_{C-H}	1130–1175	1155 IR R *s p*	1151 IR R *s p*	1155	*ms*	1155	*m*	*p*	1155	*m*	15

Table 2. (*Continued*)

Designation of mode[a,b]	Description of mode	Expected range	1,2,4-TMB[c]	4F,1,2-DMB[c]	Present work					Earlier work[d]		
					IR	*I*	Raman	*I*	Polarization	IR	*I*	Assignment
ν_{13}	18b β_{C-H}	1065–1135	1125 IR R *s p*	1105 IR R *s p*	1122‡	*w*	1120	*vw*				
ν_{14}	7b ν_{C-X}	820–1005	925 IR R *s p*	947 IR R *s p*	933	*mw*	933	*s*	*p*			
ν_{15}	12 ϕ_{C-C-C}	685–800	746 IR R *s p*	746 IR R *s p*			778	*vs*	*p*			
ν_{16}	1 Ring Breath	630–740	717 IR *R p*	719 IR R *p*	716	*ms*	717	*vvs*	*p*			
ν_{17}	6a ϕ_{C-C-C}	440–570	555 IR R *vs p*	547 IR R *p*	562	*sh*	560	*vs*	*p*			
ν_{18}	6b ϕ_{C-C-C}	395–505	472 IR R *s p*	482 R *p*	482	*mw*	482	*s*	*p*			
ν_{19}	9b β_{C-X}	295–445	439 R *p*	445 R *p*			445	*m*	*p*			
ν_{20}	9a β_{C-X}	200–345	320 IR R *s*	343 IR R	341	*mw*	341	*m*	*p*?			
ν_{21}	15 β_{C-X}	200–290	210 R *m*	214 IR R	211	*m*	210	*ms*	*p*?			
Species a″												
ν_{22}	17b γ_{C-H}	930–990	943 IR *vw*	931 IR *w*	946‡	*mw*	950	*sh*				
ν_{23}	5 γ_{C-H}	840–915	871 IR *s*	860 IR *s*	875	*m*	876	*vw*				
ν_{24}	11 γ_{C-H}	780–855	806 IR *vs*	809 IR *s*	814	*vs*	814	*vw*				

ν_{25}	4 $\delta_{C-C-C-C}$	675–740	705 IR s	695 IR	740	*ms*				735	*mb*	10
ν_{26}	16a $\delta_{C-C-C-C}$	530–620	540 IR *vs*	567 IR	551	*s*				555	*s*	6
ν_{27}	16b $\delta_{C-C-C-C}$	415–535	438 IR *vs*	451 IR	440	*s*				440	*m*	6
ν_{28}	10a γ_{C-X}	200–400	285 R *w*	312 IR R	284	*mw*	284	*m*	*dp*			
ν_{29}	10b γ_{C-X}	150–250	237 IR		241	*mw*						
ν_{30}	17a γ_{C-X}	100–165	146 IR R	149 R	158	*w, b*	155	*w*	*dp*			

[a]: Mulliken's notation (1955); [b]: Wilson's notation (1934), after Varsanyi (1974); [c]: Green *et al* (1971); [d]: Prasad 1975); *: Observed at 223 K; †: Observed at 123 K; ‡Observed in CS_2 solution (for other abbreviations, see the footnote of table 1).

Table 3. Ground state fundamental frequencies (cm^{-1}) in 2,4 dimethylaniline associated with substituent groups, in comparison with some similar mole

Designation of mode[a, b]	Description of mode	Expected range	1,2,4-TMB[c]	4F,1,2-DMB[c]	Present work					Earlier work[d]		
					IR	*I*	Raman	*I*	Polarization	IR	*I*	Assignm
CH_3 group												
ν'_1	$\nu_{asym}(CH)^{Str.}_{asym}$	2960–2990	2969 IR	2974 IR R *p*	2969	*m*	2975	*w*	*p*	2950	*sh*	ν_{asym}(CH
ν'_2	$\nu_{asym}(CH)^{Str.}_{asym}$	2925–2960	2940 IR R	2947 IR R *p*	2936	*sh*						
ν'_3	$\nu_{sym}(CH)^{Str.}_{sym}$	2860–2935	2921 IR R *p*	2924 IR R *p*	2922	*s*	2922	*ms*	*p*	2930	*mb*	ν_{asym}(CH
ν'_4	$\delta^{+}_{asym}(CH_3)^{Def.}_{asym}$	1455–1470	1467 IR	1460 IR	1463	*ms*	1463	*sh*	*dp*	1460	*mb*	δ^{+}_{asym}(CH
ν'_5	$\delta^{+}_{asym}(CH_3)^{Def.}_{asym}$	1445–1460	1455 IR	1459 IR R *dp*			1458	*mw*				
ν'_6	$\delta^{+}_{asym}(CH_3)^{Def.}_{asym}$	1440–1455			1444	*ms*	1445	*mw*	*dp*	1440	*mb*	δ^{+}_{asym}(CH
ν'_7	$\delta^{+}_{asym}(CH_3)^{Def.}_{asym}$	1410–1445					1438	*sh*				
ν'_8	$\delta_{sym}(CH_3)^{Def.}_{sym}$	1330–1395	1383 IR R *p*	1388 IR R *p*	1379	*m*	1381	*s*	*p*	1380	*w*	δ_{sym}(CH
ν'_9	$\delta_{sym}(CH_3)^{Def.}_{sym}$	1330–1395	1377 R	1379 IR R *p*			1373	*sh*				
ν'_{10}	$\delta^{-}_{asym}(CH_3)$Rock	1020–1070	1038 IR	1014 IR	1035	*m*	1040	*w*	*p*	1040	*wb*	β_{asym}(NH
ν'_{11}	$\delta^{-}_{asym}(CH_3)$Rock	1000–1025	999 IR	1005 IR	1012	*m*	1011	*w*	*p*	1020	*m*	δ^{-}_{asym}(CH
ν'_{12}	$\delta^{-}_{asym}(CH_3)$Rock	960–1000			984	*mw*	982	*w*	*p*	990	*w*	12
ν'_{13}	$\delta^{-}_{asym}(CH_3)$Rock	800–900			883*	*m sh*						
ν'_{14}	$\tau(CH_3)$Tors.	165–200			185	*w*	184	*w*				
NH_2 group												
ν''_1	$\nu_{as}(NH)^{Str.}_{as}$	3400–3500			3441	*s*	3442	*vw*		3470	*mb*	ν_{asym}(NH
ν''_2	$\nu_{sy}(NH)^{Str.}_{sy}$	3300–3420			3354	*s*	3370	*v*	*p*	3370	*mb*	ν_{sym}(NH
ν''_3	$\beta_{sy}(NH_2)^{Def.}_{sy}$	1600–1650			1626	*s*	1626	*ms*	*p*	1625	*vs*	β_{sym}(NH
ν''_4	$\beta_{as}(NH_2)$Twist	1020–1130			1076	*w*	1076	*vw*				
ν''_5	$\gamma_{sy}(NH_2)$o.p. wag	550–700			590	*vw*	588	*w, sh*				
ν''_6	$\tau'(NH_2)$Tors.	200–300			274	*vvw*						

weak band at 883 cm^{-1} (in the infrared spectra recorded at 123 K, figure 3) which has been tentatively assigned to δ^{-}_{asym} (ν'_{13}).

5.1d *CH_3 torsions*: Two torsional modes related to the CH_3 groups are expected in 2,4-DMA in the frequency interval 165–200 cm^{-1}. The infrared spectra recorded in the polyethylene matrix (figure 5) reveal the presence of a band at 185 cm^{-1} with its Raman partner appearing at 184 cm^{-1} only as a suggestion. This frequency has been assigned to $\tau(\nu'_{14})$. The other torsional frequency could not be observed.

5.2 *Normal modes associated with the amino group*

The infrared spectra show up two bands at 3441 and 3354 cm^{-1} (figure 1). The corresponding Raman lines are observed at 3442 and 3370 cm^{-1} (this Raman line is very broad). In any event, the infrared bands at 3441 and 3354 cm^{-1} have been assigned to $\nu_{asym}(\nu''_1)$ and $\nu_{sym}(\nu''_2)$ respectively.

In benzene derivatives (Varsanyi 1974) containing an amino group, NH_2 deformation β_{sym}, generally appears with good intensity. The strong Raman and infrared bands at 1626 cm^{-1}, in the case of 2,4-DMA, are then assigned to $\beta_{sym}(\nu''_3)$. Taking into consideration the frequencies of NH_2 twisting mode observed in 2,3-DMA (Shukla *et al* 1986) and *p*-toludene (Abasbegovic *et al* 1977), the weak bands observed in the spectra of 2,4-DMA (figure 2, table 3) at 1076 cm^{-1} are assigned to $\beta_{asym}(\nu''_4)$. The NH_2 wagging is expected in the frequency interval 550–700 cm^{-1} and one finds a weak band at 590 cm^{-1} in the infrared spectra taken in a polyethylene matrix and a weak Raman line at 588 cm^{-1}, both only as suggestions (figures 4 and 5). We tentatively assign these frequencies to $\nu_{sym}(\nu''_5)$.

The infrared spectrum of 2,4-DMA, recorded by trapping the molecules in a polyethylene matrix reveals the presence of three frequencies at 231, 274, and 310 cm^{-1} (figure 5). One of these frequencies probably corresponds to the NH_2 torsional mode which can be identified by the method of Kydd and Krueger (1978) used for benzene derivatives containing an amino group. According to these workers, if ν_τ represents the frequency of the NH_2 torsion and ν_i that of the inversion of the NH_2 group, the frequencies corresponding to $(\nu_\tau + \nu_i)$ and $(\nu_\tau - \nu_i)$ generally appear in the spectra. We have identified the frequency at 310 cm^{-1} as $(\nu_\tau + \nu_i)$ and at 231 cm^{-1} as $(\nu_\tau - \nu_i)$ from which one can calculate ν_τ which turns out to be $\approx$ 271 cm^{-1}. This leads us to believe that the weak infrared band at 274 cm^{-1} most probably corresponds to $\tau'(\nu''_6)$.

6. Observed spectral changes due to hydrogen bonding

The presence of intermolecular or intramolecular hydrogen bonding in a molecular system is known to considerably affect (Murthy and Rao 1968) its infrared and Raman spectra. Some spectral changes have been observed by us in 2,3-DMA (Shukla *et al* 1986). Since 2,4-DMA also possesses an amino group, one can expect similar changes as one goes from CS_2-solution to liquid and to solid at 223 and 123 K. The spectral changes are expected to be quite significant in the N–H stretching modes, although some effects can be seen in the NH_2 deformation modes also. Some marked spectral changes are presented in table 4. In view of the results obtained and discussed in detail for 2,3-DMA

Table 4. Observed spectral changes in different phases of 2, 4 dimethylaniline with some calculated results giving evidence of hydrogen bonding due amino group.

Phase	Temperature	Observed frequency (cm^{-1})				ν_{sym}(cal.)		Half band width (cm^{-1})			Integrated intensity			k[c] mdynes/Å corresponding to N–H stretch	An H–I (deg
		β_{sym}	ν_{asym}	$\Delta\nu$	ν_{sym}	B[a]	S[b]	β_{sym}	ν_{asym}	ν_{sym}	β_{sym}	ν_{asym}	ν_{sym}		
CS_2 Solution	Room	1623	3477	86	3391	3391	3407							6·54	
$\Delta\nu$		−03	36		37										
Liquid	Room	1626	3441	87	3354	3360	3382	46	102	92	132	74	120	6·40	
$\Delta\nu$		−01	21		11										
Solid	223°K	1627	3420	77	3343	3341	3352	53	108	139	121	80	105	6·34	
$\Delta\nu$		−02	10		2										
Solid	123°K	1629	3410	69	3341	3333	3342	73	139	156	168	144	150	6·32	

[a] Calculated value using Bellamy and Williams' relation (1957); [b] calculated value using Stewart's relation (1959); [c] calculated value using Linnett's relation (1945).

(Shukla *et al* 1986), it appears that a symmetric N–H . . . N (Shukla *et al* 1986; Bellamy and Williams 1957) type intermolecular hydrogen bonding exists in 2,4-DMA also, which slowly breaks down as the liquid is cooled down. At 123 K, the crystallization seems to be almost complete and the intermolecular hydrogen bonding assumes an asymmetric nature (Shukla *et al* 1986; Stewart 1959).

Like in 2,3-DMA (Shukla *et al* 1986), if one assumes that the interaction between the stretching and deformation modes of the NH_2 group is negligibly small and the magnitude of the force constant for the two N–H stretches, ν_{sym} and ν_{asym} is almost the same, one can use the relation proposed by Linnett (1945) and calculate the force constant k and the angle θ (H–N–H) in 2,4-DMA by the procedure adopted for 2,3-DMA (Shukla *et al* 1986). The results have been presented in table 4. It can be seen that the bond angle H–N–H at 223 K is 109·8° and is distinctly different from the values at room temperature and at 123 K. This indicates the anomalous behaviour of 2,4-DMA at 223 K and further suggests a phase transition of the molecule between 223 and 123 K.

Acknowledgements

One of us (ARS) is thankful to the UGC and CSIR, New Delhi, for financial support. The authors are grateful for facilities to Professor C N R Rao, IISc, Bangalore. The authors are thankful to Dr D N Sathyanarayana, IISc, Bangalore, for giving valuable help in interpreting parts of the low temperature spectra.

References

Abasbegovic N, Colombo L and Bleckmann P 1977 *J. Raman Spectrosc.* **6** 92
Bellamy L J and Williams R L 1957 *Spectrochim. Acta* **9** 341
Evans J C 1960 *Spectrochim. Acta* **16** 428
Green J H S 1970 *Spectrochim. Acta* **A26** 523, 1913
Green J H S, Harrison D J and Kynaston W 1971 *Spectrochim. Acta* **A27** 807
Hainer R M and King G W 1950 *Nature* **166** 1029
Kuwac A and Machida K 1978 *Spectrochim. Acta* **A34** 785
Kydd R A and Krueger P J 1978 *J. Chem. Phys.* **69** 827
Le Calve N and Labarbe P 1960 *Spectrochim. Acta* **16** 106
Linnett J W 1945 *Trans. Faraday Soc.* **41** 223
Mulliken R S 1955 *J. Chem. Phys.* **23** 1977
Murthy A S W and Rao C N R 1968 *Appl. Spectrosc. Rev.* **2** 69
Prasad M 1975 *Indian J. Pure Appl. Phys.* **13** 718
Shukla A R, Pathak C M, Dongre N G, Asthana B P and Shamir J 1986 *J. Raman Spectrosc.* **17** (in press)
Stewart J 1959 *J. Chem. Phys.* **30** 1259
Varsanyi G 1974 *Assignments for vibrational spectra of seven hundred benzene derivatives* (New York: John Wiley and Sons) vol. I
Wilson E B 1934 *Phys. Rev.* **45** 706
Young C W, Du Vall R B and Wright N 1951 *Anal. Chem.* **23** 709

Proc. Indian Acad. Sci. (Chem. Sci.), Vol. 97, No. 2, September 1986, pp. 117–123.
© Printed in India.

Preparation, characterization and thermal analysis of rare earth and uranyl hydrazinecarboxylate derivatives

G V MAHESH, P RAVINDRANATHAN and K C PATIL*

Department of Inorganic and Physical Chemistry, Indian Institute of Science, Bangalore 560 012, India

Ms received 12 February 1986; revised 16 May 1986

Abstract. Hydrazinecarboxylate derivatives of rare earth elements $Ln(N_2H_3COO)_3 \cdot 3H_2O$ (Ln = Ce, Pr, Nd, Sm, Eu, Gd, Tb, Dy, Ho, Er, Yb, and Y) and $UO_2(N_2H_3COO)_2 \cdot N_2H_4 \cdot H_2O$ have been prepared and characterized by chemical analysis and infrared spectra. Simultaneous TG-DTG-DTA of the rare earth complexes show that the thermal decompositions occur through carbonate and oxycarbonate intermediates to the respective oxides. The oxide formation temperatures are lower than the corresponding oxalates and acetates. The uranyl complex decomposes to U_3O_8 as the final product of decomposition.

Keywords. Hydrazinecarboxylate derivates; infrared spectra; thermal analysis.

1. Introduction

Metal hydrazinecarboxylates are of interest as precursors to fine particle oxide materials (Macek *et al* 1976; Ravindranathan and Patil 1985). In our earlier study we reported the preparation, characterization and thermal analysis of transition metal hydrazinecarboxylate derivatives. In continuation of this study, we now describe the preparation, characterization and thermal analysis of $Ln(N_2H_3COO)_3 \cdot 3H_2O$ (Ln = Ce, Pr, Nd, Sm, Eu, Gd, Tb, Dy, Ho, Er, Yb and Y) and $UO_2(N_2H_3COO)_2 \cdot N_2H_4 \cdot H_2O$.

2. Experimental

Hydrazine hydrate ($N_2H_4 \cdot H_2O$) 99–100% BDH was used in all the reactions. Rare earth oxides (99·9% pure) were obtained from Indian Rare Earths Limited.

2.1 *Preparation of rare earth hydrazinecarboxylate hydrates*

The corresponding rare earth oxide was dissolved in the minimum quantity of dilute HCl required and the solution was then treated with hydrazine hydrate. The precipitate formed dissolved when CO_2 gas was bubbled through the solution. Crystalline solid products separated from the clear solution in a couple of days and these were washed with alcohol and ether and stored under vacuum. Their

2.2 *Preparation of uranyl hydrazinecarboxylate hydrazine hydrate*

Hydrazine hydrate was added to a solution of uranyl nitrate, $UO_2(NO_3)_2 \cdot 6H_2O$ (May and Baker). The precipitate initially formed was dissolved by passing CO_2 gas through the solution and the resulting clear solution was kept open to the atmosphere. Light yellow crystals were formed after 10–15 days, which were washed with alcohol and ether and stored under vacuum. The composition of the crystals was fixed by chemical analysis to be $UO_2(N_2H_3COO)_2 \cdot N_2H_4 \cdot H_2O$.

2.3 *Analysis*

The metal contents in the rare earth complexes were determined by EDTA complexometric titrations. The uranium(VI) in the complex was determined gravimetrically using oxine. The hydrazine content was determined volumetrically using 0·025 M KIO_3 solution under Andrews' conditions (Vogel 1961).

2.4 *Physicochemical studies*

The infrared spectra of the complexes were recorded as nujol mulls using a Perkin-Elmer 781 spectrophotometer. Simultaneous TG-DTG-DTA of the samples were recorded using an Ulvac Sinku-Riko TA 1500 Instrument. All the experiments were carried out using 3–6 mg samples under ambient conditions. The heating rate employed was 10°C/min. The oxides were characterized by the x-ray powder diffraction patterns recorded on a Philips PW 1050/70 diffractometer using CuK_α radiation. The BET surface areas of oxides were measured by nitrogen adsorption using a Micromeritics Accusorb 2100E instrument.

3. Results and discussion

The reaction of rare earth ions (Ln^{3+}) with $N_2H_4 \cdot H_2O$ in the presence of CO_2 yields the corresponding hydrazinecarboxylate hydrates, $Ln(N_2H_3COO)_3 \cdot 3H_2O$ (Ln = Ce, Pr, Nd, Sm, Eu, Gd, Tb, Dy, Ho, Er, Yb and Y) as reported (Macek *et al* 1976). Our attempts to obtain any hydrazinium, $N_2H_5Ln(N_2H_3COO)_3 \cdot xH_2O$ or hydrazine, $Ln(N_2H_3COO)_3 \cdot xN_2H_4$ derivatives were not successful. Use of $N_2H_3COON_2H_5$ (Ravindranathan and Patil 1985) instead of $N_2H_4 \cdot H_2O$ also resulted in the formation of the $Ln(N_2H_3COO)_3 \cdot 3H_2O$ type of complexes. It is surprising that the corresponding lanthanum derivative $La(N_2H_3COO)_3 \cdot 3H_2O$ could not be obtained under similar experimental conditions.

3.1 *Infrared spectra*

The infrared absorption spectra of $Ln(N_2H_3COO)_3 \cdot 3H_2O$ type complexes are all identical as is expected. A typical IR spectrum of $Nd(N_2H_3COO)_3 \cdot 3H_2O$ is shown in figure 1. The IR spectra of these complexes show the characteristic N–N stretching frequency of $N_2H_3COO^-$ in the region 990–1000 cm^{-1}. Other IR absorption frequencies of $N_2H_3COO^-$ are similar to those reported for $M(N_2H_3COO)_2 \cdot xH_2O$ type complexes (Patil *et al* 1983). The IR spectrum of

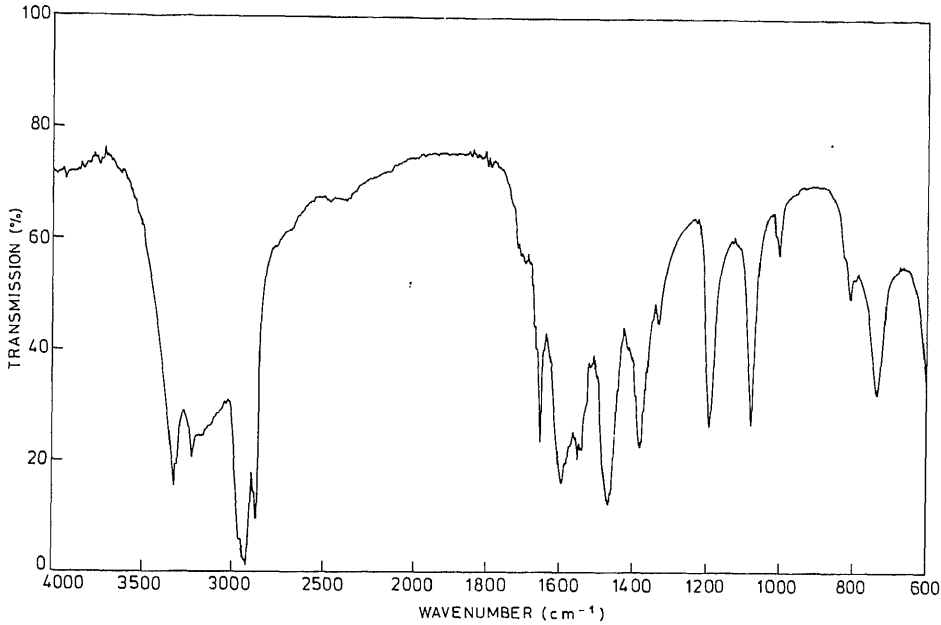

Figure 1. Infrared spectrum of $Nd(N_2H_3COO)_3 \cdot 3H_2O$

3.2 *Thermal analysis*

The results of TG-DTA of the $Ln(N_2H_3COO)_3 \cdot 3H_2O$ complexes and $UO_2(N_2H_3COO)_2 \cdot N_2H_4 \cdot H_2O$ are summarized in table 1. The thermal analysis curve of $Nd(N_2H_3COO)_3 \cdot 3H_2O$ is shown in figure 2. The composition of the intermediates are those which best fit the observed weight loss in TG.

All the complexes, $Ln(N_2H_3COO)_3 \cdot 3H_2O$, lose the water of hydration initially in a single step to yield the corresponding metal hydrazinecarboxylates. The dehydration takes place at fairly high temperatures (120–200°C) indicating the coordination of the water molecules to the metal.

The hydrazinecarboxylates obtained after dehydration decompose exothermically to the respective metal carbonates $Ln_2(CO_3)_3$. The DTA curve shows two exotherms while the TG curve shows a single step for the decomposition to $Ln_2(CO_3)_3$. In certain cases, like in Pr, Nd and Gd complexes, the TG shows breaks (~22% weight loss) indicating decomposition through a very unstable intermediate. On the basis of our earlier studies (Patil *et al* 1979; Ravindranathan and Patil 1985), the observed weight loss appears to suggest the formation of an intermediate of the type $Ln_2(C_2O_4)_3 \cdot 3N_2H_4$. This intermediate could not be isolated as the TG curve shows continuous reaction in this region. In the case of lighter rare earths, the respective carbonates decompose through the oxycarbonates ($Ln_2O_3 \cdot CO_2$) (as indicated by TG) which then decompose endothermically to the respective oxides. However, this step is not observed in the heavier rare earth complexes which give

Table 1. Thermal analysis data of rare earth hydrazinecarboxylate hydrates, $Ln(N_2H_3COO)_3 \cdot 3H_2O$ and $UO_2(N_2H_3COO)_2 \cdot N_2H_4 \cdot H_2O$

Name of Ln in complex	Thermogravimetry: Step	Temperature range °C	% weight loss: Found	% weight loss: Calculated	DTA peak temperature °C	Solid product
Ce	1	100–160	13·00	12·88	145 (endo)	$Ce(N_2H_3COO)_3$
	2	160–280	59·00	58·93	240 (exo)	CeO_2
Pr	1	120–160	13·00	12·86	150 (endo)	$Pr(N_2H_3COO)_3$
	2	160–290	22·00	23·57	275 (exo)	$Pr_2(C_2O_4)_3 \cdot 3N_2H_4$
	3	290–335	42·00	45·01	310 (exo)	$Pr_2(CO_3)_3$
	4	335–450	53·00	55·48		$Pr_2O_3 \cdot CO_2$
	5	450–510	60·00	59·45	475 (endo)	Pr_6O_{11}
Nd	1	135–170	13·00	12·75	150 (endo)	$Nd(N_2H_3COO)_3$
	2	170–290	23·00	23·39	255 (exo)	$Nd_2(C_2O_4)_3 \cdot 3N_2H_4$
	3	290–330	39·00	36·56	310 (exo)	$Nd_2(CO_3)_3$
	4	330–560	57·00	55·05	380 (endo)	$Nd_2O_3 \cdot CO_2$
	5	560–600	61·00	60·24	560 (endo)	Nd_2O_3
Sm	1	120–160	13·00	12·57	155 (endo)	$Sm(N_2H_3COO)_3$
	2	160–310	45·00	44·02	260,305 (exo)	$Sm_2(CO_3)_3$
	3	310–550	57·00	54·26	455 (endo)	$Sm_2O_3 \cdot CO_2$
	4	550–590	61·00	59·39	575 (endo)	Sm_2O_3
Eu	1	135–175	13·00	12·53	165 (endo)	$Eu(N_2H_3COO)_3$
	2	175–275	43·00	43·85	245,265 (exo)	$Eu_2(CO_3)_3$
	3	275–515	56·00	54·06	420 (endo)	$Eu_2O_3 \cdot CO_2$
	4	515–575	60·00	59·17	560 (endo)	Eu_2O_3
Gd	1	150–195	13·00	12·37	185 (endo)	$Gd(N_2H_3COO)_3$
	2	195–305	23·00	22·69	280 (exo)	$Gd_2(C_2O_4)_3 \cdot 3N_2H_4$
	3	305–370	40·00	43·32	335 (exo)	$Gd_2(CO_3)_3$
	4	370–670	58·50	58·45	650 (endo)	Gd_2O_3
Tb	1	130–170	13·00	12·33	160 (endo)	$Tb(N_2H_3COO)_3$
	2	170–310	44·00	43·16	260,300 (exo)	$Tb_2(CO_3)_3$
	3	310–480	54·50	53·20	455 (endo)	$Tb_2O_3 \cdot CO_2$
	4	480–610	58·00	57·31	610 (endo)	Tb_4O_7
Dy	1	130–170	13·00	12·23	165 (endo)	$Dy(N_2H_3COO)_3$
	2	170–310	45·00	42·80	250,305 (exo)	$Dy_2(CO_3)_3$
	3	310–575	55·00	52·77	425 (endo)	$Dy_2O_3 \cdot CO_2$
	4	575–610	59·00	57·75	590 (endo)	Dy_2O_3
Ho	1	130–180	12·50	12·16	175 (endo)	$Ho(N_2H_3COO)_3$
	2	180–315	46·00	42·57	270,310 (exo)	$Ho_2(CO_3)_3$
	3	315–655	59·00	57·44	630 (endo)	Ho_2O_3
Er	1	130–175	13·00	12·10	175 (endo)	$Er(N_2H_3COO)_3$
	2	175–310	45·00	42·35	260,305 (exo)	$Er_2(CO_3)_3$
	3	310–620	57·00	57·14	615 (endo)	Er_2O_3
Yb	1	120–170	12·00	11·94	155 (endo)	$Yb(N_2H_3COO)_3$
	2	170–305	45·00	41·81	245,300 (exo)	$Yb_2(CO_3)_3$
	3	305–655	58·00	56·41	455 (endo)	Yb_2O_3
Y	1	135–175	16·00	14·67	170 (endo)	$Y(N_2H_3COO)_3$
	2	175–315	56·00	51·37	260,310 (exo)	$Y_2(CO_3)_3$
	3	315–640	72·00	69·31	415,640 (endo)	Y_2O_3
$UO_2(N_2H_3COO)_2 \cdot N_2H_4 \cdot H_2O$						

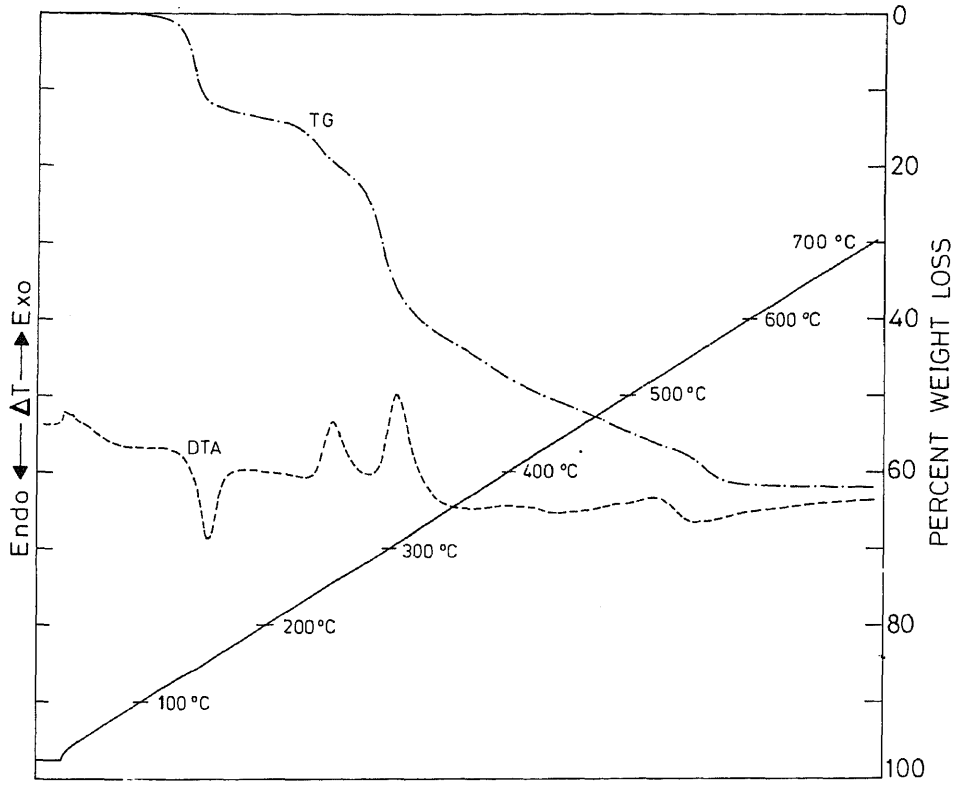

Figure 2. TG-DTA curves of $Nd(N_2H_3COO)_3 \cdot 3H_2O$

The cerium complex, $Ce(N_2H_3COO)_3 \cdot 3H_2O$, behaves differently, as compared to the other rare earth complexes. It loses its water of hydration in the region 100–160°C forming $Ce(N_2H_3COO)_3$, which then decomposes exothermically in a single step to the oxide, CeO_2.

The general decomposition sequence of the rare earth hydrazinecarboxylate hydrates may be represented by the following equations:

$$Ln(N_2H_3COO)_3 \cdot 3H_2O \xrightarrow{\text{endo}} Ln(N_2H_3COO)_3 \quad (1)$$

$$2Ln(N_2H_3COO)_3 \xrightarrow{\text{exo}} Ln_2(C_2O_4)_3 \cdot xN_2H_4 \quad (2)$$

$$Ln_2(C_2O_4)_3 \cdot xN_2H_4 \xrightarrow{\text{exo}} Ln_2(CO_3)_3 \quad (3)$$

$$Ln_2(CO_3)_3 \xrightarrow{\text{endo}} Ln_2O_3 \cdot CO_2 \quad (4)$$

The decomposition sequence followed by each complex is indicated in table 1.

The thermal decomposition of $Ln(N_2H_3COO)_3 \cdot 3H_2O$ is similar to those of rare earth carboxylates, e.g. acetates, oxalates, in that the intermediate stage is the carbonate which then decomposes to the oxide. The oxide formation temperatures are lower than those reported for acetates (Patil *et al* 1968), oxalates (Wendlandt 1959), and chemically prepared carbonates (Sastry *et al* 1966). No carbonate or oxycarbonate stage has been observed during the decomposition of cerium(III) acetate (Edwards and Hayward 1968) or cerium(III) oxalate (Wendlandt 1959).

The uranyl complex $UO_2(N_2H_3COO)_2 \cdot N_2H_4 \cdot H_2O$ (Slivnik *et al* 1979) decomposes in two steps to give U_3O_8 as the final product. Formation of U_3O_8 was confirmed by its XRD pattern. The minimum oxide (U_3O_8) formation temperature is ~585°C.

3.3 *BET surface area*

The decomposition behaviour of rare earth hydrazinecarboxylates is quite interesting. The decomposition of the cerium complex is autocatalytic and is accompanied by swelling due to the evolution of large volumes of gases like NH_3, H_2O, N_2 and CO_2. The decomposition product is voluminous fine particle CeO_2 having a surface area of 90 $m^2 g^{-1}$. However, other rare earth complexes do not exhibit autocatalytic decomposition behaviour and yield oxides with lower surface areas e.g. $Eu_2O_3 - 33$ $m^2 g^{-1}$, $Sm_2O_3 - 27$ $m^2 g^{-1}$ and $Dy_2O_3 - 17$ $m^2 g^{-1}$. The observed variation in the surface areas may be attributed to the higher oxide formation temperatures as well as the different decomposition paths followed by the heavier rare earth complexes.

4. Conclusions

The following general observations emerge from the present study.

(i) All the rare earths with the exception of lanthanum form $Ln(N_2H_3COO)_3 \cdot 3H_2O$ complexes under similar experimental conditions.

(ii) The decomposition proceeds through carbonates similar to the decomposition of rare earth acetates and oxalates.

(iii) The oxide formation temperatures of $Ln(N_2H_3COO)_3 \cdot 3H_2O$ are lower than those of the corresponding rare earth acetates and oxalates.

(iv) The cerium complex decomposes autocatalytically with swelling to give CeO_2 with large surface area.

Acknowledgements

The authors thank the Department of Science and Technology and the Department of Atomic Energy, Government of India, for financial support.

References

Edwards D A and Hayward R N 1968 *Can. J. Chem.* **46** 3443

Patil K C, Chandrasekhar G V, George M V and Rao C N R 1968 *Can J. Chem.* **46** 257
Patil K C, Budkuley J S and Pai Verneker V R 1979 *J. Inorg. Nucl. Chem.* **41** 953
Patil K C, Soundararajan R and Goldberg E P 1983 *Synth. React. Inorg. Met.-Org. Chem.* **13** 29
Ravindranathan P and Patil K C 1985 *Proc. Indian Acad. Sci. (Chem. Sci.)* **95** 345
Sastry R L N, Yoganarasimhan S R, Mehrotra P N and Rao C N R 1966 *J. Inorg. Nucl. Chem.* **28** 1165
Slivnik J, Rahten A and Sedej B 1979 *Vestn. Slov. Kem. Drus.* **26** 461; *Chem. Abst.* **92** 225831w
Vogel A I 1961 *A text book of quantitative inorganic analysis* 3rd edn (London: Longmans Green) p. 380
Wendlandt W W 1959 *Anal. Chem.* **31** 408

$RuCl_2(PPh_3)_3$ catalyzed oxidation of secondary alcohols with N-methylmorpholine N-oxide

K VIJAYASRI, J RAJARAM and J C KURIACOSE*
Department of Chemistry, Indian Institute of Technology, Madras 600 036, India

MS received 21 November 1985; revised 29 March 1986

Abstract. Catalytic amounts of $RuCl_2(PPh_3)_3$ in the presence of excess of N-methylmorpholine N-oxide (NMO) in DMF, oxidizes secondary alcohols to ketones. Spectral and electrochemical studies reveal the formation of an oxocomplex of Ru(IV), on adding excess of NMO. In the proposed mechanism, the Ru(IV)-oxo complex formed from Ru(II) and NMO, attacks the substrate in the rate determining step.

Keywords. Oxidation; secondary alcohols; N-methylmorpholine N-oxide; catalysis by Ru(II).

1. Introduction

Dichloro*tris*(triphenylphosphine)ruthenium(II) has wide application as a homogeneous catalyst in hydrogenation, isomerization, hydrosilylation and transfer hydrogenation reactions (Jardine 1984). In many ways it is complementary to Wilkinson's catalyst, $RuCl(PPh_3)_3$ (Jardine 1981). The oxidation of organic compounds catalyzed by $RuCl_2(PPh_3)_3$ has not received much attention. At room temperature $RuCl_2(PPh_3)_3$ catalyzes the oxidation of styrene (Turner and Lyons 1973) and alcohols (Tsuji *et al* 1984) by *t*-butyl hydroperoxide. In the presence of iodosobenzene, $RuCl_2(PPh_3)_3$ catalyzes the oxidation of alcohols (Muller and Godoy 1981a) and acetylene (Muller and Godoy 1981b). Sharpless *et al* (1976) have carried out reactions using several N-oxides to oxidize cholestanol, geraniol, etc. in the presence of $RuCl_2(PPh_3)_3$. There are no significant reports on the kinetics of ruthenium(II)-catalyzed oxidation of secondary alcohols. The oxidation of cyclohexanol, 1-phenylethanol and 2-propanol by N-methylmorpholine N-oxide (NMO) in DMF as the solvent is reported in this paper. A suitable mechanism is proposed based on the spectral, electrochemical and kinetic data.

2. Experimental

N-methylmorpholine N-oxide monohydrate (Fluka) was used as such. All the secondary alcohols were purified according to standard procedures. $RuCl_2(PPh_3)_3$ was prepared as per Stephenson and Wilkinson (1966), while DMF was purified as

per Faulkner and Bard (1968). Ruthenium(II) solutions were estimated by the thiourea method (Ayres and Young 1950).

Kinetic studies were carried out at 35±0·1°C. The concentration of unreacted NMO at any instant was determined titanometrically as reported earlier (Vijayasri *et al* 1985). For low concentrations of NMO (below 0·05 M) the titanometric method not being very accurate, the ketone formed from the alcohol was estimated spectrophotometrically by the method of Lappin (1951).

Electronic spectra were recorded on a Shimadzu UV-240 spectrophotometer while EPR spectra were recorded at 77°K on a Varian E4 spectrometer and IR spectra were recorded on a Perkin-Elmer 983G spectrometer. Voltammograms were recorded on a Princeton Applied Research Model 173, 175 and 179 electrochemistry system equipped with an *X–Y* recorder. The cell used was of conventional three-electrode design, consisting of Pt-wire as the working electrode, Pt-foil as the counter electrode and silver wire as the reference electrode. Tetra-*n*-butylammonium perchlorate is used as the supporting electrolyte.

3. Results and discussion

Cyclohexanol, 1-phenylethanol and 2-propanol are oxidized by NMO, in the presence of $RuCl_2(PPh_3)_3$, to the corresponding ketones. There is no oxidation of the alcohol by NMO in the absence of the catalyst. There is no reaction between $RuCl_2(PPh_3)_3$ and the alcohol in the absence of NMO as evidenced by the electronic spectra. Keeping the concentration of the substrate at a large constant value, a plot of log[NMO] vs time is linear showing that the order in NMO is unity. The orders with respect to the catalyst and the substrate ([substrate] > 0·5 M) are determined to be one and zero respectively from the pseudo first order rate constants (table 1). The order with respect to the substrate is fractional at low concentrations (0·05 to 0·2 M, figure 1). Experimental investigations could not be carried out for concentrations of substrate below 0·05 M owing to inaccuracies in the isolation and estimation of the ketone formed in these cases. The ketone formed by the catalytic oxidation of the alcohol in the concentration range 0·05 to 1·0 M corresponds to that of the NMO consumed which gives a stoichiometry of 1 : 1 between the substrate and NMO.

The absorption spectrum of $RuCl_2(PPh_3)_3$ showed significant changes when the oxidant was present in the system and hence, the electronic and EPR spectra of the $RuCl_2(PPh_3)_3$-NMO system were examined. $RuCl_2(PPh_3)_3$ in DMF (figure 2a) has absorption bands at 615 nm ($\epsilon = 388\ M^{-1}\ cm^{-1}$) and 330 nm ($\epsilon = 3107\ M^{-1}\ cm^{-1}$). Ruthenium(II) a low spin, d^6 system can have *d–d* transitions, $^1A_{1g} \rightarrow {}^1T_{1g}$ and $^1A_{1g} \rightarrow {}^1T_{2g}$ apart from MLCT and LMCT spectra (M = metal, L = ligand and CT = charge transfer). The CT bands generally obscure the *d–d* bands (Lever 1984b). Absorptions at 330 and 615 nm may be due to LMCT and MLCT respectively. The band at 615 nm is assigned to MLCT as metal ions like ruthenium(II) generate fairly low energy, CT absorption of the MLCT class (Lever 1984a). When NMO is added to ruthenium(II), a new absorption band appears at 385 nm (figure 2b). This new absorption at 385 nm, observed within one to two

Table 1. Determination of the order of reaction with respect to the reactants at high concentrations of the substrate (temperature = 35±0·1°C; solvent = DMF).

Substrate	[NMO] (M)	[S] (M)	$[RuCl_2(PPh_3)_3] \times 10^3$ (M)	$k' \times 10^3$ (min^{-1})	$\frac{k'}{[Ru(II)]} = k_1$ $M^{-1}\ min^{-1}$
Cyclo-hexanol	0·10	1·0	1·0	19·75	19·75
	0·07	1·0	1·0	20·56	20·56
	0·05	1·0	1·0	19·33	19·33
	0·05	0·70	1·0	18·70	18·70
	0·05	0·50	1·0	18·96	18·96
	0·05	1·0	0·75	13·99	19·65
	0·05	1·0	0·50	9·75	19·50
			k_1(mean) = 19·35±0·62 $M^{-1}\ min^{-1}$		
2-Propanol	0·10	1·0	0·75	12·48	16·64
	0·07	1·0	0·75	12·91	17·21
	0·05	1·0	0·75	12·52	16·69
	0·05	0·50	0·75	12·44	16·59
	0·05	0·70	0·75	12·98	17·31
	0·05	1·0	0·50	8·54	17·08
	0·05	1·0	1·00	17·92	17·92
			k_1(mean) = 17·06±0·44 $M^{-1}\ min^{-1}$		
1-Phenyl ethanol	0·10	1·0	0·75	16·61	22·15
	0·07	1·0	0·75	16·39	21·85
	0·05	1·0	0·75	16·44	21·92
	0·05	0·50	0·75	16·46	21·95
	0·05	0·70	0·75	17·02	22·69
	0·05	1·0	1·0	23·33	23·33
	0·05	1·0	0·50	11·08	22·16
			k_1(mean) = 22·29±0·50 $M^{-1}\ min^{-1}$		

k' = pseudo first order rate constant ($[S] \gg [NMO]$);
k_1 = overall second order rate constant.

state of ruthenium. This can be Ru(IV) since a 1 : 1 stoichiometry is observed between Ru(II) and NMO. The formation of the Ru(IV) species (d^4 system) could be established by EPR studies since $RuCl_2(PPh_3)_3$ (low spin, d^6 system) is not expected to give EPR signals. However, both $RuCl_2(PPh_3)_3$ as well as a mixture of $RuCl_2(PPh_3)_3$ and NMO are not found to give EPR signals. For d^4 systems like Ru(IV) there are difficulties in detecting EPR signals due to very short spin-lattice relaxation times and large zero field splittings (McGarvey 1966). In the absence of any evidence from EPR studies, cyclic voltammetric studies on solutions of $RuCl_2(PPh_3)_3$ in DMF were undertaken. The voltammogram (figure 3) shows three peaks A_a, B_a and C_a during anodic oxidation and three peaks A_c, B_c and C_c during cathodic reduction. The peak-to-peak potential separations of the oxidative and reductive waves range from 65 to 70 mV, which are characteristic of one-electron reversible process (Bard and Faulkner 1980). Peak A_a and its reduction cycle counterpart A_c can be assigned to Ru(III)/Ru(II) interconversion. Similarly peaks at B_a and B_c can be assigned to Ru(IV)/Ru(III) interconversion. Peaks C_a and C_c

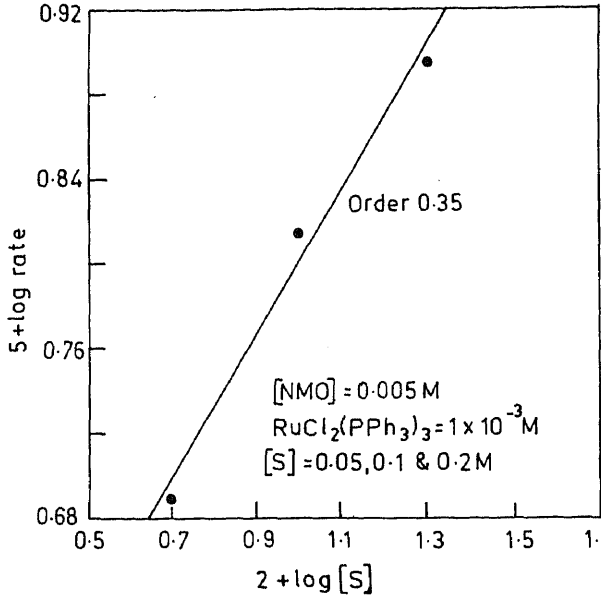

Figure 1. Order with respect to cyclohexanol at low concentrations.

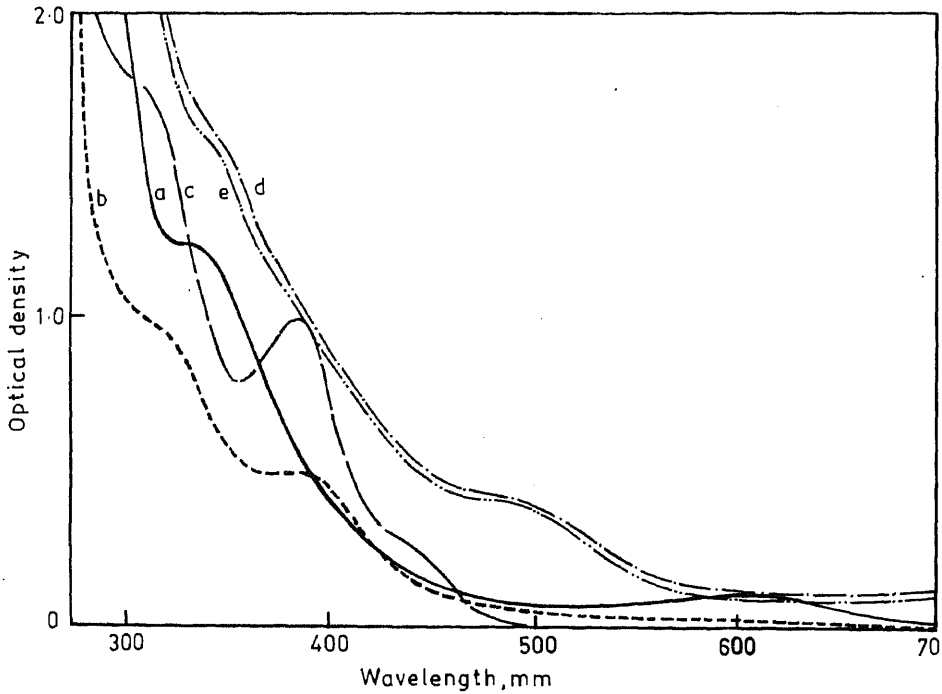

Figure 2. Absorption spectra of (a) $RuCl_2(PPh_3)_3(4\times10^{-4}$ M) in DMF, (b) $RuCl_2(PPh_3)_3(4\times10^{-4}$ M)+NMO (0·2 M) in DMF (spectrum recorded 1 hr after mixing), (c) Ru(IV) generated electrochemically from $RuCl_2(PPh_3)_3$ in DMF, (d) triphenylphos-

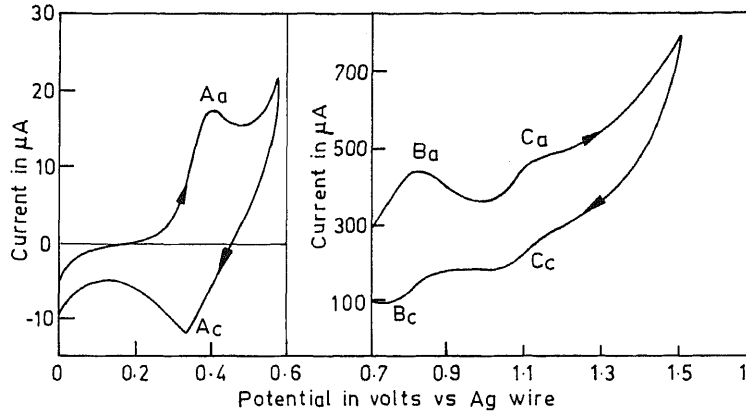

Figure 3. Cyclic voltammograms of $RuCl_2(PPh_3)_3$ in DMF in the region **a.** 0 to 0·6 V, **b.** 0·7 to 1·5 V.

controlled potential oxidation of $RuCl_2(PPh_3)_3$ in DMF at 1·0 V gives a UV-VIS spectrum (figure 2c) similar to that of the spectrum got immediately after mixing $RuCl_2(PPh_3)_3$ and NMO (figure 2b). The intermediate can be an oxo or a non-oxo species of Ru(IV). Both the oxo-Ru(IV) complexes, like (trpy)(bpy)$Ru^{IV}O^{+2}$ and (bpy)py RuO^{+2} (Thompson and Meyer 1982), and non-oxo Ru(IV) amine complexes (Tovrog *et al* 1979) have been used as oxidants for alcohols like 2-propanol. The oxo species of Ru^{IV} is likely to be the active species since N-oxides are known to form metal oxo complexes, the metal undergoing a two-electron change (Powell *et al* 1984). It is difficult to locate the Ru = O frequency in IR as most of the peaks of PPh_3 group of $RuCl_2(PPh_3)_3$ appear in the region from 700–900 cm^{-1}. Ru(IV) generated electrochemically also oxidizes alcohols in stoichiometric amounts but these Ru(IV) complexes are not found to be stable. Complexes of Ru(IV) like (bpy)py $Ru^{IV}O^{+2}$ and (trpy)(bpy)$Ru^{IV}O^{+2}$ (Moyer 1981) are known. However, it has not been possible to isolate the Ru^{IV}-oxo complex prepared from $RuCl_2(PPh_3)_3$. Hence, it has to be formed only *in situ* and used in catalytic amounts with N-oxide. The instability might be due to the PPh_3 ligands which are known to stabilize lower oxidation states.

When the mixture of $RuCl_2(PPh_3)_3$ and N-oxide is allowed to react for a long time a new absorption band appears at 500 nm (figure 2e). Figure 2e is similar to that of the spectrum of authentic sample of triphenylphosphine oxide complex of Ru(II) (figure 2d). The formation of the triphenylphosphine oxide complex of Ru(II) can be explained only if Ru^{IV} is present as the oxo species. This type of oxygen transfer from Ru^{IV} oxo species to PPh_3 is reported in the case of (bpy)py RuO^{+2} (Moyer 1981). The authentic sample of triphenylphosphine oxide complex, prepared *in situ* by passing oxygen through $RuCl_2(PPh_3)_3$ (Cenini *et al* 1971, 1972)

species. The formation of a triphenylphosphine oxide complex of Ru(II) after a long reaction time could be explained if the oxygen from the oxo species is transferred to PPh_3. There is inhibition by added triphenylphosphine, provided $[PPh_3]$ is high and so dissociation of PPh_3 from $RuCl_2(PPh_3)_3$ is given in the first step. In the absence of any inhibition by added N-methylmorpholine (NM) a prior equilibrium step involving this as the product is excluded.

Mechanism:

$$RuCl_2(PPh_3)_3 + NMO \underset{k_{-1}}{\overset{k_1}{\rightleftharpoons}} [(NM)(PPh_3)_2Cl_2Ru^{+4}(O)] + PPh_3$$

$$[(NM)(PPh_3)_2Cl_2Ru^{+4}(O)] + R_1\text{–}\underset{R_2}{\overset{|}{C}}\text{–CHOH} \xrightarrow[k_2]{\text{slow}} \left[(PPh_3)_2Cl_2(O)Ru^{+4} \leftarrow\!- -\overset{\overset{-\delta}{|}}{O}\text{—}\underset{R_2}{\overset{\overset{+\delta}{|}}{CH}}\text{–}R_1\right] + NM$$

Adduct

$$\text{Adduct} \longrightarrow R_1\text{–}\underset{R_2}{\overset{\overset{+}{|}}{C}}\text{–OH} + Cl(O)Ru^{IV}(H)(PPh_3)_2 + Cl$$

$$R_1\text{–}\underset{R_2}{\overset{\overset{+}{|}}{C}}\text{–OH} \xrightarrow{\text{fast}} R_1\text{–}\underset{R_2}{\overset{|}{C}}\text{=O} + H^+$$

$$Cl(O)Ru^{IV}(H)(PPh_3)_2 + H^+ + Cl^- + PPh_3 \longrightarrow RuCl_2(PPh_3)_3 + H_2O$$

Ruthenium compounds are known to form adducts with organic compounds (Rajeshwar Rao *et al* 1979). There is no shift in the NMR signal of the –OH proton of the alcohol when $RuCl_2(PPh_3)_3$ alone is present. But if NMO is present along with $RuCl_2(PPh_3)_3$ there is a shift in the NMR signal of the –OH proton of the alcohol towards a lower τ value which indicates an adduct formation between Ru(IV) and alcohol. The UV-VIS spectrum of the mixture of $RuCl_2(PPh_3)_3$ and alcohol is the same as that of $RuCl_2(PPh_3)_3$ itself, which rules out the possibility of a complex formation between alcohol and $RuCl_2(PPh_3)_3$. Ruthenium compounds are known to be good hydride ion abstracting agents (Sasson and Rempel 1974). In the present study the kinetic isotopic effect is negligible ($k_H/k_D = 1{\cdot}1$). This indicates that the cleavage of the C–H bond is not involved in the rate-determining step. The mechanism given above leads to the rate expression (1).

$$\text{Rate} = \frac{k_1k_2[RuCl_2(PPh_3)_3][NMO][S]}{k_{-1}[PPh_3] + k_2[S]}, \quad S = \text{substrate.} \tag{1}$$

Equation (1) can be rearranged to give (2) and (3).

$$\text{Rate} = \frac{k_1[S][RuCl_2(PPh_3)_3][NMO]}{(k_{-1}/k_2)[PPh_3] + [S]}, \tag{2}$$

$$\frac{1}{\text{rate}} = \frac{k_{-1}[PPh_3]}{k_1k_2[S][RuCl_2(PPh_3)_3][NMO]} + \frac{1}{k_1[RuCl_2(PPh_3)_3][NMO]} \tag{3}$$

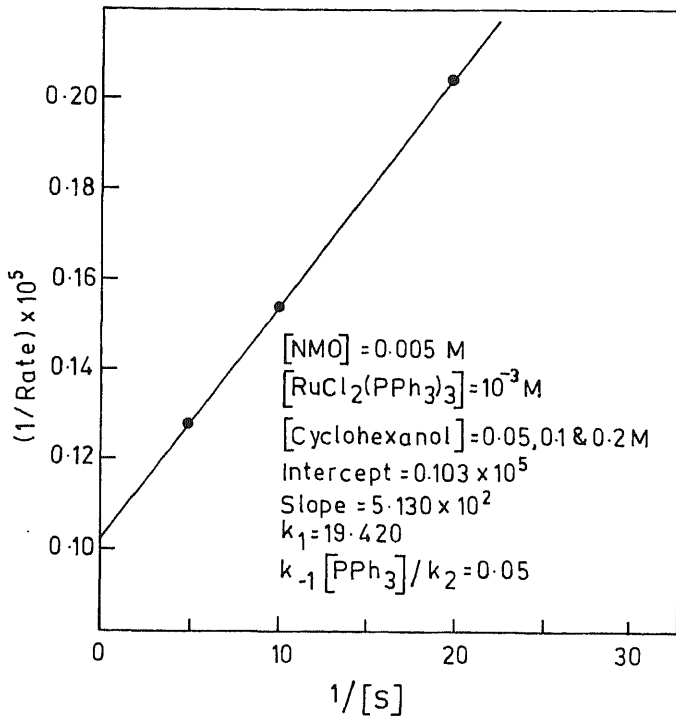

Figure 4. Evaluation of k_1 and $k_{-1}[PPh_3]/k_2$ from 1/rate vs. $1/[S]$ plot.

From the double reciprocal plot (3) (figure 4) k_1 and $(k_{-1}/k_2)[PPh_3]$ have been evaluated for a representative substrate like cyclohexanol, $k_1 = 19{\cdot}42\ M^{-1}\ min^{-1}$, $(k_{-1}/k_2)\ [PPh_3] \simeq 0{\cdot}05$. The concentration of the catalyst being kept constant, $[PPh_3]$ available from the dissociation step can be considered constant. Under experimental conditions, *i.e.* at low concentrations of the substrate (0·05 to 0·2 M) $(k_{-1}/k_2)[PPh_3]$ cannot be neglected compared to $[S]$. This explains the observed fractional order in substrate at low concentrations. At high concentrations of the substrate ($[S] > 0{\cdot}5$ CM) $(k_{-1}/k_2)[PPh_3]$ can be neglected when compared to $[S]$. This explains the zero order in substrate in this concentration range. A good agreement between the values of k_1 got from figure 4 and from the pseudo first-order rate constants in the case of cyclohexanol (table 1) supports the mechanism given above.

Acknowledgements

One of the authors, KV, thanks the CSIR, New Delhi, for financial support and

References

Ayres G H and Young F 1950 *Anal. Chem.* **22** 1277

Bard A J and Faulkner L R 1980 *Electrochemical methods, fundamentals and applications* (New York: John Wiley) p. 229

Cenini S, Fusi A and Capparella G 1971 *J. Inorg. Nucl. Chem.* **33** 3576

Cenini S, Fusi A and Capparella G 1972 *Inorg. Nucl. Chem. Lett.* **8** 127

Cotton F A, Barnes R D and Bannister E 1960 *J. Chem. Soc.* 2199

Faulkner L R, and Bard A J 1968 *J. Am. Chem. Soc.* **90** 6284

Jardine F H 1981 *Prog. Inorg. Chem.* (ed.) S J Lippard (New York: John Wiley and Sons) vol. 28, p. 6

Jardine F H 1984 *Prog. Inorg. Chem.* (ed.) S J Lippard (New York: John Wiley and Sons) vol. 31, p. 26

Lappin G R 1951 *Anal. Chem.* **23** 541

Lever A B P 1984a *Inorganic electronic spectroscopy* 2nd edn (Amsterdam: Elsevier) p. 205

Lever A B P 1984b *Inorganic electronic spectroscopy* 2nd edn (Amsterdam: Elsevier) p. 473

McGarvey B R 1966 in *Transition metal chemistry* (ed.) R L Carlin (New York: Marcel Dekker) vol. 3 p. 167

Moyer B A, Sipe B K and Meyer T J 1981 *Inorg. Chem.* **20** 1475

Muller P and Godoy J 1981a *Tetrahedron Lett.* **22** 2361

Muller P and Godoy J 1981b *Helv. Chim. Acta* **64** 2531

Powell M F, Pai E F and Bruice T C 1984 *J. Am. Chem. Soc.* **106** 3277

Rajeshwar Rao Y, Rajanna K C and Saiprakash P K 1979 *Indian J. Chem.* **A17** 297

Sasson Y and Rempel G L 1974 *Can. J. Chem.* **52** 3825

Sharpless K B, Akashi K and Oshima K 1976 *Tetrahedron Lett.* 2503

Stephenson T A and Wilkinson G 1966 *J. Inorg. Nucl. Chem.* **28** 945

Thompson M S and Meyer T J 1982 *J. Am. Chem. Soc.* **104** 4106

Tovrog B S, Diamond S E and Mares F 1979 *J. Am. Chem. Soc.* **101** 5067

Tsuji Y, Ohta T, Ido T, Minbu H and Watanabe Y 1984 *J. Organomet. Chem.* **270** 333

Turner J O and Lyons J E 1973 *German Patent* 2231678

Vijayasri K, Rajaram J and Kuriacose J C 1985 *Curr. Sci.* **54** 1279

Effect of dielectric constant of various mixed aqueous solvents on the proton-ligand and metal-ligand formation constants of N-methylisatin-β-amidinohydrazone

K SARKAR and B S GARG*
Department of Chemistry, University of Delhi, Delhi 110 007, India

MS received 27 August 1984; revised 7 April 1986

Abstract. The proton-ligand formation constant of N-methylisatin-β-amidinohydrazone (β-MIAG) and the metal-ligand formation constant of its complexes with UO_2(II), Cu(II), Ni(II), Co(II), Pb(II), Zn(II), Cd(II) and Mn(II) have been determined at a definite ionic strength, $\mu = 0{\cdot}1$ M $NaClO_4$, and at temperature $30 \pm 0{\cdot}5$°C, in aqueous organic solvents of different compositions. The variance of pK_a and log β_n with the inverse of the dielectric constant or the mole fraction of the solvent has also been studied. The pK_a and log β_n increases with the decrease of dielectric constant and the increase of the mole fraction of organic solvent of the media. In all the systems, the order of log β_n values of M(II)-β-MIAG chelates is in accordance with Irving-William's series.

Keywords. Potentiometric determination; formation constants; N-methylisatin-β-amidinohydrazone; dielectric constant of solvents.

1. Introduction

Derivatives of isatin and N-methylisatin are known to possess pharmacological activity. They act as central nervous system depressants and are used for the prevention of small pox etc. (Lozyuk 1974). The antimicrobial, antineoplastic, antihypotensive, analgesic, anti-inflammatory and cysticidal activity of isatin derivatives are well-known (Verma and Khan 1978). However, perusal of the literature reveals that no analytical work has been done on isatin and its derivatives. Hence, we have chosen N-methylisatin-β-amidinohydrazone as a ligand to study its interaction with bivalent metal ions.

2. Experimental

2.1 *Instruments*

A digital pH-meter (ECIL Model, pH-5651) with a single glass-calomel electrode assembly was used for pH measurements. It was standardised with suitable buffers before performing the titrations.

Constant temperature was maintained (to an accuracy of ±0·5°C) by using an

MLW, West Germany, NEB type thermostat. Presaturated nitrogen was passed through the solution during the titration. The pH values in aquo-organic mixtures were corrected using the method of Van Uitert and Haas (1953) and volume corrections were applied by the method of Rao and Mathur (1969).

2.2 *Reagents*

N-methylisatin-β-amidinohydrazone (β-MIAG) was prepared by refluxing equimolar quantities of N-methylisatin and aminoguanidine nitrate in alcohol. Its purity was further checked by IR, elemental analysis and TLC, m.p. 210–211°C. The solution of the ligand was prepared in freshly distilled dioxan. All the metal ion solutions were prepared from AR, (BDH) samples of the corresponding nitrates or sulphates and were standardised by conventional methods. Sodium perchlorate (Riedel) was used to keep the ionic strength constant. A 0·05 M solution of tetramethyl ammonium hydroxide (TMAH) (E Merck) was used as titrant. It was standardised with a standard solution of oxalic acid. The dioxan used was purified by refluxing with sodium metal for 24 hr and was freshly distilled over sodium before use. All other chemicals used were of reagent grade.

2.3 *pH-titration procedure*

The method of Bjerrum (1947) as modified by Irving and Rossotti (1953) was used to determine $\bar{n}$ and pL values. The experimental procedure involved potentiometric titrations of the following solutions against 0·05 M TMAH in various aquo-organic media, at 0·1 M $NaClO_4$ ionic strength and 30±0·5°C.

(i) $HClO_4$ $(1{\cdot}5\times10^{-3}\text{M})$
(ii) $HClO_4$ $(1{\cdot}5\times10^{-3}\text{M})+\beta$-MIAG $(2{\cdot}5\times10^{-3}\text{M})$
(iii) $HClO_4$ $(1{\cdot}5\times10^{-3}\text{M})+\beta$-MIAG $(2{\cdot}5\times10^{-3}\text{M})+M^{2+}(0{\cdot}5\times10^{-3}\text{M})$

These titrations have been repeated for β-MIAG in different aquo-organic solvents (50, 60, 75% v/v dioxan–water, 75% v/v acetone–water and 75% v/v alcohol–water) in order to determine the variation of its pK_a and the stability of its metal complexes with change of dielectric constant and the mole fraction of the organic solvent.

3. Results and discussion

The parameters $\bar{n}_A$, the average number of protons bound per free ligand ion, $\bar{n}$, the average number of ligand bound per metal ion, and pL, the free ligand exponent were determined by the expressions described by Irving-Rossotti, in order to evaluate the pK_a of the ligand and the metal ligand stability constants, log β. The stability constants were computed on an IBM 360 FORTRAN IV computer

nearest to zero, by minimizing

$$S\{\ S=\sum_{i=1}^{I} U^2(x_i y_i z_i)\ \},$$

with respect to variation in β_n.

S_{min} has the same statistical distribution as χ^2 with K degrees of freedom, and with weight defined in accordance with Rydberg and Sullivan (1959). The dissociation constant pK_a and the stability constants of the metal complexes in various concentrations of organic solvents are given in tables 1 and 2. In 75% v/v organic solvent compositions, the sequence of $1/\epsilon$ values is

dioxan–water > acetone–water > ethanol–water.

However, for the same v/v compositions, the pK_a values are in the sequence

acetone–water > dioxan–water > ethanol–water.

This indicates that the sequence does not follow the order of dielectric constants of the media.

In a mixed aqueous solvent the proton-ligand formation constant may be influenced by different solvent characteristics. These effects can be due to:

(1) dielectric constant of the mixed solvents;
(2) change of the hydrogen-bonding in water in the presence of organic solvents;
(3) proton solvation of the organic solvent.

(1) Bates *et al* (1966) and Rorabacher *et al* (1971) have explained the change of log K_H with solvent composition considering both electrostatic and non-electrostatic effects. They have concluded that the non-electrostatic phenomenon becomes increasingly important in solvents containing the organic solvent (OS) in more than 50% concentration.

Table 1. Dissociation constants i.e. pK_a of β-MIAG in mixed aqueous solvents at 30±0·5°C and 0·1 M $NaClO_4$ ionic strength.

Solvent composition (% v/v)	Mole fraction	Reciprocal of dielectric constant ($1/\epsilon$)	pK_a
Dioxan–water			
50	0·174	0·0293	7·95
60	0·240	0·0388	8·07
75	0·388	0·0699	8·52
Acetone–water			
75	0·422	0·0290	8·65
Alcohol–water			
75	0·479	0·0272	7·69

Table 2. Stability constant of bivalent metal complexes of β-MIAG in different mixed aqueous solvents at 30±0·5°C and 0·1 M $NaClO_4$ ionic strength.

System	Stability constant	Solvent composition (% v/v)				
		Dioxan–water			Acetone–water	Alcohol–water
		50	60	75	75	75
UO_2(II)-β-MIAG	log K_1	7·008	7·206	7·819	7·571	7·251
	log K_2	6·279	6·527	6·664	6·398	6·566
	S_{min}	0·13533	0·11934	0·14215	0·15108	0·11219
Cu(II)-β-MIAG	log K_1	6·815	7·158	7·795	7·395	7·112
	log K_2	5·413	5·759	6·360	6·272	5·978
	S_{min}	0·02101	0·65244	0·36559	0·28168	0·26277
Ni(II)-β-MIAG	log K_1	5·847	6·394	7·140	6·745	6·454
	log K_2	5·159	5·729	6·380	6·061	5·771
	S_{min}	0·05705	0·04840	0·06901	0·05541	0·05421
Pb(II)-β-MIAG	log K_1	5·533	5·801	6·502	5·948	5·626
	log K_2	4·225	4·540	5·240	4·777	4·458
	S_{min}	0·04152	0·03981	0·04567	0·10963	0·10223
Co(II)-β-MIAG	log K_1	5·303	5·620	6·134	5·852	5·654
	log K_2	4·135	4·184	5·044	4·765	4·241
	S_{min}	0·04584	0·03665	0·11028	0·10894	0·02253
Zn(II)-β-MIAG	log K_1	5·296	5·459	6·127	5·831	5·509
	log K_2	3·600	3·773	4·458	4·157	3·823
	S_{min}	0·02857	0·03314	0·04526	0·04164	0·03479
Cd(II)-β-MIAG	log K_1	4·463	4·638	5·171	4·873	4·536
	log K_2	3·380	3·463	3·750	3·448	3·388
	S_{min}	0·00957	0·00776	0·01153	0·00984	0·00849
Mn(II)-β-MIAG	log K_1	4·189	4·405	4·846	4·548	4·506
	S_{min}	0·02756	0·00234	0·10342	0·01331	0·00232

Protonation is viewed (Rorabacher *et al* 1971) as a two-step process,

$$H^+ + L^{-b} \overset{K_{OS}}{\rightleftharpoons} H^+ \ldots\ldots L^{-b} \overset{K_{H-L}}{\rightleftharpoons} HL^{+1-b} \qquad (1)$$

solvent separated ion pair

where, $K_H = K_{OS} \cdot K_{H-L}$. (2)

The values of K_{OS}, representing the diffusion controlled equilibrium constant for ion pair formation, can be calculated from Fuoss' (1958) equation.

$$K_{OS} = (4/3)\pi a^3 N_A 10^{-3} \exp\left[-(Z_H Z_L e_0^2)/\epsilon akT\right] \qquad (3)$$

where, a = distance of closest approach between the solvated proton and base in

teraction is related to the proton acceptance property of the medium and the roton solvation of the organic solvent as discussed below. Taking the logarithm of 2) and including the Fuoss expression for K_{OS} we have

$$\log K_H = \log(4/3)\pi N_A 10^{-3} + 3\log a + \log K_{H-L} - [Z_H Z_L e_0^2/2{\cdot}303kTa]\cdot(1/\epsilon) \quad (4)$$

Putting in the values of Z_L ($=-1$), it is seen that with decreasing dielectric onstant (ϵ) of the medium, log K_H increases.

2) According to Braude and Stern (1948), the tetrahedral lattice structure of ater gradually breaks down with the addition of organic solvent, and owing to the enser packing and the smaller extent of hydrogen-bonding between water olecules, the stability of the hydroxonium ion increases and the proton-donating roperty of the medium falls. This may imply that the proton-accepting property of ie solvent increases. It is also said that the H-bonded structure is less prevalent in ure ethanol in comparison of water and largely absent in pure acetone and pure ioxan. Gergely and Kiss (1977) have indicated that the dioxan molecules rogressively break down the H-bonded structure of water, whereas ethanol can rm H-bonded association with water. Hence, it is expected that the extent of -bonding in ethanol–water is greater than that in dioxan–water or in acetone–ater.

3) Protonation of the organic solvent: When the amount of organic solvent ecomes sufficiently large in a water–organic mixture, the proton solvation of the rganic solvent molecules takes place. Braude (1948) has reported that the asicities of the pure solvent molecules decrease in the following order:

water > dioxan > ethanol > acetone

hus the proton solvation of pure acetone is the least.

Effects (2) and (3) depend upon the concentration of the mixed aqueous media nd they may be counteracting with respect to the proton acceptance property of ie media. The more a solvent accepts protons the more the ligand acid is issociated. Thus the pK_a will tend to decrease.

The foregoing solvent effects influence the pK_a of the ligand conjugate acid in ie following manner:

a) With increase of solvent dielectric constant pK_a of the ligand decreases and ice-versa.

b) On decreasing the extent of hydrogen bonding in water by the organic solvent, ie proton accepting property of water increases. Hence, pK_a of the ligand ecreases.

c) Increasing proton solvation by the organic solvent decreases the pK_a of ligand nd vice-versa.

he sequence for pK_a values in the different solvents is almost the same as that for ielectric constants of the solvents except in acetone which is in the top place lightly higher than dioxan). Dioxan comes second, because it has the lowest ielectric constant but has greater proton solvation capacity and greater capacity to

In case of a dioxan–water mixture (50% v/v, to 75% v/v), the log pK_a increase with the increase of dioxan content of the mixture (table 1). However, there i some deviation from linearity because both the effects (b) and (c) for dioxan lead t lowering of the pK_a.

The stability constants log K_1 and log K_2, however, have some correlation wit the $1/\epsilon$ sequence in the different solvents, as proton solvation may not have an

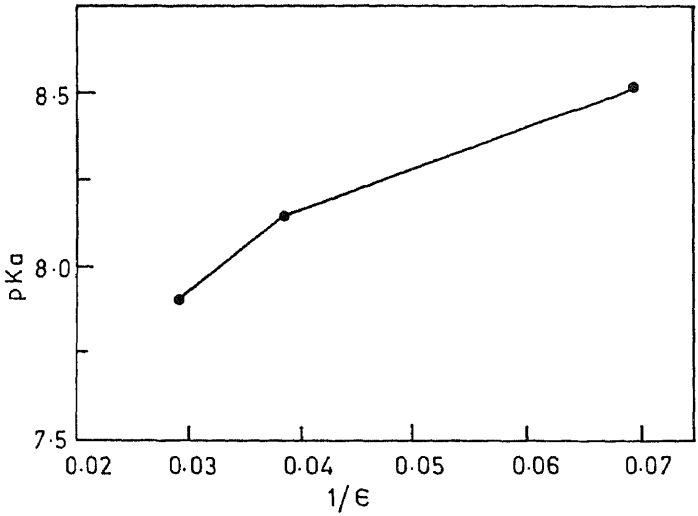

Figure 1. Plot of pK_a of β-MIAG vs. $1/\epsilon$ for dioxan water.

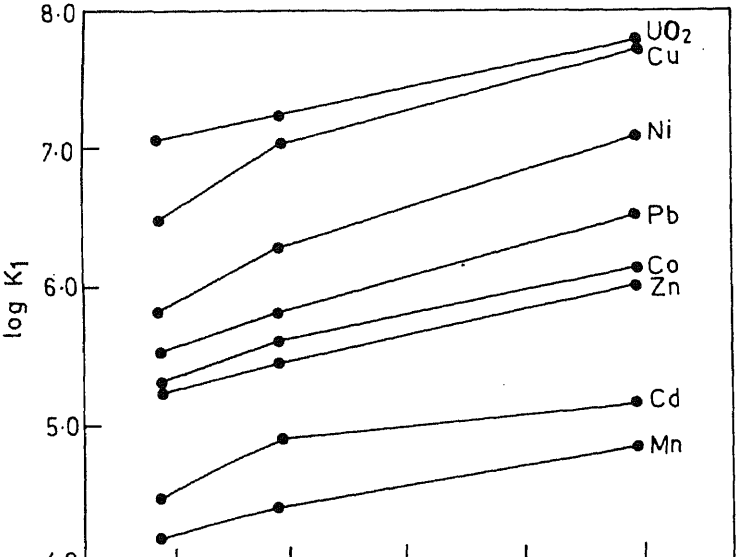

direct influence. The order of log β_n has become almost similar to the $1/\epsilon$ sequence(figures 1 and 2). Here again, it may be noted that the nature of the metal ions has little effect on the order. Comparison of the values of stability constants at 75% v/v shows the following sequence in the solvent mixtures for both log K_1 and log K_2 values:

dioxan–water > acetone–water > ethanol–water.

Acknowledgement

One of the authors (KS) is thankful to CSIR, New Delhi, for financial assistance.

References

Bates R G, Paabo M and Robinson R A 1966 *J. Phys. Chem.* **70** 247
Bjerrum 1941 Metal amine formation in aqueous solution (Copenhagen: Hasse and Son)
Braude E A 1948 *J. Chem. Soc.* 1971
Braude E A and Stern E S 1948 *J. Chem. Soc.* 1976
Fuoss R M 1958 *J. Am. Chem. Soc.* **80** 5059
Gergely A and Kiss T 1977 *J. Inorg. Nucl. Chem.* **39** 109
Irving H M and Rossotti H S 1953 *J. Chem. Soc.* 3397
Lozyuk L V 1974 *Mikrobiol. Zh. (Kiev)* **36** 224
Rao B and Mathur H B 1969 *Indian J. Chem.* **7** 1234
Rorabacher D B, Mackeller W J, Shu F R and Bonavita M 1971 *Anal. Chem.* **43** 561
Rydberg J and Sullivan J C 1959 *Acta Chem. Scand.* **13** 2059
Sullivan J C, Rydberg J and Miller W F 1959 *Acta Chem. Scand.* **13** 2023
Van Uitert L G and Haas C G 1953 *J. Am. Chem. Soc.* **75** 451
Varma R S and Khan I A 1978 *Def. Sci. J.* **28** 191

Synthesis and spectral studies of tin(IV) complexes with Schiff bases derived from sulpha drugs

ANIL VARSHNEY and J P TANDON*

Department of Chemistry, University of Rajasthan, Jaipur 302 004, India

MS received 2 July 1985; revised 13 January 1986

Abstract. Reactions of tin(IV) chloride with Schiff bases having ONN donor systems have been investigated and on the basis of elemental analysis, IR, PMR and ^{119}Sn Mössbauer spectral studies, possible structures have been indicated for the resulting new compounds. The Schiff bases used in these studies are the condensation products of salicylaldehyde with sulphathiazole, sulphaphenazole, sulphadiazine, sulphaguanidine, 2-(*p*-aminobenzene sulphonamide)-4,5-dimethyl oxazole, sulphisoxazole, sulphapyridine and sulphanilamide.

Keywords. Tin(IV) chloride; Schiff bases; sulpha drugs; infrared spectra; proton magnetic resonance spectra; Mössbauer spectra.

1. Introduction

Compounds containing the sulphonamide group have long been used as drugs for diseases like cancer, tuberculosis (Vaichaulis 1966), diabetes (Dietrich 1968), malaria (Schmidt 1969) and convulsions (Aktiesel and Kabet 1968). It has now been observed that some of these drugs show increased biological activity when administered in the form of metal complexes (Williams 1972; Frust and Haro 1969; Tiwari and Mishra 1980).

A number of references are now available to show that the condensation products of sulpha drugs with aldehydes, ketones or their derivatives are very active biologically, besides having good complexing ability, and their activity increases on complexation with metal ions (Jain and Chaturvedi 1977; Lal and Shukla 1981). It was, therefore, considered of interest to synthesize tin(IV) derivatives of Schiff bases, derived by the condensation of salicylaldehyde with some of the well-known sulpha drugs. In this paper we report the results of these studies.

2. Results and discussion

The equimolar reactions of stannic chloride with Schiff bases derived by condensation of salicylaldehyde with various sulpha drugs (SBH_2) can be represented by the following equation

$$SnCl_4 + SBH_2 \rightarrow SnCl_4 \cdot SBH_2.$$

repeated washing with cyclohexane and their purity was further checked by thin layer chromatography on silica gel G using anhydrous dimethyl formamide as the solvent – all the complexes moved as single spots.

All these complexes of tin(IV) are monomeric as evidenced by their molecular weight determination by the Rast camphor method. The low values of molar conductivity (8–14 ohm^{-1} cm^2 mol^{-1}) of the complexes in anhydrous dimethyl formamide show their non-electrolytic nature.

2.1 *IR spectra*

The ligands exhibit two broad peaks in the region 3400–3100 cm^{-1} due to the hydrogen-bonded OH and NH (Varshney and Tandon 1985). In the spectra of the complexes, the band due to OH gets shifted to the higher wave number region showing the coordination of the ligand through the phenolic oxygen. However, the ν NH band remains approximately at the same position, which clearly indicates the non-involvement of NH in complexation. A strong band in the region 1600–1620 cm^{-1} assignable to νC–N is observed in all the ligands. A slight shift of this band towards the higher frequency region in the case of tin(IV) derivatives may be due to an increase in the bond order of the azomethine group (Busch and Bailar 1956).

A medium intensity band in the ligand spectrum at $\sim$ 1280 cm^{-1} due to the C–O vibrations gets shifted to the higher frequency region ($\sim$ 1300 cm^{-1}) in the complexes suggesting the participation of phenolic oxygen in complexation (Biradar and Kulkarni 1971). Further, new strong bands in all the tin(IV) derivatives, appearing in the region 420–400 and 500–530 cm^{-1} are due to the Sn $\leftarrow$ N (Varshney and Tandon 1985c) and Sn $\leftarrow$ O (Saxena *et al* 1982) respectively.

2.2 *PMR spectra*

The ^{1}H NMR spectra of ligands show NH proton signals at δ 10·09 ppm while all the ligands show an OH proton signal at δ 12·10 ppm. The signal due to the NH proton remains unchanged in the compounds showing its non-involvement in coordination. However, the signal due to the OH proton gets shifted downfield indicating the coordination of the phenolic oxygen to the tin atom. A signal at δ 8·15 ppm is observed in the complexes due to the azomethine proton, which moves downfield in comparison to its original position in the free ligand, thereby indicating the coordination of the azomethine nitrogen to the metal atom. An appreciable change is also observed in the position of the aromatic phenyl protons appearing as a complex multiplet at δ 6·44–7·86 ppm.

2.3 *Mössbauer Spectra*

The Mössbauer spectrum of one of the complexes ($SnCl_4 \cdot C_{14}H_{14}N_4SO_3$ is recorded at 80°K using a liquid nitrogen cryostat. The isomer shift value is 0·35 mm sec^{-1}, which is lower than the 0·80 mm sec^{-1} observed in the case of tin(IV) chloride. Thus a decrease in the isomer shift value as compared to

the parent compound indicates complexation, which the magnitude of this fall is directly proportional to the donor strength of the ligand (Huggins *et al* 1969).

Since, the complex has no quadrupole splitting, it can be concluded that the spherical charge distribution around the tin nucleus is unchanged after complexation. This further indicates that there is no marked difference in the polarities of the tin-ligand bonds as reported earlier as well (Saxena *et al* 1984).

Thus on the basis of the above spectral evidence the structures in scheme 1 can be proposed for the resulting tin(IV) complexes.

3. Experimental

All the reactions were carried out under strictly anhydrous conditions and analytical grade chemicals were used for all experiments.

3.1 *Preparation of Schiff bases*

The Schiff bases have been synthesized by the condensation of salicylaldehyde with sulphathiazole(*I*), sulphaphenazole(*II*), sulphadiazine(*III*), sulphaguanidine(*IV*), 2-(*p*-aminobenzene sulphonamide)-4,5-dimethyloxazole(*V*), sulphisoxazole(*VI*), sulphapyridine(*VII*) and sulphanilamide(*VIII*) in 1:1 molar ratio using ethanol as the reaction medium. The solution was refluxed on a water bath for 3–4 h and then allowed to cool to room temperature. The products so obtained were recrystallised from acetone. The ligands used in these studies are as follows.

(1)	Salicylaldehyde sulphathiazole ($C_{16}H_{13}N_3S_2O_3$) m.p. 222°C	H_2ONN-1
(2)	Salicylaldehyde sulphaphenazole ($C_{22}H_{18}N_4SO_3$) m.p. 185°C	H_2ONN-2
(3)	Salicylaldehyde sulphadiazine ($C_{17}H_{14}N_4SO_3$) m.p. 240°C	H_2ONN-3
(4)	Salicylaldehyde sulphaguanidine ($C_{14}H_{14}N_4SO_3$) m.p. 230°C	H_2ONN-4
(5)	2-(*p*-amino benzene sulphonamide)-4,5-dimethyloxazole ($C_{18}H_{17}N_3O_4S$) m.p. 140°C	H_2ONN-5
(6)	Salicylaldehyde sulphisoxazole ($C_{18}H_{15}N_3O_3S$) m.p. 160°C	H_2ONN-6
(7)	Salicylaldehyde sulphapyridine ($C_{18}H_{17}N_3O_3S$) m.p. 200°C	H_2ONN-7
(8)	Salicylaldehyde sulphanilamide ($C_{13}H_{12}N_2O_3S$) m.p. 150°C	H_2ONN-8

3.2 *Analytical methods and physical measurements*

The complexes were analysed as reported earlier (Varshney and Tandon 1984, 1985) and the infrared spectra were recorded on a Perkin Elmer 577 IR

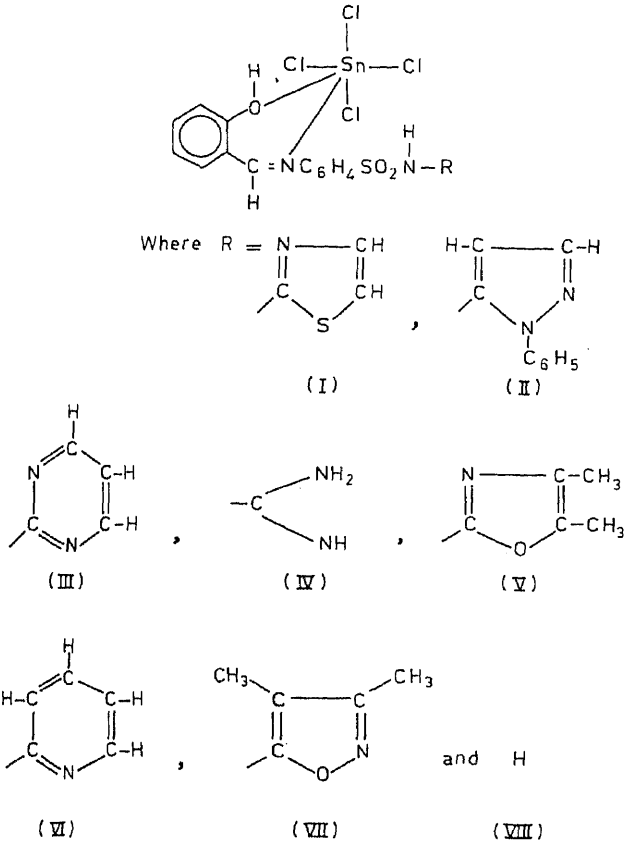

Scheme 1.

spectra employing deuterated dimethyl sulphoxide or deuterated chloroform as the solvent and tetramethyl silane as the internal standard.

^{119}Sn Mössbauer spectra were obtained using a constant acceleration microprocessor spectrometer (Cryophysics Ltd., Oxford) with a 512 channel data store. A 15 mci Ba $^{119m}SnO_3$ source was used at room temperature and samples were packed in perspex discs and cooled to 80°K using a liquid nitrogen cryostat. The experimental error in the measured values of the isomer shift (δ) and quadrupole splitting (Δ *Eq*) parameters was $\pm 0{\cdot}05$ mm sec^{-1}.

Molar conductance measurements were made in anhydrous dimethylformamide at 36 ± 1°C using a Systronics conductivity bridge Model 305. Molecular weight determinations were carried out by the Rast camphor method.

3.3 *Preparation of Sn(IV) complexes*

Equimolar amounts of stannic chloride and the ligand were mixed in a flask using benzene as the reaction medium. The colour of the reaction changed immediately. The resulting solution was stirred on a magnetic stirrer for about 4 h. Excess of

Table 1. Synthesis and characteristics of tin(IV) complexes (the tin compound used in all cases was $SnCl_4$, while the molar ratio of compound and ligand was 1 : 1).

Reactant ligand	Compound colour and state	m.p. °C	Analysis Observed (calculated) Sn	N	S	Mol. Wt obs. (calc.)
H_2ONN-1	$SnCl_4 \cdot C_{16}H_{13}N_3S_2O_2$	205	18·86	6·25	9·86	607
	Light yellow solid		(19·15)	(6·78)	(9·86)	(619·7)
H_2ONN-2	$SnCl_4 \cdot C_{22}H_{18}N_4SO_3$	180	16·94	8·86	4·92	659
	Orange solid		(17·49)	(9·04)	(5·16)	(678·7)
H_2ONN-3	$SnCl_4 \cdot C_{17}H_{14}N_4SO_3$	272	19·42	8·96	4·92	582
	Yellow solid		(19·96)	(9·42)	(5·38)	(594·7)
H_2ONN-4	$SnCl_4 \cdot C_{14}H_{14}N_4SO_3$	190	19·96	9·23	5·21	563
	Dark yellow solid		(20·51)	(9·68)	(5·53)	(578·7)
H_2ONN-5	$SnCl_4 \cdot C_{18}H_{17}N_3O_4$	145	18·24	6·32	4·92	615
	Dirty yellow solid		(18·79)	(6·65)	(5·07)	(631·7)
H_2ONN-6	$SnCl_4 \cdot C_{18}H_{15}N_3O_3S$	170	18·96	6·21	5·01	601
	Yellow solid		(19·34)	(6·84)	(5·21)	(613·7)
H_2ONN-7	$SnCl_4 \cdot C_{18}H_{17}N_3O_3S$	185	18·86	6·53	4·69	604
	Canary yellow solid		(19·28)	(6·82)	(5·19)	(615·7)
H_2ONN-8	$SnCl_4 \cdot C_{13}H_{12}N_2O_3S$	140	21·95	4·96	5·24	521
	Yellow solid		(22·12)	(5·22)	(5·96)	(536·7)

Acknowledgements

The authors are highly thankful to Dr A J Crowe, International Tin Research Institute, UK, for very kindly recording the Mössbauer spectrum. One of us (AV) is also thankful to the UGC, New Delhi for financial assistance. Thanks are also due to Hindustan Ciba-Geigy Limited for a free gift of sulphathiazole.

References

Aktiesel A and Kabet F 1968 *Danish Patent* 108626
Busch D M and Bailar J C Jr 1956 *J. Am. Chem. Soc.* **78** 1137
Biradar N S and Kulkarni V H 1971 *Z. Anorg. Allg. Chem.* **281** 312
Dietrich H 1968 *Swiss Patent* 454874
Frust A and Haro R T 1969 *Prog. Exp. Tumur Res.* **12** 102
Huggins K G, Parrett F W and Patel H A 1969 *J. Inorg. Nucl. Chem.* **71** 1209
Jain P and Chaturvedi K K 1977 *J. Inorg. Nucl. Chem.* **39** 901
Lal K and Shukla R K 1981 *J. Indian Chem. Soc.* **58** 115
Saxena A, Tandon J P, Molloy K C and Zuckerman J J 1982 *Inorg. Chim. Acta* **63** 71
Saxena A, Tandon J P and Crowe A J 1984 *Inorg. Chim. Acta* **84** 195
Schmidt L H 1969 *Annu. Rev. Microbiol.* **23** 427
Tiwari G D and Mishra M N 1980 *Curr. Sci.* **49** 8
Vaichaulis J M 1966 *US Patent* 3272352
Varshney A and Tandon J P 1984 *Proc. Indian Acad. Sci.(Chem. Sci.)* **93** 1259
Varshney A and Tandon J P 1985a *Indian J. Chem.* **A24** 70
Varshney A and Tandon J P 1985b *Proc. Indian Acad. Sci.(Chem. Sci.)* **94** 509

Proc. Indian Acad. Sci. (Chem. Sci.), Vol. 97, No. 2, September 1986, pp. 147–152.
© Printed in India.

Water-insoluble polyacrylamide XII : Polychelates based on poly (N-methacryloyl-*m*-amino benzoic acid)

KISHORE PATEL, TRUSHAR DESAI and BHIKHU SUTHAR*
Chemistry Department, Sardar Patel University, Vallabh Vidyanagar 388 120, India

MS received 26 August 1985; revised 16 May 1986

Abstract. Six new polychelates of Fe(II), Co(II), Ni(II), Cr(III), UO_2(II) and Zn(II) were prepared from the chelex poly(N-methacryloyl-*m*-amino benzoic acid). All these polychelates are coloured, amorphous powders, insoluble in all common organic solvents. They are characterized by electronic reflectance spectra, IR spectra elemental analyses and magnetic susceptibility measurements. All the polychelates show a six co-ordinated structure and suggest octahedral geometry. Conductometric studies indicated that these polychelates are non-electrolytes. Their thermal stabilities were established by thermogravimetric studies.

Keywords. Poly(N-methacryloyl-*m*-aminobenzoic acid); chelex; polychelate; diffuse reflectance Spectra; thermal stability; conductance.

1. Introduction

Literature concerning water-insoluble polyacrylamides (Joshi 1962; Patel *et al* 1985a) revealed that such polymers may find interesting applications. Only sparse reports have appeared (mostly in patents) about acryloyl-amino-benzoic acids and their polymers (Frantisek *et al* 1975; Yoshikazu *et al* 1975). Such polymeric ligands have provided a basis for the syntheses of polychelates from transition metals (Mykytiuk *et al* 1980; Kraus and Moore 1953; Desai and Suthar 1985). Chelex is a polymer containing pendant functional groups which act as chelating groups in binding polyvalent metal ions. Such properties of chelex have been exploited in diverse applications such as ion exchangers (Patel and Patel 1979), in metal separations (Dunn *et al* 1980) and preconcentration of metals (Mykytiuk *et al* 1980) and as therapeutic complexes in many biological models (Haner *et al* 1984). To understand such functions we have reported a series of metal chelates from chelex based on N-substituted carboxyphenyl acrylamide polymers (Patel and Suthar 1985a, 1985b; Patel *et al* 1985b). The present communication deals with the syntheses of the polychelates of Fe(II), Co(II), Ni(II), Cr(III), UO_2(II) and Zn(II) with chelex poly(N-methacryloyl-*m*-aminobenzoic acid). We have studied their diffuse reflectance spectra, infrared spectra, magnetic susceptibilities, elemental analyses and thermogravimetric properties.

2. Experimental

2.1 *Materials*

All chemicals used were of analytical grade purity. N-methacryloyl-*m*-a nobenzoic acid (MMAB) was synthesized from *m*-aminobenzoic acid according Patel *et al* (1985b). MMAB was recrystallized from alcohol, m.p. 190°C, yield 86 It is soluble in alcohol, dioxane THF, DMF and DMAC.

Analysis: N 6·78%; $C_{11}H_{11}NO_3$ requires 6·83% N.

The chelex poly(N-methacryloyl-*m*-aminobenzoic acid) (PMMAB) was prepa and characterized according to Patel *et al* (1985a).

2.2 *Preparation of polychelates*

All the metal polychelates were prepared as follows: Poly(N-methacryloyl- aminobenzoic acid, PMMAB) (5 g) was dissolved in dimethyl formamide (50 ml). this solution, metal nitrate (3 g in 50 ml DMF) was added. Sodium acetate (1 g) v then added to the reaction mixture. It was refluxed for 6 hr. The precipita material was filtered, washed with boiling DMF followed by hot water and fina with ethanol.

The Fe(II) polychelate was prepared according to the method mentioned abo using ferrous ammonium sulfate instead of ferrous nitrate. All the polychela were dried in an oven at around 60°C.

2.3 *Analytical methods*

All the physico-chemical measurements were made at 30°. The diffuse reflectar spectra were obtained on a Beckman DU Spectrophotometer. IR spectra w recorded on a Perkin Elmer 983 Spectrophotometer as KBr pellets. Magne measurements were made on a Sartorius semi-micro Gouy Balance. T thermogravimetric analyses were carried out using a Du Pont 951 thermal analy at a heating rate of 10°C/min in air. Conductances were measured on Konductoskop Metrohm Herisau, Switzerland, conductometer. For estimat elemental composition, the metal content in each polychelate was determined independent gravimetric and volumetric methods. Carbon, hydrogen and nitrog analyses were made on a Coleman C–H–N analyser.

3. Results and discussion

All the polychelates were dark coloured solids. They were insoluble in all comm organic solvents including water. Hence, it was not possible to characterize them conventional methods such as viscometry and osmometry. It was also not possi

Table 1. Characterization of polychelates from poly(N-methacryloyl-*m*-aminobenzoic acid).

Sample code	Analysis (%)*				μ_{eff} (B.M.)	Specific conductance (10^6) (mho cm^{-1})	Decomposition temperature (°C)
	C	H	N	Metal			
Chelex-PMMAB	64·46	5·36	6·86	–			
	(64·39)	(5·37)	(6·83)			1·40	310
Fe(II)-PMMAB	57·10	4·40	6·12	12·20			
	(56·92)	(4·31)	(6·04)	(12·04)	40·70	1·50	440
Co(II)-PMMAB	56·64	4·28	6·02	12·62			
	(56·54)	(4·28)	(5·99)	(12·58)	4·70	1·20	415
Ni(II)-PMMAB	56·72	4·32	6·02	12·66			
	(56·57)	(4·29)	(5·99)	(12·58)	3·60	0·98	368
Cr(III)-PMMAB	57·87	4·40	6·12	11·50			
	(57·39)	(4·35)	(6·09)	(11·30)	3·96	1·30	362
UO_2(II)-PMMAB	39·24	2·99	4·10	39·99			
	(38·94)	(2·95)	(4·13)	(39·83)	Dia	1·38	410
Zn(II)-PMMAB	55·82	4·30	5·99	13·90			
	(55·79)	(4·23)	(5·92)	(13·81)	Dia	1·40	450

* Theoretical values in bracket.

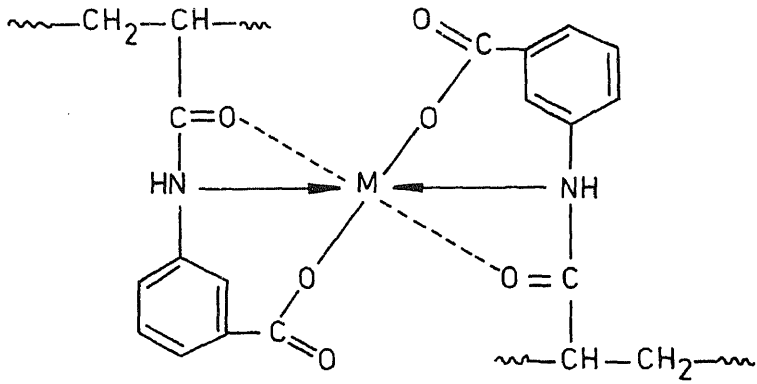

Fig. 1.

3.1 *Reflectance spectra*

The diffuse reflectance spectrum of chelex PMMAB shows two high intensity bands at 21400 and 19506 cm^{-1} which may be attributed to $\pi \rightarrow \pi^*$ and $n \rightarrow \pi^*$ transitions respectively (Rao 1975).

Iron (II) : The diffuse reflectance spectrum of the Fe(II) polychelate shows bands at 9620, 11270 and 15600 cm^{-1}. The latter two bands may be attributed to the spin

symmetry ligand field (Mani 1979). The Fe(II) polychelate shows very high magnetic moment (40 B.M.) indicating its ferromagnetic behaviour.

Cobalt (II): The diffuse reflectance spectrum of the Co(II) polychelate indicates bands at 8600, 15630, 21220 and 22700 cm^{-1}. The first two bands may be safely assigned to $^4T_{1g} \rightarrow {}^4T_{2g}$ and $^4T_{1g} \rightarrow {}^4A_{2g}$, respectively, in an octahedral stereochemistry. The highly intense and moderately broad band in the region 21400–20100 cm^{-1} may be the $n \rightarrow \pi^*$ band of the ligand itself. However the observed bathochromic shift compared with that of the ligand may be attributed to the extensive conjugation of the co-ordinated ligand through the metal ions. The magnetic moment (4·7 B.M.) of the Co(II) polychelate is in the range required for octahedral stereochemistry (Rastogi and Sharma 1974).

Nickel (II): The diffuse reflectance spectrum of the Ni(II) polychelate exhibits broad absorption at 9360 and 15950 cm^{-1} which may be assigned to $^3A_{2g} \rightarrow {}^3T_{2g}$ and $^3A_{2g} \rightarrow {}^3T_{1g}$ transitions respectively. The Ni(II) polychelate shows high magnetic moment (3·6 B.M.) for octahedral stereochemistry (Calvin and Barkenlew 1964).

Chromium (III): The diffuse electronic spectrum of the Cr(III) polychelate exhibits bands at 11300 cm^{-1} and 16090 cm^{-1}. The former band may be due to $^4A_{2g} \rightarrow E_g$ transition (Foster 1969) while the latter may be due to $^4A_{2g} \rightarrow {}^4T_{2g}$ transition in an octahedral stereochemistry (Koenig 1971). The magnetic moment is in agreement with the octahedral stereochemistry.

The UO_2(II) and Zn(II) polychelates are found to be diamagnetic in nature as is expected.

3.2 *Infrared spectra*

The IR spectra of chelex and all the metal polychelates (figure 2) resemble each other in general appearance. However, there is a noticeable difference in certain vibrational frequencies.

Examination of the IR spectrum of chelex PMMAB shows a medium broad band around 3400–3100 cm^{-1} which may be assigned to the carboxylic –OH and amide –NH stretching vibrations (Silverstein *et al* 1981). This obscured region may be due to the mixing of intermolecular and intramolecular H bonding due to –NH and –OH groups. The chelex shows strong bands at 1685 and 1665 cm^{-1} which may be attributed to the carbonyl stretching frequencies of the aromatic carboxylic and amide groups. All the polychelates show the absence of the band at 1695 cm^{-1} and a shift in the band of the amide group around 1665–1635 cm^{-1}. It is quite possible that the band due to the carboxylic carbonyl group is involved in co-ordination with metal ions while the amide carbonyl group is not participating in direct metal-chelex bonding. The IR spectra of all the polychelates reveal the presence of two bands around 1600 and 1460 cm^{-1}. This may be due to the carboxylate ion (Nakamoto *et al* 1961). It is well established that the band around 1600 cm^{-1} is due to the antisymmetric stretching and the band around 1460 cm^{-1} is due to the symmetric stretching vibrations of the carboxylate (Sandhu *et al* 1969).

A strong band around 1280 cm^{-1} in the spectrum of chelex may be due to H-bonded OH in-plane bending vibration. All the polychelates show this band shifted to 1250 cm^{-1} which may be due to –O–*M* suggesting co-ordination through

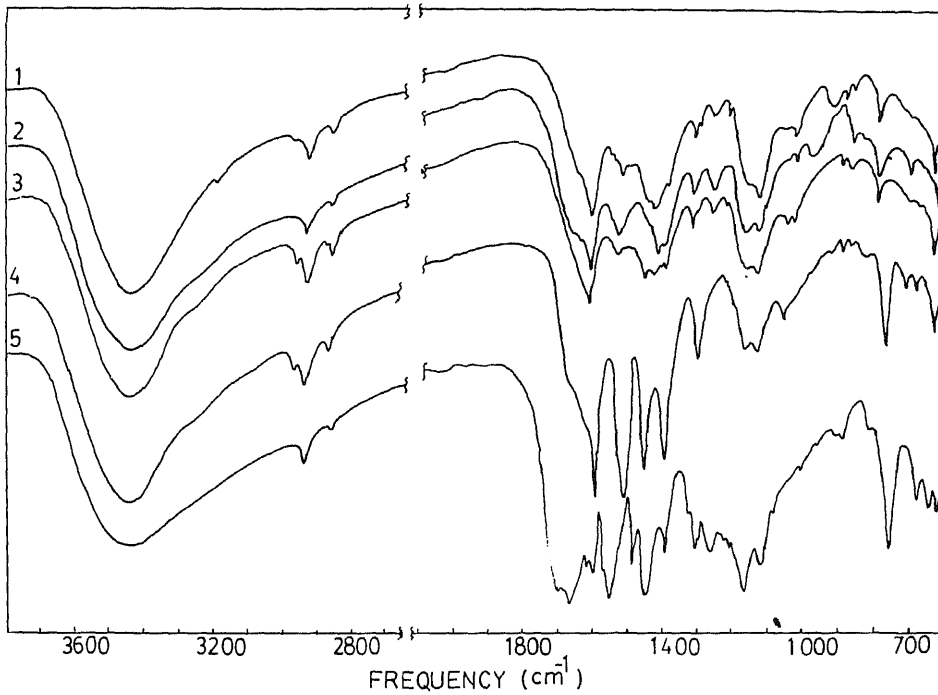

Fig. 2.

3.3 *Thermogravimetric*

The thermograms of all these polychelates were compared with that of chelex PMMAB. The polychelates are more stable than chelex PMMAB. The examination of the thermograms of the polychelates indicates the absence of water molecules in the co-ordination sphere. The loss in weight of Fe(II), Co(II), Ni(II), Cr(III), UO_2(II) and Zn(II) polychelates at 400°C are 7, 10, 15, 50, 10 and 6% respectively. The decomposition temperatures are listed in table 1 and reveal the following trend in thermal stabilities:

$$Zn > Fe > Co > UO_2 > Ni > Cr > \text{PMMAB}.$$

References

Bellamy L J 1958 *The spectra of complex organic molecules* 2nd edn (New York: John Wiley)
Calvin M and Barkenlew C H 1964 *J. Am. Chem. Soc.* **68** 2267
Desai T and Suthar B P 1986 *Synth. React. Inorg. Met.-Org. Chem.* **10** 29
Dunn M F, Pattison E S, Strum M C and Quiel E 1980 *Biochemistry* **19** 718
Foster L S 1969 *Transition met. chem.* **5** 1
Frantisek H and Jiri W 1975a Czech. Patent 157, 429; *cf* 1976 *Chem. Abstr.* **84** 169669
Frantisek H and Jiri W 1975b Czech. Patent 158, 428; *cf.* 1976 *Chem. Abstr.* **84** 5860
Haner M, Henzl M, Raissouni B and Birnbawn E R 1984 *Anal. Biochem.* **138** 233
Joshi R M 1962 *J. Polym. Sci.* **56** 313
Kraus K A and Moore G E 1953 *J. Am. Chem. Soc.* **75** 1460

Mani F 1979 *Inorg. Nucl. Chem. Lett.* **15** 297
Nakamoto K, Morimola Y and Martell A E 1961 *J. Am. Chem. Soc.* **83** 4528
Patel K, Desai T and Suthar B 1985a *Makromol. Chem.* **186** 1151
Patel K, Desai T, Schultz R and Suthar B 1985b *J. Indian Chem. Soc.* (communicated)
Patel K and Suthar B 1985a *Angew. Makromol. Chem.* **135** 177
Patel K and Suthar B 1985b *Bull. Soc. Chim. Fr.* (communicated)
Patel S R and Patel B S 1979 *Makromol. Chem.* **180** 1159
Prabhakaran C P and Patel C C 1972 *J. Inorg. Nucl. Chem.* **34** 3485
Rastogi D K and Sharma K C 1974 *J. Inorg. Nucl. Chem.* **36** 2209
Rao C N R 1975 *Ultraviolet and visible spectroscopy* (London: Butterworths)
Sandhu S S, Manhas B S, Mittal M R and Parmar S S 1969 *Indian J. Chem.* **7** 286
Silverstein R M, Bassler G C and Morrill T C 1981 *Spectrophotometric identification of orgar compounds* (New York: John Wiley)
Yoshikazu K, Kuro S, Jung K and Nichiko J 1975 Japan Kokei 151, 526; *cf.* 1976 *Chem. Abstr.* **85** 2735

© Printed in India

2-Hydroxy-1-naphthaldehyde guanylhydrazone as analytical reagent for spectrophotometric estimation of vanadium

F SALINAS, J J BERZAS NEVADO* and A ESPINOSA
Department of Analytical Chemistry, Faculty of Science, University of Extremadura, 06071 Badajoz, Spain

MS received 20 November 1985; revised 15 March 1986

Abstract. A spectrophotometric determination of V(V) with 2-hydroxy-1-naphthaldehyde guanylhydrazone can be performed in a concentration range varying from 0·70–8·70 ppm of vanadium; the molar absorptivity is $7{\cdot}7 \times 10^3$ litres mol^{-1} cm^{-1} at 405 nm and the relative error is ± 0·60. The stoichiometry (1 : 1) of the complex was established by different methods. This method of spectrophotometric determination has been applied satisfactorily to the determination of vanadium in steel.

Keywords. Vanadium(V); spectrophotometric determination; 2-hydroxy-1-naphthaldehyde guanylhydrazone.

1. Introduction

Guanylhydrazones are Schiff's bases that can be obtained by a condensation between aminoguanidine and an aldehyde or ketone. These compounds have been synthesized previously for use in pharmacological applications but a few have been studied as analytical reagents. We have initiated the utilization of these compounds in chemical analysis with pyridine-2-aldehyde guanylhydrazone (PAG) (Roman *et al* 1981) and we have studied its reactions with some cations. Salicylaldehyde guanylhydrazone (SAG) (Berzas *et al* 1984) has also been spectrophotometrically studied and a method of estimating iron using it has been described. 2-Hydroxy-1-naphthaldehyde guanylhydrazone (NAG) has also been synthesized and applied to spectrophotometric and extractive-spectrophotometric determination of iron (Salinas *et al* 1985).

In this work, the reaction between NAG and vanadium is studied and a new spectrophotometric method for the determination of vanadium in steel is described.

2. Experimental

2.1. *Reagents and apparatus*

All solvents and chemical reagents used were of analytical grade.

NAG solutions in dimethylformamide (DMF) were used at different concentrations. A standardized solution of V(V) (0·8510 g/l) was used. A buffer solution of

pH = 4·5 was prepared by dissolving 34·00 g of sodium acetate in 20·8 ml of acetic acid and diluting to 1 litre with demineralized water.

A Beckman 25 spectrophotometer with 1·0 cm glass or quartz cells as well as a Crison 501 digital pH-meter with a glass–AgCl electrode were used.

2.2. *Recommended procedure for the determination of vanadium*

To a vanadium solution, containing 0–217 μg of vanadium(V), in a 25 ml standard flask was added 5 ml of 0·08% (wt/wt) solution of NAG in DMF and 5 ml of a buffer solution of pH = 4·5. After dilution with water the absorbance at 405 nm was measured against a reagent blank prepared similarly.

Beer's law is obeyed between 0–8·7 ppm of vanadium. The optimum concentration range, evaluated by Ringbom's method, is 1·3–6·0 ppm of vanadium. The molar absorptivity at 405 nm is $7{\cdot}70 \times 10^3$ litres mol^{-1} cm^{-1}. The relative error (95% confidence level) for 3·50 ppm of vanadium is $\pm 0{\cdot}60\%$.

3. Results and discussion

3.1. *Spectral characteristics and effects of experimental variables*

NAG forms a yellow complex with V(V) in an acid medium which is slightly soluble in water and very soluble in a DMF-water mixture. The absorption spectra of the vanadium complex were recorded for samples containing 20% of DMF and the maximum absorption occurred at 405 nm.

3.1a *Influence of pH:* Samples were prepared in 25 ml volumetric flasks containing 3·50 ppm of V(V), 5 ml of 0·5 M KCl and 5 ml of 0·2% NAG solution in DMF and variable amounts of HCl and NaOH, to obtain the desired pH value. The formation of the yellow vanadium(V) complex is pH independent between 3–6·5 pH values (figure 1). A buffer acetate solution of pH = 4·5 is recommended.

3.1b *Influence of the concentration of NAG:* The effect of the chromogenic reagent was examined by measuring the absorbance of solution containing 3.50 ppm of

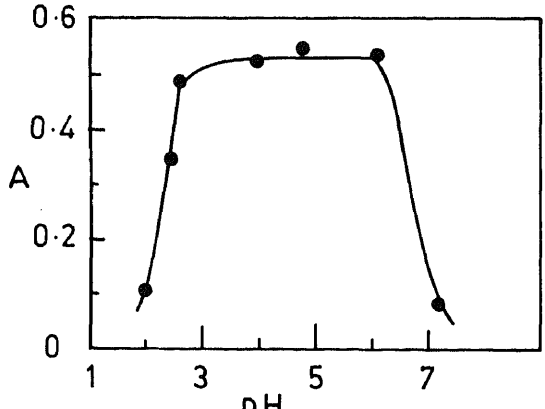

vanadium and variable amounts of NAG. It was found that 2 ml of 0·2% (W/V) NAG solution sufficed to complex the amount of V(V) taken; with higher concentrations the absorbance was essentially constant. Five millilitres of 0·2% NAG solution are recommended as a suitable amount of reagent.

3.1c *Influence of amount of DMF:* The effect of the DMF content in the medium was examined. It was found that a 16% (v/v) of DMF is necessary for keeping the complex in solution. A 20% (v/v) of DMF is recommended for subsequent studies.

3.1d *Influence of the order of addition:* From experiments in which the order of addition of reagents was varied in all possible ways, it was deduced that the reaction between V(V) and NAG is independent of the order of addition.

3.1e *Stability of the vanadium(V) complex:* The stability of samples containing 1·00, 3·5 and 7·0 ppm of V(V) was studied. The absorbance at 405 nm is constant over a period of 14 hr.

3.1f *Stoichiometry and stability constant:* The metal–reagent ratio ($m : n$) for the yellow vanadium(V) complex was determined by Job's method and was 1 : 1, metal : reagent. The stability constant calculated from these results following the method described by Meites and Thomas (1958) was $\log K = 5{\cdot}65$.

The stability constant was also determined by Gonzalez *et al* (1980) method. This method permits the differentiation between mononuclear and polynuclear complexes and it is based on the effect of dilution on the degree of dissociation of the complex. In this method the following general equation is used:

$$[(\beta A)^{1/m+n}]/[(b_0/\beta)^{m+n-1/m+n}] = (Km^m A_0(b_0)/n^{m-1})^{1/m+n}[1-\beta A/A_0(b_0)]$$

where β is the dilution factor, b the metal concentration, and $A_{0(b_0)}$ the absorbance for complete complexation at metal concentration b_0. This equation must be a straight line when the correct values are given to m and n. The equation has been applied for $n = m = 1$ and $n = m = 2$. In figure 2 it can be observed that the vanadium(V) complex is a monomer of stoichiometry 1 : 1. The stability constant was $\log K = 5{\cdot}65$, in accordance with the value obtained when of Meites and Thomas' method (1958) was applied.

3.1g *Interferences:* The effect of diverse ions was studied for the determination of 3·5 ppm of vanadium. An error of 2% in the absorbance was considered as tolerable. The results obtained are presented in table 1.

3.2 *Applications*

The recommended procedure has been applied satisfactorily to the determination of vanadium(V) in steel.

The samples were dissolved according to the following procedure: Dissolve 2·5 g

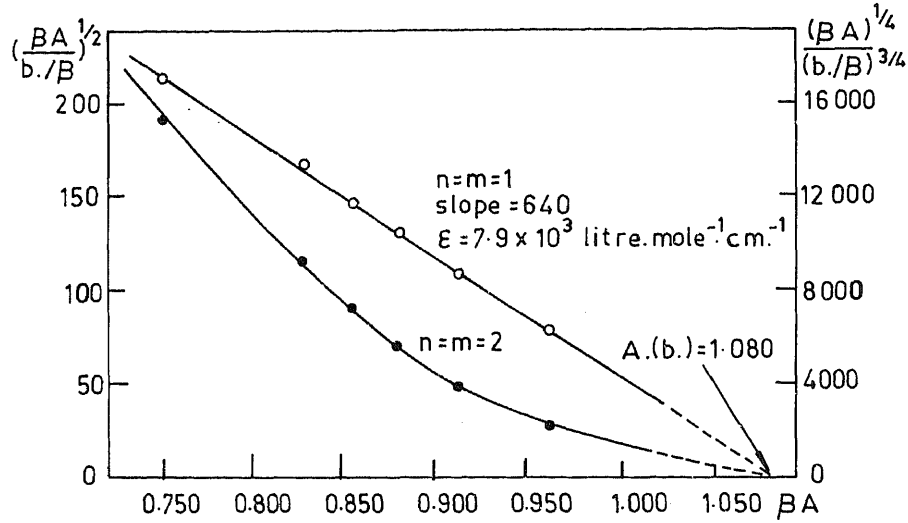

Figure 2. The method of Gonzalez *et al* (1980) applied to the V(V) complex.

Table 1. Effect of diverse ions in the spectrophotometric estimation of 3·50 ppm of vanadium(V).

Maximum tolerance diverse ion/V(V) ratio (wt/wt)	Ions
< 1	EDTA, $C_2O_4^{2-}$, Ti(IV).
1	W(VI), Ag(I).
2	Fe(III).
10	Cu(II)*, Mn(II), Pb(II), Bi(III)*
30	Citrate, Al(III)**, Zn(II), Cr(III)**, As(III), As(V)**, Mo(VI), Hg(II).
70	DCTA, thioglycollic acid.
200	Fluoride, tartrate.
1500	N,N-*bis*(2-hydroxy ethyl glycine, bicine), phosphate
7000	Triethanolamine.

* In the presence of 6·25 mg of 1,2-diaminocyclohexane-N,N,N′,N′-tetracetic acid (DCTA);
** In the presence of 0·61 g of triethanolamine.

A conventional ion exchange column 1·5 cm in diameter containing strong-acid cation exchanger (6 cm) are prepared and the column is purified according to Fritz and Abbink (1962).

Place on the column, 1 ml of the steel sample and elute the vanadium with 50 ml

demineralized water. Aliquots of the above solutions were taken and a standard addition method was used to apply the proposed method.

The result obtained for the analysis of steel (Bureau of Analysed Samples, England, 64 b of composition: C 0·90%, Cr 4·55%, V 1·99%, Mo 4·95%, W 7·05%) is 1·95% (the average of three determinations).

Acknowledgements

We thank the Comision Asesora de Investigacion Cientifica y Tecnica del Ministerio de Educacion y Ciencia de España for supporting this study (project number 2903–83).

References

Berzas J J, Espinosa A and Valiente P 1984 *Microchem. J.* **30** 380
Fritz J and Abbink J 1962 *Anal. Chem.* **34** II 1080
Gonzalez D V, Arrebola A and Roman M 1980 *Talanta* **28** 545
Meites L and Thomas H C 1958 *Advanced analytical chemistry* (New York: McGraw-Hill)
Roman M, Berzas J J and Espinosa A 1981 *Talanta* **28** 134
Salinas F, Berzas J J and Espinosa A 1985 *Bull. Soc. Chim. Belg.* **94** 719

Synthesis, identification and analytical properties of the 2-pyrilideniminobenzohydroxamic acid

F SALINAS*, M JIMÉNEZ-ARRABAL and I DURÁN MERÁS
Department of Analytical Chemistry, Faculty of Sciences, University of Extremadura, 06071 Badajoz, Spain

MS received 25 November 1985; revised 23 April 1986

Abstract. 2-Pyrilideniminobenzohydroxamic acid (PIBHA) has been synthesized by the reaction of *o*-aminobenzohydroxamic acid and pyridine-2-carbaldehyde. Its solubility in several solvents, spectral characteristics and pK_a values are reported. Its reactivity with inorganic ions, in aqueous media and by extraction with chloroform, isoamyl alcohol, toluene, and a toluenic solution of trioctylmethylammonium chloride (Adogen 464) has been investigated. The pK values corresponding to the formation constants of the complexes formed between PIBHA and Cd(II), Mn(II), Co(II), Ni(II) and Cu(II) in ethanol-water medium are also reported.

Keywords. 2-Pyrilideniminobenzohydroxamic acid; physicochemical properties; analytical properties; formation constants.

1. Introduction

Hydroxamic acids constitute a group of analytical reagents frequently used (Brandt 1960; Bass and Yoe 1966; Majumdar 1971; Bhaduri 1956; Poddar *et al* 1966; Agrawal 1980; Agrawal and Patel 1980), however, between the numerous used derivatives, the azomethinic group is rarely found. This group endows a good reactivity to Schiff bases, another important group of analytical reagents (Jungreis and Thabet 1969).

Among this kind of reagents we know the use of the 2-salicylideniminobenzohydroxamic acid as an indicator in the complexometric titration of Fe(III) (Springer and Kopecka 1984), its reactivity as well as the reactivity of 2-benzylideniminobenzohydroxamic acid with inorganic ions, and some of their applications as spectrophotometric reagents (García Martín 1985; Salinas *et al* 1986b).

Data about the synthesis, analytical properties and spectrophotometric determination of iron with thienylmethylene-2-iminobenzohydroxamic acid are reported (Salinas *et al* 1986a).

In this paper, the synthesis, properties and analytical aspects of 2-pyrilideniminobenzohydroxamic acid (PIBHA, *I*) are reported. This compound has in its structure the azomethinic and hydroxamic groups in proper positions to intervene simultaneously in the formation of chelates with inorganic ions. Also, this compound has an N pyridinic group. So, we expect it to have an improved chelating ability.

* To whom all correspondence should be addressed.

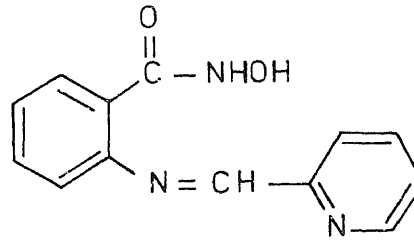

Chart 1.

2. Experimental

2.1 *Reagents and apparatus*

All solvents and chemicals used were of analytical grade. Stock solutions of the metals were standardized by well-known methods. Deionized water was employed for all purposes. Infrared spectra were recorded with a Perkin-Elmer 339 IR spectrophotometer in the 4000–400 cm^{-1} range, using the KBr pellet technique. The absorption spectra of solutions were obtained using a Beckman 25 UV-VIS spectrophotometer (1 cm quartz cells). pH measurements were carried out with a Crison Digit 501 pH-meter equipped with a glass-calomel combination electrode. The solubility of PIBHA in several solvents, was measured by the method of Wittemberger (1950) at 25 ± 0·1°C. To determine the dissociation constants of PIBHA, the potentiometric methods of Schwarzembach *et al* (1947), in several proportions of ethanol, and Irving and Rossotti (1954), and the spectrophotometric method described by Wilson and Lester (1963), were applied. To determine the formation constants of the complexes formed between PIBHA and several inorganic ions in ethanol-water (1 : 1) medium, the potentiometric methods of Irving and Rossotti (1954), Bjerrum (1941) and Chaberek and Martell (1952) were applied.

2.2. *Synthesis of PIBHA*

PIBHA was synthesized by condensation of orthoaminobenzohydroxamic acid and pyridine-2-carbaldehyde. Orthoaminobenzohydroxamic acid (5 g), synthesized employing Blatt's method (Blatt 1963) was taken in a hot mixture of ethanol : water (25 : 50, v/v) and 3·15 ml of pyridine-2-carbaldehyde was slowly added. The solution was kept stirred and warm for a few minutes. After cooling a yellow solid precipitated. The product was filtered and purified by recrystallisation from water : ethanol (2 : 1, v/v) to obtain a yellowish white product (m.p. 139 ± 1°C). Elemental analysis – found: C, 64·86%; H, 4·65%; N, 17·32%. Calculated: C, 64·71%; H, 4·60%; N, 17·42%; for $C_{13}H_{11}O_2N_3$.

3. Results and discussion

3.1 *Physicochemical properties of PIBHA*

Table 1. Spectral properties of PIBHA.

Infrared		Ultraviolet		
Vibration mode	Frequency (cm^{-1})	Solvent	λ Maxima	$\epsilon(lmol^{-1}cm^{-1})$
ν NH	3220 *s**	Water	228 nm, λ_1	$16{,}02 \times 10^3$
ν C=O (amide I band)	1620 *s*		335 nm, λ_2	$2{,}40 \times 10^3$
ν OH hydroxamic	2850 *w*	$ClCH_3$	250 nm, λ_1	$9{,}23 \times 10^3$
ν OH phenolic	3080 *s*, *b*		335 nm, λ_2	$2{,}50 \times 10^3$
δ NH (amide II band)	1570 *w*	Ethanol	235 nm, λ_1	$11{,}90 \times 10^3$
ν C–N (amide III band)	1290 *m*		335 nm, λ_2	$2{,}75 \times 10^3$
ν NO	955 *m*	Isoamyl alcohol	240 nm, λ_1	$8{,}85 \times 10^3$
			340 nm, λ_2	$2{,}86 \times 10^3$

* Abbreviations: *s* = strong; *m* = medium; *w* = weak and *b* = broad.

and the amide II band (1570 cm^{-1}) are analogous to that of the NH group of N-substituted amides and secondary amines (Davies *et al* 1955; Miyazawa *et al* 1956; Rao and Venkataraghavan 1962). Accordingly, it is possible to affirm that PIBHA has, in the solid state, the "keto" structure, *I*a, being similar to other hydroxamic acids (Exner 1968; Bracher and Small 1970; Larsen 1978; Salinas *et al* 1982).

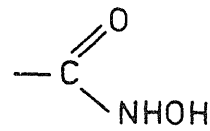

Chart Ia.

Since the stretching frequency of the free NH group appears around 3400 cm^{-1}, the decrease for PIBHA, as well as for other hydroxamic acids (Mathis 1961) can be attributed to the formation of hydrogen bonding. This point is also confirmed by observing the vibrational frequencies due to CO (1600 cm^{-1}); OH (phenolic, 3180 cm^{-1}) and OH (hydroxamic, 2850 cm^{-1}). The low frequency of these bands indicates hydrogen bonding (Hadži and Prevoršek 1957; Mathis 1961; Agrawal and Roshama 1978). Thus, it is concluded that the structural type II represents the most probable configuration of PIBHA.

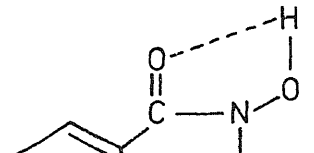

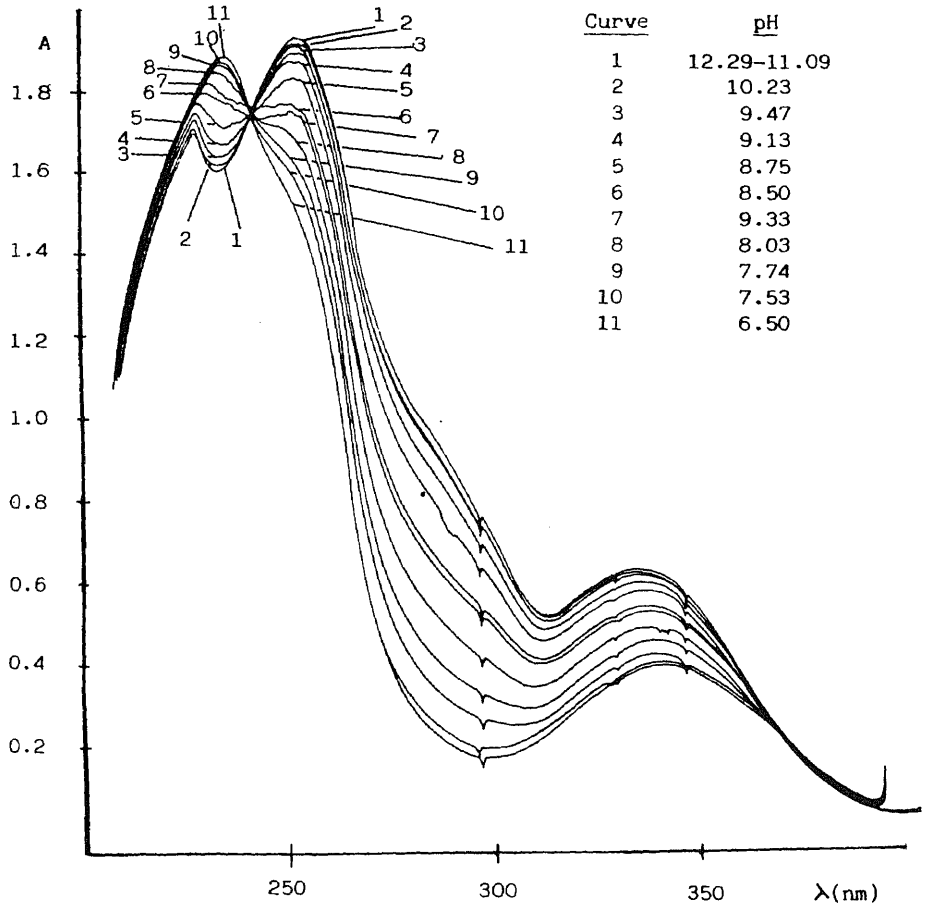

Figure 1. Variation of the absorption spectra of PIBHA for values of pH between 12·29 and 6·50. $[PIBHA] = 1{\cdot}66 \times 10^{-4}$ M, $[KCl] = 0{\cdot}1$ M.

The absorption maxima of PIBHA and their molar absorptivities (ϵ) in aqueous, ethanolic, isoamyl alcohol and chloroform solutions are given in table 1.

The absorption spectrum of PIBHA in aqueous solution shows a remarkable pH dependence. In the pH range of 12 to 6 (figure 1), the absorption maximum at 235 nm shows hyperchromic and bathochromic effects as the pH is decreased. At the same time, the maximum at 255 nm shows hypochromic and hypsochromic effects, while the maximum at 330 nm shows a hypochromic effect. Finally, one isosbestic point appears at 242 nm. This isosbestic point is indicative of the existence of two acid-base equilibrium forms that must correspond to the dissociation of the hydroxamic group and to the corresponding keto-enolic equilibrium.

In the pH range of 5–1·05 (figure 2), the maximum at 235 nm reveals

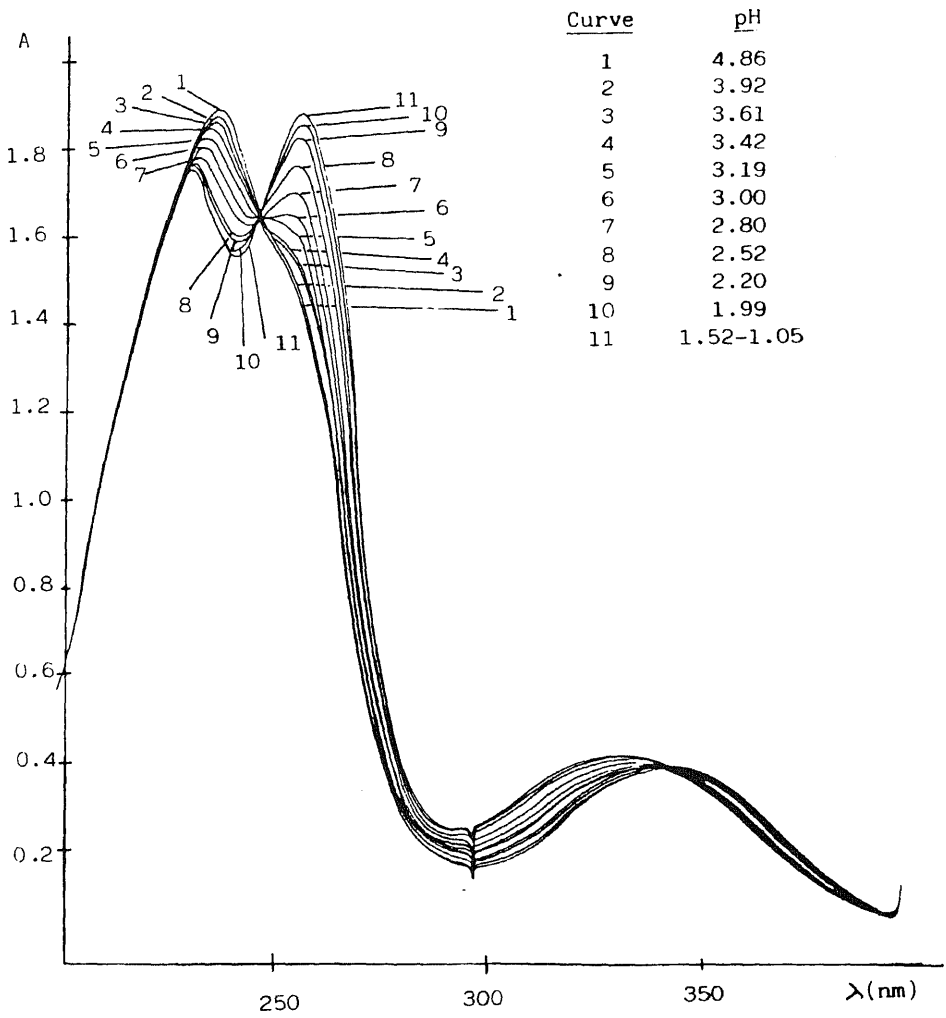

Figure 2. Variation of the absorption spectra of PIBHA for values of pH between 4·9 and 1·05. $|PIBHA| = 1{\cdot}66 \times 10^{-4}$ M, $|KCl| = 0{\cdot}1$ M.

3.1b *Solubility of PIBHA in several solvents*: The solubility of PIBHA in several solvents, was studied at 25 ± 0·1°C and the results obtained indicate that PIBHA is relatively soluble in ethanol and in methylisobutylketone (7·4 g l^{-1} and 1·8 g l^{-1} respectively) and sparingly soluble in chlroform and deionized water (0·6 g l^{-1} and 0·2 g l^{-1} respectively).

3.1c *Dissociation constants*: Table 2 presents the values of the dissociation

Table 2. Dissociation constants of PIBHA in different media (mol l^{-1}).

	Water	Ethanol-water				
	100%	80–20%	70–30%	60–40%	50–50%	Reference
pK_1	2·00	2·15	2·12	2·08	2·04	Schwarzembach *et al* (1947)
pK_2	2·70	2·30	2·35	2·40	2·45	Schwarzembach *et al* (1947)
pK_3	8·32* ± 0·08	—	—	—	—	Wilson and Lester (1963)
	8·19† ± 0·01	—	—	—	—	Irving and Rossotti (1954)
	—	—	—	—	9·25	Irving and Rossotti (1954)

* Average of the results obtained at 340 nm, 255 nm and 235 nm; † average of two determinations.

Table 3. Reactions of PIBHA with metallic ions and its extraction with several solvents.

Ion	Compound used	Colour of complex	Optimum pH range	*pD*	Solvent	Optimum pH range	*pD*
Ag(I)	$AgNO_3$	Violet	3–5	4·8	Adogen-toluene*	3–5	4·0
Mn(II)	$Mn(NO_3)_2 \cdot 4H_2O$	White	3–5	3·7	—	—	—
Hg(II)	$Hg(NO_3)_2 \cdot H_2O$	White	7–9	3·0	Adogen-toluene*	5–9	3·0
Ni(II)	$Ni(NO_3)_2 \cdot 6H_2O$	Green-yellow	3–5	4·0	—	—	—
Cd(II)	$Cd(NO_3)_2 \cdot 4H_2O$	White	3–5	4·0	—	—	—
Co(II)	$Co(NO_3)_2 \cdot 6H_2O$	Light yellow	3–7	4·0	—	—	—
Cu(II)	$Cu(NO_3)_2 \cdot 3H_2O$	Yellow	3–7	5·0	Isoamyl alcohol	3–5	5·0
Fe(II)	$Fe(NH_4)_2(SO_4)_2 \cdot 6H_2O$	Red	3–5	5·5	Chloroform	3–5	5·0
Fe(III)	$Fe(NO_3)_2 \cdot 9H_2O$	Red	3–5	5·7	Chloroform	3–5	5·7
Ti(IV)	$TiCl_4$	Yellow	3–5	5·5	Isoamyl alcohol	3–5	5·5
V(V)	NH_4VO_3	Brown	3–5	5·5	Isoamyl alcohol	3–5	5·7
Mo(VI)	$(NH_4)_6Mo_7O_2 \cdot 4H_2O$	Yellow	3–5	5·0	Isoamyl alcohol	1–3	5·4
W(VI)	$Na_2WO_2 \cdot 2H_2O$	Yellow	1–5	4·7	—	—	—

* Toluenic solution of trioctylmethylammonium chloride (Adogen 464) 1 g l^{-1}

3.2 *Chelating properties of* PIBHA

3.2a *Reactions of* PIBHA *with 54 metal ions in aqueous medium*: The complex-formation reactions of PIBHA with metal ions at different pH values, are summarized in table 3. The pH range over which the sensitivity was maximum for each metal ion and their detection limits (pD) are also shown in the same table. Reaction has been observed only with 13 of these metal ions. Almost in all cases the respective complex compounds were precipitated, except those of Co(II) and Cu(II). Coloured solutions were obtained only with Fe(III) and Fe(II) in strongly acidic medium.

Only 8 reactions have pD values between 4·5 and 6, the sensitivity of the reactions is generally not high. The ions whose reactions are the most sensitive are Fe(III), Fe(II), Ti(IV), V(V) and all of these have been observed in acetic medium.

Similar reactions are observed with 2-benzylideniminobenzohydroxamic and 2-salicylideniminobenzohydroxamic acids (García Martín 1985). These reagents produce reactions, with detection limits $pD > 4$, with the ions Sn(II), La(III), Bi(III), In(III), Y(III), Al(III), Ga(III) and Ce(IV) in acetic and neutral media in addition to the reactions with PIBHA.

3.2b *Extraction of the complexes*: The observed colour reactions, after extraction into $CHCl_3$, isoamyl alcohol, toluene and a toluenic solution of Adogen 464, are given in table 3. Only 8 ions were found to be extracted indicating that the selectivity of PIBHA can be improved by resorting to extraction. The sensitivities are of equal order, with pD values varying between 5 and 6, the more sensitive reactions being with Fe(III), Ti(IV), V(V) and Mo(VI). In a previous paper (Salinas *et al* 1985), the references of the extraction of hydroxamic acids complexes with inorganic ions have been summarized. The colour of the solutions and the pH range in which they are produced, are in good agreement with those observed with PIBHA.

3.3 *Determination of the formation constants of the complexes*

In table 4 the values of the formation constants of the complexes between PIBHA and Co(II), Cd(II), Ni(II), Mn(II) and Cu(II) are given. These values show that ease of formation of the complexes is in the following sequence:

$$\text{Cu(II)} > \text{Ni(II)} > \text{Co(II)} > \text{Cd(II)} > \text{Mn(II)}.$$

This is in accordance with the values suggested by Irving and Williams (1948) for complexes between metal divalent ions and chelates with N as a donor atom.

Table 4. Determination of the formation constants of the complexes at 25 ± 0·1°C and in ethanol : water medium (50 : 50%, v/v)

	$\log K_1$	$\log K_2$
Cu(II)	8·50	7·71
Ni(II)	7·19	6·15
Co(II)	6·71	5·80

Acknowledgements

We thank the Comisión Asesora de Investigación Científica y Técnica Ministerio de Educación y Ciencia de España for supporting this study (Projec 2903-83).

References

Agrawal Y K 1980 *Rev. Anal. Chem.* **4** 4
Agrawal Y K and Patel S A 1980 *Rev. Anal. Chem.* **5** 1, 2
Agrawal Y K and Roshama R 1978 *J. Chem. Eng. Data* **23** 259
Bass V C and Yoe J C 1966 *Talanta* **13** 735
Bhaduri A S 1956 *Z. Anal. Chem.* **151** 109
Bjerrum J 1941 *Metal amine formation in aqueous solution* (Cophenhagen: P Haase and S
Blatt A 1963 *Organic syntheses* (New york: John Wiley)
Bracher B H and Small R W H 1970 *Acta Crystallogr.* **B26** 1705
Brandt W W 1960 *Rec. chem. prog.* **21** 159
Chaberek S and Martell A E 1952 *J. Am. Chem. Soc.* **74** 5052
Davies M, Evans J C and Lumley Jones R 1955 *Trans. Faraday Soc.* **51** 761
Deshpande R G and Jahagirdar D V 1977 *J. Inorg. Nucl. Chem.* **39** 1385
Exner O 1968 *Dansk. tiddskr. farm.* **42** 145
García Martín J P 1985 *Analytical applications of 2-benzylideniminobenzohydroxamic 2-salicylideniminobenzohydroxamic acids* Ph. D. thesis, University of Extremadura, Badajoz,
Hadži D and Prevoršek 1957 *Spectrochim. Acta* **10** 38
Irving H M and Rossotti H S 1954 *J. Chem. Soc* 2904
Irving H M and Williams R P S 1948 *Nature (London)* **162** 746
Jungreis E and Thabet S 1969 *Chelates in analytical chemistry* (eds) H A Flaschka and A J Barr (New York: Marcel Dekker) vol. 2, pp. 149–177
Larsen I K 1978 *Acta Crystallogr.* **B34** 962
Majumdar A K 1971 *N-benzoylphenylhydroxilamine and its analogues* (eds) R Belcher and H I (Braunschweig: Pergamon Press)
Mathis F 1961 *Ann. Fac. Sci. Univ. Tolouse Sci. Math. Sci. Phys.* **25** 125
Miyazawa T, Shimanovchi T and Mizushima 1956 *J. Chem. Phys.* **24** 408
Poddar S N, Sengupta N R and Adhya J N 1966 *Indian J. Chem.* **3** 135
Rao C N R and Venkataraghavan R 1962 *Spectrochim. Acta* **18** 273
Salinas F, Capitán Vallvey L F and Gázquez D 1982 *Microchem. J.* **27** 188
Salinas F, Espinosa A and Sánchez Casas J 1986a *Ann. Chim.* (in press)
Salinas F, Mahedero M C and García Martín J P 1986b *Bull. Soc. Chim. Belg.* **95** 89
Salinas F, Martínez-Vidal J L and González Parra J 1985 *Proc. Indian Acad. Sci. (Chem. Sci.)*
Schwarzembach G, Willi A and Bach R 1947 *Helv. Chim. Acta* **30** 1303
Springer V and Kopecka B 1984 *Ceskolav Farm.* **33** 6
Wilson R F and Lester G W 1963 *Talanta* **10** 319
Wittemberger W 1950 *Chimische laboratoriumstechnik* 4th Edn (Vienna: Springer) p. 101

Proc. Indian Acad. Sci. (Chem. Sci.), Vol. 97, No. 2, September 1986, pp. 167–170.
© Printed in India.

Abietane diterpene quinones and a new diterpene epoxide from *Salvia moorcraftiana*

BEENA BAKSHI, N B MULCHANDANI*† and J SHANKAR
Centre of Research for Development, University of Kashmir, Srinagar 190 006, India
†Bio-Organic Division, Bhabha Atomic Research Centre, Trombay, Bombay 400 085, India

MS received 14 March 1986; revised 12 May 1986

Abstract. A new abietane diterpene epoxide and five known abietane diterpene quinones have been isolated for the first time from *Salvia moorcraftiana* roots. The epoxide has been identified as 5α-hydroxy-abieta 8,11,13-triene-7-one-1,10-epoxide and the diterpene quinones have been characterised as royleanone; 7α-hydroxyroyleanone; 7β-hydroxyroyleanone; 7α-acetoxyroyleanone and 7-oxoroyleanone.

Keywords. *Salvia moorcraftiana* Wall.; Labiatae; abietane diterpenoids.

1. Introduction

The seeds and roots of *Salvia moorcraftiana* are used as emetics against cough and also in haemorrhoids (Nadkarni 1976). A few diterpene quinones have been isolated earlier from other Salvia species (Watson and Taira 1976; Baojin *et al* 1981; Kakisawa *et al* 1969; Vlasova *et al* 1969, 1971). In our earlier investigations on this plant we have shown the presence of 6,7-dehydroroyleanone (Bakshi *et al* 1984) and a novel phenalenone (Bakshi *et al* 1986).

2. Results and discussion

In this communication we wish to report the isolation of five known abietane diterpene quinones, viz., royleanone (*I*), 7α-hydroxyroyleanone (*II*), 7β-hydroxyroyleanone (*III*), 7α-acetoxyroyleanone (*IV*), 7-oxoroyleanone (*V*) and one new abietane diterpene epoxide, viz., 5α-hydroxyabieta-8,11,13-triene-7-one-1,10-epoxide (*VI*) from the benzene extract of the roots of the plant. The structure of the new compound is elucidated on the basis of chemical and spectral analyses. This is also the first report of 7-oxoroyleanone from the genus *Salvia*.

Compound (*VI*), $C_{19}H_{24}O_3$, m.p. 78°, $[\alpha]_D^{23} + 356°$ showed UV absorption at 244 nm ($\log \varepsilon$ 4·01), 250 (3·99) and 336 (3·84), characteristic of an acetophenone

carbonyl) cm^{-1}. In its NMR spectrum, a six-proton singlet seen at δ 0·78 was attributed to gem dimethyl. A double doublet integrating for six protons centred at δ 1·22 was assigned to isopropyl methyl protons. The presence of isopropyl group was further inferred from the appearance of one C(15)-methine proton septet at δ 3·12 (Brieskorn and Buchberger 1973). This was finally confirmed by the appearance of a fragment ion in its mass spectrum at *m/z* 257 (due to the loss of the isopropyl group) (Parker and Johnson 1968). Angular methyl at C(10) which is commonly found in many of the abietane diterpenes was found to be absent in this compound.

The position of the epoxide moiety was fixed between C(1) and C(10) from the NMR and MS spectral analyses of the compound. In NMR a triplet integrating for one proton was seen at δ 3·59, which could only be due to the proton at C(1), because if the epoxide was linked to C(2) and C(3), then one would expect two doublets, integrating for one proton each, appearing at two different positions (Silva *et al* 1973). Moreover, in its MS a fragment ion at *m/z* 187 (scheme 1) clearly indicated that the epoxide is linked between C(1) and C(10). Also a one-proton singlet, D_2O exchangeable, seen at δ 4·51 could only be attributed to the tertiary hydroxyl at C(5). This finding was further supported by its resistance to acetylation. Besides, the presence of a two-proton singlet at δ 2·31 attributed to the C(6)-H confirmed the presence of a hydroxyl at C(5). In the low field region a singlet due to C(14)-H was seen at δ 6·95. Two doublets at δ 6·88 and 7·05, integrating for one aromatic proton each, were assigned to C(11)-H and C(12)-H. In the MS of this epoxide, the molecular ion peak was seen at *m/z* 300. The base peak was observed at *m/z* 231. The other fragment ion (M^+-15) appeared at *m/z* 285.

Thus on the basis of the above observations the compound (VI) was identified as 5α-hydroxyabieta-8,11,13-triene-7-one-1,10-epoxide.

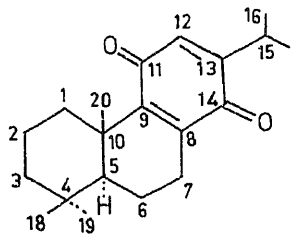

I

II 7 α-Hydroxy
III 7 β-Hydroxy
IV 7 α-Acetoxy
V 7-oxo

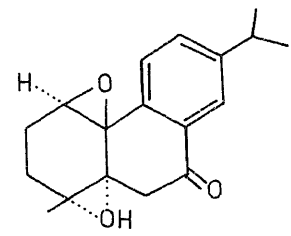

VI

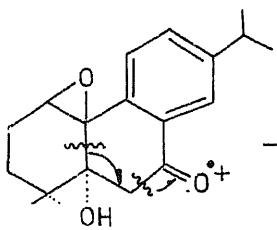

IV

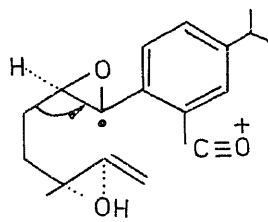

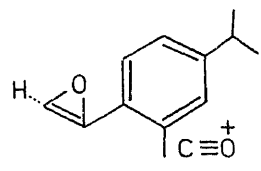

m/z 187

3. Experimental

UV spectra were measured on a Shimadzu-240 spectrophotometer using methanol (spectroscopic grade) as the solvent. IR spectra were taken on a Perkin-Elmer Infracord 137-B as KBr pellets. The optical rotations were measured in chloroform(c.0.1% or 0.2%) on a Perkin-Elmer model 141 polarimeter. ^{1}H NMR spectra were recorded on Varian model XL-100 A or Brucker WII 270 machines in $CDCl_3/CD_3OD$ using tetramethylsilane as the internal standard. M.P. are uncorrected. Column chromatography was carried out using silica gel (Acme India). Thin layer chromatograms were examined under a UV lamp for detection of spots. These were also detected by exposure to I_2 vapour, NH_3 vapour or by spraying with sulphuric acid (10%) or 2,4-dinitrophenylhydrazine as required and subsequently heating the plate at 100° in an oven.

Air dried finely powdered roots (1·5 kg) of the plants were extracted with C_6H_6 in a Soxhlet apparatus for 48 hr. The extract was concentrated under vacuum and the concentrate so obtained was subjected to column chromatography over silica gel. A total number of 350 fractions (50 ml each) were collected and monitored on TLC. Like fractions were pooled together and concentrated under vacuum. Five such concentrates were found to contain diterpenes. The concentrate A (2·5 g) contained a mixture of three compounds. The major component was separated by repeated crystallisation from MeOH: rectangular prisms, 100 mg, m.p. 169–71° TLC, silica gel, (C_6H_6: EtOAc, 95:5, Rf 0·65). This compound was identified as 6,7-dehydroroyleanone (Bakshi *et al* 1984). It was converted into its 6,7-dihydro (royleanone) and 12-methoxy derivatives.

Two compounds present in the mother liquor were separated by reverse phase TLC, ($MeOH:H_2O$, 20:80) and subsequent normal preparative TLC. The second compound was crystallised from MeOH as orange-red crystals, 30 mg, m.p. 181° $[\alpha]_D^{23}+134°(CHCl_3)$. Its IR, UV, NMR, MS spectral data were similar to those reported for royleanone (I) (Edwards *et al* 1962). The third compound was a new diterpene epoxide (VI).

5α-Hydroxyabieta-8,11,13-triene-7-one-1,10-epoxide: This was obtained as a pale yellow solid on crystallisation from petroleum ether (60–80°), 15 mg, m.p. 78°, $[\alpha]_D^{23}+356°$ ($CHCl_3$), calculated for $C_{19}H_{24}O_3$; C, 75·99; H, 8·05; found C, 76·02; H, 7·98%, UV λ_{max} (MeOH) nm (log ϵ): 244 (4·01), 250(3·99), 336(3·84); IR ν_{max} (KBr) cm^{-1}: 3600, 3030, 1685, 1613, 1481, 1410, 1389, 1270, 1101, 1036, 990, 970; ^{1}H NMR ($CDCl_3$) δ 0·78 [*s*, 6H, C(4)-methyls], 1·22 [*dd*, 6H, isopropyl methyls], 2·31 [*s*, 2H, C(6)-H_2], 3·12 [septet, 1H, J = 7 Hz, isopropyl methine-H], 3·59 [*t*, 1H, C(1)-H], 4·51 [*s*, 1H, C(5)-OH, D_2O exchangeable], 6·95 [*s*, 1H, C(14)-H], 6·88 and 7·05 [*2d*, 2H, C(11)-H, C(12)-H].MS *m/z* (%) 300 (M^+,18), 285 (M^+-15), 257 (M^+-43), 233, 231 (100), 215, 211, 203, 187, 173, 167, 143, 130.

7α-Acetoxyroyleanone: Column rechromatography of fraction 3 (2·5 g) yielded this compound as a yellow crystalline solid, 550 mg, m.p. 211·5° $[\alpha]_D^{23}-14°$(c,0·2). Its spectral data (UV, TR, NMR, MS) were found to be the same as that reported in

yellow crystalline product, 55 mg, m.p. 172–73°, $[\alpha]_D^{23}-131°$. Spectral data (UV, IR, NMR) were in total agreement with the literature values (Brieskorn and Buchberger 1973; Janot and Potier 1964).

7β-Hyroxyroyleanone: It was obtained as the second compound from fraction 4, 42 mg, m.p. 215°, $[\alpha]_D^{23}+215°$. Its spectral data (UV, IR, NMR) were in accordance with values reported in the lit. (Hensch *et al* 1975).

7-Oxoroyleanone: This was obtained as orange-red needles on column rechromatography of fraction 5, 12 mg, m.p. 196–97°, $[\alpha]_D^{23}-268°$. The compound was characterised on the basis of UV, IR, NMR, MS spectral data (Hensch *et al* 1975).

References

Bakshi B, Hassarajani S A, Mulchandani N B and Shankar J 1984 *Planta Med.* **50** 355
Bakshi B, Mulchandani N B and Shankar J 1986 *Planta Med.* (in press)
Baojin Y, Mingkun Q, Guowei Q and Zhenxiong C 1981 *Yaoxue Xuebao* **16** 837
Bredenberg B, McChesney J D and Wenkert E 1964 *J. Org. Chem.* **29** 2293
Brieskorn C H and Buchberger L 1973 *Planta Med.* **24** 190
Edwards O E, Feniak G and Los M 1962 *Can. J. Chem.* **40** 1540
Hensch M, Ruedi P and Eugster C H 1975 *Helv. Chim. Acta* **58** 1921
Janot M and Potier P 1964 *Ann. Pharm.* **22** 387
Kakisawa H, Hayashi T and Yamazaki T 1969 *Tetrahedron Lett.* 301
Nadkarni K M 1976 in *Indian Materia Medica* (ed.) (Bombay: Popular Prakashan) **1** p. 1094
Parker W L and Johnson F J 1968 *J. Am. Chem. Soc.* **90** 4716
Silva M, Bittner M and Sammes P G 1973 *Phytochemistry* **12** 883
Vlasova G F, Romanova A S, Perelson M E and Bankovskii A I 1969 *Khim. Prir. Soedin* **5** 317
Vlasova G F, Romanova A S and Bankovskii A I 1971 *Rast. Resu* **7** 74
Watson W M and Taira J 1976 *Tetrahedron Lett.* 2051

© Printed in India.

^{13}C NMR Data of flavonol methyl ethers of *Solanum pubescens*

G N KRISHNA KUMARI, L JAGAN MOHAN RAO and N S PRAKASA RAO

Department of Chemistry, Nagarjuna University, Nagarjuna Nagar 522 510, India

MS received 25 November 1985; revised 13 May 1986

Abstract. The ^{13}C NMR data of flavonol-3-methyl ethers indicated that the methylation of one of the hydroxyl groups in the *o*-dihydroxy system causes an upfield shift in the unsubstituted *o*-carbon as usual but with the other hydroxylated *o*-carbon the shift is always downfield. The spectra of the acetates indicated that 5-O$\underline{C}$OCH$_3$ and 5-OCO$\underline{C}$H$_3$ resonated downfield compared to that of other acetoxyl groups. The ^{13}C NMR data of these compounds is being reported for the first time.

Keywords. Flavonol methyl ether; ^{13}C NMR; *Solanum pubescens*; Solanaceae.

1. Introduction

The usefulness of ^{13}C NMR data in the structural elucidation of flavonoids was demonstrated by many workers (Calvert *et al* 1979) and well-reviewed (Agarwal and Rastogi 1981). The study of the ^{13}C NMR of kaempferol-3,7,4′-trimethyl ether (1), quercetin, 3,7,3′4′-tetramethyl ether (2), quercetin, 3,7,3′-trimethyl ether (3), quercetin-3,7,4′-trimethyl ether (4), quercetin-3,3′-dimethyl ether (5), myricetin-3,7,3′-trimethyl ether (6) isolated from *Solanum pubescens* Willd (Krishna Kumari *et al* 1984, 1985), and their acetates, was found to be useful in locating the 5-OH group and the position of the methoxyl group in *o*-dioxygenated systems.

2. Experimental

The natural abundance ^{13}C NMR spectra were obtained in the pulse Fourier transform mode with a JEOL-FX 100 spectrometer operating at 25·14 MHz.The samples, ranging in quantity from 20 mg to 100 mg, were examined as solutions in spinning tubes at 27°C. TMS was used as the internal reference. A pulse width of 7–10 sec was used (45°) with repetition times ranging from 5–10 sec as necessary. The spectral width was 6024 Hz with 8k data points. The compounds 1–6 were isolated as mentioned at our earlier reports (Krishna Kumari *et al* 1984, 1985). The data are given in table 1.

3. Results and discussion

The 5-acetoxyl group in 1 and 2 acetates gives signals at δ 169·4 (5-O$\underline{C}$OCH$_3$) and

Table 1. ^{13}C NMR data of flavonoid methyl ethers.

Compound \ Position	2	3	4	5	6	7	8	9	10	1′	2′	3′	4′	5′	6′	OMe
Kaempferol *7	146·8	135·6	175·9	160·7	98·2	163·9	93·5	156·2	103·1	121·7	129·5	115·4	159·2	115·4	129·5	
($CDCl_3^1$ + DMSO-d_6	154·6	137·5	177·3	160·5	96·7	164·2	90·9	155·5	104·7	121·4	128·9	113·0	160·5	113·0	128·9	58·8, 54·7
	(+7·8)	(+1·9)	(+1·4)		(−1·5)	(+0·3)	(−2·6)					(−2·4)	(+1·3)	(−2·4)		54·3
Luteolin***8	164·5	103·3	182·2	162·1	99·2	164·7	94·2	157·9	104·2	122·1	113·8	146·2	150·2	116·4	119·3	
Diosmetin***9	163·6	103·7	181·8	161·7	99·0	164·4	94·0	157·9	104·0	123·3	113·1	146·9	151·2	112·1	118·7	55·8
										(+1·2)		(+0·7)	(+1·1)	(−4·3)		
Chrysoeriol***10	163·7	103·8	181·8	161·6	98·8	164·2	94·0	157·4	103·3	121·7	110·2	150·8	148·0	115·8	120·4	56·0
											(−3·6)				(+1·1)	
Quercetin*11	146·9	135·5	175·8	160·7	98·2	163·9	93·5	156·2	103·1	122·1	115·5	145·0	147·6	115·6	120·0	
($CDCl_3$+^{2}DMSO-d_6)	154·6	137·7	177·5	160·6	96·9	164·4	91·1	155·7	104·8	121·7	110·6	147·8	150·5	110·3	121·3	59·0, 55·1
	(+7·7)	(+2·2)	(+1·7)		(−1·3)	(+0·5)	(−2·4)				(−4·9)	(+2·8)	(+2·9)	(−5·3)		55·0
3	155·4	137·7	177·8	160·8	97·4	164·3	92·0	155·9	105·0	122·1	112·1	147·3	149·7	115·5	120·7	59·4, 55·7
	(+8·5)	(+2·2)	(+2·0)		(−0·8)	(+0·4)	(−1·5)				(−3·4)	(+2·3)	(+2·1)	(−0·1)		
4	155·3	138·0	177·8	160·8	97·5	164·9	91·9	156·0	105·0	120·2	115·0	146·2	150·1	111·7	121·1	59·5, 55·8
	(+8·4)	(+2·5)	(+2·0)		(−0·7)	(+1·0)	(−1·6)					(+1·2)	(+2·5)	(−3·9)		55·5
5	155·3	137·6	177·7	161·5	98·5	164·0	93·7	156·2	104·1	122·1	112·1	147·3	149·6	115·5	120·8	59·5, 55·7
	(+8·4)	(+2·1)	(+1·9)								(−3·4)	(+2·3)	(+2·0)			
Isorhamnetin***12	147·1	136·1	176·3	161·2	98·6	164·4	93·9	156·8	103·5	122·6	112·7	149·4	147·9	116·0	122·2	56·2
											(−2·8)				(+2·2)	
Myricetin**13	147·1	136·1	176·0	161·0	98·5	164·2	93·5	156·4	103·3	121·2	107·5	146·0	136·1	146·0	107·7	
6	155·8	138·0	177·9	160·9	97·6	165·1	92·2	156·2	104·5	119·6	105·1	148·1	138·1	145·6	109·8	59·6, 56·2
	(+8·7)	(+1·9)	(+1·9)		(−0·9)	(+0·9)	(−1·3)				(−2·4)	(+2·1)	(+2·0)			56·0
Eriodictyol***14	78·4	42·2	196·0	163·6	95·9	166·7	95·1	162·9	102·0	129·7	114·5	145·3	145·7	115·6	117·9	
Homoerio-dictyol***15	78·7	42·1	196·3	163·5	95·8	166·6	95·0	162·9	101·8	129·4	111·1	147·5	146·9	115·2	119·6	55·6
											(−3·4)	(+2·2)	(+1·2)		(+1·7)	
Hesperetin***16	78·5	42·3	196·2	163·8	96·2	166·9	95·4	163·0	102·1	131·4	114·3	146·7	148·1	112·0	118·0	55·9
										(+1·7)		(+1·4)	(+2·4)	(−3·2)		

The solvent in all cases is DMSO-d_6 unless specified otherwise.
δ values in ppm from TMS at 25·14 MHz; figures in brackets are $\Delta\delta$ values.
$^+$, $^{++}$ assignments have to be interchanged;
* Markham *et al* 1978.
** Gaydoum and Bianchini 1977;
*** Markham *et al* 1982.

Table 2. ^{13}C NMR data of the acetates of flavonol methyl ethers.

Compound \ Position	2	3	4	5	6	7	8	9	10	1′	2′	3′	4′	5′	6′	OMe	OAc
Ac	154·1	140·7	173·0	150·5	107·9	163·1	98·6	157·7	110·5	122·9	129·8	113·9	161·3	113·9	129·8	59·9, 55·9 55·3	169·4 21·13
-Ac	153·8	140·6	173·2	151·2	108·0	163·2	98·6	157·7	111·0	123·1	111·0	148·8	150·5	111·4	121·9	60·0, 56·1 56·0	169·4 21·1
Ac	153·0	141·2	172·4	150·5	108·1	163·4	98·6	157·7	111·0	129·2	112·6	151·1	141·6	122·9	121·1	60·2, 56·0 55·9	169·4, 168·4 21·1, 20·6
Ac	152·9	140·9	172·9	150·7	108·0	163·2	98·5	157·5	111·1	122·7	123·0	139·5	152·7	112·0	127·4	59·8, 55·9	169·4, 168·6 21·1, 20·6
Ac	153·7	141·7	173·0	150·1	113·2	156·4	108·8	158·3	113·2	128·8	112·4	151·0	143·5	122·9	121·2	60·2, 56·0	169·2, 168·5 167·9, 21·0 20·6
Ac	152·2	141·7	172·9	150·4	108·3	163·4	98·5	157·6	111·2	128·6	109·8	152·1	133·7	143·3	115·3	60·2, 56·2 56·0	169·4, 168·2 167·3, 21·1 20·6, 20·2

values in ppm from TMS at 25·14 MHz; the acetates of the respective compounds have been studied; all spectra were taken in $CDCl_3$.

(δ 167·3–168·6 and 20·2–20·6 ppm respectively). Diacetates of compounds 3 and 4 show signals at δ 169·4, 168·4 and 169·4, 168·6 ppm for acetyl carbonyl carbons and at δ 21·1, 20·6 and 21·1, 20·6 ppm for acetyl methyl carbons, respectively. As both the compounds contain a 5-$OCOCH_3$ group in common along with the signals at δ 169·4 and 21·1 ppm, these signals are assigned to 5-O$\underline{C}$O$\underline{C}H_3$ and 5-OCO$\underline{C}H_3$ respectively analogous to the signals of compounds 1 and 2 monoacetates. The other signals at δ 168·4 and 20·6 ppm in the compound-3-acetate are assigned to 4′-O$\underline{C}$O$\underline{C}H_3$ and 4′-OCO$\underline{C}H_3$, respectively, as that is the only other acetoxyl present. Similarly, signals at δ 168·6 and 20·6 of the compound-4-acetate are assigned to 3′-O$\underline{C}$O$\underline{C}H_3$ and 3′-OCO$\underline{C}H_3$ respectively. Hence, the above values can be considered diagnostic for 5-acetoxyl rendering support for the presence of 5-hydroxyl group in flavonol-3-methyl ethers. The deshielding can be attributed to the anisotropic effect of 4-carbonyl group (table 2).

A comparison of the spectra of compound-3-diacetate with that of compound-5-triacetate shows the 7-acetoxyl carbonyl upfield (δ 167·9). One of the acetoxyl groups in an *o*-diacetoxy system as in 6-acetate is also observed upfield (δ 167·3 ppm). Except for these three characteristic differences, all other acetoxyl carbonyls appear between δ 168·4–168·6 ppm. However, no shift difference is observed for other –O$\underline{C}$O$\underline{C}H_3$ groups and appears between δ 20·2–20·6 ppm except for 5-OCO$\underline{C}H_3$. Hence, the downfield carbonyl signals can be assigned to 5-O$\underline{C}$O$\underline{C}H_3$ and the upfield signal to either 7-O$\underline{C}$O$\underline{C}H_3$ or one acetoxyl group in an *o*-diacetoxy system as the case may be.

The ^{13}C NMR assignments of compounds 1 to 6 were made on the basis of earlier assignments (Pelter *et al* 1976; Markham *et al* 1978; Agarwal and Rastogi 1981). When a phenolic hydroxyl is methylated, the *o*-carbons are reported to move upfield and the *ipso*-carbon downfield (Agarwal and Rastogi 1981). But when one of the hydroxyls in an *o*-dihydroxy system in ring-B is methylated, only the unsubstituted *o*-carbon moves upfield, while the hydroxylated *o*-carbon moves downfield. The above observation was made by a comparison of the spectra of 3 and 4 with quercetin (11, Markham *et al* 1978) and 6 with myricetin (13, Gaydoum and Bianchini 1977, table 1). The signals for the 4′-carbon of homoeriodictyol (15) and the 3′-carbon of hesperetin (16) appear at δ 146·9 and δ 146·7 respectively showing downfield shifts (Δδ +1·2 and Δδ +1·4 ppm), respectively, when compared with 4′(δ 145·7) and 3′ (δ 145·3) carbons of eriodictyol (14) (Markham *et al* 1982). Similarly the 3′-carbon of diosmetin (9) is observed more downfield (δ 146·9) than that of luteolin (8) (δ 146·2) supporting our observation (Markham *et al* 1982) (table 1).

The earlier assignments of chrysoeriol (10) and isorhamnetin (12) (Markham *et al* 1982) are to be interchanged [C-3′(δ 150·8→ 148·0), C-4′ (δ 148·0→ 150·8) in 10 and C-3′ (δ 149·4→ 147·9), C-4′ (δ 147·9→ 149·4) in 12] (table 1), respectively, to account for the downfield shifts (Δδ0·7 and Δδ1·8) observed in other flavonoids for the *o*-hydroxylated carbon. The steric repulsion between the *o*-hydroxylated methoxyls can be expected to dominate over the mesomeric effect, causing this abnormality. The extent of the downfield shift varies froom Δδ0·7 to 2·1 ppm. It is possible to locate the position of a methoxyl group in the B-ring from this observation.

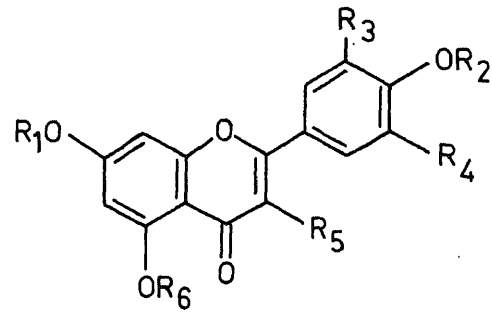

Chart 1.

1. $R_1 = R_2 = Me$, $R_3 = R_4 = H$, $R_5 = OMe$, $R_6 = H$
1 Ac $R_1 = R_2 = Me$, $R_3 = R_4 = H$, $R_5 = OMe$, $R_6 = Ac$
2. $R_1 = R_2 = Me$, $R_3 = OMe$, $R_4 = H$, $R_5 = OMe$, $R_6 = H$
2 Ac $R_1 = R_2 = Me$, $R_3 = OMe$, $R_4 = H$, $R_5 = OMe$, $R_6 = Ac$
3. $R_1 = Me$, $R_2 = H$, $R_3 = OMe$, $R_4 = H$, $R_5 = OMe$, $R_6 = H$
3 DiAc $R_1 = Me$, $R_2 = Ac$, $R_3 = OMe$, $R_4 = H$, $R_5 = OMe$, $R_6 = Ac$
4. $R_1 = R_2 = Me$, $R_3 = OH$, $R_4 = H$, $R_5 = OMe$, $R_6 = H$
4. DiAc $R_1 = R_2 = Me$, $R_3 = OAc$, $R_4 = H$, $R_5 = OMe$, $R_6 = Ac$
5. $R_1 = R_2 = H$, $R_3 = OMe$, $R_4 = H$, $R_5 = OMe$, $R_6 = H$
5 TriAc $R_1 = R_2 = Ac$, $R_3 = OMe$, $R_4 = H$, $R_5 = OMe$, $R_6 = Ac$

6. $R_1 = Me$, $R_2 = H$, $R_3 = OMe$, $R_4 = OH$, $R_5 = OMe$, $R_6 = H$
6 TriAc $R_1 = Me$, $R_2 = Ac$, $R_3 = OMe$, $R_4 = OAc$, $R_5 = OMe$, $R_6 = Ac$
7. $R_1 = R_2 = R_3 = R_4 = H$, $R_5 = OH$, $R_6 = H$
8. $R_1 = R_2 = H$, $R_3 = OH$, $R_4 = R_5 = R_6 = H$
9. $R_1 = H$, $R_2 = Me$, $R_3 = OH$, $R_4 = R_5 = R_6 = H$
10. $R_1 = R_2 = H$, $R_3 = OMe$, $R_4 = R_5 = R_6 = H$
11. $R_1 = R_2 = H$, $R_3 = OH$, $R_4 = H$, $R_5 = OH$, $R_6 = H$
12. $R_1 = R_2 = H$, $R_3 = OMe$, $R_4 = H$, $R_5 = OH$, $R_6 = H$
13. $R_1 = R_2 = H$, $R_3 = R_4 = R_5 = OH$, $R_6 = H$

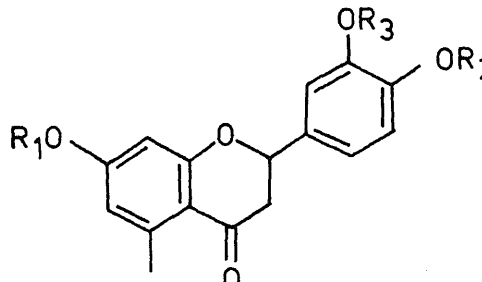

Acknowledgements

The authors are highly grateful to the University of Hyderabad for the ^{13}C NMR spectra. Two of the authors (GNKK and LJMR) thank the CSIR, New Delhi, for fellowships.

References

Agrawal P K and Rastogi R P 1981 *Heterocycles* **16** 2181 (and references therein)
Calvert D J, Cambie R C and Davis B R 1979 *Org. magn. reson.* **12** 583 (and references therein)
Gaydoum E M and Bianchini J P 1977 *Ann. Chim.* **2** 303
Krishna Kumari G N, Jagan Mohan Rao L and Prakasa Rao N S 1984 *Phytochemistry* **23** 2701
Krishna Kumari GN, Jagan Mohan Rao L and Prakasa Rao N S 1985 *Lloydia* **48** 149
Markham K R, Mohanchari V and Mabry T J 1982 *In the flavonoids* (eds) J B Harbourne and T J Mabry (London: Chapman and Hall) pp.19–134
Markham K R, Ternai B, Stanely R, Geiger H and Mabry T J 1978 *Tetrahedron* **34** 1389
Pelter A, Ward R S and Gray T I 1976 *J. Chem. Soc. Perkin I* 2475

Proc. Indian Acad. Sci. (Chem. Sci.), Vol. 97, No. 2, September 1986, pp. 177–184.
© Printed in India.

ESR Bonding parameter studies of single and mixed ligand complexes of copper(II)

Y ANJANEYULU*, N V S RAO, R PRABHAKARA RAO and V G K M PISIPATI

Faculty of Physical Sciences, Nagarjuna University, Nagarjuna Nagar 522 510, India

MS received 17 October 1985; revised 18 March 1986

Abstract. ESR and optical absorption studies are described for a number of copper(II) single and mixed ligand complexes formed with substituted salicylic acids and acetylacetone. ESR spectra of all these complexes give well-resolved spectra in DMF both at room and liquid nitrogen temperatures. The molecular orbital coefficients are estimated assuming an axial symmetry. A partial covalency is observed in all the single ligand complexes while the in-plane π-bonding is as strong as the σ-bonding in all the mixed ligand complexes. No regular trend is observed in the value of χ (which is proportional to hyperfine constants) with the change in the overall electron withdrawing capacity of the substituent on salicylic acid, either in single ligand or in mixed ligand complexes. However, the χ values for all the complexes (except in the case of *bis*(acetylsalicylato)copper(II) and (acetylacetonato)-(3,5-dinitrosalicylato)copper(II)) are in agreement with the computed value of $\chi = -3{\cdot}61$ for single crystals of copper-acetylacetonate possessing the same environment of four oxygens around copper(II).

Keywords. ESR studies; bonding parameters; acetylacetone; salicylic acids; copper(II).

1. Introduction

As part of our current studies on single ligand (Pisipati *et al* 1981, 1984) and mixed ligand (Anjaneyulu *et al* 1983, 1986) complexes of copper(II), we have carried out ESR and optical absorption studies on seven single ligand and seven mixed ligand complexes of copper(II) with acetylacetone (AA) and substituted salicylic acids (SA) as mixed ligands. In all the complexes the immediate environment of copper(II) is made up of four oxygen atoms in a square planar arrangement, except in the thio complex where the oxygen atom is replaced by a sulphur atom. The studies are undertaken in order to infer the nature of the molecular orbital coefficients, and it is found that these parameters exhibit similar qualitative characteristics for substances with similar environments around the copper(II) atom irrespective of the ligand chemical structure. Such studies on copper complexes, where Cu(II) is surrounded by [4N] (Pisipati *et al* 1981; Lancione *et al* 1976, 1979), [3N, O] (Kwik *et al* 1980), [2N, 2O] (Allen and Scullane 1978; Scullane and Allen 1978) and [N, 3O] (Anjaneyulu *et al* 1983), show consistency in molecular orbital coefficients for a particular type of environment irrespective of substituents on the ligand.

the hyperfine contact term K and given by

$$\chi = (4\pi/S_T)\,\langle\psi|\sum_i \delta(r_i)S_{Zi}|\psi\rangle, \tag{1}$$

where χ = the effective field per unpaired electron, S_T = the total spin of the ion, $\delta(r_i)$ = the delta function term and S_{Zi} = the spin of the ith electron, is found to be remarkably constant for a particular type of environment. McGarvey (1967) carried out extensive calculations on a variety of complexes and concluded that it can vary as much as 30% depending upon the ligand, the host lattice and the geometry of the chelate.

Recently χ values of −3·70 (Pisipati *et al* 1981; Lancione *et al* 1976, 1979), −3·79 (Kwik *et al* 1980), −3·92 (Allen and Scullane 1978, Scullane and Allen 1978) and −3·83 (Anjaneyulu *et al* 1983) for [4N], [3N, O], [2N, 2O] and [3O, N] arrangements respectively, resulting from different types of ligands around copper, are reported. No such systematic studies are carried out for copper complexes with [4O] environment. All the copper compounds studied in the present work possess the [4O] coordination except for the thio complex.

2. Experimental

The preparation and characterisation of all these complexes were reported in our earlier paper (Anjaneyulu and Prabhakara Rao 1986).

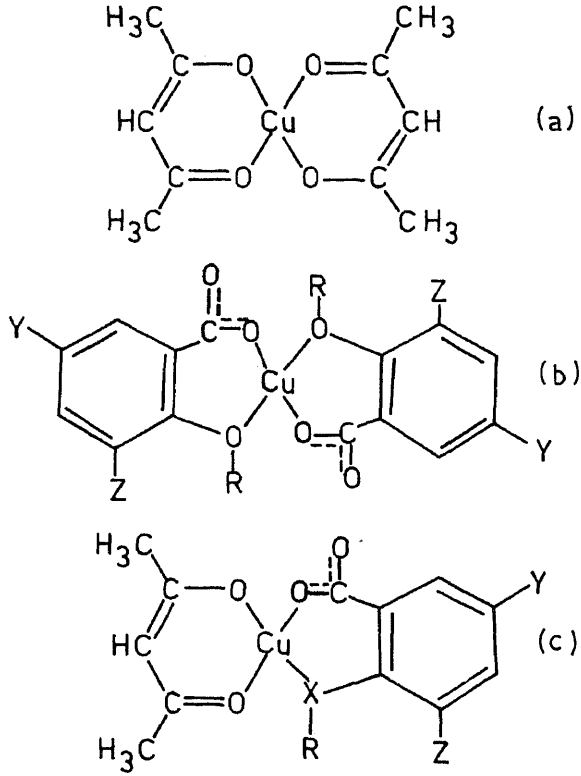

Table 1. Nomenclature of the structural formulae shown in figure 1.

Figure number	Compound number	Name of the complex	Abbreviation	Substituents			
				Y	*Z*	*R*	*X*
1a	1	*Bis*(acetylacetonato)-copper(II)	$Cu(AA)_2$	—	—	—	—
1b	2	*Bis*(salicylato)copper(II)	$Cu(SA)_2$	H	H	H	—
	3	*Bis*(5-chlorosalicylato)-copper(II)	$Cu(Cl\text{-}SA)_2$	Cl	H	H	—
	4	*Bis*(3,5-dibromosalicylato)-copper(II)	$Cu(2Br\text{-}SA)_2$	Br	Br	H	—
	5	*Bis*(3,5-diiodosalicylato)-copper(II)	$Cu(2I\text{-}SA)_2$	I	I	H	—
	6	*Bis*(3,5-dinitrosalicylato)-copper(II)	$Cu(2NO_2\text{-}SA)_2$	NO_2	NO_2	H	—
	7	*Bis*(acetylsalicylato)-copper(II)	$Cu(Acetyl\text{-}SA)_2$	H	H	$COCH_3$	—
1c	8	(Acetylacetonato) (salicylato)copper(II)	Cu(AA) (SA)	H	H	H	O
	9	(Acetylacetonato)5-chlorosalicylato)copper(II)	Cu(AA) (Cl-SA)	Cl	H	H	O
	10	(Acetylacetonato) (3,5-diiodosalicylato)-copper(II)	Cu(AA) (2I-SA)	I	I	H	O
	11	(Acetylacetonato) (5-nitrosalicylato)copper(II)	Cu(AA) (NO_2-SA)	NO_2	H	H	O
	12	(Acetylacetonato) (3,5-dinitrosalicylato) copper(II)	Cu(AA) ($2NO_2$-SA)	NO_2	NO_2	H	O
	13	(Acetylacetonato) (thiosalicylato)copper(II)	Cu(AA) (thio-SA)	H	H	H	S
	14	(Acetylacetonato) (acetylsalicylato)copper(II)	Cu(AA) (acetyl-SA)	H	H	$COCH_3$	O

The ESR spectra were recorded in dimethyl formamide (DMF) solution at room (RT) and liquid nitrogen temperatures (LNT) using a varian E4-X-band ESR spectrometer. The optical absorption spectra were recorded in solution using Beckman DK-2 ratio recording spectrophotometer. The molecular orbital coefficients are evaluated by an iterative procedure. The structural formulae of the complexes are shown in figure 1 and their nomenclature given in table 1.

3. Results and discussion

In all these single ligand and mixed ligand complexes the crystal field symmetry of the copper ion may be taken as distorted tetragonal arising out of four oxygen atoms forming a distorted square planar configuration (except in the thio complex where one sulphur atom replaces an oxygen atom) with the possibility of the

Electronic and ESR spectra of copper complexes with square planar and octahedral geometry can be easily understood using ligand field splitting of the energy levels (Reedijk 1981). Such a distortion will be small for strongly coordinating axial ligands and will increase when the coordinating power of the axial ligands decreases, resulting in the observation of only one overlapping band. However, Gersmann and Swalen (1962) reported three *d–d* transitions for Cu $(AA)_2$ in a frozen solution for which the solvent was a mixture of chloroform and toluene. In the present work all these complexes exhibited only a broad asymmetric band in solution (DMF) in between 15,000–16,000 cm^{-1} at room temperature (table 2) indicating that more than one transition is buried under each of the absorption envelopes and the solvent molecules may be weakly coordinating in the long axial positions.

Well-resolved ESR spectra of transition metal complexes in solution are solvent-dependent. Different authors have proved that a particular solvent or solvent mixture provides the best lattice and gives a well-resolved ESR spectrum at liquid nitrogen temperature, in their studies on single ligand complexes of copper(II)-acetylacetonate (Kuska *et al* 1967; Toy *et al* 1971; Belford and Duan 1978), copper diethyldithiocarbomate and mixed ligand complexes of copper(II) formed with diethyldithiocarbomate and other different ligands (Toy *et al* 1971; Yordanov and Shopov 1976; Tirant and Smith 1980). In the present work the spectra of copper substituted salicylic acids and mixed ligand complexes of

Table 2. Experimental ESR solution data at RT and LNT, with ΔE values.

	Frozen solution data at LNT				Solution data (RT)		
			$A_{\parallel} \times 10^4$	$A_{\perp} \times 10^4$			ΔE
Compound	$g_{\parallel}$	$g_{\perp}$	cm^{-1}	cm^{-1}	g_0	A_0	cm^{-1}
$Cu(AA)_2$	2·291	2·061	159	15	2·129	64	16,129
$Cu(SA)_2$	2·284	2·054	142	19	2·102	54	16,129
$Cu(Cl\text{-}SA)_2$	2·280	2·051	150	22	2·100	60	16,000
$Cu(2Br\text{-}SA)_2$	2·292	2·057	147	19	2·110	58	16,129
$Cu(2I\text{-}SA)_2$	2·292	2·055	147	20	2·105	51	16,129
$Cu(2NO_2\text{-}SA)_2$	2·300	2·061	141	18	2·110	53	16,129
Cu(acetyl-$SA)_2$	2·280	2·060	153	25	2·100	55	16,129
Cu(AA) (SA)	2·289	2·064	149	11	2·141	68	15,873
	2·240	2·040	175	16			
Cu(AA) (Cl-SA)	2·299	2·060	149	14	2·145	67	15,873
	2·244	2·050	179	15			
Cu(AA) (2I-SA)	2·295	2·051	149	18	2·146	68	15,675
	2·242	2·048	172	16			
Cu(AA) (NO_2-SA)	2·296	2·052	146	19	2·144	68	15,625
	2·234	2·046	174	17			
Cu(AA) ($2NO_2$-SA)	2·300	2·069	144	17	2·146	68	15,675
	2·238	2·060	177	14			
Cu(AA) (thio-SA)	2·295	2·051	140	11	2·150	62	15,150
Cu(AA) (acetyl-SA)	2·276	2·056	149	19	2·145	67	15,675
	2·235	2·048	175	18			

temperatures and exhibit four spin-dependent hyperfine lines as expected.

The mixed ligand complexes showed well-resolved spectra both at RT and LNT similar to those observed in the extensively studied copper acetylacetonate systems. All the four parallel and perpendicular lines are visible exhibiting an axial symmetry. The interesting features observed in the spectra are as follows. An unusual feature of the parallel lines splitting *i.e.*, the $m_i = 3/2$ line splits into three while $m_i = 1/2, -1/2, -3/2$ lines split into two lines (Chi-Lin O'Young *et al* 1978), we believe that the splitting of lines is solvent-dependent and it is in accordance with similar data for different copper complexes. The characteristic splitting of $m_i = 3/2$ line is assigned to ^{63}Cu and ^{65}Cu isotopes and it is also found in all the mixed ligand complexes. The splitting due to the solvent effect is observed on the parallel and perpendicular lines in the case of Cu(AA) (2I-SA), Cu(AA) (NO_2-SA), Cu(AA) (Acetyl-SA), Cu(AA) (Cl-SA) and Cu(AA) (SA). The splitting on the

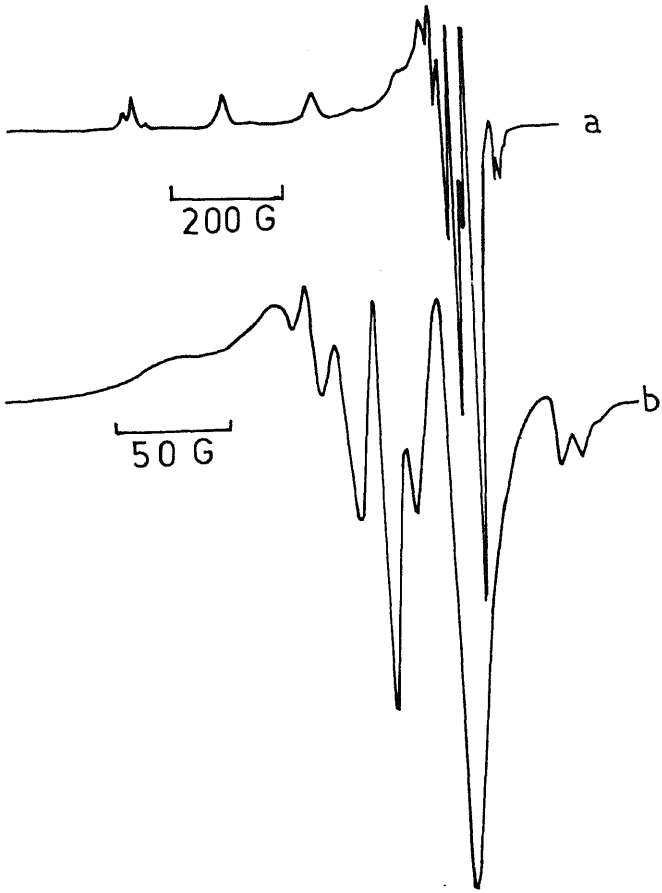

Figure 2. ESR spectra of Cu(AA) ($2NO_2$-SA) at (a) liquid nitrogen temperature, and (b) resolved perpendicular line at liquid nitrogen temperature.

Table 3. Values of $Z_{\parallel}$, $Z_{\perp}$, molecular orbital coefficients and χ.

Compound	$Z_{\parallel}$	$Z_{\perp}$	α^2	α'^2	β^2	$-\chi$
$Cu(AA)_2$	1·07	1·05	0·77	0·30	0·96	3·53
$Cu(SA)_2$	1·06	1·06	0·73	0·35	0·99	3·48
$Cu(Cl\text{-}SA)_2$	1·07	1·05	0·74	0·33	0·95	3·59
$Cu(2Br\text{-}SA)_2$	1·06	1·05	0·75	0·33	0·99	3·53
$Cu(2I\text{-}SA)_2$	1·06	1·05	0·75	0·33	0·99	3·59
$Cu(2NO_2\text{-}SA)_2$	1·06	1·05	0·77	0·31	0·99	3·56
$Cu(acetyl\text{-}SA)_2$	1·07	1·05	0·74	0·34	0·97	3·76
Cu(AA) (SA)	1·07	1·05	0·78	0·29	0·92	3·47
	1·09	1·05	0·80	0·27	0·75	3·51
Cu(AA) (Cl-SA)	1·06	1·05	0·78	0·29	0·97	3·57
	1·08	1·04	0·82	0·25	0·75	3·61
Cu(AA) (2I-SA)	1·06	1·05	0·75	0·30	0·97	3·53
	1·09	1·05	0·79	0·28	0·77	3·54
Cu(AA) (NO_2-SA)	1·07	1·05	0·76	0·32	0·96	3·55
	1·10	1·05	0·78	0·29	0·73	3·54
Cu(AA) ($2NO_2$-SA)	1·07	1·05	0·77	0·30	0·98	3·52
	1·09	1·05	0·81	0·26	0·72	3·70
Cu(AA) (thio-SA)	1·08	1·05	0·76	0·31	0·91	3·32
Cu(AA) (acetyl-SA)	1·08	1·05	0·74	0·33	0·92	3·54
	1·09	1·05	0·79	0·29	0·73	3·57

parallel line only is observed for Cu(AA) ($2NO_2$-SA) (figure 2). Even such splitting is not observed for Cu(AA) (Thio-SA) on the parallel line.

We believe that the species *I* can be identified as one of the single ligand complexes (either copper acetylacetonate or copper substituted salicylic acids) reported in the present work, while species *II* belongs to the mixed ligand complexes. We cannot identify the exact binary species because the g and A tensor values are very close for both the copper acetylacetonate and copper substituted salicylic acids. The formation of a single ligand species in solution at liquid nitrogen temperature may be arising out from the partial dissociation of the mixed ligand complexes into single ligand species (Anjaneyulu *et al* 1983). The g_0, A_0, ΔE values and the g and A tensor values at LNT are presented in table 2.

4. Molecular orbital coefficients and χ-parameter

Since the g and A tensors are essentially axially symmetric the molecular orbital coefficients were calculated taking the values $T(n) = 0{\cdot}220$ and $S = 0{\cdot}093$ for oxygen. Following McGarvey (1967) and adopting the notation used in our earlier paper (Pisipati *et al* 1981),

$$A_{\parallel} - A_{\perp} = (6/7)\alpha^2 P + (g_{\parallel} - 2{\cdot}0023)PZ_{\parallel} - (5/14)\,(g_{\perp} - 2{\cdot}0023)PZ_{\perp}, \tag{2}$$

$$A_{\parallel} + 2A_{\perp} = -3K + (g_{\parallel} - 2{\cdot}0023)PZ_{\parallel} + 2(g_{\perp} - 2{\cdot}0023)PZ_{\perp}, \tag{3}$$

in which

$$Z_{\parallel} = (\alpha\beta)/[\alpha\beta - \alpha'\beta S - \alpha'(1-\beta^2)^{1/2}T(N)/2], \tag{4}$$

and K is the isotropic contact term. The usual value of $P = 360 \times 10^{-4}$ cm^{-1} is used. α and α' are subjected to the normalisation condition,

$$\alpha^2 + \alpha'^2 - 2\alpha\alpha' S = 1, \tag{6}$$

Equations (2), (3) and (6) and the usual expressions for the g tensor are taken to solve for the molecular orbital coefficients using the d–d transition energies. For these complexes only the lowest energy d–d transition is observed and is assigned as $E_{xy} - E_{x^2-y^2}$. In view of this δ^2, the out-of-plane π-bonding coefficient could not be calculated. It is further observed that the value of δ^2 varies from 0·9 to 1·0 and the change in χ value is found to be 2% only. Thus $\delta^2 = 1$ is assumed while calculating the α^2, α'^2, β^2. These coefficients are obtained by the iterative procedure. The initial value of α^2 is determined from (2) assuming $Z_\parallel = Z_\perp = 1$. Initial values of α'^2 and β^2 are obtained from (6) and the equation for $g_\parallel$ respectively (Pisipati *et al* 1981). These three values are used to calculate $Z_\parallel$ and $Z_\perp$ from (4) and (5), which are substituted in (1) to determine the refined value of α^2. The α^2, α'^2 and β^2 values converge after three to four iterations and are presented in table 3. Using the molecular orbital coefficients the isotropic contact term K is evaluated. The isotropic contact term is proportional to the effective field per unpaired electron χ which is given by

$$\chi = (3/2)\ (hca_0^3/2{\cdot}0023\, g_N \beta_N \beta_e)\, K.$$

The computed values of χ are presented in table 3.

The molecular orbital coefficients, for all the single ligand complexes, are found to exhibit similar qualitative characteristics. The in-plane π-bonding (β^2) is weak compared to the σ-bonding (α^2) for all the single ligand complexes (table 3). It is found that the in-plane π-bonding for the mixed complexes is as strong as that of σ-bonding. The $Z_\parallel$ and $Z_\perp$ values also showed consistency for all the complexes. The average value of the effective field per unpaired electron $\chi = 3{\cdot}57$ is in reasonable agreement with the computed value of 3·61 obtained from the reported data of g, A and ΔE values for copper acetylacetonate single crystal possessing [4O] coordination (Kuska *et al* 1967). Furthermore, no regular trend is observed in the magnitude of the parameter χ with increase in overall electron-withdrawing capacity of the substituent in the salicylic acid, either in the single ligand or in the mixed ligand complexes. Previous studies (Scullane and Allen 1978) had indicated that the magnitude of χ is constant and is independent of ligand substitution. In view of the present observations further work is in progress to generalise the effect of electron-withdrawing and -donating groups in the ligand substituent on the magnitude of χ.

Acknowledgements

We are grateful to Prof. Jan Reedijk, Gorlaeus Laboratories, State University of Leiden, The Netherlands, for help in recording ESR spectra and gratefully

References

Abragam A, Horowitz and Pryce M H L 1955 *Proc. R. Soc.* **230** 169

Allen Jr H C and Scullane M I 1978 *J. Coord. Chem.* **8** 93

Anjaneyulu Y, Pisipati V G K M, Rao N V S, Murthy L N, Rao R P and Swamy R Y 1986 *Indian J. Pure Appl. Phys.* (in press)

Anjaneyulu Y and Prabhakara Rao R 1986 *Synth. React. Inorg. Met.-Org. Chem.* (in press)

Anjaneyulu Y, Rao N V S, Swamy R Y, Rao R P and Pisipati V G K M 1983 *Can. J. Chem.* **61** 2154 *Chem.* **61** 2154

Belford R L and Duan D C 1978 *J. Magn. Reson.* **29** 293

Chi-Lin O'Young, Dewan J C, Lilienthal H R and Lippard S J 1978 *J. Am. Chem. Soc.* **100** 7291

Gersmann H R and Swalen J D 1962 *J. Chem. Phys.* **36** 3221

Kuska H A, Rogers M T and Drullinger R E 1967 *J. Phys. Chem.* **71** 109

Kwik W L, Ang K P and Chen G 1980 *J. Inorg. Nucl. Chem.* **42** 303

Lancione R L, Allen Jr H C and Buntacine J R 1976 *J. Coord. Chem.* **6** 7

Lancione R L, Allen Jr H C and Buntacine J R 1979 *J. Coord. Chem.* **8** 201

McGarvey B R 1967 *J. Phys. Chem.* **71** 51

Newton W J and Tabner B J 1981 *J. Chem. Soc., Dalton Trans.* 466

Pisipati V G K M, Rao N V S, Muralikrishna V, Murthy V S and Kesavan T 1984 *Org. Magn. Reson.* **22** 629

Pisipati V G K M, Satyanandam G and Rao N V S 1981 *Org. Magn. Reson.* **17** 235

Reedijk J 1981 *Transition Met. Chem.* **6** 195

Scullane M T and Allen Jr H C 1978 *J. Coord. Chem.* **7** 181

Tirant S and Smith T D 1980 *J. Chem. Soc., Dalton Trans.* 2517

Toy A D, Chaston S H H, Pilbrow J R and Smith T D 1971 *Inorg. Chem.* **10** 2221

Yordonov N D and Shopov D 1976 *J. Inorg. Nucl. Chem.* **38** 137

© Printed in India.

Reaction of 2-hydrazino-4-methyl-6-substituted quinolines with ethylacetoacetate: A structural reinvestigation

RADHE K VAID*† and SHIV P SINGH

Department of Chemistry, Kurukshetra University, Kurukshetra 132 119, India
†Present address: Department of Chemistry, University of Illinois at Chicago, Post Box 4348, Chicago, USA.

MS received 11 December 1985; revised 6 May 1986

Abstract. 1-(6′-substituted-4′-methyl-2′-quinolyl)-3-methyl-pyrazol-5-ols are obtained by the reaction of 2-hydrazino-4-methyl-6-substituted quinolines with ethylacetoacetate rather than the reported 6-substituted-4-methylquinolino(2,3-c)-3-methyl-4,5-dihydro-1H-1,2-diazepin-5-ones. Pyrazol-5-ol structure is assigned on the basis of IR, ^{1}H NMR, ^{13}C NMR (SFORD spectrum) and high resolution mass spectroscopy.

Keywords. Quinolylhydrazine; ethylacetoacetate; ^{13}C NMR spectra; mass spectra.

1. Introduction

In continuation of our studies on the electron-impact induced fragmentation of pyrazoles (Singh *et al* 1982, 1983, 1984), we needed 1-(6′-substituted-4′-methyl-2′-quinolyl)-3-methylpyrazol-5-ols (3). The most convenient route to synthesize (3) is the treatment of ethylacetoacetate with the corresponding hydrazines (Wiley and Wiley 1964; Kamal *et al* 1985), but a survey of literature (Surana *et al* 1972) revealed that the product of the reaction of 2-hydrazino-4-methylquinoline (1a) with ethylacetoacetate is 4-methylquinolino-(2,3-c)-3-methyl-4,5-dihydro-1H-1,2-diazepin-5-one (2) rather than 1-(4′-methyl-2′-quinolyl)-3-methylpyrazol-5-ol (3a). Considering the reaction conditions and the mechanistic grounds which require the formation of hydrazone by the reaction of (1) and ethylacetoacetate, followed by cyclization through an intramolecular Friedel-Crafts reaction for the formation of 2, we thought it worthwhile to reinvestigate the reaction.

2. Results and discussion

On performing the reaction under literature conditions (Surana *et al* 1972) using a standard procedure (Wiley and Wiley 1964; Kamal *et al* 1985) in ethanol-HCl, the product obtained was the same as reported (Surana *et al* 1972) (mixed m.p., superimposable IR and co-TLC: ethylacetate/$CHCl_3$) (scheme 1). The product obtained had a m.p. 168° while that reported for 2a was 150°. The evidence presented in support of structure (2a) included absorption at 1700 and 1600 cm^{-1} in the IR spectrum and 7·2–8·05 (4H, aromatic protons), 2·6 and 2·50 (two singlets,

* To whom all correspondence should be addressed

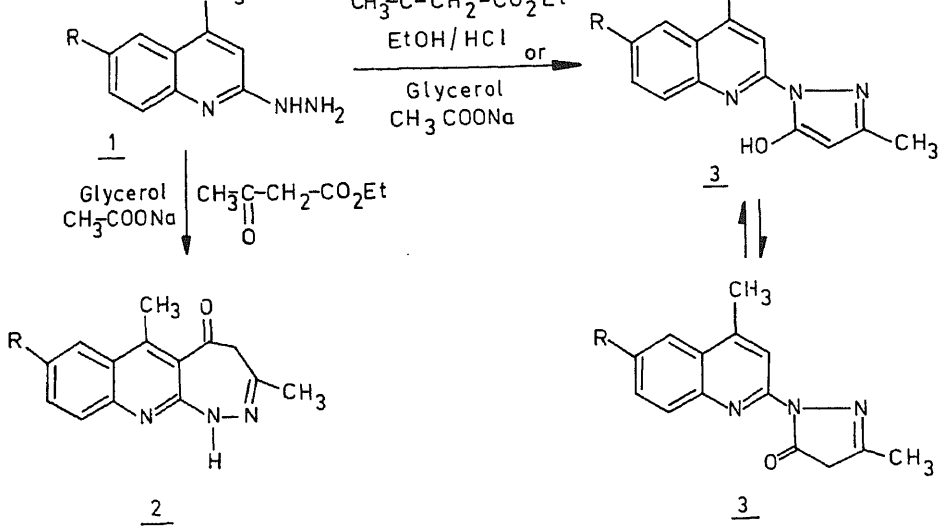

Scheme 1. 1, 2, 3, a. R = H, b. R = OCH_3, c. R = Cl, d. R = F

2-C$\underline{H}_3$), 3·10 (singlet methylene protons), a proton at 8·85 (N$\underline{H}$) and the absence of quinolin-3$\underline{H}$ appearing at 6·4 in hydrazine (1a) in ^{1}H NMR spectrum. However, no N-H stretching in IR and deuterium exchange for the N$\underline{H}$ proton in ^{1}H NMR spectra were observed for 2 by the earlier worker (Surana *et al* 1972).

The spectra, IR and ^{1}H NMR, recorded in our case, however, showed some vital differences. In the IR spectrum, a broad band around 3100–2600 cm^{-1}, due to O–H bonded vibrations, was observed. There was no band at 1700 cm^{-1}, but a sharp band at 1640 cm^{-1} due to ring carbonyl stretching was observed. ^{1}H NMR of 3a in $CDCl_3$ showed signals at 2·3 (s, 3H, pyrazol-3-C$\underline{H}_3$), 2·7 (s, 3H, quinolin-4-C$\underline{H}_3$), 5·4 (s, 1H, pyrazol-4-$\underline{H}$), 7·2–7·9 (m, 5H, aromatic protons), 14·8 (s, 1H, O–$\underline{H}$) exchanged with H_2O. It may be argued that the integration of the aromatic region might be in error but it is difficult to explain the position of the other signals. The absence of quinolin-3$\underline{H}$ presented to support the structure (2) was, in fact, the deshielding of the aromatic proton due to the formation of the pyrazol-5-ol nucleus, as it is observed that protons ortho to the hydrazine or the amino group are always shielded (Silverstein *et al* 1981). As no solvent was mentioned for ^{1}H NMR spectra, the spectrum was taken in a protic solvent to observe the keto form. The spectrum of 3a was scanned in TFA, where the compound exists in keto and enol forms (60 : 40), and exhibits signals at 2·3 and 2·5 (two singlets totally integrating for 3$\underline{H}$ of pyrazol-3-C$\underline{H}_3$ of the keto-enol form respectively), 2·7 (s, 3$\underline{H}$, quinolin-4-C$\underline{H}_3$), 3·95 and 5·45 (two singlets integrating for 2$\underline{H}$ of methylene of keto and 1$\underline{H}$ of 4-H of enolic form), 7·5–8·25 (m, 5H, aromatic protons).

The diazepinone structure (2) was ruled out by comparing the carbon resonances of the pyrazol-5-ol nucleus of 3b in ^{13}C NMR spectra. C-3, C-4 and C-5 resonated at 151·115, 88·266 and 157·572, respectively, which are in complete agreement with

spectrum of 3b, which appeared as doublet and singlet respectively, the pyrazol-5-ol structure for 3b was confirmed. The SFORD spectrum of 3b showed five tertiary carbons and seven quaternary carbons. Had it been a diazepin-5-one structure (2b), we should have observed one secondary, three tertiary and eight quaternary carbons.

Finally, the pyrazol-5-ol structure was confirmed by a study of electron-impact induced fragmentation of 2a. Linked scan data on 2a showed that the parent ion at *m/z* 239·1058 (100%; calculated for $C_{14}H_{13}N_3O$ 239·1059), which undergoes homolytic fission of two moieties to generate ions at *m/z* 142·0652 (8%; calculated for $C_{10}H_8N$ 142·0655) and *m/z* 97·0404 (3%; calculated for $C_4H_5N_2O$ 97·0401) (scheme 2). Had it been a diazepin-5-one structure, such type of cleavage would have been absent.

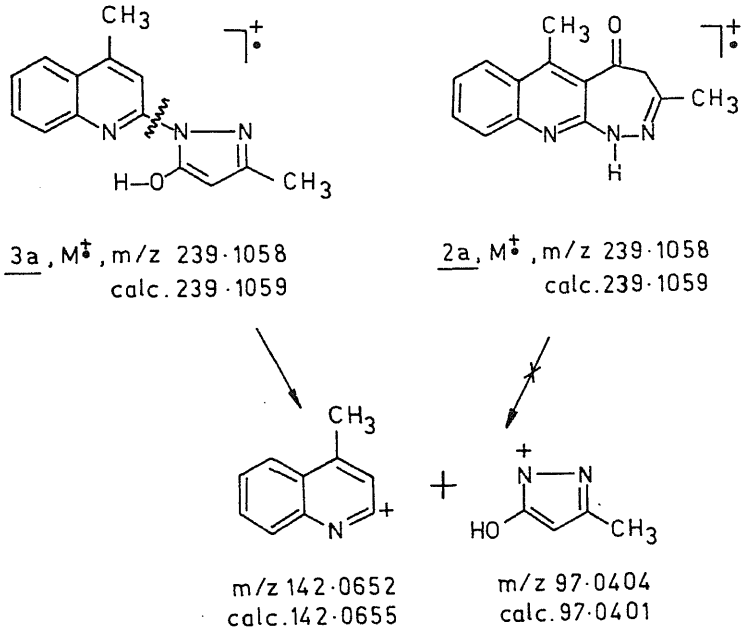

Scheme 2.

3. Experimental

Melting points were taken in open capillary tubes in a liquid bath and are uncorrected. Infrared spectra were recorded on a Beckman IR-20 spectrophotometer. PMR spectra were taken on a R-32 Perkin-Elmer (90 MHz) instrument. ^{13}C NMR spectra were obtained on JEOL FX-60 FT NMR spectrometer operating at 15·03 MHz with 8K data points. Samples taken as 10% v/v solutions in $CDCl_3$ with 2% TMS as reference. The deuterium of the solvent provided the lock signal and the probe temperature was kept at 298±1 K. Mass spectra were scanned on an Hitachi

Table 1. Physical data of 1-(6′-substituted-4′-methyl-2′-quinolyl)-3-methylpyrazol-5-ols (3)*.

Compound	R	m.p. °C	Yield %	Molecular formula	Found (Required %) C	H	N
3a	H	168	53	$C_{14}H_{13}N_3O$	70·29 (70·24)	5·40 (5·43)	17·60 (17·57)
3b	OCH_3	184	54	$C_{15}H_{15}N_3O_2$	66·88 (66·91)	5·54 (5·57)	15·65 (15·61)
3c	Cl	212	60	$C_{14}H_{12}N_3ClO$	61·58 (61·53)	4·36 (4·39)	15·43 (15·38)
3d	F	196	56	$C_{14}H_{12}N_3FO$	65·33 (65·36)	4·69 (4·66)	16·29 (16·34)

All compounds (3) were recrystallized from ethanol

RMU-60 mass spectrometer. High resolution mass spectral data and *B/E* linked scan measurements were obtained through JEOL JMS-D-X 300 mass spectrometer linked to a JEOL, JMA 3100 data system at 70 eV, ionizing current 300 μA accelerating voltage 3·0 kV, and ion source temperature 150°C.

3·1 *2-Hydrazino-4-methyl-6-substituted quinolines*

2-Hydrazino-4-methyl-6-substituted quinolines (1) were prepared following the literature procedure (Potts *et al* 1972; Mehrotra *et al* 1980; Vaid 1984).

3·2 *1-(6′-Methoxy-4′-methyl-2′-quinolyl)-3-methylpyrazol-5-ol*

2-Hydrazino-4-methyl-6-methoxyquinoline (0·203 g, 0·001 mol) and ethyl acetoacetate (0·130 g, 0·001 mol) were taken in ethanol (60 ml) containing two drops of concentrated HCl and the mixture was heated under reflux for 4–5 hr. Half of the solvent was removed and the reaction mixture kept at room temperature overnight. The product 1-(6′-methoxy-4′-methyl-2′-quinolyl)-3-methylpyrazol-5-d (2a) obtained after filtration was washed with ethanol and recrystallized from ethanol (54%), m.p. 184°; IR: 3100–2800 (OH-bonding vibration), 1640 cm^{-1} (ring carbonyl stretching), ^1H NMR ($CDCl_3$) : 2·3 (s, 3H, pyrazol-3-CH_3), 2·7 (s, 3H, quinolin-4-CH_3), 4·0 (s, 3H, OCH_3), 5·45 (s, 1H, pyrazol-4-H), 7·1–7·9 (m, 4H, aromatic protons), 14·8 (b, 1H, OH exchanged with D_2O on shaking), M^+ , *m/z* 269·1155. $C_{15}H_{13}N_3O_2$ (calculated 269·1164).

Other compounds (3) thus prepared are listed in table 1.

Acknowledgements

We are grateful to Dr K Loening, Chemical Abstracts Service, USA, for providing the nomenclature for compounds, Prof. K Pihlaja, University of Turku, Finland, for ^{13}C NMR spectra and Prof. T Maruyama, Taiho Pharmaceutical Co. Ltd., Japan,

References

Feeny J, Newman C A and Panwele P J S 1970 *J. Chem. Soc.*(C). 1842

Kamal A, Reddy A V N and Sattur P B 1985 *Indian J. Chem.* **B24** 414

Kodali D R 1980 *Heterocyclic compounds of potential medicinal interest* Ph.D. thesis, Kurukshetra University, Kurukshetra

Mehrotra S, Barthwal J P, Pandey B R, Bhargava K P and Parmar S S 1980 *J. Heterocycl. Chem.* **17** 1213

Potts K T, Bhattacharya J, Standford L S, Hrig A M and Girard C A 1972 *J. Org. Chem.* **37** 4410

Silverstein R M, Bassler T C and Morriel T C 1981 *Spectrometric identification of organic compounds* (New York: John Wiley and Sons) p. 231

Singh S P, Kodali D R, Dhindsa G S and Sawhney S N 1982 *Indian J. Chem.* **B21** 314

Singh S P, Kodali D R, Prakash I, Prakash O and Sawhney S N 1984 *Indian J. Chem.* **B23** 125.

Singh S P, Prakash I, Tomer R K, Prakash O and Sawhney S N 1983 *Indian J. Chem.* **B22** 43

Surana A, Tyagi R R and Joshi B C 1972 *Phillipp. J. Sci.* **49**

Vaid R K 1984 *Synthesis and mass spectral studies of some thiazole and pyrazole derivatives of medicinal interest*, Ph.D. thesis, Kurukshetra University, Kurukshetra

Wiley R H and Wiley P 1964 *Pyrazolones, pyrazolidones and derivatives* (New York: John Wiley and Sons) p. 20.

Proc. Indian Acad. Sci. (Chem. Sci.), Vol. 97, No. 2, September 1986, pp. 191–207.
© Printed in India.

Vibrational–rotational (v–J) levels of HD^+, evaluated in the adiabatic approximation for the electronic ground state ($1s\sigma_g$)

R S BHATTACHARJEE, R P SAXENA*, P K SRIVASTAVA and K V SANE†

Department of Physics and Astrophysics, and
†Department of Chemistry, University of Delhi, Delhi 110 007, India

MS received 31 January 1986

Abstract. The vibrational–rotational (v–J) energies of HD^+ in the electronic ground state ($1s\sigma_g$) are calculated in the 'adiabatic' approximation. The accurate wave functions and energies calculated in the approximation, where the nuclei are 'infinitely heavy', are used as the basis for the calculation, and thus the (v–J) energies are believed to be better. Furthermore, meticulous attention has been paid to the numerical evaluation of the (v–J) energies, ensuring that the possible numerical truncations, at each stage, are reduced to a minimum, thus enhancing the credence that the energy eigenvalues within the limits of the approximation, are better than the ones reported earlier.

Keywords. Born–Oppenheimer approximation; adiabatic approximation; nonadiabatic approximation; clamped nuclei; infinitely heavy nuclei.

1. Introduction

The charge asymmetry in the HD^+ molecule makes it possible to observe the vibrational–rotational spectrum as an infrared spectrum as opposed to only a Raman spectrum for the H_2 molecule (Herzberg 1966). This permits observation of the vibrational–rotational frequencies with much greater accuracy, thereby enabling one to obtain the vibrational–rotational energy eigenvalues (v, J) of the HD^+ molecule with great precision (Wing *et al* 1976; Spezeski 1977). We recently calculated (Bhattacharjee *et al* 1983) *extremely precise* energy eigenvalues and eigenfunctions of the three-body quantum mechanical problem. It is well known (Born and Oppenheimer 1927) that these wave-functions can be used as a basis for studying the nuclear motion in the H_2^+ or the HD^+ molecule in a series of successive approximations, viz, the Born–Oppenheimer (BO) approximation, the adiabatic approximation and the non-adiabatic approximation. The present paper is an attempt to compute the v–J energy levels of the HD^+ molecule in the BO and the adiabatic approximations using the static wave functions of the HD^+ molecule (the nuclei being infinitely heavy) obtained in our earlier paper (Bhattacharjee *et al* 1983).

Hunter and Pritchard (1967) had obtained the (v,J) levels in the electronic

et al (1977) yielded excellent confirmation of Hunter's and Pritchard's theory – there being a discrepancy of the order of 0·1 cm^{-1} between the predicted and experimental frequencies. However, Hunter and Pritchard never presented a proof of the convergence of their numerical procedure, nor did they show the orthogonality of their basis functions. More accurate experiments by Spezeski (1977) and by Carrington *et al* (1982) showed the need for further theoretical improvement. This was also done by Wolneiwicz and Poll (1978) who performed a second order perturbation for the 'non-adiabatic' Hamiltonian in the space of 'adiabatic' wave functions calculated by Bishop (1974) using a 'clamped nuclei' approximation. Bishop and Cheung (1977) had also estimated the radiative corrections, to the vibrational–rotational energy levels of the HD^+ molecule using an empirical formula. When these radiative corrections are added to the perturbative results of Wolneiwicz and Poll (1978), the agreement with the experiments is truly phenomenal – of the order of 0·001 cm^{-1} for the low lying levels and about 0·01 cm^{-1} for high values of v and J. Later on in the paper, we shall present a comparison of our results with those of Wolneiwicz and Poll (1978).

We wish to end this section with a final remark about the present work. In our earlier paper (Bhattacharjee *et al* 1983) we had calculated the energy eigenvalues of the three-body quantum mechanical problem (e.g. the HD^+ molecule in the limit of infinitely heavy nuclei) as the *limits* of the successive truncations of *convergent* infinite Hill determinants. The energy eigenvalues and the eigenfunctions thus found were accurate to 1 part in 10^8 and the eigenfunctions were demonstrated to be orthogonal. With *these* eigenfunctions (called static eigenfunctions) as bases we have calculated the vibrational–rotational energy levels for the HD^+ molecule in the $1s\sigma_g$ electronic state in the BO and the adiabatic approximations.

The paper is arranged as follows. In §2 we review the theoretical formulation of the three-body problem in the 'adiabatic' and the 'non-adiabatic' approximations. In §3 we describe the evaluation of the nuclear potential (due to electronic motion) in the BO and the 'adiabatic' approximations. Section 4 deals with an accurate variational solution to the problem of nuclear motion. A comparative study of our results with those from experiments and the earlier theoretical papers (Hunter and Pritchard 1967; Wolneiwicz and Poll 1978) is presented in §5.

2. Theoretical formulation of the three-body problem

The non-relativistic Schrödinger equation for the three-body quantum mechanical problem with Coulomb interactions is:

$$\left\{\frac{-\hbar^2}{2}\sum_{i=1}^{3}\frac{1}{m_i}\nabla_i^2+\sum_{i=1}^{3}\sum_{j>i}\frac{Z_iZ_j}{|\mathbf{R}_j-\mathbf{R}_i|}\right\}\psi=E\psi, \tag{1}$$

where $\mathbf{R}_1$, $\mathbf{R}_2$, $\mathbf{R}_3$ are the position vectors of the masses m_1, m_2 and m_3, respectively, and Z_i is the charge on the ith particle. Under the standard centre of mass and relative coordinate transformation, one gets:

$$= E_I \psi_I(\mathbf{R}_a, \mathbf{R}_b). \tag{3}$$

Here $\mathbf{R}_{\text{c.m.}}$ is the centre of mass (c.m.) of the three-body system, $M = m_1 + m_2 + m_3$, $(E - E_I)$ the kinetic energy of the centre of mass, $\mathbf{R}_a = \mathbf{R}_1 - \mathbf{R}_2$, $\mathbf{R}_b$ is the relative coordinate of m_3 with respect to the c.m. of m_1 and m_2 [i.e. $\mathbf{R}_3 - (m_1\mathbf{R}_1 + m_2\mathbf{R}_2)/(m_1 + m_2)$], E_I is the energy of internal motion and

$$\begin{aligned} \mu_1 &= m_1 m_2/(m_1 + m_2), \\ \mu_2 &= m_3(m_1 + m_2)/M. \end{aligned} \tag{4}$$

We now choose $m_3 = m_e$ (the mass of an electron) and work in natural atomic units $\hbar = m_e = e = 1$. We further make use of the dimensional homogeneity of (3) and perform the transformations:

$$\begin{aligned} &m_1 = \alpha_1 m_3; \; m_2 = \beta_1 m_3; \; \gamma = 1 + [1/(\alpha_1 + \beta_1)]; \\ &\mu_1' = \alpha_1 \beta_1 \gamma/(\alpha_1 + \beta_1); \\ &\epsilon_I = E_I \gamma; \; \mathbf{R}_{a'} = \gamma \mathbf{R}_a; \; \mathbf{R}_{b'} = \gamma \mathbf{R}_b. \end{aligned} \tag{5}$$

Equation (3) can now be recast in the form

$$[-(1/2\mu_1')\nabla_{a'}^2 + H_0]\psi_I(\mathbf{R}_a, \mathbf{R}_b) = \epsilon_I \psi_I(\mathbf{R}_a, \mathbf{R}_b), \tag{6}$$

where

$$H_0 = -\tfrac{1}{2}\nabla_{b'}^2 - \frac{Z_1}{|\mathbf{R}_{b'} + [\alpha_1/(\alpha_1 + \beta_1)]\mathbf{R}_{a'}|} - \frac{Z_2}{|\mathbf{R}_{b'} - [\beta_1/(\alpha_1 + \beta_1)]\mathbf{R}_{a'}|} + \frac{Z_1 Z_2}{|\mathbf{R}_{a'}|} \tag{7}$$

The most general solution for the wave-function $\psi_I(\mathbf{R}_{a'}, \mathbf{R}_{b'})$ is of the form (Born and Huang 1954)

$$\psi_I(\mathbf{R}_{a'}, \mathbf{R}_{b'}) = \sum_n \psi_n(\mathbf{R}_{a'})\phi_n(\mathbf{R}_{a'}, \mathbf{R}_{b'}), \tag{8}$$

where $\phi_n(\mathbf{R}_{a'}, \mathbf{R}_{b'})$ is the complete set of orthonormal wave functions for the electronic problem in the field of 'infinitely heavy' nuclei. These are solutions of

$$H_0 \phi_n(\mathbf{R}_{a'}, \mathbf{R}_{b'}) = \Phi_n(|\mathbf{R}_{a'}|)\phi_n(\mathbf{R}_{a'}, \mathbf{R}_{b'}). \tag{9}$$

In (9) the relative nuclear coordinate $\mathbf{R}_{a'}$ plays only a parametric role, not a dynamic one. Using the orthogonality of the ϕ_n, one can rewrite (6) in the form

$$\begin{aligned} &[-(1/2\mu_1')\nabla_{a'}^2 + \Phi_n(|\mathbf{R}_{a'}|) - \epsilon_I]\psi_n(\mathbf{R}_{a'}) \\ &\qquad + \sum_{n'} C_{nn'}(\mathbf{R}_{a'}, \nabla_{a'})\psi_{n'}(\mathbf{R}_{a'}) = 0, \end{aligned} \tag{10}$$

where

$$C_{nn'} = A_{nn'} \nabla_{a'} + B_{nn'}, \tag{11}$$

$$A_{nn'} = -(1/\mu_1') \int \phi_n(\mathbf{R}_{a'}, \mathbf{R}_{b'}) \nabla_{a'} \phi_{n'}(\mathbf{R}_{a'}, \mathbf{R}_{b'}) \mathrm{d}^3\mathbf{R}_{b'} \tag{12}$$

and

$$B_{nn'} = (1/2\mu_1') \int \nabla_{a'}\phi_n(\mathbf{R}_{a'}, \mathbf{R}_{b'}) \cdot \nabla_{a'}\phi_{n'}(\mathbf{R}_{a'}, \mathbf{R}_{b'}) \mathrm{d}^3\mathbf{R}_{b'}. \tag{13}$$

It is trivial to show that A_{nn} is zero. Thus, (10) can be rewritten as:

$$[-(1/2\mu_1')\nabla_{a'}^2 + U_n(|\mathbf{R}_{a'}|) - \epsilon_I]\psi_n(\mathbf{R}_{a'}) + \sum_{n' \neq n} C_{nn'}(\mathbf{R}_{a'}, \nabla_{a'})\psi_{n'}(\mathbf{R}_{a'}) = 0 \tag{14}$$

with

$$U_n(|\mathbf{R}_{a'}|) = \Phi_n(|\mathbf{R}_{a'}|) + B_{nn}. \tag{15}$$

Φ_n represents the nuclear potential in the BO approximation, while U_n is the potential in the adiabatic approximation. The complete potential in the non-adiabatic approximation is the nonlocal form involving the term $C_{nn'}$. In the present work, we have attempted to solve (14) neglecting the non-adiabatic terms using the complete set of eigenfunctions ϕ_n ($\mathbf{R}_{a'}$, $\mathbf{R}_{b'}$) and eigenvalues $\Phi_n(|\mathbf{R}_{a'}|)$ of the 'static' electronic problem found in Bhattacharjee *et al* (1983).

3. Numerical evaluation of the nuclear potential in the adiabatic approximation

In the adiabatic approximation, the nuclear motion, although coupled to the electronic motion, does not induce transitions among the electronic states [see (13) and (15)]. For the electronic ground state $1s\sigma_g$ (denoted by $n = 0$) the relevant part of the nuclear potential is

$$B_{00} = (1/2\mu_1') \int\{\nabla_{a'}\phi_0(\mathbf{R}_{a'}, \mathbf{R}_{b'})\}^2 d^3\mathbf{R}_{b'}, \tag{16}$$

where the coordinate system has its origin at the centre of mass of the nuclei, $\mathbf{R}_{a'}$ the relative distance between m_1 and m_2 and $\mathbf{R}_{b'}$ the position of the electron. Since the 'static' electronic wave function is normalized at each $|\mathbf{R}_{a'}| = R$, one can write in the standard confocal ellipsoidal coordinates

$$\xi = (r_1 + r_2)R, \quad \eta = (r_1 - r_2)R, \quad \omega \tag{17}$$

$$\phi_0(\mathbf{R}_{a'}, \mathbf{R}_{b'}) = \mathcal{N}_0(R)\chi_0(R, \xi, \eta, \omega). \tag{18}$$

As shown by us (Bhattacharjee *et al* 1983)

$$\chi_0(R, \xi, \eta, \omega) = \left\{\exp(-p\xi)(\xi+1)^\sigma \sum_{k=0}^{\infty} C_k[(\xi-1)/(\xi+1)]^k\right\} \times \sum_{l=1}^{\infty} a_l P_{2l-2}(\eta), \tag{19}$$

where

$$p^2 = -\tfrac{1}{2}R^2[\Phi_0(R) - Z_1Z_2/R], \tag{20}$$

and

$$\sigma = (R/p) - 1. \tag{21}$$

The integral in (16) can now be expressed as a double summation over certain

straightforward. Thus one gets

$$B_{0,0}=\frac{1}{2\mu_1'}\left\{\frac{\pi}{4}\mathcal{N}_0^2R\left(\sum_{i=1}^{6}t_i+\sum_{i=1}^{2}z_i\right)+\frac{\pi}{2}\mathcal{N}_0\frac{\partial\mathcal{N}_0}{\partial R}R^2\sum_{i=1}^{4}c_i\right.$$

$$\left.+\sum_{i=1}^{25}g_i+\sum_{i=1}^{6}y_i+\left(\frac{\partial\mathcal{N}_0}{\partial R}\right)^2\frac{1}{\mathcal{N}_0^2}\right\}. \tag{22}$$

Here each of the expressions t_i, z_i, c_i, g_i and y_i is a double summation over some Whittaker functions of the type

$$\sum_{k,k'} f(k,\ k')\,C_kC_{k'}\Gamma(\lambda)\,W_{\lambda,\mu}(Z), \tag{23}$$

the indices λ and μ depend on k, k' and $Z=4p$ (Bateman Manuscript Project 1953) (for details see appendix A). To evaluate these double summations numerically one must have some idea of the convergence of the double sum over the indices k and k'. Using the Stirling formula for the asymptotic behaviour of Γ-functions and the asymptotic behaviour of the Whittaker functions (Gradshteyn and Ryzhik 1965), $\lambda\sim c-k-k'$, one gets

$$\Gamma(\lambda)\,W_{-\lambda,\mu}(Z)\underset{\lambda\to\infty}{\sim}(Z/4\lambda)^{1/4}\exp[-2(2\lambda Z)^{1/2}]. \tag{24}$$

Furthermore, as proved by us (Bhattacharjee *et al* 1983)

$$(C_{k+1}/C_k)\underset{k\to\infty}{\longrightarrow}1-2(p/k)^{1/2}+O(1/k^2). \tag{25}$$

Thus all the double sums of the type (23) will be uniformly convergent. Retaining about fifteen terms each in the double sums yields results correct to at least eight significant places. Also as shown earlier (Bhattacharjee *et al* 1983)

$$(a_{l+2}/a_l)\underset{l\to\infty}{\longrightarrow}O(1/l^2). \tag{26}$$

The resultant integrals, (A49)–(A62), are also uniformly convergent sums and hence, to achieve eight figure accuracy, one needs only to keep about ten terms in each sum.

Clearly for an accurate evaluation of double summations of the type (25), one needs to compute Whittaker functions rather well. To the best of our knowledge, no reliable account of an accurate evaluation of the Whittaker functions, in regions of parameters that may be doubly asymptotic (λ and Z both large) has ever been published, much less used in a physical computation. Our method for numerical evaluation of $W_{\lambda\mu}(z)$ for $\lambda\gtrsim 35$, $\mu\sim 1$, $Z\gtrsim 20$, correct to one part in 10^8 is outlined in appendix B.

The logarithmic integrals quoted in appendix A (A45–A48) can be expressed in terms of the derivatives of the Whittaker functions with respect to the indices λ or μ. No well-known series expansion is found in the literature for such functions. Hence, we decided to evaluate these integrals using a 25-point Gauss–Laguerre quadrature, thereby yielding at least 8-figure accuracy. The derivatives $\partial C_k/\partial R$, $\partial a_l/\partial R$, $\partial\mathcal{N}_0/\partial R$, $\partial\sigma/\partial R$ and $\partial p/\partial R$ have also to be evaluated numerically. It is well known that a straightforward polynomial fit to numerical data for plotting the slope

part in 10^8.

Thus all the expressions t_i, z_i, c_i, g_i and y_i of appendix A can now be evaluated. Since we had already evaluated the 'static' energy eigenvalues (Bhattacharjee *et al* 1983) correct to 1 part in 10^8, the overall accuracy of our nuclear potential computation in either the BO or the adiabatic approximation is 1 part in 10^8.

4. Solution of the nuclear wave equation

The nuclear wave function $\psi_0^I(R)$ satisfies the wave equation (14)

$$[-(1/2\mu_1')\nabla_R^2 + U_0(R) - \epsilon_I]\psi_0^I(R) = 0, \tag{27}$$

where ϵ_I denotes the vibrational rotational (v, J) energy level of the nuclei,

$$U_0(R) = \Phi_0(R), \tag{28}$$

in the Born–Oppenheimer (BO) approximation, and

$$U_0(R) = \Phi_0(R) + B_{0,0}, \tag{29}$$

in the adiabatic approximation. Since the potential in either case is spherically symmetric, one can reduce the wave equation by the substitution:

$$\psi_0^I(R) = R^{-1} g_{v,J}(R)\, Y_{J,M}(\theta, \phi). \tag{30}$$

Finally one gets

$$\left\{\frac{d^2}{dR^2} + \frac{2(J+1)}{R}\frac{d}{dR} + 2\mu_1'(\epsilon_I - U_0(R))\right\} g_{v,J}(R) = 0. \tag{31}$$

To solve (31), one uses a variational principle. A plot of the potential clearly shows a harmonic-oscillator-like structure. Thus the low lying (v, J) levels are expected to be centred around a certain equilibrium distance R_E of the nuclei. A variational expansion of the type

$$g_{v,J}(R) = \exp(-\tfrac{1}{2}y^2) \sum_{m=0}^{\infty} A_m \Theta_m(y), \tag{32}$$

where

$$\Theta_m(y) = (2^m m!\, \pi^{1/2})^{-1/2} H_m(y), \tag{33}$$

$H_m(y)$ being the Hermite polynomial,

$$y = \alpha(R - R_E),\ \alpha = (\mu_1'\ k)^{1/4}. \tag{34}$$

R_E is the equilibrium distance and k is the stiffness constant, which should be particularly suitable for our problem. On substituting the ansatz (32) in (31), the wave equation reduces to the secular form

$$|\mathcal{H} - \epsilon S| = 0 \tag{35}$$

where

$$\mathcal{H}_{mn} = \int_{-\alpha R_E}^{\infty} \exp(-y^2/2)\,\Theta_m(y)\left(-\frac{d^2}{dR^2} - \frac{2(J+1)}{R}\,\frac{d}{dR} + U_0(R)\right) \times \exp(-y^2/2)\,\Theta_n(y)\,dy, \tag{36}$$

$$\mathcal{S}_{mn} = \int_{-\alpha R_E}^{\infty} \exp(-y^2)\,\Theta_m(y)\,\Theta_n(y)\,dy. \tag{37}$$

These integrals are evaluated using a combination of Simpson's rule and Newton's 3/8 rule. The secular equation (35) is then solved for the energy eigenvalues using the standard IBM Scientific Subroutine package. The eigenvalues are computed using 5×5, 10×10, 15×15 and 20×20 matrices. We show in tables 1 and 2 the convergence of various v, J energy levels of the HD^+ molecule in the BO and the adiabatic approximations, respectively.

5. Results and discussion

We first report our results on the vibrational–rotational energy levels of the H_2^+ molecule in the BO approximation along with those obtained by Hunter and Pritchard (1967). These are shown in table 3. It should be noted that the energy levels reported by us are consistently lower than the ones obtained by Hunter and Pritchard (1967). Since we have used a variational procedure for estimating the energy levels, and as discussed earlier, our numerical procedure seems to be free

Table 1. Convergence (showing the numerical stability) of the vibrational–rotational (v, J) energy levels for the HD^+ in the Born–Oppenheimer approximation.

(v, J)	Energy calculated with 15×15 matrices in units of $\mu_2^{-1}=1$	Energy calculated with 20×20 matrices in units of $\mu_2^{-1}=1$
(0,0)	−0·5980912143904	−0·5980912143960
(1,0)	−0·5893729503489	−0·589372950673
(2,0)	−0·5810928920305	−0·58109294572
(3,0)	−0·573235772321	−0·573238115462
(0,1)	−0·5978913193175	−0·5978913193197
(1,1)	−0·58918218315837	−0·5891821834022
(2,1)	−0·5809110018880	−0·580911029035
(3,1)	−0·573063326248	−0·573064826452
(0,2)	−0·5974927256149	−0·5974927256152
(1,2)	−0·5888018015923	−0·5888018018166
(2,2)	−0·5805482918897	−0·5805483070056
(3,2)	−0·5727182880570	−0·5727192900602
(0,3)	−0·5968978028556	−0·59689780285678
(1,3)	−0·5882340890285	−0·5882340891886
(2,3)	−0·58000697050486	−0·5800069810595

Table 2. Convergence (showing the numerical stability) of the vibrational–rotational (v, J) energy levels for the HD^+ in the adiabatic approximation.

(v, J)	Energy calculated with 15×15 matrices in units of $\mu_2^{-1}=1$	Energy calculated with 20×20 matrices in units of $\mu_2^{-1}=1$
(0,0)	−0·5980306649362	−0·5980306649417
(1,0)	−0·5893134758705	−0·5893134761971
(2,0)	−0·5810344169400	−0·5810344708600
(3,0)	−0·5731782142855	−0·5731805658438
(0,1)	−0·5978307994191	−0·59783079942136
(1,1)	−0·5891227365139	−0·58912273675883
(2,1)	−0·5808525530387	−0·5808525803175
(3,1)	−0·5730057958317	−0·5730073015029
(0,2)	−0·5974322645952	−0·5974322645955
(1,2)	−0·5887424103911	−0·5887424106154
(2,2)	−0·5804898951693	−0·5804899103624
(3,2)	−0·5726608081420	−0·5726618138116
(0,3)	−0·5968364295767	−0·5968364295779
(1,3)	−0·5881747804351	−0·5881747805957
(2,3)	−0·5799486513899	−0·5799486619943
(3,3)	−0·5721455485833	−0·5721462323434

Table 3. Comparison between our calculated values and those calculated by Hunter and Pritchard (1967) for the vibrational–rotational (v, J) energy levels of the H_2^+ in the BO approximation.

(v, J)	BO energy for H_2^+ as calculated by Hunter and Pritchard (1967) in atomic units	BO energy for H_2^+ as calculated by us in atomic units
(0,0)	−0·5972283	−0·59728814
(0,1)	−0·5872474	−0·5873036

Table 4. The vibrational–rotational (v, J) energy levels, calculated by us, for the HD^+ in the BO and adiabatic approximation.

	$v=0$	$v=1$	$v=2$	$v=3$
BO energies in units of $\mu_2^{-1}=1$				
$J=0$	−0·59809121439	−0·5893729506	−0·58109294	−0·57323811
$J=1$	−0·597891319319	−0·5891821834	−0·58091102	−0·57306482
$J=2$	−0·597492725615	−0·5888018018	−0·580548307	−0·5727192
$J=3$	−0·59689780285	−0·5882340891	−0·580006981	−0·5722036
Adiabatic energies in units of $\mu_2^{-1}=1$				
$J=0$	−0·5980306649	−0·589313476	−0·58103447	−0·5731805
$J=1$	−0·59783079942	−0·5891227367	−0·58085258	−0·5730073

Table 5. Comparison in values of the transition frequencies of the vibrational–rotational (v, J) energy levels as observed in experiments, values calculated by us and the values reported by other authors.

Transition levels (v, J)–$(v'J')$	Experimental values for the transition frequencies (cm^{-1})	Transition frequencies as calculated by us in the BO approximation (cm^{-1})	Transition frequencies as calculated by HP* in adiabatic approximation (cm^{-1})	Transition frequencies as calculated by us in the adiabatic approximation (cm^{-1})	Transition frequencies in the non-adiabatic approximation by HP* (cm^{-1})	Non-adiabatic values** (cm^{-1})
(1,0)–(0,1)	1869·134	1869·226	1869·28	1868·997	1869·21	1869·135
(1,1)–(0,2)	1823·533	1823·621	1823·67	1823·399	1823·59	1823·533
(1,2)–(0,3)	1776·459	1776·544	—	1776·328	—	1776·461
(2,1)–(1,0)	1856·778	1856·841	1856·92	1856·615	1856·82	1856·779
(3,1)–(2,0)	1761·616	1761·649	1761·74	1761·440	1761·48	1761·616
(3,2)–(2,1)	1797·522	1797·570	1797·64	1797·340	1797·41	1797·519
(3,1)–(2,2)	1642·108	1642·137	1642·23	1641·945	1641·98	1642·111
(3,3)–(2,2)	1831·083	1831·21	—	1830·900	—	1831·078

* HP – Hunter and Pritchard (1967); ** Wolneiwicz and Poll (1978).

from errors to the extent of at least one part in 10^8, we believe our results to provide better lower bounds to the actual energy levels.

Our results in the BO as well as the adiabatic approximation are reported in table 4. From these results it is easy to provide a comprehensive comparison of our results with those of other authors as well as with the experiments. For the sake of convenience, we have displayed in table 5 the transition frequencies for the HD^+ molecule as computed by us in the BO and the adiabatic approximations, the ones calculated by Hunter and Pritchard (1967) in the adiabatic and nonadiabatic approximations, the nonadiabatic results of Wolneiwicz and Poll (1978) and the frequencies found in experiments (Carrington *et al* 1982).

It is to be noted that the transition frequencies obtained by us, in the BO approximation are almost the same as those reported by Hunter and Pritchard (1967) in their most accurate nonadiabatic computation; the difference between these frequencies seems to be of the order of 0·01 cm^{-1}–0·1 cm^{-1}. As we have already discussed the superiority of the BO procedure (see table 3), very little needs to be said in comparing our results with those of Hunter and Pritchard.

The next improvement occurs in our results of the adiabatic approximation. These frequencies are consistently lower than experiments by almost the same amount that the BO ones as reported by us are higher. Thus the situation vis-a-vis agreement with experiment in our calculations does not seem to have improved. However, there seems to be scope for improvement in our calculations. The nonadiabatic corrections and the relativistic effects like spin-spin and spin-orbit couplings, radiative corrections etc., may be taken into account.

It should be noted that the theoretical results of Wolneiwicz and Poll (1978) agree extremely well with experiments. It is of interest to observe that the general order of magnitude of nonadiabatic corrections in their paper is of the order of 0·1 cm^{-1} and the radiative corrections are of the order of 0·008 cm^{-1} for almost all frequencies. Further, the discrepancy between our adiabatic result and that from the experiments is of the order mentioned above. Work is in progress on the nonadiabatic and other effects.

We conclude this with a final remark about the extreme precision of the work of Wolneiwicz and Poll (1978). They used second order perturbation theory for their nonadiabatic calculations, in the space of the adiabatic wave functions computed by Bishop and Cheung (1974). It may be noted that Bishop and Cheung (1974) gave no proof regarding the orthonormality of these adiabatic wave functions. It is also claimed in their work that the evaluation of the infinite sum in the second order perturbation energy converges to a limit with an increasing number of terms, although no detailed numerical figures are given in support of the above assertion.

Acknowledgements

The completion of this work would have been rendered impossible without the numerous thought provoking and enlightening discussions we had with Dr V S Verma of the Physics Department, and V M Khanna of the Chemistry Department, to whom we are sincerely indebted. Thanks are also due to the Director and staff of

$$t_2 = -2p\sigma\left[\alpha^2 H \sum_{k,k'} C_k C_{k'}\, \delta_{2,1}^{k,k'} + S1 \sum_{k,k'} C_k C_{k'}\, \delta_{2,0}^{k,k'}\right], \tag{A2}$$

$$t_3 = -4p\left[\alpha^2 H \sum_{k,k'} (k+1) C_{k+1} C_{k'}\, \delta_{3,1}^{k,k'} + S1 \sum_{k,k'} (k+1) C_{k+1} C_{k'}\, \delta_{3,0}^{k,k'}\right], \tag{A3}$$

$$t_4 = \sigma^2\left[\alpha^2 H \sum_{k,k'} C_k C_{k'}\, \delta_{3,1}^{k,k'} + S1 \sum_{k,k'} C_k C_{k'}\, \delta_{3,0}^{k,k'}\right], \tag{A4}$$

$$t_5 = 4\sigma\left[\alpha^2 H \sum_{k,k'} (k+1) C_{k+1} C_{k'}\, \delta_{4,1}^{k,k'} + S1 \sum_{k,k'} (k+1) C_{k+1} C_{k'}\, \delta_{4,0}^{k,k'}\right], \tag{A5}$$

$$t_6 = 4\left[\alpha^2 H \sum_{k,k'} (k+1)(k'+1) C_{k+1} C_{k'+1}\, \delta_{5,1}^{k,k'} + S1 \sum_{k,k'} (k+1)(k'+1) C_{k+1} C_{k'+1}\, \delta_{5,0}^{k,k'}\right], \tag{A6}$$

$$z_1 = A \sum_{k,k'} C_k C_{k'}\, \delta_{1,1}^{k,k'}, \tag{A7}$$

$$z_2 = -\alpha^2 B \sum_{k,k'} C_k C_{k'}\, \delta_{1,0}^{k,k'}, \tag{A8}$$

$$c_1 = -pS1 \sum_{k,k'} C_k C_{k'}\, (\delta_{0,0}^{k,k'} - \delta_{1,0}^{k,k'}), \tag{A9}$$

$$c_2 = \sigma S1 \sum_{k,k'} C_k C_{k'}\, (\delta_{1,0}^{k,k'} - \delta_{2,0}^{k,k'}), \tag{A10}$$

$$c_3 = 2S1 \sum_{k,k'} (k+1) C_{k+1} C_{k'}\, (\delta_{2,0}^{k,k'} - \delta_{3,0}^{k,k'}), \tag{A11}$$

$$c_4 = F \sum_{k,k'} C_k C_{k'}\, \delta_{1,1}^{k,k'}, \tag{A12}$$

$$y_1 = -\frac{\pi}{2} \mathcal{N}_0 \frac{\partial \mathcal{N}_0}{\partial R} R^3 \frac{\partial p}{\partial R}\left\{\sum_{k,k'} C_k C_{k'}\left[H(\delta_{2,2}^{k,k'} + \delta_{1,1}^{k,k'}) + S1(\delta_{0,0}^{k,k'} - \delta_{1,0}^{k,k'})\right]\right\}, \tag{A13}$$

$$y_2 = -\frac{\pi}{2} \mathcal{N}_0 \frac{\partial \mathcal{N}_0}{\partial R} R^2\left\{\sum_{k,k'} C_k C_{k'}\left\{\left[H(\delta_{2,2}^{k,k'} + \delta_{1,1}^{k,k'}) + S1(\delta_{2,1}^{k,k'} + \delta_{1,0}^{k,k'})\right](-p) + \sigma\left[H(\delta_{3,2}^{k,k'} + \delta_{2,1}^{k,k'}) + S1(\delta_{3,1}^{k,k'} + \delta_{2,0}^{k,k'})\right]\right\} + 2\sum_{k,k'} (k+1) C_{k+1} C_{k'}\left[H(\delta_{4,2}^{k,k'} + \delta_{3,1}^{k,k'}) + S1(\delta_{4,1}^{k,k'} + \delta_{3,0}^{k,k'})\right]\right\} \tag{A14}$$

$$y_3 = -\frac{\pi}{2} \mathcal{N}_0 \frac{\partial \mathcal{N}_0}{\partial R} R^2\left[\sum_{k,k'} C_k C_{k'}\, (F\delta_{1,1}^{k,k'} - N1\, \delta_{1,0}^{k,k'})\right], \tag{A15}$$

$$g_1 = \frac{\pi}{4}\mathcal{N}_0^2 R^3 \left(\frac{\partial p}{\partial R}\right)^2 \left\{ \sum_{k,k'} C_k C_{k'} [H(\delta_{1,2}^{k,k'} + \delta_{1,1}^{k,k'}) + S1(\delta_{1,1}^{k,k'} + \delta_{1,0}^{k,k'})] \right\}, \quad \text{(A17)}$$

$$g_2 = -\frac{\pi}{2}\mathcal{N}_0^2 R^2 \frac{\partial p}{\partial R} H \left\{ \sum_{k,k'} C_k C_{k'} [p(\delta_{1,2}^{k,k'} + \delta_{1,1}^{k,k'}) - \sigma(\delta_{2,2}^{k,k'} + \delta_{2,1}^{k,k'})] \right.$$

$$\left. -2 \sum_{k,k'} (k+1) C_{k+1} C_{k'} (\delta_{3,2}^{k,k'} + \delta_{3,1}^{k,k'}) \right\}, \quad \text{(A18)}$$

$$g_3 = -\frac{\pi}{2}\mathcal{N}_0^2 R^2 \frac{\partial p}{\partial R} N1 \sum_{k,k'} C_k C_{k'} (\delta_{0,0}^{k,k'} - \delta_{1,0}^{k,k'}), \quad \text{(A19)}$$

$$g_4 = -\frac{\pi}{2}\mathcal{N}_0^2 R^3 \frac{\partial p}{\partial R} \sum_{k,k'} C_k C_{k'} \{ O1(\delta_{2,2}^{k,k'} + \delta_{1,1}^{k,k'})$$

$$+ (O1 - P1)(\delta_{0,0}^{k,k'} - \delta_{1,0}^{k,k'}) \}, \quad \text{(A20)}$$

$$g_5 = \frac{\pi}{4}\mathcal{N}_0^2 R p^2 \sum_{k,k'} C_k C_{k'} \{ H\delta_{1,2}^{k,k'} + D\delta_{1,1}^{k,k'} - S1\delta_{1,0}^{k,k'} \}, \quad \text{(A21)}$$

$$g_6 = -\pi\mathcal{N}_0^2 R p \sum_{k,k'} (k+1) C_{k+1} C_{k'} \{ H\delta_{3,2}^{k,k'} + D\delta_{3,1}^{k,k'} - S1\delta_{3,0}^{k,k'} \}, \quad \text{(A22)}$$

$$g_7 = -\frac{\pi}{2}\mathcal{N}_0^2 R p \sigma \sum_{k,k'} C_k C_{k'} \{ H\delta_{2,2}^{k,k'} + D\delta_{2,1}^{k,k'} - S1\delta_{2,0}^{k,k'} \}, \quad \text{(A23)}$$

$$g_8 = \frac{\pi}{4}\mathcal{N}_0^2 R \sigma^2 \sum_{k,k'} C_k C_{k'} \{ H\delta_{3,2}^{k,k'} + D\delta_{3,1}^{k,k'} - S1\delta_{3,0}^{k,k'} \}, \quad \text{(A24)}$$

$$g_9 = \pi\mathcal{N}_0^2 R \sum_{k,k'} (k+1)(k'+1) C_{k+1} C_{k'+1} \{ H\delta_{5,2}^{k,k'} + D\delta_{5,1}^{k,k'} - S1\delta_{5,0}^{k,k'} \}, \quad \text{(A25)}$$

$$g_{10} = \pi\mathcal{N}_0^2 R \sigma \sum_{k,k'} (k+1) C_{k+1} C_{k'} \{ H\delta_{4,2}^{k,k'} + D\delta_{4,1}^{k,k'} - S1\delta_{4,0}^{k,k'} \}, \quad \text{(A26)}$$

$$g_{11} = \frac{\pi}{2}\mathcal{N}_0^2 R^2 O1 \left\{ \sum_{k,k'} C_k C_{k'} [p(\delta_{2,2}^{k,k'} + \delta_{1,1}^{k,k'}) - \sigma(\delta_{3,2}^{k,k'} + \delta_{2,1}^{k,k'})] - \right.$$

$$\left. 2 \sum_{k,k'} (k+1) C_{k+1} C_{k'} (\delta_{4,2}^{k,k'} + \delta_{3,1}^{k,k'}) \right\}, \quad \text{(A27)}$$

$$g_{12} = -\frac{\pi}{4}\mathcal{N}_0^2 R \sum_{k,k'} C_k C_{k'} \{ (A+B)\delta_{1,1}^{k,k'} + M1\delta_{1,0}^{k,k'} \}, \quad \text{(A28)}$$

$$g_{13} = \frac{\pi}{2}\mathcal{N}_0^2 R^2 N2 \sum_{k,k'} C_k C_{k'} \delta_{1,0}^{k,k'}, \quad \text{(A29)}$$

$$g_{14} = \frac{\pi}{4}\mathcal{N}_0^2 R^3 \sum_{k,k'} C_k C_{k'} \{ O2\delta_{1,1}^{k,k'} + (O2 - P2)\delta_{1,0}^{k,k'} \}, \quad \text{(A30)}$$

$$g_{15} = \frac{\pi}{2}\mathcal{N}_0^2 R^3 \frac{\partial p}{\partial R} \frac{\partial \sigma}{\partial R} \sum_{k,k'} C_k C_{k'} \{ D\mathcal{C}_{1,1}^{k,k'} - H\mathcal{A}_1^{k,k'} \}, \quad \text{(A31)}$$

$$g_{16} = \frac{\pi}{4}\mathcal{N}_0^2 R^3 \left(\frac{\partial\sigma}{\partial R}\right)^2 \sum_{k,k'} C_k C_{k'} \{H\mathcal{F}_2^{k,k'} + S1\mathcal{F}_1^{k,k'}\}, \tag{A32}$$

$$g_{17} = \frac{\pi}{2}\mathcal{N}_0^2 R^2 \left(\frac{\partial\sigma}{\partial R}\right) H\Bigg[\sum_{k,k'} (p\mathcal{C}_{1,0}^{k,k'} - \sigma\mathcal{C}_{2,0}^{k,k'}) C_k C_{k'} - 2\sum_{k,k'} \mathcal{C}_{3,0}^{k,k'} (k+1) C_{k+1} C_{k'} \Bigg], \tag{A33}$$

$$g_{18} = \frac{\pi}{2}\mathcal{N}_0^2 R^2 \frac{\partial\sigma}{\partial R} N1 \sum_{k,k'} C_k C_{k'} \mathcal{D}_0^{k,k'}, \tag{A34}$$

$$g_{19} = \frac{\pi}{2}\mathcal{N}_0^2 R^3 \frac{\partial\sigma}{\partial R} \sum_{k,k'} C_k C_{k'} \{O1\mathcal{D}_1^{k,k'} + (O1 - P1)\mathcal{D}_0^{k,k'}\}, \tag{A35}$$

$$g_{20} = -\frac{\pi}{2}\mathcal{N}_0^2 R^3 \frac{\partial p}{\partial R} \sum_{k,k'} C_k \frac{\partial C_{k'}}{\partial R} \{H(\delta_{2,2}^{k,k'} + \delta_{1,1}^{k,k'}) + S1(\delta_{0,0}^{k,k'} - \delta_{1,0}^{k,k'})\}, \tag{A36}$$

$$g_{21} = \frac{\pi}{2}\mathcal{N}_0^2 R^3 \frac{\partial\sigma}{\partial R} \sum_{k,k'} C_k \frac{\partial C_{k'}}{\partial R} \{H\mathcal{D}_1^{k,k'} + S1\mathcal{D}_0^{k,k'}\}, \tag{A37}$$

$$g_{22} = \frac{\pi}{2}\mathcal{N}_0^2 R^2 H \Bigg\{ \sum_{k,k'} C_k \frac{\partial C_{k'}}{\partial R} [p(\delta_{2,2}^{k,k'} + \delta_{1,1}^{k,k'}) - \sigma(\delta_{3,2}^{k,k'} + \delta_{2,1}^{k,k'})] - 2\sum_{k,k'} (k+1) C_{k+1} \frac{\partial C_{k'}}{\partial R} (\delta_{4,2}^{k,k'} + \delta_{3,1}^{k,k'}) \Bigg\}, \tag{A38}$$

$$g_{23} = \frac{\pi}{2}\mathcal{N}_0^2 R^2 N1 \sum_{k,k'} C_k \frac{\partial C_{k'}}{\partial R} \delta_{1,0}^{k,k'}, \tag{A39}$$

$$g_{24} = \frac{\pi}{4}\mathcal{N}_0^2 R^3 \sum_{k,k'} \frac{\partial C_k}{\partial R} \frac{\partial C_{k'}}{\partial R} (H\delta_{1,1}^{k,k'} + S1\delta_{1,0}^{k,k'}), \tag{A40}$$

$$g_{25} = \frac{\pi}{2}\mathcal{N}_0^2 R^3 \sum_{k,k'} C_k \frac{\partial C_{k'}}{\partial R} [O1\delta_{1,1}^{k,k'} + (O1 - P1)\delta_{1,0}^{k,k'}], \tag{A41}$$

$$y_5 = \frac{\pi}{2}\mathcal{N}_0 \frac{\partial\mathcal{N}_0}{\partial R} R^3 \sum_{k,k'} C_k \frac{\partial C_{k'}}{\partial R} (H\delta_{1,1}^{k,k'} + S1\delta_{1,0}^{k,k'}), \tag{A42}$$

$$y_6 = \frac{\pi}{2}\mathcal{N}_0 \frac{\partial\mathcal{N}_0}{\partial R} R^3 \frac{\partial\sigma}{\partial R} \sum_{k,k'} C_k C_{k'} \{H\mathcal{D}_1^{k,k'} + S1\mathcal{D}_0^{k,k'}\}, \tag{A43}$$

$$\delta_{l,j}^{k,k'} = \frac{\Gamma(k_+ + j + 1)}{2p^{[\sigma + (3+2j-l)/2]}} W_{[\sigma - k_+ - (l-1)/2]\ (\sigma + j + 1 - l/2)}^{(4p)}, \tag{A44}$$

k_+ being $k + k'$,

$$\mathcal{C}_{l,j}^{k,k'} = \frac{\exp(-2p)}{2p^{(2\sigma + 5 - l - 2j)}} \int_0^\infty \exp(-y)(y+4p)^{(2\sigma - k_+ - l - j + 2)} y^{(k_+ - j + 1)} (y+2p)$$

$$\mathcal{F}_l^{k,k'} = \frac{\exp(-2p)}{2p^{(2\sigma+2l-1)}} \int_0^\infty \exp(-y)(y+4p)^{(2\sigma-k_+ +l-1)} y^{(k_+ +l-1)} \times [\ln(2+y/2p)]^2 \, dy, \tag{A46}$$

$$\mathcal{D}_l^{k,k'} = \frac{\exp(-2p)}{2p^{(2\sigma+2l+1)}} \int_0^\infty \exp(-y)(y+4p)^{(2\sigma-k_+ +l)} y^{(k_+ +l)} \ln(2+y/2p) \, dy, \tag{A47}$$

$$\mathcal{A}_1^{k,k'} = \frac{\exp(-2p)}{2p^{(2\sigma+4)}} \int_0^\infty \exp(-y)(y+4p)^{(2\sigma-k_+)} y^{k_+} (y+2p)^3 \ln(2+y/2p) \, dy, \tag{A48}$$

$$H = 2 \sum_{l=1}^{\infty} a_l^2 \frac{1}{(4l-3)}, \tag{A49}$$

$$D = 4 \sum_{l=1}^{\infty} a_l a_{l+1} \frac{2l(2l-1)}{(4l-3)(4l-1)(4l+1)} + 2 \sum_{l=1}^{\infty} a_l^2 \frac{1}{(4l-3)^2} \left\{ \frac{(2l-1)^2}{(4l-1)} + \frac{(2l-2)^2}{(4l-5)} \right\}, \tag{A50}$$

$$A = 2 \sum_{l=2}^{\infty} \sum_{l'=2}^{\infty} (2a_l a_{l'} - \delta_{l,l'} a_l^2) \sum_{k=0}^{l'-2} (4l' - 4k - 5), \tag{A51}$$

$$B = 2 \sum_{l=2}^{\infty} a_l^2 \frac{(2l-1)^2}{(4l-3)}, \tag{A52}$$

$$F = 2 \left(\sum_{l=1}^{\infty} \sum_{l'=l+1}^{\infty} a_l a_{l'} + \sum_{l=2}^{\infty} a_l^2 \frac{(2l-2)}{(4l-3)} \right), \tag{A53}$$

$$M1 = 2 \sum_{l=2}^{\infty} a_l^2 \left\{ \frac{2l(2l-1)(2l-2)^2}{(4l-1)(4l-3)^2} + \frac{(2l-3)(2l-2)(2l-1)^2}{(4l-5)(4l-3)^2} \right\} + 4 \sum_{l=2}^{\infty} \frac{2l(2l+1)(2l-1)(2l-2)}{(4l+1)(4l-1)(4l-3)} a_l a_{l+1}, \tag{A54}$$

$$N1 = -2 \left[\sum_{l=2}^{\infty} a_l^2 \frac{(2l-1)(2l-2)}{(4l-1)(4l-3)(4l-5)} + \sum_{l=1}^{\infty} a_l a_{l+1} \frac{2l(2l+1)(2l-1)}{(4l+1)(4l-1)(4l-3)} - \sum_{l=2}^{\infty} a_l a_{l+1} \frac{2l(2l-1)(2l-2)}{(4l+1)(4l-1)(4l-3)} \right], \tag{A55}$$

$$N2 = 2\left[\sum_{l=2}^{\infty} \frac{\partial a_{l+1}}{\partial R}\, a_l \frac{(2l+1)(2l-1)(2l-3)}{(4l+1)(4l-1)(4l-3)}\right.$$

$$+ \sum_{l=2}^{\infty} \frac{\partial a_l}{\partial R}\, a_l \frac{(2l-1)(2l-2)}{(4l-1)(4l-3)(4l-5)}$$

$$\left. - \sum_{l=2}^{\infty} \frac{\partial a_{l+1}}{\partial R}\, a_l \frac{2l(2l-1)(2l-2)}{(4l+1)(4l-1)(4l-3)}\right], \tag{A57}$$

$$O1 = 2\sum_{l=2}^{\infty} a_l \frac{\partial a_l}{\partial R} \frac{1}{(4l-3)}, \tag{A58}$$

$$O2 = 2\sum_{l=2}^{\infty} \left(\frac{\partial a_l}{\partial R}\right)^2 \frac{1}{(4l-3)}, \tag{A59}$$

$$P1 = 2\left\{\sum_{l=2}^{\infty} a_{l+1} \frac{\partial a_l}{\partial R} \frac{2l(2l-1)}{(4l+1)(4l-1)(4l-3)}\right.$$

$$+ \sum_{l=2}^{\infty} a_l \frac{\partial a_l}{\partial R} \frac{1}{(4l-3)^2}\left[\frac{(2l-1)^2}{(4l-1)} + \frac{(2l-2)^2}{(4l-5)}\right]$$

$$\left. + \sum_{l=1}^{\infty} a_l \frac{\partial a_{l+1}}{\partial R} \frac{2l(2l-1)}{(4l+1)(4l-1)(4l-3)}\right\}, \tag{A60}$$

$$P2 = 4\sum_{l=2}^{\infty} \frac{\partial a_{l+1}}{\partial R} \frac{\partial a_l}{\partial R} \frac{2l(2l-1)}{(4l+1)(4l-1)(4l-3)}$$

$$+ 2\sum_{l=2}^{\infty} \left(\frac{\partial a_l}{\partial R}\right)^2 \frac{1}{(4l-3)^2}\left[\frac{(2l-1)^2}{(4l-1)} + \frac{(2l-2)^2}{(4l-5)}\right]. \tag{A61}$$

Appendix B

To evaluate the Whittaker functions $W_{a,b}(z)$ numerically, one recasts them as confluent hypergeometric functions (Bateman Manuscript Project 1953),

$$W_{a,b}(4p) = \exp(-2p)(4p)^{(2b+1)}\psi[(\tfrac{1}{2}-b+a),\ (2b+1),\ 4p], \tag{B1}$$

where

$$\psi(\alpha,\ \beta,\ z) = \frac{\Gamma(1-\beta)}{\Gamma(\alpha-\beta+1)}\ \phi(\alpha,\ \beta,\ z)$$

$$+ \frac{\Gamma(\beta-1)}{\Gamma(\alpha)}\, z^{(1-\beta)}\phi[(\alpha-\beta+1),\ (2-\beta),\ z], \tag{B2}$$

and

$$\phi(\alpha,\ \beta,\ z) = \frac{\Gamma(\beta)}{\Gamma(\alpha)} \sum_{n=0}^{\infty} \frac{\Gamma(\alpha+n)}{\Gamma(\beta+n)} \frac{z^n}{\Gamma(n+1)}. \tag{B3}$$

For our purpose, we need integral values of α and fractional values of β.

Further, as discussed in §3 we require $\alpha \gtrsim 35$, for the $1s\sigma_g$ state at various values of R' varies over a small range, while z varies almost from 0 to 20 or 25. A straightforward evaluation of the series expansion in (B2) suffers from the severe defect of numerical round-off errors in the region of moderate z, e.g. $2{\cdot}8 \leq z \leq 16{\cdot}0$. For the $1s\sigma_g$ state for $\beta = -1{\cdot}652564622694$, $z = 3{\cdot}4097454608$ at $\alpha = 1$, the two series in (B2) cancel each other resulting in the loss of three significant digits, whereas at $\alpha = 8$ the loss in accuracy is eight significant digits. For $z = 2{\cdot}8$ and α (moderate) the loss in accuracy was insignificant. Thus for $z \leq 2{\cdot}8$ and higher values of α, one could try to use a recurrence relation of the type (Bateman Manuscript Project 1953)

$$\psi(\alpha+) = \frac{1}{[\alpha(\alpha-\beta+1)]}\,[(2\alpha-\beta+z)\psi(\alpha)-\psi(\alpha-)], \tag{B4}$$

where $\alpha\pm = \alpha\pm 1$. Unfortunately (B4) is subject to serious numerical truncations and the method outlined above has to be abandoned.

In the region of large numerical truncations (i.e. $z \geqslant 2{\cdot}6$ and α moderate to large) an integral representation,

$$\psi(\alpha,\ \beta,\ z) \ = \ \frac{1}{\Gamma(\alpha)z^{(\alpha-1)}} \int_0^\infty \exp(-t)\,t^{(\alpha-1)}(t+z)^{(\beta-\alpha-1)}\,\mathrm{d}t, \tag{B5}$$

is found useful. A straightforward numerical evaluation of the integral in (B5) using 24-point and 32-point Gauss–Laguerre quadrature for various values of α and β and $1 \leq z \leq 16$ was found to be convergent to about eight to ten significant places. For $z < 1$, the singularity in the factor $(t+z)^{\beta-\alpha-1}$ in (B5) starts coming closer and closer to the lower limit of integration and thus renders the numerical procedure unreliable. However, even for $z < 1$ for large $\alpha \sim 25$ the Gauss–Laguerre quadrature will work quite well, because a large number of derivatives of the integrand at the lower limit would be zero, thus rendering the integrand smooth near $t = 0$. Thus the strategy for the evaluation of the Whittaker functions becomes clear. For large values of α and z, given β and z, one uses (B5) to evaluate the Whittaker function. For the same β and z and lower values of α the $W_{a,b}$'s are evaluated by the backward recurrence relation

$$\psi(\alpha-) = (2\alpha-\beta+z)\psi(\alpha) - \alpha(\alpha-\beta+1)\psi(\alpha+). \tag{B6}$$

For large α, the multiplying factors of the various in ψ's (B6) are of order 2α and $-\alpha^2$ and for small α they are $z-\beta$ and $\alpha(\beta-1)$. In either case the multiplying factors are of different orders of magnitude and cannot lead to round-off errors. For different values of β one uses the recurrence relation,

$$\psi(\beta+) = (1/z)\,[(\beta-1+z)\psi + (\alpha+1-\beta)\,\psi(\beta-)], \tag{B7}$$

where $\beta\pm = \beta\pm 1$. This relation for $z \geqslant 4$ exhibits no truncations and was used in

References

Bateman Manuscript Project 1953 *Higher transcendental functions* (New York: McGraw Hill) vol. 1, p. 248

Bhattacharjee R S, Saxena R P, Srivastava P K and Sane K V 1983 *Phys. Rev.* **A28** 2042

Bishop D M 1974 *Mol. Phys.* **28** 1397

Bishop D M and Cheung L M 1977 *Phys. Rev.* **A16** 640

Born M and Huang K 1954 *Dynamical theory of crystal lattices* (Oxford: Clarendon) appendix

Born M and Oppenheimer J R 1927 *Ann. Phys.* (*Leipzig*) **84** 457

Carrington A, Buttershaw J and Kennedy R A Jr 1982 *J. Mol. Struct.* **80** 47

Gradshteyn I S and Ryzhik I H 1965 *Table of integrals, series and products* (New York: Academic Press) p. 320

Herzberg G 1966 *Molecular spectra and molecular structure* (New York: D Van Nostrand) vol. 1

Hunter G and Pritchard H O 1967 *J. Chem. Phys.* **46** 2153

Spezeski J J 1977 Ph.D thesis, University of Yale

Wing W H, Ruff G A and Lamb W E Jr 1976 *Phys. Rev. Lett.* **36** 1488

Wolneiwicz L and Poll J D 1978 *J. Mol. Spectrosc.* **72** 264

Solution of difficult crystal structures: New, simple, economic and time saving approaches†

S S TAVALE and T N GURU ROW*
Physical Chemistry Division, National Chemical Laboratory, Pune 411 008, India

MS received 2 July 1986

Abstract. MULTAN is the most widely used package for structure determination. However, there are situations where even after utilizing all possible built-in routes the solution is not reached and these become "difficult structures". If such a structure (a) has one or more heavy atoms, (b) is "chicken-wire" with predominant aromatic character, (c) has weak diffraction data, the new approaches discussed will lead to a unique structure solution by introducing simple, economic and time saving ideas into the MULTAN package.

Keywords. Difficult crystal structures; new approaches; MULTAN package.

During the last two decades, advances in structure determination via "Direct Methods" have made extensive progress in terms of automation and several standard packages are currently in use. One such widely used package is MULTAN (Germain *et al* 1971) which normally leads to a unique structure solution in a single automatic run. Several versions of MULTAN are now in use and we shall restrict ourselves to MULTAN 78 (Main *et al* 1978), the version currently available in our laboratory. MULTAN 78 comprises mainly of four routines, NORMAL, MULTAN, FFT and PEAKSEARCH. In case a routine automatic run of MULTAN 78 fails, there are several alternate suggested built-in routes which involve increasing the total number of E values, modifying temperature factors, increasing the number of reflections in the starting set, feeding-in known chemical information, using a fragment for recycling of phases, giving correctly known orientation or partial position information etc. When all these approaches fail, we have a "difficult structure" and at this stage, normally the user tends to give up this structure determination.

The philosophy underlying the new methods suggested below for such difficult situations involves a careful study of the characteristics of the structure, the constituents of the molecule, systematic features in data sets and above all a non-mechanical use of MULTAN. In addition, these methods aim at a reduction of the computer time and memory budget, and the total man hours. The net effect, however, is an unambiguous structure solution. The following are the various steps involved in solving a structure.

†NCL Communication No. 4099

Patterson space group (monochilic : $P2/m$, orthorhombic: $Pmmm$ etc.) for analysis.

Step 2: Input a pseudo-fragment with one of the heavy atoms at (0, 0, 0) and four hydrogen atoms at arbitrary positions, since the FFT package needs a minimum of five atoms input to NORMAL.

Step 3: Compute FFT with $F_{observed}$ values (effectively $|F|$ synthesis). The limits in the PEAKSEARCH program have to extend to half the unit cell so as to get all possible interactions.

Step 4: From these interactions the heavy atom positions can easily be deduced and subsequent runs of FFT in the original space group will give the structure.

This entire operation takes 3 min (3000 reflections) on an ICL1904S machine. The procedure at the outset is not very different from a Patterson synthesis. However, the ease with which the structure can be obtained without any bias to incorrect assumptions about space group symmetry, incorrect information on the constituents of the structure or slips in interpreting the Patterson function, makes this a unique one. A somewhat similar approach is already in use (Buerskens *et al* 1984) but the methodology explained above also takes care of reduction in computer time and memory. A routine MULTAN run takes approximately 30 min for a structure with about 50 atoms.

(b) *Structure with predominant aromatic character (rings)*

Step 1: A routine MULTAN run to start with to get a "chicken-wire" solution.

Case (i): Only one aromatic ring.

Step 2: Generate equivalent data to get a triclinic system.

Step 3: Fix one of the atoms at (0, 0, 0) and shift the other ring atoms without changing the orientation as obtained from step 1, "chicken-wire" run.

Step 4: Compute the Fourier map using FFT in $P1$, locate the symmetry and generate the corresponding molecule or the molecular fragment. Use this information to get the rest of the atoms in the structure using the FFT run in the original space group.

Case (ii): Two or more aromatic rings. Only three different orientations of any two fused aromatic rings are possible. All three are subjected to the procedure under case (i) and one of these will generate the entire structure. The choice of only two fused rings is adequate to arrive at the correct structure even in cases with many rings.

Case (iii): A large number of aromatic rings with one ring containing a heavy atom.

The above procedures described under (a) and (b) may not work due to a large number of parallel vectors. After case (i) step 2, the heavy atom is placed at (0, 0, 0) and the ring formed around the heavy atom also has only three possibilities. The geometry around the heavy atom is adjusted to the standard values and the procedure under case (i) is repeated to get the entire structure.

Each of these operations take only 2 to 3 min of computer time after the initial routine run (about 30 min).

Table 1. Examples* of structures solved by these methods.

	Code**				
	RUTH	IITB	MOGHE	IYDY	ALBA
Molecular formula	$C_{42}H_{30}ClO_2.P_2S_2RU$	$C_{19}H_{25}NO_2$	$C_{18}H_{23}N_2O_3Cl$	$C_{26}H_{16}SO_2$	$C_{39}H_{32}O_8$
Method	a	b(i)	b(ii)	b(iii)	c
Space Group	$P\bar{1}$	*Pcab*	$P\bar{1}$	$P\bar{1}$	$P2_12_12_1$
a(Å)	10·042(1)	7·781(1)	6·037(1)	7·500(2)	28·337(5)
b	11·216(1)	9·959(1)	10·208(3)	9·164(1)	15·961(5)
c	17·772(2)	43·031(4)	15·499(3)	14·330(2)	8·188(4)
α (deg)	99·80(1)	90	103·98(2)	108·06(1)	90
β	93·26(1)	90	82·68(2)	83·71(1)	90
γ	90·86(1)	90	108·56(2)	100·72(1)	90
Z	2	8	2	2	4
R	0·078	0·057	0·062	0·063	0·156

** RUTH, communicated to *Polyhedron;*
IITB, communicated to *Acta Crystallogr. (C)*;
MOGHE, communicated to *Acta Crystallogr. (C)*;
IYDY, *Dyes and Pigments* **7** 81 (1986);
ALBA, *Tetrahedron Lett.* **24** 3013 (1983).
* Several structures have been solved in our laboratory by these methods and this table gives only one example per method.

(c) *Weak diffraction data*

These situations occur while dealing with structures of natural products since in these cases getting a good crystal is often a severe limiting step. There will be very few reflections for a decent 'Direct Method' run. The procedure described below is for non-centric space groups.

Step 1: About 30–40 highest E values (including origin specifiers and enantiomorphs) are given random equal phases (for example $\phi = 20°$; $\phi = 30°$; $\phi = 40°$).
Step 2: A routine run of MULTAN for all these three cases is done and from the map a repetitive fragment (4 or 5 atoms) is extracted.
Step 3: A Karle recycling is run on this fragment to get additional atoms and then a routine FFT yields the entire structure.

Table 1 gives examples for each of these methods. In conclusion, it is felt that these modified procedures would be of immense value to a practising crystallographer with even a small computer and a limited budget.

References

Buerskens P T, Bruins Slot H J, Haltiwanger R C and Van Havare W K L 1984 *J. Crystallogr. Spectrosc. Res.* **14** 599

Germain G, Main P and Woolfson M M 1971 *Acta Crystallogr.* **A27** 368

Main P, Hull S E, Lessinger L, Germain G, Declercq J P and Woolfson M M 1978 MULTAN 78 A

Reactions of halogens with 2,2′-azino*bis*-(3-ethylbenzothiazole-6-sulphonate): Stopped-flow kinetics of formation of radical cations and dications

P MARUTHAMUTHU*, L VENKATASUBRAMANIAN and P DHARMALINGAM

Department of Energy, University of Madras, Guindy Campus, Madras 600 025, India

MS received 10 March 1986; revised 27 June 1986

Abstract. Fast reactions of halogens with 2,2′-azino*bis*-(3-ethylbenzothiazole-6-sulphonate) (ABTS) were investigated by the stopped-flow-spectrophotometric technique. Iodine was found to undergo a reversible reaction with $K = 1{\cdot}43 \times 10^2$. The difference in redox potential, $\Delta E°$, for the reaction was calculated and agreed very well with the theoretically calculated value. Bromine was found to form the stable radical cation ($ABTS^{\cdot+}$) whereas chlorine generated a decomposed product via the radical cation and the dication ($ABTS^{++}$). The individual rate constants for these reactions were measured. The reactivities of the halogens are compared and discussed.

Keywords. 2,2′-Azino*bis*-(3-ethylbenzothiazole-6-sulphonate); stopped-flow kinetics; radical cation; radical dication.

1. Introduction

The study of the formation and reactivity of radical cations from electron sacrificial agents in solution has greatly helped in understanding the mechanism of charge separation processes in the chemical routes to solar energy conversions. Investigations on the redox couples, TMPD/$TMPD^{\cdot+}$ (TMPD = N,N,N′,N′-tetramethyl-*p*-phenylenediamine) (Aruchamy and Wrighton 1980; Maruthamuthu *et al* 1986) and $MV^{2+}/MV^{\cdot+}$ (MV^{2+} = methylviologen) (Gratzel 1982; Dominey *et al* 1981) and the reactions of $MV^{\cdot+}$ with several oxidizing agents (Levey *et al* 1981; Levey and Ebbesen 1983) are worth mentioning. From the general behaviour of azines (mentioned later), the substrate chosen for the present investigation, 2,2′-azino*bis*-(3-ethylbenzothiazole-6-sulphonate) is thought to function as a potential electron relay similar to TMPD and MV^{2+}. The earlier report (Mahuzier *et al* 1975) on 2,2′-azino*bis*-(3-ethylbenzothiazole-6-sulphonate) (ABTS) deals with the use of this compound as an analytical reagent for the spectrophotometric identification of periodic acid. Polarographic oxidation (Huenig *et al* 1964) of 2,2′-azino*bis*-(3-ethylbenzothiazole) reveals the formation of a radical cation and dication. However, no kinetic measurements on the formation and stability of the radical cation and dication have been carried out. In this communication, for the first time, we report the reactions of halogens with ABTS and $ABTS^{\cdot+}$ in aqueous solution.

2. Experimental

All the reactions were carried out under pseudofirst-order condition, by making the halogen concentration at least ten times that of ABTS or $ABTS^{\cdot+}$. The kinetic measurements were made by the use of applied photophysics (London) Model-1705 stopped-flow-spectrophotometer. Absorption output was digitised using a Datalab Model-902 transient recorder equipped with a variable input sensitivity and variable sampling interval. Signals were monitored by a Trio Model-CS-1562 A oscilloscope. About 700 data points were collected for each kinetic measurement and at least six such determinations were made for each value of $k_{observed}$. The data obtained were stored and analysed by CBM-3032 personal computer. The kinetic plots were plotted on a Hewlett-Packard Model-7470 A graphics plotter. All the solutions were prepared with double distilled water. Cyclicvoltammogram studies were done with a PAR Model 173/175 electrochemical set up using a platinum wire as the working electrode and KCl as the supporting electrolyte. ABTS was obtained from Boehringer, Mannheim (West Germany), in the form of a diammonium salt and was used as such. Other chemicals used were of the analytical grade. The reactions were carried out with deaerated solutions and monitored by following the appearance of the radical cation ($ABTS^{\cdot+}$) at 417 nm ($\epsilon_{417} = 2{\cdot}70\times10^4\ M^{-1}\ cm^{-1}$).

3. Results and discussion

The reactions of ABTS with halogens (X_2) were found to follow a total second-order kinetics, first-order each in [ABTS] and [X_2]. The rates were measured at 25°C, taking [X_2] in the range $2\text{–}5\times10^{-4}$ M and [ABTS] in the range $2\text{–}5\times10^{-5}$ M. The second-order rate constants were calculated from the slopes of the plots of $k_{observed}(sec^{-1})$ vs. [X_2]. The first visible observation was that molecular iodine in water oxidized ABTS to $ABTS^{\cdot+}$ instantaneously, but I_2 in excess KI (~ 5%) did not oxidize instantaneously suggesting the reaction equilibrium,

$$2\ ABTS + I_2 \underset{k_r}{\overset{k_f}{\rightleftharpoons}} 2\ ABTS^{\cdot+} + 2\ I^- \qquad (1)$$

The forward reaction was studied by following the formation of the radical cation for various concentrations of ABTS with different amounts of molecular iodine in water, in 10–15 msec time scale. The second-order rate constant, k_f calculated was $6{\cdot}28\times10^2\ M^{-1}\ sec^{-1}$. The reverse reaction was monitored by following the disappearance of $ABTS^{\cdot+}$, for various concentrations of $ABTS^{\cdot+}$ ($1{\cdot}0-5{\cdot}0\times10^{-5}$ M) and I^- ($2{\cdot}0-8{\cdot}0\times10^{-2}$ M). $ABTS^{\cdot+}$ used was prepared separately in deaerated solution by reacting ABTS and peroxomonosulphate (HSO_5^-) in the ratio 2:1 respectively. It was found to be stable for more than a week in the absence of any other additive. The stability of this radical cation is discussed later. The second-order rate constant, k_r, for the reverse reaction was calculated as $4{\cdot}40\ M^{-1}\ sec^{-1}$ and the estimated equilibrium constant is

found to be $\Delta G^\circ = -1{\cdot}23 \times 10^4$ J mol^{-1}. The difference in the standard redox potentials between the two one-electron redox couples in (1) is calculated as

$$\Delta E^\circ = \Delta G^\circ / F = -0{\cdot}127 \text{ V}$$

The standard redox potential for ABTS$^{\cdot+}$/ABTS, $E^\circ = +0{\cdot}43$ V vs. SCE was measured in an aqueous medium by the cyclicvoltammetric technique using a platinum wire as the working electrode. The standard redox potential for I_2/I^- is $E^\circ = +0{\cdot}54$ V (vs. SCE) (Latimer 1961). The theoretical value of the standard electrode potential for (1) is calculated as

$$\begin{aligned}\Delta E^\circ &= E^\circ(\text{ABTS}^{\cdot+}/\text{ABTS}) - E^\circ(I_2/I^-) \\ &= (+0{\cdot}43) - (+0{\cdot}54) \\ &= -0{\cdot}11 \text{ V}\end{aligned}$$

which agrees very well with our experimental value, $-0{\cdot}127$ V.

In the case of reactions of Br_2 and Cl_2 individually with ABTS, such an equilibrium reaction was not observed. Molecular bromine in water or aqueous Br_2/KBr oxidised ABTS to ABTS$^{\cdot+}$ in a 0·1 to 0·5 msec time scale and the calculated rate constant for the stoichiometric reaction,

$$2 \text{ ABTS} + Br_2 \longrightarrow 2 \text{ ABTS}^{\cdot+} + 2 Br^- \qquad (2)$$

is $1{\cdot}00 \times 10^5$ M^{-1} sec^{-1}. There was no detectable reaction of ABTS$^{\cdot+}$ either with Br_2 or Br^-. The radical cation ABTS$^{\cdot+}$ formed in this case is also stable in presence of either Br_2 or Br^-. This unusual stability of this radical cation is due to the distribution of an odd number of electrons over an even number of atoms arranged in a chain. In fact, there is a class of radical ions classified as violenes by Huenig (1966). Azaviolenes are obtained by interchanging the methine groups with nitrogen and are represented as follows:

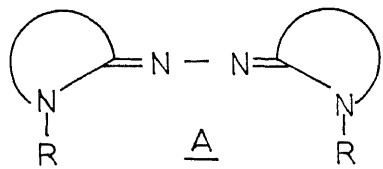

A

Chart 1

This arrangement involves a strong delocalization of the single electron into the π-cloud, symbolized by the two resonance structures, B and C, thus causing a high stability and long wavelength absorption.

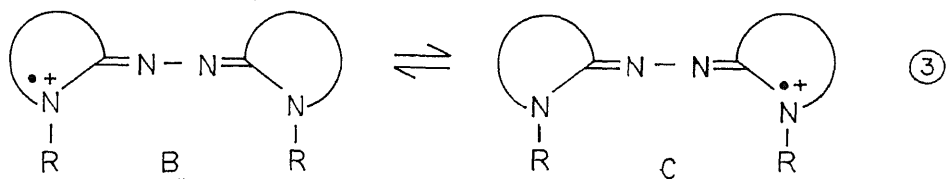

(3)

In principle the redox system is a reversible one and all the three members A, B (or C) and D are reasonably stable in the reaction medium.

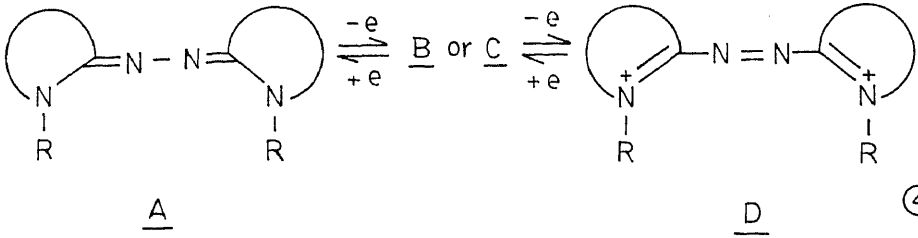

Chart 3.

In the case of azines A, which include an amidine system, the acid-base equilibria may be written as:

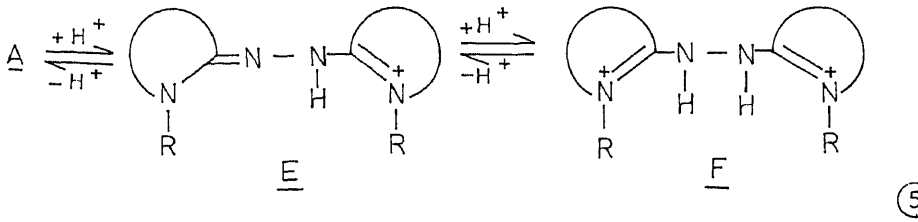

Chart 4.

Among such azines only benzothiazole azine is so weakly basic that it resists protonation from pH 11 down to pH 2·3. Since ABTS also belongs to this class, it does not exhibit protonation around the neutral pH region of the present study.

In the case of Cl_2, the first stage oxidation (scheme 1a) was very fast and took place within the mixing time of the instrument (0·2 msec). The second stage oxidation (scheme 1b) to colourless decomposed product occurred via the dication ($ABTS^{++}$) intermediate confirmed by the transient absorption spectrum, λ_{max} = 513 nm. The kinetics of this process was followed by monitoring the disappearance of $ABTS^{\cdot+}$ at 417 nm, for various concentrations of $ABTS^{\cdot+}$ prepared as mentioned earlier in this text. The kinetics of the decay process followed total second-order, first-order each with respect to $[ABTS^{\cdot+}]$ and $[Cl_2]$ ($[ABTS^{\cdot+}]$ = $1\text{–}3\times10^{-5}$ M; $[Cl_2] = 1\text{–}3\times10^{-2}$ M). The second-order rate constant k_d is 2·40 M^{-1} sec^{-1}. From the magnitudes of the rate constants, the trend of reactivity of the halogens with ABTS can be given as $Cl_2 > Br_2 > I_2$, the two latter halogens forming only the one-electron oxidation product, $ABTS^{\cdot+}$. The trend of reactivity

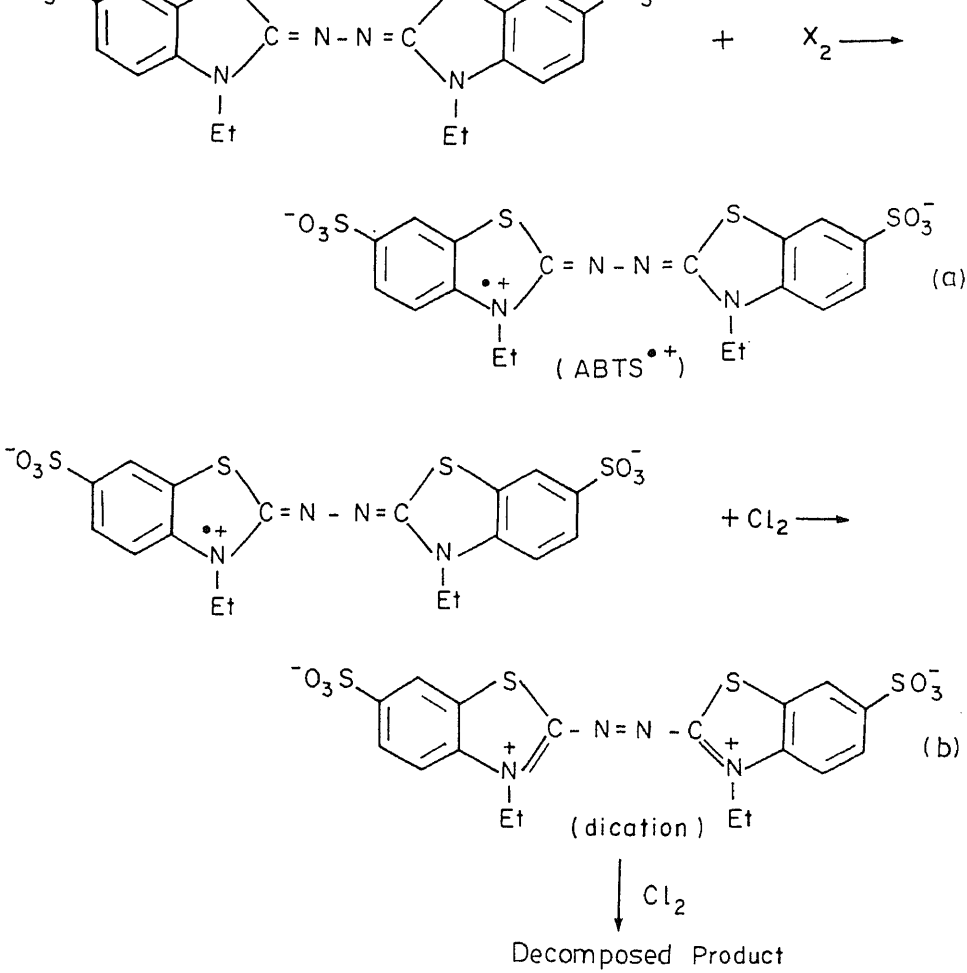

Scheme 1.

from $S_2O_8^{2-}$ and dissolving in water, is reconverted to the radical cation, ABTS$^{\cdot+}$, probably via oxidation of water,

$$\text{ABTS}^{++} \xrightarrow{H_2O} \text{ABTS}^{\cdot+} \tag{6}$$

The reversibility of the reaction $\text{ABTS}^{\cdot+} \underset{+e}{\overset{-e}{\rightleftharpoons}} \text{ABTS}^{++}$ is similar to $\text{ABTS} \underset{+e}{\overset{-e}{\rightleftharpoons}} \text{ABTS}^{\cdot+}$ and it may provide a method of using ABTS as a potential electron-relay similar to the reactions of TMPD and MV^{2+}.

Acknowledgement

The authors thank the DST, New Delhi, for financial support.

References

Aruchamy A and Wrighton M S 1980 *J. Phys. Chem.* **84** 2848

Dominey R N, Lewis N S and Wrighton M S 1981 *J. Am. Chem. Soc.* **103** 1261

Grätzel M 1982 *Acc. Chem. Res.* **14** 376

Hüenig S 1966 *Free radicals in solution* (Michigan: International Symposium, IUPAC) p. 109

Hüenig S, Balli H, Cornard H and Schott A 1964 *Ann. Chem.* **676** 52

Latimer W M 1961 *Oxidation potentials* (New Jersey: Prentice-Hall) p. 63

Levey G and Ebbesen T W 1983 *J. Phys. Chem.* **87** 829

Levey G, Rieges A L and Edwards J O 1981 *J. Org. Chem.* **46** 1255

Maruthamuthu P, Venkatasubramanian L and Dharmalingam P 1986 *J. Chem. Soc., Faraday Trans. I* **82** 359

Mahuzier G, Kirkacharian B S and Harfouche-Obeika C 1975 *Anal. Chim. Acta* **76** 79

Prof. K S G Doss

Attaining the age of eighty is a great event, and provides an occasion to salute and honour wise men. Professor K S G Doss reached eighty this August, and as a tribute to his services to Indian Science, especially electrochemistry and sugar technology, and to the Indian Academy of Sciences of which he is a Founder member, this special issue of the Proceedings is dedicated to him.

Kadarundalige Sitarama Gururaja Doss was born on the 10th August 1906 in Nagamangala of the then Mysore state. His early education in Mysore and Bangalore was marked with proficiency and excellent attainments. During an active academic period spanning three decades (1927–1957) that followed, he taught in the Central College, Bangalore, and in the National Sugar Institute, Kanpur, where he officiated as its Director. In 1957, he moved to the Central Electrochemical Research Institute (CECRI), Karaikudi, for organising research in fundamental and industrial electrochemistry in a big way. As Director of the CECRI during 1957–1967, he imparted to the Institute great strength and high reputation. Since his retirement in 1967, he has been busy as a technical adviser and consultant for several industrial units.

Prof. Doss's research spans a wide area, all the way from adsorption films, wetting phenomena, techniques for measurement of fast reactions and trace concentrations, to many applied R & D projects. He participated fully in the excitement of the Langmuir–Adam–McBain era and spread it in India in the 1930's. His later contributions to electrochemical interfaces are too many to recount here, the most well-known being the discovery of the Faradaic rectification. The latter opened up a very interesting field of study connected with polarography and fast reaction kinetics. There is not a single aspect of modern electrochemistry, on which he has not bestowed attention – be it potential of zero charge or mechanism of oxide film formation and electrochemical oscillations or a very successful solution to the industrial problem of porous carbon electrodes for air depolarized cells – name any! The international electrochemical community honoured him on his reaching the 70th year, by publishing in 1975 a Festschrift of the Journal of Electroanalytical Chemistry (Elsevier).

Prof. Sir C. V. Raman had a great influence on Prof. Doss in several aspects – his fascination for discovery and his penchant for clarity in presentation. Prof. Doss has trained and inspired a large number of young scientists and fostered electrochemical research in the country. He is a founder member of the Academy and served in the Council during 1971–73. He was elected to the Indian National Science Academy in 1957 and is a member of several professional bodies.

It is with great pleasure we convey the felicitations of the members of the Academy and the Indian Scientific Community on this occasion, wishing him longevity and happiness.

S K Rangarajan
S R Rajagopalan

C N R Rao
Editor of Publications

Solvation model for inner-sphere nuclear reorganization in the photoionization of univalent anions in solution[§]

PAUL DELAHAY* and ANDREW DZIEDZIC[†]

Department of Chemistry, New York University, New York, NY 10003, USA
[†]The Perkin-Elmer Corporation, 50 Danbury Road, Wilton, Conn 06897, USA

Abstract. The energy of inner-sphere reorganization for the photoionization of univalent anions in aqueous solution is calculated from a discrete model of solvation. A multipole expansion is used to account for electrostatic interactions, and only the terms corresponding to nuclear motion are retained in the expansion to the exclusion of induced moments. London dispersion, Born repulsion, cavity formation and hydrogen bonding are also taken into account. The theory is applied to eight inorganic anions. Calculated reorganization energies are compared to experimental values deduced from threshold energies for photoelectron emission by aqueous solutions of eight anions in the 6 to 11 eV range of photon energies. Standard reduction potentials for the corresponding radical-anion couples are calculated from threshold energies and theoretical reorganization energies.

Keywords. Anion; electron transfer; inner sphere; nuclear reorganization; outer sphere; photoelectron emission; radical; solvation; threshold energy.

1. Introduction

It is a pleasure to dedicate this paper to our distinguished colleague, K S G Doss, on the occasion of his eightieth birthday and as a tribute to his contributions to science and to electrochemistry in particular. The recently developed theory of inner-sphere reorganization (Delahay and Dziedzic 1986a) will be applied to the photoionization of eight inorganic univalent anions not previously considered. The results will be used in the calculation of the standard reduction potentials for radical-anion couples in solution. A brief introduction to photoelectron spectroscopy of aqueous solutions will be given first. Further details on this method can be found in an extensive review (Delahay 1984).

2. Photoelectron spectroscopy of aqueous solutions

Optical electron transfer can be investigated by measuring the current for photoelectron emission by aqueous solutions (salts, molecules) as a function of the photon energy E (6 to 11 eV). The current is measured by collecting electrons by means of an electrode in the gas phase above the liquid. A rotating disk target (figure 1) is used for continuous renewal of the irradiated surface of the solution. The yield is calculated as the number of collected electrons per incident photon,

[§] Dedicated to Prof. K S G Doss on his eightieth birthday
* To whom all correspondence should be addressed.

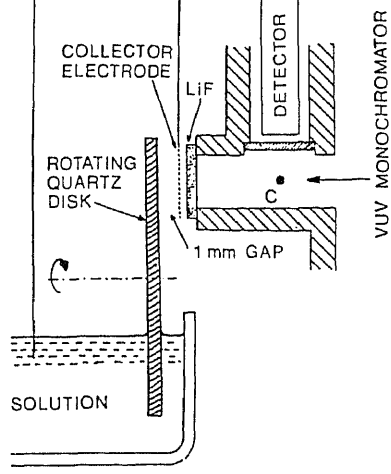

Figure 1. Schematic diagram of instrument for the determination of emission spectra (Delahay 1982).

and results are displayed as a plot of the yield Y as a function of photon energy E (figure 2, curve A).

Theory (Brodsky and Tsarevsky 1976; Brodsky 1980) predicts and experiment confirms that plots of $Y^{1/2}$ against E are linear and extrapolate to the threshold energy E_t (figure 2, line B). The exponent 1/2 of the yield Y generally holds at photon energies exceeding the threshold energy by a few tenths of electronvolt (Brodsky 1980). Plots of $Y^{1/2}$ against E exhibit a fine structure consisting of "wiggles." This fine structure, which is primarily determined by the nature of the solvent, results from a nonequilibrium electronic contribution to the energetics of photoionization on account of dielectric dispersion (Delahay and Dziedzic 1986b). The effect of this contribution, in general, averages out over the usual extrapolation range 7 to 10 eV for aqueous solutions and represents a rather negligible ($< 0{\cdot}1$ eV) error on threshold energies obtained by extrapolation from plots of $Y^{1/2}$ against E. This effect therefore is neglected in the following treatment. However, in the case of nonaqueous solvents the dispersion contribution may not be negligible and must be considered.

Threshold energies of some common inorganic anions in aqueous solution are listed in table 1. All these values are below the threshold energy of liquid water, $E_t = 10{\cdot}06$ eV, except for the fluoride ion. The value $E_t = 10{\cdot}6$ eV for this anion was recently determined by subtracting at each photon energy the emission yield for water from the total yield measured for a 5 M potassium fluoride solution (Delahay and Dziedzic 1986a). A platinum rotating disk and a plastic-lined cell were used to avoid spurious emission resulting from leaching of glass under the action of fluoride solution.

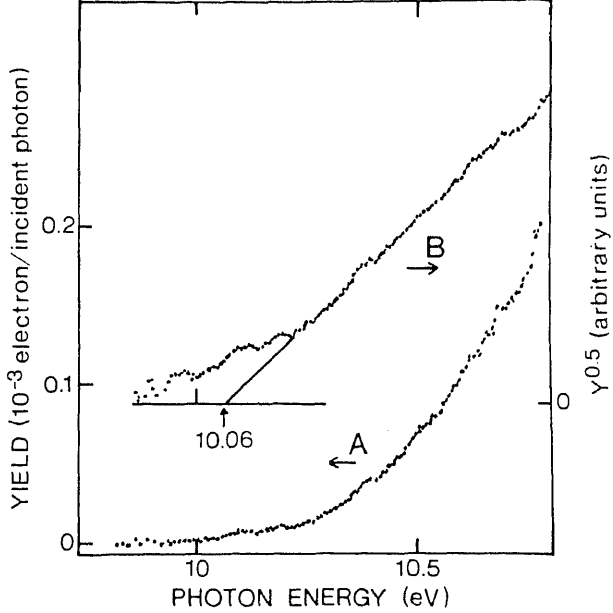

Figure 2. Photoelectron emission spectrum of liquid water at 1·5°C consisting of the plot of the yield Y against the photon energy E (curve A). Plot of $Y^{1/2}$ against E (line B). Extrapolated threshold energy $E_t = 10{\cdot}06$ eV (Delahay and von Burg 1981).

Table 1. Experimental threshold energies (eV) of anions in aqueous solution*.

OH^- (8·6)
F^- (10·6), Cl^- (8·9), Br^- (8·15), I^- (7·4)
ClO_3^- (8·2), BrO_3^- (7·9), IO_3^- (7·4)
ClO_4^- (8·5)
NO_2^- (7·6), NO_3^- (8·5), N_3^- (7·4)
HCO_3^- (9·1), SCN^- (7·2)

*From Delahay and Dziedzic 1984a; Delahay and Dziedzic 1986a.

3. Energetics of photoionization in aqueous solution

3.1 *Threshold energy*

The following basic equation for the threshold energy E_t for photoionization emission by anions in aqueous solution is derived from a thermodynamic cycle and consideration of nuclear reorganization (von Burg and Delahay 1981; Delahay 1984):

$$E_t = \Delta G_H + \Delta G + R + |e|\Delta\chi \qquad (1)$$

reactions

$$1/2H_2(g) = H^+(aq) + e^-(g), \tag{2}$$

$$A^-(aq) + H^+(aq) = A(aq) + 1/2H_2(g); \tag{3}$$

R is the free energy for nuclear reorganization of the product of photoionization; and $\Delta\chi$ is the difference between the surface potentials of the solution of A^- (aq) and water. The last term in (1) is generally very small (< 0·05 eV) and can be neglected. The contribution to E_t from nonequilibrium electronic polarization arising from dielectric dispersion is not included in (1) because it is generally negligible as noted in §2. The threshold energy E_t is equated in (1) to the free energy for electron emission. Equation (1) will be applied in §6.

The threshold energy E_t is also related to the electron affinity (EA) of the atom or radical A(g) by the following equation derived from a thermodynamic cycle (Delahay 1982):

$$E_t \approx \mathrm{EA} + \Delta G_n + \Delta G_s + R \tag{4}$$

where ΔG_n and ΔG_s are the solvation free energies of the species A(g) and $A^-(g)$, respectively. Equation (4) is approximate because the electron affinity is an enthalpy and the equation should be written in terms of enthalpies rather than free energies. The error can be significant (e.g., 0·5 eV) if the entropy contribution to ΔG_s is important. Equation (4) will be applied in §6.

Equations (1) and (4) give the threshold energy E_t for emission of electrons into the gas phase above the aqueous solution of A^-(aq). The free energy for production of quasifree electrons in the *bulk of liquid water* by photoionization of species A^-(aq) is given by $E_t - V_0$, where V_0 is the difference between the electron vacuum level and the bottom of the conduction band of liquid water. One has $V_0 \sim 1{\cdot}2$ eV (Gurevich *et al* 1980) and consequently photoionization of a species in aqueous solution begins to occur in aqueous solution at photon energies lower by $\approx 1{\cdot}2$ eV than the threshold energy for emission into the gas phase by this species.

3.2 *Free energy of nuclear reorganization*

Photoionization of A^-(aq) produces the species denoted by A(aq)* which initially has the solvation configuration of the ion A^-(aq). Subsequent nuclear reorganization of this *nonequilibrium* solvation configuration yields the atom or radical A(aq) having its equilibrium solvation configuration. The free energy for the spontaneous nuclear reorganization of the solvent about the photoionization product in the process A(aq)* → A(aq) is $-R$, where R is taken to be a positive quantity. Additionally, a significant contribution from vibrational relaxation of A(aq)* may also be included in this term.

Two regions are distinguished about the ion being photoionized: (i) the inner-sphere region comprising the first layer of solvent molecules around the central ion, and (ii) the outer-sphere region beyond the inner-sphere region generally treated as a continuous medium. The boundary between these two

where R_{IN} and R_{OUT} pertain to the inner- and outer-sphere regions, respectively.

The value of R_{OUT} was calculated first by Marcus (1956) who developed the required theory of *nonequilibrium* polarization of a continuous medium. Thus,

$$R_{OUT} = (\varepsilon_{op}^{-1} - \varepsilon_s^{-1})e^2/2a \tag{7}$$

where ε_{op} and ε_s are the optical and dielectric constants of the solvent, respectively, e is the electronic charge, and a is given by (5). The free energy R_{OUT} is determined by the *change* of ionic valence caused by photoionization rather than by the absolute values of the species involved in the photoionization process. Equation (7) shows that the free energy R_{OUT} is the difference between the free energies of electronic and total polarization of the continuous medium. Thus, R_{OUT} is the change in the free energy of orientation polarization of the medium resulting from the change of ionic valence upon photoionization.

The inner-sphere reorganization energy was calculated initially for thermal electron exchange between cations from a harmonic oscillator model of bond stretching (George and Griffith 1959). A transition state was assumed and the corresponding generalized coordinate was obtained by minimizing the energy of activation. This approach is *not* applicable directly to photoionization because no transition state is formed prior to optical electron transfer and there is reorganization about only *one* species, e.g., the ferric ion produced by photoionization of a ferrous ion. Conversely, there is reorganization about *two* species in thermal electron exchange, e.g., about the ferrous and ferric ions between which an electron is exchanged. The energy of inner-sphere reorganization U_{IN} for the photoionization of cations was calculated by Delahay and Dziedzic (1984b) for the harmonic oscillator model, and the resulting values agreed with experiment for hydrated transition metal cations and metal complexes. This matter will not be discussed further since inner-sphere reorganization about anions is treated by using a different model in the next section.

4. Solvation model for inner-sphere reorganization about univalent anions

The close relationship between solvation in the Born model and outer-sphere reorganization can be extended to inner-sphere reorganization in the photoionization of univalent anions (Delahay and Dziedzic 1984a). This relationship was fully developed recently (Delahay and Dziedzic 1986a). Thus, solvation of $A^-(g)$ can be regarded as the formation of a cavity of radius r_i in the solvent and the orientation of N_i solvent molecules in the inner-sphere region of $A^-(aq)$. Conversely, photoelectron emission by a solution of $A^-(aq)$ entails the removal of the charge $e^-(g)$ and a change of the cavity radius from r_i to the value r_f for the radical or atom thus produced. Nuclear reorganization of the inner-sphere shell changes the solvent configuration around the species produced by photoionization. The number of surrounding solvent molecules may also change from N_i to N_f. The energy U_{IN} for

inner-sphere reorganization therefore is

$$U_{IN} = U^f(\text{nucl}) - U^i(\text{nucl}) \tag{8}$$

where U^f(nucl) and U^i(nucl) represent, respectively, the terms in the equations for the hydration energies of A(aq) and A^-(aq) which correspond *only to nuclear motion* in the hydration of these species. The energy U^f(nucl) in (8) is the nuclear contribution to the solvation energy of the species A(aq) surrounded by the *equilibrium* inner-sphere shell of solvent. The energy U^i(nucl) in (8) is the nuclear contribution from the species A(aq)* surrounded by the *nonequilibrium* inner-sphere solvent shell of the ion A^-(aq).

The terms in the energies U^f(nucl) and U^i(nucl) in (8) are taken from a fairly standard model of ionic solvation involving a multipole expansion of the ionic field (*cf*, e.g., Morf and Simon 1971). The model is modified to take into account the different orientations of water molecules around cations and anions. One has (Delahay and Dziedzic 1986a)

$$\begin{aligned} U_{IN} = &- U^i(ep) - U^i(eq) - U^i(pp) - U^i(pq) - U^i(qq) \\ &+ \Delta U_{disp} + \Delta U_{rep} + \Delta U_v + \Delta U_c, \end{aligned} \tag{9}$$

where the first five terms on the right hand side represent interaction energies involving the *change* (e) of ionic charge upon photoionization, solvent permanent dipoles (p) and quadrupoles (q). Each of the last four ΔU-terms are equal to the difference $U^f - U^i$ for the following processes: ΔU_{disp} for London water–water dispersion; ΔU_{rep} for Born water–water repulsion; ΔU_v for the volume change of the solvent upon solvation; ΔU_c for cavity formation and the breaking up of the solvent structure in the solvation process. Explicit forms of the terms in (9) are given by Delahay and Dziedzic (1986a).

5. Calculation of the reorganization energy U_{IN} for various univalent anions

The contributions to the inner-sphere reorganization energies U_{IN} are listed in table 2 for various inorganic anions not considered previously by Delahay and Dziedzic (1986a). The thermochemical radii (table 3) were used for all the anions except for ClO_4^- and N_3^- for which Pauling radii were available. The following assumptions were made in the calculation: (i) The radii r_i and r_f of the anion and radical, respectively, were assumed to be equal. This assumption affects only the calculation of ΔU_{disp} and ΔU_{rep} in (9). The former is negligible even for very different values of r_i and r_f (Delahay and Dziedzic 1986a) and the latter is not sensitive to the choice of radii. (ii) The values $N_i = 6$ and $N_f = 4$ were adopted. This choice is fully justified, for instance, for the halide ions (Delahay and Dziedzic 1986a) and it appears reasonable for the anions of table 2. (iii) The water orientation was assumed in which the field vector of the negative point charge of the anion and the dipole moment of water make a 52·23° angle. This orientation is justified for the halides (Delahay and Dziedzic 1986a) and it should also prevail for other anions. (iv) The electrical field of the anions was assumed to have spherical symmetry. This approximation seems justified for ClO_4^-, for instance, but is more

Table 2. Contribution to the inner-sphere reorganization energy U_{IN}*.

Anion	$-U^i(ep)$	$-U^i(eq)$	$-U^i(pp)$	$-U^i(pq)$	$-U^i(qq)$	ΔU_{rep}	ΔU_v	ΔU_c	U_{IN}
	(all units in eV)								
ClO_3^-	2·14	−0·61	−0·19	0·08	−0·02	−0·18	0·04	−0·27	0·99
BrO_3^-	2·40	−0·72	−0·23	0·10	−0·02	−0·19	0·15	−0·27	1·22
ClO_4^-	1·39	−0·32	−0·10	0·04	−0·01	−0·14	≈0	−0·27	0·59
NO_2^-	1·88	−0·50	−0·16	0·06	−0·01	−0·16	−0·23	−0·27	0·61
NO_3^-	2·03	−0·56	−0·18	0·07	−0·02	−0·17	0·05	−0·27	0·95
N_3^-	1·75	−0·45	−0·14	0·06	−0·01	−0·15	–	−0·27	0·79
HCO_3^-	2·36	−0·71	−0·23	0·10	−0·02	−0·19	0·03	−0·27	1·07
SCN^-	1·66	−0·42	−0·13	0·05	−0·01	−0·15	0·13	−0·27	0·86

*Thermochemical radii (table 3) used for all anions except ClO_4^- and N_3^- (Pauling radii). No calculation for IO_3^- because of uncertainty on the thermochemical radius. The value $\Delta U_v = 0{\cdot}15$ eV for BrO_3^- is more likely to be comprised between the values of 0·04 and 0·10 eV for ClO_3^- and IO_3^-, respectively.

Table 3. Pauling and thermochemical radii*.

Anions	Pauling radius (Å)	Thermochemical radius (Å)
OH^-	1·47	1·33±0·03
F^-	1·36	1·26±0·03
Cl^-	1·81	1·72±0·05
Br^-	1·95	1·88±0·06
I^-	2·16	2·10±0·08
ClO_3^-	–	1·71±0·06
BrO_3^-	–	1·54±0·08
IO_3^-	–	1·22±0·72
ClO_4^-	2·45	2·40±0·05
NO_2^-	–	1·92±0·11
NO_3^-	–	1·79±0·06
N_3^-	2·04	1·95±0·02
HCO_3^-	–	1·56±0·02
CNS^-	–	2·13±0·10

*Pauling radii as given by Halliwell and Nyburg (1963); thermochemical radii according to Jenkins and Thakur (1979).

(v) Vibrational contribution to reorganization was neglected. This assumption is justified for NO_2^- (Warnek 1969) and N_3^- (Jackson *et al* 1981), for instance, but an additional vibrational contribution to U_{IN} of a few tenths of an electronvolt cannot be ruled out for some of the anions.

One has

$$U_v^i = -(v_{int} - v_{pm})/\beta_c \tag{10}$$

where v_{int} and v_{pm} are the intrinsic and partial molar volumes of the anion, respectively, and β_c is the compressibility of water. The negative sign on the right

assigning a positive sign to R since $-R$ is the change of free energy for the spontaneous process $A(aq)^* \rightarrow A(aq)$. Removal of electrostriction around $A(aq)^*$ is also spontaneous and therefore the quantity

$$\Delta U_v = U_v^f - U_v^i \tag{11}$$

in (9) is taken as positive (just as R). The energy U_v^f in (11) is assumed to be equal to zero for the neutral species A(aq). The required volumes were taken from tables (Akitt 1980; Marcus 1977; Padova 1964).

The term ΔU_c in (9) was obtained by noting that solvation of the radical $A(g)$ involves only the rotation of two of the four water molecules surrounding A(aq) without a net change of the number of hydrogen bonds and with conservation of tetrahedral symmetry (Delahay and Dziedzic 1986a) for the value $N_f = 4$. Conversely, the substitution of A(aq) by the ion $A^-(aq)$ involves a change from tetrahedral to octrahedral symmetry on the assumption that $N_i = 6$. This process involves the breaking of a bond. The reverse process therefore involves the net formation of a hydrogen bond and consequently $\Delta U_c = -0{\cdot}27$ eV (Morf and Simon 1971).

It is seen from table 2 that the terms $-U^i(ep)$ and $-U^i(eq)$ in (9) are dominant in determining the energy U_{IN}. Thus, the energy U_{IN} is determined primarily by the charge-dipole and charge-quadrupole interactions. Next in importance come the contributions ΔU_c for hydrogen bonding, $-U^i(pp)$ for dipole–dipole interaction, and ΔU_{rep} for Born repulsion. The term ΔU_{disp} of (9) is equal to zero since the radii r_i and r_f were assumed to be equal. In any case, ΔU_{disp} is negligible ($\sim 0{\cdot}01$ eV) even when r_i and r_f are significantly different (e.g., for photoionization of halide ions).

The charge-dipole energy $U^i(ep)$ is inversely proportional to the square of the cavity radius r_i, that is, to the sum of the ionic radius and the crystallographic radius of water (1·38 Å). Likewise, the charge-quadrupole interaction energy is inversely proportional to r_i^3. Since $-U^i(ep)$ and $-U^i(eq)$ are the dominant terms in (9), one can expect a monotonic decrease of U_{IN} with increasing ionic radius. The following sequences hold for the data of tables 2 and 3:

$$ClO_4^- < NO_2^- < N_3^- < SCN^- < NO_3^- < ClO_3^- < HCO_3^- < BrO_3^- \text{ (for } U_{IN}),$$

$$ClO_4^- > SCN^- > N_3^- > NO_2^- > NO_3^- > ClO_3^- > HCO_3^- > BrO_3^-$$
(for thermochemical radii).

The expected trend is essentially observed except for NO_2^-. The N_3^-/SCN^- inversion is minor, and may arise from the neglect of the unavailable value of ΔU_v in the calculation of U_{IN} for N_3^-. The exception for NO_2^- arises from the abnormally large thermochemical radius of this ion. Evidence from lyotropic numbers (Morris 1958) suggests that NO_2^- is smaller than NO_3^- whereas the opposite conclusion follows from the radii of table 2. The term $\Delta U_v = -0{\cdot}23$ eV for NO_2^- is also abnormal in comparison with the ΔU_v's for the other anions in table 2. The NO_2^- ion is V-shaped, the ONO angle being 115° (Cotton and Wilkinson 1980), and this pronounced departure from the spherical symmetry inherent to a point-charge model may account for the abnormal results for NO_2^-. Further comments on NO_2^- are made in §6.

theoretical values of U_{IN} and experimental values of R_{IN} for the halide and hydroxide ions. The R_{IN}-values were computed from (1), (6) and (7). Three additional experimental values of R_{IN} will be calculated for NO_2^-, NO_3^- and N_3^-.

The values $R_{IN} = 1{\cdot}27$ and $0{\cdot}85$ eV for NO_2^- and NO_3^-, respectively, were calculated from (1) for $E_t = 7{\cdot}6$ and $8{\cdot}5$ eV (table 1), $\Delta G = 1{\cdot}0$ and $2{\cdot}3$ eV (Berdnikov and Bazhin 1970), and $R_{OUT} = 0{\cdot}85$ and $0{\cdot}87$ eV [from (7) for the thermochemical radii of table 3]. The free energy ΔG for the N_3^-/N_3 couple is not available, and R_{IN} was obtained from (4). The value $\Delta G_n = 0{\cdot}15$ eV was taken by analogy with solvation of other radicals. The value $\Delta G_s = -2{\cdot}92$ eV was computed from the solvation enthalpy $-3{\cdot}09$ eV of N_3^- (Halliwell and Nyburg 1963) and the entropy correction of $0{\cdot}17$ eV calculated from data in Friedman and Krishnan (1973). Furthermore, one has $E_t = 7{\cdot}4$ eV (table 1) for N_3^-, EA $= 2{\cdot}70$ eV (Jackson *et al* 1981), $R_{OUT} = 0{\cdot}82$ eV for $r_c = 2{\cdot}40$ Å (Conway 1981), and consequently $R_{IN} = 0{\cdot}81$ eV from (4). The N–N distances in $N_3^-(g)$ and $N_3(g)$ are the same within $0{\cdot}006$ Å and the NNN angle is the same according to Jackson *et al* (1981). The vibrational contribution to R_{IN} therefore should be minor.

Values of R_{IN} thus obtained are listed in table 4. These free energies R_{IN} calculated from threshold energies by means of (1) are essentially *experimental* quantities since only model considerations enter in the calculation of R_{OUT} and the contribution of this term is not sensitive to r_c ($R_{OUT} = 0{\cdot}96$ eV for F^- vs $R_{OUT} = 0{\cdot}80$ for I^-). Furthermore, the continuous medium model used in calculating R_{OUT} is fully satisfactory for the outer-sphere region. Values of R_{IN} and U_{IN} in table 4 agree very well with the error of $\approx \pm 0{\cdot}1$ eV on R_{IN} except for NO_2^-. The error on R_{IN} arises from the uncertainty in the extrapolation procedure used to obtain threshold energies and the error on the free energy ΔG appearing in (1). The entropy contribution to R_{IN} is probably within the error on this quantity. The theory should hold best for anions such as the halide ions which exhibit spherical symmetry, but the agreement between R_{IN} and U_{IN} is also good for ions not

Table 4. Experimental free energies R_{IN} versus theoretical energies U_{IN}*.

Anions	R_{IN} (eV)	U_{IN} (eV)
OH^-	1·38	1.24
F^-	1·56	1·42
Cl^-	1·00	0·94
Br^-	0·83	0·84
I^-	0·72	0·71
NO_2^-	1·27	0·61
NO_3^-	0·85	0·95
N_3^-	0·81	0·79

*Results for the halide and hydroxide ions from Delahay and Dziedzic (1986a).

Table 5. Change of free energy ΔG for reaction (1) for various anion–radical couples in aqueous solution*.

Anion	E_r	R_{IN} (all in eV)	R_{OUT}	ΔG
ClO_3^-	8·2	0·99	0·89	1·8
BrO_3^-	7·9	1·22	0·92	1·3
ClO_4^-	8·5	0·59	0·76	2·7
NO_3^-	8·5	0·95	0·87	2·2
N_3^-	7·4	0·79	0·82	1·3
HCO_3^-	9·1	1·07	0·92	2·6
SCN^-	7·2	0·86	0·81	1·1

*E_r-values from table 1; R_{IN} from table 2; R_{OUT} computed from (7) for the thermochemical radii of table 3 except for ClO_4^- and N_3^- (Pauling radii).

satisfying conditions, i.e., OH^- (linear), N_3^- (linear) and NO_3^- with D_{3h}-symmetry (Cotton and Wilkinson 1980).

The decrease of U_{IN} with increasing ionic radius discussed in §5 is confirmed for R_{IN} except for NO_2^-. The following sequences prevail:

$$I^- < N_3^- < Br^- < NO_3^- < Cl^- < NO_2^- < OH^- < F^- \quad \text{(for } R_{IN}\text{)},$$

$$I^- > N_3^- > NO_2^- > Br^- > NO_3^- > Cl^- > OH^- > F^-$$

(for thermochemical radii).

The values of R_{IN} for OH^-, NO_2^- and Cl^- in table 4 indicate that either the ionic radius of NO_2^- is comprised between the radii of OH^- and Cl^- and/or that the point-charge model is inadequate for this V-shaped ion (§5).

7. Calculation of the free energy change ΔG for radical-anion couples

Values of ΔG computed from (1) and the threshold energies of table 1 are listed in table 5. The values of U_{IN} of table 2 were used instead of R_{IN} and the free energies R_{OUT} were computed from (7). The free energies ΔG in table 5 show that the radicals produced by photoionization of anions in aqueous solution are generally powerful oxidizing agents. Thus, the values $\Delta G = 2{\cdot}7$ eV for $ClO_4(aq)/ClO_4^-(aq)$ and $\Delta G = 2{\cdot}6$ eV for $HCO_3(aq)/HCO_3^-(aq)$ may be compared with $\Delta G = 2{\cdot}55$ eV for $Cl^-(aq)/Cl(aq)$. The value $\Delta G = 2{\cdot}2$ eV for $NO_3^-(aq)/NO_3(aq)$ agrees very well with the value $2{\cdot}3 \pm 0{\cdot}1$ eV given by Berdnikov and Bazhin (1970). This is to be expected in view of the agreement between R_{IN} and U_{IN} for NO_3^- in table 4.

Conclusion

The solvation model of inner-sphere nuclear reorganization yields results in

electrochemistry, namely ionic solvation, could be transposed to the study of nuclear reorganization in the photoionization in solution. Furthermore, application of the solvation model to photoionization allows the calculation of the free energy change ΔG characterizing the energetics of anion/radical couples in aqueous solution.

Acknowledgement

This work was supported by the Office of Naval Research.

References

Akitt J W 1980 *J. Chem. Soc. Faraday I* **76** 2289
Berdnikov V M and Bazhin N M 1970 *Russ. J. Phys. Chem. (Engl. Transl.)* **44** 398
Brodsky A M 1980 *J. Phys. Chem.* **84** 1886
Brodsky A M and Tsarevsky A V 1976 *J. Chem. Soc. Faraday Trans. 2* **72** 1781
Cotton F A and Wilkinson G 1980 *Advanced inorganic chemistry* (New York: Wiley Interscience) pp. 421, 423, 889
Delahay P 1982 *Acc. Chem. Res.* **15** 40
Delahay P 1984 in *Electron spectroscopy: theory, techniques and applications* (eds) C R Brundle and A D Baker (London: Academic Press) p. 123ff
Delahay P and Dziedzic A 1984a *J. Chem. Phys.* **80** 5381
Delahay P and Dziedzic A 1984b *J. Chem. Phys.* **80** 5293
Delahay P and Dziedzic A 1986a *Chem. Phys. Lett.* **128** 372
Delahay P and Dziedzic A 1986b *J. Chem. Phys.* **84** 936
Delahay P and von Burg K 1981 *Chem. Phys. Lett.* **83** 250
Friedman H L and Krishnan C V 1973 in *Water* (ed.) F Franks (New York: Plenum Press) vol. 3, p. 1ff
George P and Griffith J S 1959 in *The enzymes* (eds) P D Boyer, H Lardy and K Myrback (New York: Academic Press) p. 347ff
Gurevich Yu Ya, Pleskov Yu V and Rotenberg Z A 1980 *Photoelectrochemistry* (transl.) H S Wroblowa (New York: Consultants Bureau) p. 91
Halliwell H F and Nyburg S C 1963 *Trans. Faraday Soc.* **59** 1126
Jackson R L, Pellerite M J and Brauman J I 1981 *J. Am. Chem. Soc.* **103** 1802
Jenkins H D B and Thakur K P 1979 *J. Chem. Educ.* **56** 576
Marcus R A 1956a *J. Chem. Phys.* **24** 966
Marcus R A 1956b *J. Chem. Phys.* **24** 979
Marcus Y 1977 *Introduction to liquid state chemistry* (New York: Wiley) p. 250ff
Morf W E and Simon W 1971 *Helv. Chim. Acta* **54** 794
Morris D F C 1958 *J. Inorg. Nucl. Chem.* **6** 295
Padova J 1964 *J. Chem. Phys.* **40** 691
von Burg K and Delahay P 1981 *Chem. Phys. Lett.* **78** 287
Warnek P 1969 *Chem. Phys. Lett.* **3** 532

Proton and hydrogen transfer reactions in solution[§]

P P SCHMIDT
Department of Chemistry, Oakland University, Rochester, Michigan 48063, USA

Abstract. Proton transfer is involved in many chemical reactions, including reactions of electrochemical interest. In this paper, an analysis is presented in which individual bond potential energy functions which operate between the migrating proton (or hydrogen atom) and the remainder of the molecular framework are used in the account of the rate of transfer. This work builds upon and extends an analysis which was introduced to account for the inversion of ammonia in terms of individual, discrete intramolecular atomic interactions. The role of the environment in the transfer is discussed in terms of Metropolis/Monte Carlo methods. Algorithms for the determination of the transition state are considered: in particular, saddle point methods. Techniques for handling the determination of the saddle point when the migrating species is represented as a quantum mechanical wave-packet are discussed in addition to the more familiar methods based on the direct differentiation of the potential energy function for the reactive system.

Keywords. Proton transfer; individual bond potential energy functions; intramolecular atomic interactions; Metropolis/Monte Carlo methods; saddle point methods.

1. Introduction

The role of the proton in electrochemistry is nearly as celebrated as that of the electron (Bell 1959, 1975). It has certainly proved to be as worthy a subject of study, and indeed, a worthy adversary, eluding many efforts to characterize it unambiguously and to understand its reactions; the age-old example of the hydrogen evolution reaction springs readily to mind (Conway 1965; Frumkin 1961, 1963; Krishtalik 1970). In view of the simplicity of the atomic electronic structure, and in view of the smallness of mass, one does not easily relinquish the notion that there ought to be some relatively straightforward, clear physical interpretation of the various processes which involve this particle. Moreover, the behaviour of the proton is certain to manifest the quantum mechanical limit. Therefore, it should be possible to formulate a theory which spans all limits. It is clear that the simple proton and the hydrogen atom still have many secrets.

In this paper, an analysis of the proton/hydrogen transfer is explored in which discrete bond potential energy functions are used to build the interaction between the migrating species and its environment. The use of a relatively new, but straightforward symmetry-adapted form of the Taylor series allows one to expand the interactions between hydrogen and its surroundings (McKinley and Schmidt 1982, 1984). It is possible to carry out calculations of the tunnel-coefficients which can be associated with the transfer. Finally, one can include the interaction between the migrating proton and the environment in such a manner as to be able in principle to make accurate predictions of the activation energy for the process.

[§]Dedicated to Professor K S G Doss on his eightieth birthday.

The following topics are considered. To begin, the transition state theory of the reaction is discussed. The characterization of the solute and solvent and their contributions to the expression for the rate constant is examined. The application of Metropolis/Monte Carlo methods (Metropolis *et al* 1953) to the evaluation of the specific expression for the rate constant in the transition state theory is described. The diabatic and adiabatic limits for individual configurations of the ensemble of states are established. Techniques for determining the transition state are described and tests for adiabaticity, or the lack of it, are established. Particular attention is paid to the problem of determining the transition state when the migrating species exhibits behaviour which can only be described by the use of quantum mechanical methods. The role of local molecular vibrations is examined and included in the Monte Carlo average through the use of techniques for evaluating Franck-Condon integrals which were considered by Siebrand (1967, 1971) and Fischer (1970). Finally, the separate analyses are incorporated into a computational theory of the transition state.

2. Background

Proton transfer has been studied almost exclusively with the use model potential energy functions which represent the system as a pair of square or harmonic oscillator wells in a one-dimensional representation. The analyses based on the use of these potentials can emphasize the tunnel transfer, which certainly is important (Bell 1975). Nevertheless, activation and transfer of the proton across the barrier, in the manner of the Born–Oppenheimer and Condon approximations, is possible (Marcus 1968; Babamov and Marcus 1981; Babamov *et al* 1983; Dogonadze *et al* 1967, 1968; Levich *et al* 1970). Both adiabatic and diabatic transfers are possible (Bell 1975). For transfers in the diabatic limit, there has been considerable effort on the part of the Russian school (Dogonadze *et al* 1967, 1968; Levich *et al* 1970) to combine electronic overlap/exchange factors with the transfer of the proton (or hydrogenic species). It cannot be said at this point that one view (diabatic) or another (adiabatic, with predominant atom transfer character) commands an exclusive or even major representation of the mechanism of transfer. Until recently, a paucity of methods to handle the collection of discrete interactions which operate within the reactive system forced one to rely heavily on arbitrary model potential energy functions for the collective effects of the environment, the dielectric continuum (see, in particular, the work of the Russian school; Dogonadze *et al* 1967, 1968; Levich *et al* 1970 and later contributions). Moreover, the possibility of diabatic transfer without the specific and necessary use of the electronic terms of the Hamiltonian operator of the system has only been addressed to any extent by Marcus and his colleagues (Marcus 1968; Babamov and Marcus 1981; Babamov *et al* 1983). Although much progress has been made in the characterization of the forms and strengths of interactions which *ought* to apply, many conclusions rest upon an amount of heuristic justification without the benefit of solid results to back them up. This is especially true of the diabatic mechanisms which rely to some degree upon electronic overlap to account for the transfer. Finally, an absence of any truly useful form of handling the pair-potentials which

formalism in order to attempt to convolute the intramolecular vibrations into the analysis. In view of these limitations, therefore, it is not at all surprising that there are many inconclusive results.

My colleagues and I (Schmidt *et al* 1980; McKinley and Schmidt 1982, 1984) recently introduced a symmetry-adapted form of the Taylor series which makes it possible to consider molecular vibrations in terms of the individual contributions of atomic motions to high orders in the expansion. The expansion has been used in a quantum mechanical study of the inversion of the ammonia molecule (Schmidt and Chang 1986). The results which were obtained with the use of Morse potentials for the N–H bonds agreed well with experiment; one- and two-centre forms of expansion were used, and in both cases the agreement was equally good. The two-centre form of treatment is particularly well-suited to the investigation of the tunnel-factors for the proton/hydrogen transfer reaction. Nevertheless, both the one- and two-centre analyses find use here as well. In addition, it is possible to bring a natural and simple account of the environment into the analysis. This form of handling the potential energy functions has been applied to the problem of the vibrations of lithium in solution (Chang *et al* 1985, 1986).

The type of transformation to be modelled is illustrated reasonably well by the keto-enol transformation:

For an isolated molecule, it is possible to carry out a variety of quantum chemical computations in order to determine the potential energy surface for the intramolecular atomic deformations. The assumption is made that there is a set of atom-pair, bond potential energy functions which accounts for interactions of the migrating species (proton or hydrogen atom) in the initial, transition, and final states.

The process of determining the rate constant for the transformation is the following. First, the system, in the gas, liquid or solid phases, is equilibrated with its surroundings by the use of Metropolis/Monte Carlo techniques. Optimum (energy-minimum) configurations are determined for the separate initial and final states. Along a straight-line trajectory which connects these initial and final configurations, one begins to search for a saddle-point which is the transition state. As is discussed later, the configurations of the transition state are then tested to see if they have been attained via an adiabatic transition or not. If the test is negative, then it is necessary to determine the nearest optimum (energy-minimum) precursor state from which tunnelling can take place. The tunnel-factors are determined and the contributions to the overall rate constant are established.

The activation energy is determined as the difference between the average value of the energy of the transition state less the average value of the energy of the initial state. An average value of the pre-exponential frequency/tunnel factor is also determined. The overall value of the rate constant is the assembly of these averages

3. The transition state theory and Metropolis sampling

It has been argued elsewhere (Schmidt 1984a,b, 1985, 1986) that it is possible to calculate rate constants which are associated with atom, ion, and molecular group transfer reactions with the use of the Metropolis/Monte Carlo methods (Metropolis *et al* 1953). Configurations of limited numbers of solute and solvent are allowed to adjust according to the values assigned to coordinates via a pseudo-random number generation routine. The total energy of each randomly generated configuration is determined. Each newly generated energy is compared, in turn, with the energy of the preceding acceptable configuration. If the new energy is less than the old, the energy and associated configuration are retained and the values of any variables associated with the configuration so generated are included in the average. If the energy is greater than the preceding energy, then a Boltzmann factor in the difference is determined. If this factor is a number which is larger than another independently generated random number, the configuration and associated energy are retained. If the test fails, then the preceding configuration is retained and the values of all variables which are associated with it are included again in the averages. In this manner, a Markoff chain is built. The configurations of the limited system – which is constructed in such a way as to minimize the effects of boundaries – model elements of the ensemble of states which build a canonical ensemble.

The Metropolis/Monte Carlo method of calculating the statistical mechanical average is an optimization routine which seeks a minimum by seeking a minimum *energy*. The transition state of a reaction is defined to be a *saddle-point* (McIver and Komornicki 1972; Poppinger 1975; Bell *et al* 1981, 1984; Simons *et al* 1983; Banerjee *et al* 1985). Thus, there appears an immediate difficulty in applying the Monte Carlo method to the determination of the rate constant: the determination of the rate constant requires, as is shown shortly, the calculation of average quantities which are associated with the non-stationary transition state. It is necessary, therefore, to look for new methods which allow one to retain configurations which represent the transition state so that averages of the values of variables appropriate to this state can be assembled. This problem has been discussed in several exploratory efforts (Schmidt 1984a,b, 1985, 1986). It is pursued further in this paper; in particular, saddle-point optimizations which are under development to determine the transition state of an atom transfer reaction within the framework of some of the familiar quantum chemical routines (*cf* Bell *et al* 1981; Bell and Crighton 1984; Simons *et al* 1983; Banerjee *et al* 1984) will be considered. However, in the interest of maintaining a certain amount of initial simplicity, lest the analysis should lead us early into obscuring the physical interpretation, a simple approach, suggested in part by the work of Sinclair and Fletcher (1974), is specifically considered.

The key to unlocking part of the mystery of the transition state is the Born–Oppenheimer approximation which is applied here to the separation of the environment from the solute. In terms of strengths of interactions, the Born–Oppenheimer approximation is clearly an adequate means of separating subsystems. Indeed, if there are locally strong interactions between solute and solvent (or

The Metropolis/Monte Carlo method generates individual elements of the set of configurations which, on average, eventually make up the ensemble. The following observation has been made concerning the attainment of the reactive transition state in any individual configuration of the ensemble (Schmidt 1985, 1986).

The transition state is defined to be a saddle-point in the energy-coordinate space of the whole system. The transition state is normally identified for systems of atomic species by requiring that the eigenvalues of the matrix of second derivatives of the energy with respect to the coordinates have one and only one element which is negative definite. All remaining eigenvalues must be positive definite. If there are particles, protons or electrons, for example, which behave as quantum mechanical particles in the transition state, it is not possible simply to apply the same types of search methods to determine the saddle-point/transition state. Particularly for the electron, there is no interior hard core which leads to the usual forms of repulsions common in most atomic species; such atomic species can usually be modelled reasonably well by Lennard–Jones or Morse potential functions. For these quantum mechanical particles, therefore, it is necessary to investigate other means of determining the location of the transition state. The energy criterion still applies. However, for the distribution of matter – electronic or atomic – it is the location of the centre-of-mass which migrates and it is the location of the centre-of-mass which occupies a position in the transition state. The representation of the transfer-species as a *wave packet* is satisfactory in this instance. This point is taken up again shortly.

At this point, two possibilities arise in with reference to the eigenvector which is associated with the one and only one negative definite eigenvalue of the matrix of force constants (Schmidt 1984a,b, 1985, 1986). The first possibility is that the system, although *globally unstable*, is *locally* mechanically stable in the motions of the transfer-species when that species is located in the configuration of the transition state. Global instability in this instance must therefore be associated with an unstable configuration of the environment. In particular, because the transfer-species occupies a mechanically stable position locally, it is inferred that the migrating species has been carried along from the initial to the transition state via the fluctuation of the environment. This situation has been called an *adiabatic* transfer. It is possible to derive an expression for the rate constant under the assumption that each transfer in the ensemble of transition state configurations occurs by means of an adiabatic mechanism.

On the other hand, it is possible that the eigenvector which is associated with the single negative definite eigenvalue describes a principal axis motion for the transfer species which is *intrinsically* unstable locally. The configuration of the environment can therefore amount to a mechanically equilibrated response to this locally unstable configuration.. However, because the transfer-species cannot occupy a position of local mechanical equilibrium in the transition state, it must transfer from some transient and locally stationary *precursor* state near to the transition state via a tunnel mechanism to a final transient and locally stationary postcursor state which resembles more the thermodynamic final state than the initial state. Given that it is possible to establish the configurations of the pre and postcursor states, which is indeed possible, it is then necessary to determine the

tunnel-transfer rate constant. At this point, one notes that it is also possible to establish a value of the rate constant for the case that every transfer occurs via a diabatic tunnel-transfer.

Each configuration of the transition state, which is generated by some suitable means consistent with the Metropolis/Monte Carlo methods of sampling, is attained either by an adiabatic transfer or requires a tunnel-transfer through the residual barrier in order to complete the transfer to the final state. There are, it is clear, only *two* choices possible for any individual configuration. As is noted shortly, much of the form of the rate constant in the adiabatic and diabatic limits is the same. The two limiting forms differ mainly in the pre-exponential factor which accounts for the tunnelling, or lack of it. Thus, with specific reference to Monte Carlo methods of simulation, it is possible to consider the average value of the pre-exponential quantity as a sum of tunnel-transfer probabilities (Schmidt 1986): if the transfer occur via an adiabatic path in an individual configuration, the tunnel-factor is unity; if the transfer occurs via a diabatic tunnel-transfer, then the tunnel-factor is the quantity which is calculated in the appropriate manner. As a result, it is possible to simulate a transfer which, in principle, accurately reflects the degree of adiabaticity of the transfer.

An ensemble of transfers which take place in the adiabatic limit yields an expression for the rate constant which is the following (Schmidt 1985, 1986):

$$k_a = \frac{1}{(2\pi m^{1/2})} \frac{|A|_{3n}^{1/2}}{|A^+|_{3n-1}^{1/2}} \exp\{-\beta(V^+ - V_0)\}. \tag{1}$$

In this expression, V^+ is the complete system potential energy function which has been evaluated with the set of optimal coordinates of the transition state. The quantity V_0 is the potential energy of the system in its initial state. The determinant of the force constant matrix is given by $|A|$; in the transition state, for which the eigenvalue associated with the principal transfer axis is negative, the determinant of the force constant matrix is formed by deleting the normal mode which is associated with the negative eigenvalue: viz. $|A^+|_{3n-1}$. The mass which is associated with the transfer-species is m. Finally, $\beta = 1/k_B T$ where k_B is the Boltzmann constant.

For a system in which all of the transfers take place via a diabatic path, tunnelling must be accounted for. A relatively simple form of tunnel-transfer, only along the transfer-axis, yields the following form of rate constant (Schmidt 1984a,b, 1985)

$$k_d = \frac{(2\pi\beta)^{1/2}}{\hbar} \frac{|A|_{3n}^{1/2}}{|A^+|_{3n-1}^{1/2}} \frac{|L_{i\gamma,j\delta}|^2}{|\Delta F|} \exp\{-\beta(V^+ - V_0)\}. \tag{2}$$

The $|A|$-quantities are (assumed to be) the same as before and the potential energies are found in the same manner as for the adiabatic transfer. The quantity $L_{i\gamma,j\delta}$ is the matrix element which couples the initial and final states. The general form of this expression has been discussed previously, and will be taken up again later in this paper. The quantity $|\Delta F|$ is the absolute value of the difference of slopes of the intersecting, parabolic mappings of the potential energy functions for the initial and final states. The origin of this term also has a [illegible]

$$k = \frac{\langle \tau \rangle}{2\pi m^{1/2}} \frac{|A|_{3n}^{1/2}}{|A^+|_{3n-1}^{1/2}} \exp\{-\beta(V^+ - V_0)\}. \tag{3}$$

The average value of the tunnel-factor, $\langle \tau \rangle$, is defined as

$$\langle \tau \rangle = \frac{1}{N} \sum_{n=0}^{N} \tau_n, \tag{4}$$

with

$$\tau_n = 1, \text{ adiabatic transfer limit} \tag{5}$$

$$\tau_n = \frac{(2\pi)^{3/2} (m\beta)^{1/2}}{\hbar} \frac{|L_{i\gamma,j}\delta|^2}{|\Delta F|}, \text{ diabatic transfer limit.}$$

It can be seen that, within the limits of validity of the assumption of similarity between diabatic and adiabatic transfers, a particular transfer can be simulated via a Monte Carlo calculation to yield an accurate value of the transfer tunnel-factor. Thus, it is possible to realize limits of transfer which do not necessarily fall only into the adiabatic or diabatic limits.

The following issues remain to be resolved: (1) the means of generating the transition state; (2) the test for mechanical stability of the transfer species in the transition state; and, (3) the evaluation of the tunnel-factors.

4. Mechanics of the transition state

As it is usually carried out, a Monte Carlo calculation is an energy-minimum optimization. The problem of determining the transition state by means of any kind of saddle-point calculation is not trivial. There are, of course, well-established means for determining saddle points. In particular, the best-known require the search for configurations which assure one and only one negative eigenvalue of the determinant of the force constants for the system. Methods based on this requirement are not particularly fast, especially when used within very large quantum chemical programmes (Bell and Crighton 1984). The task of applying the notion to the Metropolis/Monte Carlo scheme of sampling becomes almost daunting. Nevertheless, there are features of some of the more efficient routines which seem to apply to the Monte Carlo method of optimization; in particular, the method of Banerjee *et al* (1985) and Simons *et al* (1983) seems to be well suited. This method is discussed here.

To begin, it is necessary to specify the mechanics of the system more precisely. Because of the instability of the transition state in the diabatic limit, it cannot be specified completely without taking quantum mechanical effects into consideration.

The distinction between solute and solvent is not a firm one. There is no necessarily sharp boundary between the two entities. If, for example, there are strong local interactions between the *actual* reactive species and the solvent, then it is possible, as stated above, to consider the aggregate to be the reactive solute. There generally occurs a region about a reactive system at which the solvent-solvent interactions take on the predominant character they have in the absence of solute (Schmidt 1984a). This region, therefore, separates the effective, operational solute from the remainder of the system, the solvent.

The complete Hamiltonian operator for the system (the collection of reactive solute and surrounding solvent) consists of a sum of terms,

$$H = T+V, \tag{6}$$

in which T represents the collections of kinetic energy operators and V the complete sum of pairwise interactions. It is possible, of course, to separate from the sum those terms which belong specifically to the reactive transfer species within the solute. Define the Hamiltonian operator for the transfer-species as

$$H_t = T_t+V_t. \tag{7}$$

The difference

$$H_{\text{env}} = H-H_t, \tag{8}$$

represents the 'environmental' Hamiltonian operator. This quantity, in fact, contains all interactions with the surroundings – intramolecular vibrations as well as weaker solvent/transfer-species interactions.

The 'channel' decomposition of the transfer Hamiltonian, H_t, is carried out as follows. With reference to initial and final states, which are labelled 'a' and 'b', let

$$\begin{aligned} H_t &= H_a+V_t-V_a \\ &= H_b+V_t-V_b, \end{aligned} \tag{9}$$

and

$$H_{a(b)} = T_t+V_{a(b)}, \tag{9'}$$

in which H_a and H_b are model Hamiltonian operators which describe, to a reasonable approximation, the behaviour of the transfer species in the neighbourhood of the stationary state configurations 'a' and 'b'. If there exist basis sets of functions which are solutions to the local, soluble eigenvalue problems

$$\begin{aligned} H_a\phi_a &= \varepsilon_a\phi_a, \\ H_b\phi_b &= \varepsilon_b\phi_b, \end{aligned} \tag{10}$$

then it is possible to construct state functions as linear combinations of these functions:

$$\Psi = \Sigma_i X_i\phi_i. \tag{11}$$

This state function is a solution to the general problem

The expansion coefficients X_i become the intramolecular/environmental
tional wavefunctions in the usual form of the Born–Oppenheimer–H
(Holstein 1959) (abbreviated as BOH in the following paragraphs) analy

By means of the use of the BOH form of adiabatic separation, one finds t
matrix elements $L_{i\gamma,j\delta}$ are given by

$$L_{i\gamma,j\delta} = \sum_{k,\varepsilon} S^{-1}_{i\gamma,k\varepsilon}\, V^{j}_{k\varepsilon,j\delta},$$

in which $S^{-1}_{i\gamma,j\delta}$ is an element of the inverse of the overlap matrix, and (S
1984a,b, 1985, 1986)

$$V^{j}_{k\varepsilon,j\delta} = \langle k\varepsilon | V - V_j | i\delta \rangle,$$

in which V_j is the model system potential energy function [cf. (10), $j = a$,
addition, there are elements which involve the kinetic energy operators; as it
yet clear how important these quantities are, attention focuses only on the
elements of the potential energy operator.

The central, and most important, issue at this point has to do with the role
analysis in the determination of the transition state.

If the transition state is adiabatically attained, then, by implication, the tr
species *adiabatically* follows the fluctuations of the environment which bring
the transformation. The strong adiabatic limit of the BOH form of sepa
applies in this case. The interactions are strong, and, more important, there
tunnelling involved. Therefore, the activation energy can be determin
the difference in the energy of the optimized initial and transition states
pre-exponential factor depends simply upon the ratio of the square roots
determinants of the matrices of the force constants, as indicated by (1)

The BOH analysis yields terms which act as perturbative couplings and th
account for the reactive transition of the system in the diabatic limit. Trans
this type take place via a tunnel mechanism. It is still the case, however, tha
are precursor and postcursor states in which the transfer-species executes
mechanical motions. The system, as a whole, however, does not need to b
state of thermodynamic equilibrium while the pre and postcursor stat
occupied. It is important to note that the Condon approximation is satisfied
process of transfer by a tunnel step. This means simply that the environm
coupled to the reactive subsystem weakly enough to allow the vibrational o
factors to separate exactly in the same manner as occurs for the electron tr
system. On the other hand, it is likely that important quantum mechanical
operate within the local solute intramolecular modes; these effects need
considered in the process of activation. This is an issue which is not pursued f
here, although it must eventually be reckoned with (Marcus 1984).

4.2 *Quantum mechanical interactions in the transition state*

As long as the electron is not involved, as a first approximation for the tran
the diabatic limit one can determine a transition state in the classical mech

particle must occupy some nearby precursor state within which the particle is locally and mechanically stable. From this configuration, the particle *tunnels* to the final postcursor state. Nevertheless, the transition state is still defined with the particle located in a genuine saddle-point of the combined classical solvent and quantal solute (transfer-species) system. It is necessary, therefore, to specify a saddle-point calculation which also takes into account the delocalized nature of the transfer-species in the transition state. This requirement forces one to bring the quantum mechanical character of the description of the system into a consistent form of saddle-point optimization involving the remaining particles which act in the classical limit.

Before it is possible to consider a general method of finding the saddle-point which represents the transition state, it is necessary to consider the quantum mechanical limit for the motion of the light protonic or hydrogenic species. This analysis also provides the necessary formulae to evaluate the matrix elements which are associated with the tunnel-transition in the diabatic limit.

The process which is considered is that of the migration of a proton or hydrogen atom from one site to another within a larger molecular aggregate. Although it is not strictly accurate to do so, for the purpose of simplifying the analysis to the point where reasonable, practical calculations can be carried out, the environment is regarded as fixed during the actual quantal limit transfer of the proton from one site to another – provided the transfer takes place as a tunnel-transition. It is therefore possible to consider the analysis of the motion of the proton in one dimension. The single dimension is that dimension which connects the initial and final potential energy wells within which the proton can exist. In order to carry out the analysis, it is necessary to be able to manipulate the interatomic, intermolecular potential energy functions which describe the interaction between the migrating protonic species and the environment.

As was indicated in the last section, the Hamiltonian operator for the transfer process is given by (7). The potential energy V_t in (7) is expressed as a sum of terms which account for the interaction between the proton, labelled 'p', and the remaining species 'i' in solution:

$$V_t = \sum_i V(r_p - r_i). \tag{15}$$

The problem now is to translate this into an expression which reflects the projection of the interaction along the transfer-axis, hereafter called the z-axis. In the following, it is assumed that all interactions are scalar.

Given a scalar potential energy which is expressed functionally as

$$V(r) = Y_{00}(\hat{r})[(4\pi)^{1/2} v_0(r)] \tag{16}$$

in which $Y_{l,m}(\hat{r})$ is the spherical harmonic function and $\hat{r}$ is the unit vector in r-space, it is possible to express an expansion in a symmetry-adapted Taylor series as by McKinley and Schmidt (1982),

$$G(\mathbf{r}+\mathbf{R}) = (4\pi)^{3/2} \sum_{n=0}^{\infty} (r^n/n!) \sum_{l,m} \frac{A_{nl}}{2l+1} Y^*_{lm}(\hat{r}) Y_{lm}(\hat{R}) I_{nl}(R). \tag{17}$$

The coefficient $A_{n,l}$ is

$$A_{nl} = \frac{n!(2l+1)}{(n-l)!!(n+l-1)!!}, \quad n \geq l \text{ and } n-l = \text{even}, \tag{18}$$

$$= 0, \qquad n < l \text{ and } n-l = \text{odd}$$

and $I_{n,l}(R)$ is

$$I_{n,l}(R) = \frac{(-1)^{n+l}}{\sqrt{4\pi}} R^l \left(\frac{\mathrm{d}}{R\mathrm{d}R}\right)^l \frac{1}{R} \left(\frac{\mathrm{d}}{\mathrm{d}R}\right)^{n-l} RV_0(R). \tag{19}$$

The projection of any source onto the z-axis reduces (17) to (Schmidt and Chang 1986):

$$V(z) = \sum_{n=0}^{\infty} z^n C_n(R), \tag{20}$$

where the expansion coefficient $C_n(R)$ is

$$C_n(R) = \frac{1}{n!} \sum_{l=0}^{n} \sum_{i} An_l P_l(\cos\,\theta_{R_i}) I_{nl}(R_i), \tag{21}$$

in which $P_l(\cos\,\theta)$ is the Legendre polynomial and θ is the angle between R and the z-axis.

The form of (20) for the one-dimensional potential energy operator projected along the z-axis is used in the quantum mechanical analysis of the motion of the migrating proton or hydrogen atom.

The specific form of the kinetic energy operator is

$$T_r = -\frac{\hbar^2}{2m} \frac{\mathrm{d}^2}{\mathrm{d}z^2}. \tag{22}$$

The expansion, (21), can be used both for the one- and two-centre analyses. The basis functions for the expansion of the state function are the solutions to the one-dimensional harmonic oscillator problem:

$$\phi_n(z) = \left(\frac{1}{2^n(\pi n!)^{1/2}}\right)^{1/2} \exp(-\tfrac{1}{2}\alpha^2 z^2) H_n(\alpha z), \tag{23}$$

in which $H_n(x)$ is the Hermite polynomial. In terms of the functions (23), the state function is

and the total energy is

$$E = \sum_{i,j} C_i C_j \langle i|H|j\rangle. \tag{25}$$

The matrix elements of the momentum operator are well known, and are given by

$$\langle i|p^2|i\rangle = \tfrac{1}{2}(2i+1), \tag{26}$$

$$\langle i|p^2|i+2\rangle = -\tfrac{1}{2}(i+1)\ (i+2). \tag{27}$$

The matrix elements of the coordinate operator can be found from the recursion relation for the oscillator functions (Schmidt and Chang 1986):

$$\langle k|q^n|m\rangle = \frac{1}{2^{1/2}}\ [(m+1)^{1/2}\langle k|q^{n-1}|m+1\rangle + (m)^{1/2}\langle k|q^{n-1}|m-1\rangle]. \tag{28}$$

The application of Ehrenfest's theorem shows that there is an optimum point of expansion for the single centre analyses, and at that point the energy will satisfy similar requirements to those for the transition state involving a classical particle. This process is illustrated with the use of a model system for which symmetry dictates where the optimum should be. An analysis – in the absence of the use of any arguments of symmetry – confirms the result.

The model system consists of a ring of massive species through which the hydrogen atom (or proton) can pass either via an adiabatic or diabatic, tunnel path (cf. figure 1). The hydrogen atom interacts with the environmental masses – in this illustration – through identical Morse potentials:

$$V_M(r) = De^{a(r_0-r)}\ (e^{a(r_0-r)} - 2), \tag{29}$$

for which

$$I_{nl}(R) = De^{ar_0}[2^n e^{ar_0} 2(2aR\ k_{l-1}(2aR) - (n-l)k_l(2aR)) - 2(aR\ k_{l-1}(aR) - (n-l)k_l(aR))], \tag{30}$$

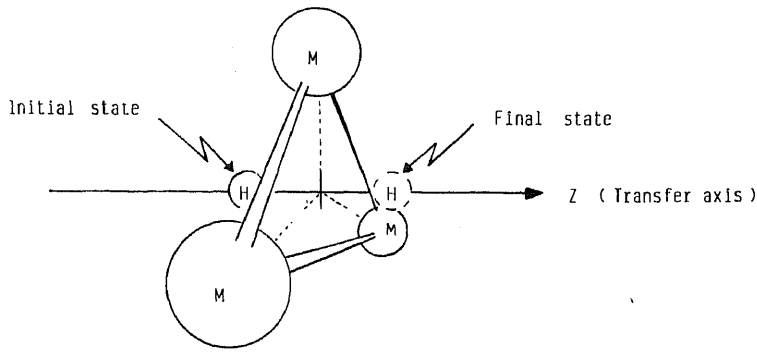

Figure 1. The arrangement of heavy masses in a 'ring' configuration through which the single, mobile proton (or hydrogen atom) migrates. In the classical limit, if the 'radius of

and $k_n(x)$ is the modified spherical Bessel function of the third kind (Arfken 1970).

The optimum point of expansion is the centre of the ring. Figure 2 shows a series of plots of the energy of the quantum mechanical component of the interaction energy; i.e., $\langle\Psi_0|V - V_0|\Psi_0\rangle$ using the Taylor series expansion, and Ψ_0 is the ground state function. The individual plots are associated with differing values of the 'ring radius'. The centre of the wavepacket is expanded at points along the C_3-axis which passes through the centre of the ring. Thus, each point on a particular curve is an energy which is associated with the ground state wavepacket which has been expanded at a point on the C_3 transfer-axis. As noted for classical systems (McKinley and Schmidt 1982), when the radius of the ring is less than a critical value (a value dictated by the choice of pair-potential used), the centre of the ring is mechanically unstable. The figures illustrate that the same holds for the quantum mechanical wavepacket. Figures 3, 4 and 5 illustrate the behaviour of the expectation values of the operators x and x^2, and the variance $\langle 0|x^2|0\rangle - \langle 0|x|0\rangle^2$; x and x^2 are the first two *operators* which emerge in the Taylor series expansion. It appears that for a quantum mechanical wavepacket, it is possible to find a locally stable configuration for values of the radius of the ring which would yield instabilities in the classical limit. In figure 5, the remarkably sharp, narrow peaks for the variance about the point of expansion in the centre of the ring suggests that this quantity might be useful in the determination of the transition state of a

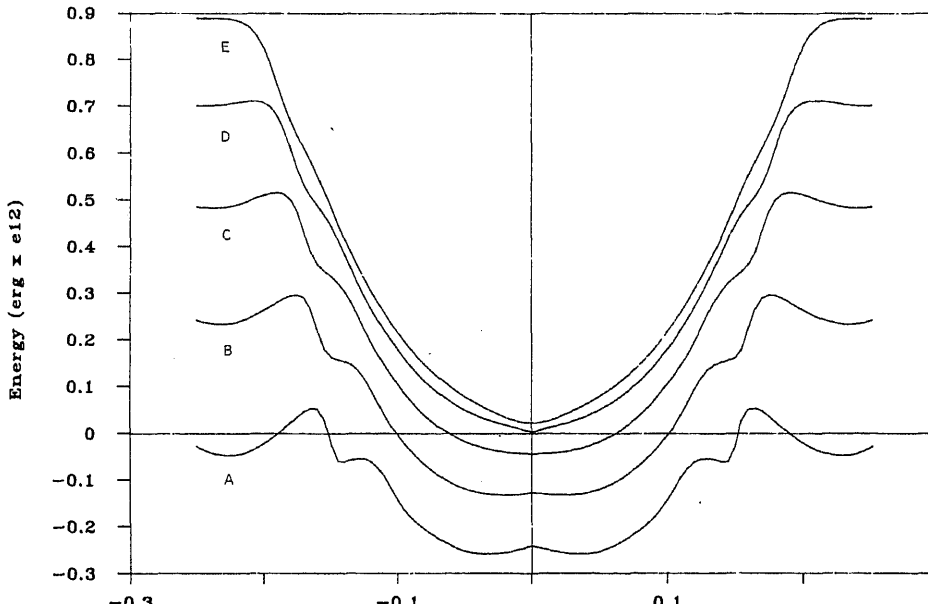

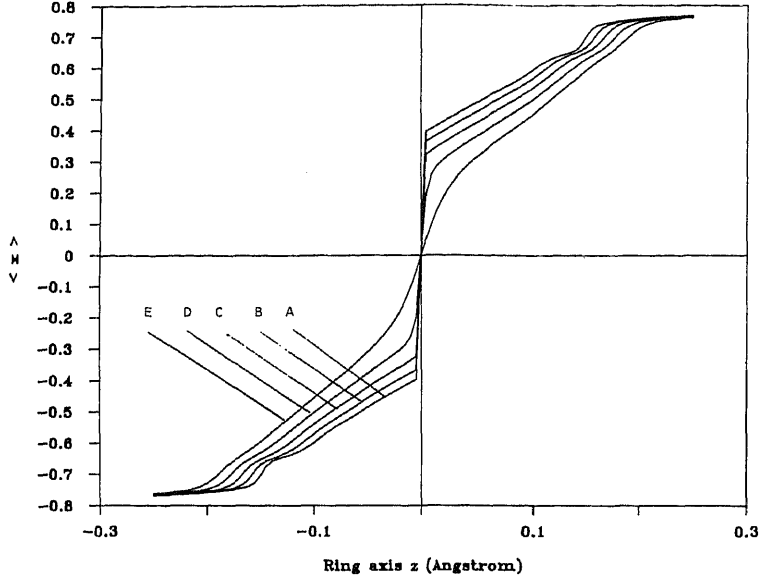

Figure 3. This figure is a plot of the ground state expectation value of the operator X, $\langle X \rangle = \langle 0|X|0 \rangle$, where x is the displacement away from the point of expansion along the C_3-axis which passes through the centre of the ring. Note the strong discontinuity at the origin at the centre of the ring. The strongest discontinuity holds for the wavepacket in the presence of the ring with the smallest 'radius'. In this calculation, the centre of the wavepacket was moved along the C_3-axis as in the case of the evaluation of the energy. The plots are for increments of the ring-radius in units of 0·01 A from 0·95 A.

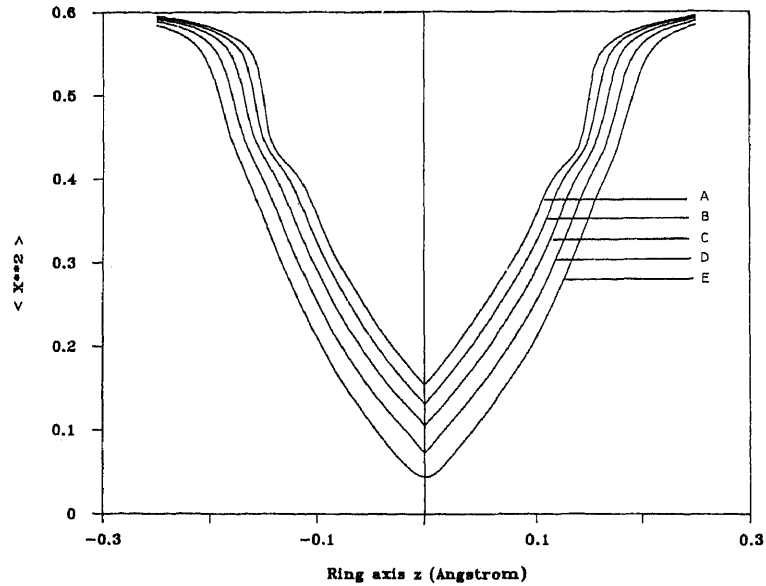

Figure 4. This figure illustrates the plots of the ground state expectation value of the operator X^2, $\langle X^2 \rangle = \langle 0|X^2|0 \rangle$ in terms of the wavepacket as the centre of the wavepacket is moved along the C_3-axis. The plots are for increments of the ring-radius in units of

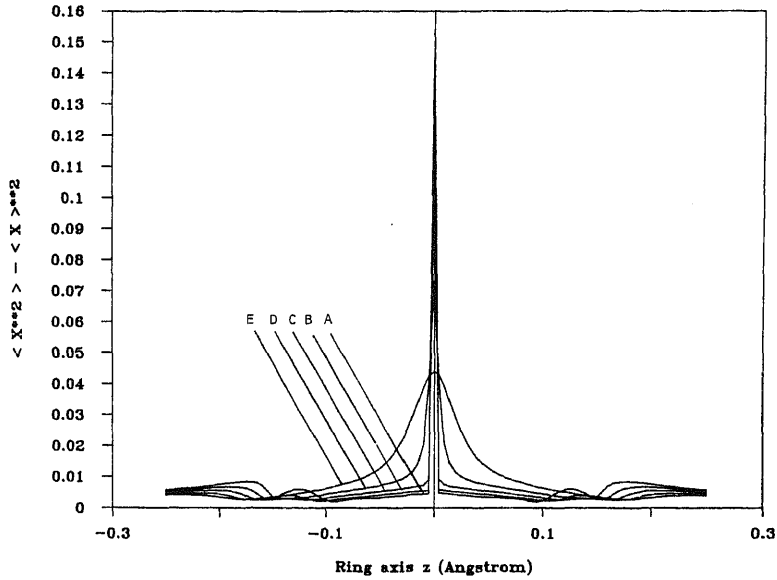

Figure 5. This figure combines the last two as the variance of the expectation value in the ground state: var = $\langle 0|X^2|0\rangle - \langle 0|X|0\rangle^2$. The plots are for increments of the ring-radius in units of 0·01 A from 0·95 A.

reaction which involves a quantum mechanical particle, viz., the electron or proton.

The conclusion is simply that it is possible to handle a quantum mechanical matter density in the same manner as is done in the classical limit. The quantal-limit matter distribution is simply moved to its optimum location by moving the location of the centre of the wavepacket. This is accomplished with the use of Ehrenfest's theorem which states that $d\langle V\rangle/dx = \langle I|dV/dx|I\rangle$ for a particular given state $|I\rangle$.

4.3 *Matrix elements of the perturbation driving the transfer*

The matrix elements $L_{i\gamma,j\delta}$ are now evaluated in a two-centre representation. The terms arise in a manner which is similar to that of the electron transfer theory (Kestner *et al* 1974, Schmidt 1984a). The development in the succeeding paragraphs follows in part that of Schmidt (1984a) for the atom transfer problem and Schmidt and Chang (1986) for the inversion of ammonia.

The two-centre analysis of the transfer uses initial and final state configurations in which the proton is located first in one part of the system and then in another. An accessible transition state exists on a potential barrier which separates the initial and final states. It is useful initially to consider a straight-line trajectory for the migration. Straightline trajectories may occur in some instances because proton transfer is sensitive to the size of the overlap factors. If the distance is too great (even 1 Å is a large distance), the tunnel-transfer will be nearly vanishing simply because the overlap integrals nearly vanish. On the other hand, it is also likely to be the case in many instances that the vector from the initial state to the transition

The analysis for the straightline trajectory is the following. Assume a transfer of the proton from an initial ground vibrational state to a final ground vibrational state. This assumption complies with the Born–Oppenheimer separation and implies that the separation of local vibrational states from the collective states of the environment can be made. In essence, this has been proved to be the case for the inversion of ammonia; that is, the tunnelling associated with the inversion doubling of the ν_2 normal mode is assumed to be separate from the remaining normal modes (Schmidt and Chang 1986).

The ground state functions have the form:

$$\phi_0(x_a) = {}^4(\alpha/\pi)^{1/2} \exp(-\tfrac{1}{2}\alpha x_a^2). \tag{23a}$$

Given an environment which is dissimilar on either side of the location of the transition state, the ground state functions in the initial and final states must be distinguished from one another: choose

$$\phi_0(x_b) = {}^4(\beta/\pi)^{1/2} \exp(-\tfrac{1}{2}\beta x_b^2), \tag{23b}$$

for the ground state function in the final state. The matrix element which is most important in the evaluation of the perturbation driving the tunnel-transition is $\langle a|V|b\rangle$. Unlike its counterpart in the simple elecron transfer theory, this quantity does not specifically involve the attraction between the migrating species and a potential energy operator whose focus of attraction (or repulsion) is the centre to which the species migrates. In this example of the hydrogen/proton transfer, the transfer matrix element is evaluated for the complete effect of the system on the migrating species. Thus, while in the transition state, the migrating species feels the attraction to the final state to which it is moving and the initial state from which it came. It is clear, therefore, that if the attraction to the initial state is greater than the attraction to the final state while the transfer-species is in the transition state, then the probablility for a successful transfer will be small, as it should be.

The point of expansion for the hybrid mass density $\phi(a)\phi(b)$ is the point which is located at the origin of the x-axis. This point does not necessarily correspond to the location of the saddle point of the transition state on the x-axis. If x_p is measured from the coordinate origin, then the displacements of the transfer species with respect to its two stationary state positions are

$$x_a = x_p + l_a \qquad x_b = x_p - l_b \tag{31}$$

and l_a, l_b give the locations of the initial and final states along the x-axis. The point of expansion is found in the usual manner for Gaussian functions (Shavitt 1963) to be

$$d_x = (\alpha l_a - \beta l_b)/(\alpha + \beta). \tag{32}$$

Thus, as usual, the overlap integral is

$$S_{12} = \left[\frac{2(\alpha\beta)^{1/2}}{\alpha+\beta}\right]^{1/2} \exp\left[-\frac{1}{2}\frac{\alpha\beta R^2}{\alpha+\beta}\right], \tag{33}$$

$$\langle\alpha|V|\beta\rangle = \sum_n P_n(R)\langle\alpha|x^n|\beta\rangle. \tag{34}$$

Here P_n is the quantity C_n from (21) evaluated with reference to d_x as the origin on the x-axis. The matrix element $\langle a|x^n|b\rangle$ now is found to be

$$\begin{aligned}\langle\alpha|x^n|\beta\rangle &= \frac{(\alpha\beta)^{1/2}}{\sqrt{\pi}} e^{-Q^2} \int_{-\infty}^{\infty} \mathrm{d}y (y-d)^n \exp(-\tfrac{1}{2}(\alpha+\beta)y^2) \\ &= \frac{1}{\sqrt{2}} \frac{(\alpha\beta)^{1/2}}{(\alpha+\beta)^{1/2}} e^{-Q^2} \sum_{m=0}^{n} \binom{n}{m} (-d)^{n-m} \\ &\quad \times \{1-(-1)^m\}\,(m-1)!! \frac{1}{(\alpha+\beta)^{m/2}},\end{aligned} \tag{35}$$

in which $\binom{n}{m}$ is the binomial coefficient and

$$Q = \alpha\beta R^2/(\alpha+\beta). \tag{36}$$

The remaining quantity in $L_{i\gamma,j\delta}$ is $V^j_{i\gamma,j\delta}$. As the basis functions are simple oscillator functions, it is possible simply to use the harmonic oscillator potential $\frac{1}{2}m\omega^2x^2$ to get

$$\tfrac{1}{2}m\omega^2\langle\alpha|x^2|\beta\rangle = \frac{m\omega^2}{\sqrt{2}} \frac{(\alpha\beta)^{1/2}}{(\alpha+\beta)^{3/4}} e^{-Q^2}\{1+\alpha l_a/(\alpha+\beta)\}. \tag{37}$$

At this point, it is worth noting that the potential energy function, V_t, in (7) is simply the complete potential expanded about one centre, the centre of influence of the transfer-species. The environmental Hamiltonian involves the same terms which are manipulated differently.

The general transfer does not necessarily occur along a straightline trajectory from initial through transition to final states. As a consequence, it is necessary either to make use of curvilinear coordinates or to use some other means of handling this non-direct migration. There are means available and they have evolved in the electronic LCAO-MO methods.

The saddle-point which defines the transition state can be seen to involve at least two intersecting planes: in one plane along the path which passes through the location of the transition state, the energy reaches a maximum value; in the other plane along the path which passes through the transition state, the energy is a minimum. The plane which contains the minimum (the plane of the Cantle and Pommel), defines a natural division between the initial and final states. Refer to the two states as 'left' and 'right' respectively – 'initial' and 'final' are not material at this point. The following discussion applies only to the ground states of the left and right sides. The analysis is generalized easily to handle excited states.

Two levels of calculation are now carried out. At the lower level, one constructs

basis states for the left and right hand sides of the problem. These functions describe the state of the migratory species – proton or hydrogen – in their respective equilibrium states. At the next level of treatment, the two states are combined as basis states in the tunnel transfer. The basis states for the left and right hand sides are combined in the matrix elements of the transfer.

In order to account for the possibility that the transfer to and from the dividing plane for the transition state is oblique, it is necessary to consider a point of expansion in the plane. Thus, define the following four basis functions: ϕ_{L1}, ϕ_{L2}, ϕ_{R1}, ϕ_{R2}. These functions, moreover, are locally orthonormal and assumed to be orthonormal across the L–R space (Oppenheimer 1928; Duke 1965). Let ϕ_{L1} be

$$\phi_{L1} = u_0(x_a), \tag{38}$$

where $u_0(x_a)$ is given by (23a), for example. A similar definition applies to ϕ_{R1}. The use of Gram–Schmidt orthogonalization (Morse and Feshbach 1953) gives for ϕ_{L2}

$$\phi_{L2} = \frac{1}{(1-S_{at}^2)^{1/2}} \{u_0(x_t) - S_{at} u_0(x_a)\}. \tag{39}$$

Now, let the left and right hand basis functions be given by

$$\begin{aligned} \Psi_L &= a_{L1}\phi_{L1} + a_{L2}\phi_{L2}, \\ \Psi_R &= a_{R1}\phi_{R1} + a_{R2}\phi_{R2}. \end{aligned} \tag{40}$$

In the usual manner, the variational calculation yields the energy eigenvalues

$$\varepsilon_L = \tfrac{1}{2}(H_{11} + H_{22}) \pm \tfrac{1}{2}((H_{11} - H_{22})^2 + 4H_{12}^2)^{1/2}. \tag{41}$$

Let c_{L1}^0 and c_{L2}^0 be the coefficients which are associated with the *lowest* energy eigenvalue. The *left* hand basis function for the combined left-right system is $\Psi_L^0 = c_{L1}^0 \phi_{L1} + c_{L2}^0 \phi_{L2}$. Now, construct orthonormal basis functions for the two sides. Write

$$\chi_L^0 = \psi_L^0, \tag{42}$$

and

$$\chi_R^0 = \frac{1}{(1-S_{LR}^2)^{1/2}} \{\psi_R^0 - S_{LR}\psi_L^0\}. \tag{43}$$

The overlap S_{LR} is given by

$$\begin{aligned} S_{LR} = {} & C_{L1}^0 C_{R1}^0 S_{13} + \frac{C_{L1}^0 C_{R2}^0}{(1-S_{23}^2)^{1/2}} \{S_{12} - S_{23}S_{13}\} \\ & + \frac{C_{L2}^0 C_{R1}^0}{(1-S_{12}^2)^{1/2}} (S_{23} - S_{12}S_{13}) \\ & + C_{L2}C_{R2} \end{aligned} \tag{44}$$

$$E = \tfrac{1}{2}(H_{LL}+H_{RR}) \pm \tfrac{1}{2}((H_{LL}-H_{RR})^2+4H_{LR}^2)^{1/2}. \quad (45)$$

In terms of the non-orthonormal basis set, the matrix elements expand as

$$H_{LL} = (C_{L1}^0)^2 H_{aa} \quad \frac{(C_{L2}^0)^2}{(1-S_{at}^2)} \quad (H_{tt}+S_{aa}H_{aa}-2S_{at}H_{at}), \quad (46)$$

with a similar term for H_{RR}. The cross term H_{LR} is

$$H_{LR} = \frac{1}{(1-S_{LR}^2)^{1/2}} \quad \Bigg(C_{L1}^0 C_{R1}^0 H_{ab} + \frac{C_{L1}^0 C_{R2}^0}{(1-S_{tb}^2)^{1/2}} \quad (H_{at}-S_{tb}H_{ab})$$

$$+\frac{C_{L2}^0 C_{R1}^0}{(1-S_{at}^2)^{1/2}} \quad (H_{bt}-S_{at}H_{ab}) + \frac{C_{L2}^0 C_{R2}^0}{\{(1-S_{at}^2)\,(1-S_{tb}^2)\}^{1/2}}$$

$$(H_{tt}-S_{at}H_{at}-S_{tb}H_{bt}+S_{at}S_{bt}H_{ab}) - \varepsilon_L^0 S_{LR} \Bigg). \quad (47)$$

In terms of the L/R basis set which is constructed above, the matrix elements of the perturbation which drives the tunnel-transfer $L_{i\gamma,j\delta}$ are now expressed as (13) with $V^j \equiv V - V_j$. The potential energy function V_j consists of the interactions between the transfer species and the surroundings expanded about an origin of coordinates which is located at the stationary point j; the point j lies either to the right or left of the location of the transition state. The potential energy function V is the complete potential function. In view of the manner in which the basis functions are constructed and optimized, V_j is the potential energy function of the initial state. Thus, the difference is the interaction between the transfer-species and its well in the final stationary state.

The specific forms of the matrix elements in terms of the non-orthonormal expansion set are the following. The generic form is

$$V_{S0,S'0}^j = \langle S0|V^j|S'0\rangle, \quad (48)$$

in which S and S' stand for 'side' with reference to the transition state. In particular, $V_{L0,L0}^j$ is

$$\langle \chi_L^0|V^j|\chi_L^0\rangle = (C_{L1}^0)^2 V_{a0,a0}^j + \quad \frac{(C_{L2}^0)^2}{(1-S_{at}^2)} \quad (V_{t0,t0}^j + S_{at}^2 V_{a0,a0}^j - 2S_{at}V_{a0,t0}^j), \quad (49)$$

$$\langle \chi_L^0 | V^j | \chi_R^2 \rangle = \frac{1}{(1-S_{LR}^2)^{1/2}} \left\{ C_{L1}^0 C_{R1}^0 V_{a0,b0}^j + \frac{C_{L1}^0 C_{R1}^0}{(1-S_{tb}^2)^{1/2}} \right.$$

$$(V_{a0,t0}^j - S_{tb} V_{a0,b0}^j) + \frac{C_{L2}^0 C_{R1}^0}{(1-S_{at}^2)^{1/2}} \quad (V_{b0,t0}^j - S_{at} V_{a0,b0}^j)$$

$$+ \frac{C_{L2}^0 C_{R2}^0}{((1-S_{at}^2)\,(1-S_{tb}^2))^{1/2}} \quad (V_{t0,t0}^j - S_{at} V_{a0,t0}^j - S_{bt} V_{b0,t0}^j$$

$$+ S_{at} S_{bt} V_{a0,b0}^j) - S_{LR} \left((C_{L1}^0)^2 V_{a0,a0}^j + \frac{(C_{L2}^0)^2}{(1-S_{at}^2)} \right.$$

$$\left. \left. (V_{t0,t0}^j + S_{at}^2 V_{a0,a0}^j - 2 S_{at} V_{a0,t0}^j) \right) \right\}. \tag{50}$$

In each of these general matrix elements there are several matrix elements which are evaluated in terms of the non-orthonormal basis functions $u_0(r_{(a,b,t)})$. At this point, the behaviour of these matrix elements and an assessment of their contribution to the perturbation driving the tunnel-transfer can be illustrated with the use of a relatively simple analysis. The non-orthonormal basis set consists of three zeroth-order functions of the form (23a) centred respectively at a, t, and b.

In view of the process by which the left/right basis set was constructed, and in view of the nature of the expansion of the complete potential energy function, matrix elements of the form $\langle u_0(a)|V - V_a|u_0(a)\rangle = 0$. On the other hand, matrix elements of the form $\langle u_0(a)|V - V_b|u_0(a)\rangle$ are non-vanishing. In particular, for this matrix element one finds

$$V_{b0,b0}^a = \langle u_0(b)|V_b|u_0(b)\rangle - \langle u_0(b)|V_a|u_0(b)\rangle, \tag{51}$$

where the point of expansion for V is the same as the coordinate origin for the product of functions $u_0(b)$. This integral is

$$\langle u_0(b)|V_b|u_0(b)\rangle = \sum_{n=0}^{\infty} \sum_{I=2}^{N} C_{2n}(R_{Ib}) \frac{(2n-1)!!}{2^n \alpha^n}, \tag{52}$$

and $C_{2n}(R_{Ib})$ is a function of the distance R_{Ib} between the location b and the species (solvent or solute atom) I. The second integral in (51), however, is

$$\langle u_0(b)|V_a|u_0(b)\rangle = \sum_{n=0}^{\infty} \sum_{I=2}^{N} C_n(R_{Ia}) \sum_{\substack{s=0 \\ \text{even}}}^{n} \binom{n}{s} (-L)^{n-s} \frac{(s-1)!!}{2\alpha^{s/2}}, \tag{53}$$

in which L is the distance between a and b. In the case of integrals of the form

$\langle u_0(t)|V_j|u_0(t)\rangle$ where $j = a, b$ and $u_0(t)$ is the basis function for the transfer-species centred at the location of the transition state, one finds

$$\langle u_0(t)|V_j|u_0(t)\rangle = \sum_{n=0}^{\infty} \sum_{I=2}^{N} C_n(R_{Ij}) \sum_{\substack{s=0 \\ \text{even}}}^{n} \binom{n}{s} (-l)^{n-s} \frac{(s-1)!!}{(2\alpha)^{s/2}} , \qquad (54)$$

and l is the distance from the location of the transition state to a or b. The expansion of the potential v in the general integral $\langle u_0(t)|V|u_0(t)\rangle$ is carried out in the coordinates of $u_0(t)$. Hence the integral has the same form as (52). The quantities $C_{2n}(R)$ are evaluated in terms of the distance R_{It} between the species I and the transfer-species located in the transition state.

Finally, the mixed terms $\langle u_0(a)|V^j|u_0(b)\rangle$ and $\langle u_0(a)|V^j|u_0(t)\rangle$, etc. are found. First, for the a-b mixed term, one finds

$$\langle u_0(a)|V - V_j|u_0(b)\rangle = \langle u_0(a)|V|u_0(b)\rangle - \langle u_0(a)|V_j|u_0(b)\rangle. \qquad (55)$$

Expand V at the optimal point for the product of Gaussians: $u_0(a)u_0(b)$. Hence,

$$\langle u_0(a)|V|u_0(b)\rangle = e^{-q^2} \sum_{n=0}^{\infty} \sum_{I=2}^{N} C_{2n}(R_{Ip}) \frac{(2n-1)!!}{(2\alpha)^n} . \qquad (56)$$

The second integral expands as

$$\langle u_0(a)|V_j|u_0(b)\rangle = e^{-q^2} \sum_{n=0}^{\infty} \sum_{I=2}^{N} C_{2n}(R_{Ip}) \sum_{\substack{s=0 \\ \text{even}}}^{n} \binom{n}{s} (-\lambda)^{n-s} \frac{(s-1)!!}{(2\alpha)^{s/2}} , \qquad (57)$$

where λ here is the distance between j and the point of expansion P.

It is clear that points of expansion of both the wavefunction and the potential have an influence on the size of the integrals involved in the transfer of the proton (or hydrogen) from the initial to the final state. It is equally clear that the overall size of the matrix elements depends, in large part, on the amount of matter density which resides near to the transition state when the system is in its initial or final states. The use of only one zeroth-order, s-type basis functions is certainly a gross oversimplification of the interactions which are likely to exist. This simplification has been chosen only for purposes of illustration. It is obvious that an enlargement of the basis set of function $\{u_i(j)\}$ is possible. Thus, for example, it is possible to mix various p- and d-characteristics ($l = 1, 2$) into the analysis in order to account for the fact that in an asymmetric environment, the local stationary states of the proton/hydrogen must possess a strong angular component of the displacement with respect to any arbitrary axis through the system.

transition state. If one sets the coefficients C_{L2} and C_{R2} equal to zero, it is immediately clear that the simpler direct analysis is automatically contained in the more general description just outlined.

As is the case for the electronic energy states of a molecule, here as well, one finds that the actual system in an asymmetric environment yields strongly angle-dependent overlap quantities. Thus, transfer to and from the transition state may be great or vanishing as the size of these overlap quantities are large or small. Note that in the expressions for the matrix elements of the perturbation which drives the transfer, terms which account for the direct transfer from *a* to *b* as well as terms which account for the transfer from *a* to *t* (the transition state) to *b* also appear. Thus, in effect, the formalism allows for the transfer of a proton via the transition state as well as a tunnel-transfer directly from *a* to *b* through a wider part of the barrier which separates initial and final states. This transfer formalism does not depend, however, upon the additional use of any higher orders of perturbation theory.

4.4 *Frank–Condon factors associated with proton/hydrogen transfers*

In this section, we consider the matter of the contribution of vibrational overlap in the environment as the transfer of a proton takes place.

In addition to the determination of the energy of activation as the difference between the energy of the transition state and the energy of the initial state, it is necessary for transfers which take place in the diabatic limit to consider the slight vibrational reorientation which must accompany the migrating species as it moves from its initial to the final state. Metropolis/Monte Carlo analyses generate individual configurations of the ensemble of states of the system, and one must analyse each configuration to determine the transfer probability for that configuration alone. As a result, the determination of the Franck–Condon factors within a configuration must be done in the zero-temperature limit. An approximate analysis can be carried out in a straightforward manner and is summarized briefly here.

The transition probability for a transfer which takes place within a particular configuration of the ensemble is

$$w_{if} = \frac{2\pi}{\hbar} \sum_f |H'_{if}|^2 \delta(E_i - E_f) \tag{58}$$

in which the summation over final states must be carried out because of the accessibility, in principle, of each to the initial state, even at zero temperature. In this expression, H'_{if} is the matrix element of the perturbation which drives the tunnel-transfer. With the use of the integral representation of the delta function, (58) can be recast as

$$w_{if} = \frac{2\pi}{\hbar^2} \int_{-\infty}^{\infty} \mathrm{d}t \, |H'_{if}|^2 \exp[-i(E_i - E_f)t/\hbar \,]. \tag{59}$$

At this point, the usual simplification common to radiationless transition theory is made that the Condon approximation applies. Write $V_{\ }$ for the specific part of the

$$w_{if} = \frac{}{\hbar^2} |V|^2 \int_{-\infty} dt \, \langle i|\exp(iH_f t/\hbar) \exp(-iH_i t/\hbar)|i\rangle, \qquad (60)$$

in which the completeness of final states has been used to eliminate the summation over f.

Assume that the remaining vibrational distortions of the environment which accompany the migration of the proton from the precursor state to the final state through the transition state are small. As a consequence there is a considerable simplification. In particular, the environmental Hamiltonian is assumed to retain the same fundamental normal mode frequencies for any state of the mobile species (the proton) in its reactive configuration.

The assumption that there is little change in the character of the environmental vibrations as the proton makes the short-distance transit from initial to final state allows one to write

$$H_f = H_i(q - q_0), \qquad (61)$$

which relates the final to the initial environmental Hamiltonian. Assume the harmonic limit applies. Then the vibrational matrix elements within the transition probability change to

$$\langle i|\exp(iH_f t/\hbar)\exp(-iH_i t/\hbar)|i = \langle i|\exp(-iq_0 p(0)/\hbar)\exp(iq_0 p(t)/\hbar|i\rangle, \qquad (62)$$

with $p(t) = p(0)\cos\omega t - m\omega q(0)\sin\omega t$. Further simplification of this expression uses the Baker–Hausdorff expression (Louisell 1964)

$$\exp(A+B) = \exp(A)\exp(B)\exp(\tfrac{1}{2},A,B) \qquad (63)$$

to get

$$\exp(iq_0 p(t)/\hbar) = \exp(iq_0 p(0)\cos\omega t/\hbar) \times \exp(-i\alpha^2 q_0 q(0)\sin\omega t)\exp(-i\alpha^2 q_0^2 \sin\omega t\cos\omega t), \qquad (64)$$

with α defined as

$$\alpha^2 = m\omega/\hbar. \qquad (65)$$

The evaluation of $\langle i|\Gamma(t)|i\rangle$ with the ground state vibrational wavefunction is

$$\langle i|\Gamma(t)|i\rangle \equiv \langle i|\exp(-iqp(0)/\hbar)\exp(iqp(t)/\hbar|i\rangle = \exp(-(\alpha^2 q_0^2/2)(1-\exp(-i\omega t)). \qquad (66)$$

This exponential function can be expanded with the result that

$$\langle i|\Gamma(t)|i\rangle = \exp(-\tfrac{1}{2}\alpha^2 q_0^2) \sum_{n=0}^{\infty} \frac{1}{n!} (\alpha^2 q_0^2/2)^n \exp(-in\omega t). \qquad (67)$$

When this is replaced in the expression for the transition probability and the

integration over time carried out, a sequence of delta functions in the energy emerges:

$$w_{if} = \frac{2\pi}{\hbar} |V|^2 \exp(-\tfrac{1}{2}\alpha^2 q_0^2) \sum_{n=0}^{\infty} \frac{1}{n!} (\alpha^2 q_0^2/2)^n \, \delta(E_0 + n\hbar\omega). \qquad (68)$$

Note that $E_0 = -n\hbar\omega$. Thus, one sees, at zero temperature, there must be vibrational relaxation which accompanies the transfer of the proton. This is reasonable as one assumes that the transfer takes place at zero temperature and there can be no further thermal activation. Nevertheless, the configuration of the ensemble within which the transfer takes place can represent a higher energy state of the system. Thus, relaxation into the vibrational manifold is expected.

The analysis which has been carried out above involved only one vibrational mode. It is extended easily to more than one mode. The argument of the delta function is modified by the inclusion of a sum of frequencies $\Sigma_i n_i \hbar\omega_i$. The coefficients which multiply the delta functions in (68) are changed into products. The exponents n_i for $(\alpha^2 q_{0i}^2/2)^{n_i}$ must, in sum, satisfy the energy equilibration set by the delta function.

5. The Monte Carlo simulation of the proton transfer

As previously noted, the Monte Carlo method of evaluation of the statistical mechanical averages is an energy minimization algorithm. Previous attempts to model atom transfer reactions within the limits of the Monte Carlo method have used constraints on the system in order to force the sampling to seek configurations of the transition state.

Metropolis/Monte Carlo methods achieve successful agreement with experiment in part through the use of averages which involve large numbers of representative ensemble elements. It is obvious that the generation of large numbers of these elements for a complicated system is computationally expensive. As a consequence of this expense, one looks for simpler, but still accurate, methods. The exploration of the application of Metropolis sampling to the determination of the transition state is still in its infancy. In the following paragraphs, I discuss a method which appears to work, although, admittedly it has only been applied to a two-dimensional system. Time has not yet permitted the extensive testing and exploration of accuracy which the method deserves.

Chemical intuition is both a blessing and a trap. The use of intuition to try to construct efficient algorithms for the determination of the transition state can lead to agonizingly time-consuming exercises with the computer. Nevertheless, even in apparent failure there can be a small, hard-won but nourishing fruit which is harvested as a result of the labour. Consider the construction of the initial and final states of the reaction.

The system which has been examined is simple. It consists of a bent ABA molecule immersed in a small collection of spherical solvent. The entire calculation

inversion in the gas phase clearly involves the linear transition state. The transition state for ABA in a solvent can be near-linear, but the presence of the solvent can allow other, slightly bent configurations to contribute to the ensemble of transition states.

The initial and final states for ABA, or any reactive solute, are locally stable, thermodynamically equilibrated states. Therefore, each state, initial or final, can be sought independently with an energy *minimization* routine. Even for the simple ABA molecule, however, one finds very soon that the independent minimization of the initial and final states makes it difficult-to-impossible to determine the transition state for these *uncorrelated* elements of the ensemble. As a result, it is necessary to carry out a coupled minimization of the initial and final states for the transfer in order to be able to determine the transition states. The following sequence seems reasonable.

First, carry out an independent, uncoupled, or uncorrelated, optimization to determine the absolute thermodynamic energy of the initial and final states. One finds when such calculations are carried out that the path which might link the initial to the final state involves considerable translational and rotational reorientation before the actual transfer can take place. One assumes that this reorganization is part of the work which is necessary to bring the system to a reactive configuration. This part of the process is always assumed to be attained by a sequence of adiabatic steps.

Next, carry out a parallel optimization of the initial and final states in which these states are correlated. The question is how to introduce the correlation. It seems reasonable to assume that the 'principle of least nuclear motion', originally formulated by Rice and Teller (1938) later by Ehrenson (1974), applies. This notion asserts simply that the reactions which involve the least atomic and electronic rearrangement will be favoured. This was accomplished by calculating the square of the displacement of the final to the initial state location for each particle as it was selected for optimization in the Metropolis sampling routine. In the ABA simulation, the unbiased sum of squares was used in the expression for the energy of a particular configuration. However, in a more realistic representation, mass-weighted coordinates and force constants could be used as weight factors in a manner which has been discussed by Ehrenson (1974). Such a weighting is clearly needed, as some parts of the system can be 'stiffer' than others.

The equilibration of the constrained initial and final states proceeded to yield energies which were not very far removed from the energies found in unconstrained minimization. The elements of the ensemble of states which are generated from the system which is equilibrated in this manner can be used as initial states in the determination of the transition states. The technique which was used here follows the suggestion for determining the saddle-point given by Banerjee *et al* (1985) with a trial starting estimate as suggested originally by Sinclair and Fletcher (1974).

The initial states as generated by the Metropolis sampling are used directly in the determination of the transition probability. It is certain that in the generation of Metropolis samples, a certain number of elements, if not all, will not yield a zero gradient norm:

$$\Gamma = \mathbf{g}^T\mathbf{g} = 0, \tag{69}$$

made, however, that a given configuration, representative of an arbitrary element of the ensemble, is not far removed from mechanical and thermodynamic equilibrium. In the process of establishing the actual expression for the transition probability in the definition of the rate constant

$$k = \int_0^\infty \mathrm{d}\mathbf{v}\mathrm{d}\mathbf{r}\dot{x}_i P(\mathbf{r},\mathbf{v}) \tag{70}$$

($v = \mathrm{d}r/\mathrm{d}t$), one begins with

$$P(\mathbf{r},\mathbf{v}) = \exp[-\beta H]/\int \mathrm{d}\mathbf{v}\mathrm{d}\mathbf{r} \exp[-\beta H], \tag{71}$$

in which H is the classical Hamilton function: $H = T+V$, and T is the kinetic energy. The complete configurational integral is defined as

$$\int \mathrm{d}\mathbf{r} \exp(-\beta V). \tag{72}$$

Given the fact that a small non-equilibrium configuration can also contribute to the integral, one considers the expansion,

$$V(\mathbf{r}) = V(\mathbf{r}_0) + \mathbf{g}^T\mathbf{r} + 1/2\mathbf{r}^T\mathbf{A}\mathbf{r}, \tag{73}$$

in which the coefficients are evaluated in terms of the instantaneous location of each of the species. Because of the non-vanishing of the linear term in (73), the actual energy is displaced permanently from the true equilibrium energy V_0. It is still possible to carry out the indicated integrations and the results are only slightly altered from those obtained from an expansion about the equilibrium configuration ($\mathbf{g}^T\mathbf{g} = 0$) (Aitken 1956):

$$\int \mathrm{d}\mathbf{r} \exp[-\mathbf{g}^T\mathbf{r} - \tfrac{1}{2}\mathbf{r}^T\mathbf{A}\mathbf{r}] = (2\pi)^{n/2}|A|^{-1/2} \exp(\tfrac{1}{2}\mathbf{g}^T\mathbf{A}\mathbf{g}), \tag{74}$$

and now the energy,

$$V(\mathbf{r}_0) - \tfrac{1}{2}\mathbf{g}^T\mathbf{A}\mathbf{g}, \tag{75}$$

represents the energy of a particular configuration. It seems reasonable to expect that, on average,

$$\langle \mathbf{g}^T\mathbf{A}\mathbf{g} \rangle = 0, \tag{76}$$

that is, the average force should vanish. Thus, even though the Metropolis simulation may generate individual non-equilibrium configurations, the sum over large numbers of these configurations should yield energies which accurately reflect true equilibrium quantities.

There is a practical consideration which lies behind the above analysis. If it were not possible to use near-equilibrium configurations, optimization to local minima would be required. This is an expensive process computationally, and if required, would greatly increase the time needed to simulate a reaction.

The determination of the transition state begins with the use of a suggestion made by Sinclair and Fletcher (1974). The location of the transition state is initially estimated with the use of the initial and final states of an individual configuration of the ensemble. The vector $\mathbf{c}_{if} = \mathbf{c}_f - \mathbf{c}_i$, which directly links the initial and final

argue that along the line $\mathbf{c}_{if}$ there must be a maximum. The line for the search is $\mathbf{x} = \mathbf{c}_i + \alpha\mathbf{s}$, where $\mathbf{s} = \mathbf{c}_{if}(0 \leq \alpha \leq 1)$.

After the initial search for the transition state has been made, the refinement of the search to establish the saddle point can proceed with the use of a variety of methods. It is important to note that as of this writing, there is no best method. The problem of saddle-point optimization is under active investigation in particular with reference to the determination of transition state configurations via quantum chemical calculations. The major obstacle to surmount for any algorithm is the length of time it takes to reach an optimum configuration. The question of whether an optimum is global versus local is less of an issue, as it is possible to constrain the optimization to search regions of a mechanical system where one 'knows' by intuition that there should be a reasonable transition state. At this point, it is necessary to admit that the model calculations which I have carried out to simulate the proton transfer, as an illustration of this discussion, have not proceeded as far as I should have liked. The problem is time. For example, although the algorithm definitely determines the saddle-point for the transfer, for any particular related pair of initial and final states, the optimization to the transition state (with the use of the Honeywell Level 68 computer) takes approximately 66 seconds. To obtain a reasonable sample of approximately 50,000 configurations would take 40 days on our machine. There is an unambiguous need to 'trim' the system, to focus the optimization on a subsystem of the whole system, and thereby accelerate convergence to an optimum for each configuration of the Metropolis sample. In the remaining paragraphs of this paper, therefore, I shall simply discuss the saddle point optimization which I have employed, warning the reader fairly – I believe – that improvements are needed and indeed under development.

In order to refine the search for the optimum, I initially chose to use the conjugate gradient method proposed by Sinclair and Fletcher (1974). This method has been refined by Bell *et al* (1981) and by Bell and Crighton (1984) by combining the conjugate gradient search with Newton–Raphson types of optimization. I believe that this method offers real possibilities for rapid optimization, but I found that there were difficulties in coding the algorithm in a way which ensured convergence to energy minima in directions conjugate to the direction along which one finds the energy maximum of the saddle point. These initial attempts made use of the simpler approach of Sinclair and Fletcher (1974) only to avoid the added burden of coding the Newton–Raphson steps.

The method I eventually found to work with certainty was the direct Newton–Raphson method. The calculation employed analytical gradients and Hessian matrices (matrices of the force constants). As noted by Banerjee *et al* (1985), if $\mathbf{H}$ is the Hessian matrix and $\mathbf{g}$ the gradient vector, the stationary condition yields

$$\mathbf{Hx} + \mathbf{g} = 0. \tag{77}$$

If $\mathbf{H}$ is diagonalized by a unitary matrix $\mathbf{U}$, then (with diagonal elements h_i)

$$\mathbf{h} = \mathbf{U}^{+}\mathbf{HU} \tag{78}$$

and

As a result, with q the vector of principal modes, optimization takes the form of N simple equations

$$q_i = -G_i/h_i. \tag{80}$$

Stationary points have $G_i = 0$. Thus, the q_i can be used as steps in the direction of the optimum along each axis. If $h_i < 0$, the search will find a maximum, and if $h_i > 0$ the search will find a minimum.

The determination of the transition state involved, therefore, the following steps after the initial estimate of its location. The analytical gradient vector and Hessian matrix were determined with reference to these cartesian coordinates. The Hessian matrix was then diagonalized and the resulting eigenvectors (one column for each eigenvalue) were used as the unitary matrix to transform the coordinate vector of the transition state and the associated gradient to the principal axis representation. Equations (80) were solved, and the q_i were used together with a scale factor, to estimate shifts in the direction of the optimum. Convergence to the transition state was determined when the ratio of the energy difference to previous energy was less than a preset tolerance (0·01, or 1%).

6. Discussion

There are several observations which can be made even with only the preliminary results which have been obtained with the use of the optimization outlined above. Part of these observations come from the earlier work which used a simpler, but far less accurate, form of estimating the transition state.

Two calculations were carried out. In the first calculation, the transition state for the ABA inversion in vacuum was determined. Symmetry dictates that it should be linear in the transition state, and indeed it is found to be so. This calculation served as a check on the routine. In addition, however, because the calculations alone required very little time – there was no solvent optimization involved, it was possible to explore the stability of the transition state in order to see if the transfer could take place via an adiabatic path or not. The test for adiabaticity is very simple when one uses Newton–Raphson methods of optimization. The determination of the Hessian matrix is already an accomplished step in the routine. Therefore, it remains necessary only to diagonalize the force constants for the migrating species in the field of the remaining species. The results, listed in table 1, include the eigenvalues which are associated with the principal axes for the motion of the transfer-species in the transition state. If one of the eigenvalues is negative, then the transition state cannot be reached via an adiabatic path, as asserted in the preceding discussion.

One would think that for the simple bent ABA system, there ought to be an accessible adiabatic transition state when the A–A interaction is allowed to vanish. This was not found. There is an explanation for the result. For such a system, there cannot be a transition state. The transformation along a path of *lowest* overall energy is isoenergetic. That is, a constant bond-length, bond-binding transforma-

Table 1. The evaluation of the transition state for the bent ABA molecule in vacuum.
The parameters of the (Lennard–Jones) potential energy functions are r_0(A–B) = 1.41 A; E_0(A–B) = 2.5×10^{-12} erg; r_0(A–A) = 2.83 A; E_0(A-A) variable, as listed below.

nteraction	Optimised state energies					Optimised coordinates						
erg)	Initial	Final	Eigenvalues	Eigenvectors	Transition state energy	State	x(B)	y(B)	x(A1)	y(A1)	x(A2)	y(A2)
)	−5·900	−5·900	−4·2955	1·0000	−5·785	Initial	−0·33305	0·00000	−0·00013	1·37453	−0·00013	−1·37453
				−0·0000		Final	0·33305	0·00000	0·00013	1·37453	0·00013	−1·37453
			266·0267	0·0000		Transition	−0·00508	0·00000	0·00254	1·38713	0·00254	−1·38713
				1·0000								
)	−5·600	−5·600	−4·2174	1·0000	−5·487	Initial	−0·33287	0·00000	−0·00022	1·37456	−0·00022	−1·37456
				−0·0000		Final	0·33287	0·00000	0·00022	1·37456	0·00022	−1·37456
			264·5227	0·0000		Transition	−0·00507	−0·00000	0·00254	1·38753	0·00254	−1·38753
				1·0000								
)	−5·000	−5·000	−4·0760	1·0000	−4·891	Initial	−0·33330	0·00000	−0·00000	1·37440	−0·00000	−1·37440
				−0·0000		Final	0·33330	0·00000	0·00000	1·37440	0·00000	−1·37440
			261·7999	0·0000		Transition	−0·00509	0·00000	0·00254	1·38827	0·00254	−1·38827
				1·0000								

initial and final states with the A–A distance frozen at its initial state length. Thus, in fact, a search is carried out along translational axes and a false transition state is found. It is clear that in cases such as this, the walking algorithm of Simons *et al* (1983) and Banerjee *et al* (1985) should be used in order to avoid the unphysical focus on a local optimum (here, a saddle-point). The correct result should automatically be an isoenergetic transformation.

On the other hand, when the A–A interaction is nonvanishing, a true transition state is found which reflects the balance in forces between the A–A attraction and the A–B repulsions in the transition state.

The introduction of a solvent complicates the analysis simply by increasing the number of interactions which must be considered. However, for this simple system, the result in solution is not that very different from that of the vacuum calculation. The presence of solvent can force the transition state to be slightly off-centre from that predicted for the vacuum. However, the adiabaticity of the transition will be essentially that which is found in the vacuum.

Table 2 presents the results of one saddle-point determination which was carried out on one pair of initial and final state configurations. The initial and final state configurations were generated from a system in which the bent ABA molecule in its initial and final states was equilibrated with 24 additional molecules of disk-like solvent in a two-dimensional system. The method of minimum images was used to reduce or eliminate boundary effects. Table 2, lists the eigenvector analysis of the transfer species in the transition state. The first eigenvalue is negative; it is associated with an eigenvector for the displacement of the transfer species, the proton, along the C_3-transfer axis. The second eigenvalue is positive definite; thus, transverse motions of the proton in the transition state are stable. The conclusion of this part of the analysis is that this particular configuration is not stable. Thus, if the transfer is to take place, it must do so by means of a tunnel-transfer. This type of calculation can be carried out with the use of the methods which have already been summarized above. A simple form of analysis has been presented before (Schmidt 1985, 1986).

Before concluding this discussion, it is necessary to note one point which has been set aside until now. To be specific, the question of the combined electron and proton/hydrogen transfer has not yet been addressed. This is an issue which has been examined in some detail by Levich *et al* (1970). Their approach to the hydrogen evolution reaction in particular has been to employ a 'double adiabatic hypothesis' to separate, first, the electronic degrees of freedom from those of the proton and the environment and then to consider the separation of the proton from the environment. The transfer in the diabatic limit, as evaluated with the use of the quantum mechanical expression for the first order time-dependent perturbation, then involves interactions of the various subsystems. At least part of the notion which is involved assumes that there is in effect a simultaneous electron and atom transfer. There is unfortunately no strong evidence which supports or denies this position (Conway 1982). It is nevertheless a possible mechanism.

The issue with reference to the approach taken in this paper is simply how one incorporates electron-transfer into the atom-transfer. The answer is that the seed of a theory is sown in the suggestion that one follow the migration of a quantal

Table 2. An examination of the transition state of A–A–B in solution.

This calculation determined the transition state for one configuration of the coupled initial and final states in a Metropolis/Monte Carlo simulation in which the bent ABA molecule was equilibrated in its initial and final states with 24 disk-like molecules of solvent in a two-dimensional array. The minimum image approximation was used to eliminate boundary effects. The system was equilibrated at 300 K and 10,000 additional cycles were executed before the sample configuration was isolated. The parameters within the molecule are those of table 1, with $E_0(\text{A–A}) = 0{\cdot}9 \times 10^{-12}$ erg.

Starting energies for this simulation:
−7·97813 −8·09295

Initial estimate of transition state energy:
−7·9453

Stability analysis of the transition state eigenvalues
−4·7681 284·3724

eigenvectors
1·0000 0·0002
−0·0002 1·0000

$E(\text{trans})=$ −7·9453

Coordinates of the transition state:

Solute, ABA

x(B)	y(B)	x(A1)	y(A1)	x(A2)	y(A2)
0·00000	0·00000	0·08367	1·38099	−0·01873	−1·38088

Solvent species

x	y	x	y	x	y
−5·99013	7·23441	−7·39451	4·23746	−5·98359	1·57997
−6·36082	−1·73176	−7·24766	−5·16724	−4·67376	4·60817
−1·78148	4·67485	−3·15053	1·52756	−3·39582	−1·37241
−4·23240	−5·27276	−0·31894	7·33602	−3·22267	7·08074
−1·93476	−4·06618	2·57178	−2·46083	2·52242	6·61329
0·70885	4·75163	2·95082	3·22716	2·89630	0·74764
1·05938	−5·25535	6·06341	7·27071	4·64411	5·09055
5·48582	2·39117	5·50340	−2·19837	3·83310	−4·85590

migrating species, the determination of the transition state would involve that species. The test for the adiabaticity of attainment of the transition state for the electron needs to be perfected; it is clearly insufficient to treat the electron in its interaction with its surroundings in the same manner as has been done here for the atom. In any event, the search for and the realization of the transition state involves not only the electron but also the displacement of all the particles of the system. Thus, automatically, in terms of the simulation, one finds that it is possible – in appropriate situations – to find the simultaneous electron and atom transfer which one would expect perhaps for the hydrogen evolution reaction. This fascinating possibility needs to be developed, in my opinion. The realization of the transition state and the modelling of the transition state through computer simulation ought,

Monte Carlo method. The principal results are (1) the construction of an algorithm which connects the initial and final state configurations in individually generated Metropolis samples, and (2), a demonstration that it is possible to find a transition state for the initial/final state pair by means of the use of a relatively simple Newton–Raphson optimization. Incidental issues which have received attention are, one, the matter of the determination of the transition state when a particle obeys the quantum mechanical limit – i.e., experiences a considerable uncertainty spread. The quantum mechanically diffuse particle is 'moved' by moving the centre-of-gravity of the wavepacket. Two, oblique tunnel-transfers have been handled with the use of basis sets located at the initial, transition, and final states. And, finally, the additional environmental reorganization necessary to accompany a tunnel-transfer has been evaluated in terms of a zero-temperature evaluation of the quantum mechanical transition probability.

The results, in sum, seem to point the way to a computational theory of the transition state. A considerable amount of work remains to be done. The discussion contained in this paper merely offers an initial suggestion. Nevertheless, it is a suggestion which seems to me to be reasonable.

Acknowledgement

This work was supported in part by contract with the Office of Naval Research, Arlington, Virginia.

References

Aitken A C 1956 *Determinants and matrices* (Edinburgh: Oliver & Boyd) edn. 9
Arfken G 1970 *Mathematical methods for physicists* (New York: Academic Press) edn. 2
Babamov V K and Marcus R A 1981 *J. Chem. Phys.* **74** 1790
Babamov V K, Lopez V and Marcus R A 1983 *J. Chem. Phys.* **78** 5621
Banerjee A, Adams N, Simons J and Shepard R 1985 *J. Phys. Chem.* **89** 52
Bell R P 1959 *The proton in chemistry* (Ithaca: Cornell Univ. Press) Chap. 10 p. 155.
Bell R P 1975 *Faraday symposia of the chemical society* **10** 7
Bell S and Crighton J S 1984 *J. Chem. Phys.* **80** 2464
Bell S, Crighton J S and Fletcher R 1981 *Chem. Phys. Lett.* **82** 122
Chang S S, Severson M W and Schmidt P P 1985 *J. Phys. Chem.* **89** 2892
Chang S S, Schmidt P P and Severson M W 1986 *J. Phys. Chem.* **90** 1046
Conway B E 1965 *Theory and principles of electrode processes* (New York: Ronald Press) Chap. 8
Conway B E 1982 *Faraday Discuss. Chem. Soc.* **74** 267
Dogonadze R R, Kuznetsov A M and Levich V G 1967 *Elektrokhimiya* **3** 739
Dogonadze R R, Kuznetsov A M and Levich V G 1968 *Electrochim. Acta* **13** 1025
Duke C B 1965 *Tunneling in solids, solid state physics* Suppl. **10** (New York: Academic Press)
Ehrenson S 1974 *J. Am. Chem. Soc.* **96** 3778
Fischer S 1970 *J. Chem. Phys.* **53** 3195
Frumkin A N 1961 *Adv. Elecrochem. Electrochem. Eng.* **1** 65
Frumkin A N 1963 *Adv. Electrochem. Electrochem. Eng.* **3** 287

Louisell W 1964 *Radiation and noise in quantum electronics* (New York: McGraw-Hill)
Marcus R A 1968 *J. Phys. Chem.* **72** 891
Marcus R A 1984 *J. Chem. Phys.* **81** 4494
McIver J W and Komornicki A 1972 *J. Am. Chem. Soc.* **94** 2625
McKinley J M and Schmidt P P 1982 *J. Chem. Soc. Faraday 2* **78** 867
McKinley J M and Schmidt P P 1984 *Chem. Phys. Lett.* **110** 379
Metropolis N, Rosenbluth A W, Rosenbluth M N, Teller A H, and Teller E 1953 *J. Chem. Phys.* **21** 1087
Morse P M and Feshbach H 1953 *Methods of mathematical physics* (New York: McGraw-Hill)
Oppenheimer J R 1928 *Phys. Rev.* **31** 66
Poppinger D 1975 *Chem. Phys. Lett.* **35** 550
Rice F O and Teller E 1938 *J. Chem. Phys.* **6** 489
Schmidt P P 1977 *J. Electroanal. Chem.* **82** 29
Schmidt P P 1984a *J. Chem. Soc. Faraday 2* **80** 157
Schmidt P P 1984b *J. Chem. Soc. Faraday 2* **80** 181
Schmidt P P 1985 *J. Chem. Soc. Faraday 2* **81** 341
Schmidt P P 1986 *J. Chem. Soc. Faraday 2* **82** 1399
Schmidt P P and Chang S S 1986 *J. Phys. Chem.* **90** 4945
Schmidt P P, Pons B S, and McKinley J M 1980 *J. Chem. Soc. Faraday 2* **76** 979
Shavitt I 1963 *Methods Comput. Phys.* **2** 1
Siebrand W 1967 *J. Chem. Phys.* **46** 440
Siebrand W 1971 *J. Chem. Phys.* **54** 636
Simons J, Jorgensen P, Taylor H and Ozment J 1983 *J. Phys. Chem.* **87** 2745
Sinclair J E and Fletcher R 1974 *J. Phys.* **C7** 864

New theories for the electric double layer at a metal/electrolyte solution interface[§]

EZEQUIEL LEIVA and WOLFGANG SCHMICKLER*
Institute of Physical Chemistry, University of Bonn, Wegelerstrasse-12 D-5300 Bonn, Federal Republic of Germany

Abstract. Recent models for the electrochemical double layer are reviewed, in which the metal is represented by "jellium" and the solution by an ensemble of hard sphere ions and dipoles. The predictions of the model are compared with experimental data, and some extensions are discussed.

Keywords. Jellium; hard spheres; double layer; interface.

1. Introduction

On experimental grounds, it has been largely accepted that the inverse capacity of a metal/electrolyte interface in the absence of specific adsorption can be written as:

$$1/C = 1/C_{\text{diff}} + 1/C_i \,, \tag{1}$$

where the 'diffuse layer' contribution C_{diff} depends on the concentration of the ions while the so-called 'inner layer' capacity C_i is independent of it. For dilute solutions, a planar electrode, and a z–z electrolyte, the former is given by the Gouy–Chapman expression (Reeves 1980),

$$C_{\text{diff}} = \left[\frac{2z^2F^2\varepsilon C_i}{RT} \right]^{1/2} \cosh \frac{zF\varphi}{2RT} \tag{2}$$

In the conventional model, this mathematical separation into two terms was thought to arise from a spatial separation of the solution into two parts: a monolayer of solvent molecules on the metal surface, the 'inner layer', into which the ions cannot penetrate, and a 'diffuse layer', where the charge on the metal is screened by the ions; the metal was thought to be a perfect conductor, which makes no contribution to the capacity. So the inner layer capacity was explained solely through the dielectric properties of the inner layer, the experimentally observed metal dependence was attributed to chemical interactions of the electrode with the first solvent layer, resulting in each case in a different 'effective inner dielectric constant' ε_i. In this respect, it is interesting to recall the values of ε_i calculated by Trassatti (1981) by using the equation:

$$\varepsilon_i = C_{i0} \,.\, X_i \,/\, \varepsilon_0 \tag{3}$$

where C_{i0} is the inner layer capacity at the potential of zero charge, ε_0 is the

[§] Dedicated to Prof. K S G Doss on his eightieth birthday

Table 1. Double layer capacity for the interphase solvent/*sp* metal at the PZC.

Metal	C_i/μFcm^{-2}	ε_i
(a) H_2O		
Hg	28	9·8
Tl	33·5	11·6
Cd	52	18·2
In(Ga)	60	21·0
Zn	100	47·0
(b) DMSO		
Hg	23	15·8
In(Ga)	53	36·5
Ga	93	64·5

The bulk dielectric constants of water and DMSO are 78·3 and 46·6 at room temperature respectively. After Trasatti (1981).

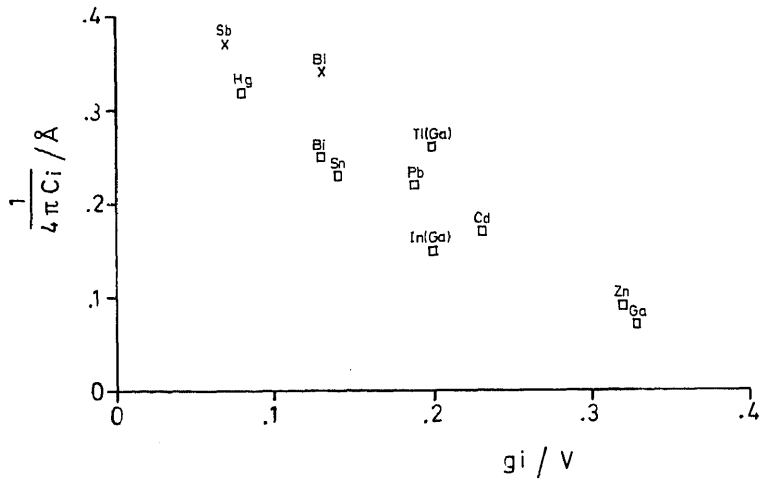

Figure 1. Inverse 'inner layer' capacity at the PZC versus water dipole potentials g_i. Dipole potentials were taken from Trasatti (1977, 1979). Boxes denote 'inner layer' capacity values taken from Trasatti (1981), while crosses indicate values of Frumkin *et al* (1974).

permittivity of the vacuum and X_i the thickness of the inner layer estimated from the molar volume of the liquid. These results, reproduced in table 1 for water and DMSO show a considerable variation of ε_i with the metal, which is attributed to a different restricted rotation of the solvent molecules at the interface.

Two problems arise from the interpretation of these results (Schmickler 1984). The first one is how to explain in the case of the interface Ga/DMSO an ε_i which is larger than the bulk dielectric constant of DMSO. The second problem appears if we plot the inverse capacity versus the dipole potentials of water (g_i), as was done by

However, a more strongly bonded molecule should give rise to a lower, and not to a higher effective dielectric constant, since it is less free to rotate. Only artificial models for the solvent, postulating the existence of two types of solvent molecules, monomers and clusters, in the inner layer, were able to explain the increase of the capacity with the dipole potential of water. However, they could not reproduce the experimental features for several metals, unless parameters pertaining to the solvent were also changed with the metal.

It is now clear that, though the validity of (1) is empirically justified (i.e. through the Parsons–Zobel extrapolation plots (Parsons and Zobel 1965)), this does not imply that the above described physical picture is necessarily true. For example, at low and moderate electrolyte concentrations, there is a considerable field penetration in the solution, which extends over several solvent layers. If we think of solvent molecules as dipoles, cooperative alignment of these entities could occur over the same distance which the diffuse ion layer extends. This would produce a relatively wide region over which the bulk properties of the solvent are not reached. Thus, the assignment to it of a dielectric constant (a macroscopic bulk quantity) would be rather misleading.

Looking at the metal side, we can easily show that it cannot be considered as a perfect conductor on the atomic scale. The Thomas–Fermi length λ_{TF} provides a measure of the penetration depth of a field into the metal. Comparing a typical value of λ_{TF} of 1 Å (Kittel 1975), with an estimation of the thickness of the double layer of about 3 Å Trassatti (1981), we see that a quantum mechanical model of the metal is required for a correct description of the interface.

Early attempts to calculate C_i in a quantum mechanical approach were made by Rice (1928). The inner layer capacity was attributed to the metal, and calculated from the Thomas–Fermi model, which gives in esu:

$$C_m = \lambda_{TF}[(\varepsilon_b)^{1/2}/4\pi \tag{4}$$

where λ_{TF} is a function of the electron density and ε_b is the background dielectric constant of the ion cores. As shown by Kornyshev *et al* (1982), (4) predicts very low values for the capacity, and cannot explain its dependence on temperature and charge. These and other difficulties, like the too small dependence of the capacity on the nature of the metal, caused its relevance to the double layer properties to be forgotten for several decades.

In this way, many theories of the double layer were developed without taking notice of the considerable progress in related areas of solid state and surface physics. On these grounds, a reexamination of the role which the metal plays in the electrode/solution interface was made Kornyshev *et al* (1982). Applying the formalism of nonlocal electrostatics, Kornyshev *et al* (1982) studied two different models. In the first one, they considered a sharp phase boundary, while in the second a spillover of the metal electrons into the solution was allowed. The extension of the electronic density into the solution produced an increase of the capacity C_{i0}, which was in better qualitative agreement with the experiment. In this way, the search for a microscopic model which contemplated the spillover of the electrons in the solution was strongly stimulated. Steps in this direction were later taken by Badiali *et al* (1980, 1981, 1983a) and Schmickler (1983), who used the

Carnie and Chan (1980) and Blum and Henderson (1981) analysed the integral equations for the ionic and solvent profiles of a model electrolyte near a charged wall. The capacity of this system, which consisted of charged hard spheres as ions and dipolar hard spheres as solvent, could be obtained for small charges on the electrode. Though the final expression for the capacity at low ionic concentrations is simple and similar to that given by the Gouy–Chapman theory, the representation of the solvent by a uniform dielectric medium was shown to be completely inadequate.

The above mentioned developments in solid state physics and statistical mechanics of electrolyte solutions culminated in a new, comprehensive model of the metal/solution interface (Badali *et al* 1983b; Schmickler and Henderson 1984b) which can explain many experimental features concerning both the metal and the solution.

We shall concentrate here on the contribution that these new lines of ideas have made to the understanding of double layer processes in the absence of specific adsorption. In order to provide a better understanding of the recent model, a short description of the main features of the jellium and hard spheres models will be given.

The plan of the article is as follows: In §2 we present the jellium model for the metal and the hard spheres model for the solution, as well as the separate influence that both exert on the double layer capacity. Section 3 deals with the unified description or the metal/solution interface by means of the jellium/hard spheres model. In §4 we analyse the role played by some approximations made in §3, which were relaxed in recent improvements of the model.

2. Jellium A model for *sp* metals

Hohenberg and Kohn (1964) showed that the ground state energy of an interacting electron gas in an external potential $V(r)$ can be written as:

$$E(n)=\int V(r)\ n(r)\ \mathrm{d}r+\frac{1}{2}\int\frac{n(r)n(r')}{|r-r'|}\ \mathrm{d}r\mathrm{d}r'+G(n) \tag{5}$$

where $n(r)$ is the electron density at the point r. The first term of (5) represents the interaction of the electrons with the external potential, the second term is the self interaction energy and $G(n)$ is a universal function of the density which accounts for kinetic, exchange and correlation energy.

In order to calculate surface properties within this formalism, a model for the metal is required. For example, some assumptions must be made about the distribution of the positively charged ions in order to calculate $V(r)$. In the case of the *sp* metals, it is reasonable to suppose a regular distribution of ionic cores, each of them bearing a charge (Z_n-n_c), where Z_n is the charge of the nucleus and n_c the number of core electrons. If this positive charge distribution is smeared out into a homogeneous positive background of density $\bar{n}$ (for $x<0$) that terminates abruptly at a plane ($x=0$), we have the so-called 'jellium' model of a metal surface (figure

2a). This is probably the most elementary model which yields quantitative results for basic surface properties such as the work function (Lundquist and March 1983).

Due to their small mass, the electrons spillover the metal surface, so that a small negative surface charge exists on the vacuum side, which for an uncharged surface is balanced by an equivalent positive excess charge on the metal side (figure 2b). Thus a surface dipole appears at the jellium edge, giving rise to a potential drop D_e perpendicular to the surface plane. It can be rigorously demonstrated that D_e makes an important contribution to the electronic work function (Lang and Kohn 1971).

$$\Phi = D_e - \tilde{\mu}, \tag{6}$$

where $\tilde{\mu}$ is the bulk chemical potential of the electrons relative to the mean electrostatic potential in the metal.

There are several ways of employing (5) for the calculation of jellium properties (Lundquist and March 1983). We concentrate here on those which provide both satisfactory results for surface properties and a reasonable numerical complexity, making them appropriate for application to electrochemical systems.

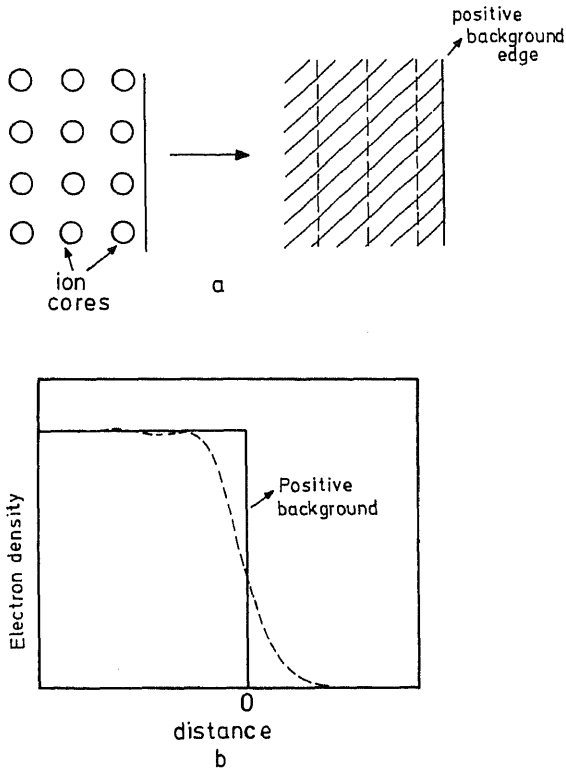

Figure 2. (a) How to construct the positive background in the jellium model. The circles represent the positive cores (right hand side), which are smeared out in a uniform, positive charge density. The broken lines depote the primitive position of the ions, the first

variational approach for the solution of (5) was made by Smith (1969). He used for $G(n)$ the following expansion:

$$G(n) = \frac{3}{10}(3\pi^2)^{2/3}\int n^{5/3}\,dr - \frac{3}{4}\left(\frac{3}{\pi}\right)^{1/3}\int n^{4/3}\,dr - 0{\cdot}056 \times \int \frac{n^{4/3}}{0{\cdot}079 + n^{1/3}}\,dr + \frac{1}{72}\int \frac{(\nabla n)^2}{n}\,dr, \tag{7}$$

where the terms on the right hand side represent the kinetic, exchange, correlation and first-order inhomogeneity corrections respectively.

The electron density $n(x)$ was represented through:

$$n(x) = \begin{cases} \bar{n} - \frac{\bar{n}}{2}\ \exp(\beta x)\ , & x < 0 \\ \frac{1}{2}\ \bar{n}\ \exp(-\beta x)\ , & x > 0. \end{cases} \tag{8}$$

The surface energy σ was then obtained as a function of the free parameter β:

$$\sigma = E(n(x)) - E(\bar{n}) = f(\beta) \tag{9}$$

The minimization of (9) with respect to β yields an approximate solution to the electronic density profile, from which the desired surface energy σ, the work function, and the jellium surface dipole D_e can be calculated.

Within the above described approximation, reasonable results were obtained for electron work functions and surface potential characteristics, so that a similar approach should also be useful for calculating double layer properties. In this respect, when a charge is present at the metal surface, the following family, due to Partenskii and Smorodinskii (1974) can be used:

$$n(x) = \begin{cases} \bar{n} - \frac{1}{2}\ [\bar{n} + \beta q]\exp(\beta x),\ x < 0 \\ \frac{1}{2}\ [\bar{n} - \beta q]\exp(\beta x),\ x > 0. \end{cases} \tag{10}$$

The quality of the approximations made within the variational scheme can be checked by comparing the calculated properties with the self consistent results of Lang and Kohn (1970) for jellium.

A trial function $n(x)$ for the density profile must fulfil three requirements: charge balance, continuity of $n(x)$ and continuity of $n'(x)$. There is, however, a fourth condition that the exact solution of the electron density should satisfy: the Budd and Vannimenus sum rule (Budd and Vannimenus 1973; Vannimenus and

$$\bar{n}\ [\ \varphi_0 - \varphi_{-\infty}\ ] = \frac{q}{2} - \frac{K_F}{2}\left[\ 0{\cdot}4 - 0{\cdot}0829 r_s - \frac{0{\cdot}0796 r_s}{(\ r_s + 7{\cdot}8\ )^2}\ \right] \qquad (11)$$

where $K_F = (3\pi^2\ \bar{n}\ )^{(1/2)}$ is the Fermi momentum, and r_s is the radius of the sphericalized Wigner Seitz cell. This equation can be obtained from a pressure balance condition Heinrichs and Kumar (1975).

Schmickler and Henderson (1984a) introduced this condition in the variational calculation of jellium properties. The trial family they used is:

$$n(x) = \begin{cases} \bar{n}\ [1 - A\ \exp(\alpha x)\cos(\Gamma x + d)]\ , & x < 0 \\ \bar{n}\ B\exp(-\beta x), & x > 0. \end{cases} \qquad (12)$$

The oscillatory term for $x<0$ was introduced in order to account for the so called 'Friedel oscillations', which appear in the self consistent solution of jellium (Lang and Kohn 1970). These two new elements in the variational calculation gave rise to a large improvement of the results for surface properties. The calculated values of work function and effective image plane position for small surface charges excess were found to be in very good agreement with the exact results of Lang and Kohn (Schmickler and Henderson 1984a). The accuracy of the variational results for charge densities that lie within the usual electrochemical range for double layer measurements has also been confirmed by the recent self consistent calculations of Gies and Gerhardts (1986). We shall see later that these properties are very important in determining the electrochemical behavior of the metal in the double layer.

In order to investigate the contribution of the metal to the double layer capacity, we shall proceed like Schmickler and Henderson (1984c), and start from the Poisson equation for a system of charges and dipoles:

$$\Delta\varphi(x) = -4\pi[\rho_m\ (x) + \rho_s(x) - \frac{\mathrm{d}}{\mathrm{d}x}\ P(x)\ ], \qquad (13)$$

where $\rho_m\ (x)$ is the charge density of the jellium, consisting of a positive ionic background at $x<0$ and a negative electron gas, ρ_s is the ionic charge density of the solution, which extends in the region $x>0$, and $P(x)$ is the solvent polarization. The last two contributions must be calculated, as we shall later see, from a microscopic model for the electrolyte. Integrating twice, we get:

$$\varphi_\infty - \varphi_{-\infty} = 4\pi \int_{-\infty}^{+\infty} x\,\rho_m(x)\ \mathrm{d}x + 4\pi \int_{0}^{+\infty} x\,\rho_s(x)\ \mathrm{d}x + 4\pi \int_{0}^{+\infty} P(x)\,\mathrm{d}x. \qquad (14)$$

Differentiating with respect to the surface charge density, we can obtain the total

$$\frac{1}{4\pi C} = \frac{1}{4\pi C_m} + \frac{1}{4\pi C_s}, \tag{15}$$

where

$$\frac{1}{4\pi C_m} = -\frac{\partial}{\partial q} \int_{-\infty}^{+\infty} x\,\rho_m(x)\,\mathrm{d}x, \tag{16}$$

and

$$\frac{1}{4\pi C_s} = -\frac{\partial}{\partial q} \int_{0}^{+\infty} [\,x\rho_s\,(x) + P(x)]\mathrm{d}x. \tag{17}$$

We note here that C_m and C_s are not independent, but rather coupled through some interactions. For example, it could be expected that the electron plasma interacts with both ions and dipoles in the solution. On the other hand, the electron cloud of the solvent molecules should also affect the electron distribution in the metal through repulsive interactions.

We discuss now the metal contribution (16). We can write $\rho_m(x) = \rho_m^0(x) + \delta\rho_m(x)$, where $\rho_m^0(x)$ represents the charge density for the uncharged metal. Replacing in (16) and applying (11), we obtain:

$$\frac{1}{4\pi C_m} = -\frac{q}{\tilde{n}} - \frac{\partial}{\partial q} \int_{0}^{\infty} x\delta\rho_m\,(x)\mathrm{d}x. \tag{18}$$

But in the linear response regime, it can be shown that (Lang and Kohn 1973)

$$\frac{\partial}{\partial q} \int_{0}^{\infty} x\,\delta\rho_m\,(x)\,\mathrm{d}x = X_i, \tag{19}$$

where X_i is the effective image plane of jellium. At the point of zero charge this is always a positive quantity and typically of the order of 0·5 A. If we now replace in (17) for $q=0$, we can obtain the contribution of the metal to the capacity at the potential of zero charge:

$$C_{m(q=0)} = -\frac{1}{4}\,\pi X_i. \tag{20}$$

The negative contribution to the capacity can be physically understood in the following way: Let us place a uniformly charged sheet at $x=D$ in front of a previously grounded perfect metal located at $x=0$ (figure 3a). An image charge is induced on the second one, and the relation between charge and potential

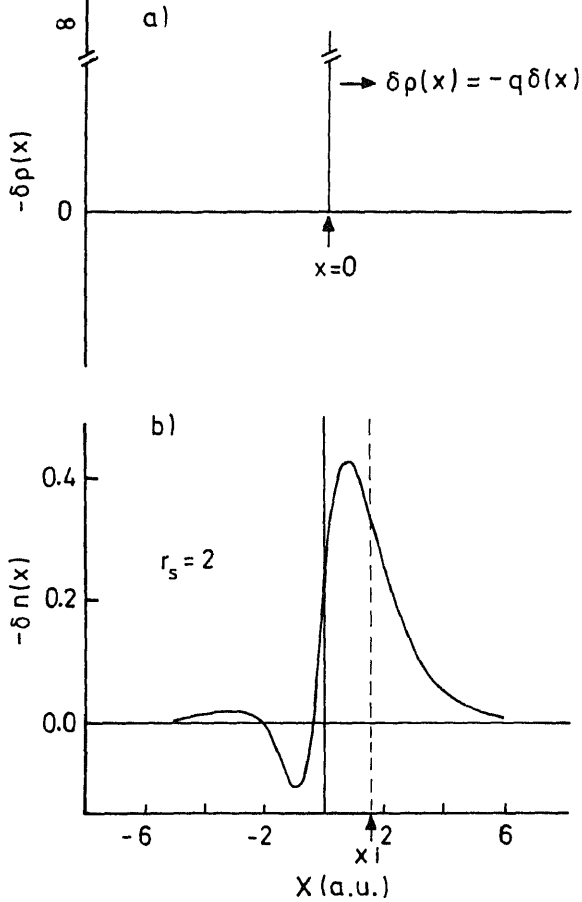

Figure 3. Charge induction by a charge located at a distance D far apart from: (**a**) a perfect metal (**b**) jellium.

difference on the metal-charged sheet is given by the capacity:

$$\frac{1}{4}\pi C = D. \tag{21}$$

If instead of a perfect metal we take now jellium with the positive background edge at $x=0$, the image charge is not located at the point $x=0$ but distributed in the x coordinate, with its center of mass located at X_i (figure 3b). For small charges, the inverse capacity of this system is:

$$\frac{1}{4}\pi C = D - X_i. \tag{22}$$

That is, the effective plate separation is smaller than the plate separation for a perfect conductor by an amount X_i. Since the thickness of the double layer is of the same order of magnitude as X_i, a very important influence of the metal on the

electron density of jellium, so that different effective double layer thickness should appear on these grounds.

Capacity calculations

The role that the electron density plays in the determination of capacity/charge curves was shown by Schmickler (1983a), who proposed a jellium dipole model for the electrochemical double layer. In this model the solvent was represented by a hexagonal lattice of point dipoles which could take up three orientations (spin one model). The dipole-dipole interactions were treated quantitatively by a 'periodic cluster approximation' (Schmickler 1983a), and a self consistent calculation with the interdependent jellium-dipoles equations was performed.

Capacity/charge curves obtained with this model are shown in figure 4, where an increase of the capacity is observed at the PZC with the electron density of the metal. This prediction is in qualitative agreement with the experimental results for simple *sp* metals.

The correct dependence of the capacity hump was also obtained. At higher temperatures, the hump becomes smaller, since the dipoles are oriented less by the field.

PZC calculations

The jellium-dipole model was also used to calculate the potential of zero charge of metal electrodes (Schmickler 1983b). For this purpose, a perfectly polarizable metal electrode Me was considered, which is in contact with an aqueous solution containing a standard hydrogen reference electrode (H_2/Pt); a platinum wire is supposed to be connected to the metal electrode. When the metal electrode is at the potential of zero charge, the potential difference of the cell is:

$$E_{PZC} = \psi_{Pt} - \psi_{ref}, \tag{23}$$

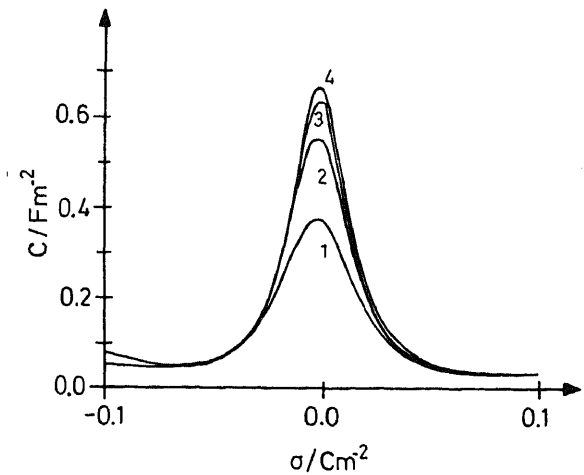

Figure 4. Theoretical capacity-charge curves for various values of the bulk electron

where ψ_{Pt} and ψ_{ref} are the outer potentials of the platinum wire and the reference electrode respectively. Equation (22) can be rewritten in terms of quantities pertaining to the metal and the solution:

$$E_{PZC} = (\psi_{Pt} - \psi_{Me}) + (\psi_{Me} - \psi_{sol}) + (\psi_{sol} - \psi_{ref}), \tag{24}$$

where Me and sol represent metal and solution respectively. The interfaces contributing to the first and third term on the right hand of (24) are in equilibrium, so that we may replace them by the corresponding work function differences to obtain:

$$E_{PZC} = (\psi_{Me} - \psi_{sol}) + 1/e(\Phi_{Me} - \Phi_{H_2/H_2O}). \tag{25}$$

The inner layer potential difference metal-solution $(\varphi_{Me} - \varphi_{sol})$ can be calculated from our model, so we re-express (25) in terms of this quantity:

$$E_{PZC} = (\psi_{Me} - \varphi_{Me}) + (\varphi_{Me} - \varphi_{sol}) + (\varphi_{sol} - \psi_{sol}) + 1/e(\Phi_{Me} - \Phi_{H_2/H_2O}) \tag{26}$$

The first term represents the potential difference metal/vacuum [D_e in (6)], which can also be calculated for jellium; Φ_{H_2/H_2O} is a measurable quantity, independent of the metal interface; $\varphi_{sol} - \psi_{sol}$ is a characteristic of the solvent, which must be estimated from solvent models; and Φ_{Me} can be taken from measurements or calculated from (6).

The dipole model was a hexagonal lattice of point dipoles as before, but the interaction of the dipoles with each other was considered in the mean field approximation, and an infinite number of orientations in space was allowed. Since in the case of small fields this approach was shown to give results practically identical with those of the Monte Carlo method (Schmickler, 1983c), it should work particularly well in this case, where the only external field acting on the dipoles is that due to the spillover of the electrons from jellium.

Some of the results obtained for E_{PZC} are shown in table 2, where the jellium work function was used for the calculations. The theoretical values are in general too low, a fact which was explained remembering that jellium predicts very low

Table 2. Calculated and experimental values of the potential of zero charge of some *sp* metals.

Metal	calc E_{PZC}	exp E_{PZC}
Hg	−1·54	−0·193
Ga	−1·43	−0·69
Tl	−1·50	−0·71
Cd	−1·53	−0·75
In(Ga)	−1·48	−0·65
Pb	−1·45	−0·56

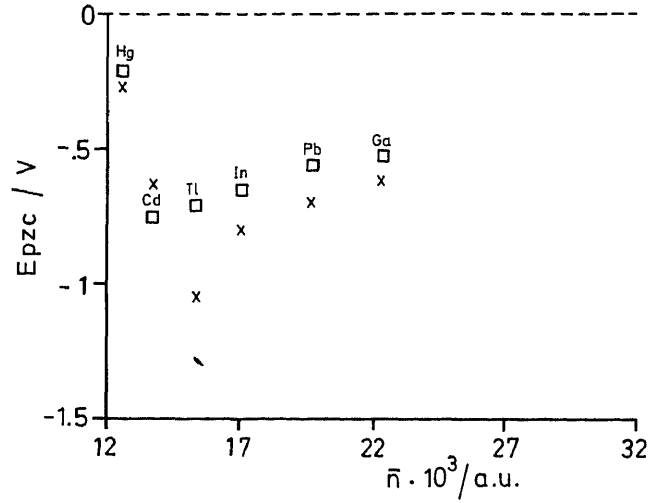

Figure 5. Calculated (x) and experimental (□) values of the potential of zero charge as a function of the electron density (Schmickler 1983b). Experimental values of Φ_{Me} were used here.

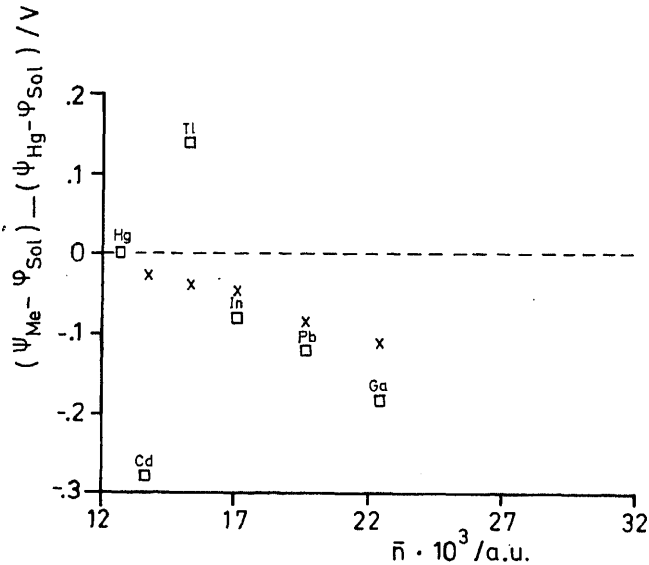

Figure 6. Dipole potential with respect to mercury as a function of the electron density. (x) Theoretical (Schmickler 1983b). (□) Experimental.

values for the work function. When instead of theoretical values experimental data for Φ_{Me} were used in calculating E_{PZC}, the results shown in figure 5 were obtained. The better agreement reflects the large contribution that Φ_{Me} makes in (25), as compared to the other terms.

The influence of Φ_{Me} disappears if we compare the experimental and the theoretical values of the dipole potential ($\psi_{Me} - \varphi_{sol}$). Furthermore, if we adopt a reference metal (e.g. Hg) for the comparison, we also get rid of the assumed values

endency with the electron density in both experiment and theory, Cd and Tl show different behavior. This may be due to the contribution of some specific factor, like he crystalline structure or atomic density, not contemplated in the homogeneous background jellium model. It is however gratifying that the correct qualitative behavior is predicted.

The model of hard spheres for electrolyte solutions

An approximate solution for the density profiles of an ensemble of hard spheres with embedded point charges, in a solvent of hard spheres with embedded point dipoles against a hard wall with smeared out surface charge, has been derived by Carnie and Chan (1980) and Blum and Henderson (1981). The detailed solution of his and other related systems is a very interesting problem which would require a whole chapter by itself, if not a book. Here, we just point out those aspects of the theory which are necessary for understanding the general model to be presented later, and note the main physical features which differentiate it from the conventional picture of the double layer.

In order to get the capacity of the system, a mathematical expression for the charge density of the ions $\rho_i(x)$ and the solvent polarization P_s is required. Correlation (h) and distribution functions (g) can be defined for ions and solvent:

$$g_i(X_i) = h_i(X_i) + 1 = \rho_i(X_i)/\rho_i, \tag{27}$$

$$g_d(X_d) = h_d(X_d) + 1 = \rho_d(X_d)/\rho_d, \tag{28}$$

where the distances $X_i(X_d)$ are measured perpendicularly to planes passing through the centers of spheres of diameters σ_i (σ_d) in contact with the hard wall, and ρ_i and ρ_d represent the mean bulk values for ion and dipole densities respectively. $g_d(X_d)$ is the first term in the expansion of the wall-dipole correlation function:

$$g_d(X_1\theta) = g_d^0(X_d) + (3)^{1/2}\,\Delta h_d(X_d)\cos\theta + \ldots, \tag{29}$$

where θ is the angle between the dipole and the normal to the surface.

For small charges, low electrolyte concentrations and equal sizes of ions and solvent molecules, g_i and $g_d(X,\theta)$ can be written in the form:

$$g_i(X) = g_0(X) + \Delta h_i(X), \tag{30a}$$

$$g_d(X_d,\theta) = g_0(X) + (3)^{1/2}\Delta h_d(X)\cos\theta, \tag{30b}$$

where $g_0(X)$ is the density profile of hard spheres near a discharged hard wall. Under these conditions, the transforms of $\Delta h_i(X)$ and $\Delta h_d(X)$ may be obtained (Henderson and Blum 1982).

$$\tilde{\Delta h}_i(S) = \frac{\beta' Z_i e_0 E}{\varepsilon K}\exp(-S\sigma/2)\left\{\frac{1}{K+S}\right.$$

$$\bar{\Delta}h_d(S) = -\frac{E\beta'\mu\beta_6^2}{(3)^{1/2}\beta_3}\exp(-S\sigma/2)\left\{1-\frac{K\sigma}{4}\frac{\beta_3}{\beta_{12}}\right.$$

$$\left.\times\left[\frac{\beta_6^2}{\beta_3^2}+2\varphi_1(S)\right]\right\}\Big/(K+S)\;A(S), \tag{32}$$

where K is the inverse Debye screening length, Z_i the ion charge, E the field, ε the bulk dielectric constant, $\beta' = 1/kt$, σ the diameter of the spheres, $\beta_3 = 1-b/3$, $\beta_6 = 1-b/6$; $\beta_{12} = 1+b/12$, where b is determined by:

$$\varepsilon = (\beta_{12}^4\,\beta_3^2)/\beta_6^6, \tag{33}$$

and μ by:

$$\mu^2 = \frac{3}{4\pi\rho_s\beta'}\left[\frac{\beta_3^2}{\beta_6^4}-\frac{\beta_6^2}{\beta_{12}^4}\right]. \tag{34}$$

The other functions in (31) and (32) are:

$$A(S) = 1-2\varphi_1(S)\,b(\beta_{12}/\beta_6^2) - 2\varphi_2(S)\,b(\beta_3/\beta_6^2),$$

$$\varphi_1(S) = (1-S\sigma-\exp(-S\sigma)/S^2\sigma^2, \tag{35}$$

$$\varphi_2(S) = (1-S\sigma+S^2\sigma^2/2-\exp(-S\sigma)/S^3\sigma^3.$$

By using (31), (32) and the second and third terms of (14), the potential difference across the interface can be calculated. Henderson *et al* (1983) found, after neglecting higher order terms in K:

$$\varphi_\infty - \varphi_{-\infty} = (E/\varepsilon K) + (E\sigma/2\bar{\varepsilon}), \tag{36}$$

where:

$$\bar{\varepsilon} = \varepsilon/[1+(\beta_6/\beta_3)(\varepsilon-1)]. \tag{37}$$

This equation is formally similar to the one which one would obtain from a Gouy–Chapman model of the double layer, in which the solvent is regarded as a uniform dielectric with constant ε in the diffuse layer, and a different dielectric constant $\bar{\varepsilon}$ in the inner layer. Does this mean that an inner layer, distinct from the rest of the fluid, actually exists? In order to investigate this, Henderson *et al* (1983)

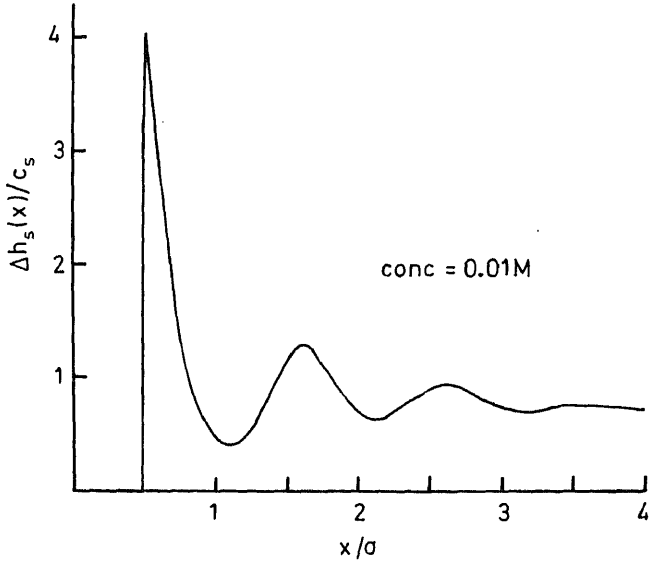

Figure 7. Inverse transform of (31) for a 0·01 M ion dipole monovalent electrolyte $\sigma = 0{\cdot}276$ nm. $T = 298$. $\varepsilon = 78{\cdot}4$. c_s is $-(\beta E \mu \beta_6^4)/(3^{1/2}\beta_3^2)$. Henderson *et al* (1983).

An oscillatory behavior, similar to that of Δh_d was also encountered for the oulombic potential felt by the ions, and a difference of the order of ten per cent vith respect to the prediction of the Gouy–Chapman theory was found for noderate electrolyte concentrations.

Summarizing, we can say that these results show a new picture for the double ayer, where the interfacial region of the solvent is as diffuse as the so-called ion iffuse layer. Moreover, experimental facts like the observed Parsons–Zobel plots Parsons and Zobel 1965) appear as a natural consequence of the theory. Just one lement is missing here, and that is the complex nature of the metal. It is the ubject of the next section.

. The jellium-hard spheres model

The above theoretical approaches for the metal and the solution were combined in Badiali *et al* (1983b) and Schmickler and Henderson (1984). We concentrate at first on the model which is more familiar to us (Schmickler and Henderson 1984), and later point out the essential differences with respect to the representation given in Badiali *et al* (1983b). A scheme of the model is shown in figure 8.

Several new features appeared in this description of the metal-solution interface:

The first layer of solvent molecules is oriented under the influence of the jellium tail extending into the solution. This must be contemplated in (30b), which was modified in the following way:

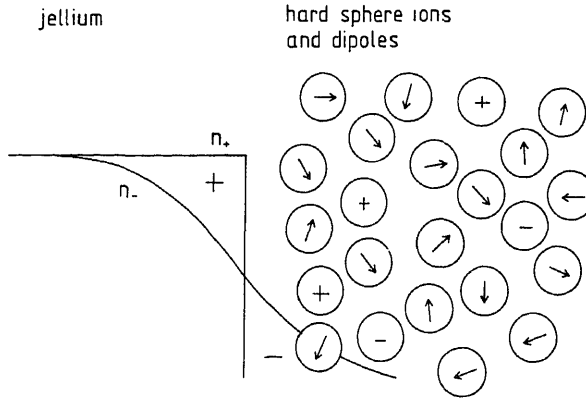

Figure 8. Schematic diagram of the jellium/hard spheres electrolyte model.

penetration of the solvent at the point $x = \sigma_d/2$ ($E_j = E(\sigma_d/2) - q/4\pi$). This constant was estimated from a previous Monte Carlo simulation (Schmickler 1983c), and found equal to:

$$a = 3\, g_0(\sigma_d/2)\, 1.10 \times 10^4\, E_j. \tag{39}$$

In this way, the new term in (38) accounts for the solvent dipole potential at the PZC.

A further improvement was the generalization of Schmickler and Henderson (1984b) for ions and solvent molecules of different radii (σ_d and σ_i):

$$\bar{\Delta}h_d = -\frac{E\beta'\mu\beta_6^2}{(3)^{1/2}\beta_3}\exp(-S\sigma_d/2)\left\{1-\frac{K(\sigma_d-\sigma_i)}{2}-\frac{K\sigma_d\beta_3}{4\beta_{12}}\right.$$
$$\left.\times\left[\frac{\beta_6^2}{\beta_3^2}+2\varphi_3(S)\right]\right\}\Big/(K+S)\;A(S) \tag{40}$$

where

$$A(S) = 1-2\varphi_1(S)\,b\,\frac{\beta_{12}}{\beta_6^2}-2\varphi_2(S)\,b\,\frac{\beta_3}{\beta_6^2},$$

$$\varphi_1(S) = \frac{1-S\sigma_d-\exp(-S\sigma_d)}{S^2\sigma_d^2}, \tag{41}$$

$$\varphi_2(S) = \frac{1-S\sigma_d+S^2\sigma_d^2/2-\exp(-S\sigma_d)}{S^3\sigma_d^3},$$

Three new terms were introduced in (9) for the surface energy of jellium: The electrostatic interaction of the electron plasma with the ions in the solution:

$$E_{\text{ion}} = \int_{\sigma_i/2}^{\infty} \varphi_j(x)\, \rho_c(x)\, \mathrm{d}x, \tag{42}$$

where ρ_c is the charge density profile in the solution.

The interaction between the jellium field and the solvent polarization is

$$E_{\text{dip}} = -\int_{\sigma_d/2}^{\infty} E_j(x)\, \rho(x)\, \mathrm{d}x, \tag{43}$$

The repulsion of the metal electrons from the closed shell of electrons on the olvent molecules:

$$E_{\text{rep}} = \int_{0}^{\infty} V_{\text{rep}}\, n(x)\, \mathrm{d}x, \tag{44}$$

where V_{rep} is a repulsive potential pertaining to the solvent molecules. Ideally, this otential should come from a quantum mechanical model of the solvent. Since such xpressions were not available, a repulsive barrier of the form,

$$V_{\text{rep}} = V_b\, \theta(x), \tag{45}$$

vas used. V_b was the only free parameter in the theory, and was chosen on a emiempirical basis for each particular solvent.

Using the trial functions of (10) for the metal and the correlation functions for he hard spheres system, the metal-solution potential difference in (14) was shown o be:

$$\varphi_{\infty} - \varphi_{-\infty} = \frac{4\pi\tilde{n}}{\beta^2} - \frac{4}{3}\, \rho_d \mu a + 4\pi q \left[\frac{\beta_6}{\beta_3} \frac{\sigma_d}{2} + \frac{1}{K\varepsilon} \left(1 + \frac{K\sigma_i}{2} - \frac{K\sigma_d}{2\lambda} \right) \right], \tag{46}$$

Note that if we now set $\sigma_d = \sigma_i$ and take the limit for $\beta \to \infty$, we get (36), which lescribes the system hard wall/hard spheres.

On the other hand, if the energy equation of jellium is solved for $q = 0$ and for a mall charge, the inverse capacity of the jellium-hard spheres interface can be umerically obtained. By applying this procedure, the influence of four parameters n the double layer capacity at the PZC was studied by Schmickler and Henderson 1984b): electrolyte concentration; temperature; electron density of the metal; olvent.

In all cases, a surprisingly good agreement with the experimental results was btained. We now consider each of these points.

In table 3, experimental and theoretical values of capacity are compared for

Table 3. Double layer capacity of mercury as a function of the electrolyte concentration.

c(M)	10^{-3}	10^{-2}	10^{-1}	1	∞
calc					
$C(\mu F.cm^{-2})$	6·0	13·6	22·6	28·7	32·5
exp					
$C(\mu F.cm^{-2})$	6	13	21	26	28·7
BH					
$C(\mu F.cm^{-2})$	5·1	9·8	13·8	15·9	17·1

After Schmickler and Henderson (1984).

Table 4. Inner layer capacity of mercury in contact with an aqueous solution.

t(C)	0	25	50	75
calc				
$C_H(\mu F.cm^{-2})$	34·2	32·5	30·8	29·3
exp				
$C_H(\mu F.cm^{-2})$	31·2	28·7	27·3	25·9

Experimental values are after Grahame (unpublished results, given by Parsons 1954). The theoretical values were taken from Schmickler and Henderson (1984).

presence of jellium brings to the theory, the results of the previous calculation for the system hard wall/hard spheres of Blum and Henderson (1981) are also quoted.

The temperature, electron density, and solvent effects were considered for the inner layer capacity. In this case, the experimental results were obtained by extrapolating the data according to (1). It is worth mentioning here that for small electrolyte concentration the theory also predicts a relationship of the type of (1):

$$1/C = 1/C_i + 4\pi/\varepsilon K. \tag{47}$$

However, the concentration independent term C_i now includes contributions to the capacity from both, the metal and the solution. Furthermore, this term involves not only the polarization of the first solvent layer but the contribution from the whole solution region.

Theoretical and experimental values of C_i at different temperatures are shown in table 4. The prediction of a lower C_i with increasing temperature is again in good agreement with the experimental data.

The nature of the metal, a factor very often omitted in the conventional theories of the double layer, was shown to play a very important role. In the homogeneous jellium model, the metal is completely characterized by its free electron density, so that this magnitude was used to represent C_i for different metals in figure 9. The increase of the surface polarizability with the electron density of jellium produces the corresponding increase of the calculated capacity. The second and third

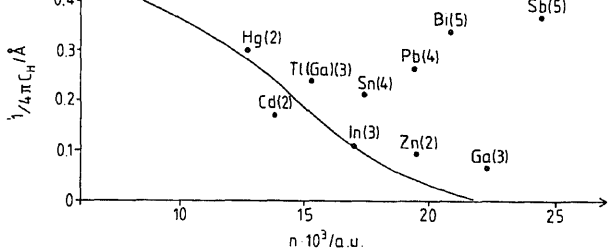

Figure 9. Inverse inner double layer capacity of the interphase water/*sp* metal as a function of the electron density (Schmickler and Henderson 1984): (——) Theory; (●) Experiment.

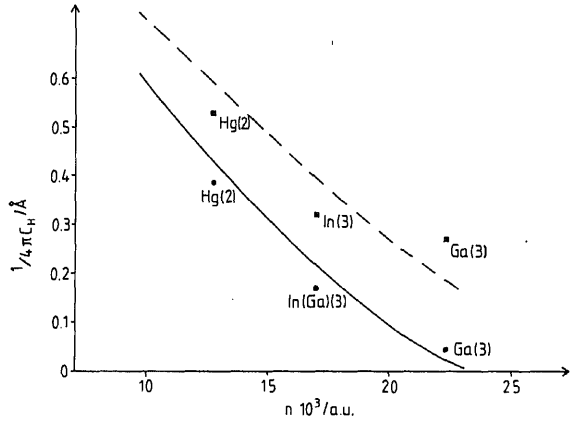

Figure 10. Inverse double layer capacity of *sp* metals. (●) and solid line DMSO, (■) and broken line acetonitrile. (Schmickler and Henderson 1984).

predictions quite well, while the fourth and fifth group elements Sb, Pb, Bi and Sb are out of line. This deviation can be attributed to chemical features which are not considered in the homogeneous background model. We shall see later that an improvement of this model is possible. Considering the discrete nature of the ion lattice in the pseudopotential approach, the results for the fourth and fifth group metals will be brought in better agreement with the experimental data. Also the divergence that appears in the theoretical results for large electron densities in figure 9 will be shown to be correctable. This can be done by employing better trial functions for the electron density.

Finally, the jellium/hard spheres model was also able to predict the correct trend for capacity results obtained with different solvents. In figure 10, experiment and theory are compared for DMSO and ACN (acetonitrile) as solvents.

The above presented jellium/hard spheres model differs in several aspects from that of Badiali *et al* (1983b). There, the diameter of ions and solvent molecules were assumed to be the same, while in Schmickler and Henderson (1984b) they were allowed to be different. A net orientation of the solvent at the PZC was also

introduced in Schmickler and Henderson (1984b). The most important difference is, however, in the treatment of jellium. Badiali *et al* (1983b) introduced pseudopotentials into the jellium model, which we shall also do below, and averaged these potentials over the whole metal region up to the jellium edge. The usual procedure is that the first layer of pseudopotentials must be half a lattice spacing behind the jellium edge, since this choice alone guarantees charge balance at the surface. In addition, Badiali and coworkers introduced an additional separation distance between the jellium edge and the ensemble of hard spheres; this introduces a second undetermined parameter into the model, which prevented them from obtaining quantitative results. However, conceptually these two works are very close.

4. Improvements on the jellium-hard spheres model

4.1 *Trial functions for the electron density. Heuristic extension for large charges on the electrode*

The effect of various approximations for the electronic density profile on the calculated capacity values was investigated in Schmickler and Henderson (1986). Two different types of trial functions were used there, and the results were compared with those obtained with the simple functions (10). They were:

$$n(X) = \begin{cases} \bar{n}[1-A\exp(\alpha X)], & X<0, \\ \bar{n}B\exp(-\beta X - KX^2), & X>0, \end{cases} \tag{48}$$

$$n(X) = \begin{cases} \bar{n}\,[1-A\exp(\alpha X)\cos(\Gamma X+\delta)], & X<0, \\ \bar{n}B\exp(-\beta X - K^2X^2), & X>0. \end{cases} \tag{49}$$

Both the functions and their first derivatives were required to be continuous, and the charge balance condition was applied. This led to two independent parameters in the first case, which were used for the variational procedure. The family (49) was additionally subjected to the half moment condition (11), so that the number of free parameters was reduced to three.

In the expansion (7) a second gradient correction ot the form:

$$E^{(2)} = \frac{1}{540(3\pi^2)^{2/3}} \int_{-\infty}^{\infty} n(X)^{-1/3} \left[\frac{1}{n(X)^2} \left(\frac{\mathrm{d}^2 n(X)}{\mathrm{d}X^2} \right)^2 - \right. \tag{50}$$

$$\left. - \frac{9}{8} \frac{1}{n(X)^3} \left(\frac{\mathrm{d}^2 n(X)}{\mathrm{d}X^2} \right) \left(\frac{\mathrm{d}n(X)}{\mathrm{d}X} \right)^2 + \frac{1}{3n(X)^4} \left(\frac{\mathrm{d}n(X)}{\mathrm{d}X} \right)^4 \right] \mathrm{d}X$$

With the two-parameter family the calculations were performed for a repulsive barrier of constant height (V_b = 1·6 eV) and of constant slope (V_s = 1·0 eV/A). The two resulting inverse capacity-electronic density curves were very close to each other (figure 11), indicating that the shape of the barrier is not a critical factor in the model. It is worth noting here that with a better trial function the divergence in the capacity has been shifted to more positive electronic densities. With the three parameter trial functions and a sloping barrier of 2·0 eV/A a divergence was not found over the investigated electron density range, while the best correlation with the experimental points was obtained.

Since the same qualitative behavior was obtained for all the variational profiles $n(X)$ employed, it can be expected that the error introduced by using an approximate solution is smaller than those due to the idealization for the model itself (e.g. the lack of structure of the metal). In the vaccum, the trial functions of (49) give results which are very close to the exact solution of Lang and Kohn (1970, 1971).

The influence of the family of trial functions on the capacity-charge curves was also studied in Schmickler and Henderson (1986). As previously stated, the polarization for a system of hard sphere dipoles and ions can be solved only for small charges on the electrode. A heuristic extension of the theory for larger charges was made on the following grounds: For small charges, the concentration independent contribution by the hard spheres to the potential difference is (Carnie and Chan 1980; Blum and Henderson 1981).

$$\Delta\phi_{\mathrm{hs}} = 4\pi q[\sigma_d/2\lambda + (\sigma_i - \sigma_d)/2\varepsilon]. \tag{51}$$

On the other hand, at very high fields, dielectric saturation of the solvent occurs and the potential difference has the form:

$$\lim_{q\to\infty} \Delta\phi_{\mathrm{hs}} = 2\pi\sigma_i q + \mathrm{const.} \tag{52}$$

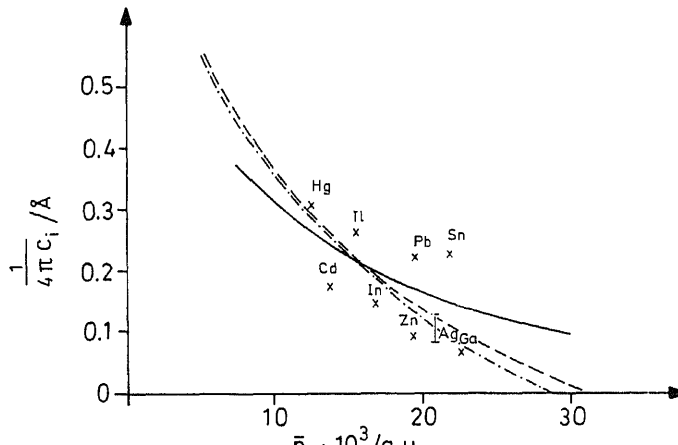

An interpolation formula between (51) and (52) must be based on a suitable function which gives the orientation of dipoles as a function of the field they experience. A natural choice is the Langevin function:

$$L\left(\frac{\mu E}{KT}\right) \; j \; L(x) = \coth(x) - (1/x), \tag{53}$$

where μ is the dipole moment, with the following result:

$$\Delta\phi_{hs} = 2\pi q\sigma_i - 2\pi\rho_d\mu\sigma_i \, L\left[4\pi q\mu \frac{q}{\lambda^2(\lambda+2)^2} \frac{(1-\sigma_d/\lambda\sigma_i)}{KT}\right]. \tag{54}$$

Calculations with the aid of (54) and the usual variational procedure showed similar capacity charge curves for the three families of equations (10), (48) and (49) at positive charge densities and in the proximities of the PZC (figure 12). However, the quality of the functions employed became a critical factor at negative charge densities, where the family (10) produces a sudden rise in the capacity and instead of a hump a shoulder is observed.

4.2 *Charge-dependent position of the effective hard wall for the hard spheres*
After analyzing a continuum model for the metal solution interphase, Kornyshev and Vorotyntsev (1984) suggested that a field-induced interfacial relaxation could play an important role on determining the capacity-charge behavior of this system. With this in sight, the influence of the previous assumption about the charge independent position of the effective hard wall was also investigated in Schmickler

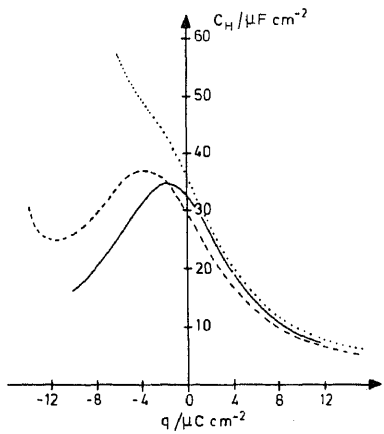

Figure 12. Capacity-charge characteristics for Hg ($\bar{n} = 0{\cdot}0128$ a.u.) with jellium representations of various quality. Dotted line: one-parameter family (10), constant barrier ($V_b a = 3$ eV); dashed line: two-parameter family (48), sloping barrier ($V_s = 1$ eV/A); full

with the charge density in such a way, that it is always at the same electronic density, namely the density at the jellium edge at zero charge. The change that this shift produces was shown to be:

$$\Delta\left(\frac{1}{4\pi C_i}\right) = X_w + q\frac{\partial X_w}{\partial q}, \tag{55}$$

resulting in reasonable electron densities in a second order effect.

4.3 *Pseudopotentials*

We have already seen that in the jellium model the metal is completely characterized by its free electron density n. In figures 9 and 10 it was also shown that this model gives good results for the inner layer capacity of *sp* metals of the second and third column of the periodic table. However, metals with high valence (IV–V) showed a systematic deviation, their capacities being lower than expected. The question arises whether this behavior is related to the discrete nature of the ionic lattice. Furthermore, experimental results for Ag single crystal surfaces (Valette and Hamelin 1973; Valette 1981, 1982) showed different capacity values for the 111, 110 and 100 faces, which does indicate an influence of the lattice.

The jellium/hard spheres model was extended by Henderson and Schmickler (1985), who calculated the capacity for different Ag crystal faces. We give here a short description of the features introduced in the model.

Following Lang and Kohn (1970), the constant positive background of jellium was replaced by a lattice of local ion pseudopotentials of the Ashcroft type (Ashcroft 1966):

$$V_{sp}\begin{cases} 0 & r \leqslant r_c \\ -Z/r & r > r_c, \end{cases} \tag{56}$$

where Z is the ionic charge, r is the radius measured from the lattice point and r_c is a cutoff radius which is determined for each metal to give a correct description of its bulk properties. The first plane of pseudopotentials stays at one half of the distance between lattice planes (d) from the surface (figure 13).

Two new terms appear in the equation for the jellium surface energy (9). One represents the cleavage energy of the infinite metal to form two new surfaces, where the electron density is held uniform up to the nominal metal boundary:

$$\delta\sigma_{\mathrm{cl}} = \Omega Z\bar{n}, \tag{57}$$

where Ω is a dimensionless constant which can be calculated on purely electrostatic basis. The second term is:

$$\delta\sigma_{\mathrm{ps}} = \int^{+\infty} \delta_v(X)[n(X) - \bar{n}\theta(-X)]\,\mathrm{d}X, \tag{58}$$

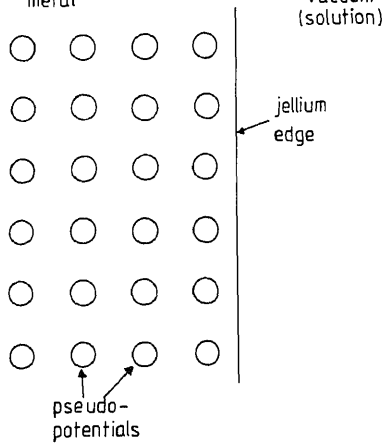

Figure 13. Jellium with a pseudopotential lattice.

where $\delta_v(X)$ is the average over the plane perpendicular to the metal surface of the sum of the ionic pseudopotentials of the half lattice, minus the potential due to the semi-infinite uniform charge background. Equation (58) thus represents the energy difference between two relaxation processes: that of the initial uniform electron density to its actual form $n(X)$ in the pseudopotential model, and the same change in the uniform background model.

$\delta\sigma_{cl}$ is independent of the form of the trial function employed, so that it can be excluded from the minimization procedure. An expression for $\delta_v(X)$ was also derived in Lang and Kohn (1971)

$$\delta_v(X) = 2\pi\bar{n}\,\{d[r_c - |x+(l+1/2)|]\,\theta(r_c - |x+(l+1/2)d|) - \\ -[x+ld+d\theta(-x-\frac{d}{2})]^2\}, \tag{59}$$

where $l = 0,1,2,3\ldots$ labels the lattice planes. By using (58), (59) and the trial function of (10), it can be shown that:

$$\delta_v(X) = (2\pi\bar{n}/\beta^3)\,(\bar{n}+\beta q)[1-\beta d\exp(-\beta d/2)\cosh(\beta r_c)/(1-\exp(-\beta d)]. \tag{60}$$

Theoretical and experimental values of capacity for Ag single crystal surfaces in contact with water are shown in table 5. Both, experimental and theoretical values of capacity present the same sequence: $C_{110} > C_{100} > C_{111}$, which can be correlated with the lower polarizability that the more compact faces show. Only qualitative agreement was expected, since Ag is an *sd* metal, and the jellium model is not quantitatively adequate for the description of such systems. The same general trend can be formulated for the capacity of other single crystal surfaces: The more compact faces should have the lower capacity. This is the case of Bi (Pal'm *et al* 1977), where the sequence $C_{111} > C_{011} > C_{211}$ corresponds with an increasing

Table 5. Interfacial inner layer capacity for Ag single crystal surfaces in aqueous electrolyte solutions.

face	d/nnd[a]	exp $C(\mu\text{Fcm}^{-2})$	calc $C(\mu\text{Fcm}^{-2})$
111	$(2/3)^{1/2}$	69	18·3
100	$1/(2)^{1/2}$	90	19·3
110	1/2	108	25·2

After Henderson and Schmickler (1985).

Table 6. Charge number Z and Ashcroft radius r_c (in a.u.) of several *sp* metals.

Metal	Z	r_c^1	r_c^2
Zn	2	1·11	1·06
Cd	2	1·23	1·19
Hg	2	1·25	1·10
Ga	3	1·11	1·05
In	3	1·12	1·15
Tl	3	1·13	1·11
Sn	4	1·12	1·11
Pb	4	1·08	1·04
Sb	5	1·06	–
Bi	5	1·08	–

[1] From Harrison (1980); [2] after Appapillai and Heine (1973) quoted by Hietschold *et al* (1975).

Since most experimental data for the inner layer capacity of *sp* metals refer to polycrystalline surfaces, some averaging of the pseudopotentials should be made in order to compare theory and experiment. One possibility consists in taking a given crystal structure (i.e. *fcc*), and averaging the pseudopotential energy over the principal crystal planes. Calculations using this procedure for different metals were performed by Leiva and Schmickler (1986). Since at this time a generalization of the Budd and Vannimenus theorem for jellium with pseudopotentials was not available, the one parameter family functions of equation (10) were employed. Two sets of pseudopotential radii were used, which were derived from different bulk properties. Their values are given in table 6.

As previously stated, experimental and theoretical results can be compared by plotting the inverse capacity as a function of the electron density. However, in the jellium (pseudopotential) model the capacity is not only a function of the electron density but also of the pseudopotential radius r_c and of the atomic density n_A. In fact, the distance between lattice planes has the form:

$$d = (3/4\pi n_A)^{1/3} G, \tag{61}$$

where G is a geometrical factor which depends on the face and lattice type.

A second possibility for comparing experiment and theory, providing at the same

inner layer capacity can be written in the form:

$$1/C_i = 1/C_m + 1/C_s, \tag{62}$$

where C_m and C_s represent the contribution to the capacity by the metal and the

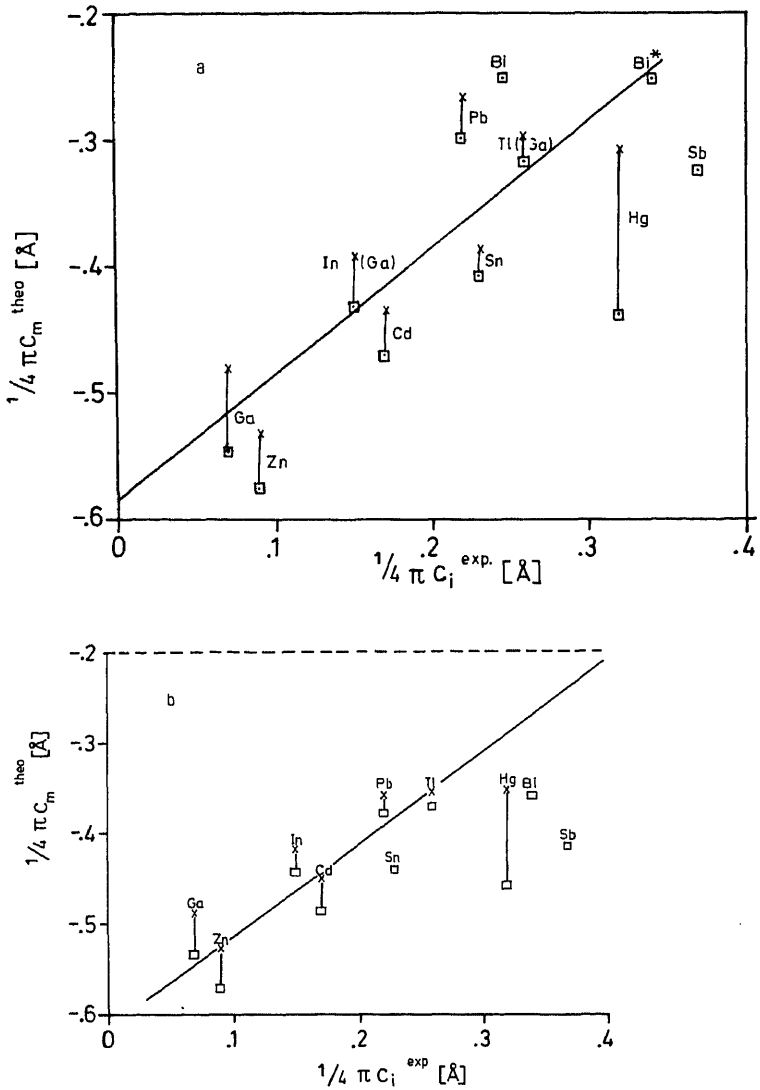

Figure 14. (**a**) Plot of the calculated inverse metal capacity versus the experimental inverse inner layer capacity of aqueous solutions (Leiva and Schmickler 1986). The experimental values are from Trasatti (1981) except for Sb, which is from Frumkin *et al* (1974). For Bi, the values given both by Trasatti and by Frumkin (asterisk) are indicated. Crosses denote values calculated from the Appapillai and Heine potentials, boxes from the Harrison's values. (**b**) Calculations similar to those of (**a**), but using the two

olution respectively. From (62) we get:

$$1/C_m = 1/C_i - 1/C_s. \tag{63}$$

f we represent now the theoretical values of $1/C_m$ as a function of experimental alues of $1/C_i$, a straight line with slope unity should be obtained, with an ordinate vhich contains the contribution of the solution. This is shown in figure 14. A linear elation with a slope of one is obtained, with an intercept on the ordinate axis which s practically equal to that predicted by the hard spheres model. For these alculations, the barrier which represents the interaction of the electron plasma vith the solvent was set equal to zero, so we can say that the theory is now arameter free. Thus, one could quickly conclude that the interaction with the olvent can be neglected. However, some kind of compensation may arise, since he trial functions used were of the type of (10). The lower polarizability which hese one-parameter functions confer is that jellium could compensate the lack of a epulsive barrier. This has been confirmed by recent calculations (E Leiva and W chmickler, unpublished results) where the family (12) was used applying the Budd–Vannimenus theorem as the boundary condition. If we do not impose a epulsive barrier, we obtain again a linear correlation of the type (63), but the ntercept is unreasonably small. Only on application of a repulsive barrier do we btain a reasonable value for the solvent contribution to the inverse capacity (see igure 14b).

. Conclusions

Ve have taken a bird's eye view of the new theories for the electrochemical double ayer. In the most successful of these models, both metal and solvent contribute lmost equally to the double layer capacity. The contribution of the metal comes rom the polarizability of the electronic plasma. On the solution side, the presence f the metal affects not only the first solvent layer, but a region of a similar spacial xtension as the diffuse double layer. For quantitative calculations, at the most one emiempirical parameter is required, which is constant for a particular solvent. So ar, the theory has correctly predicted the dependence of the double layer capacity n:

1) the electrolyte concentration; (2) the temperature (for the interface Hg/H_2O); 3) the nature of the metal (for *sp*-metals); (4) the solvent (for water, DMSO, and cetonitrile); (5) the crystalline face of the metal for single crystal surfaces (so far or Ag and Bi in contact with aqueous solution); (6) first order deviations from the arsons and Zobel plot (see Blum *et al* 1984); (7) the correct trend for dipole otentials at the PZC.

Concerning the last point, it is interesting to return to figure 1, where an mpirical correlation between inverse capacity and dipole potential was shown. A imilar plot of the calculated inverse capacity of the metal vs. calculated dipole

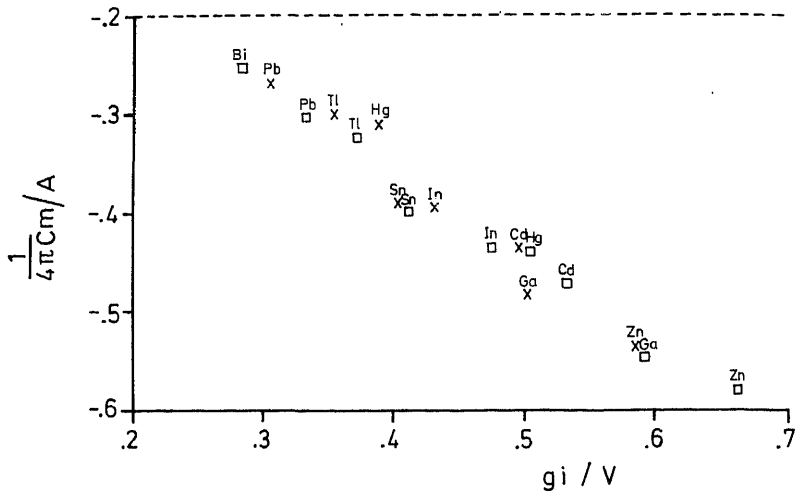

Figure 15. Calculated inner layer capacity, as a function of theoretical values for the dipole potential $-(\psi_{Me}-\varphi_{sol})$ for aqueous solutions. Appapillai (x) and Harrison (□) pseudopotentials.

the capacity of the metal is related to the capacity of the solution through:

$$1/C_m = 1/C_i - 1/C_s.$$

Secondly, g_i of figure 15 is defined according to:

$$g_i = (\psi_{Me} - \varphi_{sol}),$$

that is, g_i contains information about the change of the dipole potentials of both, metal ($\delta\chi_{Me}$) and solution ($\delta\chi_{sol}$). On the other hand, the dipole potentials of figure 1 should correspond only to those of water in the presence of the metal. However, as Trassati assumed $\delta\chi_{Me}$ to be the same for all metals, so the change of g_i in figure 1 should reflect also the differences in $\delta\chi_{Me}$ for the different metals. So, our values differ by a constant from those of Trasatti (1979). However, the relative changes of g_i should be comparable.

It is clear that the theoretical trend of figure 15 reflects well the experimental correlation of figure 1. The absolute position of the points in figure 15 depends on the kind of the pseudopotentials used, but the general trend indicates that a higher capacity is related to a higher dipole potential.

Acknowledgements

One of the authors, WS acknowledges financial support by the Deutsche Forschungsgemeinschaft and by the Fond der Chemischen Industrie

thank the Deutscher Akademischer Austauschdienst and the Consejo Nacional
e Investigaciones Cientificas y Tecnicas (Argentina) for scholarships.

eferences

ppapillai M and Heine V *Tech. Rep. Cavendish Lab.*, No. 5(973)
shcroft N W 1966 *Phys. Lett.* **23** 48
ıdiali J P, Goodisman J and Rosinberg M 1980 *J. Electroanal. Chem.* **150** 2949
ıdiali J P, Goodisman J and Rosinberg M 1981 *J. Electroanal. Chem.* **130** 31
ıdiali J P, Goodisman J and Rosinberg M 1983a *J. Electroanal. Chem.* **143** 73
ıdiali J P, Rosinberg M L, Vericat F and Blum L 1983b *J. Electroanal. Chem.* **158** 253
ım L and Henderson D 1981 *J. Chem. Phys.* **74** 1002
ım L, Henderson D and Parsons R 1984 *J. Electroanal. Chem.* **172** 389
ıdd H F and Vannimenus J 1973 *Phys. Rev. Lett.* **31** 1212, 1430(E)
ırnie S L and Chan D Y C 1980 *J. Chem. Phys.* **73** 2949
ımkin A, Damaskin B, Grigoryev N and Bagotskaya I 1974 *Electrochim. Acta* **19** 69
es P and Gerhardts R R 1986 *Phys. Rev.* **B33** 982
arrison W A 1980 *Electronic structure and the properties of solids* (San Francisco: W H Freeman and Co.) table after p. 550
enderson D and Blum L 1982 *J. Electroanal. Chem.* **132** 1
enderson D, Blum L and Lozada-Cassou M 1983 *J. Electroanal. Chem.* **150** 291
enderson D and Schmickler W 1985 *J. Chem. Phys.* **82** 2825
etschold M, Paasch G and Ziesche P 1975 *Phys. Status Solidi* **B70** 653
einrichs J and Kumar N 1975 *Phys. Rev.* **B12** 802
ohenberg P and Kohn W 1964 *Phys. Rev.* **B136** 864
ttel C 1975 *Introduction to solid state physics* (New York: John Wiley & Sons)
ornyshev A A, Schmickler W and Vorotyntsev 1982 *Phys. Rev.* **B25** 5244
ornyshev A A and Vorotyntsev M A 1984 *J. Electroanal. Chem* **167** 1
ng N D and Kohn W 1970 *Phys. Rev.* **B1** 4555
ng N D and Kohn W 1971 *Phys. Rev.* **B3** 125
ng N D and Kohn W 1973 *Phys. Rev.* **B7** 3541
iva E and Schmickler W 1986 *J. Electroanal. Chem.* **205** 323
ndquist S and March N H (eds) 1983 *Theory of the inhomogeneous electron gas* (New York: Plenum Press)
a C Q and Sahni V 1979 *Phys. Rev.* **B19** 1290
l'm U V, Pyarnoya M P and Salve M 1977 *Elektrokhimiya* **13** 873
rsons R 1954 in *Modern aspects of electrochemistry* (ed.) J O'M Bockris (London: Butterworths) vol. 1, p. 148
rsons R and Zobel F G R 1965 *J. Electroanal. Chem.* **9** 333
rtenskii M and Smorodinskii Ya 1974 *Sov. Phys. Solid State (Engl. Transl.)* **16** 423
ice D and Halley J W 1983 *J. Electroanal. Chem.* **150** 347
eeves R 1980 in *Comprehensive treatise of electrochemistry* (eds) J O'M Bockris, B E Conway and E Yeager (New York: Plenum press) vol. 1, chap. 3
ce O K 1928 *Phys. Rev.* **31** 1051
hmickler W 1983a *J. Electroanal. Chem.* **150** 19
hmickler W 1983b *Chem. Phys. Lett.* **99** 135
hmickler W 1983c *J. Electroanal. Chem.* **157** 1
hmickler W 1984 Proceedings of the NATO Summer School on Trends in Interfacial Electrochemistry, Viana de Castelo, Portugal
hmickler W and Henderson D 1984a *Phys. Rev.* **B30** 3081
hmickler W and Henderson D 1984b *J. Chem. Phys.* **80** 3381
hmickler W and Henderson D 1984c *J. Electroanal. Chem.* **176** 383
hmickler W and Henderson D 1986 *J. Chem. Phys.* (in press)

Trasatti S 1977 in *Advances in electrochemistry and electrochemical engineering* (eds) H Gerisc
C W Tobias (New York: Wiley-Interscience) vol. 10
Trasatti S 1979 in *Modern aspects of electrochemistry* (eds) B E Conway and J O'M Bockris (Ne
Plenum Press) vol. 13
Trasatti S 1981 *J. Electroanal. Chem.* **123** 121
Valette G and Hamelin A 1973 *J. Electroanal. Chem.* **45** 301
Valette G 1981 *J. Electroanal. Chem.* **122** 285
Valette G 1982 *J. Electroanal. Chem.* **138** 37
Van den Eeden A L G, Sluyters J H and Van Leuthe J H 1984 *J. Electroanal. Chem.*
Vannimenus J and Budd H F 1974 *Solid State Commun.* **15** 1739

Calculation of the density profile of a system of hard spheres near a hard wall using the Henderson–Plischke and related approximations[§]

DOUGLAS HENDERSON * and MICHAEL PLISCHKE **

IBM Almaden Research Center, 650 Harry Road, San Jose, California 95120–6099, USA
** Department of Physics, Simon Fraser University, Burnaby, BC V5A 1S6, Canada

Abstract. The first Born–Green equation for an inhomogeneous fluid, which relates the density profile and an integral of the pair distribution of the fluid, is solved for the particular case of a system of hard spheres near a hard wall. The recent approximation of Henderson and Plischke, which is constructed from the Kirkwood superposition approximation and the Percus shielding approximation, is used for the pair distribution function. The results for the density profile are in reasonably good agreement with Monte Carlo simulations; they are very good near the wall but at larger distances are slightly worse than earlier analytic results obtained from the less sophisticated singlet theory which does not involve the inhomogeneous fluid pair correlation function.

Keywords. Density profile; Born–Green equation; Henderson–Plischke approximation; hard sphere/hard wall system.

Introduction

ome years ago, Henderson *et al* (1976) obtained the singlet Ornstein–Zernike quation for the density profile of an inhomogeneous fluid. The advantage and isadvantage of this approach is that only pair functions of the homogeneous (bulk) uid and singlet density profiles of the inhomogeneous fluid appear and one is not ced with the need to approximate pair functions of the inhomogeneous fluid.

Henderson *et al* (1976) using the singlet Ornstein–Zernike equation and the ercus–Yevick approximation (Percus and Yevick 1958) obtained an analytic xpression for the Laplace transform of the density profile. This transform was ubsequently inverted analytically by Smith and Henderson (1978). Except in the nmediate vicinity of the wall, this density profile is in good agreement with the omputer simulations of Snook and Henderson (1978) and Henderson and van wol (1984) of the hard sphere/hard wall system.

At contact with the hard wall, this singlet Percus–Yevick (hereinafter called PY1) ensity profile falls to satisfy the exact relation, obtained from force balance onsiderations,

$$n(0) = \beta p \ , \tag{1}$$

here $n(z)$ is the density and z is the perpendicular distance from the wall, $= 1/kT$ (T is the temperature and k is the Boltzmann constant), and p is the ressure, but instead gives the incorrect result

---

§ Dedicated to Professor K. S. G. Doss on his eightieth birthday

where $\rho = n(\infty)$ is the bulk density of the fluid. Waisman *et al* (1976) and Henderson and Plischke (1985) have proposed simple semiempirical corrections to the PY1 $n(z)$ for the hard sphere/hard wall system which satisfy (1) and are generally in good agreement with the simulation results at all z. The only remaining problem with these semiempirical $n(z)$ for the hard sphere/hard wall system is that the first minimum in $n(z)$, near $z = 0{\cdot}5d$, where d is the hard sphere diameter, is too deep. Generally this is a minor failing. However, at very high densities this minimum becomes negative, which is unphysical.

The singlet Ornstein–Zernike equation approach has been applied to electrochemical problems. Blum (1977) has used the mean spherical approximation to study the charged hard sphere/charged hard wall (double layer) system and Henderson *et al* (1979), Carnie *et al* (1981), Lozada-Cassou *et al* (1982), Lozada-Cassou and Henderson (1983), and Carnie (1985) have used the hypernetted chain approximation (hereinafter called HNC1) to study this system. The HNC1 results are generally quite good. However, instead of satisfying the exact contact condition,

$$n(0)kT = p + E^2/8\pi\varepsilon, \tag{3}$$

the HNC1 $n(z)$ satisfies

$$n(0)kT = \frac{1}{2}\,\rho kT\left(1+\beta\,\frac{\partial p}{\partial \rho}\right)+E^2/8\pi\varepsilon. \tag{4}$$

In many applications this error is not serious because the second term, $E^2/8\pi\varepsilon$, dominates. Also for electrolytes, if a continuum model of the solvent is used. the density of hard spheres is low and the difference between $\beta p/\rho$ and $\frac{1}{2}(1+\beta(\partial p/\partial\rho))$ is not too great. However, if discrete models of the solvent are used or if a high density system of charged hard sphere is used to describe a fused salt double layer, the error in the first term on the right hand side of (4) is much more serious.

Recently, Croxton and McQuarrie (1979, 1981), Henderson *et al* (1981), Lozada (1981), Blum *et al* (1983) and Caccamo *et al* (1986) have used the first Born–Green (BG) equation (Born and Green 1946) to study double layer problems. They obtain results which are as reliable as those of the HNC1 approach. In contrast to the HNC1 approach, the BG theory requires that the pair correlation function be approximated. However, because the BG equation is obtained from force balance considerations, the density profile obtained from the BG equation automatically gives the correct value for the density profile at contact, no matter what approximation is used for the pair correlation function, provided, of course, that this approximate pair correlation function is correct in the bulk.

The modified Poisson–Boltzmann (MPB) approximation (Outhwaite 1978, 1983; Levine and Outhwaite 1978; Outhwaite *et al* 1979, 1980, 1981; Bhuiyan *et al* 1979, 1981; Levine *et al* 1981; Outhwaite and Bhuiyan 1982, 1983) is also accurate for electrolytes and is similar in spirit to the BG approximation in as much as an approximation for the pair correlation function must be introduced before $n(z)$ can be calculated.

In the above applications of the BG and MPB theories, the pair correlation

Zernike equation for the inhomogeneous fluid self consistently with the first BG equation, or an equivalent relation between pair and single functions, to obtain the pair correlation function and the density profile. Depending upon whether the Percus–Yevick or hypernetted chain approximations are used in the inhomogeneous Ornstein–Zernike equation, we refer hereinafter to these systems of equations as the PY2 of HNC2 equations.

To date PY2 and HNC2 results have been obtained only for the hard sphere/hard wall system and the Lennard–Jones fluid/hard wall system. However, in principle at least, the method can be applied to electrochemical problems. The Plischke–Henderson procedure is very promising but computationally very difficult. As a result, simple approximations for the pair correlation functions are still of great interest.

Because of the relative complexity of the charged hard sphere/charged hard wall system, the approximations used for the pair correlation function in the Croxton–McQuarrie and Caccamo *et al* BG calculations and in the MPB calculations cannot be tested directly (at present, at least). Instead the approximations are tested by examination of the resulting density profile.

Values for the pair correlation function of an inhomogeneous fluid, obtained by computer simulation, exist only for the hard sphere/hard wall system (Snook and Henderson 1978; Henderson and van Swol 1984). As a result it seems worthwhile to consider this system and examine available approximations for the pair correlation function both by direct comparison with the simulation results and by study of the density profiles obtained by a self consistent solution of the BG equation.

2. Theory

The first Born–Green (BG) equation is obtained by formally differentiating the density profile $n(z)$ with respect to z,

$$-kT\frac{\partial \ln n(z)}{\partial z} = \frac{\partial V(z)}{\partial z} + 2\pi\int_{-\infty}^{\infty}(z-z')n(z')\mathrm{d}z' \times \int_0^{\infty} g(r', z, z')\frac{\partial u(R')}{\partial R'} r'\mathrm{d}r' , \tag{5}$$

where cylindrical coordinates, r' and z', have been used. In (5) $V(z)$ is the external potential due to the wall and $u(R)$ is the pair potential between fluid particles separated by a distance R, $g(r', z, z')$ is the pair correlation for 2 particles at z and z' separated by a distance, R' which is related to r' and z' by

$$R'^2 = r'^2 + (z-z')^2. \tag{6}$$

For the specific case of the hard sphere/hard wall system, (5) becomes

$$\frac{\partial \ln n(z)}{\partial z} = 2\pi \int_{[0,\, z-d]}^{z+d} (z-z')n(z')G(z,z')\mathrm{d}z', \tag{7}$$

where $[0, z-d]$ indicates that the maximum of 0 and $z-d$ is to be used, d is the hard sphere diameter, and $G(z, z')$ is the value of $g(r', z, z')$ when the two spheres at z and z' are in contact.

It is necessary to specify $G(z, z')$. The best known approximation for $g(r, z, z')$ is the superposition approximation (Kirkwood 1935),

$$g(r, z, z') = g(r), \tag{8}$$

where $g(r)$ is the radial distribution function of the bulk fluid. Recently, Percus (1980) has proposed the approximation

$$g(r, z, z') = [\rho/n(z_{\max})]g(r), \tag{9}$$

where $\rho = n(\infty)$ and $z_{\max}$ is the height of the sphere which is furthest from the wall. Physically, (9) implies that the inner sphere shields the outer sphere from the wall and for this reason Percus called (9) the shielding approximation.

Comparison with computer simulations shows that (8) is best (at high densities, at least) for $z_1 = z_2$ while (9) is best for $r = 0$ or $R = |z-z'|$. This suggests that a hybrid approximation incorporating the best features of the superposition and shielding approximations would be useful. Henderson and Plischke (Plischke and Henderson 1984; Henderson and Plischke 1985) have constructed such an approximation. They write

$$\begin{aligned} G(z_1, z_2) = {} & |z_1 - z_2|\,[\rho d^{-1}/n(z_{\max})]g(d) \\ & + (1 - |z_1 - z_2|/d)\,[1 + c(z_1, z_2)h(d)], \end{aligned} \tag{10}$$

where $n(z_{\max}) = n(0{\cdot}75d)$ for $z_{\max} < 0{\cdot}75d$, $h(d) = g(d) - 1$, $g(d)$ is the radial distribution function at contact for the bulk fluid, and

$$c(z_1, z_2) = \begin{cases} c - \dfrac{1-c}{2}\,[3(z_1+z_2) - (z_1+z_2)^3], & z_1 + z_2 < d \\ 1, & z_1 + z_2 > d. \end{cases} \tag{11}$$

The function $A\ (z_1, z_2)$ of Caccamo *et al* (1986) seems to play the same role as $c(z_1, z_2)$. The parameter c has been determined from theoretical considerations by Henderson and Plischke (1985). For simplicity, the fit

$$c = 0{\cdot}5 + 1{\cdot}03\rho d^3 - 0{\cdot}5\rho^2 d^6, \tag{12}$$

can be used. To complete (10) we must specify $g(d)$. We use the essentially exact Carnahan and Starling (1969) result,

$$g(d) = (1 - \eta/2)/(1-\eta)^3, \tag{13}$$

where $\eta = \pi\rho d^3/6$.

When $|z_1 - z_2| = d$

$$G(z_1, z_2) = [\rho/n(z_{\max})]\, g(d), \tag{14}$$

$$G(z_1, z_2) = 1 + c(z_1, z_2)h(d). \tag{15}$$

At high densities $c(z_1, z_2) \simeq 1$ and (14) becomes the superposition approximation. At low densities

$$G(0,0) = 1 + \frac{1}{2}h(d), \tag{16}$$

which is exact, the factor of $\frac{1}{2}$ accounting for the exclusion of the hard spheres from half of the space.

Thus, (10) yields the correct limits. Direct comparison with computer simulations shows it to be a reliable approximation.

3. Results

We have calculated $n(z)$ by numerical integration, with 1001 Trapezoid rule integration points, of either

$$n(z) = \rho - 2\pi \int_z^\infty n(z')\mathrm{d}z' \int_{[0,z'-d]}^{z'+d} (z'-z'')n(z'')G(z',z'')\mathrm{d}z'' \tag{17}$$

or

$$\ln n(z) = \ln \rho - 2\pi \int_z^\infty n(z')\,\mathrm{d}z'$$

$$\times \int_{[0,z'-d]}^{z'+d'} (z'-z'')n(z'')G(z',z'')\mathrm{d}z'' \tag{18}$$

It is worth noting that for the shielding and superposition approximations, one integral in (17) or (18) can be obtained analytically by reversing the order of integration (Henderson *et al* 1981; Wertheim 1986). Wertheim (1986) further gives analytic results for $n(z)$ for the shielding approximation for the hard sphere/hard wall system but gives no numerical results for this system. Since our main interest is the Henderson-Plischke approximation, we do not make use of any of these simplifications since they do not apply to this approximation.

The calculation proceeded by using the Henderson *et al* (1976) PY1 $n(z)$ as an initial guess and then iterating, using as subsequent iterates

$$n_{\mathrm{in}}^k(z) = \alpha n_{\mathrm{out}}^k(z) + (1-\alpha)\, n_{\mathrm{in}}^{k-1}(z), \tag{19}$$

with $\alpha = 0{\cdot}05$, until self consistency was achieved. The solution was deemed self consistent if

$$\sum_{i=1}^{1001} \{n_{\mathrm{out}}^k(z_i) - n_{\mathrm{out}}^{k-1}(z_i)\}^2 < 10^{-5}. \tag{20}$$

At low densities the iteration was very fast. Even at high densities only slightly more than 100 iterations were needed, requiring no more than a few minutes of

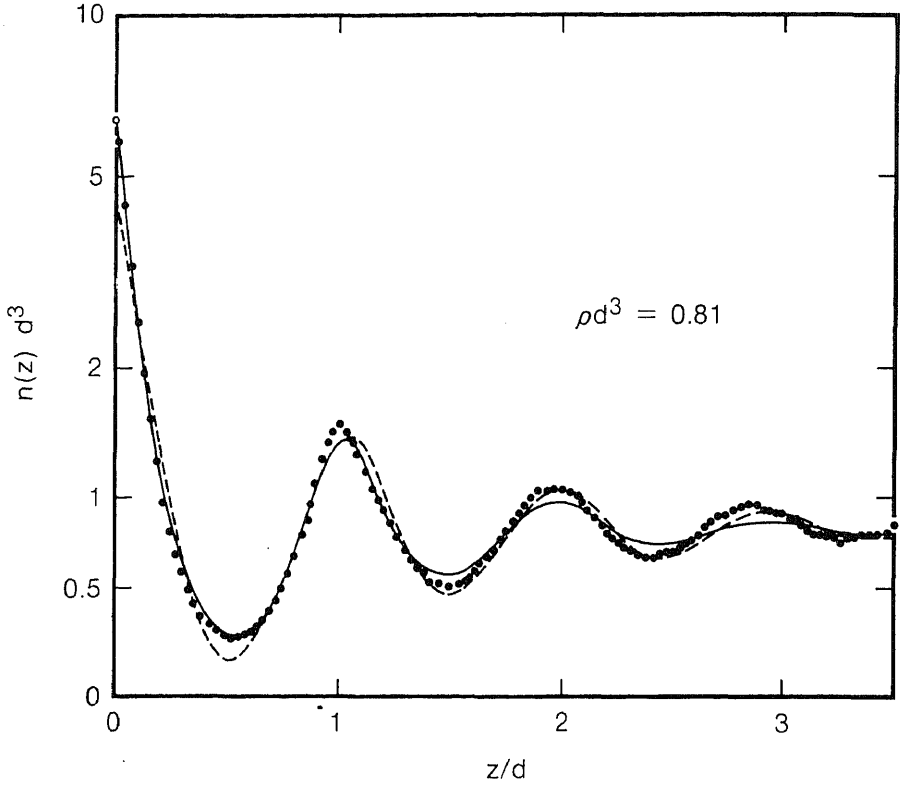

Figure 1. Density profile for hard spheres of diameter d near a hard wall for $\rho d^3 = 0{\cdot}81$. The points given over the computer simulation values of Snook and Henderson (1978) and the solid and broken curves gives the values obtained from (7) and (10), the Henderson–Plischke approximation, and from the PY1 theory (Henderson *et al* 1976), respectively.

required slightly fewer iterations and gave slightly more accurate results, judged from the values of $n(0)$.

In figure 1 we give the resulting values of $n(z)$ at $\rho d^3 = 0{\cdot}81$, calculated using the Henderson–Plischke approximation. The agreement with computer simulation results (Snook and Henderson 1978) is good. It is better than the PY1 result at small z but is somewhat inferior at larger z.

It is of interest to examine the BG results using the superposition approximation and the shielding approximation. We were unable to obtain a solution at $\rho d^3 = 0{\cdot}81$ using the superposition approximation. For this reason we examine the results of these approximations at lower density, $\rho d^3 = 0{\cdot}7028$, in figure 2. Comparison with the simulation results (Henderson and van Swol 1984) shows that the superposition approximation results in an overestimation of the oscillations in $n(z)$ whereas the shielding approximation underestimates these oscillations. Both approximations result in $n(z)$ which are out of phase with the computer simulation results. On the whole the shielding approximation yields better results.

Finally, it is interesting to examine the superposition, shielding, and Henderson–Plischke approximations for $G(z_1, z_2)$. We do this at $\rho d^3 = 0{\cdot}81$ because we do not

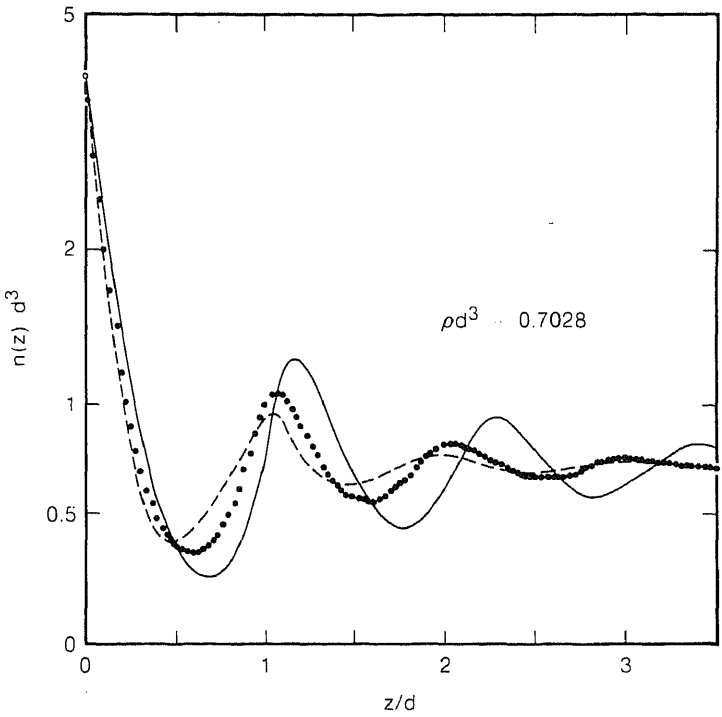

Figure 2. Density profile for hard spheres of diameter d near a hard wall for $\rho d^3 = 0{\cdot}7028$. The points give the computer simulation values of Henderson and van Swol (1984) and the solid and broken curves give the values obtained from (7) with the superposition and shielding approximations, respectively.

values of $n(z)$ are not needed to produce $G(z_1, z_2)$ from the superposition approximation.

As pointed out by J R Henderson and van Swol, the Snook and D Henderson simulation values for $g(r_{12}, z_1, z_2)$ are somewhat in error near the wall. It would be preferable to use their values. However, the only available values, at least to us, from their simulation are for $z_1 = z_2 = 0$. Thus, we have no alternative but to use the Snook and D Henderson results for $G(z_1, z_2)$. They are plotted for $z_1 = 0$, $0 < z_2 < d$ in figure 3. We corrected the Snook and D Henderson simulation results in an *ad hoc* but reasonable manner. The results of J R Henderson and van Swol indicate that near $\rho d^3 \sim 0{\cdot}81$, $G(0, 0) \sim g(d)$. Therefore, we have subtracted from the Snook and D Henderson results an amount sufficient to make $G(0, 0) = g(d)$ and have subtracted a linearly decreasing correction such that the Snook and D Henderson results are uncorrected when $z_2 = d$. Although *ad hoc*, this procedure seems reasonable and probably preferable to using the uncorrected results. The correction is not large and does not affect our conclusions.

As is seen in figure 3, the Henderson–Plischke approximation for $G(z_1, z_2)$ is very good whereas neither the superposition approximation nor the shielding approximation are satisfactory, except near $z_2 = 0$ and $z_2 = d$, respectively.

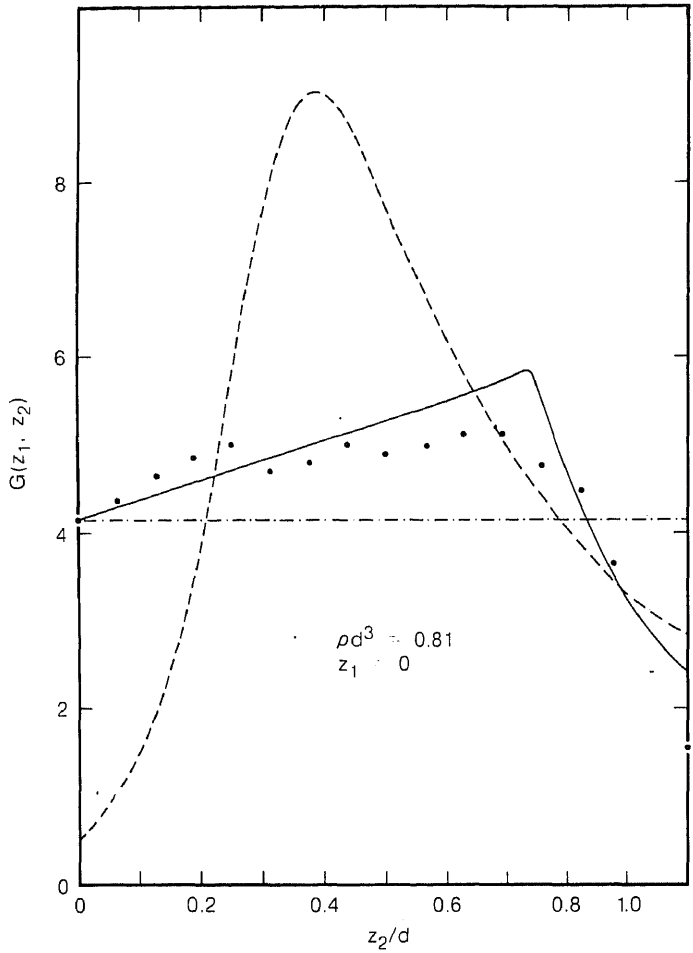

Figure 3. $G(z_1, z_2)$ for hard spheres of diameter d near a hard wall for $z_1 = 0$ and $\rho d^3 = 0{\cdot}81$. The points give the computer simulation values of Snook and Henderson (1978), corrected as described in the text, and the solid, broken and dot dash curves give the Henderson–Plischke, shielding and superposition approximations, respectively.

4. Conclusions

Despite the fact that the Henderson–Plischke approximation is quite good, the resulting self consistent $n(z)$ is a little disappointing at larger z. The oscillations at larger z are damped compared to the simulation results. Evidently there is still a little too much of the screening approximation in the Henderson–Plischke approximation.

The results are a little disappointing for the hard sphere/hard wall system because a simple, analytic, reasonably reliable result (PY1) is available. However, in a larger sense the present results are not so disappointing, since for most systems, although the PY1 and HNC1 theories still will be simple, they will not be analytic and

ear the wall, provided that an approximation for the pair correlation function is sed which is reasonable in the bulk.

However, the present results seem to indicate that for overall good results, a very ccurate approximation for $g(r_{12}, z_1, z_2)$ is required. This seems not to have been he case in the BG and MPB double layer calculations. Perhaps the low densities sed in these calculations or the overwhelming influence of the electric field makes difference. Possibly the hard sphere/hard wall system is particularly sensitive to he approximation used for $G(r_{12}, z_1, z_2)$. In any case the method is worth ursuing.

cknowledgment

his work was supported in part by NSERC of Canada.

eferences

huiyan L B, Outhwaite C W and Levine S 1979 *Chem. Phys. Lett.* **66** 321
huiyan L B, Outhwaite C W and Levine S 1981 *Mol. Phys.* **42** 1271
lum L 1977 *J. Chem. Phys.* **81** 136
lum L, Hernando J and Lebowitz J L 1983 *J. Phys. Chem.* **87** 2825
orn M and Green H S 1946 *Proc. R. Soc.* (*London*) **A188** 10
arnahan N F and Starling K E 1969 *J. Chem. Phys.* **51** 635
accamo C, Pizzimenti G and Blum L 1986 *J. Chem. Phys.* **84** 3327
arnie S L 1985 *Mol. Phys.* **54** 509
arnie S L, Chan D Y C, Mitchell J and Ninham B W 1981 *J. Chem. Phys.* **74** 1472
roxton T L and McQuarrie D A 1979 *Chem. Phys. Lett.* **68** 489
roxton T L and McQuarrie D A 1981 *Mol. Phys.* **42** 141
enderson D, Abraham F F and Barker J A 1976 *Mol. Phys.* **31** 1291
enderson D, Blum L and Bhuiyan L B 1981 *Mol. Phys.* **43** 1185
enderson D, Blum L and Smith W R 1979 *Chem. Phys. Lett.* **63** 381
enderson D and Plischke 1985 *Proc. R. Soc.* (*London*) **A400** 163
enderson J R and van Swol F 1984 *Mol. Phys.* **51** 991
irkwood J G 1935 *J. Chem. Phys.* **3** 300
evine S and Outhwaite C W 1978 *J. Chem. Soc. Faraday Trans. II* **74** 670
evine S, Outhwaite C W and Bhuiyan L B 1981 *J. Electroanal. Chem.* **123** 105
ozada M 1981 *Chem. Phys. Lett.* **81** 472
ozada-Cassou M and Henderson D 1983 *J. Phys. Chem.* **87** 2821
ozada-Cassou M, Saavedra-Barrera R and Henderson D 1982 *J. Chem. Phys.* **77** 5150
uthwaite C W 1978 *J. Chem. Soc. Faraday Trans. II* **74** 1214
uthwaite C W 1983 *J. Chem. Soc. Faraday Trans. II* **79** 1315
uthwaite C W and Bhuiyan L B 1982 *J. Chem. Soc. Faraday Trans. II* **78** 775
uthwaite C W and Bhuiyan L B 1983 *J. Chem. Soc. Faraday Trans. II* **79** 707
uthwaite C W, Bhuiyan L B and Levine S 1979 *Chem. Phys. Lett.* **64** 150
uthwaite C W, Bhuiyan L B and Levine S 1980 *J. Chem. Soc. Faraday Trans. II* **76** 1388
uthwaite C W, Bhuiyan L B and Levine S 1981 *Chem. Phys. Lett.* **78** 413
ercus J K 1980 *J. Stat. Phys.* **23** 657
ercus J K and Yevick G J 1958 *Phys. Rev.* **110** 1
lischke M and Henderson D 1984 *J. Phys. Chem.* **88** 6544
lischke M and Henderson D 1986a *J. Chem. Phys.* **84** 2846
lischke M and Henderson D 1986b *Proc. R. Soc.* (*London*) (in press)
mith W R and Henderson D 1978 *J. Stat. Phys.* **19** 191
nook I and Henderson D 1978 *J. Chem. Phys.* **68** 2134

oc. Indian Acad. Sci. (Chem. Sci.), Vol. 97, Nos 3 & 4, October 1986, pp. 307–331.
Printed in India.

pectral functions and Green's functions: A critique§

A K MISHRA and S K RANGARAJAN*

Department of Inorganic and Physical Chemistry, Indian Institute of Science, Banglore 560 012, India

Abstract. The various relations linking the spectral functions and the Green's functions e.g., $J_{AB}(\varepsilon) = [\text{Im } G^R_{AB}(\varepsilon)]/[1+\gamma e^{-\beta\varepsilon}]$, are usually established via Lehmann's approach. We demonstrate here how the same can be deduced elegantly through their respective superoperator representations. There are contexts in which the said relationships may not be strictly true and have to be modified through a $c\delta(\varepsilon)$ term (c, a constant) e.g., $J_{AB}(\varepsilon) = [\text{Im } G^R_{AB}(\varepsilon)]/[1+\gamma e^{-\beta\varepsilon}] + c\delta(\varepsilon)$. The origin and unambiguous analysis of such situations are presented. A proper bilinear form for the causal Green's function is derived.

The 'displaced harmonic oscillator' is analysed in detail, to illustrate the issues raised above.

The superoperator representation of the imaginary time Green functions is also given, in passing.

Keywords. Spectral functions; Green's functions; Lehmann's approach; superoperator representation; displaced harmonic oscillator.

. Introduction

he Fourier-transforms of the retarded, advanced and causal Green's Functions GF) are conveniently expressed in terms of superoperator (§2) resolvents. Distinguished by their analytic (or non-analytic) behaviour in the transform ariable, such a representation, in turn, motivates different versions of bilinear orms to be defined in the space generated by the superoperator. These bilinear roducts are convenient for accommodating the commutation or the anti-ommutation operations involved in the definitions of GF and the Fermi or Bose haracter of the operators. A proper bilinear form for the causal GF is derived here nd the relationships among the various GF and the spectral functions are stablished (§3).

In §3, we show that the usual (but incorrect) inner projection form for the real me causal GF

$$G^C_{BA}(\varepsilon) = \left\langle P\frac{1}{\varepsilon-\hat{L}}B,\ A-\gamma A,\ P\frac{1}{\varepsilon-\hat{L}}B\right\rangle - i\pi\langle\delta(\varepsilon-\hat{L})\ B,\ A+\gamma\ A,\ \delta(\varepsilon-\hat{L})\ B\rangle$$

enables us to recover only the principal part $G^{C,I}_{BA}(\varepsilon)$. An appropriate inner projection form for $G^{C,II}_{BA}(\varepsilon)$– wherein the bilinear form used is defined as

$$\langle X | Y \rangle = \langle [X^+, Y]_\gamma \rangle ,$$

is deduced (§3) by us. The resulting expression is

$$G^{C,II}_{BA}(\varepsilon) = -\frac{1}{2}\gamma \left[\left\langle A^+ \left| \frac{1}{\varepsilon - \hat{L} - i\eta} \right| B \right\rangle - \left\langle A^+ \left| \frac{1}{\varepsilon - \hat{L} + i\eta} \right| B \right\rangle \right]. \quad (1)$$

In (§4) we consider some specific cases to demonstrate explicitly the applicability of (1). The systems we have selected for this purpose are:

(1) the grand canonical ensemble of free electrons, and
(2) the displaced harmonic oscillator.

During the course of analysis, the inconsistency of reported superoperator inner projection representation of $G^{C}_{BA}(\varepsilon)$, viz

$$G^{C}_{BA}(\varepsilon) = -\gamma \left(A^+ \left| \frac{1}{\varepsilon - \hat{L}} \right| B \right); \; (X | Y) = \langle [X^+, Y]_{-\gamma} \rangle$$

vis-a-vis $G^{C,II}_{BA}(\varepsilon)$ will be illustrated.

The relation between spectral functions and GF, and also between different kinds of GF is usually obtained via the Lehmann approach. Here, one provides a representation of the Hamiltonian in a complete multi-particle space, through appropriate uses of the identity operator. As a result, the algebra becomes tedious. Alternatively, the above mentioned relations can be obtained in an elegant fashion by using the superoperator notion. In §5, we describe the details of this approach.

In certain instances, the relation between the spectral function and GF may involve an additional, additive term $c\,\delta(\varepsilon)$ where the constant c is non-zero. In §6, we consider the origin of such additional terms in the above mentioned relation. The procedure to obtain c has also been delineated.

The superoperator technique has hitherto been used in the context of real time GF (Paul 1982; Mc-Weeny and Pickup 1980). In §7, a superoperator representation for the imaginary time GF, relevant to finite temperature analysis is given.

2. Time Development : the Heisenberg picture and superoperators

(i) While dealing with a many-body system, we formulate the problem in two ways (Abrikasov *et al* 1963; Mattuck 1976): in the first approach, the system is considered to be isolated and N, the total particle number is specified at the beginning. The fixed N acts as an independent variable and the chemical potential μ is subsequently obtained as a function of N. In the second approach, we do not start with an isolated system but describe it using a grand canonical ensemble, wherein particle exchange is permissible. Now, the chemical potential acts as the

In the first approach, the time development of any operator O in the Heisenberg epresentation is

$$O_H(t) = e^{iHt}\ O\ e^{-iHt};\ O = O(0), \tag{2}$$

hereas in the second approach, the same is represented as

$$O_K(t) = e^{iKt}\ O\ e^{-iKt}, \tag{2}'$$

here

$$K = H - \mu N, \tag{3}$$

known as the thermodynamic potential operator (Paul 1982, p.109) or the odified Hamiltonian (Mattuck 1976). H refers to the system's Hamiltonian and, ow, N is the corresponding total particle number operator.

Since N commutes with H, (2) can be rewritten as*

$$O_K(t) = e^{iHt}\ [e^{-i\mu Nt}\ O\ e^{i\mu Nt}]e^{-iHt} \tag{4}$$

When O is a particle creation operator, say O_1^+, the term inside the bracket in (4) implifies to $e^{-i\mu t}\ O_1^+$. Similarly, when O is an annihilation operator, say O_1, the ame reduces to $e^{i\mu t}O_1$. Consequently, we have

$$O_{1K}^+(t) = e^{-i\mu t}\ O_{1H}^+(t), \tag{5}$$

$$O_{1K}(t) = e^{i\mu t}\ O_{1H}(t). \tag{6}$$

n general, when O is expressed as a product of creation/annihilation operators, the elation between the thermodynamic and ordinary Heisenberg representations .e. between $O_K(t)$ and $O_H(t)$] is obtained by appropriate applications of (5) and 6).

i) Corresponding to the two approaches discussed earlier for handling the any-body system, the time development of operator O can be formally epresented as (Jorgensen and Simons 1981; Paul 1982, p. 245)

$$O_H(t) = e^{-i\hat{H}t}\ O \tag{7}$$

$$O_K(t) = e^{-i\hat{K}t}\ O \tag{8}$$

n the above expressions, we are yet to specify the meaning of the action of perators H and K. To arrive at this specification, we recall the usual time epresentations given by (2) and (2)′. It follows from these that connections etween $\hat{H}$, H and $\hat{K}$, K are provided by

$$\hat{H}\ O = [O, H]_-, \tag{9}$$

$$\hat{K}\ O = [O, K]_-. \tag{10}$$

ince the above expressions specify the mode of action of $\hat{H}$ and $\hat{K}$, these can e considered as the definitions of $\hat{H}$ and $\hat{K}$. As the operands in (9) and (10) are

themselves operators, we call H and K the respective superoperators corresponding to H and K. For notational convenience we introduce a superoperator $\hat{L}$ as

$$O_L(t) = e^{-i\hat{L}t}\, O; \quad \hat{L}\, O = [O,\, L]_-; \quad O_L(0) = O, \tag{11}$$

and identify $\hat{L}$ with $\hat{H}$ for isolated system and with $\hat{K}$ for grand canonical description. Similarly, L can either be H or K.

When $L = L_1 + L_2$, the corresponding superoperators L_1, L_2 satisfy the following identity

$$\hat{L}\, O = \hat{L}_1\, O + \hat{L}_2 O. \tag{12}$$

Also for operator product $O_1 O_2$,

$$\hat{L}(O_1 O_2) = (\hat{L} O_1)\, O_2 + O_1 (\hat{L} O_2). \tag{13}$$

For further details regarding the mathematical structure of superoperators, we may refer to the papers by Lowdin (1982) and Weiner (1983).

3. Green's functions and superoperator representation

Green's function methods provide a systematic approach to describe the equilibrium and non-equilibrium characteristics of many-body systems – both at zero and finite temperatures. We usually come across different types of GF, differing in their analyticity (Economov 1979, pp. 145, 169). Important among them are: (i) retarded GF: G^R, (ii) advanced GF: G^A and, (iii) causal GF: G^C. Though these are defined over different time domains, there exist general relationships (Economou 1979, pp. 145, 169) among them. The retarded/advanced GF appear as the response functions in 'Linear Response Formalism' and hence are directly related to experimentally measurable quantities. The causal GF describes the propagation of disturbance in a system caused by adding (removing) a specific number of particles at a certain instant of time and removing (adding) them at a later instant. One of the important features of G^C is that it leads directly to the 'equal time operator product average' in suitable limiting cases. Further, the singularities in the Fourier transforms of the above GF are related to the energy spectrum of the system.

We define these Green's functions as

(a) Retarded GF

$$G^R_{BA}(t) = -i\theta(t)\langle [B_L(t),\, A_L(0)]_{-\gamma}\rangle$$

$$= (i)^\gamma\, \theta(t)\langle [A_L(0),\, B_L(t)]_{-\gamma}\rangle. \tag{14}$$

(b) Advanced GF

$$G^A_{BA}(t) = i\theta(-t)\langle [B_L(t),\, A_L(0)]_{-\gamma}\rangle$$

$$= (-i)^\gamma\, \theta(-t)\langle [A_L(0),\, B_L(t)]_{-\gamma}\rangle. \tag{15}$$

(c) Causal GF

$$G^{C}_{BA}(t) = -i\langle T\{B_L(t)\ A_L(0)\}\rangle$$

$$= (-i)^{\gamma}\ \langle T\{A_L(0)\ B_L(t)\}\rangle, \tag{16}$$

where T, the time ordering operator is defined as

$$T\{B_L(t)\ A_L(0)\} = B_L(t)\ A_L(0),\ t > 0$$

$$= \gamma\, A_L(0)\ B_L(t),\ 0 > \mathrm{t}.$$

Using the above definition, causal GF can be explicitly written as

$$G^{C}_{BA}(t) = -i\theta(t)\langle B_L(t)\ A_L(0)\rangle - i\gamma\,\theta(-t)\langle A_L(0)\ B_L(t)\rangle. \tag{16a}$$

In the above expressions, γ takes the value: (a) -1 when operators A and B have Fermi character and, (b) $+1$ when both of them have Bose character or one of them has Fermi and the other Bose character (Abrikasov *et al* 1963, p. 50; Paul 1982). The quantity $[X_L(t), Y_L(0)]_{-\gamma}$ denotes anti-commutation in the case (a) and commutation in (b). An operator X which contains an odd number of fermion creation/annihilation operators, and also the product of such an X with any number of boson operators have Fermi character. Products of even numbers of fermion creation/annihilation operators, boson operators and their products, and also the products of these two classes of operators have Bose character. The symbol $\langle \ldots \rangle$ denotes the expectation value over the exact normalized ground state wavefunction of the interacting system for zero temperature case, and the statistical average over grand canonical ensemble for finite temperature case. If in the above definitions we replace B by a column vector of operators, say $\bar{B}$, and A by a row vector $\bar{A}$, we obtain the corresponding generalized Green's functions (Linderberg and Ohrn 1973).

It is important to realize that when one of the operators appearing in the expressions (14) to (16) has Fermi character and the other Bose character, the Fermion particle number conservation does not hold good for the product $B_L(t)\ A(0)$, [or $A(0)\ B_L(t)$].* Consequently, the averages of such products become zeros. This feature can be further generalized to include all those cases wherein the required particle number conservation is violated by the operator products appearing inside $\langle \ldots \rangle$ (Bonch-Bruevich and Tyablikov 1962, p. 7).

Imaginary time GF: A different kind of GF, $\overline{G}_{BA}(\tau)$, known as imaginary time (or Matsubara or temperature) GF, is defined for fictitious times $\tau_i = it_j$, $i = \sqrt{-1}$ over the interval $(0,\beta)$ (Fetter and Walecka 1971)

$$\overline{G}_{BA}(\tau_1 - \tau_2) = -\langle T_\tau\{B_K(\tau_1)A_K(\tau_2)\}\rangle$$

$$= i\langle T_\tau\{B_K(\tau_1 - \tau_2)A(0)\}\rangle, \tag{17}$$

* Here we consider the particle number conservation for fermions only because for certain types of bosons having zero mass, e.g. photon, phonons, collective excitations etc., particle number conservation is not required. Also for such systems, chemical potential μ is identically zero. Next, $A(0) \equiv A_L(0)$

wherein we have used a modified Heisenberg representation*

$$O_K(\tau) = e^{K\tau} O e^{-K\tau}. \tag{17a}$$

T_τ is again a time ordering operator [cf. (17)], but now it orders the operators according to their arguments τ_i. $\langle \ldots \rangle$ denotes the average over a grand canonical ensemble and $\tau(=\tau_1 - \tau_2)$ lies within the interval $[-\beta, \beta]$.

From the cyclic property of trace it follows that

$$\overline{G}_{BA}(\tau) = \gamma \overline{G}_{BA}(\tau+\beta);\ 0 < \tau+\beta < 2\beta, \tag{17b}$$

which shows that $\overline{G}_{BA}$ is a periodic/antiperiodic function in the interval $[-\beta, \beta]$ with the period β.

We shall take up the aspects connected with the superoperator representation of imaginary time GF later, in § 7.

Instead of working directly with the GF defined in time domain, it is often convenient to work with their Fourier transforms. In the Fourier plane, the analytical properties of various GF, their relationships with each other and with spectral density function become more transparent.

We define the Fourier transform (FT) of $X(t)$ as†

$$X(\varepsilon) = \int_{-\infty}^{\infty} e^{i\varepsilon t - \eta|t|} X(t)\, dt : \eta \to 0^+,\ \varepsilon \text{ real}. \tag{18}$$

The positive infinitesimal η ensures convergence as $t \to \pm\infty$. From (11), (14)–(16) and (18), the FT of various GF are written as

$$G^R_{BA}(\varepsilon) = \left\langle \frac{1}{\varepsilon - \hat{L} + i\eta} B,\ A - \gamma A,\ \frac{1}{\varepsilon - \hat{L} + i\eta} B \right\rangle \tag{19}$$

$$G^A_{BA}(\varepsilon) = \left\langle \frac{1}{\varepsilon - \hat{L} - i\eta} B,\ A - \gamma A,\ \frac{1}{\varepsilon - \hat{L} - i\eta} B \right\rangle \tag{20}$$

$$G^C_{BA}(\varepsilon) = \left\langle \frac{1}{\varepsilon - \hat{L} + i\eta} B,\ A - \gamma A,\ \frac{1}{\varepsilon - \hat{L} - i\eta} B \right\rangle \tag{21}$$

The symbol ',' appearing in the above expressions is to remind us that the operator $(\varepsilon - \hat{L} \pm i\eta)^{-1}$ known as superoperator resolvent (SOR), acts only on B. In a special situation corresponding to the zero temperature case, wherein the ground state refers to the true vacuum state, the action of SOR in (19)–(21) is equivalent to that of $(\varepsilon - H \pm i\eta)^{-1}$.

The various GF can be expressed as the appropriate matrix elements of the SOR, thus leading to their superoperator representation. In this subsection, we consider the cases of G^R and G^C.

---

* When we consider τ as a complex number and analytically continue it to 'it' in the RHS of (17a), we formally obtain the usual Heisenberg representation.

† Strictly speaking, in the present context, ε and η should be replaced in what follows by $\varepsilon\hat{I}$ and $\eta\hat{I}$ where

Using

$$\langle A_L(0) B_L(t) \rangle = \langle A_L(-t) B_L(0) \rangle, \tag{23}$$

in the definitions of GF, we see that $(\varepsilon + \hat{L} \mp i\eta)^{-1} A$, which now appears in the FT of GF, generates operators like

$$[A, L]_-; [[A, L]_-, L]_-; [[[A, L]_-, L]_-, L]_-; \ldots . \tag{24}$$

We define

(a) a linear operator space V containing A, B and all the other operators contained in (22) and (24). In the case when A and B themselves are matrices, say $\bar{A}$ and $\bar{B}$, V contains $\bar{A}$, $\bar{B}$ and elements of the type (22), (24) for each element of $\bar{A}$, $\bar{B}$.

(b) An identity superoperator $\hat{I}$ on V as

$$\hat{I}X = X \qquad \forall X \in V. \tag{25}$$

We note here that the earlier definition of superoperator $\hat{L}$ [cf. (11)] holds for every element in V, i.e.,

$$\hat{L}X = [X, L]_- \qquad \forall X \in V. \tag{11a}$$

The linear space V can be metrized by introducing a proper bilinear product. Depending on the nature of operators, the problem, and also otherwise, more than one type of bilinear form have been reported (Banwell and Primas 1963; Dalgaard and Simons 1977; Löwdin 1982). We give the definitions of some specific bilinear products which are to be used in subsequent analysis* (Paul 1982, p. 245; Bowen 1975; Jorgensen and Simons 1981).

$$\text{(i)} \quad (X|Y) = \langle X^\dagger Y \rangle, \tag{26}$$

$$\text{(ii)} \quad (X|Y) = \langle [X^\dagger, Y]_{-\gamma} \rangle. \tag{27}$$

For boson operators, the bilinear form (27) is not positive definite. It is obvious that the bilinear form (27) can also be expressed in terms of (26) as

$$(X|Y) = (X|Y) - \gamma (X|Y), \tag{28}$$

$$\text{(iii)} \quad ((X|Y)) = \langle [\hat{L}Y, X^\dagger]_- \rangle. \tag{29}$$

where X and Y have Bose character. It has been shown that bilinear form (29) is positive definite (Bowen 1975). We can also write

$$((X|Y)) = ((L|Y)^\dagger X^\dagger) - (X|\hat{L}Y) \tag{30}$$

Finally, keeping the further development of GF theory in view, we let

$$|\bar{h}) = [|h_1), |h_2), \ldots |h_n), \ldots], \tag{31}$$

be a linearly independent, not necessarily orthogonal, basis for the space V. Then, the identity superoperator admits the following resolution

---

* With the help of the discussion provided in §(4), these bilinear forms can be shown to be zero when one of the operators has Fermi and the other has Bose character.

$$\hat{I} = |\bar{h})\,(\bar{h}|\bar{h})^{-1}\,(\bar{h}|, \tag{32}$$

where $(\bar{h}|\bar{h})$ refers to any one of the above bilinear products. We also note here that superoperator $\hat{L}$ is hermitian.

Using the bilinear form (27), retarded and advanced GF can be recast as the following matrix elements of SOR

$$G^R_{BA}(\varepsilon) = -\gamma\left(A^\dagger \left| \frac{1}{\varepsilon + i\eta - \hat{L}} \right| B\right), \tag{33}$$

$$G^A_{BA}(\varepsilon) = -\gamma\left(A^\dagger \left| \frac{1}{\varepsilon - i\eta - \hat{L}} \right| B\right), \tag{34}$$

Equations (33) and (34) can be viewed as the superoperator representation for G^R and G^A. In principle, we could have also used appropriately the other bilinear forms to express G^R, G^A. For example, when A and B have Bose character G^R is equivalently written as* (Bowen 1975)

$$G^R_{BA}(\varepsilon) = \frac{1}{\varepsilon + i\eta}\langle\, BA - AB\rangle + \frac{1}{\varepsilon + i\eta}\left(\left(A^\dagger \left| \frac{1}{\varepsilon + i\eta - \hat{L}} \right| B\right)\right). \tag{35}$$

The above expression can be obtained directly from (33) by using the identity

$$\frac{1}{\varepsilon + i\eta - \hat{L}} = \frac{1}{\varepsilon + i\eta} + \frac{1}{\varepsilon + i\eta}\,\hat{L}\,\frac{1}{\varepsilon + i\eta - \hat{L}} \tag{36}$$

and rewriting the resulting expression in terms of bilinear form (29). This manipulation also brings out an equivalent bilinear form

$$((X|Y)) = \langle\, [\hat{L}Y, X^+]_+ \,\rangle, \tag{37}$$

for operators having Fermi character.

The criteria for using a particular type of bilinear product depend, apart from the structure of the problem, on the associated algebraic structure of various forms. For example, corresponding to Fermi operators A and B, the bilinear form (27) recasts the algebra in terms of a fundamental anti-commutation relationship associated with the bare operators A and B. In contrast, the bilinear product form (37), while retaining the anti-commutation form, employs modified operator $\hat{L}B$, thus making the algebra more cumbersome.

Next we consider the superoperator representation for causal GF. To arrive at the same, the following strategies have been employed in the literature:

1. Dropping the imaginary convergence parameter η altogether (Mc-Weeny and Pickup 1980):

. Not retaining the differences in the sign of η (Paul 1982, p. 245). Then

$$\varepsilon + i\eta \ (= \varepsilon - i\eta) = Z$$

nd

$$G^C_{BA} = -\gamma \left(A^+ \left| \frac{1}{Z - \hat{L}} \right| B \right). \tag{39}$$

. Starting with (38) and finally reintroducing η in a somewhat arbitrary manner Dalgaard 1977): We see that in the first approach, the criterion for negotiating the ingularities in causal GF is completely unspecified; whereas in the second case, depending on whether $Z = \varepsilon + i\eta$, or $\varepsilon - i\eta$, G^C reduces to G^R or G^A. Finally, in he third approach, the process involved in resubstitution of the $i\eta$ term with proper ign has not been discussed and this procedure may become quite confusing for the general case. To avoid these complications, it is important to retain '$i\eta$' properly, right from the beginning, while arriving at the superoperator representation for G^C.

We start with the identity (see, for e.g., Newton 1966, p. 179).

$$\underset{\eta \to 0^+}{\text{Lim}} \frac{1}{X \pm i\eta} = P \frac{1}{X} \mp i\pi\delta(X) \tag{40}$$

P denotes the principal part and using it, we rewrite the causal GF in the frequency domain as

$$\begin{aligned} G^C_{BA}(\varepsilon) &= \left\langle P \frac{1}{\varepsilon - \hat{L}} B,\ A - \gamma A,\ P \frac{1}{\varepsilon - \hat{L}} B \right\rangle \\ &\quad - i\pi \langle \delta(\varepsilon - \hat{L}) B,\ A + \gamma A,\ \delta(\varepsilon - \hat{L}) B \rangle \\ &= G^{C,\mathrm{I}}_{BA}(\varepsilon) + i G^{C,\mathrm{II}}_{BA}(\varepsilon). \end{aligned} \tag{41}$$

It is clear that whereas $G^{C,\mathrm{I}}_{BA}(\varepsilon)$ can be expressed in terms of bilinear form (27) (used for G^R, G^A), i.e.,

$$G^{C,\mathrm{I}}_{BA}(\varepsilon) = -\gamma \left(A^+ \left| P \frac{1}{\varepsilon - \hat{L}} \right| B \right), \tag{42}$$

the same is not the case with $G^{C,\mathrm{II}}_{BA}(\varepsilon)$. Instead, we have to employ the following bilinear form for $G^{C,\mathrm{II}}_{BA}(\varepsilon)$

$$\langle X | Y \rangle = \langle [X^+,\ Y]_\gamma \rangle \tag{43}$$

$$= (X|Y) + \gamma(X|Y). \tag{43A}$$

Using (42) and (43) in (41), we write the proper super-operator representation for the causal GF as

$$G^{C}_{BA}(\varepsilon) = -\gamma \left(A^{+} \left| P \frac{1}{\varepsilon - \hat{L}} \right| B \right) - i\pi\gamma \langle A^{+} | \delta(\varepsilon - \hat{L}) | B \rangle. \tag{44}$$

A more symmetric representation for the second term on the RHS of the above equation is*

$$iG^{C,\mathrm{II}}_{BA}(\varepsilon) = -\frac{1}{2}\gamma \operatorname*{Lim}_{\eta \to 0^{+}} \left[\left\langle A^{+} \left| \frac{1}{\varepsilon - i\eta - \hat{L}} \right| B \right\rangle \right.$$

$$\left. - \left[\left\langle A^{+} \left| \frac{1}{\varepsilon + i\eta - \hat{L}} \right| B \right\rangle \right] \right]. \tag{45}$$

Further, using the identity (40) we also get [cf. (19), (20)]

$$G^{R}_{BA}(\varepsilon) = \left\langle P \frac{1}{\varepsilon - \hat{L}} B, A - \gamma A, P \frac{1}{\varepsilon - \hat{L}} B \right\rangle$$
$$- i\pi \langle \delta(\varepsilon - \hat{L}) B, A - \gamma A, \delta(\varepsilon - \hat{L}) B \rangle$$

$$\equiv G^{R,\mathrm{I}}_{BA}(\varepsilon) + iG^{R,\mathrm{II}}_{BA}(\varepsilon). \tag{46}$$

$$G^{A}_{BA}(\varepsilon) = \left\langle P \frac{1}{\varepsilon - \hat{L}} B, A - \gamma A, P \frac{1}{\varepsilon - \hat{L}} B \right\rangle$$
$$+ i\pi \langle \delta(\varepsilon - \hat{L}) B, A - \gamma A, \delta(\varepsilon - \hat{L}) B \rangle$$

$$\equiv G^{A,\mathrm{I}}_{BA}(\varepsilon) + iG^{A,\mathrm{II}}_{BA}(\varepsilon). \tag{47}$$

From (41), (46) and (47), we have the following relations (see also appendix A)

$$G^{C,\mathrm{I}}_{BA} = G^{R,\mathrm{I}}_{BA} = G^{A,\mathrm{I}}_{BA} \tag{48}$$

$$G^{R,\mathrm{II}}_{BA} = -G^{A,\mathrm{II}}_{BA} \neq G^{C,\mathrm{II}}_{BA} \tag{49}$$

4. Applicability of the new superoperator inner projection form for $G^{C,\mathrm{II}}(\varepsilon)$: some illustrations

4.1 *Grand canonical ensemble of free electrons*

The Hamiltonian for the present system is given as

$$L = K = \sum_{i} (\varepsilon_i - \mu) c_i^{+} c_i \tag{50}$$

and the Fourier transform of single particle causal GF corresponding to state 'a', viz

$$G^{C}_{aa}(t) = -i\langle T\{C_a(t)\, C_a^{+}(0)\}\rangle, \tag{51}$$

is written as (Bonch-Bruevich and Tyablikov 1962, p. 7)

$$G^{C}_{aa^{\cdot}}(\varepsilon) = \frac{n_F(a)}{\varepsilon - (\varepsilon_a - \mu) - i\eta} + \frac{1 - n_F(a)}{\varepsilon - (\varepsilon_a - \mu) + i\eta}, \tag{52}$$

we consider $G^{C,\mathrm{II}}_{aa^{\cdot}}(\varepsilon)$ which is equal to $\mathrm{Im}\, G^{C}_{aa^{\cdot}}(\varepsilon)$. We employ (45) which contains the modified inner projection form and obtain

$$\mathrm{Im}\, G^{C}_{aa^{\cdot}}(\varepsilon) = \pi[2(n_F(a)) - 1]\,\delta(\varepsilon - \varepsilon_a + \mu), \tag{53}$$

where

$$n_F(a) = \langle C_a^{+} C_a \rangle = [1 + e^{\beta(\varepsilon_a - \mu)}]^{-1}. \tag{54}$$

[Note:

When the usual superoperator representation (38) is employed, we have

$$G_{aa^{\cdot}}(\varepsilon) = \left(C_a \left| \frac{1}{\varepsilon - \hat{K}} \right| C_a \right) = \frac{1}{\varepsilon - (\varepsilon_a - \mu)}, \tag{55}$$

which obviously differs from the exact expression (52). We note that whereas (52) contains the thermal parameter β, $G^{C}_{aa^{\cdot}}(\varepsilon)$ obtained from (56) is temperature independent! In fact, it is not difficult to verify that, provided we take ε as $\varepsilon + i\eta$, (56) is the Fourier transform of the retarded GF.

Comparing (52) and (55) we also see that the principal parts of $G^{C}_{aa^{\cdot}}(\varepsilon)$ and $G^{R}_{aa^{\cdot}}(\varepsilon)$ are identical [cf. (48)]].

4.2 *Displaced harmonic oscillator* ($T = 0$)

The Hamiltonian for a displaced harmonic oscillator is given as (Haken 1976, p. 13)

$$H = \omega_0 b^{+} b + \lambda(b + b^{+}). \tag{56}$$

and the causal GF corresponding to the displacement operator

$$\phi = b + b^{+} = \phi^{+} \tag{57}$$

is defined as (Abrikasov *et al* 1963)

$$D^{C}_{\phi\phi}(t) = -i\langle \psi_0 | \, T\{\phi(t)\,\phi(0)\} \, | \psi_0 \rangle. \tag{58}$$

Direct evaluation of (58) is possible via canonical transformation

$$S = e^{(b - b^{+})\lambda/\omega_0}, \tag{59}$$

which diagonalizes H as

$$S^{-1} H S = H' = \omega_0 b^{+} b - \frac{\lambda^2}{\omega_0} \tag{60}$$

The exact ground state wavefunction, $|\psi_0\rangle$ of H can now be represented in terms of ground state wavefunction $|0\rangle$ of canonically transformed Hamiltonian H', i.e.,

$$|\psi_0\rangle = S|0\rangle \tag{61}$$

Substitution of (61) in (58), and use of the identity (Fong 1975)

$$e^{\xi M} N e^{-\xi M} = N + \xi[M, N] + \frac{\xi^2}{\underline{|2}}[M, [M, N]_-]_- + \ldots \tag{62}$$

(ξ is c-number; M, N are operators) finally leads to

$$D^C_{\phi\phi}(t) = -i\theta(t)\left[e^{-i\omega_0 t} + \frac{4\lambda^2}{\omega_0}\right] - i\theta(-t)\left[e^{i\omega_0 t} + \frac{4\lambda^2}{\omega_0}\right]. \tag{63}$$

or

$$D^C_{\phi\phi}(\varepsilon) = \left[\ \frac{1}{\varepsilon - \omega_0 + i\eta} - \frac{1}{\varepsilon + \omega_0 - i\eta}\ \right] - \frac{8\pi i\lambda^2}{\omega_0^2}\delta(\varepsilon). \tag{64}$$

[Note:

When we evaluate the $D^C_{\phi\phi}(\varepsilon)$ from the wrong expression (38) by using either the EOM method or the superoperator inner projection technique, we obtain

$$D^C_{\phi\phi}(\varepsilon) = \frac{2\omega_0}{\varepsilon^2 - \omega_0^2}. \tag{65}$$

Comparing (65) with the exact $D^C_{\phi\phi}(\varepsilon)$ from (64), we observe that the two expressions are not identical. Whereas the exact result contains the parameter λ, (65) is independent of λ! Indeed it can be seen that when ε is replaced by $\varepsilon + i\eta$, $(\eta \to 0^+)$, the right hand side of (65) is the Fourier transform of retarded GF

$$D^R_{\phi\phi}(t) = -i\theta(t)\langle[\phi(t),\ \phi(0)]_-\rangle, \tag{66}\ \textbf{]}$$

We shall now use the equation of motion (EOM) approach to show that the correct result for $D^{C,\mathrm{II}}_{\phi\phi}(\varepsilon) = \mathrm{Im}\ D^C_{\phi\phi}(\varepsilon)$ can only be obtained by employing (45). We write

$$-\mathrm{Im}\ D^C_{\phi\phi}(\varepsilon) = \frac{1}{2i}\operatorname*{Lim}_{\eta \to 0^+}\left[\left\langle \phi \left| \frac{1}{\varepsilon - \hat{H} - i\eta} \right| \phi \right\rangle - \left\langle \phi \left| \frac{1}{\varepsilon + \hat{H} - i\eta} \right| \phi \right\rangle\right] \tag{67}$$

The EOM for $\langle\phi|1/(\varepsilon - \hat{H})|\phi\rangle$ leads to the following set of equations (appendix B)

$$\varepsilon d_{\phi\phi}(\varepsilon) = 2\langle\phi^2\rangle + \omega_0 d_{\pi\phi}(\varepsilon), \tag{68}$$

$$\varepsilon d_{\pi\phi}(\varepsilon) = \omega_0 d_{\phi\phi}(\varepsilon) + \frac{4\lambda\langle\phi\rangle}{\varepsilon}, \tag{69}$$

where

$$d_{BA}(\varepsilon) = \left\langle A^+ \left| \frac{1}{\hat{\Omega}} \right| B \right\rangle. \tag{70}$$

$$d_{\phi\phi}(\varepsilon) = \frac{2\varepsilon\langle\phi^2\rangle}{\varepsilon^2-\omega_0^2} + \frac{4\lambda\omega_0\langle\phi\rangle}{(\varepsilon^2-\omega_0^2)\varepsilon}. \tag{71}$$

Evaluating $\langle\phi^2\rangle$ and $\langle\phi\rangle$ by using (61), we have

$$\langle\phi^2\rangle = 1 + \frac{4\lambda^2}{\omega_0^2}\,;\ \langle\phi\rangle = -\frac{2\lambda}{\omega_0}. \tag{72}$$

From (71) and (72)

$$d_{\phi\phi}(\varepsilon) = \frac{2\varepsilon}{\varepsilon^2-\omega_0^2} + \frac{8\lambda^2}{\omega_0^2}\frac{1}{\varepsilon}. \tag{73}$$

Substituting (73) (with proper '$i\eta$' terms) in (65)

$$\begin{aligned}\operatorname{Im} D^{C}_{\phi\phi}(\varepsilon) &= -\frac{1}{2i}\lim_{\eta\to 0}\left[\frac{2(\varepsilon-i\eta)}{(\varepsilon-i\eta)^2-\omega_0^2} - \frac{2(\varepsilon+i\eta)}{(\varepsilon+i\eta)^2-\omega_0^2}\right.\\ &\quad\left. + \frac{8\lambda^2}{\omega_0^2}\left(\frac{1}{\varepsilon-i\eta} - \frac{1}{\varepsilon+i\eta}\right)\right]\\ &= -\pi[\delta(\varepsilon-\omega_0)+\delta(\varepsilon+\omega_0)] - \frac{8\pi\lambda^2}{\omega_0^2}\delta(\varepsilon).\end{aligned} \tag{74}$$

Comparing (74) with exact Im $D^{C}_{\phi\phi}(\varepsilon)$ obtained from (64), we see that the equation of motion approach for evaluating the expression (67) yields the correct result.

Lastly, we consider the superoperator inner projection technique for evaluating Im $D^{C}_{\phi\phi}(\varepsilon)$, or more specifically, the auxiliary function $d_{\phi\phi}(\varepsilon)$.

The auxiliary function $d_{BA}(\varepsilon)$ [cf. (70)] is written in the superoperator inner projection form as

$$d_{BA}(\varepsilon) = \langle A^+|\bar{h}\rangle\langle\bar{h}|\varepsilon-\hat{H}|\bar{h}\rangle^{-1}\langle\bar{h}|B\rangle, \tag{75}$$

where $\bar{h}$ is the basis set spanning the space $\langle\hat{H}^n A \cup \hat{H}^n B\rangle_{n=0}^{\infty}$. To arrive at (75), we have used the following representation of the identity superoperator

$$\hat{I} = |\bar{h}\rangle\langle\bar{h}|\bar{h}\rangle^{-1}\langle\bar{h}|. \tag{76}$$

Substituting in (75) $A = B = \phi$ and the basis set $\bar{h}$ as $[\phi, \pi, 1]$, we once again obtain the exact expression (73) for $d_{\phi\phi}(\varepsilon)$. For the details of various steps involved, we may refer to appendix C.

5. Interrelation among spectral functions: a superoperator approach

Here, we consider the relation between the spectral functions $J_{BA}(\varepsilon)$, and $J_{AB}(\varepsilon)$, which are defined as the Fourier transforms of the time correlation functions

$\langle B_L(t)A(0)\rangle$ and $\langle A(0)B_L(t)\rangle$ respectively. Writing $B_L(t)$ in terms of superoperator $\hat{L}$, viz, $B_L(t) = e^{-i\hat{L}t}B(0)$, we have*

$$J_{BA}(\varepsilon) = \int_{-\infty}^{\infty} \langle B_L(t)A(0)\rangle e^{i\varepsilon t}\,dt$$
$$= 2\pi\langle\delta(\varepsilon-\hat{L})B, A\rangle, \tag{77}$$

$$J_{AB}(\varepsilon) = \int_{-\infty}^{\infty} \langle A(0)B_L(t)\rangle e^{i\varepsilon t}\,dt$$
$$= 2\pi\langle A, \delta(\varepsilon-\hat{L})B\rangle. \tag{78}$$

Here $A = A(0)$, $B = B(0)$.
Since

$$e^{-\beta L}\delta(\varepsilon-\hat{L})B, A = e^{-\beta L}(\varepsilon-\hat{L})Be^{\beta L}, e^{-\beta L}A$$
$$= e^{\beta\hat{L}}\delta(\varepsilon-\hat{L})B, e^{-\beta L}A : \text{using the definition of the superoperator,}$$
$$= e^{\beta\varepsilon}\delta(\varepsilon-\hat{L})B, e^{-\beta L}A : \text{from the property of the } \delta \text{ function,} \tag{79}$$

we have

$$J_{BA}(\varepsilon) = 2\pi e^{\beta\varepsilon}\mathrm{Tr}\{\delta(\varepsilon-\hat{L})B, e^{-\beta L}A\}/\mathrm{Tr}\,e^{-\beta L}. \tag{80}$$

From the cyclic property of trace,

$$J_{BA}(\varepsilon) = 2\pi e^{\beta\varepsilon}\mathrm{Tr}\{e^{-\beta L}A, \delta(\varepsilon-\hat{L})B\}/\mathrm{Tr}\,e^{-\beta L}, \tag{81}$$

or, from (78) and (81)

$$J_{BA}(\varepsilon) = e^{\beta\varepsilon}J_{AB}(\varepsilon). \tag{82}$$

The above expression denotes the fundamental relation (Lehmann 1954) between J_{BA} and J_{AB}. Further, since the different types of GF in the time domain are defined as appropriate linear combinations of time correlation functions† [cf. §3] the relation between J_{BA} and J_{AB} also determines the interrelation between different GF.

6. The "$C\delta(\varepsilon)$" term in $J_{BA}(\varepsilon)$ and illustrations

The expressions relating the imaginary parts of various GF and the spectral function J_{AB} are generally valid, as shown through the analysis in appendix A and § 5. But, as mentioned in passing in a footnote by Bonch–Bruevich [1962] (p.7) these equations, viz, (A 19) and (A 20) are not strictly true, always. The exception arises for the retarded and advanced GF when we deal with boson operators, and for the

$$J_{BA} = \frac{-2}{1-e^{-\beta\varepsilon}} \; G^{R,\mathrm{II}}_{BA} + c\delta(\varepsilon) = \frac{2}{1-e^{-\beta\varepsilon}} \; G^{A,\mathrm{II}}_{BA} + c\delta(\varepsilon)$$

(for bosons), (83)

$$J_{BA} = \frac{-2}{1-e^{-\beta\varepsilon}} \; G^{C,\mathrm{II}}_{BA} + c\delta(\varepsilon) \text{ (for fermions).} \tag{84}$$

We can prove that (83) and (84) are indeed true and the presence of the δ function centred at $\varepsilon = 0$ has its origin at the inversion stage [refer to (A 14), (A 15) and (A 17)].

The fact that arbitrary c-numbers in (83) and (84) occur, does not necessarily mean that $c \neq 0$ and this does not imply either that c is arbitrary or undetermined, for, the identity

$$\langle B(0)\; A(0)\rangle = \langle BA\rangle = \frac{1}{2\pi} \int_{-\infty}^{\infty} J_{BA}(\varepsilon)\mathrm{d}\varepsilon \tag{85}$$

can be used to determine c in terms of $\langle BA\rangle$.

Illustrations

(i) Grand canonical ensemble of electrons

In §4 we have already considered the problem of the grand canonical ensemble of electrons. Substituting $B = c_a$, $A = c_a^+$ and the relations (84), (53) in (85) and solving the resulting expression for c, it can be shown that in the present case, the constant c is identically zero.

(ii) *Displaced harmonic oscillator*

The constant c appearing in the spectral function-retarded (advanced) GF relation [cf. (83)] can be obtained in a straightforward manner by using (85). Substituting $B = A = \phi$ in (85), and using the relations† (83), (72) and

$$D^{R,\mathrm{II}}_{\phi\phi} = \mathrm{Im}\; D^{R}_{\phi\phi} = -\pi[\delta(\varepsilon-\omega_0) + \delta(\varepsilon+\omega_0)], \tag{86}$$

we obtain

$$1 + \frac{4\lambda^2}{\omega_0^2} = \int_{-\infty}^{\infty} \frac{1}{1-e^{-\beta\varepsilon}}[\delta(\varepsilon-\omega_0) + \delta(\varepsilon+\omega_0)]\mathrm{d}\varepsilon + \frac{c}{2\pi} \tag{87}$$

Solving the above expression for c, we obtain a non-zero value of c in the present case, viz,

$$c = (8\pi\lambda^2)/\omega_0^2 \,. \tag{88}$$

† Presently, we consider only the retarded GF. The c appearing in advanced GF can be obtained in a similar fashion.

It is interesting to note that in the case $\lambda \equiv 0$, $c = 0$ [refer to (88)] which means that the $c\delta(\varepsilon)$ correction becomes unnecessary for a simple harmonic oscillator (i.e. $\lambda = 0$)!

7. Superoperator representation of imaginary time GF

We have already introduced the imaginary time GF, $\overline{G}_{BA}(\tau)$ in §3 [equation (17)]. Presently, we consider the superoperator inner projection representation of frequency* GF, $\overline{G}_{BA}(\varepsilon_n)$, obtained from the Fourier series expansion of $\overline{G}_{BA}(\tau)$

$$\overline{G}_{BA}(\tau) = \frac{1}{\beta} \sum_{n=-\infty}^{\infty} e^{-i\varepsilon_n \tau} \overline{G}_{\mathrm{BA}}(\varepsilon_n) \ . \tag{89}$$

We write $\overline{G}_{BA}(\varepsilon_n)$ as

$$\overline{G}_{BA}(\varepsilon_n) = \int_0^\beta e^{i\varepsilon_n \tau} \ \overline{G}_{\mathrm{BA}}(\tau) \, \mathrm{d}\tau \tag{90}$$

$$\begin{aligned} \varepsilon_n &= (2n+1)\pi/\beta \text{ for fermions,} \\ &= 2n\pi/\beta \text{ for bosons.} \end{aligned} \tag{91}$$

Obviously superoperator representation for $\overline{G}_{BA}(\tau)$ follows from that of $\overline{G}_{BA}(\varepsilon_n)$ via (89). Substituting $\overline{G}_{BA}(\tau)$ from (17) in (90), we get

$$\begin{aligned} \overline{G}_{BA}(\varepsilon_n) &= -\int_0^\beta \mathrm{d}\tau e^{i\varepsilon_n \tau} [\theta(\tau)\langle B_K(\tau) A(0)\rangle \\ &\quad + \gamma\theta(-\tau)\langle A(0) B_K(\tau)\rangle]\mathrm{d}\tau \\ &= -\int_0^\beta \mathrm{d}\tau e^{i\varepsilon_n \tau}\langle B_K(\tau) A(0)\rangle \end{aligned} \tag{92}$$

Substituting [cf. (11), (17a)]

$$B_K(\tau) = e^{-\dot{K}\tau} B, \ B = B(0), \tag{93}$$

in (92), we get*

$$\begin{aligned} \overline{G}_{BA}(\varepsilon_n) &= -\int_0^\beta \mathrm{d}\tau \langle e^{(i\varepsilon_n - \dot{K})} B, A\rangle \mathrm{d}\tau \\ &= -\mathrm{Tr}\left\{e^{-\beta K} \int_0^\beta \mathrm{d}\tau e^{(i\varepsilon_n - \dot{K})} B, A\right\} \Big/ Z; \end{aligned}$$

---

*'Frequency dependent GF' according to Mahan (1981, p. 123).

$$|Z = \mathrm{Tr}\{e^{-\beta K}\}| \tag{94}$$

$$= -\mathrm{Tr}\left\{e^{-\beta K}\left|\frac{e^{i\varepsilon_n\tau - \hat{K}\tau}}{i\varepsilon_n - \hat{K}}\right|_0^\beta B,\ A\right\} \Big/ Z. \tag{95}$$

From (91) it can easily be seen that

$$e^{i\varepsilon_n\beta} = \gamma, \tag{96}$$

where $\gamma = -1$, when A, B have Fermi character, and $\gamma = +1$ when they have Bose character [cf. §3, above]. As a result, we have

$$\overline{G}_{BA}(\varepsilon_n) = -\mathrm{Tr}\left\{e^{-\beta K}\left(\frac{\gamma e^{-K\beta}}{i\varepsilon_n - \hat{K}} B,\ A - \frac{1}{i\varepsilon_n - \hat{K}} B,\ A\right)\right\} \Big/ Z \tag{97}$$

Next, let

$$X = \mathrm{Tr}\left\{e^{-\beta K}\, e^{-\hat{K}\beta}\, \frac{\gamma}{i\varepsilon_n - \hat{K}} B,\ A\right\}, \text{ which we can rewrite as}$$

$$X = \mathrm{Tr}\left\{e^{-\beta K}\, e^{\beta K}\, \frac{\gamma}{i\varepsilon_n - \hat{K}} B e^{-\beta K},\ A\right\}, \tag{98}$$

Since ' , ' restricts the action of superoperator $\hat{K}$ only, we have

$$X = \mathrm{Tr}\left\{\frac{\gamma}{i\varepsilon_n - \hat{K}} B,\ e^{-\beta K},\ A\right\}, \tag{99}$$

or, from the cyclic property of the trace

$$X = \mathrm{Tr}\left\{e^{-\beta K} A, \frac{\gamma}{i\varepsilon_n - \hat{K}} B\right\}, \tag{100}$$

Substituting (100) in (97), we get

$$\overline{G}_{BA}(\varepsilon_n) = -\gamma \mathrm{Tr}\left\{e^{-\beta K}\left(A, \frac{1}{i\varepsilon_n - \hat{K}} B - \gamma \frac{1}{i\varepsilon_n - \hat{K}} B,\ A\right)\right\} \Big/ Z \tag{101}$$

Finally, using the bilinear form defined by (45), $\overline{G}_{BA}(\varepsilon_n)$ is written as

$$\overline{G}_{BA}(\varepsilon_n) = -\gamma\left(A^\dagger \left| \frac{1}{i\varepsilon_n - \hat{K}} \right| B\right), \tag{102}$$

which is the superoperator representation for frequency GF.

8. Summary and conclusions

(2) the correctness of such a representation is demonstrated through its application to (a) a free-electron system, and (b) displaced harmonic oscillator, and comparing the same with the exact results;
(3) the well-known relations between the spectral functions and the various GF are deduced through their superoperator representations, thus by-passing the apparently more tedious Lehman approach;
(4) the problem of the 'the $c\delta(\varepsilon)$ ambiguity' as pointed out in connection with relating the spectral J_{AB} and Green's functions G^{i}_{AB} (i = causal, when A, B are Fermions and i = advanced/retarded when A, B are Bosons) is analysed in detail. An unambiguous method of determining the coefficient c is outlined. Both the possibilities viz. $c = 0$, $c \neq 0$, are illustrated through the Fermi gas and the displaced harmonic oscillator models;
(5) finally, the superoperator representation for the imaginary time causal GF is derived.

Appendix A. Relation between Green's functions and spectral functions

Spectral functions are directly associated with time correlation functions and represent their Fourier transforms. The spectral function corresponding to the time correlation function $\langle A(0)\ B_L(t)\rangle$ is defined as:

$$J_{AB}(\varepsilon) = \int_{-\infty}^{\infty} e^{i\varepsilon t} \langle A(0)\ B_L(t)\rangle \mathrm{d}t. \tag{A1}$$

Similarly,

$$J_{BA}(\varepsilon) = \int_{-\infty}^{\infty} e^{i\varepsilon t} \langle B_L(t)\ A(0)\rangle \mathrm{d}t\ . \tag{A2}$$

For further discussion, it is important to obtain the relation between J_{BA} and J_{AB}. We consider here $T \neq 0$ case. The zero temperature result can be obtained from it by taking appropriate limits.

It has been shown that for real ε, spectral functions are real quantities. From the knowledge of spectral functions, time correlation functions are obtained by using the inverse FT

$$\langle B_L(t)\ A(0)\rangle = \frac{1}{2\pi}\int_{-\infty}^{\infty} e^{-i\varepsilon t} J_{BA}(\varepsilon)\ \mathrm{d}\varepsilon\ , \tag{A3}$$

$$\begin{aligned}\langle A(0)\ B_L(t)\rangle &= \frac{1}{2\pi}\int_{-\infty}^{\infty} e^{-i\varepsilon t} J_{AB}(\varepsilon)\ \mathrm{d}\varepsilon\ , \\ &= \frac{1}{2\pi}\int_{-\infty}^{\infty} e^{-i\varepsilon t}\ e^{-\beta\varepsilon} J_{BA}(\varepsilon)\ \mathrm{d}\varepsilon\ ,\end{aligned} \tag{A4}$$

$$\int_{-\infty}^{\infty}$$

ere, we note that the expectation value of equal time operator product can be irectly obtained from causal GF. From (16a)

$$\langle AB \rangle = i\gamma \lim_{t \to 0^-} G^C_{BA}(t) \tag{A6}$$

Our next step is to consider the relation between various GFS and spectral nctions. Employing the inverse FT and the relation $J_{BA}(\varepsilon) = e^{\beta\varepsilon} J_{AB}(\varepsilon)$ as ell as (14)–(16), (A1) and (A2),

$$G^R_{BA}(t) = -i\theta(t) \int_{-\infty}^{\infty} e^{-i\varepsilon' t} \left[1 - \gamma e^{-\beta\varepsilon'}\right] J_{BA}(\varepsilon') \frac{d\varepsilon'}{2\pi}, \tag{A7}$$

$$G^A_{BA}(t) = i\theta(-t) \int_{-\infty}^{\infty} e^{-i\varepsilon' t} \left[1 - \gamma e^{-\beta\varepsilon'}\right] J_{BA}(\varepsilon') \frac{d\varepsilon'}{2\pi}, \tag{A8}$$

$$G^C_{BA}(t) = -i\theta(t) \int_{-\infty}^{\infty} e^{-i\varepsilon' t} J_{BA}(\varepsilon') \frac{d\varepsilon'}{2\pi} - i\gamma\theta(-t) \int_{-\infty}^{\infty} e^{-i\varepsilon' t} J_{AB}(\varepsilon') \frac{d\varepsilon'}{2\pi}, \tag{A9}$$

lternatively [Bonch–Bruevich and Tyblikov 1962]

$$G^R_{BA}(\varepsilon) = \frac{1}{2\pi} \int_{-\infty}^{\infty} (1 - \gamma e^{-\beta\varepsilon'}) \frac{J_{BA}(\varepsilon')}{\varepsilon - \varepsilon' + i\eta} d\varepsilon' \tag{A10}$$

$$G^A_{BA}(\varepsilon) = \frac{1}{2\pi} \int_{-\infty}^{\infty} (1 - \gamma e^{-\beta\varepsilon'}) \frac{J_{BA}(\varepsilon')}{\varepsilon - \varepsilon' - i\eta} d\varepsilon' \tag{A11}$$

$$G^C_{BA}(\varepsilon) = \frac{1}{2\pi} \int_{-\infty}^{\infty} \left(\frac{1}{\varepsilon - \varepsilon' + i\eta} - \gamma \frac{e^{-\beta\varepsilon'}}{\varepsilon - \varepsilon' - i\eta} \right) J_{BA}(\varepsilon') \, d\varepsilon' . \tag{A12}$$

hus, in the complex ε plane (i.e. in z)

$$\frac{1}{2\pi i} \int_{-\infty}^{\infty} (1 - \gamma e^{-\beta\varepsilon'}) \frac{i J_{BA}(\varepsilon')}{z - \varepsilon'} \frac{d\varepsilon'}{2\pi} = \begin{cases} G^R_{BA}(z), & \mathrm{Im}\, z > 0 \\ G^A_{BA}(z), & \mathrm{Im}\, z < 0 \end{cases} \tag{A13}$$

n fact, G^R and G^A together can be considered as a single analytical function $G(z)$, efined over the whole complex plane except on the real axis, where it has ngularities (either isolated poles or branch cut, depending on the spectrum of L)

[Ter Haar 1962, p. 119]. When we approach the real axis from the upper or lower sides, we have

$$G_{BA}(\varepsilon + i\eta) \equiv G^R_{BA}(\varepsilon) = P\int_{-\infty}^{\infty}(1-\gamma e^{-\beta\varepsilon'})\,\frac{J_{BA}(\varepsilon')}{\varepsilon-\varepsilon'}\,\frac{d\varepsilon'}{2\pi} - \frac{i}{2}(1-\gamma e^{-\beta\varepsilon})\,J_{BA}(\varepsilon) \tag{A14}$$

or

$$G_{BA}(\varepsilon - i\eta) \equiv G^A_{BA}(\varepsilon) = P\int_{-\infty}^{\infty}(1-\gamma e^{-\beta\varepsilon'})\,\frac{J_{BA}(\varepsilon')}{i\varepsilon-\varepsilon'}\,\frac{d\varepsilon'}{2\pi} + \frac{i}{2}(1-\gamma e^{-\beta\varepsilon})\,J_{BA}(\varepsilon) \tag{A15}$$

From (A14) and (A15), we obtain the following important relation

$$J_{BA}(\varepsilon) = \frac{i}{1-\gamma e^{-\beta\varepsilon}}\,[G^R_{BA}(\varepsilon) - G^A_{BA}(\varepsilon)], \tag{A16}$$

which in conjunction with (A3)–(A5) can be used to obtain various observables. From (A9), we can write the FT of causal GF as

$$G^C_{BA}(\varepsilon) = P\int_{-\infty}^{\infty}(1-\gamma e^{-\beta\varepsilon'})\,\frac{J_{BA}(\varepsilon')}{\varepsilon-\varepsilon'}\,\frac{d\varepsilon'}{2\pi} - \frac{i}{2}(1+\gamma e^{-\beta\varepsilon})\,J_{BA}(\varepsilon). \tag{A17}$$

Causal GF is non-analytical in the complex plane [Mattuck 1976]. This can be ascertained from the fact that real and imaginary parts of causal GF do not satisfy the dispersion relation associated with analytical functions.

From the above discussion [cf. (48), (A14)–(A17)], it also follows that

$$G^{i,I}_{BA}(\varepsilon) = P\int_{-\infty}^{\infty}(1-e^{-\beta\varepsilon'})\,\frac{J_{BA}(\varepsilon')}{\varepsilon-\varepsilon'}\,\frac{d\varepsilon'}{2\pi}, \tag{A18}$$

where $i = [R,A,C]$
and*

$$= \frac{2}{1-\gamma e^{-\beta\varepsilon}} G_{BA}^{A,II}(\varepsilon). \tag{A19}$$

From (41) and (A17), $J_{BA}(\varepsilon)$ can also be written in terms of causal GF as

$$J_{BA}(\varepsilon) = -\frac{2}{1+\gamma e^{-\beta\varepsilon}} G_{BA}^{C,II}(\varepsilon) . \tag{A20}$$

Finally we notice that when $J_{BA}(\varepsilon)$ is real

$$G_{BA}^{i,I}(\varepsilon) = \text{Re } G_{BA}^{i}(\varepsilon) , \tag{A21}$$

and

$$G_{BA}^{i,II}(\varepsilon) = \text{Im } G_{BA}^{i}(\varepsilon) . \tag{A22}$$

Needless to say that, in general, the expressions (A18)–(A20) can be used to generate the other GFS from the knowledge of any particular type of Green's function.

Appendix B. Evaluation of (30) and (31)

(a) EOM for $d_{\phi\phi}$ is

$$\left\langle \phi \left| \frac{1}{\varepsilon - \hat{H}} \right| \phi \right\rangle = \frac{1}{\varepsilon} \left\langle \phi \middle| \phi \right\rangle + \frac{1}{\varepsilon} \left\langle \phi \left| \frac{1}{\varepsilon - \hat{H}} \hat{H} \right| \phi \right\rangle. \tag{B1}$$

Next

$$\langle \phi | \phi \rangle = \langle \phi^{+} \phi + \phi \, \phi^{+} \rangle = 2\langle \phi^{2} \rangle \qquad \text{[cf. (2)]}, \tag{B2}$$

and $$\hat{H}\phi = \omega_0 \pi. \tag{B3}$$

From (B1) – (B3)

$$\varepsilon d_{\phi\phi} = 2\langle \phi^{2} \rangle + \omega_0 d_{\pi\phi}, \tag{B4}$$

which is (30).

(b) EOM for $d_{\pi\phi}$ is

$$\left\langle \phi \left| \frac{1}{\hat{H}} \right| \pi \right\rangle = \frac{1}{\varepsilon} \left\langle \phi \middle| \pi \right\rangle + \frac{1}{\varepsilon} \left\langle \phi \left| \frac{1}{\hat{H}} \hat{H} \right| \pi \right\rangle. \tag{B5}$$

Since

$$\hat{H}\pi = [\pi, \omega_0 b^+ b + \lambda\phi]_-$$
$$= \omega_0\phi + \lambda(\pi\phi - \phi\pi). \tag{}$$

We have

$$\left\langle \phi \left| \frac{1}{\varepsilon - \hat{H}} \hat{H} \right| \pi \right\rangle = \omega_0 \left\langle \phi \left| \frac{1}{\varepsilon - \hat{H}} \right| \phi \right\rangle + \lambda \left\langle \phi \left| \frac{1}{\varepsilon - \hat{H}} \right| \pi\phi - \phi\pi \right\rangle. \tag{}$$

Further using (13)

$$\hat{H}(\pi\phi - \phi\pi) = (\hat{H}\pi)\phi + \pi(\hat{H}\phi) - (\hat{H}\phi)\pi - \phi(\hat{H}\pi) = 0. \tag{}$$

From (B7) and (B8)

$$\left\langle \phi \left| \frac{1}{\varepsilon - \hat{H}} \right| \pi\phi - \phi\pi \right\rangle = \frac{1}{\varepsilon} \left\langle \phi \left| \pi\phi - \phi\pi \right. \right\rangle. \tag{}$$

Now,

$$\langle \phi | \pi\phi - \phi\pi \rangle = \langle \phi^+ \pi\phi + \pi\phi\phi^+ \rangle - \langle \phi^+ \phi\pi + \phi\pi\phi^+ \rangle$$
$$= \langle \pi\phi\phi - \phi\phi\pi \rangle. \tag{B}$$

Substituting the identity

$$\phi\pi - \pi\phi = -2, \tag{B}$$

obtained from the commutation $[\phi, \pi]_-$, in (B10), we get

$$\langle \phi | \pi\phi - \phi\pi \rangle = 4\langle \phi \rangle. \tag{B}$$

From (B9) and (B12)

$$\left\langle \phi \left| \frac{1}{\varepsilon - \hat{H}} \right| \pi\phi - \phi\pi \right\rangle = \frac{4\langle \phi \rangle}{\varepsilon}, \tag{B}$$

or from (B7) and (B13)

$$\left\langle \phi \left| \frac{1}{\varepsilon - \hat{H}} \hat{H} \right| \pi \right\rangle = \omega_0 \left\langle \phi \left| \frac{1}{\varepsilon - \hat{H}} \right| \phi \right\rangle + \frac{4\lambda\langle \phi \rangle}{\varepsilon}. \tag{B}$$

Next,

$$\langle \phi | \pi \rangle = \langle \phi^+ \pi + \pi\phi^+ \rangle = \langle \phi\pi + \pi\phi \rangle, \tag{B}$$

which using (B11) can be rewritten as

low using (23) and (24), we have

$$\langle \phi\pi \rangle = \langle \psi_0 | \phi\pi | \psi_0 \rangle = \langle 0 | S^{-1}\phi S S^{-1}\pi S | 0 \rangle$$

$$= \left\langle 0 \left| (\phi - \frac{2\lambda}{\omega_0})\pi \right| 0 \right\rangle = -1. \tag{B17}$$

ubstituting (B17) in (B16)

$$\langle \phi | \pi \rangle = 0. \tag{B18}$$

inally, (B5), (B14) and (B18) leads to

$$\varepsilon \left\langle \phi \left| \frac{1}{\varepsilon - \hat{H}} \right| \pi \right\rangle = \omega_0 \left\langle \phi \left| \frac{1}{\varepsilon - \hat{H}} \right| \phi \right\rangle + \frac{4\lambda \langle \phi \rangle}{\varepsilon} \quad ,$$

hich is (31).

ppendix C. Evaluation of $d_{\phi\phi}$ via superoperator inner projection method

efore proceeding for the derivation of $d_{\phi\phi}$, we evaluate certain relevant bilinear roducts.

1) $$\langle \pi | \phi \rangle = \langle \pi^+ \phi + \phi \pi^+ \rangle. \tag{C1}$$

ince $\pi^+ = (b - b^+)^+ = -(b - b^+) = -\pi$

$$\langle \pi | \phi \rangle = -\langle \pi\phi + \phi\pi \rangle = -\langle \phi | \pi \rangle \, ,$$

r from (B18)

$$\langle \pi | \phi \rangle = \langle \phi | \pi \rangle = 0. \tag{C2}$$

2) $$\langle \pi | \pi \rangle = \langle \pi^+ \pi + \pi \pi^+ \rangle = -2\langle \pi^2 \rangle.$$

rom (23)

$$\langle \pi | \pi \rangle = -2\langle 0 | S^{-1}\pi^2 S | 0 \rangle = 2. \tag{C3}$$

3) $$\langle \pi | \pi\phi - \phi\pi \rangle = \langle -\pi\pi\phi - \pi\phi\pi \rangle - \langle -\pi\phi\pi - \phi\pi\pi \rangle$$

$$= \langle -\pi\pi\phi + \phi\pi\pi \rangle. \tag{C4}$$

rom the above expression and (B11)

$$\langle \pi | \pi\phi - \phi\pi \rangle = -4\langle \pi \rangle.$$

sing (23) to evaluate $\langle \pi \rangle$, we get

$$\langle \pi | \pi\phi - \phi\pi \rangle = 0. \tag{C5}$$

4) $$\langle 1 | A \rangle = 2\langle A \rangle \, , \tag{C6}$$

$$\langle A | 1 \rangle = 2\langle A^+ \rangle \, , \tag{C7}$$

Now, from (37) and (A4)

$$d_{\phi\phi} = \langle \phi|\bar{h}\rangle\langle \bar{h}|\varepsilon - \hat{H}|\bar{h}\rangle^{-1}\langle \bar{h}|\phi\rangle$$

$$= [\langle \phi|\phi\rangle\langle \phi|\pi\rangle\langle \phi|1\rangle]$$

$$\begin{bmatrix} \langle \phi|\varepsilon-\hat{H}|\phi\rangle & \langle \phi|\varepsilon-\hat{H}|\pi\rangle & \langle \phi|\varepsilon-\hat{H}|1\rangle \\ \langle \pi|\varepsilon-\hat{H}|\phi\rangle & \langle \pi|\varepsilon-\hat{H}|\pi\rangle & \langle \pi|\varepsilon-\hat{H}|1\rangle \\ \langle 1|\varepsilon-\hat{H}|\phi\rangle & \langle 1|\varepsilon-\hat{H}|\pi\rangle & \langle 1|\varepsilon-\hat{H}|1\rangle \end{bmatrix}^{-1} \begin{bmatrix} \langle \phi|\phi\rangle \\ \langle \pi|\phi\rangle \\ \langle 1|\phi\rangle \end{bmatrix} \tag{C8}$$

Using (B2), (B3), (B6), (B12), (C2), (C3),(C5)–(C7) and

$$\hat{H}1 = 0;\ \langle 1|1\rangle = 2, \tag{C9}$$

the expression (C8) is written as

$$d_{\phi\phi} = [2\langle \phi^2\rangle\ 0\ 2\langle \phi\rangle]$$

$$\begin{bmatrix} 2\varepsilon\langle \phi^2\rangle & -2\omega_0\langle \phi^2\rangle - 4\lambda\langle \phi\rangle & 2\varepsilon\langle \phi\rangle \\ -2\omega_0 & 2\varepsilon & -2\varepsilon\langle \pi\rangle \\ 2\varepsilon\langle \phi\rangle & 2\varepsilon\langle \pi\rangle & 2\varepsilon \end{bmatrix}^{-1} \begin{bmatrix} -2\langle \phi^2\rangle \\ 0 \\ 2\langle \phi\rangle \end{bmatrix} \tag{C10}$$

Substituting $\langle \phi\rangle$ and $\langle \phi^2\rangle$ from (34) and [cf.(23)]

$$\langle \pi\rangle = 0, \tag{C11}$$

in (C10), we get

$$d_{\phi\phi} = \frac{2\varepsilon}{\varepsilon^2 - \omega_0^2} + \frac{8\lambda^2}{\omega_0^2}\frac{1}{\varepsilon} \tag{C12}$$

which is (35) of the text.

References

Abrikasov A A, Gorkov L P, Dzyaloshinski I E 1963 *Methods of quantum field theory in statistical physics* (Englewood Cliffs, NJ: Prentice-Hall)

Banwell C N and Primas H 1963 *Mol. Phys.* **6** 225

Bonch–Bruevich V L and Tyablikov S V 1962 *The Green function method in statistical mechanics* (Amsterdam: North-Holland)

Bowen S P 1975 *J. Math. Phys.* (*N.Y.*) **16** 620

Dalgaard E 1977 *J. Phys.* **B10** 147

Dalgaard E and Simons J 1977 *J. Phys.* **B10** 2767

Economou E N 1979 *Green's functions in quantum physics* (Berlin: Springer Verlag)

Felter A L and Walecka J D 1971 *Quantum theory of many-particle systems* (New York: Mc-Graw Hill)

Fong F K 1975 *Theory of molecular relaxation* (New York: Wiley-Interscience) Chap. 4, p. 61

Haken H 1976 *Quantum field theory of solids* (Amsterdam: North-Holland) Chap. 2, p. 13

Jorgensen P and Simons J 1981 *Second quantization-based methods in quantum chemistry* (New York: Academic Press)

Lehmann H 1954 *Nuovo Cimento* **11** 342
Mahan G D 1981 *Many-particle physics* (New York: Plenum Press)
Mattuck R D 1976 *A guide to Feynman diagrams in the many-body problem* (New York: Mc-Graw Hill)
Mc-Weeny R and Pickup B T 1980 *Rep. Prog. Phys.* **43** 1065
Newton R G 1966 *Scattering theory of waves and particles* (New York: Mc-Graw Hill)
Paul R 1982 *Field theoretical methods in chemical physics* (Amsterdam: Elsevier)
Ter Haar D 1962 *Fluctuation relaxation and resonance in magnetic systems* (London: Oliver and Boyd)
Thouless D J 1972 *The quantum mechanics of many-body systems* (New York: Academic Press)
Weiner B 1983 *J. Math. Phys.* (*N.Y.*) **24** 1791

Proc. Indian Acad. Sci. (Chem. Sci.), Vol. 97, Nos 3 & 4, October 1986, pp. 333–347.
© Printed in India.

The adsorption of D-(+)-xylose at the mercury–water interface§

ROGER PARSONS* and ROBERT PEAT
Department of Chemistry, The University, Bristol BS8 1TS, England
Present address: Department of Chemistry, The University, Southampton SO9 5NH, England

Abstract. The construction of an apparatus for measuring electro capillary curves of the mercury-electrolyte interface is described based on the maximum bubble pressure technique. The adsorption of D-(+)-xylose at the mercury-aqueous 0·7953 M NaF interface is described and compared with sucrose and its isomer D-ribose.

Keywords. D-(+)-xylose adsorption; electro capillary curves; mercury-electrolyte interface; maximum bubble pressure technique.

1. Introduction

An essential feature in the understanding of electrode kinetics and double layer properties is a knowledge of the distribution of the components of the electrolyte in space and time in the vicinity of the electrode surface. In particular, emphasis has been placed on the structure of the solvent in the immediate vicinity of the electrode. The study of an organic molecule is useful in this respect as it represents the simple replacement of a layer of water adjacent to the electrode by a monolayer of an organic species. In a previous paper we have speculated from a consideration of results on a variety of polyhydroxy compounds that subtle differences in adsorption behaviour may be due to interaction of the organic species with the interfacial solvent structure (Parsons and Peat 1980). In particular sucrose lowers the interfacial tension at a mercury interface while it raises the surface tension of water and this can be attributed to a different solvent structure at the two interfaces (Frumkin 1928; Parsons and Peat 1981). Another important biological molecule that is a constituent of nucleic acids is D-ribose. The adsorption of this molecule has been studied by Brabec *et al* (1978). An isomer of D-ribose is D-xylose and the small structural change between these two molecules is manifest in the bulk solution properties. Ribose shows a marked salting in effect in the presence of sodium chloride whereas for xylose, salting out occurs (Brill 1978). This suggests a strong association between ribose and the salt. The adsorption of xylose at the mercury interface has been studied to compare its behaviour with that of sucrose and its isomer D-ribose.

concentrations of D-xylose in aqueous solutions containing 0·7953 NaF as base electrolyte. The electrode potential was measured to ±0·1 mV against a 0·7953 M NaCl calomel electrode and the temperature was maintained at 25·00±0·05°C. Analar NaCl and KCl were twice recrystallised from water and dried at red heat in a platinum crucible. NaF and D-xylose were BDH Analar high purity grade and were used without further purification.

Differential capacitance was measured using methods previously described (Hills and Payne 1965; Parsons *et al* 1975) and the point of zero charge was determined using a streaming electrode (Grahame 1952). All measurements were recorded at a frequency of 800 Hz and a peak to peak amplitude of 10 mV. The capacitance was independent of the frequency over the range 400–3000 Hz for all concentrations studied.

The electrocapillary curves were obtained using a high precision electrometer based on the maximum bubble pressure technique (Schiffrin 1969; Lawrence and Mohilner 1971). A consequence of the Young–Laplace equation (Adamson 1967) applied to the extrusion of a mercury drop from a capillary tube is that the interface will only be stable until the growing drop is hemispherical. Any further increase in pressure produces an unstable condition forcing the drop to grow spontaneously and break away from the tube. The pressure corresponding to the hemispherical condition is the maximum bubble pressure and is directly proportional to the interfacial tension.

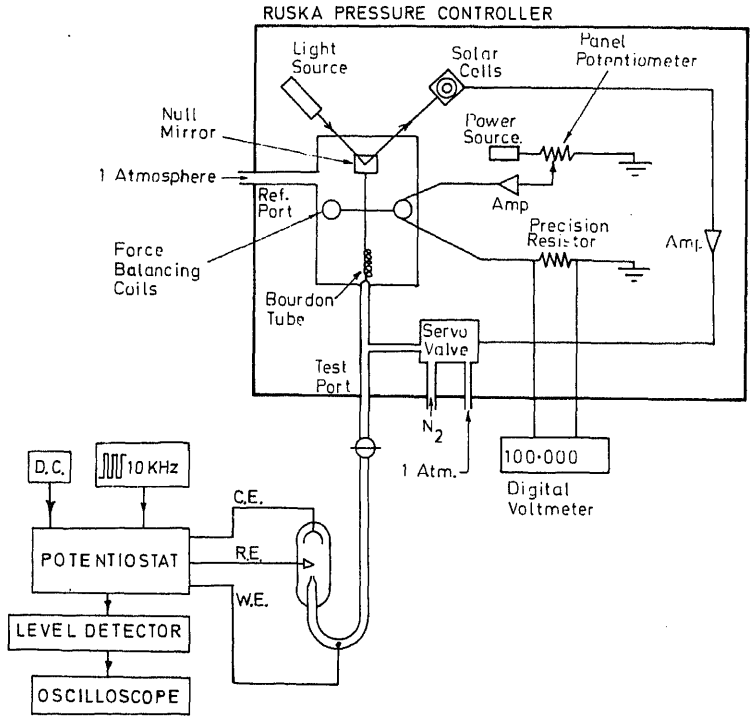

Figure 1. Schematic diagram of the maximum bubble pressure electrometer.

obtainable is due to the development of automatic pressure controlling equipment. The pressure system consists of a Ruska Pressure Controller (Model DDR-6000) coupled with a Datron, $5\frac{1}{2}$ digit, voltmeter (Model 1051) for the direct reading of pressure as an output voltage.

The controller consists of a chamber containing an electromagnetic coil, a quartz Bourdon tube and a null mirror. Application of a current through the coils of the tube causes movement of the null mirror. Furthermore, any movement of the mirror causes a variation in the intensity of light striking the solar cells and produces a proportional current in the external circuit. To control the pressure within the chamber, a constant current is passed through the force balancing coil by adjusting a potentiometer. The magnetic field produces a rotation of the null mirror and causes a current to flow in the external circuit. This current is amplified and used to drive a servo motor which opens a valve and lets pressurised nitrogen into the test port of the Bourdon tube. The movement of the Bourdon tube acts counter to the coils and rotates the mirror back to a null. The servo valve therefore maintains sufficient pressure in the system to balance the torque of the Bourdon tube against the torque produced by the coils. The current passing through the coils is directly proportional to the differential pressure across the Bourdon tube and is read by measuring the voltage drop across a standard precision resistor. The Bourdon tube used had a maximum differential pressure limit of 100 cm of Hg and read the pressure accurately to 0·006% of the full scale reading.

The pressure was applied to the mercury reservoir of the cell shown in figure 2. Electrical contact was made to the mercury with a platinum wire which was silver soldered to a tungsten contact fused into a side arm of the mercury reservoir. An inverted U tube capillary carried the mercury into the solution compartment of the cell. This tube was connected to the reservoir by a ball and socket joint and held secure with O rings and an aluminium clamp. This arrangement allowed a certain flexibility to the U tube and a pressure tight seal. The capillary was drawn to a diameter of 0·01 mm which is capable of supporting a mercury head of the order of 70 cm of Hg. It was upturned as this is reported to produce more reproducible results (Lawrence and Mohilner 1971; Vos *et al* 1974). The solution compartment has two optical windows allowing the capillary tip and mercury meniscus in the reservoir to be aligned with a cathetometer. The pressure, P, applied to the reservoir is then directly the pressure across the mercury-solution meniscus minus a small correction due to the hydrostatic pressure of the solution. The interfacial tension, γ, can be calculated directly from the expression:

$$\gamma = K[P-(h_{\text{soln}}\,\rho_{\text{soln}}/\rho_{\text{Hg}})] \qquad (1)$$

where h_{soln} is the depth of the capillary tip below the solution/air meniscus, ρ_{soln} and ρ_{Hg} are the densities of the solution and the mercury at the temperature of the experiment and K is a calibration constant obtained from a solution of known properties. This equation should contain an expression for the density of air but the correction is negligible.

The electrode potential was controlled potentiostatically and a high frequency square wave (amplitude 5 mV peak to peak) was used to detect the maximum bubble pressure by the sudden increase in charging current that occurs as the mercury breaks away (Lawrence and Mohilner 1971). The instrument was

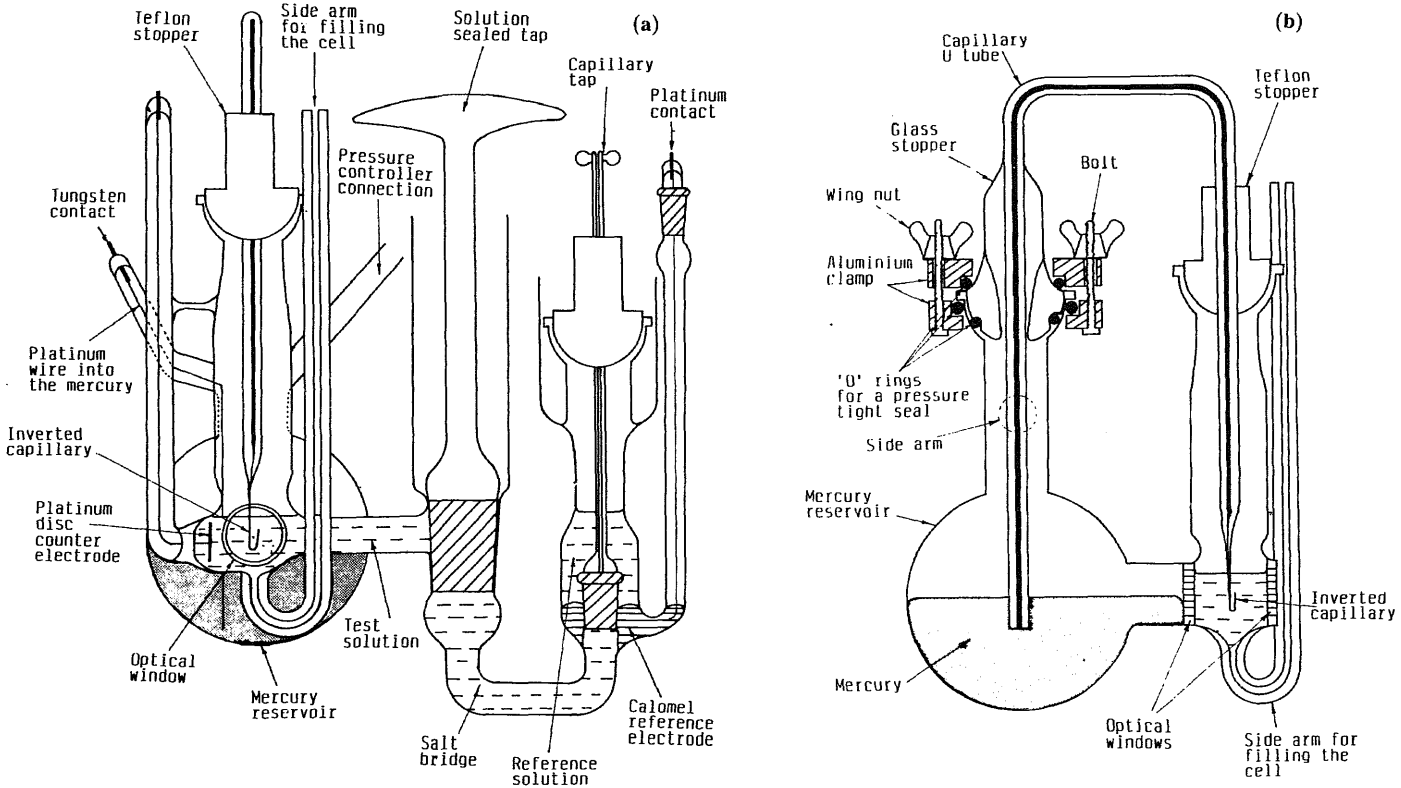

Figure 2. The electrocapillary cell **(a)** front view **(b)** left side view.

calibrated in aqueous 0·1 M KCl solution, assuming a value for the interfacial tension at the electrocapillary maximum of 426·2 mN m^{-1} (Devanathan and Peries 1954). An absolute determination by Vos and Los (1980) shows that this value is 0·6 mN m^{-1} too high. However, this leads to a proportional error of 0·15% in the derived quantities which is quite negligible. The design of the cell is such that the depth of immersion of the capillary below the solution is very small and consequently the error associated with measuring this distance becomes insignificant when converted to an equivalent mercury pressure. The variation of the density of the solution with increasing concentration of adsorbate and the increase in hydrostatic pressure due to the accumulation of mercury at the bottom of the cell are also negligible. An assessment of all errors leads to a total error on the interfacial tension of $\pm 0{\cdot}04\%$, the major contribution arising from the accuracy of the pressure controller. The cell was supported on a rack in a water bath and the whole assembly was mounted on a vibration free table.

The densities of the working solutions were measured using a pycnometer that had previously been calibrated with distilled water.

3. Results and discussion

Differential capacitance curves for xylose in the concentration range 10–1000 mM are shown in figure 3. Any variation of liquid junction potentials was assumed negligible as data is not available to make the necessary corrections. The curves display features typical of an organic species with maximum adsorption occurring around the point of zero charge (PZC). The adsorption/desorption peaks are poorly defined, which is a characteristic of a weak interaction between molecules in the adsorbed layer, and desorption is incomplete at the extremes of polarisation except for the lowest concentration. At the highest concentration the adsorption is approaching saturation as demonstrated by the constant capacitance minimum at 17·20 μF cm^{-2} between the potential $-0{\cdot}6$ V to $-1{\cdot}05$ V.

Electrocapillary curves for xylose in 0·7953 M NaCl are shown in figure 4. The rounded shape is consistent with Gouy's data (Gouy 1906) and with the poorly defined adsorption/desorption peaks displayed in the capacitance plots. The slight flattening at higher concentrations of organic compound around the pzc mirrors the capacitance minimum of figure 3. The adsorption behaviour is therefore similar in the presence of either chloride or fluoride anions. The corresponding electrocapillary curves in NaF were difficult to reproduce. These peculiarities of fluoride solutions are well documented (DeBattisti *et al* 1978) but require further detailed experimental investigation. The following analysis is based on the double integration of the capacitance curves to obtain the electrode charge and the interfacial tension. The integration constants are the point of zero charge and the interfacial tension at a known potential. The latter was obtained from the electrocapillary data by assuming that the interfacial tension measured at high negative field is independent of the anionic species. The coordinates of the point of zero charge are recorded in table 1. The charge/potential curves obtained by integration cross at a unique concentration independent potential corresponding to the position of maximum adsorption. The coordinates of this point are $\sigma^{M}_{max} = +2{\cdot}6\,\mu C\ cm^{-2}$ and $E_{max} = -0{\cdot}382$ V. This is consistent with the

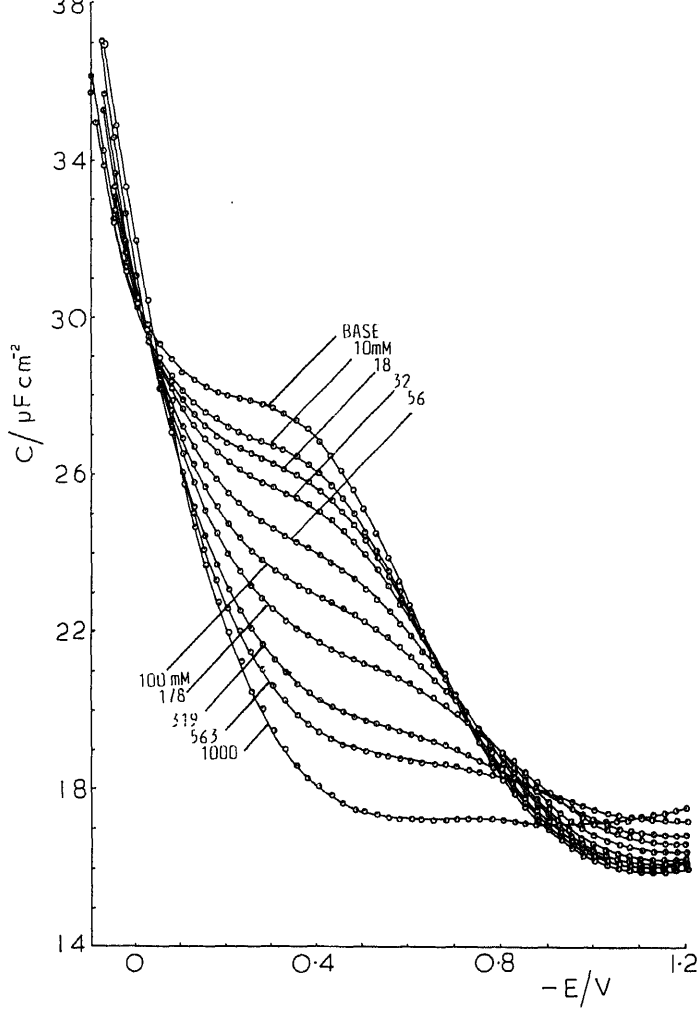

Figure 3. Differential capacity curves of a mercury electrode in contact with aqueous 0·7953 M NaF containing xylose. The concentration of xylose is indicated on each curve in mmol l^{-1}.

The surface pressure, ϕ ($= \xi_{base} - \xi$) at constant charge, was obtained from the auxiliary function $\xi(= \gamma + \sigma E)$ and the composite curve is shown as a function of concentration at the charge of maximum adsorption in figure 5. A similar curve can be obtained at constant electrode potential. The experimental scatter is of the order of $\pm 0{\cdot}3$ mN m^{-1}. Comparison of the composite isotherm with the generalised isotherms (Parsons 1961) calculated from the Frumkin equation [$\log \beta c = \log[\theta/(1-\theta)] + a\theta/2{\cdot}303$] predicts a value for the interaction coefficient, a, of $-0{\cdot}25$ corresponding to a weak attractive interaction between the adsorbed molecules; the saturation coverage Γ_s was obtained from

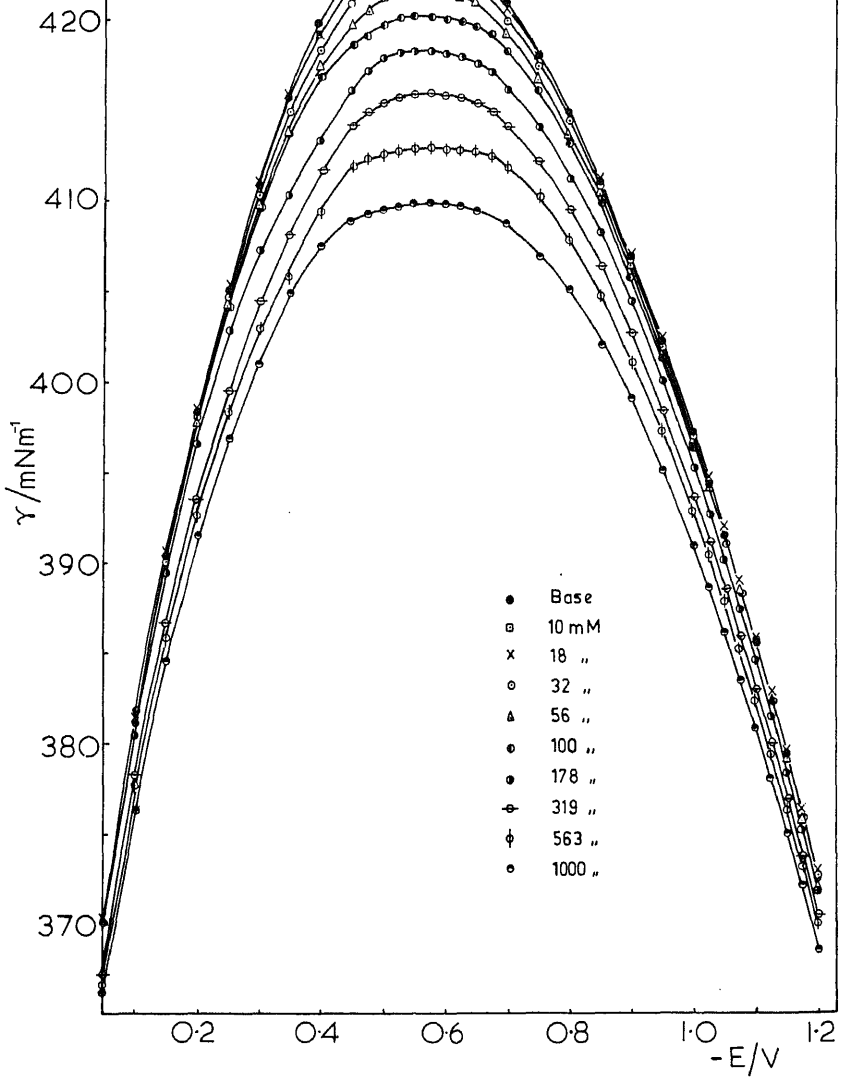

Figure 4. Electrocapillary curves for a mercury electrode in contact with aqueous 0·7953 M NaCl containing xylose.

ivalent to a molecular area of 0·5 nm^2, implying from space filling models ure 6) that xylose is adsorbed with the plane of the ring flat on the electrode; the ıe of log β was +0·79. The theoretical surface pressure corresponding to these ameters is compared with experimental data in figure 7. The generalised herms for the Virial and Volmer equations are unable to describe the shape of ıposite curves. However, as previously pointed out (Krishnan and de Levie 2) the validity of these isotherm fitting procedures must be treated with caution.

Table 1. Coordinates of the pzc of mercury in contact with 0·7953 mol l^{-1} NaF containing D-xylose at 25°C. Potentials are measured with respect to an aqueous 0·7953 mol l^{-1} NaCl calomel electrode.

c/mmol l^{-1}	$-E_{pzc}$/V	γ_{pzc}/mN m^{-1}	C_{pzc}/μF cm^{-2}
0	0·4810	428·0	25·39
10	0·4833	427·4	24·82
18	0·4850	427·2	24·52
32	0·4877	426·7	24·04
57	0·4919	425·5	23·16
100	0·4976	424·0	22·21
178	0·5039	421·7	21·15
319	0·5110	418·9	19·67
563	0·5175	415·4	18·87
1000	0·523	410·8	17·30

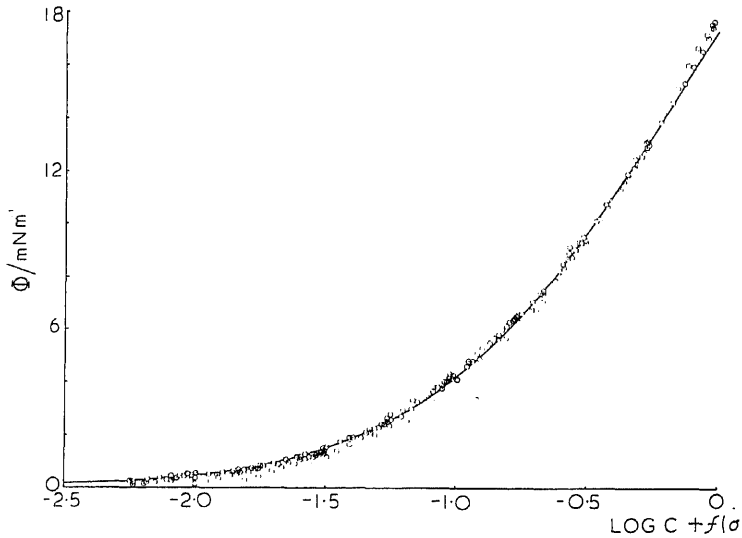

Figure 5. Composite surface pressure curve for xylose adsorbed on mercury in contact with 0·7953 M NaF at 25°C. The line was calculated from the Frumkin isotherm with $a = -0{\cdot}25$, $\Gamma_s = 3{\cdot}32 \times 10^{-10}$ mol cm^{-2}, and $\log \beta = 0{\cdot}79$.

The relative surface excess (Γ) of xylose was determined at constant charge by numerical differentiation of the function ξ with respect to the logarithm of xylose concentration. It was assumed that the activity could be approximated by the concentration, as the activity coefficients in the ternary mixture NaF + water + xylose are not available. However, some results show that xylose (Brill 1978) behaves like

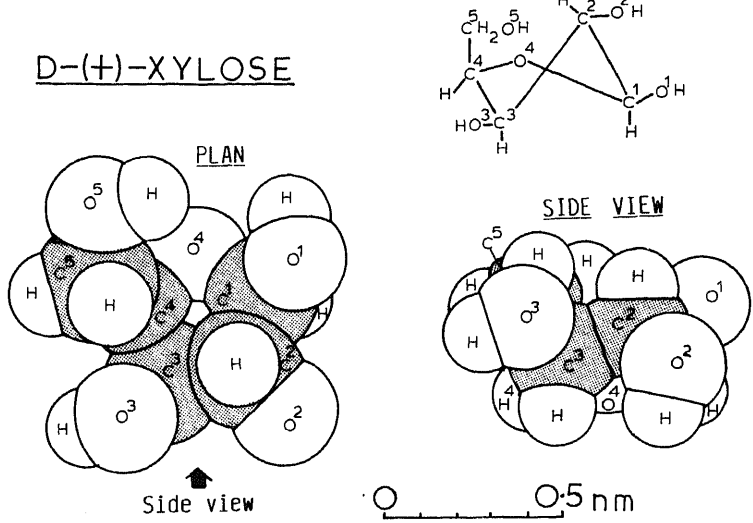

Figure 6. Schematic structure and scale drawing of a molecule of D-(+)-xylose.

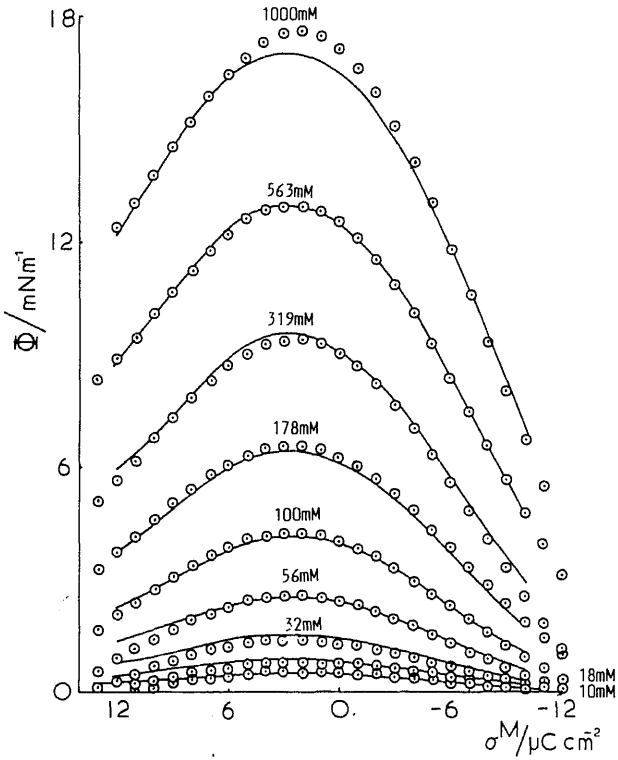

Figure 7. The surface pressure of xylose as a function of charge density on the mercury surface at 25°C. The xylose concentration in mmol l^{-1} is indicated on each curve. The lines were calculated from the Frumkin isotherm with $a = -0{\cdot}25$, $\Gamma = 3{\cdot}32 \times 10^{-10}$

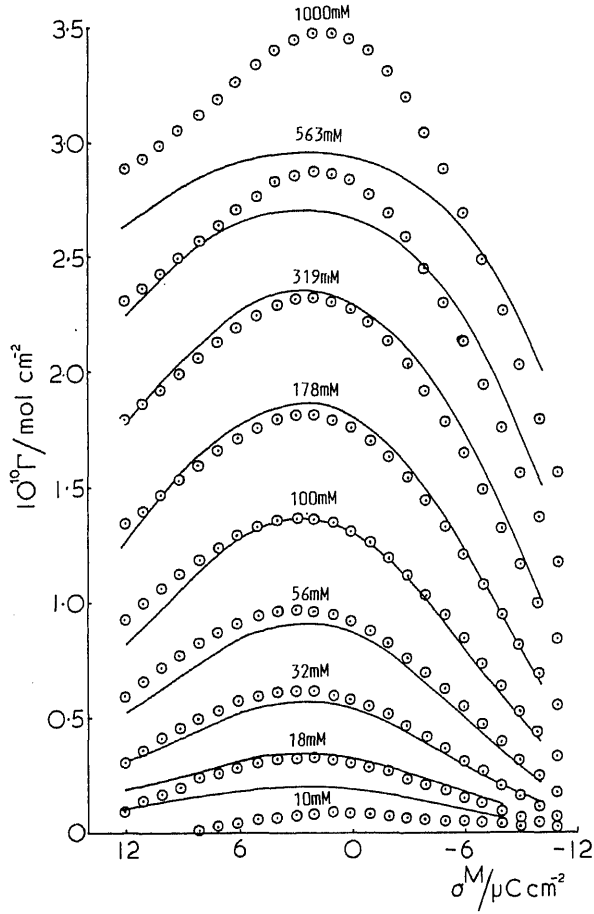

Figure 8. The relative surface excess of xylose as a function of charge density on the mercury surface at 25°C. The concentration of xylose in mmol l^{-1} is indicated by each curve. The lines were calculated from the Frumkin isotherm with $a = -0{\cdot}25$, $\Gamma_s = 3{\cdot}32 \times 10^{-10}$ mol cm^{-2}, log $\beta = 0{\cdot}79$ and experimental values of $f(\sigma)$.

(Parsons and Peat 1981) and become significant only for concentrations above 0·5 mol l^{-1}. The results are shown in figure 8. The agreement with the Frumkin isotherm is satisfactory except for the end concentrations which is probably a result of the numerical differentiation technique. The resulting data may be fitted to the Langmuir isotherm arranged in a linear form

$$c/\Gamma = c/\Gamma_s + 1/\Gamma_s\beta, \tag{2}$$

where c is the concentration of adsorbate. The linear relationship at constant charge was displayed in the concentration range 0–0·3 mol l^{-1} with parameters Γ_s of $3{\cdot}3 \times 10^{-10}$ mol cm^{-2} and log β of $+0{\cdot}84$ that agree favourably with surface

coefficient ($\log \beta = 0{\cdot}79$) by assuming that the adsorption process corresponds to a solvent displacement equilibrium. If the standard states are chosen as unit mole fraction for the adsorbate and solvent in the bulk phase and on the surface then:

$$\beta = [1/c_{s,b}]\exp(-\Delta\bar{G}^{\circ}/RT) \tag{3}$$

where $c_{s,b}$ is the bulk solvent concentration. Substituting the value of β into this equation gives $-14{\cdot}47$ kJ mol^{-1} for the standard Gibbs energy of adsorption at the point of maximum adsorption $\Delta\bar{G}^{\circ}_{max}$). This value is considerably less than the value of -22 kJ mol^{-1} for sucrose (Parsons and Peat 1981). A decrease in the standard Gibbs energy of adsorption for xylose compared to sucrose would be expected due to its smaller molecular size. This can be assumed from the work of Kaganovich and Gerovich (1966) who claim that the adsorption of aliphatic amines, acids and alcohols forming an homologous series conforms to the Traube rule. This is equivalent to the condition that the Gibbs energy is an additive function of the number of $-CH_2-$ groups in the molecule. Also Dryhurst and coworkers (Brabec *et al* 1977; Kinoshita *et al* 1977) have studied the adsorption of some nucleosides and claim from their results (Brabec *et al* 1978) that the standard Gibbs energy of adsorption is given by the sum of the standard Gibbs energy of the free base (purine or pyrimidine) with that of the free sugar (ribose or deoxyribose). Sucrose consists of D-glucose and D-fructose joined by a glycosidic linkage so a substantially smaller standard Gibbs energy might be expected for the single ring compound. However, the standard Gibbs energy is a complex quantity dependent upon metal-adsorbate, metal-solvent, adsorbate-adsorbate, adsorbate-solvent and solvent-solvent interactions in both the surface and the bulk phases. Xylose is less soluble in aqueous solution than sucrose and in this respect would be expected to be adsorbed to a greater extent. As the converse is true then the difference in behaviour of the two compounds is likely to be due to interactions within the surface phase, rather than to a difference in the energy of the molecules in solution. This may be due to a strong chemical interaction with the metal because of the presence of $-OH$ groups, although this seems unlikely as the values for the standard Gibbs energy are similar to those expected for physical adsorption. Alternatively we have argued previously in a comparison of the air/water and metal/water interfaces that there could be a specific solvent structure that is induced by the metal or the organic molecule that is favourable for the adsorption of sucrose but unfavourable for xylose (Parsons and Peat 1980). Dramatic changes in adsorption behaviour that are thought to be due to subtle changes in solvent structure have been demonstrated recently for the stereoisomers mannitol and sorbitol (Peat and Shannon 1983). D-ribose and 2-deoxy-D-ribose have been studied (Brabec *et al* 1978) and these adsorbates also show weak adsorption with the molecules adsorbed with the plane of the ring flat on the electrode surface. However, there is a distinct difference in that the D-ribose shows a maximum adsorption at -2 μC cm^{-2} compared with $+2{\cdot}6$ μC cm^{-2} for xylose. Furthermore, substitution of a single $-OH$ for a H atom in 2-deoxy-D-ribose shifts the maximum adsorption to -4 μC cm^{-2}. This is difficult to explain qualitatively from a structural aspect due to the complex molecular conformations involved but does indicate that small structural changes in the molecule can cause marked changes in adsorption behaviour.

The variation of standard Gibbs energy with electric field was determined

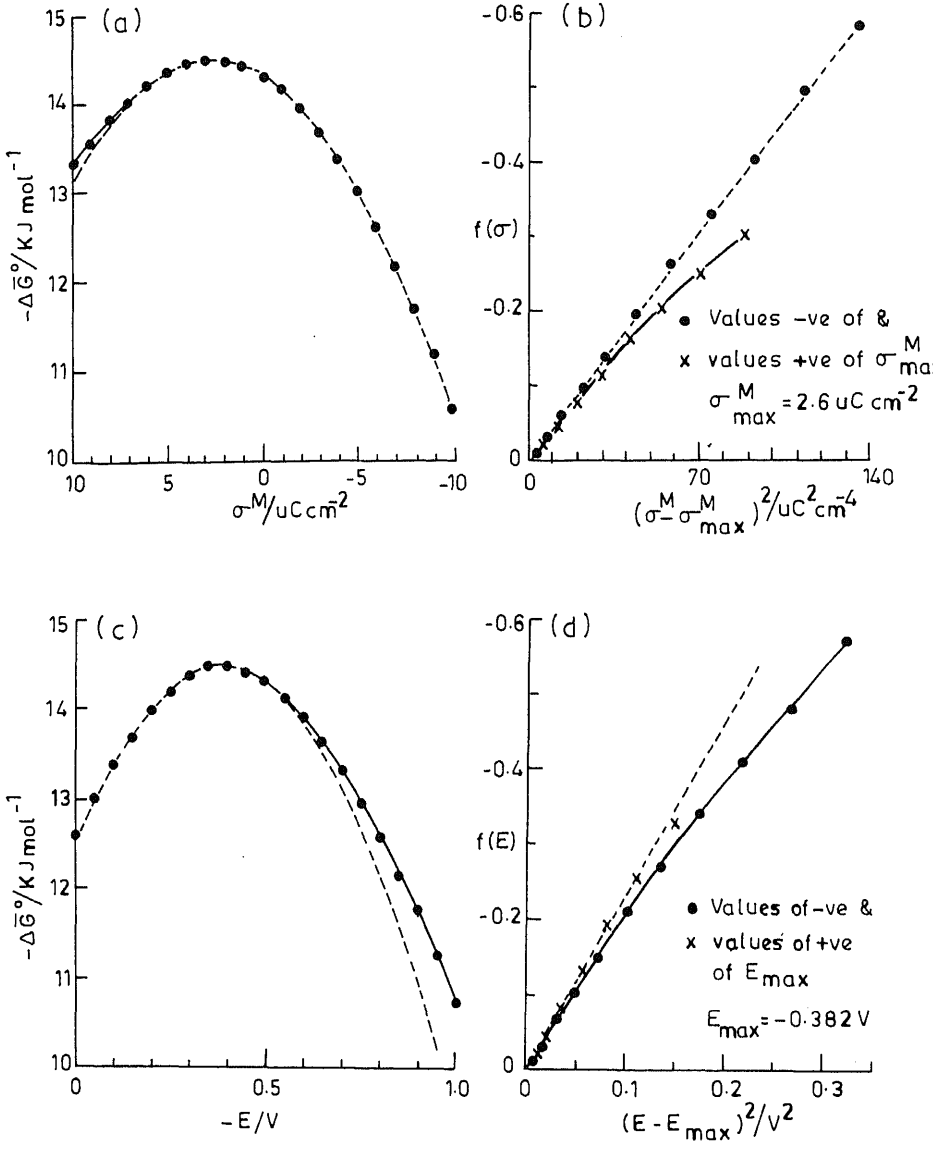

Figure 9. The variation of the standard Gibbs energy of adsorption of xylose with charge (**a**) and potential (**c**). The same data plotted as a function of $(\sigma-\sigma^{M})^{2}$ (**b**) and $(E-E_{max})^{2}$ (**d**) The broken lines are calculated from (4) and (6) with b = 0·0043 cm^{4} μC^{-2} and α = 2·31 V^{-2} respectively.

nergy is given by

$$f(\sigma) = \log \beta - \log \beta_{max} = -b(\sigma^m - \sigma^m_{max})^2, \quad (4)$$

here

$$b = (1/2\times 2{\cdot}303\ RT\Gamma_s) - 1\ (C_1^{-1} - C_0^{-1}), \quad (5)$$

nd where C_0 is the capacity corresponding to zero coverage. This model is satis-actory in the charge range $+7$ to $-10\ \mu C\ cm^{-2}$ with $b = 0{\cdot}0043\ cm^4\ \mu C^{-2}$ igure 9b). The alternative plot at constant potential corresponds to Frumkin's odel of two capacitors in parallel for which (Parsons 1976)

$$f(E) = \log \beta - \log \beta_{max} = -\alpha(E - E_{max})^2, \quad (6)$$

here

$$\alpha = (C_0 - C_1)/2{\cdot}303\ RT\Gamma_s. \quad (7)$$

s the charge-potential curves pass through a concentration-independent point orresponding to the point of maximum adsorption, it follows that the series and arallel models coverage at this unique point and

$$\sigma^m_{max} = -E_N C_1 C_0/(C_0 - C_1) = E_{max}\ C_0, \quad (8)$$

here E_N is the shift of the point of zero charge due to the adsorption of organic ompounds and E_{max} is measured with respect to the point of zero charge. Substituting he values for σ^m_{max} and E_{max} into (8) leads to a value for C_0 of $26{\cdot}24\ \mu F\ cm^{-2}$. aking the experimental values for b and Γ_s and the calculated value for C_0 in (5), hen C_1 has a value of $18{\cdot}38\ \mu F\ cm^{-2}$. Substituting σ^M_{max}, C_0 and C_1 back into (8) redicts a calculated value of $-0{\cdot}042$ V for the shift of the point of zero charge due o adsorption of the organic species. Similar conclusions can be drawn from the hift of potential caused by the adsorption of xylose which is plotted in figure 10.

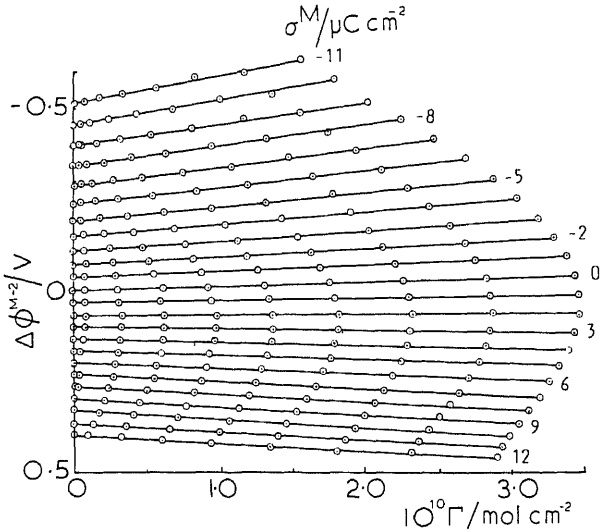

Figure 10. The change of rational potential drop across the inner layer upon adsorption of xylose at constant charge. Charge values are indicated by each curve.

Here $\Delta\phi^{m-2}$ is the change in the rational potential drop across the inner layer. It was calculated from:

$$\Delta\phi^{m-2} = E_\sigma^N - E_{\sigma=0}^{\text{base}} - \phi_\sigma^{2-s}, \tag{9}$$

where ϕ_σ^{2-s} is the diffuse layer potential drop, E_σ^N is the measured potential in the presence of adsorbate and $E_{\sigma=0}^{\text{base}}$ is the pzc of the base electrolyte. The linear relationship implies congruence of the isotherm with respect to electrode charge and the zero gradient at $+2{\cdot}6\ \mu\text{C cm}^{-2}$ corresponds to the charge of maximum adsorption. The shift of the potential of zero charge due to adsorption of a monolayer of xylose can be obtained by extrapolation of the data at $\sigma^m = 0$ to Γ_s. The value of $-0{\cdot}042$ V is in excellent agreement with the previous calculations using the capacitors in series model. Similar arguments based on the value of $\alpha = 2{\cdot}31\ \text{V}^{-2}$ from figure 9d predict a value of $-0{\cdot}050$ V for E_N which does not agree with the experimental value.

Increasing evidence suggests that water is adsorbed at the point of zero charge with its oxygen atom adjacent to the metal and that the surface potential, $g_{(M)}^{\text{H}_2\text{O}}$ (dip), is of the order of $-0{\cdot}080$ V (Trasatti 1970). The negative shift in potential upon replacing water by xylose also implies that this molecule is adsorbed with the negative end of its dipole towards the metal. At saturation coverage the shift of the point of zero charge is given by:

$$E_N = g_{(M)}^N\ (\text{dip}) - g_{(M)}^{\text{H}_2\text{O}}\ (\text{dip}) \tag{10}$$

where $g_{(M)}^N$ (dip) has the value $-0{\cdot}122$ V and is the surface dipole potential for xylose on the uncharged surface. The negative sign confirms the orientation for xylose with the negative end of its dipole towards the metal. Assuming a value for ε of 9·78 based on the thickness of the water layer as 0·33 nm and a C_0 value of $26{\cdot}24\ \mu F\ \text{cm}^{-2}$ then the effective dipole moment for xylose is 5×10^{-30} c.m. This compares favourably with a dipole moment of $2{\cdot}0 \times 10^{-29}$ c.m estimated by Franks *et al* (1973) for several similar compounds in aqueous solution.

Acknowledgements

We are grateful to Drs R M Reeves and I Williams who designed and built the maximum bubble pressure electrometer and to the Science Research Council for a maintenance grant to R Peat.

References

Adamson A W 1967 *Physical chemistry of surfaces* (London: John Wiley and Sons)
Brabec V, Christian S D and Dryhurst G 1977 *J. Electroanal. Chem.* **85** 389
Brabec V, Christian S D and Dryhurst G 1978 *J. Electrochem. Soc.* **125** 1236
Brill R V 1978 *Tech. Res. Commun., Curr. Data News* **6** No. 6
DeBattisti A, Amadelli R and Trasatti S 1978 *J. Colloid Interface Sci.* **63** 61
Devanathan M A V and Peries P 1954 *Trans. Faraday Soc.* **50** 1236
Franks F, Reid D S and Suggett A 1973 *J. Solution Chem.* **2** 99

rahame D C, Coffin E M, Cummings J I and Poth M A 1952 *J. Am. Chem. Soc.* **74** 1207
ills G J and Payne R 1965 *Trans. Faraday Soc.* **61** 326
aganovich R I and Gerovich V M 1966 *Elektrokhimiya* **2** 977
inoshita H, Christian S D and Dryhurst G 1977a *J. Electroanal. Chem.* **83** 151
inoshita H, Christian S D and Dryhurst G 1977b *J. Electroanal. Chem.* **85** 377
rishnan M and de Levie R 1982 *J. Electroanal. Chem.* **131** 97
awrence J and Mohilner D M 1971 *J. Electrochem. Soc.* **118** 259, 1596
arsons R 1961 *Proc. R. Soc. London* **A261** 79
arsons R 1963 *J. Electroanal. Chem.* **5** 397
arsons R 1976 *Croat. Chem. Acta* **48** 597
arsons R and Peat R 1980 *J. Res. Inst. Catal., Hokkaido Univ.* **28** 321
arsons R and Peat R 1981 *J. Electroanal. Chem.* **122** 299
arsons R, Peat R and Reeves R M 1975 *J. Electroanal. Chem.* **61** 151
eat R and Shannon S 1983 *J. Electroanal. Chem.* **159** 229
rasatti S 1970 *J. Electroanal. Chem.* **28** 257
chiffrin D J 1969 *J. Electroanal. Chem.* **23** 168
os H, Wiersma J and Los J M 1974 *J. Electroanal. Chem.* **52** 27
os H and Los J M 1980 *J. Colloid Interface Sci.* **74** 360

Polymer films on electrodes. 21. Electrochemical behavior of tetramethyltetraselenafulvalene incorporated into a Nafion-coated electrode[§]

ROGER D MOULTON[1], ALLEN J BARD* and JACK M WILLIAMS[2]

[1] Department of Chemistry, University of Texas, Austin, Texas 78712, USA
[2] Chemistry Division, Argonne National Laboratory, Argonne, IL 60439, USA

Abstract. The cyclic voltammetry of tetramethyltetraselenafulvalene (TMTSF) in CH_2Cl_2 is described. Controlled potential coulometry yielded a suspension of $(TMTSF)_2ClO_4$ crystals. The incorporation of TMTSF onto a Pt electrode coated with the perfluorinated ion exchange polymer Nafion and the electrochemical behavior of the electrode in aqueous $NaClO_4$ is described and compared to the related compound tetrathiafulvalene (TTF). A pair of peaks separated by about 400 mV is observed and is ascribed to the couple $TMTSF/(TMTSF)_2^+ClO_4^-$. However, formation of the needle-like crystals found with Nafion/TTF was not seen with TMTSF.

Keywords. Tetramethyltetraselenafulvalene; cyclic voltammetry; controlled potential coulometry; Nafion; tetrathiafulvalene.

1. Introduction

Considerable attention has been directed towards the modification of the electrode surface by attachment of a thin layer of the perfluorinated cation exchange polymer Nafion[†] (Rubinstein and Bard 1980, 1981; White *et al* 1982; Martin *et al* 1982a, b; Buttry and Anson 1982, 1983, 1984; Prieto and Martin 1984; Leddy and Bard 1985; Leddy *et al* 1985). Electroactive molecules can be preconcentrated in the polymer film, which can exhibit novel electrochemical behavior. In a previous study from this laboratory, tetrathiafulvalenium (TTF^+) was incorporated into a Nafion-coated Pt electrode (Henning *et al* 1981, 1982; Henning and Bard 1982) (denoted Pt/Naf, TTF^+). Electrochemical cycling of this electrode resulted in the growth of electrically conductive domains and crystals of $TTF^+Br_{0.7}$ inside the polymer matrix. The recent report of the superconducting properties of a compound related to TTF, $(TMTSF)_2ClO_4$ (TMTSF = tetramethyltetraselenafulvalene) (Bechgaard 1982; Engler *et al* 1982; Lee *et al* 1982) led us to explore the electrochemical behavior of a Pt/Naf, $TMTSF^+$ electrode, with the goal of growing crystals of the superconducting salt in the Nafion film. In this paper, the electrochemical behavior of a Pt/Naf, $TMTSF^+$ electrode is described. We were guided in our study by the previous work with TTF; however, the properties of the system involving TMTSF were very different, and no conductive crystal could be produced by the electrochemical procedure.

[§] Dedicated to Prof. K S G Doss on his eightieth birthday.

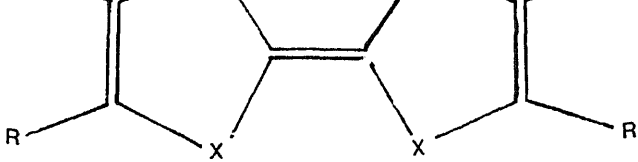

TTF: R=H, X=S
TMTSF: R=CH_3, X=Se

Chart 1.

2. Experimental

2.1 *Materials*

Tetramethyltetraselenafulvalene (TMTSF) was prepared as previously described (Wudl and Nalewajek 1980) and was stored under N_2 at 5°C. $(TMTSF)Cl_x$ was prepared photochemically from TMTSF and CCl_4 as previously described (Scott *et al* 1976). Aqueous solutions were made from $NaClO_4$ (Fischer Scientific) and triply distilled water. 970 equivalent weight Nafion dissolved in ethanol (2% by weight) was a gift from E I duPont de Nemours and Co.

2.2 *Electrochemical synthesis of* $(TMTSF)_2ClO_4$

50 mg TMTSF were dissolved in 20 ml CH_2Cl_2/0·4 M TBAP and cyclic voltammetry performed at a Pt disk. The solution showed two well-formed oxidation waves. Controlled potential coulometry at a Pt mesh electrode at a potential midway between the waves resulted in the consumption of 0·49 Faradays/eq. The purple solution immediately began to darken with a suspended crystalline precipitate, which was collected after the coulometry was complete by decanting the solution. The precipitate was washed several times with CH_2Cl_2 and air dried. The total yield was 43 mg (77%).

2.3 *Apparatus*

All electrochemical measurements employed a Princeton Applied Research (PAR) Model 175 universal programmer, Model 173 potentiostat and Model 179 digital coulometer. The working electrode was a platinum disk (area = 0·05 cm^2) imbedded in a glass rod. A platinum mesh was used as a counter electrode and a saturated calomel electrode (SCE) was used as the reference electrode. The cell was of a two-compartment design, as discussed previously (Malpas *et al* 1979).

2.4 *Procedure*

Two methods were employed to incorporate TMTSF into a Nafion film on the electrode surface. Method A: The Pt electrode was polished with 0·05 μm alumina on a felt pad and the electrode was then rinsed with water and covered with a 5 μL aliquot of the Nafion solution mixed with a solution of $(TMTSF)_2ClO_4$ dissolved in MeCN. The amount of TMTSF solution was controlled to give equal stoichiometry of the $(TMTSF)_2^+$ and sulfonate groups in the polymer. The liquid layer on the

electrode was then allowed to evaporate for 15 min before the electrode was immersed in solution. The thickness of the film created in this manner was measured with a Sloan–Dektak profile measuring device. Films of dry thickness of 0·5 μm tended to be the most reproducible. Method B: 5 μL of a solution of Nafion in EtOH was deposited onto an electrode allowed to dry for 10 min. The electrode was then immersed in an aqueous solution of TMTSF Cl_x to extract $(TMTSF)^+$. After 30 min, the electrode was removed and placed in the cell, and electrochemical experiments were begun immediately to avoid ion exchange with the electrolyte ($NaClO_4$).

3. Results

3.1 *TMTSF in solution*

The electrochemical behavior of TTF and its analogues in nonaqueous solution has been studied (Chambers *et al* 1977; Coffen *et al* 1971; Kaufman *et al* 1976; Kacemi and Lamache 1985). Both tetrathia- and tetraselenafulvalenes are oxidized in two distinct processes to the +1 and +2 oxidation states. Each oxidation has been ascribed to the removal of an electron from a formally $7e^-$ ring to form an aromatic cationic heterocycle (Perlstein 1977; Engler *et al* 1975). Electrochemical methods have been employed in the synthesis of the conductive salts of TMTSF (Bechgaard 1982; Engler *et al* 1982; Lee *et al* 1982), but apparently no detailed study of the voltammetry has been reported. We therefore examined the redox behavior of TMTSF for comparison with that previously reported to TTF and its analogues.

TMTSF shows two reversible oxidation waves by cyclic voltammetry in CH_2Cl_2/0·4 M TBAP (figure 1). The peak potentials of the waves were estimated vs an aqueous standard hydrogen electrode by adding ferrocene to the solution as an internal standard (Gritzner and Kuta 1982), and were found to be +0·543 and +0·917 V vs NHE. The values are somewhat different from the values reported in CH_2Cl_2/0·1 M $TBABF_4$ (Wudl *et al* 1981). Evidently, complexation or ion pair formation with the supporting electrolyte anion is important in the stability of the

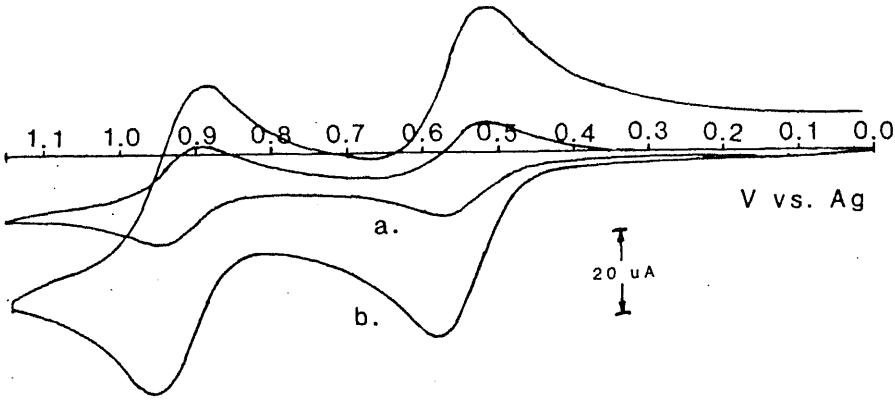

Figure 1. Cyclic voltammetry of 4·0 mm TMTSF in CH_2Cl_2/0·4 M TBAP (a) 50 mV/sec

electrode can be represented by

$$ClO_4^- + 2\ TMTSF \rightarrow (TMTSF)_2ClO_4(solid) + e^-. \quad (1)$$

However, on the time scale of cyclic voltammetry, the oxidation is reversible with no loss of material due to precipitation (figure 2a). Precipitation of the product must therefore occur on a time scale intermediate between that of the voltammetry and coulometry. experiments. To determine at what point nucleation occurs, the following experiment was performed: After a scan over the first oxidation wave, the potential was held constant for different periods of time (τ), and then the reverse (cathodic scan) carried out (figure 2b–d). If the potential of the electrode was held at the first oxidation wave for $\tau > 10$ sec, a decrease was observed in the cathodic peak current with the appearance of "noise" in the voltammogram, especially at potentials following the cathodic peak. Visual examination of the solution showed a cloud of dark material near the electrode at this time. If the potential was held for longer times, the cathodic peak current was further decreased and the "noise" became more noticeable. The results suggest that nucleation occurs after about 10 sec so that the cathodic peak current decreases

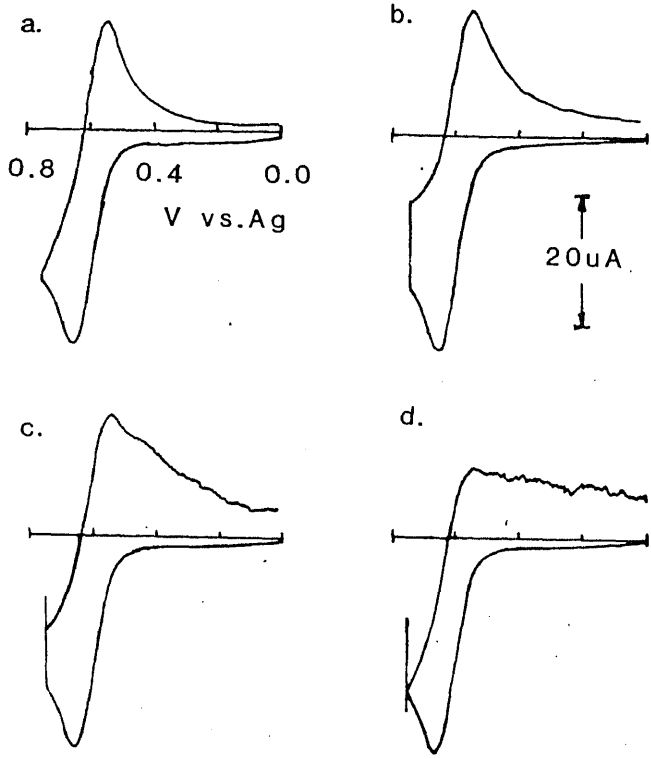

Figure 2. Single scan voltammograms of 5·0 mm TMTSF in CH_2Cl_2/0·4 M $TBAP_4$. Scan rate = 100 mV/sec, with the electrode held at the switching potential (+0.75 V) for (a) 0, (b) 10, (c) 20, (d) 40 sec.

is attributed to small individual crystals of the salt that encounter the electrode and are reduced in a process aided by the electrical conductivity of the crystal. Because the nucleation process is slow, most crystals do not precipitate on the electrode surface.

3.2 *Behavior of TMTSF in Nafion*

The redox behavior of a Pt/Naf, TMTSF electrode in aqueous $NaClO_4$ prepared by the two methods is similar; the observed currents were larger when the electrode was prepared using method A (see above). On the first reductive scan, a large wave was seen (figure 3). This wave typically showed some diffusional tailing, especially at high scan rates or with thick films. On the subsequent scans, a small oxidation wave appeared at 0·35 V, and on reversal, a new reduction peak appeared at −0·05 V. The area under these waves suggests that < 10% of the (TMTSF)$_2^+$ reduced on the first scan remained electroactive. Continued cycling shows a small change in the peak potentials and a steady decrease in peak currents was observed over several hours. The pair of peaks found after the first reduction scan are separated by about 400 mV and are perhaps slightly sharper than the theoretical 90 mV ($n=1$) width at half-maximum expected for a nernstian thin layer process (Bard and Faulkner 1980).

An attempt was made to characterize the nature of the peaks by studying the effect of scan rate and electrolyte concentration on peak potential and current. Unfortunately, the observed waves were not reproducible, so that unambiguous data to determine the exact stoichiometry of the processes could not be obtained.

3.3 *Effect of changing the electrolyte*

An electrode prepared by method A was cycled in 5 M $NaClO_4$ until essentially steady state behavior was obtained. The electrode was removed from solution in the oxidized state and placed in a 5 M NaCl solution. The first reduction showed a large peak similar to that seen on the scan of a freshly prepared electrode (figure 4). Continued cycling showed new electrochemical behavior in which the reduction

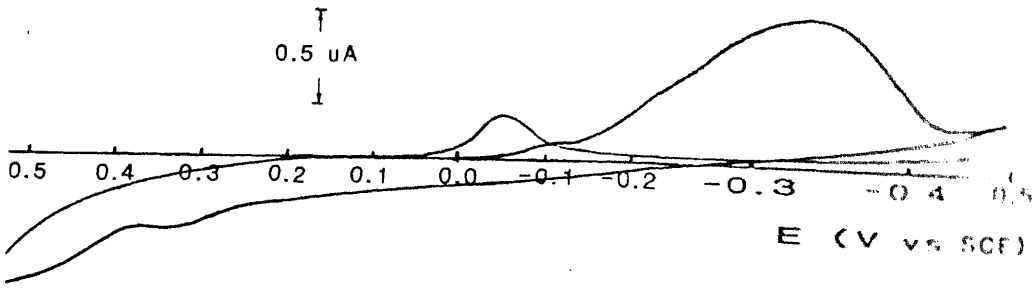

Figure 3. First scan and second scan of a Pt/Naf, TMTSF electrode in 5 M NaClO$_4$.
Scan rate, 2 mV/sec; film thickness, 0·5

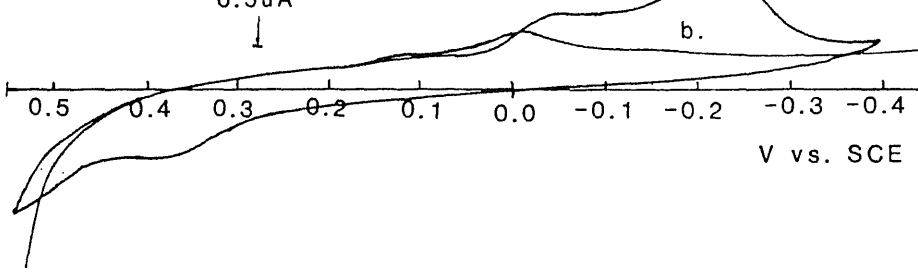

Figure 4. First (a) and second (b) scans of a Pt/Naf, TMTSF electrode previously cycled in 5 M $NaClO_4$ and then placed in 5 M NaCl. Film thickness, 0·5 μm, scan rate, 2 mV/sec. The electrode was prepared by the same procedure as in figure 3 (method A).

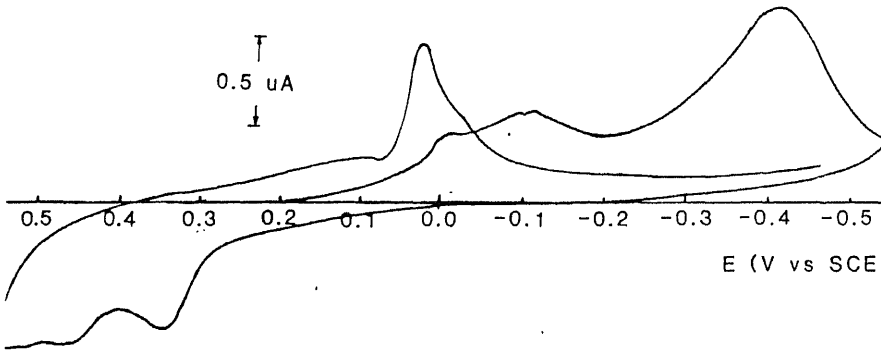

Figure 5. First scan and second scan in 5 M $NaClO_4$ of a Pt/Naf, TMTSF electrode made by method A and with benzonitrile as the solvent. Scan rate = 2 mV/sec; film thickness, 0·5 μm.

peak was shifted to positive potentials by ca. 50 mV and the amount of electroactive TMTSF was observed to be smaller – less than 50% of that previously observed in $NaClO_4$.

To establish that $(TMTSF)_2^+$ was not being expelled from the Nafion film by exchange with Na^+ from the 5 M NaCl solution, the electrode was replaced in the original $NaClO_4$ solution. After 1 cycle, essentially steady state behavior was observed as before. The electroactivity had returned to the previous level, confirming that the compound had not left the film.

3.4 *Effect of trapped solvent in the film*

An electrode prepared by method A showed that < 10% of TMTSF reduced on the first scan remained electroactive. However, if the film was cast from a benzonitrile solution, rather than an acetonitrile solution, the amount of TMTSF which remained electroactive on the second and following cycles was much greater (figure 5). The potential of the reduction peak was also shifted to positive values by 75 mV.

The difference in the films prepared by the two methods is probably a result of the effects of trapped benzonitrile in the film. Whereas method A involving acetonitrile gave reproducible films as described above following evaporation of

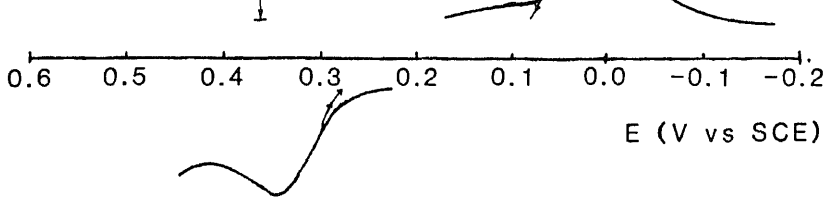

Figure 6. Scan reversal experiment of the electrode shown in figure 5. Reversal occurred at the steepest part of the rising portion of each wave. Scan rate, 2 mV/sec.

the solvent for 15 min, the use of benzonitrile required evaporation overnight to achieve the same degree of reproducibility. Even after 12 hr, some of the benzonitrile used to cast the film probably remained trapped in pockets inside the Nafion.

3.5 *Effect of switching potential*

The presence of strong positive interactions between molecules (as between monomers in a one-dimensional conductor) can be demonstrated by a scan reversal at points less extreme than the peak potential of a CV wave (Laviron 1975, 1981; Angerstein-Kazlowaska *et al* 1977). This technique was used previously to show that strong interactions exist between TTF molecules in Pt/Naf, TTF (Henning and Bard 1983). A similar experiment is shown in figure 6. As the potential of the scan approached the peak potential, the scan was reversed. The current on the reverse scan slightly exceeded that on the forward scan for a few seconds. This crossover pattern suggests that, as with TTF^+Br^-, there are interactions in the $(TMTSF)^+ClO_4^-$ that decrease upon reduction of part of the lattice, allowing the remaining molecules to be reduced more easily. A similar effect, however, was not observed in the oxidation of Nafion-bound TMTSF. The strength of the interactions in the $TMTSF^+ClO_4^-$ lattice is less than that with TTF^+Br^- and TTF in Pt/Naf, TTF^+, since the crossover pattern was much less pronounced.

4. Discussion

Comparison of the electrochemical behavior of a Pt/Naf, $TMTSF^+$ electrode to the previously described Pt/Naf, TTF^+ electrode leads to some qualitative similarities. The first reductive scan shows a broad wave, which disappears on subsequent scans in favor of a pair of slightly sharper waves at widely separated potentials. The initial scan is assigned to the reduction of $TMTSF^+$ [or $(TMTSF)_2^+$] bound to the sulfonate groups of the Nafion film to neutral TMTSF. Continued cycling results in the incorporation of ClO_4^- into the film, and we propose for the overall redox reaction in the film

$$2\ TMTSF + ClO_4^- \rightleftarrows (TMTSF)_2^+ClO_4^- + e^-. \qquad (2)$$

We propose a "square scheme" to explain the behavior of the Nafion/TMTSF system, by analogy to that previously deduced for Nafion/TTF (Henning *et al* 1981, 1982; Henning and Bard 1983). The first cathodic wave represents reduction of $(TMTSF)_2^+$ associated with sulfonate groups to neutral TMTSF. The oxidation of this species occurs with incorporation of ClO_4^- to form $(TMTSF)_2^+ClO_4^-$. Subsequent reductions involve this species to TMTSF as shown in (3).

$$\begin{array}{ccc} (TMTSF)_2^+ClO_4^- + e & \xrightarrow{-0{\cdot}05\ V} & (TMTSF)_2 + ClO_4^- . \\ \uparrow\ \text{fast} & & \downarrow\ \text{fast} \\ 2TMTSF^+ + ClO_4^- + e & \xleftarrow{+0.35\ V} & 2TMTSF + ClO_4^- \end{array} \quad , \qquad (3)$$

where $(TMTSF)_2$ and $2\,TMTSF^+ + ClO_4^-$ imply structures different from the equilibrium ones, TMTSF and $(TMTSF)_2^+ClO_4^-$, respectively.

One can also contrast the behavior of TMTSF with TTF in Nafion. Visual examination of a Pt/Naf, TMTSF electrode before and after cycling does not show formation of the needles of crystalline TMTSF in the film, as found during electrochemical formation of $TTFBr_{0.7}$ in Pt/Naf, TTF. The failure to achieve this goal may be attributed to the lack of a high concentration of electroactive TMTSF in the film. Even when benzonitrile is present in the film, which increases by several times the electroactivity of the TMTSF in the film, the concentration is evidently too low to initiate nucleation (to form bulk solid phase $(TMTSF)_2ClO_4$); TMTSF is also less hydrophilic than TTF^+, so that it may preferentially migrate to hydrophobic zones of the Nafion (Yeo and Eisenberg 1977; Falk 1980; Yeager and Steck 1981), where it can no longer participate in electron transfer to the Pt substrate. This could account for the progressive loss of electroactivity even when the TMTSF is apparently not leached from the film, and the better waves observed when the film contains benzonitrile. Unfortunately, this difference in behavior prevents the electrochemical growth of microcrystals of conductive material.

Acknowledgements

The support of this research by the National Science Foundation (CHE8402135) is gratefully acknowledged.

References

Angerstein-Kazlowaska H, Klinger J and Conway B E 1977 *J. Electroanal. Chem. Interfacial Electrochem.* **75** 45

Bard A J and Faulkner L R 1980 *Electrochemical methods* (New York: Wiley) pp. 522

Bechgaard K 1982 *Mol. Cryst. Liq. Cryst.* **79** 1

Buttry D A and Anson F C 1982 *J. Am. Chem. Soc.* **104** 4824

Buttry D A and Anson F C 1983 *J. Am. Chem. Soc.* **105** 685

Buttry D A and Anson F C 1984 *J. Am. Chem. Soc.* **106** 59
Chambers J Q, Green D C, Kaufman F B, Engler E M, Scott B A and Schumaker R R 1977 *Anal. Chem.* **49** 802
Coffen D L, Chambers J Q, Williams D R, Garrett P E and Canfield N D 1971 *J. Am. Chem. Soc.* **93** 2258
Engler E M, Greene R, Haen P, Tomkiewicz Y, Mortenson K and Berendzen J 1982 *Mol. Cryst. Liq. Cryst.* **79** 15
Engler E M, Kaufman F B, Green D C, Klots C E and Compton R N 1975 *J. Am. Chem. Soc.* **97** 2921
Engler E M and Patel V V 1975 *Tetrahedron Lett.* **14** 1259
Falk J 1980 *Can. J. Chem.* **58** 1495
Gritzner G and Kuta J 1982 *Pure Appl. Chem.* **54** 1527
Henning T P and Bard A J 1983 *J. Electrochem. Soc.* **130** 613
Henning T P, White H S and Bard A J 1981 *J. Am. Chem. Soc.* **103** 3937
Henning T P, White H S and Bard A J 1982 *J. Am. Chem. Soc.* **104** 5862
Kacemi K E and Lamache M 1985 *Nouveau J. Chem.* **9** 273
Kaufman F B, Engler E M, Green D C and Chambers J Q 1976 *J. Am. Chem. Soc.* **98** 1596
Laviron E 1975 *J. Electroanal. Chem. Interfacial Electrochem.* **63** 245
Laviron E 1981 *J. Electroanal. Chem. Interfacial Chem.* **122** 37
Leddy J and Bard A J 1985 *J. Electroanal. Chem.* **189** 203
Leddy J, Bard A J, Maloy J T and Saveant J M 1985 *J. Electroanal. Chem.* **187** 205
Lee M M, Stokes J P, Wygul F M, Kistenmacher T J, Cowan D O, Poehler T O, Bloch A N, Fuller W W and Gubser D U 1982 *Mol. Cryst. Liq. Cryst.* **79** 145
Malpas R E, Itaya K and Bard A J 1979 *J. Am. Chem. Soc.* **101** 2535
Martin C R, Rhoades T A and Ferguson J A 1982 *Anal. Chem.* **54** 1641
Martin C R, Rubinstein I and Bard A J 1982 *J. Am. Chem. Soc.* **104** 4817
Perlstein J H 1977 *Angew. Chem. (Int. Ed. Engl.)* **16** 519
Prieto N E and Martin C R 1984 *J. Electrochem. Soc.* **131** 751
Rubinstein I and Bard A J 1980 *J. Am. Chem. Soc.* **102** 6641
Rubinstein I and Bard A J 1981 *J. Am. Chem. Soc.* **103** 5007
Scott B A, Kaufman F B and Engle E M 1976 *J. Am. Chem. Soc.* **98** 4342
White H S, Leddy J and Bard A J 1982 *J. Am. Chem. Soc.* **104** 4811
Wudl F, Aharen-Shalom E and Bertz S H 1981 *J. Org. Chem.* **46** 4612
Wudl F and Nalewajek D 1980 *Chem. Commun.* 866
Yeager H L and Steck A 1981 *J. Electrochem. Soc.* **128** 1880
Yeo S C and Eisenberg A J 1977 *J. Appl. Polym. Sci.* **21** 875

© Printed in India.

High performance electrode materials for the hydrogen evolution reaction from alkaline media[§]

B V TILAK*, A C RAMAMURTHY and B E CONWAY†

Occidental Chemical Corporation, Research Center, Long Road, Grand Island, NY 14072, USA

†Department of Chemistry, University of Ottawa, Ottawa, Ontario KIN 9B4, Canada

Abstract. One of the main component electrochemical reactions in alkaline water electrolyzers, chlor-alkali and chlorate cells is the hydrogen evolution reaction. Development of high performance materials for this reaction is receiving ever increasing attention in an effort to lower the energy consumption involved in these processes.

Kinetic data for the hydrogen evolution reaction from alkaline media on various materials is presented with focus on (i) the differences in the mechanistic behavior observed during transition from smooth to high surface area, and (ii) the electrocatalytic effects arising from the incorporation of metals (e.g., Ir, Ru, Co, W, Ti, Sn, Re, Mo, etc.) and non-metals (S, P, B, Bi, Sb, etc.) into the nickel lattice, and the influence of ion-implantation of Pt into Fe. In addition, the criteria required of electrode materials for efficient performance under industrial operating conditions is highlighted.

Keywords. Hydrogen evolution reaction; high performance materials; alkaline media; mechanistic behavior; electrocatalytic effects; overvoltage.

1. Introduction

Energy conservation in electrochemical industries is receiving ever increasing attention since the oil embargo in 1974, when the power costs started skyrocketing. In the past five years, the average increase in the cost of power in the United States has been 76% and further escalation is anticipated in the future (Anon 1982, 1985).

Chlor-alkali, chlorate and water electrolysis operations are among the largest consumers of electricity in electrolytic industries. One of the major achievements in the chlor-alkali industry was the introduction of metal anodes in the early sixties. The changeover from carbon to noble metal-coated anodes resulted in a voltage savings of over 0·2 V and permitted smooth operation of the cells at high current densities. Commercialization of DSA® anodes worldwide also provided impetus in the water electrolysis (Ohta *et al* 1985; Tilak *et al* 1981) industry to develop materials such as mixed oxides as anodes and high surface area nickel based electrodes as cathodes to achieve reduction in energy consumption.

Table 1 illustrates the components of cell voltage for a typical chlor-alkali, chlorate and a water electrolyzer system in which a savings of 10% in energy costs can be achieved if the cathodic overpotential is reduced by 0·2 to 0·3 V. Reduction in energy consumption via overpotential minimization depends on the characteris-

Table 1. Components of cell voltage.

	Chlor-alkali cell (c.d:* 0·232 A/cm^2)	Chlorate cell (c.d: 230 A/cm^2)	Water electrolyzer (c.d: 0·15 A/cm^2)
$E°th$	2·23 V	1·67 V	1·19 V
η_a	0·06 V	0·04 V	0·30 V
η_c	0·38 V	0·84 V	0·30 V
IR_d	0·36 V	0·21** V	0·36 V
IR_s	0·47** V		
Cell voltage	3·50 V	2·76 V	2·15 V

* c.d refers to current density and the values quoted in parentheses refer to the normal industrial operating conditions.
** Includes hardware drop.

tics of the overpotential (η) – current-density (i) relationship which has the form:

$$I/A = i = i_0 \exp(\eta/b),$$

or

$$\eta = b \ln (I/i_0 A),$$

where A refers to the surface area, b to the Tafel slope, $d\eta/d\ln i$, and i_0 to the true exchange current density. The magnitude of the overpotential at any given i depends on i_0 and b, which depend on the slow step controlling the kinetics of the overall reaction (Conway and Bai 1984).

The strategy to obtain high performance materials for the discharge of hydrogen from high alkaline media has been two-fold:

a) selection of materials with high i_0 and low b,
b) enhancement of the surface area.

It is desirable to have materials exhibiting high i_0 and low Tafel slopes since high operating current densities can be achieved without significant increase in the overpotential as shown qualitatively in figure 1. However, kinetic treatment of the generally accepted pathways during the hydrogen evolution reaction (h.e.r.) shows that participation of adsorbed intermediates in the slow-step during h.e.r. results in low Tafel slopes (Tilak *et al* 1977; Bockris and Subramanyan 1971) (table 2). Since atomic hydrogen participating in the slow-step diffuses into the bulk metal, metals exhibiting low Tafel slopes act as sinks for adsorbed hydrogen resulting in lattice expansion/distortion (Bockris and Subramanyan 1971; Flitt and Bockris 1982). While the presence of absorbed hydrogen is sometimes advantageous under some conditions (e.g., 'buffering' the 'reverse currents' encountered during shut-downs), it is mostly deleterious to the structural integrity of the metal. Hence, the choice should be a material exhibiting high i_0 for the h.e.r. with discharge as the slow-step. Another obvious but non-trivial factor is the enhancement of the area, which brings about a decrease in the overpotential which is exploited in the preparation of high surface area materials.

The main criteria relevant for selecting a high performance cathode material from a technological point of view are:

a) cost/life, b) electrocatalytic activity, c) stability under open circuit conditions

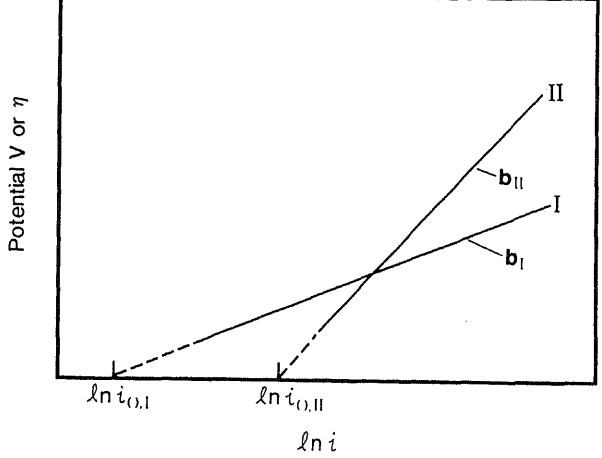

Figure 1. Relative polarization behavior of two processes at an electrode having two possible i_0 and b values. Process I offers better performance at high c.d. even though the i_0 is low.

Table 2. Pathways involved during H_2 evolution.

Mechanism	$\frac{F}{RT}\frac{d\eta}{d \ln i}$
Discharge	
$M+H^+ + e \rightarrow MH$	2
Recombination	
$MH+MH \rightarrow H_2+2M$	$1/2(1-\theta)$
Electrochemical desorption	
$MH+H^+ + e \rightarrow H_2+2M$	$1/(1{\cdot}5-\theta)$

The hydrogen evolution reaction has been extensively investigated on various metals in acid and alkaline media. A review of the studies in alkaline solutions is summarized by Tilak *et al* (1981) and Appleby *et al* (1982), and some recent investigations with specific reference to application in chlor-alkali cells is cited by Caldwell (1981) and Hine *et al* (1986). While the data reported in the literature is informative, comparative evaluation of the kinetic behavior is difficult in view of the differences in electrolyte composition and temperature in these investigations. The purpose of this communication is to discuss the interrelated criteria 'b' to 'e', noted above, with special reference to application in the chlor-alkali industry.

Kinetic studies presented here were carried out for comparison of the hydrogen evolution characteristics on various surfaces in typical chlor-alkali catholyte, containing 15% NaOH + NaCl at 95% C, using table 1 as the starting point to evaluate and develop high performance materials for the hydrogen evolution

that are required for determination of mechanistic pathways is recognized, the present studies were restricted to an examination of the polarization characteristics of h.e.r. on a variety of substrates with various electrode compositions so that a comparative evaluation of several materials could be made.

A brief survey of the literature is presented here on the various methods that have been attempted to obtain high performance catalytic cathode materials in the chlor-alkali industry. Much of the work has been reported in the form of patents, and table 3 lists a few methods that have been reported in the literature.

Among the various methods, electroplating, or in some instances electroless plating, of a metal or alloy has received considerable attention. Plating typically involves a ferrous substrate (steel) on which metals such as Ni, Mo, Co, Cd and W or their alloys have been deposited and the coatings tested for their catalytic activity in highly alkaline environments at elevated temperatures. A variation of the plating scheme involves co-deposition of elements such as Zn or Al with Ni and subsequent chemical leach treatment to form a high surface area porous matrix. Other variations include deposition of a thin layer of a noble metal such as Pt on an intermediate non-porous Ni layer.

The thermal or flame spray method for catalytic coatings involves either spraying or painting a substrate (or preplated substrate) with a chloride salt of the appropriate metal followed by high temperature treatment in air to form the corresponding oxide. In some instances, the oxides have been reduced to the metallic form by heating in the presence of hydrogen with an optional sintering procedure. Metals coated by this method include Ni, Co, Zr, Rh and Ir to mention a few.

Table 3. Catalytic cathode patent literature.

Patent assignee	Elements in coating/technique	Patent #
Diamond Shamrock	Ni, (Zn)/electroplating	US 4, 104, 133 (1978)
Osaka Soda	Ni, Mn/electroplating, thermal	Japan 79, 38, 277 (1979)
Tokuyama Soda	Ni, S/electroplating	German offen. 2, 811, 472 (1978)
Showa Denko	Ni, (Al)/electroplating	Japan 79, 71, 084 (1979)
Showa Denko	Ni, Co, P, Se/electroplating	Japan 79, 75, 481 (1979)
Showa Denko	Fe/oxide formation	Japan 79, 80, 282 (1979)
Tokuyama Soda	Ni, Ru, Ir/electroplating	Japan 79, 90, 080 (1979)
Chlorine Engineers	Ni, noble metals/electroplating and flame coating	Japan 79, 110, 983 (1979)
Metallgesellschaft	Fe, Co, Ni, Ag/thermal	German offen. 2, 829, 901 (1980)
PPG	Ni, P, (Fe)/electroplating	US 4, 184, 941 (1980)
British Petroleum Co.	Co, Fe, Ni, Mo, W, V/thermal	Europ. Pat. Appl. 9, 406 (1980)
PPG	W and Ni and/or Co/electroless plating	US 4, 086, 149 (1978)
Chlorine Engineers	Ni, RuO_2/electroplating and thermal	US 4, 465, 580 (1985) US 4, 543, 265 (1985)
Diamond Shamrock	Co-ZrO_2/flame coating	US 3, 992, 278 (1976)
PPG	Hydroxy carboxylic or aromatic acid/addition to electrolyte	US 3, 954, 581 (1976)
Olin	Noble metal ion additions	German offen. 2, 818, 306 (1978)
Occidental Chemical	Ni, Mo, Cd/electroplating	US 4, 354, 915 (1982)

Of more fundamental interest are reports of catalysis of h.e.r. brought about by ne addition of surface active agents to the catholyte (Carlin 1976) where the nechanism is presumably due to a diffuse double layer effect, by under potential eposited (UPD) metals (Korovin *et al* 1980) or the 'intrinsic properties' of new naterials (Onuchukwu 1982).

A recent paper by Riley and Moran (1986) describes catalysis of h.e.r. on pure Ni n 30% KOH brought about by deposition of small quantities of iron. Catalysis was ttributed to surface roughening following the codeposition of iron, and was onfirmed by SEM studies. deCarvalho *et al* (1985) have reported two Ni-Fe lectrodeposits which show catalytic activity to h.e.r. in 28% KOH solutions at levated temperatures. An η value of 162 mV was reported at a current density c.d.) of 135 mA/cm^2 and no details as to the nature of the surface were given. In a nore recent exhaustive study of amorphous metals, Kreysa and Håkansson (1986) ave studied twelve metallic glasses (see table 1 of their paper) containing elements uch as Fe, Ni, Mo, Si, B and Ti. Polarization behavior of these materials were btained in 1 M KOH at temperatures ranging from 30 to 90°C (see table 2 of Kreysa and Håkansson 1986, for a comparison of the kinetic parameters). Among ne materials investigated, $Fe_{60}Co_{20}Si_{10}B_{10}$ showed maximum reduction in η and high i_0 value. These materials were prepared in a smooth form but the nature of he surface and its surface composition after subjecting the specimen to prolonged athodic polarization has not been reported in this work. The mechanism of lectrocatalysis in these materials was not addressed in this work and further omparison of our data obtained on various high performance materials is not ossible at the present moment due to the choice of the test medium in these nvestigations.

. Experimental

All polarization studies were carried out at 95 ± 2°C in an all-glass three ompartment cell which was thoroughly cleaned in a hot $HNO_3 + H_2SO_4$ mixture nd rinsed in triple distilled water. The electrolyte used in this study analyzed 15% NaOH + 17% NaCl to simulate the catholyte composition of a diaphragm type hlor-alkali cell and was prepared from Analar grade chemicals and triple distilled vater.

Steady-state polarization data was obtained using a transient galvanostatic echnique and a Tektronix 564 B oscilloscope employed for measuring potentials ollowing a current perturbation (Tilak 1979). All the potentials reported in this vork have been corrected for the *iR* drop in the solution. A large area platinum gauze served as the counter electrode and the potential of the working electrode vas measured with respect to a freshly prepared reversible hydrogen electrode RHE) placed in the test solution. The cell was deaerated with purified hydrogen Matheson Hydrogen Purifier, Model #8366). The potential of the RHE was hecked periodically against a Hg/HgO reference electrode to ensure its stability. Prior to each experiment, the electrodes were subjected to cathodic polarization at

estimated using the technique described by Periassamy and Krishnaswamy (1975).

Electrodes used in this investigation were either obtained in high purity or prepared by methods mentioned below. High purity (99·99%) platinum, iridium, rhodium, iron, cobalt and nickel were obtained from Johnson–Matthey (Malvern, PA). Ruthenium, titanium, tin, rhenium, molybdenum, tungsten carbide, titanium carbide and nickel carbide were obtained from Research Organic and Inorganic Chemical Corporation (Sun Valley, CA), NiSb, Ni_2Si, $NiSi_2$ and NiB from CERAC (Minomonee Falls, WI) and vitreous carbon from Atomergic Chemetals Corporation (Plainsview, NY).

Ni-Ir, Ni-W, Ni-Co and Ni-Ti alloys were prepared (Lu and Srinivasan 1978) using an electric arc furnace under an argon atmosphere and were kindly supplied by Dr S Srinivasan of the Los Alamos National Laboratory, the teflon bonded platinum screen by Energy Research Corporation (Danbury, CT), and the sintered nickel plaque by Dr K V N Rao of Gould Inc. (Fort Erie, Canada).

Platinum ion-implantation into an iron matrix was done at the Atomic Energy Research Establishment, Harwell, England, at a dosage level corresponding to a monolayer coverage at a depth of penetration of approximately 100 Å.

Ni-S, Ni-Zn, Ni-Re, Ni-Mo, Ni-Mo-Cd and Ni-Sn alloy coatings were obtained by electroplating on to nickel substrates. Nickel substrates were initially degreased in trichloroethylene at room temperature for half an hour followed by rinsing in acetone-ethyl alcohol and water. The substrates were activated in a 1:1 mixture of concentrated HNO_3 and glacial acetic acid for 5 minutes prior to plating. Ni-S coatings (Hine *et al* 1979) were deposited from a modified Watts nickel bath containing 150 g/l $NiSO_4$, 47·5 g/l $NiCl_2$, 30 g/l H_3BO_3 and 30 g/l KSCN (pH ~ 4) at 45°C and at a current density of 20 ma/cm^2 for 1 hour. Ni-Zn coatings were prepared from solutions containing 330 g/l $NiSO_4$, 45 g/l $NiCl_2$, 37·5 g/l H_3BO_3 and 20 g/l $ZnCl_2$ (pH ~ 4·5) at 50°C and at a current density of 3 ma/cm^2 for 1 hour. Plating conditions and baths employed for electrodepositing Ni-Re (Netherton and Holt 1951; Komnikov 1964), Ni-Mo (Hovey *et al* 1963), Ni-Mo-Cd (Stachurski *et al* 1982) and Ni-Sn (Bennett and Tompkins 1976) are noted in references cited in parentheses.

Ni-Mo, Ni-Al and Ni-Si coatings were plasma sprayed on nickel coupons at Heany Industries, Inc. (Scottsville, NY). Ni substrates were first degreased and sandblasted with 20 mesh Al_2O_3. Nickel and the second constituent, in powder form (0–200 to +325 mesh size), were mixed and fed to the plasma gun powered at 30 kilowatts (at a temperature of ~ 10,000°F) in a working argon atmosphere. The substrates were maintained at 250–300°C by external cooling and the mixtures were sprayed at a rate of 1/1000″ per pass till the required thickness was achieved.

Surface compositions of most of the coatings were either obtained using either EDAX (X-ray) or ESCA/Auger techniques.

3. Results and discussion

3.1 *Electrocatalytic effects for the H_2 evolution reaction in alkaline media*

zation behavior of various metals in smooth form was first examined. Results presented in figures 2 to 4 show overvoltages > 300 mV at a current density of 230 ma/cm^2 which is commonly employed in industrial operations. Pt and Rh exhibited dual Tafel slopes of 70 mV in the low c.d. region and ~ 170 in the high c.d. region. The polarization behavior of Ir and Ru is complex in the sense that there are three distinct slopes indicating simultaneous or coupled reaction pathways.

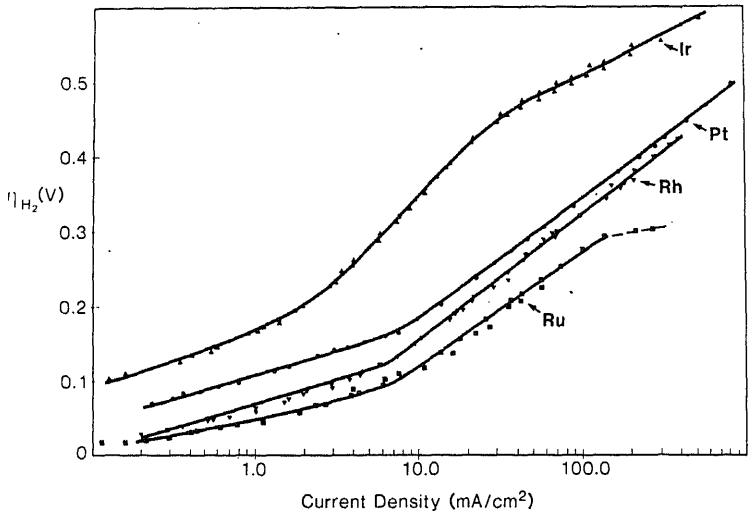

Figure 2. Cathodic polarization behavior of Pt, Ir, Rh and Ru in 15% NaOH + 17% NaCl solutions at 95°C.

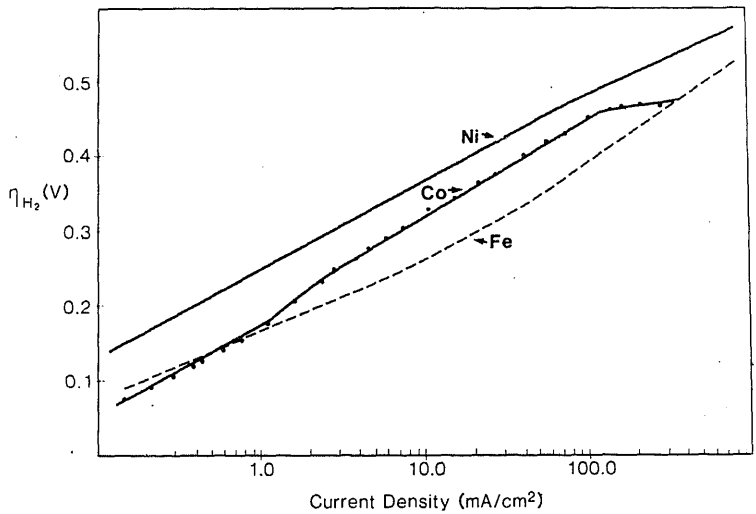

Figure 3. Cathodic polarization behavior of transition metals in 15% NaOH + 17%

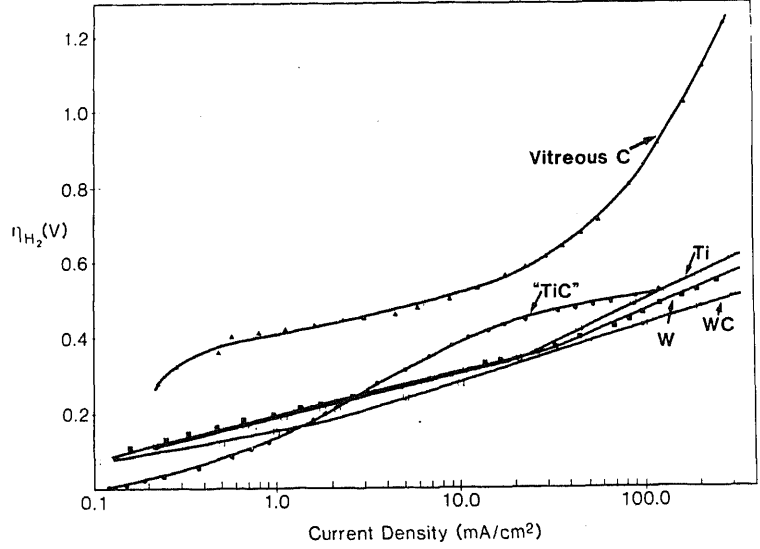

Figure 4. Cathodic polarization behavior of Ti, W and C in 15% NaOH + 17% NaCl solutions at 95°C.

Table 4. Kinetic parameters for the hydrogen evolution reaction from 15% NaOH + 17% NaCl solutions at 95°C.

	Exchange current density (ma/cm²)*			Tafel slope (mV)*		
	Low η region		High η region	Low η region		High η region
Pt	0·022		0·80	65		170
Ir	0·006	0·25	0·002	70	220	110
Rh	0·08		1·3	70		170
Ru	0·05	1·8	0·00001 (?)	50	155	45 (?)
Fe	0·014		0·24	100		150
Co	0·032	0·038	0·00001	120	135	40
Ni	0·009		0·003	130		100
Ti	0·02		0·80	120		240
C	0·0001		7 (?)	120		700 (?)
W	0·02		0·54	120		200
Sn	–		0·00002	–		140
Re	0·002		1·0	50		160
Mo	0·0013		0·01	96		120
TiC	1·2	0·35	0·0003	120	260	130
WC	0·015		0·13	100		160

* Values obtained by extrapolation from the linear regions at low and high overpotentials (η).

Based on the magnitude of the Tafel slopes (table 4), the mechanism of h.e.r. on Pt, Ir and Rh appears to be fast discharge-slow electrochemical desorption, in agreement with the earlier studies in 0·1 to 0·5 N NaOH solutions at 25°C (Mannan

Pt, Ir and Rh exhibited positive open circuit potentials (E_{ocp}) whereas the E_{ocp} of Ru varied in the range of -5 to -25 mV. Analysis of the current-voltage curves Around E_{ocp} with Ru, following the methodology outlined by Periassamy *et al* (1975) (1978), indicates the absence of metal dissolution and hence it appears that the negative E_{ocp} is reflective of equilibrium reactions such as $Ru + H_{ads} \rightarrow RuH_x$. The low Tafel slope observed with Ru in the high current density region is probably a consequence of the changes in the mechanism of h.e.r. due to variations in the surface composition.

Comparison of the polarization data on Fe, Co and Ni shows that Fe is a better catalyst than Co or Ni (See figure 5 for the polarization behavior of steel and Ni-plated steel). However, Fe dissolves under open circuit conditions – the corrosion rate of Co and Ni being negligible in caustic media under the same conditions. The Tafel slopes of 100–130 mV on Fe, Co and Ni in the low current density region are indicative of fast discharge-slow electrochemical desorption mechanism for the h.e.r. as proposed for Ni in alkaline media (Miles *et al* 1976).

One of the techniques employed to improve the corrosion resistance of metals is ion-implantation with noble metals. Hence, Fe electrodes were implanted with Pt at a dosage level corresponding to a monolayer coverage at a depth of penetration of < 100 Å, and their corrosion and polarization behavior examined. Figure 6 compares the polarization characteristics of Pt implanted iron with that of pure iron; virtually no change in the polarization behavior is observed. Corrosion rates determined at the open-circuit potential decreased from ~ 533 $\mu A/cm^2$ to 0 as the electrode was activated. These results are not surprising since Pt atoms were "buried" beneath the surface at a depth of ~ 100 Å as verified by ion-back scattering spectra.

Ti, W, C, WC, and TiC electrodes showed high Tafel slopes and low i_0 values similar to that observed in acidic media (Tamari and Kato 1976). Thus, of the smooth materials examined in this investigation (see table 4 for a comparison of the kinetic parameters), nickel was chosen for further studies in view of its stability in

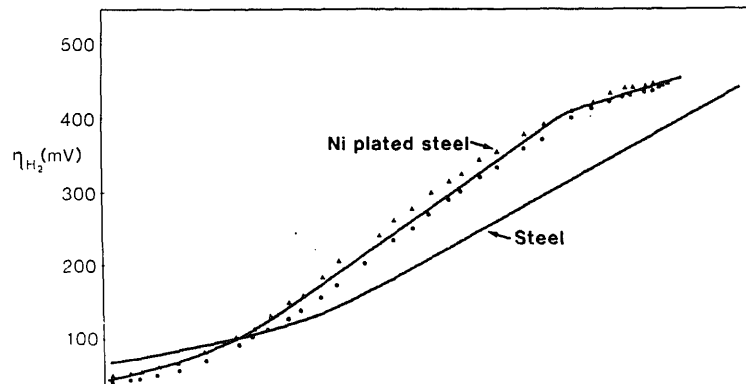

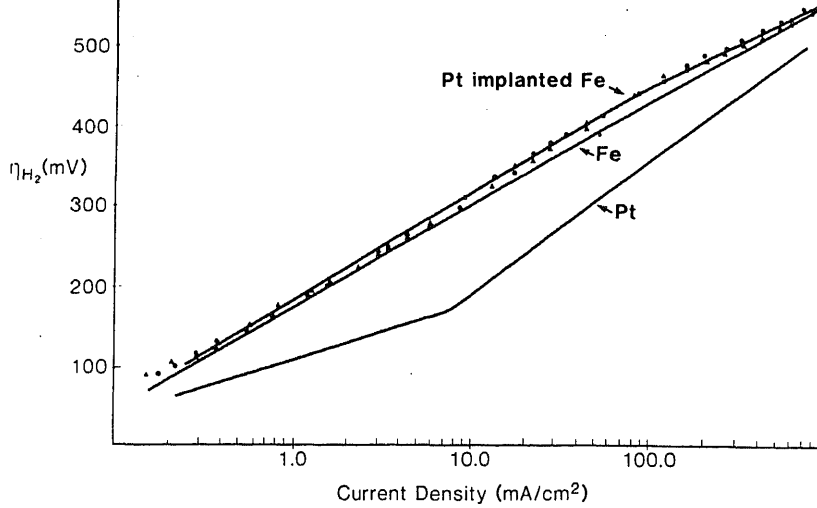

Figure 6. Effect of ion-implantation of Pt in Fe on the hydrogen evolution characteristics.

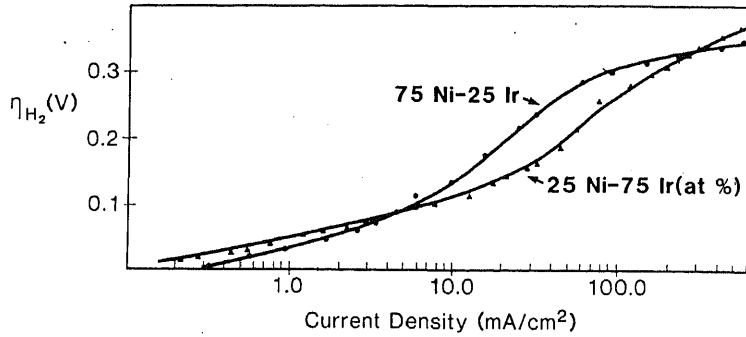

Figure 7. Effect of alloying of Ir with Ni on the η-log i curves.

caustic media under open-circuit conditions and economic considerations. To enhance its electrocatalytic activity, investigations were directed towards examining the polarization behavior of various nickel alloys and nickel compounds. The second element in these alloys and compounds was so chosen as to fall on either side of the volcano curve constructed based on heats of formation of metal-hydrogen bonds (Parsons 1969).

Results in figures 7, 8, 9 and table 5 show a significant effect of alloying in enhancing the electrocatalytic activity – the most marked influence being depicted in figure 9 where cobalt at 10 atom % weight in nickel exhibited the best activity. Ni-Sn alloy (figure 10) behaved more like nickel, but NiTi and $NiTi_2$ showed dramatic effects by exhibiting low overvoltages in the high c.d. region (figure 11). These alloys, however, were unstable since they disintegrated following electrolysis over a period of a few hours due to the formation of Ti hydrides and associated

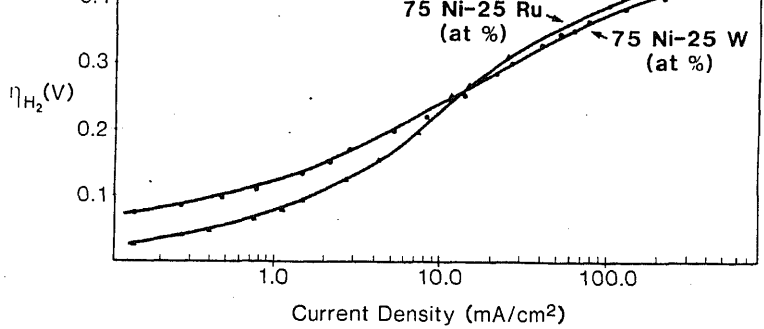

Figure 8. Effect of alloying of Ru with Ni on the cathodic polarization behavior in 15% NaOH + 17% NaCl solutions.

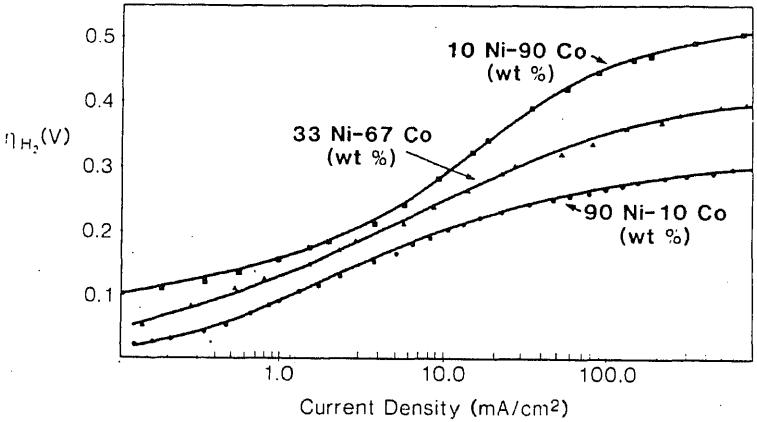

Figure 9. Cathodic polarization characteristics of Ni-Co alloys in 15% NaOH + 17% NaCl aq. at 95°C.

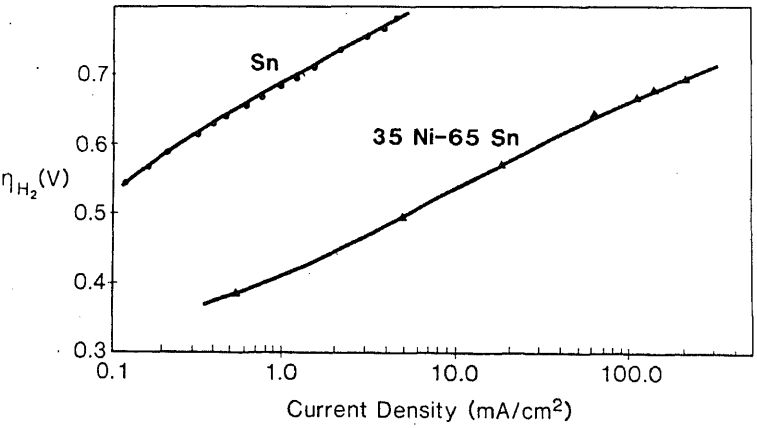

Figure 10. Effect of Sn in Ni during H_2 evolution from 15% NaOH + 17% NaCl solutions at 95°C.

Table 5. Kinetic parameters for the hydrogen evolution reaction from 15% NaOH + 17% NaCl solutions at 95°C.

	Exchange current density (ma/cm^2)*		Tafel slope (mV)*	
	Low η region	High η region	Low η region	High η region
75 Ni – 25 Ir	3	2 0·0001	60 180	60
25 Ni – 75 Ir	0·7	1·5	60	140
75 Ni – 25 Ru	0·05	0·013	60	110
75 Ni – 25 W	0·01	0·006	90	80
10 Ni – 90 Co	0·0003	0·00005	60	75
33 Ni – 67 Co	0·05	0·00005	120	60
90 Ni – 10 Co	0·012	0·00012	100	50
35 Ni – 65 Sn	–	0·006	–	130
Ni_3Ti	0·35	5·3	110	400 (?)
Ni Ti	–	2·5	–	90
Ni Ti_2	–	15	–	100
84 Ni – 16 Re	0·10	0·03	70	130
50 Ni – 50 Re	0·12	0·003	30	40
15 Ni – 85 Re	0·25	0·02	35	40
35 Ni – 65 Mo	–	0·13	–	30

* Values obtained by extrapolation from the linear regions at low and high overpotentials.

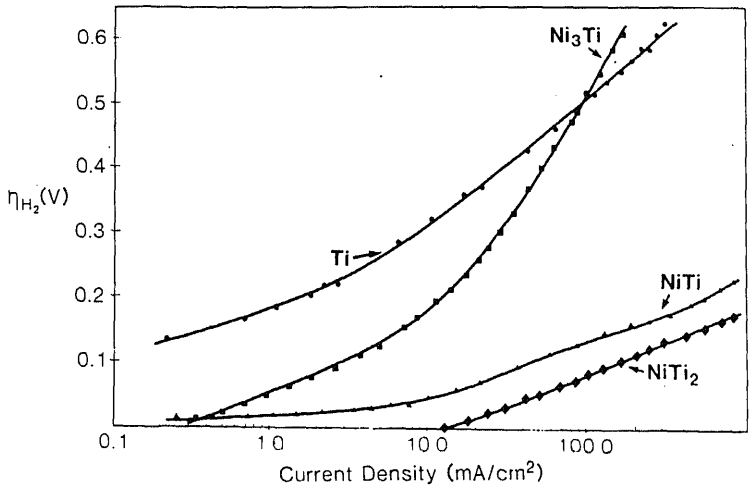

Figure 11. Cathodic polarization behavior of Ni-Ti alloys in 15% NaOH + 17% NaCl solutions at 95°C.

lattice expansion. Ni-Ir, Ni-W and Ni-Co alloys exhibited low overpotentials at a c.d. of 230 ma/cm^2 but these values are still high compared to those presently used in industry and, hence, were not investigated further.

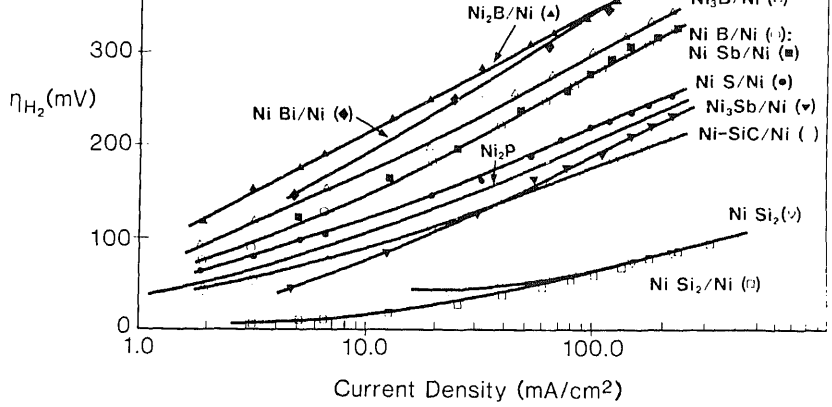

Figure 12. Effect of B, P, Bi, S, SiC, P and Si in nickel matrix during H_2 evolution from 15% NaOH + 17% NaCl solutions at 95°C.

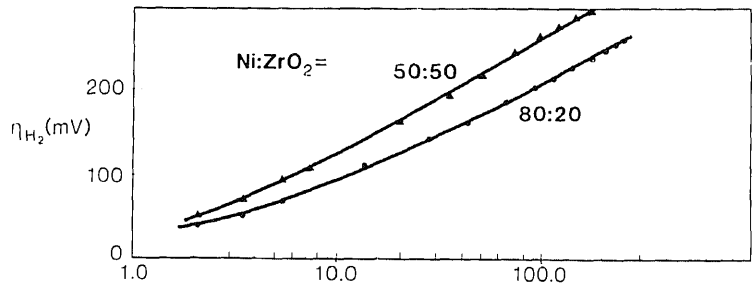

Figure 13. Cathodic polarization behavior of Ni-ZrO_2 composites in 15% NaOH + 17% NaCl solutions at 95°C.

enhancement in catalytic activity was significant but the overvoltages are still high except on NiSi and $NiSi_2$ which showed high I_0 values (defined as $i_0 A$) and low Tafel slopes. The origin of the enhanced activity is clearly due to the high surface area generated by the leaching of Si from the matrix of NiSi and $NiSi_2$. Thus, it appears that high surface nickel electrodes exhibit not only a high I_0 value but also low Tafel slopes of 20–30 mV which may be compared to a value of ~ 110 mV observed with smooth nickel surfaces.

3.1b *Polarization characteristics on high surface area nickel electrodes*: To investigate the aforementioned phenomenon further, high surface area nickel electrodes were prepared using ion-bombardment, plasma spraying, thermal decomposition and electrodeposition techniques.

Ion-bombardment is known to generate disordered structures leading to an increase in surface area and, hence, a nickel wire electrode was ion-bombarded with Ni^+ ions at 100 keV to a dosage level of 5×10^{16} ions/cm^2. Polarization

Table 6. Kinetic parameters for the hydrogen evolution reaction from 15% NaOH + 17% NaCl solutions at 95°C.

	Exchange current density* (ma/cm^2)	Tafel slope (mV)
NiB	1·0	140
Ni_2B	0·24	135
Ni_3B	0·45	130
NiBi	0·6	150
NiSb	1·0	120
Ni_3Sb	2·1	120
NiS	0·8	105
Ni_2P	1·2	100
Ni-SiC	1·7	100
$NiSi_2$	5·0	170
Ni_2Si	8·0	70
Ni-ZrO_2 (50:50)	1·3	140
Ni-ZrO_2 (80:20)	2·3	130

* Values obtained by extrapolation from the linear region at high overpotentials (η).

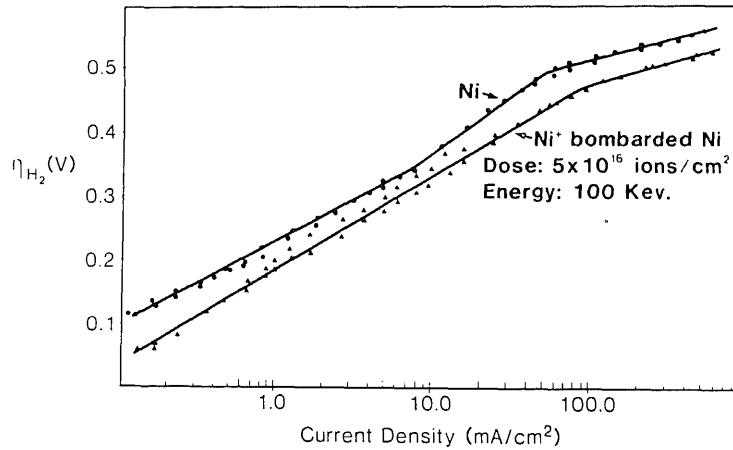

Figure 14. Effect of ion-bombardment on the cathodic polarization characteristics of Ni in 15% NaOH + 17% NaCl solutions at 95°C.

behavior of the electrode (figure 14) showed lowering of the hydrogen overpotential suggesting increased surface area by a factor of 6 which was confirmed by an analysis of the initial portion of the galvanostatic charging curves.

Figures 15 and 16 illustrate the overpotential behavior of Ni-Al blends plasma sprayed on nickel substrates from which Al was leached out in 10% NaOH by

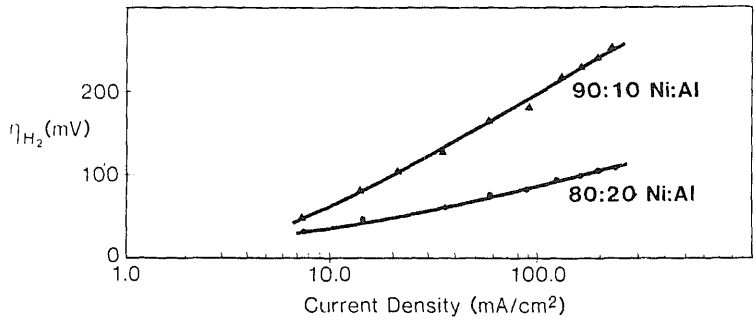

Figure 15. Cathodic polarization behavior of Ni-Al composites.

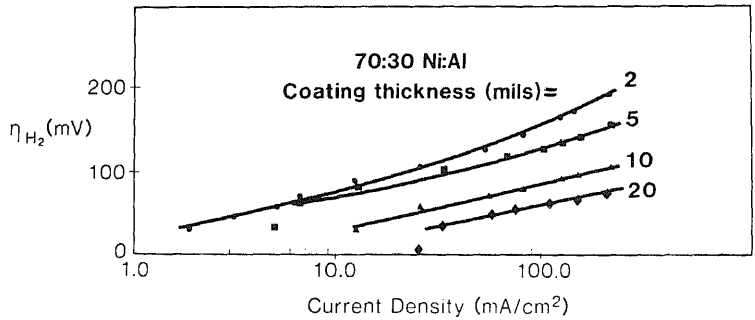

Figure 16. Effect of thickness of plasma sprayed Ni-Al mixtures on the cathodic polarization characteristics.

out. Results show substantial lowering of hydrogen overvoltage and also the Tafel slope. Since Si dissolves in NaOH, Ni-Si alloys and blends were also tested in this study. The results (figure 17) show significant enhancement in the catalytic activity for the h.e.r. on these electrodes and again a decrease in Tafel slopes.

Electrodeposited Ni-Re alloys on Ni substrates (figure 18) also exhibited catalysis and lowering of Tafel slopes. However, alloys containing 50% or more Re were very unstable and dissolved even upon cathodic polarization. Figure 19 illustrates the polarization behavior of Ni, Mo, Ni + Mo (plasma sprayed) and electrodeposited Ni-Mo. The alloys showed significant catalysis compared to their smooth metal counterparts. Also, the electrodeposited alloy showed very low Tafel slope in the high c.d. region and was more catalytic compared to the plasma sprayed coatings. It is very clear from the SEM micrographs (figures 20 to 26) that, as the surface is changed from smooth to a microfractured state, the Tafel slope and, hence, the mechanistic pathway is dramatically altered. Sintered Ni plaque and high surface area NiS (roughness factor ~ 300) also exhibited (figure 27) a behavior similar to other high surface materials mentioned above. Thus, the

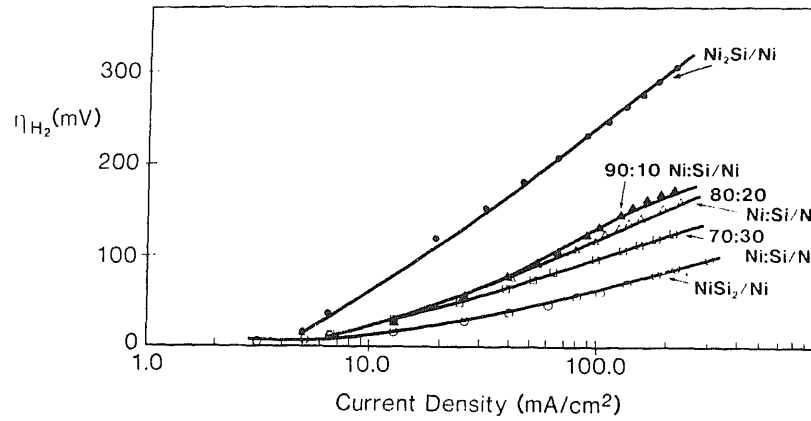

Figure 17. Effect of Ni-Si alloys and composites on the cathodic polarization behavior in 15% NaOH + 17% NaCl solutions at 95°C.

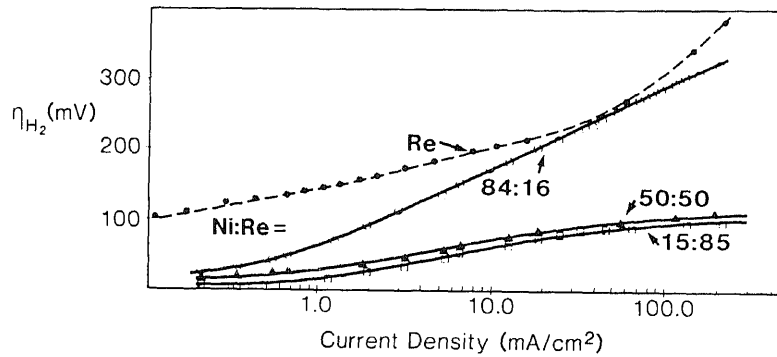

Figure 18. Cathodic polarization behavior of Ni-Re alloys.

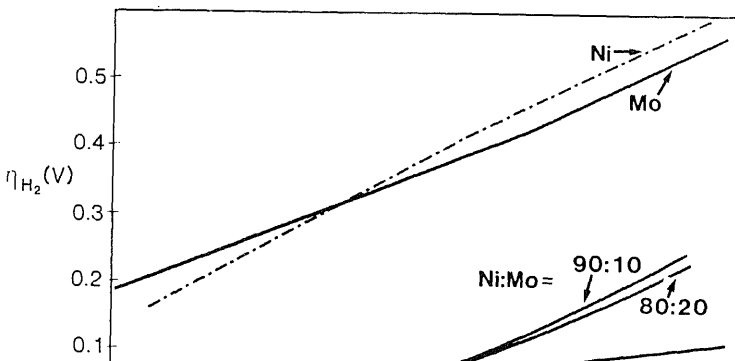

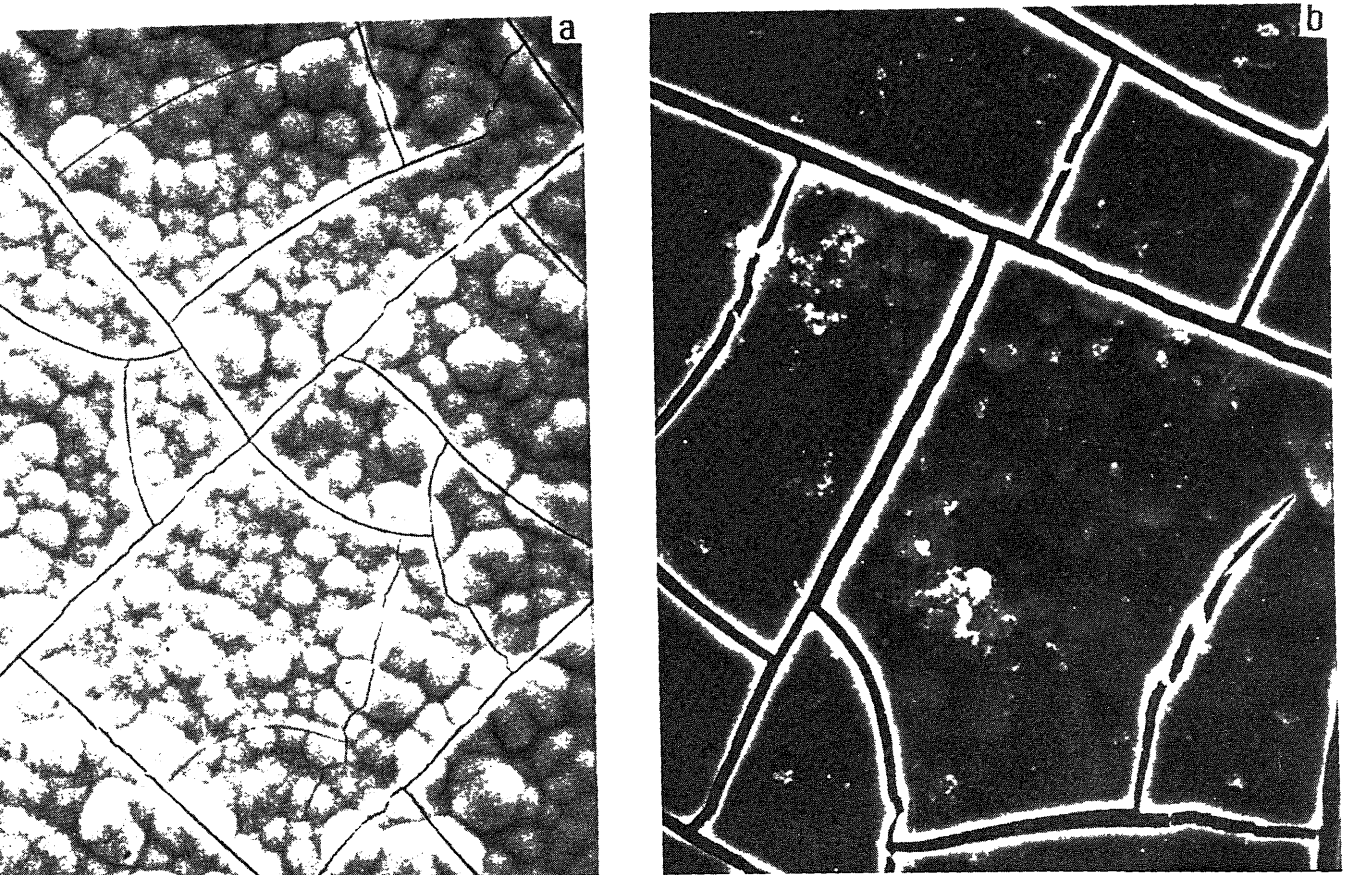

Figure 20. SEM images of NiS deposits; [**a**]-untreated; [**b**]-heat treated at 400°C for 5 min.; magnification: 1K.

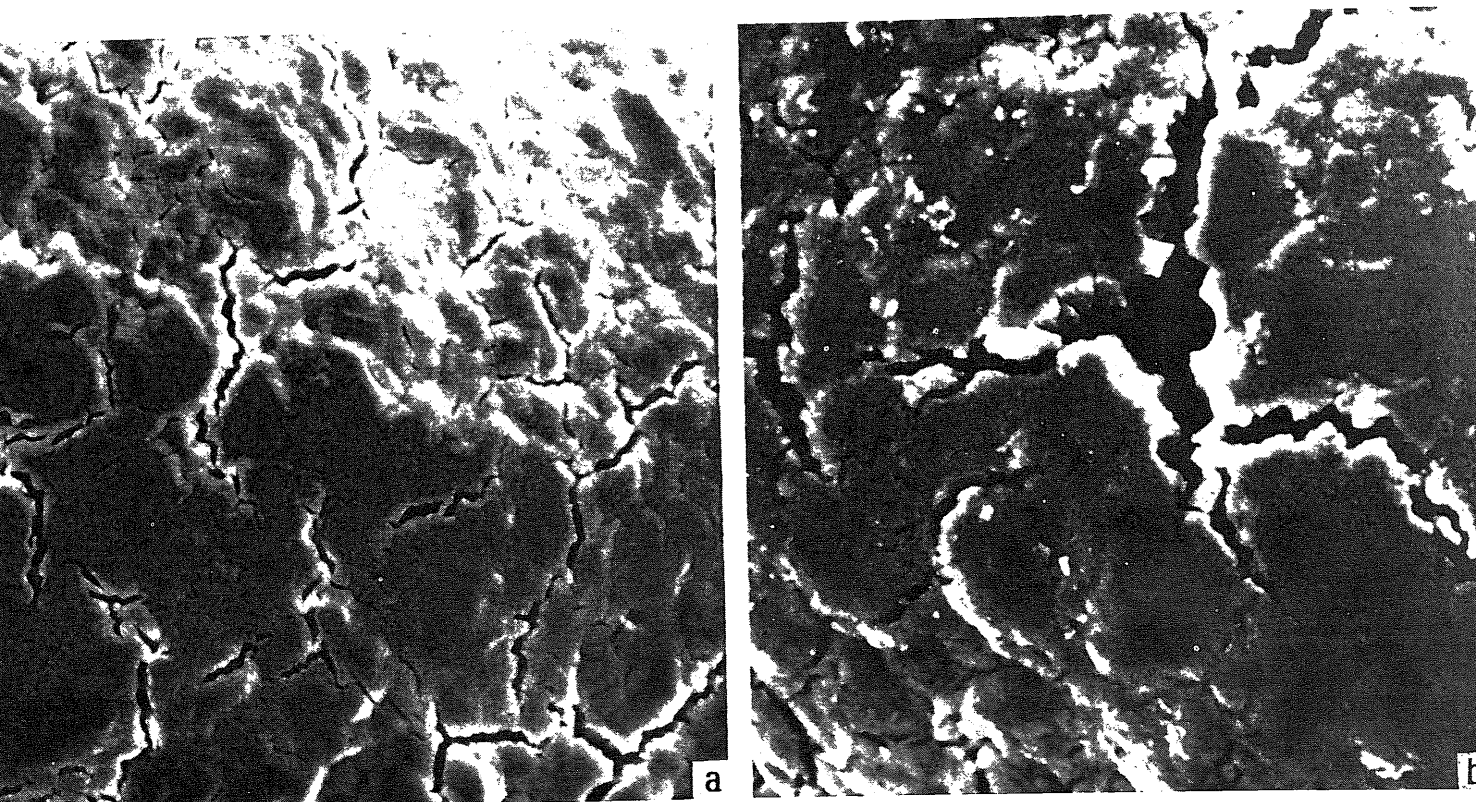

Figure 21. SEM images of Ni-Zn electrodeposits at a magnification of 1K; (**a**) untreated; (**b**) after anodic leaching for 15 hrs at 0·1 ma/cm^2.

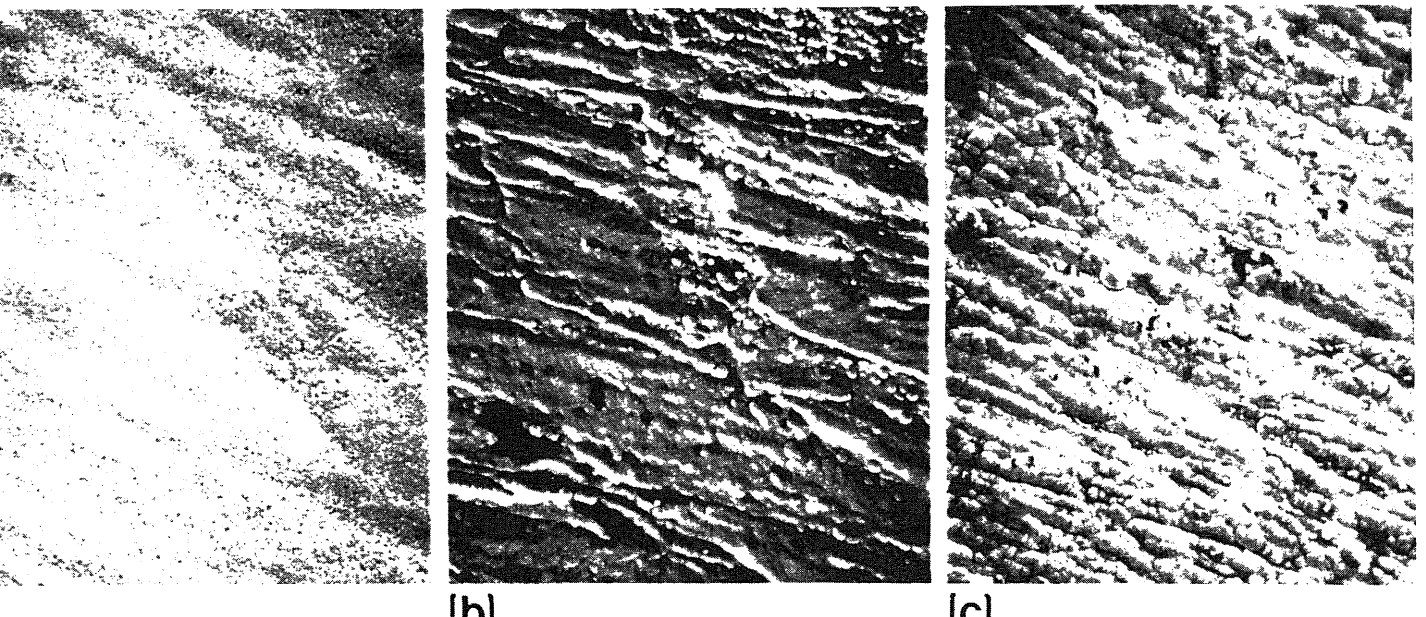

Figure 22. SEM images of Ni-Re alloys at 1000×; **a)** 84% Ni-16% Re; **b)** 50% Ni-50% Re; **c)** 15% Ni-85% Re.

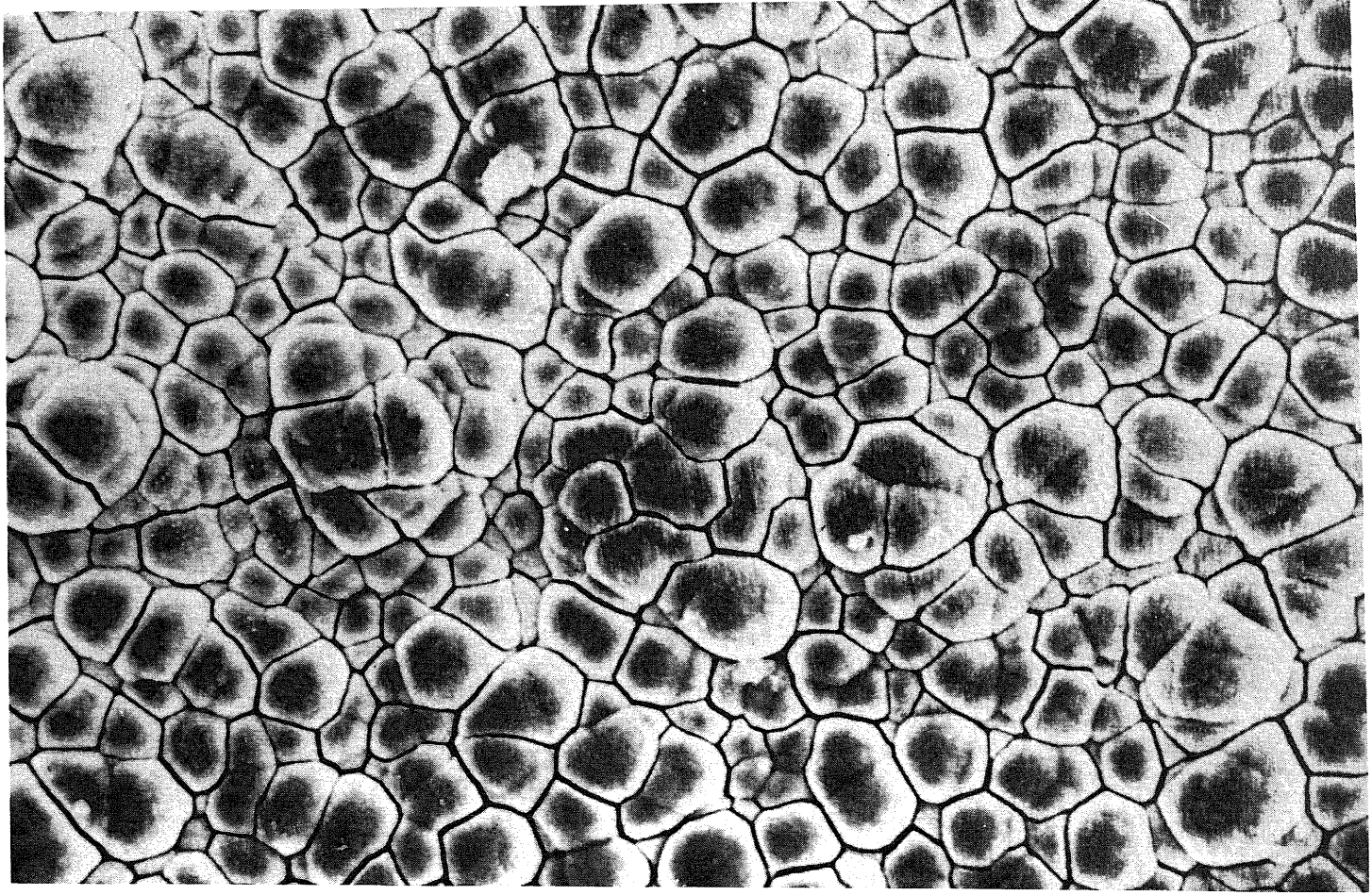

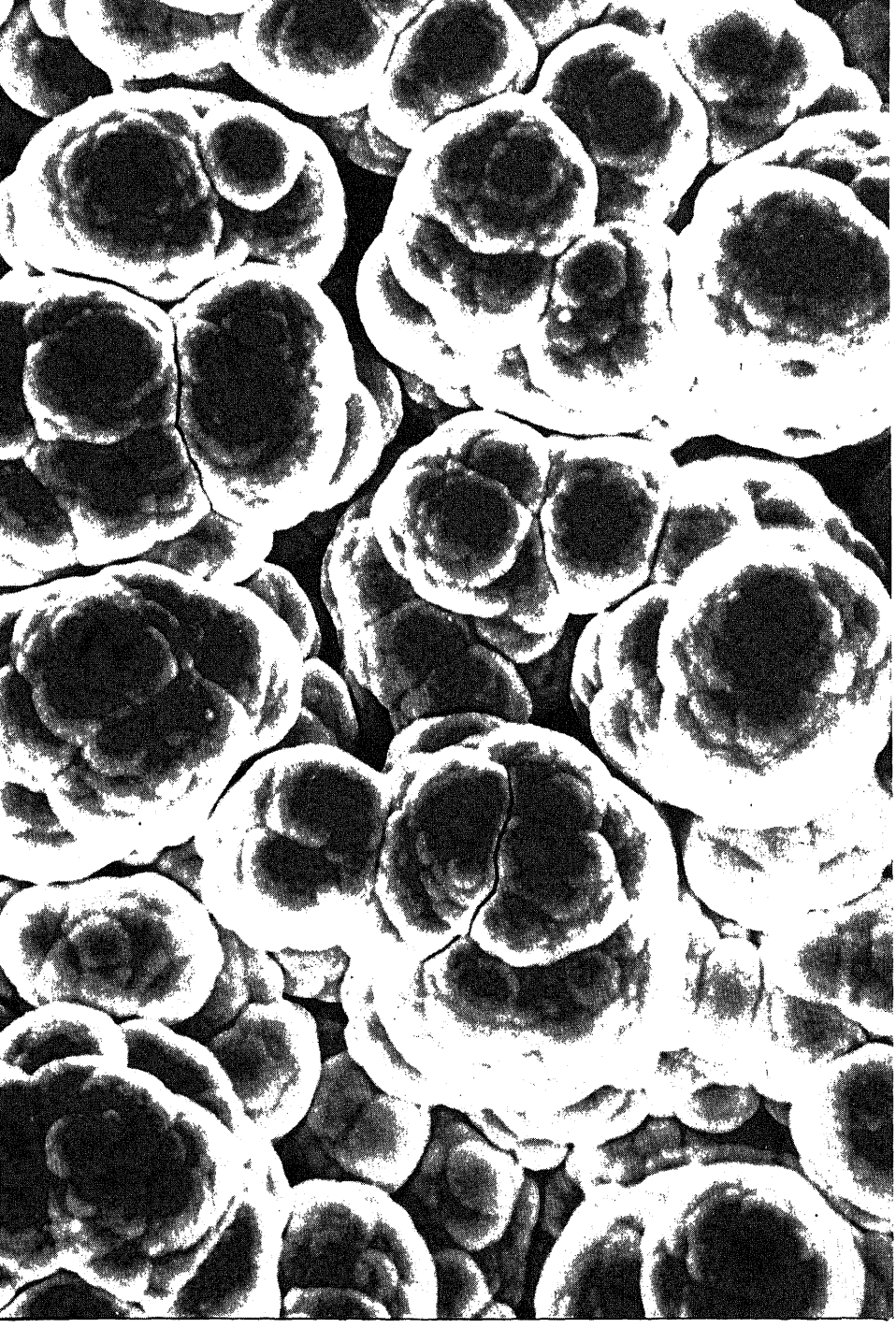

Figure 23b. SEM image of electrodeposited Ni-Mo alloy at ×1K.

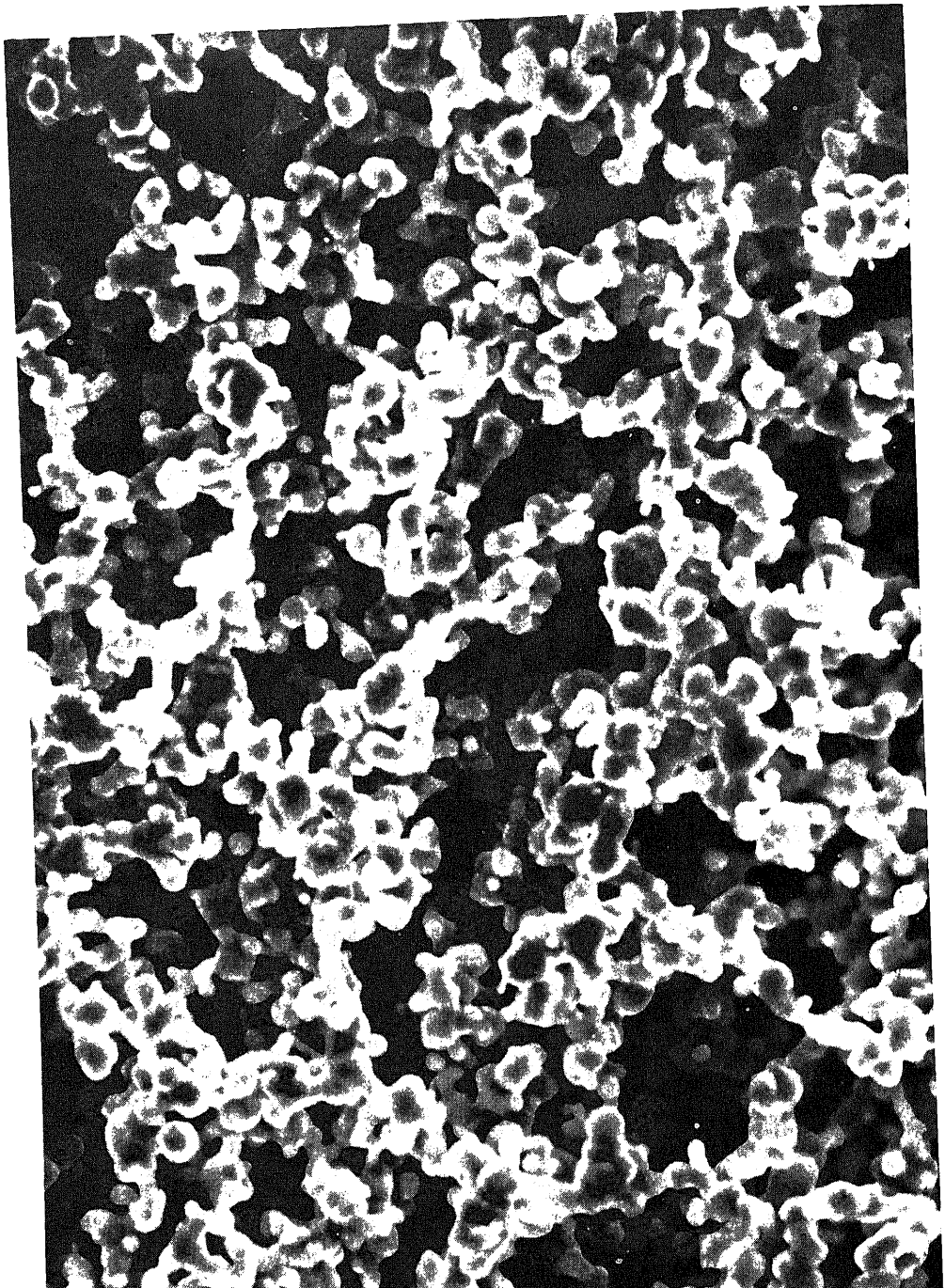

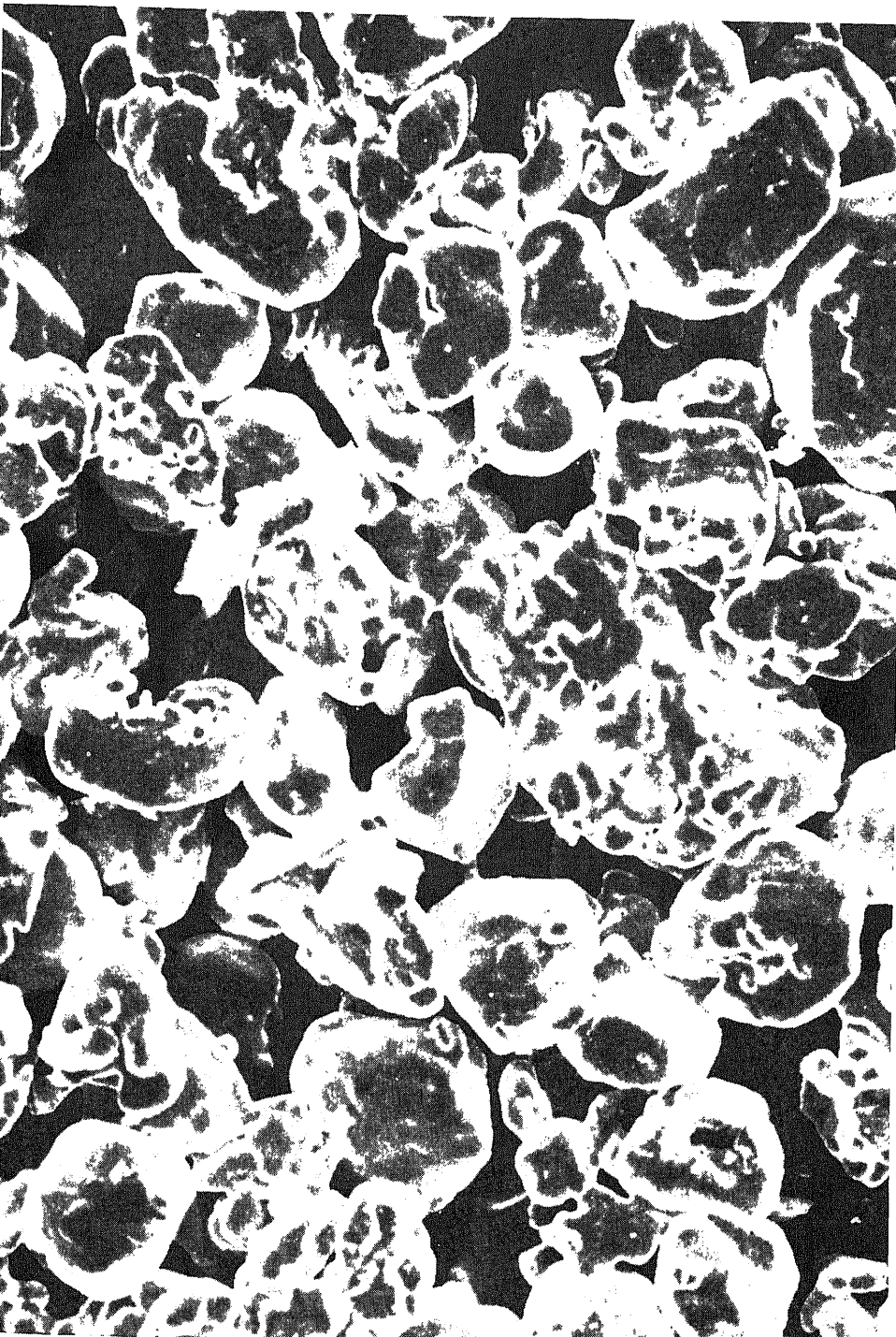

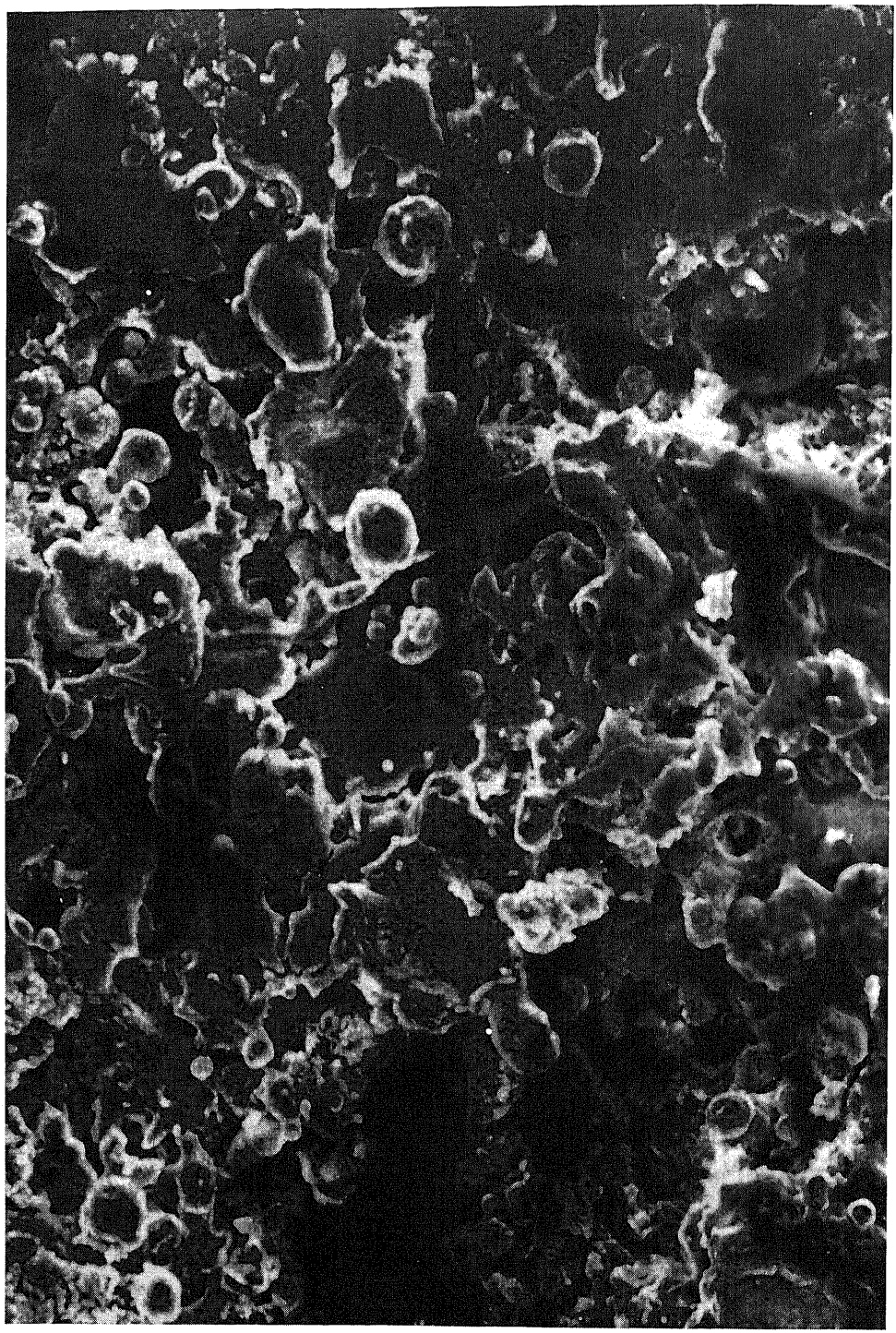

Figure 26. SEM image of leached Ni-Al composite at ×1K

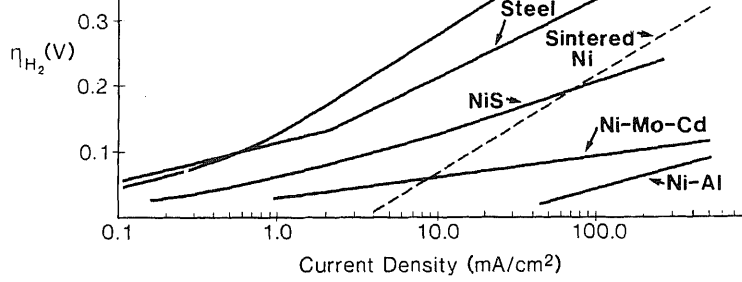

Figure 27. Effect of surface area on the polarization behavior of nickel during H_2 evolution.

η (figure 27) and a very low Tafel slope even in the high c.d. region. SEM studies of this coating (figure 28) indicate a microfractured surface similar to those shown in the earlier micrographs. The surface composition of this coating was examined using ESCA and ISS (Ion Scattering Spectroscopy) techniques. Figure 29 shows Ni $2p_{3/2}$ ESCA spectra for a typical coating before and after subjecting the specimen to a cathodic leach treatment in NaOH. The peak at 855·4 eV corresponds to $Ni(OH)_2$ but the leached sample shows an additional shoulder at 852 eV which can be attributed to metallic nickel. This suggests the possible presence of metallic nickel islands dispersed in nickel oxide. A similar feature is also observed for Mo (figure 30) where the predominant species can be attributed to MoO_3. The second peak at 227·2 eV is assigned to metallic Mo. Figure 31 shows a typical ISS analysis in which the presence of Ni ($E/E_0 = 0{\cdot}32$) and Mo ($E/E_0 = 0{\cdot}50$) can be easily distinguished. These spectra were obtained after sputtering the coating for 30 minutes. The interesting feature of this spectra is the significant change in the Mo/Ni ratio before and after the leach treatment indicating the selective removal of Mo from the coating. Figures 32 and 33 show ESCA spectra obtained following the ISS experiment which indicates the dominant species to be metallic Ni and Mo along with a small concentration of the two oxides. Hence, the bulk concentration of the coating consists of metallic Ni and Mo while the surface is predominantly composed of a thin layer of the oxides.

Further verification that the observed low Tafel slope was not an unique phenomenon observed in Ni-based systems, is obtained from the polarization behavior of three forms of Pt as shown in figure 34. These results demonstrate unequivocally that the observed low Tafel slopes and catalysis are not unique to nickel and its alloys.

A comparison of the overvoltages at 200 mA/cm^2 on the materials examined in this investigation is provided in table 7.

3.1c *Possible explanations for change in the mechanism of hydrogen evolution with high surface area electrodes*: Since hydrogen evolution is occurring on high surface area matrices, it may be postulated that the phenomenon of low Tafel slopes is associated with mechanistic changes arising from coverage variations in the porous

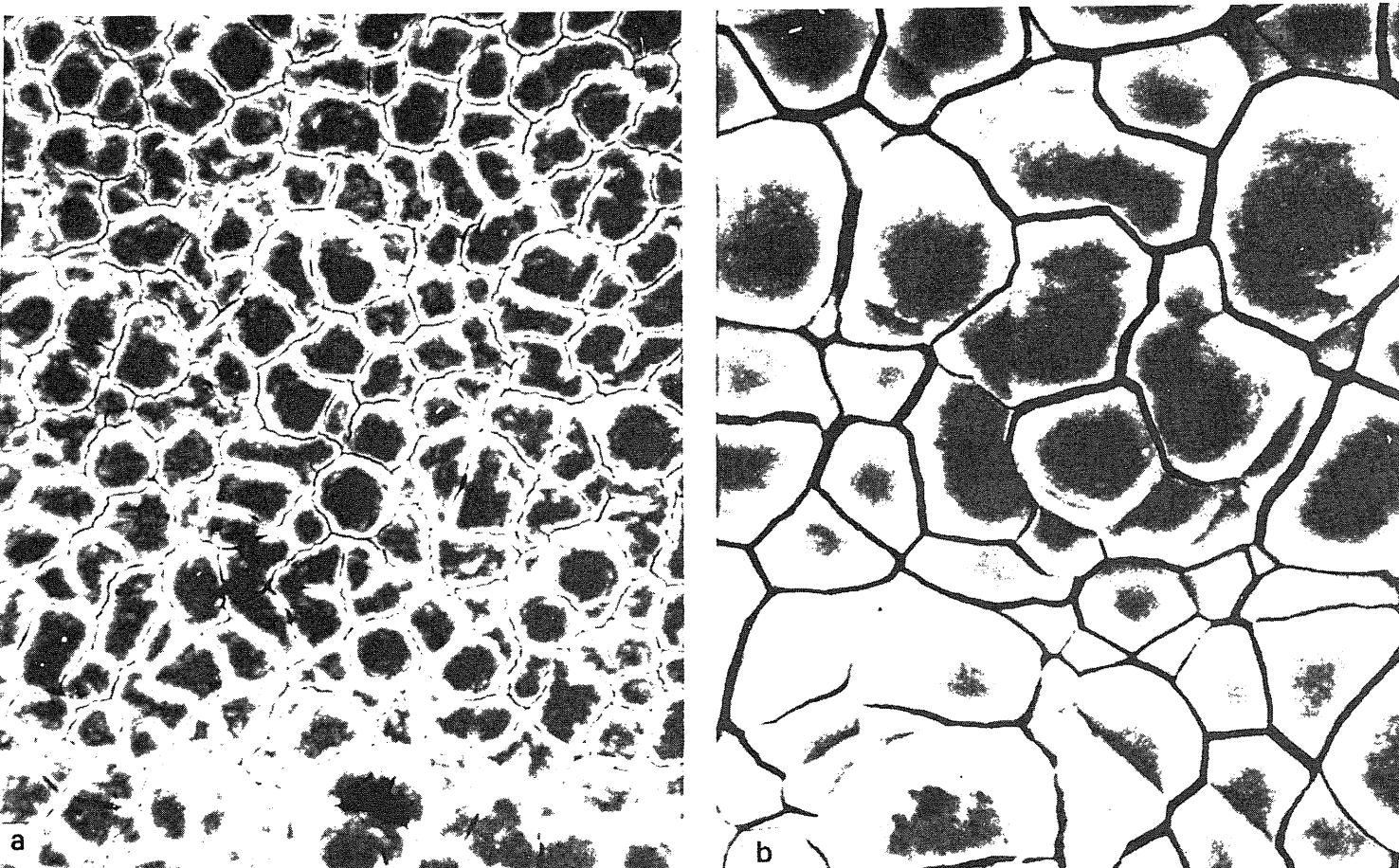

Figure 28. SEM image of electrodeposited Ni-Mo-Cd at (**a**) 1K× and (**b**) 3K×.

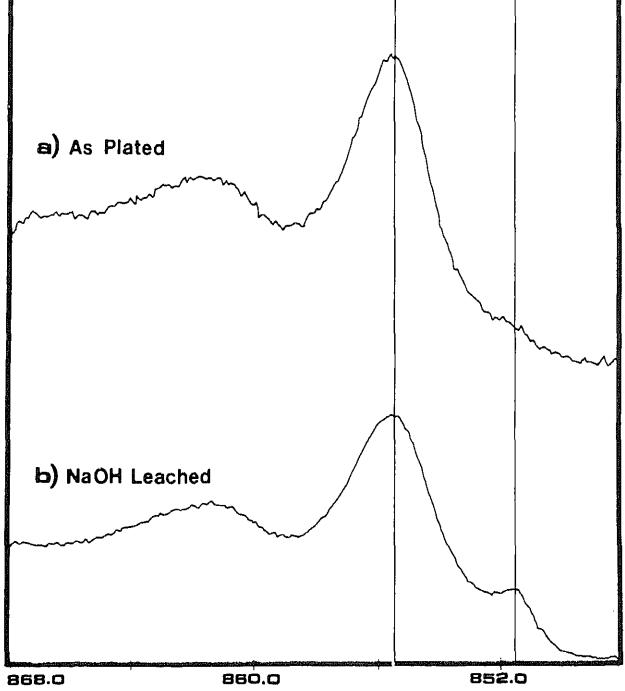

Figure 29. Ni $2P_{3/2}$ ESCA spectra of (**a**) As plated sample and (**b**) after NaOH leaching.

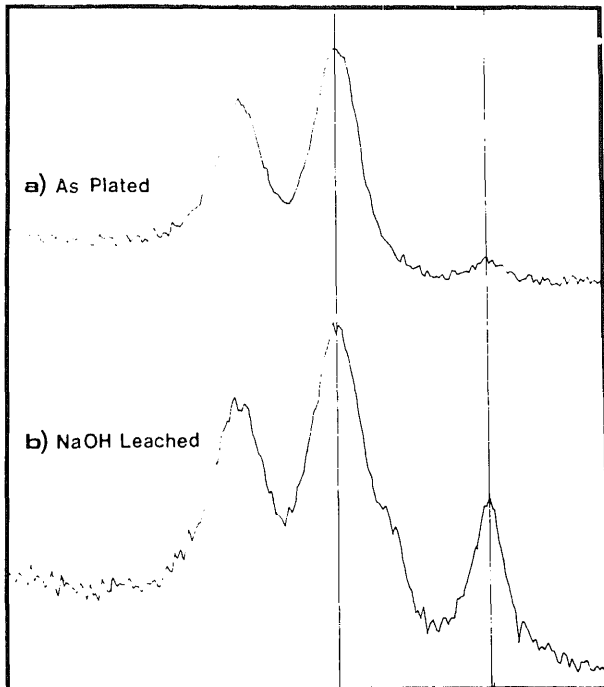

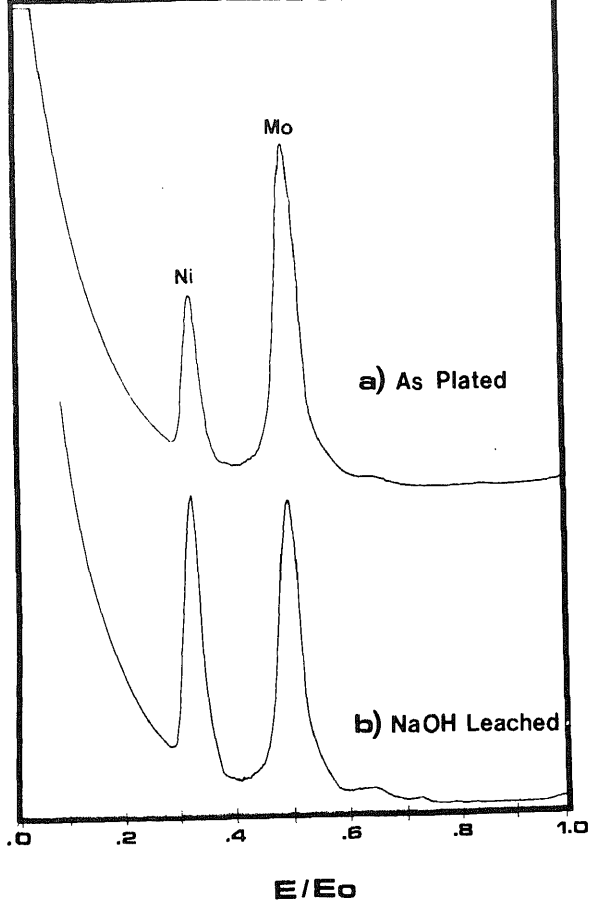

Figure 31. ^{20}Ne ISS spectra of (**a**) As plated sample and (**b**) after NaOH leaching. The spectra represent the surface composition after about 30 minutes of sputtering.

structure. This was examined by assuming a homogeneous elementary flooded pore model (Tilak *et al* 1977) (wherein the interconnected multiphase porous matrix is treated as a homogeneous phase) and deducing the current-voltage relationships taking into account the backward rate and coverage dependence on potential (B V Tilak, S Venkatesh and S K Rangarajan, unpublished results). Analysis of the results showed that Tafel slopes do indeed change, but in the wrong direction. Thus, whether the rate determining step is discharge or electrochemical desorption, the Tafel slopes change from 2 and 0·666 RT/F respectively, to 4 RT/F at high overpotentials. This is not surprising since porous structures, while offering high specific surface area, create their own problems via associated phenomena such as mass transport, finite conductivity of the electrode, etc. Furthermore, 'simple' considerations show that I_0 on a material can be increased by increasing the surface area, assuming that the chosen 'surface' can be effectively utilized for the reaction under study. The factors governing effective utilization depend, among many

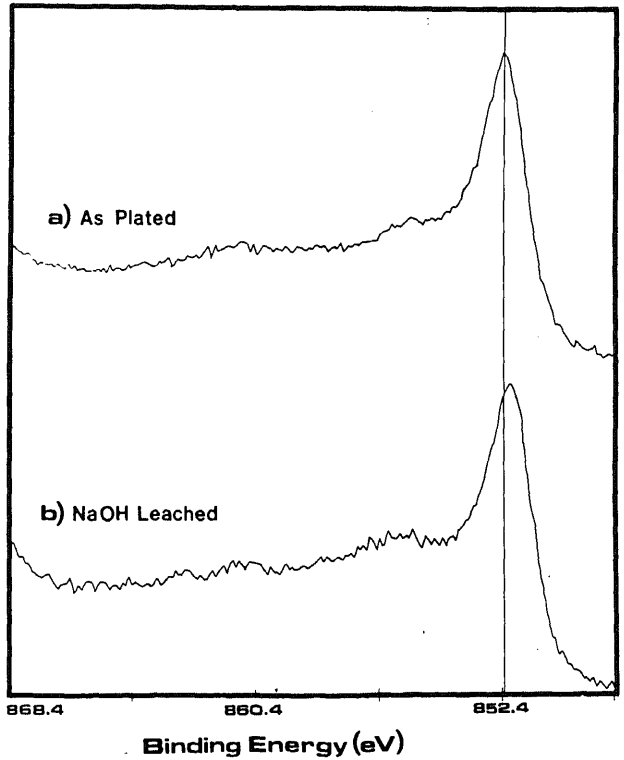

Figure 32. Ni $2P_{3/2}$ ESCA spectra of (**a**) As plated sample and (**b**) after NaOH leaching. Samples were sputtered for approximately 35 minutes with ^{20}Ne (ISS).

Thus, in the case of a flow-through electrode system, it is possible to optimize conditions for reactions with low i_0 so as to achieve substantial reaction rates for a given geometric area. However, for gas evolution reactions the criteria for effective utilization appear to be different, especially when the electrode is operated in different modes. This may be exemplified by comparing the performance of a Ni plaque having a surface area of 2·5 m^2/g (corresponding $R \sim 1200$) for N_2H_4 oxidation and H_2 evolution. In the former case, excellent results were reported, while as a cathode during H_2 evolution, results show that only a small fraction ($\ll 5\%$) of the surface was utilized. Similar behavior was observed with Ni foam metals having a surface area of $\sim 1{\cdot}7$ and 3·3 m^2/g (equivalent $R \sim 5600$ & 5200) and with thermally formed Pt-Ir coatings with a roughness factor of ~ 170.

The above findings suggest that while 'dealing' with high area surfaces for gas evolution reactions, it is necessary to distinguish between roughness and porosity – as in the former case the diffusion layer profile 'copies' the optimized surface thereby permitting greater utilization of the surface, whereas on a porous surface the liquid is in contact with only a fraction of the electrode surface. This fraction is dependent on the probability of a liquid pore belonging to the infinite continuous liquid pore system which is a function of the probabilities of closing a

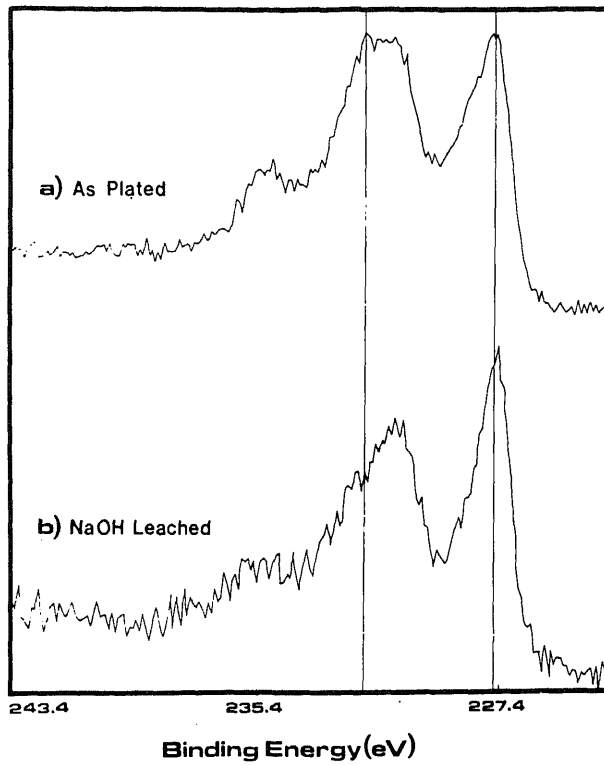

Figure 33. Mo $3d_{3/2,\,5/2}$ ESCA spectra of (**a**) As plated sample and (**b**) after NaOH leaching. Samples were sputtered for approximately 35 minutes with ^{20}Ne (ISS).

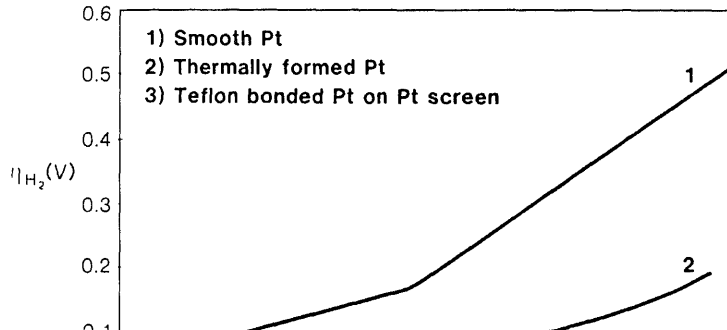

Table 7. Comparison of hydrogen overvoltage on metals/coatings investigated in the present study (15% NaOH + 17% NaCl at 95°C at a c.d of 200 ma/cm^2).

Metal/coating	Overvoltage (mv)	Metal/coating	Overvoltage (mv)
Ru	300	NiB/Ni	318
Rh	381	Ni_3B/Ni	337
Pt	400	Ni_2B/Ni	381
Ir	540	NiBi/Ni	393
Fe	440	Ni-ZrO_2 (80:20)	250
Co	465	Ni bombarded Ni	491
Ni	518	Ni-Al (80:20)	140
WC	481	Ni-Al (90:10)	243
W	531	Ni-Al 2 mils	187
Ti	581	Ni-Al 5 mils	156
Vitreous C	1087	Ni-Al 10 mils	106
Steel	375	Ni-Al 20 mils	75
Ni plated Steel	440	$NiSi_2$/Ni	73
Pt implanted Steel	481	Ni-Si (70:30)	118
Ni-Ir (75:25)	310	Ni-Si (80:20)	156
Ni-Ir (25:75)	329	Ni-Si (90:10)	169
Ni-W (75:25)	400	Ni_2Si/Ni	300
Ni-Ru (75:25)	416	Ni-Re (15:85)	100
Ni-Co (90:10)	283	Ni-Re (50:50)	108
Ni-Co (33:67)	371	Ni-Re (84:16)	325
Ni-Co (10:90)	487	Re	383
Ni-Sn (35:65)	691	Ni-Mo (Electrodeposit)	100
$NiTi_2$	100	Ni-Mo (80:20)	200
NiTi	150	Ni-Mo (90:10)	216
Ti	575	Mo	508
$NiSi_2$/Ni	94	Ni-Al	59
$NiSi_2$	94	Ni-Mo-Cd	100
Ni-SiC/Ni	200	NiS	242
Ni_3Sb/Ni	237	Sintered Ni	275
NiS/Ni	253	Thermally formed Pt	133
Ni_2P	240	Teflon bonded Pt	41

of these factors which govern the 'choking' and degree of utilization of the electrode, when porous electrodes are operated in a gas evolution mode.

Cl_2 and H_2 evolution studies on thermally formed Pt-Ir electrode, having a roughness factor of 170, showed that η Cl_2 was considerably lower than η H_2 at a given c.d. While an explanation may be attempted in terms of i_0 values for the respective processes, it is difficult to rationalize the overpotential differences on smooth Pt-Ir and high area Pt-Ir electrodes unless crystallite size effects (see Kinoshita 1982 for a discussion related to this topic) are invoked to understand the marginal increase in i_0 observed on high area Pt-Ir surfaces.

Thus, the results observed seem to suggest that there are several factors such as crystallite size effects, hitherto neglected gas bubble formation, and release energetics and dynamics, etc., that need to be considered in modelling the hydrogen evolution characteristics on high surface area cathodes.

sprayed Ni-Al coatings and from electrosorption in electrodeposited Ni-Mo-Cd coatings) on which the hydrogen evolution reaction proceeds as described below

$$X\,\mathrm{Ni} + \mathrm{H_2O} + e \rightleftharpoons \mathrm{Ni}_x\mathrm{H} + \mathrm{OH}^-$$
$$\mathrm{Ni}_x\mathrm{H} + \mathrm{H_2O} + e \rightleftharpoons (\mathrm{Ni}_x\mathrm{H})\,\mathrm{H}_{ads} + \mathrm{OH}^-$$
$$(\mathrm{Ni}_x\mathrm{H})\,\mathrm{H}_{ads} + \mathrm{H_2O} + e \rightarrow \mathrm{Ni}_x\mathrm{H} + \mathrm{OH}^- + \mathrm{H_2}\,.$$

While the two quasiequilibria preceding the slow-step will indeed give low Tafel slopes, it is difficult to comprehend hydride formation only on high surface area matrices and not on smooth electrodes. Furthermore, as noted earlier, this behavior is not unique to nickel as similar observations were noticed on Pt electrodes (figure 34).

Since high surface electrodes have 'active sites' with varying energetics, it is conceivable that the activation energy is altered resulting in mechanistic changes. However, the role of surface area in inducing mechanistic variations is yet to be unequivocally established and the proposed model should involve a 'surface-area related factor' in the exponential term $\beta\eta\, F/RT$. Investigations in progress addressing these issues will be reported in a separate communication.

3.2 *Stability under open-circuit conditions*

While most metals remain stable under cathodic polarization, many of them dissolve under open-circuit conditions because of inherent thermodynamic instability or due to 'forced' instability (which will be elaborated later). Thus, iron cathodes in NaOH solutions exhibit open-circuit potentials negative to the reversible hydrogen electrode in the same solution. This is a corrosion potential arising from the anodic dissolution of Fe as $HFeO_2^-$ – the conjugate reaction being the discharge of H^+ ions to form H_2 or the reduction of other redox species in the solution. While the former can be controlled by appropriately manipulating the pH of the medium, the forced instability caused by the reduction of other species in the solution will enhance the instability of the electrode. Thus, in a diaphragm type chlor-alkali cell, OCl^- and ClO_3^- are present in the catholyte and these ions can exacerbate the corrosion rate of transition metals since the reduction of these ions is thermodynamically favored. It is hence imperative that any high performance cathode material chosen be not only stable at the given pH of the medium but also resist further oxidation by OCl^- and ClO_3^- present in the solution.

3.3 *Other factors dictated by cell design and product quality*

In addition to electrocatalysis and stability considerations, two other criteria that are by no means trivial while selecting high performance cathode materials include the following.

3.3a *Selection of coating technique*: Several methods, such as plasma spraying, thermospraying, electrodeposition, thermal decomposition, etc., are available for generating of high surface area coatings on iron substrates. However, it is necessary to examine the generally complex electrode geometry and structure before choosing the coating technology because of the 'limited throwing power' of the various coating methods and their operating temperatures. If, for example, a

cathode finger in a H-4 chlor-alkali cell (an extremely complex structure) is to be coated entirely *in situ*, it would be a monumental task in view of the factors noted above. Furthermore, the tolerances involved in the fabrication of the cathodes are tight, with the result that any coating technique that requires operation at high temperatures will distort the cathode and, hence, the current distribution in the cell, resulting in an additional ohmic drop.

3.3b *Product purity:* In chlor-alkali operations, there are two parasitic cathode reactions, noted below, which lead to blind current efficiency losses.

$$OCl^- + H_2O + 2e \rightarrow Cl^- + 2OH^-,$$
$$ClO_3 + 3H_2O + 6e \rightarrow Cl^- + 6OH^-.$$

It was recently shown that OCl^- gets reduced under limiting current density conditions on all metals, whereas the cathodic reduction of ClO_3^- to Cl^- is kinetically slow and proceeds only on iron based surfaces at low current densities (B V Tilak and K Tari, in preparation). Since chlorate is an undesirable impurity in caustic, it is imperative that the cathode material which is electrocatalytic for the hydrogen evolution reaction is also electrocatalytic for the chlorate reduction reaction unless measures are taken to prevent its formation.

4. Conclusions

Highlights of the electrocatalytic investigations reported in this study can be summarized as follows.

a) Enhanced catalytic activity to h.e.r. in caustic media can be achieved by alloying nickel with metals such as Co, Ir, W or with non-metals such as S, P, B, Si, Bi and Sb.

b) Significant lowering of hydrogen overvoltage is observed only in the case of high surface area materials.

c) High surface area materials show high I_0 values and low Tafel slopes.

d) Increased catalytic activity observed on high surface area electrodes is just not a mere consequence of its extended surface but is a result of altered reaction pathways leading to low Tafel slopes.

e) An elementary flooded pore model description allowing for potential dependent adsorption of hydrogen does not explain the observed low Tafel slopes.

f) The 3-*D* hydride model explains the origin of low Tafel slopes solely from mechanistic considerations with no explicit reference to the "high surface area features" of the coating.

g) There is a need to quantify the observed behavior on high surface materials in terms of: i) crystallite size effects; ii) bubble formation and release energetics and; iii) more realistic visualization of a 'rough' surface.

h) It is demonstrated that a number of different approaches can be taken to obtain high performance catalytic cathodes but it is important to examine these techniques in perspective since the ultimate aim is to implement these coatings in 'real-life'

i) Some of the prerequisites for any high performance coating to be commercially viable are: i) good throwing power; ii) ability to coat *in situ*; iii) ease of recoating; iv) stability of the coating to special treatments which can include diaphragm deposition and baking procedures; v) stability to open circuit conditions and vi) catalytic activity towards ClO_3^- reduction.
j) Catalytic coatings formed by electrodeposition or better still, electroless deposition, seem to have all the practical and commercial advantages if used in tandem with protection schemes e.g., cathodic protection, addition of reagents that would instantaneously react with the oxidizing species in the anolyte in a diaphragm type chlor-alkali cell.

Acknowledgements

The authors wish to thank Mrs U I Keller for performing the electrochemical studies and Dr L Salvatti for ESCA/ISS analyses.

References

Anon 1982 *Chemical Week* September 15, p. 44; October 27, p. 80
Anon 1985 *Electrical World* April, p. 53; September, p. 51
Appleby A J, Kita H, Chemla M and Brönoel G 1982 *Encylopedia of electrochemistry of elements* (ed) A J Bard (New York: Marcel Dekker Inc) vol. 9, part A, p. 384
Bennett J E and Tompkins H G 1976 *J. Electrochem. Soc.* **123** 999
Bockris J O'M and Subramanyan P K 1971 *Electrochim. Acta* **16** 2169
Caldwell D L 1981 *Comprehensive treatise of electrochemistry* (eds) J O'M Bockris, B E Conway, E Yeager and R E White (New York: Plenum Press) vol. 2, p. 105
Carlin W W *US Patent No.* **3,** 954, 581
Conway B E, Kozlowska H A, Sattar M A and Tilak B V 1983 *J. Electrochem. Soc.* **130** 1825
Conway B E and Bai L 1984 *Hydrogen energy progress* V (eds) T N Veziroglu and J B Taylor (New York: Pergamon Press) vol. 2, p. 879
deCarvalho J, Tremilion-Filho G, Avaca L and Gonzalez R 1985 Paper No. 370 presented at the *Electrochemical Society Meeting*, Toronto, Canada, May
Flitt H F and Bockris J O'M 1982 *Int. J. Hydrogen Energy* **7** 411
Hine F, Tilak B V and Viswanathan K 1986 *Modern aspects of electrochemistry* (eds) J O'M Bockris, B E Conway and R E White (New York: Plenum Press) vol. 18
Hine F, Yasuda M and Watanabe M 1979 *Denki Kagaku* **47** 401
Hovey N W, Krohn A and Hanneken G M Jr 1963 *J. Electrochem. Soc.* **110** 362
Komnikov L 1964 *Met. Finish.* **62** 49
Korovin N V, Saveleva O N and Kozolova N I 1980 *Sov. Electrochem.* **16** 498
Kreysa G and Håkansson B 1986 *J. Electroanal. Chem.* **201** 61
Kinoshita K 1982 *Modern aspects of electrochemistry* (eds) J O'M Bockris, B E Conway and R E White (New York: Plenum Press) vol. 14, chap. 8
Lu P W T and Srinivasan S 1978 *J. Electrochem. Soc.* **125** 265
Mannan R 1967 Doctoral dissertation, University of Pennsylvania
Miles M H, Kissel G, Lu P W T and Srinivasan S 1976 *J. Electrochem. Soc.* **123** 332
Netherton L E and Holt M L 1951 *J. Electrochem. Soc.* **98** 106
Ohta T, Funk J E, Porter J D and Tilak B V 1985 *Int. J. Hydrogen Energy* **10** 571
Onuchukwu A N 1982 *Electrochim. Acta* **27** 529
Parsons R 1969 *Surf. Sci.* **18** 28
Periasamy M and Krishnaswamy P R 1975 *J. Electroanal. Chem.* **61** 349

churski J Z O, Pouli D, Ripa J and Pokrzyk G F 1982 *US Patent No.* **4** 354, 915
mari N and Kato A 1976 *Denki Kagaku* **44** 477
ak B V 1979 *J. Electrochem. Soc.* **126** 1344
ak B V, Lu P W T, Colman J E and Srinivasan S 1981 *Comprehensive treatise of electrochemistry* (eds) J O'M Bockris, B E Conway, E Yeager and R E White (New York: Plenum Press) vol. 2, p. 1
ak B V, Rader C G and Conway B E 1977 *Electrochim. Acta* **22** 1167
ak B V, Rader C G and Rangarajan S K 1977 *J. Electrochem. Soc.* **124** 1879

Electrochemical reduction of 2-nitrobenzidine in methanol-water mixtures[§]

S ARAVAMUTHAN, M S SASHIDAR, C KALIDAS and C S VENKATACHALAM*

Department of Chemistry, Indian Institute of Technology, Madras 600 036, India

Abstract. The electroreduction of 2-nitrobenzidine (2-NB) in buffered methanol-water mixtures in the composition range 20–80% (v/v) and pH range 2·80–12·00 gave a single six-electron diffusion-controlled irreversible wave. On the basis of the results obtained, a diphenoquinone-diimine intermediate is suggested in the mechanism of 2-NB reduction in methanol-water mixtures.

Keywords. 2-Nitrobenzidine; voltammetric techniques; reduction mechanism; electroreduction.

Introduction

Aromatic nitro compounds follow two distinct pathways of reduction depending on the nature of the substituents in the phenyl ring (Stocesova 1949; Shreve and Markham 1949; Heyrovsky and Vavrika 1970): (i) a two-step reduction process wherein the hydroxylamine first formed in a four-electron reduction step is further reduced at a more negative potential to the corresponding amine by a two-electron uptake, and (ii) a single step reduction process wherein the hydroxylamine formed as in (i) undergoes dehydration to give the quinoneimine intermediate which is subsequently reduced at a more positive potential to the corresponding amine. Recently, some interesting reports have appeared on the electrochemical reduction of various nitro substituted biphenyl derivatives in protic and dipolar aprotic media (John Koshy *et al* 1974, 1978, 1981, 1982; Hlavaty *et al* 1979, 1983; Voigtlander *et al* 1983). In view of the importance of some nitro substituted benzidines in the field of analytical and industrial chemistry (Braithwaite 1958; Kuhn 1959; Aravamuthan *et al* 1982), we have taken up in detail the study of the electrochemical behaviour of these compounds at the mercury cathode in different media. In continuation of our work from this laboratory in N,N-dimethylformamide solutions (Aravamuthan *et al* 1984), we report in this paper the results obtained from the electrochemical reduction of 2-NB(NB–nitrobenzidine) in buffered methanol-water mixtures (pH 2·80–12·00) at various compositions (20–80% v/v) of methanol.

Experimental

2-NB was prepared according to the literature procedure (Kovar 1964) and its purity tested by m.p. (141°C), IR, TLC and mass spectrometry. Methanol (Rechem) was

purified by standard methods (Robert 1977–78). Potassium chloride (GR) was used as the supporting electrolyte without further purification. Britton–Robinson (BR) and Clark–Lubs (CL) buffers (Britton 1955) were used to control the pH of the experimental solutions.

The polarographic measurements made in the present work using a three electrode assembly were similar to those described previously (John Koshy *et al* 1978). The dropping mercury electrode (DME) used in 0·1 M aqueous potassium chloride supporting electrolyte at 55 cm height of the mercury column (height uncorrected for back pressure) had the following capillary characteristics under open circuit conditions: $m = 0{\cdot}8814$ mg.sec^{-1}, $t = 7{\cdot}0$ sec. Details of the micro-coulometric experiments employed in the present investigation and the method of evaluating the total number of electrons (n_{app}) in the electro-reduction have been described earlier (John Koshy *et al* 1974). A microburette type hanging mercury drop electrode (HMDE, Metrohm EA 290) was used as the working electrode in cyclic voltammetric (CV) experiments. The area of the electrode was calculated to be $0{\cdot}022 \pm 0{\cdot}003$ cm^2 in aqueous methanol containing 0·1 M potassium chloride. All measurements were carried out at 30°C.

3. Results and discussion

Figure 1 shows typical polarograms of 2-NB ($5{\cdot}0 \times 10^{-4}$ M) obtained in buffered 20% (v/v) methanol-water mixture containing 0·1 M potassium chloride supporting electrolyte. It is seen from figure 1 that 2-NB gives a single well-defined d.c. wave

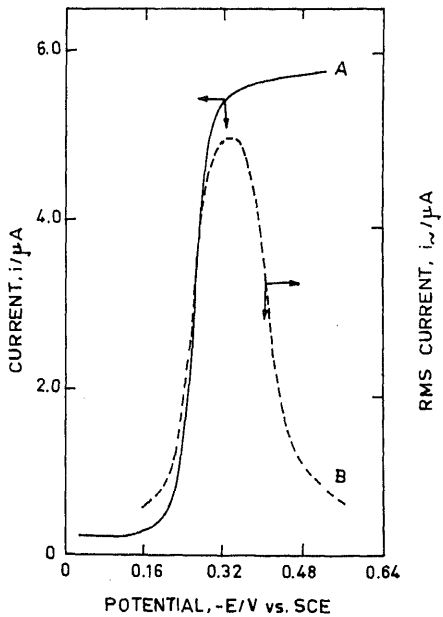

Figure 1. d.c polarogram (A) and a.c polarogram (B) of 2-NB ($5{\cdot}0 \times 10^{-4}$ M) in 20%

and the a.c. polarogram shows a single peak corresponding to the d.c. step. This observation is true for all the compositions of methanol studied at different pH values. The d.c. wave was found to be diffusion-controlled in the composition range 20–80% (v/v) methanol and in the pH range 2·80–12·00 as indicated by the linearity of the plots passing through the origin of (i) limiting current *versus* concentration of 2-NB and (ii) limiting current *versus* square root of the height of the mercury column. A slope of 0·5 in the (log i–log h) linear plot further confirmed the diffusion-controlled nature of the limiting current in buffered methanol solutions. The electrode process was found to be irreversible on the basis of larger wave slopes ($E_{3/4}-E_{1/4}$) obtained for a six-electron process ($n_{app}=6$ in the present work was confirmed subsequently by micro-coulometry) and larger negative a.c. summit potential (E_s) values in all methanol solutions of varying compositions and pH.

The electrochemical reduction of 2-NB in buffered methanol solutions is strongly dependent on the pH of the medium. The half-wave potential ($E_{1/2}$) varies linearly with pH becoming more negative as the pH is increased which indicates proton participation in the electrode process. It is also found that $E_{1/2}$ varies with the composition of methanol shifting it to more negative values as the methanol content is increased. This is attributed to the 'inhibition' of the electrode process caused by the adsorption of methanol molecules at the mercury-solution interface (Maironovsky 1968).

The total number of electrons (n_{app}) participating in the reduction of 2-NB in buffered methanol-water mixtures was determined by microscale controlled-potential electrolysis experiments (John Koshy *et al* 1974). The coulometric data presented in table 1 for different compositions of methanol at various pH values indicate that a total of six electrons are involved in the reduction of 2-NB.

Figure 2 shows typical cyclic voltammograms of 2-NB obtained at 0·100 V sec^{-1} sweep rate in 20% (v/v) methanol-water mixtures in acid (figure 2a) and alkaline (figure 2b) regions. It is found that a single cathodic peak appears in the forward scan at all compositions of the methanol-water mixture in the pH range 2·80–12·00.

Table 1. Microcoulometric data for 2-NB ($5{\cdot}0\times10^{-4}$ M) reduction in buffered methanol solutions at various compositions.

Percentage composition of methanol (v/v)	pH	Applied potential ($-E$ vs Hg pool electrode/V) at the plateau of the wave	n_{app}
	3·08	0·600	6·05
20	6·85	0·900	5·95
	11·60	1·100	6·02
	3·50	0·700	5·95
60	6·34	0·950	5·92
	10·42	1·100	6·02
	4·81	0·900	5·95
80[a]	6·99	1·100	5·98
	10·23	1·400	5·94

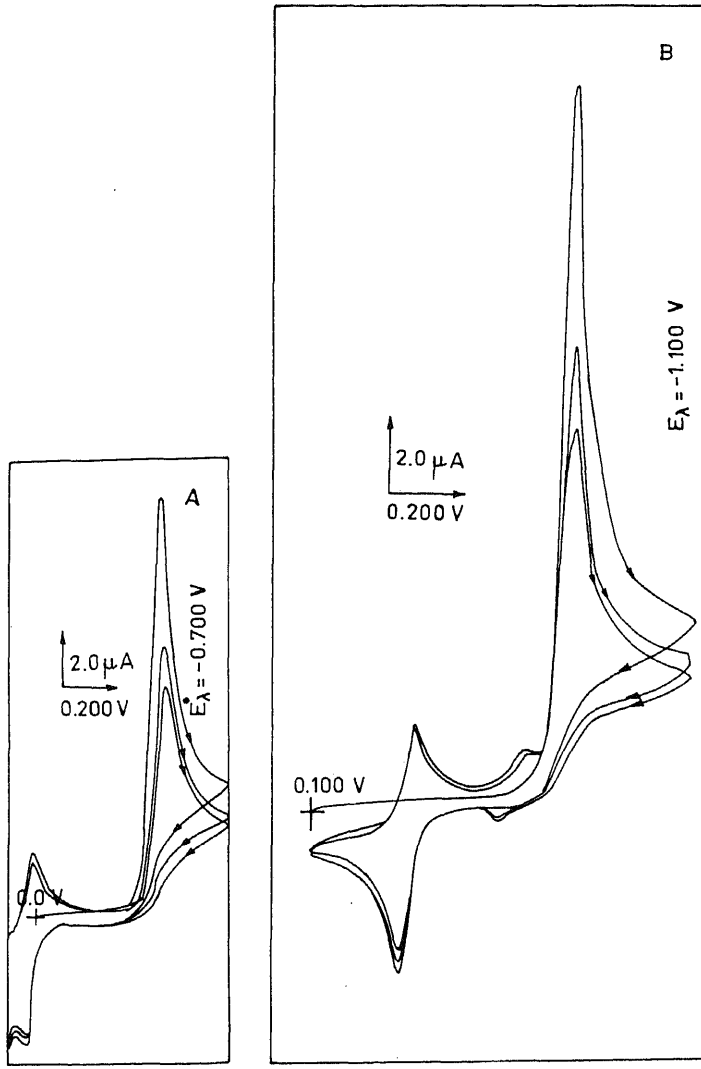

Figure 2. Cyclic voltammograms of 2-NB ($5{\cdot}0 \times 10^{-4}$ M) in buffered 20% (v/v) methanol-water mixture containing 0·1 M KCl supporting electrolyte at pH 4·94 (**A**) and 10·81 (**B**) [switching potentials, E_λ and starting voltages are indicated in the figures; sweep rate, $v = 0{\cdot}100$ V sec^{-1} in both the cases].

The peak potential corresponds to the d.c. polarographic step. The cathodic peak is said to be diffusion-controlled as evidenced by the linearity of the plot passing through the origin of i_p^c versus $v^{1/2}$. A sweep reversal past the cathodic peak gives no anodic peak which confirms the irreversible nature of the electrode process. In alkaline media, during continuous cycles a reversible one electron 'redox couple'

reverse scan itself, it might have resulted from the oxidation of the reduction product of 2-NB formed at the electrode surface and the oxidised product is once again reduced to the initial reduction product. The peak separation ($\triangle E_p$) of 0·030 V corresponds to a reversible two-electron 'redox couple' and this may be attributed to the following reaction:

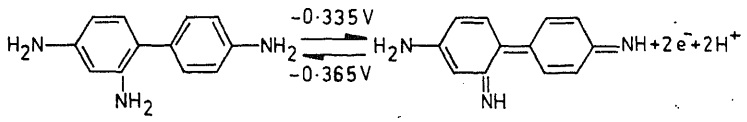

Chart 1.

In acidic solutions of methanol (pH < 4·50), it is quite likely that the 'redox couple' might be observed at more positive potentials than the zero volts *versus* SCE, but in view of the possible oxidation of mercury and the chloride ion of the supporting electrolyte, sweep experiments were not extended to more positive potential scales.

The presence of diphenoquinonediimine intermediate during the reduction of 2-NB was confirmed by CV experiments carried out on 2-aminobenzidine. 2-aminobenzidine was prepared by the chemical reduction of 2-NB using tin and hydrochloric acid. The product was recrystallised and characterised by m.p. (observed 132°C, literature value 134°C, Tauber 1890) and IR techniques. Figure 3 shows typical cyclic voltammograms of 2-aminobenzidine ($1{\cdot}09 \times 10^{-3}$ M) in buffered (pH 11·75) 50% (v/v) methanol-water mixtures containing 0·1 M KCl. It is found that a peak separation ($\triangle E_p$) of 0·035–0·040 V which corresponds to a reversible two-electron 'redox couple', is comparable to the value reported earlier for 2-NB reduction. This indicates that the 'redox couple' which appeared in the cyclic voltammogram of 2-NB is due to the oxidation of 2-aminobenzidine.

The reason for observing the cathodic peak in the forward scan (figure 3) for 2-aminobenzidine is due to the starting potential, namely, 0·0 V which is more positive than the potential required to oxidize 2-aminobenzidine (around −0·150 V vs SCE) to the diphenoquinonediimine intermediate. Hence, during the start of the experiment the oxidised form of 2-aminobenzidine is reduced to give the cathodic peak. Though the concentration of 2-aminobenzidine taken was much higher ($1{\cdot}09 \times 10^{-3}$ M), the smaller current obtained in the cyclic voltammogram is due to the low concentration of the oxidised compound formed at the electrode surface. This point has been repeatedly checked by the following experiments:

. On holding the potential at 0·0 V for few seconds, the cathodic current was found to increase; on the other hand, when the potential was held at a more negative value the peak height was found to decrease.

i. The cyclic voltammograms of 2-aminobenzidine at sweep rates 0·050 V sec^{-1} and 0·100 V sec^{-1} in the same buffered (pH 11·75) medium (50% v/v methanol) were also taken keeping the starting voltage at −0·800 V *versus* SCE and scanning the potential *backwards* (*anodically polarised*). In this case, as expected, the anodic

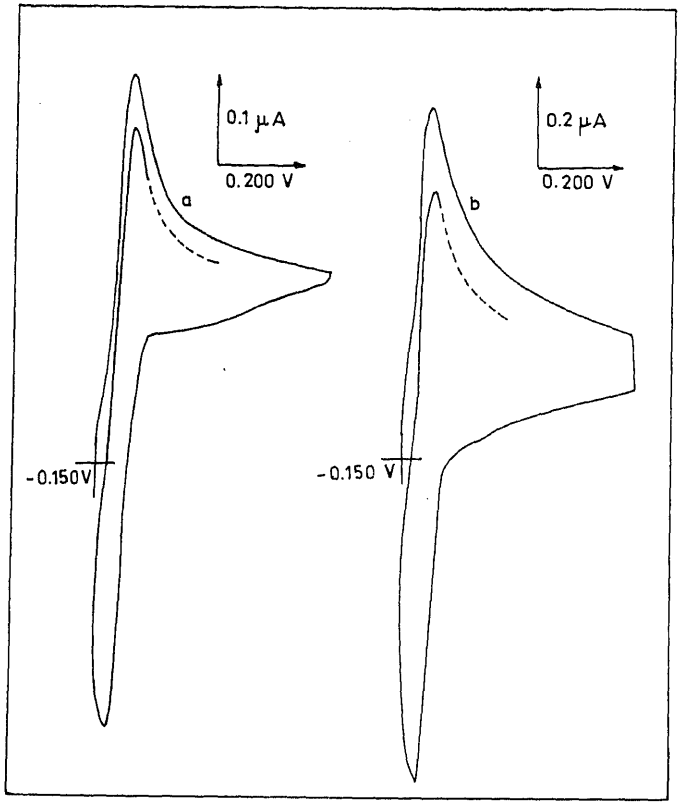

Figure 3. Cyclic voltammograms of 2-aminobenzidine ($1{\cdot}09 \times 10^{-3}$ M) showing diphenoquinonediimine species in 50% (v/v) buffered (pH 11·75) methanol-water mixtures at sweep rates, $\nu = 0{\cdot}050$ V sec^{-1}(a) and 0·100 V sec^{-1}(b). Starting voltages are indicated in the figure.

peak first appeared followed by the cathodic peak while the anodic peak current is found to be more than what has been observed earlier.

Based on the polarographic, coulometric and CV experiments, the ECE-type of mechanism is suggested for 2-NB reduction in buffered methanol-water mixtures (chart 2).

It may be pointed out that since the formation of 2-aminobenzidine occurs at a more positive potential (E_2) than the potential (E_1) at which the 2-hydroxylaminobenzidine is formed from the parent compound, a single wave is observed (figure 1) in the present investigation (Stocesova 1949; Par Michel le Guyader 1966). In the mechanism cited above it is inferred that in acidic media, the protonated form of 2-NB is reduced to 2-aminobenzidine via the protonated diphenoquinone diimine intermediate while in neutral and alkaline solutions, the unprotonated form of 2-NB is reduced. The identification of the reduction product of 2-NB from macroscale controlled-potential electrolysis through

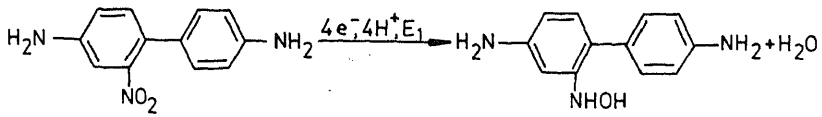

2-nitrobenzidine

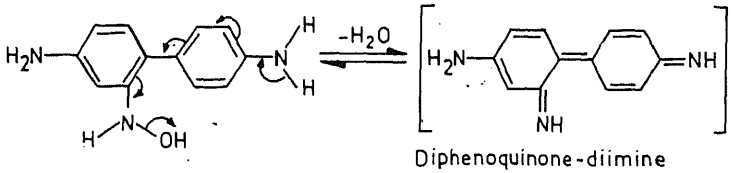

Diphenoquinone-diimine intermediate

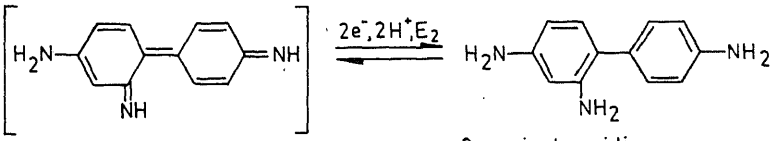

2-aminobenzidine

Chart 2.

olution after electrolysis changed its colour rapidly due to possible aerial oxidation vhen taken out of the cell.

Acknowledgements

The financial assistance to one of the authors (SA) from the Department of Atomic Energy, Bombay is gratefully acknowledged.

References

Aravamuthan S, Kalidas C and Venkatachalam C S 1982 *Proc. Indian Acad. Sci.* (*Chem. Sci.*) **91** 311
Aravamuthan S, Kalidas C and Venkatachalam C S 1984 *J. Electroanal. Chem.* **171** 293
Braithwaite R S W 1958 *J. Chem. Soc.* 4073
Britton H T S 1955 *Hydrogen ions* (London: Chapman and Hall)
Heyrovsky M and Vavrika S 1970 *J. Electroanal. Chem.* **28** 409
Illavaty J, Volke J, Manousek O and Bakos V 1979 *Electrochim. Acta* **24** 541
Illavaty J, Volke J and Bakos V 1983 *Collect. Czech. Chem. Commun.* **48** 379
John Koshy V, Venkatachalam C S and Kalidas C 1974 *Trans. Soc. Adv. Electrochem. Sci. Technol.* **9** 162
John Koshy V, Venkatachalam C S and Kalidas C 1978 *J. Electroanal. Chem.* **89** 191
John Koshy V, Venkatachalam C S and Kalidas C 1981a *Electrochim. Acta* **26** 1851
John Koshy V, Venkatachalam C S and Kalidas C 1981b *Indian J. Chem.* **A20** 49
John Koshy V, Venkatachalam C S and Kalidas C 1982 *Indian J. Chem.* **A21** 555
Kovar V 1964 *Chem. Abstr.* **60** 454h
Kuhn H 1959 *Angew. Chem.* **71** 93
Le Guyader P M 1966 *Bull. Soc. Chim. Fr.* **66** 1849
Maironovsky S G 1968 *Catalytic and kinetic waves in polarography* (New York: Plenum Press) chap. 5
Robert C 1977–78 *C R C Handbook of chemistry and physics* edn 58 (West Palm Beach, Fl: CRC Press)
Shreve O D and Markham E C 1949 *J. Am. Chem. Soc.* **71** 2993
Stocesova D 1949 *Collect. Czech. Chem. Commun.* **14** 615

Electrochemical reduction of some benzophenones in molten acetamide at 85°C[§]

R SARASWATHI and R NARAYAN*
Department of Chemistry, Indian Institute of Technology, Madras 600 036, India

Abstract. Benzophenones undergo a one-step two-electron reduction in molten acetamide containing sodium acetate, both at the mercury and the glassy carbon electrodes. The reduction process is irreversible. The $E_{1/2}$ potentials of some of the benzophenones can be fitted into a Hammett plot. The αn_a and $k^0_{f,h}$ are evaluated and discussed.

Keywords. Benzophenone; molten acetamide; half-wave potentials; Hammett plot.

1. Introduction

There are a large number of papers in the literature dealing with the electrochemical reduction of aromatic carbonyl compounds at the mercury electrode (Day *et al* 1952; Perrin 1965; Zuman *et al* 1968a). In particular, studies on the electrochemical reduction of benzophenone in the aqueous-alcoholic media have been numerous (Elving and Leone 1958; Pfister and Bonastre 1965; Sivakumar *et al* 1983), using polarography, controlled-potential electrolysis, cyclic voltammetry and chronoamperometry. The kinetics and mechanism of the reduction process in acidic, neutral and alkaline (Suzuki and Elving 1961; Zuman 1968; Nadjo and Saveant 1971) solutions have been investigated and the conditions for the formation of free radicals and radical ions have been discussed. In acidic and in neutral media benzophenone gives two equal and well-defined d.c. polarographic waves, each wave corresponding to a one-electron reduction process. In the pH range of 6–8, the two waves merge to give only one wave. At still higher pH, a third wave appears at more negative potentials.

The first one-electron wave represents the reduction of benzophenone to the free radical $(C_6H_5)_2\dot{C}OH$ which is supposed to dimerize to pinacol. The second one-electron wave is due to the reduction of the free radical to carbinol. The two-electron combined wave involves the reduction of benzophenone to carbinol through a free radical state. The third wave at a more negative potential is attributed to the more difficult reduction of the free radical ion $[(C_6H_5)_2\dot{C}O]^-$ which is formed along with the neutral free radical. The schematic representation of the mechanism suggested is given here:

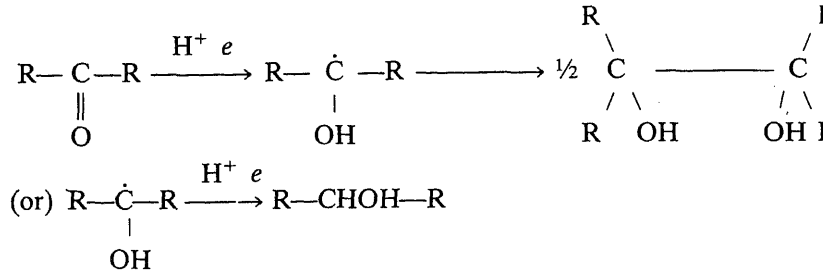

Zuman *et al* (1968) used polarography in their study of a series of substituted benzophenones in buffered aqueous-ethanolic media and the half-wave potentials were correlated with Hammett substituent constants (σ). Sivakumar *et al* (1984) have extended the study to aqueous-organic mixtures i.e. in 50% dioxane-water, 50% DMF-water and 50% isopropanol-water but have not made any correlations. Diffusion coefficients and rate constants were reported by the authors from the cyclic voltammetry results. Blazquez *et al* (1985) in their recent paper on the 'electrodimerisation of benzophenone on mercury electrode' have reported the results of a reinvestigation of the mechanism of the first reduction step of benzophenone in buffered ethanol-water solutions below a pH of 6. Current-time curves and differential capacitance-potential curves were used to establish the reversible nature of the first electron transfer.

The electrochemical reduction behaviour of benzophenone has also been investigated in non-aqueous solvents – namely formamide (Harry Letan and Gropp 1953), dimethyl formamide (Given and Peover 1960; Wawzonek and Gundersen 1960), acetonitrile (Lunnazi *et al* 1971), pyridine (Michelli and Elving 1968) and dimethyl sulphoxide (Tallant and Evans 1969). Two successive one-electron steps are observed, the first is attributed to the formation of a free radical anion and second to the benzhydrol dianion. The first reduction step is found to be more reversible that the second one. The effect of proton donors on the reduction behaviour has also been studied.

Saveant and Nadjo (1971) and Saveant and Thiebault (1978) have studied the reduction behaviour of halo-derivatives of benzophenone in DMF, DMSO, acetonitrile and liquid ammonia. The reduction of these compounds in aqueous media is found to follow the same reaction path as the unsubstituted compound (Zuman *et al* 1968b) whereas in aprotic solvents a reductive cleavage of the carbon-halogen bond is observed at potentials positive to the carbonyl group reduction. The possible reduction mechanisms are also discussed.

In our laboratory, considerable amount of work has been done in molten acetamide at 85°C on the electrochemical reduction of oxygen, metal ions and a few quinones (Phani 1984). The study indicated that molten acetamide behaves like water. The present study was undertaken to follow the electrochemical reduction of benzophenones in molten acetamide. The diffusion coefficients and the kinetic parameters are evaluated and the results are discussed.

2. Experimental

ne electrolytic cell with minimum exposure to the atmosphere and melted in a dry ydrogen atmosphere. The cell is a double-walled vessel with provision for irculation of water. The temperature of the melt is maintained at 85°C with the elp of HAAKE R20 thermostat. 1·0 M CH_3COONa is generally used as the upporting electrolyte which renders the medium slightly basic.

Commercial samples of benzophenone, 2,4-dihydroxy, 2-hydroxy-5-chloro, -hydroxy (Bio-organics) and 4-bromo benzophenones (Fluka) were used after esting for the purity of the compounds. The other compounds were prepared as rescribed in the literature.

The dropping mercury working electrode has the characteristics of $= 2{\cdot}47\ mgs^{-1}$ and an open circuit drop time of 3 sec at a height of 57 cm of the ercury column in 1·0 M CH_3COONa in molten acetamide. The hanging mercury rop electrode (HMDE) is of a Metrohm make with an area of 0·022 cm^2 for a our-division drop. The area is calculated from the average weight of several drops ssuming spherical shape for the drops. Two glassy carbon electrodes are used in ur experiments with geometrical areas of 0·06 cm^2 and 0·075 cm^2. The true urface areas of the electrodes were determined from the standard experiment of d^{+2} ion reduction in molten acetamide. Cd^{+2} undergoes a reversible reduction at ne mercury and at the glassy carbon electrodes. The diffusion coefficient of Cd^{+2} on in molten acetamide (Phani 1984) and the area of the HMDE are known. For the ame concentration and sweep rates, the i_p values at these two electrodes are ompared and the area of the glassy carbon electrode is calculated. The areas of the lectrodes are 0·07 cm^2 and 0·1 cm^2, respectively. The glassy carbon electrodes ere mounted into a Teflon cylinder with the surface flush with the edge of the ylinder. This is then made to fit snugly into a suitable glass tube using 'Araldite'. he electrical contact is by a copper wire inserted into mercury placed on top of the arbon electrode. The glassy carbon electrodes were hand-polished with various rades of fine emery papers, degreased with acetone, washed thoroughly with ater and dried before use.

The reference electrode is Ag, $AgCl/Cl^-$(saturated). It is made of a thin-walled lass bulb containing molten acetamide saturated with AgCl and KCl. Contact with ne melt is made by a wetted asbestos wick passing through a small hole in the glass ulb. A large platinum foil is used as the counter electrode.

The potential range of investigation with a mercury electrode is from $-0{\cdot}1$ V to $-1{\cdot}6$ V and with a glassy carbon electrode (GCE) is from $+0{\cdot}7$ V to $-1{\cdot}9$ V versus ne Ag, $AgCl/Cl^-$(saturated) electrode. Platinum electrodes could not be used as a rge reduction peak is observed at $-1{\cdot}0$ V. This reduction process probably occurs t highly negative potentials with mercury and glassy carbon electrodes.

A potentiostat interphased with a scan generator constructed from operational mplifiers in this laboratory is used for our experiments. The polarograms and the yclic voltammograms are recorded with an $X-Y$ recorder (Digigraphic series 000).

3. Results

Figure 1 shows the polarogram for the reduction of benzophenone in molten acetamide at different concentrations. A well-defined single wave is obtained. The reduction process is diffusion-controlled and the i_d values are proportional to the concentrations studied. A maximum is observed when the concentration exceeds about $1{\cdot}5 \times 10^{-3}$ M for all the benzophenones studied except 2-hydroxy-5-chloro benzophenone. For this compound, no maximum is observed upto a concentration of $2{\cdot}0 \times 10^{-3}$ M.

Table 1 gives the polarographic results for the reduction of benzophenones in molten acetamide. The $E_{1/2}$ values are found to change depending on the nature of the substituent. A maximum positive shift is observed with 4-bromobenzophenone and a maximum negative shift with 4-hydroxy benzophenone. The transfer coefficients (αn_a) are evaluated from the log $[(i_d - i)/i]$ versus E plots and the diffusion coefficients are calculated using the Ilkovic equation.

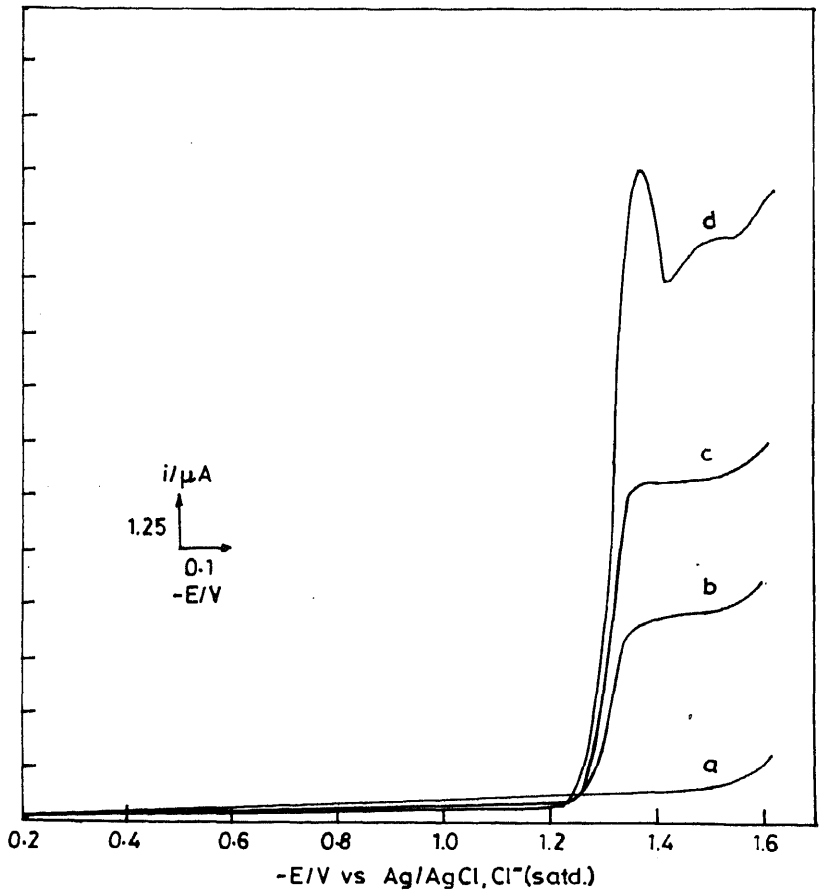

Figure 1. Polarograms for the reduction of benzophenone from molten acetamide at

at 85°C $m = 2{\cdot}47$ mg sec^{-1}; $t = 3$ sec; $n = 57$ cm. Supporting electrolyte 1·0 M CH_3COONa. Concentration of benzophenones $1{\cdot}0 \times 10^{-3}$ M. I–diffusion current constant.

Substituent	$E_{1/2}$ (V)	I	$D \times 10^6$ (cm^2 sec^{-1})	αn_a
H	1·315	3·12	4·83	1·78
2-Hydroxy	1·36	2·65	3·49	1·78
4-Hydroxy	1·49	2·60	3·366	0·845
2,4-Dihydroxy	1·48	2·32	2·6	1·52
2-Hydroxy-5-methyl	1·35	2·84	4·0	1·66
2-Hydroxy-5-chloro	1·29	2·87	4·1	1·29
2-Amino	1·43	2·92	4·2	1·18
4-Bromo	1·275	3·24	5·2	1·62
3-Nitro-4-hydroxy	0·72*	5·78*	4·21*	1·03
	1·03			
	1·51			

* For the first reduction step only.

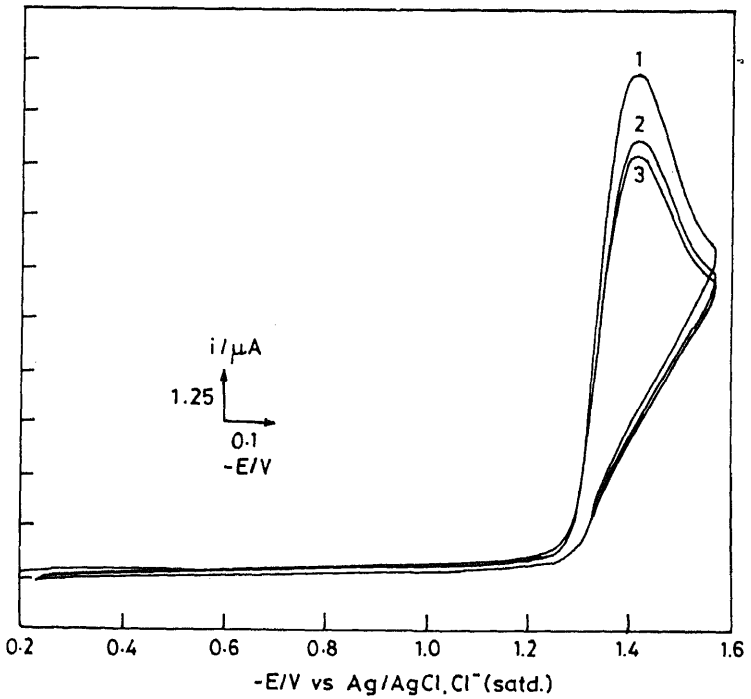

Figure 2. Cyclic voltammogram for the reduction of benzophenone from molten acetamide at 85°C. Supporting electrolyte: 1·0 M CH_3COONa at HMDE ($A = 0{\cdot}022$ cm^2). Sweep rate: 150 mVsec^{-1}, 1,2,3 correspond to the cycles. Concentration of benzophenone: $1{\cdot}18 \times 10^{-3}$ M.

res 2 and 3 show the cyclic voltammogram of benzophenone at the HMDE the GCE, respectively. The i_p values are found to be proportional to $v^{1/2}$

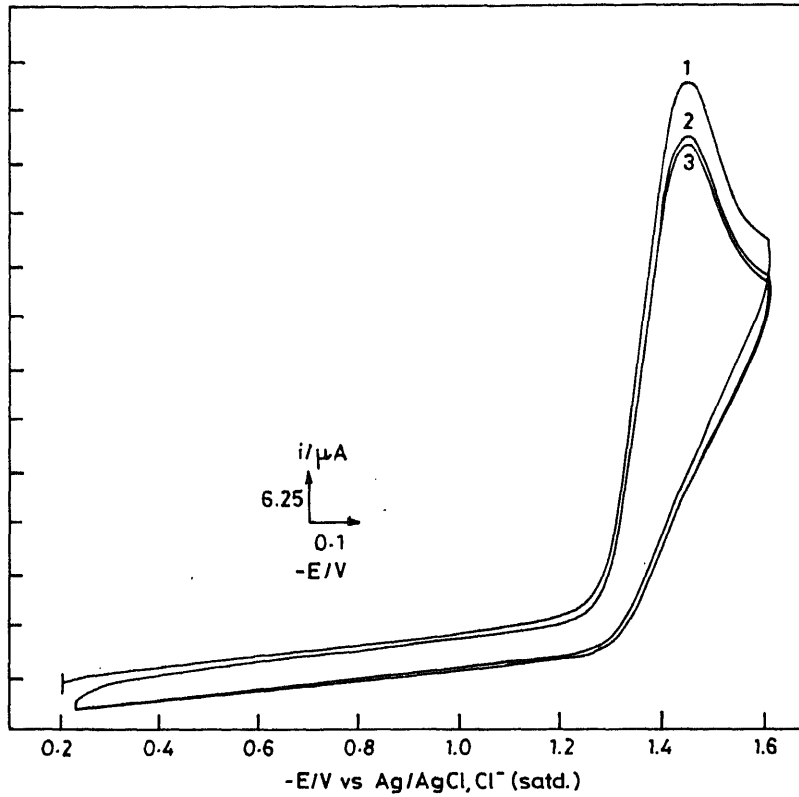

Figure 3. Cyclic voltammogram for the reduction of benzophenone from molten acetamide at 85°C. Supporting electrolyte: 1·0 M CH_3COONa at glassy carbon electrode (A = 0·1 cm^2). Sweep rate: 150 mV sec^{-1},1,2,3 correspond to the cycles. Concentration of benzophenone: $1{\cdot}5 \times 10^{-3}$ M.

(figure 4) and also to the concentrations studied. The irreversible nature of the reduction is clearly seen from the absence of an anodic peak in the reverse scan and also from the variation of E_p values with the sweep rates. E_p values for any one concentration shift with the nature of the substituent and show the same trend as $E_{1/2}$ potentials.

Tables 2 and 3 give the data for the reduction of benzophenones in molten acetamide from the above study. The E_p values are reported at a sweep rate of 20 $mVsec^{-1}$. The diffusion coefficients are evaluated using the equation

$$i_p = 3{\cdot}01 \times 10^5 n(\alpha n_a)^{1/2}\, C_0^b \nu^{1/2}, \qquad (1)$$

where i_p is the peak current in micro amperes. The transfer coefficients (αn_a) are evaluated from the $E_p - \log \nu$ (figure 5) and $E_p - \log i_p$ (figure 6) graphical plots. Since the standard potentials of benzophenones are not known in literature, the

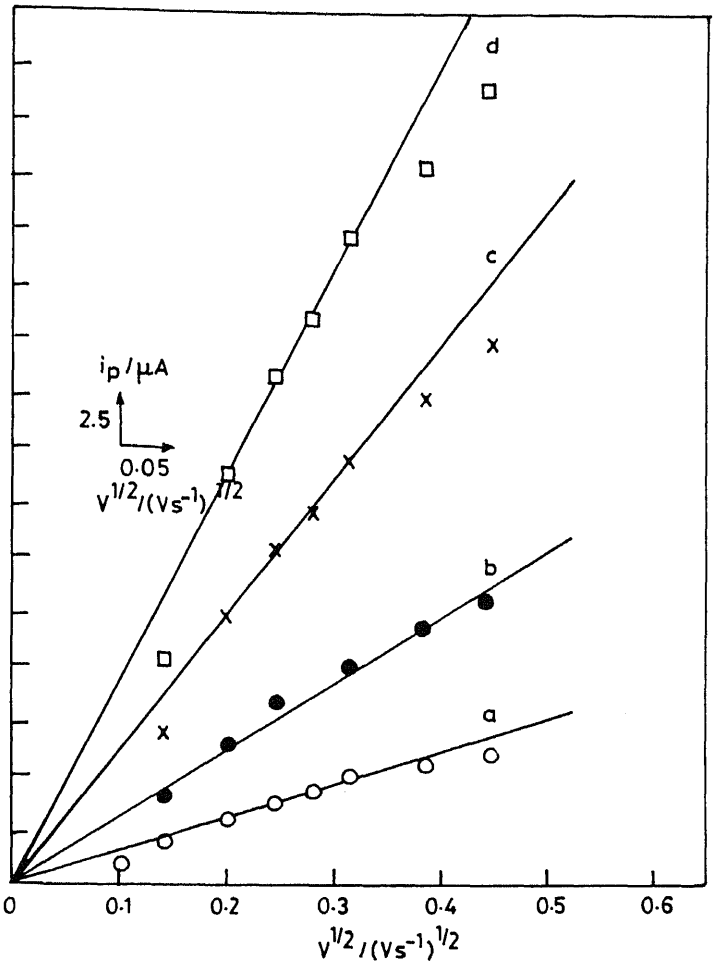

Figure 4. Plot of i_p versus $v^{1/2}$ for benzophenone reduction in molten acetamide at HMDE ($A = 0{\cdot}022$ cm^2). Supporting electrolyte 1·0 M CH_3COONa. Concentration of benzophenone (a) $0{\cdot}57 \times 10^{-3}$ M (b) $1{\cdot}18 \times 10^{-3}$ M (c) $2{\cdot}01 \times 10^{-3}$ M (d) $2{\cdot}7 \times 10^{-3}$ M.

4. Discussion

In molten acetamide one well-defined polarographic wave is obtained for the reduction of these benzophenones at all concentrations, in the potential range of $-0{\cdot}1$ V to $-1{\cdot}6$ V. Molten acetamide at 85°C is known to have ionic product of $10^{-14{\cdot}6}$ (Guiot and Tremillon 1968) which is comparable with that of water. Previous studies (Phani 1984) on the electrochemical reduction of O_2, quinones and metal ions in molten acetamide show that the reduction behaviour of these compounds is similar to that in water. In aqueous-organic solvents, in the range of pH 6 and 8, benzophenone undergoes a two-electron reduction in one step (Zuman

Table 2. Cyclic voltammetric data for the reduction of benzophenones at HMDE in molten acetamide at 85°C. Supporting electrolyte: 1·0 M CH_3COONa. Concentration of benzophenones $\sim 1 \times 10^{-3}$M.

Substituent	E_p(V) at 20 mVsec^{-1}	$D \times 10^6$ (cm^2 sec^{-1})	αn_a (E_p – log i_p)	αn_a (E_p – log ν)	$k^0_{f,h}$ at $E = 0$ V
H	1·35	5·3	0·68	0·8	$1{\cdot}6 \times 10^{-17}$
2-Hydroxy	1·39	3·9	0·68	0·66	$8{\cdot}26 \times 10^{-17}$
4-Hydroxy	1·54	3·4	0·68	0·66	$2{\cdot}02 \times 10^{-19}$
2,4-Dihydroxy	1·49	3·5	0·79	0·87	$7{\cdot}86 \times 10^{-21}$
2-Hydroxy-5-methyl	1·38	2·3	1·27	1·14	$1{\cdot}31 \times 10^{-27}$
2-Hydroxy-5-chloro	1·31	1·8	1·27	1·02	$3{\cdot}35 \times 10^{-28}$
2-Amino	1·47	5·0	0·56	0·71	$2{\cdot}65 \times 10^{-15}$
4-Bromo	1·31	4·5	0·9	1·00	$2{\cdot}0 \times 10^{-23}$
3-Nitro-4-hydroxy	0·78 1·56	3·67*	0·78*	0·71*	-

* For the first reduction step.

Table 3. Cyclic voltammetric data for the reduction of benzophenones at GCE in molten acetamide at 85°C. Supporting electrolyte: 1·0 M CH_3COONa. Concentration of benzophenones $\sim 1 \times 10^{-3}$M.

Substituent	E_p(V) at 20 mVsec^{-1}	$D \times 10^6$ (cm^2 sec^{-1})	αn_a (E_p – log i_p)	αn_a (E_p – log ν)	$k^0_{f,h}$ at $E = 0$ V
H	1·33	2·0	0·6	0·48	$1{\cdot}12 \times 10^{-17}$
2-Hydroxy	1·38	3·6	0·69	0·35	$1{\cdot}45 \times 10^{-18}$
4-Hydroxy	1·60	2·3	0·55	0·50	$1{\cdot}24 \times 10^{-17}$
2,4-Dihydroxy	1·48	2·02	0·66	0·60	$6{\cdot}0 \times 10^{-20}$
2-Hydroxy-5-methyl	1·34	2·5	0·81	0·60	$9{\cdot}8 \times 10^{-22}$
2-Hydroxy-5-chloro	1·30	1·9	0·70	0·50	$1{\cdot}79 \times 10^{-18}$
2-Amino	1·44	3·16	0·67	0·7	$1{\cdot}73 \times 10^{-20}$
4-Bromo	1·26	2·3	0·79	0·83	$5{\cdot}6 \times 10^{-20}$
3-Nitro-4-hydroxy	1·1 1·65	3·35*	0·40*	0·4*	-

* For the first reduction step.

wave with either supporting electrolyte. Hence it is inferred that benzophenone undergoes a one-step two-electron reduction in molten acetamide. The mechanism suggested in aqueous medium at this pH is (Zuman 1968):

$$\mathrm{RCOR} + \mathrm{e} \rightarrow \mathrm{R\overset{(-)}{\dot{C}}OR}$$

$$\mathrm{R\overset{(-)}{\dot{C}}OR} + \mathrm{H^+} \rightleftarrows \mathrm{R\dot{C}OHR}$$

$$\mathrm{R\dot{C}OHR} + \mathrm{e} \rightarrow \mathrm{R\overset{(-)}{\dot{C}}OHR}$$

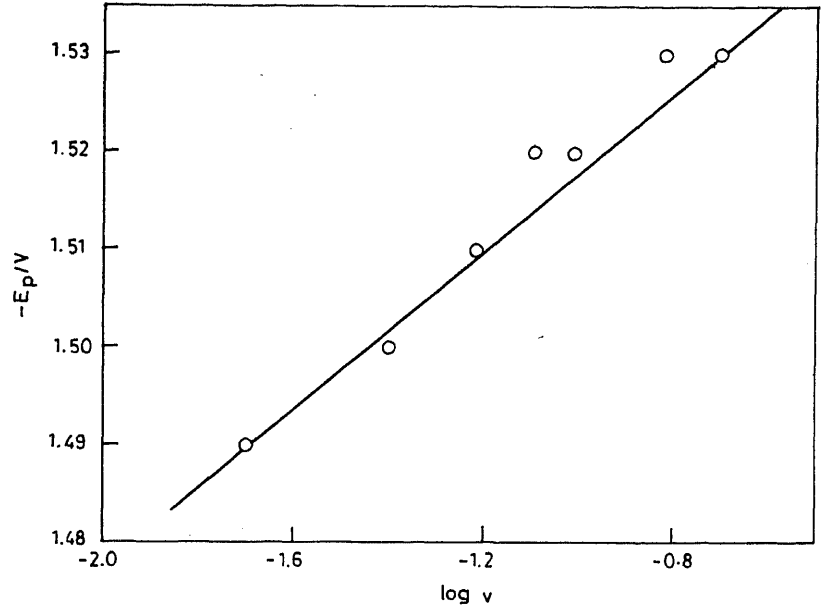

Figure 5. Plot of peak potential (CVM) versus log (sweep rate) for the reduction of 2, 4-dihydroxy benzophenone in molten acetamide at 85°C. Concentration: $0{\cdot}45 \times 10^{-3}$ M. Supporting electrolyte: 1·0 M CH_3COONa.

The log $[(i_d - i)/i]$ versus E plots are linear but the slope of approximately 50 mV indicates irreversibility of the reduction process. The αn_a values do not vary much with the substituents. The change in the $E_{1/2}$ values with various substituents on the benzophenone is found to follow the same trend as in an aqueous medium.

The addition of an electron at the carbon atom of the carbonyl group is facilitated by a low electron density at the carbonyl group and the half-wave potentials are shifted to more positive values. Hence the presence of electron withdrawing substituents makes the reduction easier. Accordingly the *p*-bromo benzophenone shows a positive $E_{1/2}$ shift of 40 mV while the *p*-hydroxy benzophenone a negative shift of 175 mV with respect to the unsubstituted compound. In the case of 2-hydroxy-5-chloro benzophenone, the presence of a hydroxyl group ortho to the carbonyl group may additionally hinder the electron addition due to the hydrogen bonding and steric effects. However, the presence of a chloro group meta to the carbonyl group gives a net positive shift of 25 mV in the $E_{1/2}$ value. The expected negative shifts in $E_{1/2}$ values are observed for the other compounds.

The half-wave potentials in buffered aqueous-ethanolic (Zuman *et al* 1968b) solvent have been correlated to the nature of the substituents through a Hammett plot. The Hammett plot ($E_{1/2}$ versus σ) for a number of para and meta substituted benzophenones gave a value of + 0·25 for the reaction constant ρ at a pH of 9·3. In the present study linearity is observed between the $E_{1/2}$ values and the substituent constants (σ) for the following compounds: 4-bromo ($\sigma = +0{\cdot}26$); 4-hydroxy ($-0{\cdot}7$); 2-hydroxy-5-chloro ($+0{\cdot}373$) and 2-hydroxy-5-methyl ($-0{\cdot}069$). The

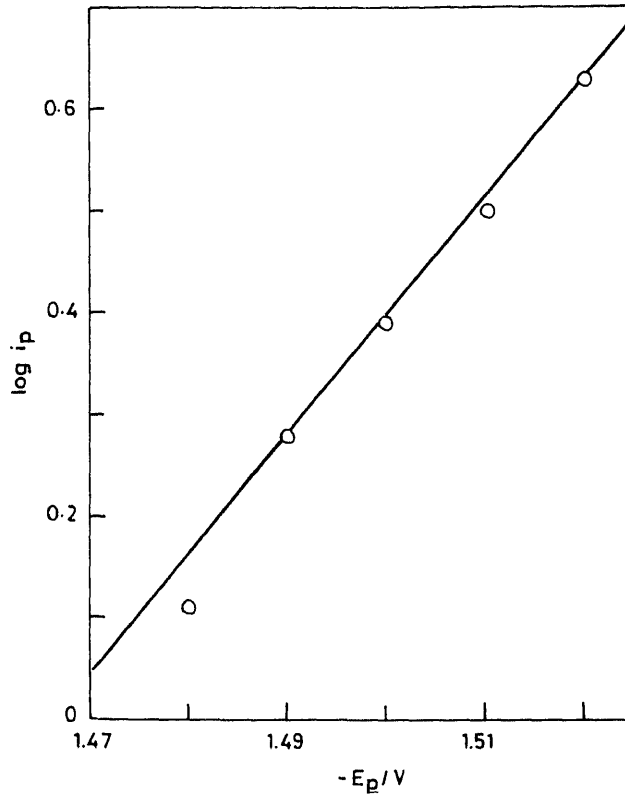

Figure 6. Plot of log (peak current) versus peak potential for the reduction of 2, 4-dihydroxy benzophenone in molten acetamide. Concentration: $0{\cdot}45 \times 10^{-3}$ M. Supporting electrolyte: 1·0 M CH_3COONa.

compounds are taken for the corresponding meta substituents. The reaction constant ρ works out to be $+0{\cdot}218$. Further experiments are to be carried out to confirm these observations.

4.1 *Diffusion coefficients*

The diffusion coefficients are evaluated from the polarographic and cyclic voltammetric results using the appropriate equations. Generally it is observed that the diffusion coefficients of the substituted compounds are smaller than the unsubstituted compound. No unusual results are observed. The reported value of the diffusion coefficient of benzophenone in aqueous medium at 25°C at a pH of 6·8 is $6{\cdot}7 \times 10^{-5}$ cm^2 sec^{-1} (Sivakumar and Jayaram Reddy 1984). The D values are found to be smaller in molten acetamide than in water. The same observation was made in earlier studies with quinones and metal ions in molten acetamide (Phani and Narayan 1985). The decrease in D value is perhaps associated with the higher value of the viscosity of molten acetamide ($\eta_{85°C}$ acetamide $-2{\cdot}01$ cP; $\eta_{25°C}$ water $-0{\cdot}892$ cP).

nitro group is a four-electron step. The D values reported in the tables are calculated from the diffusion current values of the first wave.

The wave at $-1{\cdot}51$ V is inferred to be the reduction of the carbonyl group since there is no reduction process observed at this potential range for nitrobenzene in acetamide ($E_{1/2}$ potentials are $-0{\cdot}79$ V and $-1{\cdot}03$ V, respectively). It may be mentioned however that the $E_{1/2}$ of the reduction of the nitro group is shifted to more positive values in the presence of hydroxyl groups in the ortho position and benzoyl group meta.to the nitro group. It is known from the reduction of *o*-nitro phenol in aqueous medium (Astle and McConnel 1943) that the presence of the hydroxyl group in the ortho position facilitates the reduction of the nitro group. Whether the presence of the benzoyl group has any additional effect is to be investigated. It is seen from table 1 that the presence of the nitro group has no additional effect to that of the *p*-hydroxyl group on the reduction of the carbonyl group. This is possible due to the prior reduction of the nitro group to –NHOH. Analysis of the reduction of the nitro compounds will be dealt in a subsequent communication.

The cyclic voltammograms at the HMDE and at the GCE also show a single reduction step in the range of potentials studied. The E_p values at both the electrodes are found to be nearly the same and are slightly more negative than the $E_{1/2}$ values. The diffusion controlled nature of the reduction is inferred from the $i_p - v^{1/2}$ plots passing through the origin and the i_p values are proportional to the concentrations of the benzophenones. The reduction mechanisms at both the HMDE and the GCE thus seem to be the same. The ratios of the i_p values at the HMDE and the GCE are found to be in proportion to the ratios of their areas, with due corrections for the slightly different αn_a values. The D values are obtained from the $i_p/v^{1/2}$ versus C plots using the corresponding αn_a values (tables 2 & 3). The values are found to be a little lower than the polarographic values but the same trend is followed.

4.2 *Electrochemical kinetic parameters*

The standard rate constant for a totally irreversible process can be obtained from the analysis of the polarographic wave following the procedure suggested by Koutecky. Suzuki and Elving (1961) reported a formal rate constant of 10^{-19} at $E = 0$ V with respect to SCE for the reduction of benzophenone. It is easier to obtain the rate constants from linear sweep voltammetry. Sivakumar *et al* (1983) have reported $k^0_{f,h}$ values from the cyclic voltammetric results in a number of publications for various substituted benzophenones. The $k^0_{f,h}$ values vary from 10^{-16} to 10^{-35}. The relevance of these values was not discussed and no correlations were made.

The standard rate constant k_s for a totally irreversible process can be obtained from the following equation (Galus 1976):

$$E_p = E^0 - \frac{RT}{\alpha n_a F}\left(0{\cdot}78 - \ln k_s + \ln\left(\frac{\alpha n_a F D v}{RT}\right)^{1/2}\right), \qquad (2)$$

if $E°$ is known. Alternatively,

$$E_p = 1{\cdot}14\,\frac{RT}{\alpha n_a F} + \frac{RT}{\alpha n_a F}\ln\frac{k^0_{f,h}}{D^{1/2}} - \frac{RT}{2\alpha n_a F}\ln \alpha n_a \nu, \tag{3}$$

where $k^0_{f,h}$ is the rate constant at $E = 0$ V. The peak current i_p of a totally irreversible process is also related to the standard rate constant as follows (Nicholson and Shain 1964),

$$i_p = 0{\cdot}227\, nFA\, C^b_0 k_s \exp\left(\frac{-\alpha n_a F}{RT}\,(E_p - E_0)\right). \tag{4}$$

Accordingly, a plot of $\log i_p$ versus E_p will be linear with a slope of $(\alpha n_a F/2{\cdot}303\, RT)$ and hence if the standard potential E_0 is known, k_s can be calculated from the intercept. Since the standard potentials of benzophenones are not known in acetamide, the formal rate constants $k^0_{f,h}$ are evaluated at $E = 0$ V and are tabulated (tables 2 & 3). It may not be strictly correct to compare these $k^0_{f,h}$ values since the standard potentials are reported to vary by 100–200 mV depending on the substituents (Flaig *et al* 1968). However, since these are the first values to be reported in molten acetamide, we wish to draw attention to some important observations.

(1) Even when $\Delta E_{1/2}$ is positve, the $k^0_{f,h}$ value is much lower for the reduction of *p*-bromo benzophenone than that of benzophenone.

(2) The $\Delta E_{1/2}$ is negative for 2-hydroxy benzophenone but the rate constant is nearly the same as for benzophenone.

(3) The $E_{1/2}$ shift for 2-amino benzophenone is negative but the $k^0_{f,h}$ is higher than that of the benzophenone. It has been reported that even for *p*-amino derivative the $E_{1/2}$ does not fall in the Hammett plot (Zuman 1960).

(4) The $k^0_{f,h}$ values indicate that the reduction is faster at the glassy carbon electrode than at the HMDE.

4.3 *αn_a-values*

The αn_a values are generally reported from the difference in the peak potential and the half-peak potential values by the equation,

$$E_p - E_{p/2} = (1{\cdot}857\, RT/\alpha n_a F). \tag{5}$$

It is found that a 10% error in the αn_a value results from an error of 5 mV in the peak potential values. Hence the αn_a values are evaluated from the $(\log i_p - E_p)$ and $(E_p - \log \nu)$ plots and used in our calculations. The αn_a values are close to $0{\cdot}6 \pm 0{\cdot}1$ for the reduction at the mercury electrode except for 4-bromo, 2-hydroxy 5-methyl and 2-hydroxy 5-chloro derivatives. In the work of Zuman *et al*

mechanism of reduction at the HMDE may be the cause for the higher αn_a values. Since only a single reduction step is observed and if the mechanism followed is an EHEH one, then the $\alpha = 1$ is associated with the proton transfer as the rate determining step and $\alpha = 0{\cdot}5$ with the electron transfer as the rate determining step. It is more probable that $n_a = 2$ and $\alpha = 0{\cdot}5$ in the reduction of the three compounds. The proton transfer is generally accepted as the fast step (Zuman *et al* 1968). It is not clear at present as to why the substituents bring about this variation.

This investigation is being continued with a further series of substituted benzophenones, as well in N-methyl acetamide and dimethyl acetamide.

5. Conclusions

(1) Molten acetamide essentially functions like water.
(2) Substituent effects on the reduction of the carbonyl group follow the same trend as in aqueous and in aqueous-organic mixtures.
(3) The electrochemical reduction of the carbonyl group is faster on a glassy carbon surface.

Acknowledgement

The authors thank Dr K K Balasubramanian for helpful discussions.

References

Astle M J and McConnel W 1943 *J. Am. Chem. Soc.* **65** 35
Blazquez M, Rodriquex-Mellado J M and Ruiz J J 1985 *Electrochim. Acta* **30** 1527
Day R A, Milliken S R and Shults W D 1952 *J. Am. Chem. Soc.* **74** 2741
Elving P J and Leone J T 1958 *J. Am. Chem. Soc.* **80** 1021
Flaig W, Beutal Spacher H, Riemer H and Kalke E 1968 *Ann. Chem.* **719** 96
Galus Z 1976 *Fundamentals of electrochemical analysis* (Chichester: Ellis Harwood) p. 236
Given P H and Peover M E 1960 *J. Chem. Soc.* 385
Guiot S and Tremillon B 1968 *J. Electroanal. Chem.* **18** 261
Harry Letan Jr and Gropp A H 1953 *J. Phys. Chem.* **57** 965
Jaffe H H 1953 *Chem. Rev.* **53** 191
Lund H 1973 in *Organic electrochemistry* (ed.) M M Baizer (New York: Marcel Dekker) chapt. 7
Lunnazi L, Maccagnani G, Mazzanti C and Placucci G 1971 *J. Chem. Soc.* **B71** 162
Michielli R F and Elving P J 1968 *J. Am. Chem. Soc.* **90** 1989
Nadjo L and Saveant J M 1971 *J. Electroanal. Chem.* **33** 419
Nicholson R S and Shain I 1964 *Anal. Chem.* **36** 706
Perrin C L 1965 *Progress in physical organic chemistry* (eds) S G Cohen, A Streitwieser and R W Taft (New York: Interscience) Vol. 3, p. 221
Pfister G and Bonastre J 1965 *Bull. Soc. Chim. Fr.* 1993
Phani K L N 1984 *Electrochemical studies in molten acetamide* Ph.D. thesis, Indian Inst. Technol., Madras
Phani K L N and Narayan R 1985 *J. Electroanal. Chem.* **187** 187
Saveant J M and Nadjo L 1971 *J. Electroanal. Chem.* **30** 41
Saveant J M, Halla F M and Pinson J 1978 *J. Electroanal. Chem.* **89** 347
Saveant J M and Thiebault 1978 *J. Electroanal. Chem.* **89** 335
Sivakumar A and Jayarama Reddy S 1984 *Trans. Soc. Adv. Electrochem. Sci. Technol.* **19** 295

Sivakumar A, Jayarama Reddy S and Krishnan V R 1983a *Indian J. Chem.* **A22** 800
Sivakumar A, Jayarama Reddy S and Krishnan V R 1983b *J. Electrochem. Soc. India* **32** 129
Sivakumar A, Jayarama Reddy S and Krishnan V R 1984 *J. Electrochem. Soc. India* **33** 177
Suzuki M and Elving P J 1961 *J. Phys. Chem.* **65** 391
Tallant D R and Evans D H 1969 *Anal. Chem.* **41** 835
Wawzonek S and Gundersen A 1960 *J. Electrochem. Soc.* **107** 537
Zuman P 1960 *Collect. Czech. Chem. Commun.* **25** 3225
Zuman P 1968 *Collect. Czech. Chem. Commun.* **33** 2548
Zuman P, Barnes D and Ryvolova-Kejharova A 1968a *Discuss. Faraday. Soc.* **45** 202
Zuman P, Exner O, Rekker R F and Nauta T H 1968b *Collect. Czech. Chem. Commun.* **33** 3213

Proc. Indian Acad. Sci. (Chem. Sci.), Vol. 97, Nos 3 & 4, October 1986, pp. 417–430.
© Printed in India.

Cyclic voltammetric studies of dioxygen-bridged dinuclear cobalt(III) complexes[§]

S ILANGOVAN and P NATARAJAN*

Department of Inorganic Chemistry, School of Chemistry, University of Madras, Guindy Campus, Madras 600 025, India

Abstract. Cyclic voltammetric studies were carried out for dioxygen-bridged dinuclear cobalt(III) complexes using platinum electrodes at different values of pH and ionic strength. Reversible electrode reactions occur particularly for the dioxygen complexes $[(phen)_2Co(\mu\text{-}O_2,NH_2)Co(phen)_2]\ (ClO_4)_4 2H_2O$ and $[(bpy)_2Co(\mu\text{-}O_2,NH_2)Co(bpy)_2]\ (ClO_4)_4 \cdot H_2O$ with 1,10-phenanthroline (phen) and 2,2-bipyridine (bpy) as the non-bridging ligands. For complexes with ammonia (NH_3) ethylenediamine (en) as the terminal ligands, there is quasi-reversible electrode behaviour at pH <3 due to protonation of the peroxo complexes which subsequently undergo equilibration with isomeric forms. Such behaviour is well-marked for the peroxo complex $[(en)_2Co(\mu\text{-}O_2 NH_2)Co(en)_2](NO_3)_3$. The decaammine complex $[(NH_3)_5Co(\mu\text{-}O_2)Co(NH_3)_5](NO_3)_5$ shows only a cathodic peak due to intramolecular charge transfer decomposition in solution after reduction at the electrode. Diffusion coefficients for all the dioxygen complexes were determined from the plots of I_p vs. $\nu^{1/2}$.

Keywords. Cyclic voltammetric studies; dioxygen-bridged dinuclear Co(III) complexes; superoxo complexes; peroxo complexes; coordinated dioxygen systems.

1. Introduction

Redox behaviour of dioxygen molecule in aqueous solution at different values of pH has been studied in great detail (Sawyer and Valentine 1981). It is of immense interest to study the electrodic behaviour of coordinated dioxygen systems for understanding the mechanisms of oxygenation and related biological redox reactions (McLendon and Martell 1976; Jones *et al* 1979). Considerable attention has been paid recently to these dioxygen coordinated metal complexes, since vital biological functions such as oxygen transport and many enzymatic reactions take place involving oxygen in different oxidation states (Wilkins 1971; Hayaishi 1975). Although the existence of cobalt complexes coordinated to dioxygen has been known for a long time, no specific biological functions are attributed to these species (Sykes and Weil 1970; Lever and Gray 1978). Depending upon the ligands and the conditions of oxygenation, the cobalt(II) ion forms 1 : 1 or 1 : 2 oxygen metal complexes (Basolo *et al* 1975; Jones *et al* 1979). Complexes of these types have been isolated and characterized with reference to structure, spectra and reactivity (Sykes and Weil 1970; McLendon and Martell 1976; Lever and Gray 1978; Jones *et al* 1979). Structural investigation and ESR studies of these dioxygen

electron mainly resides in the superoxo group and the two cobalt atoms are equivalent (Sykes and Weil 1970; Lever and Gray 1978).

Electron transfer reactions of the superoxo complexes with a variety of one-electron reductants have been reported earlier and in all those reactions the redox reactions are known to occur at the dioxygen bridge and not at the cobalt centre (Sykes and Weil 1970; Sykes 1974; Lever and Gray 1975). Recently, electron transfer reactions of superoxo complexes with strong reducing agents such as excited $Ru(bpy)_3^{2+}$ and $Ru(phen)_3^{2+}$ ions (Chandrasekaran and Natarajan 1980, 1981), unstable metal ions (Natarajan and Raghavan 1980a), organic radicals (Natarajan and Raghavan 1981) and free superoxide ion (Natarajan and Raghavan 1980b) have been reported and in all those reactions the products are the corresponding peroxo complexes. Redox process of these dioxygen complexes with Fe^{2+}, $Co(bpy)_3^{2+}$, $Co(phen)_3^{2+}$, $Fe(phen)_3^{2+}$ and the peroxo complex, $[(en)_2Co(\mu\text{-}O_2, NH_2)Co(en)_2]^{3+}$ occur by an outer-sphere electron transfer mechanism (Sykes 1974; Chandrasekaran and Natarajan 1980). Recently, attempts have been made to calculate the self exchange rate constants for the superoxo/peroxo couples using the Marcus relationship (Michelson *et al* 1977; McLendon and Mooney 1980; Chandrasekaran and Natarajan 1981). In order to calculate the above self exchange rate constants, a systematic study of the thermodynamics of interconversion of μ-superoxo and μ-peroxo complexes in terms of fairly accurate reduction potentials, (E values vs. normal hydrogen electrode) is required. Vleck (1960) and Hanslik and Vleck (1973) reported polarographic reduction of μ-superoxo complexes while Martell and co-workers (Harris *et al* 1980) employed cyclic voltammetry to determine the peak potentials for the oxidation of the peroxo complexes to the corresponding superoxo complexes. The observed redox potentials are interpreted in terms of metal-dioxygen bonding and the concept of charge-transfer from cobalt(II) to the dioxygen ligand. McLendon and Mooney (1980) and later Richens and Sykes (1982) have studied the electrodic reduction of some of the superoxo complexes using Pt electrodes in aqueous media. In the present investigation detailed cyclic voltammetric studies have been carried out for both the superoxo and the peroxo complexes by changing the ionic strength and pH of the solution. Cyclic voltammetry provides redox potentials as well as more information about the mechanistic details of electrode reactions of these complexes.

2. Experimental

Cyclic voltammetric studies were carried out for the following μ-superoxo and μ-peroxo complexes.

1. $[(NH_3)_5Co(\mu\text{-}O_2)Co(NH_3)_5](NO_3)_5$
2. $[(NH_3)_4Co(\mu\text{-}O_2, NH_2)Co(NH_3)_4](NO_3)_4$

7. $[(phen)_2Co(\mu\text{-}O_2,\ NH_2)Co(phen)_2](ClO_4)_3 \cdot H_2O$
8. $[(bpy)_2Co(\mu\text{-}O_2,\ NH_2)Co(bpy)_2](ClO_4)_3 \cdot 2H_2O$

The superoxo complexes 1–3 were prepared using the literature method (Davies *et al* 1972). Complexes 4–8 were prepared using the methods already reported with modifications (Mori and Weil 1967, 1968; Sasaki and Fujita 1969, 1970; Davies and Sykes 1971; Gileadi *et al* 1975). The dioxygen complexes were characterized by UV and visible spectra after recrystalization. A Hitachi Model 320 UV-visible spectrophotometer was used for spectral measurements. Cyclic voltammograms were run using PAR model 173 potentiostat/galvanostat. A PAR model 175 universal programmer was used to generate the cyclic triangular wave. Current output was monitored using PAR model 176 current follower. A Perkin–Elmer Hitachi 057 *X-Y* recorder was used for recording the cyclic voltammograms. The electrochemical cell was a three-electrode cell, cylindrical in shape with two sockets in which were inserted the working electrode and the counter electrode. The working electrode and the counter electrodes were platinum foils of one cm^2 area. A saturated calomel electrode placed in the side arm was the reference electrode and was connected to the potentiostat through a electrometer probe. Electrolytic contact was made by a luggin capillary projecting towards the working electrode. The platinum electrodes were cleaned and electrochemically treated prior to running a cyclic voltammogram. The condition of the working electrode was ascertained by running a cyclic voltammogram in 0·5 M H_2SO_4 in the range +1·3 and −0·2 V vs. SCE at a potential scan rate of 50 mV/sec and compared with that reported in the literature (Sawyer and Roberts 1974; Gileadi *et al* 1975). The reagents hydrochloric acid, nitric acid, sulphuric acid, sodium nitrate, sodium sulphate and sodium perchlorate were AnalaR grade supplied by BDH or E Merck.

Cyclic voltammograms were run in aqueous media at 25°C. The solutions for the cyclic voltammetric experiments contained usually 1×10^{-3} M of the dioxygen-bridged dicobalt(III) complex in 1×10^{-3} M acid and 0·1 M supporting electrolyte. The acids used were perchloric acid, sulphuric acid, nitric acid and hydrochloric acid, and the supporting electrolytes were sodium perchlorate, sodium sulphate, sodium nitrate and potassium chloride, respectively. Solutions were deoxygenated by passing a stream of oxygen-free N_2 gas through the solution kept in the cell for 30 minutes prior to the potential sweep. Potential sweeps were carried out in the cathodic direction for superoxo complexes and in the anodic direction for peroxo complexes at scan rates (ν) 5 to 200 mV/sec. Experiments were carried out by varying the acidity and ionic strength for all the dioxygen complexes. Measured reduction potentials (E_{ob}) were the mean values of the anodic (E_{pa}) and cathodic (E_{pc}) peak potentials at a given scan rate. The potential values mentioned hereafter are with reference to the normal hydrogen electrode (NHE) at 25°C.

3. Results

μ-Superoxo complexes are stable in solution with pH < 3 while the μ-peroxo complexes are stable in neutral or alkaline solution. In the case of μ-peroxo

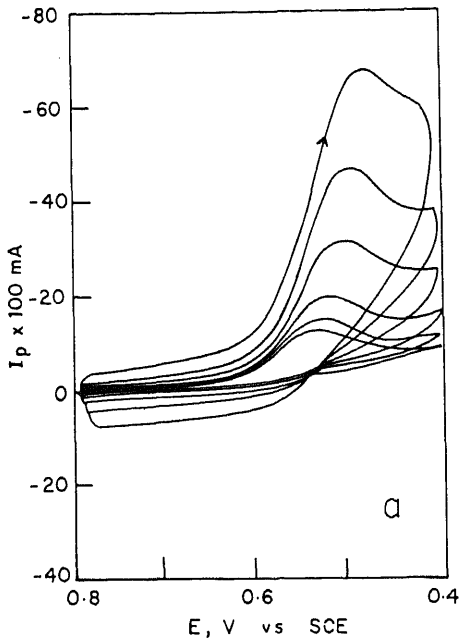
-80
-60
-40
-20
0
-20
-40
I_p x 100 mA
a
0·8
0·6
0·4
E, V vs SCE

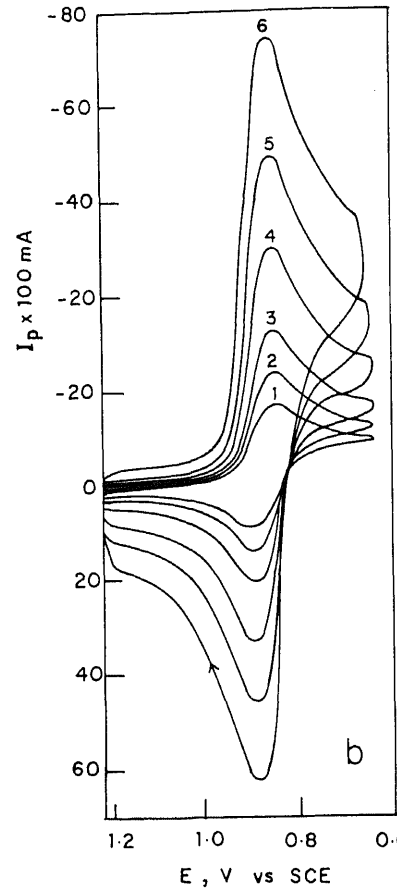
-80
-60
-40
-20
-20
0
20
40
60
I_p x 100 mA
6
5
4
3
2
1
b
1·2
1·0
0·8
0·6
E, V vs SCE

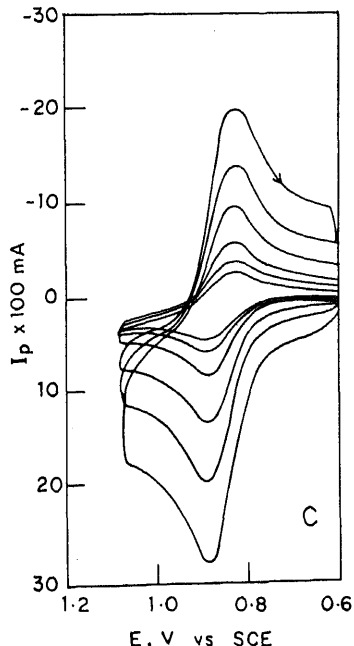
-30
-20
-10
0
10
20
30
I_p x 100 mA
c
1·2
1·0
0·8
0·6
E, V vs SCE

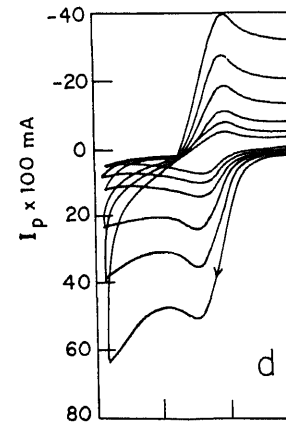
-40
-20
0
20
40
60
80
I_p x 100 mA
d

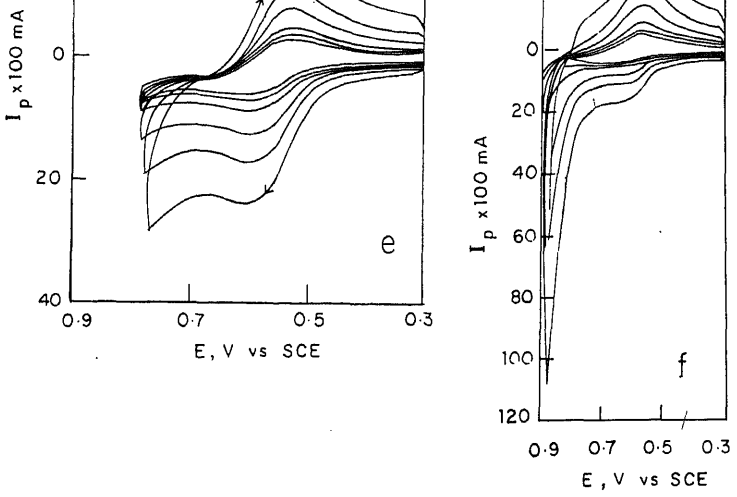

Figure 1. Cyclic voltammograms of dioxygen-bridged dicobalt(III) complexes at scan rates 5, 10, 20, 50, 100 and 200 mV/sec. (**a**) $[(NH_3)_5Co(\mu\text{-}O_2)Co(NH_3)_5](NO_3)_5$ in 0·05 M $HClO_4$; [complex] = $1{\cdot}185\times10^{-3}$ M; [$NaClO_4$] = 0·1 M. (**b**) $[(bpy)_2Co(\mu\text{-}O_2, NH_2)Co(bpy)_2](ClO_4)_4\cdot H_2O$ in 0·2 M HNO_3; [complex] = $2{\cdot}009\times10^{-3}$ M; [KNO_3] = 0·1 M. (**c**) $[(bpy)_2Co(\mu\text{-}O_2, NH_2)Co(bpy)_2](ClO_4)_3\cdot 2H_2O$ in 0·01 M H_2SO_4; [complex] = 5×10^{-4} M; [Na_2SO_4] = 0·1 M. (**d**) $[(en)_2Co(\mu\text{-}O_2, NH_2)Co(en)_2](NO_3)_3$ in 1×10^{-3} M $HClO_4$; [complex] = $1{\cdot}007\times10^{-3}$ M; [$NaClO_4$] = 0·1 M. (**e**) $[(en)_2Co(\mu\text{-}O_2, NH_2)Co(en)_2](NO_3)_3$ in 0·1 M $HClO_4$; [complex] = $9{\cdot}3\times10^{-4}$ M; [$NaClO_4$] = 0·1 M. (**f**) $[(en)_2Co(\mu\text{-}O_2, NH_2)Co(en)_2](NO_3)_3$ in 1·0 M $HClO_4$; [complex] = $9{\cdot}83\times10^{-4}$ M; [$NaClO_4$] = 0·1 M.

omplexes (Sykes and Weil 1970; Lever and Gray 1978). The μ-peroxo complex 6 n acidic solutions undergoes isomerization reaction after fast protonation and this rotonation equilibrium has been studied in considerable detail (Sykes and Weil 970; Lever and Gray 1978). There is no observable decomposition of the dioxygen omplexes during the course of the study in the media in which cyclic voltammetric xperiments were carried out as is determined from the UV and visible absorption pectra. Typical cyclic voltammograms of the dioxygen complexes are given in igure 1. The values of peak potentials (E_p), peak currents (I_p) and separation in eak potentials (E_p) were measured in all cases from the cyclic voltammograms ecorded at different potential sweep rates (Nicholson and Shain 1964; Sawyer and Roberts 1974) (table 1). For a reversible electrode couple, the peak current is elated to the potential scan rate and the concentration of the complex by the xpression (Nicholson and Shain 1964; Sawyer and Roberts 1974; Gileadi *et al* 975),

$$|I_p| = 2{\cdot}72\times10^5 n^{3/2} D^{1/2} C_0 \nu^{1/2},$$

where I_p = peak current in amperes; D = diffusion coefficient in cm^2/sec; = number of electrons involved in the electrode process, C_0 = concentration of he complex in moles/litre and ν = potential scan rate in volts/sec. Plots of I_{pc} or I_{pa}

Table 1a. Peak potentials and peak currents at different scan rates for the complex $[(NH_3)_5Co(\mu\text{-}O_2)Co(NH_3)_5](NO_3)_5$.

ν(mV/sec)	E_p(V) vs. NHE	$I_p(\mu$ A)	$I_p/\nu^{1/2}$
5	0·788	95	42·5
10	0·778	130	41·1
20	0·768	180	40·3
50	0·758	280	39·6
100	0·747	410	41·0
200	0·735	560	39·6

$[HClO_4] = 0{\cdot}05$ M; $[NaClO_4] = 0{\cdot}1$ M; [Complex] $= 1{\cdot}185 \times 10^{-3}$ M; sweep range $= +0{\cdot}8$ to $+0{\cdot}4$ V.

Table 1b. Peak potentials, peak currents and difference in peak potentials at different scan rates for the complex $[(phen)_2Co(\mu\text{-}O_2, NH_2)Co(phen)_2](ClO_{44})_4 \cdot H_2O$.

ν(mV/sec)	E_p(V) vs. NHE	ΔE_p(mV)	$I_{pa}(\mu$ A)	$I_{pc}(\mu$ A)	$I_{pa}/\nu^{1/2}$	$I_{pc}/\nu^{1/2}$	I_{pa}/I_{pc}
5	1·073	55	70	70	31·25	31·25	1·00
10	1·073	55	100	100	31·65	31·65	1·00
20	1·073	55	130	130	29·08	29·08	1·00
50	1·073	55	205	220	29·00	31·12	0·95
100	1·073	55	290	320	29·00	32·00	0·91
200	1·073	55	370	430	26·17	30·41	0·86

$[H_2SO_4] = 0{\cdot}1$ M; $[Na_2SO_4] = 0{\cdot}1$ M; [complex] $= 1{\cdot}014 \times 10^{-3}$ M; sweep rate $= +1{\cdot}2$ to $+0{\cdot}6$ V.

vs. $\nu^{1/2}$ are linear for complexes 2 to 8 in weakly acidic solutions (figure 2) and from the slopes of the above plots, the values of the diffusion coefficients were calculated. The values of peak potentials (E_p), separation of peak potentials (ΔE_p) and the values of diffusion coefficient (D) are tabulated (tables 2a–e) for complexes 2 to 8 at different acidities and ionic strengths of the medium. Redox potentials of the superoxo-bridged complexes at pH = 1 or 3 determined in the present investigation are shown in table 3.

4. Discussion

The peroxo ion having two electrons in the π_{2p} antibonding level is the least stable among the dioxygen species. In aprotic media, the peroxide dianion is a highly unstable species. When protons or metal ions stabilize the peroxide dianion the redox potentials are known to be altered (Sawyer and Valentine 1981). When the peroxide ion is coordinated to a metal ion, the stability increases as there is

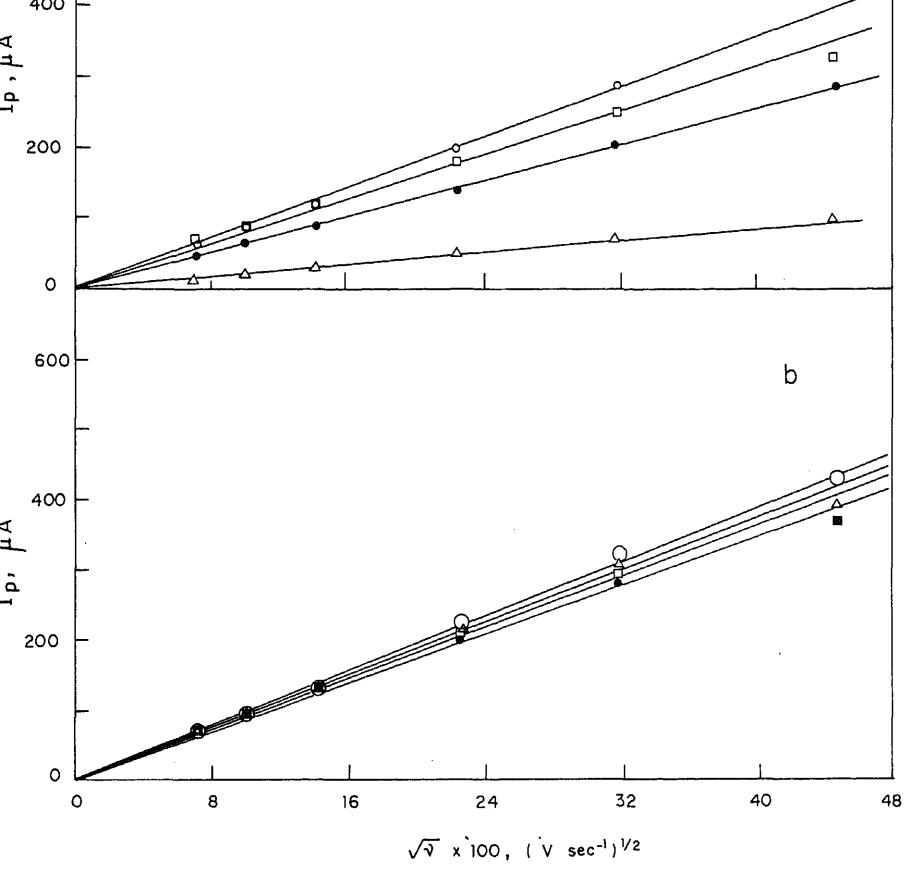

Figure 2a. I_p vs. $\nu^{1/2}$ plots for the complex $[(en)_2Co(\mu\text{-}O_2, NH_2)Co(en)_2](NO_3)_3$. (i) [complex] = $1{\cdot}007\times10^{-3}$ M; $[HClO_4] = 1\times10^{-3}$ M; $[NaClO_4] = 0{\cdot}1$ M; ○ – I_{pa} vs. $\nu^{1/2}$; □ – I_{pc} vs. $\nu^{1/2}$. (ii) [complex] = $0{\cdot}983\times10^{-3}$ M; $[HClO_4] = 1{\cdot}0$ M; $[NaClO_4] = 0{\cdot}1$ M; △ – I_{pa} vs. $\nu^{1/2}$. (iii) [complex] = $0{\cdot}930\times10^{-3}$ M in 75% CH_3CN; [NaCl] = 0·1 M; ● – I_{pa} vs. $\nu^{1/2}$. (**b**) (i) $[(phen)_2Co(\mu\text{-}O_2, NH_2)Co(phen)_2](ClO_4)_4$; [complex] = $1{\cdot}005\times10^{-3}$ M; $[H_2SO_4] = 0{\cdot}1$ M; $[Na_2SO_4] = 0{\cdot}1$ M; ○ – I_{pc} vs. $\nu^{1/2}$; □ – I_{pa} – vs. $\nu^{1/2}$. (ii) $[(phen)_2Co(\mu\text{-}O_2, NH_2)Co(phen)_2](ClO_4)_3$; [complex] = $1{\cdot}002\times10^{-3}$ M; $[HNO_3] = 0{\cdot}1$ M; $[KNO_3] = 0{\cdot}1$ M; △ – I_{pa} vs. $\nu^{1/2}$; ● – I_{pc} vs. $\nu^{1/2}$.

The superoxo complexes 2 to 5 and the peroxo complexes 6, 7 and 8 show versible one-electron transfer process at the electrode. The apparent deviation om the reversibility of the superoxo complexes 2, 3 and 6 at higher acidity is xplained on the basis of the protonation of the peroxo species in homogeneous olution. The absence of anodic peak for the ammine complex 1 in 0·05 M $HClO_4$ an be attributed either to the slow heterogeneous electron transfer of the reduced

Table 2a. Peak potentials, difference in peak potentials and diffusion coefficients for the complex $[(en)_2Co(\mu\text{-}O_2, NH_2)Co(en)_2](NO_3)_4$ at different $[H^+]$ and ionic strength.

[Medium] (M)				
H^+	Supporting electrolyte	E_p(V) vs. NHE	ΔE_p(mV)	$D\times10^5$ (cm^2/sec)
$HClO_4$	$NaClO_4$			
0·0005	0·1	0·770	63	1·868
0·0010	0·1	0·773	63	1·668
0·0050	0·1	0·768	66	1·512
0·0100	0·1	0·773	71	2·164
0·5000	0·1	0·810	73	2·138
0·0010	0·05	0·778	65	1·515
0·0010	0·20	0·766	62	1·515
0·0010	0·40	0·763	65	1·415
H_2SO_4	Na_2SO_4			
0·0005	0·1	0·708	60	1·719
0·0010	0·1	0·713	62	1·714
0·0025	0·1	0·708	70	1·647
0·0010	0·05	0·703	65	1·450
0·0010	0·4	0·683	65	1·258

$\nu = 50$ mV/sec; [complex] $= 1\times10^{-3}$ M; sweep range $= +0{\cdot}8$ to $+0{\cdot}35$ V.

Table 2b. Peak potentials, difference in peak potentials and diffusion coefficients for the complex $[(en)_2Co(\mu\text{-}O_2, NH_2)Co(en)_2](NO_3)_3$ at different $[H^+]$.

$[HClO_4]$(M)	E_p(V) vs. NHE	ΔE_p(mV)	$D\times10^6$ (cm^2/sec)
0·001	0·774	70	10·030
0·100	0·778	60	2·238
1·000	0·818	56	0·715
*75% CH_3CN	0·773	60	6·053

$\nu = 50$ mV/sec; [complex] $= 1\times10^{-3}$ M; sweep range $= +0{\cdot}3$ V to $+0{\cdot}9$ V;
* [complex] $= 9{\cdot}30\times10^{-4}$ M; supporting electrolyte $= 0{\cdot}1$ M NaCl.

Table 2c. Peak potentials, difference in peak potentials and diffusion coefficients for the complex $[(phen)_2Co(\mu\text{-}O_2, NH_2)Co(phen)_2](ClO_4)_3 \cdot H_2O$ at different $[H^+]$ and ionic strength.

[Medium] (M)				
H^+	Supporting electrolyte	E_p(V) vs. NHE	ΔE_p(mV)	$D \times 10^5$ (cm^2/sec)
HNO_3	KNO_3			
0·001	0·1	1·088	59	1·420
0·010	0·1	1·086	58	1·278
0·110	0·1	1·075	60	1·147
0·210	—	1·060	60	1·188
0·410	—	1·040	59	1·226
1·100	—	1·010	65	1·352
H_2SO_4	Na_2SO_4			
0·001	0·1	1·088	57	1·242
0·020	0·1	1·083	57	1·117
0·120	0·1	1·053	57	1·147
0·010	—	1·108	60	1·114
0·020	—	1·088	60	1·117
0·110	—	1·063	59	1·077
0·210	—	1·058	55	1·147
0·410	—	1·043	58	1·077
1·000	—	1·008	62	0·959

$\nu = 50$ mV/sec; [complex] $= 5 \times 10^{-4}$ M; sweep range = 0·6 to 1·1 V.

Table 2d. Peak potentials, difference in peak potentials a diffusion coefficients for the complex $[(bpy)_2Co(\mu\text{-}O_2, NH_2)(bpy)_2](ClO_4)$. H_2O at different $[H^+]$ and ionic strength.

[Medium] (M)				
H^+	Supporting electrolyte	E_p(V) vs. NHE	ΔE_p(mV)	$D \times 10^5$ (cm^2/sec)
HNO_3	KNO_3			
0·1	0·1	1·036	62	1·511
0·2	0·1	1·050	64	1·549
0·3	0·1	1·043	62	1·563
0·4	0·1	1·036	65	1·541
1·0	0·1	1·033	62	1·518
H_2SO_4	Na_2SO_4			
0·050	0·1	1·078	55	1·376
0·100	0·1	1·068	55	1·277
0·200	0·1	1·058	60	1·352
0·300	0·1	1·048	60	1·300
0·400	0·1	1·028	60	1·222
1·000	0·1	1·003	60	1·145
0·1	—	1·076	58	1·274
0·1	0·02	1·076	58	1·196
0·1	0·50	1·068	55	1·088
0·1	1·00	1·040	58	0·927

$\nu = 50$ mV/sec; [complex] $= 1 \times 10^{-3}$ M; sweep range = +1·2 0·6 V.

Table 2e. Peak potentials, difference in peak potentials and diffusion coefficients for the complex $[(bpy)_2Co(\mu\text{-}O_2,NH_2)Co(bpy)_2](ClO_4)_3{\cdot}2H_2O$ at different $[H^+]$ and ionic strength.

[Medium] (M)				
H^+	Supporting electrolyte	E_p(V) vs. NHE	ΔE_p(mV)	$D\times10^5$ (cm^2/sec)
HNO_3	KNO_3			
0·001	0·1	1·083	55	1·183
0·010	0·1	1·078	62	1·374
0·200	0·1	1·060	60	1·398
0·400	—	1·033	62	1·219
H_2SO_4	Na_2SO_4			
0·001	0·1	1·081	58	1·293
0·010	0·1	1·078	56	1·227
0·010	—	1·123	55	1·188
0·100	—	1·081	58	1·117
0·200	—	1·061	60	1·250
0·400	—	1·045	60	1·156

v = 50 mV/sec; [complex] = 1×10^{-3} M; sweep range = +0·6 to +1·1 V

Table 3. Redox potentials of μ-superoxo bridged dinuclear cobalt(III) complexes.

Complex	pH	E(V) vs. NHE
1	1	0·760±0·005
2	3	0·763±0·005
3	3	0·800±0·010
3	3	0·725*±0·010
4	1	1·100±0·010
5	1	1·095±0·010

* In solution containing SO_4^{2-} ions.

species at the electrode or to a quasi-reversible reaction; chemical reaction followed by electrodic reduction of the superoxo complex. Decomposition of the superoxo complex 1 in aqueous acidic medium has also been reported in the reduction of the complex using Fe^{2+} as the reductant. In a similar way for complex 1 there is fast protonation of the peroxo complex formed at the electrode in the reduction process which subsequently undergoes charge transfer decomposition as follows.

$$[(NH_3)_5Co(\mu\text{-}O_2)Co(NH_3)_5]^{5+} \xrightarrow[\text{at electrode}]{+e,\ H^+} 2Co^{2+} + 10NH_4^+ + O_2$$

Barnartt and Charles (1962) observed quantitative evolution of oxygen when this complex underwent reduction at platinum electrode. Unlike the above mono-

show reversible behaviour at the electrode under the same conditions (Jebaraj 1982). This indicates that the occurrence of the anodic peaks for the monobridged superoxo complexes depends on the stability of the protonated peroxo complexes towards intramolecular charge transfer decomposition.

μ-superoxo and μ-peroxo complexes with non-bridging ligands NH_3, en, bpy and phen in weakly acidic solution, ($[H^+] < 0{\cdot}1$ M) show reversible behaviour at electrodes. For the above systems (a) $I_p/\nu^{1/2}$ is constant, (b) I_{pa}/I_{pc} is constant at all scan rates and (c) E_p is 58 ± 2 mV ($n = 1$) characteristic of reversible redox systems. On increasing the acidity there is an anodic shift of peak potentials (E_p) particularly for the dibridged superoxo complexes 2 and 3 with NH_3 and (en) ligands, while increase of ionic strength with salts produces a slight cathodic shift of peak potentials. The observed increase in E_p (anodic shift) with increase in $[H^+]$ indicates that the peroxo analogue of 2 and 3 formed on reduction protonates readily in solution. The protonated species of the μ-peroxo complexes exist in equilibrium after isomerization as follows (Mori and Weil 1967):

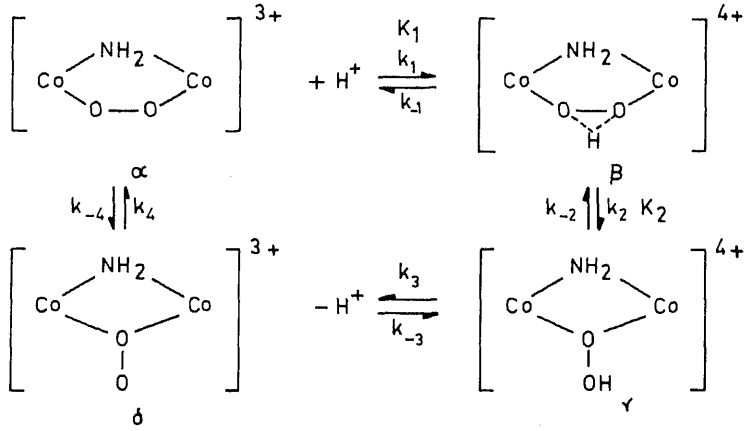

Chart 1.

Sykes and Weil (1970) studied the above equilibrium for the complex 6. The electrode phenomena of these complexes approach that of a quasi-reversible one where there is electrode reaction followed by fast homogeneous reaction when $[H^+]$ is increased. Once the μ-superoxo complex undergoes reduction at the electrode there is fast protonation of the peroxo species in solution at the electrode. The species which undergo oxidation at the electrode are not only the unprotonated form of the peroxo complex but also the isomeric forms of the protonated peroxo complex. The concentration of each species that undergoes oxidation at the electrode surface is again determined by the equilibrium constants K_1, K_2 and $[H^+]$. Richens and Sykes (1982) who observed such electrodic behaviour for these complexes on varying $[H^+]$ proposed the following correlation for the observed potentials and the formal potential

$$E_{obs} = E^0 + \frac{0{\cdot}059}{} \log\{1 + K_1(1 + K_2)[H^+]\}$$

where K_1 and K_2 are the equilibrium constants. For the complex 2, on increase of $[H^+]$ from 0·001 M to 0·5 M using $HClO_4$, the observed potential shifts anodically from 0·763 to 0·820 V. While keeping the $[H^+]$ at 1×10^{-3} M, increase of ionic strength using ClO_4^- or NO_3^- results in a small shift in E_p cathodically (table 2). In HCl medium also this complex shows redox potentials of 0·758 and 0·853 V at $[H^+]=0{\cdot}001$ M and 1·0 M, respectively, while in 1·0 M NaCl it is 0·723 V. In a similar fashion, the complex 3 shows $0{\cdot}80\pm0{\cdot}01$ V as the reduction potential in a solution at pH = 3 ($HClO_4$ or HCl) whereas Richens and Sykes (1982) report a value of 0·863 V. The peroxo analogue of complex 6 also shows a value of 0·800 V in 1×10^{-3} M $HClO_4$ and also in 90% acetonitrile (0·1 M NaCl supporting electrolyte). However, the superoxo complex 3 in 1×10^{-3} M H_2SO_4 undergoes reduction at 0·725 V which is 75 mV more cathodic than that observed in 1×10^{-3} M HNO_3 or $HClO_4$. This is presumably due to the ion-pair formation between the superoxo cation and the sulphate anion. The ion-pair then undergoes reduction at a potential more cathodic than the free superoxo ion. This type of cathodic shift has also been found for the peroxo complex 6 in acetonitrile medium when using Na_2SO_4 as the supporting electrolyte.

Although the plot of I_p vs. $\nu^{1/2}$ is linear for the peroxo complex 6, when $[H^+]$ is varied from 1×10^{-3} to 1·0 M, it has been observed that the peak current values (I_p) decrease with $[H^+]$. Consequently, there is apparent decrease in the value of the diffusion coefficient, calculated from the slope of I_p vs. $\nu^{1/2}$ plot for $[H^+]$ ranging from 1×10^{-3} to 1·0 M. Such a change in the diffusion coefficients is not seen with the superoxo complexes on varying $[H^+]$. This implies that the concentration (C_0) used in the calculation of D from the slope ($2{\cdot}72\times10^5 n^{3/2}AD^{1/2}C_0$) is not the actual concentration of peroxo ions, which are electroactive, and the actual concentration of the electroactive species is slightly less than the concentration of the peroxo complex (C_0) used in the calculation. Such a decrease in I_p with $[H^+]$ is expected for this complex since with increase in $[H^+]$, there will be a shift in the protonation equilibrium towards the γ-form of the peroxo complex. It has been reported earlier that the γ-form of the peroxo complex does not undergo oxidation with Ce^{4+} or $Fe(phen)_3^{3+}$ readily unlike the α-form (Mori and Weil 1967). The γ-form of the peroxo complex is also expected to behave in a similar way at the electrode. The diffusion coefficient values at 1×10^{-3} M and 1·0 M $[H^+]$ indicate that only 20% of the peroxo complex is electroactive form when $[H^+]=1{\cdot}0$ M.

Unlike the complexes 2, 3 and 6, the complexes with non-bridging ligands bpy and phen (complexes 4, 5, 7 and 8) show quite reversible electrodic behaviour in both HNO_3 and H_2SO_4 media. There is no observable anodic shift of the peak potentials on varying $[H^+]$. On the other hand, there is a small cathodic shift of peak potentials on increasing the acidity or ionic strength (table 2). Further, there is no decrease in peak current with increase in $[H^+]$ for the peroxo complex 7 and 8. The observed electrodic behaviour is understood to be due to the absence of protonation in the peroxo complexes 7 and 8.

There is no change in reduction potentials (E) of the dioxygen complexes to start with in either the superoxo complex or its analogue. Reduction potential (E) for

been known for mononuclear cobalt(III) complexes on changing the ligands from (phen) to CN^-, the potentials are $Co(phen)_3^{3+/2+} = 0{\cdot}37$ (Pryzystas and Sutin 1973); $Co(bpy)_3^{3+/2+} = 0{\cdot}37$ (Paglia and Sironi 1957); $Co(en)_3^{3+/2+} = 0{\cdot}18$ (Kim and Rock 1969); $Co(NH_3)_6^{3+/2+} = 0{\cdot}108$; $Co(CN)_5(H_2O)^{2-/3-} = -0{\cdot}43$ V. The ligands which stabilize the cobalt(II) complex for oxidation have higher redox potentials. Thus the redox potentials of cobalt(III) complexes increase when the degree of chelation of amine ligands increases. In superoxo/peroxo complexes also, the terminal ligands which induce electron withdrawal from the O_2 bridge stabilize the bridge for oxidation. The dioxygen complexes with chelates (bpy) or (phen) with delocalization of O_2^- electrons in the molecular orbitals of the ligands have higher potential than the complexes with terminal ligands (en) and NH_3.

Acknowledgement

The investigations reported in this paper are supported by funds provided by the Department of Science and Technology.

References

Barnartt S and Charles R G 1962 *J. Electrochem. Soc.* **109** 333
Basolo F, Hoffman B M and Ibers J A 1975 *Acc. Chem. Res.* **8** 384
Chandrasekaran K and Natarajan P 1980 *Inorg. Chem.* **19** 174
Chandrasekaran K and Natarajan P 1981 *J. Chem. Soc. Dalton Trans.* 478
Davies R, Mori M, Sykes A G and Weil J A 1972 *Inorg. Synth.* **12** 197
Davies K M and Sykes A G 1971a *J. Chem. Soc. A* 1414
Davies K M and Sykes A G 1971b *J. Chem. Soc. A* 1418
Duffy D L, House D A and Weil J A 1969 *J. Inorg. Nucl. Chem.* **31** 205
Gileadi E, Kirowa-Eishner E and Penciner J 1975 in *Interfacial electrochemistry, an experimental approach* (London: Addison Wesley)
Hanslik J and Vleck A A 1973 *Collect. Czech. Chem. Commun.* **38** 957
Harris W R, McLendon G, Martell A E, Bess R C and Mason M 1980 *Inorg. Chem.* **19** 1
Hayaishi O 1975 *Chemical models and mechanisms for oxygenases in molecular mechanisms of oxygen activation* (New York: Academic Press)
Jebaraj J C J 1982 M. Phil. Dissert., University of Madras
Jones R D, Summerville D A and Basolo F 1979 *Chem. Rev.* **79** 139
Kim J J and Rock P A 1969 *Inorg. Chem.* **8** 563
Lever A B P and Gray H B 1978 *Acc. Chem. Res.* **11** 348
McLendon G and Martell A E 1976 *Coord. Chem. Rev.* **19** 1
McLendon G and Mooney W F 1980 *Inorg. Chem.* **19** 12
Michelson A M, McCord J M and Frodovich I 1977 *Superoxide and superoxide dismutases* (London: Academic Press)
Mori M and Weil J A 1967 *J. Am. Chem. Soc.* **89** 3732
Mori M and Weil J A 1968 *J. Am. Chem. Soc.* **90** 615
Natarajan P and Raghavan N V 1980a *J. Chem. Soc., Chem. Commun.* 268
Natarajan P and Raghavan N V 1980b *J. Am. Chem. Soc.* **102** 4518
Natarajan P and Raghavan N V 1981 *J. Phys. Chem.* **85** 188
Nicholson R S and Shain I 1964 *Anal. Chem.* **36** 706
Paglia E and Sironi C 1957 *Gazz. Chim. Ital.* **81** 1125
Pryzystas T J and Sutin N 1973 *J. Am. Chem. Soc.* **95** 5545

Sasaki Y and Fujita J 1969 *Bull. Chem. Soc. Jpn.* **42** 2089
Sasaki Y and Fujita J 1970 *Bull. Chem. Soc. Jpn.* **43** 3462
Sawyer D T and Roberts J L Jr 1974 *Experimental electrochemistry for chemists* (New York: Wiley Interscience)
Sawyer D T and Valentine J S 1981 *Acc. Chem. Res.* **14** 393
Sykes A G 1974 *Chem. Br.* **10** 170
Sykes A G and Weil J A 1970 *Progr. Inorg. Chem.* **13** 1
Vleck A A 1960 *Collect. Czech. Chem. Commun.* **25** 3036
Vleck A A 1963 *Progr. Inorg. Chem.* **5** 211
Wilkins R G 1971 *Adv. Chem. Ser.* **100** 111

The translocation of cobalt dicarbollide anions across a lipid bilayer membrane: the effect of solution resistance[§]

ROBERT J ATWELL Jr, RAMAMURTHI SRIDHARAN and ROBERT DE LEVIE*

Chemistry Department, Georgetown University, Washington DC 20057, USA

Abstract. The distorted current transients obtained with potential step measurements of cobalt dicarbollide translocation through a lipid bilayer membrane can be understood quantitatively in terms of the effect of series solution resistance.

Keywords. Cobalt dicarbollide; lipid bilayer membrane; ion translocation; IR correction.

1. Introduction

Electrochemistry is an old discipline, tracing its origins to the experiments of Galvani at the end of the 18th century. Although it has, at various times, branched out into other areas, such as the study of electrolyte solutions and that of colloids, its main focus has traditionally been on the interfacial charge transfer, especially at the metal-solution boundary.

Recently, as much more has become known about the bioelectrochemical phenomena studied by Galvani, it has become clear that these, too, involve interfacial charge transfer. The main distinguishing feature is that, in the nervous system, electricity is carried by ions rather than by metal electrons. Consequently, bioelectrochemical charge transfer is predominantly linked to the passage of ions through membranes (which act as ion permeation barriers) and usually lacks the redox processes typically accompanying charge transfer at the metal-solution interface. However, having recognized this major difference, one is often struck by the remaining similarities, as will be illustrated in the present communication.

A lipid bilayer is a very thin, non-polar region of space interposed between two aqueous solutions. Because of its low dielectric permittivity, some forty times smaller than that of the surrounding water, the Born energy (Born 1920) required to bring an ion from an aqueous solution into a lipid bilayer membrane is quite high. Consequently, lipid bilayers are very efficient barriers to ion transport and are used, in living organisms, to delineate the boundaries between cells or organelles and their surroundings.

Boundary crossing is, of course, possible, provided that it can be controlled. The major mechanism for such controlled ion permeation is through ion "channels", i.e., protein-lined pores which allow ion flow, and which can be opened and closed with chemical or electrical signals. Other ion transport mechanisms involve so-called ion "carriers" and "pumps". Here we will consider an example of a small

---

[§] Dedicated to Prof. K S G Doss on his eightieth birthday

group of ions which can breach the ion permeability barrier without external assistance, because they are sufficiently large, and have enough hydrophobic interaction with the membrane interior, to overcome the Born barrier.

The simplest electrostatic model of a lipid bilayer membrane is that of a plane-parallel slab of material of low dielectric permittivity, interposed between two aqueous solutions. In such a model, the Born energy changes abruptly at the membrane-water interfaces. However, because of the extreme thinness of a lipid bilayer, of the order of 3 nm, an ion in the membrane is never more than about 15 Å away from an aqueous phase. Such ions are, therefore, still subject to image forces which, as it were, let it sense the proximity of the more polar phase. More realistic electrostatic models, then, must include such image forces (Neumcke and Läuger 1969; Parsegian 1969). If one also takes into account hydrophobic interactions, then a model emerges (Ketterer *et al* 1971) which includes the possibility of ionic adsorption in the membrane close to the membrane-water interfaces, where the (short-range) hydrophobic attraction is already effective while the (longer-range) image forces still attenuate the Born repulsion. In general, it is found that lipophilic anions indeed exhibit such adsorption while lipophilic cations do not; the latter apparently are kept away from the interface by the dipole potential (Liberman and Topaly 1969; Haydon and Myers 1973).

One can perform a number of interesting experiments with lipophilic anions. They prefer the interfaces over the interior of the membrane, but they can cross over from one side of the membrane to the other under the influence of an externally applied electric field (Andersen and Fuchs 1975). Such membrane "translocation" is accompanied by a corresponding current in the external circuit. The integral of this current reveals the total charge which has moved; at sufficiently high applied fields, this charge reaches a limiting value which is equal to the total initially adsorbed anionic charge. In this way, one can directly measure the amount of adsorbed lipophilic anions, i.e., their interfacial excess.

This quantity turns out to depend strongly on the ionic strength of the aqueous solutions adjacent to the lipid bilayer membrane: the layer of membrane-adsorbed anions is balanced electrostatically by a aqueous space charge region which repels anions and, therefore, causes the adsorption to become self-limiting (Wang and Bruner 1978). Indeed, the diffuse layer theory of Gouy (1909, 1910) and Chapman (1913) is quantitatively applicable here, once it is realized that the adsorbed anionic charge must be localized a short distance below the membrane surface (Andersen 1978), unlike an electronic charge which always sits at the very surface of the metal.

As we have briefly reported before (de Levie 1981), we have made measurements on the strongly lipophilic anion cobalt dicarbollide, i.e., the substitution-inert complex of Co(III) with two dicarba-undecaborane or "carbollide" anions. The membrane permeability of phenylcarbollide was first reported by Liberman and Topaly (1969). The synthesis and properties of cobalt dicarbollide were reported by Hawthorne and Andrews (1965), and its crystal structure was deterrmined by Zalkin *et al* (1967). The sample used here was kindly supplied by Dr Hawthorne.

The measurements were made using the "boxcar" method outlined earlier; at small applied voltages, the resulting transients were nearly exponential whereas, at

olution resistance through which the electrical current must flow, i.e., by "iR rop". This effect is quite common in metal-based electrochemistry, but is usually isignificant in measurements on lipid bilayer membranes, where the currents are, ypically, much smaller. In the present case, however, the effect of the solution esistance must be taken into account because of the high adsorbability and iembrane permeability of cobalt dicarbollide anions.

Results

he current-time transients reported earlier (figure 5 in de Levie 1981) contained a cale labeling error of a factor of ten in the current axis; the correctly labeled data or the six highest voltages are shown in figure 1. First we will analyze the central ortion of these transients; thereafter, the very beginning and end will be shown to e rationalizable as well.

We start by assuming that the ion translocation current i as a funcation of time t is iven simply by

$$i(t) = q(t)k \ \exp\ [\alpha f V(t)], \tag{1}$$

here $q(t)$ is the anionic charge adsorbed at time t at the membrane-solution nterface, k is a translocation rate constant, α is a transfer coefficient, f is shorthand or the Faraday divided by the product of the gas constant and the absolute emperature, and $V(t)$ is the potential difference driving the ion translocation from ne side of the membrane to the other. Equation (1) assumes that the ion ermeation barrier is highest in the middle of the membrane, and that the so-called single jump" formalism (Markin 1969; Läuger and Stark 1970; Ketterer *et al* 1971) pplies. Although recent results from this laboratory (van Dijk and de Levie 1985)

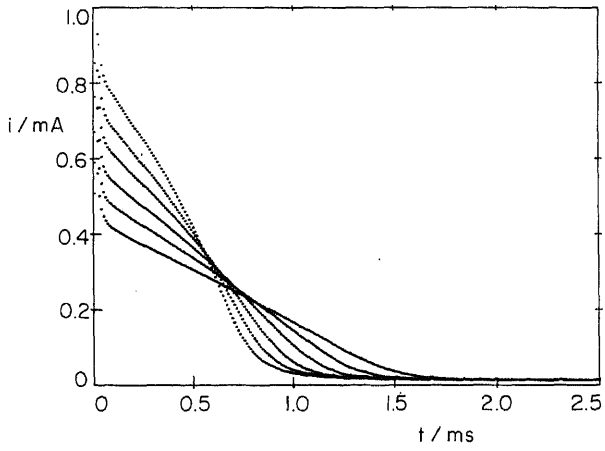

Figure 1. Current transients following potential steps of (from slow to fast decay) 250, 275, 300, 325, 350 and 375 mV amplitude, respectively, applied to a Mueller–Rudin type lipid bilayer membrane formed from 5 mg/ml diphytanoyllecithin (Avanti, Birmingham, Alabama) in *n*-decane, interposed between two identical aqueous solutions containing

have cast doubt on the correctness of this approach it is, nonetheless, used h
because of its simplicity; it appears to be adequate for the limited purpose of t
present work.

We will denote the adsorbed anionic charge at time zero, i.e., just before t
voltage step, by q_0, so that

$$q(t) = q_0 - \int_0^t i(t)\ \mathrm{d}t \qquad (3$$

hence

$$\mathrm{d}q(t)/\mathrm{d}t = -i(t), \qquad (3$$

which, when combined with (1), leads to a simple exponential transient when $V($
is constant. In general, however, $V(t)$ depends on time through the tim
dependence of the current,

$$V(t) = E - i(t)R, \qquad (4$$

where E is the constant voltage applied to the measurement cell for $t > 0$, and R
the solution resistance in series with the lipid bilayer membrane. Combination c
(1) and (4) leads to

$$i(t) = q(t)k\ \exp\ [\alpha f\{E - i(t)R\}] \qquad (5$$

for which no closed-form solution was found. Therefore, we have analyzed th
experimental data as follows. We rewrite (5) as

$$\ln\ [i(t)/q(t)] = \ln\ k + \alpha f E - \alpha f R\, i(t). \qquad (6$$

The instantaneous current $i(t)$ is, of course, directly measurable. The remainin
charge $q(t)$ is obtainable from (2); at the applied voltages used here, the integrals o
the complete transients are independent of E and are, therefore, equal to q_0, s
that $q(t)$ can be calculated. A plot of $\ln\ [i(t)/q(t)]$ versus $i(t)$ should thus be linear
with slope αfR and intercept $\ln\ k + \alpha fE$. Figure 2 shows such plots which, indeed

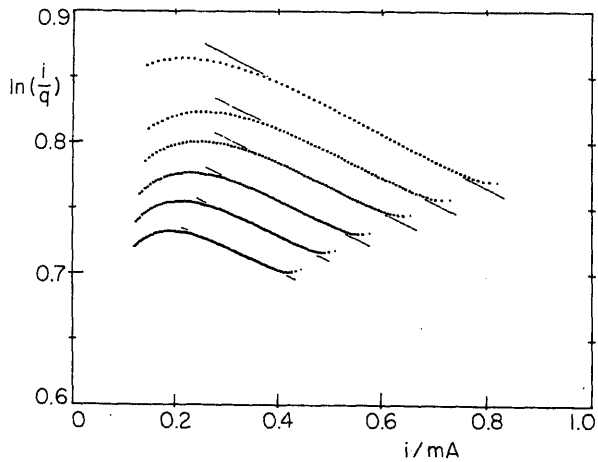

Figure 2. Analysis of the transients of figure 1 according to (6). The quotient i/q has the dimension sec^{-1}, as the numerical values used for i and q are in amperes and coulombs

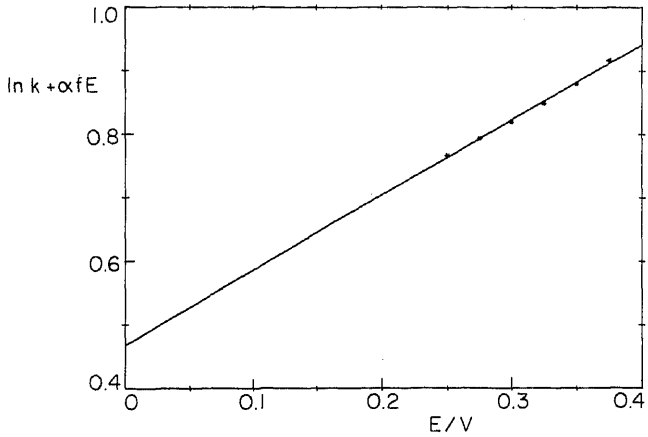

Figure 3. Extrapolation of the intercepts of figure 2 to obtain the translocation rate constant k, in sec^{-1}.

xhibit essentially parallel linear regions. Ignoring for the moment the deviations at oth ends of the curves, we can extract alpha from a plot of the intercepts versus E, s done in figure 3 and, with that value, obtain the solution resistance R from the lopes in figure 2. For the transfer coefficient we find a value of 0·30, for the esistance we obtain 317 ± 33 Ohms, while the intercept of figure 3 leads to an stimate for k of 107 sec^{-1}.

With these parameters, one can now reconstitute the entire transients. Comparison with the experimental data shows that the resulting differences at short imes fit single exponentials of the form

$$i_c = (E/R)\ \exp\ [-t/RC], \tag{7}$$

where i_c is the current necessary to charge the dielectric membrane capacitance C. Combination with the solution resistance R yields a dielectric membrane apacitance of 53 ± 4 nF.

Finally, the current transients at long times, after subtraction of the remaining teady-state current, are linear in the square root of time, indicating that, at such imes, aqueous diffusion has become rate-limiting.

. Discussion

The interesting aspect of our analysis is the striking similarity between our bservations at the membrane-solution interface and those common at its netal-solution equivalent. To a first approximation, the basic charge transfer law

chronocoulometric experiment. The Gouy-Chapman theory applies to the interfacial concentrations of the translocatable ions, and the fact that the adsorbed ions are localized below the membrane surface makes for the equivalent of a Helmholtz layer. The earliest part of the observed transient is dominated by the membrane capacitance and, at long times, membrane transport becomes controlled by aqueous diffusion. The currents can even become so large that corrections for *iR* drop must be made. In short, even though there is no change in oxidation state involved in membrane transport, the phenomenology and problems are quite analogous to those of classical electrochemistry at the metal-solution interface.

Acknowledgement

We gladly acknowledge Dr M F Hawthorne of the University of California at Riverside for his kind gift of a sample of cobaltdicarbollide, and AFOSR for financial support.

References

Andersen O S 1978 in *Membrane transport in biology: concepts and models* (eds) G Giebisch, D C Tosteson and H H Ussing, (New York: Springer Verlag) p. 369

Andersen O S and Fuchs M 1975 *Biophys. J.* **15** 795

Born M 1920 *Z. Phys.* **1** 45

Chapman D L 1913 *Philos. Mag.* **25** 475

van Dijk C and de Levie R 1985 *Biophys. J.* **48** 125

Erdey-Grúz T and Volmer M 1930 *Z. Phys. Chem.* **150** 203

Gouy G 1909 *Compt. Rend.* **149** 654

Gouy G 1910 *J. Phys.* **9** 457

Haydon D A and Myers V B 1973 *Biophys. Biochim. Acta* **307** 429

Hawthorne M F and Andrews T D 1965 *Chem. Commun.* **19** 443

Ketterer B, Neumcke B and Läuger P 1971 *J. Membr. Biol.* **5** 225

Läuger P and Stark G 1970 *Biochim. Biophys. Acta* **211** 458

de Levie R 1981 in *Futuristic aspects in electrochemical science and technology*, SAEST, p. 109

Liberman Ye A and Topaly V P 1969 *Biofizika* **14** 452

Markin 1969 *Mol. Biol.* **3** 610

Neumcke B and Läuger P 1969 *Biophys. J.* **9** 1160

Parsegian A 1969 *Nature (London)* **221** 844

Tafel J 1905 *Z. Phys. Chem.* **50** 641

Wang C C and Bruner L J 1978a *J. Membr. Biol.* **38** 311

Wang C C and Bruner L J 1978b *Nature (London)* **272** 268

Zalkin A, Hopkins T E and Templeton D H 1967 *Inorg. Chem.* **6** 1911

eak sampling – a new technique for eliminating charging current in C polarography[§]

AITHU POOJARY and S R RAJAGOPALAN*
Materials Science Division, National Aeronautical Laboratory, Bangalore 560 017, India

Abstract. Charging current (CC) in AC polarography (ACP) is proportional to dE/dt, (E = applied voltage). Though it is well known that CC is zero when dE/dt is zero, it has not been used to eliminate CC in ACP. This communication describes a new method based on this principle. This technique, termed by us as peak sampling technique, consists of sampling the cell current at the instant when applied voltage $\Delta E \sin \omega t$ is maximum or minimum and averaging the samples. Compensation of the series resistance by 'IR compensation' is a must for the effective separation of the non-faradaic current from the cell current by this technique. This method, it is shown here, actually gives the in-phase component of cell current. It is pointed out that this method achieves phase selectivity by box-car integration, which has not been used so far as a phase sensitive detector. Comparing this technique with phase selective polarography employing lock-in-amplification for realising phase selectivity, it is shown that the peak sampling technique gives signals that are $\pi/2$ times larger as compared to the other method.

Keywords. Peak sampling; phase selective AC polarography; charging current elimination; fundamental harmonic polarography; phase selective detection by box-car integration; AC polarograph for trace analysis.

Introduction

he application of AC polarography (ACP) to trace analysis is limited by the ackground, which is due to the charging of the double layer capacitance. The harging current is directly proportional to the frequency, whereas the faradaic urrent increases as the square root of the frequency. Consequently the enhanced gnal available at higher frequency is not useful, due to the poorer signal-to-ackground ratio at higher frequency. Hence, we have to employ a lower frequency Dasmaskin 1967) for analytical use and accept a lower sensitivity. Charging urrent elimination will help in realising the full potentiality of ACP.

An established approach for eliminating charging current is the phase selective echnique, which takes advantage of the fact that the charging current is 90° out of hase with applied voltage whereas the phase of faradaic current is 45° or less Smith 1966, p. 7). Practical implementation of this principle uses the lock-in-mplification technique (Smith 1966, p. 121). In this paper we present a simple, legant new method, termed as peak sampling technique for eliminating charging urrent in ACP.

where i_f is the faradaic current and i_c is the charging current. If q is the charge density and A is the area of the dropping mercury electrode (DME) then the charging current is given by

$$-i_c = Q\frac{dA}{dt} + AC_d\frac{d(E)}{dt}, \tag{2}$$

where C_d is the differential capacity of the double layer and E is the applied voltage. In the case of ACP, the change in the area of DME within a cycle is negligible and hence the first term can be neglected. Therefore, for ACP, (2) can be written as

$$-i_c = AC_d\frac{d(\delta E)}{dt}, \tag{3}$$

where $\delta E (= \Delta E \sin \omega t)$ is the superimposed AC voltage. Substituting for δE in (3) we get,

$$-i_c = AC_d\omega \cos \omega t. \tag{4}$$

From (3) it is readily seen that $i_c = 0$ when $d(\delta E)/dt = 0$. For a sine wave $d(\delta E)/dt$ will be zero at the positive and negative peak. Hence, the cell current sampled at the instant when the applied sinusoidal voltage exhibits a maximum or a minimum, is free from charging current. Another way of looking at this is as follows. From (4) it is seen that the charging current is a cos wave, while the input is a sine wave. Therefore, the zero crossing of the charging current will coincide with a phase of $\pi/2$ and $3\pi/2$ for the input voltage. Sampling the cell current when the phase of the applied sine wave is $\pi/2$ or $3\pi/2$ can therefore eliminate charging current.

The principle that charging current is zero when $(dE/dt) = 0$ is well known in transient techniques. It is surprising that it has not been exploited so far for rejecting charging current in ACP. This principle appears to be different from that of the phase selective technique. Comparing (3) and (4) we conclude that as far as AC polarography is concerned the two principles of eliminating charging current are similar.

While using the principle of measuring when $(dE/dt) = 0$, we sample the cell current at the peak of the applied voltage. Hence, we call this the peak sampling technique.

An expression for the current measured by the peak sampling technique can easily be obtained. The equivalent circuit for the impedence of a small electrode with a large counter electrode (the case of a polarographic cell), is generally represented as in figure 1a (Rehbach and Sluyters 1970). The uncompensated resistance, R_u, includes contributions from the resistance of the dropping mercury electrode (DME) and resistance of the solution included between the Luggin tip and the DME. Let us assume that R_u is exactly compensated by '*IR* compensation'. For such an ideal situation the equivalent circuit of the cell is shown in figure 1b. Unlike

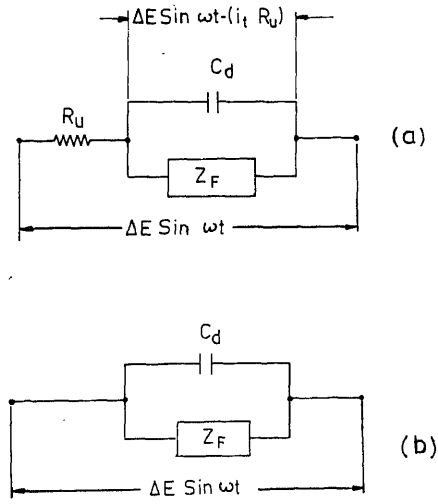

Figure 1. Equivalent circuit of a cell with a small working electrode (DME) and a large counter electrode: (a) without '*IR* compensation'. Effective voltage applied across C_d is less than the total applied voltage; (b) with '*IR* compensation'. Effective voltage is the same as applied voltage. R_u = Series uncompensated resistance (includes resistance of DME and the resistance of solution between Luggin tip and DME), C_d = differential capacity of double layer, Z_F = Faradaic impedance (includes charge transfer resistance and Warburg impedance) $\Delta E \sin \omega t$ = applied AC potential. $i_t R_u$ = ohmic drop across the series resistance due to the cell current i_t.

ıe case shown in figure 1a, here the full applied voltage is impressed across the ouble layer. We will analyse this case. Inter-relationship between the waveforms f applied voltage ($\Delta E \sin \omega t$) and the various currents are shown in figure 2. The ıarging current leads the applied voltage by 90°, while the cell current leads the pplied voltage by φ. It is seen that at the instant t_s, corresponding to a peak of the pplied voltage, i_c is zero and the cell current is entirely faradaic

$$(i_t)_{t_s} = (i_f)_{t_s} + 0. \tag{5}$$

his is a consequence of 90° separation between i_c and $\Delta E \sin \omega t$. The phase of the ell current at that instant is seen from figure 2 to be $(90+\varphi)$. Therefore

$$(i_t)_{t_s} = \mathrm{I} \sin (\omega t_s + \varphi) = \mathrm{I} \sin (90+\varphi),$$

r

$$(i_t)_{t_s} = \mathrm{I} \cos \varphi. \tag{6}$$

From (6) it is readily seen that the current measured by the peak sampling echnique is the amplitude of the in-phase component of the cell current: This echnique can therefore be looked upon as an alternative to the lock-in-mplification approach for implementing phase selective polarography.

.1 *The effect of series resistance*

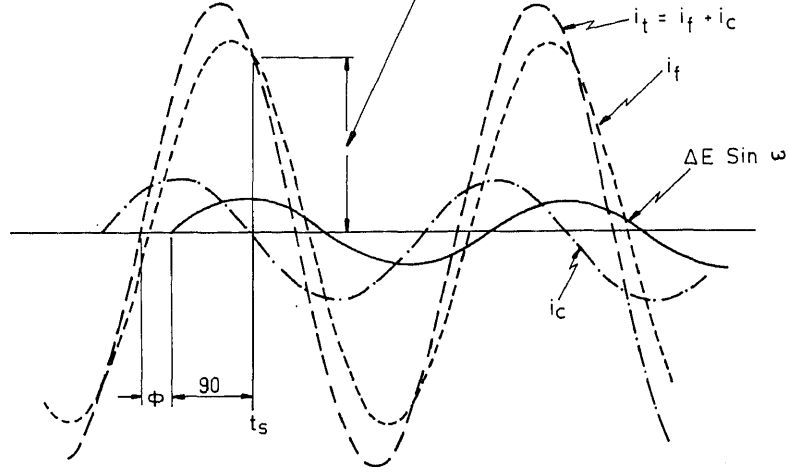

Figure 2. Schematic diagram showing the inter-relationship between voltage and current waveforms in AC polarography. $\Delta E \sin \omega t$ = applied AC potential, i_c = wave form of charging current (i_c leads $\Delta E \sin \omega t$ by 90°), i_f = faradaic current wave form, i_t = cell current wave form (phase of angle of i_t is φ, i_t is the vectorial sumof i_c and i_f), t_s = time at which $\Delta E \sin \omega t$ is maximum and the cell current is sampled in the peak sampling technique, i_{measured} = sampled value of current.

the charging current (Hayes and Bauer 1962; Smith 1963). Figure 3 shows the different current vectors for the case shown in figure 1b.

The effective AC potential, $V_e (= AC')$ impressed across the double layer is smaller than the applied potential, V, $(= AB)$ due to the ohmic drop $i_t R_u$. There is a phase difference $\varphi_{c'}$ between V_e and V. The current measured by the peak sampling technique would be $AG (= i_t \cos \varphi_m)$ if i_t is sampled when V is at its peak. It would include a contribution from i_c because i_c is 90° out of phase only with respect to the voltage across C_d i.e. V_e. The amount of charging current included in the measured value will be the projection of i_c on AB and is equal to $i_c \cos (90 - \varphi_c)$ or $i_c \sin \varphi_c)$. Even though it is smaller than $i_c \sin \varphi_m$, the charging current present in the cell current is significant. If the current is sampled when V_e is maximum, the measured current will be $AH (= i_t \cos \varphi = i_f \cos \varphi')$ and will not include any contribution from the charging current. It is not practical to make this measurement since there is no simple way of knowing the position of the peak of V_e. However, it is possible to make φ_c small and under ideal conditions zero through '*IR* compensation'. Thus the effectiveness of the rejection of the charging current by the peak sampling technique would depend on the efficiency of '*IR* compensation'.

2.2 *Need for averaging*

In principle, a single sampling at the instant of occurrence of peak in the applied voltage is all that is necessary for eliminating charging current. Such a measured

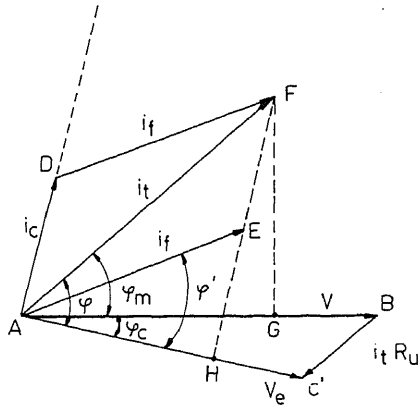

Figure 3. Schematic representation of current and voltage vectors when the series resistance R_u is present. AB = applied AC potential V, AC' = effective applied AC potential V_e when $R_u \neq 0$, $i_t R_u$ = ohmic drop across R_u due to cell current i_t, φ_c = phase angle of V_e, AD = charging current vector i_c, AE = faradaic current vector i_f, AF = cell current vector i_t (the resultant of i_c and i_f), φ' = phase angle of i_f, φ_m = phase angle of i_t with respect to applied voltage, φ = phase angle of cell current with respect to effective AC potential across the double layer, AG = current measured by sampling when V is maximum, AH = current measured when V_e is maximum.

value will be heavily corrupted by noise, especially at low current levels. To overcome this problem it is essential that the sampling operation should be repeated for several waves and the results averaged. The operation of sampling and averaging the sampled data is nothing but box-car integration. Therefore peak sampling technique can be considered as achieving phase selective detection through box-car integration. Though several applications of box-car integration other than signal-to-noise ratio improvement are known, there is no mention of its use as a phase selective device (Malmstadt *et al* 1974). This is the first time, at least in electrochemistry, that it is being used for phase sensitive detection.

3. Implementation of the peak sampling technique

The block diagram for eliminating charging current by the peak sampling technique is shown in figure 4. The steps in signal processing are: (a) isolation of the fundamental harmonic of i_t (b) producing a finite number of sampling pulses (coinciding with the maxima of applied AC potential) during the current measuring interval in each drop (c) sampling the current isolated in step (a) by the pulses produced in step (b) and averaging them, and (d) recording the average value of sampled current against DC potential to get the charging current eliminated AC polarogram.

The circuit is briefly described below. An adder type potentiostat (McKubre and Macdonald, 1984, p. 45) is used to impress the input functions on to the cell, viz, E_{DC}, ramp and $\Delta E \sin \omega t$. The cell current is converted into voltage by the

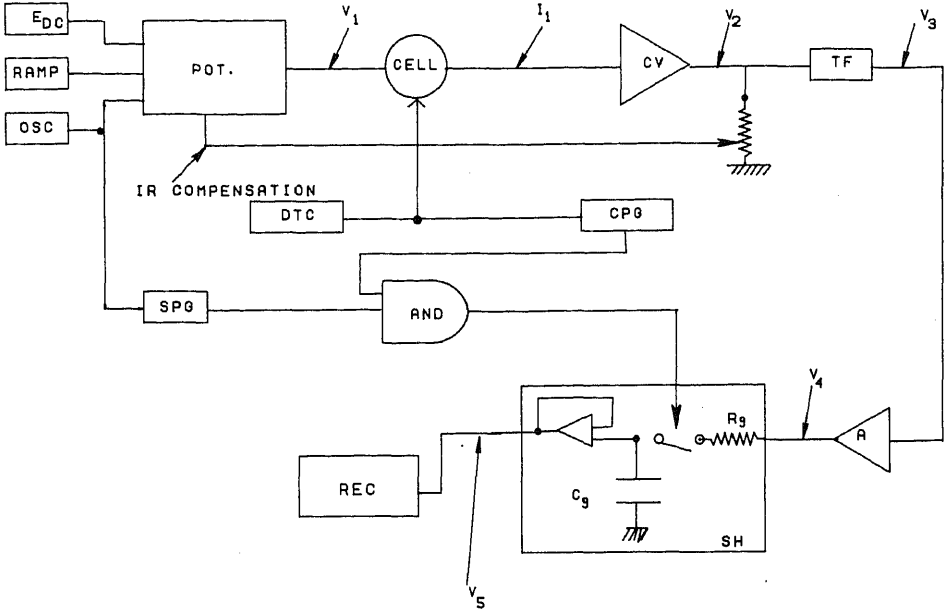

Figure 4. Block diagram of the circuit used for implementing the peak sampling technique. E_{DC} = initial DC potential, RAMP = Ramp generator, OSC = sinusoidal oscillator, POT = potentiosat, CV = current-to-voltage converter, TF = tuned band pass filter, DTC = drop time controller, CPG = command pulse generator, SPG = sampling pulse generator, AND = AND gate, SH = sample hold, A = amplifier, REC = recorder, R_gC_g = charging time constant of sample hold, $V_1 = E_{DC} + bt + \Delta E \sin \omega t$, $I_1 = I_t \sin(\omega t + \varphi)$, $V_2 = R\, I_t \sin(\omega t + \varphi)$ + harmonics, $V_3 = R\, I_t \sin(\omega t + \varphi)$, $V_4 = GR\, I_t \sin(\omega t + \varphi)$, $V_5 = GR\, I_t \cos \varphi$ (b = slope of Ramp and GR 'gain' due to CV and A).

Q of 10. Drop time is controlled by an electro-mechanical knocker operated by the droptime controller. Sampling pulse train of required width (80 μs) and position is derived from the oscillator in the following way. The sinusoid from the oscillator is converted into a squarewave in a standard trigger circuit (Smith 1966, p. 119). Sharp needle pulses coinciding with the positive peak of the applied voltage are derived from the square-wave by the use of one-shots. This will produce the pulse train.

In order to minimise the contribution to the charging current from the area change, the current should be sampled towards the end of the drop life when dA/dt is small (figure 5a). For this purpose, the sampling pulses should occur only during the current measurement interval in each drop.

A scheme for realising this is described below. From the drop knocker pulse (figure 5b) a command pulse is produced such that it occurs during the current measuring interval and it has a width equal to the current measuring time, 40 msec, in this work (figure 5c). These command pulses generated by CPG are AND gated with the sampling pulse train produced by SPG (figure 4). This operation results in the production of a finite number of sampling pulses during the current measuring interval (figure 5D).

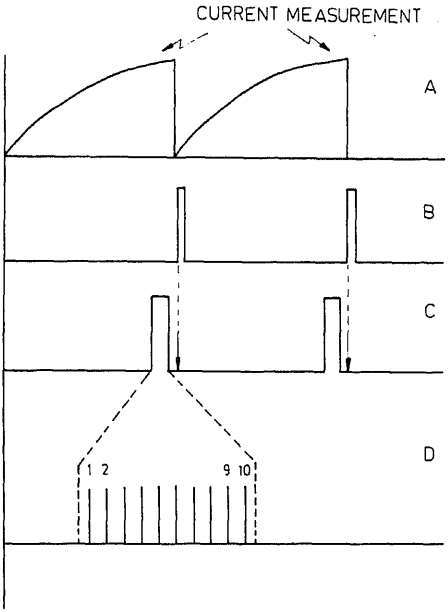

Figure 5. Timing diagram showing the relationship of various pulses to the drop time. A. Area change within a drop time, B. drop knocker pulse train, C. command pulse train generated by command pulse generator, arrow denotes drop fall, D. position of sampling pulse train in a drop life.

gate. As a result of these operations, each wave of the cell current occurring within the sampling interval gets sampled at instants corresponding to successive positive peaks of applied voltage. The time constant $R_g C_g$ of SH is such, that it averages the sampled data. The output of SH is recorded against DC potential.

It is worthwhile to point out that circuit elements should not introduce any spurious phase change. Such phase changes would vitiate the results because the applied voltage then loses its reference character.

'*IR* compensation' is provided by positive feed back (McKubre and Macdonald 1984, p. 49). The positive feed back is obtained from the output of the current-to-voltage converter. The amount of '*IR* compensation' is adjusted by varying the fraction of the output that is fed-back.

4. Comparison between peak sampling and lock-in-amplifier (LIA) techniques

In LIA technique, the signal $[I \sin(\omega t + \varphi)]$ is multiplied by a reference square wave and the product averaged by passing through a low pass filter (LPF). It is easily shown that the in-phase component is recovered when the reference square wave is in-phase with the applied voltage. For this case the output of LIA will be

$$V_{LIA} = (2/\pi) V_x \cos \varphi, \tag{7}$$

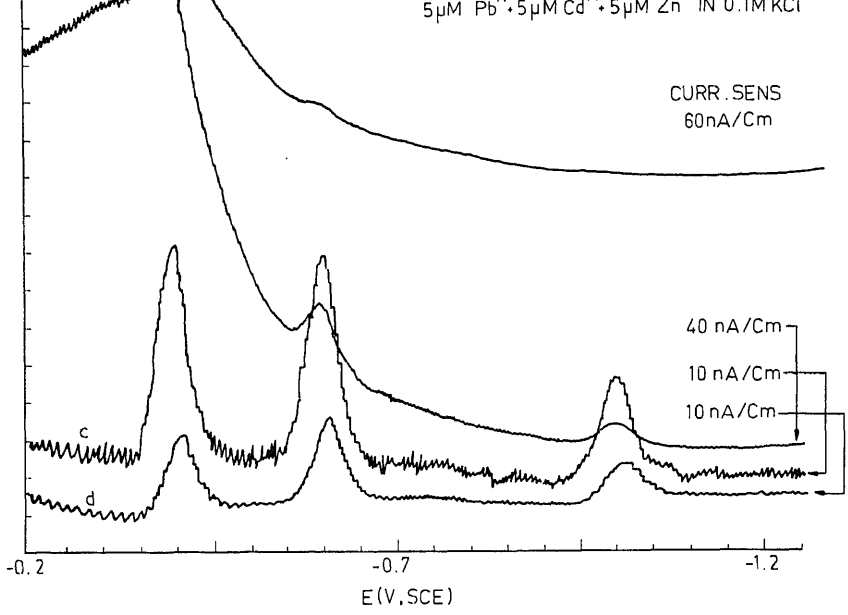

Figure 7. AC polarograms of 1·0 ppm Pb^{++} + 0·6 ppm Cd^{++} + 0·3 ppm Zn^{++} in 0·1 M KCl drop time = 0·5 sec. (a) Total cell current polarogram recorded at a current sensitivity of 60 nA/cm. Large background current has swamped completely the waves due to lead and zinc. Cadmium peak is barely visible. (b) 'Peak sampled' polarogram without '*IR* compensation' recorded at a current sensitivity of 40 nA/cm. Due to the presence of R_u, charging current elimination is incomplete. Even with a partial elimination of charging current, the cadmium and zinc peaks are seen. (c) 'Peak sampled' polarogram obtained with proper '*IR* compensation' recorded at 10 nA/cm. Peaks due to lead, cadmium and zinc are distinctly seen. (d) Phase selective polarogram using LIA technique recorded at a current sensitivity of 10 nA/cm. Proper '*IR* compensation' was used. Area of electrode in this case alone was 40% smaller. All the three peaks are distinctly seen.

measured with better accuracy. The area of the electrode used for getting 'LIA phase selective' polarograms is 40% smaller than that used for 'peak sampled' polarograms. After correcting for the difference in area, the ratios of the peak heights for the two techniques for lead, cadmium and zinc are 1·93, 1·72 and 1·93, respectively. On the basis of theory, it is shown in §4 that the wave height of a "peak sampled" polarogram should be $\pi/2$ (= 1·57) times larger than that of a "LIA phase selective" polarogram. Comparing the experimentally observed ratio with the theoretical one, it is found that the experimental values are 10 to 23% higher. Though the theoretically expected trend, viz, that peak sampling gives a larger signal as compared to LIA is verified, the quantitative agreement between theory and experiment is not very good. Further investigations are needed to understand the larger difference between theory and experiment.

As expected (§4), the noise level in peak sampled polarograms is larger than that in LIA phase selective polarogram. However, they are not unacceptably noisy. It is

samples by sampling at the negative peak, (b) averaging over a number drops as was done by Barker and Gardner (1958). These approaches have not been tried in this work.

Importance of '*IR* compensation' is demonstrated by the curve (b) which has been recorded by the peak sampling technique but without using '*IR* compensation'. Comparing curves (a) and (b) it can be inferred that there has been a partial rejection of charging current. That is the reason for the peaks due to cadmium and zinc in curve (b). At potentials anodic to $-0{\cdot}5$ V, the charging current is large and the lead wave is completely masked. The incomplete elimination of charging current in curve (b) is due to the effect of series resistance R_u. For the perfect rejection of charging current correct amount of *IR* compensation is a must.

Rapid polarography, i.e., polarography with short drop time, about 0·2 second, and large ramp rates has become popular in analytical work because polarographic "run times" are less than one minute (Bond 1970; Smith 1971). In the case of short drop times, dA/dt does not tend to a consant value even at the end of the drop life. Consequently, contribution to the charging current due to area change will exist. With a view to examine the effectiveness of peak sampling technique in eliminating charging current in 'rapid polarography', peak sampled polarograms with 0·2 sec and 1·0 sec drop times are compared in figure 8. The flatness of the base line is not

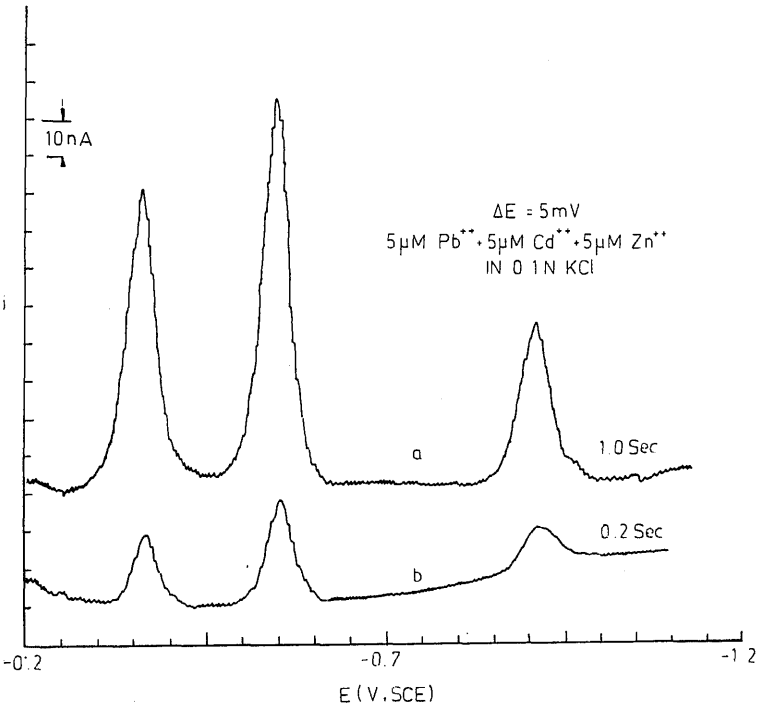

Figure 8. AC polarograms of 5 μm each of Pb^{++}, Cd^{++} and Zn^{++} in 0·1 M KCl at different drop times; (a) 'peak sampled' polarogram with drop time 1·0 sec, (b) 'peak sampled' polarogram with drop time of 0·2 sec; in both the cases all the three peaks are seen distinctly, two different DMEs were used, the ratio of the areas of DME for curves (a)

A Wenking potentiostat (Model LB75M) coupled with a Wenking Scan Generator (Model VSG 72) is used for controlling the potential. The range of potentials covered in the CV experiments corresponds to 0 to −2·2 V vs SCE. An *X-Y* recorder (Digitronic Model 2000 series) is used to record the *i-E* curves. All the potentials are expressed vs SCE and the measurements are made at 32 ± 1°C. Potential sweeps are effected with (i) equal slopes for forward and backward scans and (ii) unequal slopes for forward and backward scans.

3. Results and discussion

Figure 1A shows the ASV curves of 10^{-5} M $ZnSO_4$ solutions in which the forward cathodic sweep of the CF was extended to −2·2 V and they demonstrate the beneficial influence of *in situ* deposited sodium on the anodic peak current obtained in the reverse scan. The potential sweep rate has been kept constant in both

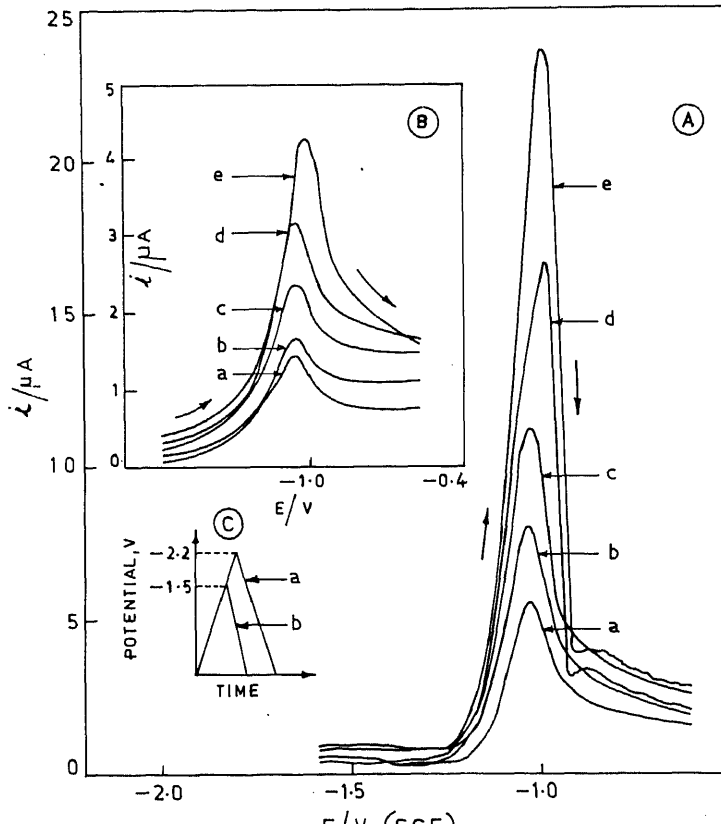

orward and backward directions of CV (See inset of figure 1c for the input time profile). For comparison, the ASV curves of the same solution in which the forward athodic potential sweep was limited to −1·5 V only (thus ensuring the absence of odium deposition) and the resulting anodic sweep voltammograms are shown in igure 1B (inset). The observed anodic peak currents were also linear and thus irectly proportional to the concentration of the metal ion in solution. A omparison of such calibration plots, obtained in the presence and in the absence of odium amalgamation, have been given in figure 2, and it clearly reveals the anodic ignal enhancement in the case of forward scan extended to sodium deposition otential.

Confirmation for the involvement of *in situ* sodium deposition and its role in the nhancement of the anodic peak currents has been verified by running CVs using a upporting electrolyte which is completely devoid of sodium ions, viz., tetramethyl mmonium chloride again taking the case of cadmium as an example (Prabhakara Rao and Varadharaj 1983). The proportionality in the increase of the anodic peak eight obtained to the concentration of the sodium ion in solution in the case of nixed supporting electrolyte of tetraalkyl chloride and sodium carbonate and nclusion of sodium deposition potential has also been verified (Varadharaj 1984).

These anodic peak currents are expected to respond to the scan rate of the otential, their magnitudes increasing with the increase in sweep rate for a given concentration. However, it may be realised that such peak heights will not bear a square root dependence on the scan rate expectations based on Randles-Sevcik equation (Randles 1948; Sevcik 1948), because the concentration of the metal in the amalgam available for stripping differs in each case from one sweep rate to the other arising out of different amounts of metal being deposited and exchanged

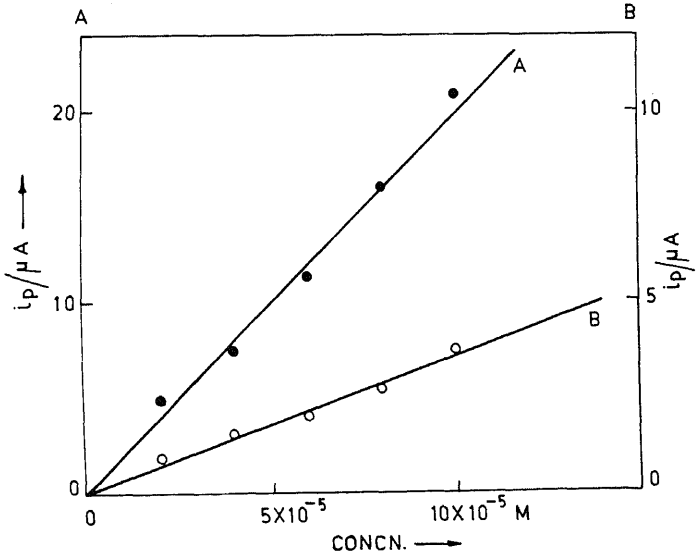

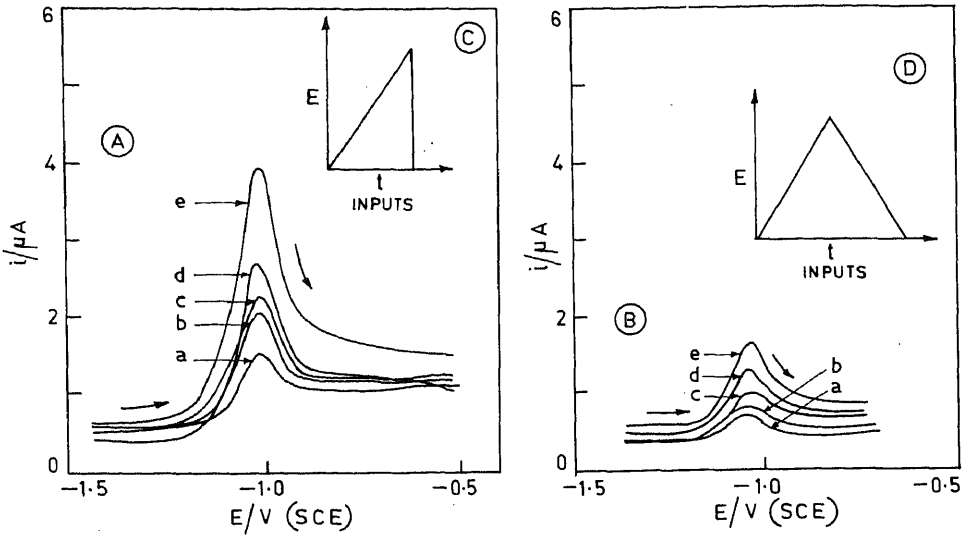

Figure 5. **(A)** Stripping curves obtained for a solution containing (a) 2, (b) 3, (c) 4, (d) 5 and (e) 6 μ M $ZmSO_4$ and using programmed time-potential inputs. Sweep rate of forward scan is 50 mV Sec^{-1} and reverse scan is 200 mV Sec^{-1}. **(B)** As (A) but using inputs in which sweep rates of forward and reverse scan are identical i.e. 50 mV Sec^{-1}. **(C)** and **(D)** are potential input profiles for recording the curves in (A) and (B) respectively.

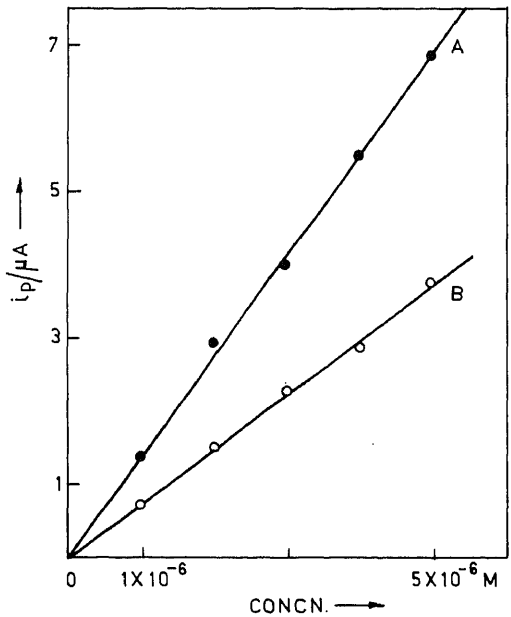

Figure 6. **(A)** Plot of i_p vs concentration of Cd^{2+} ion obtained using programmed inputs. Sweep rate of forward scan is 50 mV Sec^{-1} and reverse scan is 150 mV Sec^{-1}. **(B)** As (A)

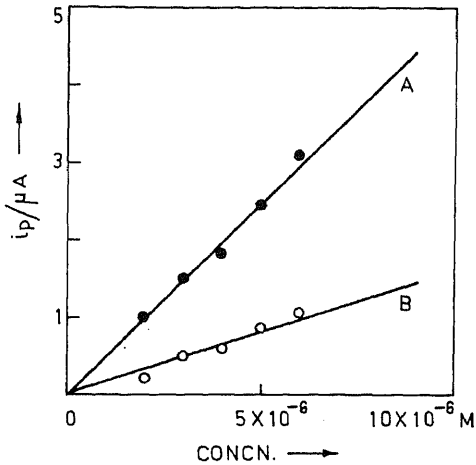

Figure 7. (A) Plot of i_p vs concentration of Zn^{2+} ion obtained using programmed inputs sweep rate of forward scan is 50 mV Sec^{-1} and reverse scan is 200 mV Sec^{-1}. (B) As (A) but using inputs in which sweep rates of forward and reverse scan are identical i.e. 50 mV Sec^{-1}.

ate of exchange reaction taking place between the metal ion in solution and the odium in amalgam, (iii) solubility considerations for the respective metal in Hg, nd (iv) the rate of potential sweep of the forward scan (which is analogous to the ime of pre-electrolysis in the conventional ASV).

From the above experimental data one can conclude that a good enhancement of he anodic signal is possible in ASV by favouring additional accumulation of metal on in HMDE via a displacement reaction between sodium metal in mercury and netal ions present in solution, the former being generated *in situ* on HMDE using a rogrammed time-potential input. This technique, besides enhancing estimation of ndividual metal ions at low levels, could also be expected to work well in the case f a mixture of metal ions in the solution under consideration.

cknowledgement

he authors wish to express their thanks to Mr R Srinivasan and Professor K I Vasu or their encouragement.

eferences

emula W, Rakowska E and Kublik Z 1959 *J. Electroanal. Chem.* **1** 205
ozun L F, Popova T V and Dzhasymbehov A K 1981 *Electrokimiya* **17** 655
rabhakara Rao G and Varadharaj A 1983 *J. Electroanal. Chem.* **145** 205
andles J E B 1948 *Trans. Faraday Soc.* **44** 327
evcik A 1948 *Collect. Czech. Commun.* **13** 349

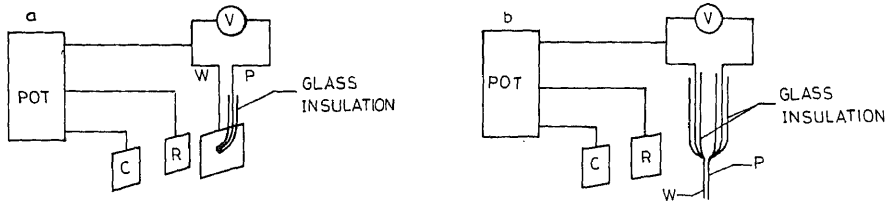

Figure 1. Schematic illustration of the electrode configuration used for measurement of polymer resistance. (a) Polymer deposited on a foil electrode, (b) Polymer deposited on and between two parallel wires.

investigation can be deposited. An insulated Pt wire (diameter = 1 mm) probe is positioned close to the foil surface such that when a polymer of sufficient thickness is deposited on the foil, the probe tip is just embedded in the polymer. This probe can be used to monitor the surface potential of the polymer. A similar configuration has been used by Fan *et al* (1984) to determine the surface potential of conducting layers on semiconductors. The resistance of the polymer film is determined as follows. When the polymer is under potentiostat control a current i flows across the polymer/electrolyte interface. This causes a voltage drop, V, across the polymer film due to the resistance of the polymer. This voltage drop V is measured between W and P. The resistance of the polymer is given by V/i.

The second configuration figure 1b is adapted from that used by Paul *et al* (1985). It consists of two parallel platinum wires (diameter = 1 mm) aligned very close to each other. When polymerization is carried out simultaneously on both the wires, the polymer layer grows on the two wires and eventually bridges the gap between the wires. One of the wires is then used for potentiostatic control of the polymer (W) and voltage drop in the polymer is measured using the second wire (P). The resistance of the polymer is obtained as before by taking the ratio of voltage drop to potentiostatic current.

Polyaniline films were produced by the procedure described by Diaz and Logan (1980). All chemicals were AR grade. Aniline was further purified by distillation under nitrogen. Sulphuric acid was purified by distillation under dry air. 0·5 M H_2SO_4 used as supporting electrolyte for resistance measurements was purified by pre-electrolysis for 48 hours. The following solutions were used for measuring the pH dependence of resistance: pH = 0·74, 0·5 M H_2SO_4; pH = 1–2, chloride buffer; pH = 3–5, phthalate buffer; pH = 6·5, phosphate buffer.

Potential control was done using a PARC 362 Scanning Potentiostat and potentiodynamic data were recorded on a Hewlett-Packard 7035B X–Y Recorder. Voltage drop across the polymer was measured using HIL 2161 Digital Multimeter.

Polymerization was carried out by potentiodynamic cycling between −0·2 V to +0·8 V vs SCE in 0·1 M aniline + 0·1 M H_2SO_4 at 50 mVsec^{-1}. Polymerization time of 30 minutes produced a film of thickness sufficient to provide contact between W and P. All measurements were made with 30 minute films.

3. Results and discussion

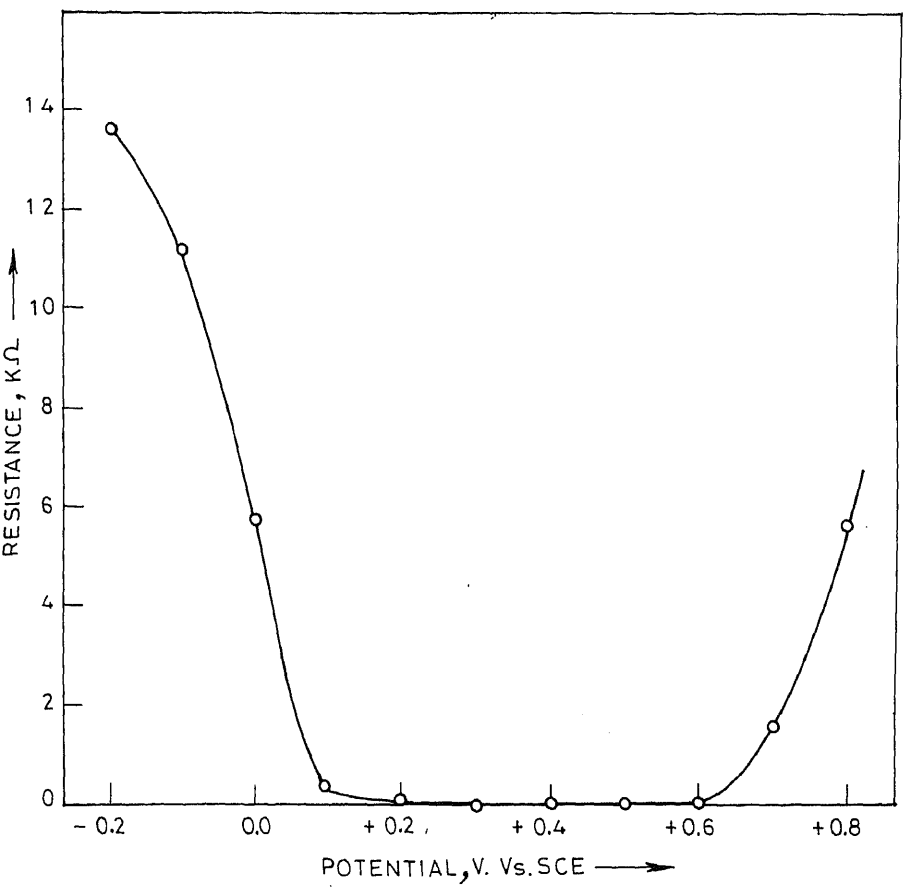

Figure 2. Resistance of a supported polyaniline film as a function of applied electrochemical potential in 0·5 M H_2SO_4 (pH = 0·74).

decrease of the resistance. A broad minimum in resistance is observed between 0·1 V and +0·6 V with sharp increase in resistance on further anodic polarization. These observations are in agreement with the results reported by Paul *et al* 985). The resistance change with our films is generally of the order of 10^4. Paul *et* (1985) have reported a change in resistance of $> 10^6$. This difference may be rtly due to the fact that our films are thicker (≈ 100 μm) than those used in the rlier study (≈ 5 μm). Identical results were obtained when the second configuration was used for resistance measurement.

It has been recognized that the chemistry of polyaniline is sensitive to pH. The pen-circuit potential of polyaniline electrodes is pH-dependent (Jozefowicz *et al* 969) as also the conductivity (MacDiarmid *et al* 1985). It has been suggested that olyaniline may have application as a pH sensor in a limited range. Thus it is of terest to obtain a quantitative dependence of conductivity on pH.

The dependence of polymer resistance on the pH of the supporting electrolyte is

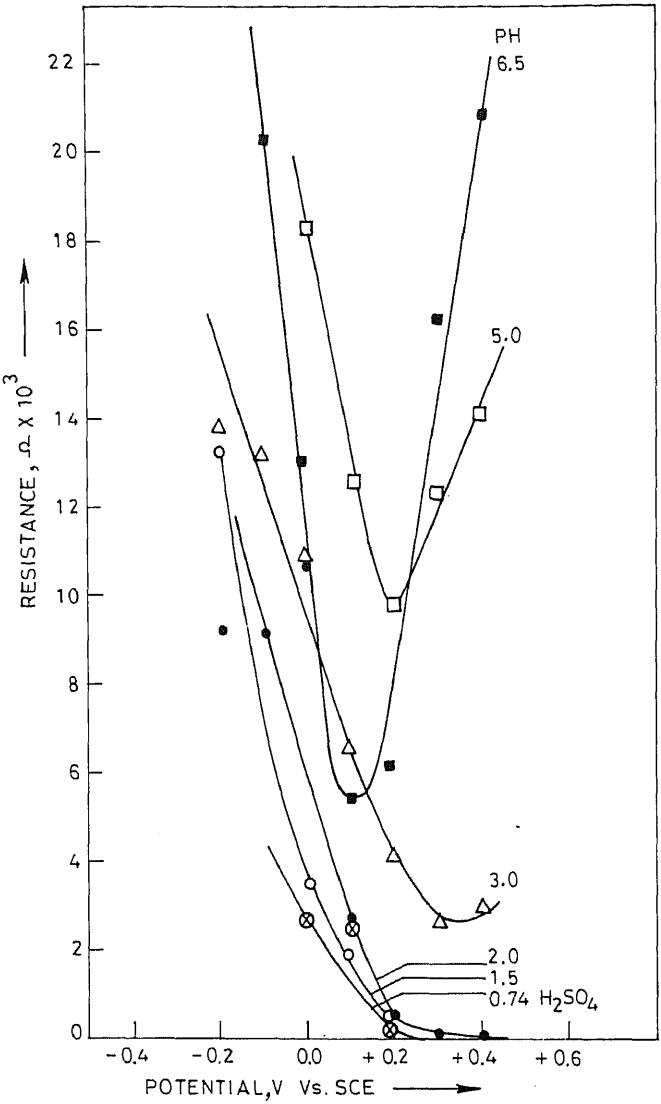

Figure 3. Resistance of a polyaniline film as a function of applied electrochemical potential in buffers of various pH.

potentials. The resistance of the polymer increases with pH in agreement with the earlier report. There is a slow evolution in the resistance-electrochemical potential behaviour with the resistance minimum becoming sharper at higher pH.

These data were used to generate a conductance surface, 'state-diagram' as shown in figure 4. Such a 'state-diagram' has been suggested as an aid in the discussion of various properties of polyaniline. Salaneck *et al* (1986) have proposed a surface curvature based on the data at pH = 1 and the pH-dependent resistance of

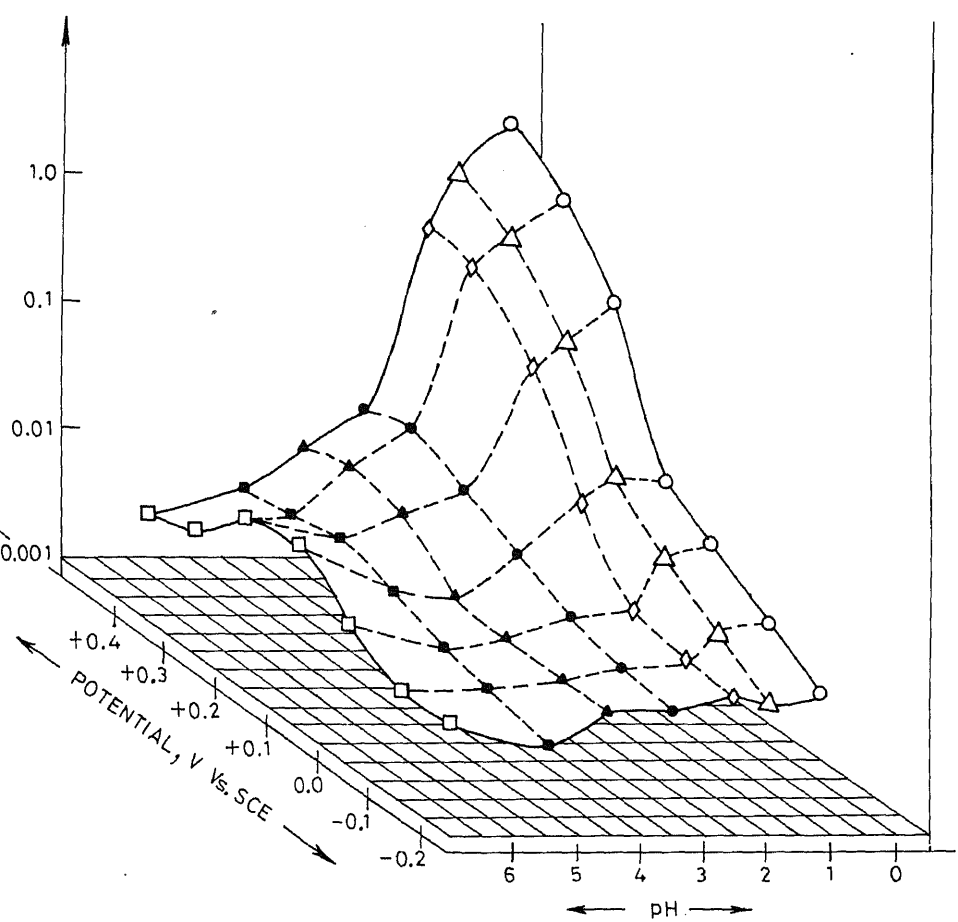

Figure 4. A conductance surface 'state-diagram' of polyaniline generated from the data shown in figure 3.

Polymer resistance and electrochemical activity

he cyclic voltammogram of polyaniline in 0·5 M H_2SO_4 and the steady-state esistance of the polymer in the same solution are shown in figure 5. It is apparent iat the electrochemical activity of the polymer film occurs mainly in the resistance indow between +0·1 V and +0·6 V. Similarly it has been observed by Oyama *et l* (1983) that the ability of the polymer to drive redox reactions is determined by ie equilibrium redox potential of the couples concerned. Couples whose redox otential is within the range +0·1 V to +0·6 V exhibit reaction rates which are not ubstantially different from those observed at pyrolitic graphite. Couples whose quilibrium potentials are outside this range are inhibited.

A direct relation between polymer resistance and electrochemical activity is also

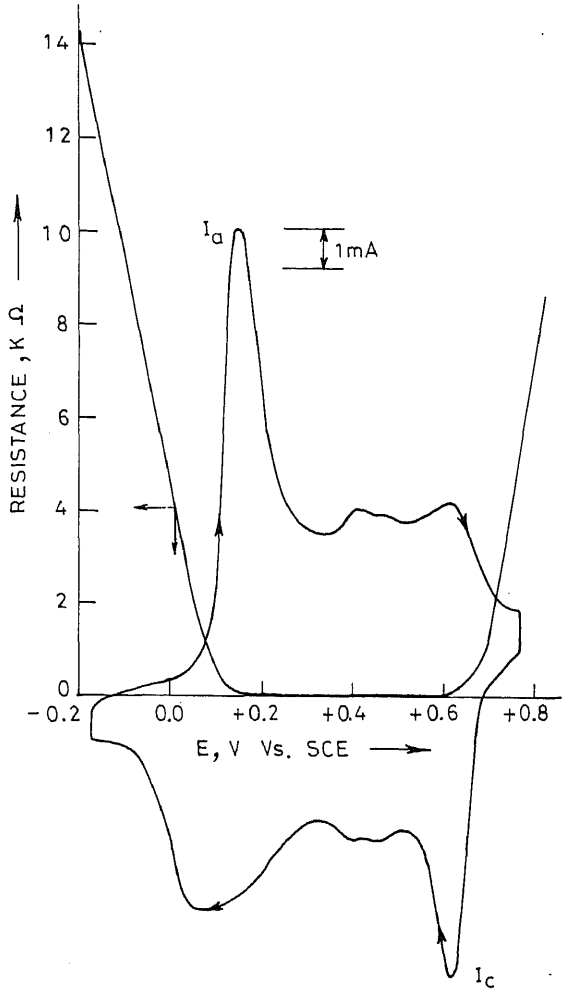

Figure 5. Cyclic voltammogram of polyaniline in 0·5 M H_2SO_4 and corresponding resistance profile. The resistance was obtained from steady-state measurements.

of changes which can be observed with increasing pH. The *i–V* curve in pH = 0·74 (figure 5) is quite complex and at least four peaks can be distinguished. With increasing pH some of these peaks coalesce or disappear and at pH = 5·0 a single peak is observed. Simultaneously, the potential range in which high currents are observed becomes narrower and at pH = 5·5 the polymer is virtually electroinactive. These changes are in qualitative agreement with resistance measurements where the resistance window becomes higher and narrower with increasing pH.

Polyaniline has been used as a protective coating for the prevention of passivation/dissolution of small band gap semiconductors such as *n*-Si. The polymer films were found to function satisfactorily when used to drive redox reactions such as $Fe^{3+/2+}$ or I_3^-/I^- but were virtually inactive for oxidation of water (Noufi *et al*

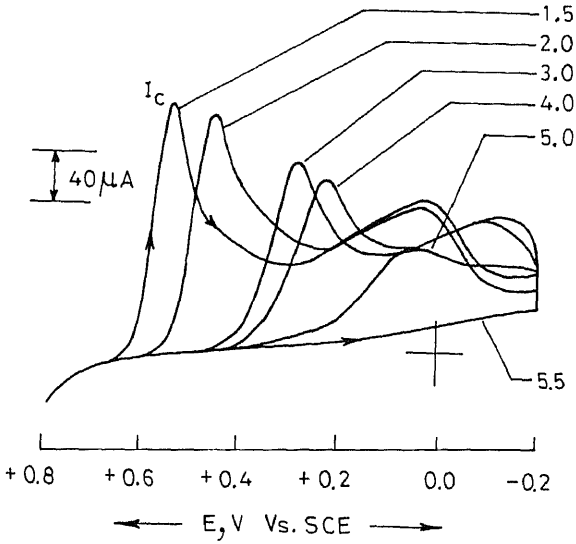

Figure 6. Cathodic scans of polyaniline in buffers of various pH.

ıe change in resistance of polyaniline. The equilibrium potential of the redox ɔuples are within the resistance window between +0·1 V and +0·6 V while the quilibrium potential of water oxidation (+1·0 V) lies in a region where the ɔlymer is highly resistive.

Conclusion

has been shown that resistance of conducting polymer films can be measured *in tu* by a procedure which is simpler than has been used earlier. The worth of such udies in understanding electrode kinetics has been seen particularly in relation to e variation of pH. However, a more quantitative analysis of the influence of sistance on the electrochemical behaviour is required.

In situ resistance measurements in the presence of redox couples should be of terest in understanding their kinetics. Such studies are currently in progress in our boratory.

cknowledgement

his work was partly supported by a grant from BRNS/DAE.

eferences

iaz A F and Clarke T C 1980 *J. Electroanal. Chem.* **111** 115
iaz A F and Logan J A 1980 *J. Electroanal. Chem.* **111** 111

Kittlesen G P, White H S and Wrighton M S 1984 *J. Am. Chem. Soc.* **106** 7389
MacDiarmid A G, Jin-Chih Chiang, Wu Song Huang, Humphrey B D and Somasiri N L D 1985 *Mo*
Cryst. Liq. Cryst. **125** 309
Noufi R, Tench D and Warren L F 1980 *J. Electrochem. Soc.* **127** 2709
Noufi R, Nozik A J, White J and Warren L 1982 *J. Electrochem. Soc.* **129** 2261
Oyama N, Ohnuki Y, Chiba K and Ohsaka T 1983 *Chem. Lett.* **1759**
Paul E W, Ricco A J and Wrighton M S 1985 *J. Phys. Chem.* **89** 1441
Salaneck W R, Lundstrom I, Huang Wu-S and MacDiarmid A G 1986 *Synth. Met.* **13** 291
Skotheim T, Lundstrom I and Prejza J 1981 *J. Electrochem. Soc.* **128** 1625
Tourillon G and Garnier F 1982 *J. Electroanal. Chem.* **135** 173
White H S, Kittlesen G P and Wrighton M S 1984 *J. Am. Chem. Soc.* **106** 5375

pplications of exponential relaxation methods for corrosion studies nd corrosion rate measurement[§]

V LAKSHMINARAYANAN and S R RAJAGOPALAN*†

Raman Research Institute, Bangalore 560 080, India

† Materials Science Division, National Aeronautical Laboratory, Bangalore 560 017, India

Abstract. Investigations on the use of an exponential relaxation technique for studying corrosion systems are reported. It is shown that the polarisation resistance and the double layer capacitance of corrosion systems can be obtained by the small amplitude exponential relaxation technique (SAERT). It is demonstrated, that the rate of corrosion can be measured by the large amplitude exponential relaxation technique (LAERT). This technique yields 'accelerated Tafel plot' only when the charging current is negligible, which is seldom so. Methods for correcting for double layer charging are described. Double layer capacitance as a function of potential is obtained from LAERT. Therefore it can be used for studies on inhibitors. The utility of LAERT for corrosion systems with only one of the conjugate reactions under activation control is established. The effect of series resistance (R_e) is discussed and an *in situ* method for its determination is described. A procedure for correcting the experimental data for errors due to R_e is given.

Keywords. Corrosion rate; polarisation resistance; ohmic drop and double layer capacitance; small amplitude exponential relaxation technique; large amplitude exponential relaxation technique; single transient and multi transient; accelerated Tafel plot.

Introduction

wo exponential relaxation techniques were proposed by Rangarajan (1971) and rabhakara Rao and Rangarajan (1974) for the study of electrode kinetics. One of em employed a small amplitude exponentially decaying current pulse as input ch that the resulting polarisation was in the linear regime of the current-potential lationship. This was called the exponential linear relaxation technique (Rangajan 1971). The second technique which was termed the accelerated Tafel plot TP) (Prabhakara Rao and Rangarajan 1974) employed as input, a large nplitude exponentially decaying current pulse to polarise the electrode to the afel region. This technique, for reasons put forth in this paper, would be more tly described by the term 'large amplitude exponential relaxation technique' AERT).

In spite of several attractive features of these techniques, they have been seldom sed for the study of corrosion systems. There is no reported work on the use of xponential linear relaxation techniques for measuring polarisation resistances (R_p) f corrosion systems. There is one paper (Prabhakara Rao and Yegnaraman 1982) escribing the use of ATP for measuring the corrosion rate (i_{corr}) of the system, iron

---

§ Dedicated to Prof K. S. G. Doss on his eightieth birthday

* To whom all correspondence should be addressed

in 0·5 M H_2SO_4. However, the results show an anomaly, namely i_{corr} is a function of the time constant, τ, of the exponential current signal. The present authors showed that the anomaly is due to the neglect of double layer charging current and described methods of obtaining i_{corr} uncorrupted by charging current from the potential–time transient obtained in the so-called ATP technique (Lakshminarayanan and Rajagopalan 1985). In this paper, we show for the first time, that the small amplitude exponential relaxation technique (SAERT) could be used for measuring R_p and double layer capacity, C_d, of corrosion systems. In addition, we present here the results of the study of several corrosion systems by the ATP technique and show that it gives true i_{corr} and gives information on C_d as a function of potential as well.

2. Theory

2.1 *Small amplitude exponential relaxation technique* (SAERT)

Using the results of Rangarajan we give below the expressions, suitably modified for the corrosion systems, which are characterised by a pair of conjugate reactions. When an exponentially decaying current input of small magnitude is applied to a corrosion system which is purely under activation control, the linearised current-potential relationship takes the form,

$$-C_d \frac{d\eta}{dt} - \frac{(\alpha_c+\beta_a)nF\eta i_{corr}}{RT} = i = \triangle I \exp\left(-\frac{t}{\tau}\right) \tag{1}$$

where $\triangle I \exp(-t/\tau)$ represents the current input, C_d is the double layer capacitance of the corrosion system, α_c and β_a are respectively the transfer coefficients of the cathodic and anodic conjugate reactions of the corrosion system, and i_{corr} is the corrosion rate.

The solution of (1) is given by,

$$\eta = \frac{\triangle I\ R_p\ \tau_d}{(\tau_d - 1)}\left[\exp\left(-\frac{t}{\tau}\right) - \exp\left(-\tau_d\frac{t}{\tau}\right)\right], \tag{2}$$

where $R_p = \dfrac{RT}{(\alpha_c + \beta_a)\ nF\ i_{corr}}$ and $\tau_d = \dfrac{\tau}{R_p C_d}$.

From (2) it is evident that the potential–time transient exhibits a maximum. This arises due to a time lag in over-potential (η) following current (i). We discuss below the methods of obtaining R_p and C_d from η-t transient.

2.1a *Single transient method for measurement of R_p and C_d*: For a corrosion system under activation control, the double layer charging current $[-C_d\,(d\eta/dt)]$ is zero at the maximum point and the entire current is purely faradaic. Utilising this fact it can be shown,

It can also be shown for the same case,

$$T_{\max} = \left(\frac{t_{\max}}{\tau}\right) = \frac{\ln \tau_d}{(\tau_d - 1)} \,. \tag{4}$$

It is clear that using (3) and (4) R_p and C_d can be obtained from a single transient for a corrosion system, which is under activation control.

Another method of obtaining R_p and C_d would be by fitting a curve represented by (2) to the experimental data.

2.1b *Multi transient method for measurement of R_p and C_d:* A third method is to plot $\eta_{\max}$ against i (corresponding to $t_{\max}$) obtained from several transients and evaluate the slope $(d\eta/dt)$ which is equal to R_p.

All the three methods yield R_p values uncorrupted by double layer charging, since at $\eta_{\max}$, $(d\eta/dt) = 0$ and therefore the charging current is also zero whatever be the value of C_d.

Most of the systems exhibiting uniform corrosion fall into one of the following categories.

(i) Both cathodic and anodic reactions are one-step tafelian electron transfers and are under activation control.

(ii) The anodic reaction is a one-step tafelian electron transfer and is under activation control, but the cathodic reaction is partly under mass transfer control or is mass transfer limited.

$$R_p = (RT)/(\beta_a n F i_{\text{corr}}).$$

(iii) The anodic reaction is passive dissolution while the cathodic reaction is a one-step tafelian electron transfer on the passive area

$$R_p = (RT)/(\alpha_c n F i_{\text{corr}}).$$

In all these cases R_p and C_d can be measured by the small amplitude exponential relaxation technique (SAERT). In the case (i) R_p can be found by polarising in either direction. In the case (ii) it is found by polarising in the anodic direction, while cathodic polarisation is to be employed for the case (iii).

2.1c *Effect of series resistance*: The model considered above is C_d across R_p. Experimental measurement always includes a series resistance, R_e. This may have contributions from the resistance of the working electrode, resistance of electrolyte existing between working electrode and the Luggin tip. The presence of R_e, in a current controlled experiment, leads to an additional ohmic drop being included in the measured potential and hence (2) is to be modified as,

$$\frac{\triangle I R_p \tau_d}{(\tau_d - 1)}\left[\exp\left(-\frac{t}{\tau}\right) - \exp\left(\tau_d \frac{t}{\tau}\right)\right] + \triangle I \; R_e \; \exp\left(-\frac{t}{\tau}\right). \tag{5}$$

The coordinates of the maximum of $\eta - t$ transient change due to the presence of R_e. Employing (5) it can be shown

$$\eta^*_{max} = \eta_{max}\left[\exp\left(\frac{-\ln a^*}{\tau_d - 1}\right)\right]\left[1 + \frac{R_e}{R_p}\,\frac{(\tau_d - 1)}{\tau_d}\right], \tag{7}$$

where $a^* = R_p/\left[R_e\dfrac{(\tau_d - 1)}{\tau_d} + R_p\right]$.

η^*_{max} and T^*_{max} are coordinates of the maximum of the η–t transient, when $R_e \neq 0$, and η_{max} and T_{max} are coordinates of the maximum of η–t transient when $R_e = 0$.

It is readily seen from (6) and (7) that in the presence of series resistance, it is not possible to calculate R_p from η^*_{max} and T^*_{max} if R_e is not known. Generally, in current controlled experiments, the error due to ohmic drop in R_e is easily corrected since the value of current is precisely known at each instant if the value of R_e is known. However, the real problem is in knowing the value of R_e.

The exponential relaxation technique provides an elegant method for the *in situ* measurement of R_e. When $R_e \neq 0$, at $t = 0+$, a potential jump occurs in the η–t transient, which is due to the ohmic drop, iR_e. From the magnitude of the potential drop, R_e can be readily calculated. Using this value of R_e recovered experimentally, the η–t profile can be corrected for the ohmic drop due to R_e by using the relation

$$(\eta)_t = (\eta^*)_t - R_e \Delta i \exp(-t/\tau). \tag{8}$$

This technique can therefore be used to evaluate R_p and C_d even without *a priori* knowledge of R_e.

2.2 *Large amplitude exponential relaxation technique* (LAERT)

When a current input of the form $\Delta I \exp(-t/\tau)$, where ΔI is sufficiently large to keep the system in the Tafel region, is applied to a corrosion system under activation control, the resulting current–potential relationship can be shown to be

$$i = \Delta I \exp\left(-\frac{t}{\tau}\right) = -C_d\frac{d\eta}{dt} + i_{corr}\exp\left(\frac{2{\cdot}303\eta}{bc}\right), \tag{9}$$

or

$$i = \Delta I \exp\left(-\frac{t}{\tau}\right) = -C_d\frac{d\eta}{dt} - i_{corr}\exp\left(\frac{2{\cdot}303\eta}{ba}\right), \tag{10}$$

where bc and ba are the Tafel slopes of cathodic and anodic reactions of the corrosion system. If the charging current $[= -C_d(d\eta/dt)]$ is zero, then (9) and (10) become Tafel relations. Under such conditions, $\eta - t$ transient will be a straight line in the large polarisation range, and an accelerated Tafel plot (ATP) is obtained. However, charging current is generally not zero for corrosion systems when transient methods are used for studying them. Therefore, corrosion rates calculated from the linear section of the $\eta - t$ transient will be in error. Even when the double layer charging current cannot be neglected, it can easily be corrected using an elegant approach suggested by Rangarajan (1971) and Prabhakara Rao and Rangarajan (1974). Hence, this method is better called the large amplitude exponential relaxation technique (LAERT) rather than accelerated Tafel plot (ATP). Methods of obtaining true i_{corr} by LAERT after correcting for charging current are described below.

ntirely faradaic since $(d\eta/dt)$ is zero at that instant. Hence a Tafel plot free from e effects of double layer charging can be derived from η_{max} and i at t_{max} of several ansients, obtained by varing ΔI at constant τ. Getting I_{corr}, ba and bc from the afel plot is straightforward.

2b *Single transient method for measurement of* i_{corr} *and* $C_d(E)$: The double yer charging current can be corrected using a single η–t transient. At each η lue, the total current is equal to the sum of faradaic current (i_F) and non-faradaic rrent (i_{nF}). For every η (excepting η_{max}) there are two values of current; one in e rising (i_{t_1}) and another in the falling portion (i_{t_2}). However, as i_F is the same, oth in the rising and falling portions, at constant η, it is easy to show,

$$(i_F)_{t_1} = (i_{t_1}) + C_d\left(\frac{d\eta}{dt}\right), \tag{11}$$

here

$$C_d = [(i_{t_2}) - (i_{t_1}) / \left[\left(\frac{d\eta}{dt}\right)_{t_1} - \frac{d\eta}{dt}\right)_{t_2}\right]. \tag{12}$$

A similar expression has been given by Rangarajan (1973) while discussing the eory of double pulse galvanostatic technique. At each η, i_F can be calculated by 1). By plotting these values of i_F against the corresponding values of η on semilog per, i_{corr} and Tafel slopes can be found. Incidentally C_d as a function of potential recovered from (12).

It is worthwhile pointing out that in LAERT also the presence of R_e will lead to an ror in the measurement of i_{corr}. The method of correction described in §2.1c is lid here also.

Employing the methods described above, i_{corr} can be measured for the following pes of corrosion systems:

) When both the conjugate reactions are under activation control: In this case i_{corr} obtained by polarising in both the directions.

) In the case of systems having one conjugate reaction under activation control d the other partially mass transfer controlled, i_{corr} is obtained by polarising in the rection of the activation controlled reaction.

i) If one of the conjugate reactions is activation controlled and the other diffusion nited, then faradaic current is related to overpotential by

$$i_a = i_{corr}\left[1 - \exp\left(\frac{2{\cdot}303\eta}{ba}\right)\right], \tag{13}$$

the cathodic reaction is diffusion limited ($bc \to \infty$) and

$$i_a = i_{corr}\left[\exp\left(-\frac{2{\cdot}303\eta}{bc}\right) - 1\right], \tag{14}$$

the anodic polarisation has an infinite slop ($ba \to \infty$).

To obtain i_{corr} in this case, the system will have to be polarised in the direction of e reaction which is under activation control and the true faradaic current lculated by the above methods. Using this current, i_{corr} can be obtained from (13) d (14) by curve fitting.

3. Experimental

An ASTM G–72 type corrosion cell is used for the study. The electrode specimen is masked with Araldite (an epoxy resin) to define the area exposed to the electrolyte. The systems studied are (i) mild steel in 0·5 M H_2SO_4, (ii) Armco iron in 0·5 M H_2SO_4, (iii) mild steel in 1 M HCl (for inhibitor study), (iv) copper in 1 M NaCl, (v) Armco iron in 0·52 M NaCl.

For the first four systems, the electrolyte was deaerated with oxygen-free hydrogen. For copper in neutral 1 M NaCl, experiments were conducted both in aerated and deaerated conditions. Measurements were carried out one hour after the attainment of the steady state. Steady state logarithmic polarisation measurements of i_{corr} were carried out immediately after recording ATP.

The block diagram of the experimental set-up is shown in figure 1. An exponentially decaying waveform is generated by applying a rectangular pulse to a *RC* net work and half-wave rectifying the resulting waveform. This is applied to the cell using a fast response potentiostat in the galvanostatic mode developed for this purpose (V Lakshminarayanan, Aithu Poojary and S R Rajagopalan 1981, unpublished results). The transients obtained by SAERT and LAERT are corrected for ohmic drop due to R_e by the method given in § 2.1c.

4. Results and discussions

Figure 2 shows a typical η–t transient obtained for mild steel in 0·5 M H_2SO_4.

R_p values obtained by all the three methods described above are given in table 1 for several corrosion systems studied in this work. They are in good agreement with the steady state linear polarisation value. Hence, the small amplitude exponential relaxation method can be considered a transient analogue of the linear polarisation technique.

To assess the validity of the method of correction for the ohmic drop due to R_e given in § 2.1c, experiments were conducted using a dummy cell ($R_e = 100\,\Omega$, $R_p' \equiv 10\,\Omega\,cm^2$ and $C_d' \equiv 10\,\mu F/cm^2$). The values of R_p' calculated from uncorrected and corrected transients are 108·4 Ω and 9·83 Ω respectively. It is clear that the method suggested in this work effectively corrects for the ohmic drop due to R_e.

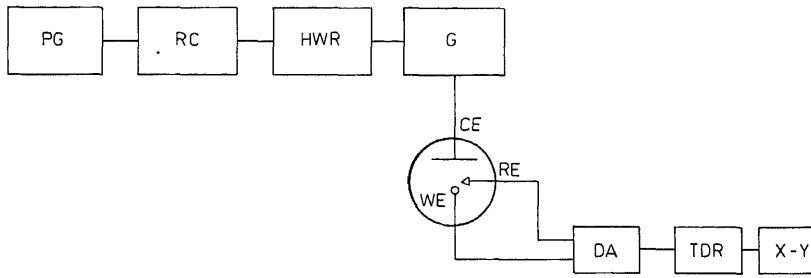

Figure 1. Block diagram of the set-up used for exponential relaxation technique. PG - pulse generator; RC – RC network; HWR – half-wave rectifier; G – galvanostat; CE – counter electrode; RE – reference electrode; WE – working electrode; DA – dif-

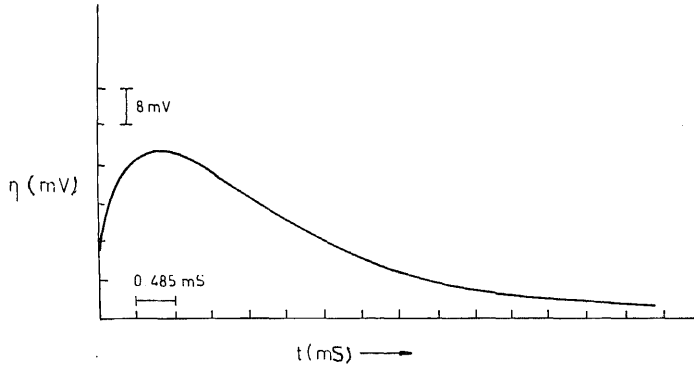

Figure 2. Potential–time transient obtained at $\tau = 1$ ms and $\Delta I = 10$ mA/cm^2 for MS/0·5 M H_2SO_4.

Table 1. Polarisation resistance (R_p) of some corrosion systems obtained by SAERT.

System	Method	τ (m sec)	R_p from cathodic polarisation (ohm cm^2)	R_p from anodic polarisation (ohm cm^2)
MS/0·5 M H_2SO_4 (deaerated)	Method 1 [by using (3)]	1	14·71	14·21
		1000	13·98	14·56
	Method 2 (by curve fitting)	1	15·38	14·25
	Method 3 (Multi-transient approach)	1	14·85	14·52
		1000	13·72	13·85
	Steady state linear polarisation (SSLP)	—	14·02	14·07
Armco iron/ 0·5 M H_2SO_4 (deaerated)	1	100	194	208
		1000	196	197·2
	2	100	201·6	205·1
	3	100	202·3	207·2
		1000		
	SSLP	—	205·0	205·0
Armco iron in 0·5 M NaCl (aerated)	1	100	—	79·48
		1000	—	82·34
	2	100	—	80·10
	3	100	—	81·50
		1000	—	80·90
	SSLP	—	—	82·00
Copper in 1 M NaCl (aerated)	1	100	—	292
		1000	—	312
	2	100	—	305
	3	100	—	295
		1000	—	301
	SSLP	—	—	310
Copper in 1 M NaCl (deaerated)	1	500	—	$3{\cdot}55 \times 10^3$
		5000	—	$3{\cdot}57 \times 10^3$
	2	500	—	$3{\cdot}33 \times 10^3$
	3	500	—	$3{\cdot}70 \times 10^3$
		5000	—	$3{\cdot}45 \times 10^3$

C_d values obtained by SAERT are given in table 2. The values of C_d obtained for systems containing acid solutions or deaerated NaCl are of the expected order of magnitude. In the case of systems having aerated NaCl solution C_d values are large. This is presumably due to large pseudo-capacitance. Similar observation has been reported in literature (Kanno *et al* 1980) for mildsteel in aerated NaCl.

Figure 3 shows i_{corr} of MS in 0·5 M H_2SO_4 (deaerated) obtained from the straight line portion of the η–t curve. No correction for charging current has been carried out in this case. It is seen that i_{corr} increases with increasing τ and $\triangle I$. It tends to a value corresponding to steady state logarithmic polarisation at higher time constants and lower $\triangle I$. Table 3 gives i_{corr} of MS in 0·5 M H_2SO_4 obtained at various τ values after correcting for charging current by using the procedures described. It is seen that i_{corr} calculated after correcting for double layer charging is independent of τ. This clearly shows that the correction for charging current is a must in this transient technique for getting true i_{corr}. It is also seen that i_{corr}

Table 2. Double layer capacitance (C_d) for some corrosion systems obtained by SAERT.

System	Method	τ (m sec)	C_d from cathodic polarisation ($\mu F/cm^2$)	C_d from anodic polarisation ($\mu F/cm^2$)
MS/0·5 M H_2SO_4	Curve fitting (i)	1	86·71	93·56
	From η_{max} and t_{max} [using (3) and (4)] (ii)	1	89·78	91·80
Armco iron/ 0·5 M H_2SO_4	(i)	100	83·13	77·15
	(ii)	100	80·0	78·00
Armco iron in 0·52 M NaCl (aerated)	(i)	100	—	1395
	(ii)	100	—	827
Copper in 1 M NaCl (aerated)	(i)	500	—	290
	(ii)	500	—	275
Copper in 1 M NaCl (deaerated)	(i)	500	—	134
	(ii)	500	—	139

Table 3. Corrosion rate of MS in 1 M H_2SO_4 (deaerated) obtained at various τ values by LAERT.

Method	τ (m sec)	i_{corr} (mA/cm^2) from cathodic Tafel line	i_{corr} (mA/cm^2) from anodic Tafel line	bc (mV)	ba (mV)
Multi-transient	1	1·45	1·30	93	76
	100	1·40	1·35	99	83
	1000	1·35	1·35	99	83
Single transient	5	1·40	1·40	103	83
	10	1·40	1·40	96	86
	50	1·40	1·40	96	83
Logarithmic					

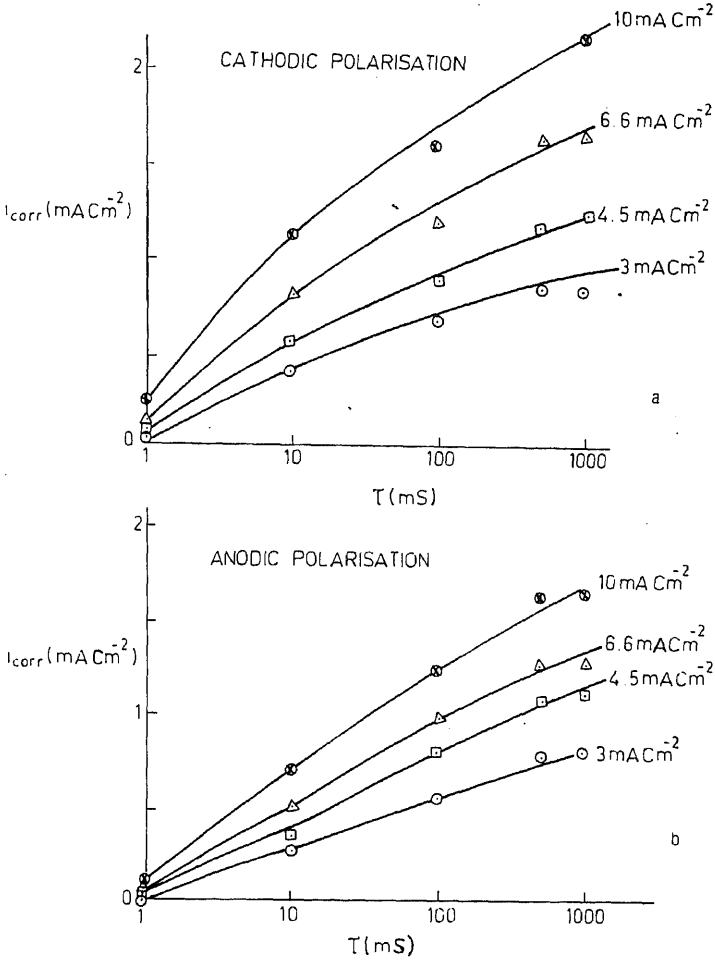

Figure 3. **(a)** Plot of i_{corr} vs. η obtained at several applied current densities (ΔI) from cathodic accelerated Tafel plots. **(b)** Plots of i_{corr} vs. η obtained at several applied current densities (ΔI) from anodic accelerated Tafel plots.

tained by the two procedures of correcting for charging current are in good reement with logarithmic polarisation value.

Table 4 gives the i_{corr} obtained for the systems Armco iron in 0·5 M H_2SO_4, mco iron in 3% NaCl (0·52 M) and copper in 1 M NaCl. The values obtained by th single and multi-transient methods are in good agreement with the steady te logarithmic polarisation.

In the case of copper and iron in NaCl, the cathodic reactions are under partial ss transfer control while the anodic reaction is under activation control. Hence these, corrosion rate has been obtained from anodic transients alone.

From (4) it is seen that any errors in the estimation of slope will affect the culation of charging current, which in turn will affect the accuracy of calculation

Table 4. Corrosion rates of some corrosion systems obtained by LAERT.

System	Method	τ (m sec)	From cathodic plot (mA/cm^2)	From anodic plot (mA/cm^2)	bc (mV)	ba (mV)
Armco iron in 0·5 M H_2SO_4	Multi-transient	100	0·074	0·074	93	73
		1000	0·074	0·072	93	73
	Single transient	100	0·074	0·074	90	73
		1000	0·070	0·070	90	76
	Logarithmic polarisation	—	0·072	0·072	93	73
Copper in 1 M NaCl	Multi-transient	100	—	0·062	—	51·5
		1000	—	0·060	—	56·0
	Single transient	100	—	0·065	—	52·5
		1000	—	0·068	—	57·1
	Logarithmic polarisation	—	—	0·060	—	53·5
Copper in 1 M NaCl (deaerated)	Multi transient	500	—	0·0032	—	53
		5000	—	0·0034	—	54·8
	Single transient	500	—	0·0030	—	53
	Logarithmic polarisation	—	—	0·0032	—	56·48
Armco iron in 3% NaCl (aerated)	Multi-transient	100	—	0·180	—	79·7
		1000	—	0·180	—	79·7
	Single transient	100	—	0·180	—	79·7
		1000	—	0·170	—	83·7
	Logarithmic polarisation	—	—	0·180	—	83·7

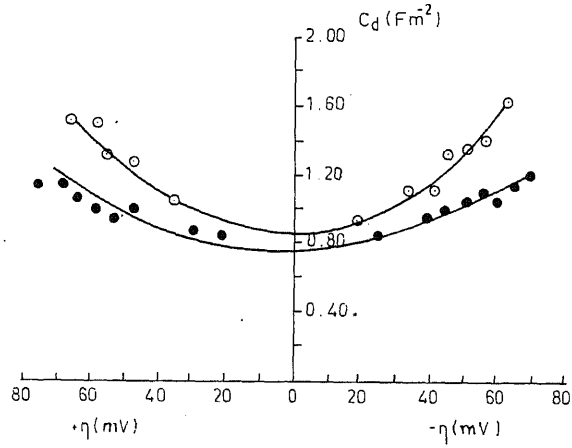

Figure 4. C_d as a function of potential for the system of MS in 0·5 M H_2SO_4 (deaerated) with and without hexamine inhibitor. ⊙ without inhibitor; ● with 10 mM hexamine inhibitor.

non faradaic. The ratio of faradaic to non faradaic

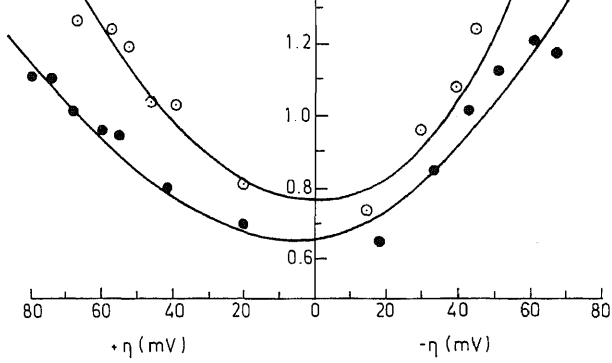

Figure 5. C_d as a function of potential for the system of MS in 1 M HCl (deaerated) with and without acetyl acetone inhibitor. ⊙ without inhibitor; ● with 0·1 M acetyl acetone inhibitor.

Table 5. Effect of inhibitors on corrosion rates.

ystem	τ (m sec)	Inhibitor	Inhibitor concentration (M)	i_{corr} (mA/cm^2) Single transient From cathodic Tafel line	From anodic Tafel line	i_{corr} (mA/cm^2) Multi-transient From cathodic Tafel line	From anodic Tafel line
IS/0·5 M H_2SO_4	50	Hexamine	0	1·393	1·428	1·428	1·428
			0·01	0·385	0·385	0·385	0·400
IS/1 M HCl	20	Acetyl-acetone	0	0·7	0·7	0·72	0·70
			0·1	0·310	0·320	0·300	0·310

t low τ. As a rule of thumb, it is better to use $\tau \geq 10\ R_pC_d$. Too large a τ should be voided since it might lead to concentration polarisation at large ΔI.

Figure 4 shows C_d as a function of potential for MS in 0·5 M H_2SO_4 obtained at = 50 msec. The effect of adding hexamine (10 mM) is also shown in figure. The owering of C_d brought about by the adsorption of inhibitor is clearly seen. Figure 5 hows similar behaviour for MS in 1 M HCl with 0·1 M acetyl acetone as inhibitor. Table 5 shows the effect of hexamine (10 mM) on the corrosion rate of MS in 0·5 M H_2SO_4 and the effect of acetyl acetone on the corrosion rate of MS/1 M HCl.

. Conclusions

. SAERT can be considered a transient analogue of the steady state linear olarisation technique, while LAERT can be considered that of the steady state ogarithmic polarisation technique. The straight line portion of the η–t curve

cannot be considered the 'accelerated Tafel plot' (ATP) as it contains contributions from the double layer charging current also. Hence it is preferable to call this the large amplitude exponential relaxation technique (LAERT).

2. SAERT involving both multitransients and single transients can be used to obtain polarisation resistances R_p and double layer capacitances C_d of corrosion systems.

3. With the single transient method one can get either R_p (by SAERT) or i_{corr} (by LAERT) by perturbing the electrode for very small time periods and thus preventing excessive polarisation of the electrode. Besides, the single transient method is quite fast for close monitoring of R_p and I_{corr}.

4. LAERT using a single transient provides information on C_d as a function of potential which is useful in the study of inhibitors and for investigating area changes with time.

5. Both the relaxation techniques have an in-built advantage of *in situ* measurement of R_e which permits correction for the ohmic drop due to R_e.

Acknowledgement

The authors thank Professor S K Rangarajan for the many stimulating discussions they had with him.

List of symbols

b_a and b_c – anodic and cathodic Tafel slopes of conjugate reactions of the corrosion system;
C_d – double layer capacitance;
ΔI – amplitude of exponentially decaying current input;
i_{corr} – corrosion rate;
i_F – faradaic current;
i_{nF} – non-faradaic current;
i_{t_1} – total applied current at the rising portion of η–t curve;
i_{t_2} – total applied current at the falling portion of η–t curve;
R_p – polarisation resistance;
R_e – solution resistance;
t_{max} – time corresponding to maximum of $\eta - t$ curve;
T_{max} – t_{max}/τ;
T^*_{max} – t_{max}/τ in the presence of solution resistance;
α_c and β_a – cathodic and anodic transfer coefficients respectively for the conjugate reactions of the corrosion sytem;

References

anno K, Suzuki M and Sato Y 1980 *Werkst. Korros.* **31** 364

akshminarayanan V and Rajagopalan S R 1985 *Proc. International conference on corrosion science and technology* Indian Institute of Metals and Indian Institute of Technology – Kharagpur, February, Calcutta, (in press)

rabhakara Rao G and Rangarajan S K 1974 *J. Electroanal. Chem.* **55** 151

rabhakara Rao G and Yegnaraman V 1982 *Proc. Indian Natl. Sci. Acad.* **A48** 392

angarajan S K 1971 *J. Electroanal. Chem.* **32** 329

angarajan S K 1973 *J. Electroanal. Chem.* **41** 491

Electrobioluminescence – a novel method for understanding bioluminescent mechanisms[§]

K S V SANTHANAM
Tata Institute of Fundamental Research, Colaba, Bombay 400 005, India

Abstract. The chemistry of the formation of excited states in living systems is probed by using the electrochemical techniques. A new method of using a living animal as an electrode provides mechanistic details on the various steps involved and the overall energetics of the process of excited state formation. This is discussed in detail with reference to the newly developed earthworm electrode which glows upon potential sweep or step programme in an electrochemical cell.

Keywords. Electrobioluminescence; earthworm bioluminescence; firefly bioluminescence; electron injection; cyclic-voltammetry of living animals.

1. Introduction

The phenomenon of some living animals generating bioluminescence has been known and investigated (Adams and Cilento 1982; Hastings 1983a) for understanding the chemistry of the excited states. The approach has been to isolate the chromophore and the enzyme for simulating the observed emission features. The energetics of such reactions have been considered in detail (Kosower 1981; Ward and Cormier 1978; Hastings 1983b) in selected systems. An interesting outcome of these studies has been the identification of new pathways for excited state formations and a realization that some of the living systems produce excited states at efficiencies $> 90\%$. So far it has seldom been possible to study bioluminescent mechanisms in the living state. A method which has recently been developed called electrobioluminescence (EBL) offers some unusual advantages for investigating the mechanistic schemes, sensitivity to external conditions in generating the excited states and the effect of electrolytes on the production efficiencies of excited states. This has been based on the generation of bioluminescence by living animals under the influence of an externally impressed voltage (Ismail and Santhanam 1984; Limaye and Santhanam 1986a and b). It may be considered as stimulated bioluminescence where a chemical reaction is initiated by the application of an appropriate voltage resulting in the overall production of the excited state. A photon is emitted upon the excited state returning to the ground state. A primary requisite for the study is that the animal chosen is amenable for its development as an electrode.

The formation of the excited state in living systems is caused by the generation reaction

$$\mathrm{L} + \mathrm{Lase} \xrightarrow{\mathrm{R}} \text{products} + h\nu, \qquad (1)$$

where L represents luciferin, Lase represents the enzyme luciferase and R represents the activator. The chromophore of luciferin is significantly different

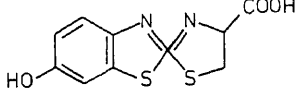	Firefly	552–590
	Bacteria	470–500
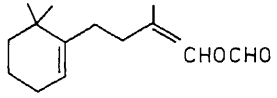	Latia	535
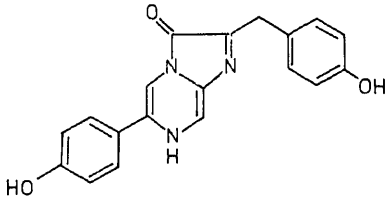	Coelenterazine (Renilla, Aequorea)	470
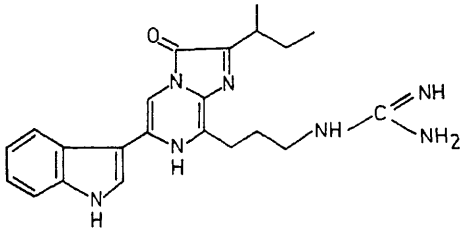	Cypridina	462
Earthworm luciferin (?)	Lampito mauritii	495

from one species to another. The EBL reaction may also be represented by (1). A few examples of luciferins are shown in table 1.

2. Chemical mechanisms: from chemical bonds to photons

One of the complex questions that arise in considering reaction (1) is about the nature of the chemical process which would release enough energy in one step to form the excited state. Here the nature of L and R would control the reaction. Another important question is the efficiency of bioluminescence and how it changes from one system to another. The answers to these questions can be generated by a study of EBL; it provides a comparison of *in vivo* to *in vitro* bioluminescence.

(a) *Electron transfer reactions of radical ion annihilation*: The chemiluminescence that is often produced by the reaction of oppositely charged aromatic ion radicals in aprotic solvents has been considered as a one-step excitation to give the product in the excited state. It is considered as an electron transfer reaction with no intermediate formation of a bond. A typical reaction is shown in figure 1. Here the free energy released in the electron transfer reaction is taken as one parameter and the changes in solvation as the other (Periasamy and Santhanam 1977; Kulkarni *et al* 1978a, 1978b). Marcus (1965, 1970) pioneered this model based on dielectric polarization, where

$$G_{\text{pol}} = m^2 e^2 \left(\frac{1}{2r_+} + \frac{1}{2r_-} - \frac{1}{R} \right) \left(\frac{1}{D_O} - \frac{1}{D_S} \right) \tag{2}$$

r_+ and r_- are the radii of the cation and anion, R the interionic distance, D_O and D_S the optical and dielectric constants and m the reaction coordinate for solvent dipole reorientation. The above expression can be simplified to $G_{\text{pol}} = m^2\ \lambda$ where

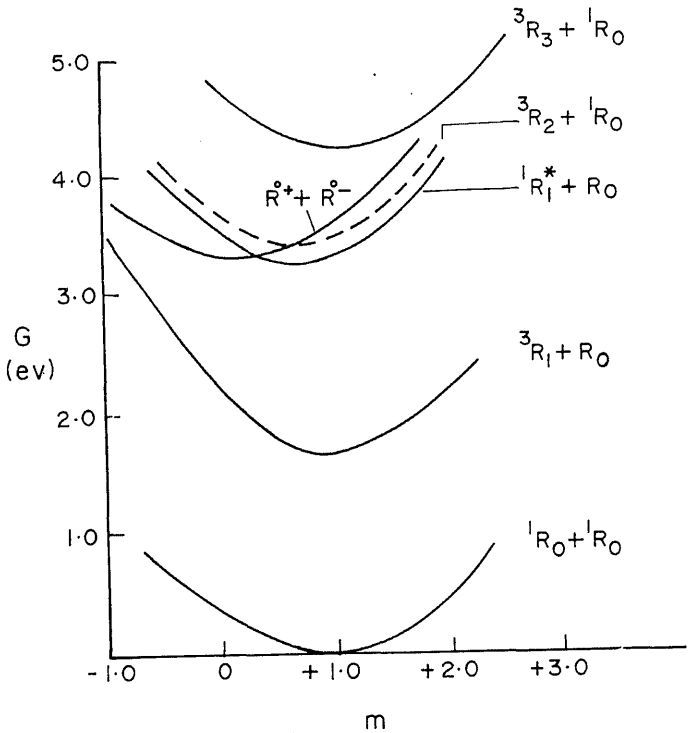

Figure 1. Free energy curves for electron transfer bioluminescence. $^1R_0$ = ground singlet state, $^3R_1$ = first triplet state, $^3R_2$ = second triplet state, $^1R^*$ = first excited single state, $\dot{R}^+$ = free radical cation, and $\dot{R}^-$ = free radical anion; m represents the parameter defined in the text.

λ constitutes the product of the parameters in the brackets multiplied by the charge. The free energy of the product molecules is considered with

$$\Delta G_{pol} = E_{S_1} \text{ (or } E_{T_1}) + (m-1)^2,$$

where E_{S_1} and E_{T_1} are the energies of first singlet and first triplet states respectively. The region of intersection of the separated ions and products is defined by m^* which has direct relationship to E_{S_1} or E_{T_1} and the ΔG^0 of the reaction. The accessibility of the product states is given by the intersection region and the rate of formation of the product state is defined by

$$k_s = gpz \exp\left\{-\frac{\lambda}{4RT}\left[1+\frac{E_{S_i}+\Delta G^0}{\lambda}\right]^2\right\}, \tag{3}$$

where g is the spin statistical factor, p the probability factor and z the collision frequency. For the triplet state E_{S_1} will have to be replaced by E_{T_1} and the appropriate ΔG^0 (Periasamy and Santhanam 1977).

The free energy of the reaction is calculated from the electrochemical potentials. For the reactions

$$R + e \rightleftarrows R^{\cdot -}, \; E^0 \; (R/\dot{R}^-), \tag{4}$$

$$R - e \rightleftarrows R^{\cdot +}, \; E^0 \; (\dot{R}^+/R), \tag{5}$$

$\Delta G^0 = E^0_{(R/R^-)} - E^0_{(R^+/R)}$. The ΔG^0 is generally large for several electron transfer reactions of the above type and in the range of 1–4 eV; in several cases the emitting state is the excited singlet state. Thus, with the available energy, chemi-excitation is in general possible. Table 2 lists selected examples of the electron transfer reactions. However, in some situations ΔG^0 is less than the excited singlet state and in such situations, the energy is enough to populate the accessible triplet state ($\Delta G^\circ \geq E_T$). The resulting triplets annihilate to produce the excited singlet state of the molecule (Periasamy *et al* 1973). The chemi-excitation process is generally efficient in electron transfer reactions. However, this type of electron transfer reactions has not been considered in bioluminescence until recently, mainly

Table 2. Electron transfer reactions[a].

Type of Reaction	$-\Delta G^0$ (eV)	E_{S_1} (eV)	E_{T_1} (eV)	λ (nm)
$DP\dot{A}^- + D\dot{P}A^+$	3·08	3·00	1·84	440
$Rub^- + R\dot{u}b^+$	2·29	2·30	1·10	600
$A\dot{N}^- + A\dot{N}^+$	3·36	3·20	1·80	420
$DP\dot{A}^- + TMP\dot{D}^+$	1·97	3·00 (DPA)	1·80 (DPA)	440
$Rub^- + TMP\dot{D}^+$	1·56	2·30 (Rub)	1·10 (Rub)	600

[a] Reactions carried out in aprotic solvents containing 0·1 M $(C_4H_9)_4NClO_4$. DPA = 9,10-diphenylanthracene, Rub = rubrene, AN = anthracene, TMPD = N,N,N^1,N^1 tetramethyl-*p*-phenylene diamine.

o be modified in the light of this factor; in these situations also, electron transfer eactions must be involved before the excited state is formed, and hence, a hybrid eaction mechanism should be considered.

b) *Reactions of the peroxide type*: The reaction mechanisms considered here use xygen as the component of the reaction and the peroxide $-O-O-$ bond is ormed prior to the formation of the excited state. The discovery by Kopecky and Mumford (1969) that isolated ring peroxides produce high yields of electronically xcited products led to several postulates of peroxides in bioluminescence. The reakdown of the peroxide ring can generate about 4 eV which would be enough to orm a product in an excited state. McCapra and Richardson (1964) proposed the -O-O- bond formation in bioluminescent systems such as firefly and cypridina. The following sequence has been visualized

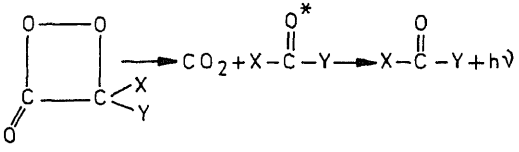

(6)

Chart 1.

X and Y represent the chromophores. Kosower (1981) considered the energetics of he above reaction scheme in detail and suggested that the thermal decomposition f the $-O-O-$ bridged compound may not be a one-step process but may be aused by an electron transfer step (see subsequent section). Interestingly it has een shown (Stone 1968) that for every O_2 (the earlier step to the formation of -O-O- bridge) that is consumed in the reaction, a CO_2 molecule and a carbonyl noiety are produced. A quantum yield close to unity has been demonstrated Seliger and McElroy 1960). Later Plant *et al* (1968) used labelled ^{14}C-carboxy uciferin and demonstrated the quantitative liberation of CO_2 in the reaction. The verall reaction can be represented as

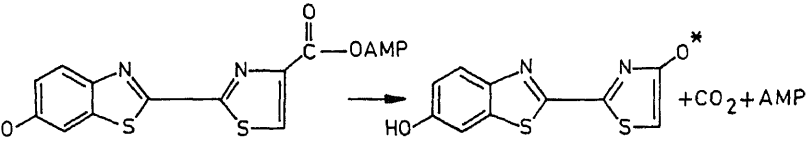

(7)

Chart 2.

The formation of ring peroxides in bioluminescent reactions opens up new athways for combining electron transfer reactions and the excited state formation.

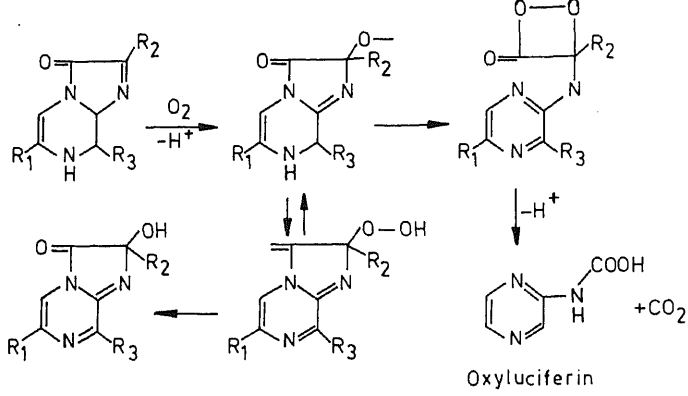

(8)

Chart 3.

The proposed oxidative mechanisms were discussed by Shimomura *et al* (1977) and the proposed mechanism is shown below.

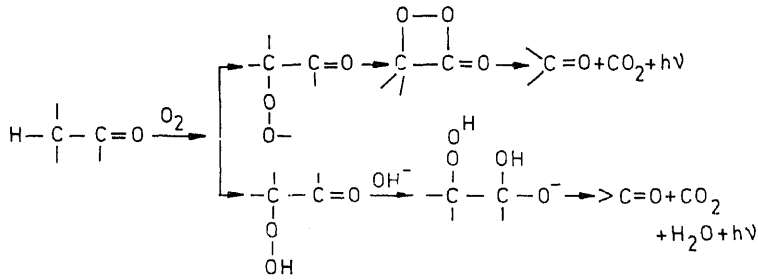

(9)

Chart 4.

As can be seen in the above reaction scheme, the upper path involves a dioxetane bridge formation and the latter involves the participation of the solvent. The experimental results support the upper pathway. The two mechanisms were differentiated by using labelled $H_2^{18}O$ and $^{16}O_2$ and $H_2^{16}O$ and $^{18}O_2$ (DeLuca and Dempsey 1973; Shimomura *et al* 1977).

Peroxide bridge formation is also recognized in aequoera (jellyfish). However the photoprotein will emit light upon addition of calcium ion (Shimomura and Johnson 1975). Here an enzyme substrate peroxide intermediate is produced and stored in the cell. The intermediate is able to react with calcium and emit flashes (Hastings and Morin 1969).

Although cyclic peroxide formation is overwhelmingly established, laboratory experiments with such cyclic peroxides generate triplet states rather than excited singlet states; this step requires thermal decomposition. If the triplet state is produced, then the excited singlet state formation would require an energy

eld, the reaction scheme requires a higher energy conservation step. Hence an ectron transfer scheme [such as that discussed in (a)] and a peroxide mechanism ould be required. The electron transfer scheme is by far the most efficient emi-excitation process. One such proposal is that the disintegration of peroxide used by an electron transfer reaction (Adams and Cilento 1982; Koo and huster 1977) charge annihilation and chemi-excitation follows the above action. With a view to test such a process the following reaction has been rformed between several radical cations (R^+) and diphenyl peroxide (DPP). The llowing reaction sequence is proposed.

$$R + DPP \rightarrow (R^+ + DPP^-)_{cage}. \tag{10}$$

ith the low stability of the radical anion, it undergoes decarboxylation.

$$(R^+ + DPP^-)_{cage} \rightarrow (R^+ + BC^- + CO_2)_{cage}. \tag{11}$$

C is the product of the decarboxylation of DPP (benzocoumarin). As BC^- is a werful reducing agent (E^0 of the redox couple is very negative), the electron nsfer reaction in the cage will occur to produce the excited state.

$$(R^+ + BC^- + CO_2)_{cage} \rightarrow ({}^1R^* + BC + CO_2)_{cage}. \tag{12}$$

nce the cage reaction should be sensitive to the dielectric constant of the medium, e above reaction occurs spontaneously in solvents like DME, THF, etc.
For bioluminescence the following charge transfer resonance structure of the oduct state is expected on the basis of the above scheme.

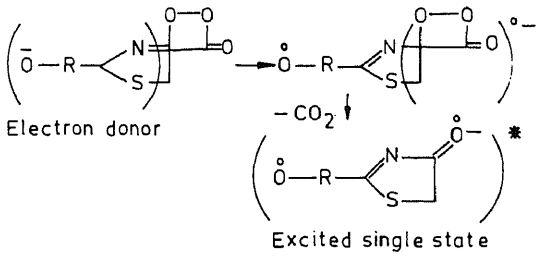

(13)

Chart 5.

is pathway can produce high quantum yields.

) *Reactions involving specific ions*: A specific ion requirement has been noticed the bioluminescence of marine animals. *Renilla* bioluminescence requires Ca^{2+} r binding to the protein (Cormier *et al* 1970, Cormier 1978). The nerve impulse is ked through Ca^{2+} and the protein; the latter is a single peptide chain of olecular weight 18,500 and contains two high affinity Ca^{2+} binding sites. The tive protein carries luciferin (one mole) and is referred to as blue fluorescent otein (BP–LH_2) [the luciferin (LH_2) is bound to the protein]. Here the linkage

has been considered to be noncovalent. The addition of BP–LH_2 to luciferase does not produce emission of light because bound LH_2 is sterically hindered for the reaction. When Ca^{2+} is added to it, the ion displaces the LH_2 due to a conformational change in BP–LH_2 and light emission occurs.

The following sequence of reactions is required for the ion formation

$$BP-LH_2+Ca^{2+} \rightleftarrows BP-Ca+LH_2, \tag{14}$$

$$BP-Ca+LH_2+E \rightleftarrows E-LH_2+Ca-BP, \tag{15}$$

$$E-LH_2+Ca-BP \rightarrow \text{Oxyluciferin}^*-E+CO_2. \tag{16}$$

In contrast to aequorea, the emission of radiation occurs only upon the addition of Ca^{2+} (Shimomura and Johnson 1975); the substrate (LH_2) is bound to the enzyme and its release occurs upon addition of Ca^{2+}. The reaction sequence may be visualized as

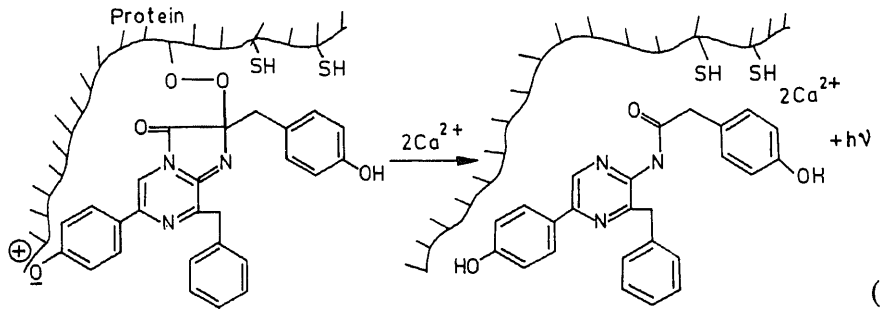

(17)

Chart 6.

2.1 *Mechanisms investigated by* EBL

The *in vivo* understanding of bioluminescence is most challenging due to the interlinking of reactions. Self-triggering mechanisms generally operate to produce bioluminescent chemicals. However, some animals generate bioluminescence under chemical or electrochemical excitation–which may be termed external control. Of these two types, chemical excitation results in the excitor being a component of the reaction scheme and often this results in the destruction of the animal. The electrical excitation offers an advantage over this except that in this case electrochemical reactions may be occurring on the surface of the animal. The development of an earthworm (*Lampito mauritii*) electrode (Limaye and Santhanam 1985) has the potentiality for investigating bioluminescent reaction mechanisms. This electrode is used in an electrochemical cell carrying an electrolytic solution; the role of specific ion requirement can be investigated by this method. Here the excited state is produced on the surface of a "live electrode".

A typical set up for EBL is shown in figure 2. The earthworm electrode (EWE) is prepared by carefully washing the earthworm in distilled water and following the procedure described earlier (Limaye and Santhanam 1986a). Using the EWE as the working electrode and a large mesh platinum grid [1·0 cm × 1·0 cm] as the auxiliary electrode, the potential of the EWE is swept linearly with time and the resulting

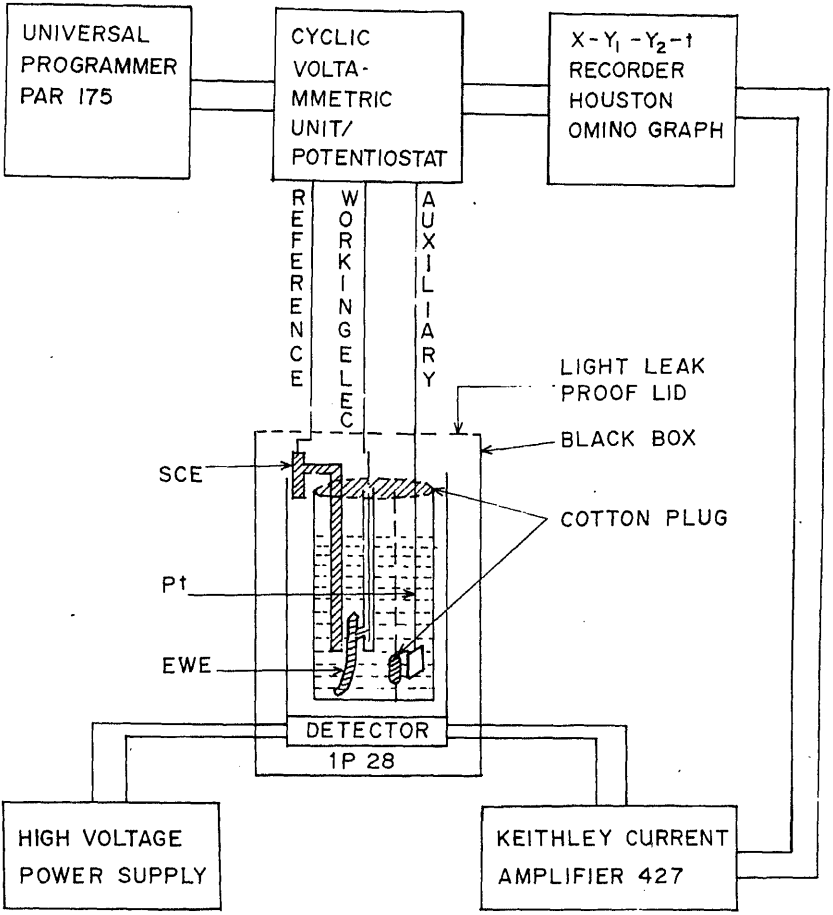

Figure 2. Experimental set-up for EBL. Reference, working and auxiliary electrodes are as shown.

lectrode in this scheme. The recording of the current-voltage curve provides the nset potential for luminescence and the resulting current as a measure of the eactions at the electrode. The onset potential is characteristic of the reaction itiating the electron transfer step. With EWE, the onset potential is −0·56 V vs CE and suggests a 2*e* reduction of O_2 as the initiator of the luminescence. Experiments conducted by saturating the electrolyte solutions with O_2 and removal f O_2 by degassing produce drastic changes in the bioluminescence output. Further

The influence of the electrolyte in the medium produces marked changes in the output of the EWE. Table 3 shows the EBL output of the EWE in different electrolytes. Ca^{2+} in the medium produces the highest EBL output, while Fe^{2+} or Fe^{3+} or Cu^{2+} in the medium produces the lowest (Limaye and Santhanam 1986a). The influence of Ca^{2+} on the bioluminescence output has been investigated by isolating the bioluminescence chemicals. Experiments *in vitro* do not produce higher luminescence output than has been obtained with other electrolytes such as K_2SO_4 or $MgSO_4$. The chemiluminescent kinetics in the above experiments were very similar. These results in comparison with EBL suggests Ca^{2+} is not an ingredient of the bioluminescent scheme as in *aequorea*; it does not release the substrate-bound protein. The highest EBL output in Ca^{2+} medium arises from the process of coelomic cell displacement on the electrode. A relative comparison of the EBL emission durations in Ca^{2+} to any other ion such as K^+ or Mn^{2+} is much longer i.e. 320 s to 100 s; the rate of decay in Ca^{2+} solution is slower than in K^+ or Mn^{2+} ion solution. The EBL output shows a correlation with action potential; the amplitude of the action potential is related to Ca^{2+} concentration. It changes from -30 mV to $+30$ mV from negligible Ca^{2+} concentration 0·1 mM to 100 mM. Ito *et al* (1970) obtained a linear relationship between Ca^{2+} concentration and the intracellularly evoked spikes. These plots had a slope of (26)/10 mV$\times$(Ca^{2+}). The membrane potential of the longitudinal muscle does not show a change from its -35 mV upon addition of Ca^{2+}.

The EWE does not generate any luminescence in solutions of Fe^{2+}. Two possible explanations may be offered; (a) it is known to decompose H_2O_2 through (Halliwell and Gutteride 1984),

$$Fe^{2+} + H_2O_2 \rightarrow Fe^{3+} + OH^{\cdot} + OH^{-}, \tag{18}$$

Table 3. Relative photonic output of EWE in different electrolytes[a].

Medium	Relative photonic output
0·1 M K_2SO_4	1·00
0·1 M $FeSO_4$	0·00
0·1 M $Fe_2(SO_4)_3$	0·00
0·1 M $CuSO_4$	0·00
0·1 M $CaCl_2$	1·98
0·1 M $MnCl_2$	0·63

[a] The potential step programming is done from 0 to $-1{\cdot}0$ V. The data collected is an average of 25 worms. The EWE is stable after the experiment. The earthworm is not visually damaged. The relative photonic output is calculated with reference to the output in 0·1 M

ill precede O_2 reduction at the EWE. The effect of Fe^{3+} on EWE output is more mplex; the presence of Fe^{3+} in bioluminescent *in vitro* reaction does not affect e emission intensity. Hence the enzyme in activation of the reaction (1) by specific nding of Fe^{3+} or Fe^{2+} can be conclusively ruled out. With iron salts, aber–Weiss reaction

$$H_2O_2+O_2^- \rightarrow OH^{\cdot}+OH^-+O_2 \tag{19}$$

also likely to occur; in this situation the EBL reaction will have to be considered as ccurring as follows

$$O_2+e \rightleftarrows O_2^-, \tag{20}$$

$$2O_2^-+2H^+ \rightarrow 2HO_2 \rightarrow H_2O_2+O_2 \tag{21}$$

$$O_2+2e \rightarrow O_2^{-}{}^-+2H^+ \rightarrow H_2O_2\,. \tag{22}$$

he rate of formation of H_2O_2 in mitochondria (Boveris and Turrens 1980) reflects ie rate of univalent reduction of oxygen and it has been demonstrated to reach 5% of the total O_2 consumption (Boveris and Turrens 1980). Hence the presence f Fe^{3+} in the medium appears to inactivate the displacement of coelomic cells on ie EWE. For similar reasons Cu^{2+} also inhibits the EBL output.

3 *Correlation of the Faradaic current and EBL*

he Faradaic current during EBL has been shown to have a quantitative correlation the photons liberated (Limaye and Santhanam 1986a); this produced a correlation f electron input to the photon output. Figure 2 shows the results obtained with WE in a K_2SO_4 electrolyte. The linearity observed in this correlation suggests the osence of other biological stimulii on this electrode. It is noteworthy that in none f the experiments with EWE has there been an output of one photon per electron iput. Considering the first step in EBL as oxygen reduction (initiator of ioluminescence) consumption of $2e$ would be expected. The observed correlation ere suggests there are other side reactions operating along with the above eaction. Nevertheless in the above reaction a maximum efficiency of 50% is chieved for the best EWE prepared in our experiments.

The general current decay pattern of a species in solution undergoing an lectrode reaction by a process of diffusion control, is defined by (Bard and aulkner 1980)

$$i_f = nFAD^{1/2}C^*/(\pi^{1/2}\,t^{1/2}), \tag{23}$$

nd the current decaying pattern at an EWE markedly deviates from the above efinition because of significant convection at the electrode due to the orderly ovement of the earthworm. This aspect is reflected in the current-time curve own in figure 3. The extent to which these oscillations occur in a slow sweep lectrochemical experiment (such as cyclic voltammetry) is too small for its

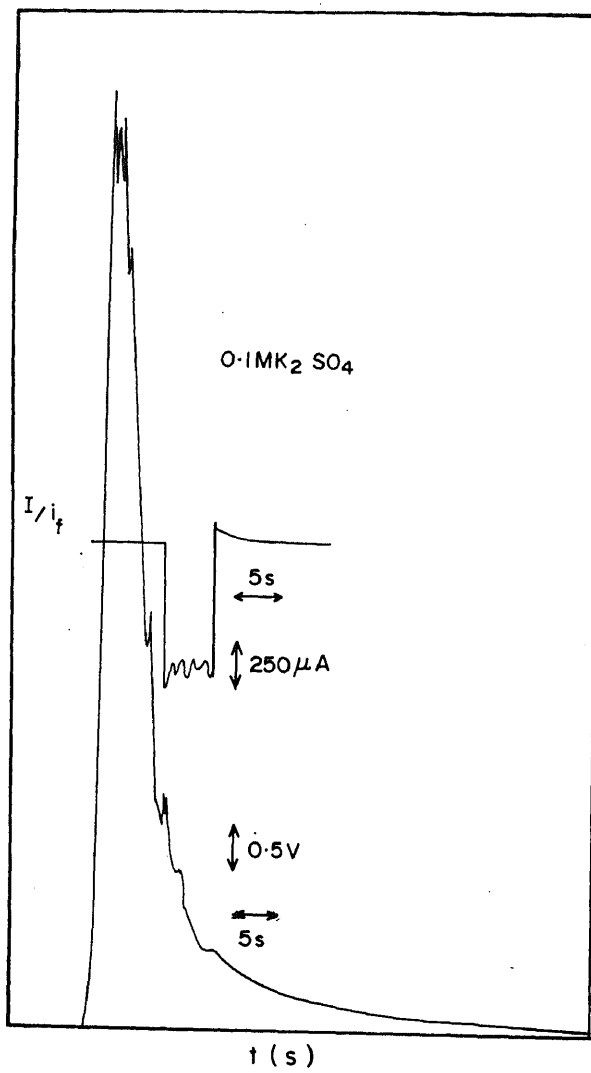

Figure 3. Current-time curve (at the centre) for potential step electrolysis of the *Lampito mauritii* electrode in 0·1 M K_2SO_4 media. Step potential 0 to −1·0 V vs SCE. i_f represents the current. Intensity-time curve during the above potential step. I = intensity.

observations by the slow perturbation techniques. Nevertheless the electron input to photon output correlations discussed earlier would be significant.

2.4 *Experiments with dissected* EWE

The data on the distribution of coelomocytes in the EWE have been obtained by using EBL. Here the major question that has arisen is whether the coelomocytes are displaced to the surface of the EW uniformly or there are marked regional

of these experiments has been that a *post-clitellar* electrode always produces an order of magnitude higher photonic output. This difference stems from the excretary acts in the two regions; the excretion is accomplished by a funnel and nephrostone which opens into the coelom.

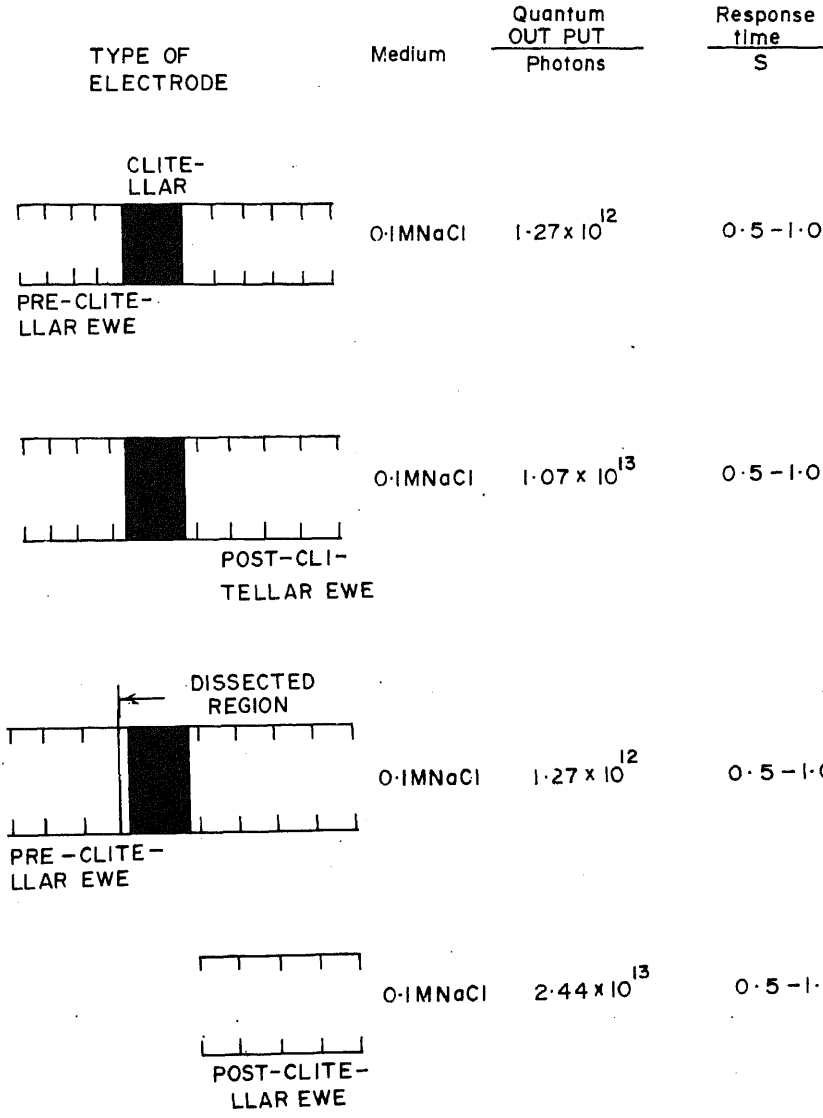

Figure 4. Representation of the output photons and response times at an EWE. The electrode type is shown diagrammatically.

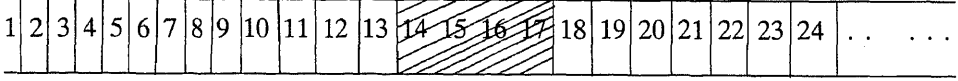

$$\text{The total EBL output} = \sum_{i=1}^{13} (h\nu)_i + \sum_{i=18}^{n} (h\nu)_i + \sum_{i=14}^{17} (h\nu)_i, \tag{24}$$

i refers to the segmental number. The last term contributes very little to the total output and hence is neglected and therefore,

$$I = \int_0^\infty I_1 \, dt + \int_0^\infty I_2 \, dt + \int_0^\infty I_3 \, dt + \ldots, \tag{25}$$

where I_1, I_2, $I_3 \ldots$ are considered the intensities of each of the segments and are time dependent. Since the photon is released in the biochemical reaction,

$$\frac{dI}{dt} = \left[\frac{dS}{dt}\right] \frac{(I_{max}-I)^2}{K_S I_{max}}, \tag{26}$$

and when I reaches zero the above expression simplifies to

$$\frac{dI}{dt} = \left[\frac{dS}{dt}\right] \frac{I_{max}}{K_S}, \tag{27}$$

where S refers to substrate concentration and K_S is Michaelis constant. The above discussion shows the segmental displacement when it occurs in EBL, the microscopic analysis shows the variance in the emission intensity distribution. However, from the above results it is clear that

$$\sum_{i=1}^{13} (h\nu)_i < \sum_{i=18}^{n} (h\nu)_i, \tag{28}$$

and furthermore $\sum_{i=18}^{n} (h\nu)_i$ in the dissected EWE is nearly the same (factor of two difference) as the live *post-clitellar* EWE. The electrolyte consumption by the EWE (through the mouth) does not result in the sustained production of coelomic cells; if it is so then the production rate is small. Consequently, it follows that the EBL of the EWE arises from the *post-clitellar* region. A closer examination of the current-time response at an EWE shows negligible Faradaic current flowing upon reversal of the potential setp (i.e. 0 V) when a *post-clitellar* EWE is used; with the *pre-clitellar* electrode it is significant.

3. Development of a firefly electrode

The larvae of the firefly *Pteroptyx malaccae* generate pulsed light emission with $\lambda = 530$ nm at 500 msec intervals. The emission features are represented by a short

about 8·0 sec. The interesting aspect of this electrode is its sensitivity to adaptability for an electrolytic medium. With $CaCl_2$ as the electrolyte, the emission intensity decreases slowly and after about 138 sec, the intensity reaches very low levels; at the end of the experiment the firefly is not destroyed (cf. the effect of $CaCl_2$ with the earthworm). The Ca^{2+} appears to inhibit the generalized firefly reaction

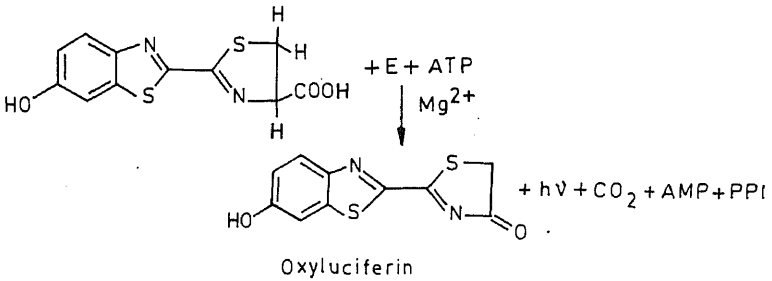

(29)

Chart 7.

probably by binding specifically to E. The first step in the above reaction is the enzyme-bound luciferyl adenylate and pyrophosphate (PPi). Preliminary investigations have shown that in EBL, oxygen is reduced causing a lower photonic output. Currently investigations are in progress to correlate the photonic output with Faradaic current flow and for a fuller understanding of the reaction mechanism. It appears from the results that oxygen is a component of the reaction (29) and that peroxide intermediate formation is less likely for the generation of the excited state.

4. Conclusions

The development of EBL has generated results for a mechanistic understanding of bioluminescent reaction schemes. A significant feature of this method is the *in situ* probing of the excited state formation. With the earthworm electrode, it has been conclusively shown that ions like Fe^{2+} or Fe^{3+} inhibit the bioluminescent reaction; this does not occur when the bioluminescent reaction is carried out with the isolated chemiluminescent material. Furthermore, the enhancement of the emission of radiation with EWE in the presence of Ca^{2+} follows a mechanism different from the conventional reaction mechanism operating with marine bioluminescence. It is also shown that the EBL of the earthworm electrode predominantly arises from the *post-clitellar* segments; the emission intensity is a

composite of the reactions occurring in the individual segments and is caused by the overlapping decay curves.

Acknowledgement

The author is thankful to Ms N M Limaye, Ms Achala Chande and Dr Ismail for helpful discussions.

References

Adams S W and Cilento G 1982 *Chemical and biological generation of excited states* (New York: Academic Press)

Bard A J and Faulkner L R 1980 *Electrochemical methods* (New York: Wiley) p. 143

Boveris A and Turrens J F 1980 in *Chemical and biochemical aspects of superoxide and superoxide Dismutase* (eds) J V Bannister and H A O Hall (FEBS Symposium) p. 84

Cormier M J 1978 in *Bioluminescence in action* (ed.) P J Herring (London: Academic Press) pp. 75–108

Cormier M J, Hori K and Karhanis Y D 1970 *Biochemistry* **9** 1184

Duluca M and Dempsey M E 1973 in *Chemiluminescence and bioluminescence* (eds) M J Cormier, D M Hercules and J Lee (New York: Plenum Press) p. 345

Halliwell B and Gutteridge J M C 1984 *Biochem. J.* **219** 1

Hastings J W 1983a *J. Mol. Evolution* **19** 309

Hastings J W 1983b *Bull. Mar. Sci.* **33** 818

Hastings J W and Morin J G 1969 *Biochem. Biophys. Res. Commun.* **37** 493

Ismail S A and Santhanam K S V 1984 *Bioelectrochem. Bioenerg.* **12** 535

Ito Y, Kuriyama and Tashiro N 1970 *J. Exp. Biol.* **52** 79

Koo J Y and Schuster G B 1977 *J. Am. Chem. Soc.* **99** 6107

Kopecky K R and Mumford C 1969 *Can. J. Chem.* **47** 409

Kosower E W 1981 in *Bioluminescence and chemiluminescence* (eds) M A Deluca and W D McElroy (New York: Academic Press) p. 365

Kulkarni B B, Sundaresan N S and Santhanam K S V 1978a *Trans. Soc. Adv. Electrochem. Sci. Technol.* **13** 329

Kulkarni B B, Swayambunathan V and Santhanam K S V 1978b *J. Photochem.* **9** 174

Limaye N M and Santhanam K S V 1985 *Bioelectrochem. Bioenerg.* **14** 405

Limaye N M and Santhanam K S V 1986a *Bioelectrochem. Bioenerg.* **15** 341

Limaye N M and Santhanam K S V 1986b *Bioelectrochem. Bioenerg.* (in press)

McCapra F and Richardson D G 1964 *Tetrahedron Lett.* **3167**

Marcus R A 1965 *J. Chem. Phys.* **24** 679, 2654

Marcus R A 1970 *J. Chem. Phys.* **52** 2803

Periasamy N and Santhanam K S V 1977 *Chem. Phys. Lett.* **51** 442

Periasamy N, Shah S J and Santhanam K S V 1973 *J. Chem. Phys.* **58** 821

Plant P J, White E H and McElroy W D 1968 *Biochem. Biophys. Res. Commun.* **31** 98

Seliger H H and McElroy W D 1960 *Arch. Biochem. Biophys.* **88** 136

Shimomura O, Goto T and Johnson F H 1977 *Proc. Natl. Acad. Sci. USA* **74** 2799

Shimomura O and Johnson F H 1975 *Nature (London)* **256** 236

Stone H 1968 *Biochem. Biophys. Res. Commun.* **31** 386

Ward W W and Cormier M J 1978 *Methods Enzymol.* **57** 252

Proc. Indian Acad. Sci. (Chem. Sci.), Vol. 97, Nos 3 & 4, October 1986, pp. 495–511.
© Printed in India.

Corrosion of austenitic stainless steels in aqueous environments§

J B GNANAMOORTHY
Materials Development Laboratory, Indira Gandhi Centre for Atomic Research, Kalpakkam 603 102, India

Abstract. Aqueous corrosion of austenitic stainless steels and their weldments has been reviewed, with particular reference to the results of the studies conducted at the Indira Gandhi Centre for Atomic Research at Kalpakkam. Different aspects of pitting and crevice corrosion, intergranular corrosion and stress corrosion cracking in stainless steels have been discussed. Since secondary phases present in these stainless steels have a significant influence on the corrosion behaviour of these steels, the methods of estimation of these secondary phases have also been discussed.

Keywords. Austenitic stainless steels; aqueous corrosion; pitting; crevice corrosion; stress corrosion cracking; sensitization; intergranular corrosion; secondary phases; carbides; delta-ferrite; sigma; chi-phase; weldments.

1. Introduction

Stainless steels are extensively used as materials of construction because of their good corrosion resistance, and in many applications problems due to corrosion do not arise. However, attempts to extend their use to more demanding technological applications has continued to generate interest in their corrosion resistance, often with a view to defining limits for their use. Austenitic stainless steels, which are the modifications of the classic 18% Cr-8% Ni iron based alloys and designated by the 300 series of the American Iron and Steel Institute (AISI), represent the largest category of stainless steels produced in the world. From among the austenitic steels type 316 stainless steel has been used as the material for fuel cladding as well as for most of the structural components of the sodium cooled fast breeder reactors. Various aspects of the corrosion behaviour of this stainless steel and other related alloys in aqueous environments have been extensively studied since 1975 in the Materials Development Laboratory of the Indira Gandhi Centre for Atomic Research at Kalpakkam. A review of these studies is presented here.

2. Pitting corrosion

Usually adequate allowance in the wall thickness of the component is made at the design stage to take into account the possible loss of material by uniform corrosion during its service life. A serious mode of attack of stainless steels is localized corrosion such as pitting, crevice corrosion, intergranular corrosion and stress corrosion cracking. Therefore, detailed studies are very essential for understanding

It is well-recognized that pitting corrosion of metals takes place only at potentials higher than a critical value for each alloy/environment system (Gnanamoorthy and Balachandra 1973). During the evaluation of the critical potential for AISI type 316 ss in 0·1 N H_2SO_4 containing 0·5 N Cl^- ions by the potentiostatic method (Dayal and Gnanamoorthy 1980b), it was observed that before stable and self-propagating pits are formed, unstable pits are nucleated and repassivated. The initiation of unstable pits is indicated by the rise of the current in the form of either flicks or a gradual increase and then a sudden decrease before a steady rise of current at the stable pitting potential during anodic polarization. The incubation periods for nucleation of unstable and stable pitting were determined at various constant potentials for a maximum exposure period of 24 hr. The plots of inverse of incubation time (i.e., rate of initiation of pits) vs. potential were found to be linear for both unstable and stable pitting (figure 1). Since the critical potential for the stable pitting (E_{sp}) and the critical potential for unstable pitting (E_{up}) are those potentials at which the rates of initiation of stable and unstable pits, respectively, are zero (i.e., incubation periods are infinite), they can be more accurately determined as the intercepts of these linear plots obtained by the least square method. The values of E_{sp} and E_{up} (+537 and +449 mV, respectively) thus determined were quite close to the ranges of values evaluated by the experiments.

Two more critical potentials, namely the instantaneous potential for unstable pits, E_{iup}, and the instantaneous potential for stable pits, E_{isp}, were also identified. At these critical potentials, the incubation periods for nucleation of unstable pits and stable pits respectively were zero, and pitting started instantaneously. The values of E_{iup} and E_{isp} could be determined accurately from the intercepts of the linear plots of potential vs. incubation time (figure 2). It was also shown that the pit nucleation potentials obtained by potentiodynamic as well as semi-potentiostatic experiments correspond to the nucleation of unstable pitting. The critical pit passivation potential, E_{pp}, defined as that potential more active

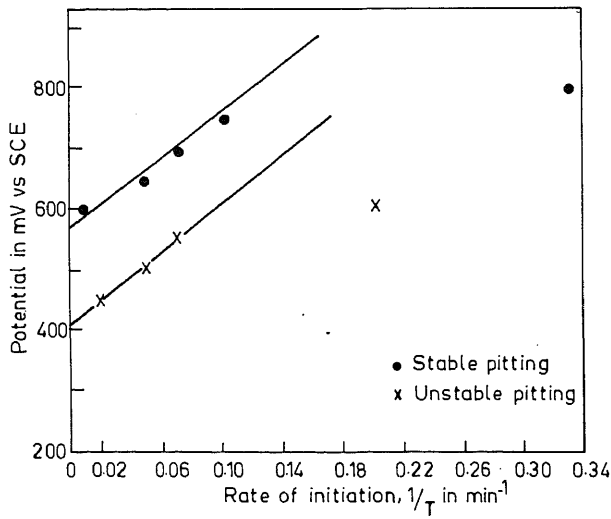

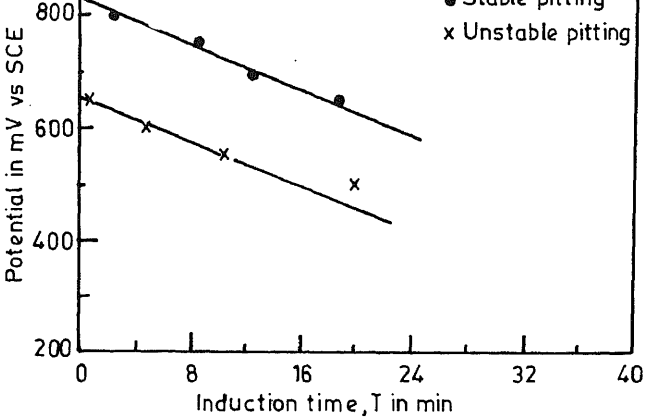

Figure 2. Plots of applied potential vs. induction time for stable and unstable pitting.

which neither new pits can nucleate nor existing pits propagate, can be nsidered as a unique material property, provided that the value of E_{pp} is etermined by universally standarized experimental conditions and the pit growth alue limited to about 0·1 mA/cm^2 (Dayal and Gnanamoorthy 1979, 1980b). The kinetics of pit growth has been generally observed to follow a relationship of e type $i = kt^b$ where i is the increase in the current density after a time t that has apsed after the initiation of the pit. The value of the exponent b depends on a umber of factors such as the alloy composition, applied potential, composition of e medium and pit density. In the case of unstable pits, the values of b at different otentials and chloride concentrations were found to vary randomly, indicating that ey do not follow any regular kinetics. In the case of stable pit growth, at lower pplied potentials and chloride concentrations two distinct values of b were found, dicating a change in kinetics after the initial growth of the pits. At higher applied otentials and chloride concentrations, a value close to 2 was obtained for b roughout the period of growth of the pit (figures 3 & 4). It was also observed that e pits initiated at the interface of the alloy and the inclusion, and that the orphology of the pit gradually changed from a regular to an irregular shape uring different stages of the pit growth (Dayal and Gnanamoorthy 1979, 1982).

In general, the corrosion of a weld metal is known to be inferior to that of the ase metal because of the inhomogeneous, dendritic microstructure produced in e former after welding. On prolonged exposure at high temperatures, the icrostructure undergoes further changes due to precipitation of more secondary hases. Gill *et al* (1986a) have studied the pitting corrosion behaviour of weld eposit metal of type 316L ss after thermally ageing it at 773, 873 and 973 K for fferent durations of time ranging from 0·5 to 5000 h. They found that the pitting orrosion resistance of the weld metal decreases with ageing time at all the mperatures studied (figure 5). With the decrease in the pit nucleation potential here was a corresponding increase in the reactivation peak current density igure 6). The delta-ferrite and sigma phases in the weld metal remained

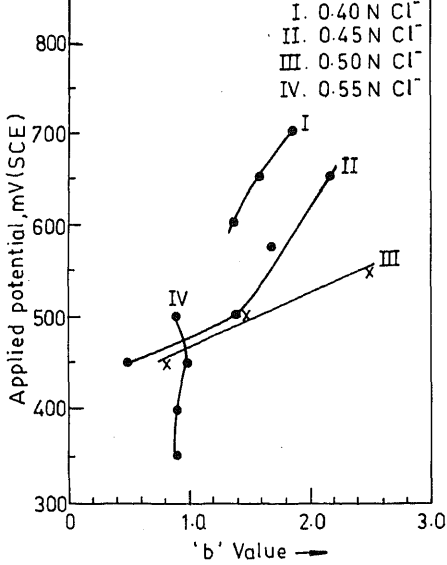

Figure 3. Variation of *b* value with respect to applied potential for different chloride ion concentrations during stable pit growth.

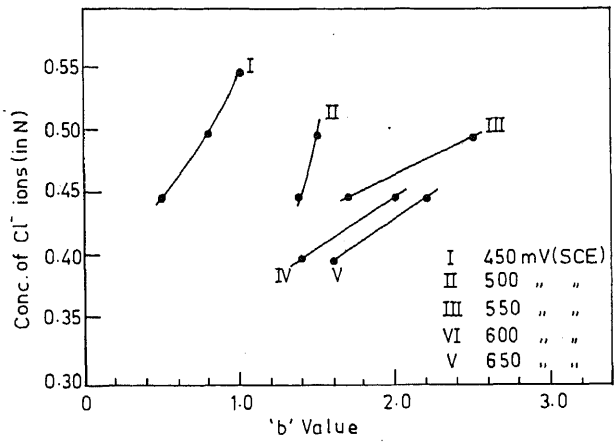

Figure 4. Variation of *b* value with respect to applied potential for different chloride ion concentrations during unstable pit growth.

unattacked during pit growth because of their relatively nobler electrochemical properties.

Recently it has been reported that the addition of small amounts of nitrogen to the weld metal as well as wrought metal improves their pitting corrosion and sensitization resistances and their mechanical properties. Kamachi Mudali *et al* (1986) have studied the role of nitrogen in improving the pitting corrosion resistance of weldments of 304 and 316 stainless steels. Weld metal samples with

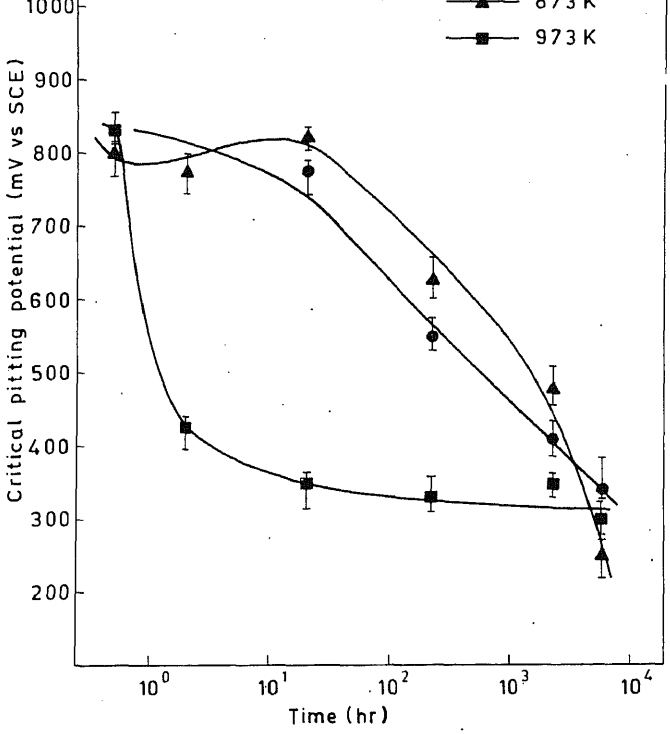

Figure 5. Variation in the critical pitting potential with ageing time at 773, 873 and 973 K.

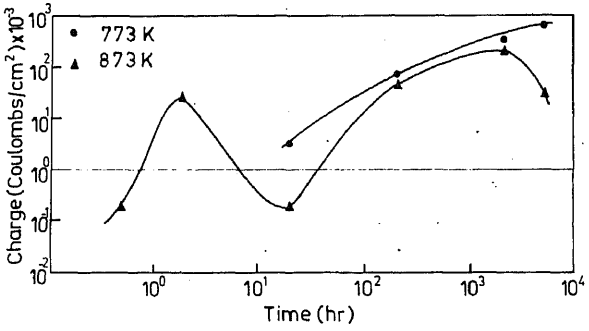

Figure 6. Change in the reactivation peak current density with ageing time at 773 and 873 K.

varying proportions of argon-nitrogen mixtures as the shielding gas. The nitrogen content in the weld metal was found to increase as the volume percent of nitrogen in the argon gas was increased (figure 7). While there was no delta-ferrite present in the weld metals of type 316 ss even at very low levels of nitrogen in the metal, delta-ferrite was absent in type 304 ss weld metal samples only when the concentration of nitrogen in the weld metal was very high (~1400 ppm).

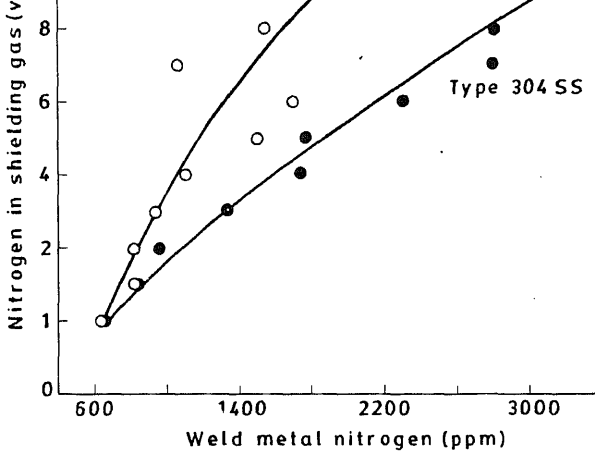

Figure 7. Nitrogen contents in weld metals of types 304 and 316 ss as a function of the volume percent of nitrogen gas mixed with shielding argon gas.

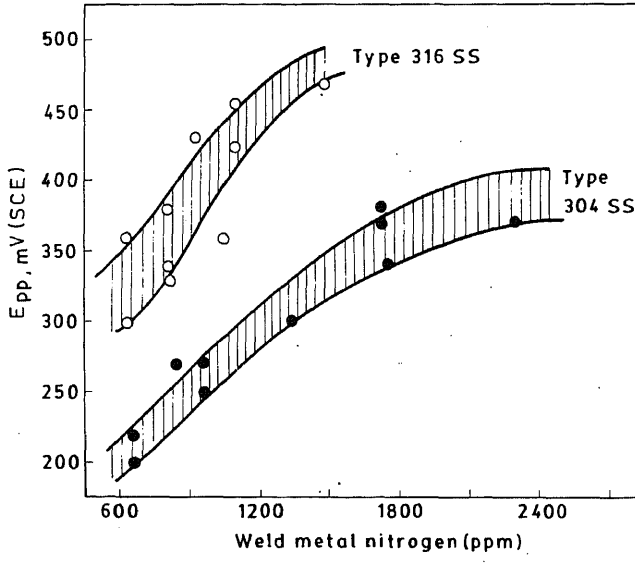

Figure 8. Critical pitting potentials of types 304 and 316 ss weld metals as a function of their nitrogen content.

Potentiodynamic anodic polarization studies in 0·5 M NaCl solution (deaerated by hydrogen) showed that weldments of both types of steel had increased resistance to pitting as the nitrogen content in the steel was increased (figure 8).

The specific role of nitrogen in improving the pitting corrosion resistance was studied by ESCA evaluation of the pitted samples. The passive film on the samples showed the absence of nitrogen and molybdenum; however, these elements were

found to be enriched at the metal/film interface. A 4 eV peak shift in the nitrogen found at the pit site indicated the presence of a nitrogen compound at the pit. This lent credence to the hypothesis of the dissolution of nitrogen to form NH_4^+ ions and subsequently other inhibiting compounds which repassivate the pit surface to improve the pitting corrosion resistance.

Examination of the pitted samples of type 316 ss weldments by scanning electron microscopy and optical microscopy showed that pits had initiated at triple points of austenite/austenite boundaries as well as at centres of the austenite grains. Triple points are the regions where the impurities or the minor alloying elements such as S and P segregate to the maximum extent during primary austenite solidification. The occurrence of pits at austenite centres could be due to the fact that these areas have the lowest concentrations of Cr and Mo compared to the grain boundary regions in the weld metal. In the case of type 304 ss weld metal samples, pits were found to initiate at austenite/delta-ferrite interfaces and grow into the austenite matrix leaving the Cr-rich delta-ferrite unattacked.

Based on the available results and observations, a generalized mechanism for pitting could be put forward:

1. At a potential more noble to a critical value, due to the presence of certain inhomogenities on the metal surface, passivity is momentarily destroyed by either penetration or adsorption of aggressive ions or by film breaking mechanisms.
2. The metal dissolution process produces M^{n+} ions inside the pit.
3. Due to the excess positive charge inside the pit, negative ions like Cl^- are attracted to attain electrical neutrality and thus the metal chloride (MCl_n) is formed.
4. Hydrolysis MCl_n generates a very low pH, and insoluble corrosion products are formed inside the localized area.
5. The highly acidic environment increases the dissolution rate further which attracts more Cl^- ions and the process becomes autocatalytic.
6. Besides the activating Cl^- ions, other non-activating ions such as OH^- and SO_4^{--} present in the bulk solution are also attracted to the local site. The autocatalytic process is retarded and the film is likely to be rendered stable again. Stable pitting takes place only if conditions are created at localized areas for autocatalytic process (like low pH, high Cl^- concentration etc.). Unstable pitting occurs when any of the conditions for autocatalytic process is not met, so that a pit could be repassivated.

3. Crevice corrosion

Another form of localized corrosion which is a major practical problem affecting stainless steels is crevice corrosion. This occurs in shielded areas of metal surfaces formed at the interfaces of pipe couplings, threaded or rivetted connections, gasket fittings, spot welded lap joints, porous welds, coiled or stacked sheets of metals etc. Extensive investigations have been carried out towards understanding the

Initially, the anodic dissolution ($M \rightarrow M^+ + e$) and cathodic reduction ($O_2 + 2H_2O + 4e \rightarrow 4OH^-$ in neutral solution) processes occur uniformly over the entire metal surface, including the crevice exterior. The oxygen in the shielded crevice area is consumed after some incubation period, but the decrease in cathodic reduction rate is negligible because of the small area involved. Consequently the corrosion of the metal inside and outside the crevice continues at the same rate. With cessation of the cathodic reactions producing hydroxide, the migration of negative ions (e.g. chlorides) into the crevice area is required to maintain charge balance. The resulting metal chloride hydrolyses to insoluble metal hydroxides and free acid. Both the chloride ions and low pH accelerate crevice corrosion in a manner similar to autocatalytic pitting, while the reduction reaction cathodically protects the exerior surface.

Initiation of crevice corrosion attack can be influenced by a number of factors such as the crevice geometry, alloy composition and its microstructure, bulk solution chemistry as well as physical characteristics such as temperature, velocity and volume. Dayal *et al* (1983a) have used a potentiodynamic polarization method for assessing the influence of these various factors on the crevice corrosion

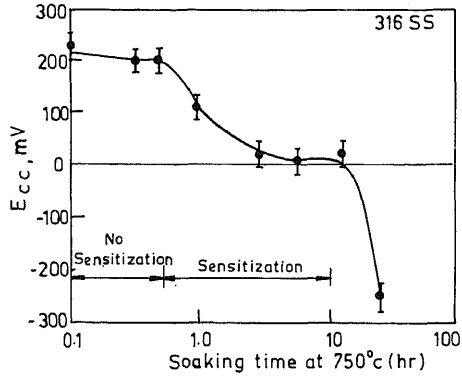

Figure 9. Relationship between critical crevice corrosion potential, E_{cc}, and soaking time (degree of sensitization).

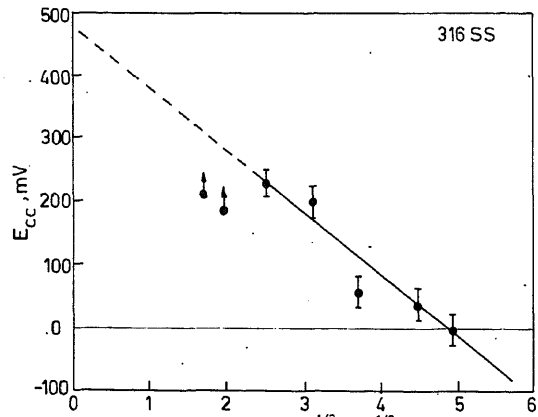

sed as the index to the crevice corrosion resistance of a given system (a more ctive E_{cc} value indicating a higher susceptibility to crevice attack). Dayal and nanamoorthy (1984) observed that sensitized samples of type 316 ss in 0·5 M aCl solution exhibit increased susceptibility to crevice corrosion and suffer tergranular attack inside the crevice (figure 9). They also found that the sistance to crevice corrosion decreases with decrease in the grain diameter (d) llowing a linear relationship between E_{cc} and $d^{-1/2}$ (figure 10). Investigations on ld worked stainless steels of types 304, 310 and 316 stainless steels indicated that $_{cc}$ decreases with cold work up to 5 to 15% and that further increase in cold work d not produce any further change in E_{cc} value. These effects were attributed to e increase in the number of defect sites and change in texture produced by cold ork (Dayal *et al* 1984).

Sensitization and intergranular corrosion

hen austenitic stainless steels are heated in the temperature range of 723 to 23 K, the chromium present in them combines with carbon and precipitates at e grain boundaries as chromium-rich carbides such as $Cr_{23}C_6$. This carbide ecipitation with the accompanying depletion of chromium in the vicinity of the ain boundaries is known as sensitization. The chromium concentration in the eas adjacent to the grain boundaries may fall below the minimum required value bout 12%) for maintaining passivity, if the component is heated for a sufficiently ng time in this temperature range. When this happens the component is liable to ndergo selective grain boundary attack during its service, resulting in intergranu- r corrosion. Optimum parameters for heat treatment to avoid sensitazation can be btained from time-temperature-sensitization (TTS) diagrams for the required ainless steels. Dayal *et al* (1978) have established the TTS diagram for a modified pe 316 stainless steel. The influence of different degrees of cold work (0 to 25% eduction in thickness by cold rolling) on the sensitization behaviour of type 316 ss as also been studied (Dayal *et al* 1981). The TTS diagrams for these cold worked eels showed that the temperature range increases as the cold work increased up to 0%. However, the time required for sensitization is reduced around the nose mperatures with increase in cold work up to 10%. At higher cold work levels, oth the temperature range of sensitization and the time required for sensitization emain almost the same.

While the TTS diagram can be used for evaluating the sensitization time for any othermal heat treatment, it cannot be used directly to determine the extent of ensitization when the material is continuously cooled through a range of emperatures. Dayal and Gnanamoorthy (1980a) have developed a method to redict the extent of sensitization in stainless steels during continuous cooling. The rinciple of this method is similar to that used for relating time-temperature- ansformation behaviour on continuous cooling. Using this method the critical near cooling rate to avoid sensitization can be calculated for a material whose TTS iagram is known. Dayal *et al* (1981) have shown that based on this method a ontinuous cooling sensitization (CCS) diagram can also be established from the othermal TTS diagram and the different cooling curves.

Many incidents of stress corrosion cracking in stainless steel components, especially in water cooled nuclear reactors, have been experienced throughout the world. Intergranular cracking has been widely reported in weld-sensitized regions. In many cases intergranular or transgranular cracking has been found in regions away from the welds as well as in components that were not welded. Such crackings have been attributed to the presence of chloride and oxygen in water. In view of the seriousness of the problems posed by stress corrosion cracking in critical reactor components, systematic investigations of the factors affecting the phenomenon have been carried out. Khatak and Gnanamoorthy (1979) have studied the stress corrosion cracking of type 304 ss in water containing zero to 50 ppm of oxygen and 10 and 50 ppm of chloride ions at 280°C with the C-ring specimens stressed to 70% and 100% of the yield strength of the alloy. The results showed that the specimens stressed to 70% yield strength and exposed to a solution containing no oxygen but 10 ppm of chloride ions did not undergo any cracking up to 340 days of exposure. However, under similar experimental conditions except for an increase in oxygen ion concentration (achieved by not adding hydrazine), the specimens had cracked after an exposure period of 225 days. When the chloride ion concentration was increased to 50 ppm the cracking time was reduced to 162 days. Similarly, any increase in the stress level or oxygen level further decreased the time to cracking. In all the cases the cracking was transgranular. Thus, it was shown that both chloride and oxygen levels in water need to be simultaneously controlled to avoid stress corrosion cracking.

There are many instances cited in the literature where residual stresses in combination with aggressive ions such as chlorides have caused cracking in austenitic stainless steels. In fact, more failures have been due to unaccounted residual stresses than the actual applied loads. For numerous applications using stainless steels, cold deformation is the final manufacturing operation. Any inhomogeneous deformation can result in residual stresses and such stresses, sometimes as high as the yield stress, could exist as a result of even a simple operation like straightening or bending. In large components where heat treatment is not possible, it is necessary to know to what extent cold work can be permitted without the risk of stress corrosion cracking. Khatak *et al* (1979) have carried out studies on the susceptibility of types 316 ss with different degrees of cold work, in boiling 45% $MgCl_2$ solution. Their results showed that cold working up to 15% reduction in thickness renders these steels susceptible to stress corrosion cracking. The maximum time for crack appearance was 10 hr for specimens without any external stress. For specimens with external stress, there was a further progressive decrease in cracking time with increase in cold work. Muraleedharan *et al* (1985) found that almost similar effects are seen in type 316 ss. For both steels at all stresses, SCC initiated in the transgranular mode. The fracture mode changed to intergranular in the case of 316 ss while in the case of type 304 ss transition from transgranular to intergranular mode occurred only in specimens that have been cold worked to very high levels (26 and 56%). There was a general tendency for an increase in the intergranular fracture area with increased level of cold work and applied stress. Bandyopadhyay *et al* (1981) investigated the stress corrosion

welded specimens have a higher susceptibility to stress corrosion cracking.

Depending on the method of stressing test specimens, test procedures for stress corrosion cracking evaluation can be grouped into: (1) the constant load method, (2) the constant strain method, and (3) the slow dynamic straining method. Among these methods, the dynamic straining test has been the most favoured technique today because it is a severe test capable of producing cracking in a relatively short time with good reproducibility. However, there is scepticism about the use of the dynamic straining method for comparing the SCC susceptibility of similar alloys with different metallurgical/microstructural conditions and therefore having a wide difference in their ductilities. Khatak *et al* (1984) have evaluated the effect of cold rolling on the SCC propensity of type 316 ss using different test methods with a view to establishing the suitability of these methods, especially the dynamic straining method, by comparing the SCC resistance of materials having wide variations in their mechanical properties. These investigations showed that the use of parameters such as the ratio of UTS, ratio of total elongations and cracking index obtained through dynamic straining tests on such materials might give erroneous results and that crack growth rate could be a suitable criterion for evaluation of SCC susceptibility.

. Estimation of secondary phases

When austenitic stainless steel and its weld metal are exposed to elevated temperatures during service, precipitation of various phases such as carbides, chi and sigma takes place. Relatively minor amounts of these phases can have major effects on the corrosion properties of the stainless steels. Therefore, a knowledge of the type, amount, and physical parameters of all phases is vital for the achievement of the optimum properties in stainless steels.

Some of the necessary information about the phases present can be obtained from microstructural analysis by physical methods like optical metallography, x-ray diffraction, electron microscopy and electron probe microanalysis. However, for a multi-phase alloy, it is also advantageous to know the precise distribution of elements between the different phases, the quantity of the individual phases and their lattice parameters. This is possible by separating the phases and consolidating them free of matrix contamination. The essential principle of separation of the phases is based on the selective dissolution of the matrix under appropriate conditions. Generally, the schemes of separation are based either on chemical and/or electrochemical techniques. The chemical reagents, like an alcoholic solution of bromine, are not always specific. The electrolytic anodic dissolution technique using electrolytes such as hydrochloric acid in a miscible organic solvent is widely used. This electrochemical technique is quantitative for the separation of the carbide phase but it is semi-quantitative for the separation of the delta-ferrite and sigma phases.

5.1 *Estimation of delta-ferrite*

The presence of delta-ferrite between 2 and 10% in the austenitic stainless steel welds is necessary to avoid the incidence of hot cracking. Techniques and standard procedures for measuring ferrite levels to the required accuracy are not available so

far. The magnetic (probe), x-ray diffraction, and metallographic methods make only surface or limited volume measurements. Schaeffler and DeLong diagrams can also be used for the measurement of delta-ferrite if the chemical composition of the weld deposit is known. But the accuracy of such a measurement is only 3 to 4%. The absolute content of delta-ferrite, however, can be determined by using an electrochemical technique (Gill *et al* 1979).

The technique consists of exposing a sample of the weld to an electrolyte (3·6 N H_2SO_4 containing 0·1 N NH_4SCN) at a fixed potential (−80 mV vs SCE) as shown in figure 11. At this critical potential, the austenite of the duplex austeno-ferrite microstructure is selectively dissolved while ferrite which becomes passive remains undissolved. The undissolved ferrite is then cleaned in a mixture of H_2SO_4 and HNO_3 and washed with methanol, dried and weighed.

The complete dissolution of austenite requires exposure of the sample for a long period, which depends on the thickness of the specimen and its ferrite content. During this long period some loss of ferrite is bound to occur. The error thus introduced can be eliminated if a correction factor is applied with respect to the loss of ferrite in its passive state. Calculation shows that maximum error introduced due to ferrite dissolution in this condition is only 1% of the estimated ferrite value.

This technique can also be used to study the following:

[a] The morphology of delta-ferrite after the austenite phase has been selectively dissolved from the duplex structure.
[b] The chemical composition of delta-ferrite.
[c] The decay kinetics of delta-ferrite during elevated temperature ageing in stainless steels (e.g. type 308) where other magnetic phases like martensite nucleate and interfere with the evaluation of ferrite content by magnetic methods.

6.2 *Estimation of other secondary phases*

While it is possible to individually separate various phases from the austenitic stainless steel matrix by careful adjustment of electrode potentials by a potentiostat,

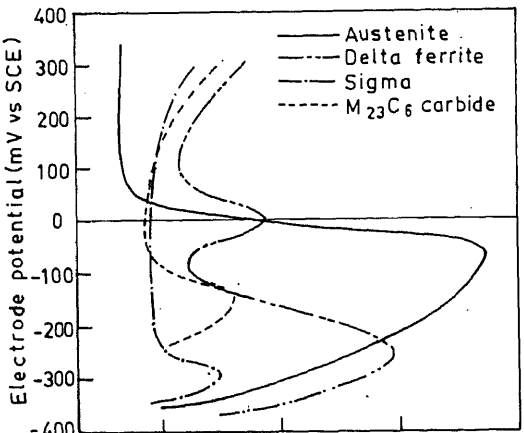

y the electrochemical technique (as described for the separation of delta-ferrite) nd then individually separate the phases by selective chemical dissolution, since reparation of the powders of the secondary phases into electrodes for electroche- ical separation is a very involved and time consuming process.

A sample containing a mixture of secondary phases like delta-ferrite – $M_{23}C_6$, gma – $M_{23}C_6$ or Chi – $M_{23}C_6$ dispersed in the austenite matrix can be analyzed r the estimation of individual phases by a combination of electrochemical and emical techniques (Gill and Gnanamoorthy 1982). For chemically separating the ases, a 5% $Br_2 - CH_3OH$ solution is employed. As shown in figure 12, the lta-ferrite and sigma phases dissolve rapidly in this solution and dissolution is mplete in 50 and 70 minutes respectively. The complete dissolution of the Chi ase (not shown in the figure) takes about 40 minutes in this solution. But the ssolution rate of $M_{23}C_6$ is relatively slow. In 70 minutes, when the other secondary ases are dissolved completely, only about 1% $M_{23}C_6$ is dissolved. The weight actions of various phases can then be calculated as shown in figure 13.

3 *Growth kinetics of secondary phases – application of phase separation chniques*

number of samples were sectioned from type 316L stainless steel weld deposit nd heat treated at 773, 873 and 973 K for durations ranging from 0·5 to 5000 hr. he electrochemical extraction of the precipitate was carried out as described arlier. The residue obtained from the electrochemical extraction process was nalysed by X-ray diffraction using CuK_α radiation (Gill *et al* 1986b). In the -deposited sample, only delta-ferrite was present, whereas samples aged at 773 K ontained sigma, chi and $M_{23}C_6$ in addition to untransformed ferrite. However, the sidue obtained from samples aged at 873 and 973 K contained sigma and $M_{23}C_6$. The data for the total amount of extract obtained as a function of ageing time at fferent ageing temperatures are shown in figure 14. There is a general increase in

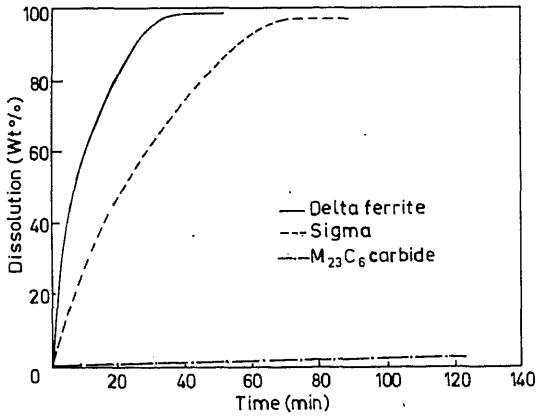

Figure 12. Dissolution behaviour of delta-ferrite, sigma and $M_{23}C_6$ in 5% Br_2-CH_3OH

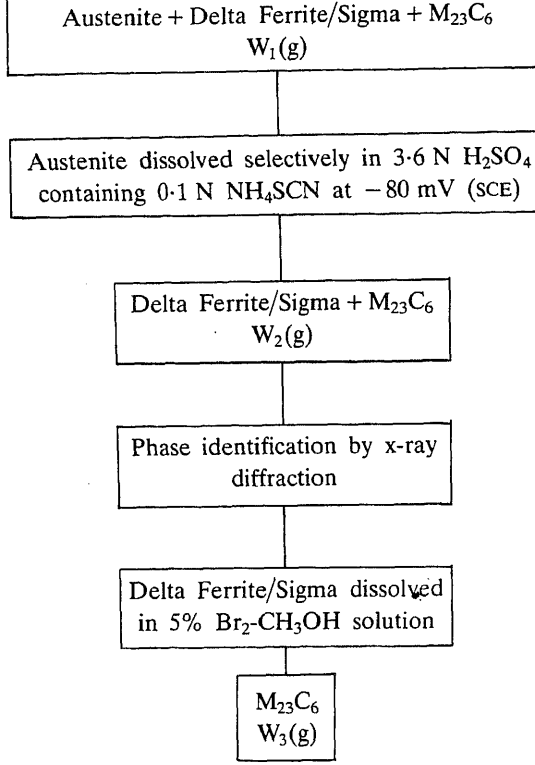

$$\text{Wt. \% delta-ferrite/sigma} = \frac{W_2 - W_3}{W_1} \times 100$$

$$\text{Wt. \% } M_{23}C_6 = \frac{W_3}{W_1} \times 100$$

Figure 13. A schematic plan of the electrochemical and chemical techniques for the separation and estimation of secondary phases in austenitic stainless steels.

the content of secondary phases with increasing temperatures. But the increase is higher as the temperature of ageing is raised.

The results for the chemical separation of $M_{23}C_6$ and sigma from the extracts obtained from the electrochemical extraction process are shown in figures 15 and 16 respectively. It is noted that the carbide grows rapidly at an ageing temperature of 773 K. However, at higher temperatures of ageing, the carbide growth is rapid during the initial stages of ageing but the dissolution process sets in on further ageing. The time of ageing needed to dissolve the carbide depends on the temperature of ageing. For example, an ageing time of 200 hr is needed at 873 K and about 20 hr at 973 K for the dissolution process to be predominant.

It is also interesting to note that the plateau regions observed in the growth kinetics of sigma (figure 16) correspond to the ageing times when $M_{23}C_6$ starts

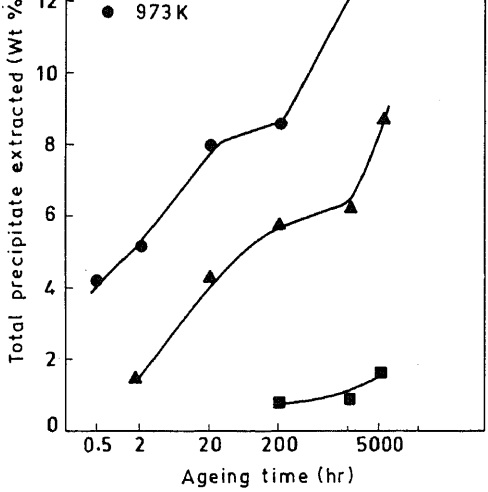

Figure 14. Total amount of precipitate extracted from the aged samples as a function of ageing time.

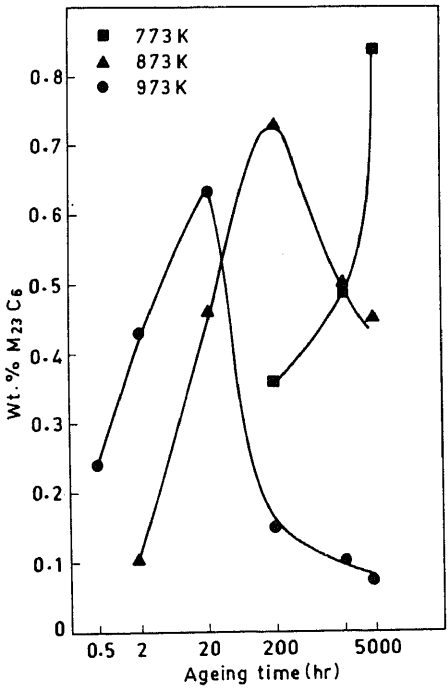

Figure 15. Amount of $M_{23}C_6$ formed during ageing as a function of ageing time.

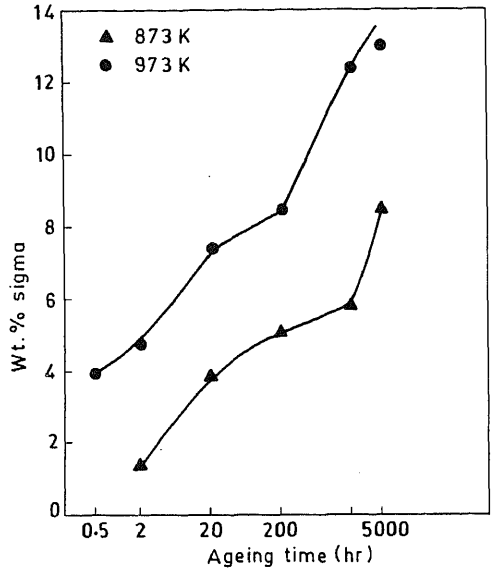

Figure 16. Amount of sigma formed as a function of ageing time.

and the dissolution of the carbides. The formation and resolution of $M_{23}C_6$ during thermal ageing has also been observed by other investigators using electron microscopy. However, the electrochemical and chemical methods of phase separation provide a method of studying this phenomenon quantitatively.

7. Conclusion

Most of the corrosion problems occurring in stainless steel structures and equipment can be prevented or minimised by (i) the proper choice of the construction material, welding electrodes and welding procedures, (ii) adopting scrupulous cleanliness during handling, and (iii) controlling the water chemistry of the environment at all stages of fabrication, storage and service.The optimum metallurgical condition of the material should be ensured so that it is free from sensitization or residual stresses. With these precautionary measures at the design and fabrication stages, the service-life of the austenitic stainless steel structures could be extended to very many years without costly shut-down and maintenance.

References

Bandyopadhyay G, Khatak H S, Mannan S L, Gnanamoorthy J B and Rodriguez P 1981 *Proc. workshop on experience in the fabrication and use of stainless steel equipment in DAE projects* (Kalpakkam: Reactor Research Centre) vol. **3** C-66

Dayal R K and Gnanamoorthy J B 1979 *Chem. Age India* **30** 483

Dayal R K and Gnanamoorthy J B 1980a *Corrosion (Houston)* **36** 104

Dayal R K and Gnanamoorthy J B 1980b *Corrosion (Houston)* **36** 433

Dayal R K and Gnanamoorthy J B 1983b *Corros. Maintenance* **6** 301
Dayal R K and Gnanamoorthy J B 1984 *Proc. Ninth Int. Cong. Met. Corros* **3** 141
Dayal R K, Parvathavarthini N, Gnanamoorthy J B, Rodriguez P and Prasad Y V R K 1984 *Mater. Lett.* **2** 248
Dayal R K, Parvathavarthini N, Venkadesan S, Mannan S K and Gnanamoorthy J B 1981 *Proc. workshop on experience in the fabrication and use of stainless steel equipment in DAE projects* (Kalpakkam: Reactor Research Centre) vol. **3**, C-66
Dayal R K, Venkadesan S and Gnanamoorthy J B 1978 Reactor Research Centre, Kalpakkam, *Time-temperature sensitization diagrams for Virgo 14 Sb steel* Report No. RRC-35.
Gill T P S, Dayal R K and Gnanamoorthy J B 1979 *Welding Res. Suppl.* **58** 375-s
Gill T P S and Gnanamoorthy J B 1982 *J. Mater. Sci.* **17** 1513
Gill T P S, Gnanamoorthy J B and Padmanabhan K A 1986a *Corrosion* (in press)
Gill T P S, Vijayalakshmi M, Gnanamoorthy J B and Padmanabhan K A 1986b *Welding Res. Suppl.* **65** 122-s
Gnanamoorthy J B and Balachandra J 1973 *J. Electrochem. Soc. India* **22** 257
Kamachi Mudali U, Dayal R K, Gill T P S and Gnanamoorthy J B 1986 *Werkst. Korros.* (in press)
Khatak H S and Gnanamoorthy J B 1979 *Proc. Second Natl. Conf. on Corrosion and its control* (Karaikudi: SAEST) 1.6, p. 73
Khatak H S, Mannan S L, Gnanamoorthy J B and Rodriguez P 1979 *Chem. Age India* **30** 491
Khatak H S, Muraleedharan P, Gnanamoorthy J B, Rodriguez P and Padmanabhan K A 1984 *Proc. sixth international conference on fracture*, Poster papers, pp. 153
Muraleedharan P, Khatak H S, Gnanamoorthy J B and Rodriguez P 1985 *Metal. Trans.* **A16** 285

© Printed in India.

Fuel cells: Problems and prospects[§]

A K SHUKLA*, K V RAMESH and A M KANNAN
Solid State and Structural Chemistry Unit, Indian Institute of Science, Bangalore 560 012, India

Abstract. In recent years, fuel cell technology has advanced significantly. Field trials on certain types of fuel cells have shown promise for electrical use. This article reviews the electrochemistry, problems and prospects of fuel cell systems.

Keywords. Fuel cells; invariant electrode-electrolyte system; energy-conversion devices; electrocatalysts.

1. Introduction

In the literature (Bagotzky and Skundin 1980; Kordesch 1978; Liebhafsky and Cairns 1968; Vielstich 1970; Bockris and Srinivasan 1969), several publications have covered the history of fuel cells. William Grove in 1839 was the first to have proclaimed the discovery of fuel cells, but the impetus in fuel cell research and development started as late as 1950. This led to the successful use of H_2-O_2 fuel cells for main on-board power supply in Apollo and Gemini spacecrafts in the sixties. However, research and development of fuel cells for terrestrial applications declined in the late sixties due to their high cost, noble-metal requirements and short life. Fuel cell activity was further revived in the early seventies and was greatly enhanced in 1973 after the energy crisis (Tilak *et al* 1981).

A fuel cell is an electrochemical cell which can continuously change the chemical energy of a fuel and an oxidant to electrical energy by a process involving essentially invariant electrode-electrolyte system. The difference between a fuel cell and a battery is that in the former, the fuel is continuously and externally fed to the electrode, whereas in the latter the reactants are stored within. Fuel cells produce electrical energy as long as they are supplied with a fuel and an oxidant. Fuels that can be used include H_2, CH_4, NH_3, N_2H_4 and CH_3OH or H_2-rich gas derived from oil or coal or recovered from biomass. The oxidant is generally oxygen or air; other oxidants such as halogens and H_2O_2 could also be used.

The simplest type of fuel cell, viz., a H_2-O_2 fuel cell is shown schematically in figure 1. A typical unit produces voltages of less than 1 volt and current of the order of 1 A/ft^2. A number of such cells are stacked together in series or parallel to produce sizeable outputs. A fuel cell power plant consists of three major sub-systems, viz., fuel reforming, power generating and power conditioning units. The layout of a fuel cell power plant is shown schematically in figure 2. The fuel reforming processes can be in-built in the power section itself. In the power

[§] Dedicated to Prof. K S G Doss on his eightieth birthday

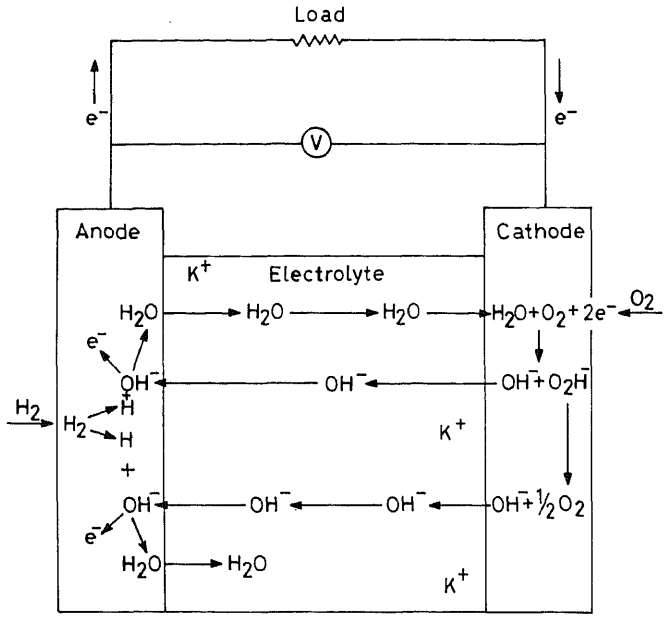

Figure 1. Electrochemical processes occurring in an alkaline H_2–O_2 fuel cell.

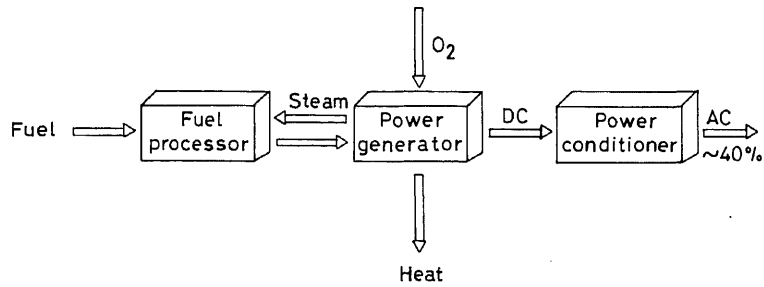

Figure 2. Fuel cell power plant.

generator, the reformate reacts with O_2 electrochemically on the electrode surfaces producing d.c. electricity and heat in the form of hot water or steam; this heat can be fed back to the fuel-reforming section.

2. Advantages of fuel cells

The efficiencies of different types of energy conversion devices are given in table 1. It can be seen that the demonstrated efficiencies of fuel cells are considerably higher in relation to other energy-conversion devices. The direct conversion of chemical energy to electrical energy in a fuel cell makes its efficiency free from

Table 1. Efficiencies of direct energy conversion devices.

Energy converter	% efficiency
Thermoelectric	10
Thermionic	22
Photovoltaic	18
Magnetohydrodynamics	60
Low temperature fuel cells	60
High temperature fuel cells	60
Gas turbines	30
Internal combustion engines	30
Diesel engines	40

(Tilak *et al* 1981)

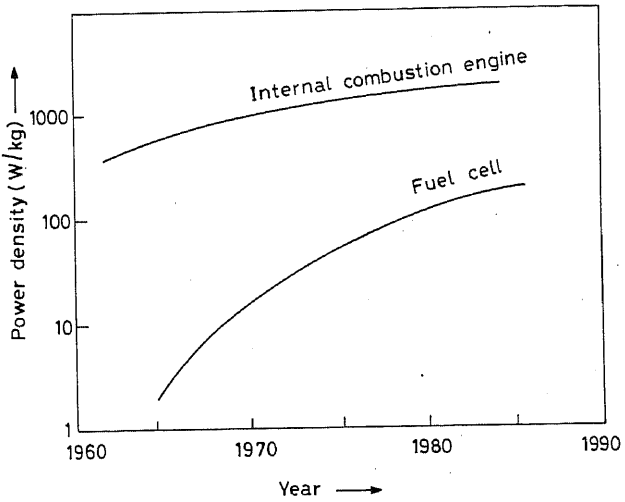

Figure 3. Historical trend in power densities for fuel cell and internal combustion engines.

esired temperature range and multifuel capability. Furthermore, fuel cells roduce d.c. electricity which is attractive to industries that use large amounts of .c. power, viz., chloralkali and aluminium industries. Since fuel cells feed on H_2, ney are suited to industries that generate this gas as a by-product, such as the etrochemical industry. Fuel cells can be run on almost any fuel, viz., naphtha, nethanol, natural gas or any H_2-rich fuel. Non-conventional fuels such as ewage-treated gases can also be used. Siting power plants close to the load keep ransmission losses to a minimum and save the heavy expense of laying down ransmission lines. Fossil-fuel power plants with capacities as high as 1000 MW utilize their exhaust heat to generate additional electrical energy thereby further

of load. Also the efficiency of a fuel cell does not depend on its size. Only fossil-fuel plants with capacities larger than 1000 MW can approach the efficiency of a fuel cell. The modular design of fuel cells allows a utility to expand its generating capacity in small increments closely matching the needs for load following and peaking service.

Fuel cell technology has undergone substantial development (Brusaglino *et al* 1982; Shukla *et al* 1983) since 1960 (see figure 3) and it is believed that in the years to come fuel cells will become commercially feasible.

3. Types of fuel cells

Fuel cells may be generally classified as in table 2. A broad distinction between direct and regenerative fuel cells, which are similar to primary and secondary batteries, has been made. Reformer and biochemical fuel cells have been grouped under indirect fuel cells. The direct type has been further subdivided based on the temperature of operation, viz., low (<200°C), medium (200–750°C) and high (>750°C). The types of fuels employed in fuel cells are also indicated in the table. Fuel cells have also been grouped according to the type of electrolyte. The promising electrolytes are acids (H_3PO_4), alkali (KOH), molten carbonates (Li^+, K^+, $Na^+-CO_3^{2-}$), solid polymers (RSO_3H) and solid oxides ($ZrO_2-Y_2O_3$).

3.1 *Acid fuel cells*

In acidic fuel cells ion conduction through the electrolyte is provided by hydrogen or hydronium ions. Platinum or platinum alloys are employed as electrocatalysts with carbon (or graphite) based electrodes.

Table 2. Classification of fuel cells.

Fuel cells					
Direct			Indirect		Regenerative
Low temperature (<200°C)	Medium temperature (200–750°C)	High temperature (>750°C)	Reformer	Biochemical	
Hydrogen-oxygen	Hydrogen-oxygen	Hydrogen-oxygen	Natural gas	Glucose	Thermal
Organic compounds-oxygen	Carbon monoxide-oxygen	Carbon monoxide-oxygen	Naphtha	Carbo-hydrate	Electrical
Nitrogeneous compounds–oxygen or hydrogenperoxide	Ammonia-oxygen		Methanol Ethanol	Urea	Photo-chemical
Hydrogen-halogen			Coal		Radio-chemical
Metal-oxygen or			Ammonia		

ıe stability of the carbon and the platinum catalyst arises. The advantages of PAFC re that the phosphoric acid is very stable and can be highly concentrated (≈100%) uch that the water vapour pressure is low and hence keeping the steady-state water emoval by the reactant gases equal to the product water rate. Besides, at 200°C, ıe anode performance is good even with fuels containing carbonmonoxide upto %. The major disadvantage of PAFC is that the cathode, i.e., the oxygen-reducing ectrode performance is poor. At present one of the objectives of R and D work n PAFC is to improve the performance of oxygen cathode. Field trials on PAFC for rrestrial applications have shown promises for commercialization (Cameron 985).

2 *Alkaline fuel cells*

his is the most promising system for space applications and has been successfully sed in Apollo and other space shuttles. Ion conduction in alkaline fuel cells is rovided by hydroxyl ions. A wide range of electrocatalysts including nickel, silver etal oxides, spinels and noble metals can be used. The advantages of alkaline fuel ells are that the cathode performance is much superior to that in acid fuel cells and ıe construction materials are relatively less costly in the former cells. The main isadvantage is that the alkaline electrolytes react with carbon oxides to form arbonates which severely limit the cell performance. This necessitates scrubbing of O_2 in the system.

3 *Molten carbonate fuel cells (MCFC)*

he electrolyte employed is generally a mixture of alkali-metal carbonates and the n conduction is through the carbonate ions. Since these salts function as ectrolytes only in the liquid phase, the cells operate at 600–700°C. The electrodes e made of alloys of Ir, Pt, Rh, Ni. The half-cell reactions in this cell are:

t the anode: $H_2 + CO_3^{2-} \rightarrow H_2O + CO_2 + 2e^-$

$$CO + CO_3^{2-} \rightarrow 2CO_2 + 2e^-$$

t the cathode: $\frac{1}{2}O_2 + CO_2 + 2e^- \rightarrow CO_3^{2-}$

The MCFC's have several advantages over acid fuel cells. They have high power ensity and higher voltages than the acid cells. Since the cell is tolerant to CO, eforming process can occur within the fuel cell and hence reformers and shift onvertors are not required. Higher efficiency is achieved since the reforming rocess absorbs heat which is supplied *in situ* by heat produced at the electrodes of ıe cell. However, high temperatures impose severe constraints on materials uitability for long time operations.

.4 *Solid-polymer fuel cells (SPFC)*

he electrolyte in these cells is an ion-exchange membrane which is impermeable to ases. Generally, cation-exchange membranes e.g. RSO_3H, are used due to their etter stability and higher conductivity as compared to anion-exchange resins. The dvantages of solid-polymer fuel cells are that the electrolyte being a solid cannot

Types of fuel cells	Largest Unit tested (kW)	Longest stack tested (h)
Alkaline	35–60	10,000
Phosphoric acid	4,500	16,000
Molten carbonate	2	5,000
Solid polymer	5	10,000
Solid oxide	<1	5,000

change or vapourize from the system and the only liquid in the fuel cell is water; this minimizes corrosion problems. The main disadvantages are: the necessity to humidize the electrolyte; working temperatures and pressures are too low to yield good current densities and life of cells are limited due to oxidative degradation of polymers with time.

3.5 *Solid-oxide fuel cells (SOFC)*

These employ a solid, non-porous metal-oxide electrolyte with ion conduction occurring through the migration of oxide ions in the crystal lattice. Stabilized zirconia is commonly used as electrolyte and the operating temperatures of the cells are between 900°–1000°C. Solid-oxide fuel cells have distinct advantages over aqueous fuel cells as these employ no liquids and hence the problems associated with flooding of porous electrodes and maintenance of three-phase interface are totally averted. Also the electrolyte composition remains invariant and independent of the composition of the fuel and oxidant. Since the cell operates at high temperatures, losses due to activation polarization are minimal; this avoids the use of noble-metal catalysts. In addition, these cells do not suffer from the constraints in molten carbonate cells which require recycling of CO_2 at the cathode. The main disadvantages are the high temperatures of operation and severe material limitations imposed at these temperatures. A comparison of the performance of different types of fuel cells is given in table 3 (Phadke 1985).

4. Fuel cell electrodes

One of the important components of a fuel cell is its electrodes. The main functions of electrodes are: to contain the gas/liquid/solid interface, to hold the catalyst and to serve as an electron conductor. The electrode materials must be inexpensive, structurally rigid, non-corrosive and non-reactive so that they are long lasting and electrolyte resistant.

Previously, platinum black was used as the catalyst in fuel cell electrodes. Although the electrode showed good activity, the catalyst loading was rather high. The maximum surface area that can be achieved with platinum black dispersions is about 30 m^2/g of platinum but it is rapidly reduced during cell operation due to sintering, thereby reducing fuel cell efficiencies. Effective noble-metal utilization is

btained by dispersing the metal uniformly on a conducting support.

Porous carbon as support has proven to be most effective especially for ow-temperature fuel cells. Besides being inert at temperatures upto 200°C, the ectrodes can be designed with large surface area. Due to many microscopic actures and fissures, that produce pores from 10^{-3} to 10^{-7} cm in diameter, the ternal surface area of 1 cc of some of the porous carbons is around 1000 m^2. By spersing platinum on to porous carbon supports, metal areas greater than 50 m^2/g of platinum can be achieved. Moreover, platinum-supported carbon ectrodes have fairly good resistance to sintering of platinum crystallites as well as nproved mass-transfer properties during cell operation.

The major disadvantage of these electrodes, however, is that flooding occurs hen capillary action draws the electrolyte too far into the pores and deactivates e reaction zone. This problem can be circumvented by making the electrode ydrophobic. Polyethylene, polytetrafluoroethylene (PTFE), paraffin etc., have een used as hydrophobisizers which at the same time also act as binders for the ectrodes. The structural and performance characteristics of the hydrophobic ectrodes depend on the preparation technique and the mode of operation. arameters influencing the electrode performance are the radius of the catalyst articles, the radius of the binder particles, porosities of the catalyst and binder and orosity of the support, effective electrolyte conductivity, concentration and stribution of active catalytic species, mode of impregnation of catalyst on the pport, pretreatment of the electrode, gas pressure, temperature etc. (Chirkov 975). In hydrophobic electrodes, not all the particles are wetted and it is a function f binder concentration as well as the method of fabrication. The pore structure of e electrode consists of two types of pores, viz., pores in the inner space between ydrophilic and hydrophobic layers and the pores in the hydrophobic layer with nall chains of porous agglomerates of the binder. The latter factor plays a gnificant role. Also, the pores with radii between 25–200 Å make significant ontribution to the electrochemical activity which increases with micropore olume. Successful operation of a fuel cell electrode requires the establishment of as/electrolyte/solid interface. However, for aqueous electrolytes, there is general- no genuine three-phase junction as the pore walls on the gas side are covered ith a thin liquid film. Hence, the electrochemical reaction occurs in a reaction one of finite extension (Vielstich 1970). In actual electrodes, the pores are regular with varying diameters and lengths.

Theoretical analysis of porous electrodes is an intricate task due to lack of precise ructural details, non-linear, multi-dimensional and coupled equations and roblems involved in defining the operating regions, e.g., the three phase oundaries. To overcome these complexities, an idealization of various types of ore structures has been assumed and several models have been proposed for escribing operational behaviour of porous electrodes (Bartell and Shephard 1953; iner and Hunter 1969; Chirkov 1972).

Surface area, exchange current-density, double-layer capacitance, polarization esistance etc., are some of the parameters characterizing the electrode perform-

$$\eta = E - E_r = \eta_{act} + \eta_{conc} + \eta_{ohm}, \tag{1}$$

where η_{act} is the activation overpotential (arising from charge transfer); η_{conc} is the concentration overpotential (due to low concentration of reactants or high concentration of products at the electrode surface, especially at high current-densities); and η_{ohm} $(-IR_i)$ is the ohmic overpotential which increases linearly with current (R_i being the internal resistance mainly comprising of the resistivities of the electrolyte and the electrode).
For a planar electrode,

$$\eta_{act} = (RT/\alpha\mathcal{F})\ln i_0 - (RT/\alpha\mathcal{F})\ln(I/A), \tag{2}$$

and

$$\eta_{conc} = (RT/n\mathcal{F})\ln(1 - I/I_L), \tag{3}$$

where i_0 is the exchange current-density (expresses equilibrium reaction rate at $I = 0$); α is the transfer coefficient $(0 < \alpha < 1)$; $\mathcal{F}$ is the Faraday constant; A is the area of the electrode; and I_L is the limiting current. It is evident from (2) that the activation overpotential at an electrode can be reduced by increasing i_0 or A. Thus electrodes should have high exchange current-densities and high surface areas.

Substituting (2) and (3) in (1), rearranging and differentiating, the differential resistance is given by,

$$\frac{dE}{dI} = \frac{RT}{\alpha\mathcal{F}I} - \frac{RT}{n\mathcal{F}(I_L - I)} - R_i \tag{4}$$

Equation (4) implies that at low current-densities, the major contribution to differential resistance is from activation overpotential. As current increases, differential resistance is mainly governed by R_i linearly. When the current approaches the limiting value, the differential resistance is controlled by mass-transfer limitations resulting in the rapid decrease of the electrode potential. This description is valid only if $|\eta| \ll (RT/\mathcal{F})$. For porous gas-diffusion electrodes, however, the mathematical treatments are much more complex than (4); these are discussed in detail in several publications (Berger 1968; Bagotzky and Vasilev 1966; Breiter 1969; Srinivasan *et al* 1967).

4.2 *Electrocatalysis of fuel cell electrodes*

Low temperature fuel cells, which operate at temperatures below 100°C, require an adequate catalytic activity of electrode materials. The electrocatalyst should have high exchange current density and/or low Tafel-slopes. By an appropriate choice of an electrocatalyst, a particular electrode reaction can be accelerated by minimizing the overpotential. It is found that electrocatalysts are almost always based on transition metals or ions irrespective of their being present as metals, alloys, semiconductors (oxides in particular), and complexes (metal phthalocyanines and

orphyrins). This is because of the unpaired *d*-electrons and unfilled *d*-orbitals resent in them which facilitate bond-formation with adsorbates. The free energy adsorption will depend strongly on the number of unpaired *d*-electrons per metal om and also on their energy levels, which in turn depend on the nature of the ansition metal and its chemical environment. The chemical environment around e transition metal ion affects the properties of the metal-absorbate bond. Since ectrocatalytic reactions involve both formation and cleavage of metal-absorbate onds, most effective electrocatalysis is observed when the bond is of intermediate rength; weak bonding leads to insufficient coverage by adsorbate for it to be an fective catalyst, while a high free energy of adsorption will cause the rate of the eavage step to be slow. This dependence on the rate of hydrogen evolution action is discussed in the form of a volcano curve by Parsons (1958).

An alternative method of achieving effective catalysis is to change the properties the catalyst itself during the reaction sequence leading to the weakening of the etal-adsorbate bond, such as change in oxidation state etc. In addition, geometric rangement of the catalyst centres also affects the catalytic activity especially for ncerted reactions and adsorption of large molecules involving more than one talytic site. Further, since large surface area of the catalyst increases the rate of sorption of reactants, the catalyst surface is deliberately roughened to increase e current-density at an electrode. Generally, expensive electrocatalysts such as atinum are dispersed on a high surface area substrate. The substrate must be a od electronic conductor, inexpensive and corrosion-resistant to the electrolyte. rbon is a suitable substrate for this purpose. It is found that the origin and etreatment of carbon substrates control the activity of an electrocatalyst. rther, it is desirable that the catalyst structure be highly disordered to achieve gher activity. The presence of grain boundaries, lattice defects, kinks, screw slocations etc., is important. However, the development of electrocatalysts as of day has been essentially empirical. Characterization studies for the surface ucture of electrodes and the electrode-electrolyte interface (both *ex-situ* and *in u*) are desirable (Sherwood 1985; Kinoshita and Stonehart 1977). There are veral publications which review electrocatalysis in detail (Appleby 1974; onehart and Ross 1975; McNicol 1978; Fickett 1977; Fletcher 1984). Generally, ble-metal catalysts are supported on high-surface area substrates to achieve aximum utility of the catalyst and higher electrochemical reaction rates. Carbon a substrate has many attractive properties, such as chemical stability, high rface area, electrical conductivity and both macroscopic and microscopic rosities (Appleby 1983). A wide variety of carbon substrates (Hillenbrand and cksonen 1965; McBreen *et al* 1981) have been employed both as electrocatalyst pports and as electrocatalysts for oxygen reduction. It is reported (Nicolau *et al* 59; Hillenbrand and Lacksonen 1965; Ross *et al* 1974) that the surface oxides on rbon as well as the catalyst-support interactions exercise a considerable influence the catalytic activity of the electrodes. Recently an ashless coconut-shell carbon s been reported (Manoharan and Shukla 1983; Manoharan *et al* 1984; anoharan and Shukla 1984; Shukla *et al* 1985; Goodenough *et al* 1985; amesh and Shukla 1985; Ramesh 1986) to be an excellent substrate for hydrogen idation and oxygen reduction in fuel cells.

(Grubb and Mckee 1966). These materials are corrosion resistant and possess high electrical conductivity. Pervoskites such as $La_xSr_{1-x}CoO_3$ and $AB'_{0.5}B''_{0.5}O_3$ (where A = Li, Cs, Ca, Ba, Sr, La etc. and B' = V, Cr, Mn, Fe, Co, Ni, Ru etc. and B'' = Ti, Zr, Sn, V, Nb, Ta etc.) as well as certain ruthenates e.g. $Pb_2Ru_2O_7$ have also been investigated as substrates (McHardy and Stonehart 1975). The conductivity of these oxide materials is increased by incorporation of certain dopants but these are not sufficiently acid resistant. If the electronic conductivities and the corrosion resistances of these materials are improved, these could offer an alternative to carbon.

4.3. *Hydrogen oxidation electrodes*

The mechanism of the hydrogen-ionization reaction has been studied in detail in view of the revived interest in fuel cells (Breiter 1969; Appleby 1974; McNicol 1978). In acid electrolytes, the hydrogen reaction is given by

$$H_{ad} + H_2O \rightleftharpoons H_3O^+ + e^-, \tag{5}$$

and in alkaline solution by

$$H_{ad} + OH^- \rightleftharpoons H_2O + e^- \tag{6}$$

Partial reaction steps of (5) are given by:

(a) transport of molecular hydrogen to and adsorption on the electrode surface either from the gas phase or from the electrolyte:

$$H_2 \text{ or } H_{2(\text{dissolved})} \rightarrow H_{2_{ad}},$$

and (b) hydration and ionization of the adsorbed hydrogen which may proceed by two alternative reaction paths:

(1) dissociation of the molecules into atoms

$$H_{2_{ad}} \rightarrow H_{ad} + H_{ad} \text{ (Tafel reaction)},$$

followed by hydration and ionization at discrete sites on the electrode surface.

$$H_{ad} + H_2O \rightarrow H_3O^+ + e^- \text{ (Volmer reaction)}$$

(ii) hydration and partial ionization (Heyrovsky–Volmer mechanism)

$$\begin{aligned} H_{2_{ad}} + H_2O &\rightarrow [H_{ad}\ H_3O^+] + e^- \\ &\rightarrow H_{ad} + H_3O^+ + e^-, \\ H_{ad} + H_2O &\rightarrow H_3O^+ + e^-. \end{aligned}$$

Partial reaction steps in alkaline solution can also be written in a similar manner.

Studies on anodic oxidation of hydrogen on platinum in phosphoric acid have shown that dual-site dissociation of hydrogen on platinum is the rate-determining

Only metals capable of chemisorbing hydrogen are suitable for establishment of he reversible hydrogen potentials, VIII-group metals with partially filled *d*-orbitals meet this requirement. At room temperature, platinum metals, specially in finely divided form such as platinum black, will establish the reversible ydrogen potential over the entire pH range, and Raney nickel will do so in lkaline electrolytes.

A large number of phosphides, arsenides, selenides and tellurides of Fe, Co and Ni have been investigated as electrocatalysts for hydrogen oxidation in sulphuric cid at temperatures less than 100°C (Mund *et al* 1973; Luft *et al* 1974). Of these, CoP_3 is the most promising and is also less prone to CO poisoning. Tungsten arbide has also been found to be an effective electrocatalyst besides being tolerant o CO poisoning (Bohm and Pohl 1968; Von Benda *et al* 1972). However, the rate onstant for hydrogen oxidation on this material is two orders of magnitude lower han for Pt metal. The highest exchange-current densities of 10^{-3} A/cm^2 are btained for the platinum-group metals. At present, the best electrocatalyst in acid lectrolytes remains to be platinum dispersed on carbon with an acceptable loading of ·25 mg/cm^2 (Cameron 1985).

Although Raney nickel is unstable in alkaline media, Ti-and Cr-containing Raney nickels (Mund *et al* 1977; Kenjo 1985) have been reported to possess higher atalytic activity and stability. The higher activity is attributed to increased *d*-band acancy caused by the addition of Ti or Cr to Raney nickel. Nickel boride also xhibits moderate activity (Jasinski 1965) in alkaline electrolytes. Recently, Ta_5Si_3, Tb_4O_7 and $3Y_2O_3.2ZrO_2$ have been investigated as catalysts for hydrogen oxidation in acid electrolytes. Of these, $3Y_3O_3.2ZrO_2$ exhibits the highest activity Tanase *et al* 1982). Noble-metal alloys such as Pt-Pd and Pt-Ru (Niedrach *et al* 967; Stonehart 1982) have also been employed as electrocatalysts for hydrogen nodes. Pt-Ru containing carbon electrodes have been reported to possess higher atalytic activity than Pt both for hydrogen oxidation as well as oxygen reduction. Characterization studies of these electrodes reveal that the presence of Ru liminates the formation of surface platinum oxides, thereby enhancing their ctivity (Ramesh 1986).

4.3 *Methanol-oxidation electrodes*

The direct methanol-air fuel cell enjoys a number of unique advantages as compared to other power generators and to other fuel cells. The challenge facing the development of a commercially viable methanol cell is to obtain adequate current/voltage characteristics. Attempts to build commercially viable, direct methanol fuel cells have encountered problems mainly concerned with inadequate anode activity. In addition, performance has been affected by electrode deterioration, possibly arising from the accumulation of the decomposition products of methanol. In order to improve the efficiency of the anode, it is necessary to examine not only the specific activity of the catalyst, but also a number of other parameters affecting electrode performance. In particular, the electrode substrate affects the rate of mass transfer of reactants and products to and from the catalytic sites. In spite of extensive research on non-noble catalysts, platinum metals still

happen to be the only useful catalyst for methanol electrodes operating below 80°C.

In acidic media, methanol could be oxidized at the Pt electrode to carbon dioxide and water, while in alkaline media the main oxidation product is the formate ion. The mechanism of methanol oxidation in these media is as follows.

(a) *In acid medium*: $CH_3OH \rightarrow CH_3OH_{ad} \rightarrow CH_2O_{ad} \rightarrow HCOOH_{ad} \rightarrow CO_2$,

In alkaline medium: $CH_3OH \rightarrow CH_2O \rightarrow HCOO^- \rightarrow CO_3^{2-}$.

Systems using acid electrolytes have the advantage of spontaneous carbon dioxide removal but at the same time acid electrolytes are corrosive and the air electrodes in acid media perform poorly. As already indicated, alkaline systems exhibit less material problems and the use of carbon supports and silver catalysts make them cost effective.

A major improvement in electrode performance has been achieved with bifunctional catalysts. It is believed that one component of the catalyst facilitates the adsorption of methanol and the second provides an active oxygen. However, the performance of catalysts has depended to a very marked degree on the interaction of the two components both with each other and with the substrate. In the light of this fact, platinum group bi-metal catalysts, viz., Pt-Ru, Pt-Pd and Pd-Ru have been found to be more effective than the individual platinum-group metals (Binder *et al* 1972; McNicol *et al* 1976; Shropshire 1965).

4.4 *Oxygen-reducing electrodes*

Owing to the complexity of reaction and difficulties in the formation and breaking of the O–O bond, the kinetics of oxygen reduction is poor with almost all electrode materials. Oxygen reduction at the electrodes proceeds by the following pathways (Yeager 1976; Tarasevich *et al* 1983; Hoare 1968).

(a) Direct 4-electron pathway: In alkaline solutions, oxygen is reduced to OH^- through

$O_2 + 2H_2O + 4e^- \rightarrow 4OH^-$, the reaction potential being 0·401 V vs NHE at 25°C.

In acid solutions, oxygen is reduced to water

$O_2 + 4H^+ + 4e^- \rightarrow 2H_2O$, the reaction potential being 1·229 V vs NHE at 25°C.

(b) Peroxide pathway: In alkaline solutions, oxygen is first reduced to peroxide

$O_2 + H_2O + 2e^- \rightarrow HO_2^- + OH^-$, the reaction potential being −0·065 V vs NHE at 25°C.

It is subsequently reduced through

$HO_2^- + H_2O + 2e^- \rightarrow 3OH^-$, the reaction potential being 0·867 V vs NHE at 25°C.

Or the decomposition through,

$H_2O_2 + 2H^+ + 2e^- \rightarrow 2H_2O$, the reaction potential being 1·77 V vs NHE at 25°C.

The peroxide may as well undergo decomposition as follows,

$$2H_2O_2 \rightarrow 2H_2O + O_2.$$

Oxygen reduction on most of the carbon substrates proceeds mainly through the peroxide pathway (Fischer and Heitbaum 1980). Consequently, the electrode potentials correspond to 2-electron reduction of oxygen resulting in large overpotentials at open circuits itself. Incorporation of additional catalyst which promotes the peroxide elimination is therefore necessary. Rotating-ring-disc electrode (RRDE) studies on platinum and platinum alloys indicate that oxygen reduction on these materials proceeds by both direct 4-electron and peroxide pathways with the former being predominant (Tarasevich *et al* 1983; Fischer and Heitbaum 1980; O'Grady *et al* 1982). Generally, oxygen reduction kinetics is faster in alkaline electrolytes than in acid media.

Noble metals and their alloys (Peuckert *et al* 1986; Ramesh 1986; Yeager 1982; Manoharan 1984) metal oxides (Garcia *et al* 1980; Matsumura and Sato 1980; Manoharan and Shukla 1984, 1985) transition-metal macrocycles, viz., metal phthalocyanins and porphyrins (Yeager 1981; Van Veen and Van Baar 1982; Shukla *et al* 1985a; Goodenough *et al* 1985) have been studied as oxygen-reducing catalysts. Further, it is reported that heat treatment of metal-macrocycles adsorbed on carbon enhances their catalytic activity but they lack long term stability. Different oxides with spinel, perovskite and pyrochlore structures have also been reported to exhibit high catalytic activity towards oxygen reduction (Trasatti 1981; Horowitz *et al* 1983; Manoharan and Shukla 1985; Goodenough *et al* 1985; Yeager 1982). Activated carbon itself is a good catalyst for oxygen reduction in alkaline media. Various kinds of carbon have been studied as oxygen-reducing electrodes. Coconut-shell carbon reportedly reduces di-oxygen to water without peroxide formation. At present, platinum dispersed on carbon with Pt loadings of 0·5 mg/cm^2 remains the most practical catalyst (Fletcher 1984).

5. Conclusion

Fuel cell development is yet in its infancy. Like the internal combustion engines, at the end of the 19th century, there is both optimism and pessimism about their commercial potential. Stationary fuel cell power plants have a better chance of succeeding than mobile vehicular fuel cells mainly on the basis of the maximum cost/kW which the consumer can afford.

The life of alkaline H_2–O_2 fuel cells has to be improved and the costs reduced ten-fold. The cost of PAFC's has to be reduced by 50%; power densities need to be increased together with proven life. Although the efficiency and other performance

characteristics of MCFC's are satisfactory, their power sections can be quantified and made available for utility purposes only after efficient coal-gasifier facilities are available. A ten-fold increase in stack life and stack size of MCFC's is needed. It is expected that within ten years MCFC's will be competing with the advanced PAFC's especially for larger utility purposes. Solid-oxide fuel cells and their stack progress are excellent. However, fabrication techniques have to be improved to ensure reproducibility when large number of cell stacks are produced.

In the case of solid-polymer fuel cells, factors such as development of the humidification process, CO_x tolerance, cost reduction have to be optimized. One of the greatest problems in the area of catalysts for fuel cells with acid electrolytes continues to be the development of low-cost catalysts for oxygen-reducing electrodes. The catalyst should at least display an activity equal to platinum and preferably give potentials close to the well known four-electron oxygen reduction. Development of catalysts till now has been purely empirical; surface characterization studies, both *ex situ* as well as *in situ*, on electrodes could be useful in identifying the active catalytic species. It is believed that with continued world-wide efforts in appropriate areas of research, both in the scientific and engineering aspects, fuel cells would become feasible for power generation and other utilities.

Acknowledgement

The authors are thankful to Professor C N R Rao for his interest in this work.

References

Alkire R and Place B 1972 *J. Electrochem. Soc.* **119** 1687

Appleby A J 1974 *Modern aspects of electrochemistry* (eds) B E Conway and J O'M Bockris (New York: Plenum Press) vol. **9** p. 369

Appleby A J 1983 *Proceedings of the workshop on the electrochemistry of carbon* (New Jersey: The Electrochemical Society)

Bagotzky V S and Skundin A M 1980 *Chemical power sources* (London: Academic Press)

Bagotzky V S and Vasilev Yu B 1966 *Fuel cells–their electrochemical kinetics* (New York: Consultants Bureau)

Bartell F E and Shephard J W 1953 *J. Phys. Chem.* **57** 211

Berger C 1968 *Handbook of fuel cell technology* (New Jersey: Prentice Hall)

Binder H, Kohling A and Sandstede G 1972 *From electrocatalysis to fuel cells* (ed.) G Sandstede (Seattle: University of Washington Press) p. 59

Bockris J O'M and Srinivasan S 1969 *Fuel cells–their electrochemistry* (New York: Mc-Graw Hill)

Bohm H and Pohl F A 1968 *Wiss. Ber. AEG–Telefunken* **41** 46

Breiter W 1969 *Electrochemical processes in fuel cells* (New York: Springer–Verlag)

Brusaglino G, Ostano P and Thione L 1982 *Solid state protonic conductors II for fuel cells and sensors* (eds) J B Goodenough, J Jensen and M Kleitz (Odense: University Press) p. 86

Cameron D S 1985 *Platinum Met. Rev.* **29** 107

Chirkov Yu G 1972 *Sov. Electrochem. (Engl. Trans.)* **8** 358

Chirkov Yu G 1975 *Sov. Electrochem. (Engl. Trans.)* **11** 503

De Levie R 1967 *Adv. Electrochem. Electrochem. Eng.* **6** 239

Fischer P and Heitbaum J 1980 *J. Electroanal. Chem. Interfacial Electrochem.* **112** 231

Fickett A P 1977 *Proceedings of the symposium on electrode materials and process for energy conversion and storage* (eds) J D E McIntyre, S Srinivasan and F G Will (New Jersey: Electrochemical Society)

Garcia P F, Shannon R D, Bierstedt P E and Flippen F B 1980 *J. Electrochem. Soc.* **127** 1974
Giner J and Hunter C 1969 *J. Electrochem. Soc.* **116** 1124
Goodenough J B, Shukla A K, Palitiero C, Jamieson K R, Hamnett A and Manoharan R 1985 *Br. Pat.* GB 2164785A
Grubb W T and Mckee D W 1966 *Nature* **210** 192
Hillenbrand L J and Lacksonen J W 1965 *J. Electrochem. Soc.* **112** 249
Hoare J P 1968 *The electrochemistry of oxygen* (New York: Interscience)
Horowitz H S, Longo J M and Horowitz H H 1983 *J. Electrochem. Soc.* **130** 1851
Jasinski R 1965 *Am. Chem. Soc. Fuel Cell Symp.*, (New York: Am. Chem. Soc.) p. 95
Kenjo T 1985 *J. Electrochem. Soc.* **132** 383
Kinoshita K and Stonehart P 1977 *Modern aspects of electrochemistry* (eds) J O'M Bockris and B E Conway (New York: Plenum Press) vol. **12** p. 183
Kordesch K V 1978 *J. Electrochem. Soc.* **125** 77c
Liebhafsky H A and Cairns E J 1968 *Fuel cells and fuel batteries–modern processes for the electrochemical production of energy* (New York: John Wiley)
Luft G, Mund K, Richter G, Schulte R and Von Sturm F 1974 *Siemans Forsch-Entwicklungsber* **3** 177
Manoharan R 1984 *Oxygen-reducing carbon electrodes for alkaline fuel-air fuel cells and metal-air batteries* Ph.D. thesis, Indian Institute of Science, Bangalore
Manoharan R, Sarma D D and Shukla A K 1984 *J. Power Sources* **13** 275
Manoharan R and Shukla A K 1983 *J. Power Sources* **10** 333
Manoharan R and Shukla A K 1984 *Bull. Mater. Sci.* **6** 259
Manoharan R and Shukla A K 1985 *Electrochim. Acta* **30** 205
Matsumura Y and Sato E 1980 *Electrochim. Acta* **25** 585
McBreen J, Olender H, Kordesch K V and Srinivasan S 1981 *J. Appl. Electrochem.* **11** 787
McHardy J and Stonehart P 1975 *International review of science, physical chemistry series 2* (ed.) J O'M Bockris (London: Butterworths) p. 171
McNicol B D 1978 *Catalysis* **2** 243
McNicol B D, Short R T, and Chapman A G 1976 *J. Chem. Soc. Faraday Trans.* **72** 2735
Mund K, Richter, Schulte R and Von Sturm F 1973 *Ber. Bunsenges. Phys. Chem.* **77** 839
Mund K, Richter and Von Sturm F 1977 *J. Electrochem. Soc.* **124** 1
Nicolas C S, Thom H G and Pobitschka E 1959 *Trans. Faraday Soc.* **55** 1430
Niedrach L, McKee, Parynter J and Danzig I F 1967 *J. Electrochem. Technol.* **5** 318
O'Grady W E, Taylor E J and Srinivasan S 1982 *J. Electroanal. Chem. Interfacial Electrochem.* **132** 137
Parsons R 1958 *Trans. Faraday Soc.* **54** 1053
Peuckert M, Yoneda T, Dalla Betta R A, and Boudart M 1986 *J. Electrochem. Soc.* **133** 944
Phadke R S 1985 *Paper presented at the National Workshop on Fuel cells* (TERI: New Delhi)
Ramesh K V 1986 *Preparation and characterization of fuel cell electrodes* Ph.D. thesis, Indian Institute of Science, Bangalore
Ramesh K V and Shukla A K 1985 *J. Power Sources* **15** 201
Rangarajan S K 1969 *J. Electroanal. Chem. Interfacial Electrochem.* **22** 89
Ross P N, Kinoshita K and Stonehart P 1974 *J. Catal.* **32** 163
Sherwood P M A 1985 *Chem. Soc. Rev.* **14** 1
Shukla A K, Manoharan R, Goodenough J B, Hammett A and Palitiero C 1985a *J. Appl. Electrochem.* **15** 774
Shukla A K, Manoharan R and Ramesh K V 1983 *Bull. Mat. Sci.* **5** 267
Shukla A K, Ramesh K V, Manoharan R, Sarode P R and Vasudevan S 1985b *Ber. Bunsenges. Phys. Chem.* **89** 1261
Shropshire J A 1965 *J. Electroanal. Chem.* **9** 90
Srinivasan S, Hurwitz H D and Bockris J O'M 1967 *J. Chem. Phys.* **46** 3108
Stonehart P 1982 *Adv. Hydrogen Energy* **3** 1149
Stonehart P and Ross P N 1975 *Catal. Rev. Sci. Eng.* **12** 1
Tanase S, Higachi S and Takahashi S 1982 *Prog. Batt. Solar Cells* **4** 235
Tarasevich M, Sadkowshi A and Yeager E 1983 *Comprehensive treatise of electrochemistry* (eds) B E Conway, J O'M Bockris, B Yeager, S Khan and R E White (New York: Plenum Press) vol. **7** p. 301

Ternary complexes of substituted catechols and catecholamines

P K BHATTACHARYA*, N A EMANUEL and N D KULKARNI
Department of Chemistry, Faculty of Science, M S University of Baroda, Baroda 390 002 India

MS received 25 October 1985; revised 6 March 1986

Abstract. Stability constants of the ternary complexes [CuAL] where A = 5-Nitro-1,10-phenanthroline, *bis*(2-pyridyl) ketone (DPK) or *bis* (2-pyridyl)amine (DPA) and L is the dianion of catechol, tiron, protocatechic acid, pyrogallol, 1,8-dihydroxynaphthalene, catecholaldehyde, 2,3-dihydroxynaphthalene, dopamine or adrenaline have been determined by potentiometric titration in dioxane water (1 : 1 v/v) medium using a SCOGS computer programme. The observed trend of stability is explained on the basis of the nature of substitution over the ligands, chelate ring size and also the composition of mixed solvent in case of DPK. Structural changes in DPK have also been discussed as a function of pH, composition of medium and coordinating mode of the secondary ligand in the ternary complexes.

Keywords. Ternary complex; Cu(II) complex; complexes of catechol and derivatives; effect of substitution on ligand.

1. Introduction

In recent years, considerable attention has been paid to the coordination behaviour of heteroaromatic N-bases (A) in ternary transition metal complexes because of their similarity to imidazole systems commonly occurring in metalloenzymes. Contrary to the expectations from statistical consideration, the formation constants, log K^{MA}_{MAL}, of the mixed ligand complexes are found to be much greater than the binary systems. This has been explained in terms of $M \rightarrow A\pi$ interaction (Sigel 1967; Huber *et al* 1969; Griesser and Sigel 1970; Chidambaram and Bhattacharya 1970). The influence of the electronic character of the ligands on the stability of ternary complexes has, further, been confirmed by observing the discriminating behaviour of [MA] complexes towards the secondary ligands L having N or O^- coordinating sites (Walker *et al* 1972; Gopalkrishnan and Bhattacharya 1982a, b; Patel *et al* 1982a). Also the nature of substitution on two ligands has been shown to affect the stability of ternary complexes (Huber and Sigel 1972; Fischer and Sigel 1974, 1979; Sigel 1980; Patel and Bhattacharya 1985).

The present investigation considers potentiometric study of three series of ternary complexes [CuAL] where A = 5-nitro-1,10-phenanthroline (A^1), 2,2′-bipyridylketone (DPK, A^2), *bis* (2-pyridyl)amine (DPA, A^3) and L = catechol (L^1), tiron (L^2), protocatechuic acid (L^3), pyrogallol (L^4) 1,8-dihydroxynaphthalene (L^5), 2,3-dihydroxynaphthalene (L^6), catecholaldehyde (L^7), dopamine (L^8) or adrenaline in aqueous-dioxan (1 : 1, v/v) medium. The structures of catecholamines L^8 and L^9 are shown in chart 1.

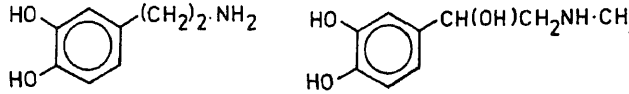

(L^8) Chart 1. (L^9)

2. Experimental

The instruments used and the method of determination of proton ligand and binary metal ligand formation constants were as detailed earlier (Patel *et al* 1982b).

For determination of formation constants of the ternary complexes [CuAL], potentiometric titrations were performed in dioxan-water medium at 30°C and I = 0·2M ($NaClO_4$). Calculations were done using computer programme SCOGS (Sayce 1968, 1971; Sayce and Sharma 1972) and considering the species LH_2, LH, L, AH, A, Cu(II), [CuA], [CuA_2], [CuL], [CuL_2] and [CuAL] to be present in the solution.

Electronic spectra of DPK and [CuDPK] were recorded at various pH on a Carl Zeiss Specord UV-VIS recording spectrophotometer.

3. Results and discussion

The formation constant calculations in the present study indicate that the formation of ternary complexes [CuAL], where $A = A^1$ to A^3 and $L = L^1$ to L^9, is in two steps, $Cu + A \rightleftharpoons [CuA]$ and $[CuA] + L \rightleftharpoons [CuAL]$ as in cases where A is *o*-phenanthroline (A^4) or dipyridyl (A^5) (Patel *et al* 1982b, Patel and Bhattacharya 1985). However, special attention is required for the [Cu DPK L] systems because of the special characteristics associated with DPK.

DPK is known to absorb a water molecule and exist in geminal diol form (DPK·H_2O). One of these two – OH protons can get dissociated at higher pH (> 5) (deprotonation is favoured in the presence of a metal ion) and the free O^- competes with one of the pyridyl nitrogens for coordination with the metal ion. Thus $(DPK{\cdot}OH)^-$ exhibits ambidentate nature with N–N or N–O^- as coordinating sites (Fischer and Sigel 1975, 1979). However, in the present study computer assisted calculations of formation constants of [Cu DPK L^{1-9}] in pH ranges 3 to 4·5 or 3 to 7 gave identical results, indicating that in these systems, DPK probably coordinates from the N–N end till high pH. To further confirm this, pH titration curves of [Cu DPK L] were compared with the corresponding curves for [Cu DIPY L]. Representative curves are shown in figure 1. The two curves run parallel till pH ~ 7·0 and there is no difference in the [Cu DPK L] and [Cu DIPY L] curves. This indicates that DPK continues to coordinate from the N–N site up to pH 7 as in the case of dipyridyl. Coordination from the – OH site in DPK would liberate extra protons resulting in deviation of the [Cu DPK L] curve from the [Cu DIPY L] curve. A reason for the preference for N–N coordination in [Cu DPK L] could be found in the

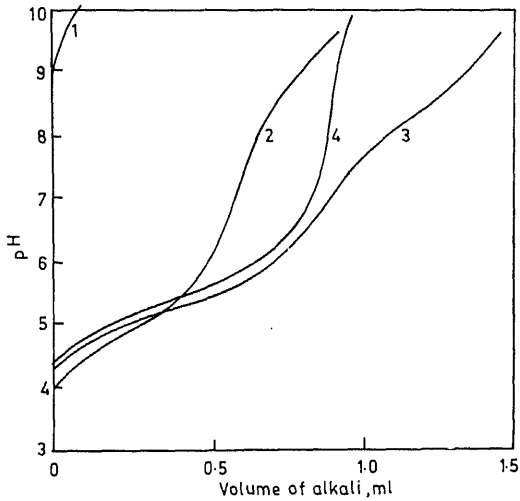

Figure 1. Titration curves for (1) DPK(0·001 M); (2) CuDPK (1 : 1); (3) CuDPK catechol (1 : 1 : 1); (4) CuDIPY catechol (1 : 1 : 1); solutions containing 0·01 M each of the ligands and/or Cu^{2+} have been titrated.

Verification of table 1 shows that $[CuA^2L]$ complexes are more stable than other $[CuAL]$ complexes. This can be explained only when DPK is considered to be in keto form. Loss of planarity of the chelate ring in gem-diol form with sp^3 hybridized carbon will result in considerable reduction in $M \rightarrow$ DPK. $H_2O\pi$-interaction which will destabilize the ternary complex.

An observation of the spectra of DPK and [CuDPK] at various pH supports this fact. In between pH 2 to 7 DPK exhibits two bands at 274 nm (π_1) and 244 nm (π_2) corresponding to transitions in the pyridyl ring. The π_2 band is shifted to lower energy due to the presence of the keto group. The weak $n \rightarrow \pi^*$ transition of the keto group occurs at $\sim$ 320 nm and is hidden under intense π_2 transition.

In the case of [Cu DPK] the corresponding π bands are observed at 248 and 272 nm with a small shift due to coordination with the metal ion. The presence of a π_2 band at higher wavelength (248 nm) till pH $\sim$ 5·5 indicates the existence of the keto form of the coordinated DPK and supports the following equilibrium.

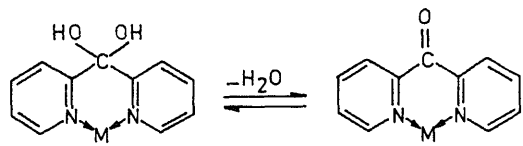

Table 1. Stability constants log K^{CuA}_{CuAL} for ternary complexes of Cu(II).

Ligands[a]	A^1	$\Delta \log K$	A^2	$\Delta \log K$	A^3	$\Delta \log K$	A^{4b}	$\Delta \log K$	A^{5b}	$\Delta \log K$
L^1	13·76 (±0·10)	+0·96	14·65 (±0·08)	+1·85	13·58 (±0·03)	+0·78	13·48	+0·68	13·60	+0·80
L^2	14·56 (±0·07)	+0·15	15·06 (±0·05)	+0·65	14·35 (±0·09)	−0·06	14·25	−0·16	14·39	−0·02
L^3	15·51 (±0·10)	+0·10	15·66 (±0·04)	+0·25	15·39 (±0·03)	−0·02	14·77	−0·64	15·04	−0·37
L^4	16·05 (±0·07)	+0·49	15·90 (±0·07)	+0·34	14·88 (±0·10)	−0·68	15·24	−0·32	15·04	−0·52
L^5	10·66 (±0·10)	+0·09	10·18 (±0·10)	−0·39	9·54 (±0·08)	−1·03	8·93	−1·64	9·05	−1·52
L^6	15·35 (±0·09)	+0·80	15·15 (±0·10)	+0·60	14·80 (±0·09)	+0·25	14·71	+0·16	14·92	+0·37
L^7	14·39 (±0·09)	+0·54	14·35 (±0·09)	+0·50	13·39 (±0·10)	−0·06	13·70	−0·15	14·13	+0·28
L^8	14·28 (±0·05)	+0·28	14·78 (±0·07)	+0·78	13·85 (±0·10)	−0·15	13·47	−0·53	13·94	−0·06
L^9	15·67 (±0·10)	+1·01	16·11 (±0·10)	+1·45	15·48 (±0·05)	+0·82	15·22	+0·56	15·27	+0·61

Values in dioxane water (1:1, v/v) and μ = 0·2M $NaClO_4$ at 30°C, with standard deviation $\sigma\beta$ in parenthesis;
[a]See text for ligand description; [b]Values for A^4 and A^5 are taken from earlier work (Bhattacharya and Patel 1985), where A^4 = 1,10-phenanthroline and A^5 = 2,2′-dipyridyl.

Table 2. Stability constant of ternary complexes of [Cu DPK L] t = 30°C, μ = 0·2 mol dm^{-3} ($NaClO_4$) in different percentages of dioxan-water medium.

Percentage of dioxan	log $K^{CuA}_{CuAL^1}$	Δlog K	log $K^{CuAL^8}_{CuAl}$	Δlog K
Aqueous	14·78[a]	+0·82	10·91	+0·05
25%	14·14	+1·34	11·53	+0·53
50%	14·65	+1·85	14·78	+0.78

[a]Sigel *et al* (1971)

queous 25% and 50% dioxan-water media. The value of $K^{CuA}_{CuAL^1}$ in aqueous olution is taken from literature (Fischer and Sigel 1979), where the conditions used or the determination are different, and hence the value of $K^{CuA}_{CuAL^1}$ is higher. Iowever, both temperature and ionic strength affect binary and ternary formation onstants to the same extent and hence the $\Delta \log K$ value can be considered for omparison with the present study. It is observed that there is an increase in the ositive value of $\Delta \log K$ with increase in dioxan content of the medium, indicating hift of equilibrium (I) towards right. The keto form being more π acidic in haracter stabilizes the ternary complex.

$\Delta \log K$ values for the complexes $[CuA^1L]$ are higher than those for orresponding DIPY or PHEN complexes. This is because of the presence of electron ithdrawing $-NO_2$ group which depleted the electron density over the ring, making a stronger π acid. As a result, the class *A* character of the metal ion is increased nd coordination with a $O^- - O^-$ containing ligand is favoured resulting in greater tabilization of the ternary complex. The electron releasing > NH group over DPA hould decrease the π-acidity of the ligand. However, there is no destabilization of he ternary complex involving DPA. This may be because of the larger size of the helate ring formed by DPA.

Comparison within the series of secondary ligands indicates that $\Delta \log K$ values or [Cu*A* catecholate] are higher than those for the respective complexes formed by iron, photocatechuic acid, catechol aldehyde or 2,3-dihydroxynaphthalene. This is ecause of the electron withdrawing nature of the substitutents, sulphonate, arboxylate, carbonyl or phenyl, respectively, over the catecholate ring. These ecrease the electron density over the coordinating O^- resulting in lower release of epulsion in the ternary complex than in the binary complex and ultimately lower tabilization of the ternary complex. The ternary complexes formed by 1,8-lihydroxy naphthalene are still less stable probably because of the direct articipation of the second phenyl ring in electron delocalization and formation of a ix-membered chelate ring.

In case of catecholamines the amino group remains protonated and hence exert an lectron withdrawing effect. Consequently, in ternary complexes of dopamine, $\Delta \log K$ values are lower than those for [Cu *A* catecholate]. However, in adrenaline

References

Chidambaram M V and Bhattacharya P K 1970 *J. Inorg. Nucl. Chem.* **32** 3271
Fischer B E and Sigel H 1974 *Z. Naturforsch.* **B29** 654
Fischer B E and Sigel H 1975 *J. Inorg. Nucl. Chem.* **37** 2127
Fischer B E and Sigel H 1979 *Inorg. Chem.* **18** 425
Gopalkrishnan K and Bhattacharya P K 1982a *J. Chem. Soc., Dalton Trans.* 353
Gopalkrishnan K and Bhattacharya P K 1982b *J. Chem. Soc., Dalton Trans.* 543
Griesser R and Sigel H 1970 *Inorg. Chem.* **9** 1238
Griesser R and Sigel H 1971 *Inorg. Chem.* **10** 2229
Huber P R, Griesser R, Prijs B and Sigel H 1969 *Eur. J. Biochem.* **10** 238
Huber P R and Sigel H 1972 *Z. Naturforsch.* **B27** 1319
Patel V K and Bhattacharya P K 1985 *Proc. Indian Acad. Sci. (Chem. Sci.)* **94** 495
Patel P J, Patel V K and Bhattacharya P K 1982a *Indian J. Chem.* **A21** 590
Patel P J, Patel V K and Bhattacharya P K 1982b *Inorg. Chem.* **21** 3163
Sayce I G 1968 *Talanta* **15** 1397
Sayce I G 1971 *Talanta* **18** 653
Sayce I G and Sharma V S 1972 *Talanta* **19** 831
Sigel H 1967 *Chimia* **21** 489
Sigel H 1980 *Inorg. Chem.* **19** 1411
Sigel H, Huber P R and Pasternack R F 1971 *Inorg. Chem.* **10** 2226
Walker F A, Sigel H and McCormic D B 1972 *Inorg. Chem.***11** 2756

© Printed in India.

Exchange reactions of copper complexes with amines

M N PATEL* and K B PATEL
Chemistry Department, Sardar Patel University, Vallabh Vidyanagar 388 120, India

MS received 29 July 1985

Abstract. Square planar mixed ligand complexes of the type [CuLL′] where L = 5-chlorosalicylaldehyde and L′ = acetoacetanilide, have been synthesized on treatment with ammonia. Amine exchange of the above Schiff base complexes has been carried out on treatment with different amines. The reaction with ethanol amine is quite interesting compared to other amines. It reacts with 5-chlorosalicylaldehyde to form a Schiff base, while the β-diketone part is removed in the complex formation. All the complexes were characterized by elemental analysis, spectral studies, magnetic measurement, TLC, and conductane.

Keywords. Mixed ligand copper complexes; amine exchange; Schiff bases.

. Introduction

The present work was undertaken in order to explore the synthesis, structure and eactions of the corresponding mixed ligand complexes of copper(II). Mixed ligand omplexes of the type [CuLL′], where L = 5-chlorosalicylaldehyde is a primary igand and L′ = acetoacetanilide the secondary ligand, are prepared. The mixed igand complex on treatment with ammonia gives a mixed imine Schiff base (SB) omplex. Amine exchange (transamination) reactions were also carried out by reatment of the mixed imine Schiff base complex with methyl amine [*M*], -butylamine [NB], aniline [*A*], *m*-toludine [MT], *p*-toludine [PT], *p*-anisidine [PA], -phenilidine [PP], α-naphthylamine [*N*] and ethanol amine [*E*].

. Experimental

All the chemicals used were of AnalaR or chemically pure grade.

.1 *Preparation of parent complexes (type I)* [*Cu-SB*$_1$-*AAA*]

To an aqueous solution (1 M) of copper acetate in excess ammonia, alcoholic olution of respective 5-chlorosalicylaldehyde (1 M) and acetoacetanilide *AAA*] (1 M) were added. The mixture was stirred well, and the solid that eparated out was filtered and washed successively with water and 50% alcohol. The product was recrystallised from chloroform.

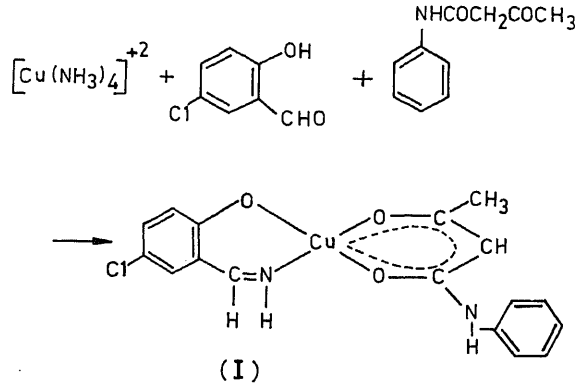

(I)

2.2 *Preparation of complexes using methyl and other amines (type II)*

An ethanolic solution (0·005 M) of a copper(II) complex of the type (I) was warmed for half an hour on a water-bath. Using methyl amine [*M*] (30 ml) as solvent the contents were refluxed for two hours. The product was obtained by pouring water into the reaction mixture, filtering, washing with water and 50% ethanol, and finally recrystallizing from chloroform.

The amine exchange reactions of *n*-butyl amine, aniline, *m*-toludine, *p*-toludine, *p*-anisidine, *p*-phenilidine, and α-naphthylamine were carried out as described above.

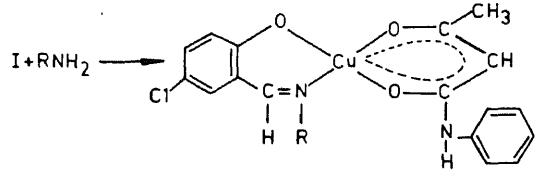

Chart 2.

where R = CH_3, C_4H_{10}, C_6H_5, *m*-C_7H_7, *p*-C_7H_7, *p*-C_7H_7O, *p*-C_8H_9O, and α-C_8H_7.

2.3 *Preparation of complexes using ethanol amine (type III)*

Copper(II) mixed ligand complexes containing salicylaldimine and β-diketone (type I) were treated with an ethanolic solution of ethanolamine (0·05 M, 20 ml) on a waterbath for 2–3 hours. The solid product precipitated on addition of water to the reaction mixture was filtered, washed with water and finally with 50% ethanol. The complex was recrystallized from chloroform. Analysis of the products showed that the β-diketone part was replaced by a water molecule and the basic bidentate Schiff base is converted to a tridentate.

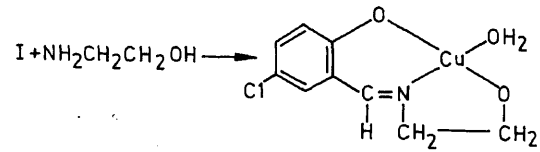

2.4 *Elemental analyses*

Carbon, hydrogen and nitrogen were estimated by C–H and N Coleman analysers. Halogen was estimated by the well-known Carius method.

2.5 *Metal contents in the complexes*

The metal content of each of the complexes was estimated by volumetric analysis. Weighed quantities of metal chelates of copper(II) were decomposed with a mixture of perchloric acid, nitric acid, sulphuric acid and hydrochloric acid, all AR grade. After carefully evaporating to dryness, the residue in powder form was extracted with distilled water and diluted to a finite volume. The metal ion in solution was estimated by titration against standard EDTA solution using an appropriate indicator.

2.6 *Physical measurements*

The effective magnetic moments were calculated from the equation

$$\mu_{\text{eff}} = 2{\cdot}83[(\chi_A - N_\alpha)T]^{1/2},$$

where χ_A is the molar magnetic susceptibility corrected using Pascal's constants and N_α is the temperature independent paramagnetism per gram-ion of copper (II). N_α was assumed to be 60×10^{-6} cgs (Muto and Tukki 1972).

TLC analysis of all the complexes was carried out on silica gel (Sichem) using a mixture of chloroform and ether (6 : 4) as solvent. The solvent was selected after several trials. Solutions of the copper (II) complexes were prepared. The solution indicated two spots in TLC whereas the mixed ligand complex is pure and a single compound rather than the mixture of *bis* complexes of the two ligands.

Conductivity measurements were carried out in chloroform using a Toshniwal conductivity bridge, model CLO/O1A.

ESR measurements of the powdered samples were carried out at room temperature on a Varian E-4 EPR spectrometer operating at 9·5 GHz with 100 kHz field modulation.

Reflectance spectra in the visible region were recorded on a Beckman-Du-Spectrophotometer at room temperature fitted with a standard Beckman reflectance attachment; MgO (BDH) was used as diluent.

The infrared spectra of the complexes were taken as KBr pellet on a Perkin-Elmer 983 IR spectrophotometer. Percentage transmission was recorded against wave number.

3. Results and discussion

The aldehyde part undergoes Schiff base formation. The β-keto-anilides, however, remain unaffected. No Schiff base formation takes place in the β-ketoanilide part of the molecules. The amine exchange reaction proceeds by a nucleophilic attack of the exchanging amine on the electron deficient carbon of the polarised imine (Olsgawski and Martin 1965). Amine exchange was carried out using excess amine

(acetoacetanilide part) is completely removed and the aldimine part reacts with ethanolamine to form a tridentate ligand, in which the –OH group of ethanolamine provides the third coordination site, the final compound (III) attained is tetracoordinated through coordination of water molecules (Bhattacharya and Uma 1979).

The elemental analyses of Cu(II) complexes are in agreement with the suggested structures (table 1). All the Schiff base complexes obtained are soluble in chloroform. They are found to be non-conducting, indicating their non-electrolytic nature.

All the Cu(II) complexes are paramagnetic showing the presence of one unpaired electron. The room temperature magnetic moments in the present amine exchange complexes lie in the range 1·8–2·0 B.M. (table 2) are within the range expected for square planar Cu(II) complexes (Hathaway and Thomlinson 1970).

The diffuse reflectance spectra of copper(II) mixed ligand complex and its amine exchange are shown in figure 1 and summarized in table 2. Copper(II) mixed ligand complex, derived from SB_1–*AAA* exhibits two bands at 16,395 and 25,640 cm^{-1} and is consistent with square planar stereochemistry (Aly and Asmal 1981). The first band is assigned to *d–d* transition while the band at 25,640 cm^{-1} can be attributed to charge transfer or interligand transition (Dave *et al* 1974). All the amine exchange complexes showed these two bands in the region 15000–17000 cm^{-1} and 24000–26000 cm^{-1} respectively.

Table 1. Analytical data of [Cu-SB_1-*AAA*] and its amine exchange complexes.

Compound	Experimental (theoretical) %				
	Metal	Carbon	Hydrogen	Nitrogen	Halogen
Cu-SB_1-*AAA*	16·47 (16·14)	50·84 (51·47)	3·39 (3·80)	7·42 (7·106)	9·39 (9·01)
Cu-SB_1*M*-*AAA*	14·6 (15·57)	52·57 (52·94)	4·0 (4·16)	6·54 (6·86)	8·32 (8·70)
Cu-SB_1NB-*AAA*	13·92 (14·76)	55·79 (56·0)	4·78 (5·1)	6·08 (6·22)	7·59 (7·88)
Cu-SB_1*A*-*AAA*	14·21 (13·95)	58·96 (58·72)	3·72 (4·04)	5·67 (5·95)	7·29 (7·55)
Cu-SB_1MT-*AAA*	13·38 (13·13)	59·11 (59·61)	4·1 (4·33)	5·52 (5·78)	7·15 (7·33)
Cu-SB_1PT-*AAA*	14·24 (13·13)	59·34 (59·51)	4·16 (4·33)	5·6 (5·78)	7·46 (7·33)
Cu-SB_1PA-*AAA*	12·08 (12·07)	57·96 (57·6)	4·44 (4·2)	5·84 (5·6)	6·83 (7·1)
Cu-SB_1PP-*AAA*	12·13 (11·72)	55·07 (55·45)	4·1 (4·25)	5·33 (5·17)	6·33 (6·56)
Cu-SB_1*N*-*AAA*	12·18 (12·82)	61·03 (60·60)	4·54 (4·24)	5·38 (5·65)	6·87 (7·17)
[Cu-SB_1*E*]·H_2O	24·21 (22·78)	39·24 (38·70)	3·24 (3·58)	5·19 (5·01)	12·49 (12·78)

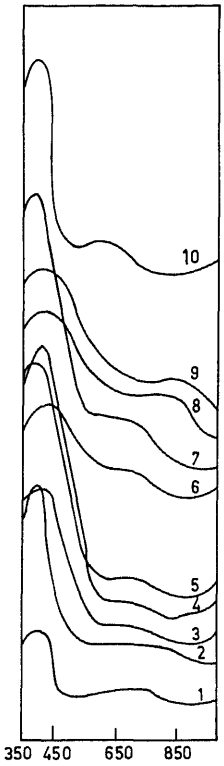

Figure 1. Reflectance spectra of copper(II) complexes.
1. Cu-SB_1-*AAA*;
2. Cu-SB_1M-*AAA*;
3. [Cu-SB_1E]·H_2O;
4. Cu-SB_1NB·*AAA*;
5. Cu-SB_1*A*-*AAA*;
6. Cu-SB_1MT-*AAA*;
7. Cu-SB_1PT-*AAA*;
8. Cu-SB_1PA-*AAA*;
9. Cu-SB_1PP-*AAA*;
10. Cu-SB_1*N*-*AAA*.

The ESR spectra of powder samples of Cu–SB_1–*AAA* and Cu–SB_1*A*–*AAA* have $g\perp = 2{\cdot}0027$ and $g\perp = 2{\cdot}025$, respectively. It may be concluded that square planar eometry is possible around copper(II) (Gajapathy *et al* 1983).

The IR spectra of mixed ligands complexes are complicated and difficult to nterpret. However, only those peaks that could be assigned with reasonable ertainty are listed. Mixed imine Schiff base complexes of Cu(II) show stretching requency at 1605 cm^{-1} when R is H, which disappears after amine exchange eaction and a new band appears around 1630 cm^{-1} (table 3). The band at 615 cm^{-1} is due to ν C=N of the imine linkage. The band around 1570 cm^{-1} is ue to ν C=O of diketone. There is also a band around 3220 cm^{-1} corresponding o the free ν N–H of diketone.This band indicates that there is no bonding through he nitrogen of the diketone.

The IR spectrum of complex [Cu–SB_1E]·H_2O exhibits a broad band around 3410 cm^{-1} corresponding to O–H stretch, confirming the presence of water. There is also a band around 800 cm^{-1} corresponding to the O–H out-of-plane deformation. This indicates the presence of coordinated water.

A further examination of the IR spectra, indicates that the copper is coordinated through C=N and the oxygen of water molecule. The C=N stretching frequency is observed at 1630 cm^{-1} (Nakamoto 1970). The disappearance of the ν N–H band

Table 2. Spectral (electronic and ESR) and magnetic moment data of Cu-SB_1-*AAA* and its amine exchange complexes.

Compound	Absorption maxima (cm^{-1})	Assignment	$g_\perp$ value	Magnetic moment (B. M.)
Cu-SB_1-*AAA*	16,395 25,640	$^2B_{1g}$–$^2A_{1g}$ Charge transfer	2·00277	1·8
Cu-SB_1*M*-*AAA*	15,615 25,925	Charge transfer	—	1·83
Cu-SB_1NB-*AAA*	16,360 24,995	Charge transfer	—	1·89
Cu-SB_1*A*-*AAA*	16,190 24,990	Charge transfer	2·025	1·97
Cu-SB_1MT-*AAA*	16,715 24,965	Charge transfer	—	1·9
Cu-SB_1PT-*AAA*	16,530 24,770	Charge transfer	—	1·86
Cu-SB_1PA-*AAA*	16,480 25,645	Charge transfer	—	1·93
Cu-SB_1PP-*AAA*	15,145 24,990	Charge transfer	—	1·84
Cu-SB_1*N*-*AAA*	15,875 24,895	Charge transfer	—	2·0
[Cu-SB_1*E*]·H_2O	15,530 25,640	Charge transfer	2·019	1·78

Table 3. Infrared frequencies of Cu-SB_1·*AAA* and its amine exchange complexes (cm^{-1}).

Compound \ Group	N–H	C=N	C=O	*m*–O	*M*–N	H_2O
Cu-SB_1-*AAA*	3220 *b*	1615 *s*	1570 *m*	690 *s*	515 *w*	—
Cu-SB_1*M*-*AAA*	3280 *b*	1635 *s*	1550 *s*	665 *ms*	500 *w*	—
Cu-SB_1NB-*AAA*	3285 *mb*	1620 *s*	1590 *s*	670 *m*	545 *m*	—
Cu-SB_1*A*-*AAA*	3260 *w*	1615 *s*	1590 *m*	680 *mw*	545 *w*	—
Cu-SB_1MT-*AAA*	3245 *w*	1625 *ms*	1580 *s*	700 *s*	535 *b*	—
Cu-SB_1PT-*AAA*	3260 *b*	1610 *m*	1590 *m*	680 *m*	540 *m*	—
Cu-SB_1PA-*AAA*	3230 *b*	1620 *s*	1515 *m*	680 *m*	545 *b*	—
Cu-SB_1PP-*AAA*	3250 *mb*	1630 *s*	1555 *s*	660 *m*	530 *b*	—
Cu-SB_1*N*-*AAA*	3290 *b*	1625 *s*	1575 *s*	675 *m*	520 *b*	—
[Cu-SB_1*E*]·H_2O	—	1630 *s*	—	660 *s*	540 *w*	3410 *b*

References

Aly M M and Asmal S E 1981 *J. Inorg. Nucl. Chem.* **43** 45
Bhattacharya P K and Uma C 1979 *J. Indian Chem. Soc.* **56** 751
Dave L D, Kothari H K and Sudhamshumoullp 1974 *Indian J. Chem* **12** 771
Gajapathy D, Govindarajan S, Patil K C and Manohar H 1983 *Polyhedron* **2** 865
Hathaway B J and Thomlinson A G 1970 *Coord. Chem. Rev.* **5** 1
Muto Y and Tukki T 1972 *Bull. Chem. Soc. (Jpn)* **51** 139
Nakamoto K 1970 *IR spectra of inorganic and coordination compounds* (New York: Wiley-Intersc
Olsgawski E J and Martin D A 1965 *J. Inorg. Nucl. Chem.* **25** 345
Samantaray A, Panda P K, and Mahapatra B K 1983 *J. Indian Chem. Soc.* **60** 293

oc. Indian Acad. Sci. (Chem. Sci.), Vol. 97, Nos 5&6, December 1986, pp. 543–546.
Printed in India.

nfluence of electrostatic effect on the stability of mixed-ligand omplexes: Uranyl-complexone-phenol/phenolic acid ternary systems

ANUSHREE SAMANTA, S N LIMAYE and M C SAXENA*
Department of Chemistry, Dr. Harisingh Gour Vishwavidyalaya, Sagar 470 003, India

MS received 24 December 1985; revised 8 April 1986

Abstract. The formation constants (log K^{MA}_{MAL}) of the complexes of the type $(UO_2.A.L]$ (where A = IMDA, NTA or EDTA; L = catechol, resorcinol, phloroglucinol, pyrogallol, β-resorcylic acid or protocatechuic acid) have been determined potentiometrically at 25°C and ionic strength, I = 0·2 (mol dm^{-3}, $NaClO_4$) using the Irving–Rossotti approach. The formation constants of the binary complexes (log K^{M}_{MA}) have been found to lie in the sequence IMDA < NTA < EDTA, whereas those for the mixed ligand complexes (log K^{MA}_{MAL}) follow the reverse sequence, IMDA > NTA > EDTA, due to the electrostatic effect.

Keywords. Ternary uranyl-complexone-phenol/phenolic acid complexes; electrostatic effect; formation constant; stability of mixed-ligand complexes.

Introduction

he statistical aspects of solution stabilities of mixed-ligand complexes have been scussed by some workers (Marcus and Eliezer 1961, 1962; Kida 1956, 1961; ewitt and Watters 1954; Bhattacharya 1981). Bjerrum (1941) had proposed the -called "total effect" in order to explain the gradual decrease in stability of the ccessive binary complexes of a given metal ion with a certain ligand. statisticality involved in the stability of some mixed-ligand complexes of the type CuAL] (where A = 2,2′-dipyridyl, or *o*-phenanthroline, L = catechol or a similar condary ligand) has been reported recently (Bhattacharya and Patel 1982). The ffects of electrostatic and other astatistical factors on the stabilities of ternary nthanide-EDTA complexes with alizarine-red sulphonic acid and some unsatu-ted aliphatic carboxylic acids have been reported by us (Limaye and Saxena 1984, 985).

In the present work the formation constants of (1:1:1) mixed-ligand complexes f UO_2^{2+} have been determined using IMDA, NTA and EDTA as primary ligands and techol (cat), resorcinol (res), phloroglucinol (phl), pyrogallol (pyr), pro-catechuic acid (pca) and β-resorcylic acid (β-res) as secondary ligands. The role f electrostatic effect in the variation of stabilities of these ternary complexes has een discussed.

2. Experimental

Uranyl nitrate of BDH analar grade and other chemicals of Merck GR or Fluka AR grade were used. The solutions were prepared in double distilled water. The metal-ligand formation constants were determined potentiometrically by using the Irving–Rossotti approach (Irving and Rossotti 1953, 1954; Chidambaram and Bhattacharya 1970) at 25°C and an ionic strength, $I = 0{\cdot}2$ (mol dm^{-3}, $NaClO_4$). The usual titration sets (Limaye and Saxena 1982) were prepared and titrated after equilibration with a carbonate free 0·2 mol dm^{-3} NaOH solution using an Elico digital (model LI-120) pH-meter. Reproducible pH data were used for evaluating the formation constants. The proton-ligand formation constants of the secondary ligands were redetermined to obtain their values under experimental conditions. The experimental values of the formation functions were subjected to the *Q-test* (Pecsok *et al* 1976) so as to reject any suspect value. Only statistically valid values were used for calculating the formation constants. The formation constants, $\log K^{M}_{ML}$, $\log K^{M}_{MA}$ and $\log K^{MA}_{MAL}$ (the terms have their usual meanings) are presented in table 1. The quantities in parentheses represent standard deviations.

3. Results and discussion

The formation of the mixed-ligand complexes in the present work (titration curves not shown) proceeds following the equilibria

$$M + A \rightleftharpoons MA;\ MA + L \rightleftharpoons MAL \text{ (charges omitted).}$$

Chelation with the primary ligand takes place in a lower pH region (pH $\lesssim$ 3·0) and the primary complex *MA* remains stable up to a sufficiently high pH ($\sim$ 8·0). The secondary ligand *L* combines with *MA* in the pH range $\sim$ 4·0–6·0. No hydrolysis of the complexes is indicated. Dilute solutions (1×10^{-3} mol dm^{-3}) were used to avoid any possibility of the formation of polynuclear species. Plots (not shown) of $\bar{n}/[L]$ vs $[L]$ ($\bar{n}$ = formation function of the complex, $[L]$ = free ligand concentration) were found to be smooth indicating the absence of any polynuclear species.

Table 1. Formation constants of the binary (*MA* and *ML*) and ternary (*MAL*) complexes of UO_2^{2+}. Temperature = 25°C; $I = 0{\cdot}2$ (mol dm^{-3}, $NaClO_4$).

Formation constant	Primary ligand (*A*)	Secondary ligand (*L*)					
		cat	res	phl	pyr	pca	β-res
$\log K^{M}_{ML}$	–	14·90 (±0·002)	9·66 (±0·01)	8·34 (±0·0005)	13·81 (±0·02)	15·47 (±0·001)	8·10 (±0·002)
$\log K^{MA}_{MAL}$	IMDA	13·80 (±0·002)	8·96 (±0·00)	7·46 (±0·02)	13·55 (±0·02)	15·04 (±0·003)	7·41 (±0·002)
	NTA	13·40 (±0·004)	8·64 (±0·002)	7·08 (±0·05)	12·85 (±0·002)	14·50 (±0·008)	6·97 (±0·003)
	EDTA	10·42	6·71	5·28	10·31	11·63	4·85

The $\log K^{M}_{MA}$ values are expectedly found to lie in the sequence IMDA < NTA < EDTA. The denticity of these ligands (three, four and six, respectively) causes gradually increasing chelate effect in this sequence. Further, the combination of the ligands A^{2-}, A^{3-} and A^{4-} (corresponding to IMDA, NTA and EDTA, respectively) with UO_2^{2+} should be associated with increasing entropy effect in this order. The metal chelates of these ligands with the 3*d*- and 4*f*- metal ions are actually reported (Ashcroft and Mortimer 1970) to be stabilised chiefly due to the entropy factor. The entropy effect should mainly originate from the rupture of the hydration sphere of the uranyl ion and the desolvation of the acetate groups of these ligands.

In contrast to the stability sequence of the binary *MA* complexes, a reverse order of stability has been observed (see table 1) for the ternary complexes, IMDA > NTA > EDTA. The complexation of the three chelons with the uranyl ion followed by a further chelation with the secondary ligand, L^{2-} may be represented as:

$$UO_2^{2+} + \text{IMDA}^{2-} \rightleftharpoons [UO_2.\text{IMDA}]^0;$$
$$[UO_2.\text{IMDA}]^0 + L^{2-} \rightleftharpoons [UO_2.\text{IMDA}.L]^{2-}, \quad (1)$$
$$UO_2^{2+} + \text{NTA}^{3-} \rightleftharpoons [UO_2.\text{NTA}]^-;$$
$$[UO_2.\text{NTA}]^- + L^{2-} \rightleftharpoons [UO_2.\text{NTA}.L]^{3-}, \quad (2)$$
$$UO_2^{2+} + \text{EDTA}^{4-} \rightleftharpoons [UO_2.\text{EDTA}]^{2-};$$
$$[UO_2.\text{EDTA}]^{2-} + L^{2-} \rightleftharpoons [UO_2.\text{EDTA}.L]^{4-}, \quad (3)$$

Equations (1), (2) and (3) clearly show that with IMDA the incoming secondary ligand (negatively charged) experiences no electrostatic repulsion during the formation of the mixed-ligand complex. With NTA and EDTA, however, gradually increasing electrostatic repulsion is involved. The $\Delta \log K$ ($= \log K^{MA}_{MAL} - \log K^{M}_{ML}$) values (table 1) are negative. Statistically also the combination of L^{2-} with *MA* in the three cases should be less favoured in the observed sequence. What is important here is not so much the negative value of $\Delta \log K$ but its magnitude which leads to a reverse order of stability of the ternary *MAL* complexes as compared to that of the binary *MA* complexes.

It is observed that in general the increase in charge (on *MA*) from -1 to -2 causes much greater increase in the numerical value of $-\Delta \log K$ as compared to the change from 0 to -1. Statistically, therefore, the second step of complexation ($MA + L \rightleftharpoons MAL$) becomes much less favourable on going from NTA to EDTA than from IMDA to NTA which seems reasonable in view of their denticities.

The stability sequence (for binary, *ML* as well as ternary, *MAL* complexes) follows the order of ligand basicity pca > cat > pyr > res > phl > β-res. The effect of ring size of the chelate with the secondary ligand is also reflected in the stability. Both cat and pyr form similar five-membered rings; the presence of one additional –OH group in the latter causes a reduction in electron density over the two donor oxygens resulting in the sequence cat > pyr. Six-membered rings are

higher values of log K^{M}_{ML} and log K^{MA}_{MAL} than those with cat, although both form otherwise similar five-membered rings. With β-res a six-membered ring involving the carboxylate and hydroxyl groups seems to be formed leaving behind one –OH group and hence the stability of β-res complexes is the least in the series.

Acknowledgements

One of the authors (MCS) is thankful to the Madhya Pradesh Council of Science & Technology for the award of a research grant, and the other (AS) for a junior research fellowship under the research project.

References

Ashcroft S J and Mortimer C T 1970 *Thermochemistry of transition metal complexes* (London: Academic Press) pp. 119, 127, 391

Bhattacharya P K 1981 *J. Sci. Ind. Res.* **40** 382

Bhattacharya P K and Patel V K 1982 *J. Indian Chem. Soc.* **59** 1244

Bjerrum J 1941 *Metal amine formation in aqueous solutions* (Copenhagen: P Haase & Sons) chap. 4

Chidambaram M V and Bhattacharya P K 1970 *J. Inorg. Nucl. Chem.* **39** 2471

Dewitt R and Watters J 1954 *J. Amer. Chem. Soc.* **76** 3810

Irving H M and Rossotti H S 1953 *J. Chem. Soc.* 3397

Irving H M and Rossotti H S 1954 *J. Chem. Soc.* 2904

Jejurkar C R, Mavani I P and Bhattacharya P K 1972 *Indian J. Chem.* **10** 1190

Kida S 1956 *Bull. Chem. Soc. Jpn.* **29** 805

Kida S 1961 *Bull. Chem. Soc. Jpn.* **34** 962

Limaye S N and Saxena M C 1982 *J. Indian Chem. Soc.* **59** 698, 916

Limaye S N and Saxena M C 1984 *J. Indian Chem. Soc.* **61** 748

Limaye S N and Saxena M C 1985 *J. Inst. Chem. India* **57(11)** 83

Marcus Y and Eliezer I 1961 *Bull. Res. Counc., Israel,* **A10** 23

Marcus Y and Eliezer I 1962 *J. Phys. Chem.* **66** 1661

Pecsok R L, Shields L D, Cairns T and McWilliams I G 1976 *Modern methods of chemical analysis* 2nd edn (New York: John Wiley & Sons) chap. 24

Proc. Indian Acad. Sci. (Chem. Sci.), Vol. 97, Nos 5&6, December 1986, pp. 547–553.
© Printed in India.

Molecular and crystal structure of 1-hydroxy-2-methyl-11-methylene-tricyclo $(5.3.1.0)^{2,7}$-undecan-5-one, $C_{13}O_2H_{18}$

S KRISHNASWAMY and VASANTHA PATTABHI*

Department of Crystallography and Biophysics, University of Madras, Guindy Campus, Madras 600 025, India

MS received 29 May 1986; revised 22 September 1986

Abstract. The title compound is orthorhombic with $a = 26{\cdot}132(6)$, $b = 11{\cdot}023(2)$, $c = 8{\cdot}317(5)$, Å; space group *Iba*2; $Z = 8$, $D_m = 1{\cdot}21(1)$, $D_c = 1{\cdot}192$ Mg m^{-3}, $\frac{1}{2}(H_2O)$ per molecule in asymmetric unit; λ (*MoK*α) = 0·7107 A; $\mu = 0{\cdot}46$ cm^{-1}; $F(000) = 936$. The structure was solved by direct methods and refined to $R(F)$ value of 0·069 using 327 reflections with $F \geqslant 5\sigma(F)$ out of 727 independent reflections for 2θ max = 46°. The *trans* fused cyclohexane and cyclohexanone rings form layers along the *a-b* plane. The axial methyl attached at the bridge-head, interlocks with the translated methylene of the cyclobutane fused across the cyclohexane ring. The equatorial hydroxyl at the bridge-head adjacent to the methyl junction and the water molecule on the two-fold form a water bridge along the *z* axis. The packing is reminiscent of that observed for the cholesterols used in membrane structure studies.

Keywords. X-ray structure; tricyclic; cyclobutane; cholesterol packing.

1. Introduction

The title compound was obtained through an unusual reductive cyclisation (Kannan *et al* 1984) (figure 1). Such a cyclisation, leading to the formation of a cyclobutane ring in metal ammonia reactions, had not been reported earlier. The X-ray structure determination of this compound was taken up primarily to verify the difficult cyclisation and the structure proposed by chemists using ^{13}C NMR evidence. The X-ray structure confirms the proposed structure (figure 2). An interesting feature that emerges from the structure solution is the tendency of this rigid tricyclic alcohol to mimic the crystal packing of cholesterols, in terms of interlocking of the projecting groups and alternation of hydrophobic and hydrophilic layers.

2. Experimental

The compound in the form of crystals was supplied courtesy Prof. S Swaminathan,

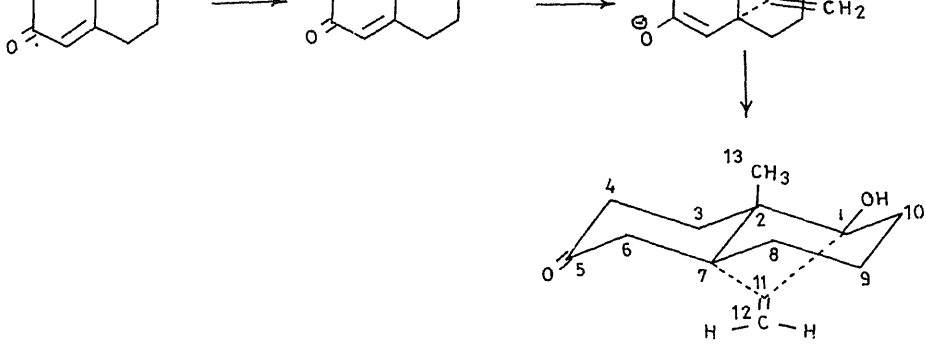

Figure 1. Schematic diagram of molecule and reduction scheme.

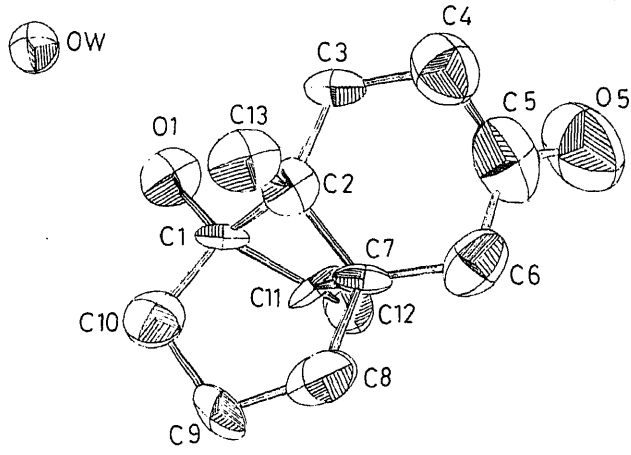

Figure 2. ORTEP diagram (Johnson 1965) showing thermal ellipsoids at 50% probability level.

applied. In the total of 727 reflections for 2θ max of 46°, 463 reflections had $F \geq 3\sigma(F)$ and 327 reflections had $F \geq 5\sigma(F)$. The results appertaining to the crystal and the data collection are listed in table 1.

3. Structure solution and refinement

The space group *Iba*2 was assigned based on the non-centric distribution of the E statistics. The structure was solved using a direct method and the Karle recycling procedure through the program MULTAN 80 (Main *et al* 1980). Initially the data beyond $3\sigma(F)$ limit were used for refinement. The z coordinate of the atom C(1) was held constant for fixing the origin on the two-fold axis. Block diagonal

Table 1. Crystal data.

Formula $C_{13}O_2H_{18}\cdot\frac{1}{2}H_2O$			$Mr = 215{\cdot}29$
System orthorhombic			Space group *Iba2*
$a = 26{\cdot}132(6)$	$b = 11{\cdot}023(2)$		$c = 8{\cdot}317(5)$ Å
$D_m = 1{\cdot}21(1)$	$D_c = 1{\cdot}192$ Mg m^{-3}	$Z = 8$	$F(000) = 926e$
$\lambda(MoK\alpha) = 0{\cdot}7107$Å			$\mu = 0{\cdot}46$ cm^{-1}
Crystal size $0{\cdot}4 \times 0{\cdot}13 \times 0{\cdot}08$ mm			
$\frac{\sin\theta \text{ max}}{\lambda}$	$0{\cdot}55$ Å^{-1}		
Total hkl	727		
$F \geq 5\sigma(F)$	327		
R	0·069		

Table 2. Fractional coordinates ($\times 10^4$) and equivalent thermal parameters ($\times 10^4$) for non-hydrogen atoms. e.s.d. values in parentheses.

$U_{eq} = \frac{1}{3}\sum_i\sum_j U_{ij} a_i^* a_j^* a_i a_j$

Atom	*X*	*Y*	*Z*	U_{eq}(Å^2)
C1	9250 (5)	2208 (11)	−653 (19)	386 (31)
C2	8796 (5)	2001 (12)	478 (15)	527 (34)
C3	8538 (5)	802 (9)	210 (18)	505 (32)
C4	7969 (6)	839 (16)	449 (21)	957 (37)
C5	7741 (6)	1768 (16)	−645 (22)	900 (37)
C6	7946 (5)	3004 (13)	−587 (19)	666 (34)
C7	8516 (5)	3017 (10)	−483 (17)	406 (33)
C8	8721 (6)	4276 (12)	50 (20)	737 (37)
C9	9292 (6)	4449 (12)	−182 (16)	572 (36)
C10	9601 (5)	3234 (14)	−204 (18)	639 (35)
C11	8865 (5)	2648 (10)	−1859 (19)	376 (33)
C12	8794 (5)	2541 (14)	−3458 (18)	598 (35)
C13	8887 (5)	2157 (14)	2299 (16)	627 (36)
O1	9554 (4)	1174 (8)	−1131 (15)	675 (29)
O5	7379 (4)	1483 (11)	−1552 (18)	1341 (35)
				U_{iso}(Å^2)
OW	10000	0	1401 (17)	518 (33)

finement (Shiono 1968) with isotropic temperature factors converged at = 0·15. The anisotropic temperature factor of C(1) was nonpositive definite. ıe water oxygen was treated isotropically. The clamp on the z coordinate of C(1) ıs shifted to the centre of mass of the molecule and the refinement was restarted. owever the anisotropic temperature factors of C(2), C(3) and C(7) were ınpositive definite. The quality of the data prompted the use of a higher cut off, mely 5σ (F). The refinement was restarted from the Karle output stage. otropic refinement converged at $R = 0{\cdot}122$. Anisotropic refinement converged at = 0·106 and the anisotropic temperature factors were normal. The hydrogens ere fixed stereochemically. The water and hydroxyl hydrogens were not included.

procedure in SHELX 76 (Sheldrick 1976). A few cycles of refinement brought the R index to 0·08. At this stage 20 reflections had a $F(\text{obs})/F(\text{calc})$ ratio of 1·5. Six of these, (3,1,0), (1,1,0), (28,2,0), (21,7,0), (22,0,2) and (7,1,2), which had a bad intensity profile in the data collection, were removed. A few cycles of damped refinement resulted in $R = 0{\cdot}069$. On further refinement the anisotropic temperature factors of C(1), C(4) and C(11) were nonpositive definite. The refinement was terminated at $R = 0{\cdot}069$ as no further improvement of the geometry was expected with the present data set. The maximum shift to esd ratio in the parameters was 0·3. The difference map had no peak greater than 0·25eÅ^{-3}. The weighted R was 0·055 with $w = 3{\cdot}003/\sigma^2$ (F) $(0{\cdot}0002F^2)$ and the goodness of fit $S = 2{\cdot}78$.

4. Results and discussions

The coordinates, bond lengths and bond angles involving the non-hydrogen atoms are listed in tables 2 to 4. The cyclohexane ring is in the sofa form with C(2)

Table 3. Bond lengths (Å) involving non-hydrogen atoms. e.s.d. values in parentheses.

Atoms	Distance	Atoms	Distance
C1–C2	1·53 (2)	C5–C6	1·47 (2)
C1–C10	1·50 (2)	C5–O5	1·25 (2)
C1–C11	1·50 (2)	C6–C7	1·49 (2)
C1–O1	1·45 (2)	C7–C8	1·55 (2)
C2–C3	1·50 (2)	C7–C11	1·52 (2)
C2–C7	1·56 (2)	C8–C9	1·52 (2)
C2–C13	1·54 (2)	C9–C10	1·56 (2)
C3–C4	1·50 (2)	C11–C12	1·35 (2)
C4–C5	1·49 (2)		

Table 4. Bond angles (°) involving non-hydrogens e.s.d. values in parentheses.

Atoms	Angle	Atoms	Angle
C2–C1–C10	116 (1)	C4–C5–O5	120 (2)
C2–C1–C11	87 (1)	C6–C5–O5	122 (2)
C2–C1–O1	119 (1)	C5–C6–C7	112 (1)
C10–C1–C11	109 (1)	C2–C7–C6	119 (1)
C10–C1–O1	109 (1)	C2–C7–C8	110 (1)
C11–C1–O1	116 (1)	C2–C7–C11	85 (1)
C1–C2–C3	113 (1)	C6–C7–C8	112 (1)
C1–C2–C7	87 (1)	C6–C7–C11	124 (1)
C1–C2–C13	118 (1)	C8–C7–C11	104 (1)
C3–C2–C7	110 (1)	C7–C8–C9	115 (1)
C3–C2–C13	108 (1)	C8–C9–C10	114 (1)
C7–C2–C13	120 (1)	C1–C10–C9	109 (1)
C2–C3–C4	114 (1)	C1–C11–C7	89 (1)

ckered. The C(9) end is flattened to accommodate the cyclobutane ring. The clobutane ring is puckered with a dihedral angle of 38(1)° between the planes rough the atoms C(1), C(2), C(7) and C(1), C(11), C(7). The cyclohexanone ring in the favoured chair form with puckering at C(2) and C(5). The torsion angles volving the rings are given in table 5. The bond angles and lengths within the rings e in agreement with the standard values expected for C(sp^3)–C(sp^3), within perimental error (Eliel *et al* 1967; Allen 1984). The hydroxyl oxygen O(1) is quatorial, whereas the methyl C(13) and the cyclobutane forming C(11) are axial ith respect to the cyclohexane ring.

The hydrogen bonding and packing features are shown in figures 3 and 4. The ethyl and methylene groups are nearly at right angles to the decalin-like ring

Table 5. Selected torsion angles (°) involving the ring atoms. e.s.d. values are given in parentheses.

Cyclohexane	
C1–C2—C7–C8	−77 (1)
C2–C7—C8–C9	59 (1)
C7–C8—C9–C10	−24 (2)
C8–C9—C10–C1	23 (2)
C9–C10—C1–C2	−60 (1)
C10–C1—C2–C7	83 (1)
Cyclohexanone	
C2–C3—C4–C5	57 (2)
C3–C4—C5–C6	−54 (2)
C4–C5—C6–C7	42 (2)
C5–C6—C7–C2	−34 (2)
C6–C7—C2–C3	39 (2)
C7–C2—C3–C4	−50 (1)
Cyclobutane	
C1–C2—C7–C11	26 (1)
C2–C7—C11–C1	−27 (1)
C7–C11—C1–C2	27 (1)
C11–C1—C2–C7	−26 (1)

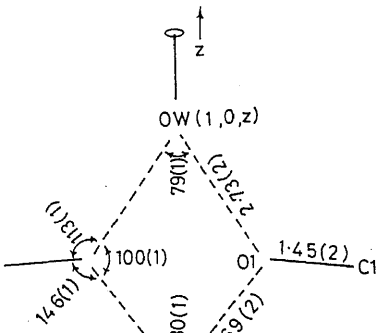

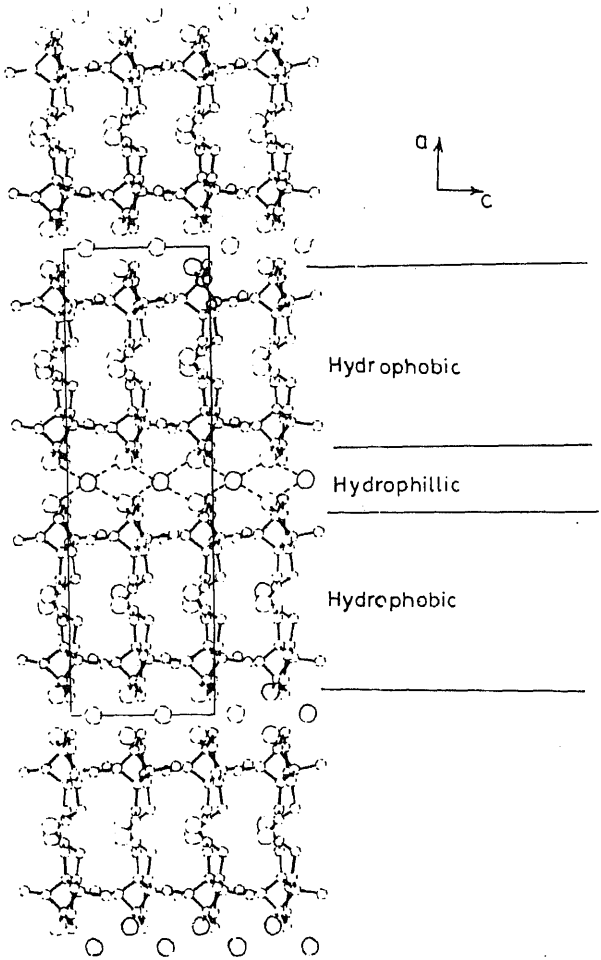

Figure 4. Packing diagram down *b* axis showing the water bridge and the alternate hydrophobic and hydrophilic layers. The methyl-methylene interlocking can also be seen.

system. These ring systems along the a-b plane are interlocked by the methyl and the methylene groups (C(13)....C(12) $(x, y, z+1)$:3·56Å). The packing of cholesteryl myristate (Craven and De Titta 1976) shows similar methyl interlocking involving the axial methyls of the steroid rings. Likewise, the alternate hydrophilic and hydrophobic layers seen in figure 4, are similar to the packing of the cholesterol monohydrate structure (Craven 1976).

References

Allen F H 1984 *Acta Cryst.* **B40** 64
Craven B H 1976 *Nature (London)* **260** 727
Craven B M and De Titta G T 1976 *J. Chem. Soc., Perkins Trans.* **II** 814
Eliel E L, Allinger N L, Angyal S J and Morrison G A 1967 *Conformational analysis* (New York: Interscience)
Johnson C K 1965 ORTEP, Report ORNL-3794, Oak Ridge National Laboratory, Tennessee, USA
Kannan R, Geetha P and Swaminathan S 1984 *Tetrahedron Lett.* **25** 1601
Main P, Fiske S J, Hull S E, Lessinger L, Germain G, Declercq J P and Woolfson M M 1980, MULTAN 80. A system of computer programs for the automatic solution of crystal structures from x-ray diffraction data, Universities of York, England and Louvain, Belgium
Sheldrick G M 1976 SHELX 76. A program for crystal structure determination, University of Cambridge, England
Shiono R 1968 Block diagonal least squares program, Department of Crystallography, University of Pittsburg, USA

Mechanism of the oxidation of alkyl aryl and diphenyl sulphoxides by peroxomonosulphate

R SUTHAKARAN, P SUBRAMANIAM and C SRINIVASAN*
School of Chemistry, Madurai Kamaraj University, Madurai 625 021, India

MS received 12 May 1986; revised 17 October 1986

Abstract. Detailed kinetic investigations of the oxidation of methyl phenyl sulphoxide and diphenyl sulphoxide by peroxomonosulphate in aqueous acetic acid medium reveal that the reactions are first-order, both in the sulphoxide and in the oxidant. Studies with substituted phenyl methyl sulphoxides and 4,4'-disubstituted diphenyl sulphoxides show that electron-releasing groups accelerate the rate of oxidation and electron-withdrawing groups retard it. A fair correlation between log k_2 and Hammett substituent constants has been observed in the two series. The mechanism proposed involves the rate-determining nucleophilic attack of the sulphoxide sulphur at the outer terminal peroxo oxygen atom of HSO_5^-.

Keywords. Peroxomonosulphate; oxidation of sulphoxides; structure-reactivity relationship.

Introduction

The synthetic utility of potassium hydrogen persulphate or potassium peroxomonosulphate (Kennedy and Stock 1960) as an oxidant has been studied in detail. The chemoselective oxidation of sulphides to sulphones by peroxomonosulphate (PMS) have been noticed (Trost and Curran 1981). PMS has been recently employed for the epoxidation of *trans*-cinnamic acid (Curci *et al* 1980) and alkenes (Bloch *et al* 1985). However, there are only a few kinetic studies with PMS as the oxidant. The kinetics of oxidation of halide (Fortnum *et al* 1960; Secco and Venturini 1976), nitrite (Edwards and Muller 1962), thiocyanate ion (Smith and Wilson 1966, 1967), alkyl thiocyanates (Bridgart and Wilson 1971), azide and azidopentammine-chromium(III) (Thompson *et al* 1979), oxovanadium and peroxovanadium (Thompson 1981, 1982), amino acids (Ramachandran and Vivekanandam 1984; Ramachandran *et al* 1984) and dimethyl sulphoxide (Pandurengan and Maruthamuthu 1981) have been investigated. Because aromatic sulphoxides can act as either nucleophiles or electrophiles in the kinetics of peroxobenzoic acid oxidations (Curci and Modena 1964), a detailed kinetic study on the oxidation of sulphoxides would be of great interest with PMS. In this paper we report our results on the kinetics of oxidation of methyl phenyl sulphoxide (MPSO), diphenyl sulphoxide (DPSO), several substituted phenyl methyl sulphoxides and diphenyl sulphoxides by PMS. A plausible mechanism, based on the kinetic results, has also been proposed.

2.1. *Materials*

All the substituted phenyl methyl sulphoxides were prepared from the corresponding sulphides by chromium trioxide oxidation (Baliah and Satyanarayana 1978). Methyl *p*-nitrophenyl sulphoxide was obtained by the oxidation of corresponding sulphide with nitric acid (Zincke and Lenhardt 1913). *p*-Acetylphenyl methyl sulphoxide was prepared by the potassium peroxodisulphate oxidation of the corresponding sulphide (Srinivasan *et al* 1986). The Friedel-Crafts reaction of benzene with thionyl chloride furnished diphenyl sulphoxide and similarly disubstituted diphenyl sulphoxides were obtained from substituted benzenes (Cumber *et al* 1965; Leonard and Sutton 1948; Sugaswa and Sakurai 1940). 4,4′-Dinitrodiphenyl sulphoxide was obtained by the hydrogen peroxide oxidation of the corresponding sulphide (Szmant and McIntosh 1951). All the sulphoxides were purified by distillation or recrystallization before kinetic use. The purity of the sulphoxides was established by means of sharp melting behaviour with solids, single spot on TLC and by spectral studies. Doubly distilled water was used throughout, the second distillation being from permanganate. Peroxomonosulphate, $2KHSO_5 . KHSO_4 . K_2SO_4$ (Oxone), sulphuric acid (AR) and potassium bisulphate (GR) were used as such. Acetic acid was purified by refluxing with chromium trioxide (Orton and Bradfield 1924).

2.2 *Kinetic measurements*

The oxidation studies with aryl methyl sulphoxides were conducted in 50% acetic acid-50% water (v/v) under pseudo first-order conditions with a ten-fold excess of the substrate over that of the oxidant concentration. The studies with 4,4′-disubstituted diphenyl sulphoxides were carried out in 80% acetic acid-20% water (v/v) due to their poor solubility in 50% acetic acid-50% water (v/v) medium. The progress of the reaction was followed by estimating the unconsumed PMS iodometrically by taking aliquot at regular intervals of time. The pseudo first-order rate constants (k_1) were calculated from the slope of the linear plot of log $(a - x)$ vs time by the method of least-squares using a IBM 1130 computer. The correlation coefficient for each run is $> 0{\cdot}995$. Straight lines were generally obtained for at least 60% of the reaction. The second-order rate constants were obtained from the relation $k_2 = k_1/[\text{substrate}]$.

2.3 *Product analysis*

The reaction mixture from actual kinetic run was neutralised with sodium carbonate, the solution was evaporated to dryness and ether extracted. Removal of ether gave solid product. On the basis of m.p. and TLC methyl phenyl sulphone and diphenyl sulphone were identified as the final products in the oxidations of MPSO and DPSO respectively.

2.4 *Reaction stoichiometry*

The stoichiometry of the reaction was determined by estimating the unreacted PMS after completion of the reaction by allowing an excess of it to react with substrate

(R = Me, Ph)

3. Results and discussion

3.1 *Oxidation of MPSO*

The kinetic studies were carried out under pseudo first-order conditions in the presence of MPSO in 50% acetic acid-50% water (v/v) mixture. Plots of log [PMS] against time were linear with slopes that were independent of the initial concentration of PMS, indicating the first-order dependence on the oxidant. The constant pseudo first-order constants (k_1) (see table 1) at different initial concentrations of PMS also reveal the first-order dependence on PMS. The linear dependence of log k_1 on log [MPSO] with a slope of 1·05 (r = 0·999) and the constant values of second-order rate constants at different concentrations of [MPSO] (table 1) indicate a first-order dependence on MPSO. The rate law may, therefore, be expressed as

$$\frac{-\mathrm{d[PMS]}}{\mathrm{d}t} = k_2[\mathrm{MPSO}]\,[\mathrm{PMS}].$$

The rate of oxidation is almost acid independent ([H^+] was maintained by the addition of H_2SO_4, see table 2). The kinetic data in table 2 also show that the rate is unaffected by the change in the ionic strength of the medium maintained by the addition of sodium bisulphate. This may be due to the reaction between an ion and

Table 1. Pseudo-first-order and second-order rate constants for the oxidation of MPSO and DPSO with PMS in 50% (v/v) aqueous acetic acid[a].

10^2[Sulphoxide] (M)	10^3[PMS] (M)	MPSO at 30°C		DPSO at 27·5°C	
		10^4k_1(sec^{-1})	10^2k_2(M^{-1} sec^{-1})	10^4k_1(sec^{-1})	10^2k_2(M^{-1} sec^{-1})
0·75	0·75	5·15 ± 0·25	6·86 ± 0·33	1·90 ± 0·16	2·53 ± 0·21
1·00	0·75	6·35 ± 0·32	6·35 ± 0·32	2·67 ± 0·14	2·67 ± 0·14
1·50	0·75	9·79 ± 0·53	6·52 ± 0·35	3·99 ± 0·18	2·66 ± 0·12
2·00	0·75	13·2 ± 0·88	6·59 ± 0·44	5·31 ± 0·55	2·66 ± 0·28
2·50	0·75	16·9 ± 1·2	6·77 ± 0·48	6·70 ± 0·53	2·68 ± 0·21
3·00	0·75	19·5 ± 0·70	6·51 ± 0·23	7·93 ± 0·35	2·64 ± 0·12
4·00	0·75	26·9 ± 1·0	6·74 ± 0·26	9·25 ± 0·33	2·31 ± 0·08
5·00	0·75	32·4 ± 1·6	6·48 ± 0·32	11·7 ± 0·65	2·35 ± 0·13
1·50	0·50	9·87 ± 0·63	6·58 ± 0·42	3·78 ± 0·48	2·52 ± 0·32
1·50	1·00	10·3 ± 0·41	6·84 ± 0·27	3·93 ± 0·12	2·62 ± 0·08
1·50	1·25	9·79 ± 0·37	6·52 ± 0·25	3·95 ± 0·28	2·63 ± 0·19
1·50	1·50	10·1 ± 0·48	6·75 ± 0·32	4·18 ± 0·05	2·79 ± 0·03

[a][H_2SO_4] = 0·10 M; I = 0·60 M. The error quoted in k is the 95% confidence limit of Student's t-test (Srinivasan *et al* 1982).

Table 2. Effect of varying $[H^+]$, I, and percentage of solvent composition on the rate of oxidation[a].

	MPSO[b,c]	DPSO[c,d]	I (M)	MPSO[b,e]	DPSO[d,e]	AcOH–H_2O	MPSO[b,f]	DPSO[d,f]
$10[H_2SO_4]$ (M)	$10^4k_1(sec^{-1})$	$10^4k_1(sec^{-1})$		$10^4k_1(sec^{-1})$	$10^4k_1(sec^{-1})$	(v/v)	$10^4k_1(sec^{-1})$	$10^4k_1(sec^{-1})$
0·25	5·12 ± 0·16	1·92 ± 0·02	0·40	5·67 ± 0·21	2·03 ± 0·10	10–90	10·6 ± 0·69	4·87 ± 0·30
0·50	5·18 ± 0·14	2·00 ± 0·07	0·60	5·15 ± 0·25	1·90 ± 0·16	30–70	7·77 ± 0·53	2·53 ± 0·18
1·00	5·15 ± 0·25	1·90 ± 0·16	0·70	5·38 ± 0·09	1·87 ± 0·10	50–50	5·15 ± 0·25	1·90 ± 0·16
1·50	5·55 ± 0·21	2·05 ± 0·16	0·90	5·18 ± 0·18	1·83 ± 0·09	70–30	4·41 ± 0·28	1·65 ± 0·07
1·90	5·75 ± 0·21	2·27 ± 0·09	1·00	5·18 ± 0·07	1·90 ± 0·12			

[a][Sulphoxide] = $7·5 \times 10^{-3}$ M; [PMS] = $7·5 \times 10^{-4}$ M; [b] T = 30°C; [c] I = 0·60 M; solvent 50:50; AcOH–H_2O (v/v); [d] T = 27·5°C; [e] $[H_2SO_4]$ = 0·10 M; solvent 50:50 AcOH–H_2O (v/v); [f] I = 0·60 M; $[H_2SO_4]$ = 0·10 M.

possible formation of a charged activated complex in the transition state which is more hydrated than those of the reactants. Such a solvent effect is observed in the oxidation of methyl phenyl sulphoxide by N-bromo-succinimide (Srinivasan *et al* 1983), alkyl aryl sulphides by peroxodisulphate (Kuthalingam 1980; Sundararajan 1981) and phenyliodosodiacetate (Srinivasan *et al* 1982), and phenylmercaptoacetic acids by peroxodisulphate (Srinivasan and Pitchumani 1979). In the Cr(VI) oxidation of aryl methyl (Baliah and Satyanarayana 1978) and diaryl sulphoxides (Srinivasan *et al* 1981) and of sulphides (Srinivasan *et al* 1985) the formation of charge-separated complex in the rate-limiting step has been excluded as the rate constant increases with increase in the content of the acetic acid in the medium in these oxidations. Since the rate is also not influenced by the addition of acrylonitrile, a free radical mechanism has been excluded.

3.2 *Oxidation of* DPSO

Our interest in the oxidation of DPSO and substituted diphenyl sulphoxides stems from some of our recent interesting observations with MPSO and DPSO in certain oxidations. In the peroxodiphosphate (Srinivasan and Rajagopal 1979; Rajagopal 1984) and N-bromosuccinimide oxidations (Srinivasan *et al* 1983) of MPSO, the reaction is first-order in substrate in each case, while zero-order dependence is observed in DPSO in its reactions with the two oxidants. But with both cases the order with respect to the oxidant is one. In contrast, the oxidations of MPSO and DPSO by Cr(VI) (Baliah and Satyanarayana 1978; Srinivasan *et al* 1981) and by peroxobenzoic acid (Curci and Modena 1966; Curci *et al* 1966) follow second-order kinetics.

Detailed studies with DPSO in 50% acetic acid-50% water (v/v) indicate that the order with respect to each reactant is unity as evidenced by the linearity of the plot of log $(a-x)$ vs time, constant pseudo first-order rate constants at different initial [PMS] and by the constant k_2 values at different initial [DPSO] (table 1). A plot of log [DPSO] vs log k_1 is linear with a slope of 1·03 ($r = 0{\cdot}999$). As observed with MPSO, the reaction rate is not influenced by the variations in $[H^+]$ and ionic strength and the rate constants decrease with decrease in the percentage of water (table 2).

3.3 *Substitutent effects*

The structure-reactivity relationship has been examined by studying the rates of PMS oxidation of several substituted phenyl methyl sulphoxides and 4,4′-disubstituted diphenyl sulphoxides at three temperatures (tables 3 and 4). The data in tables 3 and 4 reveal that while electron-releasing substituents increase the rate of oxidation, electron-withdrawing substituents retard it. The correlation of log k_2, with Hammett substituent constants, σ, is only fair in the two series ($\rho = -0{\cdot}40$, $r = 0{\cdot}957$, $s = 0{\cdot}04$, 95% confidence limit on $\rho = \pm 0{\cdot}10$ for aryl methyl sulphoxides at 30° and $\rho = -0{\cdot}40$, $r = 0{\cdot}981$, $s = 0{\cdot}06$, 95% confidence limit on $\rho = \pm 0{\cdot}09$ for substituted diphenyl sulphoxides at 27·5°). The use of σ^+/σ^- has not improved the correlation. The nearly identical ρ values for the two series of sulphoxides show that in both cases the electron deficient transition state almost

Table 3. Second-order rate constants and enthalpies and entropies activation for the oxidation of $XC_6H_4SOCH_3$ by PMS[a].

X	10^2k_2(M^{-1} sec^{-1}) 10°C	20°C	30°C	$\Delta H^{\neq}$(KJ mol^{-1})	$-\Delta S^{\neq}$(JK^{-1} mol^{-1})
H	1·72 ± 0·10	3·81 ± 0·16	6·86 ± 0·33	54·3 ± 3·6	88·0 ± 13
p-MeO	2·59 ± 0·08	5·22 ± 0·12	10·8 ± 0·37	56·2 ± 2·1	78·1 ± 7·7
p-Me	2·12 ± 0·07	4·17 ± 0·06	8·14 ± 0·24	52·9 ± 2·0	91·4 ± 7·2
p-Et	1·98 ± 0·07	4·07 ± 0·24	8·48 ± 0·73	57·0 ± 4·3	77·4 ± 16
p-Br	1·64 ± 0·12	3·44 ± 0·12	6·36 ± 0·49	46·6 ± 4·4	114 ± 16
p-Cl	1·56 ± 0·07	3·03 ± 0·20	5·71 ± 0·33	50·8 ± 4·0	101 ± 15
p-$COCH_3$[b]	1·28 ± 0·09	2·92 ± 0·19	4·84 ± 0·19	45·8 ± 4·2	119 ± 15
m-Cl	0·933 ± 0·03	2·52 ± 0·19	4·32 ± 0·33	53·3 ± 4·4	94·9 ± 16
p-NO_2	0·821 ± 0·03	1·95 ± 0·03	3·77 ± 0·24	53·7 ± 2·8	95·0 ± 10

[a] [Sulphoxide] = $7·5 \times 10^{-3}$ M; [PMS] = $7·5 \times 10^{-4}$ M; [H_2SO_4] = 0·10 M; I = 0·60 M; solvent 50:50 AcOH–H_2O (v/v). [b]The Bayer-Villiger oxidation has been ruled out as acetophenone was not oxidised under our experimental conditions.

Table 4. Second-order rate constants and enthalpies and entropies of activation for the oxidation of disubstituted diphenyl sulphoxides by PMS[a].

Sulphoxide	10^2k_2(M^{-1} sec^{-1}) 12·5°C	27·5°C	37·5°C	$\Delta H^{\neq}$(KJ mol^{-1})	$-\Delta S^{\neq}$(JK^{-1} mol^{-1})
Diphenyl	0·946 ± 0·03	2·43 ± 0·12	5·43 ± 0·24	48·8 ± 2·5	99·0 ± 8·9
4,4′-Diacetamido-diphenyl	1·77 ± 0·09	3·92 ± 0·09	6·39 ± 0·30	35·7 ± 2·4	153 ± 8·6
4,4′-Dimethyl-diphenyl	1·37 ± 0·08	3·89 ± 0·16	6·78 ± 0·28	45·3 ± 2·8	122 ± 10
4,4′-Difluoro-diphenyl	0·960 ± 0·03	2·67 ± 0·16	5·53 ± 0·47	49·4 ± 3·5	111 ± 13
4,4′-Dichloro-diphenyl	0·733 ± 0·02	2·25 ± 0·13	4·38 ± 0·32	50·5 ± 3·0	109 ± 11
4,4′-Dibromo-diphenyl	0·710 ± 0·03	2·12 ± 0·14	3·89 ± 0·18	48·3 ± 3·2	117 ± 12
4,4′-Dinitro-diphenyl	0·256 ± 0·03	0·693 ± 0·03	1·09 ± 0·03	40·5 ± 3·7	152 ± 13

[a][Sulphoxide] = $7·5 \times 10^{-3}$ M; [PMS] = $7·5 \times 10^{-4}$ M; [H_2SO_4] = 0·10 M; I = 0·40 M; solvent 80:20 AcOH–H_2O (v/v).

resembles each other. However, the low ρ values point out that the transition state cannot be as electron-deficient as pictured for electrophilic aromatic substitution.

The activation parameters for the oxidation of the two series of sulphoxides are also listed in tables 3 and 4. In both series the observed range of experimental $\Delta H^{\neq}$ value is $> 2\delta$ i.e. the error criterion (Petersen *et al* 1961; Wiberg 1964) is satisfied and hence the relation between $\Delta H^{\neq}$ and $\Delta S^{\neq}$ can be assumed to be valid. The

lphoxides and $r = 0{\cdot}963$ for diphenyl sulphoxides) suggesting that the oxidation ccurs for all substrates by a similar mechanism in each series.

4 *Mechanism of oxidation*

aqueous solution, peroxomonosulphate ion mainly exists as HSO_5^-, a weak acid ith an ionisation constant 4×10^{-10}. However, in alkaline medium the concentration of HSO_5^- is much low (Ogata and Tabushi 1958). It has been reported that round pH = 10, HSO_5^- exists principally as SO_5^{2-} (Ball and Edwards 1956),

$$HSO_5^- + H_2O \rightleftharpoons SO_5^{2-} + H_3O^+.$$

he absence of any effect on the rate of oxidation on the addition of a strong acid dicates (i) SO_5^{2-} is not the active species and (ii) HSO_5^- is the active species as the rst ionization of peroxomonosulphuric acid lies in the very high acid region (Ball nd Edwards 1956). Because of the unsymmetrical nature of the peroxide link, SO_5^- is very reactive to strong nucleophiles (Ball and Edwards 1956).

Scheme 1.

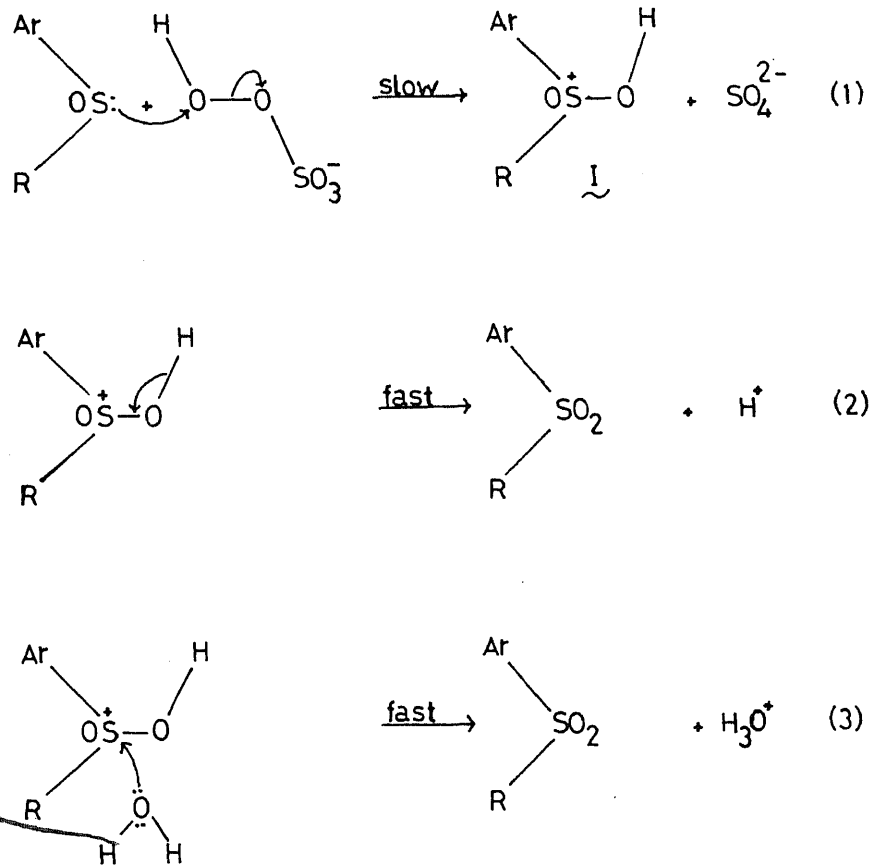

In the proposed mechanism (scheme I) it is envisaged that the rate-determining step involves the nucleophilic attack of sulphoxide sulphur at the outer terminal peroxo oxygen atom of HSO_5^- to form an intermediate (I) analogous to the mechanism suggested for the peroxodisulphate oxidation of sulphides (Arumugam *et al* 1978; Srinivasan *et al* 1978) and to the general mechanism proposed for many peroxide reactions (Edwards 1962). As addition of potassium sulphate has not influenced the rate constant, it is concluded that (1) is not reversible. The intermediate (I) decomposes to give the sulphone with a loss of proton. The formation of the sulphonium ion intermediate (I) in the slow step accounts for the observed substituent effect and solvent effect. In the reactions of peroxomonosulphate with azidopentamminechromium(III) and with azide employing H_2O^{18}, $O_3^{18}SO^{18}OH^-$ (non-terminally labelled) and $O_3SOO^{18}H^-$ (terminally labelled), it has been shown that the reactions proceed by transfer of a terminal peroxide oxygen of the peroxomonosulphate to the reactants (Thompson *et al* 1979). It has also been demonstrated that Caro's acid is the source of oxygen in the oxidation of nitrite to nitrate (Anber and Taube 1954), and of phosphite to phosphate (Lunenok-Burmakina *et al* 1968). The intermediate (I) may also decompose to give the sulphone by the attack of water as shown in (3). This possibility is excluded as it has been reported (Gragerov and Levit 1963) that the treatment of diphenyl sulphide with a solution of ethanol, acetic acid, H_2O^{18} and peroxomonosulphate for 5 hours at 0° gave diphenyl sulphoxide devoid of O^{18}; similar oxidation at 20–25° gave diphenyl sulphone devoid of O^{18}. It is, therefore, concluded that the source of oxygen in the present study is PMS itself.

Acknowledgements

The authors thank E I du Pont du Nemours Co. (Inc.), for a generous gift of Oxone. RS and PS thank the Madurai Kamaraj University for the award of Fellowships.

References

Anber M and Taube H 1954 *J. Am. Chem. Soc.* **76** 6243
Arumugam N, Srinivasan C and Kuthalingam P 1978 *Indian J. Chem.* **A16** 478
Baliah V and Satyanarayana 1978 *Indian J. Chem.* **A16** 966
Ball D L and Edwards J O 1956 *J. Am. Chem. Soc.* **78** 1125
Bloch R, Abecassis J and Hassan D 1985 *J. Org. Chem.* **50** 1544
Bridgart G J and Wilson I R 1971 *Aust. J. Chem.* **24** 2481
Cumber C W N, Read J F and Vogel A I 1965 *J. Chem. Soc.* 5860
Curci R, Fiorentino M, Troisi L, Edwards J O and Pater R H 1980 *J. Org. Chem.* **45** 4758
Curci R, Giovine A and Modena G 1966 *Tetrahedron* **22** 1235
Curci R and Modena G 1964 *Gazz. Chim. Ital.* **94** 1257
Curci R and Modena G 1966 *Tetrahedron* **22** 1227
Edwards J O 1962 *Peroxide reaction mechanism* (New York: John Wiley) p. 67
Edwards J O and Muller J J 1962 *Inorg. Chem.* **1** 696
Fortnum D H, Battaglia C J, Cohen S R and Edwards J O 1960 *J. Am. Chem. Soc.* **82** 778
Gragerov T and Levit A F 1963 *Zh. Obshch. Khim.* **33** 543; 1963 *Chem. Abstr.* **58** 13831

eonard N J and Sutton L E 1948 *J. Am. Chem. Soc.* **70** 1564
unenok-Burmakina V A, Alleva G P and Franchuk T M 1968 *Russ. J. Inorg. Chem.* (*Engl. Transl.*) **13** 509
gata Y and Tabushi I 1958 *Bull. Chem. Soc. Jpn.* **31** 969
rton K J P and Bradfield A E 1924 *J. Chem. Soc.* 960
andurengan T and Maruthamuthu P 1981 *Bull. Chem. Soc. Jpn.* **54** 3551
etersen R C, Markgraf J H and Ross S D 1961 *J. Am. Chem. Soc.* **83** 3819
ajagopal S 1984 *Kinetics and mechanism of oxidation of organic compounds*, Ph.D. thesis, Madurai Kamaraj University, Madurai
amachandran M S and Vivekanandam T S 1984 *J. Chem. Soc. Perkin Trans.II* 1341
amachandran M S, Vivekanandam T S and Mani Raj R P 1984 *J. Chem. Soc. Perkin Trans.II* 1345
ecco F and Venturini M 1976 *J. Chem. Soc. Dalton Trans.* 1410
mith R H and Wilson I R 1966 *Aust. J. Chem.* **19** 1365
mith R H and Wilson I R 1967 *Aust. J. Chem.* **20** 1353
rinivasan C, Kuthalingam P and Arumugam N 1978 *Can. J. Chem.* **56** 3043
rinivasan C and Rajagopal S 1979 *React. Kinet. Catal. Lett.* **12** 45
rinivasan C and Pitchumani K 1979 *Indian J. Chem.* **A17** 162
rinivasan C, Venkatasamy R and Rajagopal S 1981 *Indian J. Chem.* **A20** 505
rinivasan C, Chellamani A and Kuthalingam P 1982 *J. Org. Chem.* **47** 428
rinivasan C, Rajagopal S and Thirunavukarasu N 1983 *Oxidation Communications* **4** 403
rinivasan C, Chellamani A and Rajagopal S 1985 *J. Org. Chem.* **50** 1201
rinivasan C, Subramaniam P and Radha S 1986 *Indian J. Chem.* (in press)
undararajan G 1981 *Oxidation of aryl methyl sulphides by peroxodisulphate – Solvent effects*, M.Phil. thesis, Madurai Kamaraj University, Madurai
ugaswa S and Sakurai K 1940 *J. Pharm. Soc. Jpn.* **60** 22
zmant H H and McIntosh J J 1951 *J. Am. Chem. Soc.* **73** 4356
hompson R C 1981 *Inorg. Chem.* **20** 3745
hompson R C 1982 *Inorg. Chem.* **21** 859
hompson R C, Wieland P and Appleman E H 1979 *Inorg. Chem.* **18** 1974
rost B M and Curran D P 1981 *Tetrahedron* **22** 1287
/iberg K B 1964 *Physical organic chemistry* (New York: Wiley) p. 376
incke Th and Lenhardt S 1913 *Ann.* **400** 14

Electron impact ionization of amines using crossed electron-molecular beams

S V KRISHNA KUMAR* and D MATHUR

Tata Institute of Fundamental Research, Homi Bhabha Road, Colaba, Bombay 400 005, India

MS received 1 May 1986; revised 4 July 1986

Abstract. Ionization energy functions of triethyl amine, tri-*n*-propyl amine, N,N-dimethyl-benzenamine and N,N-diethyl-benzenamine, and appearance energy functions of major products of dissociative ionization have been measured using a high sensitivity crossed electron beam-molecular beam apparatus incorporating a quadrupole mass spectrometer and an on-line laboratory computer. The data obtained is useful in understanding the role of dopants in gas laser plasmas.

Keywords. Electron impact; ionization energy; appearance energy.

. Introduction

An understanding of the gas phase chemistry of laser plasmas requires knowledge of ionization processes resulting from collisions of electrons with atoms and molecules. In order to produce a uniform discharge and to enhance the output power from electric discharge lasers, some polyatomic molecules, such as the amines, have recently been used as dopants in laser gas mixtures (Kline and Denes 1982). The introduction of amines results in the formation of large numbers of both parent ions as well as fragment ions due to electron impact. In some cases, the fragment ions are found to dominate the parent ions even at energies just above the threshold for ionization. This necessitates the measurement of ionization efficiency curves of the parent ion as well as the major fragment ions in making the right choice of dopants to be used in the lasers without inducing much dissociation. Recently, amine dopants have also been used in nitrogen lasers (Krishna Kumar and Mitra 1986).

In order to understand the atomic and molecular collision processes responsible for altering the plasma characteristics and excited state populations, accurate information on ionization energies (IE) of parent ions and appearance energies (AE) of fragment ions are essential. However, literature values show a large spread in IE data pertaining to such amines. For instance, in the case of N,N-dimethyl-benzenamine, reported IE values range from 7·10 to 7·92 eV (Levin and Lias 1982). Most of these measurements report the vertical IE (rather than the adiabatic values) which are of actual consequence in laser plasmas; these have been measured using either photoelectron spectroscopy or with photoionization techniques. AE data for most of the fragment ions of the amines are not available. Electron impact ionization near the threshold yields vertical IE and AE values (Field and Franklin 1957) and hence makes it a good choice for their determination.

*To whom all correspondence should be addressed.

As there is a paucity of accurate electron impact data, high sensitivity experiments were conducted using a crossed electron beam-molecular beam apparatus incorporating a quadrupole mass spectrometer to determine IE, AE and ionization efficiency curves of some amines which may be of use in gas laser plasmas.

2. Experimental

The experimental apparatus used, shown schematically in figure 1, has been described extensively in recent publications (Mathur 1980; Maccoll and Mathur 1981; Mathur and Badrinathan 1984, 1986) and therefore, only the salient features pertaining to the present study are briefly mentioned here. A well-collimated beam of intensity $\sim 10^{-8}$ A, with an energy resolution of $\sim$ 120 meV (full width at half maximum), intersects a molecular beam at right angles in a field free region enclosed by a highly transparent molybdenum wire mesh. Fast differential pumping in the collision zone yields a base pressure of 2×10^{-8} torr. Ions produced by electron impact which drift towards the mass spectrometer (in the direction of the molecular beam) are extracted by a weak three-element lens into a quadrupole mass spectrometer which has unit resolution at mass 300. The mass spectrometer is

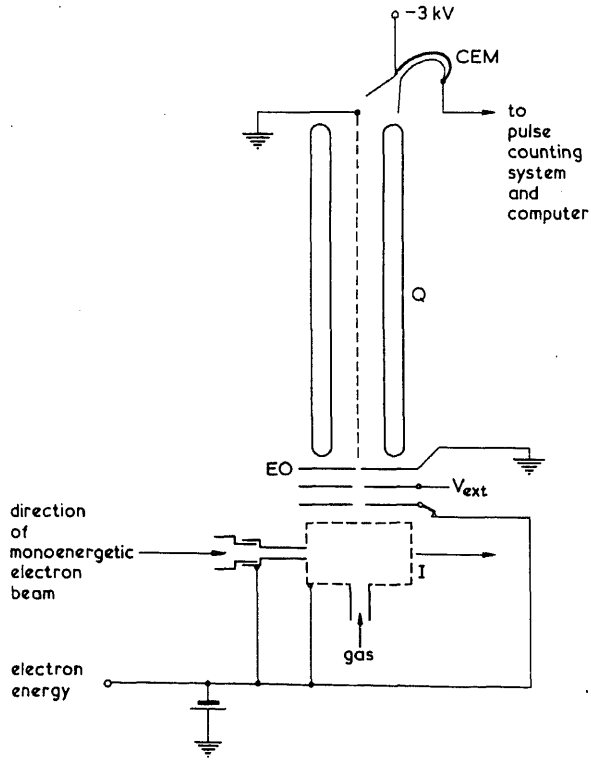

controlled by a laboratory computer which accomplishes on-line multiple scanning of electron beam energy and synchronous storage of ion intensities in the computer memory. The use of quadrupole mass spectrometer has the advantage of high ion transmission efficiency. Ions are detected by an off-axis channel electron multiplier which prevents detection of spurious signals due to photons and fast neutral metastables.

The electron energy scale for all the IE and AE values reported here was calibrated by admixing small amounts of argon (IE = 15·76 eV) for which IE is well established. This is necessary to take into account the energy differences which arise due to contact potentials and other field inhomogeneities in the collision zone. To obtain good signal to noise ratio in the threshold region for ionization, signal averaging is done over at least 100 scans in the electron energy range from 5 to 20 eV. The system was stabilized and checked for drift over the time taken for data acquisition, which was found to be negligible. Typical threshold ionization efficiency curves pertaining to N,N-dimethyl-benzenamine and argon are shown in figure 2. The method of establishing ionization thresholds is discussed in the context of our present data in the following section.

3. Results and discussion

Electron-impact mass spectra and ionization efficiency curves have been measured for triethyl amine, tri-*n*-propyl amine, N,N-dimethyl-benzenamine and N,N-diethyl-benzenamine. Typical mass spectra obtained at an electron impact energy of 20 eV are shown in figure 3 whilst figures 4–7 illustrate threshold IE curves for molecular ions and AE curves for the major dissociative fragmentation ions. For the sake of clarity, only the range from threshold energy to a few eV is plotted taking

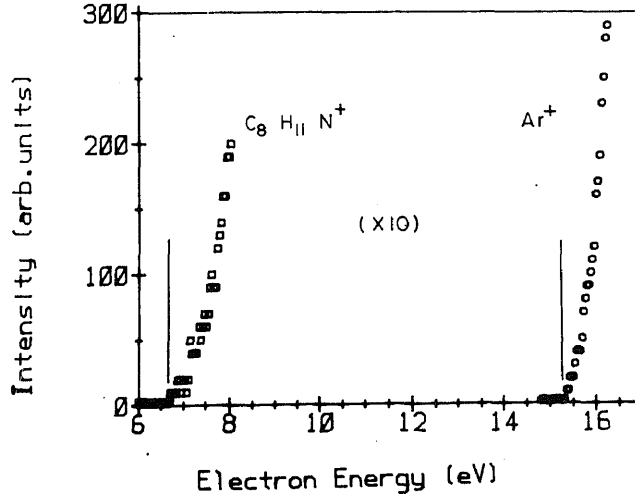

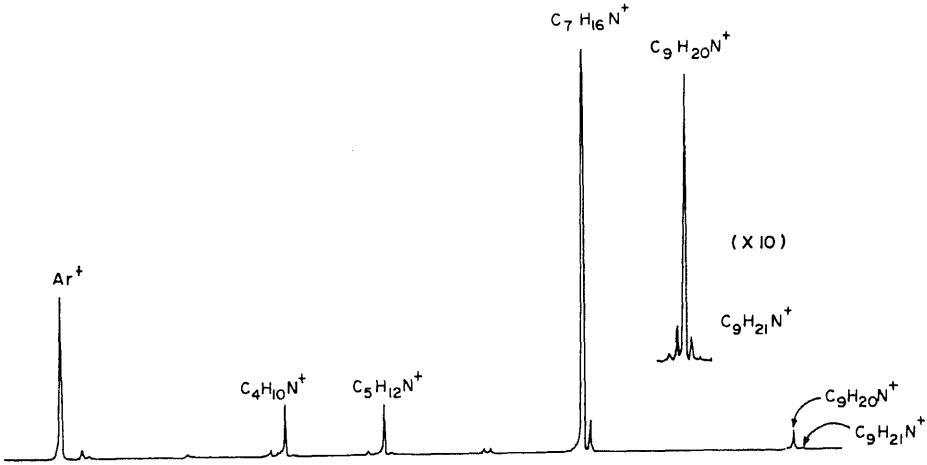

Figure 3. Mass spectrum of tri-*n*-propyl amine and argon mixture at an electron impact energy of 20·0 eV.

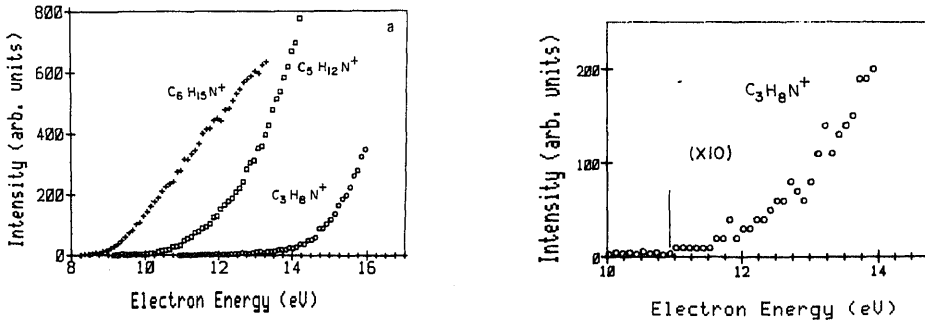

Figure 4. (**a**) Ionization efficiency curves near the threshold of the molecular and some major fragment ions of triethyl amine. (**b**) Threshold region of $C_3H_8N^+$ fragment ion at 10 times greater sensitivity shows pronounced tailing of the AE function.

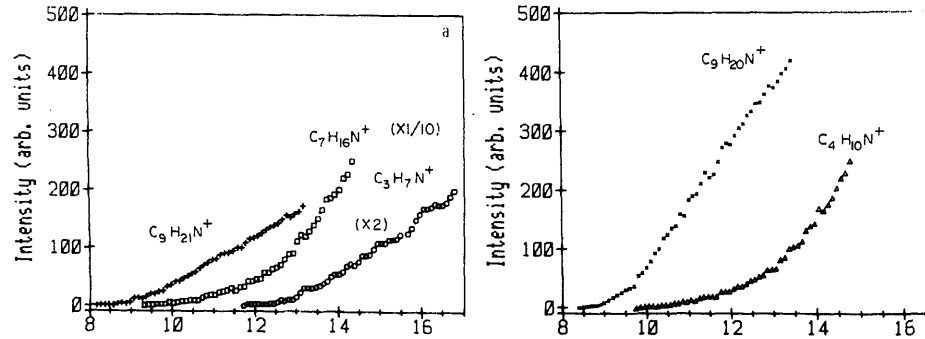

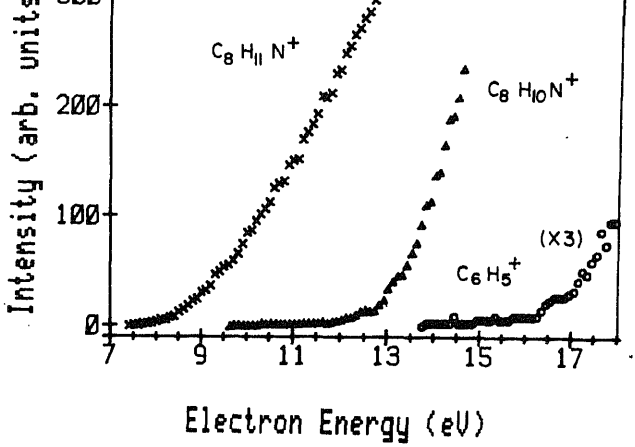

Figure 6. Ionization efficiency curves of N,N-dimethyl-benzenamine and its fragment ions.

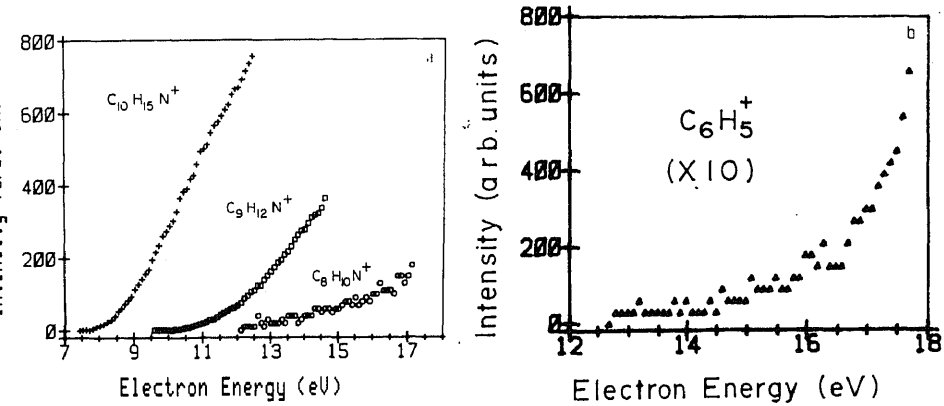

Figure 7. (**a**) Ionization efficiency curves of N,N-diethyl-benzenamine and its fragment ions $C_9H_{12}N^+$ and $C_8H_{10}N^+$. (**b**) AE functions for $C_6H_5^+$.

very tenth data point stored in the computer memory. It can be seen from figure 3 at at electron energies as low as 15 eV the intensity of fragment ions is much ore than the intensity of molecular ions except in the case of N,N-dimethyl-enzenamine. Tri-*n*-propyl amine stands out with a two-orders of magnitude fference in intensity between the fragment ion $C_7H_{16}N^+$ and the molecular ion $_9H_{21}N^+$. In all the molecular species studied, the positive charge is localised on e heteroatom. Consequently, following ionization, nitrogen becomes isoelectro-c with carbon. This can result in the formation of an sp^2-hybridised nitrogen ructure with an unpaired electron which may lead to a π-bond with the electron tuated on the carbon atom being ejected as a result of the cleavage of the β-bond. Most of the earlier values of IE and AE that have been reported rely on either the milog plot technique or the linear extrapolation technique of determining onsets. the semilog plot technique, the logarithm of the ion current, usually normalized 50 eV impact energy, is plotted as a function of electron energy for the sample

and also for a reference gas whose ionization energy is known accurately. The resulting curves, in general, show approximately linear and parallel sections at about 1 to 0·5% of the ion currents at 50 eV impact energy and the differences in the ionization or appearance energies are given by the separation of the curves along the energy axis. In the linear extrapolation method, the ionization efficiency curves are plotted upto a few eV above the threshold. The curve above the threshold, which is taken to be approximately linear, is extrapolated to the energy axis. The intercept is taken as the IE or AE. Both these methods fail to take into account the shape of the curve near the threshold. Any curvature in the ionization efficiency curve is assumed to be solely due to the high energy tail of the electron energy distribution. However, even in experiments that are carried out using monoenergetic electron beams with an energy width as low as 30 meV, pronounced 'tailing' of threshold IE and AE curves (extending over several eV in certain cases) is found to occur (Maccoll and Mathur 1981). Curvature at the threshold is not due only to the contribution from the high energy part of the electron energy distribution; other physical factors such as the threshold behaviour of the ionization cross-section, reaction competition (in the case of fragment ions) as well as instrumental factors such as detection sensitivity, signal to noise ratio and ion residence time in the interaction region must also be taken into account when considering thresholds and inelastic onsets. Neither the semilog plot technique nor the method of linear extrapolation can yield accurate onset information in cases where some of the above factors result in a pronounced tailing of the AE curves.

We have attempted to circumvent some of the problems of onset determination by adopting the vanishing current method. We employ a single particle counting technique to determine the minimum energy at which ionization or fragmentation occurs. For such a method to be feasible, the using of the channel electron multiplier in a pulse-output mode and employment of multiple scanning techniques is mandatory.

The IE and AE of some major fragments have been determined for triethyl amine, tri-*n*-propyl amine, N,N-dimethyl-benzenamine and N,N-diethyl-benzenamine and are given in table 1. The present results agree closely with the vertical IE determined by photoelectron spectroscopy.

The ionization onset results from ejection of a single electron from the b_1 or b_1-like π orbitals which are contributed either from the substituent groups' n or π orbitals, or alternately, from the benzene e_{1g} π orbitals. HeI photoelectron angular distributions have been measured by Kobayashi (1978) and others (Sell and Kuppermann 1978) and the β asymmetry parameter has been determined from the first photoelectron band in N,N-dimethyl-benzenamine as well as for the corresponding π bands of the reference compound trimethyl amine and the first band in benzene. Reasonably close correspondence is observed for β values obtained for the lowest energy thresholds in N,N-dimethyl-benzenamine and the substituent group, indicating that electron ejection is most probably from one of the π orbitals of the substituent groups attached to the benzene ring in the compounds investigated in the present study.

Though there are only a few results to compare with for AE values, the results

Table 1. Ionization energy and appearance energy of major fragment ions.

	IE or AE (eV)	
	Present work	Earlier work
$C_6H_{15}N^+$	8·27 ± 0·11	8·08 (V) [PE][b]
		8·19 ± 0·05 (V) [PE][b]
$C_5H_{12}N^+$	9·16 ± 0·12	11·48 [EI][b]
$C_3H_8N^+$	10·93 ± 0·05	–
$C_9H_{21}N^+$	8·17 ± 0·05	8·04 ± 0·3 (V) [PE][b]
		7·23 [PI][a]
$C_9H_{20}N^+$	8·41 ± 0·09	–
$C_7H_{16}N^+$	9·33 ± 0·17	–
$C_4H_{10}N^+$	9·75 ± 0·13	–
$C_3H_7N^+$	11·72 ± 0·27	–
$C_8H_{11}N^+$	7·42 ± 0·05	7·45 (V) [PE][b]
		7·51 (V) [PE][a]
$C_8H_{10}N^+$	9·64 ± 0·29	10·75 ± 0·05 [PI][a]
		10·56 ± 0·05 [PI][b]
$C_6H_5^+$	9·88 ± 0·1	15·7 ± 0·1 [EI][a]
$C_{10}H_{15}N^+$	7·44 ± 0·07	7·51 (V) [PE][a]
		7·20 (V) [PE][b]
$C_9H_{12}N^+$	9·61 ± 0·04	–
$C_8H_{10}N^+$	12·12 ± 0·04	–
$C_6H_5^+$	12·68 ± 0·06	–

[a] Rosenstock *et al* 1977; [b] Levin and Lias 1982; PE: photoelectron spectroscopy; PI: photoionization; EI: electron impact.

rve near the threshold, and to the high sensitivity of the instrument which has en used in the present experiments.

Our present data indicates that in the case of ionization of the parent molecules, e resulting IE curves have a fairly sharp and structureless onset. In the case of agment ions, on the other hand, the threshold AE function generally exhibits rly pronounced tailing, which extends over a range of upto 3 eV in some cases. the case of the phenyl positive ion formation some distinct structure is also served about 2 eV above the initial onset. This is possibly indicative of the istence of a low-lying excited state of the fragment ion, though lack of ectroscopic information precludes specific identification of the electronic nfiguration of such a state at present.

We have attempted to estimate the cross-sections for ionization and dissociative nization by considering the electron flux in the interaction zone as well as the mber density of neutral molecules. Our estimates indicate cross-sections in the 10^{-16} to 10^{-17} cm^2 range, although the uncertainties involved in determining the

Acknowledgements

We are grateful to Dr C Badrinathan for assistance with the computer-controlled data acquisition system, and to Mr Thimmappa and Dr Pradeep Mathur, Indian Institute of Technology, Bombay, for providing ultra pure samples. We also thank Prof. S K Mitra and Prof. S K Bhattacharjee for their encouragement.

References

Field F H and Franklin J L 1957 *Electron impact phenomena and the properties of gaseous ions*, (New York: Academic Press) chap. 3.

Kline L E and Denes L J 1982 *Applied atomic collision physics*, (eds) H S W Massey, E W McDaniel and B Bederson vol. 3, p. 402

Kobayashi T 1978 *Phys. Lett.* **A69** 105

Krishna Kumar S V and Mitra S K 1986 *J. Appl. Phys.* **60** 2177

Levin R D and Lias S G 1982 *Ionization potential and appearance potential measurements, 1971–1981, NSRDS-NBS71* (Washington, DC: National Bureau of Standards)

Maccoll A and Mathur D 1981 *Org. Mass Spectrom.* **16** 261

Mathur D 1980 *J. Phys.* **B13** 4703

Mathur D and Badrinathan C 1984 *Int. J. Mass Spectrom. Ion Process.* **57** 167

Mathur D and Badrinathan C 1986 *Int. J. Mass Spectrom. Ion Process.* **68** 9

Rosenstock H M, Draxl K, Steiner B W and Herron J T 1977 *J. Phys. Chem. Ref. Data* **6** (suppl. 1)

Sell J A and Kuppermann A 1978 *Chem. Phys.* **33** 367

Printed in India.

Reaction of the phosphate radical with amines — A flash photolysis study

P SUBRAMANIAN, V RAMAKRISHNAN, J RAJARAM and J C KURIACOSE*

Department of Chemistry, Indian Institute of Technology, Madras 600 036, India

MS received 15 May 1986

Abstract. Rate constants for the reaction of phosphate radical with some aromatic and aliphatic amines have been determined by the flash photolysis technique. The products formed under conditions of continuous irradiation have been identified. In the case of an aromatic amine the major product is the azo compound while in the case of an aliphatic amine a carbonyl compound is formed.

Keywords. Flash photolysis; phosphate radical; rate constants; aromatic and aliphatic amines.

Introduction

In recent years considerable amount of attention has been paid to studies relating to the generation and reactions of inorganic radicals (Ross and Neta 1979; Gorkovnik and Okhlobystein 1979). Most of these radicals are oxidising in nature and are postulated as intermediates in many thermal reactions. However, the intermediates or stable products in such reactions have been identified only in a limited number of cases and a systematic study in this respect is lacking. In thermal reactions, though radical generation and radical reaction steps have been postulated, the corresponding rate constants have not been evaluated. In this paper, we report the results of a study on the oxidation of amines with the phosphate radical.

The phosphate radical is a good oxidising agent and in general, two types of reactions take place, viz, hydrogen abstraction and electron transfer (Maruthamuthu and Neta 1977b; Maruthamuthu and Neta 1978). The acid-base forms and the corresponding optical absorption properties of phosphate radical are summarized in table 1 (Maruthamuthu and Neta 1978).

Table 1. Acid base forms and optical absorption properties of phosphate radical.

	$H_2PO_4^{\cdot}$	$HPO_4^{-\cdot}$	$PO_4^{2-\cdot}$
pK_a	5·7	8·9	
λ_{max}	520	510	530 nm
ϵ_{max}	1850	1550	2150 M^{-1} cm^{-1}

Only analytical grade chemicals were used in this investigation. Lithium peroxydiphosphate ($Li_4P_2O_8 \cdot 4H_2O$) was prepared and purified as reported in the literature (Creaser and Edwards 1972; Maruthamuthu 1974; Maruthamuthu and Neta 1977a). Freshly distilled samples of amines were used for preparing the solutions. In the case of some solid amines, recrystallised samples were used and their purity checked from their melting points.

2.2 *Measurements*

Flash photolysis experiments were carried out in a Nortech Flash Photolysis apparatus described previously (Elango *et al* 1984). The half width of the flash duration was about 30 microseconds. The decay of the phosphate radical was monitored by following the absorbance at 530 nm and measurements were made at $23{\cdot}0 \pm 1{\cdot}0$°C. Continuous photolysis experiments were carried out with 48 W low pressure Hg lamps (Rayonet RUL 2537 Å). All solutions were prepared with triply distilled water and deaerated with purified nitrogen before flashing. The flash experiments were done within 20 min after mixing the solutions and used only for a single flash.

2.3 *Product analysis*

Continuous irradiation experiments were carried out to identify the end products. In a typical experiment, a well-cooled deaerated aqueous solution containing 5 mM peroxydiphosphate and 1 mM amine at pH 11·0 (NaOH was used to adjust the pH) was irradiated in a quartz tube with 254 nm radiation for about 30 min. Immediately after irradiation, the organic materials were extracted into ether from the alkaline medium. The ether extract after drying over anhydrous $MgSO_4$ was evaporated to a small volume and analysed.

The reaction products were carbonyl compounds in the case of aliphatic amines, as determined by GLC. These have also been identified by comparing the IR spectra of the phenylhydrazones of these compounds with those of authentic samples.

In the case of aniline, the products were analysed by TLC. 4-Aminodiphenylamine, azobenzene and benzidine are the major products, and 2-aminodiphenylamine and hydrazobenzene are formed in trace amounts. In addition, phenylhydroxylamine is also formed. Azobenzene is formed by the rapid oxidation of hydrazobenzene. Therefore, in these experiments, azobenzene was obtained as the major product and hydrazobenzene as a minor product. UV spectra of these separated products compared well with those of authentic samples. The separated amines were also mixed with *p*-dimethylaminobenzaldehyde and the visible spectra of the resulting derivatives (Zechner *et al* 1976) compared with those of authentic samples. Under these conditions aniline itself, without added peroxydiphosphate, underwent photolysis yielding the same products other than phenylhydroxylamine, but in considerably reduced yields. Experiments were also conducted leaving the reaction mixture in the dark, where it was noticed that the peroxydiphosphate does not oxidise aniline and hence thermal oxidation of aniline by peroxydiphosphate is

f no consequence in our studies. These results show that the greater yield of -aminodiphenylamine, azobenzene, benzidine and 2-aminodiphenylamine that re obtained on irradiating the peroxydiphosphate with aniline results from the eaction of the phosphate radical with aniline.

. Results and discussion

The phosphate radical, $PO_4^{2-\cdot}$, is produced by the flash photolysis of a deaerated olution containing 1×10^{-5} M peroxydiphosphate at pH 11·0 (Lussier *et al* 1970; Sida *et al* 1973).

$$P_2O_8^{4-} \xrightarrow{h\nu} 2PO_4^{2-\cdot} \qquad (1)$$

The absorption of $PO_4^{2-\cdot}$ at 530 nm ($\varepsilon = 2150\ M^{-1}\ cm^{-1}$) (Maruthamuthu and Neta 1978) was observed immediately after the light pulse. The transient bsorption spectrum of the phosphate radical at pH 11·0 is shown in figure 1. The lash output energy and the concentration of the peroxydiphosphate were so djusted as to produce initially 1×10^{-6} M of the phosphate radical. The decay of he radical is second order in the absence of any scavenger as shown in the insert of igure 1 and the decay rate constant (k_r) is $2 \times 10^8\ M^{-1}\ sec^{-1}$. This indicates that

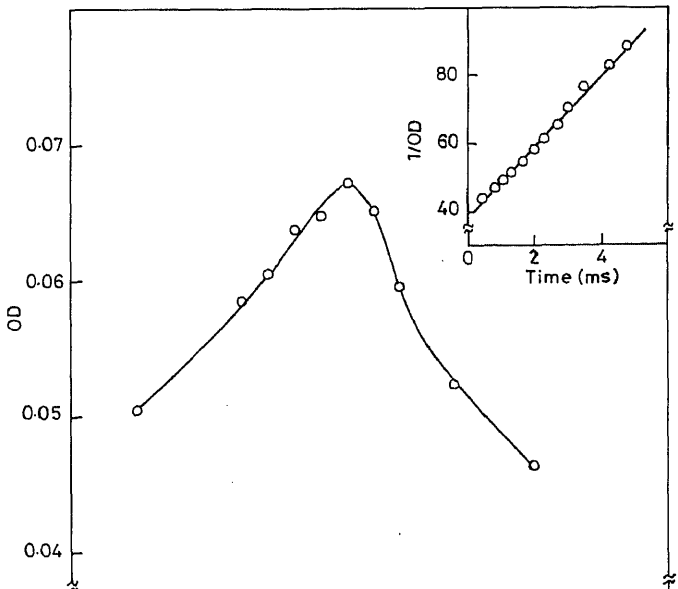

the disappearance of the radical is largely by a recombination process.

$$2\ PO_4^{2-\cdot} \xrightarrow{k_r} P_2O_8^{4-} \qquad (2)$$

In the presence of an excess of amine (scavenger), reaction 3 will compete with the self decay,

$$PO_4^{2-\cdot} + R\ddot{N}H_2 \xrightarrow{k_s} \text{products.} \qquad (3)$$

A pseudo-first order behaviour is observed. This will lead to a composite rate law,

$$-d[PO_4^{2-\cdot}]/dt = k_s[\text{amine}]\ [PO_4^{2-\cdot}] + 2k_r[PO_4^{2-\cdot}]^2. \qquad (4)$$

The mixed-order kinetics have been analyzed by the graphic method (Zwicker and Grossweiner 1963) and by computer simulation (Closs and Rabinow 1976). Both of them need the initial concentration of the radical, $[PO_4^{2-\cdot}]_0$ or initial absorbance (A_0), which involves an element of uncertainty because of the emission of the flash lamp. Nakamura *et al* (1980) attempted to remove the initial concentration of the radical or A_0 from the equation by differentiation with respect to time at an appropriate absorbance A^*; (5) was thus derived,

$$[d \ln A_t/dt]_{A^*} = -\{k_s[Y^\cdot]_0 + (2k_r/\varepsilon 1)A^*\}, \qquad (5)$$

where $[Y^\cdot]_0$ is the quantity of the scavenger added.

In eqn. 5, the left term is obtained from the tangential line at the appropriate absorbance (A^*) in the first order plot. The slope in the plot of these values against the initial concentration of scavenger yields k_s.

In our studies, the plot of first order rate constants vs [amine] gave a straight line (second order rate constants determined from the slope) passing through the origin indicating that in the presence of excess scavenger the self decay is negligible. The pseudo-first order rate constants were determined for at least three different initial concentrations of scavenger and at each concentration at least three kinetic curves were processed. The second order rate constants (k_s) obtained for some of the aromatic and aliphatic amines are given in table 2. The data are subject to the

Table 2. Rate constants for the reaction of $PO_4^{2-\cdot}$ radical with amines at pH 11·0 (k_s for $CO_3^{-\cdot}$ given for comparison).

Amine	$PO_4^{2-\cdot}$ $k_s(M^{-1}\ s^{-1})$	$CO_3^{-\cdot}$ $k_s(M^{-1}\ s^{-1})$
Aniline	$7{\cdot}10\times10^8$	$5{\cdot}40\times10^8$
	$1{\cdot}47\times10^9$ (pH 7·0)[a]	$5{\cdot}50\times10^8$ (pH 7·0)
	$\sim 10^{10}$ (pH 5·0)[b]	$5{\cdot}30\times10^8$ (pH 5·0)

rors inherent in flash photolysis studies (±10%). The rate constants for rbonate radical reaction (Elango *et al* 1984, 1985) are given for comparison. The rate constants, k_s, for aromatic amines are higher than those for aliphatic nines as in the case of the carbonate radical. Hence the reaction pathway of $O_4^{2-\cdot}$ is likely to be similar to that for $CO_3^{-\cdot}$. The products obtained under nditions of steady state irradiation were the same whether peroxydiphosphate or rbonate were employed as the source of the radical.

1 *Reaction of phosphate radical with aromatic amines*

ne effect of pH on the rate constant for the reaction of phosphate radical with iline has been studied. The rate constants are markedly different in the pH range -11, showing that the intrinsic reactivity of the three forms of phosphate radicals, z, $H_2PO_4^{\cdot}$, $HPO_4^{-\cdot}$ and $PO_4^{2-\cdot}$, towards aniline is different. However, in the case the carbonate radical, the rate constants displayed extremely poor dependance pH showing that the protonated and basic forms of this radical, $HCO_3^{\cdot}$ and $CO_3^{-\cdot}$ spectively, ($pK_a = 9{\cdot}6 \pm 0{\cdot}3$) (Cope and Hoffman 1972; Chen *et al* 1973) reacted the same rate. The carbonate radical reacts with aniline to form an adduct which rther dissociates via an electron transfer mechanism (Elango *et al* 1984). ccording to the theoretical calculations of Eberson (1982), the non-bonded direct ectron transfer from aromatic compounds is possible only in the case of the $SO_4^{-\cdot}$ dical and not in the case of $OH^{\cdot}$ and $CO_3^{-\cdot}$ radicals. The reactions of phosphate dicals are very similar to that of $SO_4^{-\cdot}$. All these suggest that the reaction of $O_4^{2-\cdot}$ with aniline is likely to involve a direct electron transfer from aniline to $O_4^{2-\cdot}$ without adduct formation. Hence attempts have been made to identify the ssible anilino-radical intermediate. For the protonated ($C_6H_5\dot{N}^+H_2$) and basic $C_6H_5\dot{N}H$) forms of the anilino radical, absorption maxima of 423 and 300 nm spectively, have been reported by Land and Porter (1963).

When a solution containing 0·1 mM peroxydiphosphate and 0·1 mM aniline at H 11·0 is flashed with about 200 J of energy there is very little absorption in the 3 nm region. The absorption around 300 nm could not be followed due to nitations of the monitoring source. But on flashing the same solution with the me energy at pH 6·0, a transient absorption around 424 nm has been observed msec after the start of the flash. This transient absorption is identical with that ported for $C_6H_5\dot{N}^+H_2$ (Land and Porter 1963; Christensen 1972).

Similarly with *p*-nitroaniline at pH 5·0, transient absorption having maxima at 0 and 490 nm was observed. This absorption is due to the formation of the nitroanilino cation radical, $p\text{-}NO_2C_6H_4\dot{N}^+H_2$ (Testa and Wollenben 1977). In e absence of peroxydiphosphate, aniline and *p*-nitroaniline showed only very tle absorption in these regions. At pH 11·0 the anilino cation radical that is rmed probably gets deprotonated to give the anilino radical, $C_6H_5\dot{N}H$ ($K_a = 7{\cdot}0$) (Land and Porter 1963), which can further dimerise to give drazobenzene and other observed products as shown in the mechanism in heme 1. In the case of the $CO_3^{-\cdot}$ radical, this scheme is still valid except that step I volves the intermediacy of an adduct.

Due to the resonance structures of anilino radical ($C_6H_5\dot{N}H$) the ortho- and ra-positions are active. When two radicals couple, the coupling products can as

Scheme 1.

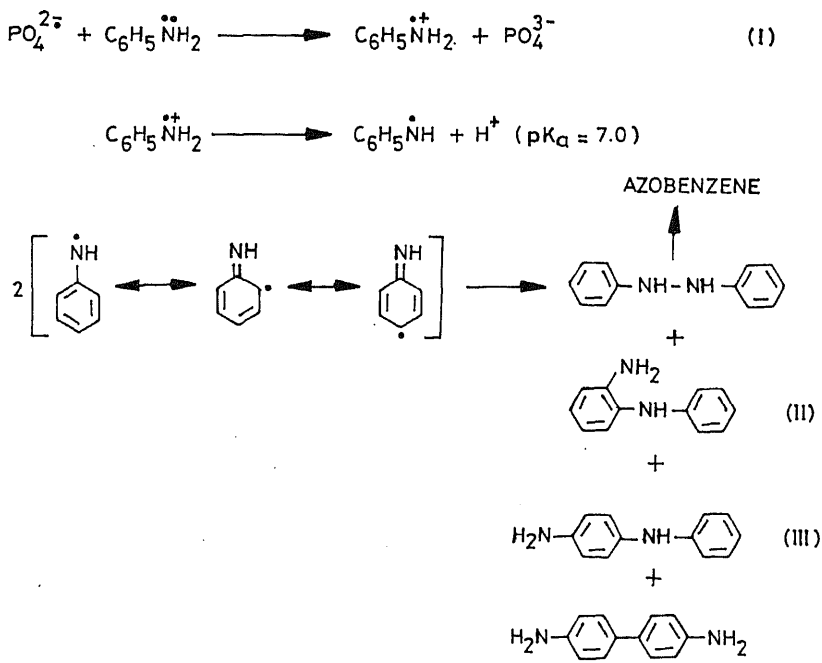

of the other molecule. Formation of products such as II and III are therefore to be expected.

It would be interesting to compare the reaction of the $OH^{\cdot}$ radical (Christensen 1972; Rao and Hayon 1975) and phosphate radical with aniline. The highly reactive $OH^{\cdot}$ radical reacts with aniline to give both the cyclohexadienyl type and the anilino radicals. The less reactive $PO_4^{2-\cdot}$ radical is more selective and gives only an anilino radical.

3.2 *Reaction of the phosphate radical with aliphatic amines*

In the case of aliphatic amines there can be two possible mechanisms for the oxidation of amines by one-electron oxidants, which involve (i) direct-electron transfer and (ii) H-atom abstraction as the rate determining steps (Chow 1980; Hull *et al* 1967). Scheme 2 explains these two modes of attack of the $PO_4^{2-\cdot}$ radical on the aliphatic amines.

Both the mechanisms indicate the eventual formation of the same aminoalkyl radical ($R\dot{C}HNR_2'$ or $R\dot{C}HNH_2$). In the electron transfer mechanism this radical is formed by the deprotonation (Anderson and Norman 1971) of aminium cation radical [equation (2) in scheme 2]. The aminoalkyl radical is a strong reducing agent (Anderson and Norman 1971) and readily undergoes oxidation to imine in

Scheme 2.

(i) a) *Direct one-electron transfer*

$$RCH_2\ddot{N}R_2' + PO_4^{2-\cdot} \longrightarrow RCH_2\dot{N}^+R_2' + PO_4^{3-} \quad (1)$$

$$RCH_2\dot{N}^+R_2' \xrightarrow{-H^+} R\dot{C}HNR_2' \quad (2)$$

$$RCHNR_2' \xrightarrow{OX} RCH{=}\overset{+}{N}R_2' \quad (3)$$

$$RCH{=}\overset{+}{N}R_2' \xrightarrow{OH^-/H_2O} RCHO + HNR_2' \quad (4)$$

b) *Electron transfer via an adduct*

A variant of (i) (a) is as follows:

$$RCH_2\ddot{N}R_2' + PO_4^{2-\cdot} \longrightarrow \text{adduct} \longrightarrow RCH_2\overset{+}{N}R_2' + PO_4^{3-}$$

and steps 2, 3 and 4 as before.

(ii) *α-Hydrogen abstraction*

$$RCH_2NH_2 + PO_4^{2-\cdot} \longrightarrow R\dot{C}HNH_2 + HPO_4^{2-} \quad (5)$$

$$2R\dot{C}HNH_2 \longrightarrow RCH{=}NH + RCH_2NH_2$$

or

$$\begin{array}{l} \\ \\ RCH\text{—}CHR \\ \quad | \quad\ | \\ \quad NH_2 \quad NH_2 \end{array} \quad (6)$$

$$R\dot{C}HNH_2 \xrightarrow{ox} RCH{=}NH \quad (7)$$

$$RCH{=}NH \xrightarrow{OH^-/H_2O} RCHO + NH_3 \quad (8)$$

Table 3. Products identified in the reaction of $PO_4^{2-\cdot}$ radical with some aliphatic amines.

Amine	Product	Method
n-Butylamine	*n*-Butyraldehyde	by GLC and as 2,4-dinitrophenyl-hydrazone derivative
Cyclohexylamine	Cyclohexanone	by GLC and as 2,4-dinitrophenyl-hydrazone derivative
Di-*n*-propylamine	*n*-Propionaldehyde	as 2,4-dinitrophenyl-hydrazone derivative
Triethylamine	Acetaldehyde	as 2,4-dinitrophenyl-hydrazone derivative

product. The reaction products identified with some of the aliphatic amines are given in table 3.

Detail studies regarding the mode of attack of $PO_4^{2-\cdot}$ on aliphatic amines and

References

Anderson N H and Norman R O C 1971 *J. Chem. Soc.* B 993

Bida G, Curci R and Edwards J O 1973 *Int. J. Chem. Kinet.* **5** 859

Chen S N, Cope V W and Hoffman M Z 1973 *J. Phys. Chem.* **77** 1111

Chow Y L 1980 *Reaction intermediates* (New York: Plenum) vol. 1, p. 151

Christensen H 1972 *Int. J. Radiat. Phys. Chem.* **4** 311

Closs G L and Rabinow B E 1976 *J. Am. Chem. Soc.* **98** 8190

Cope V W and Hoffman M Z 1972 *Chem. Commun.* 227

Creaser I I and Edwards J O 1972 in *Topics in phosphorus chemistry* (eds) E J Griffith and M Grayson (New York: Wiley Interscience) vol. 7, p. 379

Eberson L 1982 in *Advances in physical organic chemistry* (New York: Academic Press) vol. 18, p. 148

Elango T P, Ramakrishnan V, Vancheesan S and Kuriacose J C 1984 *Proc. Indian Acad. Sci. (Chem. Sci.)* **93** 47

Elango T P, Ramakrishnan V, Vancheesan S and Kuriacose J C 1985 *Tetrahedron* **41** 3837

Hull L A, Davis G T, Rosenblatt D H, Williams H K R and Weglein R C 1967 *J. Am. Chem. Soc.* **89** 1163

Kumar A and Neta P 1980 *J. Am. Chem. Soc.* **102** 7284

Land E J and Porter G 1963 *Trans. Faraday Soc.* **59** 2027

Lussier R J, Risen Jr W M and Edwards J O 1970 *J. Phys. Chem.* **74** 4039

Maruthamuthu P 1974 *Kinetics of oxidation of substrates (oxidation studies involving peroxy diphosphate)* Ph.D. Thesis, Madras University

Maruthamuthu P and Neta P 1977a *J. Phys. Chem.* **81** 937

Maruthamuthu P and Neta P 1977b *J. Phys. Chem.* **81** 1622

Maruthamuthu P and Neta P 1978 *J. Phys. Chem.* **82** 710

Morkovnik A F and Okhlobystein O Yu 1979 *Russ. Chem. Rev. (Engl. Transl.)* **48** 1055

Nakamura M, Ito O and Matsuda M 1980 *J. Am. Chem. Soc.* **102** 698

Rao P S and Hayon E 1975 *J. Phys. Chem.* **79** 1063

Ross A B and Neta P 1979 *National Standard Reference Data Series* (Washington: *US Natl. Bur. Stand.*) No. 65

Testa A C and Wollenben J 1977 *J. Phys. Chem.* **81** 429

Zechner J, Prangova Lilia St, Grabner G I and Getoff N 1976 *Z. Phys. Chem. (Neue Folge)* **102** 137

Zwicker E F and Grossweiner L I 1963 *J. Phys. Chem.* **67** 549

nderpotential deposition studies of copper on glassy carbon

S JAYA, T PRASADA RAO and G PRABHAKARA RAO*

Central Electrochemical Research Institute, Karaikudi 623 006, India

MS received 7 March 1986; revised 4 August 1986

Abstract. Studies on the deposition and dissolution of copper from 0·5 M sulphuric acid solutions onto glassy carbon (GC) using potential sweep techniques indicated that an additional peak occurs at higher positive potentials than the bulk stripping peak. This peak is identified as due to the stripping of underpotential deposited (UPD) copper. Results of investigations on the effect of sweep rate, deposition potential and time of deposition on the peak characteristics of UPD and bulk deposited copper are also reported.

Keywords. Underpotential deposition of copper; glassy carbon; potential sweep technique; bulk stripping peak; deposition potential.

Introduction

large number of studies pertaining to the underpotential deposition (UPD) of rious metals on solid electrodes have appeared in the literature for understanding e electrochemical and electrocatalytic properties of such systems (Kolb 78). Very few studies were made on carbonaceous electrodes (Morcos 1975; ainina *et al* 1972; Kiekens *et al* 1983) inspite of their widespread use in analytical d technical chemistry. The UPD of copper on polycrystalline graphite by using -ray fluorescence technique (Vassos and Mark 1967) revealed that copper starts owing as three-dimensional nuclei at specific sites after the completion of a onolayer. The occurrence of an UPD peak was observed during the studies on position of mercury on glassy carbon (GC) by correlating the potential difference tween the bulk and monolayer peak potentials to the difference in work nctions of substrate and depositing metal (Kiekens *et al* 1983). However, no tailed studies have appeared on the deposition of mercury or other metals on GC. is paper reports the results of UPD studies of copper on GC by using potential eep techniques.

Experimental

xperiments were carried out in 0·5 M sulphuric acid solutions prepared by uting 98% sulphuric acid (BDH, AR) in conductivity water. Copper sulphate DH, AR) was added to the 0·5 M H_2SO_4 supporting electrolyte corresponding to $^{-6} - 10^{-4}$ M range in UPD studies of copper. The working electrode is a lycrystalline GC (Tokai & Co., Japan) with a geometric area of 0·0707 cm^2. The

* whom all correspondence should be addressed

electrode surface was polished with various emery papers of increasing fineness (1/0 to 4/0). A bright platinum foil counter electrode and NCE (1 M KCl) as the reference electrode were employed in a three-electrode cell assembly.

3. Results and discussion

The cyclic voltammetric curve for the deposition and dissolution of 10^{-3} M copper in 0·5 M sulphuric acid solution on GC shows peaks corresponding to the bulk deposition of copper (–0·05 V) and its stripping (0·03 V). However, new peaks appear when the potential scan is limited to 0 to 0·5. The peaks at 0·4 and 0·3 V are due to deposition and dissolution, respectively.

3.1 *Underpotential deposition of copper on GC*

The cyclic voltammetric peak currents appearing at ~ 0·4 and 0·3 V are too small to be analyzed to elucidate the reason for their occurrence. To overcome this, sensitivity enhancement has been achieved by running anodic sweep voltammograms on samples of deposits of copper obtained by prior cathodic deposition of GC under varied conditions in all subsequent experiments. Hence, further studies were conducted by carrying out experiments in which the potential of the electrode is held at the cathodic limit for varying times followed by a potential sweep in the anodic direction to follow the anodic peaks for the above purpose. The electrodeposition of copper from x M copper sulphate ($10^{-6} \geqslant x \leqslant 10^{-4}$ M) in 0·5 M H_2SO_4 onto GC is achieved by holding the potential in the range $-0{\cdot}1$ to $-0{\cdot}5$ V for a certain time (t_d). Figure 1 shows typical cases wherein copper ($x = 10^{-5}$ M) was deposited at a potential (E_d) of $-0{\cdot}5$ V for 2, 4 and 10 min, following which the deposits were anodically stripped. It is clear from the figure that there are two stripping peaks corresponding to the oxidative dissolution of copper at $-0{\cdot}05$ V (peak 1) and 0·220 V (peak 2). Of these, peak 1 is identified as being due to the oxidation of bulk deposited copper as copper (II) (Stulikova and Vydra 1973). Peak 2 is characterised as the one arising from the stripping of underpotentially deposited copper as copper(II), as described below.

The possibility of peak 2 occurring at 0·22 V due to the oxidation of bulk deposited Cu(0) to Cu(1) is ruled out as Cu(0)/Cu(1) peak is expected at potentials ~0·05 V (Stulikova and Vydra 1973). Hence the large potential shift in the positive direction to bulk deposition potential can be ascribed to the UPD of copper or the stripping of the first layer (monolayer) of deposited copper.

After examining the underpotential shifts of various metals deposited on different substrates, a relation was proposed (Kolb *et al* 1974) between the underpotential shift ($\Delta E_p = E_m - E_b$) and the difference in electronic work function ($\Delta\phi$) of the substrate and adsorbate,

$$E_p = 0{\cdot}5\ \Delta\phi.$$

Since, the work function of carbon and copper are 5·0 (Weast 1978) and 4·45 electron volts (Trasatti 1971), respectively, the monolayer stripping peak is

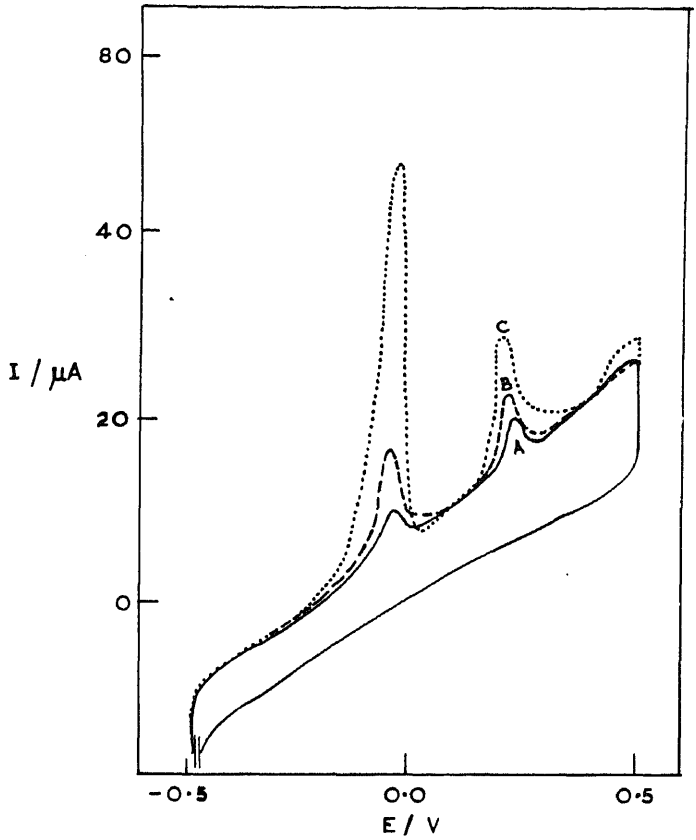

Figure 1. Potentiodynamic *I-E* profile at 11 mV/s obtained in 0·5 M H_2SO_4 + 10 ^{5}M $CuSO_4$. Anodic scan is effected after holding for 2, 4 and 10 min at −0·5 V on GC (curves A, B and C respectively).

e due to the stripping of the UPD monolayer of copper. This view is further onfirmed by the fact that the charge associated with this peak corresponds to 10 μc nd is varied over a range of 0·63 μc to 10 μc under all the experimental conditions tudied but always less than the charge expected for stripping of the fully covered nonolayer i.e. 24·5 μc for the area of the electrode employed (Bowles 1966; Furuya and Motoo 1979). Systematic studies were then carried out to understand he effects of copper concentration, time of deposition, sweep rate and deposition otential on the stripping pattern of bulk and underpotentially deposited copper.

.2 *Effect of copper concentration*

Table 1 shows the stripping peak potentials of UPD and bulk deposited copper as a unction of concentration of copper in solution. It is interesting to note from the able that with increase in the concentration of copper, the UPD and bulk stripping

Table 1. Effect of concentration of copper on underpotential shifts.
($E_d = -0{\cdot}5$ V; $t_d = 4$ min; $V = 11$ mV/s).

Concentration of Cu^{2+}(M)	E_b	E_m	ΔE_p
5×10^{-6}	$-0{\cdot}08$	0·190	0·270
10^{-6}	$-0{\cdot}065$	0·200	0·265
10^{-5}	$-0{\cdot}050$	0·220	0·270
10^{-4}	$-0{\cdot}025$	0·245	0·270

E values in volts (NCE); ΔE_p values in volts.

Table 2. Effect of time of deposition on underpotential shifts and on charges associated with UPD and bulk stripping peaks.
($[Cu^{2+}] = 10^{-5}$M; $E_d = -0{\cdot}50$V; $V = 11$ mV/s).

t_d (min)	E_m	E_b	ΔE_p	Q_m	Q_b
2	0·220	$-0{\cdot}050$	0·270	2·10	2·05
4	0·220	$-0{\cdot}050$	0·270	4·00	3·85
6	0·220	$-0{\cdot}045$	0·265	8·00	7·90
8	0·230	$-0{\cdot}035$	0·265	10·00	9·90
10	0·230	$-0{\cdot}040$	0·270	10·40	34·30

E values in volts (NCE); ΔE_p values in volts; Q values in μ Coulombs.

3.3 *Effect of time of deposition*

The effect of time of deposition on electrooxidation charges of UPD and bulk deposited copper and their stripping peak potentials was then carried out and results are furnished in table 2. From table 2, it is clear that the charges associated with UPD and bulk deposition of copper increase with increase in time of deposition as per expectations. On the other hand, the increase of time of deposition has no appreciable effect on UPD peak potential (E_m) and bulk peak potential (E_b). It is also significant to note that the underpotential shift (ΔE_p) is practically unaltered (cf. figure 1 and table 2).

3.4 *Effect of sweep rate*

Typical results obtained during the sweep rate variation studies on the stripping behaviour of underpotential and bulk deposited copper are shown in table 3. The increase in sweep rate from 6 to 270 mV/s shifts both monolayer and bulk stripping peak potentials towards more positive potentials while retaining a constant ΔE_p value, as observed in the case of the deposition of thallium onto silver (Kolb 1978). The charges corresponding to the stripping of the monolayer and bulk deposited

Table 3. Effect of sweep rate on underpotential shifts and charges associated with UPD and bulk stripping peaks.
($[Cu^{2+}] = 10^{-5}$M; $E_d = -0{\cdot}50$V; $t_d = 4$ min).

Sweep rate (mV/s)	E_m	E_b	ΔE_p	Q_m	Q_b
6	0·21	−0·06	0·270	4·00	3·85
11	0·22	−0·05	0·270	4·00	3·90
30	0·22	−0·05	0·270	3·95	4·00
50	0·23	−0·03	0·260	4·00	4·00
100	0·24	−0·02	0·260	4·00	3·95
188	0·25	−0·015	0·265	3·90	3·95
270	0·26	−0·005	0·265	4·00	3·95

E values in volts (NCE); ΔE_p values in volts; Q values in μ Coulombs.

Table 4. Effect of deposition potential on stripping characteristics of UPD and bulk stripping peaks.
($[Cu^{2+}] = 10^{-5}$M; $t_d = 4$ min; $V = 11$ mV/s).

E_d (V vs NCE)	E_m	E_b	ΔE_p	Q_m	Q_b
−0·20	—	—	—	—	—
−0·25	—	—	—	—	—
−0·30	0·22	−0·050	0·270	0·63	0·60
−0·35	0·22	−0·045	0·265	1·88	1·90
−0·40	0·22	−0·050	0·270	3·25	3·25
−0·45	0·22	−0·050	0·270	2·88	2·85
−0·50	0·22	−0·050	0·270	4·00	4·00

E values in volts (NCE); ΔE_p values in volts; Q values in μ Coulombs.

5 *Effect of deposition potential*

he dissolution behaviour of copper was studied as a function of deposition otential (E_d) by holding the potential in the range −0·25 to −0·5 V in steps of 05 V for 4 min in 10^{-5} M copper sulphate in 0·5 M sulphuric acid solution. As is ear from table 4, the UPD and bulk deposition of copper occur only when E_d is aintained at potentials more negative than −0·3 V. With change of E_d from −0·3 o −0·5 V, the charges corresponding to the stripping of UPD and bulk deposited opper increase while retaining the expected constancy for E_m, E_b and E_p values.

. Conclusions

ll the above described results clearly establish the formation of UPD of copper

constant is noticed with increase in concentration of copper in solution and sweep rate.

Acknowledgement

The authors wish to express their gratitude to Professor K I Vasu, for his keen interest and encouragement.

References

Bowles B J 1966 *Nature (London)* **212** 1456
Brainina K Z, Zakarchuk N F, Synkova D P and Yudelevich I G 1972 *J. Electroanal. Chem.* **35** 165
Furuya N and Motoo S 1979 *J. Electroanal. Chem.* **98** 189
Kiekens P, Van Den Boecke F, Bogaert M and Temmerman E 1983 *Bull. Soc. Chim. Belg.* **92** 929
Kolb D M 1978 in *Advances in electrochemistry and electrochemical engineering* (eds) H Gerischer and Tobias Ch (New York: Wiley) vol. 2
Kolb D M, Przasynski M and Gerischer H 1974 *J. Electroanal. Chem.* **54** 25
Morcos I 1975 *J. Electroanal. Chem.* **66** 250
Stulikova M and Vydra F 1973 *J. Electroanal. Chem.* **49** 117
Trasatti S 1971 *J. Electroanal. Chem.* **33** 251
Vassos B H and Mark H B 1967 *J. Electroanal. Chem.* **13** 1
Weast R C 1978 in *CRC handbook of chemistry and physics* 59th edn (West Palm Beach, Fl: CRC Press) E81

© Printed in India.

Stereochemistry and structural phase transition of Cu(II) complexes containing orthophosphate ions and pyridine/picoline

M S SASTRY* and M D SASTRY**

*Chemistry Division and **Radiochemistry Division, Bhabha Atomic Research Centre, Bombay 400 085, India

MS received 1 March 1986; revised 23 August 1986

Abstract. Copper complexes of the type $Cu(L)_4(H_2PO_4)_2$ designated as complex (I), and $Cu(L)_4\ HPO_4$ designated as complex (II), (where L = pyridine (py) or γ-picoline (pic)) have been synthesised, characterised by chemical analyses, IR, and electronic and magnetic susceptibility data. From ESR studies it is concluded that complexes (I) have elongated *trans* octahedral stereochemistry. The temperature dependence of the ESR spectrum of $Cu(py)_4(H_2PO_4)_2$ suggests a fluxional behaviour in the immediate coordination of Cu(II), whereas very little variation of the ESR spectrum of the $Cu(pic)_4(H_2PO_4)_2$ complex indicates that the stereochemistry of this complex is essentially static in nature. The differential scanning calorimetric studies in the case of $Cu(py)_4(H_2PO_4)_2$ complex have given clear evidence for the occurrence of a structural phase transition at 147 K. The absence of any abrupt changes in the ESR spectrum at that temperature excludes the possibility of any changes in the immediate environment of Cu(II).

Keywords. Copper(II) complexes; octahedral stereochemistry; differential scanning calorimetric studies; structural phase transition.

1. Introduction

Structural studies of transition metal complexes with phosphate coordination have been reported by a number of investigators (Siebert 1958; Schmidt and Taube 1963; Lincoln and Stranks 1968; Ojima and Nonoyama 1973). Recently we have reported ESR and electronic spectral studies of some copper (II) bipyridyl/1, 10-phenanthroline complexes containing orthophosphate ions (Sastry *et al* 1984). Some of these complexes were found to exhibit temperature dependent fluxional behaviour. The present work is aimed at extending these investigations to Cu(II) phosphate complexes containing unidentate ligands such as pyridine and substituted pyridines. This paper describes the preparation and structural elucidation of $Cu(L)_4(H_2PO_4)_2$ and $Cu(L)_4HPO_4$ complexes from IR, electronic spectral, ESR and magnetic susceptibility data. Differential scanning calorimetric (DSC) studies were also conducted to see if any structural phase change occurs in these compounds.

2. Experimental

2.1 *Chemicals*

All chemicals were of reagent grade and were used without further purification.

2.2 *Preparation of complexes*

The complexes were prepared by reaction between $Cu(H_2PO_4)_2/Cu(HPO_4)$ and the neutral ligand (L) in dry methanol-2,2′ dimethoxy propane medium.

2.2a *Cu(py/pic)$_4$(H_2PO_4)$_2$*: $Cu(H_2PO_4)_2$ was prepared by dissolving $CuCO_3$ (2·0 g 10 mM) in the minimum amount of 85% orthophosphoric acid by warming and stirring. Green coloured $Cu(H_2PO_4)_2$ (identified by chemical analysis) was precipitated from the clear green coloured solution by the addition of dry methanol. To the slurry of this compound in dry methanol-2,2′-dimethoxy propane mixture (1:1 ratio, 20 ml), freshly distilled dry pyridine/gamma-picoline (50·0 mM) was added drop by drop with constant stirring for about five hours with occasional warming. The green coloured slurry changed to greenish blue colour slowly and same coloured compound was precipitated out. The precipitate was filtered, washed with 1% py in methanol-dimethoxypropane mixture and dried in a vacuum desiccator. Yield, $Cu(py)_4(H_2PO_4)_2$, 3·00 gm. Analysis: Found – Cu, 11·02; P, 10·56; N, 9·52; Calc. for $Cu(py)_4(H_2PO_4)_2$ Cu, 11·07; P, 10·80; N, 9·75. Yield, $Cu(pic)_4(H_2PO_4)_2$ 3·50 g. Analysis: Found – Cu, 9·98; P, 9·65; N, 8·45; Calc. for $Cu(pic)_4(H_2PO_4)_2$; Cu, 10·08; P, 9·98; N, 8·89.

2.2b *Cu(py)/(pic)$_4$(HPO_4)*: The preparation of this complex (dark blue) is similar to that of $Cu(L)_4(H_2PO_4)_2$ complexes, except that $CuHPO_4$ was prepared by dissolving cupric oxide in 85% orthophosphoric acid, always keeping CuO in excess while dissolving in the acid. Yield, $Cu(py)_4(HPO_4)$, 2·00 g. Analysis: Found – Cu, 13·20; P, 6·9; N, 11·65; Calc. for $Cu(py)_4(HPO_4)$; Cu, 13·35; P, 6·5; N, 11·76. Yield, $Cu(pic)_4(HPO_4)$, 2·40 g. Analysis: Found – Cu, 11·77; P, 5·89; N, 10·55; Calc. for $Cu(pic)_4(HPO_4)$ Cu, 11·94; P, 5·83; N, 10·52.

2.3 *Instrumental methods*

IR spectra of the complexes were recorded on a Perkin Elmer 577 spectrophotometer using nujol and hexachlorobutadiene (HCBD) mulls. Electronic absorption spectra of nujol mulls were recorded on a Cary-14 spectrophotometer. ESR spectra of powdered samples were recorded on a Varian V-4502 spectrometer operating at X-band frequency. DPPH was used as a g-marker and the magnetic field was measured using an NMR gaussmeter. Magnetic susceptibilities of the compounds were measured by the Gouy method on powdered samples using $Hg[Co(CNS)_4]$ as standard. DSC experiments were carried out on a Perkin Elmer 2-C instrument.

3. Results and discussion

3.1 *Results*

The ESR spectrum of polycrystalline $Cu(py)_4(H_2PO_4)_2$ at room temperature was isotropic with the g value ($g = 2{\cdot}010 \pm 0{\cdot}001$), while at 77 K, the spectrum was anisotropic with $g_{\parallel} = 2{\cdot}18 \pm 0{\cdot}001$ and $g_{\perp} = 2{\cdot}008 \pm 0{\cdot}001$ (figures 1a, b). The ESR spectrum of $Cu(py)_4(HPO_4)$ and $Cu(pic)_4(HPO_4)$ were isotropic at room tempera-

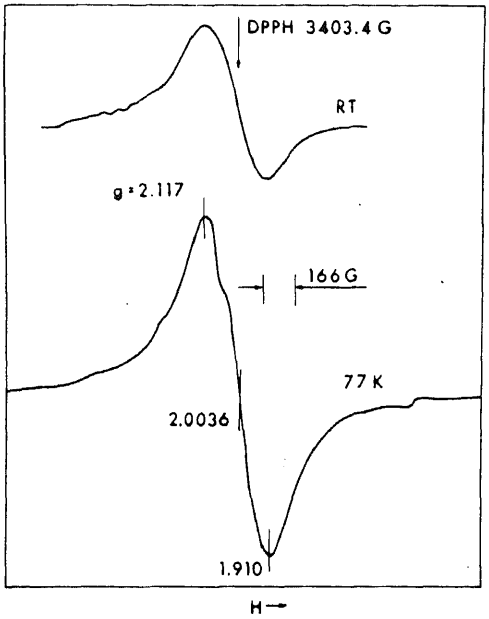

Figure 1. EPR spectrum of $Cu(py)_4(H_2PO_4)_2$ at room temperature (A) and at 77 K (B). The anisotropic features, with parallel components on the lower field side, can be observed at 77 K.

ith partially resolved hyperfine structure. The spectrum yielded the values $= 2{\cdot}19 \pm 0{\cdot}001$, $g_\perp = 2{\cdot}010 \pm 0{\cdot}001$, $A_\parallel = 181 \pm 1G$ and $A_\perp < 25G \pm 1G$. The oom temperature magnetic moments of $Cu(py)_4(H_2PO_4)_2$ and $Cu(pic)_4(H_2PO_4)_2$ ere 1·85 and 1·83 B.M. respectively, while the values for the corresponding PO_4^{2-} complexes were 1·80 and 1·90 B.M.

The IR spectra obtained for the compounds investigated in the region 00–4000 cm^{-1} are consistent with the reported values for the internal modes of all onstituent groups (Chapman and Thirlwell 1964; Gill *et al* 1961; Choca *et al* 1972; aito *et al* 1973; Biagetti *et al* 1966). Further, the IR spectra have provided evidence or the metal (copper) – oxygen, and metal – nitrogen vibration suggesting the oordination of neutral ligand and phosphate ions to the metal. The frequencies for ese vibrations are:

a) Cu – N stretching; 270 cm^{-1} (Cu $py_4(H_2PO_4)_2$) 295, 285, 258, 250 cm^{-1} (Cu $y_4(H_2PO_4)_2$), 260 cm^{-1} (Cu pic_4 HPO_4) and 290, 275, 265, 260 cm^{-1} (Cu pic_4 PO_4).

b) Cu – O stretching: 255 cm^{-1} (Cu $py_4(H_2PO_4)_2$), 310 cm^{-1} (Cu py_4 HPO_4), 50 cm^{-1} (Cu $pic_4(H_2PO_4)_2$) and 300 cm^{-1} (Cu pic_4 HPO_4).

The electronic absorption (mull) spectra of all these complexes were found to be milar, with broad absorption peaks in 650–950 nm. Whereas the spectrum of Cu $y_4(H_2PO_4)_2$ and Cu $pic_4(H_2PO_4)_2$ contained a dominant absorption at 650 nm ith an unresolved shoulder at 800 nm, the corresponding complexes of type II

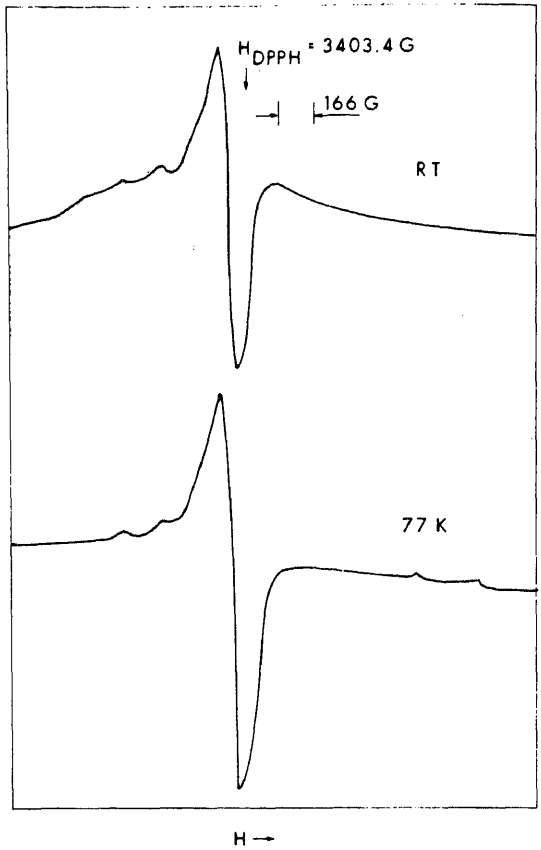

Figure 2. EPR spectrum of $pic_4(H_2PO_4)_2$ at room temperature and at 77 K.

3.2 *Discussion*

From the ESR spectra of $Cu(L)_4(H_2PO_4)_2$ complexes, the g values observed for the $Cu(py)_4(H_2PO_4)_2$ complex at 77 K ($g_{\parallel} > g_{\perp} > 2{\cdot}0$) shows that the unpaired electron has predominant (x^2-y^2) character. This suggests that the Cu(II) ion in the complex has *trans* octahedral geometry with elongation along the z-axis. The dynamic behaviour at room temperature resulting in an isotropic spectrum and the anisotropicity at 77 K were interpreted as being due to temperature dependent motional effects of CuL_4O_2 chromophore resulting in averaging of anisotropies at room temperature. This can be visualised either as temperature dependent hindered motion or temperature dependent vibronic coupling (Hathaway *et al* 1981). Lowering the temperature of such complexes leads to the freezing out of the dynamical distortions and, in certain cases, such a process is accompanied by first-order structural phase transition (Hathaway *et al* 1981). DSC experiments indicated phase transition at 147 K with a sharp peak, in the case of Cu

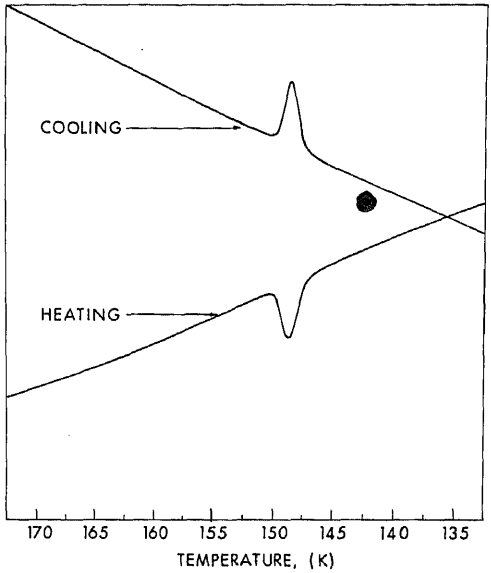

Figure 3. DSC scan of Cu $(py)_4(H_2PO_4)_2$ below room temperature.

round the Cu(II) ion. The ESR spectra of $Cu(L)_4(HPO_4)$ complexes were found to e essentially temperature independent. DSC experiments indicated the absence of ny phase changes in the temperature range 300 to 77 K. The ESR spectrum of $Cu(pic)_4(H_2PO_4)_2$ (figures 2a,b) showed an axial spectrum both at room emperature and at 77 K, with well-resolved hyperfine structure. DSC experiments ave not shown any peaks in the range 300 to 77 K. The g values ($g_\parallel > g_\perp > 2$) ndicate an elongated octahedron with $d(x^2-y^2)$ as the ground state. The $A_\perp$ and $A_\parallel$ values obtained for this complex are in agreement with those reported for etragonally distorted $Cu(py)_4(CF_3COO)_2$ complexes (Pradillas *et al* 1979). The ery little variation of the ESR spectrum with temperature indicates that the oordination around Cu(II) in this complex is essentially static in nature. The room emperature magnetic moment values for all these $Cu(L)_4(H_2PO_4)_2$ and $Cu(L)_4(HPO_4)$ complexes are in the range expected for the octahedral complexes.

The far IR spectra of $Cu(L)_4(H_2PO_4)_2$ complexes showed two bands in the region 50–200 cm^{-1}, conforming to *trans* octahedral stereochemistry (D_{4h}), which is also onsistent with the evidence from the ESR data, whereas the far IR spectra of $Cu(L)_4(HPO_4)$ complexes showed a large number of bands conforming to *cis* ctahedral stereochemistry. The metal-nitrogen and metal-oxygen stretching nodes for these complexes have been assigned in accordance with the reported ata. Although two copper-oxygen stretching bands are expected in the case of $Cu(L)_4(HPO_4)$ complexes, only one broad band is observed in each case. It is erhaps possible that the other band might have been obscured in the broad nvelope.

geometry, are in accordance with the reported observations for this type of complexes (Pradillas *et al* 1979; Hathaway *et al* 1981).

4. Conclusions

ESR and IR have shown that the complexes $Cu(py)_4(H_2PO_4)_2$ and $Cu(pic)_4(H_2PO_4)_2$ have coordinating H_2PO_4 groups in the *trans* positions and py/pic molecules in the equatorial plane. The electronic and ESR spectral features similar to the above complexes have also been observed for the elongated *trans* octahedral $Cu(py)_4(CF_3COO)_2$ complex (Pradillas *et al* 1979), and thus the $Cu(L)_4(H_2PO_4)_2$ complexes are also expected to have similar structures. It is interesting that the stereochemistry of $Cu(py)_4(H_2PO_4)_2$ is fluxional in nature, while that of $Cu(L)_4(H_2PO_4)_2$ is essentially static. This is probably due to the presence of hydrogen-bonding between the hydrogen of the methyl group in picolene and phosphate ions. The differences in the IR and electronic spectral data of $Cu(L)(HPO_4)$ complexes from that of $Cu(L)_4(H_2PO_4)_2$ complexes have indicated a more distorted octahedron conforming to *cis* octahedral stereochemistry for the former complexes. Spectral features similar to $Cu(L)_4(HPO_4)$ complexes have also been observed in the *cis* octahedral Cu(II) complexes (Hathaway *et al* 1981). Although axial spectra are expected for the *cis* octahedral Cu(II) complexes, only temperature independent isotropic spectra were observed for the $Cu(L)(HPO_4)$ complexes. A similar observation was reported in the case of the $Cu(L)_4(H_2PO_4)_2$ (L = 1,10, phenanthroline) complex at room temperature (Sastry *et al* 1984), although at 77K the phen-complex gave an anisotropic spectrum. A temperature lower than 77 K might be required to observe the anisotropicity in the ESR spectra of the py/pic analogue.

Acknowledgements

We are thankful to Dr R M Iyer, for his helpful suggestions and keen interest in the work. We also wish to thank Dr S K Kulshreshtha for his help in the DSC experiments.

References

Biagetti R V, Bohrer, William G and Haendler H M 1966 *Inorg. Chem.* **5** 379

Chapman A C and Thirlwell L E 1964 *Spectrochim. Acta* **20** 937

Choca M, Ferraro J R and Nakamoto K 1972 *J. Chem. Soc., Dalton Trans.* **2297**

Gill N S, Nuttal R H, Scaife D E and Sharp D W A 1961 *J. Inorg. Nucl. Chem.* **18** 1979

Hathaway B J, Harry Duggan, Angela Murphy, John Mullane, Chris Power, Andrew Walsh and Walsh B 1981 *Coord. Chem. Rev.* **36** 267

Lincoln S F and Stranks D R 1968 *Aust. J. Chem.* **21** 37

Ojima H and Nonoyama K 1973 *Z. Anorg. Allgem. Chem.* **401** 195

Pradillas J, Chen H W, Koknat F W and Fackler J P Jr 1979 *Inorg. Chem.* **18** 3519

Saito Y, Schdanfer C W, Corden M and Nakamoto K 1973 *Appl. Spectrosc.* **27** 213

nfrared and Raman spectra of vicinally trisubstituted 2-methyl, -chloroaniline and 2-methyl, 6-chloroaniline

A R SHUKLA[1], C M PATHAK*, N G DONGRE[2], B P ASTHANA and JACOB SHAMIR[†]

Laser and Spectroscopy Laboratory, Department of Physics, Banaras Hindu University, Varanasi 221 005, India

[†]Department of Inorganic and Analytical Chemistry, The Hebrew University of Jerusalem, Jerusalem, Israel

[1]Present address: Department of Non-Conventional Energy Sources, Block No. 14, CGO Complex, New Delhi 110 003, India

[2]Department of Physics, Harish Chandra Post-graduate College, Varanasi 221 001, India

MS received 18 March 1986; revised 8 July 1986

Abstract. The IR and Raman spectra of 2-methyl, 3-chloroaniline (2-M, 3-CA) and 2-methyl, 6-chloroaniline (2-M, 6-CA) have been recorded at room temperature in the region 3600–100 cm^{-1}. A vibrational analysis has been made using additional frequencies obtained from IR studies at 223 and 123 K and also including the polarization measurement of the Raman lines. A comparative study of these two molecules together with the spectra of 2,3-dimethylaniline (2,3-DMA), investigated earlier, has been presented. The anomalous behaviour of certain normal modes at low temperatures indicates the presence of an intermolecular hydrogen bonding of the N–H...N type in 2-M, 3-CA and 2,3-DMA, whereas, in 2-M, 6-CA, an intramolecular hydrogen bonding of the type N–H...Cl has been detected owing to the presence of the highly electronegative Cl atom at the ortho position.

Keywords. Infrared and Raman spectra; normal modes; spectral changes; hydrogen bonding, inter-and intra-molecular; phase transition.

Introduction

he near IR spectra of 2-M, 3-CA and 2-M, 6-CA were first investigated by Sharma nd Dwivedi (1976) who have reported the frequency assignments of 35 and 37 ormal modes in the respective molecules out of a possible 45 normal modes in ach molecule. Our recent study on 2,3-DMA (Shukla *et al* 1986), and earlier studies n substituted benzenes (Varsanyi 1974) have revealed that more fundamentals can e observed if the spectra are recorded at low temperatures. In an attempt to vestigate the influence of the three vicinal substitutions in benzene on the normal odes of the benzene frame, a comparative study of the normal modes of the olecules under investigation has been presented, along with those of 2,3-DMA Shukla *et al* 1986). The investigation of the low temperature spectra has led to bservation of many new fundamental frequencies. With the help of frequencies bserved and analysed, it has been possible to propose frequency assignments for l the 45 normal modes in each molecule under discussion. The solution spectra as ell as the low temperature spectra have further given strong evidence that both

*To whom all correspondence should be addressed.

the molecules are involved in one or the other kind (intermolecular or intramolecular) of hydrogen bonding as expected.

2. Experimental

The samples of 2-M, 3-CA and 2-M, 6-CA, both liquids at room temperature (b.p. 225°C), were obtained from Koch-Light, England. The reported purity was better than 98·5% in both the samples. The samples were redistilled several times under reduced pressure before use. The experimental details of recording the near IR, far IR and Raman spectra at room temperature, and IR spectra at 223 and 123 K, using a variable temperature cell, have been described elsewhere (Shukla *et al* 1986). The IR and Raman spectra of 2-M, 3-CA only has been reproduced in figure 1 covering the spectral region 3600–100 cm^{-1}. The observed spectral features in 2-M, 3-CA are compared with those of 2,3-DMA (Shukla *et al* 1986), wherever necessary. The accuracy of measurement was nearly ± 2 cm^{-1} to ± 5 cm^{-1}. The frequencies of the normal modes of the benzene frame and their assignments, in Wilson's notation (1934), have been collected for the above three molecules in table 1. The observed

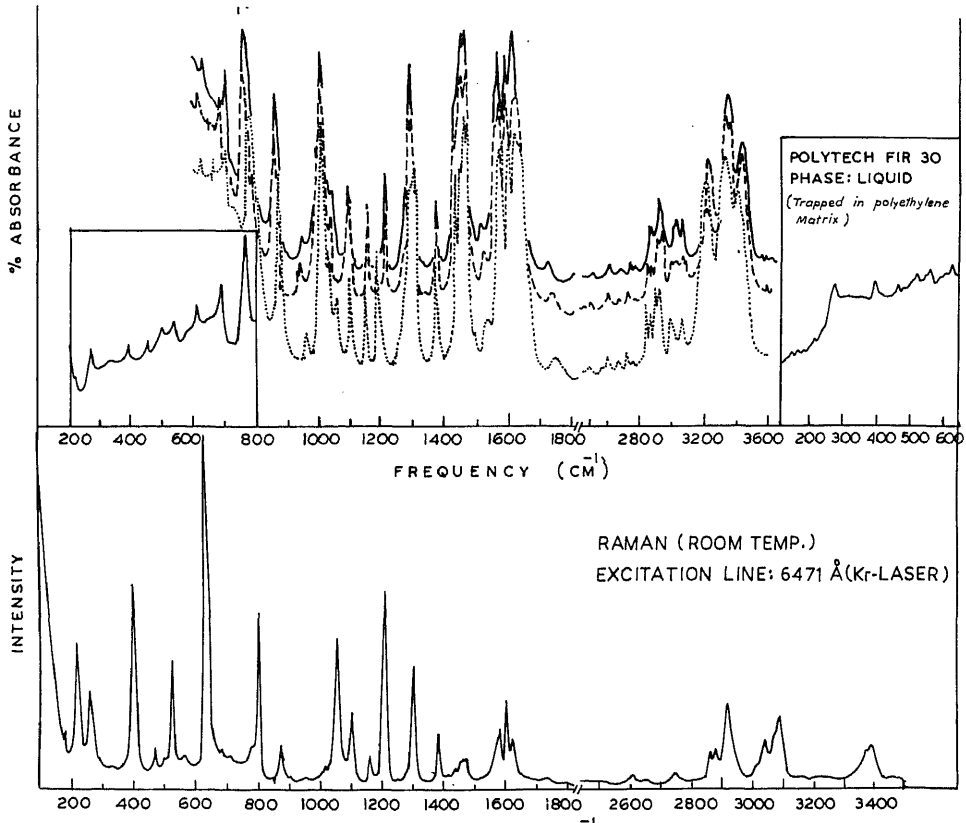

Table 1. Comparison of the frequencies[@] of ring modes (cm^{-1}) in 2M, 3-CA, 2M, 6-CA and 2,3-DMA.

Designation of mode (*a*)	Description of mode (*b*)		Present work					
			2M,3-CA		2M,6-CA		2,3-DMA[c]	
Species a'								
ν_1	2	ν_{C-H}	3084[#]	IR, *mw*			3070	IR, *m*
			3085	*R,m,p*	3080	*R,ms,p*	3075	*R,m,p*
ν_2	20b	ν_{C-H}	3064	IR,*mw*	3069	IR,*m*	3023	IR,*ms* (ν_3)
			3070	*R,sh,p*	3069	*R,sh,p*	—	
ν_3	7a	ν_{C-H}	3028	IR,*mw*	3025	IR,*m*	3040	IR,*ms* (ν_2)
			3038	*R,m,p*	3031	*R,m,p*	3044	*R,ms,p*
ν_4	8b	ν_{C-C}	1599	IR,*s*	1591	IR,*s*	1599[#]	IR,*vs*
			1599	*R,m,dp*	1595	*R,w,dp*	1596	*R,s,p*
ν_5	8a	ν_{C-C}	1577	IR,*s*	1574	IR,*s*	1574	IR,*sh*
			1578	*R,m,p*	1574	*R,ms,p*	1582	*R,sh,p*
ν_6	19a	ν_{C-C}	1476	IR,*vs*	1473	IR,*vs*	1472	IR,*vs* (ν_7)
			1474	*R,w,p*	1473	*R,ms,p*	1474	*R,w,p*
ν_7	19b	ν_{C-C}	1463	IR,*vs*	1468*	IR,*vs*	1483	IR,*vs* (ν_6)
			1463	*R,w,p*	—		1485	*R,mw,dp*
ν_8	14	ν_{C-C}	1303*	IR,*s*	1311	IR,*ms*	1308*	IR,*sh*
			—		1310	*R,m,p*	1308	*R,sh,p*
ν_9	20a	ν_{C-X}	1296	IR,*s*	1285	IR,*ms*	1295	IR,*vs*
			1298	*R,ms,p*	1285	*R,s,p*	1295	*R,vs,p*
ν_{10}	3	β_{C-H}	1253*	IR,*sh*	1250	IR,*ms*	1260	IR,*ms*
			1252	*R,vw*	1250	*R,w,p*	1260	*R,s,p*
ν_{11}	13	ν_{C-X}	1213	IR,*m*	1195	IR,*mw*	1200	IR,*mw*
			1202	*R,s,p*	1195	*R,ms,p*	1200	*R,s,p*
ν_{12}	9b	β_{C-H}	1158	IR,*m*	1150	IR,*w*	1166	IR,*m*
			1168	*R,mw,dp*	1150	*R,mw,dp*	1168	*R,m,dp*
ν_{13}	18a	β_{C-H}	1101	IR,*m*	1102**	IR,*sh*	1094	IR,*vs* (ν_{14})
			1100	*R,m,p*	1099	*R,sh,p*	1094	*R,s,p*
ν_{14}	6b	ϕ_{C-C-C}	867	IR,*s*	849	IR,*ms*	542	IR,*mw* (ν_{17})
			867	*R,m,p*	848	*R,w,p*	540	*R,s,p*
ν_{15}	12	ϕ_{C-C-C}	799	IR,*ms*	828	IR,*m*	821	IR,*s*
			799	*R,s,p*	825	*R,s,p*	814	*R,vw*
ν_{16}	1	Ring	631	IR,*s*	632	IR,*s*	662	IR,*s*
		breath	632	*R,vvs,p*	633	*R,vvs,p*	667	*R,vvs,p*
ν_{17}	6a	ϕ_{C-C-C}	524	IR,*ms*	527	IR,*w*	490	IR,*m* (ν_{18})
			523	*R,ms,p*	528	*R,m,p?*	490	*R,s,dp*
ν_{18}	18b	β_{C-X}	468	IR,*m*	471	IR,*m*	472	IR,*m* (ν_{19})
			469	*R,mw,p*	469	*R,ms,p*	473	*R,vw,dp*
ν_{19}	7b	ν_{C-X}	399	IR,*ms*	390	IR,*m*	1128	IR,*m* (ν_{13})
			399	*R,s,p*	390	*R,s,p*	1120	*R,w,p*
ν_{20}	9a	β_{C-X}	326	IR,*wb*	329	IR,*vw*	335	IR,*wb*
			330	*R,vvw*	329	*R,w,p*	330	*R,mw,p*

Table 1. (*Continued*)

Designation of mode (*a*)	(*b*)	Description of mode	Present work 2M,3-CA	2M,6-CA	2,3-DMA[c]
Species a''					
ν_{22}	5	γ_{C-H}	957 IR,*mw* 958 *R*,*vvw*	950 IR,*w* 952 *R*,*vw*	952 IR,*mw* —
ν_{23}	17a	γ_{C-H}	904 IR,*vvw* 903 *R*,*vvw*	895 IR,*w* 896 *R*,*vw*	898 IR,*mw* 899 *R*,*vw*
ν_{24}	11	γ_{C-H}	772 IR,*vs* 772 *R*,*sh*,*dp*	760 IR,*s* 765 *R*,*vw*	773 IR,*vs* 773 *R*,*vw*
ν_{25}	4	$\delta_{C-C-C-C}$	704 IR,*s* 708 *R*,*w*,*dp*	723 IR,*s* —	713 IR,*vs* 715 *R*,*vw*
ν_{26}	16b	$\delta_{C-C-C-C}$	561 IR,*ms* 561 *R*,*w*,*dp*	538 IR,*ms* 542 *R*,*w*,*dp*	555 IR,*ms* 557 *R*,*w*,*dp*
ν_{27}	16a	$\delta_{C-C-C-C}$	— 498 *R*,*w*,*dp*	— 502 *R*,*w*,*dp*	505 IR,*mw* 512 *R*,*vw*,*dp*
ν_{28}	10b	γ_{C-X}	— 261 *R*,*ms*,*dp*	250 IR,*w* 245 *R*,*ms*,*dp*	258 IR,*w* —
ν_{29}	10a	γ_{C-X}	221 IR,*w* 221 *R*,*s*,*dp*	228 IR,*w* 228 *R*,*ms*,*dp*	235 IR,*w* 235 *R*,*s*,*dp*
ν_{30}	17b	γ_{C-X}	143 IR,*vw* —	140 IR,*w* 145 *R*,*w*,*dp*	145 IR,*vw* 145 *R*,*vw*

[a] Mulliken's notation (1955); [b] Wilson's notation (1934); [c] Shukla *et al* (1986); The assignment of the modes in Wilson's (1934) notation remains the same for all the three molecules, but in Mulliken's (1955) notation they differ at certain places in the case of 2,3-DMA and these are given in parenthesis against the corresponding frequencies.

* Observed at 223 and 123 K; ** Observed at 123 K; # Observed at 223 K; IR, infrared; *R*, Raman; *p*, polarized; *dp*, depolarized; *b*, broad; *s*, strong; *m*, medium; *w*, weak; *ms*, medium strong; *mw*, medium weak; *vw*, very weak; *vs*, very strong; *vvs*, very very strong; *vvw*, very very weak; *sh*, shoulder.

frequencies of the normal modes associated with the substituent groups in the above three molecules have been collected separately in table 2.

3. Comparative study of the various ring modes

For the sake of comparison of the various ring modes in the two molecules under investigation, with those of 2,3-DMA (Shukla *et al* 1986), all the normal frequencies are collected together in table 1.

3.1 *C–H stretches*

The three C–H stretches in a vicinally trisubstituted benzene correspond to the modes 2, 20b and 7a (table 1). All the three frequencies have been observed in the

Table 2. Comparison of group frequencies[a] (cm^{-1}) in 2M, 3-CA, 2M, 6-CA and 2,3-DMA.

Designation of mode	Description of mode	Present work		
		2M,3-CA	2M,6-CA	2,3-DMA[c]
NH_2 group:				
ν_{as}	$(NH)_{as}^{str.}$	3472 IR,*ms* 3470 *R*,*w*,*dp*	3480 IR,*s* 3479 *R*,*w*	3449 IR,*s* —
ν_{sy}	$(NH)_{sy}^{str.}$	3385 IR,*s* 3385 *R*,*mb*,*p*	3389 IR,*s* 3390 *R*,*b*,*p*	3367 IR,*vs* 3370 *R*,*m*,*p*
β_{sy}	$(NH_2)_{sy}^{def.}$	1622 IR,*vs* 1622 *R*,*mw*,*p*	1617 IR,*vs* 1617 *R*,*s*,*p*	1621 IR,*vs* 1621 *R*,*m*,*p*
β_{as}	$(NH_2)^{twist}$	1045 IR,*m* 1048 *R*,*s*,*p*	1079 IR,*s* 1080 *R*,*s*,*p*	1045 IR,*m* 1045 *R*,*s*,*p*
γ_{sy}	$(NH_2)^{o.p.wag}$	610 IR,*mv* 608 *R*,*w*,*sh*	590 IR,*wb* 585 *R*,*wb*	626 IR,*s* 630 *R*,*vvw*
τ'	$(NH_2)^{tors}$	284 IR,*sh* —	293 IR,*vw* 298 *R*, *vw*	274 IR,*sh* —
CH_3 group(s)				
ν_{as}	$(CH)_{as}^{str.}$	— —	— —	— 2978 *R*,*w*,*p*
ν_{as}	$(CH)_{as}^{str.}$	— 2965 *R*,*w*	2975 IR,*m* 2980 *R*,*w*,*p*	2967 IR,*s* —
ν_{as}	$(CH)_{as}^{str.}$	2935 IR,*m* 2937 *R*,*sh*,*p*	2933 IR,*ms* 2934 *R*,*w*	2941 IR,*s* —
ν_{sy}	$(CH)_{sy}^{str.}$	2916 IR,*m* 2918 *R*,*ms*,*p*	2916 IR,*ms* 2919 *R*,*ms*,*p*	2923 IR,*s* 2923 *R*,*s*,*p*
ν_{sy}	$(CH)_{sy}^{str.}$	— —	— —	2904* IR,*s* 2910 *R*,*s*,*p*
δ_{as}^{+}	$(CH_3)_{as}^{def.}$	— —	— —	— 1462 *R*,*s*,*h*
δ_{as}^{+}	$(CH_3)_{as}^{def.}$	1450** IR,*s* 1450 *R*,*w*	1442 IR,*s* 1445 *R*,*m*,*dp*	1455** IR,*sh* 1450 *R*,*mw*
δ_{as}^{+}	$(CH_3)_{as}^{def.}$	— —	— —	1444 IR,*s* 1443 *R*,*mw*
δ_{as}^{+}	$(CH_3)_{as}^{def.}$	1438 IR,*s* 1438 *R*,*w*,*p*	1437 IR,*s* 1437 *R*,*m*,*p*	1437* IR,*s* 1438 *R*,*mw*
δ_{sy}	$(CH_3)_{sy}^{def.}$	1380 IR,*m* 1380 *R*,*mw*,*p*	1378 IR,*m* 1379 *R*,*m*,*p*	1383 IR,*ms* 1383 *R*,*s*,*p*
δ_{sy}	$(CH_3)_{sy}^{def.}$	— —	— —	1376# IR,*w* 1376 *R*,*sh*,*p*
δ_{as}^{-}	$(CH_3)^{rock}$	1028* IR,*m* 1023 *R*,*vw*,*p*	1033 IR,*m* 1035 *R*,*mw*,*p*	1043* IR,*m* —
δ_{as}^{-}	$(CH_3)^{rock}$	1011 IR,*vs* 1012 *R*,*vw*,*p*	994 IR,*m* 997 *R*,*m*,*p*	1018 IR,*m* 1021 *R*,*w*,*p*
δ_{as}^{-}	$(CH_3)^{rock}$	— —	— —	991 IR,*ms* 991 *R*,*s*,*p*
δ_{as}^{-}	$(CH_3)^{rock}$	— —	— —	871 IR,*ms* —
τ	$(CH_3)^{tors.}$	188 IR,*w*	185 IR,*w*	185 IR,*w*

3.2 *C–C stretches*

The various C–C stretches, in Wilson's (1934) notation, correspond to the modes 8a, 8b, 14, 19a and 19b (table 1). The frequency of mode 14 is usually insensitive to any type of substituent (Varsanyi 1974) and its frequency has been found to be fairly constant in the present study also. It may be noted that the IR band corresponding to this mode 14 overlapped with the C-NH_2 stretch in the case of 2-M, 3-CA, similar to that observed in 2,3-DMA (Shukla *et al* 1986), in the room temperature IR spectra, but the two modes got well separated in the spectra recorded at low temperatures.

The next two C–C stretching modes, 8a and 8b have been distinctly observed and assigned in both the molecules. It is obvious from table 1 that the frequencies of this pair of vibrations (8a and 8b) are fairly insensitive to the nature and position of the substituents in the case of all the three vicinally trisubstituted benzenes. The high degree of depolarization of the mode 8b in the Raman spectra, as measured in the present study, is more or less a characteristic property of this mode and has been found in a large number of molecules (Herz 1941). The other pair of C–C stretching modes, 19a and 19b appears characteristically with good intensity and the frequency of mode 19b gets affected by the nature of the substituents, whereas the frequency of mode 19a remains almost unaffected.

3.3 *C–H in-plane bends*

The three C–H in-plane bends in 2-M, 3-CA and 2-M, 6-CA correspond to modes 3, 9b and 18a. The frequency of mode 3 is lower, whereas the frequency of mode 18a has been found to be higher than the frequency of the corresponding modes in benzene and monosubstituted benzenes (Varsanyi 1974). It has been noticed that the intensity of mode 18a is lower in 2-M, 3-CA and 2-M, 6-CA as compared to that in 2,3-DMA (Shukla *et al* 1986). The frequency of mode 9b shows a variation in intensity which may be attributed to the nature and position of the substituent in the ring.

3.4 *C–H out-of-plane waggings*

The three C–H out-of-plane waggings correspond to modes 5, 11, and 17a. Modes 5 and 17a have been observed with very weak intensity, whereas, mode 11 appears with fairly good intensity. The frequency of mode 11 is, however, lowest among the three and its magnitude has been found to vary only with the relative position of the substituents, whereas the frequency of mode 5 has been found to change with the relative position as well as the nature of the substituents.

3.5 *Radial skeletal vibrations*

The seven radial skeletal vibrations in the molecules under investigation, correspond to modes 1, 12, 6a, 6b, 4, 16a and 16b. The radial skeletal modes 1 and

2 have been observed with good intensity in both the molecules and these two nodes couple strongly with the C–X (X = light) stretch as a result of which, the requencies corresponding to modes 1 and 12 assume relatively lower magnitude as ompared to that observed in benzene. In the case of 2,3-DMA (Shukla *et al* 1986), ne frequencies of the skeletal modes 6a and 6b both, were found to decrease as ompared to that in benzene, whereas in the case of 2-M, 3-CA and 2-M, 6-CA, mode a behaves in a similar fashion as in 2,3-DMA (Shukla *et al* 1986), but the frequency f mode 6b increases considerably because of its coupling with the C–Cl stretching node. Further, the frequencies of the skeletal modes 16a and 16b have been found o be higher than the corresponding frequencies in the parent molecule benzene ecause of their coupling with the C–X (X = substituent) out-of-plane wagging nodes. The last skeletal mode 4 has been found to be almost insensitive to ubstitution in both the molecules.

.6 *C–X (X = substituent) stretching, bending and wagging modes*

The C–X stretching vibrations in these molecules correspond to modes 7b, 13 and 0a. All the three modes, which appear at their characteristic frequencies, have been observed in the present work, and the values are listed in table 1. The C–NH_2 tretch, observed in the frequency interval 1270–1300 cm^{-1}, corresponds to mode 0a. This frequency appears with quite good intensity in the IR spectra and as a trongly polarized line with sufficiently good intesity in the Raman spectra. There eems to be a slight effect of relative position and nature of the substituents to node 13. The relative position of the Cl atom, in methyl chloroaniline isomers nvestigated in this work, does not seem to affect the frequency of the C–CH_3 tretching mode 7b much, which is observed around 400 cm^{-1} in both the nolecules.

In benzene derivatives with vicinal trisubstitution (Varsanyi 1974), the in-plane C–X bends correspond to the modes 9a, 15 and 18b, and out-of-plane C–X wags orrespond to the modes 10a, 10b and 17b. The frequencies of all these modes lie in he far IR region (figure 1). Only some slight influence of the substituent groups can e seen on the magnitude of the frequencies of these modes, which may be ttributed to the relative position and/or the nature of the substituents.

. Vibrations of the substituent groups and spectral changes due to hydrogen onding

The two molecules under investigation have NH_2 and CH_3 groups as substituents. t is fairly well-known that in anilines and substituted anilines (Murthy and Rao 968), the hydrogen atoms of the NH_2 group make an intermolecular hydrogen ond of N–H...N type and cause some spectral changes. Some special spectral eatures and changes were observed in 2,3-DMA (Shukla *et al* 1986). Similar spectral hanges are expected in the cases of 2-M, 3-CA and 2-M, 6-CA and only some elevant points are discussed here. One finds that in the case of 2-M, 3-CA, the difference between the two values of asymmetric N–H stretching frequency, one

hydrogen bond formation in the case of 2-M, 3-CA, almost similar to the case of 2,3-DMA (Shukla *et al* 1986). However, the behaviour of 2-M, 6-CA is quite different as regards the integrated intensities of the three bands related to the normal modes of the NH_2 group, two N–H stretches and one H–N–H bend, which actually decrease in going from liquid phase to the condensed phases. Furthermore, in 2-M, 6-CA, unlike 2-M, 3-CA the difference between the two values of the asymmetric N–H stretching frequency, one observed in solution and the other in the liquid phase, is different from the corresponding difference for the symmetric N–H stretching. It is also seen that the frequencies of the N–H stretching modes in 2-M, 6-CA do not follow the Bellamy and Williams (1957) empirical relation

$$\nu_{sym} = 345{\cdot}5 + 0{\cdot}876\ \nu_{asym},$$

as closely as in 2-M, 3-CA or in 2,3-DMA (Shukla *et al* 1986).

The above facts suggest that in 2-M, 6-CA, the two N–H bonds do not behave in an identical fashion during the hydrogen bonding. This is most probably due to the coexistence of intramolecular hydrogen bonding along with N–H...N type intermolecular hydrogen bonding. In fact, according to Krueger (1962), the presence of an electronegative atom in the vicinity of NH_2 group in a molecule gives rise to intra-molecular hydrogen bonding and therefore it is quite likely that such hydrogen bonding of the type N–H...Cl coexists along with the inter-molecular hydrogen bonding in 2-M, 6-CA.

Acknowledgements

One of us (ARS) is thankful to the UGC and CSIR, New Delhi, for financial support during the period of this work and NGD is grateful to UGC for the award of a fellowship. A part of the experimental work was carried out at the Indian Institute of Science, Bangalore, in the laboratory of Professor C N R Rao, and the help rendered by him is gratefully acknowledged.

References

Bellamy L J and Williams R L 1957 *Spectrochim. Acta* **9** 341
Herz E 1941 *Monatsh. Chem.* **74** 160
Krueger P J 1962 *Can. J. Chem.* **40** 2300
Mulliken R S 1955 *J. Chem. Phys.* **23** 1977
Murthy A S N and Rao C N R 1968 *Appl. Spectrosc. Rev.* **2** 69
Sharma S N and Dwivedi C P D 1976 *Indian J. Phys.* **50** 25
Shukla A R, Pathak C M, Dongre N G, Asthana B P and Shamir J 1986 *J. Raman Spectrosc.* **17** 299
Varsanyi G 1974 *Assignments for vibrational spectra of seven hundred benzene derivatives* (New York: John Wiley and Sons) vol. 1
Wexler A S 1967 *Appl. Spectrosc. Rev.* **1** 29
Wilson E B 1934 *Phys. Rev.* **45** 706

SCF perturbation calculations on metalloporphyrins

K K BHATTACHARJEE, J SUBRAMANIAN*, D P SANTRY** and J-H FUHRHOP†

Department of Chemistry, North-Eastern Hill University, Shillong 793 003, India
** Department of Chemistry, McMaster University, Hamilton, Ontario, Canada L8S 4M1
† Institut für Organische Chemie FB21 WE02, Freie Universität Berlin, 3 Takustrasse, 1000 Berlin 33, Federal Republic of Germany

MS received 6 June 1986; revised 16 October 1986

Abstract. The influence of metal ion on the oxidation and ionisation potentials of metalloporphyrins is investigated by the simple electrostatic model using SCF perturbation theory. The zero order wavefunctions are obtained from PPP and CNDO/2 methods. The wide variations in redox potentials with metal and the relative insensitivity of the optical transitions with metal are very well accounted for by the perturbation approach.

Keywords. SCF perturbation calculations; metalloporphyrins; CNDO perturbation calculations.

1. Introduction

Metalloporphyrins occur as chromophores in many biological systems. Hence a considerable number of studies have been made on the various physicochemical aspects of these systems (Smith 1975; Dolphin 1978). A number of molecular orbital calculations have been made on metalloporphyrins and related systems in varying levels of sophistication (Maggiora 1973; Gouterman 1978; Almlöf 1974; Maggiora and Weiman 1974; Sangler *et al* 1977; Case and Karplus 1977; Petke *et al* 1978; Christofferson 1979; Ohno 1979; Dedieu *et al* 1982; Edward and Zerner 1983; Rawlings *et al* 1984).[§] It has been noticed that with a few exceptions, in the metalloporphyrins the redox potentials are very sensitive to the nature of the metal ion but the visible electronic spectra are relatively independent (Fuhrhop *et al* 1973; Felton 1978; Davis 1978) of the metal ion. This behaviour has been qualitatively interpreted as arising from the coulombic perturbation of the π electron energy levels of the porphyrin ligand by the metal ion (Felton 1978; Davis 1978). Recent results of photoelectron spectroscopic studies on metalloporphyrins have also been interpreted on this basis (Kitagawa *et al* 1979). An attempt has been made in this work to investigate this model quantitatively. The metal ion is assumed to perturb the energy levels of the porphyrin ligand. A simple perturbation of the type $H' = (-Ze^2/r)$ is used where Ze is the effective nuclear charge on the metal ion. We have used the SCF perturbation theory to obtain the first order changes in the energy levels arising out of the coulombic perturbation (Stevens *et al* 1963; Geralt and Mills 1968; Pople *et al* 1968; Santry 1974, 1976). The wave function for the

---

* To whom all correspondence should be addressed

§ Only a few representative references are given. The literature cited is by no means exhaustive.

by the CNDO/2 method. The results are encouraging and we obtained good correlations between the oxidation potential of the π-ligand and the charges on the metal ion.

2. Methods of calculation

The SCF perturbation theory is well-documented (Santry 1974, 1976), and only the salient features are presented here for the sake of continuity. This method aims at calculating the first order corrections, namely $E^{(1)}$ and $W^{(1)}$ to the molecular orbital energy matrix and the total energy respectively, in the presence of a perturbation, $H^{(1)}$. The zeroth order Fock, overlap and coefficient matrices are given by $F^{(0)}$, $S^{(0)}$ and $C^{(0)}$. The corresponding matrices for the first order correction are respectively $F^{(1)}$, $S^{(1)}$ and $C^{(1)}$. Starting with Roothan's matrix equations,

$$FC = SCE \tag{1}$$

it is expanded in a perturbation series to first order. Our zeroth order functions are calculated in the ZDO framework and hence $S^{(1)}$ is ignored. The first order corrections to the m.o. energies are given by

$$E_i^{(1)} = \mathcal{F}_{ii} = \sum_{\mu}\sum_{\nu} C_{\mu i}^{(0)} F_{\mu\nu}^{(1)} C_{\nu i}^{(0)}, \tag{2}$$

where i, j, k etc. refer to the m.o. energy levels and μ, ν to the atomic orbitals. The corresponding coefficient matrix $C^{(1)}$ is given by

$$C^{(1)} = C^{(0)}A, \tag{3}$$

where the mixing matrix A is given by

$$A_{ik} = \mathcal{F}_{ik}/(E_k^{(0)} - E_i^{(0)}), \tag{4}$$

and

$$A_{ii} = 0.$$

The first order correction to the bond-order matrix is

$$P^{(1)} = 2\sum_{i}^{\text{occ}}\sum_{k}^{\text{vac}} A_{ki}\,(C_{\mu i}^{(0)} C_{\nu k}^{(0)} + C_{\mu k}^{(0)} C_{\nu i}^{(0)}) \tag{5}$$

Only those A_{ki} terms are involved for which the i belong to the occupied levels and the k to the vacant ones. The first order correction to the total energy is given by

$$W^{(1)} = (\tfrac{1}{2}) \sum_{\mu}\sum_{\nu} \{ P_{\mu\nu}^{(0)}\,(H_{\mu\nu}^{(1)} + F_{\mu\nu}^{(1)}) + P_{\mu\nu}^{(1)} H_{\mu\nu}^{(0)} \}. \tag{6}$$

given by Santry (1974). $W^{(1)}$ is calculated by an iterative procedure using the dependence of $F^{(1)}$ on $P^{(1)}$. In the first cycle of calculations, $F^{(1)}$ is set equal to $H^{(1)}$. The $H^{(1)}$ matrix is given by

$$H^{(1)}_{\mu\mu} = (-Z/R_\mu) \text{ in au,} \tag{7}$$

and

$$H^{(1)}_{\mu\nu} = 0 (\text{for } \mu \neq \nu) \tag{8}$$

where R_μ is the distance of the atomic orbital μ from the central metal ion. The zeroth order functions have been obtained for porphin dianion with D_{4h} symmetry. The geometry used is that of Zerner and Gouterman (1966). In the PPP method, the elements of the $F^{(1)}$ matrix are given by

$$\begin{aligned} F^{(1)}_{\mu\mu} &= H^{(1)}_{\mu\mu} + (\tfrac{1}{2})\, P^{(1)}_{\mu\mu}\, \gamma_{\mu\mu} + \sum_{\mu \neq \nu} P^{(1)}_{\nu\nu}\, \gamma_{\mu\nu}, \\ F^{(1)}_{\mu\nu} &= -(\tfrac{1}{2})\, P^{(1)}_{\mu\nu}\, \gamma_{\mu\nu}, \end{aligned} \tag{9}$$

and the corresponding elements in the CNDO/2 formalism are

$$\begin{aligned} F^{(1)}_{\mu\mu} &= H^{(1)}_{\mu\mu} + (\tfrac{1}{2})\, P^{(1)}_{\mu\mu}\, \gamma_{AA} + \sum_{B} Q^{(1)}_{B}\, \gamma_{AB}, \\ F^{(1)}_{\mu\nu} &= -(\tfrac{1}{2})\, P^{(1)}_{\mu\nu}\, \gamma_{AB}. \end{aligned} \tag{10}$$

3. Results and discussion

The aim of the SCF perturbation calculations presented here is to understand the effect of a residual positive charge on the π electron energy levels of a porphyrin. The residual charge on the metal arises out of the ionic character of the sigma bonds formed by the metal ion and the nitrogen atoms. Thus, in a crude model, the metalloporphyrin π levels are considered to arise out of the perturbation of the π levels of the dianion by the residual charge on the metal. This approach requires a reliable set of energy levels and wave functions for the π electrons in the porphyrin dianion. We have taken the results of CNDO/2 calculation on porphyrin dianion as the starting point (Maggiora 1973). The changes in the π m.o. energies (2) and the total energy of the system (6) as functions of perturbing charge were calculated (table 1). The total orbital energies, $E_i^{(0)} + E_i^{(1)}$ as functions of perturbing charges are presented in figure 1 for the HOMO and LUMO levels. Similar calculations were done using the PPP wavefunctions. In the PPP formalism, it is not possible to distinguish explicitly between a porphyrin dianion and a metalloporphyrin. In choosing the "standard parameters" for PPP-calculations on a metalloporphyrin,

Table 1. Correlation of oxidation potentials[a] ($E_{1/2}^{OX}$ values), ionisation potentials and the charges obtained from the SCF perturbation calculations. (The experimental data are for metal octaethyl porphyrins, OEP).

System	Charge (PPP)	Charge (CNDO/2)	$E_{1/2}^{(OX)}$ (volts) (vs SCE)	*IP* (eV)
Mg(II)OEP	1·30	1·52	0·54	6·21
Zn(II)OEP	1·31	1·56	0·63	6·26
Ni(II)OEP	1·32	1·58	0·73	6·32
H_2OEP	1·34	1·59	0·81	6·36
Ag(II)OEP	1·38	1·63	1·10	6·53
Al(III)OEP(OH)	1·36	1·61	0·95	6·44[b]
Sn(IV)OEP$(OH)_2$	1·43	1·68	1·40	6·70[b]

[a] $E_{1/2}^{(OX)}$ values are taken from reference (Fuhrhop *et al* 1973).
[b] *IP* values are estimated using (11); other values are experimental data from Kitagawa *et al* 1979).

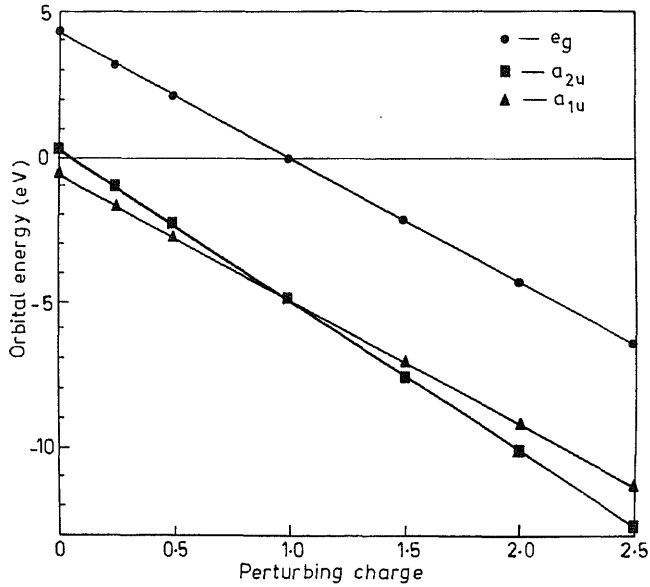

Figure 1. Energies of HOMO and LUMO levels of porphyrin dianion obtained by SCF perturbation method using PPP wavefunctions.

the orbital energy, $E_i^{(0)} + E_i^{(1)}$ vs the perturbing charge using the PPP-data is presented in figure 2. The results of the perturbation calculations indicate (i) that the outermost energy levels, $a_{1u}(\pi)$, $a_{2u}(\pi)$ and $e_g(\pi)$ are affected to different extents by the point charge perturbation; (ii) a_{1u} and a_{2u} levels cross in the neighbourhood of a perturbing charge equal to +1 unit. The crossing of a_{1u} and a_{2u} levels has an experimental basis. It has been noticed that the visible electronic

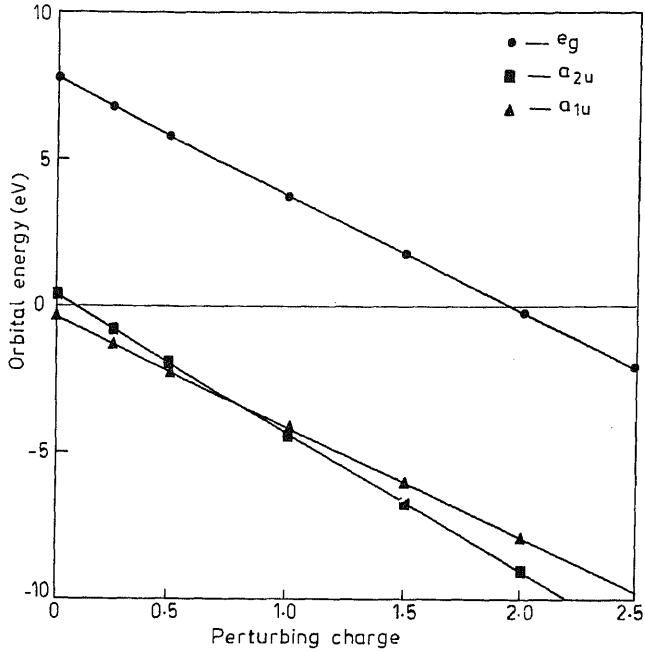

Figure 2. Energies of HOMO and LUMO levels of porphyrin dianion obtained by SCF perturbation method using CNDO/2 wavefunctions.

(a_{1u} and a_{2u}) (Dolphin *et al* 1971; Hanson *et al* 1981). The presence of the counter-ion changes the residual charge on the metal ion and the electrostatic effect explains the situation.

The energy levels obtained from above perturbation calculations may be correlated with ionisation potentials and redox potentials (Kitigawa *et al* 1979) have observed a linear correlation of the experimental ionisation potentials and oxidation potentials of metallo-octaethyl porphyrins. Hence we have fitted the available ionisation potential values of metallo-octaethyl porphyrins with their corresponding $E_{1/2}^{(OX)}$ values as follows:

$$IP\ (\text{eV}) = 5{\cdot}896 + 0{\cdot}5766\ E_{1/2}^{(OX)}, \tag{11}$$

with a standard deviation of 0·036 eV and linear correlation coefficient of 0·922.

From the ionisation potential values [experimental or estimated according to (11)], using Koopman's theorem we have obtained the charges on the metal ions in various metalloporphyrins, using figures 1 and 2. As pointed out earlier, these charges may be considered as residual charges on the metal ion. A value of 1·34 (PPP) and 1·5 (CNDO/2) for Mg leads to an ionic character of 65% to 75% in the Mg-N σ bond. On the basis of electronegativity difference between Mg and N we expect an ionic character of 55%. Hence these numbers are not unreasonable. We

ese calculations is that from Mg(II) to Sn(IV) porphyrins the range of the residual harges is only 0·13 to 0·16 eV. This small range will lead only to marginal ifferences in the energy gaps between the occupied and the unoccupied π m.o. evels. Hence one does not expect much dependence of the electronic spectral ransition energies on the metal in the metalloporphyrins. On the other hand, this mall range of residual charge leads to an amplified range of oxidation potentials 0·54 V – 1·40 V vs SCE).

The electrostatic model, to a limited extent, does explain the observed trends in ne electronic spectra and oxidation potentials of metalloporphyrins.

Acknowledgements

The authors are thankful to the staff of the Regional Computer Centre, Jadavpur, or their cooperation in the computations. One of the authors (JS) wishes to cknowledge the financial support from the Council of Scientific and Industrial Research, New Delhi and the Department of Atomic Energy, for the computational work.

References

Almlöf J 1974 *Int. J. Quantum Chem.* **8** 915
Case D A and Karplus M 1977 *J. Am. Chem. Soc.* **99** 6182
Christofferson R E 1979 *Int. J. Quantum Chem.* **16** 573
Davis D G 1978 in *Porphyrins* (ed.) D Dolphin (New York: Academic Press) vol. 5, p. 127
Dedieu A, Rohmer M and Veillard A 1982 *Adv. Quantum Chem.* **16** 43
Dolphin D (ed.) 1978 in *Porphyrins* (New York: Academic Press) vol. 1–7
Dolphin D, Forman A, Borg D C, Fajer J and Felton R H 1971 *Proc. Natl. Acad. Sci. USA*, **68** 614
Edward W D and Zerner M C 1983 *Int. J. Quantum Chem.* **23** 1407
Felton R H F 1978 in *Porphyrins* (ed.) D Dolphin (New York: Academic Press) vol. 5
Fuhrhop J H, Kadish K M and Davis D G 1973 *J. Am. Chem. Soc.* **91** 5140
Geralt J Mills I M 1968 *J. Chem. Phys.* **49** 1719
Gouterman M 1978 in *Porphyrins* (ed.) D Dolphin (New York: Academic Press) vol. 3, pp 1–156
Hanson L K, Chang C K, Davis M S and Fajer J 1981 *J. Am. Chem. Soc.* **103** 663
Kitagawa S, Morishima I, Yonezawa J and Sato N 1979 *Inorg. Chem.* **18** 1345
Maggiora G M 1973 *J. Am. Chem. Soc.* **95** 6555
Maggiora G M and Weiman L J 1974 *Int. J. Quantum Chem., Quantum Biology Symp.* **1** 179
Ohno K 1979 in *Horizons of quantum chemistry* (eds.) K Fukui and B Pullman (Dordrecht: Reidel) p. 245
Petke J D, Maggiora G M, Shipman L L and Christofferson R E 1978 *J. Mol. Spectrosc.* **71** 64
Pople J A, Mciverjr J W and Ostlund N S 1968 *J. Chem. Phys.* **49** 2960, 2965
Rawlings D C, Davidson E R and Gouterman M 1984 *Int. J. Quantum Chem.* **26** 237
Sangler D, Maggiora G M, Shipman L L and Christofferson R E 1977 *J. Am. Chem. Soc.* **99** 7470, 7487
Santry D P 1974 in *Electronic structure of polymers and molecular crystals* (eds.) J M Andre and J Ladik (New York: Plenum) p. 479
Santry D P 1976 *Theor. Chim. Acta* **42** 67
Smith K M (ed.) 1975 in *Porphyrins and metalloporphyrins* (Amsterdam: Elsevier)
Stevens R H, Pitzer R M and Lipscomb W N 1963 *J. Chem. Phys.* **38** 550

Proc. Indian Acad. Sci (Chem. Sci.), Vol. 97, Nos 5&6, December 1986, pp. 607–615.
© Printed in India.

Exchange studies of 5-sulphosalicylic acid in amberlite IRA 401 Cl anion exchange resin

NOOMAN A KHALAF and G S NATARAJAN*
Laxminarayan Institute of Technology, Nagpur University, Nagpur 440 010, India

MS received 10 November 1983; revised 6 August 1986

Abstract. Exchange studies of 5-sulphosalicylic acid in Amberlite IRA 401 Cl anion exchange resin have been carried out at 25°C in a stirred vessel. The exchange rates have been interpreted on the basis of a simple diffusion model.

Keywords. Ion exchange; kinetics; diffusion; anion exchange resin; exchange rate studies; 5-sulphosalicylic acid.

1. Introduction

Interest in ion exchange kinetics has grown rapidly in recent years. Knowledge of rate constants, mass transfer coefficients or diffusion coefficients, derived from rate investigations will be extremely useful in the design of ion exchange columns. Several authors have used kinetic models (Thomas 1944) in explaining ion exchange rates and some have used the mass transfer coefficient (Guggenheim 1944; Barrer 1948; Gregor *et al* 1955; Bonner *et al* 1956) concept in relating the mass transfer coefficient to the physical properties of the system. Glueckauf and Coates (1947) used a slightly modified approach where it is assumed that the rate at any time is proportional to the distance the system is from equilibrium. Smith and Dranoff (1964) have clearly brought out the merits and demerits of various approaches to the treatment of ion exchange kinetic data and have said that fairly reliable and accurate analysis of such data could be easily obtained by the simplest approach.

In the present work the exchange of 5-sulphosalicylic acid in Amberlite IRA 401 Cl resin has been studied over a range of concentrations. The data have been interpreted by a simple model.

2. Experimental

All exchange experiments were carried out in a 500 ml Corning beaker whose base

measured by a stroboscope. This speed was chosen after it was found that beyond this speed there was no effect on the rate of exchange when the speed of the stirrer was increased. Each experimental run utilised 200 ml of solution at a definite concentration of 5-sulphosalicylic acid. The sulphosalicylic acid was of BDH AR grade and was estimated by potentiometric titration against standard alkali. Exchange experiments were carried out with 0·5 g of resin Amberlite IRA 401 Cl (25–60 mesh, BSS, exchange capacity 3·6 m equivalents/g), carefully weighed and allowed to swell overnight by immersion in water. The resin was filtered and dried with filter paper before each experiment and added to the experimental solution maintained at 25° ± 1°C. Variation of the conductance of the solution was monitored by a conductivity cell (cell constant 0·1) whose resistance was measured by a Leeds and Northrup Bridge Cat. 7645 through a Null detector (Ajco-Poona). Figure 1 represents plots of conductance of sulphosalicylic acid solution with time for several concentrations. The data are represented in table 1.

3. Discussion

The results in figure 1 indicate the variation of conductance of the experimental solutions with time. The plot of log concentration of sulphosalicylic acid remaining in solution with time is found to be fairly linear after about 2 minutes of the run indicating that the exchange follows an exponential trend.

The hydroxyl group in the sulphosalicylic acid is expected to remain ionised in solution to a small extent in view of its low dissociation constant ($32{\cdot}3 \times 10^{-4}$ at 25°C). It is therefore to be expected that the anion of the acid will exchange with

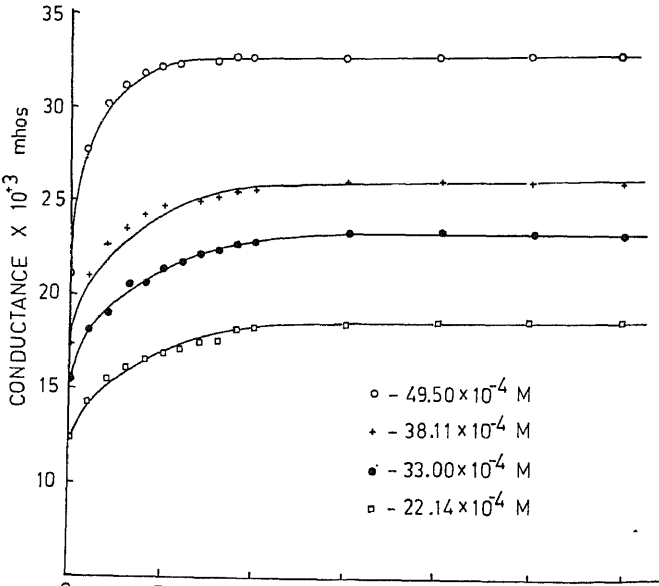

Table 1. Exchange rate data of 5-sulphosalicylic acid in Amberlite IRA 401 Cl at 25°C at various concentrations of sulphosalicylic acid.

Time	$49{\cdot}5\times10^{-4}$ M				$38{\cdot}11\times10^{-4}$ M				$33{\cdot}0\times10^{-4}$ M				$22{\cdot}14\times10^{-4}$ M			
(min)	$A\times10^{+3}$	$B\times10^{+4}$	$C\times10^{+4}$	D	$A\times10^{+3}$	$B\times10^{+4}$	$C\times10^{+4}$	D	$A\times10^{+3}$	$B\times10^{+4}$	$C\times10^{+4}$	D	$A\times10^{+3}$	$B\times10^{+4}$	$C\times10^{+4}$	D
0	24·00	49·50	26·97		17·40	38·11	22·47		15·40	33·00	20·27		12·40	22·14	15·09	
1	27·70	35·40	15·18	0·883	20·80	25·67	12·04	0·784	17·99	23·92	12·33	0·578	14·17	16·38	10·09	0·421
2	29·90	28·45	10·78	1·639	22·50	19·50	8·27	1·348	18·90	20·29	9·83	0·861	15·30	11·95	6·55	0·886
3	30·90	25·50	9·43	2·064	23·49	17·55	7·05	1·629	20·50	14·18	6·60	1·409	16·00	9·95	5·27	1·129
4	31·60	23·50	8·40	2·580	24·20	15·24	5·86	2·009	20·60	14·15	6·17	1·511	16·50	7·74	3·95	1·458
5	32·08	22·00	7·67	3·236	24·70	14·22	5·30	2·250	21·40	13·20	5·38	1·734	16·89	7·08	3·47	1·611
6	32·10	21·75	7·55	3·400	24·75	13·62	4·98	2·428	21·60	11·55	4·63	1·999	17·00	6·53	3·12	1·737
7	32·18	21·60	7·50	3·478	25·00	13·25	4·82	2·527	22·00	10·23	4·03	2·285	17·39	5·53	2·59	1·973
8	32·30	20·50	7·44	3·580	25·10	12·75	4·55	2·722	22·20	9·73	3·76	2·443	17·40	5·42	2·47	2·035
9	32·56	20·50	7·04	4·830	25·50	11·13	4·00	3·294	22·59	8·25	3·13	2·949	18·00	3·66	1·65	2·601
10	32·59	20·40	6·94	5·810	25·60	10·93	3·89	3·463	23·70	7·93	3·00	3·105	18·20	3·33	1·46	2·786
15	32·59	20·40	6·94	–	26·00	9·53	3·32	–	23·10	6·64	2·44	–	18·60	1·66	1·44	–
20	32·65	20·30	6·88	–	26·00	9·43	3·28	–	23·30	5·94	2·19	–	18·70	1·33	0·57	–
30	32·65	20·30	6·88	–	26·00	9·43	3·28	–	23·30	5·94	2·19	–	18·70	1·33	0·57	–

A – Conductance of solution, mhos; B – Total concentration of sulphosalicylic acid from standard graph moles/litre; C – Calculated concentration of ionised form of sulphosalicylic acid g ions/litre; D – ln $(C_{A_0}-C_{A_e})/(C_{A_t}-C_{A_e})$, C_{A_e} in each case is estimated from figure 1.

two chloride ions of the resin, as per the mechanism,

$$2R^+Cl^- + (SA^{2-})H^{2+} \rightarrow 2R^+(SA^{2-}) + 2H^+ + 2Cl^- \quad (1)$$

where (SA^{2-}) represents the anion of the sulphosalicylic acid, less both dissociable protons. This type of exchange was verified by chloride estimation of the solution at the end of the experiment. In order to follow the exchange after equation (1), sulphosalicylic acid of the same concentration as that used in the experiment (mole/lit) was used in preparing various mixtures of solutions by volume, with hydrochloric acid of double the strength as of the weak acid. This is because one mole of 5-sulphosalicylic acid is replaced in solution by two moles of HCl. A plot of conductance of these mixtures against their composition served as a standard curve for each experimental run from which the composition of the sulphosalicylic acid and chloride ion present at a given conductance value could be estimated. For a given value of conductance in figure 1 it was possible therefore to estimate the amount of chloride ion and sulphosalicylic acid present in solution at any given instant (cf. column B, in table 1). With the help of the dissociation constant of the OH^- group of the acid it was possible to calculate the concentration of the anion (SA^{2-}) (cf. column C, table 1).

The following simple approach could then be utilised to explain results in figure 1.

If the total concentration of exchangeable ions, i.e., (SA^{2-}) in solution is C_{A_0}, and C_{A_e}, the concentration at equilibrium, then $x_A = C_{A_e}/C_{A_0}$. Similarly if C_{A_s} represents the concentration of exchanged ions present on the resin per ml and Q_s the total concentration of exchangeable ions that could be present on the resin then $y_A = C_{A_s}/Q_s$.

From the experiments in the present case with 5-sulphosalicylic acid it can be inferred from table 1 that the corresponding value of x_A and y_A at the end of the kinetic run lie on an isotherm which is fairly linear (Coulson and Richardson 1971; Perry and Chilton 1973).

The problem is therefore simplified in the present work and the following ideas are explored. This is based on the following assumptions:

(i) it is assumed that the system has achieved a steady state over short intervals of time;
(ii) an equilibrium exists at the solid-liquid interface;
(iii) the resin is treated as a homogeneous medium;
(iv) the resin is free from the exchanging ions at time, $t = 0$;
(v) the linear driving force approximation with a correction factor of unity for solid phase diffusivity is assumed;
(vi) the experimental data is assumed to be independent of the speed of stirring;
(vii) the electrostatic forces and charge on the species are neglected;
(viii) the isotherm of y_A vs. x_A is linear.

The diagram in page 611 indicates the actual state of affairs at the resin surface-solution boundary.

Considering one cm^2 of the resin surface, then the rate of exchange reaction-

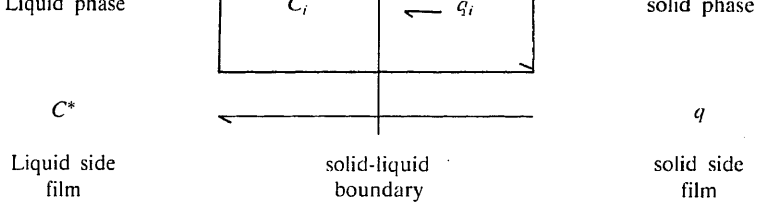

and k_S represent the liquid and solid mass transfer coefficients, respectively. C d C_i represent the concentrations of the species (SA^{2-}) in the bulk of the solution d at the surface of the resin respectively. Analogously, q_i and q represent the ncentrations of the same ion in the solid phase.

If Q represents the exchange capacity of the resin, then because of the fact that e equilibrium (1) lies on a fairly linear portion of an isotherm of y_A vs x_A one can ow that:

$$q_i/Q = p\,C_i/C_{A_0}, \tag{3}$$

ere p is a constant. Here y_A as defined earlier is equal to q_i/Q and x_A is equal to $/C_{A_0}$,C_{A_0} being the initial concentration of the species (SA^{2-}). For a given stem and at a given initial concentration of (SA^{2-}) in solution $Q\cdot P/C_{A_0}$ is constant d represented by α so that $q_i = \alpha C_i$.

From (2) it therefore follows that:

$$k_L C + k_S q = C_i(k_L + k_S\alpha). \tag{4}$$

ence,

$$C_i = (k_L C + k_S q)/(k_L + k_S\alpha). \tag{5}$$

e rate of exchange can now be rewritten as:

$$R = k_L\,[C - (k_L C + k_S q)/(k_L + k_S\alpha)], \tag{6}$$

ich on simplification gives

$$R = k_L\,[(k_S\alpha C - k_S q)/(k_L + k_S\alpha)]. \tag{7}$$

As depicted in the diagram, at any instant q will always be in equilibrium with a rresponding concentration value in the bulk, represented by C^*, so that

$$k_S q = k_S\alpha C^*.$$

therefore follows that

$$R = [k_L k_S\alpha(C - C^*)]/(k_L + k_S\alpha), \tag{8}$$

ich, on rearrangement becomes,

$$R = (C - C^*)/\left(\frac{1}{k_S\alpha} + \frac{1}{k_L}\right). \tag{9}$$

Unless $p \rightarrow \infty$ and hence $\alpha \rightarrow \infty$, k_L can have a value such that

$$k_L \gg k_S \alpha. \tag{10}$$

If we now assume that k_L is very much greater than $k_S\alpha$, then

$$R = k_S \alpha (C - C^*). \tag{11}$$

In analogy with the relation between q and C^* as mentioned above, one should expect a similar relation between C and q^* where q^* now represents the equilibrium value in the solid phase corresponding to C at any instant. It is therefore obvious, that

$$R = k_S (q^* - q). \tag{12}$$

The assumption $k_L \gg k_S \alpha$ would mean that

$$C_i = C,$$

and

$$q_i = q^*. \tag{13}$$

Using the definition, that the rate R is,

$$R = -\left(\frac{dc}{dt}\right) \frac{V \times (D/6)}{(w/d)} \tag{14}$$

(it is assumed that the resin particles are uniform spheres), then comparing (14) and (12) it follows that

$$-\left(\frac{dc}{dt}\right) = (6/D)(w/d)(k_S/V)(q^* - q). \tag{15}$$

At any instant of time one can show that

$$(C_{A_0} - C) V = (w/d) q.$$

Therefore

$$q^* - q = \alpha C - (C_{A_0} - C)(Vd/w) \tag{16}$$

At equilibrium i.e. when no more of the ionic species (SA^{2-}) are exchanged, then

$$q^* = q_e = q \text{ and } C = C_{A_e}.$$

Therefore

$$\alpha C_{A_e} = (C_{A_0} - C_{A_e})(Vd/w),$$

which leads to

$$\alpha = [(C_{A_0} - C_{A_e})/C_{A_e}](Vd/w). \tag{17}$$

Using this value of α in (16) and simplifying, it can be shown that

$$-\left(\frac{dc}{dt}\right) = (6/D)(k_S C_{A_0}/C_{A_e})(C - C_{A_e}). \quad (18)$$

ntegration of this equation between the limits 0 and t and noting that at $t = 0$, $= C_{A_0}$ and at $t = t$, $C = C_{A_t}$, leads to

$$\ln [(C_{A_0} - C_{A_e})/(C_{A_t} - C_{A_e})] = (6/D)(k_S C_{A_0}/C_{A_e})\ t. \quad (19)$$

other words a plot of

$\ln (C_{A_0} - C_{A_e})/(C_{A_t} - C_{A_e})$ vs time should be a straight line.

The values of C_{A_0}, C_{A_t} are all actual ionic concentrations present in solution, lculated as per standard procedure (Maron and Prutton 1967). Values of C_{A_t} were timated from experimental curves in figure 1.

A plot of $\ln (C_{A_0} - C_{A_e})/(C_{A_t} - C_{A_e})$ vs time is seen to be fairly linear (figure 2) ringing out the validity of (19). The slope of this plot is found to be

$$\text{slope} = (6/D)k_S(C_{A_0}/C_{A_e}).$$

nce D is 0·047 cm in the present case then for an initial sulphosalicylic acid oncentration of $22{\cdot}14 \times 10^{-4}$ M this slope has a value equal to 0·4166 leading to a alue of $k_S = 2{\cdot}05 \times 10^{-6}$ cm/sec. Since the slopes are all nearly the same as seen om figure 2, it can be inferred that the value of k_S is independent of the initial acid oncentrations. The value of the diffusion coefficient D_S calculated using the xpression

$$D_S = k_S D/10$$

orks out to $0{\cdot}964 \times 10^{-8}$ cm^2/sec suggesting that the order is as to be expected for rface diffusion.

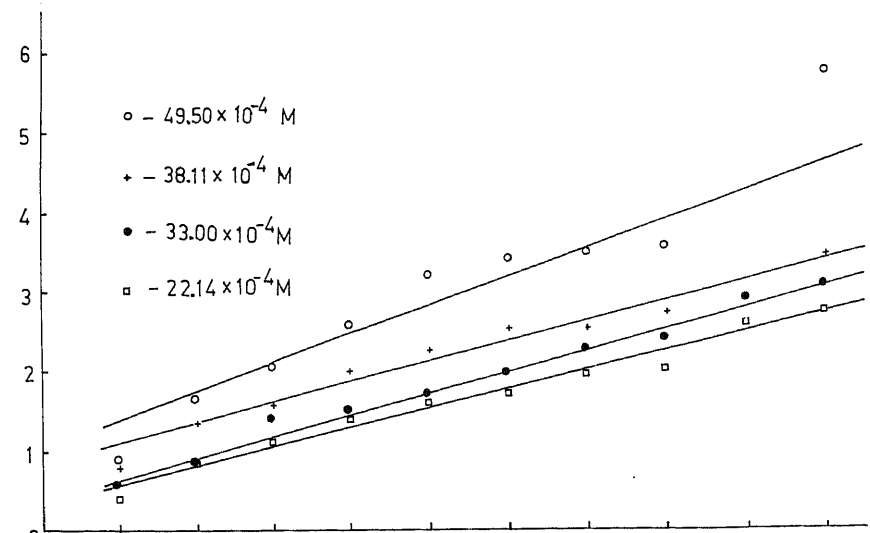

Further the value of α as calculated by the expression

$$\alpha = [(C_{A_0} - C_{A_e})/(C_{A_e})](Vd/w)$$

assuming a density of 1·1 is 1285. The assumption, $k_L \gg k_S\alpha$ would hence be valid, since $k_S\alpha = 0{\cdot}00263$, which is very small compared to the k_L values calculated from the slope at time $t = 0$ using the plot of C/C_0 vs t. This slope would give $k_L a_p$, where a_p is the outer surface area of resin particle per unit volume of particle free slurry (cm^{-1}) and a value of k_L as 0·025 was obtained in the present case.

4. Conclusion

In conclusion it can be inferred that a simple model based on the linear driving force approximation can be very well employed to explain the exchange of 5-sulphosalicylic acid anion on Amberlite IRA 401 (Cl) anion exchange resin. The diffusion coefficient value estimated in the present case justifies the assumption that the process is surface diffusion controlled.

List of symbols

C_{A_0} Initial concentration of the species (SA^{2-}) in g ions/ml;
C^* concentration of species (SA^{2-}) in equilibrium in bulk solution at any time, g ions/ml;
C concentration of the species (SA^{2-}) in the bulk of the solution (g ions/ml);
C_i concentration of the species (SA^{2-}) at the surface of the resin (g ions/ml);
C_{A_t} concentration of species (SA^{2-}) at any time, g ions/ml;
C_{A_e} concentration of species (SA^{2-}) at equilibrium, g ions/ml;
C_{A_s} concentration of exchanged ions present on the resin g ions/ml;
d density of resin particles, g/ml;
D average diameter of resin particles in cm;
D_s diffusion coefficient cm^2/sec.
k_L liquid side mass transfer coefficient, cm/sec;
k_S solid side mass transfer coefficient, cm/sec;
P constant;
Q exchange capacity of the resin in g ions/ml;
Q_s total concentration of exchangeable ions on the resin g ions/ml;
q concentration of species (SA^{2-}) on the resin at any time g ions/ml;
q^* concentration of species (SA^{2-}) on the resin at equilibrium in the solid phase, g ions/ml;
q_i concentration of species (SA^{2-}) on the surface of the resin g ions/ml;
R rate of exchange g ions of (SA^{2-}) transferred per cm^2 resin surface per unit time;
t time in minutes;
V volume of experimental solution in ml;

References

Barrer R M 1948 *Colliogue international sur les reactions dans l'et al solide* (Paris:)
Bonner O D, Holland V F and Smith L L 1956 *J. Phys. Chem.* **60** 1102
Coulson J M and Richardson I F 1971 *Chemical Engineering* vol. 3, p. 527
Glueckauf E and Coates J I 1947 *J. Chem. Soc.* 1315
Gregor H P, Belle J and Marcus R A 1955 *J. Am. Chem. Soc.* **77** 2713
Guggenheim E A 1944 *Proc. R. Soc. London* **A183** 203 213
Maron S H and Prutton C F 1967 *Principles of physical chemistry* 4th edn (London: Macmillan) p. 449
Perry R H and Chilton C H *Chemical engineer's handbook* 5th edn (Tokyo, New York: Kogakusha McGraw-Hill) pp. 16
Smith T G and Dranoff J S 1964 *Ind. Eng. Chem. Fundam.* **3(3)** 195
Thomas H C 1944 *J. Am. Chem. Soc.* **66** 1664.

© Printed in India.

Design and fabrication of an ultraviolet photoelectron spectrometer for the study of free molecules+

V JAYARAM and M S HEGDE*

Solid State and Structural Chemistry Unit, Indian Institute of Science, Bangalore 560 012, India

MS received 21 August 1986

Abstract. An ultraviolet photoelectron spectrometer for the study of free atoms and molecules has been designed and fabricated with indigeneous components. The spectrometer consists of a 100 mA HeI discharge lamp, 180° hemispherical electron energy analyser (127 mm mean dia) and electron multiplier ratemeter electron detection systems. The resolution of the spectrometer is 90 meV/and the intensity of N_2 (5σ) band is 10^5 c/sec. The sample inlet and the collision chamber can be heated to 500 K so that solids of low vapour pressure can be studied. Typical spectra of molecules recorded with the instrument are shown.

Keywords. UV photoelectron spectroscopy; electron states of molecules; free molecules.

1. Introduction

Ultraviolet photoelectron spectroscopy (UVPES) is an invaluable spectroscopic method for the study of electron states of atoms and molecules. The method involves photoionization of atoms or molecules from HeI (21·22 eV) or HeII (40·8 eV) UV radiation, the ejected photoelectrons being energy analysed. The process is given by:

$$M + h\nu \rightarrow M^+ + e, \tag{1}$$

where $h\nu$ is the energy of the photon beam and M stands for atom or molecule. Kinetic energy of the photoelectrons is given by the energy balance equation:

$$h\nu = E_{KE} + E_{BE} \tag{2}$$

where E_{KE} is the kinetic energy of the photoelectrons to be measured experimentally and knowing the photon energy $h\nu$, the binding energy of the photoelectron, E_{BE}, can be obtained. Turner *et al* (1970) were the first to develop this method and since then, a large number of molecules have been studied employing UVPES as can be seen from the reviews (Heilborner and Maier 1977; Rao *et al* 1979).

It was considered most worthwhile to fabricate a UV photoelectron spectrometer for the study of free molecules. A prototype was fabricated earlier in this laboratory (Hegde and Basu 1978). In this article we describe the design and fabrication of a photoelectron spectrometer in sufficient detail so that the information can be profitably used for the fabrication of the instrument.

2. Design and fabrication

The basic components of the spectrometer are: (a) a HeI UV lamp; (b) electron energy analyser; (c) photon-molecule collision chamber; (d) electron detection system; and (e) differential vacuum systems. Design and fabrication of each of the above systems are given below:

(a) *He lamp*: HeI radiation is obtained from a capillary discharge tube. The transition due to 2^1P-1^1S with 21·22 eV (584 Å) energy is the most intense resonance line in the helium discharge lamp which can be used as the photon source. The half-width of this line is less than 0·01 eV and therefore it is essentially monochromatic for this purpose. The wavelength of this radiation being in the far UV region, no optical window can be used. Therefore, the radiation should be obtained through a windowless capillary discharge tube. The cross-sectional view of the helium lamp and its mounting in the spectrometer chamber is shown in figure 1. The lamp consists of two aluminium electrodes connected by 1·5 mm ID, 6 mm OD, 40 mm long fused quartz capillary tube. The aluminium electrodes can be watercooled and are insulated using teflon insulators. The lamp is connected to an aluminium connector having the provision to pump out the helium gas. A brass capillary of 1 mm ID, 6 mm OD and 35 mm length is mounted on the aluminium connector through which the HeI radiation can be collimated to the collision chamber. The aluminium connector is mounted on a 30 cm dia aluminium flange of the spectrometer chamber. Pure helium gas is let in through a precision needle valve and a discharge can be struck between the electrodes by applying 3 kV, after which the pressure of helium gas is reduced and up to 100 mA discharge current obtained at 500 V. The discharge current is controlled through a potentiometer. The pressure at which discharge is maintained is about 1 torr.

The lamp should be assembled such that there should be clearance of 1 mm throughout the length of the lamp (20 cm), so that the scattering of the HeI radiation by the walls of the capillary is reduced. In order to maintain 1 torr pressure in the discharge zone, a constriction is provided through a stainless steel piece of 1 mm ID before the helium pumping line. Helium gas needs to be pumped out to minimize self absorption of the resonance radiation and also to minimise flooding of helium gas in the collision as well as the spectrometer chambers. These details can be found in figure 1.

(b) *Electrostatic electron energy analyser*: For high resolution, a 180° hemispherical sector analyser is employed here. If r_1 is the radius of the outer surface of the inner sector and r_2 is the radius of the inner surface of the outer sector, the electrons of E_{KE} energy get collimated when voltage across the analyser, V_p, is applied such that the beam enters at zero potential at the slit and is collected at zero potential. For this, the outer hemisphere is connected to $-V_p/2$ and the inner to $+V_p/2$. The relation between the kinetic energy of the photoelectrons and V_p is given by the equation

$$E_{KE} = eVp\,[(1/r_1) - (1/r_2)]. \tag{3}$$

The resolution of this analyser is given by

$$(\Delta E/E_{KE}) = (S/2r_0), \tag{4}$$

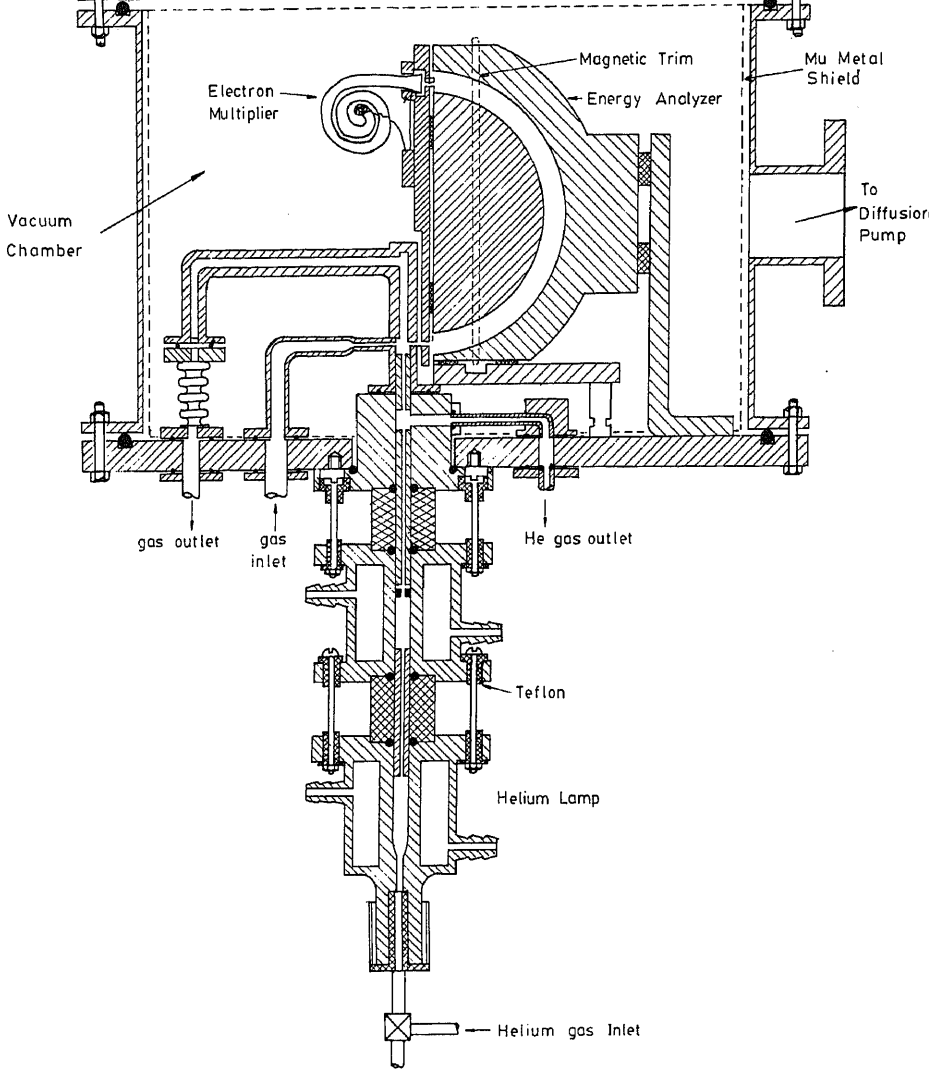

Figure 1. Cross-sectional view of the UV photoelectron spectrometer.

where $r_0 = (r_1 + r_2)/2$ and S is the slit width. The binding energy of the valence electrons in molecules vary from 7 to 20 eV, and thus, kinetic energy varies from 15·22 to 2·22 eV. Taking E_{KE} of about 10 eV and a convenient slit width of 1 mm dia, r_0 can be decided depending upon what resolution we need. Generally, ΔE of 70 to 100 meV is sufficient for most studies. Thus, when slit diameter $S_0 = 1$ mm, $\Delta E = 0{\cdot}07$ eV and $E = 10$ eV, r_0 required is 71 mm for (4) to be satisfied. It is

convenient to have a sweeping voltage of 1–10 V, and thus, hemispherical sectors of r_1 and r_2 equal to 64 and 76 mm were chosen, which meet all the above criteria. Details on the electrostatic analyser can be found in Seviere (1972).

Analyser sectors were fabricated from extruded aluminium rods. The hemispherical sectors were machined on a HMT lathe using a radial cutter. The accuracy of the surface is within ± 0·025 mm. The inner as well as the outer hemispheres are mounted on an aluminium plate wherein 1 mm dia inlet and outlet slits are provided at 180°. The analyser pieces and the plate were coated with gold by the vacuum deposition method in a vacuum system having a planetary rotation facility at the Hind High Vacuum Co, Bangalore. The inner and the outer hemisphere and the plate are insulated with teflon washers. The hemispheres are aligned within ± 0·05 mm with reference to r_0. The cross-sectional view of the analyser is shown in figure 1. Around the outer hemisphere, a magnetic trim coil of only one turn is provided to fine tune the signal. The mechanical mounting arrangement can be seen in figure 1.

(c) *Collision chamber*: A 4 mm diameter stainless steel tube collinear with the helium lamp acts as the collision chamber. A sample inlet tube with separate pumping facility is connected to the collision chamber. An orifice of 1·5 mm diameter acts as an outlet of photoelectrons from the collision chamber. The direction of photoelectrons taken from the collision chamber is perpendicular to the photon beam direction. The distance between the orifice and the electron inlet slit to the analyser is kept to a minimum of 3 mm so that the maximum solid angle is available to enable a higher number of photoelectrons to enter the inlet slit of the analyser. Also, the distance between the photon source and the electron outlet orifice is kept to a minimum so that the production of photoelectrons is maximum.

The mean free path, λ, of the photoelectrons is equal to $1/n\sigma$ where n is the number of molecules per cm^3 and σ is the photoionization cross-section (McDaniel 1964). For most molecules, σ is of the order of 10^{-16} cm^2 and taking the value of the number of molecules at 1 torr sample pressure, λ obtained is about 3·5 cm. This is about double the distance an electron has to travel before leaving the collision chamber. This means that photoelectrons ejected do not collide with the molecules before they leave the collision chamber. This is how the collision chamber dimension has been decided. If the vapour pressure is lower than 1 torr, the mean free path is even longer.

Sample inlet tubes can be heated to 500 K and thus, solids and liquids having lower vapour pressure can be studied in this instrument. The mounting of a gas inlet system and the collision chamber is also shown in figure 1.

(d) *Electron detection*: Since the number of photoelectrons obtained after the analyser stage is about 10^3–10^5 electrons/sec, an electron multiplier is used for amplification and detection. Channel electron multiplier made by Mullard (B419BL) is used in this instrument. This is the only component imported from

the ratemeter for further amplification, pulse shaping, counter and finally to the recorder. Block diagram of the ratemeter is given in figure 2.

An AMPTEK A101 PAD charge sensitive preamplifier and discriminator is used for initial amplification and pulse shaping. This amplifier is capable of sensing a nominal threshold referred to the input of 0·16 picocoulomb charge. This is equivalent to 10^6 electrons. Input charge threshold can be varied by the addition of a variable resistance from 0·16 picocoulombs to 10 picocoulombs. Output pulse width can be varied from 220 n sec to 800 n sec. Output of the amplifier can be interfaced directly with CMOS or TTL. In this ratemeter, the output pulse is given to a decade counter. If the frequency of pulse is high, we can select divide by 10 or 100 so that the number of charge pulses can be counted accurately. Output of the counter is given to the monostable for a fixed pulse width of 30 microseconds of about 4 V. A voltage translator changes the output of the monostable to a fixed 12 V pulse. These incoming voltage pulses are converted to analogue voltage using a frequency to voltage converter. The DC output voltage is given to the buffer amplifier and to the y-axis of an x-y recorder. Some of these details are given in figure 2.

(e) *Differential vacuum system*: A three-stage differential vacuum system is required in this instrument. The main vacuum system consists of a 10 cm oil diffusion pump with a liquid nitrogen trap. The spectrometer chamber made of SS sheet with aluminium flanges of 30 cm diameter can be pumped to 10^{-6} torr. The helium gas is pumped by a separate pumping line with a 100 l/min rotary pump and the sample inlet-outlet system is pumped by a 10 cm dia oil diffusion pump. The diameters of the HeI photon source and the electron outlet orifice are adjusted such that during the experiment, helium discharge can be maintained at 1 torr, the collision chamber at 1 torr, and the spectrometer chamber better than 10^{-5} torr.

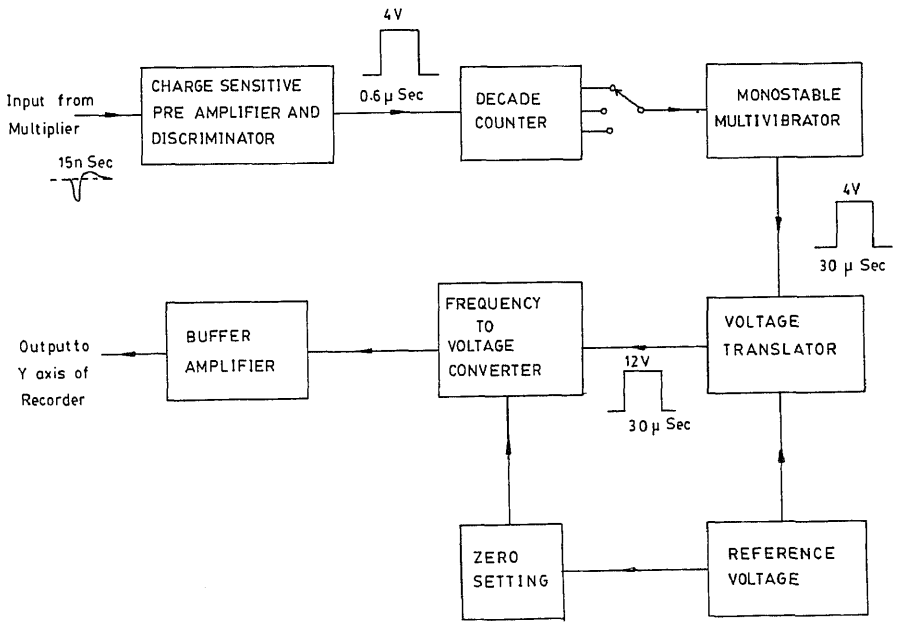

The spectrometer chamber is shielded from the earth's magnetic field by a 0·5 mm thick μ-metal sheet. This is indicated in figure 1.

3. Operation of the UV photoelectron spectrometer

The system is first pumped to 10^{-6} torr. The helium vacuum line as well as the sample inlet vacuum line are also evacuated. The electrical connections to the helium lamp, analyser and the electron detection probe are made as shown in figure 3. In addition, connections to the heating line, the sample inlet and the magnetic trim provided around the outer hemisphere of the analyser have to be made. This is also shown in figure 3. The electrical connections are taken through a ceramic vacuum feed through made by ECIL, Hyderabad.

After initiating He discharge, the pressure is adjusted to get a 100 mA discharge current. The spectrum sweeping circuit, called analyser control, consists of a magnetic trim power supply and a programmable ramp generator. The ramp voltage applied across the hemispherical sector can be programmed such that

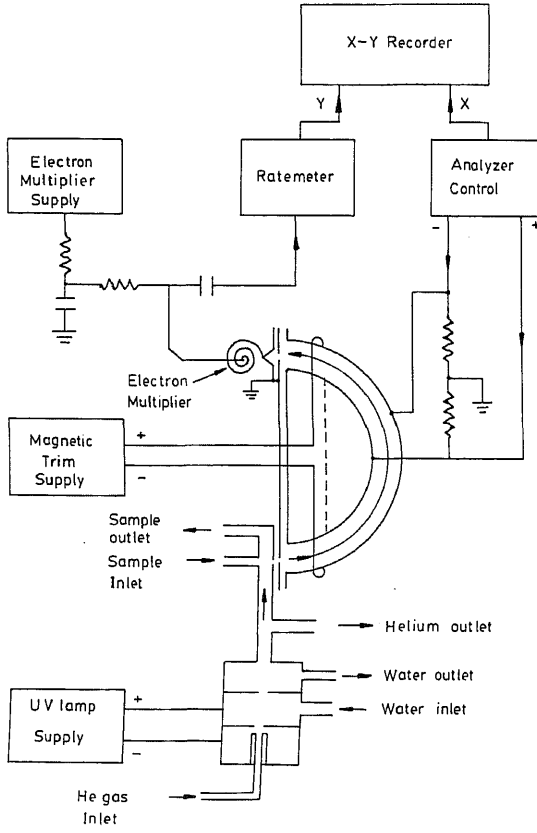

Figure 3. Electronic control in the spectrometer.

± 15 V and other parts of the circuit are designed using OP Amps. The analyser control block diagram is shown in figure 4. Put on the ratemeter and apply about 1·9 – 2 KV to the multiplier. The background count in the ratemeter should be less than 10^2 c/sec when the helium lamp is on. If not, ground the body properly so that the background signal is reduced.

Helium is known to have two autoionization states with electronic configurations $1s^1 2s^1$ and $1s^0 2s^2$. In the discharge lamp, the population of these states is sufficiently large and they get autoionized to give electrons of kinetic energy 19·64 eV. Thus, at this kinetic energy (equivalent to 24·6 – 19·64 ≡ 4·96 eV binding energy), an electron peak can be obtained with about 3×10^3 c/sec intensity. The scanning voltage to the analyser should be varied such that this peak is detected. Maximise this signal by varying helium pressure, magnetic trim supply and electron multiplier voltage. Then air can be leaked in through a fine leak value. Look for N_2 and O_2 photoelectrons which are well documented (Turner *et al* 1970) and calibrate the spectrometer. Then the vapour or gas under study can be leaked in and photoelectron spectra can be taken. A photograph of the photoelectron spectrometer is given in figure 5.

4. Results and discussions

The photoelectron spectrum of N_2 gas taken in this spectrometer is shown in figure 6. 5σ, 1π and 4σ bands of N_2 molecule are well recorded. The vibrational fine structure of 1π band corresponding to N_2^+ is clearly resolved. The FWHM of each of the photolines is about 90 meV which is close to the expected value with the design parameters of slit width and the analyser sizes chosen here. The electron counts obtained are in the 10^4 to 10^5 range for the N_2 signal and this is a sufficiently good performance for recording photoelectron spectra of molecules.

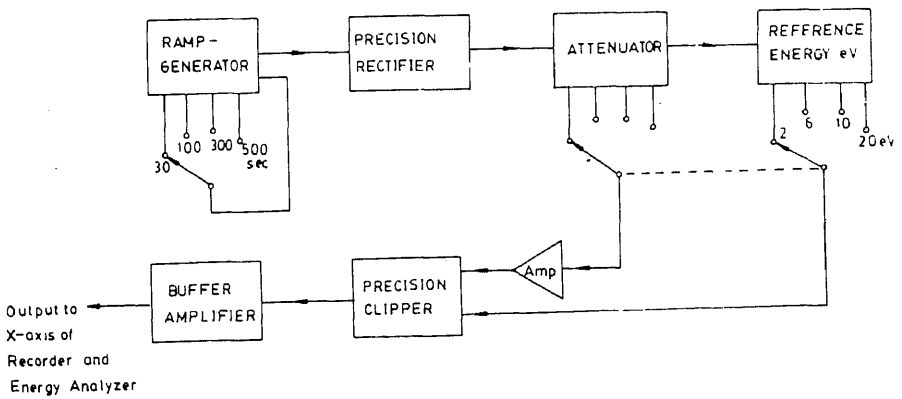

Figure 4. Block diagram of the analyser control.

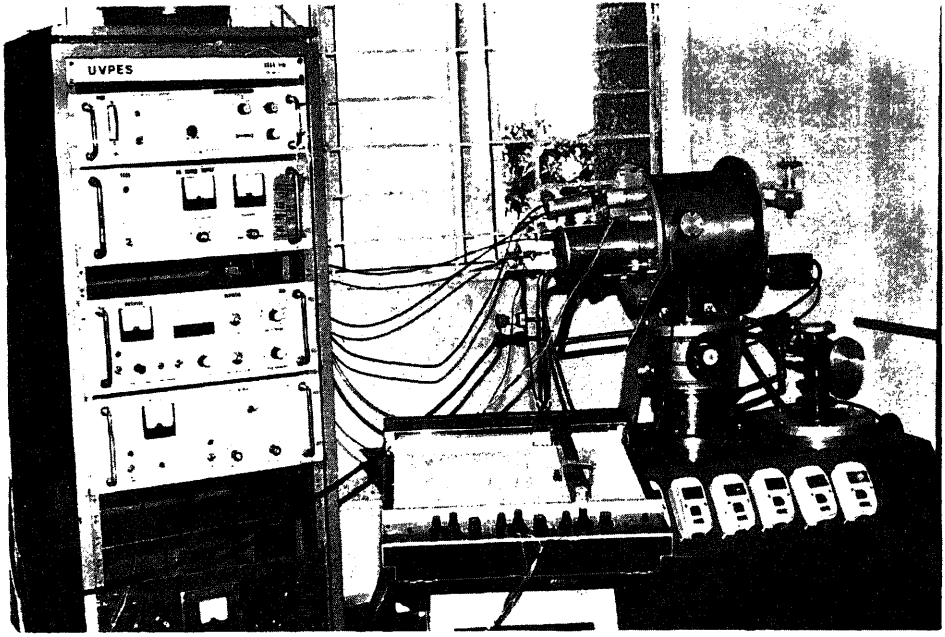

Figure 5. Photograph of the UV photoelectron spectrometer.

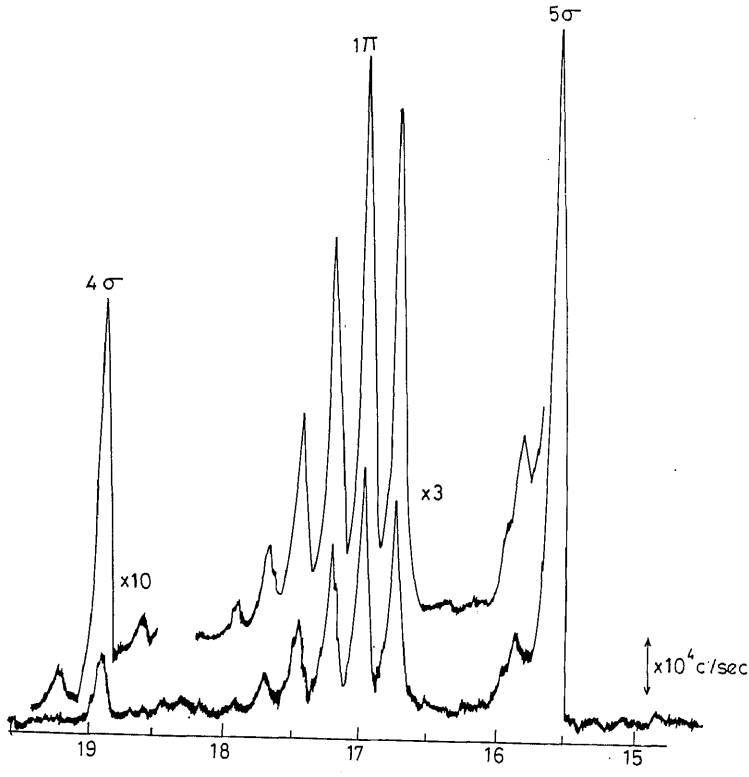

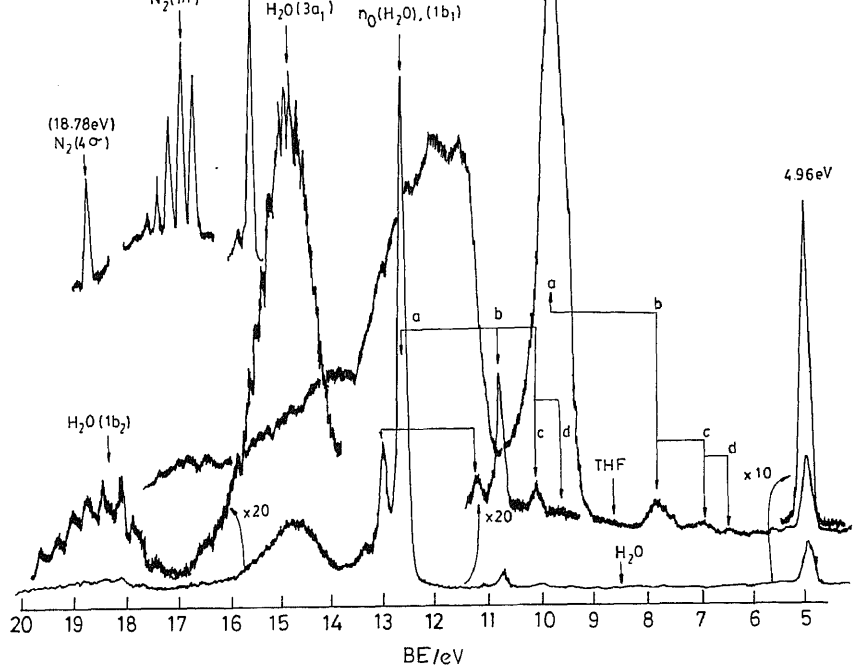

Figure 7. HeI UPS of H_2O and THF; notice autoionization peak of He at 4·96 eV; also satellites due to HeI β, HeI γ, HeI δ radiation marked b,c,d.

In figure 7, photoelectron spectra of H_2O and THF are given. Spectra of air (only the N_2 part) are also shown, which were taken for calibration. Autoionization peak of helium at 4·96 eV is also shown. The N_2 (5σ) peak at 15·6 eV and the autoionization peak at 4·96 provide spectra for complete internal calibration of H_2O and THF bands. Expanded bands of $1b_2$ and $3a_1$ of H_2O are also shown. Assignment of each of the photolines can be found in Turner *et al* (1970) and Kimura *et al* (1981).

In the helium discharge lamp, in addition to the resonance radiation due to the 2^1P-1^1S transition (HeI_α), 3^1P-1^1S, 4^1P-1^1S, and 5^1P-1^1S (HeI_β, HeI_γ, HeI_δ) are also emitted and the energies of these radiations are 23·08, 23·74 and 24·04, respectively (Eland 1984). $1b_1$ band of H_2O due to these radiations also appear as satellites marked by b, c and d in figure 7. Taking the intensity of HeI_α (21·22 eV) of 100%, HeI_β and HeI_γ are 3% and 0·5% respectively as can be seen from the figure 7. Generally, these satellites are seen for the more intense lines as can be seen for n_0 band in THF. The photoelectron spectra shown here are comparable to those obtained from commercial spectrometers (Kimura *et al* 1981).

The spectrometer has also been employed to study molecular interactions, and systems such as diethyl ether-iodine (Rao *et al* 1986) and BF_3. H_2O (Durrant *et al* 1986) have been investigated.

Acknowledgements

The authors thank Professor C N R Rao, FRS for his encouragement. Financial support from the Department of Science & Technology, Government of India is gratefully acknowledged.

References

Durrant M C, Hegde M S and Rao C N R 1986 *J. Chem. Phys.* (In print)

Eland J H D 1984 *Photoelectron spectroscopy* (London: Butterworths)

Heilbornner E and Maier J P 1977 in *Electron spectroscopy* (eds) C R Brundle and A D Baker (London: Academic Press)

Hegde M S and Basu P K 1978 *Curr. Sci.* **47** 160

Kimura K, Kastumata S, Achiba Y, Yamazaki T and Iwata S 1981 *Handbook of Hel photoelectron spectra of fundamental organic molecules* (Tokyo: Japan Sci. Societies Press)

McDaniel E W 1964 *Collision phenomena in ionized gases* (New York: John Wiley)

Seviere K D 1972 *Low energy electron spectroscopy* (New York: Wiley-Interscience)

Rao C N R, Basu P K and Hegde M S 1979 *Appl. Spectrosc. Rev.* **15** 1

Rao C N R, Hegde M S and Kamath P V 1986 *J. Mol. Struct. (Theor. Chem.)* **135** 409

Turner D W, Baker C, Baker A D and Bundle C R 1970 *Photoelectron spectroscopy* (New York: Wiley-Interscience)

Magnetic properties of $Ca_2Fe_{2-x}Mn_xO_5$[†]

A K GANGULI and J GOPALAKRISHNAN*

Solid State and Structural Chemistry Unit, Indian Institute of Science, Bangalore 560 012, India

MS received 26 November 1986

Abstract. Magnetic susceptibility of $Ca_2Fe_{2-x}Mn_xO_5$ members crystallizing in two different structures, one having octahedral (O), tetrahedral (T) and square-pyramidal (SP) coordination of transition metal atoms (OTSP structure) and the other having octahedral and tetrahedral coordination (OT structure), has been investigated. Susceptibility behaviour of the oxides with OTSP structure is different from that of the oxides with OT structure. $Ca_2Fe_{1\cdot33}Mn_{0\cdot67}O_5$ with OTSP structure shows an antiferromagnetic ordering while the corresponding oxide with OT structure shows weak ferromagnetism.

Keywords. $Ca_2Fe_{2-x}Mn_xO_5$; magnetic susceptibility.

1. Introduction

We have recently synthesized a new series of oxides of the general formula $Ca_2Fe_{2-x}Mn_xO_5$ employing the carbonate solid-solutions $Ca_2Fe_{2-x}Mn_x(CO_3)_4$ as precursors (Vidyasagar *et al* 1986). The oxides crystallize in an orthorhombic structure related to brownmillerite (B.M.) and $Ca_2Mn_2O_5$. Electron diffraction investigations of these oxides (Rao *et al* 1986) revealed a novel oxygen vacancy ordering derived from the perovskite structure indicating the presence of three different coordination polyhedra [octahedra (O), tetrahedra (T) and square-pyramids (SP)] around the transition metal atoms (OTSP structure). $Ca_2Fe_{2-x}Mn_xO_5$ with OTSP structure transform to the brownmillerite structure (OT structure) on heating at ~ 1050 K *in vacuo*. These oxides provide a rich variety of systems for investigating the magnetic properties of Fe^{3+} and Mn^{3+} in different oxygen coordinations. In this communication, we briefly report magnetic susceptibility studies of $Ca_2Fe_{2-x}Mn_xO_5$ in both the structures over the temperature range 40–800 K.

2. Experimental

$Ca_2Fe_{2-x}Mn_xO_5$ ($x = 0\cdot67$, $1\cdot00$ and $1\cdot33$) in OTSP and OT structures were prepared as described earlier (Vidyasagar *et al* 1986). Magnetic susceptibilities were measured by the Faraday method using a Cahn RG electrobalance. For measurements in the 300–800 K range, the sample held *in vacuo* at $\sim 10^{-3}$ torr was

[†]Contribution No. 398 from the Solid State and Structural Chemistry Unit.

heated using a microfurnace. For measurements in the 40–300 K range, a closed cycle helium cryostat (Air Products Displex) was employed. $HgCo(NCS)_4$ was used as the calibrant and the susceptibilities were corrected for diamagnetism.

3. Results and discussion

Magnetic susceptibility data of $Ca_2Fe_{2-x}Mn_xO_5$ are given in table 1. We see clearly an antiferromagnetic ordering around 570 K in $Ca_2Fe_{1.33}Mn_{0.67}O_5$ (1) and Ca_2FeMnO_5 (2), while in $Ca_2Fe_{0.67}Mn_{1.33}O_5$ (3) the antiferromagnetic ordering is significantly missing. Instead, the last oxide shows a weak ferromagnetism, the susceptibility increasing sharply around 680 K. Sample (1) shows an additional susceptibility maximum around 140 K. The paramagnetic Curie temperature θ_p increases with increasing Mn^{3+} content.

The susceptibility behaviour of $Ca_2Fe_{2-x}Mn_xO_5$ changes drastically on transforming to the brownmillerite (OT) structure. Significantly, the antiferromagnetic ordering noticed in samples (1) and (2) is missing in samples (4) and (5); instead, the latter show a weak ferromagnetism. Moreover, the trend in θ_p values is reversed in samples (4)–(6); θ_p becomes more negative with increasing Mn^{3+} content.

An understanding of the complex magnetic behaviour of $Ca_2Fe_{2-x}Mn_xO_5$ requires a knowledge of the various magnetic interactions that are possible in these oxides. The possible interactions are 180° $Fe^{3+}-O^{2-}-Fe^{3+}$, $Mn^{3+}-O^{2-}-Mn^{3+}$ and $Fe^{3+}-O^{2-}-Mn^{3+}$ superexchanges. Of these, the $Fe^{3+}-O^{2-}-Fe^{3+}$ interaction is strongly antiferromagnetic (Kanamori 1959), while the $Mn^{3+}-O^{2-}-Mn^{3+}$ interaction could be both ferromagnetic and antiferromagnetic; this interaction becomes anisotropic when the e_g orbitals of the Jahn-Teller Mn^{3+}: d^4 are ordered (Goodenough *et al* 1961). $Fe^{3+}-O^{2-}-Mn^{3+}$ interaction also could be both ferromagnetic and antiferromagnetic. Both $Ca_2Fe_2O_5$ and $Ca_2Mn_2O_5$ are known to order antiferromagnetically at 725 K and 350 K respectively (Grenier *et al* 1973; Poeppelmeier *et al* 1982). The antiferromagnetic ordering temperatures of samples (1) and (2) (table 1) (~570 K) are in between the ordering temperatures of the end members; the additional $Mn^{3+}-O^{2-}-Fe^{3+}$ interaction in the solid solutions apparently lowers the Néel

Table 1. Magnetic susceptibility data of $Ca_2Fe_{2-x}Mn_xO_5$ oxides.

Compound number	Composition	C_M (Experimental)	C_M (Calculated)	T_N (K)	θ_p (K)
1	$Ca_2Fe_{1.33}Mn_{0.67}O_5$	6·67	11·68	564	−384
2	Ca_2FeMnO_5	5·71	10·99	570	− 8
3	$Ca_2Fe_{0.67}Mn_{1.33}O_5$	4·00	10·31	—	248
4	$Ca_2Fe_{1.33}Mn_{0.67}O_5$ (B.M.)	6·15	11·68	—	−104
5	Ca_2FeMnO_5 (B.M.)	7·62	10·99	—	−180
6	$Ca_2Fe_{0.67}Mn_{1.33}O_5$	10·66	10·31	—	−488

temperature as compared to $Ca_2Fe_2O_5$. The magnetic behaviour of sample (3) is intriguing; there is no apparent antiferromagnetic ordering. On the contrary, the sample is weakly ferromagnetic. With Mn^{3+} ordered in O and SP layers and Fe^{3+} in T layers in the structure (figure 1), the magnetic behaviour seems to suggest that the $Mn^{3+}-O^{2-}-Mn^{3+}$ interaction becomes anisotropic and ferromagnetic in the layers. Anisotropic $Mn^{3+}-O^{2-}-Mn^{3+}$ interaction occurs in the O′– orthorhombic structure of $LaMnO_3$ and related perovskites (Goodenough *et al* 1961) and in MnF_3 (Wollan *et al* 1959).

The change in the magnetic properties of $Ca_2Fe_{2-x}Mn_xO_5$ on transformation to the OT structure may be understood in terms of the cation distribution in the brownmillerite structure (table 2). The T sites are most likely to be occupied exclusively by Fe^{3+} in samples (4) and (5). In sample (4), the O sites are occupied by both Mn^{3+} and Fe^{3+} providing additional $Mn^{3+}-O^{2-}-Fe^{3+}$ interaction pathways which probably render the sample weakly ferromagnetic. Samples (5) and (6) where the octahedral sites are occupied by Mn^{3+} do not show a definite ordering. The increase of negative θ_p values with manganese content in samples (4)–(6) indicates that the net antiferromagnetic interaction increases in the series.

The experimental molar Curie constants (C_M) of the oxides (table 1) are much smaller than the calculated values, indicating the presence of competing interactions of varying magnitude which often lead to frustration (Ferey *et al* 1979). A small C_M value has been reported in a related oxide, $Ca_3Fe_{1.65}Mn_{1.35}O_{8.02}$ (Nguyen *et al* 1984).

Further investigation of $Ca_2Fe_{2-x}Mn_xO_5$ using Mössbauer spectroscopy is in progress.

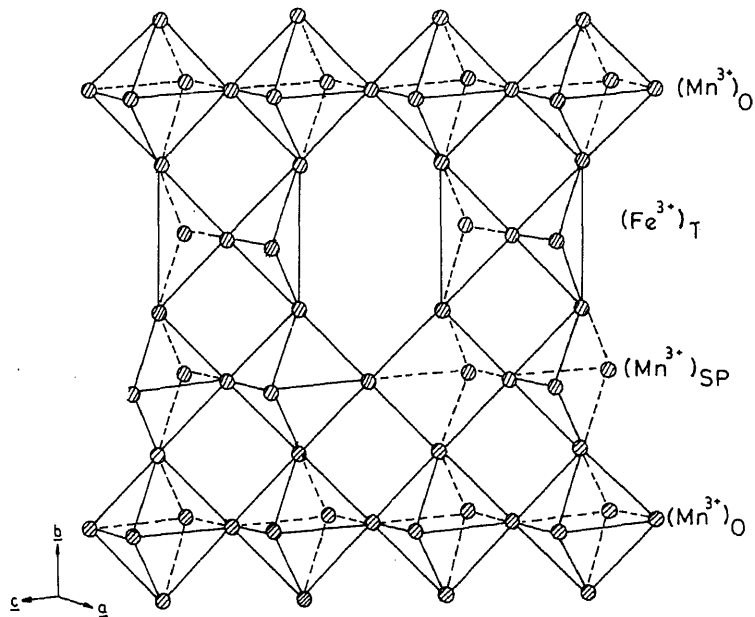

oxygen atom

Table 2. Probable cation distribution of $Ca_2Fe_{2-x}Mn_xO_5$ oxides.

Compound number[a]	Composition	Cation distribution[a]
1	$Ca_2Fe_{1.33}Mn_{0.67}O_5$ ($Ca_3Fe_2MnO_{7.5}$)	$(Fe^{3+})_O(Fe^{3+})_T(Mn^{3+})_{SP}$
2	Ca_2FeMnO_5 ($Ca_3Fe_{1.5}Mn_{1.5}O_{7.5}$)	$(Fe^{3+}_{0.5}Mn^{3+}_{0.5})_O(Fe^{3+})_T(Mn^{3+})_{SP}$
3	$Ca_2Fe_{0.67}Mn_{1.33}O_5$ ($Ca_3FeMn_2O_{7.5}$)	$(Mn^{3+})_O(Fe^{3+})_T(Mn^{3+})_{SP}$
4	$Ca_2Fe_{1.33}Mn_{0.67}O_5$ (B.M.)	$(Fe^{3+}_{0.33}Mn^{3+}_{0.67})_O(Fe^{3+})_T$
5	Ca_2FeMnO_5 (B.M.)	$(Mn^{3+})_O(Fe^{3+})_T$
6	$Ca_2Fe_{0.67}Mn_{1.33}O_5$	—

[a] Subscripts O, T and SP denote respectively octahedral, tetrahedral and square-pyramidal sites.

Acknowledgements

The authors thank Professor C N R Rao, FRS for valuable discussion and advice. Thanks are also due to the University Grants Commission, New Delhi, and the Department of Science and Technology, Government of India, for support of this research. One of us (AKG) thanks the CSIR, New Delhi, for the award of a Fellowship.

References

Ferey G, Varret F and Coey M 1979 *J. Phys.* **C12** 1531
Goodenough J B, Wold A, Arnott R J and Menyuk N 1961 *Phys. Rev.* **124** 373
Grenier J C, Pouchard M and Georges R 1973 *Mater. Res. Bull.* **8** 1413
Kanamori J 1959 *J. Phys. Chem. Solids* **10** 87
Nguyen N, Calage Y, Varret F, Ferey G, Caignaert V, Hervieu M and Raveau B 1984 *J. Solid State Chem.* **53** 398
Poeppelmeier K R, Leonowicz M E and Longo J M 1982 *J. Solid State Chem.* **44** 89
Rao C N R, Gopalakrishnan J, Vidyasagar K, Ganguli A K, Ramanan A and Ganapathi L 1986 *J. Mater. Res.* **1** 280
Vidyasagar K, Ganapathi L, Gopalakrishnan J and Rao C N R 1986 *J. Chem. Soc. Chem. Commun.* 449
Wollan E O, Child H R, Koehler W C and Wilkinson M K 1959 *Phys. Rev.* **112** 1132

High T_c superconductivity in oxides derived from $La_{1.8}Sr_{0.2}CuO_4$†

P GANGULY and C N R RAO*

Solid State and Structural Chemistry Unit, Indian Institute of Science, Bangalore 560 012, India

Abstract. Quasi two-dimensional copper oxides derived from $La_{1.8}Sr_{0.2}CuO_4$ by substitution of La, Sr or Cu show high T_c superconductivity.

Keywords. Superconductivity; two-dimensional copper oxides; $La_{1.8}Sr_{0.2}CuO_4$.

The discovery of high T_c superconductivity in La-Ba-Cu (~ 30 K) and La-Sr-Cu (~ 36 K) oxides of K_2NiF_4 structure (Cava *et al* 1987; Uchida *et al* 1987) has created widespread interest in this family of copper oxides. We have been interested in the crystal chemistry, magnetism and electrical properties of oxides of K_2NiF_4 structure for sometime (Ganguly and Rao 1984). In particular, we have reported that La_2CuO_4 exhibits a moderately low (1 ohm cm) temperature-independent resistivity (Ganguly and Rao 1973). Cu^{2+} ions in this oxide as well as other rare-earth copper oxides of the type Ln_2CuO_4 do not contribute to the magnetic susceptibility (Rao *et al* 1985). Partial substitution of La^{3+} by Sr^{2+} or Ba^{2+} in La_2CuO_4 gives rise to a mixed-valent system with a considerably lower resistivity having a value close to that found in various oxides at the borderline when the temperature coefficient of resistivity changes sign (Rao and Ganguly 1985). It appears that marginally metallic mixed-valent copper oxides of quasi two-dimensional character are good candidates for high temperature superconductivity (Rao and Ganguly 1987).

We have investigated several mixed-valent copper oxides of K_2NiF_4 structure for possible high-temperature superconductivity. We find that $La_{1.8}Sr_{0.2}CuO_4$ has a T_c of 36 K as reported by others; substitution of Sr by Ca in this oxide lowers the T_c. Thus, $La_{1.8}Sr_{0.1}Ca_{0.1}CuO_4$ exhibits the onset of superconductivity around 30 K (figures 1 and 2). Substitution of even a minute proportion of Cu by Ni appears to change T_c markedly. Thus, $La_{1.8}Sr_{0.2}Ni_{0.01}Cu_{0.99}O_4$ exhibits the onset of superconductivity around 24 K (figures 1 and 2). We are now studying the effect of substituting La by Pb and other ions, noting that both acidity and ionic size may be important in determining the superconducting transition temperature.

Substitution of La partially by Eu in $La_{1.8}Sr_{0.2}CuO_4$ has been examined. Thus $(La_{1.75}Eu_{0.25})_{1.8}Sr_{0.2}CuO_4$ exhibits a T_c of around 26 K (figure 1). It is interesting that the presence of Eu does not destroy superconductivity in this oxide system.

† Contribution No. 421 from the Solid State and Structural Chemistry Unit.

* To whom all correspondence should be addressed.

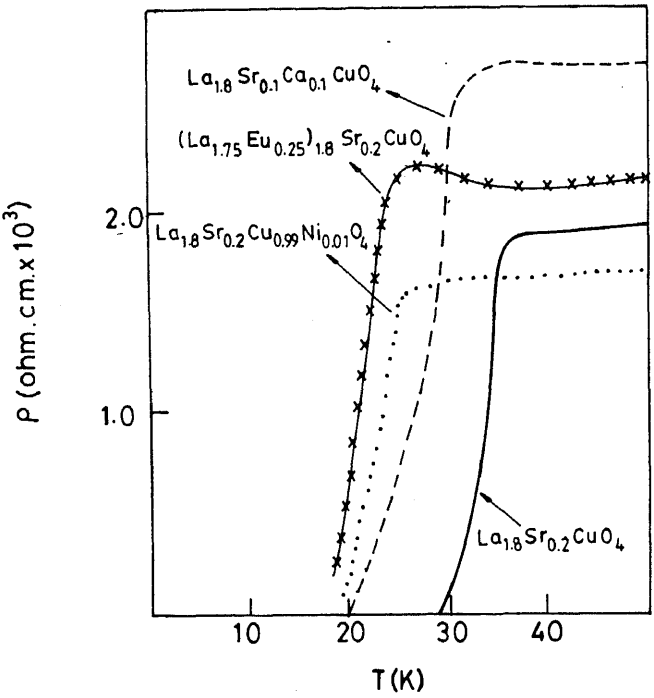

Figure 1. Resistivity data of copper oxides of K_2NiF_4 structure exhibiting superconducting transitions.

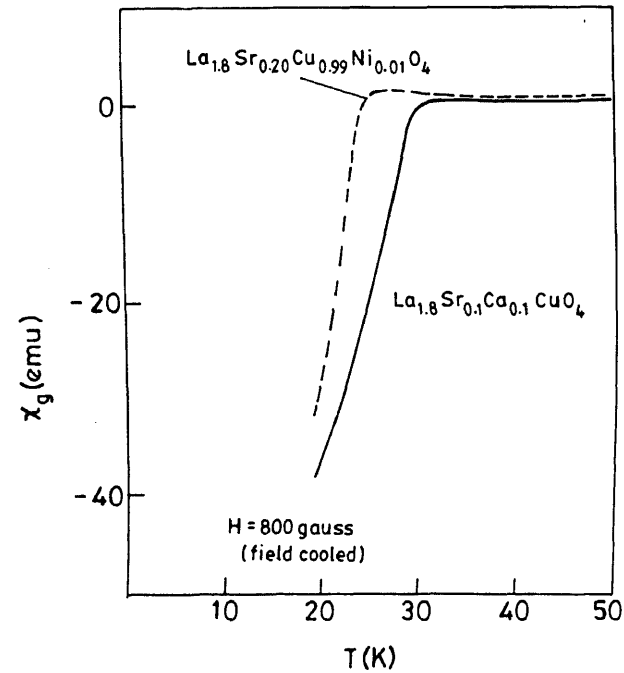

We are investigating systems of the type $(La_{1-x}Ln_x)_{2-y}B_yCuO_4$ with Ln = P or Nd and B = Sr or Ba. These systems are interesting in that only at a particula concentration of Pr or Nd, the oxide system is stable in the K_2NiF_4 structure (Singi *et al* 1982). We are now examining the relation between the lattice instability i these oxides and the superconducting transition temperature.

Acknowledgement

The authors thank the University Grants Commission and the Department o Science & Technology, Government of India, for support of this research.

References

Cava R J, van Dover R B, Batlogg B and Rietman E A 1987 *Phys. Rev. Lett.* (in press)

Ganguly P and Rao C N R 1973 *Mater. Res. Bull.* **8** 408

Ganguly P and Rao C N R 1984 *J. Solid State Chem.* **53** 193

Rao C N R and Ganguly P 1985 in *The metallic and the non-metallic states of matter* (eds) P P Edwards and C N R Rao (London: Taylor and Francis)

Rao C N R and Ganguly P 1987 *Curr. Sci.* **56** 47

Rao C N R, Rao K J and Gopalakrishnan J 1985 *Annual Reports C* (London: The Royal Society of Chemistry)

Singh K K, Ganguly P and Rao C N R 1982 *Mater. Res. Bull.* **17** 493

Uchida S, Takagi H, Kitazawa K and Tanaka S 1987 *Jpn. J. Appl. Phys.* **26** L1

SUBJECT INDEX

ietane diterpenoids
Abietane diterpene quinones and a new diterpene epoxide from *Salvia moorcraftiana* 167
celerated Tafel plot
Applications of exponential relaxation methods or corrosion studies and corrosion rate measurement 465
etylacetone
ESR bonding parameter studies of single and mixed ligand complexes of copper (II) 177
etylacetonates
Mixed ligand complexes of *bis*(acetylacetonato-)nickel(II) and cobalt(II) with N and N, N'-substituted thioureas 19
polarograph for trace analysis
Peak sampling – a new technique for eliminating charging current in AC polarography 437
abatic approximation
Vibrational-rotational (ν-J) levels of HD^+, evaluated in the adiabatic approximation for the electronic ground state ($1s\sigma_g$) 191
aline media
High performance electrode materials for the hydrogen evolution reaction from alkaline media 359
yl bromides
Kinetics of the reaction of alkyl bromides with nucleophiles containing nitrogen atoms 55
algamable metals
Use of programmed time-potential inputs in anodic stripping voltammetry with *in situ* sodium amalgamation 449
ine-alcohol interactions
Enthalpies of complex formation of dibutyl and tributyl amines with isomeric butanols 77
ine exchange
Exchange reactions of copper complexes with amines 535
ino acid
Structural studies of amino acid complexes-I EXAFS study of glutamic acid complex of copper 25
acardiaceae
Semecarpuflavanone-a new biflavanone from *Semecarpus anacardium* Linn 63
alytical properties
Synthesis, identification and analytical properties of the 2-pyrilideniminobenzohydroxamic acid 159
Anilines
Kinetics of the reaction of alkyl bromides with nucleophiles containing nitrogen atoms 55
Anion
Solvation model for inner-sphere nuclear reorganization in the photoionization of univalent anions in solution 221
Anodic stripping voltammetry
Use of programmed time-potential inputs in anodic stripping voltammetry with *in situ* sodium amalgamation 449
Appearance energy
Electron impact ionization of amines using crossed electron-molecular beams 565
Aqueous corrosion
Corrosion of austenitic stainless steel in aqueous environments 495
Aromatic and aliphatic amines
Reaction of the phosphate radical with amines-A flash photolysis study 573
Austenitic stainless steels
Corrosion of austenitic stainless steel in aqueous environments 495
2,2'-Azino*bis*-(3-ethylbenzothiazole-6-sulphonate)
Reactions of halogens with 2,2'-azino*bis*-(3-ethylbenzothiazole–6–sulphonate): Stopped-flow kinetics of formation of radical cations and dications 213
Benzophenone
Electrochemical reduction of some benzophenones in molten acetamide at 85°C 395
7,8-benzoflavanone
Photo-Fries reaction of 1-naphthyl cinnamate 41
Biflavanones
Semecarpuflavanone-a new biflavanone from *Semecarpus anacardium* Linn 63
Biflavanone SA4
Semecarpuflavanone-a new biflavanone from *Semecarpus anacardium* Linn 63
Bonding parameters
ESR bonding parameter studies of single and mixed ligand complexes of copper(II) 177
Born-Green equation
Calculation of the density profile of a system of hard spheres near a hard wall using the Henderson-Plischke and related approximations 297

electronic ground state ($1s\sigma g$) 191

$Ca_2Fe_{2-x}Mn_xO_5$
Magnetic properties of $Ca_2Fe_{2-x}Mn_xO_5^+$ 627
Calorimetry
Enthalpies of complex formation of dibutyl and tributyl amines with isomeric butanols 77
Carbides
Corrosion of austenitic stainless steel in aqueous environments 495
Catalysis by Ru(II)
$RuCl_2(PPh_3)_3$ catalyzed oxidation of secondary alcohols with N-methylmorpholine N-oxide 125
Charging current elimination
Peak sampling – a new technique for eliminating charging current in AC polarography 437
Chelex
Water-insoluble polyacrylamide XII : Polychelates based on poly (N-methacryloyl-*m*-aminobenzoic acid) 147
Chi-phase
Corrosion of austenitic stainless steel in aqueous environments 495
6-Chloro-2,4-dimethoxypyrimidine
Electronic and vibrational spectra of 2,4,6-trichloro- and 6-chloro-2,4-dimethoxypyrimidine 83
Cholesterol packing
Molecular and crystal structure of 1-hydroxy-2-methyl-11-methylene-tricyclo $(5.3.1.0)^{2,7}$-undecan-5-one, $C_{13}O_2H_{18}$ 547
2-Cinnamoyl-1-naphthol
Photo-Fries reaction of 1-naphthyl cinnamate 41
Clamped nuclei
Vibrational-rotational (ν-J) levels of HD^+, evaluated in the adiabatic approximation for the electronic ground state ($1s\sigma_g$) 191
CNDO perturbation calculations
SCF perturbation calculations on metalloporphyrins 601
^{13}C NMR
^{13}C NMR data of flavonol methyl ethers of *Solanum pubescens* 171
^{13}C NMR chemical shifts
^{13}C NMR substituent induced chemical shifts in the side-chain carbons of α,β-unsaturated sulphones 33
^{13}C NMR spectra
Reaction of 2-hydrazino -4-methyl-6-substituted quinolines with ethylacetoacetate: A structural reinvestigation 185
Cobalt
Inorganic complexation of nickel and cobalt in natural waters 1

solution resistance 431
Complexation
Inorganic complexation of nickel and cobalt in natural waters 1
Complexes of catechol and derivatives
Ternary complexes of substituted catechols and catecholamines 529
Conductance
Water-insoluble polyacrylamide XII : Polychelates based on poly (N-methacryloyl-*m*-amino benzoic acid) 147
Conductance-electrochemical activity relationship
In situ resistance measurement of a conducting polymer electrode 457
Conducting polymer film electrodes
In situ resistance measurement of a conducting polymer electrode 457
Controlled potential coulometry
Polymer films on electrodes. 21 Electrochemical behavior of tetramethyltetraselenafulvalene incorporated into a Nafion-coated electrode 349
Coordinated dioxygen systems
Cyclic voltammetric studies of dioxygen-bridged dinuclear cobalt (III) complexes 407
Coordination number
Some lanthanide metal complexes of n-isonicotinamidosalicylaldimine 13
Copper (II)
ESR bonding parameter studies of single and mixed ligand complexes of copper (II) 177
Corrosion rate
Applications of exponential relaxation methods for corrosion studies and corrosion rate measurement 465
Crevice corrosion
Corrosion of austenitic stainless steel in aqueous environments 495
Cu(II) complex
Ternary complexes of substituted catechols and catecholamines 529
Cyclic voltammetric studies
Cyclic voltammetric studies of dioxygen-bridged dinuclear cobalt (III) complexes 407
Polymer films on electrodes. 21. electrochemical behavior of tetramethyltetraselenafulvalene incorporated into a Nafion-coated electrode 349
Cyclic-voltammetry of living animals
Electrobioluminescence-a novel method for understanding bioluminescent mechanisms 479
Cyclobutane
Molecular and crystal structure of 1-hydroxy-2-methyl-11-methylene-tricyclo-$(5.3.1.0)^{2,7}$-undecan-5-one $C_{13}O_2H_{18}$ 547

Delta ferrite
Corrosion of austenitic stainless steel in aqueous environments 495
Density profile
Calculation of the density profile of a system of hard spheres near a hard wall using the Henderson-Plischke and related approximations 297
Deposition potential
Underpotential deposition (UPD) studies of copper on glassy carbon 581
Difficult crystal structures
Solution of difficult crystal structures: New, simple, economic and time saving approaches 209
Dielectric constant of solvents
Effect of dielectric constant of various mixed aqueous solvents on the proton-ligand and metal-ligand formation constants of N-methylisatin β amidinohydrazone 133
Diffuse reflectance spectra
Water-insoluble polyacrylamide XII : Polychelates based on poly (N-methacryloyl-*m*-amino benzoic acid) 147
Diffusion
Exchange studies of 5-sulphosalicyclic acid in Amberlite IRA 401 Cl anion exchange resin 607
Dioxygen-bridged dinuclear Co(III)complexes
Cyclic voltammetric studies of dioxygen-bridged dinuclear cobalt (III) complexes 407
Displaced harmonic oscillator
Spectral functions and Green's functions: A critique 307
Distorted octahedral coordination
Structural studies of amino acid complexes-I EXAFS study of glutamic acid complex of copper 25
Double layer
New theories for the electric double layer at a metal/ electrolyte solution interface 267
D−(+)−xylose adsorption
The adsorption of D−(+)−xylose at the mercury-water interface 333

Earthworm bioluminescence
Electrobioluminescence-a novel method for understanding bioluminescent mechanisms 479
Effect of substitution on ligand
Ternary complexes of substituted catechols and catecholamines 529
Electrobioluminescence
Electrobioluminescence-a novel method for understanding bioluminescent mechanisms 479
Electro-capillary curves
Electrocatalysts
Fuel cells: Problems and prospects 513
Electrocatalytic effects
High performance electrode materials for the hydrogen evolution reaction from alkaline media 359
Electron impact
Electron impact ionization of amines using crossed electron-molecular beams 565
Electron injection
Electrobioluminescence-a novel method for understanding bioluminescent mechanisms 479
Electron states of molecules
Design and fabrication of an ultraviolet photoelectron spectrometer for the study of free molecules 617
Electron transfer
Solvation model for inner-sphere nuclear reorganization in the photoionization of univalent anions in solution 221
Electroreduction
Electrochemical reduction of 2-nitrobenzidine in methanol-water mixtures 395
Electrostatic effect
Influence of electrostatic effect on the stability of mixed-ligand complexes: Uranyl-complex-one-phenol/phenolic acid ternary systems 543
Energy-conversion devices
Fuel cells: Problems and prospects 513
Enthalpy of complexes
Enthalpies of complex formation of dibutyl and tributyl amines with isomeric butanols 77
ESR date
Stereochemistry and structural phase transition of Cu(II) complexes containing orthophosphate ions and pyridine/picoline 587
ESR studies
ESR Bonding parameter studies of single and mixed ligand complexes of copper (II) 177
Estrogen receptor binding affinity
QSAR studies on estrogen receptor binding affinity of 2-phenylindoles using first-order valence molecular connectivity 91
Ethylacetoacetate
Reaction of 2-hydrazino-4-methyl-6-substituted quinolines with ethylacetoacetate: A structural reinvestigation 185
Ethyl bromoacetate
Reaction of ethyl bromoacetate with substituted naphthoate ions 47
EXAFS
Structural studies of amino acid complexes-I

Firefly bioluminescence
Electrobioluminescence-a novel method for understanding bioluminescent mechanisms 479
Flash photolysis
Reaction of the phosphate radical with amines-A flash photolysis study 573
Flavonol methyl ether
^{13}C NMR data of flavonol methyl ethers of *Solanum pubescens* 171
Formation constants
Effects of dielectric constants of various mixed aqueous solvents on the proton-ligand and metal-ligand formation constants of N-methylisatin-β amidinohydrazone 133
Synthesis, identification and analytical properties of the 2-pyrilideniminobenzohydroxamic acid 159
Influence of electrostatic effect on the stability of mixed ligand complexes: Uranyl-complex-one-phenol/ phenolic acid ternary systems 543
Fuel cells
Fuel cells: Problems and prospects 513
Fundamental harmonic polarography
Peak sampling - a new technique for eliminating charging current in AC polarography 437

Green's functions
Spectral functions and Green's functions: A critique 307

Half-wave potentials
Electrochemical reduction of some benzophenones in molten acetamide at 85°C 395
Hammet equation
Reaction of ethyl bromoacetate with substituted naphthoate ions 47
Hammett plot
Electrochemical reduction of some benzophenones in molten acetamide at 85°C 395
Hammett relationship
Kinetics of the reaction of alkyl bromides with nucleophiles containing nitrogen atoms 55
Hard sphere/hard wall system
Calculation of the density profile of a system of hard spheres near a hard wall using the Henderson-Plischke and related approximations 297
Hard spheres
New theories for the electric double layer at a metal electrolyte solution interface 267
Henderson-Plischke approximation
Calculation of the density profile of a system of hard spheres near a hard wall using the Henderson-Plischke and related approximations 297
High performance materials
Hydrazine caboxylate derivatives
Preparation, characterization and t
analysis of rare earth and uranyl hy
carboxylate derivatives
Hydrogen bonding
Kinetics of the reaction of alkyl bromid
nucleophiles containing nitrogen atoms
Infrared and Raman spectra of 2,4-dimet
line
Infrared and Raman spectra of vicinally
tituted 2-methyl, 3-chloraniline and 2-
6-chloraniline
Hydrogen evolution reaction
High performance electrode materials
hydrogen evolution reaction from a
media
2-Hydroxy-1-naphthaldehyde guanylhydra
2-Hydroxy-1-naphthaldehyde guanylhyc
as analytical reagent for spectrophot
estimation of vanadium

Individual bond potential energy functio
Proton and hydrogen transfer reacti
solution
Infinitely heavy nuclei
Vibrational-rotational (ν-J) levels of HI
aluated in the adiabatic approximation
electronic ground state ($1s\sigma_g$)
Infrared and Raman spectra
Infrared and Raman spectra of 2,4-dime
line
Infrared and Raman spectra of vicinally
tituted 2-methyl,3-chloraniline and 2-m
chloraniline
Infrared spectra
Preparation, characterization and
analysis of rare earth and uranyl hydra
boxylate derivatives
Synthesis and spectral studies of tin (I
plexes with Schiff bases derived from
drugs
Inner sphere
Solvation model for inner-sphere nucle
ganization in the photoionization of u
anions in solution
In situ
Use of programmed time-potential in
anodic stripping voltammetry with
sodium amalgamation
In situ resistance measurement of con
polymer electrode
Interface
New theories for the electric double lay
metal/electrolyte solution interface

ntramolecular atomic interactions
Proton and hydrogen transfer reactions in solution 233
nvariant electrode-electrolyte system
Fuel cells: Problems and prospects 513
on exchange
Exchange studies of 5-sulphosalicylic acid in Amberlite IRA 401 Cl anion exchange resin 607
onization energy
Electron impact ionization of amines using crossed electron-molecular beams 565
on translocation
The translocation of cobalt dicarbollide anions across a lipid – bilayer membrane: the effect of solution resistance 431
R correction
The translocation of cobalt dicarbollide anions across a lipid bilayer membrane: the effect of solution resistance 431
someric effect
Enthalpies of complex formation of dibutyl and tributyl amines with isomeric butanols 77
soselective relationship
Reaction of ethyl bromoacetate with substituted naphthoate ions 47

ellium
New theories for the electric double layer at a metal electrolyte solution interface 267

Kinetics
Kinetics of the reaction of alkylbromides with nucleophiles containing nitrogen atoms 55
Exchange studies of 5-sulphosalicylic acid in Amberlite IRA 401 Cl anion exchange resin 607

Labiatae
Abietane diterpene quinones and a new diterpene epoxide from *Salvia moorcraftiana* 167
Lanthanide metal complexes
Some lanthanide metal complexes of *n*-isonicotinamidosalicylaldimine 13
Large amplitude exponential relaxation technique
Applications of exponential relaxation methods for corrosion studies and corrosion rate measurement 465
$La_{1.8}Sr_{0.2}CuO_4$
High T_c superconductivity in oxides derived from $La_{1.8}Sr_{0.2}CuO_4$ 631
Lehmann's approach
Spectral functions and Green's functions: A critique 307
lipid bilayer membrane

Magnetic spectra
Mixed ligand complexes of *bis*(acetylacetonato) nickel(II) and cobalt(II) with N and N'-substituted thioureas 19
Magnetic susceptibility
Magnetic properties of $Ca_2Fe_{2-x}Mn_xO_5^+$ 627
Mass spectra
Reaction of 2-hydrazino-4-methyl-6-substituted quinolines with ethylacetoacetate: A structural reinvestigation 185
Maximum bubble pressure technique
The adsorption of D−(+)-xylose at the mercury-water interface 333
Mechanistic behavior
High performance electrode materials for the hydrogen evolution reaction from alkaline media 359
Mercury-electrolyte interface
The adsorption of D−(+)-xylose at the mercury-water interface 333
Metropolis/Monte Carlo methods
Proton and hydrogen transfer reactions in solution 233
Mixed ligand complex
Mixed ligand complexes of *bis*(acetylacetonato) nickel(II) and cobalt(II) with N and N,N'-substituted thioureas 19
Mixed ligand copper complexes
Exchange reactions of copper complexes with amines 535
Molecular connectivity
QSAR studies on estrogen receptor binding affinity of 2-phenylindoles using first-order valence molecular connectivity 91
Molten acetamide
electrochemical reduction of some benzophenones in molten acetamide at 85°C 395
Mössbauer spectra
Synthesis and spectral studies of tin(IV) complexes with Schiff bases derived from sulpha drugs 141
MULTAN package
Solution of difficult crystal structures: New, simple, economic and time saving approaches 209

Nafion
Polymer films on electrodes. 21. Electrochemical behavior of tetramethyltetraselenafulvalene incorporated into a Nafion-coated electrode 349
1-Naphthyl cinnamate
Photo-Fries reaction of 1-naphthyl cinnamate 41
1-naphthyl α-methyl cinnamate

Natural waters
Inorganic complexation of nickel and cobalt in natural waters 1
New approaches
Solution of difficult crystal structures: New, simple, economic and time saving approaches 209
Nickel
Inorganic complexation of nickel and cobalt in natural waters 1
Nickel(II) and cobalt(II) thioureas
Mixed ligand complexes of *bis*(acetylacetonato) nickel(II) and cobalt(II) with N and N,N'-substituted thioureas 19
N-isonicotinamidosalicylaldimine
Some lanthanide metal complexes of n-isonicotinamido- salicylaldimine 13
2-Nitrobenzidine
Electrochemical reduction of 2-nitrobenzidine in methanol-water mixtures 395
N-methylisatin β amidinohydrazone
Effect of dielectric constant of various mixed aqueous solvent on the proton-ligand and metal ligand formation constants on N-methylisatin β amidinohydrazone 133
N-methylmorpholine N-oxide
$RuCl_2(PPh_3)_3$ catalyzed oxidation of secondary alcohols with N-methylmorpholine N-oxide 125
Nonadiabatic approximation
Vibrational-rotational (ν-J) levels of HD^+, evaluated in the adiabatic approximation for the electronic ground state ($1s\sigma_g$) 191
Normal modes
Infrared and Raman spectra of 2,4-dimethylaniline 97
Infrared and Raman spectra of vicinally trisubstituted 2-methyl,3-chloraniline and 2-methyl 6-chloraniline 593
Nuclear reorganization
Solvation model for inner-sphere nuclear reorganization in the photoionization of univalent anions in solution 221

Ohmic drop and double layer capacitance
Applications of exponential relaxation methods for corrosion studies and corrosion rate measurement 465
Outer sphere
Solvation model for inner-sphere nuclear reorganization in the photoionization of univalent anions in solution 221
Oxidation
$RuCl_2(PPh_3)_3$ catalyzed oxidation of secondary alcohols with N-methylmorpholine N-oxide 125

Partition chromatography
Solid phase synthesis of the signal sequence of E.*coli* alkaline phosphatase 71
Peak sampling
Peak sampling-a new technique for eliminating charging current in AC polarography 437
Peroxo complexes
Cyclic voltammetric studies of dioxygen-bridged dinuclear cobalt (III) complexes 407
Peroxomonosulphate
Mechanism of the oxidation of alkyl aryl and diphenyl sulphoxides by peroxomonosulphate 555
Phase selective AC polarography
Peak sampling-a new technique for eliminating charging current in AC polarography 437
Phase selective detection by box-car integration
Peak sampling – a new technique for eliminating charging current in AC polarography 437
Phase transition
Infrared and Raman spectra of 2,4-dimethylaniline 97
Stereochemistry and structural phase transition of Cu(II) complexes containing orthophosphate ions and phyridine/picoline 587
Infrared and Raman spectra of vicinally trisubstituted 2-methyl, 3-chloranilines and 2-methyl, 6-chloranilines 593
2-Phenylindoles
QSAR studies on estrogen receptor binding affinity of 2-phenylindoles using first-order valence molecular connectivity 91
Phosphate radical
Reaction of the phosphate radical with amines-A flash photolysis study 573
Photoelectron emission
Solvation model for inner-sphere nuclear reorganization in the photoionization of univalent anions in solution 221
Photo-Fries reaction
Photo-Fries reaction of 1-naphthyl cinnamate 41
Physicochemical properties
Synthesis, identification and analytical properties of the 2-pyilideniminobenzohydroxamic acid 159
2-(*p*-methylcinnamoyl)-1-naphthol
Photo-Fries reaction of 1-naphthyl cinnamate 41
Pitting
Corrosion of austenitic stainless steel in aqueous environments 495
PMR and mass spectra
Semecarpuflavanone- a new biflavanone from *Semecarpus anacardium* Linn 63

Polychelate
Water-insoluble polyacrylamide XII: Polychelates based on poly (N-methacryloyl-*m*-amino benzoic acid) 147
Poly(N-methacryloyl-*m*-aminobenzoic acid)
Water-insoluble polyacrylamide XII : Polychelates based on poly (N-methacryloyl-*m*-amino benzoic acid) 147
Potentiometric determination
Effect of dielectric constant of various mixed aqueous solvents on the proton-ligand and metal-ligand formation constants of N-methylisatin-β amidinohydrazone 133
Programmed E-t inputs
Use of programmed time-potential inputs in anodic stripping voltammetry with *in situ* sodium amalgamation 449
Proton magnetic resonance spectra
Synthesis and spectral studies of tin (IV) complexes with Schiff bases derived from sulpha drugs 141
Proton transfer
Proton and hydrogen transfer reactions in solution 233
Pyrazolyl borate complex
A ruthenium(II) complex of *bis* (1-pyrazolyl) borate 9
2-Pyrilideniminobenzohydroxamic acid
Synthesis, identification and analytical properties of the 2-pyrilideniminobenzohydroxamic acid 159

Quantitative structure-activity relationship
QSAR studies on estrogen receptor binding affinity of 2-phenylindoles using first-order valence molecular connectivity 91
Quasi two-dimensional copper oxides
High T_c superconductivity in oxides derived from $La_{1.8}Sr_{0.2}CuO_4$ 631
Quinolylhydrazine
Reaction of 2-hydrazino-4-methyl-6-substituted quinolines with ethylacetoacetate: A structural reinvestigation 185

Radical
Solvation model for inner-sphere nuclear reorganization in the photoionization of univalent anions in solution 221
Radical cation
Reactions of halogens with 2,2′ aninobis-(3-ethylbenzothiazole-6-sulphonate): Stopped-flow kinetics of formation of radical cations and dications 213
Radical dication
Reactions of halogens with 2,2′-azinobis-(3-
Rate constants
Reaction of the phosphate radical with amines-A flash photolysis study 573
Reactivity selectivity principle
Reaction of ethyl bromoacetate with substituted naphthoate ions 47
Reduction mechanism
Electrochemical reduction of 2-nitrobenzidine in methanol-water mixtures 395
Reverse substituent effect
^{13}C NMR substituent induced chemical shifts in the side-chain carbons of α,β-unsaturated sulphones 33
Ruthenium (II)
A ruthenium (II) complex of *bis* (1-pyrazolyl) borate 9

Saddle point methods
Proton and hydrogen transfer reactions in solution 233
Salicylic acids
ESR bonding parameter studies of single and ligand complexes of copper (II) 177
Salvia moorcraftiana wall
Abietane diterpene quinones and a new diterpene epoxide from *Salvia moorcraftiana* 167
SCF perturbation
SCF perturbation calculations on metalloporphyrins 601
Schiff bases
Synthesis and spectral studies of tin(IV) complexes with Schiff bases derived from sulpha drugs 141
Secondary alcohols
$RuCl_2(PPh_3)_3$ catalysed oxidation of secondary alcohols with N-methylmorpholine N-oxide 125
Secondary phases
Corrosion of austenitic stainless steel in aqueous environments 495
Semecarpuflavanone
Semecarpuflavanone- a new biflavanone from *Semecarpus anacardium* Linn 63
Semecarpus anacardium
Semecarpuflavanone- a new biflavanone from *Semecarpus anacardium* Linn 63
Sensitization
Corrosion of austenitic stainless steel in aqueous environments 495
Sigma
Corrosion of austenitic stainless steel in aqueous environments 495
Signal sequence
Solid phase synthesis of the signal sequence of *E. coli* alkaline phosphatase 71
Single transient and multi transient

Small amplitude exponential relaxation technique
Applications of exponential relaxation methods for corrosion studies and corrosion rate measurement 465
Solanaceae
^{13}C NMR Data of flavonol methyl ethers of *Solanum pubescens* 171
Solanum pubescens
^{13}C NMR Data of flavonol methyl ethers of *Solanum pubescens* 171
Solid phase synthesis
Solid phase synthesis of the signal sequence of *E. coli* alkaline phosphatase 71
Solvation
Solvation model for inner-sphere nuclear reorganization in the photoionization of univalent anions in solution 221
Spectral changes
Infrared and Raman spectra of 2,4-dimethylaniline 97
Infrared and Raman spectra of vicinally trisubstituted 2-methyl, 3-chloraniline and 2-methyl, 6-chloraniline 593
Spectral functions
Spectral functions and Green's functions: A critique 307
Species pattern
Inorganic complexation of nickel and cobalt in natural waters 1
Spectrophotometric determination
2-Hydroxy-1-naphthaldehyde guanylhydrazone as analytical reagent for spectrophotometric estimation of vanadium 153
Stereochemistry
Stereochemistry and structural phase transition of Cu(II) complexes containing orthophosphate ions and pyridine/picoline 587
Steric effect
Enthalpies of complex formation of dibutyl and tributyl amines with isomeric butanols 77
Stopped-flow kinetics
Reactions of halogens with 2,2′-azino*bis*-(3-ethylbenzothiazole-6-sulphonate): Stopped-flow kinetics of formation of radical cations and dications 213
Stress corrosion cracking
Corrosion of austenitic stainless steel in aqueous environments 495
Structure-reactivity relationship
Mechanism of the oxidation of alkyl aryl and diphenyl sulphoxides by peroxomonosulphate 555
Substituent effect
^{13}C NMR substituent induced chemical shifts in
Substituted naphthoate ions
Reaction of ethyl bromoacetate with substituted naphthoate ions 47
Sulpha drugs
Synthesis and spectral studies of tin (IV) complexes with Schiff bases derived from sulpha drugs 141
Superconductivity
High T_c superconductivity in oxides derived from $La_{1.8}Sr_{0.2}CuO_4$ 631
Superoperator representation
Spectral functions and Green's functions: A critique 307
Superoxo complexes
Cyclic voltammetric studies of dioxygen-bridged dinuclear cobalt (III) complexes 407
Sweep rate
Underpotential deposition (UPD) studies of copper on glassy carbon 581

Ternary complex
Ternary complexes of substituted catechols and catecholamines 529
Tetramethyltetraselenafulvalene
Polymer films on electrodes. 21 Electrochemical behavior of tetramethyltetraselenafulvalene incorporated into a Nafion-coated electrode 349
Tetrathiafulvalene
Polymer films on electrodes. 21 Electrochemical behavior of tetramethyltetraselenafulvalene incorporated into a Nafion-coated electrode 349
Thermal analysis
Preparation, characterization and thermal analysis of rare earth and uranyl hydrazinecarboxylate derivatives 117
Thermal stability
Water-insoluble polyacrylamide XII : Polychelates based on poly (N-methacryloyl-*m*-amino benzoic acid) 147
Thermodynamic parameters
Kinetics of the reaction of alkyl bromides with nucleophiles containing nitrogen atoms 55
Threshold energy
Solvation model for inner-sphere nuclear reorganization in the photoionization of univalent anions in solution 221
Tin(IV) chloride
Synthesis and spectral studies of tin(IV) complexes with Schiff bases derived from sulpha drugs 141
Transesterification

2,4,6-trichloropyrimidine
Electronic and vibrational spectra of 2,4,6-trichloro- and 6-chloro-2,4-dimethoxypyrimidine 83
Tricyclic
Molecular and crystal structure of 1-hydroxy-2-methyl-11-methylene-tricyclo $(5.3.1.0)^{2,7}$-undecan-5-one, $C_{13}O_2H_{18}$ 547
Tridentate ligand
Some lanthanide metal complexes of n-isonicotinamidosalicylaldimine 13

Underpotential deposition
Underpotential deposition (UPD) studies of copper on glassy carbon 581
Uninegative chelating agents
A ruthenium (II) complex of *bis* (1-pyrazolyl) borate 9
α,β unsaturated sulphones
^{13}C NMR substituent induced chemical shifts in the side- chain carbons of α,β-unsaturated sulphones 33
UV and IR spectra
Electronic and vibrational spectra of 2,4,6-trichloro- and 6-chloro-2,4-dimethoxypyrimidine 83
UV Photoelectron spectroscopy
Design and fabrication of an ultraviolet photoelectron spectrometer for the study of free molecules 617

Vanadium
2-Hydroxy-1-naphthaldehyde guanylhydrazone as analytical reagent for spectrophotometric estimation of vanadium 153
Voltammetric techniques
Electrochemical reduction of 2-nitrobenzidine in methanol-water mixtures 395

Weldments
Corrosion of austenitic stainless steel in aqueous environments 495

X-ray absorption spectra
Structural studies of amino acid complexes-I EXAFS study of glutamic acid complex of copper 25
X-ray structure
Molecular and crystal structure of 1-hydroxy-2-methyl-11-methylene-tricyclo $(5.3.1.0)^{2,7}$-undecan-5-one, $C_{13}O_2H_{18}$ 547

Zinc and cadmium sulphate
Use of programmed time-potential inputs in anodic stripping voltammetry with *in situ* sodium amalgamation 449

AUTHOR INDEX

Aggarwal R C
see Rao T R 13
Bard Allen J
see Moulton Roger D 349
Anil Kumar
Inorganic complexation of nickel and cobalt in natural waters 1
Anjaneyulu Y
ESR Bonding parameter studies of single and mixed ligand complexes of copper (II) 177
Anushree Samanta
Influence of electrostatic effect on the stability of mixed-ligand complexes: Uranyl-complex-one-phenol phenolic acid ternary systems 543
Aravamuthan S
Electrochemical reduction of 2-nitrobenzidine in methanol-water mixtures 395
Atwell Robert J (Jr)
The translocation of cobalt dicarbollide anions across a lipid bilayer membrane: the effect of solution resistance 431
Asthana B P
see Shukla A R 97,593

Bajaj H C
see Khan M M Taqui 9
Beena Bakshi
Abietane diterpene, quinones and a new diterpene epoxide from *Salvia Moorcraftiana* 167
Bhardwaj R C
see Khan M M Taqui 9
Bhaskare C K
Structural studies of amino acid complexes-I EXAFS study of glutamic acid complex of copper 25

electronic ground state ($1s\sigma_g$) 191
Bhattacharya P K
Ternary complexes of substituted catechols and catecholamines 529
Contractor A Q
see Gholamian M 457
Conway B E
see Tilak B V 359
Delahay Paul
Solvation model for inner-sphere nuclear reorganization in the photoionization of univalent anions in solution 221
Desai Trushar
see Patel Kishore 147
Dharmalingam P
see Maruthamuthu P 213
Dongre N G
see Shukle A R 97
see Shukla A R 97,593
Dziedzic Andrew
see Delahay Paul 221
Emanuel N A
see Bhattacharya P K 529
Espinosa A
see Salinas F 153
Fuhrhop J H
see Bhattacharjee K K 601
Ganesan P K
see Srinivasan C 33
Ganguli A K
Magnetic properties of $Ca_2Fe_{2-x}Mn_xO_5^{\ddagger}$ 627
Ganguly P
High T_c superconductivity in oxides derived from $La_{1.8}Sr_{0.2}CuO_4$ 631
Garg B S
see Sarkar K 133
Gholamian M
In situ resistance measurement of a conducting polymer electrode 457
Gnanamoorthy J B
Corrosion of austenitic stainless steel in aqueous environments 495
Gnanasekaran C
see Rajasekaran K 47
Gopalakrishnan J
see Ganguli A K 627
Hegde M S
see Jayaram V 617
Henderson Douglas
Calculation of the density profile of a system of a hard spheres near a hard wall using the Henderson-Plischke and related approximations 297
Jacob Shamir
see Shukla A R 593
Jayachandran T
Photo-Fries reaction of 1-naphthyl cinnamate 41
Jayaram V
Design and fabrication of an ultraviolet photoelectron spectrometer for the study of free molecules 617
Jaya S
Underpotential deposition (UPD) studies of copper on glassy carbon 581
Kalidas C
see Aravamuthan S 395
Kannan A M
see Shukla A K 513
Khalaf Nooman A
Exchange studies of 5-sulphosalicylic acid in Amberlite IRA 401 Cl anion exchanged resin 607
Khan I A
see Rao T R 13
Khan M M Taqui
A ruthenium (II) complex of *bis* (1-pyrazolyl) borate 9
Kokatnur S B
see Tembe G L 19
Krishna Kumari G N
^{13}C NMR data of flavonol methyl ethers of *Solanum pubescens* 171
Krishna Kumar S V
Electron impact ionization of amines using crossed electron-molecular beams 565
Krishnaswamy S
Molecular and crystal structure of 1-hydroxy-2-methyl-11-methylene-tricyclo $(5.3.1.0)^{2,7}$-undecan-5-one $C_{13}O_2H_{18}$ 547
Kulkarni N D
see Bhattacharya P K 529
Kulkarni S Y
see Bhaskare C K 25
Kuriacose J C
see Vijayasri K 125
see Subramanian P 573
Lakshminarayanan V
Applications of exponential relaxation methods for corrosion studies and corrosion rate measurement 465
Leiva Ezequiel
New theories for the electric double layer at a metal/electrolyte solution interface 267
Levie Robert De
see Atwell Robert J (Jr.) 431

Limaye S N
see Anushree Samanta 543

Mahesh G V
Preparation, characterization and thermal analysis of rare earth and uranyl hydrazinecarboxylate derivatives 117
Manimaran T
see Jayachandran T 41
Maruthamuthu P
Reactions of halogens with 2,2′-azinobis-(3-ethylbenzothiazole-6-sulphonate) : Stopped-flow kinetics of formation of radical cations and dications 213
Mathur D
see Krishna Kumar S V 565
Meras I Duran
see Salinas F 159
Mishra A K
Spectral functions and Green's functions: A critique 307
Moulton Roger D
Polymer films on electrodes. 21. Electrochemical behavior of tetramethyltetraselenafulvalene incorporated into a Nafion-coated electrode 349
Mulchandani N B
see Beena Bakshi 167
Murty A S R
see Tembe G L 19
Murthy S S N
Semecarpuflavanone- a new biflavanone from *Semecarpus anacardium* Linn 63

Nagaraj R
see Reddy G Laxma 71
Narayan R
see Saraswathi R 403
Natarajan G S
see Khalaf Nooman A 607
Natarajan P
see Ilangovan S 437
Nevado J J Berzas
see Salinas F 153

Parsons Roger
The adsorption of D−(+)-xylose at the mercury-water interface 333
Patel K B
see Patel M N 535
Patel Kishore
Water-insoluble polyacrylamide XII : Polychelates based on poly (N-methacryloyl-*m*-amino benzoic acid) 147
Patel M N
Pathak C M
see Shukla A R 97,593
Pathak Gopal
see Pradhan Shirish D 77
Pattabhi Vasantha
see Krishnaswamy S 547
Peat Robert
see Parsons Roger 333
Pisipati V G K M
see Anjaneyulu Y 177
Plischke Michael
see Henderson Douglas 297
Poojary Aithu
Peak sampling - a new technique for eliminating charging current in AC polarography 437
Pradhan Shirish D
Enthalpies of complex formation of dibutyl and tributyl amines with isomeric butanols 77
Prasad M
see Srivastava S L 83
Punnaiah G
see Rao T Janardhan 55

Radhe K Vaid
Reaction of 2-hydrazino-4-methyl-6-substituted quinolines with ethylacetoacetate: A structural reinvestigation 185
Rajagopalan S R
see Poojary Aithu 437
see Lakshminarayanan V 465
Rajaram J
see Vijayasri K 125
see Subramanian P 573
Rajasekaran K
Reaction of ethyl bromoacetate with substituted naphthoate ions 47
Ramakrishnan V
see Subramanian P 573
Ramakrishnan V T
see Jayachandran T 41
Ramamurthy A C
see Tilak B V 359
Ramesh K V
see Shukla A K 513
Rangarajan S K
see Mishra A K 307

Rao C N R
see Ganguly P 631
Rao G Prabhakara
Use of programmed time-potential inputs in anodic stripping voltammetry with *in situ* sodium amalgamation 449
see Jaya S 581

Rao N V S
see Anjaneyulu Y 177
Rao R Prabhakara
see Anjaneyulu Y 177
Rao T Janardhan
Kinetics of the reaction of alkyl bromides with nucleophiles containing nitrogen atoms 55
Rao T Prasada
see Jaya S 581
Rao T R
Some lanthanide metal complexes of n-isonicotinamidosalicylaldimine 13
Ravindranathan P
see Mahesh G V 117
Reddy G Laxma
Solid phase synthesis of the signal sequence of *E. coli* alkaline phosphatase 71
Reddy K Veera
see Khan M M Taqui 9
Row T N Guru
see Tavale S S 209

Salinas F
2-Hydroxy-1-naphthaldehyde guanylhydrazone as analytical reagent for spectrophotometric estimation of vanadium 153
Synthesis, identification and analytical properties of the 2-pyrilidenimino benzohydroxamic acid 159
Sane K V
see Bhattacharjee R S 191
Santhanam K S V
Electrobioluminescence-a novel method for understanding bioluminescent mechanisms 479
Santry D P
see Bhattacharjee K K 601
Saraswathi R
Electrochemical reduction of some benzophenones in molten acetamide at 85°C 403
Sarkar K
Effect of dielectric constant of various mixed aqueous solvent on the proton-ligand and metal-ligand formation constants of N-methylisatin-β-amidinohydrazone 133
Sashidar M S
see Aravamuthan S 395
Sastry M D
see Sastry M S 587
Sastry M S
Stereochemistry and structural phase transition of Cu(II) complexes containing orthophosphate
Schmickler Wolfgang
see Leiva Ezequiel 267
Schmidt P P
Proton and hydrogen transfer reactions in solution 233
Shamir Jacob
see Shukla A R 97
Shankar J
see Beena Bakshi 167
Shukla A K
Fuel cells: Problems and prospects 513
Shukla A R
Infrared and Raman spectra of 2,4-dimethylaniline 97
Infrared and Raman spectra of vicinally trisubstituted 2-methyl 3-chloraniline and 2-methyl, 6-chloraniline 593
Singh Shiv P
see Radhe Vaid K 185
Shunmugasundaram A
see Srinivasan C 33
Singh P
QSAR studies on estrogen receptor binding affinity of 2-phenylindoles using first-order valence molecular connectivity 91
Singh Ranjeet
see Srivastava S L 83
Sridharan Ramamurthi
see Robert J Atwell (Jr.) 431
Srinivasan C
^{13}C NMR substituent induced chemical shifts in the side-chain carbons of α,β-unsaturated sulphones 33
see Suthakaran R 555
Srivastava P K
see Bhattacharjee R S 191
Srivastava S L
Electronic and vibrational spectra of 2,4,6-trichloro and 6-chloro-2,4-dimethoxypyrimidine 83
Subramaniam P
see Suthakaran R 555
Subramanian J
see Bhattacharjee K K 601
Subramanian P
Reaction of the phosphate radical with amines-A flash photolysis study 573
Sundaram E V
see Rao T Janardhan 55
Suresh Kumar T N
see Gholamian M 457
Suthakaran R

Tandon J P
see Varshney Anil 141
Tavale S S
Solution of difficult crystal structures:New, simple, economic and time saving approaches 209
Tembe G L
Mixed ligand complexes of *bis* (acetylacetonato) nickel(II) and cobalt(II) with N and N, N′–substituted thioureas 19
Tilak B V
High performance electrode materials for the hydrogen evolution reaction from alkaline media 359

Varadharaj A
see Rao G Prabhakara 449
Varshney Anil
Synthesis and spectral studies of tin (IV) complexes with Schiff bases derived from sulpha drugs 141
Venkatachalam C S
see Aravamuthan S 395
Venkatasubramanian L
see Maruthamuthu P 213
Vijayasri K
$RuCl_2(PPh_3)_3$ catalyzed oxidation of secondary alcohols with N-methylmorpholine N-oxide 125

Williams Jack M
see Moulton Roger D 349